

Astrophysics and Space Science Library 455

Margarita Ryutova

Physics of Magnetic Flux Tubes

Second Edition

AS
SL

 Springer

Physics of Magnetic Flux Tubes

Astrophysics and Space Science Library

Series Editor:

STEVEN N. SHORE, *Dipartimento di Fisica “Enrico Fermi”, Università di Pisa, Pisa, Italy*

Advisory Board:

F. BERTOLA, *University of Padua, Italy*

C. J. CESARSKY, *Commission for Atomic Energy, Saclay, France*

P. EHRENFREUND, *Leiden University, The Netherlands*

O. ENGVOLD, *University of Oslo, Norway*

E. P. J. VAN DEN HEUVEL, *University of Amsterdam, The Netherlands*

V. M. KASPI, *McGill University, Montreal, Canada*

J. M. E. KUIJPERS, *University of Nijmegen, The Netherlands*

H. VAN DER LAAN, *University of Utrecht, The Netherlands*

P. G. MURDIN, *Institute of Astronomy, Cambridge, UK*

B. V. SOMOV, *Astronomical Institute, Moscow State University, Russia*

R. A. SUNYAEV, *Max Planck Institute for Astrophysics, Garching, Germany*

More information about this series at <http://www.springer.com/series/5664>

Margarita Ryutova

Physics of Magnetic Flux Tubes

Second Edition

 Springer

Margarita Ryutova
Lawrence Livermore National Laboratory
Livermore
California, USA

ISSN 0067-0057 ISSN 2214-7985 (electronic)
Astrophysics and Space Science Library
ISBN 978-3-319-96360-0 ISBN 978-3-319-96361-7 (eBook)
<https://doi.org/10.1007/978-3-319-96361-7>

Library of Congress Control Number: 2018953181

© Springer Nature Switzerland AG 2018

This work is subject to copyright. All rights are reserved by the Publisher, whether the whole or part of the material is concerned, specifically the rights of translation, reprinting, reuse of illustrations, recitation, broadcasting, reproduction on microfilms or in any other physical way, and transmission or information storage and retrieval, electronic adaptation, computer software, or by similar or dissimilar methodology now known or hereafter developed.

The use of general descriptive names, registered names, trademarks, service marks, etc. in this publication does not imply, even in the absence of a specific statement, that such names are exempt from the relevant protective laws and regulations and therefore free for general use.

The publisher, the authors and the editors are safe to assume that the advice and information in this book are believed to be true and accurate at the date of publication. Neither the publisher nor the authors or the editors give a warranty, express or implied, with respect to the material contained herein or for any errors or omissions that may have been made. The publisher remains neutral with regard to jurisdictional claims in published maps and institutional affiliations.

Cover figure caption: The image is a 3-wavelength composite of solenoidal slinky at the coronal temperatures 2 MK (Fe XV 211 Å), 1.5 MK (Fe XII 193 Å) and 0.6 MK (Fe IX/X 171Å) taken by the SDO/AIA on August 31, 2012.

This Springer imprint is published by the registered company Springer Nature Switzerland AG
The registered company address is: Gewerbestrasse 11, 6330 Cham, Switzerland

To Dmitri, Alex and Dmitri, Jr.

Preface to the Second Edition

In the second edition, material of the book has been slightly rearranged and corrected. A significant amount of new material has been added with a triple goal: (1) to present more recent observational results, (2) to extend discussion to scaled laboratory experiments for possible application to solar physics, and (3) to give some practical tools in form of the solved problems that can be used for quantitative analysis of related phenomena.

Hence, four new chapters have been added. Chapter 21 contains description of recent laboratory experiments scaled to astrophysics. High repetitive rate and ability to accurately control the system parameters in the experiment allow to identify missing elements in physics of studied phenomena. The exemplary experiments have been chosen to reflect the effects observed or need to be observed in the solar atmosphere and beyond. The topics span from magnetically driven plasma jets, bow shocks, and generation of seed magnetic field to plasma instabilities and self-organization. The next chapter titled initially “What to Observe” turned out to be long and has been divided into two parts: “What to Observe in the Low Atmosphere” (Chap. 22), and “What to Observe in the Upper Atmosphere” (Chap. 23). This division is, of course, formal, because the dynamics of solar atmosphere is intrinsically governed by coupling of the photosphere/convective zone and overlying chromosphere/corona. Chapter 24 contains solution of 48 problems covering subjects of Chaps. 2–20. Most problems are made out of original papers containing fundamental results. In this way, the original paper, often based on complex theory, turns into a convenient tool for practical use and quantitative analysis.

I would like to extend my thanks to all friends and colleagues whom I mentioned in the first edition. No one complained. Many of them read the first edition of the book and gave me useful advices that helped to improve the text. During the final stage of preparation of the second edition, I was visiting Dmitri Budker of Helmholtz Institute, Johannes Gutenberg University in Mainz. Communication with Dmitri Budker and his young and mighty group was true inspiration, and I thank them all.

My very special thanks go to Dr. Claus Ascheron who encouraged me to write this book, initiated the second edition, helped me greatly, and patiently supported me to fulfill this task. I am very grateful to Elke Sauer, Adelheid Duhm, and other members of Springer for their help and support.

Once again, I would like to thank my husband Dmitri Ryutov who heroically accepted my new commitment to work on the second edition of the book. I am happy that my sons, Alex and Dmitri Jr, and my grandchildren, Dasha, Liza, and Pavel, were all involved in various phases of my work asking me good questions and proofreading some parts of the book.

Livermore, CA, USA
November 2017

Margarita Ryutova

Preface to the First Edition

The advanced space and ground-based observations show amazing details in the sun's behavior providing us with invaluable information on the sun as a star and as our own energy source. The behavior of the sun is determined by a tremendous variety of physical phenomena acting on wide range of spatial and temporal scales. Every aspect requires its own specific subject studies, and a lot of work is still needed to understand the inner workings of this fascinating things.

This book addresses one group of the phenomena: those involving finely structured magnetic fields. It has been more than five decades since the small scale intense magnetic flux tubes were found to cover the huge "magnetic free" surface of the sun outside sunspots and active regions. For the time being, the fact that all the magnetic field of the sun from its visible surface, throughout corona, and further to the interplanetary space has a fine filamentary structure, is well established. This ubiquity of the magnetic flux tubes and their obvious role in a variety of processes affecting the dynamics of the solar atmosphere and of the outflowing plasma calls for detailed study of their properties. And yet, no book on physics of magnetic flux tubes and their role in the dynamics of various magnetized objects has been available.

This book is intended to fill this gap at least partly, offering the first comprehensive account of the physics of magnetic flux tubes. The book provides side by side presentation of observations and analytical theory complemented by quantitative analysis. Many problems that are usually treated separately are presented in the book as a coupled phenomena and are treated on the unified basis. In some cases the author takes a risk to point at the effects that have not yet been looked for, or may be used for the predictability of events, and makes suggestions on what the observer should expect and what to search for in huge banks of observational data.

A major feature of the book is the application and observational test of the analytical theories that have not been previously considered in the context of the solar physics. Examples are: negative energy waves that may lead to formation of solitons propagating along flux tubes; explosive instability in the multi-wave interactions; energetically open circuit leading to understanding of the observed variety of coronal structure formation, and others. These concepts are discussed

vis-à-vis pertinent observational data. Extremely important is assessment of collective phenomena in the ensembles of magnetic flux tubes randomly distributed in space and over their physical parameters making the rarefied ensembles in the quiet sun, more crowded families in plages, and dense conglomerates in sunspots and active regions.

The book contains also examples where, conversely, the new theory developments were prompted and enabled by the observations. One can mention the observations of continuous fragmentation of flux tubes accompanied by generation of mass flows, which turned out to be consistent with magnetoacoustic streaming—an effect analogous to Faraday's acoustic streaming. Likewise, the flux tube reconnections and post-reconnection processes that occur in high plasma beta environment have clearly demonstrated the need for significant extensions of the existing theory that focused on low beta coronal reconnections.

The reader will also find descriptions of such intriguing and not fully understood phenomena as the bullwhip effect—an explosively growing amplitude of flux tube oscillation; a greenhouse-like effect, where the temperature under the prominences grows much higher than the expected coronal temperatures; and the effects of a spatio-temporal echoes in the series of recurrent flares and microflares.

The work was done in Lawrence Livermore National Laboratory. The Lab's hospitality is greatly acknowledged. I am particularly grateful to Robert Becker, Kem Cook, Jim Sharp, Charles Alcock, John Bradely, David Dearborn, Gayle Christiansen and JD Nichols.

I would like to thank my former colleagues from Landau's theoretical department, Kapitza's Institute for Physical Problems in Moscow, where I received my graduate degrees and worked for years on quantum vortices in superfluid Helium and Type II superconductors. My special thanks go to my teachers Isaak Khalatnikov, Lev Pitaevskii and Alexei Abrikosov, my PhD adviser.

My interest in Solar physics dates back to 1970s, when I once came across an early paper by Howard and Stenflo about small scale magnetic flux tubes on the sun. I was captivated by this beautiful subject. I am grateful to Jan Stenflo and Robert Howard not only for their excellent paper, which triggered my lifetime interest, but for all the meetings and discussions that I have had with them later.

I would like to thank Henk Spruit, Gene Parker, Bernie Roberts and Gene Avrett, who happened to be my first foreign correspondents in the field of solar physics. After about a decade and a half working on magnetic flux tubes (still back in the Soviet Union), I realized that my results are not known in the West. I then chose these outstanding physicists and sent them some of my offprints. All responded. Henk Spruit immediately made me an invited speaker at the IAU Symposium. Gene Parker was also quick, but I found out about it only 7 months later when I was summoned by the authorities and presented a huge tattered box full of papers for identification and explanation what it all meant. It meant that Gene Parker sent me all his papers without any note. Berny Roberts together with Eric Priest invited me to the University of St Andrews for several weeks to work together. I visited Gene Avrett in Harvard Smithsonian Center for Astrophysics several times and had

wonderful communications with him and other researchers in the CFA, especially with Shadia Habbal and Wolfgang Kalkofen whom I also thank a lot.

I am pleased to thank all my collaborators, particularly Toshi Tajima, Barry LaBonte, Jun-ichi Sakai, Shadia Habbal, Richard Woo, Tom Berger, Mandy Hagenaar and Zoe Frank. I am especially grateful to Dick Shine. Many beautiful results obtained from observations and described in this book would not have been here without his insight and help.

I would like to thank Alan Title, Philip Scherrer and Ted Tarbell for not only being my collaborators, but also as trusting people who gave me a job at Stanford Lockheed Institute for Space Research. No CV, no references, and no questions were asked.

Finally, I am extremely grateful to my husband Dmitri (Mitya) Ryutov for his patience and encouragement expressed sometimes in my native Georgian.

Livermore, CA, USA
September 2014

Margarita Ryutova

Contents

1	The Sun's Magnetic Fields	1
1.1	The Sun as a Star.....	1
1.1.1	Legacy of Ancients.....	1
1.1.2	Hidden Interior.....	3
1.1.3	Magnetic Dipole.....	4
1.2	Magnetic Surface.....	6
1.2.1	Quiet Sun.....	8
1.2.2	Sunspots and Active Regions.....	9
1.2.3	Plages.....	10
1.2.4	High Latitudes and Polar Regions.....	10
1.3	Mass Flows.....	12
1.4	Magnetic Skeleton.....	18
	References.....	20
2	A Quick Look on Small-Scale Flux Tubes	23
2.1	Early Years.....	23
2.1.1	First Direct Observational Signs of Magnetic Flux Tubes.....	24
2.1.2	The Sunspot Dilemma.....	25
2.2	Elements of Theory for De Facto Flux Tubes.....	27
2.3	Numerical Visualization and Observations.....	30
2.4	Filamentary Structures in Laboratory and Universe.....	34
2.5	Problems.....	40
	References.....	40
3	Intrinsic Properties of Flux Tubes: Wave Phenomena	43
3.1	Equations of Motion or How Are Tube Waves Excited.....	43
3.1.1	Equation of Motion for a Single Flux Tube.....	45
3.1.2	Macroscopic Motions of an Ensemble of Flux Tubes.....	46
3.2	Absorption of Acoustic Waves: Landau Resonance.....	50
3.3	Effects of Noncollinearity of Flux Tubes.....	53
3.4	Exact Theory of Linear Oscillations of Magnetic Flux Tube.....	54

3.5	Radiation of Secondary Waves by Oscillating Flux Tubes	56
3.6	Scattering of Acoustic Waves and Maximum Energy Input	58
3.7	Axisymmetric Oscillations of Flux Tube	60
3.7.1	Types of $\mathbf{m} = \mathbf{0}$ Mode	60
3.7.2	Equation of Motion for Sausage Oscillations	61
3.7.3	Dispersion Relation	63
3.7.4	Sausage and Fast Oscillations in Homogeneous Flux Tube	66
3.7.5	Effects of Radial Inhomogeneities on Sausage Oscillations	67
3.8	Problems	69
	References	73
4	Effects of Flux Tube Inhomogeneities and Weak Nonlinearity	75
4.1	Radially Inhomogeneous Flux Tube: Internal Resonances	75
4.1.1	Anomalous Resonance in Kink Oscillations	75
4.1.2	Alfvén Resonance	78
4.2	Boundary Value Problem	81
4.2.1	Phase-Mixing in Flux Tubes	82
4.2.2	Phase-Mixed Torsional Waves	83
4.2.3	Phase-Mixed Kink Oscillations	86
4.3	Longitudinal Resonances	87
4.3.1	Loss of Radial Equilibrium	88
4.3.2	Bullwhip Effect	90
4.4	Standing Resonances and the Temperature Jump	94
4.4.1	Growth of the Oscillation Amplitude: First Resonance	95
4.4.2	Spectral Density and Strong Enhancement of the Oscillation Amplitude	97
4.5	Weakly Nonlinear Waves in Flux Tubes	98
4.5.1	Nonlinear Kink Oscillations: KdV-Burgers Equation ...	98
4.5.2	Possibility of Solitary Sausage Wave	103
4.6	Problems	104
	References	105
5	Flux Tube Dynamics in the Presence of Mass Flows	107
5.1	Kelvin-Helmholtz Instability and Negative-Energy Waves	107
5.2	Shear Flow Instabilities in Magnetic Flux Tubes	112
5.2.1	Specifics of Kelvin-Helmholtz Instability Along Flux Tubes	112
5.2.2	Flux Tubes and Negative-Energy Waves (NEWs)	114
5.3	Basic Equations of Flux Tube Oscillations with Shear Flows ...	115
5.4	Dissipative Instabilities of Negative-Energy Kink Oscillations	117

5.5	Radiative Instability of Flux Tube Oscillations in Presence of Flows	119
5.5.1	Sausage Oscillations	120
5.5.2	Kink Oscillations	121
5.6	Parity of Negative and Positive Energy Waves	123
5.7	Explosive Instability of Negative-Energy Waves	125
5.8	Sub-critical Mass Flows: Absence of Instabilities	126
5.8.1	Can the Alfvén Waves Heat the Corona?	126
5.8.2	Effect of Mass Flows on the Efficiency of Heating by Alfvén Waves	127
5.9	Phase-Mixed Alfvén Waves at Sub-Alfvénic Mass Flows	130
5.9.1	Damping Rate and Height of Energy Release	130
5.9.2	Observable Morphological Effects	132
5.10	The Asymptotic Behavior of the Total Energy Flux	134
5.11	The Wave Extinction in the Presence of Downflows	137
5.12	Problems	140
	References	145
6	Collective Phenomena in Rarefied Ensembles of Flux Tubes	147
6.1	Response of Flux Tubes to Propagation of Sound Waves	147
6.1.1	Energy Exchange Between the Acoustic Waves and Ensembles of Flux Tubes	148
6.1.2	Near-Resonance Condition	150
6.2	Nonlinear Estimates of the Maximum Energy Input	152
6.3	Axisymmetric Oscillation in Flux Tube Ensembles	155
6.3.1	Equations of Motion	155
6.3.2	Dispersion Relation: Resonance and Frequency Shift... ..	157
6.4	The Interaction of Unsteady Wave Packets with an Ensemble of Flux Tubes	162
6.5	Spreading of the Energy Absorption Region: “Clouds of Energy”	165
6.5.1	Large Wave Packets	166
6.5.2	Short Wave Packets: Energy Absorption and Release	169
6.6	The Energy Transfer from Unsteady Wave Packets to the Medium	173
6.7	Problems	176
	References	177
7	Effects of Magnetic Flux Tubes in Helioseismology	179
7.1	The Time-Distance Tomography	179
7.1.1	Key Points of Time-Distance Analysis with Magnetic Fields	180
7.1.2	The Travel Times	182
7.2	The Effects of Horizontal Flows	183
7.3	Effects of Horizontal Magnetic Field	185

- 7.4 Effects of Background Inhomogeneities 186
 - 7.4.1 Weak Inhomogeneities 186
 - 7.4.2 Variations of Flow Velocities 187
- 7.5 Practical Use of the Forward-Backward Information 188
 - 7.5.1 Symmetry Properties 188
 - 7.5.2 Reconstruction of Subsurface Flow and Magnetic Fields from Observations 189
- 7.6 Magnetic Corrections in a Vertically Stratified Atmosphere 193
- 7.7 Estimate of the Energy Flux from Time-Distance Analysis 195
 - 7.7.1 Heat and Magnetic Energy Fluxes 196
 - 7.7.2 Contribution of Eddy Fluxes 198
 - 7.7.3 Reconstruction of Energy Fluxes from Observational Data 199
- 7.8 Raman Spectroscopy of Solar Oscillations 200
 - 7.8.1 Stokes and Anti-Stokes Satellites 201
 - 7.8.2 Using Raman Spectroscopy in Observations 203
- 7.9 Problem 205
- References 206
- 8 Wave Phenomena in Dense Conglomerate of Flux Tubes 207**
 - 8.1 Propagation of MHD Waves in an Ensemble of Closely Packed Flux Tubes 207
 - 8.1.1 Basic Equations and Dispersion Relation 210
 - 8.1.2 Special Cases 214
 - 8.2 Dissipative Processes 216
 - 8.2.1 Weakly Inhomogeneous Medium 217
 - 8.2.2 Medium with Moderate and Strong Inhomogeneities ... 218
 - 8.2.3 Dissipation by Thermal Conduction 220
 - 8.2.4 Dissipation by Viscosity 222
 - 8.2.5 Total Dissipation Rate 223
 - 8.3 Anomalous Damping at Small Wavevectors 226
 - 8.4 Absorption of p-Modes by Sunspots and Active Regions—Observations 228
 - 8.5 The Interpolation Formula and Comparison with Observations 231
 - 8.6 Problem 237
 - References 237
- 9 Nonlinear Wave Phenomena in Dense Conglomerate of Flux Tubes 239**
 - 9.1 Nonlinear Equations in Strongly Inhomogeneous Medium 239
 - 9.2 Formation of Shocks Across Small-Scale Inhomogeneities 244
 - 9.2.1 Validation of the Overturning Condition 245

9.3	Effect of Inhomogeneities on the Dispersion Properties of the System	247
9.3.1	Basic Equations	247
9.3.2	Dispersion Relation	249
9.3.3	KdV–Bürgers’ Equation with Strong Inhomogeneities	251
9.4	Numerical Analysis	252
9.4.1	The Model	253
9.4.2	Formation of Shock Waves	254
9.4.3	Energy Dissipation	255
9.5	Problems	259
	References	259
10	Magnetosonic Streaming	261
10.1	Secondary Flows—Boundary Layer Effects	261
10.1.1	Acoustic Streaming—History and Nature of Faraday’s Effect	261
10.1.2	Secondary Flows in Magnetohydrodynamics	263
10.2	Magnetosonic Streaming Due to the Action of Ponderomotive Force	265
10.3	Process of Filamentation and Diffusive Vanishing of Magnetic Flux Tubes	269
10.3.1	Diffusive Broadening of Flux Tube	271
10.3.2	Quantitative Estimates—Lifetimes and Spatial Scales of Flux Tubes	273
10.4	Generation of Mass Flows Due to the Absorption Mechanisms	275
10.5	Numerical Analysis	279
10.5.1	Basic Equations and Numerical Method	279
10.5.2	Numerical Results	281
10.6	Intrinsic Nature of Flux Tube Fragmentation	284
10.7	Problems	285
	References	286
11	Moving Magnetic Features (MMFs)	287
11.1	Types of MMFs and Their Observed Properties	287
11.2	Impossibility of the Origin of MMF’s in Conservative Systems	289
11.2.1	The Mechanism	291
11.3	Nonlinear Kink and Its Evolution in the Presence of Shear Flows	292
11.4	Soliton and Shocklike Formations Along the Flux Tube: Numerical Studies	295
11.5	Observations and Comparison with Theory	299
11.6	Quantitative Analysis	305
11.7	Unification of Known Types of Moving Magnetic Features	308

- 11.8 Impact of MMFs on the Overlying Atmosphere 312
- 11.9 Anticorrelation Between Population of MMF's
and Coronal Loop Formation..... 316
- 11.10 Problems 320
- References..... 320
- 12 Reconnection of Flux Tubes: Specifics of High Plasma β 323**
 - 12.1 Basics of Magnetic Reconnection 324
 - 12.2 Photospheric Reconnections: No Immediate Gain in Energy..... 328
 - 12.2.1 Specifics of Photospheric Reconnections 329
 - 12.2.2 Flux Tubes Carrying Different Amount
of Magnetic Flux 333
 - 12.2.3 Number of Events: Importance of Noncollinearity
of Flux Tubes 335
 - 12.3 Dynamics of Post-reconnection Products..... 336
 - 12.3.1 Self-similarity of Solution 337
 - 12.3.2 Energy Analysis 340
 - 12.3.3 Transsonic Motion 340
 - 12.4 Dynamics of \cup -Shaped Flux Tubes 342
 - 12.5 Dynamics of \cap -Shaped Flux Tube 344
 - 12.6 Problems 349
 - References..... 349
- 13 Post-reconnection Processes: Shocks, Jets, and Microflares 351**
 - 13.1 Key Regularities Observed in the Photosphere/Transition
Region 351
 - 13.2 Post-reconnection Shocks and Hydromagnetic Cumulation
of Energy 354
 - 13.2.1 Head-On Convergence of Shock Fronts..... 355
 - 13.2.2 Energy Distribution Between Heat, Jet, and Their
Combinations 357
 - 13.3 Observation of Photospheric Reconnections and Their
Impact on Overlying Atmosphere 361
 - 13.3.1 Microflares, Jets, and Their Combinations..... 362
 - 13.3.2 Effects of Converging Supergranular Flows 365
 - 13.4 Key Elements of Energy Production and Observation
of Shocks 368
 - 13.5 Explosive Events 371
 - 13.6 Response of the Upper Atmosphere to Reconnection
of Unipolar Flux Tubes 375
 - 13.7 Problems 377
 - References..... 377

14	Photospheric Network as Energy Source for Quiet Sun Corona	379
14.1	Post-reconnection Processes in Arbitrarily Magnetized Environment.....	379
14.1.1	Magnetic Loop Arcades in the Chromosphere.....	380
14.1.2	Post-reconnection Shocks in Upper Atmosphere: Types and Characters	383
14.2	Heights of Shock Formation.....	387
14.3	Energy Release in the Chromosphere-Transition Region	392
14.3.1	Quantitative Analysis	392
14.3.2	Total Energy Flux in Quiet Sun Atmosphere	396
14.4	Magnetic Energy Avalanche and the Fast Solar Wind	397
14.5	Problems	399
	References.....	399
15	Response of the Corona to Magnetic Activity in Underlying Plage Regions	401
15.1	Magnetic Imprint of Plage Regions in the Corona	401
15.2	Coronal Dynamics Above Unipolar and Mixed Polarity Plages.....	403
15.3	Properties of Braidlike Coronal Structures	407
15.4	Comparison of Coronal Emission Above Mixed Polarity and Unipolar Plages.....	410
15.5	Energy Extraction Mechanisms from the Ensembles of Photospheric Flux Tubes	414
15.5.1	Mixed Polarity Plage.....	415
15.5.2	Unipolar Plage.....	417
15.5.3	N-Solitons	419
15.6	Problems	423
	References.....	424
16	Electrodynamic Coupling of Active Region Corona with the Photosphere	425
16.1	The Problem of Multi-Face Corona	425
16.2	Emerging Magnetic Flux and Structure Formation in Overlying Atmosphere.....	427
16.3	Current Drive Mechanisms Associated with the Emerging Magnetic Flux	433
16.3.1	Proper Motion	434
16.3.2	Acoustic Waves.....	435
16.3.3	Alfvén Waves.....	436
16.4	Energy Flow Throughout Solar Atmosphere	438
16.4.1	An Equivalent Circuit: Earlier Attempts	439
16.4.2	LRC Circuit with Mutual Inductance (Transition Region)	441
16.5	Energetically Open Circuit	443

16.6	Evolution of Current Systems	449
16.6.1	Linear Regime	449
16.6.2	Nonlinear Regime	450
16.7	Quantitative Analysis	453
16.7.1	Examples	454
16.8	Limiting Currents and Filamentary Structures	458
16.9	Problems	461
	References	463
17	Fine Structure of Penumbrae: Formation and Dynamics	465
17.1	Peculiarities of Sunspot Penumbrae: Observations	465
17.2	Dynamics of Penumbral Filaments and Ongoing Reconnections	469
17.3	Formation of Filamentary Penumbrae	473
17.3.1	Phenomenology of Basic Mechanism	474
17.3.2	Filamentary Structure of Sunspot	476
17.3.3	Properties of Individual Filaments	476
17.4	Screw Pinch Instability and Dark Cores	478
17.4.1	More on Substructures of Filaments	481
17.4.2	Effects of Axial Flows	483
17.5	Problems	485
	References	485
18	Bow Shocks and Plasma Jetting over Penumbrae	487
18.1	Response of the Overlying Atmosphere to Penumbral Dynamics	487
18.1.1	Penumbral Transients: Double Structures and Jets	488
18.1.2	Viewing Under Different Angles	491
18.1.3	Brief Summary of Properties	496
18.2	Phenomenology and Quantitative Analysis	498
18.2.1	Dynamics of U-Shaped Filaments	499
18.2.2	Nature of Double Structures	501
18.3	Bow Shocks	503
18.4	Energy Release and Lifetime of Bright Transients	507
18.5	Problems	510
	References	511
19	Self-organization in the Corona and Flare Precursors	513
19.1	Well-Organized Multithreaded Coronal Arcades: Slinkies	513
19.2	Essential Difference Between “Regular” and Slinky-Producing Flares	516
19.3	Precursors and Predictability	522
19.4	Exemplary Case of X-Class Flare and Formation of Slinkies	525
19.5	Phenomenology of Energy Buildup and Quantitative Analysis	531

19.6	Recurrent Flares and Echoes	536
19.6.1	Landau Damping, Memory, and Spatiotemporal Echoes	537
19.6.2	Echo Effects in Slinkies	540
19.6.3	Spatial and Temporal Recurrences in Flares	542
19.7	Problems	545
	References	545
20	Quiescent Prominences	547
20.1	Background: Problem of Stability	547
20.2	Large-Scale Observed Regularities	551
20.3	Formation of Prominence Cavity and Helical Structures	555
20.3.1	The Case of the August 16 2007 Prominence.....	557
20.3.2	Phenomenology of Cavity Formation	561
20.4	Regular Series of Plumes: Multimode Regime of Rayleigh-Taylor Instability	564
20.4.1	Practical Use.....	566
20.5	Fast-Growing Plumes: Nonlinear Regime	568
20.5.1	Mushroom Formation	569
20.5.2	Bubble Competition	571
20.6	Greenhouse-Like Effect	572
20.7	Problems	576
	References.....	576
21	Laboratory Experiments Scaled to Solar and Space Plasmas	579
21.1	Criteria for Scaled Laboratory Experiments of Astrophysical MHD Phenomena	579
21.1.1	Similarity Criteria in the Ideal MHD	580
21.1.2	Invariance of Shock Boundary Conditions.....	581
21.1.3	Applicability Conditions for the MHD Similarity	582
21.2	Jets, Bow Shocks, and Instabilities.....	583
21.2.1	Magnetically Driven Plasma Jets	584
21.2.2	Bow Shocks	586
21.3	Shock–Shock Interaction, Magnetic Field Generation and Self-organization	588
21.3.1	Weibel Instability and Filamentation	589
21.3.2	Magnetic Field Generation by Biermann Battery Effect.....	589
21.3.3	Self-organization in Laser-Produced Counter-Streaming Plasmas	592
21.4	Rayleigh-Taylor Instability and Self-generated Magnetic Fields	595
21.4.1	Nonlinear Rayleigh-Taylor Instability	595
21.4.2	Self-generation of Magnetic Field by RT Instability	597
21.5	Arched Magnetic Flux Tubes and Plasma Flows.....	599

- 21.6 On the Magnetic Reconnection 602
- 21.7 Laboratory Simulation of Solar Coronal Plasmoids..... 604
- References..... 608
- 22 What to Observe in Low Atmosphere** 611
 - 22.1 Wave Phenomena 611
 - 22.2 Magnetosonic Streaming and Fragmentation of Magnetic Flux Tubes..... 616
 - 22.3 Penumbra and Moving Magnetic Features 620
 - 22.4 Post-reconnection Processes..... 624
 - 22.5 Misuse of Reconnection Physics 630
 - 22.6 Explosive Instability and Post-reconnection Jets 632
 - References..... 637
- 23 What to Observe in the Upper Atmosphere** 639
 - 23.1 Braided Magnetic Structures and Screw Pinch Instability 639
 - 23.2 Electrodynamic Coupling of Corona and Underlying Photosphere 644
 - 23.3 Evolution of Rudimentary Penumbra and Response of the Overlying Atmosphere 649
 - 23.4 Plasma Jetting and Bow Shocks..... 654
 - 23.5 Self-organization and Recurrent Flares 658
 - 23.6 Exotics in Prominences 664
 - References..... 669
- 24 Solutions** 671
 - 24.1 Problems of Chap. 2 671
 - 24.2 Problems of Chap. 3 674
 - 24.3 Problems of Chap. 4 679
 - 24.4 Problems of Chap. 5 681
 - 24.5 Problems of Chap. 6 685
 - 24.6 Problems of Chap. 7 688
 - 24.7 Problems of Chap. 8 689
 - 24.8 Problems of Chap. 9 690
 - 24.9 Problems of Chap. 10 694
 - 24.10 Problems of Chap. 11 699
 - 24.11 Problems of Chap. 12 702
 - 24.12 Problems of Chap. 13 705
 - 24.13 Problems of Chap. 14 710
 - 24.14 Problems of Chap. 15 713
 - 24.15 Problems of Chap. 16 718
 - 24.16 Problems of Chap. 17 721
 - 24.17 Problems of Chap. 18 725

24.18 Problems of Chap. 19	729
24.19 Problems of Chap. 20	731
References	734
Index	737

Acronyms

AIA	Atmospheric Imaging Assembly (on board of SDO)
BBSO	Big Bear Solar Observatory
CDS	Coronal Diagnostic Spectrometer (on board of SOHO)
CRISP	CRISP imaging spectropolarimeter on SST
DOT	Dutch Open Telescope
EIS	Extreme-Ultraviolet Imaging Spectrometer (on board of Hinode)
EIT	Extreme-Ultraviolet Imaging Telescope (on board of SOHO)
EUV	Extreme ultraviolet
GOES	Geostationary Operational Environmental Satellite
HAO	High Altitude Observatory
HEP	High energy proton (flux)
Hi-C	High Resolution Coronal Imager
HMI	Heliioseismic and Magnetic Imager (on board of SDO)
IBIS	Imaging by Interferometric Survey
IRIS	Interface Region Imaging Spectrograph
KdV	Korteweg-de Vries equation
KH	Kelvin-Helmholtz (instability)
LASCO	Large Angle and Spectrometric Coronagraph Experiment (on board of SOHO)
MDI	The Michelson Doppler Imager (on board of SOHO)
MMFs	Moving magnetic features
NEWs	Negative energy waves
NST	New Solar Telescope
RT	Rayleigh-Taylor (instability)
SDO	Solar Dynamics Observatory
SJI	Slit-jaw image
SOHO	The Solar and Heliospheric Observatory
SOT	Solar Optical Telescope (on board of Hinode)
SP	Spectropolarimeter (on board of Hinode)
SST	Swedish 1-m Solar Telescope (SST) on La Palma

SUMER	Solar Ultraviolet Measurements of Emitted Radiation (on board of SOHO)
SVST	Swedish Vacuum Solar Telescope on La Palma
SXR	Soft X-ray
SXT	Soft X-ray Telescope (on board of Yohkoh)
TIP	Tenerife Infrared Polarimeter
TRACE	Transition Region and Coronal Explorer
UV	Ultraviolet
VTT	German Vacuum Tower Telescope

Chapter 1

The Sun's Magnetic Fields



Abstract In this introductory chapter we first briefly describe some overall characteristics of the sun, and then take a closer look at the sun's magnetic surfaces. We shall see that highly advanced space and ground-based observations show various magnetic elements, their clusters, and mass flows in great detail. The chapter is concluded with the description of the magnetic skeleton of the sun showing the well-defined imprint of the photospheric magnetic field pattern at all available temperatures from low chromosphere to the outermost corona.

1.1 The Sun as a Star

1.1.1 *Legacy of Ancients*

Since ancient times all people on the earth have considered the sun as their own. They knew that they depended on it, and wanted to know why.

Back in 3000 BC the Egyptians believed that the sun is He who is above and has created himself from himself, and the earth and sky, and man was born from his tears.

The Chinese at that time pragmatically built observatories to map out time, record sunspots, flares, prominences, and eclipses. The origin of the sun and the fear to lose it was described along the lines: Of all celestial objects it is the Sun that good heaven put in the China's sky and give it to Chinese people, animals and plants, and when Dark force, the dragon, eats the sun at bad times, inspired brave people of China to scare the dragon with loud gongs. And it always worked. People of China were first to record and predict the solar eclipses.

And, yet, it was Pythagoras (569–475 BC) and his followers who formulated the first mathematical basis of the heaven ("Number is within of all things"). They postulated that the universe is in constant circular motions, and that the sun and all the heavenly objects revolve about a single central fire. They declared that the sun is spherical and has a substance similar to glass that collects rays from central fire, and transmits them to us. Most importantly, they linked geometry of harmonious motions with its physical nature. Pythagoras said: "from the sun and moon and

from the stars in so great number, and of so great size, moving so swiftly, there must necessarily arise a sound inconceivably great. . . and the sound of the stars moving on in a circle becomes musical.” Concluding that the universe exists in accordance with musical harmony, so the sun also makes a harmonious period. The Pythagoreans believed that the moon has an earthy appearance, and this is because, “like our earth, it is inhabited throughout by animals and plants, only larger and more beautiful; for the animals on it are fifteen times stronger, not having any sort of excrement, and their day is fifteen times as long as ours.”

The harmonious cosmological model of the Pythagoreans did not receive immediate development.

In words of Plutarch “Anaxagoras was the first to put in writing, most clearly and most courageously of all men, the explanation of the moon’s illumination and darkness, . . . and even his account was not common property but was still a secret, current only among a few and received by them with caution or simply on trust.” Anaxagoras (500–497 BC) declared that “the moon has a light which is not its own but comes from the sun.” Anaxagoras’s cosmology teaches that the world began with a vortex setup, that the rotatory movement began at one point and then gradually spread, taking in wider and wider circles. And then, “in consequence of the violence of the whirling motion stones were thorn from the earth and kindled into stars.”

Democritus, who according to his own account “was young when Anaxagoras was old” has in fact reinstated the views of Anaxagoras, but unlike Anaxagoras who believed that the earth is flat and rides on the air, Democritus believed that the earth remains where it is because it is in equilibrium and there is no reason why it should move one way rather than another. At the same time Democritus vision of heaven was so advanced that could fit a modern astronomy textbook: “There are worlds infinite in number and differing in size. In some there is neither sun nor moon, in others the sun and moon are greater than with us, in others there are more than one sun and moon. The distances between the worlds are unequal, in some directions there are more of them, in some fewer, some are growing, others are at their prime, and others again declining, in one direction they are coming into bang, in other they are waning. Their destruction comes about through collision with one another. Some worlds are destitute of animal and plant life and of all moisture.”

But it was not until Plato that Astronomy became a science comparable to Mathematics as it was prescribed by Pythagoras.

Plato (427 BC) said: “We shall pursue astronomy, as we do geometry, by means of problems, and we shall dispense with the starry heavens, if we propose to obtain a real knowledge of astronomy, and by that means to convert the natural intelligence of the soul from useless to a useful possession.”

And long voyage of theory of harmonious motions with earth at the center continued for centuries. It swallowed the first heliocentric model of universe by Aristarchus of Samos, who not only hypothesized that “fixed stars and the sun remain unmoved, that the earth revolves about the sun,” but also measured sizes of the earth, moon, and sun, and their distances. He described the moon as a satellite of the earth. He declared that the sizes of the earth and the sun are negligible in size

compared to the universe. He radically improved the sun-dial, and regarded time as “quantity expressed by things in motion and at rest.”

The heliocentric system was abandoned for another 1800 years until the time of Copernicus. With or without Copernicus the time came for putting the sun where it belonged.

In what follows the overall characteristic of the sun will be briefly described. Then the sun’s magnetic surfaces and its magnetic skeleton sustaining the overlying atmosphere will be presented in view of the most recent observations.

This book is devoted solely to the physics of small-scale magnetic flux tubes being the first attempt to consolidate the problems involving the intermittent magnetic fields per se. There are of course excellent books on all the aspects of solar physics accumulated during the decades of the subject studies (Athay 1976; Moffatt 1978; Parker 1979; Sturrock et al. 1986; Zirin 1988; Cox et al. 1991; Somov 1991; Strong et al. 1999; Dwivedi 2003; Severny 2004; Golub and Pasachoff 2010; Priest 2014). This fairly incomplete list of references which themselves contain rich bibliographies is given in order to direct the reader to valuable information on various solar subjects that are beyond the scope of this book.

1.1.2 Hidden Interior

The sun today belongs to a family of moderately warm yellow dwarfs, and is in its middle age.

Almost entire energy of the sun produced by nuclear fusion in the core is transported throughout the rest of solar interior, its visible atmosphere, and out into space. This process is determined by the composition of medium, its temperature, density, pressure, and internal energy. In high density and high temperature plasmas under conditions immediately outside the solar core, the energy is transported by radiation. Plasma density here is still so high that photons liberated by nuclear fusion travel a short distance and soon are either scattered or absorbed and re-emitted by other particles. At lower temperatures, but still high densities, electrons provide another mean of energy transport—conduction. This process occupies the region approximately up to $0.74 R_{\odot}$. Farther outward the plasma density and temperature rapidly drop. Sharp temperature gradient provides conditions for convective instability: a heated plasma element (not a particle!) becomes buoyant and rises some distance, called the mixing length, before it falls back due to releasing its energy into the surrounding plasma. The overall qualitative picture of the stages of energy production and transport in the solar interior is sketched in Fig. 1.1. Regions of action of various mechanisms must obviously overlap.

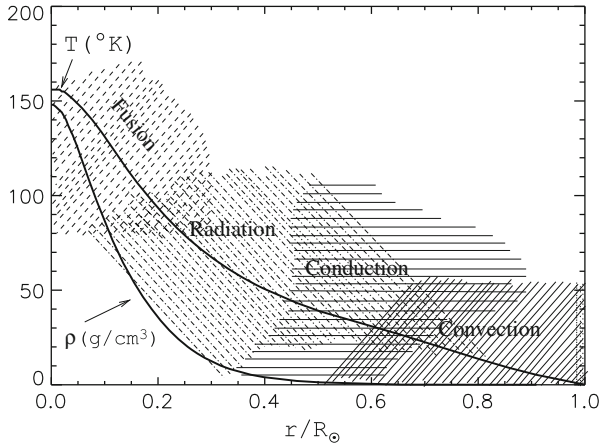


Fig. 1.1 Schematic of the energy production and transport in solar interior. Data for the temperature and density plots are taken from Bahcall and Ulrich (1988)

The sun's interior is hidden from us and its true structure and physical processes are subject of guessing and modeling. What we see well however, i.e., the photosphere, chromosphere, multi-temperature corona, and its extension to interplanetary space supply us with invaluable information for studying the sun as a star.

1.1.3 Magnetic Dipole

The sun as a star appears in the form of a modestly magnetized well-shaped dipole with a mean field intensity of about 1 G (Fig. 1.2). What seems however as a neat dipole is in fact tremendously complicated magnetic body, very inhomogeneous, intermittent, and highly dynamic. And yet, the overall properties of magnetic fields and general pattern of their behavior are in many ways quite systematic.

For example, measurements of the magnetic flux of a "dipole" over many solar cycles show that its intensity remains about the same and ranges in the interval of $1.5\text{--}2.5 \times 10^{22}$ Mx. The axis of magnetic dipole is tilted at about $\pm 7.23^{\circ}$ with respect to the ecliptic, and it also remains steady (in the sun's coordinate system). The magnetic flux of the dipole mainly comprises of the high latitude magnetic fields, where in average it is unipolar and uniquely determines the polarity of a dipole.

An ensemble of polar magnetic fields being quite irregular and variable at short timescales shows remarkably regular pattern at large timescales: the mean magnetic flux of a dipole periodically weakens and subsequently undergoes a reversal of polarity. This happens roughly every 10–11 years and is directly related to periodic

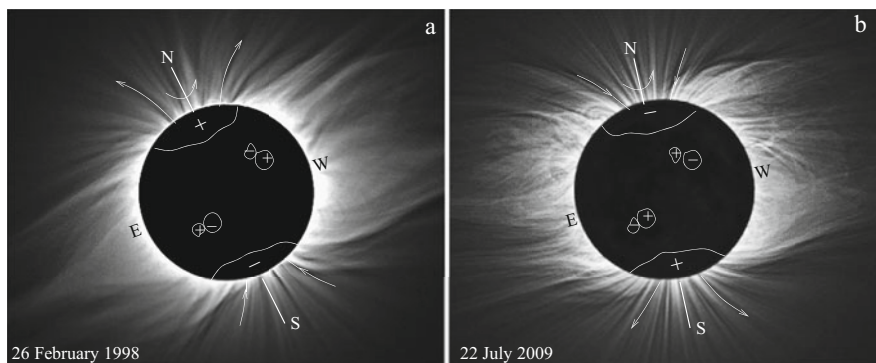


Fig. 1.2 Magnetic dipole. The background cartoons are the images of total solar eclipses: (a) 1998 February eclipse photographed by Jerry Lodriguss, and (b) 2009 July eclipse photographed by Miloslav Druckmüller. Note that the tilt of the sun's axis is different during the two eclipses. On February, 26 1998 the tilt is near its maximum. This is because when viewed from Earth the tilt is maximum during the first week of March and decreases to minimum toward the first week of June (second maximum and minimum fall to the first week of September and the first week of December, respectively). Reprinted from <http://www.zam.fme.vutbr.cz/~druck/eclipse/>. Courtesy of M. Druckmueller

change of sunspot numbers observed during the centuries and known as 11-year solar cycle.

The reversal of a dipole polarity marks the abrupt changes in the configuration of sunspots and active regions over the entire solar surface. Most remarkable is the appearance of new sunspots at latitudes of $38\text{--}40^\circ$ —this is the highest range of latitudes for sunspots to appear. New sunspot groups in both hemispheres have magnetic polarities opposite to those of previous sunspot groups, i.e., the polarity reversal occurs here as well. Farther in time, new sunspot groups emerge closer and closer to the equator in both hemispheres. The number of sunspots gradually increases and reaches the maximum in about 3–4 years. After that, fewer and fewer sunspots emerge in locations closer to the equator (Fig. 1.3). Sunspot groups are always organized in such a way that the leading sunspot tends to be closer to the equator, whereas the trailing sunspot is closer to the pole. The polarity of the following sunspot is always opposite to that of pole. At the end of cycle when the last sunspots appear in the equatorial zone, the polarity reversal of a dipole is about to happen.

The time between two consecutive minima (or maxima) in the sunspot numbers and migration of the zone of their emergence, traditionally determined as the 11-year cycle, changes considerably during the centuries, and may range from 7–17 years. And, of course, the number of sunspots in every cycle changes considerably as well. There were periods of extremely low solar activity when sunspots were not observed at all. The most well known to our knowledge is the Mounder Minimum that occurred between 1645 and 1715. This period was called the Little Ice Age, during which the Thames and the canals of Venice were covered with ice. Progress

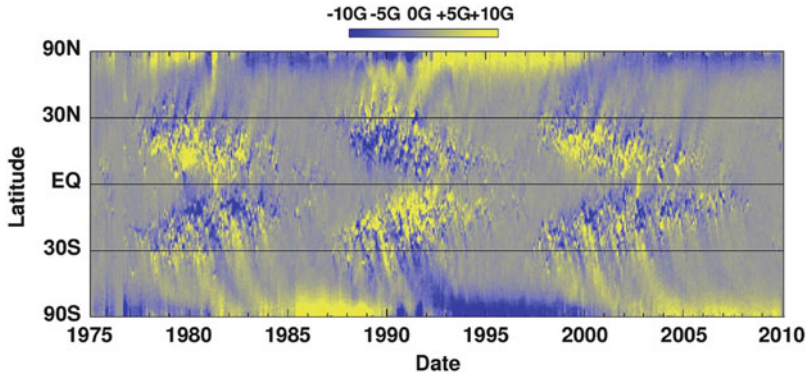


Fig. 1.3 Diagram of the distribution of the sun's magnetic field over three 11-year solar cycles. Yellow represents magnetic field directed out of the sun. Blue represents magnetic field into the sun. Sunspots themselves produce the “Butterfly” pattern at low latitudes. The sun's meridional flow from the equator to the poles in each hemisphere carries magnetic remains of the sunspots to the poles. This produces the streaks seen at higher latitudes and reverses the magnetic polarity of the sun's poles every 11 years. Reprinted from <http://solarscience.msfc.nasa.gov>. Image credit: NASA/MSFC/David Hathaway

in the analysis of radioactive Carbon 14 and Beryllium 10 that trace the influence of solar activity on the Earth provided information about the solar cycles back to hundreds of centuries (see, e.g., Lockwood (2013) and the literature therein).

It is only natural to expect that the magnetism of other stars has the same nature. But it was not until the 1980s that this fact was confirmed. Although the magnetic field concentrations are not directly observable on stars, these areas produce strong emission in the Ca II H and K resonance lines in the optical, and the Mg II H and K lines in the ultraviolet diapason. Observing variations in Ca II H and K lines in main sequence stars, Wilson (1978) found that the solar type stars of type G2 and older indeed show cyclic variations. It was also found that the magnitude of these variations is of the same order as that for the sun (Vaughan 1980; White and Livingston 1981).

But it is only our sun that provides us with unprecedented details of its magnetism and behavior.

1.2 Magnetic Surface

Highly advanced space and ground observations have revealed amazing details of solar magnetism. The surface of the sun is the best source for obtaining information on how the magnetic field emerges and evolves, and how it is distributed over the surface. At any moment of time the solar surface is covered with uneven ensembles of magnetic elements having various spatial sizes, shapes, and lifetimes.

Their distribution over space, so-called magnetic filling factor, also varies over space and time. The magnetic filling factor f_m is a convenient parameter defined as $f_m = S_m/S$, where S is the area of interest, and S_m is the area occupied by the magnetic field. In terms of the filling factor, the solar surface can roughly be categorized as follows (Fig. 1.4):

- Quiet sun—the largest regions of the solar surface covered by small magnetic flux tubes far removed from each other with average filling factor much less than unity, $f_m \ll 1$.
- Sunspots with filling factor of the order of unity, $f_m \simeq 1$.
- Active regions that are clusters of bipolar sunspots and surrounding them mixed polarity magnetic elements with average magnetic filling factor close to unity, $f_m \simeq 1$.
- Remnant active regions consisting of mixed polarity elements with magnetic filling factor in the range of $f_m \sim 0.3$ – 0.6 .
- Plages, which are rarefied ensembles of either unipolar or mixed polarity elements with filling factor in the range of $f_m \sim 0.2$ – 0.35 .

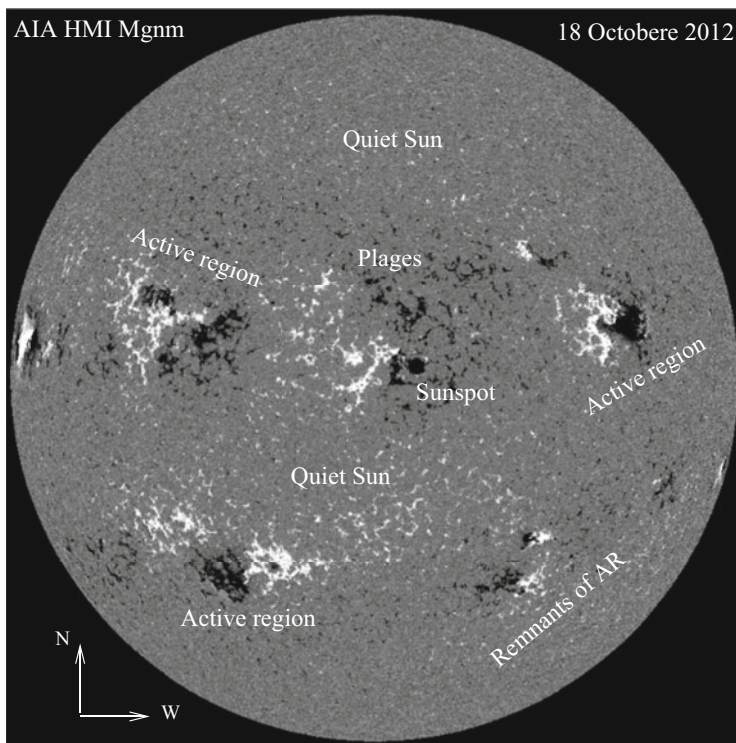


Fig. 1.4 Full disk magnetogram taken by the AIA/HMI instrument on board of SDO. White and black patches represent line-of-sight (vertical) magnetic field of positive and negative polarities

The magnetic elements that form these ensembles have their own substructures and consist of small-scale flux tubes. Size of the smallest constituents may be well below the resolution, which for the time being has reached few tens of kilometers.

1.2.1 *Quiet Sun*

Most of the solar surface, in fact 90% of it is covered by small-scale magnetic elements—magnetic flux tubes. They usually trace the convective cell boundaries at all scales, the smallest of which is the granulation network. The size of network granules ranges from a few hundred km to several arcseconds (1 arcsec = 726 km). The network picture is well recognizable in the quiet sun magnetograms, where negative and positive magnetic flux tubes trace the granulation pattern and encircle it (Fig. 1.5). Lifetime of individual magnetic flux tubes ranges from a few minutes to a couple of hours. The entire supply of the “pepper and salt” magnetic flux forming quiet sun “magnetic carpet” is replaced in about 40 h (Title and Schrijver 1997), which eventually provides a permanent energy supply to overlying atmosphere.

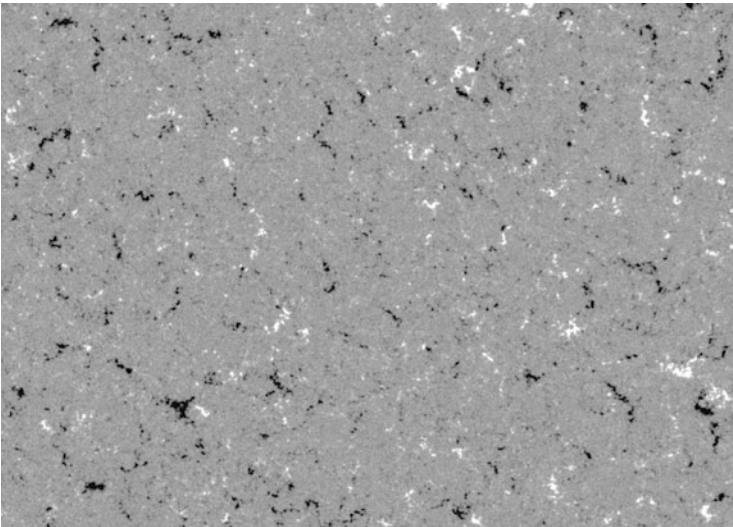


Fig. 1.5 Fragment of a quiet sun magnetogram taken by HMI/SOT at the disc center. The field of view is $346 \times 283 \text{ arcsec}^2$

1.2.2 Sunspots and Active Regions

Sunspots are huge conglomerates of magnetic flux concentrations seen as dark spots. Their temperature is about a thousand degrees lower than the average surface temperature. A closer look at sunspots reveals their extremely complex nature. For example, mature sunspots are usually surrounded by the penumbra: strong, almost vertical magnetic field of umbra becomes more and more horizontal toward the periphery forming an “uncombed” system of thin magnetic filaments arcing radially outward from the umbra and terminating in the photosphere (Fig. 1.6). The inclination of the magnetic filaments is found to vary across penumbra from 45° to 90° to the sunspot normal (Title et al. 1993). There are strong intensity inhomogeneities across the penumbra, resulting in a visual effect of interlaced dark and bright filaments.

The Evershed flow (unsteady plasma outflow at the photospheric level) is also found to be structured on the scale of the penumbral filaments. The flow is more horizontal than the mean magnetic field at all radii in the penumbra and has a spatial correlation with dark penumbral filaments (Shine et al. 1994). The bright filaments are usually less horizontal making thus some angle with the Evershed flows. Livnigston (1991), comparing images of sunspot with different exposures,

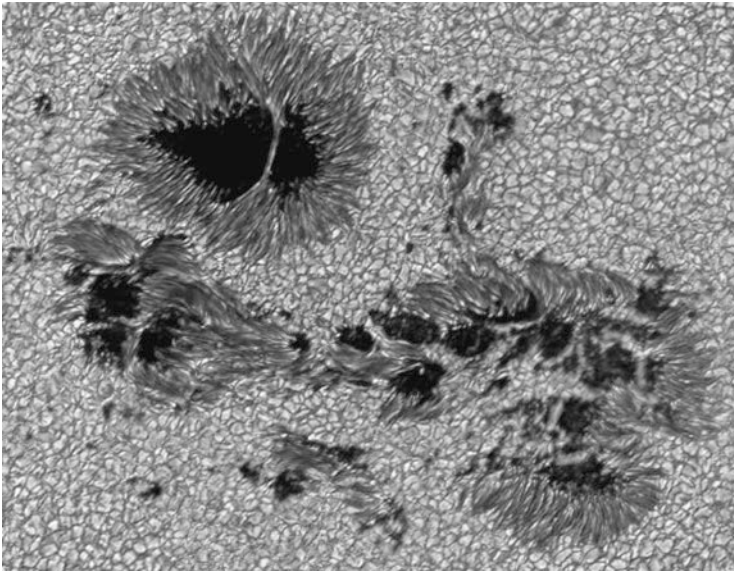


Fig. 1.6 Image of the active region (AR 10375) in 4320 \AA Blue Continuum covering 100×130 arcsec area. Both, younger sunspot (upper left) and decaying AR (bottom) show well-developed filamentary penumbrae. One can see a small bright points inside umbrae, which are signs of their filamentary structure. Image taken by DOT on June 6, 2003. Reprinted from <http://www.staffscience.uu.nl>, courtesy of R. Rutten

came to the conclusion that the sunspot umbra also has a filamentary structure, and may exhibit presence of vertical, diverging, and even horizontal filaments.

Newly emerged young sunspots sometimes do not develop penumbrae, and remain “naked.” These are called pores. Typically they are 3000–6000 km in size and live for many hours.

Sunspot formation and their appearance at a visible surface is a gradual process that may take hours and days. A complex conglomerate consisting of several sunspots and pores, such as one shown in Fig. 1.6, takes several solar rotations to form, live, and decay. Due to a close neighborhood of opposite polarity formations the active regions harbor a wide range of electromagnetic phenomena that shape the overlying atmosphere: chromosphere, transition region, and corona. The latitudes of a complex active regions are also sites of the origin of a slow solar wind.

1.2.3 *Plages*

Plages are complex conglomerates of magnetic flux concentrations with average magnetic filling factor of about $f \sim 0.2$ – 0.3 .

There are two major types of plages: mixed polarity plage and plage dominated by one polarity magnetic elements. The origin of plages is mainly associated with the decaying active regions, but they may also form due to the subsurface magnetic activity leading to elevated rate of emergence of small-scale magnetic flux tubes. An average magnetic field in the magnetic concentrations here is about 100 G. Figure 1.7 shows example of a typical plage with average magnetic field strength exceeding 100 G, and a filling factor of about $f \geq 0.3$. Usually, plages resulting from remnant active regions are bipolar formations. The decaying sunspot leads to formation of unipolar plages, which may overlap with the neighboring opposite polarity plage and form a mixed polarity region.

Dynamics of plages and their activity is extremely rich. There are common effects produced by unipolar and bipolar plages, but most importantly, each category has its own unique features.

1.2.4 *High Latitudes and Polar Regions*

As mentioned above, toward the end of 11-year cycle active latitudes “shrink,” and remaining sunspots and sunspot groups migrate toward the equator, while the 10–11 years old remnants of the previous cycle have already migrated toward poles. The polarity of the pole has a polarity of the ending cycle where small-scale magnetic elements occupy the polar and high altitude regions. At the turn of a cycle the opposite polarity sunspots and sunspot groups start to emerge at about $\pm 40^\circ$ latitudes. Newly emerged sunspots migrate toward the equator while their

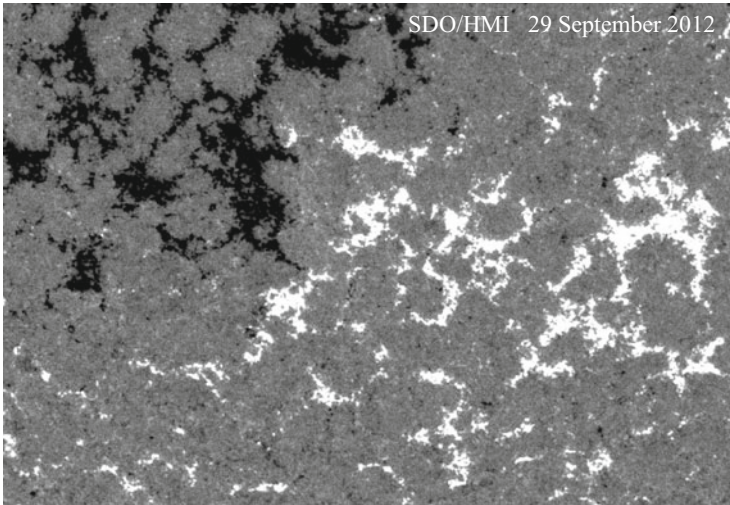


Fig. 1.7 Image of a plage taken by the HMI/SDO instrument. White and black patches corresponding to positive and negative magnetic fluxes form a typical unipolar plages. Note a well-defined supergranular pattern demarcated by magnetic flux concentrations. Field of view is 150×200 arcsec

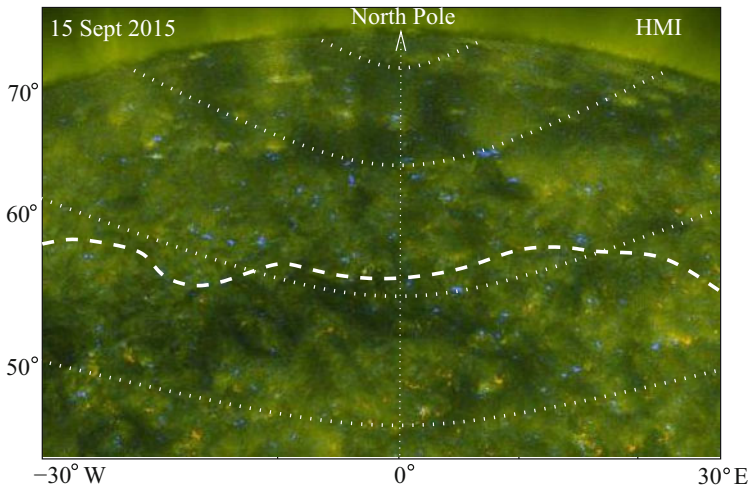


Fig. 1.8 Magnetogram of high altitude solar region near the North pole shows the encounter of the ensemble of negative polarity network elements of a previous cycle with the ensemble of positive polarity magnetic elements coming from a new cycle. White dashed line is the approximate demarcation line between these regions

peripheral magnetic elements migrate toward the polar regions. Thus in the first half of a new cycle one observes the merging of the opposite polarity ensembles of small-scale magnetic elements of the previous cycle with those of a new cycle (Fig. 1.8).

The filling factor of ensembles and the location of demarcation line between them play a crucial role in the dynamics of the overlying atmosphere, the most spectacular of which is formation and evolution of quiescent prominences and polar plumes.

1.3 Mass Flows

The entire solar atmosphere from its visible surface to interplanetary space is pierced by a great variety of mass flows. They are observed in all temperature ranges, and may have a steady, unsteady, and explosive character. Their velocities vary from a few tenths of km s^{-1} to hundreds of km s^{-1} . The presence of flows dramatically changes the physical picture of any given event, leading often to the formation of energetically open non-conservative systems. We will discuss several special cases associated with the presence of mass flows throughout the book. Here we briefly overview a few general patterns of mass flows.

The surface of the sun exhibits multiple-scale convective motions which traditionally are described as granular, mezogranular, and supergranular pattern. Irregularly shaped granules with sizes ranging from a few hundred km to arcseconds uniformly cover entire solar surface outside pores and sunspots. Average lifetime of granules is about 8 min. In the center of granule a warm plume is rising with velocity $\simeq 0.4 \text{ km s}^{-1}$ diverging and falling down at the edge of a granule. Figure 1.9 shows co-aligned images of a region containing several pores surrounded by unipolar plage and quiet sun patches. The top panels are the magnetogram and Dopplergram taken simultaneously by the SST instrument on Hinode. Line-of-sight magnetic field reaches $\sim 2300 \text{ G}$. Dopplergram measurements give the velocities ranging between ~ -1.2 and 1.6 km s^{-1} . White dots correspond to downflows, black points to upflows. Note that downflows are usually associated with magnetic flux concentrations. Bottom left in Fig. 1.9 is the same region in G-band. The black box there singles out the region of emerging flux which is enlarged on the right, where the map of horizontal velocities restored from time series of the SST data is shown. The velocities are averaged over 20 min. Arrows indicate the direction of horizontal velocities and their value.

Convective motions are also organized at larger scales. The most systematically observed motions that form cellular pattern are mesogranulation and supergranulation.

Mezogranular pattern of mass flows is characterized by advection of granular convection and associated small-scale magnetic fields. Rising velocities of plasma in a center are usually small, while horizontal velocities of diverging plasma are about 0.5 km/s . Horizontal distance between mezogranular centers is $5000\text{--}10,000 \text{ km}$ with lifetime of about 2 h.

In case of supergranulation mass flow rising from a center of neighboring cells with velocities of about 0.1 km/s diverge horizontally with velocities $0.3\text{--}0.5 \text{ km/s}$. Supergranular pattern is closely related to magnetic network consisting

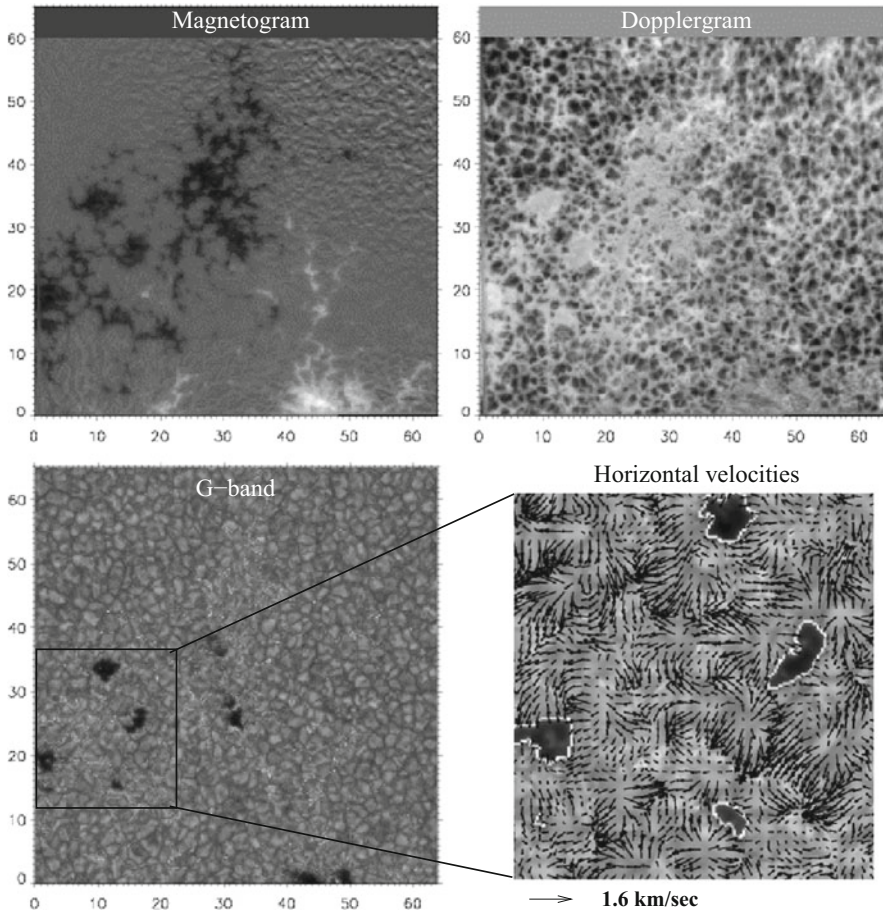


Fig. 1.9 Co-temporal and co-spatial set of images of 50×50 arcsec region taken by the SST instrument on Hinode on September 30, 2007. *Magnetogram* is scaled to maximum of ~ 2300 G. *Dopplergram* velocities range from ~ -1.2 to 1.6 km s^{-1} . *White dots* correspond to downflows, *black points* to upflows. The coordinates are expressed in arcsec. Bottom left is the same area in the G-band. Black box shows the region of emerging flux, shown enlarged on the right together with corresponding horizontal flow map. Credit: Vargas Domínguez et al. (2010), reproduced with permission from ESO

of magnetic elements with stronger than average magnetic field. Typical diameter of supergranules is of the order of 30,000 km, and lifetime of about 36 h.

A cellular pattern has multi-scale character and at all scales the inter-cellular lanes are filled by magnetic flux tubes. There they emerge, move around, and interact with each other and surrounding flows, directly affecting the overlying atmosphere.

The first to respond is the chromosphere. Here the temperature rises from 4000 K to 2.5×10^4 K in about 1500 km. Extremely dynamic, the chromosphere creates a

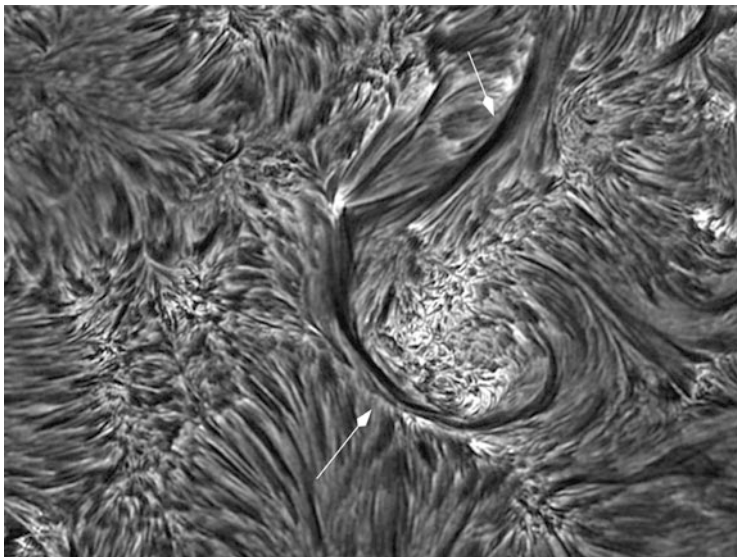


Fig. 1.10 The $H\alpha$ image of a relatively quiet sun/plage region taken by the DOT on September 23, 2006. The field of view is 86×65 Mm. Fibrils of many shapes and sizes bridging the polarity inversion lines outline the magnetic connections between the opposite magnetic elements. A huge crescent-like dark feature is an active filament (white arrows). A milky area surrounded by filament is plage. Reprinted from <http://www.staff.science.uu.nl>, courtesy of R. Rutten

narrow transition region where in another couple of hundred km the temperature jumps up to million degrees to setup the corona.

Blocked by strong emission of the photospheric white light, the chromosphere requires a narrow bandpass filters around the spectral lines emitted at chromospheric temperatures from the temperature minimum (4200 K) to its “upper boundary” (2.5×10^4 K at about 3000 km above the surface). The middle and low chromosphere are best observed in Ca II K, He II, and $H\alpha$ lines.

Especially well the chromospheric features associated with mass flows are seen in $H\alpha$ line. Here we give only a few examples of the most pervasive large-scale chromospheric flows. These are fibrils, active filaments, quiescent prominences, penumbral jets, and spicules. All these features are uniquely associated with and governed by the magnetic field.

Fibrils are elongated dark structures with characteristic sizes of 1500–7000 km. Their lifetimes are of the order of network of about 15–20 h. They overhang the polarity inversion line everywhere, in the quiet sun, in plages, and around the sunspots. Examples of fibrils are shown in Fig. 1.10. The area is located south of decaying active region which produced a huge active filament (more precisely set of filaments), marked by white arrows. The crescent part of filament carefully encircles a unipolar plage which is seen in the chromosphere as milky conglomerate of bright rosettes.

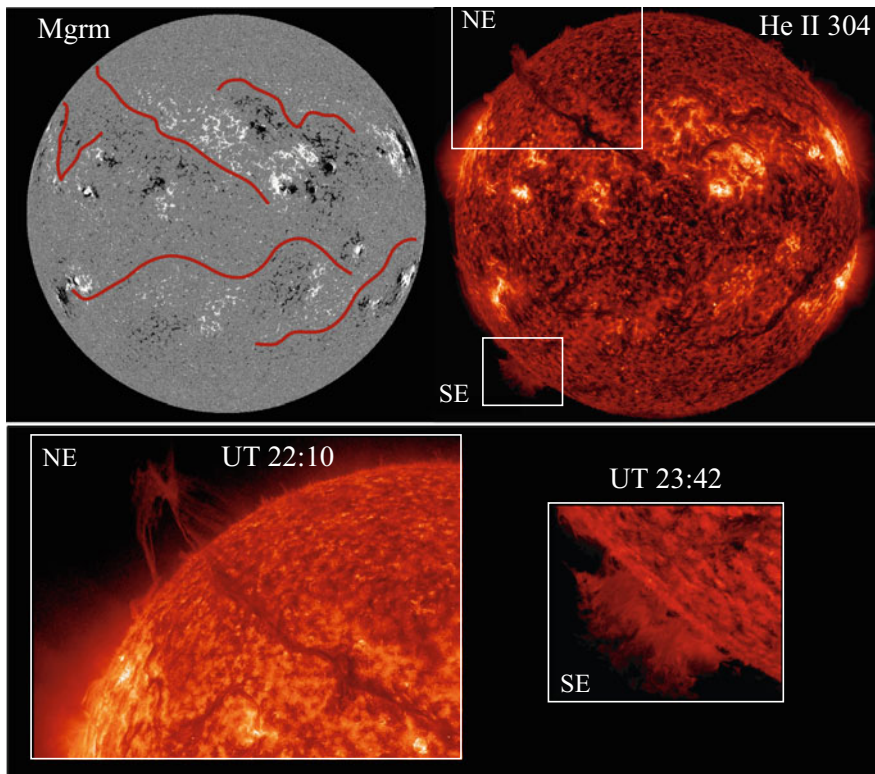


Fig. 1.11 Full disc images of the sun taken by the HMI and AIA instruments on the SDO on November 13, 2011. The red strokes on the HMI magnetogram demarcate the polarity inversion lines that coincide with the chromospheric filaments seen as long dark structures in 304 \AA He II line ($5 \times 10^4 \text{ K}$). These are quiescent prominences. Their projection on sky at North East and South East limbs is shown in inlets. Height of a limb portion of both prominences exceeds $50,000 \text{ km}$

Filaments and prominences form two classes of magnetic structures with very different patterns of mass flows. Filaments are usually associated with the active regions. They are confined mostly in the chromosphere, i.e., their height is about $1500\text{--}2000 \text{ km}$, and their length is in the range of $50\text{--}100 \text{ Mm}$. Magnetic field strength in active filaments may be as high as $500\text{--}700 \text{ G}$. Their lifetime ranges from a few hours to days, and is determined by the evolution of parental active region. Plasma streaming along the filament may reach 30 km s^{-1} . Some transverse velocities were recorded to be about $3\text{--}10 \text{ km s}^{-1}$.

At much larger scales $H\alpha$ chromosphere exhibits a huge dark features that demarcate the *global* polarity inversion lines (Fig. 1.11). These are quiescent

prominences. In fact, these complex structures are far from quiescent, and harbor wide range of plasma instabilities, from regular flow instabilities to explosive mass release. Having lifetimes from a few days to several solar rotations, their name is quite justified by their longevity. Compared to active filaments, the $H\alpha$ prominences are much longer and much taller structures. Their length may be more than solar radius. Their height *always* exceeds the coronal heights, i.e., the quiescent prominences overhang the corona. At the same time the mass density of prominences is by 2–3 orders of magnitude higher than the coronal plasma density. In other words, a heavy cool material of prominence suspended over rarefied hot gas is like an iron bar floating in thin air.

Figure 1.11 shows the sun in 304 Å He II line (5×10^4 K) taken by the SDO/AIA instrument on November 13, 2011 together with the HMI magnetogram. The red lines on the magnetogram follow the path of prominences suspended above the demarcation line dividing the quiet sun magnetic network of the opposite polarities. White boxes on the North East (NE) and South East (SE) of the chromospheric image contain a projection of a limb portion of prominences. Slightly enlarged, these images are shown in the bottom of Fig. 1.11. Note that the North East limb shows the projection of a huge prominence whose body crosses the solar disc from its center, whereas the South East limb shows the projection of prominences hidden from us on the far side of the sun.

Mass flows associated with the quiescent prominences is hard to classify. Whatever shape is taken by the prominences they all have highly intermittent filamentary structure. Small-scale filaments comprising the prominence are usually accompanied by mass flows induced by the local magnetic field and electric currents.

Among a huge variety of magnetic structures and flows, the sun has one of the most persistent phenomena—spicules. These are magnetized plasma jets coming out of magnetic network and outlining supergranular boundaries. They are as ubiquitous as large-scale convective pattern, forming regular bush-like structures arranged into the rosettes that are mainly anchored in the supergranular lanes. They have quite self-similar properties practically all over the solar surface. Their lifetime is usually several minutes. The plasma in spicules is ejected with speed of about $20\text{--}30 \text{ km s}^{-1}$, and in a few minutes, as a fountain, drops down onto photosphere. Figure 1.12 shows a beautiful picture taken by the amateur astronomer in $H\alpha$ line, showing the solar surface covered by spicules. One can see a regular chromospheric network outlined by the bushes of spicules. Two active regions destroy the regularity of network and produce characteristic fibrils and filaments around them. Along the large-scale streamers accompanying sunspots and active regions, there are very

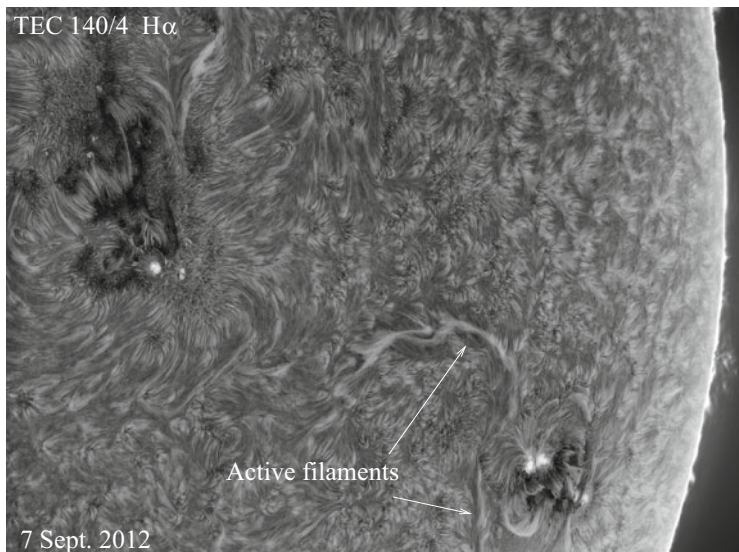


Fig. 1.12 The amateur picture of the sun in $H\alpha$ showing the active regions surrounded by filaments and a wonderful prairie of spicules forming extremely regular bushes that outline the chromospheric network. Reprinted from <http://www.stern-fan.de>. Courtesy of Rolf Geissinger

specific, always present systematic small-scale jets coming out of penumbrae with velocities of a few km s^{-1} . Their typical length is between 1000 and 4000 km, some may reach 10,000 km. Their lifetime ranges from 30 s to several minutes. When at the limb, the sunspot looks like crowned disc (Fig. 1.13).

We conclude this chapter by mentioning the polar plumes. These are long thin streamers projected on the sky as beams emanated from the north and south poles. These streamers are associated with small-scale magnetic elements and, when visible, their footpoints are seen as bright points. As we know, the polar regions are populated only by small-scale magnetic elements—remnants of dispersed magnetic clusters migrated toward the poles. Figure 1.14 shows a segment of south pole taken with the EIT instrument on SOHO in the Fe IX/X 171 Å (top) and Fe XII 195 Å (bottom) lines on May, 8 1996. Their temperature is therefore about 1 MK. They extend up to 30 Mm above the photosphere.

Note that we gave above only a few examples of the $H\alpha$ structures. In reality the filaments, fibrils, and quiescent prominences that form a broad classes of electromagnetic structures. And each class provides its own unique opportunity to study the fundamental physical processes.

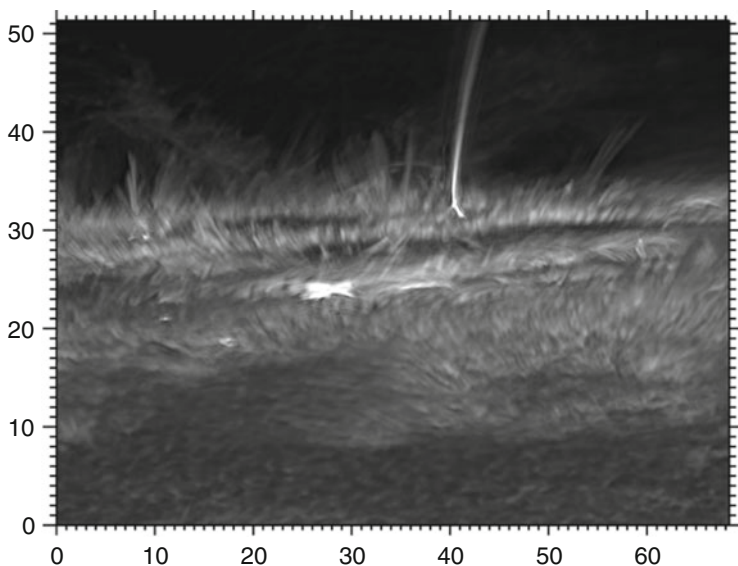


Fig. 1.13 Image of the active region (AR 10486) just before it rotated out of sight over the west limb to the backside of the sun in Ca II H line. The sunspots appear as flat dark pancakes encircled by spikes of penumbral jets and further surrounded by chromospheric fibrils. The foreground shows granulation pattern and spicules. A huge jet exceeding 15 Mm in length stands out between two sunspots. Tickmarks are arc seconds. The image is taken by the DOT on November 4, 2003. Reprinted from <http://www.staff.science.uu.nl>, courtesy of R. Rutten

1.4 Magnetic Skeleton

In a visible light radiated from the photosphere the sun looks like a smooth ball covered with a few tiny pockmarks (Fig. 1.15a). These tiny pockmarks are caused by the presence of magnetic field where temperature is significantly lower than that of surrounding photosphere. In the immediate vicinity to the surface solar atmosphere shows a “normal” behavior: its temperature and density *drop* with height. But reaching the temperature minimum of $\simeq 4400$ K at about 500 km height, the temperature quickly raises, and in about 1500 km from the temperature minimum reaches $\simeq 10^4$ K, forming the chromosphere (Fontenla et al. 2006). From that level, just in a narrow transition region of a few hundred km the temperature jumps to million degrees, forming a vast corona (for contemporary model of solar atmosphere, see, e.g., Fontenla et al. (2006) and the literature therein).

The problem of energy production, its transfer, and release throughout the solar atmosphere has been and still remains one of the major challenges in solar physics. The obvious platform for approaching this problem is understanding the

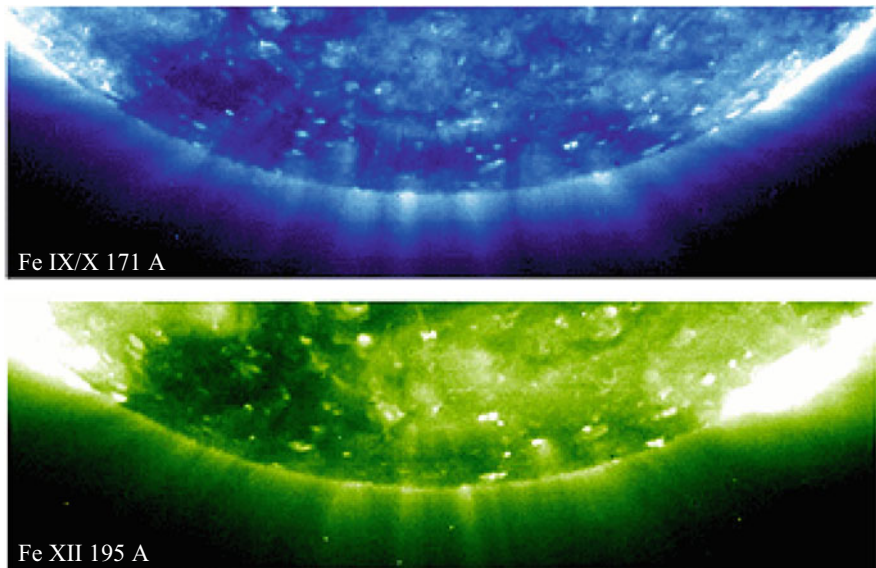


Fig. 1.14 The EUV images of the south pole with regular arrays of polar plumes, emanated radially outward from the solar surface. One can see bright footpoints of plumes which are associated with small-scale magnetic flux tubes—remnants of dispersed magnetic clusters that migrated in course of the solar cycle toward the poles

generation, structure, and evolution of magnetic fields, embedded in highly dynamic environment and interacting with it.

The overall imprint of the line-of-sight magnetic field in the overlying atmosphere and its outline is illustrated in Fig. 1.15.

The enhanced intensity of a hot plasma at all temperature levels mimics the magnetic field pattern seen at the surface. The very specifics of energy production, its transfer, and release, i.e., electromagnetic coupling of the photosphere with upper layers of atmosphere, is totally determined by characteristic features of local magnetic fields, be it the quiet sun with its rarefied ensembles of small-scale magnetic flux tubes, or dense clusters of magnetic flux tubes forming sunspots and active regions.

Throughout this book we shall study the properties of isolated flux tubes and their interaction with surrounding medium and each other. We will see that different topologies of flux tube ensembles met in the quiet sun, plages, and active regions, together with various mass flows interacting with them, result in a wide range of phenomena that are observable and may be quite well understood.

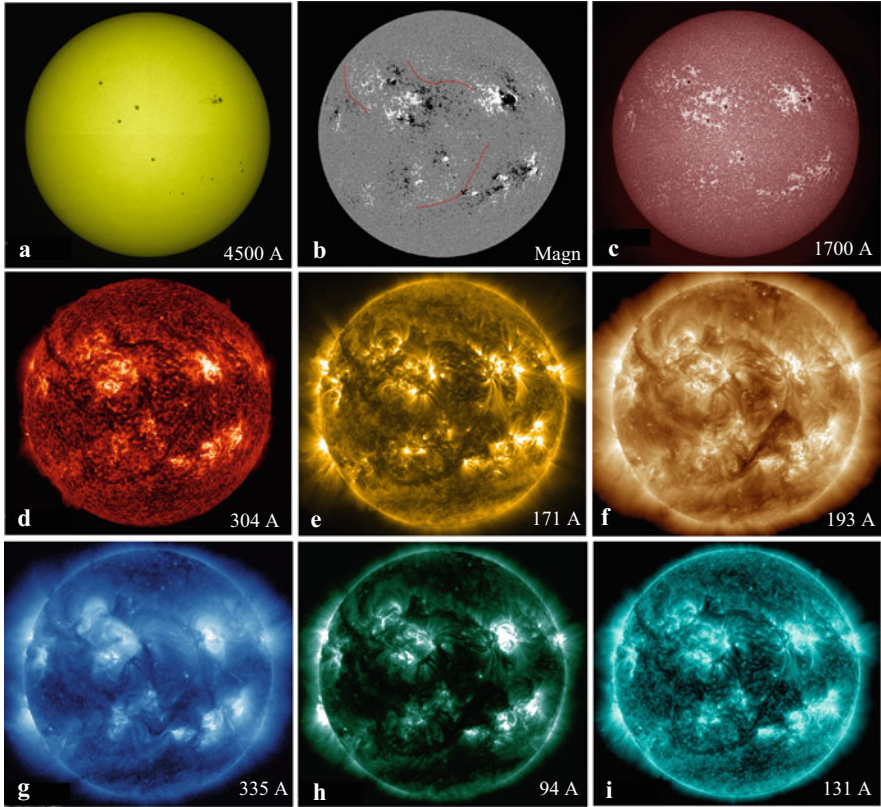


Fig. 1.15 The magnetic surface of the sun and its imprint in the overlying atmosphere: (a) The solar surface in the white light showing the atmosphere at 5500–6400 K; (b) Line-of-sight magnetogram with a few red lines demarcating the large-scale magnetic shear; the imprint of these lines, as well as the presence of magnetic fields are seen throughout the entire atmosphere; (c) The temperature minimum region in a cool emission line at about 4500–5000 K; (d) Upper chromosphere and transition region in He II line formed at $\approx 10^5$ K; (e)–(f) Corona at escalating temperatures of about 6.3×10^5 , 1.3×10^6 , 2×10^6 K (g)–(i), 6.3×10^6 K, and 2×10^7 K, respectively. Images are taken by the AIA/SDO instrument on November 10, 2011

References

- G. Athay, *The Solar Chromosphere and Corona: Quiet Sun* (D. Reidel Publishing Co., Dordrecht, 1976)
- J.N. Bahcall, R.K. Ulrich, *Rev. Mod. Phys.* **60**, 297 (1988)
- A.N. Cox, W.C. Livingston, M.S. Matthews, *Solar Interior and Atmosphere* (University of Arizona Press, Tucson, 1991)
- B.N. Dwivedi, *Dynamic Sun* (Cambridge University Press, Cambridge, 2003)
- J.M. Fontenla, E. Avrett, G. Thuillier, J. Harder, *Astrophys. J.* **639**, 441 (2006)
- L. Golub, J.M. Pasachoff, *The Solar Corona* (Cambridge University Press, Cambridge, 2010)
- W. Livingston, *Nature* **350**, 45 (1991)

- M. Lockwood, *Living Rev. Sol. Phys.* **10**, 4 (2013)
- H.K. Moffatt, *Magnetic Field Generation in Electrically Conducting Fluids* (Cambridge University Press, Cambridge, 1978)
- E.N. Parker, *Cosmical Magnetic Fields* (Clarendon Press, Oxford, 1979)
- E.R. Priest, *Magnetohydrodynamics of the Sun* (Cambridge University Press, Cambridge, 2014)
- A. Severny, *Solar Physics* (University Press Holdings Int., 2004)
- R.A. Shine, A.M. Title, T.D. Tarbell, K. Smith, Z.A. Frank, *Astrophys. J.* **430**, 413 (1994)
- B.V. Somov, *Physical Processes in Solar Flares* (Kluwer Academic Publishers, Dordrecht, 1991)
- K.T. Strong et al., *The Many Faces of the Sun* (Springer, Berlin, 1999)
- P.A. Sturrock, T.E. Holzer, D.M. Mihalas, R.K. Ulrich, *Physics of the Sun*, vols. 1–3 (D. Reidel Publishing Co., Dordrecht, 1986)
- A.M. Title, C.J. Schrijver, in *Cool Stars, Steller Systems, and the Sun*, ed. by R. Donahue, J.A. Bookbinder. Astronomical Society of the Pacific Conference Series (1997)
- A. Title et al., *Astrophys. J.* **403**, 780 (1993)
- S. Vargas Domínguez et al., *Astron. Astrophys.* **516**, A91 (2010)
- A.H. Vaughan, *Publ. Astron. Soc. Pacific* **92**, 392 (1980)
- O.R. White, W.C. Livingston, *Astrophys. J.* **249**, 798 (1981)
- O.C. Wilson, *Astrophys. J.* **226**, 379 (1978)
- H. Zirin, *Astrophysics of the Sun* (Cambridge University Press, Cambridge, 1988)

Chapter 2

A Quick Look on Small-Scale Flux Tubes



Abstract In this chapter we recall some basic steps of how magnetic flux tubes were discovered and how they were viewed in their early years. During the decades after their discovery, flux tubes evolved from an interesting novelty into a founding element of solar magnetism. Today we know that the entire magnetic field of the Sun, from sunspots to coronal loops and solar wind, has a filamentary structure. We briefly discuss the universality of filamentary structures in universe.

2.1 Early Years

For ages, solar magnetic fields were associated with sunspots. The existence of magnetic field concentrations outside sunspots has been realized only in the late 1950s. Howard (1959), observing magnetic fields in various active and quiet sun regions, found that existence of magnetic “features” with fields greater than 75 Gs outside sunspots and far removed from them is not “uncommon.” Confirming the correspondence between calcium bright points (seen at chromospheric temperatures) and photospheric magnetic fields, described earlier by Babcock and Babcock (1955), Howard writes: “A close correspondence in most small structural details between the calcium plages and magnetic field tends to indicate a real physical relationship between the two,” and finally suggests that “the magnetic field in the solar photosphere and chromosphere is in the form of more or less *vertical columns*.”

Leighton (1959) describing his observations of magnetic field in plage regions also concludes that “relatively strong field, 100 or 200 G in strength are found in extensive areas throughout plage regions, the field pattern being in striking agreement with the pattern of Ca II emission.”

The same year, Severny (1959) reports on the observations of fine structures in *sunspots*!

Such was the birth of small-scale magnetic flux tubes. Not only were the existence of small-scale magnetic features detected, but they were also found uniquely associated with two important phenomena. One was a direct correlation with heating the overlying chromosphere (Ca II emission), and the other was

formation of large-scale magnetic shear formed all over the solar surface by small-scale “columns” of opposite polarity.

Pikel’ner (1963), well before the small-scale flux tubes were directly observed, was the first to predict the existence of flux tubes. He suggested that convective motions acting on the magnetic lines of force squeeze them and crowd in toward the periphery of the granules, and that the field becomes concentrated into a network covering the sun’s surface. He also predicted that the enhanced convection contributes to chromospheric emission, so that the network becomes observable in Ca II and H α lines. Moreover, Pikel’ner found that the motion of plasma entrained in the magnetic field lines is responsible for the observed mottles consisting of granular elements streaming from the center toward the periphery, and concluded that the presence of mottling over the entire solar surface demonstrates that a “weak” field exists everywhere. The direct observation of these suggestions were still to come.

2.1.1 First Direct Observational Signs of Magnetic Flux Tubes

Using the photographic technique of Leighton for high-spatial resolution measurements of photospheric magnetic fields, Sheeley (1966, 1967) finds that as a bipolar magnetic region develops in time and as its magnetic flux spreads over a larger area, the flux density does not decrease smoothly, but is distributed in bits and fragments of progressively smaller sizes until finally, they escape detection below the threshold of photographic measurements. The magnetic field in these small magnetic features was found to range from 200 to 700 G. Sheeley states that “wherever there are adjacent regions of opposite polarity, there are disc filaments in H α .” His conclusion, that “magnetic fields of several hundred gauss occur in tiny areas easily as small as 500 km in regions of the solar surface sometimes well removed from sunspot activity,” became the turning point which, despite the predecessors, is a fact of the discovery of small-scale flux tubes.

Just at about the same time, observing magnetic fields of small sunspots and pores, Steshenko (1967) finds that the field strength of the smallest pores (1'' – 0.5–2'') is about 1400 G. In larger spots he finds very small elements with a field strength of 5350 G (!), much higher than the average field of the sunspot itself. He also observed an isolated place outside sunspots having field strengths up to 1000 G.

Beckers and Schröter (1968) performed an extremely detailed study of the small-scale magnetic structures *in* and *around* the sunspots. These studies included the measurements of velocity, intensity, and magnetic field strength in the fine elements. By these observations they confirmed and extended Sheeley’ findings, providing substantial guideline for future observations. Being quite cautious, they start the discussion as follows: “We presented in this paper evidence that most, and perhaps all, of the photospheric magnetic field around a unipolar sunspot is concentrated in a few thousand small region (1000 km in diameter) with strong magnetic fields (up to 1400 G). This, together with the other properties of the magnetic knots, shows that they are an essential part of a solar activity regions. We are, however, not yet able to

decide definitely whether they occur only in the dissolution phase or whether they are a permanent constituent of a solar activity region.”

Soon, it was found that almost the entire surface outside sunspots is covered by small-scale magnetic elements. Howard and Stenflo (1972), analyzing Mount Wilson magnetogram recordings obtained during 26 days with 17 by 17 arcsec aperture, found that more than 90% of the total flux is channeled through narrow flux tubes with very high field strength in plages and at the boundaries of supergranular cells. The flux tubes occupying a very small region in the photosphere were found rapidly spreading out with height. This spreading of the field lines and decreasing the field strength with height was dubbed the “mushroom effect,” described earlier by Pikel’ner (1963) as chromospheric mottling (Frazier and Stenflo 1972).

2.1.2 *The Sunspot Dilemma*

It is interesting that just before these fundamental results establishing the filamentary structure of Sun’s magnetic fields outside sunspots, and long before the recent high-resolution observations, Papathanasoglou (1971), along the earlier findings of Crimea group (see, e.g., Severny 1959), has observed the filamentary structure of *sunspot umbra*, and showed that the widths of umbral filaments are $<1''$, and that dark spacing between them are about $0.6''$. This amazing result was totally ignored, earning only three (!) citations, first of which was given by Livingston (1991) in his Nature article “Radial Filamentary Structure in a Sunspot Umbra,” where he also reports on the direct observations of the filamentary structure of sunspot umbra.

For many years, however, the study of small-scale filamentary structure of umbrae was overshadowed by studies of a sunspot as a whole, its stability and its impact on the surrounding and overlying atmosphere. The large-scale observational data clearly indicated that as a whole, the sunspots must be intrinsically unstable. The stability analysis of such a complex and ever changing body requires consideration of many competing effects—the job that yet has to be done. And search for the mechanisms of sunspot stability became an uphill battle. The filamentary structure of the sunspot body has been put aside by the majority of researchers. The most revealing of the acute situation of those days is, probably, an example of Piddington’s research.

The large body of Piddington’s work on solar magnetic fields may be characterized by his own words (1975): “A phenomenological model of solar magnetic fields is developed, which differs drastically from all currently popular (diffuse-field) models. Its acceptance would require a review of a major part of theoretical solar physics.”

Revision of a major part of solar theories and interpretations was not easy, and Piddington’s ideas in many aspects of solar magnetism caused various reactions, from such definitions as “Piddington’s Heresy” (Parker (1976) on role of turbulent diffusion) to a silent dropping off his works from citations. Figure 2.1 shows an

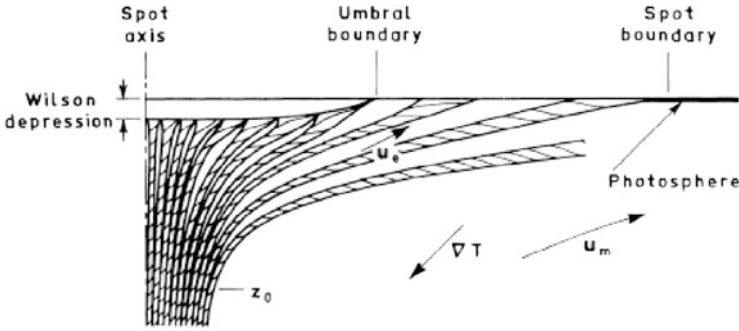


Fig. 2.1 Section of a sunspot magnetic field with the flux-rope helical twist omitted for simplicity. The individual flux tubes are shown twisted and separated by nonmagnetic plasma regions whose width increases with distance from the axis, thus accounting for the penumbral filaments. The Evershed flow u_e has different directions and velocities inside and outside the flux tubes. Reprinted from Pidington (1978) by permission from Springer Science and Business Media

example of the Piddington's model of sunspot consisting of the individual twisted flux tubes.

Meyer et al. (1977) reacted to Piddington's model of sunspot stability simply: "We shall show, using a simplified model, that a sunspot can be stable in and immediately below the photosphere. This stability can be related to the potential energy associated with the Wilson depression. *There is no need to invoke twisted fields (e.g., Pidington 1975), which have not been observed.*" (!)

By the time of this statement, from a basic plasma theory, supported by laboratory experiments, it was already well known that long magnetic cylinders are intrinsically unstable with respect to so-called screw pinch instability (Shafranov 1956; Kruskal and Kulsrud 1958; Kadomtsev 1966). A condition for screw pinch instability, known as Kruskal-Shafranov condition, is simple: flux tube with magnetic field $\mathbf{B}(0, B_\phi, B_z)$, radius R , and length L will be inevitably twisted if

$$q = \frac{2\pi R B_z}{L B_\phi} \equiv \frac{h}{L} < 1, \quad (2.1)$$

where q is the safety factor, and h is the pitch of helical configuration, i.e., the distance in which the field line makes one revolution around the flux tube. In case of solar magnetic flux tubes, the safety factor is always < 1 , which means that any magnetic flux confined in a cylinder with roughly $R \ll L$ must be twisted.

One can say that at those times Piddington's model of solar magnetic fields including sunspots (Fig. 2.1), active regions, and their environments, based on the model of twisted flux-ropes, was probably the closest to the goal. More general features of solar magnetic field visualized by Pidington (1978) are shown in Fig. 2.2. All these features, as already mentioned, have been subsequently confirmed (Ryutova et al. 2008; Su et al. 2010; Ruiz Cobo and Puschmann 2012; Stenflo 2013).

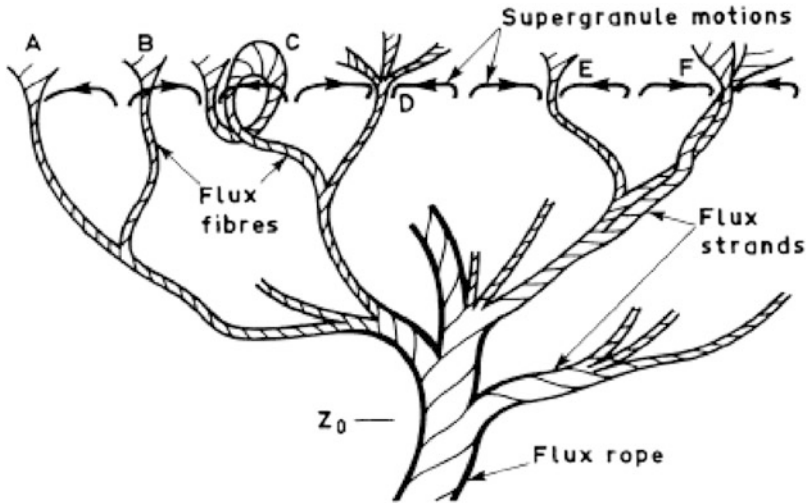


Fig. 2.2 Schematic of the main magnetic and plasma features of decaying active regions and quiet sun. The flux-rope section acts as the trunk of a tree-like structure whose main branches are flux strands. These, in turn, fray into flux fibers ($\approx 3 \times 10^{18}$ Mx) which provide the network rosettes (on disk) and bushes (at limb). These tend to be driven to the supergranular boundaries (A), but may be observed piercing the cell interior (B). The kink instability provides a loop (C). A flux fiber frays further (D) into flux threads ($\approx 3 \times 10^{17}$ Mx) which provide the photospheric filigree and chromospheric mottles. A group of fibers (E) and perhaps some flux strands (F) form a boundary and force a convective cell to turn over continuously for several days. Reprinted from Pidington (1978) by permission from Springer Science and Business Media

2.2 Elements of Theory for De Facto Flux Tubes

The theoretical approach to the origin and properties of small-scale magnetic flux tubes started to flourish only in a middle of 1970s. By that time, a decade of efforts of observers prepared a rich ground for these studies.

Parker (1974a) proposed a simple hydrodynamic mechanism associated with turbulent pumping to squeeze magnetic field into the slender tube (Fig. 2.3). He writes: “The obvious point of departure for an inquiry into the origin of intense fields in the supergranular boundaries is the well-known effect in which the outflow of fluid from the center of each supergranular sweeps the vertical component of magnetic field to the boundary.” The key element in this scheme is that the turbulent pumping of fluid downward at the supergranular boundary produces a partial vacuum within the flux tubes, just like in the water-jet vacuum pump, in which one fluid is forced along by turbulent coupling to another. In this scheme, the field is restricted by energy equipartition, $B^2/8\pi \simeq (1/2)\rho v^2$, and limits the value of the magnetic field by a maximum of about 500 G. Uncertainty in velocity fields and too low value of the magnetic field lead Parker to add yet another effect that is supposed to further concentrate the individual flux tubes, namely the Bernoulli

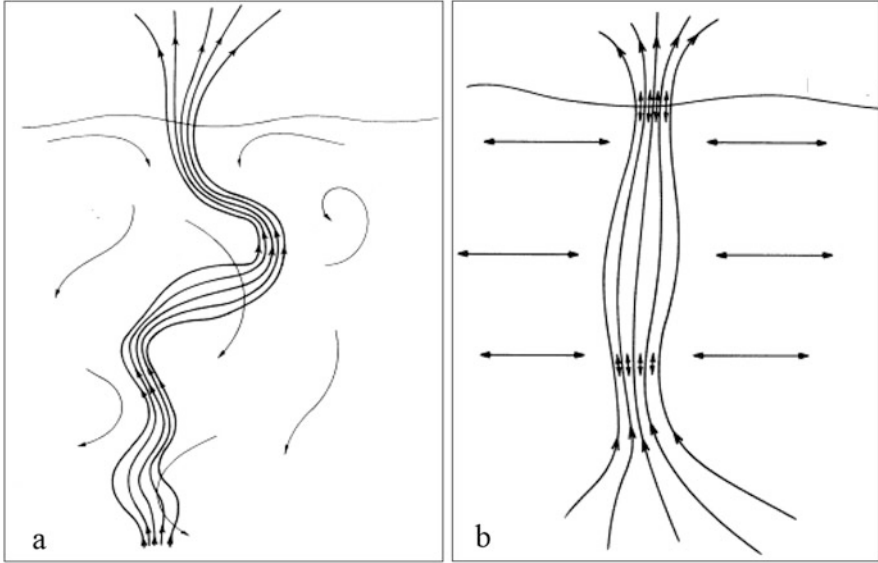


Fig. 2.3 Sketch of a magnetic flux tube extending up through the photosphere. (a) Turbulent subsiding fluid in a supergranular boundary into the tenuous chromosphere above the visible surface of the sun; (b) The magnetic field lines alternately squeezed and expanded in the turbulent convection beneath the photosphere, causing the surge up and down along the flux tube; the open ends are indicated by the short double arrows. Reprinted from Parker (1974a,b) by permission from IOP, AAS

effect. Unfortunately, this effect increases the mean magnetic field only to a fraction of the equipartition value. And Parker concludes that “we must look farther” (Parker 1974b, see also Parker 1979).

The origin of the small-scale magnetic flux tube covering the entire solar surface and making up sunspots, plagues, and active regions is still an open question.

It is therefore not surprising that the first theoretical works on fundamental properties of flux tubes were based on their de facto existence (Cram and Wilson 1975; Ryutov and Ryutova 1976; Defouw 1976; Ryutova 1977; Roberts and Webb 1978; Spruit 1981).

The basic equations employed in early attempts to study properties of magnetic flux tubes are Maxwell equations mainly in the MHD approximation:

$$\nabla \cdot \mathbf{B} = 0 \quad (2.2)$$

$$\frac{\partial \mathbf{B}}{\partial t} = \nabla \times (\mathbf{v} \times \mathbf{B}) + \eta_D \nabla^2 \mathbf{B} \quad (2.3)$$

$$\rho \frac{d\mathbf{v}}{dt} = -\nabla p + \frac{1}{4\pi} (\nabla \times \mathbf{B}) \times \mathbf{B} - \rho g(z) \quad (2.4)$$

$$\frac{d\rho}{dt} + \rho \nabla \cdot \mathbf{v} = 0 \quad (2.5)$$

$$\frac{\partial(\rho^{-\gamma} p)}{\partial t} + \mathbf{v} \nabla(\rho^{-\gamma} p) = 0 \quad (2.6)$$

where d/dt designates a full derivative ($d/dt = \partial/\partial t + \mathbf{v} \cdot \nabla$), $\eta_D = c^2/4\pi\sigma$ is magnetic diffusivity, and $\sigma = 1.96ne^2/(m_e\nu_{ei})$ is the plasma conductivity.

The magnetic flux tube, in a simple cylindrically symmetric model, may be considered as a set of magnetic field lines through some surface S bounded by the closed contour C . The lines of force are defined, in terms of $\mathbf{B}(\mathbf{r})$, as the solution of equations

$$\frac{dr}{B_r} = \frac{rd\phi}{B_\phi} = \frac{dz}{B_z} \quad (2.7)$$

Applying Gauss's theorem to (2.2) we see that the total magnetic flux across any closed surface S is zero,

$$\int_S \mathbf{B} \cdot d\mathbf{S} = 0, \quad (2.8)$$

which means that every line of force entering S must also leave, i.e., the individual lines either extend to infinity or form closed curves. It follows then that the total number of lines, i.e., the total magnetic flux through any closed contour C , is constant and can be written as

$$\Phi = \int_C \mathbf{B} \cdot d\mathbf{S} \quad (2.9)$$

which means, for example, that the strength of a flux tube increases when it narrows and decreases when it widens.

Let us now turn to question what are the requirements for the equilibrium of a flux tube. Consider the simplest case of hydrostatic equilibrium and assume that the magnetic field depends only on coordinate r , $\mathbf{B} = B(0, 0, B_z(r))$. Equation (2.4), that provides the momentum balance, is then

$$-\nabla p + \frac{1}{4\pi}(\nabla \times \mathbf{B}) \times \mathbf{B} - \rho \mathbf{g} = 0 \quad (2.10)$$

In an absence of gravity from this equation we have

$$p(r) + \frac{B_z^2(r)}{8\pi} = p_e \quad (2.11)$$

$$p(r) + \frac{B_z^2(r)}{8\pi} = p_e + \frac{B_{ze}^2(r)}{8\pi}$$

where the constant of integration, p_e , is obviously a gas pressure outside the flux tube, p_e , in case if flux tube is embedded in magnetic free environment, $p_e + B_{ze}^2/8\pi$, if the magnetic field outside flux tube is nonzero. Equations (2.11) are classical conditions for static equilibrium of magnetic flux tube.

In the presence of gravity, if it acts along the negative direction of z -axis, Eq. (2.10) gives:

$$\frac{dp}{dz} + \rho g(z) = 0 \quad (2.12)$$

Taking into account the ideal gas law, $\rho = mp/kT$ (k is Boltzmann constant) we have

$$p = p_0 \exp\left(-\int_0^z \frac{1}{\Lambda(z)} dz\right) \quad (2.13)$$

where

$$\Lambda(z) = \frac{kT}{mg} \quad (2.14)$$

is the pressure scale height. In terms of density, Eq. (2.13) becomes

$$\rho = \rho_0 \frac{T_0}{T(z)} \exp\left(-\int_0^z \frac{1}{\Lambda(z)} dz\right) \quad (2.15)$$

It is important to note that MHD equations (2.2)–(2.6) allow to study quite a limited classes of phenomena. Throughout this book, however, we will encounter the problems that will require much more elaborated approach. In each particular case, for example, such as nonlinear unsteady phenomena, dynamics of non-conservative systems, self-organized processes, and many others, we will deal with the special technique.

2.3 Numerical Visualization and Observations

One of the first exemplary models of a quasi-static flux tube was constructed numerically by Deinzer et al. (1984a,b). The full MHD equations for a compressible medium together with an energy equation were solved in two-dimensional geometry for a slender slab being in the pressure equilibrium with surrounding plasma. It was assumed that all quantities have a barometric dependence on z (cf. Eq. (2.13)).

Figure 2.4 shows an example of the numerical solution for density, magnetic field, and velocity at a time when stationary state has been evolved (half of the symmetric structure is shown). The important results obtained in this calculation are, for example, that the density is reduced inside the slab to half of the

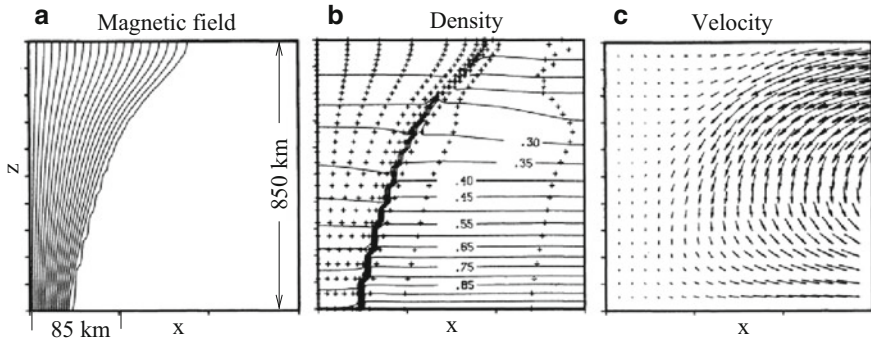


Fig. 2.4 Results of the slab modeling. **(a)** Lines of constant density normalized to $\rho_0 = 1.610^{-6} \text{ g cm}^{-3}$; the crosses indicate the location of the node points, concentrated at the edge of the slab where the steepest gradients appear. **(b)** Magnetic field lines. **(c)** Velocity field; maximum velocity is $\sim 200 \text{ m s}^{-1}$. The horizontal scale is stretched by a factor 10/3 in order to show more details of the structure. Credit: Deinzer et al. (1984a,b) reproduced with permission ESO

ambient plasma, and appearance of downflows around the magnetic slab caused by noncollinearity of the isotherms and lines of constant gravitational potential (not shown). Even these relatively early modeling (although only two-dimensional) quite adequately represent what is to be observed. The results of more advanced numerical simulations of flux tube structures and additional literature can be found, for example, in Steiner (2007). High-resolution observation with ground-based and space telescopes have allowed to study the inner structure of small-scale flux tubes and their chromospheric counterparts seen as bright points.

Figures 2.5 and 2.6 show results of the observations made with the Swedish 1-m Solar Telescope (SST) on La Palma (Scharmer et al. 2003), which may resolve the magnetic structures in the G-band 4305 \AA bandpass with 70 km resolution. Using the SST data, Berger et al. (2004) studied magnetic elements in a plage region near disk center. The SST data were complimented by a co-temporal Ca II H image, showing the network elements in low-chromosphere, and high-resolution magnetogram that resolves structures as small as 120 km with a flux sensitivity of $\simeq 130 \text{ Mx cm}^{-2}$. Figure 2.5 shows a $2.5 \times 4 \text{ Mm}$ sample region containing small-scale magnetic elements which at any moment of time fill intergranular lanes. Their lifetime is usually on the order of granular timescales ($\sim 8\text{--}10 \text{ min}$) or less. The top left panel shows G-band 4305 \AA filtergram and bottom left is magnetogram of the region. The white lines highlight a bright point across which intensities of several parameters were measured. These are shown in the right panel.

The solid curve with squares is the G-band intensity, duplicated by the Gaussian fit (dark dashed curve). The FWHM is 128 km . Also shown are plots of co-temporal and aligned data in the chromospheric Ca II H-line and 4364 \AA continuum with the corresponding magnetogram and Dopplergram signals. The peak absolute magnetic flux density is 836 Mx cm^{-2} . The peak downflow velocity measured in the Dopplergram slice is 543 m s^{-1} , displaced from the G-band peak emission by approximately 200 km on either side of the cut. This displacement of downflow

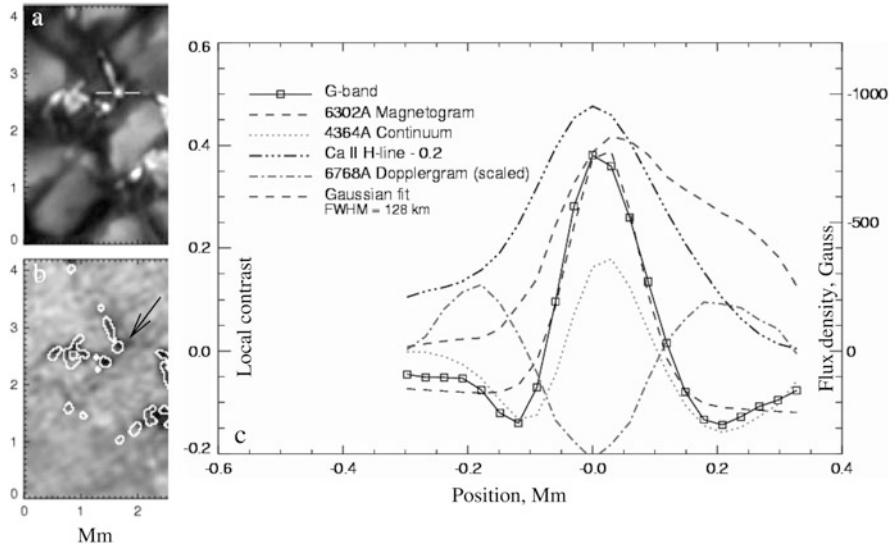


Fig. 2.5 Region containing a closely packed system of small-scale magnetic element. (a) G-band 4305 Å filtergram and (b) magnetogram. The white lines highlight a bright point across which a relative intensity profiles are shown in (c). Credit: Berger et al. (2004), reproduced with permission ESO

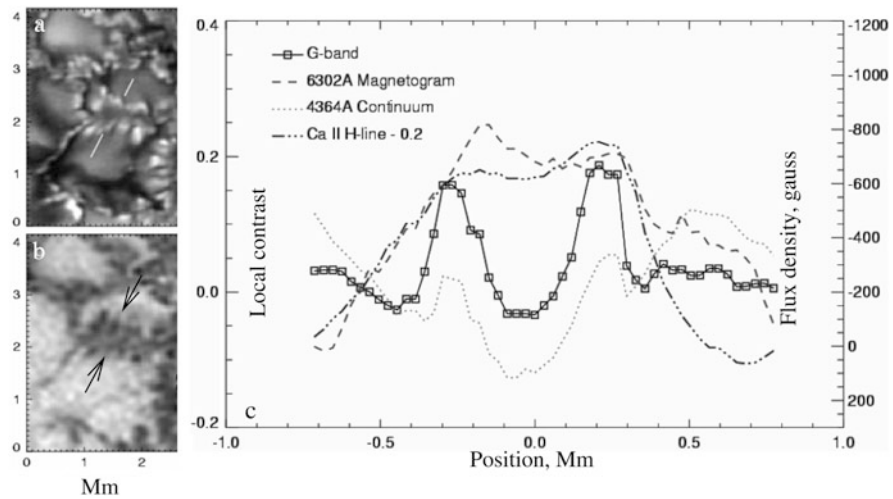


Fig. 2.6 The same as in Fig. 2.5 but for a region containing very small isolated bright point and elongated dark features. Credit: Berger et al. (2004), reproduced with permission ESO

velocity relative to the magnetic and bright point agrees well with the numerical models mentioned above (Deinzer et al. 1984a,b). This has been confirmed in more recent numerical simulations as well (e.g., Steiner et al. 1998).

Figure 2.6 is another example of the same procedure as above but for the diverging ribbon-like structure which is not resolved into individual flux tubes. The measured magnetic flux density in the ribbon structures ranges from 300 to 1500 Mx cm^{-2} .

As in the previous case, the chromospheric emission closely follows the G-band pattern and the magnetogram signal exhibits more discrete structures. The right panel shows a distinct double-peak shape in all of the emission lines indicating higher intensities and magnetic flux density at the edges of the ribbon structure. The maximum absolute-value flux density in the bright point region is 1341 Mx cm^{-2} . The magnetic flux density in the central region is also quite large, $\sim -700 \text{ Mx cm}^{-2}$, indicating that this is a complex but rather symmetric magnetic body with a darkened interior and bright walls.

This kind of structures appeared in various numerical simulations studying formation of photospheric flux tubes, pores, and light bridges (see, e.g., Steiner 2007; Jafarzadeh et al. 2013 and the literature therein). These studies are well facilitated by increasing possibilities of observations which include not only studies of individual flux tubes but their statistical properties as well.

Figure 2.7 shows an example of statistical studies performed with New Solar Telescope (NST) of Big Bear Solar Observatory. Observations were done with adaptive optics correction using TiO 7057 \AA line with 10 s time cadence (Abramenko et al. 2010). Figure 2.7 shows the probability distribution functions (PDFs) for the diameter, D , lifetime, LT , and maximum intensity, I_{max} , of bright points tracked during about 2 h period.

It was found that 98.6% of bright points live less than 120 s. The lifetime distribution function follows a log-normal approximation for all features with lifetime exceeding 100 s. The longest registered lifetime was 44 min. The size and maximum intensity of BPs were found to be proportional to their lifetimes. A majority of bright points were found to be transient events reflecting the strong

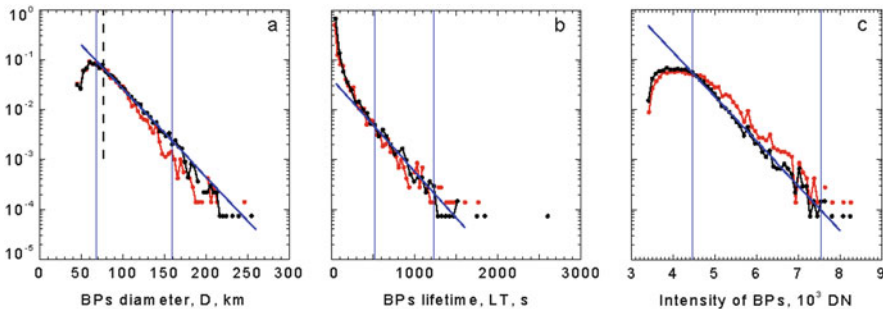


Fig. 2.7 Probability distribution functions of small-scale magnetic features: (a) diameters, (b) lifetimes, and (c) intensities. The data represent two sets of runs corresponding to lowest (black) and highest (red) threshold of intensity masks. Straight blue lines show the exponential fit showing a log-normal distribution of all the parameters. Courtesy of Abramenko, see also Abramenko et al. (2010)

dynamics of the quiet sun populated by small-scale magnetic flux tubes. The distribution function of their sizes extends to the diffraction limit of instrument, 77 km. The authors conclude that the *real minimum size of magnetic flux tubes has not yet been detected* in observations with modern high-resolution telescopes.

As a building block of the solar magnetic fields, flux tubes play a major role in all physical processes in the sun from the energy production, its transfer and release to overall global behavior of the sun. Study of these processes and the flux tubes involvement in them is the subject of this book.

2.4 Filamentary Structures in Laboratory and Universe

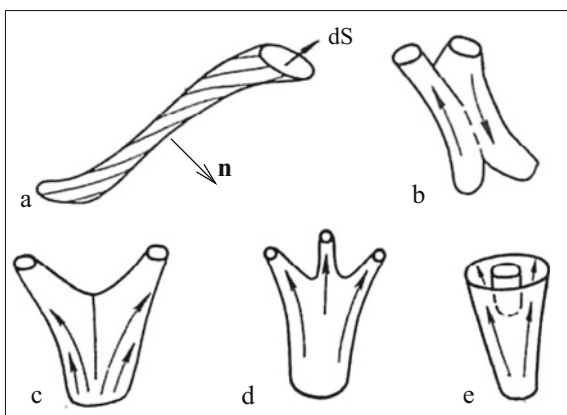
The universe consisting of ever moving elementary particles and ionized gases is pierced by inborn magnetic fields. Highly advanced observations show their ubiquitous filamentary structure. But long before this fact became evident, in studies of laboratory plasma the *concept* of magnetic flux tubes became a necessity.

Invention of tokamak and a possibility that magnetic field of the appropriate configuration could provide plasma confinement brought up the problems of plasma equilibrium and stability. This, in turn, leads to the concept of *magnetic flux tubes* (Rosenbluth and Longmire 1957; Spitzer 1958; Kadomtsev 1959). It has been realized that among the properties of the magnetic field that are needed for stable confinement of plasma, the essential role may be played by their filamentary structure (Leonovich 1965; Morozov and Solov'ev 1966; Leonovich 1966). Examples illustrating a possible configuration of flux tubes are shown in Fig. 2.8.

The concept of magnetic flux tube requires that on the surface of tube $(\mathbf{n} \cdot \mathbf{B}) = 0$, where \mathbf{n} is the normal to tube surface. Given that $\text{div}\mathbf{B} = 0$, inside flux tube magnetic flux must be conserved, $d\Phi = \mathbf{B}d\mathbf{S}$ (cf. Eqs. (2.8) and (2.9)).

Although magnetic field is divergence free, it was understood that a flux tube can branch into two or more tubes. If line of force does not branch, then it cannot

Fig. 2.8 The concept of magnetic flux tube. (a) The tube of a cross-section dS and the normal to tube surface, \mathbf{n} ; (b)–(e) Several possibilities of branching of tube which occurs at singular points having different characters (After Morozov and Solov'ev (1966))



have a beginning or an end. Hence, it was postulated that there are three classes of non-branching lines of force: (1) those that start at infinity and end at infinity; (2) those that remain in a bounded volume (closed or non-closed), and (3) field lines that originate at infinity but are trapped within a finite volume. These early studies of various magnetic field configurations and their properties form the basis for the studies of magnetic field structures and their effects on various plasmas. Since then, these studies went far beyond the tokamak devices and, along the main stream of creating energy producing devices, brought together laboratory and astrophysical plasmas.

The laboratory experiment allows one to change characteristic parameters of the object and follow a time history of the event during desired time interval. It is remarkable that the laboratory experiments that deal with targets of a spatial scale from several μm to several cm and timescales of nanoseconds and seconds can reproduce phenomena occurring in stellar coronae, galactic jets, fine structures in supernovae remnants, and solar atmosphere. Existence of a broad magnetohydrodynamic similarity (Ryutov et al. 2001; Ryutov and Remington 2007; Drake 2009) allows a direct scaling of laboratory results to astrophysical phenomena.

For the time being, a rich bank of encouraging results from laboratory experiments aimed to study the astrophysical plasma have been accumulated (Lapenta et al. 2006; Bellan 2008; Perrone et al. 2013; Brown et al. 2014).

As an example, in Fig. 2.9 we show the spheromak formation and evolution (Romero-Talamas et al. 2006), captured by a high-speed imaging system in the sustained spheromak physics experiment (SSPX) (Hooper et al. 1999; McLean et al. 2001). Spheromak is one of the topologically simplest “long-lived” configurations in form of a compact toroid. Of many applications, spheromaks can be used, for example, to study how electric currents in the plasma produce the spheromak, how it evolves, and whether it is capable of containing hot plasmas. In course of these studies it became clear that the observed regularities are often similar to phenomena observed in astrophysical plasmas, and in particular in the solar corona. Figure 2.9 shows four stages of the spheromak evolution. The plasma enters the high-speed camera field of view a few tens of microseconds after injection, and begins to balloon out of the injector gun. In about $50\mu\text{s}$ the plasma reaches the bottom of the flux conserver a column forms. This moment is shown in Fig. 2.9a. At $80\mu\text{s}$ the column acquires a kinked shape (Fig. 2.9b). Toward the end of the plasma’s lifetime, its central column becomes a collection of thin filaments and then reorganizes itself into a more regular system of filaments.

The process of filamentation and accompanying phenomena have numerous analogies, from chemistry and discharge tubes to neutron stars and supernovae. Examples of two extreme objects pierced by “thin” filaments are shown in Fig. 2.10. Top panel shows a pulsed corona discharge in atmospheric air generated between a planar high-voltage electrode and the water surface with an immersed stainless steel plate electrode. During each pulse thin glow-like filaments were formed which then propagate along the gas–liquid interface (Lukes et al. 2011). Bottom panel shows a well-defined hairy structure of #49 supernova remnant, typical to all the supernovae and their remnants.

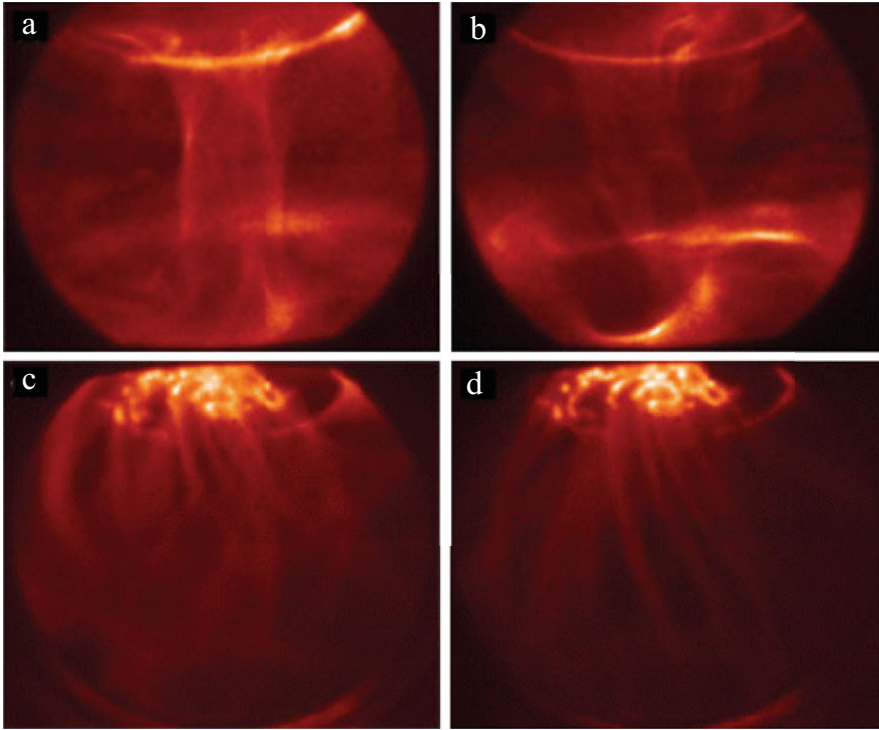


Fig. 2.9 Formation and evolution of a plasma column inside the spheromak: (a) Regime of a column formation (about $50\mu\text{s}$ after the plasma injection); (b) At $80\mu\text{s}$ the column acquires a kinked shape; (c) Regime of filamentation: central column becomes a messy collection of filaments; (d) Possible regimes of self-organization of filamentary structure (Courtesy of Harry McLean, LLNL, see also Romero-Talamas et al. (2006))

We conclude this chapter by a fascinating and known for a long time examples of filamentary structures that were predicted and discovered as macroscopic quantum phenomena.

Long before the concept of magnetic flux tubes has been introduced in a tokamak plasma, in low temperature physics filamentation of substance became a starting point in studies of amazing phenomena in superfluidity and superconductivity (Landau 1941; Onsager 1949; Feynman 1955; Abrikosov 1957). A He 4 isotope below the 2.17 K (dabbed Helium II) becomes superfluid, but in various situations, such as under action of a heat or placed in a capillary tube, behaves as a mixture of superfluid and normal components. A dual nature of Helium II is especially prominent when placed in a rotating cylinder. At some critical angular velocity there appear vortices with circulation quantized in units of h/m (h being a Planck's constant and m is the mass of the Helium atom).

By the nature the vortices are the elements of a condensate: the vortex core consists of the *normal* component, and formation of vortices transforms the

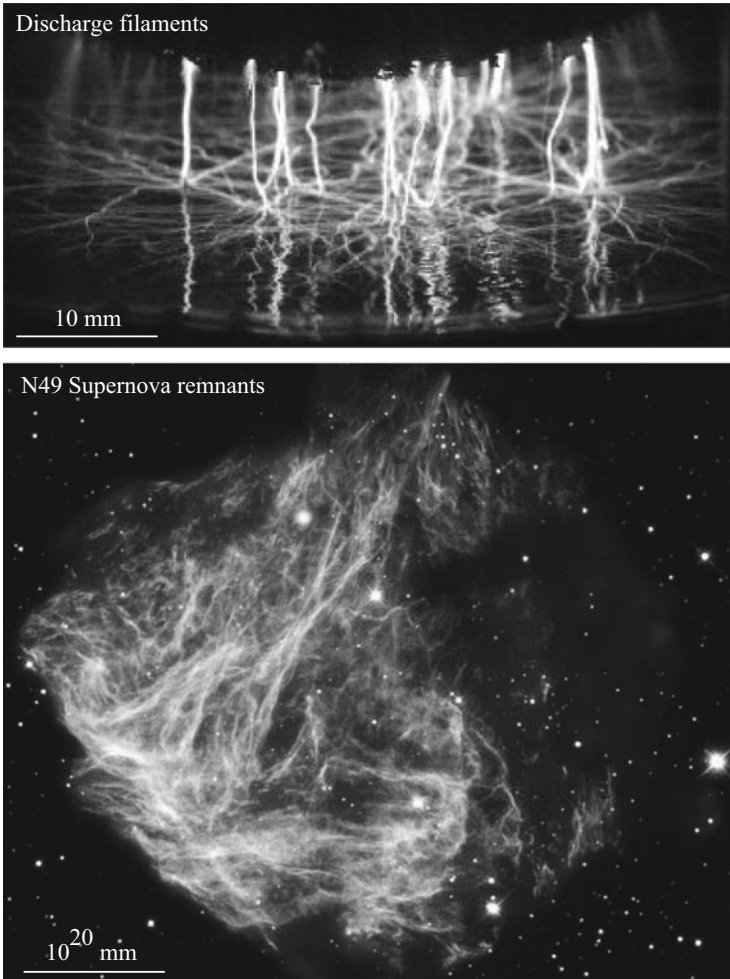


Fig. 2.10 Two extreme scales of filamentary structures. Top: The gas discharge filaments generated along the water surface (courtesy of Petr Lukes); Bottom: N49 supernova remnant located in the Large Magellanic Cloud taken by NASA's Chandra X-ray observatory (courtesy of NASA)

superfluid into the normal state. According to the theory, appearance of quantum vortices is energetically favorable. Moreover, in the established state the vortices have a minimal circulation (i.e., just h/m) and happen to form a regular lattice.

One of the first experiments demonstrating the formation of quantum vortices is shown in Fig. 2.11. One can see that with increasing the angular velocity of container there appear more and more vortices, just in agreement with theory predicting that in a container rotating at angular velocity ω , vortices should appear with a density $2\omega m/h$ (Feynman 1955). Tkachenko (1966) predicted that in equilibrium the vortices should form a triangular lattice. And they indeed do.

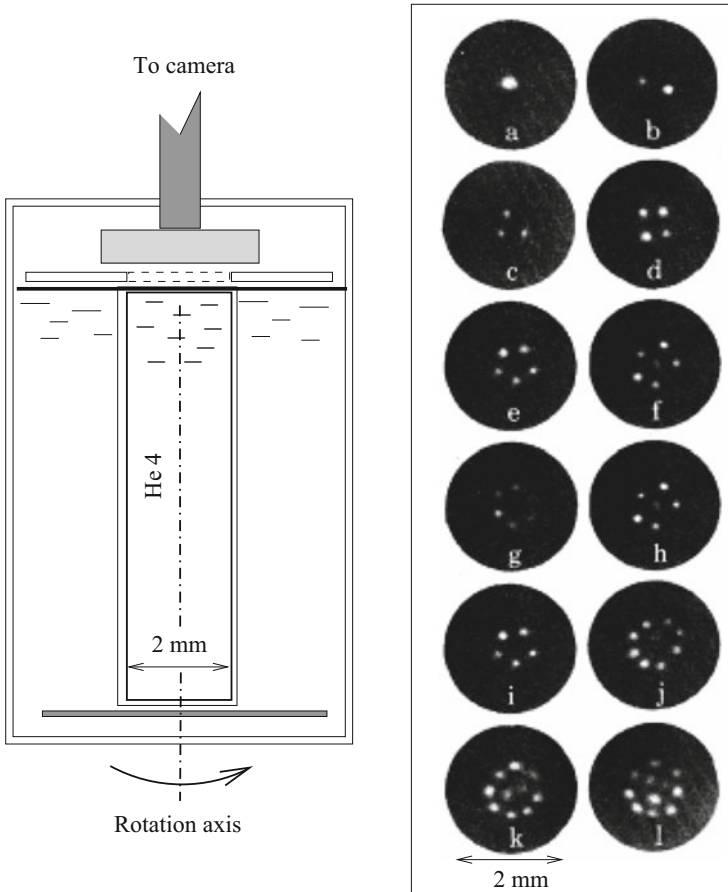


Fig. 2.11 Photographs of stable vortex arrays. Left: Schematic of the experiment. Right: Appearance of quantum vortices at different angular velocities of bucket. The diameter of the dark circles corresponds to the 2-mm bucket diameter. The angular velocities range from (a) 0.30 s^{-1} to (l) 0.59 s^{-1} with somewhat uneven intervals. Reprinted with permission from Yarmchuk et al. (1979). Copyright APS

Filamentary processes occur as well in Bose-Einstein condensates (BEC, very cold atomic gases), He-3 isotope below 0.0025, and various types of superconductors.

Metals in superconducting phase having a zero resistivity are known to expel the magnetic field. The transition from superconducting to normal state usually has a discrete quantum nature. In Type-II superconductors, for example, such a transition occurs via formation of an Angstrom size threads that carry quantized magnetic flux, Abrikosov vortices (Abrikosov 1957).

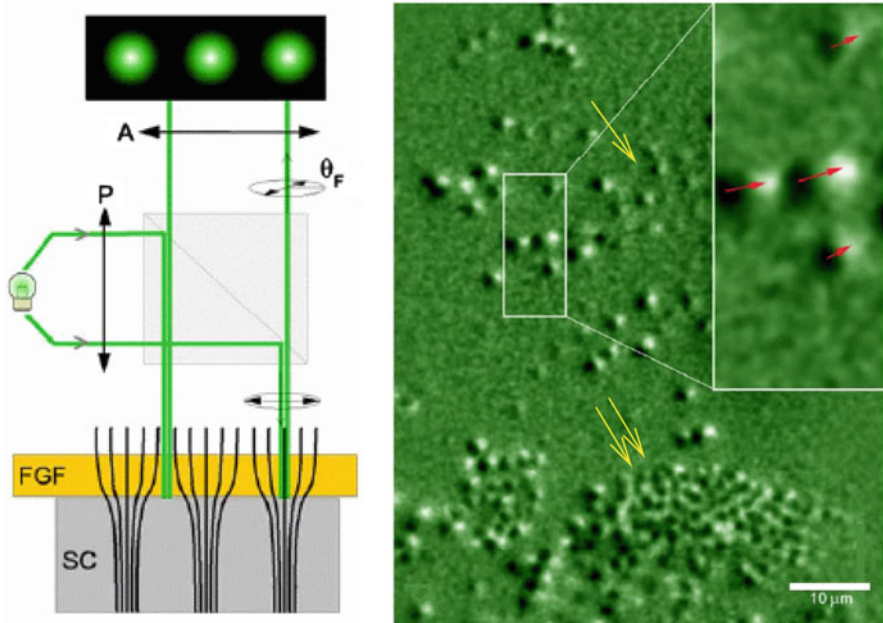


Fig. 2.12 Visualization of Abrikosov vortices and their dynamics in superconducting $NbSe_2$. Left: Schematic of the experiment setting (see text for details). Right: Magneto-optical images of vortices and their response to an increase of the applied magnetizing field by 4 mOe. The dark and bright spots represent initial and final vortex positions, respectively. The scale bar is 10 μ m. Reprinted from Goa et al. (2001) by permission from IOP Publishing

With the improved experimental technique it became possible to observe individual vortices and their dynamics. Figure 2.12 shows a real-time imaging of Abrikosov vortices in superconducting $NbSe_2$ (Goa et al. 2001).

Left panel in Fig. 2.12 shows a principle of a high-sensitivity magneto-optical (MO) imaging. The maxima of the magnetic field from vortices in a superconducting sample (SC) give maxima in the Faraday rotation F of incoming plane polarized light, which shows up in a ferrite garnet layer (FGF) near the sample. Vortices appear as bright spots when imaged using a crossed polarizer, P , and analyzer, A . Right panel shows resulted vortex dynamics during flux penetration. The image shows the change in flux distribution over a 1 s time interval after a 4 mOe increase in the applied field. The dark and bright spots represent initial and final vortex positions, respectively. Medium brightness corresponds to an unchanged flux distribution, indicating stationary vortices. The insert shows a close-up view of four vortex jumps. The arrows indicate the direction of vortex motion. Note how close is a visual resemblance between the distribution of vortices and distribution of flux tubes over the solar surface: a “filling factor” of vortices changes from very small number where they form a rarefied ensembles (white arrow) to almost unity where vortices form a dense conglomerate (double white arrows).

Vortices in superfluid Helium and superconductors, magnetic flux tubes in solar atmosphere and space, filamentation process in biology and chemistry have probably a common ground, which is to be yet established. One conclusion can be made for sure: *formation of filamentary structures in nature is energetically favorable and fundamental process.*

2.5 Problems

2.1 Is it possible to produce magnetic field configuration in which equilibrium is realized without external currents, solely by stretching the magnetic lines of force inside the equilibrium configuration? Use the energy-momentum tensor.

2.2 Show that if magnetic field confined within a closed surface S moves with plasma, then its total helicity,

$$H_m = \int_V \mathbf{A} \cdot \mathbf{B} dV \quad (2.16)$$

is an invariant of the motion only if $\mathbf{B} \cdot \mathbf{n} = 0$.

2.3 Calculate the helicity of two flux tubes linked together.

2.4 Derive validity conditions of thin flux tube approximation for static tubes.

References

- V. Abramenko et al., *Astrophys. J.* **725**, L101 (2010)
 A.A. Abrikosov, *Sov. Phys. JETP* **5**, 1174 (1957)
 H.W. Babcock, H.D. Babcock, *Astrophys. J.* **121**, 349 (1955)
 J.M. Beckers, E.H. Schröter, *Sol. Phys.* **4**, 142 (1968)
 P.M. Bellan, *Fundamentals of Plasma Physics* (Cambridge University Press, Cambridge, 2008)
 T.E. Berger, L.H.M. Rouppe van der Voort, M.G. Lfdahl et al., *Astron. Astrophys.* **428**, 613 (2004)
 M.R. Brown et al., *Micro-Physics of Cosmic Plasmas: Hierarchies of Plasma Instabilities from MHD to Kinetic* (Springer, Berlin, 2014)
 L.E. Cram, P.R. Wilson, *Solar Phys.* **41**, 313 (1975)
 R.J. Defouw, *Astrophys. J.* **209**, 266 (1976)
 W. Deinzer, G. Hensler, M. Schuessler, E. Weisshaar, *Astron. Astrophys.* **139**, 426 (1984a)
 W. Deinzer, G. Hensler, M. Schuessler, E. Weisshaar, *Astron. Astrophys.* **139**, 435 (1984b)
 R.P. Drake, *Phys. Plasmas* **16**, 5501 (2009)
 R.P. Feynman, *Progress in Low Temperature Physics*, vol. 1, Chap. 2 (Holland Publishing Co., Amsterdam, 1955)
 E.N. Frazier, J. Stenflo, *Sol. Phys.* **27**, 330 (1972)
 P.E. Goa et al., *Supercond. Sci. Technol.* **14**, 729 (2001)
 E.B. Hooper, L.D. Pearlstein, R.H. Bulmer, *Nucl. Fusion* **39**, 863 (1999)

- R. Howard, *Astrophys. J.* **130**, 193 (1959)
- R. Howard, J. Stenflo, *Sol. Phys.* **22**, 402 (1972)
- S. Jafarzadeh et al., *Astron. Astrophys.* **549**, 116 (2013)
- B.B. Kadomtsev, *Plasma Physics and the Problem of Controlled Thermonuclear Reactions*, vol. IV (Pergamon Press, New York, 1959)
- B.B. Kadomtsev, in *Reviews of Plasma Physics*, vol. 2, ed. by M.A. Leontovich (Consultants Bureau, New York, 1966), p. 153
- M.D. Kruskal, R.M. Kulsrud, *Phys. Fluids* **1**, 265 (1958)
- L.D. Landau, *J. Phys. Moscow* **5**, 71 (1941)
- G. Lapenta et al., *J. Geophys. Res.* **111**, A12S06 (2006)
- R.B. Leighton, *Astrophys. J.* **130**, 366 (1959)
- M.A. Leontovich (ed.), *Reviews of Plasma Physics*, vol. 1 (Consultants Bureau, New York, 1965)
- M.A. Leontovich (ed.), *Reviews of Plasma Physics*, vol. 2 (Consultants Bureau, New York, 1966)
- W. Livingston, *Nature* **350**, 45 (1991)
- P. Lukes, M. Clupek, V. Babicky, *IEEE Trans. Plasma Sci.* **39**, 2644 (2011)
- H.S. McLean et al., *Rev. Sci. Instrum.* **72**, 556 (2001)
- F. Meyer, H.U. Schmidt, N.O. Weiss, *Mon. Not. R. Astron. Soc.* **179**, 741 (1977)
- A.I. Morozov, L.S. Solov'ev, in *Reviews of Plasma Physics*, vol. 2, ed. by M.A. Leontovich (Consultants Bureau, New York, 1966), p. 1
- L. Onsager, *Suppl. Nuovo Cimento* **6**, 249 (1949)
- D. Papathanasoglou, *Sol. Phys.* **21**, 113 (1971)
- E. Parker, *Astrophys. J.* **189**, 563 (1974a)
- E. Parker, *Astrophys. J.* **190**, 429 (1974b)
- E. Parker, *Basic Mechanisms of Solar Activity*, IAU, ed. by V. Bumba, J. Kleczek (Oxford University Press, Oxford, 1976), p. 406
- E. Parker, *Cosmical Magnetic Fields* (Oxford University Press, Oxford, 1979)
- D. Perrone et al., *Space Sci. Rev.* **178**, 233 (2013)
- J.H. Piddington, *Astrophys. Space Sci.* **34**, 347 (1975)
- J.H. Piddington, *Astrophys. Space Sci.* **55**, 401 (1978)
- S.B. Pikel'ner, *Sov. Astron.* **6**, 757 (1963)
- B. Roberts, A.R. Webb *Sol. Phys.* **56**, 5 (1978)
- C.A. Romero-Talamas et al., *Phys. Plasmas* **13**, 2502 (2006)
- M.N. Rosenbluth, C. Longmire, *Ann. Phys.* **1**, 120 (1957)
- B. Ruiz Cobo, K.G. Puschmann, *Astrophys. J.* **745**, 141 (2012)
- D.D. Ryutov, B.A. Remington, *Astrophys. Space Sci.* **307**, 291 (2007)
- D.D. Ryutov, M.P. Ryutova, *Sov. Phys. - JETP* **43**, 491 (1976)
- D.D. Ryutov, B.A. Remington, H.F. Robey, R.P. Drake, *Phys. Plasmas* **8**, 1804 (2001)
- M.P. Ryutova, *Proceedings of XIII International Conference on Phenomena in Ionized Gases* (1977), p. 859
- M. Ryutova, T. Berger, A. Title, *Astrophys. J.* **676**, 1356 (2008)
- G. Scharmer, K. Bjelksjo, T. Korhonen, B. Lindberg, B. Petterson, in *Proceedings of SPIE in Innovative Telescopes and Instrumentation for Solar Astrophysics*, ed. by S.L. Keil, S.V. Avakyan, vol. 4853 (2003), p. 341
- A.B. Severny, *Sov. Astron.* **3**, 214 (1959)
- V.D. Shafranov, *At. Energy* **30**, 38 (1956)
- N.R. Sheeley Jr., *Astrophys. J.* **144**, 723 (1966)
- N.R. Sheeley Jr., *Sol. Phys.* **1**, 171 (1967)
- L. Spitzer, *Proceedings of the 2-nd International Conference on "Atoms for Peace"*, Geneva (1958), p. 40
- H.C. Spruit, *Astron. Astrophys.* **98**, 155 (1981)
- O. Steiner, *AIP Conference Proceedings*, vol. 919 (2007), p. 74
- O. Steiner, U. Grossmann-Doerth, M. Knoelker, M. Schuessler, *Astrophys. J.* **495**, 468 (1998)

- J. Stenflo, *Astron. Astrophys. Rev.* **21**, 66 (2013)
N.V. Steshenko, *Publ. Crimean Astrophys. Obs.* **37**, 21 (1967)
J.T. Su et al., *Astrophys. J.* **710**, 170 (2010)
V. K. Tkachenko, *Sov. Phys. JETP* **23**, 1049 (1966)
E.J. Varmchuk, M. J.V.R. Gordon, R.E. Packard, *Phys. Rev. Lett.* **43**, 214 (1979)

Chapter 3

Intrinsic Properties of Flux Tubes: Wave Phenomena



Abstract The ensembles of small-scale magnetic elements that cover 90% of the solar surface outside sunspots and active regions are embedded in highly dynamic environment. The individual flux tubes shaken by convective and interacting with the various wave trains, such as ubiquitous 5-min oscillations and magnetosonic waves, respond to these actions in various ways. First of all they are set in motion, which in a specific situation may have oscillatory character. In this chapter we shall consider conditions that are necessary for the excitation of waves propagating along the individual flux tubes, and specify their character.

3.1 Equations of Motion or How Are Tube Waves Excited

The photospheric flux tubes, constantly buffeted by convective flows and wave trains are brought into motion. The character of these motions is not a trivial question and requires detailed analysis of the flux tube behavior in a given field of flows. As flux tubes have form of long, slender cylinder, it is only natural to expect that generated motions will have an oscillatory character. We will see, however, that to successfully generate and *sustain* the oscillations *propagating* along flux tube require special conditions. If these conditions are not fulfilled the flux tube, just like a simple rope, disturbed on one end and even showing the first signs of wavy motion, quickly loses it. In other words, if not specially arranged, waves excited at one end of the rope damp out in “no time.” We will see, however, that conditions in solar atmosphere are favorable for excitation and maintenance of flux tube oscillations. Before moving to the main subject of this chapter it is tempting to see the oscillating flux tubes in action.

If we choose the photospheric flux tubes for direct illustration of oscillations, the task is challenging because flux tubes in the photosphere are aligned predominantly with the line-of-sight, and detecting their oscillations requires special decoding of the observational data (Ploner and Solanki 1997; Fujimura and Tsuneta 2009; Zlotnik et al. 2011). To see the vertical extent of flux tubes we choose for illustrative purpose the thin magnetic threads comprising prominences that are well observable at the limb.

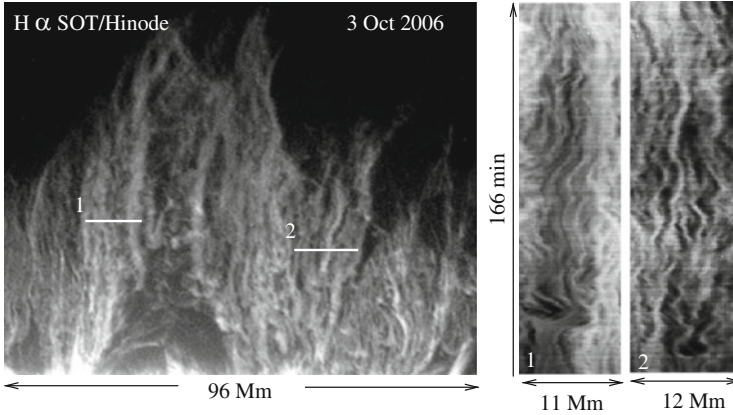


Fig. 3.1 Image of the October 3 2006 prominence taken in $H\alpha$ line by the SOT instrument on Hinode (left). Right panels show space-time images obtained from 166 min movie with 15 s cadence. Kinked oscillatory motions of elemental filaments are ubiquitous phenomena. The scale of the left panel is 1/2 of the right panels

To study a temporal variability of various small-scale formations, the special procedure, called space-time cuts, was developed for application to data compiled in movies. This procedure allows one to follow motions of all the bright and dark patches lying along the cut (straight line or circle) made on the movie snapshot. Throughout the book we will use results of this procedure many times. Figure 3.1 (left) shows a limb portion of the prominence taken on October 3 2006 in $H\alpha$ line by the SOT instrument on Hinode. Data were compiled in 166 min movie with 15 s cadence. Examples of two space-time cuts are shown by white lines marked by numbers 1 and 2. Two right panels show the results of the space-time cuts: motions of dark and bright patches lying along the cuts during 166 min time interval. One can see clear oscillatory motion in exemplary magnetic filaments.

It is important to emphasize, however, that although the kinked oscillatory motions are ubiquitous phenomena in systems of magnetic filament, not all the flux tubes are subject to regular oscillatory motions. And there must be a specific mechanism providing the conditions for excitation and, most importantly, for maintenance of propagating wave with a definite frequency and amplitude that must be specific for each individual flux tube.

Thus, the questions are:

- What makes the motion acquired by a flux tube due to its interaction with outer flows or wave trains to be a wave motion with a specific frequency and amplitude?
- Why, on the other hand, some flux tubes seemingly under the same conditions exhibit non-oscillatory motions?
- How are the physical parameters of individual flux tube and outer motions associated with final outcome?

To find answers to these basic questions we need to construct and solve the equation of motion of magnetic flux tubes in the dynamic environment. More precisely, we need to study collective phenomena in the ensembles of flux tubes interacting with outer motions and having random parameters (radius R , magnetic field, B , plasma density ρ , inclination with respect to solar surface, etc.) to see why some flux tubes are brought to oscillatory motions while others are not.

3.1.1 Equation of Motion for a Single Flux Tube

We start with the situation typical to quiet sun, i.e., when magnetic filling factor is much less than unity, $f_m = R^2/d^2$ (d is an average distance between the flux tubes), i.e.,

$$R \ll d, \quad (3.1)$$

and consider a long-wavelength limit,

$$\lambda \equiv k^{-1} \gg d. \quad (3.2)$$

As a first step we consider the motion of a separate magnetic flux tube relative to the plasma and find the force of interaction between the flux tube and the plasma. After that, by averaging over a volume containing many flux tubes (but still smaller than the wavelength λ), we obtain an expression for the volume force acting on the medium due to the ensemble of flux tubes, which subsequently allows us to write macroscopic equations for a plasma containing many magnetic flux tubes.

We take the initial direction of the flux tube as the z -axis and denote the displacement of the flux tube from its equilibrium position by a vector $\xi(z, t)$ which is transverse to the z -axis. Since the relative velocity of the plasma motion and flux tube is a first-order quantity, we can neglect the change in the size and shape of the cross section of the flux tube when evaluating the interaction force.

The equation of motion for the tube having constant circular cross section of radius R can be written as follows:

$$\rho_i \pi R^2 \frac{\partial^2 \xi}{\partial t^2} = \rho_e \pi R^2 \frac{\partial \mathbf{v}_\perp}{\partial t} + \rho_e \pi R^2 \left(\frac{\partial \mathbf{v}_\perp}{\partial t} - \frac{\partial^2 \xi}{\partial t^2} \right) + \pi R^2 \frac{B^2}{4\pi} \frac{\partial^2 \xi}{\partial z^2} \quad (3.3)$$

where \mathbf{v}_\perp is the normal component of the macroscopic velocity of the plasma, B is the magnetic field inside flux tube, and ρ_i and ρ_e are the plasma densities inside and outside flux tube, respectively. The meaning of the forces given on the right-hand side of the equation is quite simple: the first term corresponds to the Archimedes force (pushing out), acting on the tube moving in a liquid with acceleration; the second term takes into account the effect of the added mass per unit length, namely

$\pi R^2 \rho_e$ (Landau and Lifshitz 1987), also arising due to the acceleration; the third term is the effect of the magnetic tension inside the flux tube.

When using the added mass concept we assumed that the plasma is incompressible. This is valid since the velocities $\partial \xi / \partial t$ and \mathbf{v}_\perp are small compared to the sound speed while the period of the long-wave oscillations is large compared to natural periods of the radial oscillations of the flux tubes. Equation (3.3) can be written in the form

$$\frac{\partial^2 \xi}{\partial t^2} - \frac{B^2}{4\pi(\rho_i + \rho_e)} \frac{\partial^2 \xi}{\partial z^2} = \frac{2}{(1 + \rho_i/\rho_e)} \frac{\partial \mathbf{v}_\perp}{\partial t} \quad (3.4)$$

In the absence of external motions, i.e., when $\mathbf{v}_\perp = 0$, this equation describes the natural kink oscillations of the flux tube with phase speed (Ryutov and Ryutova 1976; Spruit 1981)

$$\frac{\omega}{k} = \frac{B}{\sqrt{4\pi(\rho_i + \rho_e)}} \quad (3.5)$$

It is remarkable that Eq. (3.4), which is the fundamental equation for kink oscillations of flux tube and corresponding expression for phase velocity (3.5), was first derived in such a simple way (Ryutov and Ryutova 1976). Of course, (3.4) can be derived from MHD equations as well, which will be discussed later in this chapter. It is important to note however that the equation of motion for individual flux tube only shows that the flux tube may perform the oscillations with frequency determined by its magnetic field and plasma density inside and outside it. But the equation alone does not give an answer to questions of how flux tube oscillations are excited, and what determines whether the flux tube is capable to sustain these oscillations or not. As mentioned above, for this problem we need to consider the motion of an ensemble of flux tubes randomly distributed over their parameters.

3.1.2 Macroscopic Motions of an Ensemble of Flux Tubes

To describe an ensemble of flux tubes and collective phenomena in it we have to take into account that each separate tube is characterized by its own physical parameters, radius, R , an internal plasma density, ρ_i , and temperature, T_i . For simplicity, we assume that the matter inside the flux tube is cold, $T_i \ll T_e$, and we can neglect the gas-kinetic pressure, p_i , inside the flux tubes. This assumption is not at all a principal one and can always be taken into account. Then the unperturbed state can be described by the pressure equilibrium condition:

$$\frac{B^2}{8\pi} = p_e \equiv \frac{1}{\gamma} \rho_e c_s^2 \quad (3.6)$$

where p_e is the pressure outside the flux tubes, γ is the specific heat ratio, and c_s is the sound speed.

We now introduce the dimensionless parameter

$$\eta = \frac{\rho_i}{\rho_e}, \quad (3.7)$$

which together with the tube radius, R describes the individual properties of the flux tube, which obviously may change greatly from one tube to another. So, rewriting the equation of motion (3.3) for a separate tube and henceforth labeling the displacement vector, ξ_{\perp} with the index η (emphasizing that the displacement of the tube depends on η), we have

$$\frac{\partial^2 \xi_{\eta}}{\partial t^2} - \frac{2}{\gamma} \frac{c_s^2}{(1+\eta)} \frac{\partial^2 \xi_{\eta}}{\partial z^2} = \frac{2}{1+\eta} \frac{\partial \mathbf{v}_{\perp}}{\partial t} \quad (3.8)$$

Now we proceed to the derivation of the equation for “macroscopic” quantities. By macroscopic we mean the quantities averaged over the volumes with the characteristic dimension d satisfying the inequalities (3.1) and (3.2):

$$R \ll d \ll \lambda \quad (3.9)$$

In other words, we take averages over the volumes which comprise a large number of flux tubes but are still small compared to the characteristic scale λ of variation of “macroscopic” parameters.

All the flux tubes situated in some averaging volume of the size d as in Eq. (3.9) are subject to the same external conditions (the same \mathbf{v} in (3.8)). In particular, the motion of the flux tubes with the same η in the averaging volume is just identical.

To find the macroscopic equations of motion we introduce the distribution function of flux tubes, f , with respect to the parameters R and η , and define it as follows:

$$d\alpha = f(R, \eta) dR d\eta, \quad (3.10)$$

where $d\alpha$ is the fraction of the volume which is occupied by flux tubes with values of the parameters R and η in the intervals $(R, R+dR)$, $(\eta, \eta+d\eta)$. The normalization of the function f , defined in such a way, is clearly the following:

$$\alpha = \int_0^{\infty} \int_0^{\infty} dR d\eta f(R, \eta) \quad (3.11)$$

Here α is simply the total fraction of the volume occupied by flux tubes, which simply corresponds to the magnetic filling factor of the medium. And, according to our assumption (we are considering the case of widely spaced magnetic flux tubes: $r \ll d$), $\alpha \sim R^2/d^2 \ll 1$.

It is convenient also to introduce the distribution function only over the parameter η :

$$g(\eta) = \int_0^\infty f(R, \eta) dR \quad (3.12)$$

Obviously,

$$\alpha = \int_0^\infty g(\eta) d\eta \quad (3.13)$$

From (3.3) it is clear that the force acting on the unit length of the flux tube from the side of the ambient plasma is equal to

$$\mathbf{F}_\eta = \pi R^2 \rho_e \left(2 \frac{\partial \mathbf{v}_\perp}{\partial t} - \frac{\partial^2 \boldsymbol{\xi}}{\partial t^2} \right). \quad (3.14)$$

Of course, this force is eventually produced by the momentum flux through the surface of the tube. The tube, on the other hand, acts on the ambient medium with the force $-\mathbf{F}_\eta$.

The macroscopic force $\mathbf{F}(\mathbf{r}, t)$ acting on the unit volume of the external fluid can be presented as a result of the summation of the forces $-\mathbf{F}_\eta$ (see (3.14)) over all the flux tubes occupying the averaging volume:

$$\mathbf{F}(\mathbf{r}, t) = -\rho_e \int \left[2 \frac{\partial \mathbf{v}_\perp}{\partial t} - \frac{\partial^2 \boldsymbol{\xi}}{\partial t^2} \right] g(\eta) d\eta, \quad (3.15)$$

where dependence on \mathbf{r} describes the variation of all the quantities over the volume.

The macroscopic equation of motion of the ambient plasma can now be written as

$$\rho_e \frac{\partial \mathbf{v}}{\partial t} = -c_s^2 \nabla \delta \rho_e + \mathbf{F}(\mathbf{r}, t) \quad (3.16)$$

or

$$\rho_e \frac{\partial \mathbf{v}}{\partial t} = -c_s^2 \nabla \delta \rho_e - \rho_e \int \left[2 \frac{\partial \mathbf{v}_\perp}{\partial t} - \frac{\partial^2 \boldsymbol{\xi}}{\partial t^2} \right] g(\eta) d\eta. \quad (3.17)$$

where $\delta \rho_e$ is the density perturbation of ambient plasma under the adiabatic law

$$\delta p_e = c_s^2 \delta \rho_e, \quad (3.18)$$

satisfying the continuity equation

$$\frac{\partial \rho_e}{\partial t} + \rho_e \operatorname{div} \mathbf{v} = 0 \quad (3.19)$$

In the above equations we skip the averaging sign over the macroscopic fluid velocity \mathbf{v} and macroscopic pressure perturbation δp_e .

Strictly speaking, there are additional terms of the order of α in the continuity and momentum equations: the terms which arise from the fact that the part of the averaging volume is occupied by the flux tubes. We neglect these terms because of the assumed smallness of α . If retained, these terms would give rise to the appearance of a small ($\sim\alpha$) correction of the phase velocity of sound waves. The first term in the integrand of (3.17) which after the integration over η acquires the form $-2\rho_e\partial\mathbf{v}_\perp/\partial t$ gives rise to corrections of the same order of smallness.

The role of the terms proportional to α can also be seen from the energy consideration. Indeed, multiplying (3.17) by \mathbf{v} , and taking into account (3.19) we obtain for the energy density of a plasma motion:

$$\rho_e \frac{\partial}{\partial t} \int dV \left[\frac{1}{2} \mathbf{v}^2 + \frac{1}{2} c_s^2 \left(\frac{\delta\rho_e}{\rho_e} \right) + \alpha \mathbf{v}_\perp^2 \right] = \rho_e \int dV \int g(\eta) d\eta \frac{\partial^2 \xi_\eta}{\partial t^2} \mathbf{v}_\perp \quad (3.20)$$

We see that the term containing α on the left-hand side which appeared from terms proportional to $2\partial\mathbf{v}_\perp/\partial t$ on the right-hand side of (3.17) is negligibly small. So that, accounting for this particular and analogous terms, or completely neglecting them, results in only some minor ($\sim\alpha$) redefining of the energy of fluid motion. Accordingly, when we study the energy exchange between the fluid motion and the flux tubes oscillations for the case of widely spaced flux tubes with $\alpha \ll 1$, we can omit this and analogous terms.

On the other hand, taking into account the force \mathbf{F} in (3.16), which is also of the order of α , leads to a qualitatively new effect associated with the elasticity of the flux tubes. In other words, the only term of the order of α which matters in (3.17) is that proportional to $\partial\xi_\eta^2/\partial t^2$, as this term describes the energy exchange between the oscillating flux tubes and the fluid. It is just this term that is responsible for the qualitatively new effect which consists in the Landau-like damping of the acoustic waves and transferring their energy into the energy of flux tube oscillations.

Equations (3.8) and (3.17)–(3.19) form a closet set describing large-scale, macroscopic motions of the fluid containing randomly distributed flux tubes. Note that in these motions the flux tubes behave as an ensemble, and cannot be described as an individual elements. In this sense, one can say that (3.8) and (3.17)–(3.19) describe the collective phenomena in the system of flux tubes. On the other hand, as will shall see in the next section, such an approach allows us to reveal some remarkable properties of *individual* flux tube that cannot be found without a macroscopic approach.

3.2 Absorption of Acoustic Waves: Landau Resonance

Using (3.8) and (3.17)–(3.19) we can study the interaction of the acoustic waves with an ensemble of flux tubes randomly (and widely) distributed in space and over their parameters, R , B , ρ_i , etc. Consider the eigensolutions of this set of equations in the form of traveling waves, i.e., when all perturbed quantities, ξ_η , \mathbf{v} , and $\delta\rho$, change in proportion to $\exp(-i\omega t + i\mathbf{k}\mathbf{r})$.

Using (3.8) we first express ξ_η through \mathbf{v}_\perp :

$$\xi_\eta = \frac{2i\omega\mathbf{v}_\perp}{\omega^2(1+\eta) - 2\gamma^{-1}c_s^2k^2\cos^2\theta} \quad (3.21)$$

where $k\cos\theta = k_z$ is the component of the acoustic wave vector along the flux tube, and θ is the angle between the direction of propagation of the sound wave and the flux tube axis. We consider the solution with $\text{Re } \omega > 0$. Substituting (3.21) into (3.15) we obtain

$$\mathbf{F} = i\omega\rho_e\mathbf{v}_\perp\mathcal{J}(\omega, \mathbf{k}) \quad (3.22)$$

where

$$\mathcal{J}(\omega, \mathbf{k}) = 2 \int_0^\infty \left[1 - \left(\eta + 1 - \frac{2c_s^2k^2\cos^2\theta}{(\omega + i0)^2} \right)^{-1} \right] g(\eta) d\eta \quad (3.23)$$

Obviously, as t approaches $-\infty$ the perturbations must vanish, and so we may replace ω by $\omega + i0$ in the denominator of the integrand.

The integral $\mathcal{J}(\omega, \mathbf{k})$ is of the order of α and is therefore small compared to unity. This fact allows us to easily obtain a dispersion relation. Using (3.16), (3.19) and (3.22)–(3.23), we have

$$\omega \simeq kc_s \left[1 - \frac{\sin^2\theta}{2} \mathcal{J}(\omega, \mathbf{k}) \right] \quad (3.24)$$

The effect of an ensemble of magnetic flux tubes on the oscillations of the medium enters into the problem through the integral $\mathcal{J}(\omega, \mathbf{k})$. The form of $\mathcal{J}(\omega, \mathbf{k})$ containing a resonant denominator indicates the resonance character of the interaction between the medium and the flux tubes. And the resonance condition is

$$c_s = v_{ph}\cos\theta \quad (3.25)$$

where $v_{ph} = \omega/k$ is the phase speed of flux tube oscillations (3.5). The condition (3.25) is analogous to the Cherenkov resonance condition in Landau damping theory (Landau 1946). The analogy with Landau damping is described in Appendix 1.

Thus, when condition (3.25) is satisfied, there occurs a resonant transfer of acoustic wave energy into the energy of flux tube oscillations. Since the plasma density and magnetic field are different inside different flux tubes, the phase velocity (3.5) varies from tube to tube. Thus, one can find for each angle of propagation, θ , the tubes for which the condition (3.25) is satisfied and which, therefore, remove energy from the sound wave, and maintain their own oscillatory motion.

To determine corresponding damping rate we have to evaluate $\mathcal{I}(\omega, \mathbf{k})$. To do this we can set the frequency equal to the solution of the dispersion relation for a “pure” plasma (free from flux tubes), namely $\omega = kc_s$. We must also note that taking into account the real part of \mathcal{I} leads only to an insignificant change in the frequency of the oscillations. Thus, it is sufficient to find an imaginary part of \mathcal{I} . Using the δ -function representation

$$\text{Im} \frac{1}{x + i0} = -i\pi \delta(x), \quad (3.26)$$

we find the damping rate, $\nu \equiv -\text{Im}\omega$, of the sound wave,

$$\nu = \frac{kc_s \sin^2 \theta}{2} \text{Im} \mathcal{I}(\omega, \mathbf{k}), \quad (3.27)$$

to be

$$\nu = \begin{cases} \pi kc_s \sin^2 \theta g(\eta), & \eta_0 > 0 \\ 0 & \eta_0 < 0 \end{cases} \quad (3.28)$$

where

$$\eta_0 = \frac{2\cos^2 \theta}{\gamma} - 1 \quad (3.29)$$

One could arrive to the same result by a more formal method, considering the solution of the Cauchy problem for the set (3.8)–(3.19) and using a Laplace transform—exactly in the same way as is done by Landau (1946) studying Langmuir oscillations in a rarefied plasma.

A sketch of the function $g(\eta)$, which according to our basic assumptions is a smooth broad function of flux tube parameters, is shown in Fig. 3.2. Here, $\Delta\eta$ is the width of the distribution function, i.e., the interval of parameters of all flux tubes, $\Delta\eta \gg \text{Im}\omega/\omega = \nu/\omega$, and $\delta\eta$ is the interval of resonant flux tubes, such that $\delta\eta \sim \alpha \ll \Delta\eta$. If we make the natural assumption that the plasma density inside the flux tubes, ρ_i , changes with respect to the surrounding density, ρ_e , by not more than several times from one tube to another, we can conclude that the width, $\Delta\eta$, of that region of η -values where the distribution function is essentially nonzero, is of the order of unity, then we have $g(\eta_0) \simeq \alpha$. This allows us to write the following

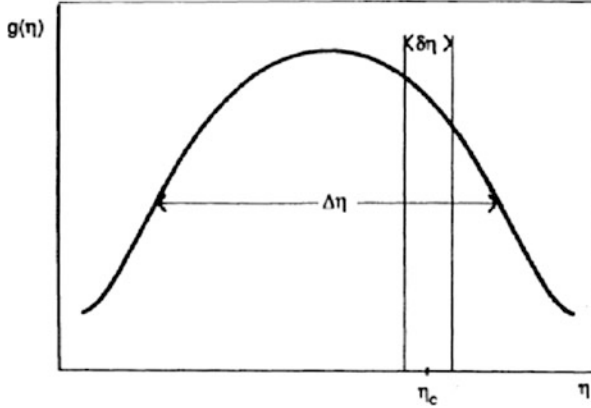


Fig. 3.2 Sketch of the distribution function of flux tubes, $g(\eta)$, as a function of the ratio of internal and external densities of the tubes, $\eta = \rho_i/\rho_e$

estimate for the damping rate

$$\frac{\nu}{kc_s} \simeq \alpha. \quad (3.30)$$

This estimate holds only for a rather narrow range of values of θ where $\eta_0 > 0$, that is, where

$$\cos^2\theta > \frac{\gamma}{2} \quad (3.31)$$

For a monatomic gas the corresponding region is about $\theta \leq \arccos(5/6)^{1/2} \simeq -5^\circ$. This restriction comes from the condition $\eta_0 > 0$ merely because of the approximation (3.6). If we remove this restriction and take into account plasma pressure inside the flux tube, then instead of (3.23), we find

$$\mathcal{I}(\omega, \mathbf{k}) = 2 \int_0^\infty d\eta dv_A g(\eta, v_A) \left[1 - \frac{\omega^2}{(1 + \eta)[(\omega + i0)^2 + c_k^2 k^2 \cos^2\theta]} \right] \quad (3.32)$$

Here v_A is the Alfvén velocity inside flux tube

$$v_A = \frac{B}{\sqrt{4\pi\rho_i}} \quad (3.33)$$

The essential difference between this result and (3.23) is that now there is no evident restriction on the propagation angle: an integration over the parameter η gives directly the Cherenkov condition for arbitrary values of parameter η and angle θ .

3.3 Effects of Noncollinearity of Flux Tubes

It is hard to imagine that magnetic flux tubes, embedded in highly dynamic environment, stay parallel to each other. Obviously, each flux tube has its own (and arbitrary) inclination with respect to surface, which means that flux tubes are essentially noncollinear. This fact turned to be very important in their interaction with the ambient atmosphere and leads to some striking effects in their dynamics.

To take into account noncollinearity of the flux tubes let us characterize the direction of a separate flux tube by a single vector \mathbf{n} directed along the flux tube axis. Denote the distribution function of flux tubes with respect to their directions by $h(\mathbf{n})$. To single out the effect of noncollinearity of the flux tubes we assume in these calculations that the parameter η is fixed. The normalization of the function $h(\mathbf{n})$ is

$$\alpha = \int h(\mathbf{n}) d\omega \quad (3.34)$$

where α is again the magnetic filling factor and $d\omega$ is an element of solid angle. The component of the macroscopic velocity at right angles to the vector \mathbf{n} is equal to $\mathbf{v} - \mathbf{n}(\mathbf{nv})$. We have thus instead of (8)

$$\xi_{\mathbf{n}} = -\frac{2i\omega[\mathbf{v} - \mathbf{n}(\mathbf{nv})]}{\omega^2(1 + \eta) - 2\gamma^{-1}c_s^2(\mathbf{kn})^2} \quad (3.35)$$

We have labeled here the displacement ξ by the index \mathbf{n} , to reflect dependence of ξ on the orientation of the flux tube.

The volume force acting on the plasma can by analogy with (3.22) be written as

$$F_i = -i\omega\rho_e K_{ij} v_j \quad (3.36)$$

where

$$K_{ij} = -2 \int d\omega h(\mathbf{n})(\delta_{ij} - n_i n_j) \left[1 - \left(\eta + 1 - \frac{2c_s^2(\mathbf{kn})^2}{\gamma(\omega + i0)^2} \right)^{-1} \right] \quad (3.37)$$

Once we have the expression for the force we can use (3.16)–(3.19) to write down the dispersion relation

$$\omega = kc_{se} \left[1 - \frac{k_i k_j}{k^2} K_{ij}(\omega, \mathbf{k}) \right], \quad (3.38)$$

and, bearing in mind that K_{ij} is small, find the small imaginary correction to the frequency:

$$\frac{\nu}{kc_s} = \int d\text{oh}(\mathbf{n}) \left[1 - \frac{(\mathbf{kn})^2}{k^2} \right] \delta \left[\eta + 1 - \frac{2(\mathbf{kn})^2}{\gamma k^2} \right] \quad (3.39)$$

In the particular case of an isotropic distribution of flux tubes we have $h(\mathbf{n}) = \alpha/4\pi$, and the expression for the damping rate is especially simple

$$\frac{\nu}{kc_s} = \frac{\sqrt{2} \alpha \gamma [2 - \gamma(1 - \eta)]}{8 \sqrt{\gamma(1 + \eta)}} \quad (3.40)$$

where we assumed that $\eta < 2/\gamma - 1$.

Thus, the contribution of noncollinearity of flux tubes into the process of absorption of sound waves and accumulation of their energy is quite essential. The more the tubes deviate from the vertical direction, the more efficient the absorption of sound waves becomes.

The fact that magnetic flux tubes are noncollinear plays an essential role in the interaction of neighboring flux tubes, namely allowing the reconnection between the *same* polarity magnetic flux tubes that leads to farther fragmentation of flux tubes and other macroscopic effects that are observed. These will be addressed in the following chapters.

3.4 Exact Theory of Linear Oscillations of Magnetic Flux Tube

The linearized set of MHD equations for the plasma *inside* the magnetic flux tube has the form

$$\rho_i \frac{\partial \mathbf{v}}{\partial t} = \frac{1}{4\pi} [(\nabla \times \mathbf{b}) \times \mathbf{B}], \quad \frac{\partial \mathbf{b}}{\partial t} = \nabla[\mathbf{v} \times \mathbf{B}], \quad (3.41)$$

where \mathbf{v} and \mathbf{b} are the perturbations of velocity and magnetic field, respectively. As the gas kinetic pressure inside the flux tubes vanishes the equation of continuity splits off.

In cylindrical coordinates (r, ϕ, z) with a z -axis directed along the flux tube, the linearized MHD equations with perturbations proportional to $\exp(-i\omega t + ik_z z + im\phi)$ imply that the velocity components inside the flux tube are as follows:

$$v_r = -\frac{\partial \psi_i}{\partial r}, \quad v_\phi = -\frac{im\psi_i}{r}, \quad v_z = 0 \quad (3.42)$$

where $m = 0, \pm 1, \pm 2, \pm 3, \pm 4, \dots$, and ψ_i satisfies the equation

$$\frac{1}{r} \frac{\partial}{\partial r} r \frac{\partial \psi_i}{\partial r} + \left(\frac{\omega^2}{v_A^2} - k_z^2 - \frac{m^2}{r^2} \right) \psi_i = 0 \quad (3.43)$$

In the non-magnetized region outside flux tube the linearized set of equations can also be reduced to a single equation for the velocity potential ψ_e ($\mathbf{v}_e = \nabla \psi_e$):

$$\frac{1}{r} \frac{\partial}{\partial r} r \frac{\partial \psi_e}{\partial r} + \left(\frac{\omega^2}{c_s^2} - k_z^2 - \frac{m^2}{r^2} \right) \psi_e = 0 \quad (3.44)$$

The perturbation of gas-kinetic pressure in terms of ψ_e is then

$$\delta p_e = \frac{i c_s^2}{\omega \gamma} \rho_e \Delta \psi_e \quad (3.45)$$

The external sound speed and Alfvén velocity are connected through the relation (cf. (3.6))

$$v_A^2 = \frac{2}{\gamma \eta} c_s^2. \quad (3.46)$$

On the surface of flux tube, at $r = R$, we must satisfy the conditions for the continuity of the normal components of velocity and total pressure,

$$v_r|_i = v_r|_e, \quad \frac{B b_z}{4\pi} = \delta p_e \quad (3.47)$$

Using (3.42)–(3.46) we can reduce the set of boundary conditions to a single equation for the logarithmic derivatives of ψ_i and ψ_e :

$$\left(\eta - \frac{2 k_z^2 c_s^2}{\omega^2} \right) \frac{\partial \ln \psi_e}{\partial r} = \frac{\partial \ln \psi_i}{\partial r} \quad \text{at } r = R \quad (3.48)$$

Inside the flux tube the solution is proportional to an m th order Bessel function $\psi_i \sim J_m(q_i, r)$, where $q_i = (\omega^2/v_A^2 - k_z^2)^{1/2}$. Outside the flux tube the solution has the form of outgoing waves: $\psi \sim H_m^{(1)}(q_e r)$, where $H^{(1)}$ is a first-order, and $q_e = (\omega^2/c_s^2 - k_z^2)^{1/2}$ (we have chosen the branch of the root corresponding to $\text{Re } q_e > 0$).

Since we are considering long-wave oscillations with $k_z R \ll 1$, the arguments of the Bessel and Hankel functions in the boundary condition (3.48) are small compared to unity. If we retain only the first nonvanishing terms in the expansion

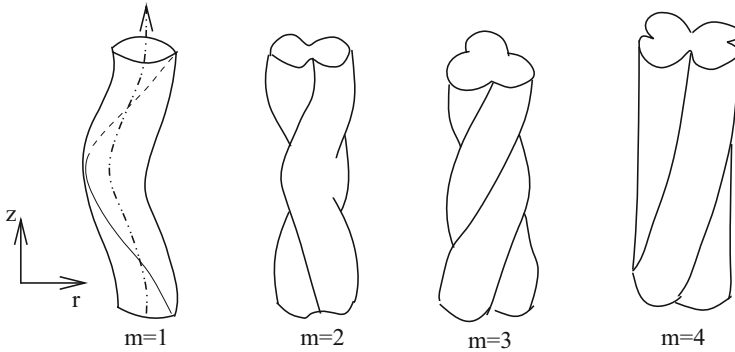


Fig. 3.3 Shape of the flux tube for various $m \neq 0$ modes

with respect to this small parameter we obtain the following dispersion relation:

$$\omega_m = \Omega \equiv k_z c_s^2 \sqrt{\frac{2}{\gamma(1+\eta)}} \quad (3.49)$$

for $m = \pm 1, \pm 2, \pm 3, \pm 4, \dots$. It is only natural that the oscillations of flux tubes may have multiple azimuthal modes. The first four modes (except $m = 0$) are shown in Fig. 3.3.

The dipole mode $m = \pm 1$ corresponds to kink oscillations of flux tube. Note that eigenfrequencies of all the modes are independent of the azimuthal number, m , and are the same, except for axisymmetric mode $m = 0$. This case requires separate consideration and will be addressed in Sect. 3.7.

Although the frequencies of all the modes are the same, their *amplitudes* and *damping rates* are quite different and strongly depend on the mode number. The oscillation amplitude in the vicinity of flux tube is proportional to $(kR)^{|m|}$, and progressively diminishing for higher order modes.

3.5 Radiation of Secondary Waves by Oscillating Flux Tubes

So far, considering the equation of motion of a separate flux tube (see (3.8)), we have neglected the compressibility of the medium surrounding the flux tube. This was justified by the smallness of the frequency of oscillations $\omega = kc_s$ as compared to c_s/R . Taking compressibility into account, i.e., higher-order terms in the parameter $\omega R/c_s \sim kR$ leads to the appearance of a new effect, namely to the radiation of secondary acoustic or MHD waves by the oscillating flux tubes.

If we retain in the boundary condition (3.48) the next order term in powers of kR , it leads, on the one hand, to a small change in the real part of the frequency and, on

the other hand, to the appearance of radiative damping of oscillations. The resulting damping rate $\nu_{\text{rad}}^{|m|}$ has following form

$$\nu_{\text{rad}}^{|m|} = \frac{\pi \Omega}{|m|!(|m| - 1)!(1 + \eta)} \left(\frac{Rk_z}{2} \right)^{2|m|} \left[\frac{2}{\gamma(1 + \eta)} - 1 \right]^{|m|} \quad (3.50)$$

Thus an oscillating flux tube may radiate secondary acoustic waves. The frequency of radiated waves is obviously the same as frequency of natural oscillations of flux tube. The corresponding radial wave number k_r is determined from the dispersion relation and is

$$k_r = \frac{(\omega^2 - k^2 c_s^2)^{1/2}}{c_s}, \quad (3.51)$$

Radiation of secondary waves occurs only if k_r is real, that is, if the phase velocity (ω/k) of flux tube oscillations is larger than c_s . For the kink mode, for example, the radiative damping rate is

$$\nu_{\text{rad}} = \frac{\pi \Omega}{(1 + \eta)} \left(\frac{Rk_z}{2} \right)^2 \left[\frac{2}{\gamma(1 + \eta)} - 1 \right] \quad (3.52)$$

The ability of flux tube to radiate the secondary acoustic or MHD waves provides one of the most important mechanisms of energy transfer from primary acoustic waves and convective motions to overlying atmosphere. Indeed, as was shown in previous sections the resonant flux tubes absorb the energy of a sound wave in a time

$$\tau_{\text{res}} \simeq \frac{1}{\nu_{\text{res}}}, \quad (3.53)$$

where $\nu \simeq \alpha k c_s$ (see (3.30) and (3.40)).

The absorbed energy is accumulated in flux tubes in the form of their natural oscillations, and then, after a considerably longer time

$$\tau_{\text{rad}} \simeq \frac{1}{\nu_{\text{rad}}}, \quad (3.54)$$

the flux tube releases the accumulated energy in the form of secondary acoustic waves, or secondary MHD waves if the surrounding plasma is magnetized.

The main condition for the above process to take place is as follows:

$$\nu_{\text{res}} > \nu_{\text{rad}}, \quad (3.55)$$

Since $\nu_{\text{res}} \simeq \omega \alpha$ and $\nu_{\text{rad}} \simeq \omega k^2 R^2$, the condition (3.55) is satisfied if $k^2 R^2 < \alpha$. Bearing in mind that the distance, d between flux tubes is of the order of R/α , we

can write that $kd \ll 1$. In other words, under the conditions when a macroscopic description of widely spaced flux tubes is applicable ($k \ll d^{-1}$), the condition (3.55) is satisfied automatically. On the other hand, these are typical conditions for quiet sun regions and rarefied plages.

3.6 Scattering of Acoustic Waves and Maximum Energy Input

The process of energy transfer to the medium can also occur without preliminary accumulation of energy in the form of flux tube oscillations. Depending on the parameters of the medium, the interaction between the primary sound wave and an ensemble of flux tubes may have a character of resonant scattering.

Suppose a plane acoustic wave, $\omega = kc_s$, is propagating with unit amplitude

$$\chi = -\frac{1}{2}\exp(-i\omega t + i\mathbf{k}\mathbf{r}) + \text{c.c.}, \quad (3.56)$$

c.c. stands for complex conjugate. In the presence of a magnetic flux tube the solution outside flux tube will be superposition of this plane wave and outgoing cylindrical waves:

$$\psi_e = e^{-i\omega t + ik_z z} \left[-\frac{1}{2}e^{-iq_e r \cos\phi} + \sum_{m=-\infty}^{\infty} A_m H_m^{(1)}(q_e r) e^{im\phi} \right] + \text{c.c.} \quad (3.57)$$

where we have used the relation $\mathbf{k}\mathbf{r} = k_z z + q_e r \cos\phi$.

Inside the flux tube the solution has the form

$$\psi_i = e^{-i\omega t + ik_z z} \sum_{m=-\infty}^{\infty} B_m J_m(q_i r) e^{im\phi} + \text{c.c.} \quad (3.58)$$

Using the identity

$$e^{iq_e r \cos\phi} \equiv \sum_{m=-\infty}^{\infty} i^m J_m(q_e r) e^{im\phi} + \text{c.c.} \quad (3.59)$$

and writing down the boundary condition (3.48) for each azimuthal harmonic m we obtain the following expression for the coefficients A_m :

$$A_m = -\frac{i^m}{2} \frac{\tilde{\eta} q_i J'_m(q_i R) J_m(q_e R) - q_e J'_m(q_e R) J_m(q_i R)}{\tilde{\eta} q_e H_m^{(1)'}(q_e R) J_m(q_i R) - q_i J'_m(q_i R) H_m^{(1)}(q_i R)} \quad (3.60)$$

where $\tilde{\eta} = \eta - 2k_z^2 c_s^2 / \gamma \omega^2$.

For long-wave oscillations with $kR \ll 1$ and $m > 0$, A_m reduces to

$$A_m = -\frac{\pi i^{|m|-1}}{|m|!(|m|-1)!(1+\eta)} \left(\frac{kR \sin\theta}{2}\right)^{2|m|} \frac{\Omega}{\omega - \Omega + i v_{\text{rad}}^{|m|}} \quad (3.61)$$

where $\Omega(\eta)$ is given by (3.49).

The power radiated in the m -th mode per unit length of the flux tube is $2\pi\rho Q_m$, where Q_m is the density of radiated energy flux

$$Q_m = |A_m|^2 \frac{\rho c_s k}{\pi r} \quad (3.62)$$

The energy density, W in the incident acoustic wave is $\rho\omega^2 c_s^2/2$. Now we can find relation between this energy and the energy, Q , of the secondary waves radiated per unit time and per unit length of the flux tube to be

$$Q = \zeta(\eta, R, \omega) W \quad (3.63)$$

where

$$\zeta = \zeta_0 + 2 \sum_{m=1}^{\infty} \zeta_m \quad (3.64)$$

with the coefficients ζ_0 and ζ_m obtained from (3.5) and (3.50) as

$$\zeta_0 = \frac{c_s^2}{k} \frac{\pi^2}{16} (kR)^2 \left(\sin^2\theta - \frac{\gamma}{2}\right), \quad (3.65)$$

$$\zeta_m = \frac{c_s^2}{k} \left[\frac{\pi}{|m|!(|m|-1)!(1+\eta)} \right]^2 \left(\frac{kR \sin\theta}{2}\right)^{4|m|} \frac{\Omega^2}{(\omega - \Omega)^2 + (v_{\text{rad}}^{|m|})^2} \quad (3.66)$$

In these expressions $\Omega(\eta)$ and $v_{\text{rad}}^{|m|}$ are determined by (3.49) and (3.50), respectively, and $\cos\theta = k_z/k$.

Equations (3.63)–(3.66) solve the problem of energy input to the medium due to the radiation of secondary waves by a single oscillating flux tube.

3.7 Axisymmetric Oscillations of Flux Tube

3.7.1 Types of $m = 0$ Mode

Axisymmetric oscillations of flux tube have their own peculiarities and should be considered separately (Cram and Wilson 1975; Defouw 1976; Roberts and Webb 1978; Ryutova 1981).

There are three types of axisymmetric modes with $m = 0$ (Fig. 3.4):

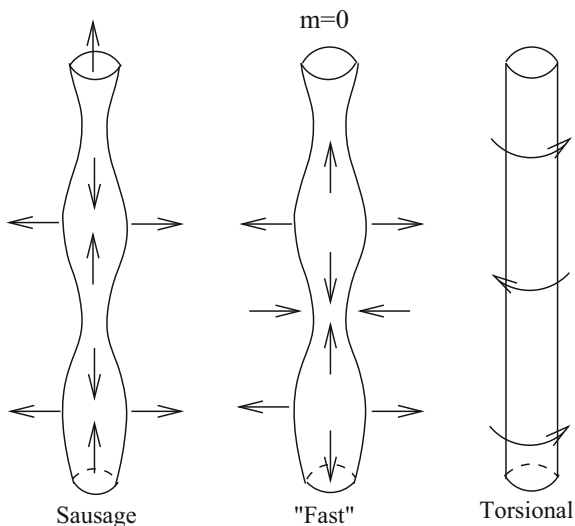
1. The analogue of slow magnetosonic waves, so-called sausage or tube waves with the phase velocity

$$c_T = \frac{\omega}{k} = \frac{c_s v_A}{\sqrt{c_s^2 + v_A^2}}; \quad (3.67)$$

These are quasi-longitudinal waves propagating along the flux tube in such a way that a compression (expansion) of a plasma inside flux tube is compensated by the decrease (increase) in the longitudinal magnetic field due to a corresponding change of the tube cross section. So that the sum of gas-kinetic and magnetic pressure in linear approximation is unperturbed, $\delta p_i + B\delta B/4\pi = 0$;

2. The high frequency fast oscillations analogous to fast magnetosonic waves with phase velocity $\sim \sqrt{c_s^2 + v_A^2}$. Because of high frequency which is of the order v_A/R , excitation of this mode is difficult. Besides, it experiences strong radiative damping.

Fig. 3.4 Types of axisymmetric oscillations of flux tube with azimuthal wave number $m = 0$



3. Torsional oscillations which are actually pure Alfvén waves. These are transverse incompressible waves. In their presence neither the tube boundary nor the surrounding plasma is disturbed. Besides, their amplitude is very small, $\sim v_{\text{conv}} R/L_{\text{conv}}$, where v_{conv} is characteristic velocity in the convective zone, and L is the convective cell size. Thus these waves have too insignificant influence on the dynamics and energy production processes.

Thus the main candidate out of these three axisymmetric tube waves is the sausage mode.

3.7.2 Equation of Motion for Sausage Oscillations

The main feature of sausage oscillations, as mentioned above, is that the total pressure, $P = p + B^2/4\pi$, remains unperturbed, i.e.:

$$\delta P = \delta p + \frac{\mathbf{b}\mathbf{B}}{4\pi} = 0 \quad (3.68)$$

Thus, in linear approximation the compression or expansion of a flux tube and the perturbations of plasma and magnetic pressure are uniform. This fact leads to quite specific features of the sausage oscillations absent in higher mode tube waves.

To observe their features we consider axially symmetric flux tube being uniform along its length, and use cylindrical coordinates (r, ϕ, z) with the z -axis directed along the unperturbed magnetic field. In other words, we assume that the unperturbed density ρ , the gas-kinetic pressure p , and the magnetic field $\mathbf{B}(0, 0, B)$ depend on r . As the magnetic field inside flux tube is much stronger than outside, we shall consider the flux tube environment magnetic-free.

We adopt the model flux tube shown in Fig. 3.5 and assume that the magnetic field decreases smoothly from a maximum value on the axis of the flux tube to zero as $r \rightarrow \infty$, and that the plasma density and pressure are also smooth functions of r .

Let us bring again the linearized set of MHD equations written in a form

$$\rho \frac{\partial \mathbf{v}}{\partial t} = -\nabla \delta p + \frac{1}{4\pi} [\nabla \times \mathbf{b}] \times \mathbf{B} \quad (3.69)$$

$$\frac{\partial \mathbf{b}}{\partial t} = \nabla \times [\mathbf{v} \times \mathbf{B}] \quad (3.70)$$

$$\frac{\partial \delta \rho}{\partial t} + \text{div} \rho \mathbf{v} = 0 \quad (3.71)$$

$$\frac{\partial \delta S}{\partial t} + \mathbf{v} \nabla S = 0 \quad (3.72)$$

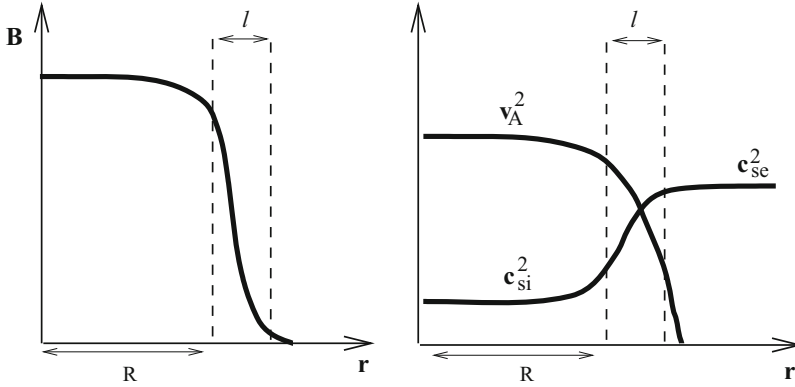


Fig. 3.5 Sketch of smooth parameter profiles of inhomogeneous flux tube with the sharp inhomogeneity confined near the tube boundary of the width $\sim l$

where $S = \rho^{-\gamma} p$ is the entropy measure, and \mathbf{v} , \mathbf{b} , $\delta\rho$, δp , and are the perturbed quantities, of the velocity, magnetic field, plasma density, and gas kinetic pressure,

$$\delta S = \rho^{-\gamma} \delta p + \gamma \rho^{-\gamma-1} S \delta \rho \quad (3.73)$$

For perturbations independent of ϕ and proportional to $\exp(-i\omega t + ikz)$, (3.69) gives

$$-i\omega\rho \left(1 - \frac{k^2 v_A^2}{\omega^2}\right) v_r = -\frac{\partial}{\partial r} \left(\delta p + \frac{b_z B}{4\pi}\right), \quad (3.74)$$

$$-i\omega\rho v_z = \frac{b_r}{4\pi} \frac{\partial B}{\partial r} - ik\delta p. \quad (3.75)$$

From (3.70),

$$b_r = -\frac{kB}{\omega} v_r, \quad b_z = \frac{1}{i\omega} \frac{1}{r} \frac{\partial}{\partial r} (r v_r B), \quad (3.76)$$

and Eqs. (3.71)–(3.73) take the form

$$-i\omega\delta\rho + \frac{1}{r} \frac{\partial}{\partial r} r\rho v_r + ik\rho v_z = 0, \quad (3.77)$$

$$\delta p - \gamma \frac{p}{\rho} \delta\rho = \frac{v_r}{i\omega} \left(\frac{\partial p}{\partial r} - \gamma \frac{p}{\rho} \frac{\partial \rho}{\partial r}\right). \quad (3.78)$$

Eliminating from last two equations $\delta\rho$ we get the equation for δp expressed through velocity perturbations. Now we substitute obtained expression for δp into (3.75) to obtain the following equation:

$$-i\omega\rho v_z = -\frac{k}{\omega}v_r\frac{\partial}{\partial r}\left(\frac{B^2}{4\pi} + p\right) - \frac{k}{\omega}\gamma p\left(\frac{1}{r}\frac{\partial}{\partial r}rv_r + i\omega kz\right) \quad (3.79)$$

The first term on the right-hand side vanishes due to the flux tube equilibrium condition, (3.68), and (3.79) takes the form

$$i\omega\left(1 - \frac{k^2c_{si}^2}{\omega^2}\right)v_z = \frac{kc_{si}^2}{\omega}\frac{1}{r}\frac{\partial}{\partial r}rv_r \quad (3.80)$$

In order to obtain the equation for v_r , we need to express the right-hand side of (3.74) through velocity perturbations. From (3.76)–(3.78) and (3.68) we have

$$\delta p + \frac{b_z B}{4\pi} = \rho\frac{c_{si}^2 + v_A^2}{i\omega}\frac{v_r}{r} + \frac{c_{si}^2}{\omega}k\rho v_z \quad (3.81)$$

Substituting here the expression for v_z from (3.80) we obtain

$$\delta p + \frac{b_z B}{4\pi} = \frac{\rho}{i\omega}\frac{\omega^2(c_{si}^2 + v_A^2) - k^2c_{si}^2v_A^2}{\omega^2 - k^2c_{si}^2}\frac{1}{r}\frac{\partial}{\partial r}rv_r, \quad (3.82)$$

and finally the equation for radial velocity perturbation takes the form

$$\frac{\partial}{\partial r}\rho\frac{\omega^2(c_{si}^2 + v_A^2) - k^2c_{si}^2v_A^2}{\omega^2 - k^2c_{si}^2}\frac{1}{r}\frac{\partial}{\partial r}rv_r + \rho(\omega^2 - k^2c_{si}^2)v_r = 0 \quad (3.83)$$

This equation describes the small axisymmetric oscillations of radially inhomogeneous plasma both inside and outside magnetic flux tube.

Note that (3.83) describes two $m = 0$ modes, the slow (sausage) and “fast” oscillations. In both cases the flux tube boundary performs the radial displacement $v_r = \partial\xi_r/\partial t$. The torsional, $m = 0$ oscillations are characterized by the azimuthal component of velocity, $v_\phi = \partial\xi_\phi/\partial t$, and will be considered in Chap. 4, Sect. 4.2.1.

3.7.3 Dispersion Relation

Outside the flux tube at large enough distances, $r \gg R$, where we can assume that the plasma is uniform and the magnetic field is negligibly small, (3.83) turns to be just a second-order Bessel equation. Bearing in mind that in the region $r \gg R$ there

are only outgoing waves, the solution to (3.83) is simply proportional to a second-order Hankel function:

$$v_r = C_1 H_1^{(2)}(qr) \quad (3.84)$$

where

$$q = \sqrt{(\omega^2/c_{se}^2) - k^2} \quad (3.85)$$

Obviously, $\text{Re}\omega > 0$, and we choose the branch of the roots with $\text{Re}q > 0$.

At small compared to k^{-1} distances from the flux tube axis (i.e., inside flux tube and its immediate neighborhood) the second term on the left-hand side of (3.83) is small compared to the first, because $k^2 R^2 \ll 1$. Neglecting the second term we have in the zeroth approximation

$$\rho \frac{\omega^2(c_{si}^2 + v_A^2) - k^2 c_{si}^2 v_A^2}{\omega^2 - k^2 c_{si}^2} \frac{1}{r} \frac{\partial}{\partial r} r v_r = C_2 \quad (3.86)$$

where C_2 is a constant.

From the condition that there be no singularities at $r \rightarrow 0$ we find

$$v_r = \frac{C_2}{r} \int_0^r \frac{(\omega^2 - k^2 c_{si}^2) r' dr'}{\omega^2(c_{si}^2 + v_A^2) - k^2 c_{si}^2 v_A^2} \quad (3.87)$$

This solution is valid for arbitrary r -dependence of $\rho(r)$ and $B(r)$. In the region $R \ll r \ll k^{-1}$ (3.84) and (3.87) have overlapping regions of applicability. This means that by matching solutions in these regions we can obtain the dispersion relation.

Consider first the behavior of the solution (3.87) in the region $r \gg R$. Here $v_A = 0$ and $c_{se} = \text{const}$, i.e., the integrand changes in proportion to r . Hence, the main term in the asymptotic expression of v_r is proportional to r . To find the next term in the expansion we add to and subtract from the expression for v_r , the term

$$\int_0^r \frac{1}{\rho} \frac{(\omega^2 - k^2 c_{se}^2)}{\omega^2 c_{se}^2} r' dr', \quad (3.88)$$

after which we get

$$\begin{aligned} v_r = & \frac{C_2}{r} \int_0^r \left[\frac{1}{\rho} \frac{\omega^2 - k^2 c_{si}^2}{\omega^2(c_{si}^2 + v_A^2) - k^2 c_{si}^2 v_A^2} - \frac{(\omega^2 - k^2 c_{se}^2)}{\rho_e \omega^2 c_{se}^2} \right] r' dr' \\ & + \frac{C_2}{r} \frac{\omega^2 - k^2 c_{se}^2}{\rho_e \omega^2 c_{se}^2} \frac{r^2}{2} \end{aligned} \quad (3.89)$$

The expression inside the square brackets decreases fast at large distances, and for $r \gg R$ we obtain

$$v_r = C_2 \frac{r}{c_{se}^2} \left[\frac{1}{\rho_e} \frac{\omega^2 - k^2 c_{se}^2}{2\omega^2} + \frac{D(\omega)}{r^2} \right] \quad (3.90)$$

where function $D(\omega)$ describes the dispersion and is defined as follows:

$$D(\omega) = c_{se}^2 \int_0^\infty \left[\frac{1}{\rho(c_{si}^2 + v_A^2)} \frac{\omega^2 - k^2 c_{si}^2}{\omega^2 - k^2 c_T^2} - \frac{1}{\rho_e c_{se}^2} \frac{\omega^2 - k^2 c_{se}^2}{\omega^2} \right] r' dr' \quad (3.91)$$

Here, c_T is the phase velocity of the axisymmetric tube oscillations (cf. (3.67)):

$$c_T^2 = \frac{c_{si}^2 v_A^2}{c_{si}^2 + v_A^2} \quad (3.92)$$

Thus, we found the next term in the asymptotic expression.

Using now expression for the Hankel function for small arguments,

$$H_1^{(2)} = \frac{qr}{2} - \frac{2i}{\pi qr}, \quad (3.93)$$

and equating the expressions obtained from (3.90) and (3.92), we find the dispersion relation:

$$D(\omega) = -\frac{2i c_{se}^2}{\pi \rho_e \omega} \quad (3.94)$$

The integrand in (3.91) for $D(\omega)$ is nonvanishing only when $r \leq R$, i.e., $D(\omega) \sim R^2$.

For the class of solutions related to axisymmetric modes with, $R \ll k^{-1}$, we have $\omega/kc_{si} \sim 1$ and $\omega/kv_A \sim 1$. In this case the ratio of the left- and right-hand sides of (3.94) is of the order of $k^2 R^2 \ll 1$. Therefore, for this class of solutions condition (3.94) can be satisfied only by a special choice of ω , such that the denominator $(\omega^2 - k^2 c_T^2)$ be close to zero. This fact by itself shows the great sensitivity of the solution to the inhomogeneity of the plasma and magnetic field inside the flux tube. In other words, the excitation and propagation of the axisymmetric tube waves are very sensitive to radial profiles of plasma and magnetic field inside the flux tube. As in realistic situations inhomogeneities certainly exist, it is necessary to consider their role in any model of the axisymmetric oscillations. We shall discuss this issue in Sect. 3.7.5.

3.7.4 Sausage and Fast Oscillations in Homogeneous Flux Tube

Consider the case of nearly homogeneous flux tube with a stepwise distribution of the plasma parameters, i.e., flux tube with a sharp boundary (i.e. $\ell \simeq 0$ in Fig. 3.5). In this case

$$D(\omega) = \frac{c_{se}^2 R^2}{2(c_{si}^2 + v_A^2)} \frac{\omega^2 - k^2 c_{si}^2}{\omega^2 - k^2 c_T^2}, \quad (3.95)$$

and from (3.94) we have

$$z \frac{z - c_{si}^2/c_T^2}{z - 1} = -iQ \frac{1}{k^2 R^2} \quad (3.96)$$

where z and Q stand for

$$z = \frac{\omega^2}{k^2 c_T^2}, \quad Q = \frac{4c_{se}^2 v_A^2}{\pi c_T^4} \quad (3.97)$$

The right-hand side of (3.95) is a large quantity, because $Q \simeq 1$ and $kR \ll 1$. This allows us to find both solutions of this equation. We define these solutions for fast and slow oscillations as z_F and z_S , respectively.

The $|z| \gg 1$ solution of (3.95)–(3.97) is obviously

$$z_F \simeq -i \frac{Q}{k^2 R^2}, \quad (3.98)$$

or, for $Re\omega > 0$

$$z_F \simeq \frac{1}{\sqrt{2}} \frac{c_T}{R} (1 - i) \quad (3.99)$$

Thus, the frequency of the fast axisymmetric oscillations is very high, and having correspondingly high imaginary part, these oscillations are rapidly damping.

Another solution of the dispersion relation (3.95) corresponding to the case when the denominator in the left-hand side of (3.95) tends to zero describes the slow oscillations, and is of the form

$$z_S \simeq 1 - i \frac{k^2 R^2}{Q} \left(\frac{c_{si}^2}{c_T^2} - 1 \right) \quad (3.100)$$

or choosing $Re\omega > 0$ and keeping in mind relations (3.97) we have

$$\omega_S \simeq kc_T \left[1 - i \frac{k^2 R^2}{2Q} \left(\frac{c_{si}^2}{c_T^2} - 1 \right) \right]. \quad (3.101)$$

Thus, the real part of (3.101) is a natural eigenfrequency of the sausage oscillations, while the imaginary part describes their radiative damping. One can see that, as far as $k \ll R$, radiative damping is small. This fact may play an important role in large scale dynamics of solar atmosphere. A smallness or radiative damping means that the oscillations excited in the photosphere where the flux tube interacts with the acoustic wave trains may propagate along the flux tube for a long time without damping.

The main problem with this process, however, is that, as mentioned above, the sausage mode is extremely sensitive to radial inhomogeneities of the plasma and magnetic field inside the flux tube. From this perspective the more slender are the flux tube, the more chance they have to sustain the sausage oscillations. We will discuss this issue in the next section.

3.7.5 Effects of Radial Inhomogeneities on Sausage Oscillations

In order to determine the conditions under which the radial inhomogeneities of flux tube start to show an appreciable effect on the sausage oscillations, we consider a model situation when the phase velocity, c_T changes with radius across the flux tube as follows:

$$c_T^2 = \begin{cases} c_{T0}^2(1 - \epsilon r^2/R^2), & r < R \\ 0, & r > R \end{cases} \quad (3.102)$$

Clearly, when $\epsilon \ll 1$, the quantities in the integral (3.91) for $D(\omega)$ inside the flux tube are independent of r . Then, in terms of parameter z , defined by (3.97), we have for $D(z)$:

$$D(z) = \frac{R^2 c_{T0}^2 c_{se}^2 (z - v_{A0}^2/c_{T0}^2)}{2 c_{si}^2 c_{T0}^2} \int_0^1 \frac{d\zeta}{z - 1 + \epsilon\zeta} \quad (3.103)$$

This integral determines an analytical function $D(z)$ in the complex z -plane with a cut between the points $z = 1 - \epsilon$ and $z = 1$ (Fig. 3.6a):

$$D(z) = \frac{R^2 c_{T0}^2 c_{se}^2}{2 v_{A0}^2 c_{si}^2} \frac{z - v_{A0}^2/c_{T0}^2}{\epsilon} \ln \frac{z - 1 + \epsilon}{z - 1} \quad (3.104)$$

The imaginary part of the logarithm changes in the interval $(-i\pi, i\pi)$.

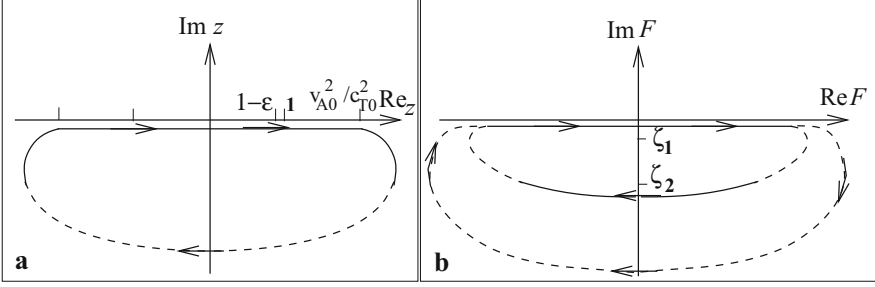


Fig. 3.6 Study of the dispersion relation: **(a)** The complex z -plane with a cut between the points $z = 1 - \epsilon$ and $z = 1$; **(b)** The hodograph in the complex F -plane corresponding to the z -plane contour shown in Panel **a**

In the framework of this model the dispersion relation has a form

$$z \left(z - \frac{v_{A0}^2}{c_{T0}^2} \right) \ln \frac{z - 1 + \epsilon}{z - 1} = -i Q \frac{\epsilon}{k^2 R^2} \quad (3.105)$$

We can modify the left-hand side of this equation at $\epsilon \rightarrow 0$ by performing an expansion in powers of ϵ . This procedure leads to the dispersion (3.96), which has the solution $z = 1$. This result is valid when $\epsilon \ll k^2 R^2$. Note that the solution corresponding to the sausage mode disappears when $\epsilon \geq k^2 R^2$.

In the opposite case, when $\epsilon \gg k^2 R^2$ but still $\epsilon \ll 1$, (3.105) does not have a solution $z = 1$. Indeed, as the imaginary part of the logarithm changes from $-i\pi$ to $i\pi$, and the absolute magnitude of the right-hand side of (3.105) is large compared to unity, the absolute value of z must also be large compared to unity, which is necessary in order to satisfy (3.105). To find the corresponding solution, we take into account that at $z \gg 1$,

$$\ln \left(1 + \frac{\epsilon}{z - 1} \right) \simeq \frac{\epsilon}{z}, \quad (3.106)$$

and (3.105) gives

$$z = -i \frac{\epsilon Q}{k^2 R^2} \quad (3.107)$$

This, on the other hand, coincides with (3.99). Thus, the solution with $z \gg 1$ corresponds to a fast mode.

To find the critical value of ϵ for which the solution vanishes, we can use a hodograph method mapping the contour shown in Fig. 3.6b onto the complex F -plane, which we define as

$$F(z) = z \left(z - \frac{v_{A0}^2}{c_{T0}^2} \right) \ln \frac{z - 1 + \epsilon}{z - 1} \quad (3.108)$$

In accordance with the Nyquist criterion the number of roots of (3.105) lying in the lower z -half-plane is equal to the number of times the hodograph of F goes round the point $-iQ\epsilon/k^2R^2$. Note that as the system initially is stable, we are interested only in roots with $\text{Im}z < 0$.

The obtained shape of the hodograph and both roots,

$$\zeta_1 = -i \frac{Q\epsilon}{k^2R^2}, \quad \zeta_2 = i\pi \left(1 - \frac{\epsilon}{2}\right) \left(1 - \frac{\epsilon}{2} \frac{v_{A0}}{c_{T0}}\right) \quad (3.109)$$

laying inside it, is shown in Fig. 3.6b. From the figure it is clear that the critical value of ϵ is determined by the equation

$$\pi \left(1 - \frac{\epsilon}{2}\right) \left(\frac{v_{A0}^2}{c_{T0}^2} + \frac{\epsilon}{2} - 1\right) = Q \frac{\epsilon}{k^2R^2} \quad (3.110)$$

Given that $kR \ll 1$ we have for the critical value of ϵ

$$\epsilon_{cr} = \frac{\pi k^2 R^2}{Q} \left(\frac{v_{A0}^2}{c_{T0}^2} - 1\right) \quad (3.111)$$

This is quite a small quantity, which means that for the sausage oscillations to survive and propagate along flux tube, there is very narrow threshold of physical parameters. On the other hand, radial pulsation of the surface of the tube with inhomogeneous parameters may become large and cause a catastrophic growth of radiative losses, and thus damping of the tube waves.

3.8 Problems

3.1 Describe the motion of a sphere oscillating in an ideal fluid and find velocity of the established oscillations. This is an important problem of added mass.

3.2 The same for a cylinder of a mass M (per unit length) and radius R oscillating in an incompressible liquid of density ρ under the action of a small sinusoidal force $F = F_0 \sin \omega t$.

3.3 Describe the adiabatic motion of plasma blob displaced vertically in stratified atmosphere and being in pressure equilibrium with its surroundings.

3.4 Find condition for magnetic buoyancy instability in case of horizontal magnetic flux tube in stratified atmosphere in presence of ambient magnetic field.

Appendix 1: Analogy with Landau Damping

Landau damping is a fundamental effect occurring in dispersive and dissipative media sustaining any kind of wave phenomena (Timofeev 1970; Tataronis and Grossmann 1970; Chen and Hasegawa 1974; Ryutov 1999).

A plasma wave of frequency ω and wave number k propagating in a collisionless plasma is subject of Landau damping because the wave distorts the particular distribution function associated with a resonance

$$\omega = kv \quad (3.112)$$

Particles having speed v are resonant with the wave and so exchange energy with it. Mathematically, the dispersion relation for plasma waves is

$$I = \frac{\omega_p^2}{k^2} \int \frac{\partial f_0 / \partial v}{v - \omega/k} dv, \quad (3.113)$$

where ω has a small imaginary part and the imaginary part of the integral gives a δ -function, so that

$$I = \frac{\omega_p^2}{k^2} \mathcal{P} \int \frac{\partial f_0 / \partial v}{v - \omega/k} dv + i\pi \frac{\partial f_0}{\partial v}, \quad (3.114)$$

This, in turn, leads to the dispersion relation

$$\omega = \omega_p + i\omega_p \frac{\pi}{2} \frac{\omega_p^2}{k^2} \left(\frac{\partial f_0}{\partial v} \right)_{v=\omega/k} \quad (3.115)$$

In our case the resonant excitation of kink and/or sausage waves produces a Landau-like damping of an incident acoustic wave. Physically, the acoustic wave damps because the wave distorts the distribution function of flux tubes. This, just like in kinetic plasma, is associated with a resonance

$$\omega \cos\theta = kc_s. \quad (3.116)$$

The flux tubes having natural phase speed, ω/k , are resonant with the acoustic wave and so exchange energy with it. The dispersion relation (3.24) for the acoustic wave becomes

$$\omega = kc_s \left[1 - \frac{1}{2} \sin^2\theta \int d\eta g(\eta) \left(1 - \frac{\omega^2}{\eta + 1 - 2c_s^2 k^2 \cos^2\theta} \right) \right] \quad (3.117)$$

where ω has a small imaginary part, and the imaginary part of the integral gives a δ -function. The resulting dispersion relation is

$$\omega = kc_s[1 - i\pi \sin^2\theta g(\eta_0)], \quad (3.118)$$

where

$$\eta_0 = 2\cos^2(\theta/2) - 1 = kc_s. \quad (3.119)$$

Resonance is where

$$\eta + 1 = \frac{2\cos^2\theta}{\gamma} \quad (3.120)$$

But

$$\frac{\omega^2}{k^2} = \frac{B^2}{4\pi(\rho_i + \rho_e)} = \frac{B^2}{4\pi\rho_e(\eta + 1)}, \quad (3.121)$$

and

$$\frac{B^2}{8\pi} = p_e = \frac{\rho_e c_s^2}{\gamma}, \quad (3.122)$$

So that the resonance condition (3.116) becomes just expression (3.120).

Appendix 2: Derivation of Equation for Kink Oscillations from MHD

The linearized set of MHD equations in the cylindrical coordinates with z -axis directed along magnetic field for the perturbations proportional to $\exp(-i\omega t + ikz + im\phi)$ have a form:

$$\omega\delta P = -i\rho \frac{\omega^2(c_{si}^2 + v_A^2) - k^2c_{si}^2v_A^2}{\omega^2 - k^2c_{si}^2} \left(\frac{1}{r} \frac{\partial}{\partial r} r v_r + \frac{1}{r} \frac{\partial}{\partial \phi} v_\phi \right), \quad (3.123)$$

$$\omega \frac{\partial}{\partial r} \delta P = -i\rho(\omega^2 - k^2v_A^2)v_r, \quad (3.124)$$

$$\omega \frac{1}{r} \frac{\partial}{\partial \phi} \delta P = -i\rho(\omega^2 - k^2v_A^2)v_\phi, \quad (3.125)$$

where $\delta P = \delta p_i + b_z B/4\pi$ is the total pressure perturbation.

From (3.124) and (3.125) it is obvious that

$$(\omega^2 - k^2 v_A^2) \nabla_z \mathbf{v} = 0 \quad (3.126)$$

Since we are not interested in pure Alfvén wave, (3.126) gives for velocity perturbations $\nabla_z \mathbf{v} = 0$, and we can introduce the velocity potential (see (3.42)) which reduces the set (3.123)–(3.125) to the single equation inside flux tube (3.43) and to (3.44) outside it. Respectively, on the surface of the flux tube, at $r = R$, the conditions for the continuity of the normal component of velocity and total pressure have a form

$$(\omega^2 - k^2 v_A^2) \nabla_z \mathbf{v} = 0 \quad (3.127)$$

$$\rho_i \left(1 - \frac{k^2 v_A^2}{\omega^2} \right) \psi_i \Big|_R = \rho_e \psi_e \Big|_R \quad (3.128)$$

Consider the motion of a magnetic flux tube in a field of a plane acoustic wave propagating with the amplitude ζ_0 (see (3.56) where we used a unit amplitude):

$$\Psi_{0e} = \frac{1}{2} \exp(-i\omega t + i\mathbf{k}\mathbf{r}) + \text{c.c.} \quad (3.129)$$

where $\mathbf{k}\mathbf{r} = k_z z + q_e r \cos\phi$, and $q_e = \omega^2 / c_{se}^2 - k_z^2$.

The solution of MHD equations outside flux tube as a superposition of this plane wave and outgoing cylindrical waves with $m = \pm 1$ has a form

$$\Psi_{0e} = \frac{1}{2} \exp(-i\omega t + i\mathbf{k}\mathbf{r}) + \text{c.c.} \quad (3.130)$$

We have taken a real part of (3.57) and retained only the first nonvanishing term in the expansion of Hankel function over a small argument. The solution inside flux tube (3.58) can be written as

$$\Psi_{0i} = e^{-i\omega t + ik_z z} B r \cos\phi \quad (3.131)$$

Using now (3.127)–(3.131) we can find coefficients A and B expressed through the amplitude of the incident sound wave ζ_0 . After some algebra we have

$$A = -\zeta_0 q_e R^2 \frac{1 - \eta(1 - k^2 v_A^2 / \omega^2)}{1 + \eta(1 - k^2 v_A^2 / \omega^2)} \quad (3.132)$$

$$B = 2\zeta_0 q_e \frac{1}{1 + \eta(1 - k^2 v_A^2 / \omega^2)} \quad (3.133)$$

Inserting now (3.132) and (3.133) into (3.130) and (3.131) and taking into account (3.42) we can express the velocity inside flux tube $\mathbf{v}_{i\perp}$ through the velocity in outer region, $\mathbf{v}_{e\perp}$:

$$\mathbf{v}_{i\perp} = 2\mathbf{v}_{e\perp} \frac{1}{1 + \eta(1 - k^2 v_A^2 / \omega^2)} \quad (3.134)$$

For a plane harmonic dependence this relationship gives the following equation for the flux displacement:

$$(1 + \eta) \frac{\partial^2 \xi_{\perp}}{\partial t^2} - \eta v_A^2 \frac{\partial^2 \xi_{\perp}}{\partial z^2} = 2 \frac{\partial \mathbf{v}_{\perp}}{\partial t} \quad (3.135)$$

Recalling that $\eta = \rho_i / \rho_e$ we see that (3.135) exactly coincides with (3.4).

References

- L. Chen, A.A. Hasegawa, J. Geophys. Res. **79**, 1033 (1974)
 L.E. Cram, P. Wilson, Sol. Phys. **41**, 313 (1975)
 R.J. Defouw, Astrophys. J. **209**, 266 (1976)
 D. Fujimura, S. Tsuneta, Astrophys. J. **702**, 1443 (2009)
 L.D. Landau, Sov. Phys. - JETP **16**, 574 (1946)
 L.D. Landau, E.M. Lifshitz, *Fluid Mechanics* (Pergamon Press, Oxford, 1987)
 S.R.O. Ploner, S.K. Solanki, Astron. Astrophys. **325**, 1199 (1997)
 B. Roberts, A.R. Webb, Sol. Phys. **56**, 5 (1978)
 D.D. Ryutov, Plasma Phys. Control. Fusion **41**, A1 (1999)
 D.D. Ryutov, M.P. Ryutova, Sov. Phys. - JETP **43**, 491 (1976)
 M.P. Ryutova, Sov. Phys. JETP **53**, 529 (1981)
 H.C. Spruit, Astron. Astrophys. **98**, 155 (1981)
 J.A. Tataronis, W. Grossmann, Z. Phys. **261**, 203 (1970)
 A. Timofeev, Soviet Physics - Uspekhi **13**, 632 (1970); A&A **98**, 155
 E.Ya. Zlotnik et al., Astron. Lett. **37**, 508 (2011)

Chapter 4

Effects of Flux Tube Inhomogeneities and Weak Nonlinearity



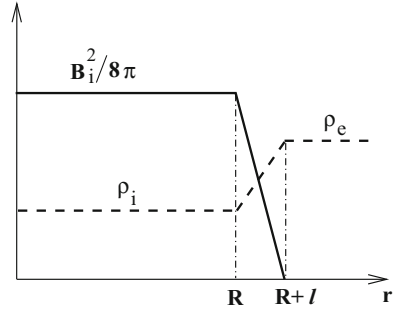
Abstract In this chapter we shall consider some special properties of magnetic flux tubes associated with their radial and longitudinal inhomogeneities. Magnetic flux tube embedded in weakly magnetized or nonmagnetic environment and kept in dynamic equilibrium by external pressure must be intrinsically inhomogeneous. Even if magnetic field and density inside flux tube are radially smooth across the most of its cross section, at the periphery they must have a finite gradient to match the physical parameters of surrounding plasma. Besides, flux tubes in the photosphere are subject to longitudinal inhomogeneity because of sharp stratification of low atmosphere. It is remarkable that this intrinsic property of flux tubes to be inhomogeneous plays a crucial role in their ability to absorb the energy of the outer motions, carry it upward, and convert it into the heat or other forms of energy. We shall discuss some macroscopic effects associated with flux tube inhomogeneities, which, in fact, are observable. We shall also study a weakly nonlinear waves in flux tubes and show that they obey a KdV-Burgers equation and may develop into shocks and solitons.

4.1 Radially Inhomogeneous Flux Tube: Internal Resonances

4.1.1 *Anomalous Resonance in Kink Oscillations*

Consider first the effect of radial inhomogeneity of flux tube, which, in fact, results in a striking property of flux tube: it turns out that even in the absence of any dissipative effects, an additional and strong damping of flux tube oscillations occurs near the singular point where the phase velocity of oscillations becomes equal to the local value of the Alfvén speed (Ryutova 1977; Ionson 1978). Existence of resonant layer inside *any* flux tube makes virtually all the flux tubes responsible for permanently acting mechanism of energy production and its transfer. It is not surprising therefore that enhanced emission in the overlying atmosphere (almost at all temperatures) mimics the pattern of small-scale flux tubes observed in the photosphere.

Fig. 4.1 Sketch of the flux tube parameters with the sharp boundary layer



To demonstrate the action of an *internal resonance* consider the kink oscillations of flux tube with somewhat simplified profile shown in Fig. 4.1, where the solid line is the magnetic pressure $B^2(r)/8\pi$, and the dashed line is the gas-kinetic pressure $p(r)$. Both functions are linear in the interval $[R, R + l]$, with $l \ll R$. We assume magnetic free environment.

For kink oscillations of flux tube with $kR \ll 1$ a plasma can be considered incompressible and the MHD system for small oscillations proportional to $\exp(-i\omega t)$, are as follows:

$$\begin{aligned} \operatorname{div} \mathbf{v} &= 0 \\ -i\omega \mathbf{b} &= \nabla \times [\mathbf{v} \times \mathbf{b}] \\ -i(\omega + i\nu)\rho \mathbf{v} &= -\nabla p + \frac{1}{4\pi} ([\nabla \times \mathbf{b} \times \mathbf{B}] + [\nabla \times \mathbf{B} \times \mathbf{b}]) \end{aligned} \quad (4.1)$$

with \mathbf{v} and \mathbf{b} being perturbed quantities.

In order to provide a proper account for singularity in a matching point of phase velocities, i.e., where $v_A = \omega/k$, we have added a small imaginary part, ν , to the frequency in the equation of motion. Physically, this addition can be attributed, for example, to the rare collisions between ions and neutrals in plasma.

We use cylindrical coordinates (r, ϕ, z) with z -axis directed along the flux tube. At $kR \ll 1$ the kink oscillations of flux tubes can be considered as a plane motion, and we can put $v_z = 0$. The other components of velocity can be expressed through the velocity potential ψ , just as we did in Chap. 3:

$$v_r = -\frac{1}{r} \frac{\partial \psi}{\partial \phi} \quad v_\phi = \frac{\partial \psi}{\partial r} \quad (4.2)$$

and reduce the system (4.1) to a single equation for ψ :

$$\frac{\partial}{\partial r} \left(\rho - \frac{k^2 B^2}{4\pi\omega^2} \right) r \frac{\partial \psi}{\partial r} - \left(\rho - \frac{k^2 B^2}{4\pi\omega^2} \right) \frac{\psi}{r} = 0 \quad (4.3)$$

The solution of (4.3) in the region $r < R$ is obviously

$$\psi_i = C_1 r, \quad (4.4)$$

and in the region $r > R + l$,

$$\psi_e = \frac{C_2}{r}. \quad (4.5)$$

To find the solution in the transition layer $(R, R + l)$, it is convenient to introduce a new variable

$$x = \frac{r - R}{l}, \quad 0 < x < 1 \quad (4.6)$$

Taking into account that $l \ll R$, (4.3) can be written as follows:

$$\frac{d}{dx}(x - x_0 - i\epsilon) \frac{d\psi}{dx} - \frac{l^2}{R^2}(x - x_0 - i\epsilon)\psi = 0 \quad (4.7)$$

where

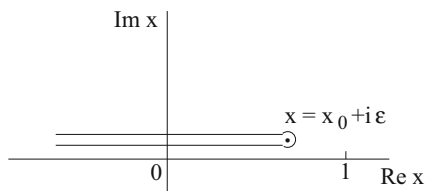
$$x_0 = \left(\frac{k^2 B_i^2}{4\pi\omega^2} - \rho_i \right) \left(\frac{k^2 B_i^2}{4\pi\omega^2} + \rho_e - \rho_i \right)^{-1}, \quad (4.8)$$

and small imaginary part $i\epsilon$ is associated with imaginary term $i\nu$ coming from the system (4.1). The specific value of ϵ is not important because it does not enter into final result. In other words, the kinetic losses which are present in plasma, act “behind the scene.”

Equation (4.7) has a single-valued solution in the complex plane x with a cut along the line $\text{Im}x = i\epsilon$. This is illustrated in Fig. 4.2. At the same time, $-\infty < \text{Re}x < x_0$. Equation (4.7), being of complex arguments, is a modified Bessel equation of zeroth order. Taking into account that $l \ll R$, solution to this equation can be written as follows:

$$\psi = A + D \ln(x - x_0 - i\epsilon) \quad (4.9)$$

Fig. 4.2 The complex x -plane with a cut along the line $\text{Im}x = i\epsilon$



At both boundaries, $r = R$ and $r = R + l$, we have to satisfy continuity conditions for the functions ψ (i.e., for solutions (4.4), (4.5), and (4.9)) and their derivative:

$$\begin{aligned} \psi_i(r) \Big|_R &= \psi(r) \Big|_R, & \frac{d\psi_i(r)}{dr} \Big|_R &= \frac{d\psi(r)}{dr} \Big|_R; \\ \psi(r) \Big|_{R+l} &= \psi_e(r) \Big|_{R+l}, & \frac{d\psi(r)}{dr} \Big|_{R+l} &= \frac{d\psi_e(r)}{dr} \Big|_{R+l} \end{aligned} \quad (4.10)$$

Now, choosing the logarithm branch single-valued in the region with the cut shown in Fig. 4.2, we obtain the following dispersion relation:

$$\ln \frac{1-x_0}{x_0} + \frac{R}{l} \left(\frac{1}{1-x_0} - \frac{1}{x_0} \right) + i\pi = 0 \quad (4.11)$$

In terms ω and k this expression becomes as follows:

$$\omega \simeq \frac{k B_i}{\sqrt{4\pi(\rho_i + \rho_e)}} \left(1 + \frac{i\pi}{4} \frac{\rho_i}{\rho_i + \rho_e} \frac{l}{R} \right). \quad (4.12)$$

This result shows that kink oscillations of flux tube with radial dependence of magnetic field and density inside it are subject to strong resonant damping. At the applicability limit, when l becomes of the order of radius, R , we have even $\text{Im } \omega \sim \text{Re } \omega$. One can show that this result is valid in the case when the magnetic field outside the flux tube is nonzero.

Physically, the nature of the damping is due to the pumping of oscillation energy into the resonance point where the dissipation occurs. The effect is similar to the wave phenomena occurring in moving inhomogeneous media (plasma and liquids) that develop at the resonant points where the velocity of the substance coincides with the phase velocity of the oscillations (Timofeev 1970).

As mentioned above, given that flux tubes in nature are always inhomogeneous across their cross section, the existence of anomalous resonance damping becomes a major agent in various processes of energy conversion. In particular, the long waves propagating in plasma with magnetic flux tubes or with any other kind of magnetic field filamentation experience a strong resonance absorption resulting a rapid transformation of oscillation energy into the heat.

4.1.2 Alfvén Resonance

The resonant absorption layer, being a site of the anomalous absorption of the kink oscillation of flux tubes, may also support the Alfvén resonance. By nature kinetic Alfvén waves are MHD waves having short cross-field scales comparable to the ion

gyroradius, $r_i = v_{Ti}/\omega_{ci}$. For such short waves the resonant layer may be considered “uniform,” which is not too principal, but allows to simplify the analysis (Ionson 1978).

The basic assumption can be summarized as follows: (1) $\mathbf{B} = B(0, 0, B)$, (2) local values of velocities are $v_{Ti} < v_A < v_{Te}$, (3) in harmonic perturbations $\sim \exp(-i\omega t + \mathbf{k} \cdot \mathbf{r})$, $k_r \gg k_\perp \gg k_z$.

The MHD equations for a warm ion-electron plasma are as follows:

$$\frac{\partial n_\alpha}{\partial t} + \nabla \cdot (n_\alpha v_\alpha) = 0 \quad (4.13)$$

$$m_\alpha \frac{dv_\alpha}{dt} = e_\alpha \mathbf{E} + \frac{1}{c} e_\alpha \mathbf{v}_\alpha \times \mathbf{B} - \frac{1}{n_\alpha} \nabla P_\alpha, \quad (4.14)$$

$$P_\alpha = n_\alpha k_B T_\alpha \quad (4.15)$$

where the subscript α refers to the particle species. It is also assumed that $(\nabla \times \mathbf{E}) = 0$ (shear waves). Linearizing the system (4.13)–(4.15) with respect to perturbations $\sim \exp(-i\omega t + \mathbf{k} \cdot \mathbf{r})$, one obtains equations for density \tilde{n}_α and current $\tilde{j}_{z\alpha}$ fluctuations:

$$\frac{\tilde{n}_\alpha}{n_\alpha} = \left[\frac{ie_\alpha k_z}{m_\alpha} \tilde{E}_z + \frac{ic\omega^2 k_r}{B\Omega_\alpha} (1 - s_\alpha) \tilde{E}_r \right] \frac{1}{\omega^2 - v_{T\alpha}^2 k_z^2}, \quad (4.16)$$

$$\tilde{j}_{z\alpha} = \frac{in_\alpha e_\alpha^2}{m_\alpha \omega} \tilde{E}_z + \frac{n_\alpha e_\alpha v_{T\alpha}^2 k_z}{\omega} \frac{\tilde{n}_\alpha}{n_\alpha} \quad (4.17)$$

where $s_\alpha = k_r^2 v_{T\alpha}^2 / \Omega_\alpha^2$, Ω_α is the cyclotron frequency, $v_{T\alpha}$ is the thermal velocity, and tilde marks small fluctuations. The term $(1 - s_\alpha)$ in (4.14) has been externally introduced by letting $\tilde{\mathbf{E}} \rightarrow (1 - s_\alpha) \tilde{\mathbf{E}}$ and represents finite gyroradius correction, or in other words, it reflects the amount by which the average field felt by the particles deviates from that at the center of their orbit. Since $v_{Ti} < v_A < v_{Te}$, and $\omega \simeq k_z v_A$, (4.14) and (4.15) reduce to

$$4\pi \tilde{n}_e e = \frac{i\omega_{pe}^2}{v_{Te}^2} \left(1 + \frac{\omega^2}{k_z^2 v_{Te}^2} \right) \frac{\tilde{E}_z}{k_z}, \quad (4.18)$$

$$4\pi \tilde{j}_{\parallel e} = -\frac{i\omega_{pe}^2 \omega}{v_{Te}^2} \frac{\tilde{E}_z}{k_z} \quad (4.19)$$

for electrons, and

$$4\pi\tilde{n}_{ie} = \frac{i\omega_{pi}^2 k_z^2 \tilde{E}_z}{\omega^2 k_z} - \frac{\omega_{pi}^2 s_i (1-s_i) \tilde{E}_r}{v_{Ti}^2 k_r} \quad (4.20)$$

$$4\pi\tilde{j}_{zi} = \frac{i\omega_{pi}^2 k_z \tilde{E}_z}{\omega k_z} \quad (4.21)$$

for ions.

Using now (4.18)–(4.21) and z -component of

$$\nabla \times (\nabla \times \tilde{\mathbf{E}}) = \frac{4\pi}{c^2} \frac{\partial \tilde{\mathbf{j}}}{\partial t} - \frac{1}{c^2} \frac{\partial^2 \tilde{\mathbf{E}}}{\partial t^2}, \quad (4.22)$$

one can easily obtain the following dispersion relation for kinetic Alfvén waves:

$$\frac{\omega^2}{k_z^2 v_A^2} = 1 + \beta + k_r^2 r_i^2 \left(1 + \frac{T_e}{T_i}\right) \quad (4.23)$$

Here T_e and T_i are the electron and ion temperatures, r_i is the ion gyroradius, and β is a local plasma beta. Note that these waves do not have magnetic shear and yet are capable of propagating across the ambient magnetic field. It is important that the existence of such waves largely depends on the inclusion of nonzero electron inertia ensuring the presence of the second term in (4.18) (inertia term) which would otherwise vanish.

Using the dispersion relation (4.23) in Maxwell's equations yields the following useful relationships between $\tilde{\mathbf{B}}$ and $\tilde{\mathbf{E}}$:

$$\frac{\tilde{\mathbf{B}}_{\perp}}{\tilde{E}_r} = \frac{1}{v_A}, \quad \frac{\tilde{B}_r}{\tilde{E}_r} = -\frac{\mathbf{k}_{\perp}}{k_r} \frac{1}{v_A} \quad (4.24)$$

$$\frac{\tilde{\mathbf{E}}_{\perp}}{\tilde{E}_r} = \frac{\mathbf{k}_{\perp}}{k_r}, \quad \frac{\tilde{E}_z}{\tilde{E}_r} = -k_r^2 r_i^2 \frac{k_z T_e}{k_r T_i} (1 - k_r^2 r_i^2) \quad (4.25)$$

The transverse structure of a kinetic Alfvén waves (i.e., $k_r \neq 0$) greatly increases viscous damping and leads to irreversible heating of the ions. Furthermore, because these waves are accompanied by a field-aligned electric field \tilde{E}_z , Joule dissipation of the field-aligned electric current can heat the electrons.

The rate at which energy is dissipated (per unit volume) due to the ions is

$$q_i = \rho v_r \left(\frac{\partial \tilde{v}_{i\perp}}{\partial r} \right)^2 \quad (4.26)$$

where ρ is the mass density, $\tilde{v}_{i\perp}$ is the ion velocity, and ν_r is the cross-field kinematic viscosity

$$\nu_r = \frac{v_{Ti}^2 v_i}{\Omega_i^2} \left(1 + \frac{v_i^2}{\Omega_i^2} \right)^{-1}, \quad (4.27)$$

where v_i is the ion-ion collision frequency. With (4.26) and (4.27) a heating rate for $v_i \ll \Omega_i$ is given by

$$q_i = k_r^2 r_i^2 v_i \frac{|\tilde{\mathbf{B}}_\perp|^2}{8\pi} \quad (4.28)$$

Here the relation $\tilde{v}_{i\perp}/v_A \simeq \tilde{B}_\perp/B$ has been used. The electron heating rate, which is given by

$$q_e = \frac{1}{2} \text{Re}(\tilde{j}_{ez} \tilde{E}_{ez}), \quad (4.29)$$

is related to the ion heating rate as follows:

$$q_e \simeq \frac{\sqrt{m_e/m_i}}{\beta} q_i. \quad (4.30)$$

Since in solar plasma $\beta \simeq \sqrt{m_e/m_i}$, electrons and ions are heated at approximately the same rate. The dissipation rates given by (4.28) and (4.30) greatly exceed those inferred by an ideal MHD description.

4.2 Boundary Value Problem

Flux tubes embedded in ever-moving environment may carry significant amount of energy stored around them. One of the important agents of energy transport is the ability of the *oscillating* flux tubes to respond to the action of surrounding changes, temperature inhomogeneities, atmospheric stratification, etc. (Ryutova and Khijakadze 1990; Solanki et al. 1996; Ploner and Solanki 1997; Garcia de Andrade 2007; Penn et al. 2011). In the next sections we discuss some particular effects resulted from the response of oscillating flux tubes to changes of the environmental conditions.

4.2.1 Phase-Mixing in Flux Tubes

As in the previous section, here again we consider the radially inhomogeneous flux tubes. Another class of phenomena caused by the inhomogeneity of flux tube parameters is associated with frequency detuning between neighboring oscillating magnetic surfaces inside flux tube. Even if the waves propagating along the radially inhomogeneous flux tube do not possess local resonances they undergo intense phase-mixing during which the oscillations of neighboring field lines become rapidly out of phase (Tataronis and Grossman 1970; Timofeev 1970; Heyvaerts and Priest 1983). This naturally leads to generation of small-scale motions, at which the dissipative effects turn on and result in strong absorption of flux tube oscillations.

To look into the effect of phase-mixing we need to consider the general case when flux tube parameters vary across the entire cross section of flux tube, as shown in Fig. 4.3a. In this case, the weakly damped wave which could be described in terms of smoothly varying radial eigenfunction does not exist any more. What happens is that if at the initial moment of time ($t = 0$) the eigenfunction had a smooth radial profile (Fig. 4.3b)

$$\psi(r, z, t)|_{t=0} = \chi(r, 0)e^{ik_z z + i\phi}, \quad (4.31)$$

with time it evolves into a strongly oscillating function concentrated in the resonance point r^* (Fig. 4.3c).

Further in time and at higher altitudes the eigenfunction becomes multi-spiky, and waves in neighboring magnetic surfaces will have different phases.

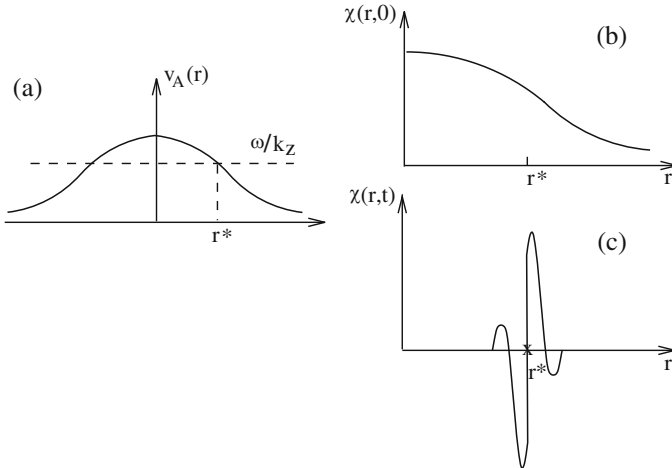


Fig. 4.3 The flux tube with the smooth radial profile across its entire cross section and the evolution of the eigenfunction: (a) The Alfvén velocity, r^* is the point where the Alfvén velocity coincides with the phase velocity of tube wave; (b) The eigenfunction at the initial moment of time; (c) Strongly oscillating eigenfunction at the resonant point, r^*

The linearized MHD equations, together with the equilibrium condition $p_i(r) + B^2(r)/8\pi = p_e(r)$, lead to the following equations for a spatial variation of the tube displacement, ξ :

$$-\omega^2 \rho \xi = \nabla \delta P + \frac{B^2(r)}{4\pi} \frac{\partial^2 \xi}{\partial z^2} \quad (4.32)$$

where $\delta P = \delta p + Bb_z/4\pi$ is a perturbation of total pressure (as earlier we use cylindrical coordinates with the z -axis directed along the tube).

The best way to solve this three-dimensional set of equations with r, ϕ, z variables is to use the Laplace transform over z , then solve the radial equation, and then apply Laplace inversion. In the next section we shall consider some special cases, namely the case of the Alfvén (torsional) waves, and then address the kink oscillations.

4.2.2 Phase-Mixed Torsional Waves

In case of torsional Alfvén waves ($m = 0$), $\xi_r = \xi_z = 0$, and the system (4.32) reduces to a single equation for ξ_ϕ :

$$-\omega^2 \xi_\phi(r, z) = v_A^2(r) + \frac{\partial^2 \xi_\phi(r, z)}{\partial z^2} \quad (4.33)$$

Laplace transform of $\xi_\phi(r, z)$ over z with $\text{Re } p > 0$ is

$$\xi_{\phi p} = \int_0^\infty e^{-pz} \xi_\phi dz \quad (4.34)$$

With this, (4.34) becomes as follows:

$$\omega^2 \xi_{\phi p}(r) + v_A^2(r) p^2 \xi_{\phi p}(r) = -v_A^2(r) \left[\xi_\phi(r, 0) + p \frac{\partial \xi_\phi(r, 0)}{\partial z} \right] \quad (4.35)$$

Thus, for $\xi_{\phi p}(r)$ we have

$$\xi_{\phi p} = -i \frac{v_A(r)}{2\omega} \left[\xi_\phi(r, 0) + p \frac{\partial \xi_\phi(r, 0)}{\partial z} \right] \left[\frac{1}{p + i\omega/v_A} - \frac{1}{p - i\omega/v_A} \right] \quad (4.36)$$

Laplace inversion

$$\xi_\phi(r, z) = -\oint e^{pz} \xi_{\phi p}(r) dp \quad (4.37)$$

requires integration to be performed along the contour which is a vertical line lying on the right of all the poles of the function $\xi_{p\phi}$. The poles are obviously at the points $p = \pm i\omega/v_A(r)$.

Shifting the contour C to the left and taking residues, one can arrive at the following solution for displacement $\xi_\phi(r, z)$:

$$\xi_\phi(r, z) = \frac{\xi'_\phi(r, 0)v_A(r)}{\omega} \sin \frac{\omega z}{v_A(r)} + \xi_\phi(r, 0) \cos \frac{\omega z}{v_A(r)} \quad (4.38)$$

Equation (4.38) shows how a profile of function $\xi_\phi(r, 0)$ changes at higher altitudes in the course of wave propagation. Indeed, if at the base of the flux tube, i.e., at $z = 0$, $\xi_\phi(r, 0)$ is a smooth function of radius, say, $\xi_\phi(r, 0) \sim r$ (i.e., a rigid rotation takes place), then at higher altitudes the dependence of ξ_ϕ on r becomes more and more spiky (Fig. 4.4).

The characteristic radial scale length of perturbations, Δr is of the order of

$$\Delta r \sim \frac{v_A^2(r)}{z\omega v'_A(r)} \sim \frac{v_A(r)r}{\omega z}, \quad (4.39)$$

and diminishes inversely with z . Respectively, the dissipative processes, like viscosity, Ohmic losses, and/or thermal losses, become more and more important at larger z . At the same time, it is obvious that the energy flux no longer depends on z exponentially.

To obtain a true picture of the dissipation process one should include the dissipative terms into (4.33). For instance, taking into account viscous losses, the right-hand side of (4.33) acquires additional term (Landau and Lifshitz Hydrodynamics):

$$\nu \frac{1}{r^2} \frac{\partial}{\partial r} \left(r^3 \frac{\partial}{\partial r} \frac{\xi_\phi}{r} \right), \quad (4.40)$$

where ν is kinematic viscosity.

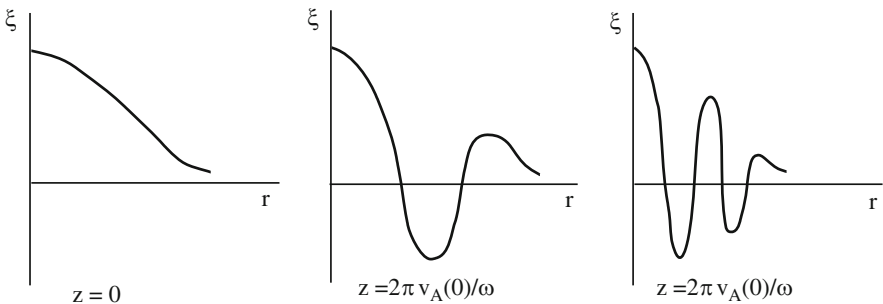


Fig. 4.4 Profiles of the eigenfunction with height in phase-mixed Alfvén wave

Let us assume that for oscillations with a smooth radial profile (on a scale of the order of flux tube radius) which initially are generated by convective motions, dissipation is slow, $\omega \gg \nu/R^2$. In this case the oscillations will propagate almost without damping up to the heights where the inverse damping rate $\Delta r^2/\nu$ (here $\Delta r \sim v_A R/\omega z$ is the scale-length of perturbations) becomes equal to the propagation time $z/v_A(r)$. The corresponding height can be estimated as

$$z = z_* \simeq \frac{v_A(r)}{\omega} \left(\frac{\omega R^2}{\nu} \right)^{1/3}. \tag{4.41}$$

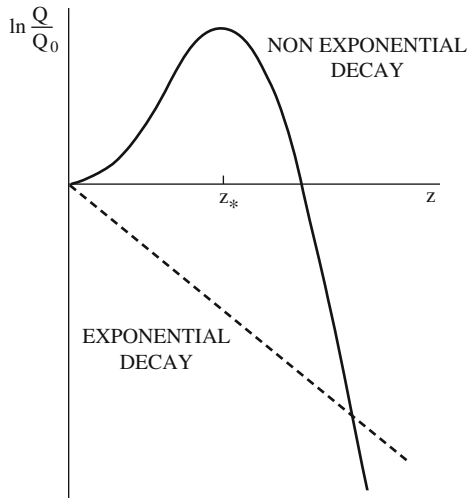
For the volume density of the power Q released by viscous dissipation we have the following estimate:

$$\sim \rho v \frac{\omega^2 \xi^2}{(\Delta r)^2}. \tag{4.42}$$

As Δr diminishes with height, Q is growing with z . At the altitude given by decreases (see Fig. 4.5). Thus, the heating power has a characteristic shape with a pronounced maximum at a certain altitude z . For comparison, the dotted line in Fig. 4.5 shows the power for the usual exponentially damping wave.

It is therefore obvious that even in the case of a smooth radial profile the flux tube oscillation can transfer energy from the photosphere and the convective zone to the upper layers of the atmosphere.

Fig. 4.5 The volume density of power released by viscous dissipation; solid line with the maximum at the definite altitude z_* (see (4.41)) represents the phase-mixed wave, while dashed line is for the regular exponentially damping wave



4.2.3 Phase-Mixed Kink Oscillations

Consider now the phase-mixing effect in the kink oscillations of flux tube (Rytova and Khijakadze 1990). In a low frequency limit, $\omega \ll v_A/R$, the linearized MHD equations can be reduced to the following equation for the r -component of the tube's displacement vector:

$$\frac{\partial^2}{\partial z^2} \left(\frac{B^2}{4\pi} \xi_r + \frac{\partial}{\partial r} \frac{B^2}{4\pi} r \frac{\partial}{\partial r} r \xi_r \right) + \omega^2 \left(\rho \xi_r + \frac{\partial}{\partial r} \rho r \frac{\partial}{\partial r} r \xi_r \right) = 0. \quad (4.43)$$

The Laplace transform for this equation has the form:

$$\frac{\partial}{\partial r} \rho (\omega^2 + p^2 v_A^2) r \frac{\partial}{\partial r} r \xi_{rp} + \rho (\omega^2 + p^2 v_A^2) \xi_{rp} = -F(0) - pF(0), \quad (4.44)$$

where ξ_{rp} is the Laplace transform for the displacement $\xi_r(z)$, and

$$F(r) = \frac{B^2}{4\pi} \xi_r + \frac{\partial}{\partial r} \frac{B^2}{4\pi} r \frac{\partial}{\partial r} r \xi_r \quad (4.45)$$

The exact solution of the boundary-value problem in this case is much more difficult than in the previous case of the torsional Alfvén waves. However, some general conclusions on the asymptotic behavior of the solution at $z \rightarrow \infty$ can be obtained in a simpler way.

The main contribution to the asymptotic solution comes from those singularities of ξ_{rp} which are nearest to the imaginary axis in the complex plane. In other words, we should consider the solution of (4.44) in the limit of $\text{Re}(p) = \epsilon \rightarrow 0$. In this limit the solution has a strongly oscillating shape near the point where the following condition is fulfilled:

$$v_A^2(r) = \frac{\omega^2}{(\text{Im} p)^2} \quad (4.46)$$

The solution in this region has a form:

$$\xi_{rp} = D(r) \ln \frac{1}{r - r_0 + i(\epsilon/\text{Im} p)(v_A(r)/v'_A(r))} \quad (4.47)$$

where $D(r)$ is a slowly varying function of p , and r_0 is determined by (4.46). As to the $v_A(r)$ and $v'_A(r) = dv_A(r)/dr$, they are taken at the point $r = r_0$.

From (4.41) and (4.47) for $\xi_{\phi p}$ we have

$$\xi_{\phi p} \sim \frac{1}{r - r_0 + i(\epsilon/\text{Im} p)[v_A(r)/v'_A(r)]} \quad (4.48)$$

One can see that the function $\xi_{\phi p}$ has poles near the points $p = \pm v_A/\omega$. i.e., the solution in this case is similar to that for the Alfvén waves (i.e., for torsional waves). The same holds for the asymptotic behavior of the solution.

4.3 Longitudinal Resonances

In this section we consider another aspect of the energy accumulation which is associated with longitudinal inhomogeneities of flux tube and/or its environment leading to longitudinal resonances. In particular, we study here the situation when magnetic flux tubes are pinned at some altitudes. This problem is also related to the coronal loops where both ends of coronal loop threads are pinned at the photosphere.

There are situations when magnetic flux tubes stretched upward from the photosphere get “pinned” at some height (Ryutova and Khijakadze 1990). At this height, almost complete reflection of the tube wave may occur, which means that standing waves can be excited and conditions for longitudinal resonances arise. Below, we discuss two examples of such resonant structures.

Consider the flux tube with a stepwise radial profile of density, magnetic field and pressure. But we will take into account the height dependence of flux tube parameters and the parameters of environment. In this case flux tube sustains weakly damped kink oscillations. It is important to note that the phase-mixing and associated effects are now absent.

For the z -dependent case the equation for kink oscillations has the form

$$4\pi R^2(\rho_i + \rho_e) \frac{\partial^2 \xi}{\partial t^2} = \frac{\partial}{\partial z} \left(R^2 B^2 \frac{\partial \xi}{\partial z} \right) \quad (4.49)$$

With the condition of flux conservation

$$R^2(z)B(z) = \text{const} \quad (4.50)$$

Equation (4.49) can be written as follows:

$$4\pi \frac{(\rho_i + \rho_e)}{B} \frac{\partial^2 \xi}{\partial t^2} = \frac{\partial}{\partial z} B \frac{\partial \xi}{\partial z} \quad (4.51)$$

We solve this equation for two types of longitudinal resonances: one is associated with loss of radial equilibrium by flux tube, which may lead to the effect similar to bullwhip effect, and another is caused by the temperature jump at some altitude along the flux tube.

4.3.1 Loss of Radial Equilibrium

To demonstrate the effect of gravity let us consider for simplicity an isothermal atmosphere. Then z -dependence of plasma parameters obeys the simple barometric law

$$\rho_i = \rho_{i0} e^{-\kappa_i z}, \quad \rho_e = \rho_{e0} e^{-\kappa_e z}, \quad \frac{B^2}{8\pi} + p_i = p_e \quad (4.52)$$

where κ_i and κ_e are inverse pressure scale-height inside and outside flux tube

$$\kappa_{i,e} \equiv \frac{1}{\Lambda_{i,e}} = \frac{mg}{k_B T_{i,e}}. \quad (4.53)$$

At $\kappa_e > \kappa_i$, i.e., in case when the pressure scale-height outside the flux tube is less than that inside ($T_e < T_i$), the flux tube rapidly expands and its mass per unit length becomes very large. Formally this means that at some height the flux tube gets “dissolved.” Indeed, from (4.52) it follows that when approaching the height (from below)

$$z_* = \frac{\Lambda_i \Lambda_e}{\Lambda_i - \Lambda_e} \ln \frac{p_{i0} + B^2/8\pi}{p_{e0}}, \quad (4.54)$$

the magnetic field tends to zero, and according to magnetic flux conservation, $R \rightarrow \infty$. Of course this is a formal statement, since at the point $z = z_*$, the equilibrium of the flux tube is no longer one-dimensional, but qualitative conclusion that in this region the flux tube rapidly expands, or, in other words, its inertia becomes infinitely large, remains valid. Respectively, the amplitude of flux tube oscillations becomes close to zero, and (4.49) should be solved with the boundary condition $\xi(z_*) = 0$. This is a typical Sturm-Liouville problem and the corresponding solution has a discrete frequency spectrum. Which means the presence of resonances in the system, and if the spectrum of the exciting force is sufficiently narrow, the amplitude of flux tube oscillations can increase at several points (namely at the gulf points) along the tube.

Consider first a quasi-classical problem of forced oscillations of flux tube with $\xi \sim \exp(-i\omega t)$. Equation (4.51) takes a form:

$$\frac{\partial}{\partial z} B \frac{\partial \xi}{\partial z} + 4\pi \frac{(\rho_i + \rho_e)}{B} \omega^2 \xi = 0 \quad (4.55)$$

In a quasi-classical approach, a local wave vector

$$q(z) = \frac{\omega B(z)}{\sqrt{4\pi[\rho_i(z) + \rho_e(z)]}} \equiv \frac{\omega}{c_k(z)} \quad (4.56)$$

is much larger than κ_i and κ_e , i.e., the wave frequency is large. In this approximation, the flux tube can be considered “locally homogeneous,” and the energy density flux of tube oscillations takes a simple form

$$S = \pi R^2 (\rho_i + \rho_e) \xi^2 \omega^2 c_k \quad (4.57)$$

It is just a product of phase velocity of kink oscillations (which in this case coincides with the group velocity), and the energy density of oscillations per unit length of the tube. The condition, $S = \text{const}$, determines the oscillation amplitude as a function of height. From (4.50) and (4.56) we have

$$\xi(z) = \frac{[\rho_{i0} + \rho_{e0}]^{1/4}}{[\rho_i(z) + \rho_e(z)]^{1/4}} \xi(0) \quad (4.58)$$

As the plasma density drops with height exponentially, the oscillation amplitude grows exponentially as well. This fact has an important consequences. For example, at large enough amplitudes, the oscillation energy will be efficiently dissipated due to nonlinear processes, of which the first to appear is generation of shock waves.

For illustration consider a particular case, when (4.55) can be solved exactly. This can be done if we assume that scale heights inside and outside flux tube are close, $\kappa_i \simeq \kappa_e$. Then, from equilibrium conditions we have

$$B(z) = B(0)e^{-\kappa z/2}, \quad \frac{\rho_i(z) + \rho_e(z)}{B(z)} = \frac{\rho_i(0) + \rho_e(0)}{B(0)} e^{-\kappa z/2} \quad (4.59)$$

With these, (4.55) becomes

$$\frac{\partial^2 \xi}{\partial z^2} - \kappa \frac{\partial \xi}{\partial z} + q^2 \xi = 0 \quad (4.60)$$

where q is given by (4.56).

A secular equation for the solution of (4.60) of the form $\sim \exp(i\mu z)$ is as follows:

$$\mu^2 + i\mu\kappa - q^2 = 0 \quad (4.61)$$

To choose a correct root of (4.61), we need to add a small imaginary part to the frequency, $\omega = \omega_0 + i\epsilon$, such that at $\omega_0 > 0$, $\epsilon \rightarrow +0$. The sign of ϵ corresponds to a slow adiabatic excitation of perturbation at $t \rightarrow -\infty$. Out of two solutions of (4.58), we need to choose the one that has $\text{Re}\mu > 0$, which corresponds to assumption that at $t \rightarrow -\infty$ the flux tube was at rest, and that the oscillations excited at $z = 0$ propagate from the origin of coordinate system to infinity, i.e.,

$$\mu = -\frac{i\kappa}{2} + \sqrt{q^2 - \frac{\kappa^2}{4}} \quad (4.62)$$

After choosing the root, we put $\epsilon = 0$. Finally,

$$\xi \sim e^{\kappa z/2} \exp(iz\sqrt{q^2 - \kappa^2/4}) \quad (4.63)$$

This solution has two slightly different branches determined by the frequency. One branch corresponds to relatively high frequencies, when $q > \kappa/2$, i.e., when

$$\omega > c_k/4\Lambda, \quad (4.64)$$

In this case the flux tube oscillations represent running waves propagating upward along flux tube with exponentially growing amplitude.

In the opposite case, when $q < \kappa/2$ and, i.e., for lower frequencies such that

$$\omega < c_k/4\Lambda \quad (4.65)$$

the solution of (4.55) has pure exponential dependence on height

$$\xi \sim e^{(\kappa/2 - \sqrt{\kappa^2/4 - q^2})z} \quad (4.66)$$

In both cases ($q > \kappa/2$ and $q < \kappa/2$), the exponential growth of oscillation amplitude will be eventually limited by some physical processes determined by specific properties of a system. First to act are nonlinear processes, and, in particular, formation of shocks and solitons.

4.3.2 Bullwhip Effect

By its nature, an unlimited growth of the amplitude of flux tube oscillations is very similar to effect of bullwhip: in both cases the growth of the oscillation amplitude is associated with *longitudinal* inhomogeneity of the object. Note that final stage, i.e., exponentially growing amplitude of flux tube, and shock formation may occur at different heights for two branches (4.64) and (4.65). One may expect that in case of $\omega > c_k/4\Lambda$ with accompanying running waves, shock formation occurs at higher altitudes and hence, at higher temperatures, than in case of $\omega < c_k/4\Lambda$.

From observational point of view such a process may be easily recognizable, especially now when high resolution and high cadence observations show great details in dynamics of various formations throughout the solar atmosphere. Examples of such events taken by the AIA instrument on SDO are shown in Figs. 4.6 and 4.7.

Figure 4.6 shows a bullwhip behavior of a flux rope captured by AIA instrument at coronal temperatures in Fe IX 171 line. Shown is formation and evolution of growing loop curvature at the “end” of the rope (marked by blue curves) accompanied in the final stage by shock formation and its farther growth (marked

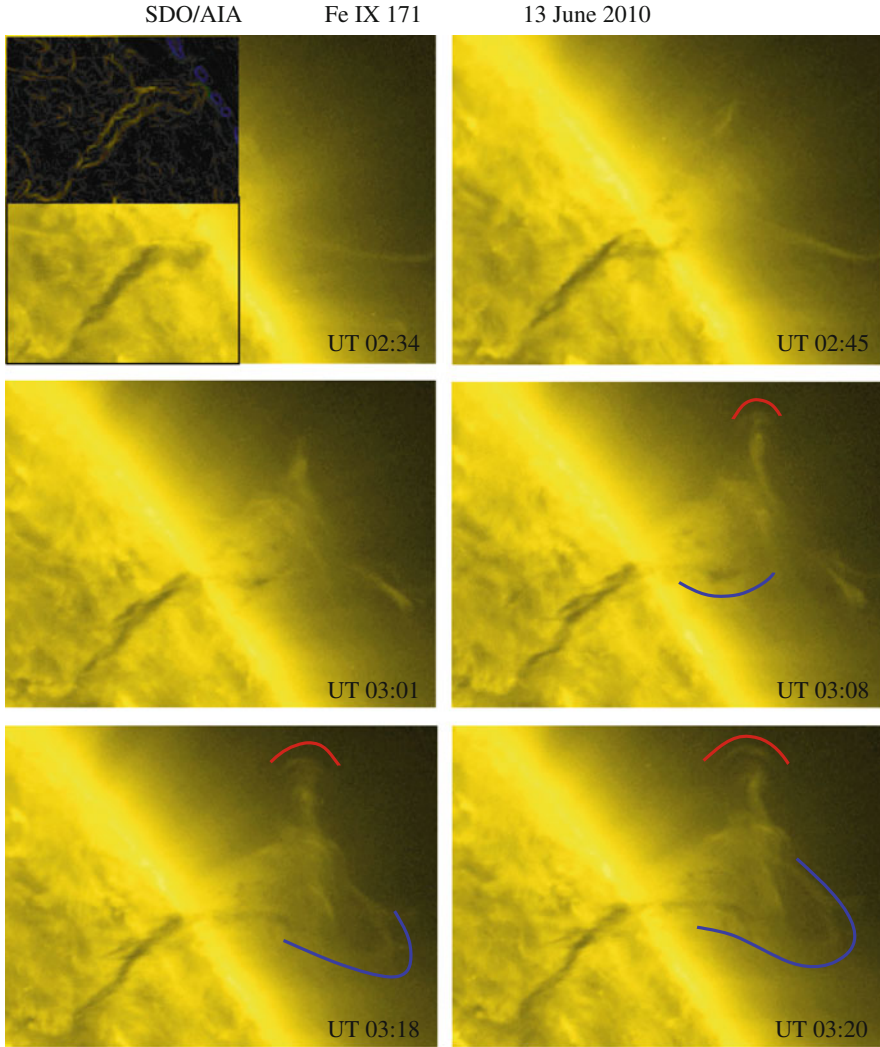


Fig. 4.6 A bullwhip behavior of a flux tube at coronal temperatures, $T \simeq 6.3 \times 10^5$ K shown at six instances of time. The dark inlet on the image at UT 02:34 is produced by the Edge Detect procedure of the area marked by box in the left lower corner clearly reveals the flux tube oscillations well seen in all subsequent snapshots. Blue curves at the final stages outline the exponentially growing amplitude. The red arcs at three last snapshots outline the growing shock front. Field of view is $153 \text{ Mm} \times 114 \text{ Mm}$

by the red curves). The dark inlet on the image at UT 02:34 is produced by the Edge Detect procedure of the area marked by box in the left lower corner of that snapshot. The inlet reveals a regular oscillations of flux tube, which farther in time (seen in the subsequent snapshots) evolve into the exponentially growing swing.

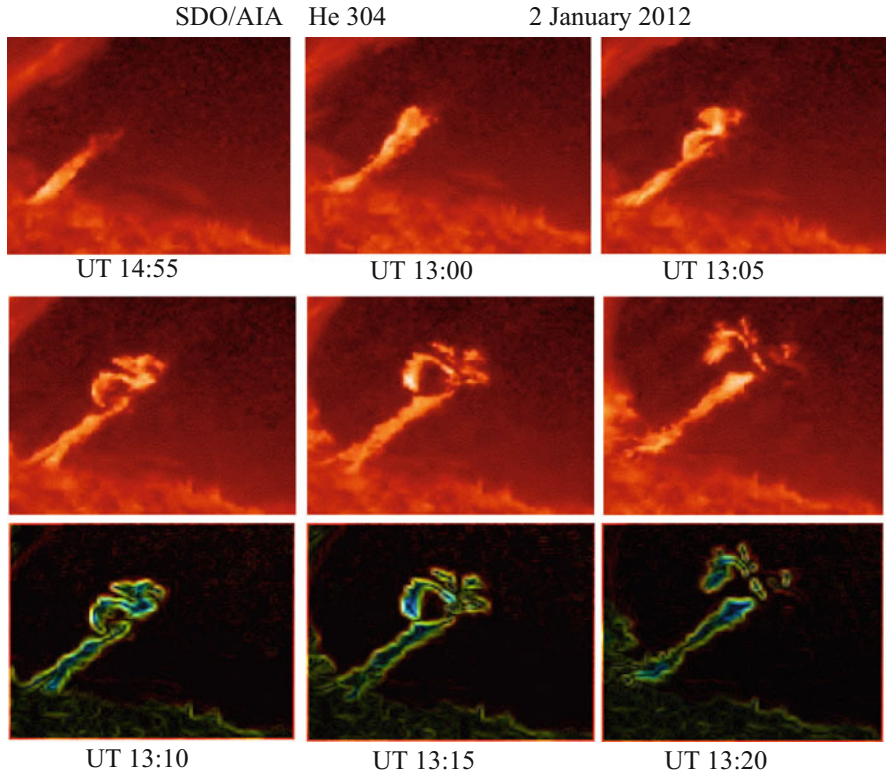


Fig. 4.7 Bullwhip behavior of a compact magnetic flux at the chromospheric temperatures, $T \simeq 6.3 \times 10^5$ K, shown at six instances of time. Last three snapshots (middle row) are reproduced in the bottom with application of the Edge Detect procedure, which reveals more clearly the oscillatory pattern throughout the process. Field of view is $68 \text{ Mm} \times 51 \text{ Mm}$

Another example of bullwhip behavior seen at lower, chromospheric temperatures, is shown in Fig. 4.7. In this case explosive growth of the flux tube amplitude and shock formation occur already at the chromospheric temperatures. Upper six images show a compact energized magnetic flux tube in the chromosphere taken by AIA instrument on the SDO in 304 emission line on January 2, 2012. The Edge Detect procedure applied to all three images in a middle row reveals both the oscillatory pattern of the body of flux tube and formation of a swing at the end of flux tube. One should bear in mind that the end of flux tube and its oscillation amplitude are governed by (4.58) and (4.63).

The bullwhip effect in solar flux tubes is a regular phenomenon and may be observed at all temperatures from the chromospheres to outer corona. All it requires, actually, is the longitudinal inhomogeneity of a flux tube and its ability to sustain the oscillatory motion. As mentioned above, these are in fact the same requirement that are needed to excite the growing oscillations along the bullwhip and produce a

crack, i.e., shock wave or exploding soliton, as different theories of bullwhip predict (Bernstein et al. 1958; Krehl et al. 1998; McMillen and Goriely 2003).

Since antiquity man used whip cracking for various reasons. The fact that the crack is associated with acceleration of the wave that reaches the supersonic velocity at the tip, and generates shock wave, has been realized only in the beginning of twentieth century.

And yet, the first obvious experiment and mathematical illustration of the effect were done only in 1958 by Bernstein et al. They studied a bullwhip operated by an expert whip cracker, using a movie camera and still photographs. They found that the crack is produced by the tip of the whip exceeding the sound speed and producing the shock wave. In their words, “in order to produce a crack it is necessary to start a sharp loop near the handle and cause this loop to propagate down toward the tip by investing the system with sufficient momentum or kinetic energy. Apparently this energy becomes concentrated near the tip end, and when the tip tries to negotiate the sharp turn around the loop, it does so with sufficient velocity to cause a shock wave in air.”

They also gave a mathematical solution for idealized whip assuming that a discontinuity in tension propagates down the whip reaching infinite values associated with decreasing of the mass of the whip. For example, they arrived to solution for the speed of a kink in a form:

$$\frac{ds}{dt} = k + \frac{c}{\sqrt{L-s}} \quad (4.67)$$

Here s is the coordinate of a kink along the whip, L is the length of the whip and k and c are constants of integration. Calculated tension, which is proportionally to $(ds/dt)^2$, also turns out to be inverse proportional to $1/\sqrt{L-s}$. This means that in a finite time, the speed of the tip and the tension increase without the limit as $s \rightarrow L$, i.e., as the kink reaches the tip.

Figure 4.8 shows a numerical solution for the wave propagating along the whip. The whip is modeled as an inhomogeneous planar elastic rod with tapered end. It was found that an impulse applied to the handle of the whip travels to the end and accelerates the tip to supersonic speed. A crack is produced when a section of the whip breaks the sound barrier. Dash-dotted curves in Fig. 4.8 are the shock waves emitted by a material point on the rod.

In the solar atmosphere, the open structures that reach the height that no longer sustains conditions of $\omega\xi_0 < c_{se}$ are all subject of explosively growing amplitude and exhibition of bullwhip effect. It is important to note that in this particular case the fact of the exponential growth of amplitude is not at all associated with the instability of a system, but rather is a consequence of the atmospheric stratification, i.e., an exponential drop of the density inside flux tube.

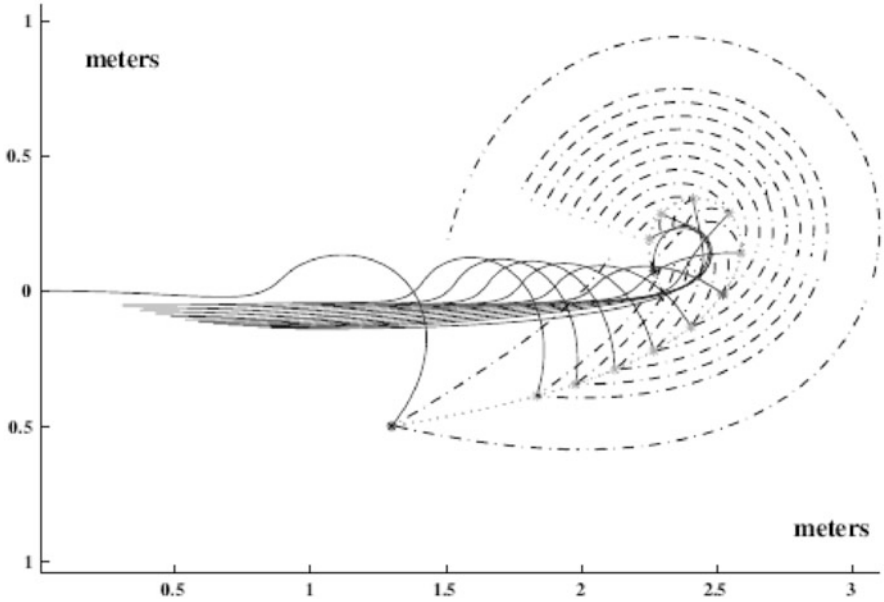


Fig. 4.8 Numerical solution for time sequence of the whip behavior. The solid curves are the rod; the dashed curve is the path the tip of the whip travels; the dash-dotted curves are the shock waves. Reprinted from McMillen and Gorieli (2003) by permission from Elsevier

4.4 Standing Resonances and the Temperature Jump

Consider now another mechanism for the formation of longitudinal resonant structures associated with temperature jump (Ryutova and Khijakadze 1990). Take, for example,

$$T = \begin{cases} T_1, & 0 < z < L \\ T_2, & z > L \end{cases} \tag{4.68}$$

We assume for simplicity that temperatures inside and outside the flux tube are about the same.

In particular case, considered in this section, the presence of a sharp discontinuity in the vertical temperature leads to formation of standing resonances along the oscillating flux tube. To avoid a possibility of shock formation, we assume that the initial amplitude of flux tube oscillations is small enough to satisfy condition $\omega\xi_0 < c_{se}$, where c_{se} is the sound speed outside flux tube.

The solution of (4.60) in the region below the temperature jump, $0 < z < L$, is as follows:

$$\xi = e^{(\kappa z/2)} \left[\xi_0 \cos(z\sqrt{q^2 - \kappa^2/4}) + A \sin(z\sqrt{\kappa^2/4 - q^2}) \right] \tag{4.69}$$

Here we took into account that boundary condition at the base of the flux tube, $z = 0$, with a given amplitude of oscillations ξ_0 , i.e., $\xi|_{z=0} = \xi_0$, provides expressions for the coefficient in front of the first term, which obviously, is ξ_0 .

In the region above the temperature jump, $z > L$, with $1/\Lambda_2 = (mg)/(kT_2)$, (4.49) has a form:

$$\frac{\partial^2 \xi}{\partial z^2} - \kappa \frac{T_1}{T_2} \frac{\partial \xi}{\partial z} + q^2 \frac{T_1}{T_2} \xi = 0 \quad (4.70)$$

Here we took into account that $1/\Lambda_2 = \kappa(T_1/T_2)$. Solution to this equation for the open end of flux tube is as follows:

$$\xi = C e^{(\sigma \kappa z/2)} \exp\left(i\sqrt{q^2 \sigma - \kappa^2 \sigma^2/4}\right), \quad \sigma = \frac{T_1}{T_2} \quad (4.71)$$

Two other arbitrary constants A and C are determined from the boundary conditions at the point $z = L$:

$$\xi \Big|_{z=L} = 0; \quad \frac{d\xi}{dz} \Big|_{z=L} = 0 \quad (4.72)$$

After a simple algebra, we get for A , describing the behavior of flux tube in region $0 < z < L$:

$$A = -\xi_0 \frac{\kappa L \cos \alpha - 2\alpha \sin \alpha - \left(\sigma \kappa L + 2i\sqrt{4\sigma q^2 L^2 - \sigma^2 \kappa^2 L^2}\right) \cos \alpha}{\kappa L \sin \alpha + 2\alpha \cos \alpha - \left(\sigma \kappa L + i\sqrt{4\sigma q^2 L^2 - \sigma^2 \kappa^2 L^2}\right) \sin \alpha} \quad (4.73)$$

where the coefficient C is included in A , and

$$\alpha = L\sqrt{q^2 - \frac{\kappa^2}{4}} \quad (4.74)$$

From the expression (4.73) it is clear that at $\sigma = T_1/T_2 \ll 1$ there appear narrow resonances in the system. Indeed, the imaginary part in the denominator is small, and when the real part of denominator tends to zero, the amplitude of oscillations becomes infinitely large.

4.4.1 Growth of the Oscillation Amplitude: First Resonance

To consider this effect in more detail, let us simplify the analysis by neglecting the terms of the order of $\sqrt{T_1/T_2}$ (and higher) in the numerator, and terms of the order

of T_1/T_2 in the denominator. In this approximation we then have

$$A = -\xi_0 \frac{\kappa L \cos\alpha - 2\alpha \sin\alpha}{\kappa L \sin\alpha + 2\alpha \cos\alpha - 2iqL\sqrt{\sigma} \sin\alpha} \quad (4.75)$$

The denominator here tends to zero at $\text{tg}\alpha = (2qL\sigma - 2\alpha)/\kappa L$. Taking into account smallness of parameter $\sigma = T_1/T_2 \ll 1$, we find that the resonance condition is determined by the equation

$$\text{tg}\alpha = -\frac{2\alpha}{\kappa L} \quad (4.76)$$

Respectively, for the set of resonance frequencies we have

$$\omega_n^2 = c_k(0) \sqrt{\frac{\alpha_n}{L^2} + \frac{\kappa^2}{4}} \quad (4.77)$$

where α_n are the roots of (4.76), $n = 1, 2, 3 \dots$

Near the resonance frequency ω_n , i.e., at $|\omega - \omega_n| \ll 0$, one can replace the numerator in (4.75) by its value at the resonance point and expand the denominator over $(\omega - \omega_n)$. This gives

$$A_n = -\xi_0 \frac{2\alpha_n(\kappa^2 L^2 - 4\alpha_n^2)}{[2\kappa L + \kappa^2 L^2 + 4\alpha_n^2] \sqrt{4\alpha_n^2 + \kappa^2 L^2}} \frac{\omega_n}{\omega - \omega_n + i\nu_n/2} \quad (4.78)$$

where

$$\nu_n = 16\omega_n \sqrt{\sigma} \frac{\alpha_n^3}{[2\kappa L + \kappa^2 L^2 + 4\alpha_n^2] \sqrt{4\alpha_n^2 + \kappa^2 L^2}} \quad (4.79)$$

are the damping rates.

As an example, let us consider the first resonance, $n = 1$, which lies in the interval $\pi/2 < \alpha_1 < \pi$. Assume that the wavelength of oscillations is comparable with L , i.e., $\kappa L \simeq 1$. Then, $\alpha_1 = 1.9$, and

$$A_1 = 5\xi_0 \left(\omega - \omega_1 + i\frac{\nu_1}{2} \right); \quad \frac{\nu_1}{\omega_1} = 1.4\sqrt{\sigma} \quad (4.80)$$

The oscillation amplitude can be found from (4.59). Near the resonance we can neglect the first term, thus obtaining

$$\xi(L) = A_1 \exp(\kappa L/2) \sin\alpha_1, \quad (4.81)$$

and for $\kappa L \simeq 1$,

$$\xi(L) = 6\xi_0 \frac{\omega_1}{\omega - \omega_1 + 0.7i\omega_1 \sqrt{T_1/T_2}} \quad (4.82)$$

Now, if, for example, $T_2 = 10T_1$, the width of the resonance is 20% of the frequency. This is a well measurable quantity in the solar atmosphere.

4.4.2 Spectral Density and Strong Enhancement of the Oscillation Amplitude

We have considered above harmonic oscillations excited at the base of the flux tube. Actually, in the region where flux tube is rooted, they experience the random displacements caused by the convective motions. Therefore, more adequate would be the description of these displacements in terms of the spectral density of oscillations, which can be represented in the form

$$(\xi_n^2)_\omega = \frac{|F|^2 (\xi_0^2)_\omega}{(\omega - \omega_n)^2 + \nu_n^2/4} \quad (4.83)$$

where $(\xi_n^2)_\omega$ is the spectral density of flux tube oscillations averaged over the “length” of the flux tube, ω_n and ν_n are, as before, the n -th order eigenfrequency and corresponding damping rate. The function F has a meaning of a form-factor which is of the order of unity and depends on the particular longitudinal structure of the eigenfunction.

To get the square average of flux tube displacement, we have to integrate (4.83) over frequencies. For narrow resonances, $\nu_n \ll \omega_n$, one can replace $(\xi_0^2)_\omega$ by the constant, $(\xi_0^2)_{\omega_n}$, to obtain

$$\overline{\xi_r^2} - \int (\xi_r^2)_\omega d\omega = \frac{1}{\nu_n} 2|F|^2 (\xi_0^2)_{\omega_n} \quad (4.84)$$

Thus, the displacement of a flux tube at some height can be much larger than at its footprint. In other words, if somewhere the resonance structure is formed, one can expect a large oscillation level and with some probability the amplitude of oscillations can be substantially larger than its time-averaged value. This means that in this region nonlinear dissipation can occur. Note that these effect may exist along the resonances described above and occurrence of a bullwhip effect.

The probability distribution function $P(\xi)$ depends on the properties of a random process $\xi_0(t)$. For example, for a Gaussian process the probability has a standard exponential form

$$P(\xi) \sim \exp\left(-\xi^2/2\overline{\xi^2}\right), \quad (4.85)$$

which gives a considerable probability for fluctuations during which ξ^2 is about six times larger than its average value $\overline{\xi^2}$, while $\overline{\xi^2}$ itself is already enhanced and is

large (see (4.84)):

$$\xi^2 \simeq 6 \overline{\xi^2}. \quad (4.86)$$

In the observations such events will manifest themselves in range of phenomena, from a temporal brightening of a flux tube region at a given height to explosive events and violent mass ejections.

Note that we did not make any assumptions regarding the properties of spectral density of exciting oscillations, so that it can be arbitrary. The results therefore are general.

4.5 Weakly Nonlinear Waves in Flux Tubes

In this section we address the problem of weakly nonlinear oscillations of flux tubes. Besides the nonlinearity, the flux tube oscillations are subject of the dispersion associated in the first place with inhomogeneity of the flux tube parameters and its environment. As in many other natural environments, if the wave amplitude steepens, the competition between nonlinearity and dispersion may lead to stabilization of the amplitude and, thus to formation of a dynamically stable kink, propagating as a solitary wave (Rayleigh (1876); Boussinesq (1871) and Korteweg and de Vries (1895)). We will see below that both, nonlinear kink and sausage oscillations may produce the solitary kink and sustain its longevity.

4.5.1 Nonlinear Kink Oscillations: *KdV-Bürgers Equation*

In this section we follow studies of weakly nonlinear long wavelength kink oscillations of flux tube performed by Ryutova and Priest (1993). We adopt, as earlier, the model of cylindrical flux tube of radius R , directed along the z -axis. Radius of the flux tubes is assumed to be much less than the wavelength $\lambda = k^{-1}$: $kR \ll 1$. The analysis is based on the ideal MHD equations which we write here for convenience:

$$\rho \frac{\partial \mathbf{v}}{\partial t} + (\mathbf{v} \nabla) \mathbf{v} = -\nabla \delta p + \frac{1}{4\pi} [\nabla \times \mathbf{B}] \times \mathbf{B} \quad (4.87)$$

$$\begin{aligned} \frac{\partial \mathbf{B}}{\partial t} &= \nabla \times [\mathbf{v} \times \mathbf{B}] \\ \frac{\partial \rho}{\partial t} + \operatorname{div} \rho \mathbf{v} &= 0 \\ p &= p_0 \left(\frac{\rho}{\rho_0} \right)^\gamma \end{aligned} \quad (4.88)$$

The set is completed by the pressure equilibrium condition.

At the surface of flux tube the boundary conditions of continuity of the normal component of velocity,

$$v_{ri}|_{r=R} = v_{re}|_{r=R}, \quad (4.89)$$

and the normal component of the momentum flux

$$p_i + \frac{B^2}{8\pi} \Big|_{r=R} = p_e \Big|_{r=R} \quad (4.90)$$

should be satisfied. These conditions lead to the following dispersion relation (see Eqs. (3.47)–(3.48), Chap. 3):

$$\eta \frac{\omega^2 - k^2 v_A^2}{\omega^2} \frac{\partial \ln \psi_e}{\partial r} \Big|_{r=R} = \frac{\partial \ln \psi_i}{\partial r} \Big|_{r=R} \quad (4.91)$$

In the long-wavelength limit the expression (4.91) is subject of expansion in powers of a small parameter (kR). The first term in this expansion gives the phase velocity of a kink mode, $c_k = B/\sqrt{4\pi(\rho_i + \rho_e)}$.

Retaining the next order terms we obtain

$$\omega = c_k k + \beta_k k^3 + i\mu k^3, \quad (4.92)$$

where

$$\beta_k = -\frac{c_k R^2}{8(1 + \eta)^2}, \quad \mu = \frac{\pi c_k R^2}{4} \frac{c_k^2 - c_s^2}{91 + \eta)c_s^2} \quad (4.93)$$

Here c_s is the sound speed *outside* flux tube.

The second term in the dispersion relation (4.92) describes a weak dispersion of the kink mode associated with the flux tube inertia, and the third term corresponds to radiative damping of flux tube oscillations.

Now we need to determine the character of the nonlinearity of the kink oscillations. Analyzing the next terms we arrive to a simple conclusion that the first nonlinear term that can affect the finite-amplitude kink oscillations is a cubic term, since the azimuthal dependence of the quadratic nonlinearity contains only terms with $m = 0$ and $m = 2$. Thus, the character of nonlinearity of a kink mode appears to be cubic.

To find the equation of kink mode corresponding to the dispersion relation (4.92) and containing a cubic nonlinearity we use the method of the stretched variables

$$\zeta = \epsilon(z - c_k t), \quad \tau = \epsilon^2 t \quad (4.94)$$

where ϵ is a key small parameter.

To carry out the adequate perturbation analysis we perform expansion of the MHD equations by representing the velocity, magnetic field and other plasma parameters in power series with respect to ϵ . For simplicity we assume that plasma inside flux tube is cold, $p_i \ll p_e$, and respectively, neglect the gas-kinetic pressure inside flux tube. This assumption is not principal but allows to simplify algebra. Thus inside the flux tube we may write

$$\begin{aligned}
 \mathbf{v}_\perp &= \epsilon^{1/2} \mathbf{v}_{1\perp} + \epsilon^{3/2} \mathbf{v}_{2\perp} + \dots \\
 v_z &= \epsilon v_{1z} + \epsilon^2 v_{2z} + \dots \\
 \mathbf{B}_\perp &= \epsilon^{1/2} \mathbf{B}_{1\perp} + \epsilon^{3/2} \mathbf{B}_{2\perp} + \dots \\
 B_z &= B_0 + \epsilon^{3/2} B_{1z} + \epsilon^{5/2} B_{2z} + \dots \\
 \rho &= \rho_0 + \epsilon \rho_1 + \epsilon^2 \rho_2 + \dots
 \end{aligned} \tag{4.95}$$

Respectively, outside the flux tube we have

$$\begin{aligned}
 \mathbf{v}_{e\perp} &= \epsilon^{1/2} \mathbf{v}_{1e\perp} + \epsilon^{3/2} \mathbf{v}_{2e\perp} + \dots \\
 v_{ez} &= \epsilon v_{e1z} + \epsilon^2 v_{e2z} + \dots \\
 p_e &= p_{e0} + \epsilon^{3/2} p_{e1} + \epsilon^{5/2} p_{e2} + \dots \\
 \rho_e &= \rho_{e0} + \epsilon^{3/2} \rho_{e1} + \epsilon^{5/2} \rho_{e2} + \dots
 \end{aligned} \tag{4.96}$$

where \mathbf{v}_\perp and \mathbf{B}_\perp are the transverse (r and ϕ) components of velocity and magnetic field.

The expansions (4.95) and (4.96), along the exact representation of a linear stage of flux tubes oscillations, describe the dispersion properties of a system that includes the oscillating flux tube and its environment. Besides, the above choice of variables allows one to specify the nature of the nonlinearity independently of the dispersive properties of a system.

Substituting (4.95) and (4.96) in the MHD equations, and equating terms of each order in ϵ , we obtain sequence of equations up to the desired order.

First, in the order of $\epsilon^{3/2}$ for a flux tube interior we have from (4.87) and (4.88)

$$-c_k \rho_0 \frac{\partial \mathbf{v}_{1\perp}}{\partial \zeta} = -\frac{B_0}{4\pi} \nabla_\perp B_z + \frac{B_0}{4\pi} \frac{\partial \mathbf{B}_{1\perp}}{\partial \zeta} \tag{4.97}$$

$$-c_k \frac{\partial \mathbf{B}_{1\perp}}{\partial \zeta} = B_0 \frac{\partial \mathbf{v}_{1\perp}}{\partial \zeta} \tag{4.98}$$

and for outer region

$$-c_k \rho_{e0} \frac{\partial \mathbf{v}_{e1\perp}}{\partial \zeta} = -\nabla_\perp p_1 \tag{4.99}$$

$$p_1 = c_s^2 \rho_1 \tag{4.100}$$

Substituting $\mathbf{B}_{1\perp} = -(B_0/c_k)\mathbf{v}_{1\perp}$ which follows directly from (4.98), into (4.97) we have

$$\left(-c_k\rho_0 + \frac{B_0}{4\pi c_k}\right) \frac{\partial \mathbf{v}_{1\perp}}{\partial \zeta} = -\nabla_{\perp} \frac{B_0 B_{1z}}{4\pi}, \quad (4.101)$$

and, respectively,

$$\left(-c_k\rho_0 + \frac{B_0}{4\pi c_k}\right) \frac{\partial \mathbf{v}_{1\perp}}{\partial \zeta} = -c_k\rho_{e0} \frac{\partial \mathbf{v}_{1\perp}}{\partial \zeta} \quad (4.102)$$

This equation coincided naturally with the basic equation for linear oscillations which gives the phase velocity of kink mode.

Now we proceed to the next, ϵ^2 , order approximation. At this order from z -component of (4.87) and the second equation in (4.88) we have

$$\rho_1 = \frac{\rho_0}{c_k} v_{1z}, \quad \rho_0 c_k v_{1z} = \frac{c_k^2 \mathbf{B}_{1\perp}^2}{v_A^2 8\pi} \quad (4.103)$$

Here we used relationship

$$\nabla_{\perp} B_{1z} = \frac{v_A^2 - c_k^2}{v_A^2} \frac{\partial \mathbf{B}_{1\perp}}{\partial \zeta}. \quad (4.104)$$

Now, in the next, $\epsilon^{5/2}$ order, the transverse components of (4.87) and the first equation in (4.88) for the flux tube interior take forms

$$\rho_0 c_k \frac{\partial \mathbf{v}_{2\perp}}{\partial \zeta} + \frac{B_0}{4\pi} \left(\frac{\partial \mathbf{B}_{2\perp}}{\partial \zeta} - \nabla_{\perp} B_{2z} \right) = \rho_0 \frac{\partial \mathbf{v}_{1\perp}}{\partial \tau} - (\rho_1 c_k - \rho_0 v_{1z}) \frac{\partial \mathbf{v}_{1\perp}}{\partial \zeta} \quad (4.105)$$

$$c_k \frac{\partial \mathbf{B}_{2\perp}}{\partial \zeta} + B_0 \frac{\partial \mathbf{v}_{2\perp}}{\partial \zeta} = \frac{\partial \mathbf{B}_{1\perp}}{\partial \tau} + \frac{\partial}{\partial \zeta} (v_{1z} \mathbf{B}_{1\perp}) \quad (4.106)$$

In the outer region at this order we have

$$\rho_{e0} c_k \frac{\partial \mathbf{v}_{e2\perp}}{\partial \zeta} - \nabla_{\perp} p_2 = \rho_{e0} \frac{\partial \mathbf{v}_{e1\perp}}{\partial \tau} + \frac{\rho_{e1}}{2} \nabla_{\perp} \mathbf{v}_{e1\perp}^2, \quad (4.107)$$

$$\rho_{e0} c_k \frac{\partial v_{e1z}}{\partial \zeta} = \frac{\partial p_1}{\partial \zeta} \quad (4.108)$$

Using $p_1 = c_s^2 \rho_{e1}$ in (4.108) and taking into account that

$$\nabla \rho_{e1} = \frac{\rho_{e0} c_k}{c_s^2} \frac{\partial \mathbf{v}_{e1\perp}}{\partial \zeta} \quad (4.109)$$

we can write (4.107) in the form:

$$\rho_{e0} c_k \frac{\partial \mathbf{v}_{e2\perp}}{\partial \zeta} - \nabla_{\perp} \left(p_2 + \frac{\rho_{e1} \mathbf{v}_{e1\perp}^2}{2} \right) = \rho_{e0} \frac{\partial \mathbf{v}_{e1\perp}}{\partial \tau} - \frac{c_k \rho_{e0}}{c_s^2} \mathbf{v}_{e1\perp}^2 \frac{\partial \mathbf{v}_{e1\perp}}{\partial \zeta} \quad (4.110)$$

Matching (4.105) and (4.110) through the boundary conditions, we obtain

$$(\rho_{i0} + \rho_{e0}) c_k \frac{\partial \mathbf{v}_{2\perp}}{\partial \zeta} + \frac{B_0}{4\pi} \frac{\partial \mathbf{B}_{2\perp}}{\partial \zeta} = (\rho_{i0} + \rho_{e0}) c_k \frac{\partial \mathbf{v}_{1\perp}}{\partial \tau} - \frac{c_k \rho_{e0}}{c_s^2} \mathbf{v}_{1\perp}^2 \frac{\partial \mathbf{v}_{1\perp}}{\partial \zeta} \quad (4.111)$$

Eliminating the second-order terms in (4.111) and (4.106) we arrive straightforwardly to nonlinear equations for kink mode written in the stretched variables:

$$2 \frac{\partial \mathbf{B}_{1\perp}}{\partial \tau} + \frac{c_k}{\rho_{i0} v_A^2} \frac{\partial}{\partial \zeta} \left(\mathbf{B}_{1\perp} \frac{\mathbf{B}_{1\perp}^2}{8\pi} \right) - \frac{c_k^2}{c_s^2} \frac{\rho_{e0} c_k}{B_0^2 (\rho_{i0} + \rho_{e0})} \frac{\mathbf{B}_{1\perp}^2}{2} \frac{\partial \mathbf{B}_{1\perp}}{\partial \zeta} \quad (4.112)$$

It is convenient to introduce instead of the transverse components \mathbf{B}_{\perp} the complex quantity $H = B_r - i B_{\phi}$, and normalize it by the unperturbed magnetic field, B_0 . Finally, the nonlinear equation for a kink mode acquires the form:

$$\frac{\partial H}{\partial \tau} + \frac{c_k}{4} \frac{\partial}{\partial \zeta} (|H|^2 H) - \frac{c_k^3}{4(1+\eta)c_s^2} |H|^2 \frac{\partial H}{\partial \zeta} = 0 \quad (4.113)$$

Equation (4.113) is a fundamental equation describing nonlinear kink oscillations of magnetic flux tubes. We see that, as expected, the character of nonlinearity is cubic.

It is interesting that the first two terms in (4.113) formally are similar to those describing hydromagnetic waves propagating along the magnetic field in a cold plasma (e.g., Mjølhus 1976). Note however that the similarity is only formal, because in cold plasma the MHD waves propagate in an unbounded plasma, whereas in case of magnetic flux tubes, we deal with an oscillating “magnetic string” which interacts with the nonmagnetic environment. The influence of the magnetic free region is represented by the last term in (4.113), and is reflected in the propagation velocity of the kink mode.

It should be emphasized that the entire procedure developed above (starting from stretched variables (4.113)) was aimed to find the character of nonlinearity. To construct the full equation describing the nonlinear kink oscillations in weakly dispersive and dissipative media, (4.113) should be supplemented with the dispersion terms obtained in the analysis of radiative damping.

Applying a standard procedure to the dispersion relation (4.92) we obtain the evolutionary equation describing a weakly nonlinear kink oscillations in weakly

dispersive medium, which includes the intrinsic dissipative process associated with radiation of secondary MHD waves by oscillating flux tube

$$\begin{aligned} \frac{\partial H}{\partial \tau} + \frac{c_k}{4} \frac{\partial}{\partial \zeta} (|H|^2 H) - \frac{c_k^3}{4(1+\eta)c_s^2} |H|^2 \frac{\partial H}{\partial \zeta} + \beta_k \frac{\partial^3 H}{\partial \zeta^3} \\ + \frac{\mu}{\pi} v.p. \int_{-\infty}^{\infty} \frac{\partial^3 H}{\partial s^3} \frac{ds}{s - \zeta} = 0 \end{aligned} \quad (4.114)$$

where β_k and μ are given by expressions (4.93).

Equation (4.114) fully describes a nonlinear oscillations of flux in a dissipative and weakly dispersive media. The equation is obviously of a type of KdV-Burgers equation (see, e.g., Karpman 1975). The final outcome depends on the interplay between the nonlinearity, dispersion and dissipation processes. If, for example, the nonlinearity prevails dispersion and dissipation, kink oscillations evolve into shock waves. In case of competitive dispersion effect, a kinked flux tube will sustain a solitary kink for a long time. The effect of radiative damping (last term in (4.114)) plays important role in development of strong plasma instabilities which will be addressed later. Here we must add that kink solitons proved to be ubiquitous in solar atmosphere, and are well observed, especially in sunspot and plage regions. This will be studied in Chaps. 11 and 15.

4.5.2 Possibility of Solitary Sausage Wave

On the possibility of symmetric, $m = 0$ mode, soliton solution in a magnetic slab was first pointed out by Roberts and Mangeney (1982). They considered a uniform, two-dimensional slab of magnetic field B , with width $2d$, embedded in a gravity-free, nonmagnetic atmosphere. Earlier, Roberts (1981) studied a long wavelength symmetric pulsations of such a slab and obtained their dispersion relation up to nonlinear terms with respect to wavenumber, k . It was found that there are two possible symmetric waves propagating along the magnetic field depending on the phase velocity, $c_T = c_{si} v_A / \sqrt{c_{si}^2 + v_A^2}$ and the sound speed outside the slab, c_{se} .

If $c_T < c_{se}$, then the dispersion relation has a form

$$\omega \simeq k c_T (1 - \alpha |k|), \quad (4.115)$$

where the constant α is a measure of the environment's inertia,

$$\alpha = \frac{1}{2} \frac{\rho_e}{\rho_i} \frac{c_T^2 c_{se}}{c_{si}^2 v_A^2} \frac{c_{si}^2 - c_T^2}{\sqrt{c_{se}^2 - c_T^2}} d \quad (4.116)$$

If $c_T > c_{se}$ or $c_{si} < c_{se}$, then the dispersion relation for slab oscillations takes a form

$$\omega \simeq kc_{se}(1 - \alpha_e k^2), \quad (4.117)$$

where

$$\alpha_e = \frac{1}{2} \frac{\rho_e}{\rho_i} \frac{c_{se}^2}{c_{si}^2 + v_A^2} \frac{c_{se}^2 - c_{si}^2}{c_{se}^2 - c_T^2} d^2 \quad (4.118)$$

Dispersion relation (4.115) corresponds to wave propagating inside the slab, and (4.117) to those outside the slab.

Using the method of stretched variables for a magnetic slab oscillations, Roberts (1985) derived nonlinear equations for sausage mode:

$$\frac{\partial v}{\partial t} + c_T \frac{\partial v}{\partial z} + \beta_T v \frac{\partial v}{\partial z} + \alpha \frac{1}{\pi} \frac{\partial^2}{\partial z^2} \int_{-\infty}^{\infty} \frac{v(z', t) dz'}{z' - z} \quad (4.119)$$

where v is the wave propagation velocity, and β_T is a coefficient of nonlinearity

$$\beta_T = \frac{1}{2} \frac{v_A^2 [3c_{si}^2 + (\gamma + 1)v_A^2]}{(c_{si}^2 + v_A^2)^2} \quad (4.120)$$

Thus, for a slab, weakly nonlinear sausage oscillations are governed by the equation similar to one-dimensional integro-differential equation obtained by Benjamin (1967) and Ono (1975) for internal waves in deep water.

One should bear in mind, however, that there are several problems with sausage oscillations. One is that they are very sensitive to radial inhomogeneity across their cross section, and can survive only if the flux tube is highly homogeneous, which, under real conditions of solar atmosphere, is quite unlikely. The same fact also works “against” nonlinearity of sausage oscillations. One of the obvious mechanisms for steepening the waves in the solar flux tubes is gravity: the waves propagating upward against gravity quickly grow, so does the cross section of flux tubes, and, sausage waves damp away earlier than they become nonlinear.

4.6 Problems

4.1 Find the length and time scales for resonant absorption of Alfvén waves in coronal loops with uniform magnetic field B_0 bounded by $z = 0$ and $z = L$. Assume that Alfvén waves with motions $v_y(x, z, t)$ are excited in the loop by footpoint driver of amplitude $A(x)$ and frequency ω_d in the continuum spectrum (Priest 2014).

4.2 Describe phase mixing of standing Alfvén waves in time. Consider a “short” coronal loops (Priest 2014).

4.3 Magnetic flux tubes anchored in the photosphere and shaken by convective motion may be roughly modeled by a bullwhip with lash of length L and mass M with an attached cracker of mass m , with $m \ll M$. Show that the cracker may move much faster than the handle of a whip (footpoint of solar flux tubes) and reach unlimited speed braking sonic barrier (Krehl et al. 1998).

References

- T.B. Benjamin, *J. Fluid Mech.* **29**, 559 (1967)
 B. Bernstein, D.A. Hall, H.M. Trent, *J. Acoust. Soc. Am.* **30**, 1112 (1958)
 J. Boussinesq, *CR Acad. Sci. Paris* **72**, 755 (1871)
 L.C. Garcia de Andrade, *Astrophys. Space Sci.* **310**, 25 (2007)
 J. Heyvaerts, E.R. Priest, *Astron. Astrophys.* **117**, 220 (1983)
 J.A. Isonson, *Astrophys. J.* **226**, 650 (1978)
 V.I. Karpman, *Nonlinear Waves in Dispersive Media* (Pergamon Press, London, 1975)
 D.J. Korteweg, G. de Vries, *Philos. Mag. Ser. 5* **39**, 422 (1895)
 P. Krehl, S. Engemann, D. Schwenke, *Shock Waves* **8**, 1 (1998)
 T. McMillen, A. Goriely, *Phys. D* **184**, 192 (2003)
 E. Mjølhus, *J. Plasma Phys.* **16**, 321 (1976)
 H. Ono, *J. Phys. Soc. Jpn.* **39**, 1082 (1975)
 M.J. Penn et al., *Astrophys. J.* **734**, 47 (2011)
 S.R.O. Ploner, S.K. Solanki, *Astron. Astrophys.* **325**, 1199 (1997)
 E.R. Priest, *Magnetohydrodynamics of the Sun* (Cambridge University Press, Cambridge, 2014)
 L. Rayleigh, *Philos. Mag. Ser. 5* **1**(4), 257 (1876)
 B. Roberts, *Sol. Phys.* **69**, 39 (1981)
 B. Roberts, *Phys. Fluids* **28**, 3280; *Sol. Phys.* **69**, 39 (1985)
 B. Roberts, A. Mangeney, *Mon. Not. R. Astron. Soc.* **198**, 7 (1982)
 M.P. Ryutova, in *Proceedings of the XIII-th International Conference on Phenomena in Ionized Gases, Part: II* (1977), p. 859.
 M.P. Ryutova, L.G. Khijakadze, *Geophys. Monogr.* **58**, 99 (1990)
 M.P. Ryutova, E.R. Priest, *Astrophys. J.* **419**, 349 (1993)
 S.K. Solanki et al., *Astron. Astrophys.* **315**, 303 (1996)
 J.A. Tataronis, W. Grossman, Decay of MHD Waves by phase-mixing. *Z. Phys.* **261**, 203 (1970)
 A. Timofeev, *Sov. Phys. Usp.* **13**, 632 (1970)

Chapter 5

Flux Tube Dynamics in the Presence of Mass Flows



Abstract Mass flows observed throughout the solar atmosphere exhibit many patterns. They are observed in a wide temperature range of 3×10^4 – 10^7 K, and can have a steady, unsteady, or explosive character. Their amplitudes vary from a few tenths of km s^{-1} at the photosphere up to hundreds of km s^{-1} in the transition region and corona. Presence of mass flows drastically changes the dynamics of magnetic structures, and most importantly, plays a crucial role in the processes of the energy production, transfer, and release. Depending on the geometry and intensity of the flow, the system of magnetic flux tubes exhibits a number of unusual phenomena that are directly observed. In this chapter we consider mainly two effects associated with presence of mass flows. One is the instability of Negative-Energy waves () and other lies in the range of velocities beyond the instability threshold, namely the effect of mass flows on the energy transfer by the phase mixed Alfvén waves.

5.1 Kelvin-Helmholtz Instability and Negative-Energy Waves

The mass flows observed in the solar atmosphere and beyond are as ubiquitous as the magnetic structures. They are predominantly collinear with the magnetic structures, with some differences between downflows, upward mass flows, and vortical motions. For example, in the chromospheres/transition region strong *downflows* are usually associated with complex dynamical structures with multiple velocities (Kjeldseth-Moe et al. 1994). Upward mass flows, also seen at chromospheres/transition region temperatures, apart the “well behaved” spicules, may be adjacent to downflows and often exhibit explosive character ejecting plasma with velocities ranging from 100 to 400 km s^{-1} (Dere et al. 1989). Nonisotropic and unsteady high velocity events often having a twisted character, such as macrospicules, are observed to move outward into the corona at velocities of 10 – 150 km s^{-1} . Mass flows in macrospicules often follow a ballistic trajectories (Withbroe et al. 1976; Habbal and Gonzalez 1991). A quiet prominences and active chromospheric filaments are in fact ever moving magnetized plasma with all kind of shapes and energetics. We shall discuss the effect of various flows throughout the

book. Here we concentrate on some basic and at the same non-trivial features of the system of flux tubes and flows.

To understand the basic dynamic processes associated with flows, we need to study their interaction with the structured magnetic fields.

One of the well-known effects of mass flow on the magnetic and nonmagnetic interface is the Kelvin-Helmholtz (KH) instability (Chandrasekhar 1961).

In the atmosphere, for example, the condition for KH instability is simple

$$u \geq \sqrt{2gd \frac{\rho_2 - \rho_1}{\rho_2 + \rho_1}} \quad (5.1)$$

Here g is the gravitational acceleration, d is a thickness of a narrow mixing layer, ρ_2 and ρ_1 are the gas densities in lower and upper layers of atmosphere, $\rho_2 > \rho_1$, and $u = u_2 - u_1$ is the shear flow associated with different velocities of a wind below and above some layer of the clouds. Consequences of condition (5.1) are observed from its simplest manifestation on our sky and waters to quantum world and biology.

Figure 5.1 shows a typical example of KH instability often seen on our sky as a result of interaction between the clouds and the wind with sheared velocities. The choice of this picture (although the oceans and large water surfaces are even more favorite objects) has been motivated by interesting fact: note that higher in the atmosphere the size and regularity of KH rolls change significantly. One can see from condition (5.2) that with height, i.e. with the drop of the atmospheric density condition for the instability changes, so does the amplitude of the KH rolls. At some point the velocity of the wind may no longer be higher than the required threshold. In this case, two different scenarios may develop. One corresponds to so low shear velocities that system is stable with respect to any drastic changes. Another scenario may develop under some special conditions determined by system parameters, when the system becomes a subject of explosively growing amplitude KH rolls. Example of such a situation may be illustrated by “the rogue wave over Alabama” shown in bottom panel of Fig. 5.1.

Figure 5.2 shows example of a quiescent prominences taken by the SDO/AIA in 304 and 193 Å lines (the image is combination of these two lines). The chromospheric, 304 Å line, clearly shows oscillatory pattern of the prominence filaments. The region occupying by the oscillating filaments slowly grows for several days. In early hours of February 27 the prominence starts to grow faster, and at about UT 03:01 bursts into explosion. Here we see this event at five instances of time from 2013 February 25 to the explosive phase.

We shall discuss below two types of KH instability characteristic to solar magnetic flux tube. Classical KH instability, just like in hydrodynamics, develops when the plasma flows associated with oscillating flux tubes exceed some threshold u_{KH} . This threshold is supersonic for any tangential discontinuity in the absence of magnetic field, and becomes super-Alfvénic when the magnetic field is involved.

Much more intriguing turned out to be the range of flow velocities below the KH threshold, i.e. when the system is stable with respect to a regular KH instability. What happens is that at the sheared mass flows having velocities less



Fig. 5.1 Two different regimes of shear flow instabilities. The upper panel is a typical KH instability caused by interaction of wind with layered clouds. Bottom panel shows another regime of flow instability leading to creation of a powerful rogue wave similar to the ocean rogue waves exhibiting explosively growing “amplitude.” In both cases the energy of a system is locally not conserved: unaccounted energy comes from the wind. The upper picture is taken by Henrik Bondo in Denmark on December 30, 2006, reprinted from <http://epod.usra.edu>, credit EPOD at NASA’s Earth Science Division and the EOS (GSFC); the lower picture, the rogue wave over Alabama, is courtesy of Xinhua photo agency, reprinted from <http://news.xinhuanet.com/english/photo>

than u_{KH} but larger than some threshold, the nonlinear dissipative instabilities may develop, which lead to the appearance of Negative-Energy waves (NEWs) (Ryutova 1988). The characteristic feature of negative energy waves is that any interaction of these waves with the medium, i.e. any mechanism of subtraction of their energy (dissipative effects, interaction with other waves, etc.) leads to fast growth of their amplitudes. Accordingly, the damping rate becomes the growth rate. This in turn results in the onset of strongly nonlinear processes and the widening of the classes of instabilities, most important of which is the explosive instability when

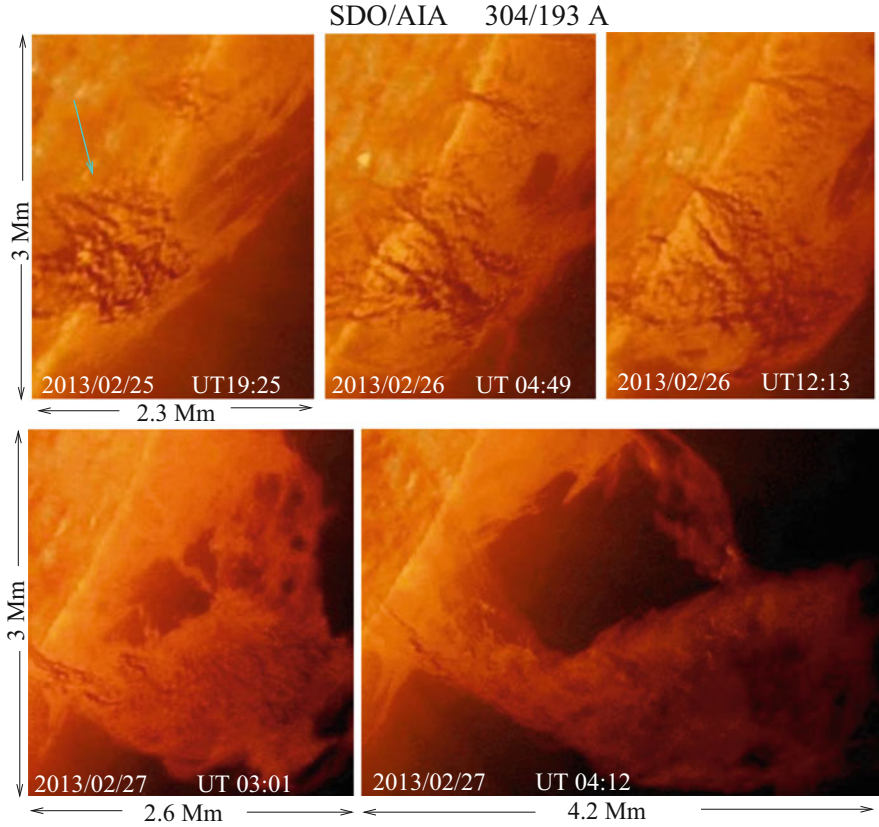


Fig. 5.2 Snapshots of the oscillating the filaments of slowly evolving quiescent prominence. The gradual “swelling” of prominence takes several days. Finally, the prominence starts to grow faster and by Feb. 27 UT 04:10 bursts out in the explosive way. Courtesy of NASA/SDO

the amplitudes of the perturbations in a system (A) reach infinitely large values in a finite time: $A \sim 1/(t-t_0)$, t_0 is the “explosion” time, and it is completely determined by the physical properties of the medium (Kadomtzev et al. 1964; Dikasov et al. 1965; Sturrock 1966; Coppi et al. 1969; Weiland and Wilhelmsson 1977; Ostrovskii et al. 1986). It is important to emphasize that Negative-Energy waves may appear only in an energetically open systems, i.e. systems with “unaccounted” energy source and sink of energy. In the system of atmospheric clouds, for example, the source is a wind energy, and the dissipation is any viscous or thermal losses.

Analytically, to recognize the Negative-Energy waves and distinguish them from usual, positive energy waves, is very simple. *Any wave will have a negative energy* if, for example, at a positive eigenfrequency the derivative of the corresponding dispersion function, $D(\omega, k) = 0$, with respect to ω becomes negative, i.e. if

$$\frac{\partial D(\omega, k)}{\partial \omega} < 0 \quad (5.2)$$

The location where this derivative becomes zero is the bifurcation point that corresponds to the upper threshold for NEW and lower threshold for classical KH instability. Hence, if along the magnetic flux tube the amplitude of the mass flow is in the interval, $u_{\text{NEW}} \leq u \leq u_{\text{KH}}$, the system is able to maintain vigorous dynamics characteristic to presence of Negative-Energy waves.

The properties and existence of Negative-Energy waves are largely determined by the dispersion properties of the system. To demonstrate their nature in a simple way, consider longitudinal electromagnetic wave with frequency ω propagating in a dispersive medium. The energy of such wave is given by the expression (Landau and Lifshitz 1984):

$$U = \frac{1}{8\pi} \frac{\partial \epsilon(\omega, k)}{\partial \omega} \omega < E^2 > \quad (5.3)$$

where $\epsilon(\omega, k)$ is the dielectric function and serves as linear dispersion relation for a system

$$\epsilon(\omega, k) = 0 \quad (5.4)$$

We see that the wave energy is proportional to the derivative $d\epsilon/d\omega$, so that the sign of energy depends on whether the medium exhibits normal dispersion, $\partial\epsilon/\partial\omega > 0$ or anomalous dispersion $\partial\epsilon/\partial\omega < 0$.

Similarly, for any other system with the dispersion function

$$D(\omega, k) = 0, \quad (5.5)$$

the energy of the wave $\sim A \exp(-i\omega t)$ is

$$W = \frac{1}{4} \omega \frac{\partial D(\omega, k)}{\partial \omega} A^2 \quad (5.6)$$

Consider now the system with any kind of dissipation, e.g. Landau damping, Ohmic, thermal conductivity, viscosity, etc., which causes appearance of small imaginary part, $i\alpha$, in the dispersion relation

$$D(\omega + i\nu, k) + i\alpha = 0 \quad (5.7)$$

This adds a small imaginary part in the wave frequency whose amplitude now is $\sim A \exp[-i(\omega + i\nu)t]$. Expanding the dispersion function with respect to the small imaginary term, ν , we obtain

$$D_0(\omega_0) + i\nu \left. \frac{\partial D}{\partial \omega} \right|_{\omega_0} + i\alpha = 0, \quad (5.8)$$

which gives

$$\nu = -\frac{\alpha}{\partial D/\partial\omega|_{\omega_0}} \quad (5.9)$$

Equations (5.6) and (5.9) show that at the normal dispersion, i.e. when $\partial D/\partial\omega > 0$, the parameter $\nu < 0$ is a damping rate and dissipative effects lead to the absorption of wave energy. In the opposite case of anomalous dispersion, i.e. when $\partial D/\partial\omega < 0$, $\nu > 0$ becomes the growth rate and any subtraction of wave energy leads to growing of the wave amplitude. It must be understood that the system which may possess the anomalous dispersion must be energetically open system, i.e. locally the energy of a system is not conserved. In this particular case the system loses the energy on the expense of growing the wave amplitude. This leads to the strong dissipative instabilities which will be considered below, and which play essential role in the dynamics of solar atmosphere.

5.2 Shear Flow Instabilities in Magnetic Flux Tubes

5.2.1 Specifics of Kelvin-Helmholtz Instability Along Flux Tubes

Consider a homogeneous magnetic flux tube of circular cross section in the presence of a flow directed along the tube axis. We adopt for a coordinate system in which the matter inside the flux tube is at rest, while the flow velocity outside the tube has a value u and is directed toward increasing z .

We begin with the kink oscillations, and describe the displacement of the tube with respect to its unperturbed position by the vector $\xi(z,t)$, which lies in the plane perpendicular to the axis of the tube. The equation for kink oscillations in presence of shear flow can be written as follows:

$$\rho_i \frac{\partial^2 \xi_{\perp}}{\partial t^2} = -\rho_e \left(\frac{\partial}{\partial t} + u \frac{\partial}{\partial z} \right)^2 \xi_{\perp} + \frac{B^2}{4\pi} \frac{\partial^2 \xi_{\perp}}{\partial z^2} \quad (5.10)$$

Equation (5.10) can be written in the form of an energy integral:

$$I = \int dz \frac{\pi R^2}{2} \left[(\rho_i + \rho_e) \left(\frac{\partial \xi_{\perp}}{\partial t} \right)^2 + \left(\frac{B^2}{4\pi} - \rho_e u^2 \right) \left(\frac{\partial \xi_{\perp}}{\partial z} \right)^2 \right] = \text{const} \quad (5.11)$$

The integrand has the meaning of the energy of the oscillations per unit length along the tube.

For sinusoidal traveling waves $\sim \exp(-i\omega t + ikz)$ the dispersion relation obtained from (5.10) has the form

$$D(\omega) = \omega^2 + \frac{1}{\eta}(\omega - ku)^2 - k^2 v_A^2 = 0 \quad (5.12)$$

where as earlier, $\eta = \rho_i / \rho_e$. From (5.12) we have

$$\omega_{\pm} = \frac{k}{1 + \eta} [u \pm \sqrt{\eta[v_A^2(1 + \eta) - u^2]}] \quad (5.13)$$

This dispersion relation describes two different kinds of instabilities, and accordingly, two branches and different thresholds for the onset of these instabilities.

One instability is analogous to a usual Kelvin-Helmholtz instability, and the other one is the instability of Negative-Energy waves (NEWs).

The condition for Kelvin-Helmholtz follows from (5.13) immediately, and corresponds to appearance of an imaginary part in frequency, i.e. when the radicand in (5.13) becomes negative:

$$u > u_c^{\text{KH}} = v_A \sqrt{1 + \eta} \quad (5.14)$$

Thus at $u > v_A \sqrt{1 + \eta}$, mass flows directed along the flux tube cause the excitation of natural oscillations flux tube, just like a strong wind causes appearance of a KH rolls at the ocean surface or along the layered clouds.

By nature the KH instability develops at a linear stage although its threshold in hydro- and gasdynamics is supersonic. In our case, when magnetic field is involved, the threshold becomes superalfvénic.

It follows from dispersion relation (5.13) that unstable perturbations propagate upstream: $\text{Re}(\omega/k) = u/(1 + \eta) > 0$. Consequently, if an upstream flow of surrounding plasma “blows over” a certain length of flux tube, the kink oscillations excited here will also propagate upstream.

This instability is remarkable in that it may be considered as an important agent for exciting oscillations in regions far from a convection zone. It is usually assumed that the excitation of oscillations of magnetic tubes requires an oscillatory motion of their point where it is shaken by an unsteady convection. Oscillations of magnetic flux tubes excited by convective motions have the frequencies of the order of the inverse timescale of the granular or supergranular motions, i.e., on the order of $l/\tau \sim 10^{-2} - 3 \times 10^{-3} \text{ s}^{-1}$. These low frequency oscillations indeed cover entire solar surface and are well observed in lower atmosphere. In upper atmosphere, however the oscillations of filamentary structures are observed to have wide range of frequencies which is hard to explain by the involvement of the convective motions.

The KH instability, on the other hand, provides another mechanism, which does not require motions at the base of the flux tube, and not just any motions but such that the resonance conditions must hold. The KH instability may act anywhere in solar atmosphere from photosphere to corona and solar wind. The frequencies of

oscillations in this case, being totally unrelated to the time scales of convection, may be arbitrary. They are determined by the local physical parameters of a system, and may be used for diagnostic goals.

5.2.2 Flux Tubes and Negative-Energy Waves (NEWs)

At a flow velocity which is less than u_c^{KH} , i.e. when the system is stable with respect to classical KH instability, the system may become subject of instability of Negative-Energy waves. It is important to emphasize that the instability of NEW is *below* the hydrodynamic instability, and require weaker, as we will see below, sub-alfv'enic, flows to trigger an exchange of energy and momentum between the magnetic flux and outer motions. Besides, as discussed above, any loss of energy by NEWs leads to the growing of their amplitude. Along the usual dissipative processes, the non-dissipative mechanisms of energy loss typical to flux tube per se naturally contribute to growing of their amplitude. This occurs due to radiation of secondary waves by oscillating flux tube, and the resonance damping (Rytova 1977; Ionson 1978). In later chapters we shall see the Negative-Energy waves in action and study various consequences of their instabilities observed throughout the solar atmosphere. Now, to understand the nature of NEWs, and find out the range of velocities for their existence let us employ the energy analysis.

Using the energy integral (5.11) and dispersion relation (5.13), we can find for traveling waves the energy density per unit length of the tube

$$W = \frac{\pi R^2}{2} \rho_e \xi_{\perp}^2 k^2 \left[(1 + \eta) \frac{\omega^2}{k^2} + \eta v_A^2 - u^2 \right] \quad (5.15)$$

or

$$W = \frac{1}{(1 + \eta)} \pi R^2 k^2 \rho_e \xi_{\perp}^2 (w^2 \pm uw), \quad (5.16)$$

where we have introduced notation

$$w = \sqrt{\eta[v_A^2(1 + \eta) - u^2]} \quad (5.17)$$

One should keep in mind that the radicand here is *positive*, i.e. we consider the velocities $u > v_A \sqrt{(1 + \eta)}$, i.e. the system is stable with respect to KH instability.

For $u > 0$, the only wave which can have a Negative-Energy is one that corresponds to the minus sign in dispersion relation (5.13), i.e. the wave which would propagate in the negative z direction in the absence of a flow. For this wave a lower branch of (5.16) gives

$$W = \pi R^2 k^2 \rho_e \xi_{\perp}^2 (\eta v_A^2 - u^2) \frac{w}{w + u}, \quad (5.18)$$

One can see that the energy of the wave becomes negative at

$$u > u_c^{\text{NEW}} = \sqrt{\eta} v_A \quad (5.19)$$

where the superscript ‘‘NEW’’ specifies that the threshold corresponds to the appearance of Negative-Energy waves. Comparing conditions (5.14) and (5.19), we see that the relation $u_c^{\text{NEW}} < u_c^{\text{KH}}$ holds with a good margin, i.e., that Negative-Energy waves have an appreciate range of parameters where they can be generated.

Thus, in the interval of sheared flow velocities

$$u_c^{\text{NEW}} < u < u_c^{\text{KH}} \quad (5.20)$$

an instability of Negative-Energy waves occurs and action of any dissipative effects or non-dissipative damping results in their enhancement and thus an increase of their amplitude.

As mentioned above, a remarkable property that magnetic tubes exhibit is that even in the absence of dissipative processes, the development and enhancement of this instability may be facilitated by the mechanism of a collisionless dissipation of kink oscillations. The most important of which are associated with two intrinsic features of flux tubes: (1) The resonant absorption of the oscillations in an Alfvén resonance layer, and (2) Lost of the energy due to the radiation of secondary waves, both acoustic and MHD. In the next section we consider several examples.

5.3 Basic Equations of Flux Tube Oscillations with Shear Flows

The linearized system of MHD equations in presence of mass flow with an unperturbed velocity \mathbf{u} is follows

$$\rho \frac{\partial \mathbf{v}}{\partial t} + (\mathbf{u} \nabla) \mathbf{v} + (\mathbf{v} \nabla) \mathbf{u} = -\nabla \delta p + \frac{1}{4\pi} ([\nabla \times \mathbf{b}] \times \mathbf{B} + [\nabla \times \mathbf{B}] \times \mathbf{b}) \quad (5.21)$$

$$\frac{\partial \mathbf{b}}{\partial t} = \nabla \times [\mathbf{v} \times \mathbf{B}] + \nabla \times [\mathbf{u} \times \mathbf{b}] \quad (5.22)$$

$$\frac{\partial \delta \rho}{\partial t} + \text{div} \rho \mathbf{v} + \text{div} \delta \rho \mathbf{u} = 0 \quad (5.23)$$

$$\frac{\partial \delta S}{\partial t} + \mathbf{v} \nabla S + \mathbf{v} \nabla \delta S = 0 \quad (5.24)$$

where \mathbf{v} , \mathbf{b} , $\delta \rho$, and δp are perturbed parameters, and $\mathbf{u} = u(0, 0, u(r))$. All the flux tube parameters are assumed to be functions only of the radius. For the perturbations

proportional to $\exp(-i\omega t + im\phi + ikz)$ from (5.21) we have

$$\begin{aligned}
 -i(\omega - ku)\rho v_r &= -\frac{\partial}{\partial r} \left(\delta p + \frac{b_z B}{4\pi} \right) + ik \frac{B}{4\pi} b_r \\
 -i(\omega - ku)\rho v_\phi &= \frac{1}{r} \frac{\partial}{\partial \phi} \left(\delta p + \frac{b_z B}{4\pi} \right) + ik \frac{B}{4\pi} b_\phi \\
 -i(\omega - ku)\rho v_z &= -ik\delta p - \rho v_r \frac{\partial u}{\partial r} - \frac{kB}{4\pi(\omega - ku)} v_r \frac{\partial B}{\partial r}
 \end{aligned} \tag{5.25}$$

Equation (5.22) gives

$$\begin{aligned}
 b_r &= -\frac{kB}{\omega - ku} v_r, \\
 b_\phi &= -\frac{kB}{\omega - ku} v_\phi, \\
 -i(\omega - ku)b_z &= -\frac{1}{r} \frac{\partial}{\partial r} r B v_r - \frac{imB}{r} v_\phi + b_r \frac{\partial u}{\partial r}
 \end{aligned} \tag{5.26}$$

Note that $\text{div} \mathbf{b} = 0$.

Equations (5.23) and (5.24) become, respectively, as follows:

$$-i(\omega - ku)\delta\rho + \frac{1}{r} \frac{\partial}{\partial r} r \rho v_r + \frac{im}{R} \rho v_\phi + ik\rho v_z = 0, \tag{5.27}$$

$$-i(\omega - ku)(\delta p - c_s^2 \delta\rho) + v_r \left(\frac{\partial p}{\partial r} - c_s^2 \frac{\partial \rho}{\partial r} \right) = 0 \tag{5.28}$$

To put system of (5.25)–(5.28) in a compact form, we express all the perturbed quantities in terms of v_r , v_ϕ and the perturbation of the total pressure, $\delta P = \delta p + b_z B/4\pi$. After some algebra we obtain the following system:

$$\begin{aligned}
 i\delta P &= \rho \frac{\Omega^2(c_s^2 + v_A^2) - k^2 c_s^2 v_A^2}{\Omega^2 - k^2 c_s^2} \left[\frac{1}{r} \frac{\partial}{\partial r} r v_r \frac{v_r}{\Omega} + \frac{im}{r} \frac{v_\phi}{\Omega} \right] \\
 \frac{\partial \delta P}{\partial r} &= i\rho(\Omega^2 - k^2 v_A^2) \frac{v_r}{\Omega}, \\
 \frac{im}{r} \delta P &= i\rho(\Omega^2 - k^2 v_A^2) \frac{v_\phi}{\Omega}
 \end{aligned} \tag{5.29}$$

where

$$\Omega = \omega - ku. \tag{5.30}$$

System (5.29) describes all types of small oscillations of a magnetic tube in presence of field aligned shear flows.

5.4 Dissipative Instabilities of Negative-Energy Kink Oscillations

Consider first the kink oscillations. In the long-wave limit, and with assumption that the fluid is incompressible, i.e. that $\text{div} \mathbf{v} = 0$, we can replace the velocity by a stream function ψ (cf. Chap. 3):

$$v_r = -\frac{1}{r} \frac{\partial \psi}{\partial \phi} \quad v_\phi = \frac{\partial \psi}{\partial r} \quad (5.31)$$

then, instead of the system (5.29) we have a single equation for kink oscillation in presence of shear flow:

$$\frac{1}{r} \frac{\partial}{\partial r} \left[\left(\rho \Omega - \frac{k^2 B^2}{4\pi \Omega} \right) r \frac{\partial \psi}{\partial r} \right] - \left(\rho \Omega - \frac{k^2 B^2}{4\pi \Omega} \right) \frac{\psi}{r^2} = 0 \quad (5.32)$$

We are assuming that ω contains a small imaginary part $i\nu$, introduced in order to bypass the singular point at $\rho \Omega = k^2 B^2 / 4\pi \Omega$ correctly. Physically, the appearance of this correction can be explained in terms of any dissipative processes present in the system, i.e. for example caused by collisions between the plasma particles. We use the model of flux tube which is homogeneous nearly throughout entire radius, except a narrow diffuse boundary layer where the plasma density and the magnetic pressure are linear functions of the radius (cf. Fig. 3.6):

$$\rho \Omega^2 = \rho_i \omega^2 \frac{R - r + l}{l} + \rho_e \Omega^2 \frac{r - R}{l} \quad (5.33)$$

$$B^2(r) = B^2 \frac{R - r + l}{l}$$

where thickness of boundary layer $l \ll R$.

Solutions of (5.32) at constant values of the density, magnetic field, and flow velocity are Bessel functions in the flux tube interior and Hankel functions outside it. To first order in $kR \ll 1$, these solutions are, respectively,

$$\psi = \begin{cases} C_1 r, & r < R \\ C_2 / r, & r > R + l \end{cases} \quad (5.34)$$

To find solutions in the transition region $R < r < R + l$ (as we did in Chap. 3, Section 8), we introduce the variable

$$x = \frac{r - R}{l}, \quad 0 < x < 1, \quad (5.35)$$

and using the smallness of parameter l/R , rewrite (5.32) in the form which (which is identical to Eq. (3.118)):

$$\frac{d}{dx}(x - x_0 - i\epsilon)\frac{d\psi}{dx} - \frac{l^2}{R^2}(x - x_0 - i\epsilon)\psi = 0, \quad (5.36)$$

where small imaginary part $i\epsilon$ comes from taking into account the dissipative properties of a system, and x_0 now includes the shear flow velocity:

$$x_0 = (k^2 v_A^2 - \omega^2) \left(k^2 v_A^2 + \frac{\rho_e}{\rho_i} \Omega^2 - \omega^2 \right)^{-1} \quad (5.37)$$

Just like in Chap. 3 (Section 3.7) we can find a single-valued solution of (5.35) in the complex plane x with a cut along the line $\text{Im}x = i\epsilon$ (see Fig. 3.6):

$$\psi = A + D \ln(x - x_0 - i\epsilon) \quad (5.38)$$

At the same time, $-\infty < \text{Re}x < X_0$. Using now continuity of ψ and $d\psi/dx$ at both boundaries, $r = R$ and $r = R + l$, we find the dispersion relation

$$\ln \frac{1 - x_0}{x_0} + \frac{R}{l} \left(\frac{1}{1 - x_0} - \frac{1}{x_0} \right) + i\pi = 0 \quad (5.39)$$

The real part of (5.39) yields

$$1 - x_0 = x_0 \quad (5.40)$$

It is easy to verify that this expression is precisely the same as the dispersion relation (5.13).

For imaginary part of the frequency (5.39) gives the following expression:

$$\frac{\gamma}{\omega} = -\frac{\pi}{4} \frac{l}{R} \frac{\eta}{(1 + \eta)^2} \frac{(\eta u \mp w)^2}{\pm w} \quad (5.41)$$

Equations (5.40) and (5.41) solve the problem of kink oscillations of flux tube with smooth radial profile and in presence of shear flows. One can see that for waves with a positive energy (the upper sign) the quantity γ corresponds to a damping rate, while for waves with a Negative-Energy (the lower sign), γ becomes positive, and thus corresponds to a growth rate.

Finally, the growth rate of the instability of NEW supported by the anomalous absorption (Alfvén resonance) is as follows:

$$\frac{\gamma_{\text{res}}}{\omega} = \frac{\pi}{4} \frac{l}{R} \frac{\eta}{(1 + \eta)^2} \frac{\left\{ \eta u + \sqrt{\eta[v_A^2(1 + \eta) - u^2]} \right\}^2}{\sqrt{\eta[v_A^2(1 + \eta) - u^2]}} \quad (5.42)$$

Note that the anomalous-absorption effect which is responsible here for the instability of Negative-Energy waves may also occur in the case of a homogeneous magnetic flux tube if the shear flow has the coordinate dependence. Since under real conditions of solar atmosphere both the magnetic flux tube and mass flows along them are inhomogeneous, the instability of negative-energy waves may be considered as one of the most natural occurrence triggering a violent phenomena in systems with filamentary magnetic fields.

5.5 Radiative Instability of Flux Tube Oscillations in Presence of Flows

In this section we address the problem of radiative damping of flux tube oscillations in the presence of sheared mass flows. We focus here on the kink and sausage modes and find the damping rates of these modes and their energy content.

We start with the density perturbations written in the form

$$\delta\rho = \cos(m\phi) \left[\frac{1}{2} f(r) \exp(-i\omega t + ikz) + \text{c.c.} \right] \quad (5.43)$$

The function f satisfies the equation

$$\frac{1}{r} \frac{d}{dr} \left(r \frac{df}{dr} \right) \frac{m^2}{r^2} - k^2 f + \frac{(\omega - ku)^2}{c_{se}^2} f = 0 \quad (5.44)$$

A solution to this equation corresponding to acoustic waves which propagate away from the tube is

$$f_e(r) = AH_m^{(1)}(k_{\perp}r), \quad (5.45)$$

where

$$k_{\perp} = \sqrt{\frac{(\omega - ku)^2}{c_{se}^2} - k^2} = \frac{k}{c_{se}} \sqrt{(v_{\phi} - u)^2 - c_{se}^2} \quad (5.46)$$

The radiation of secondary acoustic waves by flux tube is possible only if the radicand here is *non-negative*.

At large distances from the flux tube ($k_{\perp}r \gg 1$), solution (5.45) has the asymptotic behavior

$$f = a \left(\frac{2}{\pi k_{\perp}r} \right)^{1/2} \exp \left(ik_{\perp}r - \frac{im\pi}{2} - i\frac{\pi}{4} \right). \quad (5.47)$$

For $k_{\perp}r \gg 1$, solution for $\delta\rho$ (Eq. (5.43)) will still be a plane-wave,

$$\delta\rho = \frac{1}{2}\rho_0\cos(m\phi)\exp(-i\omega t + ikz + ik_{\perp}r) + \text{c.c.} \quad (5.48)$$

With this we can calculate the energy density of a radiated wave to obtain

$$W_{\text{se}} = \frac{\rho_e c_{\text{se}}^2}{2} \left| \frac{\delta\rho_0}{\rho_e} \right|^2 \frac{c_{\text{se}}\sqrt{k^2 + k_{\perp}^2} - ku}{c_{\text{se}}\sqrt{k^2 + k_{\perp}^2}} \cos^2 m\phi. \quad (5.49)$$

Under condition (5.67) (see below), W_{se} is negative. Using relation (5.47), we find

$$W_{\text{se}} = \frac{c_{\text{se}}}{\pi k_{\perp}r} \frac{|A|^2}{\rho_e} \frac{\chi c_{\text{se}} - ku}{\chi} \cos^2(m\phi) \quad (5.50)$$

here $\chi = \sqrt{k^2 + k_{\perp}^2}$.

The energy flux from a unit length of the flux tube,

$$Q = 2\pi r \langle W_{\text{se}} \rangle k_{\perp} c_{\text{se}} / \chi \quad (5.51)$$

is

$$Q = \frac{2c_{\text{se}}^2 |A|^2}{\rho_e} \frac{\chi c_{\text{se}} - ku}{\chi^2} \begin{cases} 1, & m = 0 \\ 1/2, & m = 1 \end{cases} \quad (5.52)$$

Now we need to express the coefficient A in terms of the flux tube oscillation amplitude. To do this, we shall consider the solution of (5.45) near the flux tube boundary at $k_{\perp}r \ll 1$. Corresponding analysis is presented in the next two sections separately for sausage and kink oscillations.

5.5.1 Sausage Oscillations

For sausage oscillations we have

$$f = \left(1 + \frac{2i}{\pi} \ln \frac{Ck_{\perp}r}{2} \right), \quad (5.53)$$

where C is Euler's constant. Using the system (5.21), one can see that for non-magnetic environment, the density perturbation is related to the radial component of the displacement of the fluid, ξ_r , as follows:

$$\xi_r = \frac{c_{\text{se}}^2}{\rho_e(\omega - ku)^2} \frac{\partial \delta\rho}{\partial r}. \quad (5.54)$$

Accordingly, for the displacement of the tube boundary in the sausage oscillations of the form $\xi_r = (1/2)\xi_0 \exp(-i\omega t + ikz) + \text{c.c.}$, from (5.43), (5.53), and (5.54), we get

$$A = -\frac{i\pi R\rho_e(\omega - ku)^2}{2c_{se}^2}\xi_0 \quad (5.55)$$

Finally, for sausage oscillations, the energy flux, Q_T , radiated from a unit length of the flux tube is

$$Q_T = \frac{\pi^2 \rho_e}{2} v_\phi (v_\phi - u)^2 k^3 R^2 |\xi_0|^2. \quad (5.56)$$

5.5.2 Kink Oscillations

Now we turn to kink oscillations. Using the expansion of the Hankel function $H_m^{(1)}(k_\perp r)$ at $k_\perp r \ll 1$, we find from (5.45):

$$f \simeq -\frac{2iA}{\pi k_\perp r} \quad (5.57)$$

The radial component of the flux tube displacement in the kink oscillations, $\xi_r = \cos\phi[(1/2)\xi_0 \exp(-i\omega t + ikz) + \text{c.c.}]$, follows from (5.43), (5.54), and (5.57):

$$A = -\frac{i\pi k_\perp R^2 \rho_e (\omega - ku)^2}{2c_{se}^2} \xi_0 \quad (5.58)$$

Note that for long-wavelength kink oscillations ξ_0 is, in fact, the amplitude of the tube axis displacement from its unperturbed position.

The energy flux, Q_k , radiated from a unit length of the flux tube performing kink oscillations, is

$$Q_k = \frac{\pi^2 \rho_e}{4} v_\phi (v_\phi - u)^2 [(v_\phi - u)^2 - c_{se}^2] \frac{k^5 R^4 |\xi_0|^2}{c_{se}^2} \quad (5.59)$$

Let us now find the energy of the sausage and kink oscillations for a unit length of the tube. For the kink oscillations, the result follows directly from (5.11) and acquires the following form

$$W_k = \frac{\pi R^2}{4} |\xi_0|^2 k^2 \left[(\rho_i + \rho_e) \frac{\omega^2}{k^2} + \rho_i v_A^2 - \rho_e u^2 \right] \quad (5.60)$$

In the case of the sausage oscillations, we need to carry out some calculations. First note that for these oscillations we have

$$W_T = \left\langle \frac{\rho \delta v_{\parallel}^2}{2} + \frac{\gamma \rho}{2} \left(\frac{\delta \rho}{\rho} \right)^2 + \frac{\delta B^2}{8\pi} \right\rangle \pi R^2 \quad (5.61)$$

where the averaging is done over a wave-length. When writing this expression we have assumed that the transverse velocity of the plasma motion inside the flux tube is small compared to the velocity of a shear flow. From the equations of motion, the continuity equations, and the frozen-in condition we find the following relations inside the tube:

$$\delta v_{\parallel} = \frac{c_{\text{si}}}{\rho} \delta \rho, \quad \delta B = B \frac{\xi}{2R}, \quad \delta \rho = \frac{v_A^2}{2c_{\text{si}}^2} \frac{\xi}{R} \quad (5.62)$$

using for ξ the expression (5.54), we obtain

$$W_T = \frac{\pi |\xi_0|^2}{8} \frac{\rho_i v_A^2 (v_A^2 + c_{\text{si}}^2)}{c_{\text{si}}^2} \quad (5.63)$$

Having the expressions for the energy flux, Q , radiated from a unit length of the flux tube and the energy of flux tube oscillations W , we can directly find the instability growth rates, $\gamma^{\text{rad}} = Q/2W$. Indeed, for the kink oscillations we have

$$\frac{\gamma_b^{\text{rad}}}{\omega} = \frac{\pi k^2 R^2}{2} \frac{(v_{\phi} - u)^2 [(v_{\phi} - u)^2 - c_{\text{se}}^2]}{c_{\text{se}}^2 v_{\phi} [(1 + \eta) v_{\phi} - u]} \quad (5.64)$$

and for the sausage oscillations,

$$\frac{\gamma_T^{\text{rad}}}{\omega} = \frac{\pi k^2 R^2}{4} \frac{\rho_e c_T^2 (c_T - u)^2}{\rho_i v_A^4}. \quad (5.65)$$

All the quantities entering into the both expressions are directly or indirectly measurable. The obtained results therefore allow to infer physical parameters that are not directly observable and to develop the predictability tools.

5.6 Parity of Negative and Positive Energy Waves

The radiative damping of primary flux tube oscillations in the presence of shear flows may lead to strong enhancement of the oscillations. This is possible in two cases:

1. If the flux tube oscillations have a Negative-Energy, and the radiated wave has a positive energy, and
2. If the flux tube oscillations have a positive energy, and the radiated wave has a Negative-Energy.

The dispersion relation for plane sound waves far from the flux tube is as follows:

$$\left. \frac{\omega}{k} \right|_{se} = u \pm c_{se} \sqrt{1 + \frac{k_{\perp}^2}{k^2}}, \quad (5.66)$$

where k_{\perp} is the component of the wave vector perpendicular to the z -axis, and k is the component of the wave vector along the z -axis. The subscript se specifies sound waves.

It is easy to verify that the sound wave which in the absence of a flow propagates in the negative z direction may have a Negative-Energy. This corresponds to the lower sign in dispersion relation (5.66). The condition for the flow velocity under which the energy of radiated acoustic wave becomes negative is

$$u \geq c_{se} \sqrt{1 + k_{\perp}^2/k^2} \quad (5.67)$$

The transverse component of the wave vector of this wave is found from the condition

$$(\omega/k)|_k = (\omega/k)|_s \quad (5.68)$$

Let us first find the conditions under which the kink oscillations with a positive energy radiate sound waves with a Negative-Energy, i.e., the conditions under which the following relations hold:

$$\frac{1}{1 + \eta} (u + w) = u - c_{se} \sqrt{1 + \frac{k_{\perp}^2}{k^2}} > 0 \quad (5.69)$$

where, as earlier, $w = \sqrt{\eta[v_A^2(1 + \eta) - u^2]}$.

Simple calculations show that these relations can hold under the following conditions

$$v_A > c_{se}/\sqrt{\eta}, \quad u > c_{se} + \sqrt{v_A^2 - c_{se}^2/\eta} \quad (5.70)$$

It follows from the equilibrium condition of the unperturbed tube, $p_i + B^2/8\pi = p_e$. that

$$c_{se} > v_A \sqrt{\gamma \eta / 2}, \quad (5.71)$$

where γ is the adiabatic index. Consequently, conditions (5.70) can be satisfied only if $\gamma < 2$, which holds very well for the most of the solar atmosphere.

The question is, can a Negative-Energy kink oscillation radiate a wave with a positive energy? In other words, can the condition

$$\frac{1}{1 + \eta}(u - w) = u + c_{se} \sqrt{1 + \frac{k_{\perp}^2}{k^2}} \quad (5.72)$$

be satisfied? the answer is negative: this condition cannot be satisfied since it reduces to the equation

$$-w = \eta u + (1 + \eta)c_{se} \sqrt{1 + \frac{k_{\perp}^2}{k^2}} \quad (5.73)$$

whose left side is negative, and right side is positive. Thus, we may conclude that the kink oscillations with a positive energy traveling “downstream” will become unstable due to the radiation of secondary acoustic waves with a Negative-Energy. The growth rate of this instability is given by (5.64). We have to bear in mind of course that the primary condition for this instability is that the shear flow velocity must be in the interval given by conditions (5.70).

The mechanism of the Negative-Energy instability associated with the radiative damping operates for sausage oscillations as well. Although a flow has essentially no effect on the axisymmetric oscillations, and their energy remains positive even in the presence a flow, the NEW instability may develop due to the radiation of negative-energy waves. The sound waves having Negative-Energy are those which propagate against the flow in the coordinate system of the fluid; their energy becomes negative under condition (5.67), i.e., if they are traveling downstream in the laboratory system. Now, taking into account the phase-matching condition we obtain an instability condition (cf. (5.69)):

$$c_T = u + c_{se} \sqrt{1 + k_{\perp}^2/k^2} > 0 \quad (5.74)$$

This condition can hold if

$$u > c_T + c_{se} \quad (5.75)$$

A slow wave propagating downstream may thus be unstable with respect to radiation of Negative-Energy waves. The growth rate of this instability is given by (5.65).

5.7 Explosive Instability of Negative-Energy Waves

A specific nonlinear instability, an explosive instability, occurs in a system which contains waves with energies of different signs. This instability was first studied by Dikasov et al. (1965) in the particular case of waves with random phases. Coppi et al. (1969) described the explosive instability for a “triplet” of coherent positive and Negative-Energy waves, and introduced the term “explosive instability.” A distinctive feature of an explosive instability is that the amplitudes of *all* the interacting waves reach infinitely large values in a finite time. This statement is of course formal, because at large enough, but finite amplitudes higher-order nonlinear processes turn on and limit the growth of the amplitude to a certain level. A very good account of the Negative-Energy waves and associated explosive instability is given in the book by Weiland and Wilhelmsson (1977).

Analyzing nonlinear processes, in particular, three-wave processes, it is convenient to assume that the sign of the frequency corresponds to the sign of the energy. When this approach is taken, the condition for the explosive instability of a three-wave process can be written as follows:

$$\begin{aligned}\omega_1 + \omega_2 + \omega_3 &= 0 \\ k_1 + k_2 + k_3 &= 0 \\ |m_1| \pm |m_2| \pm |m_3| &= 0\end{aligned}\tag{5.76}$$

where the indices 1, 2, 3, mark the three interacting waves. Since we are considering oscillations with $m = 0, \pm 1$, it follows from the last relation in (5.76) that either all three waves are axisymmetric, $m = 0$, or two of them have $m = \pm 1$, and the third $m = 0$.

In case of flux tube oscillations, conditions (5.76) indeed hold, providing thus development of explosive instability. We may consider, for example, the interaction of one sausage mode ($m = 0$) and two kink modes ($m = \pm 1$). Conditions (5.76) in this case reduce to the following

$$\omega_T + \omega_{k+} + \omega_{k-} = 0, \quad k_T + k_{k+} + k_{k-} = 0\tag{5.77}$$

The $k+$ and $k-$ subscripts correspond to waves traveling downstream and upstream, respectively.

It is simple to verify that conditions (5.77) are compatible if $k_T > 0$, and if the the following inequality holds:

$$u > \frac{c_T}{1 + \eta} + \sqrt{v_A^2 \eta - c_T^2 \frac{\eta(\eta^2 + 3\eta + 3)}{1 + \eta^2}},\tag{5.78}$$

which is exactly the condition for an explosive instability.

It is important to emphasize that condition (5.78) is quite powerful: even if only a single wave, e.g. a sausage wave with $k_T > 0$, has been excited in the system, and the amplitudes of the two other waves are on the level of thermal noise, then the amplitudes of these two waves will grow exponentially reaching finally the explosive phase. From dimensionality considerations it is clear that the typical growth rate is on the order of magnitude $k_T c_T$. After a time of several inverse growth rates, at which the amplitudes of all three waves become comparable, the amplitudes begin a power-law growth in accordance with (Dikasov et al. 1965; Coppi et al. 1969):

$$v_T \sim \frac{1}{t_0 - t} \quad (5.79)$$

where t_0 is the time of the “explosion.” In our case, $t_0 \simeq (k_T, v_T)^{-1}$.

5.8 Sub-critical Mass Flows: Absence of Instabilities

In this section we shall consider the effects of *sub-critical mass flows* when a system is stable with respect to both the KH and NEW instabilities. In particular, we will study the influence of mass flows on the propagation of shear Alfvén waves.

We will see that even in a simple case of regular mass flows directed along the magnetic field, their presence considerably modifies the dissipation of shear Alfvén waves, affecting both the magnitude and the height of maximum dissipation. The strongest effect occurs in the case of downflows when the flow velocity at a certain height becomes equal to the Alfvén velocity. Near that point the wave comes to extinction and gives off its energy completely. This effect can be directly associated with observed high velocity downflows in the transition region, and, in particular, can serve as a qualitative explanation for the high variability of the emission observed around 10^5 K. In the presence of upward mass flows and moderate downflows, the dissipation of Alfvén waves is accompanied by the radial redistribution of the energy input across the magnetic structure thus creating a mosaic pattern in the emitting regions. Note again that the flow velocities are assumed to be below the thresholds which correspond to the onset of hydrodynamic and dissipative instabilities.

5.8.1 *Can the Alfvén Waves Heat the Corona?*

The specific mechanism of the dissipation of the Alfvén waves is an important agent in the problem of the energy transfer and release in the solar atmosphere. One of the major mechanisms by which Alfvén waves may heat the plasma is their dissipation due to the phase mixing effect (Heyvaerts and Priest 1983). The origin

of this effect is associated with the strong distortion of the wave front which occurs at the propagation of Alfvén waves upward in the solar atmosphere (see Chap. 4, Sect. 4.2). The absorption of the wave reaches a maximum at the height where the dissipation time becomes comparable to the propagation time (z/v_A). The estimate for this characteristic damping length is:

$$z_{\max} \sim L_d \sim \frac{v_A}{\omega} \left(\frac{R^2 \omega}{\nu} \right)^{1/3} \quad (5.80)$$

where ν is the kinematic viscosity coefficient. In the higher layers of the solar atmosphere where the plasma is typically collisionless, the Reynolds number $\text{Re} = (R^2 \omega)/\nu$ is very large, $\sim 10^{10}$. Therefore, the damping length (5.80) greatly exceeds the typical length of magnetic structures in the solar atmosphere. Parker (1991) gave a detailed analysis of difficulties connected with the efficiency of phase mixing effect, which under solar conditions occurs far beyond the corona. And the search began for the effects that would make the phase mixing process to work at reasonable (e.g., coronal) heights.

Important advances were obtained by Similon and Sudan (1989) who treated the propagation of Alfvén waves in a three-dimensional geometry propagating in a complex magnetic field made up of stochastic field lines: the irregular motions at the footpoints of an inhomogeneous magnetic structure and the stochastization of the magnetic field lines lead to shortening of the damping length down to $L_d \sim \ln \text{Re}$.

Still too high. There are various models based on different physical factors, such as plasma turbulence, relaxation effects, and others, which can affect the efficiency of heating by the Alfvén waves and especially its location (Hood et al. 1997; De Moortel et al. 2000; Voitenko and Goossens 2000; Rogava et al. 2000; Walsh and Ireland 2003).

5.8.2 *Effect of Mass Flows on the Efficiency of Heating by Alfvén Waves*

We consider one more aspect, namely, the influence of background mass flows on the propagation of the Alfvén waves and their possible influence on the phase-mixing effect. We shall see that the presence of shear flows not only reduces height of energy release but leads to important topological effects that are observable.

To visualize these effects we assume that Alfvén waves excited by convective motions are subject to slow dissipation. That is, for oscillations with initially smooth radial profile over a scale on the order of flux tube radius R , the frequency

$$\omega \gg \nu/R^2 \quad (5.81)$$

In this case for pure cylindrical geometry with z -axis directed along the magnetic field, the oscillations with velocity

$$v = v_0 \cos \frac{\omega z}{v_A(r)} \quad (5.82)$$

will propagate almost without damping up to the heights z_* where the inverse damping rate $\Delta r^2(z)/\nu$ becomes equal to the propagation time $z/v_A(r)$:

$$\Delta r^2(z)/\nu \simeq z/v_A \quad (5.83)$$

Here Δr is the scale length of the perturbation at a height z estimated as

$$\Delta r(z) \sim \frac{v_A(r)}{|dv_A/dr|} \frac{v_A(r)}{\omega z} \quad (5.84)$$

If R is the characteristic radius of the magnetic structure, then

$$\frac{v_A(r)}{|dv_A/dr|} \sim R, \quad (5.85)$$

and at a height of a few wavelengths ($z \gg \frac{v_A}{\omega}$), the scale length, Δr , becomes smaller and smaller:

$$\Delta r(z) \sim R \frac{v_A}{\omega z} \ll R \quad (5.86)$$

Note that relationships (5.83) and (5.86) give straightforward estimate (5.80).

At a small scale ($\sim \Delta r$) the dissipative effects turn on and ultimately result in the strong damping of a wave at a certain altitude. The dissipative terms link the perturbations at the field lines separated by a distance not exceeding a generalized skin depth

$$\delta = \sqrt{v_* \frac{z}{v_A}} \quad (5.87)$$

where

$$v_* = \frac{\eta}{\rho} + v_m \quad (5.88)$$

At the height z_{\max} where the main dissipation occurs (Eq. (5.80)), the skin depth is given by

$$\delta = R \frac{1}{\text{Re}^{1/3}} \ll R \quad (5.89)$$

This means that considering the wave propagation and dissipation at a certain magnetic surface, we need to know the coefficients of the equation of motion only in the vicinity of this surface. In other words, after the formation of narrow spikes, the analysis becomes local (across the magnetic field), and it can be applied essentially to any field and velocity profile. In the case of an arbitrary magnetic field geometry, the velocity perturbation in the Alfvén wave is

$$\mathbf{v}(\ell, \mathbf{r}) = \mathbf{v}(\ell)e^{iS(\mathbf{r})} \quad (5.90)$$

where $S(\mathbf{r})$ is an eikonal:

$$S(\mathbf{r}) = \int_{L_0}^L \frac{\omega}{v_A(\mathbf{r}) + u(\mathbf{r})} d\ell \quad (5.91)$$

The integration is carried out along the flux tube between its footpoints.

The dependence of the velocity \mathbf{v} on the coordinates transverse to the magnetic field \mathbf{B} as in geometrical acoustics is determined by the gradient of the eikonal across the magnetic structure

$$\mathbf{v}(\ell, \mathbf{r}) = \tilde{\mathbf{v}}(\ell)e^{i\boldsymbol{\tau}\nabla_{\perp}S} \quad (5.92)$$

where $\boldsymbol{\tau}$ is a two-dimensional vector in the plane perpendicular to \mathbf{B} .

The dissipation per unit volume is

$$q \simeq \frac{1}{2}\rho v_*(\nabla_{\perp}S)^2\tilde{\mathbf{v}}^2(\ell) \quad (5.93)$$

where the dependence of $\tilde{\mathbf{v}}(\ell)$ on the coordinate ℓ along the ray trajectory is determined by the conservation of the energy flux

$$B \frac{d}{d\ell} \left(\frac{\rho\tilde{\mathbf{v}}^2}{2} \frac{1}{B} (v_A + u) \right) = -\frac{1}{2}\rho v_*(\nabla_{\perp}S)^2\tilde{\mathbf{v}}^2(\ell) \quad (5.94)$$

Here B is the absolute value of the magnetic field and the operator

$$B \frac{d}{d\ell} \left(\frac{1}{B} \dots \right)$$

in the left-hand side of (5.94) takes into account the change of the cross section of the magnetic flux.

For a given magnetic field $\mathbf{B}(\mathbf{r})$ (5.94) solves the problem of the wave dissipation and yields the dissipation rate at any point in the magnetic structure.

Let us define the expression in brackets in the left-hand side of (5.94) as a function $f(\ell)$:

$$f(\ell) = \frac{v_A + u}{B(\ell)} \frac{\rho \tilde{v}^2}{2} \quad (5.95)$$

With this function, (5.94) can be rearranged as follows:

$$\frac{df}{d\ell} = -v_* \frac{(\nabla_{\perp} S)^2}{v_A + u} f(\ell) \quad (5.96)$$

The integration of this equation is straightforward and yields:

$$f = f_0 e^{-\int^{\ell} v_* [(\nabla_{\perp} S)^2 / (v_A + u)] d\ell} \quad (5.97)$$

The dissipation rate (5.17) is then

$$q \simeq v_* (\nabla_{\perp} S)^2 \frac{B}{v_A + u} f_0 \exp\left(-\int^{\ell} v_* \frac{(\nabla_{\perp} S)^2}{v_A + u} d\ell\right) \quad (5.98)$$

This expression describes the propagation of an Alfvén wave in an arbitrary magnetic field and flow velocity directed along the same ray trajectory.

In the next section we derive the maximum energy release and the characteristic damping length for some chosen geometry of the magnetic field and aligned mass flow.

5.9 Phase-Mixed Alfvén Waves at Sub-Alfvénic Mass Flows

5.9.1 Damping Rate and Height of Energy Release

Let us consider the two-dimensional magnetic field $\mathbf{B} = \mathbf{B}(0, B_{\phi}, B_z)$ with $B_{\phi} = B_{\phi}(r)$ and $B_z = B_0 = \text{const}$. We will assume that the plasma flow is directed along the magnetic field. Consequently, the phase velocity $\mathbf{v}_{\text{ph}} = \mathbf{v}_A + \mathbf{u}$ will be $\mathbf{v}_{\text{ph}} = \mathbf{v}_{\text{ph}}(0, v_{\text{ph}\phi}(r), v_{\text{ph}z})$. The eikonal (5.91) can be written as

$$S(\mathbf{r}) = \int^L \frac{\omega}{\sqrt{v_{\text{ph}\phi}^2 + v_{\text{ph}z}^2}} d\ell \quad (5.99)$$

For the chosen geometry

$$d\ell = \sqrt{r^2 d\phi^2 + dz^2} \quad (5.100)$$

and

$$\frac{v_{\text{ph}\phi}}{v_{\text{ph}z}} = \frac{B_\phi}{B_z} \quad (5.101)$$

$$\frac{dz}{B_z} = \frac{r d\phi}{B_\phi(r)} \quad (5.102)$$

With the help of relationships (5.101) and (5.102) we can rearrange the expressions for the arc element (5.100) and phase velocity as follows:

$$d\ell = \sqrt{1 + \frac{B_\phi^2}{B_z^2}} dz \quad (5.103)$$

$$|\mathbf{v}| = \sqrt{v_{\text{ph}\phi}^2 + v_{\text{ph}z}^2} = v_{\text{ph}z} \sqrt{1 + \frac{B_\phi^2}{B_z^2}} \quad (5.104)$$

Substituting (5.103) and (5.104) into Eq. (5.99) yields

$$S(\mathbf{r}) = \int^z \frac{\omega}{v_{\text{ph}z}(\mathbf{r})} dz \quad (5.105)$$

For the transverse gradient of the eikonal, we have then

$$\nabla_\perp S(\mathbf{r}) = \frac{\partial}{\partial \mathbf{r}} \int^z \frac{\omega}{v_{\text{ph}z}(\mathbf{r})} dz = -\frac{v'_{\text{ph}z}(\mathbf{r})\omega}{v_{\text{ph}z}^2(\mathbf{r})} z. \quad (5.106)$$

With this expression, the dissipation rate (5.98) becomes as follows:

$$q = v_* \frac{\rho |v_0|^2 \omega^2 v_{\text{ph}}'^2}{2 v_{\text{ph}}^4} z^2 \exp\left(-\frac{2}{3} v_* \frac{\omega^2 v_{\text{ph}}'^2}{v_{\text{ph}}^5} z^3\right) \quad (5.107)$$

We took into account here the relationships (5.101) and (5.102) and integrated the exponent over z . For convenience, we dropped the index “ z ” of the phase velocity and will keep in mind below that v_{ph} is the z -component of $\mathbf{v}_{\text{ph}} = \mathbf{v}_A + \mathbf{u}$.

The function $f(\zeta) = \zeta^2 e^{-(2/3)\zeta^3}$ has a maximum at $\zeta = 1$ which from (5.107) gives a height where the maximum absorption of Alfvén waves occurs:

$$z_{\text{max}}(r_0) = \frac{v_{A0} + u_0}{\omega} \left[\frac{\omega(v_{A0}^2 + u_0^2)}{v_* (v'_{A0} + u'_0)^2} \right]^{1/3} \quad (5.108)$$

Here r_0 is the radius of some arbitrary magnetic surface. The subscript “0” introduced in (5.108) reflects the fact that the height of the maximum energy input depends on the radius of the magnetic surface. Thus, for the particular magnetic surface the maximum damping rate is

$$q_m = v_* \frac{\rho |v_0|^2}{2} \left[\frac{[v'_A(r_0) + u'(r_0)]\omega}{v_*[v_A(r_0) + u(r_0)]} \right]^{2/3} e^{-2/3} \quad (5.109)$$

5.9.2 Observable Morphological Effects

The presence of mass flows considerably modifies the picture of the energy release contributed by Alfvén waves. First of all, since the profiles of the Alfvén velocity and flow speed are different functions of radius, the phase velocity $v_A(r) + u(r)$ can have more than one extremum across the magnetic structure. Obviously, the maximum heating occurs at those radii where the gradients of the Alfvén velocity and plasma flows are strongest. The height of maximum absorption, given by (5.108), can be quite adequate for those regions of the atmosphere where observational evidence for an extreme fine structure is found (see, e.g., Kjeldseth-Moe et al. 1994, p. 89).

According to observations, multiple velocities in the transition region are the result of the simultaneous existence of distinctly different velocities associated with separate magnetic filaments with individual sizes of 4–40 km. Taking the magnetic field as 10 G, the temperature as 10^5 K, and the scale of the magnetic filament and mass flow as $R_1 = 10$ km and $R_2 = 40$ km (see, e.g., Dere 1994; Kjeldseth-Moe et al. 1994), we can estimate the height (5.108). For this choice of parameters, the combined kinetic coefficient is $v_* \simeq 2.1 \times 10^{10} \text{ cm}^2 \text{ s}^{-1}$, and the estimate for the height of maximum dissipation is 6300 km for the thinner filaments, and 16,000 km for the filaments with a 40 km radius.

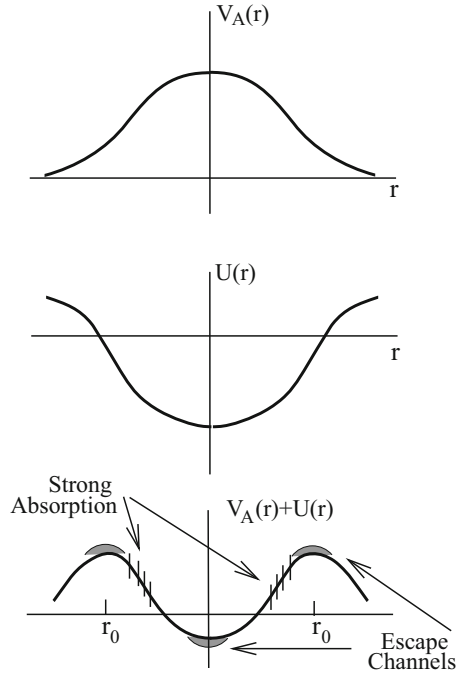
One more morphological effect caused by presence of mass flows, which can be observed, is appearance of an *escape channels* across the magnetic structure carrying energy into upper layers of atmosphere. Indeed, at those radii where

$$v'_A(r_0) + u'(r_0) \Rightarrow 0 \quad (5.110)$$

the damping of the Alfvén waves becomes negligibly small and the wave energy is carried out along these radii to higher altitudes. Thereby, along the magnetic structure, these radii form the escape channels for the energy of Alfvén waves (Fig. 5.3).

Habbal et al. (1990) comparing the morphological structure and temporal behavior of the emission from coronal bright points in a coronal hole and a quiet sun region found that the peaks of emission in the six different wavelengths from the chromosphere to corona are not always co-spatial, implying that bright points consist of a bunch of small-scale loops of different temperatures.

Fig. 5.3 Schematic example of slightly different magnetic field and flow profiles. The extrema of the phase velocity correspond to the energy escape channels, and the regions of steepest gradients are those where the strongest energy absorption occurs



It is important to note that the patchy brightenings associated with magnetic structures may be observed in a wide range of spatial and time scales. For example, the energy escape channels may be associated with the ensembles of unipolar magnetic flux tubes typical to the photosphere underlying the coronal holes (Harvey and Sheeley 1979; Tian et al. 2008). The energy transfer via *unipolar* flux tubes most probably is associated with the Alfvén waves, and being the subject of ever present mass flows, will exhibit the effect described above. In other words, the energy carried by flux tubes, depending on their parameters and associated mass flows may be deposited at different heights and at different temperatures, depending on the realization of escape channels. This may be illustrated in Fig. 5.4. The first panel here shows a snapshot of the sun in Fe XII 193 Å line at 1.26×10^6 K with a huge coronal hole region outlined by the white box. The subsequent snapshots show the coronal hole region at increasing temperatures, starting with magnetogram (Fig. 5.4b).

One can see that the chromospheric bright points (Fig. 5.4c) closely mimic the ensemble of magnetic flux tubes, i.e. almost every flux tubes “delivers” the energy at 5×10^4 K. Higher in the atmosphere, at 6.3×10^5 K (Fig. 5.4d) there are noticeably less number of bright points, although they still fill the region quite densely. At million degree temperatures (Fig. 5.4e) we see significantly less bright points which actually disappear at 2.5×10^6 K (Fig. 5.4f). At this temperature there are only a few survivors (marked by red arrows). These bright points have different origin: as seen

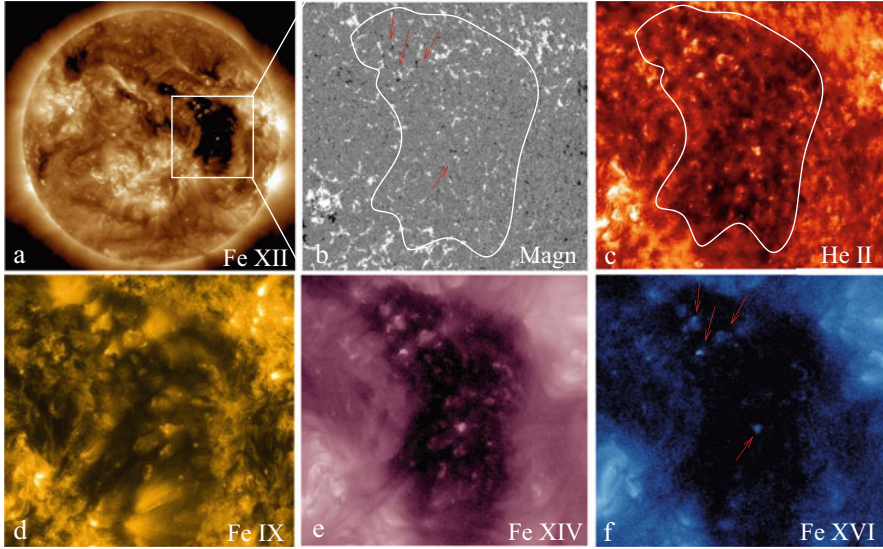


Fig. 5.4 Image of coronal hole taken on 31 May 2013 with the AIA and HMI instruments on the SDO. (a) A whole disc image in Fe XII line at 1.3×10^6 K with well-defined coronal hole; an area in white box containing coronal hole is shown in subsequent images; (b) The magnetogram under the coronal hole is dominated by a rarefied ensemble of mostly unipolar flux tubes; white curve is an approximate border of coronal hole, red arrows show some of the most prominent opposite polarity inclusions; (c)–(f) Coronal hole at the increasing temperatures, 5×10^4 K (He II), 6.3×10^5 K (Fe IX), 2×10^6 K (Fe XIV), 2.5×10^6 K (Fe XVI). Red arrows on the Fe XVI image show the only surviving bright points inside the coronal hole. Courtesy of NASA/SDO

on the magnetogram they are associated with the opposite polarity flux tubes, and the energy transfer here is associated with interaction between the opposite polarity flux tubes through the reconnection and post-reconnection processes.

The next important question associated with effect of mass flows is that of the asymptotic behavior of the total power flux in the phase mixed wave and its distribution across the magnetic structure. We proceed to this problem in the next section. This effect as well can be observed and measured.

5.10 The Asymptotic Behavior of the Total Energy Flux

The total energy flux \mathcal{P} in the wave, integrated over the cross section of the magnetic structure in the absence of a background plasma flow is

$$\mathcal{P} = \frac{\pi}{2} \int \rho |v|^2 v_A r dr \quad (5.111)$$

From the expression for the damping rate (5.109) it is clear that the slowest damping occurs near the axis of the flux tube where for a monotonic dependence of $B(r)$ and $\rho(r)$ on r , the derivative of the Alfvén speed tends to zero. Near the axis, then, the derivative of the Alfvén speed can be represented by

$$v'_A \simeq v''_A(0) r, \quad (5.112)$$

where by the order of magnitude

$$v''_A(0) \simeq \frac{v_A}{R^2} \quad (5.113)$$

From (5.92) and (5.106) in the absence of mass flows we have for $|v|^2$

$$|v|^2 = |v_0|^2 \exp \left[-\frac{1}{3} \frac{\omega^2 v_* (v''_A)^2 r^2}{v_A^5} z^3 \right] \quad (5.114)$$

Since v is a function of radius, $v = \Omega r$, we should take into account that

$$v_0 = \Omega(0)r \quad (5.115)$$

Substituting (5.114) and (5.115) into (5.111), we find that asymptotically, at a height $z \gg (v_A/\omega)(1/\text{Re}^{1/3})$ the total power flux has a power-law dependence on z :

$$\mathcal{P} = \pi \rho(0) v_A(0) \Omega^2(0) \int_0^\infty \exp \left[-\frac{2}{3} \frac{\omega^2 v_* (v''_A)^2 z^3 r^2}{v_A^5} \right] r^3 dr \quad (5.116)$$

Indeed, the integration gives

$$\mathcal{P} = \frac{1}{2} \pi \rho(0) v_A(0) \Omega^2(0) \left(\frac{3v_A^5}{2\omega^3 v_* (v''_A)^2} \right)^2 \frac{1}{z^6} \quad (5.117)$$

or

$$\mathcal{P} = \pi \rho(0) v_A(0) \Omega^2(0) R^4 \left(\frac{z_{\max}}{z} \right)^6 \quad (5.118)$$

This energy flux is produced within the central part of a magnetic structure limited by the radius

$$R_* \simeq R \left(\frac{z_{\max}}{z} \right)^{3/2} \quad (5.119)$$

The situation changes when the background plasma flows are taken into account. In this case, the maximum and/or minimum energy input is redistributed across the magnetic structure and the location of the corresponding regions is determined by those radii where the sum, $v_A(r) + u(r)$, has an extremum. With different profiles of Alfvén speed and flow velocity, as observed, there might be several points where this sum has an extremum. Therefore, the picture of a heated area across the magnetic field, as already discussed, should have quite a patchy and mosaic form. For example, in the simplest case when there is only one point, say, $r = r_0$, instead of (5.112) we will have

$$v'_A + u' \simeq (v''_A + u'')(r - r_0) \quad (5.120)$$

Respectively, the total power flux is

$$\begin{aligned} \mathcal{P} &\simeq \pi \rho(0)[v_A(r_0) + u(r_0)]\Omega^2(r_0)r_0^3 \\ &\times \int_0^\infty \exp\left[-\frac{1}{3} \frac{\omega^2(v''_A + u'')(r - r_0)^2 v_*}{v_A^5} z^3\right] dr \end{aligned} \quad (5.121)$$

this gives the following law for the z -dependence of the total power flux:

$$\mathcal{P} \sim \left(\frac{z_{\max}}{z}\right)^{3/2} \quad (5.122)$$

while in the absence of plasma flows the z -dependence of the total power flux, (5.118) is proportional to $(z_{\max}/z)^6$. Therefore, the presence of plasma flows significantly changes the distribution of energy input with height. First of all, the total energy input occurs at much lower altitudes in the presence of flows than without them. Second, the energy release and its manifestation must have a patchy character. This result seems quite natural and can be easily understood: in the absence of plasma flows the energy flux is concentrated near the center of the magnetic structure, now it is redistributed across the magnetic field, and occurs in some annular channel with a width which has a height dependence of the form:

$$|r - r_0| \sim r_0 \left(\frac{z_{\max}}{z}\right)^{3/2} \quad (5.123)$$

From observational point of view this effect seems to be ubiquitous and well observed.

5.11 The Wave Extinction in the Presence of Downflows

In the case of downflows, if at some point the flow velocity becomes equal to the Alfvén speed, the phase velocity (the denominator in (5.98)) becomes zero and the damping becomes infinite. The physical reason for this effect is quite simple: when the flow speed becomes comparable to Alfvén speed, the wave flux undergoes stagnation (in the laboratory frame), dissipating all its energy as it approaches the stagnation point. As both Alfvén and flow velocities have some radial profiles, the stagnation occurs at a height which depends on radius. This fact gives rise to a peculiar spatial distribution of the dissipated power which must be observable.

Let us consider a flux tube in which the flow is directed towards the surface of the Sun. Denote the cross section of the flux tube by A . Then from the magnetic flux conservation $BA = \text{const}$ and the mass conservation $\rho u A = \text{const}$ we find that the Alfvén velocity scales as

$$v_A \sim \frac{B}{\sqrt{\rho}} \tag{5.124}$$

or

$$\frac{v_A}{u} = \text{const} \sqrt{\rho} \tag{5.125}$$

We see that the ratio of the Alfvén velocity and flow speed, v_A/u , decreases with height as the density decreases (Fig. 5.5). Thus simple consideration shows that the condition $v_A \simeq u$ can most easily be met at higher altitudes.

Near the point $v_A(r) = u(r)$ where the phase velocity of the wave $v_{\text{ph}} = v_A + u$ becomes zero, the wave comes to extinction, and Alfvén waves propagating upward will release all their energy.

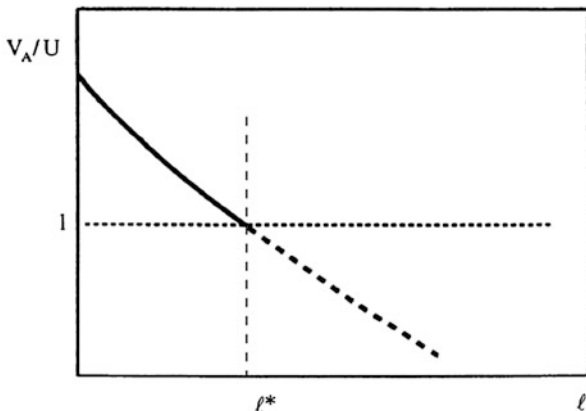


Fig. 5.5 Possible behavior of the ratio of the Alfvén and flow speeds with height

Near the point $v_A = u$ at the axis of the magnetic structure, we have

$$v_{\text{ph}}(r, l) = \frac{\partial v_{\text{ph}}}{\partial l}(l - l_0) + \frac{1}{2} \frac{\partial^2 v_{\text{ph}}}{\partial r^2} r^2 \quad (5.126)$$

As earlier, we consider an example of a simple profile for the Alfvén velocity and the mass flow and assume that they have an extremum at the center of a magnetic flux tube. Let us introduce the notations

$$\Omega_l = \frac{\partial v_{\text{ph}}}{\partial l}, \quad (5.127)$$

$$\Omega_r = R \frac{\partial^2 v_{\text{ph}}}{\partial r^2} \quad (5.128)$$

For a given field line (at a distance r from axis) the condition $v_{\text{ph}} = 0$ holds at the height

$$l^*(r) = l_0 - \frac{\Omega_r}{\Omega_l} \frac{r^2}{2R} \quad (5.129)$$

When approaching the point l^* , the eikonal diverges logarithmically; therefore, it depends weakly on the lower integration limit l_0 . Substituting the expansion (5.126) into the expression (5.91) and retaining only the first term in this expansion yields

$$S(l) = \int_{l_0}^l \frac{\omega dl}{\Omega_l |l - l^*|} = \frac{\omega}{\Omega_l} \ln \left| \frac{l - l^*}{l} \right| \quad (5.130)$$

The radial derivative of the eikonal is then

$$\frac{\partial S}{\partial r} = \frac{\omega}{\Omega_l |l - l^*|} \frac{\partial l^*}{\partial r} \quad (5.131)$$

Using now expression (5.129) we have

$$\frac{\partial S}{\partial r} = -\frac{\omega^2}{\Omega_l} \frac{r \Omega_r}{R |l - l^*|} \quad (5.132)$$

This expression allows us to find how the energy flux, or actually, the function f determined by (5.95), damps out near $l = l^*$. From (5.97) and (5.132) we have

$$f \propto \exp \left[-v_* \frac{\omega^2 \Omega_r^2 r^2}{|\Omega_l^5| R^2} \int_{\mathcal{L}_0}^l \frac{dl}{|l - l^*|^3} \right]. \quad (5.133)$$

The integration gives

$$f \propto \exp \left[-\nu_* \frac{\omega^2 \Omega_r^2 r^2}{2|\Omega_l^5| R^2} \frac{1}{(l - l^*)^2} \right]. \quad (5.134)$$

We see that near the point l^* the damping is very strong: *nothing propagates beyond this point*.

Before the wave comes to extinction at the point $l = l^*$, the strong damping occurs at the height, l_d , which is determined by the condition (for $r \sim R$)

$$\nu_* \frac{\omega^2 \Omega_r^2}{|\Omega_l^5| (l^* - l_d)^2} \sim 1 \quad (5.135)$$

We took into account here that at $r \sim R$, $l^* = l_d$ (see (5.129)). Using the estimates

$$\Omega_l \sim \frac{v_A}{l^*}, \quad \Omega_r \sim \frac{v_A}{R}, \quad (5.136)$$

we have from (5.135)

$$(l^* - l_d)^2 \sim \nu_* \frac{\omega^2 l^{*5}}{R^2 v_A^3}. \quad (5.137)$$

This expression gives the distance $\Delta = l^* - l_d$ at which the strong damping of the wave increases dramatically and ends up with the complete absorption of the wave power at the point l^* :

$$\Delta \sim l^* \left(\frac{l^*}{z_{\max}} \right)^{3/2}; \quad (5.138)$$

z_{\max} here is the characteristic damping length of the shear Alfvén waves provided by the phase-mixing effect in the absence of plasma flows (Eq. (5.80)). To estimate the axial extent of the total energy release, we take the parameters corresponding to the transition region, at 10^5 K, where the largest downflows are observed. For a magnetic field strength $B = 4$ G, a density 10^{10} cm^{-3} , $R = 40$ km, an Alfvén wave period of 100 s, the characteristic damping length in the absence of flows is $z_{\max} = 9 \times 10^4$ km. Taking the height of the transition region to be $l^* = 10^4$ km, we get the axial extent of the absorption region to be $\Delta = 370$ km.

In Fig. 5.6 we sketch the qualitative behavior of the amplitude and damping rate of the Alfvén wave with height. The amplitude (Fig. 5.6a) and the damping rate (Fig. 5.6b) in the absence of plasma flows are shown. In this case the amplitude of the Alfvén wave drops gradually with height until it reaches the height where the eigenfunction of perturbations becomes highly oscillatory so that the wave damps out due to the regular phase mixing effect. At this height, the amplitude drops rapidly

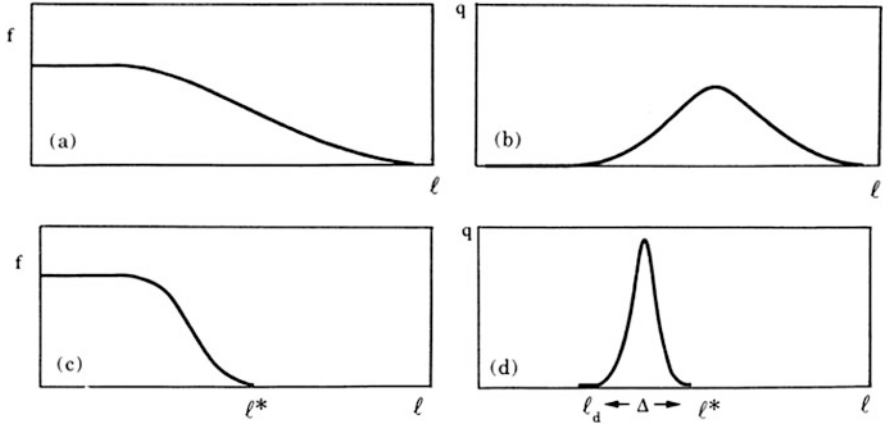


Fig. 5.6 Qualitative behavior of the amplitude and the damping rate both in the absence and in the presence of downflows. In the absence of mass flows the amplitude of the Alfvén wave (a) drops gradually with height until it reaches the height where the eigenfunction of perturbations becomes highly oscillatory so that the wave damps out due to the phase mixing effect. Near that region the damping rate (b) has a maximum. In the presence of downflows at lower altitudes the behavior of the wave amplitude (c) and the damping rate (d) are similar to those without mass flows. At the point $l = l_d$ the strong damping occurs and at a short distance of $\Delta = l^* - l_d$ the wave damps out completely, so that no portion of it propagates farther

and the damping rate has a maximum determined by (5.108) and (5.109) with $u = 0$.

In the presence of downflows the process of the wave damping has an entirely different character: at lower altitudes the behavior of the wave amplitude Fig. 5.6c and the damping rate Fig. 5.6d are similar to those without mass flows. At the point $l = l_d$ the strong damping occurs and at a short distance $\Delta = l^* - l_d$ the wave damps out completely, so that no portion of it propagates farther.

Note that the same consideration is applicable also to the other modes of flux tube oscillations, in particular kink, $m = \pm 1$, and sausage, $m = 0$ oscillations.

Hence, the physical parameters of the magnetic field and plasma flows determine the morphology of a heated area: the geometrical height where the maximum heating occurs now is not restricted by the phase-mixing effect and can be much lower than z_{\max} .

5.12 Problems

5.1 This exemplary problem is about the internal waves in an ocean. The classical Kelvin-Helmholtz instability is usually analyzed by considering a sheared mass flows of fluids in gravitational field when lighter fluid with ρ_1 is above a heavier one, $\rho_2 > \rho_1$. Find the regions of linear KH instability and nonlinear instability of Negative Energy Waves (NEWs) (Cairns 1979).

5.2 Throughout solar atmosphere, especially in the transition region and corona, repetitive pulses with explosively growing amplitudes are often observed. The solar atmosphere as energetically open system has plenty of free energy available, and thus may easily sustain the negative energy waves whose interaction with positive energy waves leads to explosive growth of all three wave amplitudes. The interplay between the processes of explosive growth and its saturation may lead to repeated peaks of the amplitude in time. Describe the process and determine the speed and the repetition rate of the peaks (Weiland and Wilhelmsson 1977; Wilhelmsson 1984).

Appendix: Equation for Alfvén Waves in the Presence of Parallel Mass Flows

In this section we derive the general equation for Alfvén waves in the presence of mass flows which can be used for solving problems other than those considered in the previous sections.

In particular, this equation will allow one to study the influence of mass flows on the resonance absorption of Alfvén waves and to explore the development of different kinds of hydrodynamic instabilities.

Consider for simplicity a magnetic field having only a z-component, $\mathbf{B}_0(0, 0, B(r))$. The background mass flow with the velocity $\mathbf{u}(r)$ is assumed to be directed along the magnetic field. All the plasma parameters are monotonic functions of radius. The perturbation of the velocity $\mathbf{v}(0, v_\varphi(r, z, t), 0)$ and the magnetic field $\mathbf{b}(0, b_\varphi(r, z, t), 0)$ are axisymmetric, and we will drop the index φ further. The MHD-equations for a given geometry which include the viscous losses have the form

$$\rho \left(\frac{\partial v}{\partial t} + u \frac{\partial v}{\partial z} \right) = \frac{B}{4\pi} \frac{\partial b}{\partial z} + \frac{1}{r^2} \frac{\partial}{\partial r} \eta r^3 \frac{\partial v}{\partial r} \quad (5.139)$$

$$\frac{\partial b}{\partial t} + u \frac{\partial b}{\partial z} = B \frac{\partial v}{\partial z} + \frac{\partial}{\partial r} \frac{1}{r} v_m \frac{\partial}{\partial r} r b \quad (5.140)$$

All notations are standard; η is ion viscosity ($\omega_i \tau_i \gg 1$) and v_m is magnetic diffusivity. Since the dissipation is weak, we have neglected in the dissipative terms the derivatives $\partial/\partial z$.

Taking the derivative $(\partial/\partial t + u\partial/\partial z)$ of (5.139) and using (5.140) we have

$$\begin{aligned} \rho \left(\frac{\partial}{\partial t} + u \frac{\partial}{\partial z} \right)^2 v &= \frac{B}{4\pi} \frac{\partial}{\partial z} \left[B \frac{\partial v}{\partial z} + \frac{\partial}{\partial r} \frac{1}{r} v_m \frac{\partial}{\partial r} r b \right] \\ &\quad + \left(\frac{\partial}{\partial t} + \frac{\partial}{\partial z} \right) \frac{1}{r^2} \frac{\partial}{\partial r} \eta r^3 \frac{\partial v}{\partial r} \end{aligned} \quad (5.141)$$

At weak dissipation, one can use in the second term in right-hand side of (5.141), the following expression for $\partial b/\partial z$:

$$\frac{B}{4\pi} \frac{\partial b}{\partial z} \simeq \rho \left(\frac{\partial v}{\partial t} + u \frac{\partial v}{\partial z} \right), \quad (5.142)$$

Now we can write a single equation for v :

$$\begin{aligned} \rho \left(\frac{\partial}{\partial t} + u \frac{\partial}{\partial z} \right)^2 v &= \frac{B^2}{4\pi} \frac{\partial^2 v}{\partial z^2} + \frac{B}{4\pi} \frac{\partial}{\partial r} \frac{1}{r} v_m \frac{\partial}{\partial r} r \frac{4\pi\rho}{B} \left(\frac{\partial v}{\partial t} + u \frac{\partial v}{\partial z} \right) \\ &+ \left(\frac{\partial}{\partial t} + u \frac{\partial}{\partial z} \right) \frac{1}{r^2} \frac{\partial}{\partial r} \eta r^3 \frac{\partial v}{\partial r} \end{aligned} \quad (5.143)$$

For the boundary value problem with

$$v|_{z=0} = v_0 e^{i\omega t} \quad (5.144)$$

and without the dissipation we have from (5.143) (see (5.82)):

$$v = v_0 \cos \frac{\omega z}{v_A(r)} \quad (5.145)$$

As discussed in Section 8, the velocity profile becomes spiky with height, and its scale (5.86) at the heights $z \gg v_A/\omega$ becomes much less than R :

$$\Delta r \ll R \quad (5.146)$$

This condition allows us to simplify (5.141). Namely, in the dissipative terms we can neglect the radial derivatives of all the functions except v . Note that the background plasma parameters $B(r)$, $\rho(r)$, and $u(r)$ change at the scale R , and from to condition (5.146) we have

$$\frac{db}{dr}, \frac{d\rho}{dr}, \frac{du}{dr} \ll \frac{\partial v}{\partial r} \quad (5.147)$$

Furthermore,

$$\frac{\partial^2}{\partial r^2} \gg \frac{1}{r} \frac{\partial}{\partial r}, \frac{1}{r^2} \quad (5.148)$$

Under these conditions (5.143) becomes:

$$\left(\frac{\partial}{\partial t} + u \frac{\partial}{\partial z} \right)^2 v = v_A^2(r) \frac{\partial^2 v}{\partial z^2} + v_* \left(\frac{\partial}{\partial t} + u \frac{\partial}{\partial z} \right) \frac{\partial^2 v}{\partial r^2} \quad (5.149)$$

where $v_* = \eta/\rho + v_m$.

One can see that in the absence of dissipation, different radii do not communicate with each other as is clearly seen from (5.149): The Alfvén waves along each cylindrical surface propagate with the speed determined only by the surface radius r , i.e. at a speed $v_A(r)$.

The dissipative term links the perturbations at the field lines separated by the distance not exceeding a generalized skin-depth (5.89), which means that considering the wave propagation and dissipation at a certain magnetic surface, we need to know the coefficients of (5.149) only in the vicinity of this surface. We denote the radius of some arbitrary surface by r_0 , and for

$$r = r_0 + x, \quad (5.150)$$

use the approximations

$$v_A(r) \cong v_A(r_0) + \left. \frac{dv_A(r)}{dx} \right|_{r_0} \quad (5.151)$$

$$u(r) \cong u(r_0) + \left. \frac{du(r)}{dx} \right|_{r_0} \quad (5.152)$$

$$v_* \cong v_*(r_0) \quad (5.153)$$

We drop the index “0” below, and will keep in mind that these quantities have a local meaning at a certain radius r_0 .

For perturbations $\sim \exp(-i\omega t)$, (5.149) reduces to

$$[u^2(r) - v_A^2(r)] \frac{\partial^2 v}{\partial z^2} - 2i\omega u(r) \frac{\partial v}{\partial z} - \omega^2 v = v_* \frac{\partial^2}{\partial r^2} \left(-i\omega v + u(r) \frac{\partial v}{\partial z} \right) \quad (5.154)$$

It is convenient to represent the velocity perturbations in a form

$$v = w(r, z, t) \exp\left(i \frac{\omega}{v_{A0} + u_0} z\right) \quad (5.155)$$

where $v_{A0} = v_A(r_0)$ and $u_0 = u(r_0)$. Simple algebra gives the following equation for w (the analogue of parabolic equation in diffraction theory):

$$\begin{aligned} \frac{\partial w}{\partial z} + i\omega \frac{v'_{A0} + u'_0}{(v_{A0} + u_0)^2} x w \\ - v_* \left[\frac{1}{2(v_{A0} + u_0)} \frac{\partial^2 w}{\partial^2 x} - \frac{u'(r)}{v_{A0}(v_{A0} + u_0)} \frac{\partial w}{\partial x} - \frac{u''(r)}{2v_{A0}(v_{A0} + u_0)} w \right] = 0 \end{aligned} \quad (5.156)$$

Prime means the derivative over radius.

Equation (5.156) is the basic equation describing the Alfvén wave propagation in the presence of plasma flows. Magnetic field and plasma parameters have a smooth

dependence on radius. This equation can be written in especially convenient form using a function Q which we define as follows:

$$w = Q(x, z, t) \exp\left(\frac{u'(x)}{v_{A0}}x\right), \quad (5.157)$$

and in the variables:

$$\xi = x \left[\frac{\omega(v'_{A0} + u'_0)}{v_*(v_{A0} + u_0)} \right]^{1/3} \quad (5.158)$$

$$\zeta = z \frac{\omega(v'_{A0} + u'_0)}{(v_{A0} + u_0)^2} \left[\frac{\omega(v'_{A0} + u'_0)}{v_*(v_{A0} + u_0)} \right]^{-1/3} \quad (5.159)$$

With (5.157)–(5.159), the basic parabolic equation (5.156) takes a form:

$$\frac{\partial Q}{\partial \zeta} + i\xi Q - \frac{\partial^2 Q}{\partial \xi^2} + \alpha(\xi) \cdot Q = 0 \quad (5.160)$$

with

$$\alpha(\xi) \sim \left[\frac{(u')^2(\xi)}{v_{A0}^2} + \frac{u''(\xi)}{v_{A0}} \right] \quad (5.161)$$

Equation (5.160) allows one to study the various instabilities in the presence of mass flows.

It is important to note that the asymptotic behavior of the total power flux of the wave varies much more slowly with height in the presence of mass flows than without them. Namely, the total power flux \mathcal{P} in the presence of flows scales with height as $\mathcal{P} \sim z^{(-3/2)}$, while it scales as $\mathcal{P} \sim z^{-6}$ in their absence.

Thus, a regular *subsonic* upward and downward mass flows modify considerably the propagation of phase mixed Alfvén waves. First of all, the radial redistribution of the energy input occurs, which is determined by the fact that the extrema of the Alfvén speed and flow velocity are not spatially coincident. In this case, the strongest absorption occurs at those radii at which the gradients of the phase velocity are steepest, while those radii at which the phase velocity has extrema form an escape channel for the wave energy. Therefore, even for moderate flow velocities (compared with the magnitude of the Alfvén speed), both upward and downward flows lead to the creation of a complex mosaic of highly localized bright regions with varying heights. These effects can be considered as a reasonable explanation for understanding the complex intermittent emission such as observed in coronal bright points (Huang et al. 2012; Alexander et al. 2011; Habbal and Withbroe 1981; Habbal et al. 1990).

Note also that the strongest effect occurs in the case of downflows: if at some geometrical height the Alfvén speed and flow velocity become equal, the wave comes to extinction and gives off its energy completely. This process is independent of the heating due to phase mixing and can occur much earlier and at lower altitudes than the onset of the latter. Near this region the absorption length $\Delta = l^* - l_d$ along the direction of the magnetic field becomes very small. Since both the Alfvén speed v_A and flow velocity u depend on r and l , the points where $v_A = u$ constitute a surface $l = l(r)$ in which essentially all the wave energy is released. This effect, as mentioned earlier, should manifest itself as a complex picture of localized bright regions, as complex as the topology of the magnetic fields and plasma flows throughout the solar atmosphere.

References

- C.E. Alexander, G. Del Zanna, R.C. Maclean, *Astron. Astrophys.* **526**, 134 (2011)
 R.A. Cairns, *J. Fluid Mech.* **92**, 1 (1979)
 S. Chandrasekhar, *Hydrodynamic and Hydromagnetic Stability* (Dover Publications, New York, 1961)
 B. Coppi, M.N. Rosenbluth, R. Sudan, *Ann. Phys.* **55**, 201 (1969)
 I. De Moortel, A.W. Hood, T.D. Arber, *Astron. Astrophys.* **354**, 334 (2000)
 K.P. Dere, *Space Sci. Rev.* **70**, 21 (1994)
 K.P. Dere, J.-D.F. Bartoe, G.E. Brueckner, *Sol. Phys.* **123**, 41 (1989)
 V.M. Dikasov, L.I. Rudakov, D.D. Ryutov, *Sov. Phys. JETP* **21** (1965)
 S.R. Habbal, G.L. Withbroe, *Sol. Phys.* **69**, 77 (1981)
 S.R. Habbal, R.D. Gonzalez, *Astrophys. J.* **326**, L25 (1991)
 S.R. Habbal, G.L. Withbroe, J.F. Dowdy Jr., *Astrophys. J.* **352**, 333 (1990)
 J.W. Harvey, N.R. Sheeley Jr., *Space Sci. Rev.* **23**, 139 (1979)
 J. Heyvaerts, E.R. Priest, *Astron. Astrophys.* **117**, 220 (1983)
 A.W. Hood, J. Ireland, E.R. Priest, *Astron. Astrophys.* **318**, 957 (1997)
 Z. Huang, M.S. Madjarska, J.G. Doyle, D.A. Lamb, *Astron. Astrophys.* **548**, 62 (2012)
 J.A. Ison, *Astrophys. J.* **226**, 650 (1978)
 B.B. Kadomtzev, A.B. Mikhailovski, A.V. Timofeev, *Sov. Phys. JETP* **20**, 1517 (1964)
 O. Kjeldseth-Moe, N. Brynildsen, P. Brekke, P. Maltby, *Space Sci. Rev.* **70**, 89 (1994)
 L. Landau, M. Lifshitz, *Fluid Mechanics* (Pergamon Press, Oxford, 1984)
 L.A. Ostrovskii, S.A. Rybak, L.Sh. Tsimring, *Sov. Phys. Usp.* **29**, 1040 (1986)
 E.N. Parker, *Astrophys. J.* **376**, 355 (1991)
 A.D. Rogava, S. Poedts, S.M. Mahajan (2000), *Astron. Astrophys.* **354**, 749
 M.P. Ryutova, in *Proceedings of XIII. International Conference, Berlin* (1977), p. 859
 M.P. Ryutova, *Sov. Phys. JETP* **67**(8), 1594 (1988)
 P.L. Similon, R.N. Sudan, *Astrophys. J.* **336**, 442 (1989)
 P.A. Sturrock, *Phys. Rev. Lett.* **16**, 270 (1966)
 H. Tian, W. Curdt, M. Eckart, H. Jansen, *Astrophys. J.* **681L**, 121 (2008)
 Yu. Voitenko, M. Goossens, *Astron. Astrophys.* **357**, 1073 (2000)
 R.W. Walsh, J. Ireland, *Astron. Astrophys. Rev.* **12**, 1 (2003)
 H. Wilhelmsson, *Phys. Scr.* **29**, 469 (1984)
 G.L. Withbroe, D.T. Jaffe, P.V. Foukal, M.C.E. Huber, R.W. Noyes, E.M. Reeves, E.J. Schmahl, J.G. Timothy, J.E. Vernazza, *Astrophys. J.* **203**, 528 (1976)
 J. Weiland, H. Wilhelmsson, *Coherent Nonlinear Interaction of Waves in Plasmas* (Pergamon Press, Oxford, 1977)

Chapter 6

Collective Phenomena in Rarefied Ensembles of Flux Tubes



Abstract In the previous chapters we have considered the properties of individual flux tubes and their dynamics due to the interaction with the surrounding medium. The solar atmosphere, however, consists of ensembles of flux tubes randomly distributed in space and over their parameters. In this chapter we shall consider the time-dependent response of a randomly magnetized medium to propagation of acoustic waves and unsteady wave packets. We will see that the collective phenomena resulted from these interactions lead to clear morphological effects that are observable. The character of these effects and the associated energy input and distribution crucially depend on the magnetic filling factor of the medium and several other factors that will be specified.

6.1 Response of Flux Tubes to Propagation of Sound Waves

The response of a randomly magnetized medium to propagation of acoustic waves and unsteady wave packets strongly depends on the distribution of magnetic elements and their individual properties (Ryutova and Priest 1993a,b). Obviously, the wave packets and other motions near the surface carry significant amount of energy, which, by various means, may be absorbed by the magnetic flux tubes and carried upward into higher layers of the atmosphere. The outcome depends not only on the properties of an individual flux tube, but strongly depends on the set of neighboring flux tubes. For illustrative purpose we show in Fig. 6.1 examples of the corona overlying two different ensembles of magnetic flux tubes. The left panels show a dense conglomerate of magnetic elements forming a small active region with magnetic filling factor on the order of unity. Hot compact loops are “customary” overlying the dense mixed polarity region. The right panels show a quiet sun region with rarefied ensemble of flux tubes with small filling factor. One can see clouds of energy, at the same, 0.5×10^5 K temperature, as active region coronal loops, but spread diffusively over the ensembles of far removed flux tubes. Later in this chapter we shall see that the appearance of hot large clouds of plasma is a natural consequence of the collective phenomena in rarefied ensembles of flux tubes.

SDO 2 June 2012

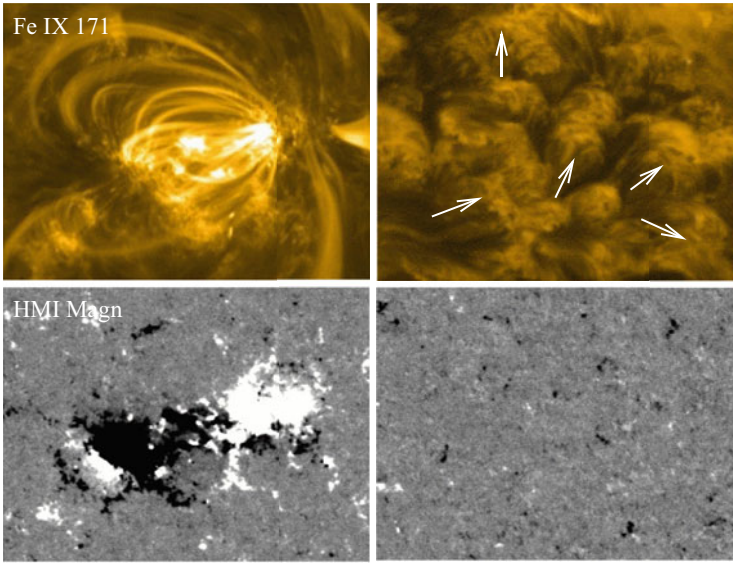


Fig. 6.1 Snapshots of two typical ensembles of magnetic elements and their overlying corona in Fe IX 171 Å line at 6.3×10^5 K. Left: The magnetogram of a compact active region forming well-defined hot loops; Right: A quiet sun region magnetogram and hot cloudy corona above it. White arrows show an approximate direction of the propagation of clouds. Field of view of each snapshot is 130×100 Mm. Courtesy of SDO/HMI

6.1.1 Energy Exchange Between the Acoustic Waves and Ensembles of Flux Tubes

We start with consideration of rarefied ensembles of flux tubes and their interaction with acoustic waves and unsteady wave packets. The subject of dense conglomerate will be studied in Chaps. 8 and 9.

The most important role here is played by resonant interaction, both absorption and scattering of the sound wave by flux tubes. Recall that in the case of resonant absorption the acoustic waves (of frequency ω) energy of the incident acoustic wave is accumulated in the system of magnetic flux tubes. The acoustic wave first damps out at a rate $\nu_L \sim (R^2/d^2)\omega$, and remains for a long time in the form of flux tube oscillations. Then, in a time ν_{rad}^{-1} which is much longer than the damping time of the sound wave, the resonant flux tubes radiate their energy as secondary acoustic (or MHD) waves, where $\nu_{\text{rad}} \sim \omega k^2 R^2$. The incident acoustic wave can also be resonantly scattered with the main contribution coming from the kink mode; it leads to a linear frequency shift and to the appearance of incoherent noise without a preliminary buildup of wave energy in flux tube oscillations.

When the distribution of flux tube natural frequencies is broader than ν_L the landau-like resonant absorption process is more important than resonant scattering,

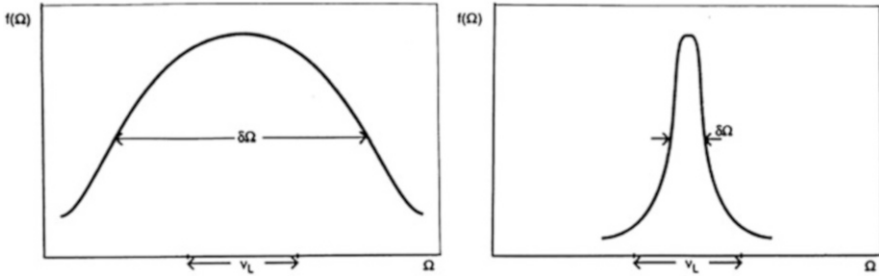


Fig. 6.2 Distribution function $f(\Omega)$ of the flux tubes as a function of their frequencies, Ω , for (a) a broad distribution with $\delta\Omega \gg \nu$; (b) a narrow distribution with $\delta\Omega \ll \nu_L$ where $\delta\Omega$ is the spread in eigenfrequencies and ν_L is the damping rate of the acoustic wave due to Landau resonance

but when the distribution is narrow the tubes are almost identical and resonant scattering may dominate.

Figure 6.2 illustrates these two cases of distribution function over the flux tube parameters. Obviously the case of broad distribution function is much more realistic than the case of almost identical flux tubes (Bogdan and Zweibel 1987). Thus, the damping of long-wavelength acoustic oscillations in the rarefied plasma ($R \ll d$) with

$$\lambda = k^{-1} \gg d, \quad (6.1)$$

is largely determined by Landau damping (Landau 1946; Timofeev 1970; Chen and Hasegawa 1974; Ryutov and Ryutova 1976; Lontano et al. 2000).

To look into the problem in depth we need to make nonlinear estimates, and consider the damping of monochromatic sound wave of finite amplitude. This will allow us to solve several problems. In particular, to find the maximum energy that can be transferred to the medium from the acoustic wave packets, and a frequency shift of the propagating waves, which is of measurable quantity.

Let a periodic acoustic wave be excited at the initial moment of time, $t = 0$, with amplitude ζ_0 and frequency ω_0 . The displacement amplitude $\xi_\eta(t)$ of a flux tube in the field of this sound wave is described by the equation:

$$\frac{\partial \xi_\eta}{\partial t^2} + \Omega^2(\eta)\xi_\eta = A\Omega^2(\eta)\zeta_0 e^{-i\omega t} \quad (6.2)$$

where $\Omega(\eta)$ is the eigenfrequency of flux tube oscillations and A is a numerical factor of order unity.

6.1.2 Near-Resonance Condition

Let us first consider the energy exchange between the acoustic wave and the flux tube in conditions close to resonance, i.e., in a region of small $(\eta - \eta_0)$. We assume that the frequency shift Δ is small:

$$|\Delta| - |\omega - \Omega| \ll \omega \quad (6.3)$$

Under this condition, for those values of η sufficiently close to η_0 the amplitude of the flux tube oscillations increases linearly in time, so that very rapidly, just in a few periods, it becomes much larger than ζ_0 , and we can neglect the initial amplitude ξ_0 ($\simeq \zeta_0$).

The solution of (6.2) corresponding to the initial conditions $\xi = 0$ and $d\xi/dt = 0$ at $t = 0$ is

$$\xi = A\zeta_0 \left[-\frac{\Omega e^{i\Omega t}}{2(\Omega + \omega)} - \frac{\Omega e^{-i\Omega t}}{2(\Omega - \omega)} + \frac{\Omega^2 e^{-i\omega t}}{\Omega^2 - \omega^2} \right] \quad (6.4)$$

The first term on the right has a nonresonant character and can be neglected. The last two terms can be combined, and using again the condition (6.3) we find

$$\xi \simeq \frac{A\zeta_0\omega}{2\Delta} e^{-i\omega t} (1 - e^{-i\Delta t}). \quad (6.5)$$

The energy density of flux tube oscillations which is proportional to $|\xi|^2$ is then estimated as

$$W \simeq \frac{|1 - e^{-i\Delta t}|^2}{\Delta^2} = \frac{\sin^2(\Delta t/2)}{\Delta^2}. \quad (6.6)$$

Let us denote the distribution function of flux tubes over their eigenfrequencies Ω by $f(\Omega)$. Then the total energy transfer to the flux tubes within time t is proportional to

$$I = \int f(\Omega) \frac{\sin^2(\Delta t/2)}{\Delta^2} d\Omega. \quad (6.7)$$

At a time $t \gg 1/\omega$, the interval of frequencies Ω that gives a significant contribution to the integral (6.7) is of the order of $(1/t) \ll \Omega$. Respectively, for a broad enough distribution function $f(\Omega)$ can be replaced by its value at $\Omega = \omega$:

$$I \simeq \frac{1}{2} f(\omega) t \int_{-\infty}^{\infty} \frac{\sin^2(x)}{x^2} dx = \frac{\pi}{2} f(\omega) t \quad (6.8)$$

Then the power absorbed by the flux tubes is proportional to $|\zeta_0|^2 f(\omega)$.

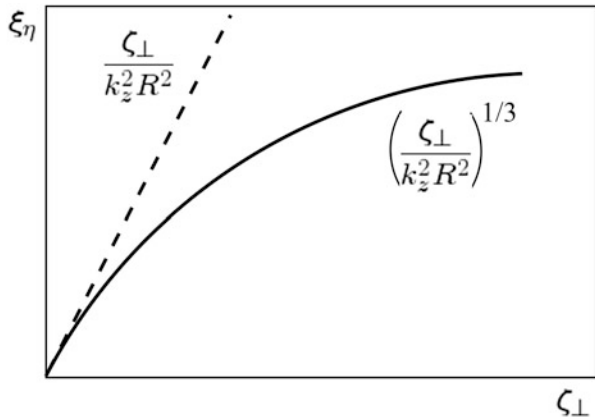


Fig. 6.3 Plots of the amplitude of flux tube displacement, ξ_η , as a function of the initial sound wave amplitude, ζ_\perp : dashed line for the linear case, and solid line for nonlinear case

By retaining all the numerical factors one can obtain in this way the damping rate, ν_L , of the acoustic wave due to the Landau resonance, which is given by (3.28) of Chap. 3. Thus in order of magnitude,

$$\nu_L (\equiv \text{Im}\omega) \simeq \alpha\omega \tag{6.9}$$

Note that this estimate holds for a broad distribution function $f(\Omega)$ with $\Delta \sim \Omega$ (Fig. 6.3).

Equation (6.7) shows that, when the damping rate of the acoustic wave equals to ν_L , the wave is absorbed by flux tubes whose

$$|\Delta| \equiv |\omega - \Omega| \leq \nu_L \tag{6.10}$$

Within a time $t_L = 1/\nu_L$ the energy of the acoustic wave is transferred to the resonant flux tubes. The oscillations of the flux tubes, in principle, are gradually dissipated in two ways: first, by radiative damping through the radiation of secondary acoustic or MHD waves with damping rate $\nu_{\text{rad}} \sim (kR)^2 \Omega$ (see (3.50)); and, second, by the usual dissipative effects (e.g., viscosity, thermal losses, etc.), with corresponding damping rate ν_{diss} .

The Landau damping mechanism corresponds to the case when

$$\nu_L \gg \nu_{\text{rad}} + \nu_{\text{diss}} \tag{6.11}$$

In this case the sequence of energy transfer phenomena is as follows:

1. Within a time $t_L = 1/\nu_L$ the energy of the acoustic wave is transferred to the flux tubes with eigenfrequencies in the range $|\omega - \Omega| \sim \nu_L$;

2. Within a time of a few inverse damping rates $|\omega - \Omega|^{-1} \sim \nu_L^{-1}$ the flux tube oscillations become phase-mixed and their oscillations become completely incoherent;
3. Within a time proportional to $(\nu_{\text{rad}} + \nu_{\text{diss}})^{-1}$ the flux tube oscillations damp away due to either or both mechanisms mentioned above, i.e. radiation and dissipative processes.

The flux tube oscillation energy is converted into heat if $\nu_{\text{rad}} > \nu_{\text{diss}}$, or into the energy of incoherent secondary acoustic noise if $\nu_{\text{rad}} < \nu_{\text{diss}}$.

It is important that if $\nu_L \gg \nu_{\text{rad}} + \nu_{\text{diss}}$, absorption of the acoustic wave occurs neither by resonant absorption nor by resonance scattering: the initial energy of the acoustic wave is instead stored for a long time, $\sim (\nu_{\text{rad}} + \nu_{\text{diss}})^{-1}$, in the form of incoherent flux tube oscillations.

6.2 Nonlinear Estimates of the Maximum Energy Input

Let us return to (6.2) and for definiteness rewrite it for the kink mode with eigenfrequency $\Omega = kc_s/\sqrt{2/\gamma(1+\eta)}$

$$\frac{\partial^2 \xi_\eta}{\partial t^2} + \Omega^2(\eta)\xi_\eta = -\omega^2 \zeta_\perp e^{-I\omega t} \quad (6.12)$$

As was already mentioned, near the resonance, in a few periods, the flux tube oscillation amplitude, ξ , far exceeds the amplitude ζ_\perp of the initial sound wave, and the oscillations become nonlinear. The first effect which saturates the growth of the amplitude is a nonlinear frequency shift, which we denote as $\Delta\omega_{\text{nl}}(\xi_\eta)$. Now the frequency of flux tube oscillations can be written as

$$\Omega_{\text{nl}} = \Omega + \Delta\omega_{\text{nl}}(\xi_\eta) \quad (6.13)$$

The first non-vanishing term in the expansion of $\Delta\omega_{\text{nl}}(\xi_\eta)$ in powers of ξ_η has the form

$$\Delta\omega_{\text{nl}}(\xi_\eta) = \Omega(k_z \xi_\eta)^2 \quad (6.14)$$

For values η that are sufficiently close to resonance value η_0 (condition (6.3)), the stationary value of the amplitude can be estimated directly from (6.12):

$$\xi(\eta) \left| \frac{d\Omega}{d\eta}(\eta - \eta_0) - \Omega k_z^2 \xi_\eta^2 \right| \sim \zeta_\perp \omega \quad (6.15)$$

Since $d\Omega/d\eta \sim \omega$, it follows from (6.14) and (6.15) that ξ_η depends on η as follows:

$$\nu \simeq \left\{ \begin{array}{l} \zeta_\perp/|\eta - \eta_0|, \quad |\eta - \eta_0| \gg (\zeta_\perp k_z)^{2/3} \\ \zeta_\perp(\zeta_\perp k_z)^{-2/3}, \quad |\eta - \eta_0| \leq (\zeta_\perp k_z)^{2/3} \end{array} \right\} \quad (6.16)$$

This expression allows us to estimate the energy which will be transferred by an ensemble of flux tubes to the medium when the amplitude of flux tube oscillations reaches saturation. Since the energy of flux tube oscillations per unit length is of the order of magnitude of $\rho_e R^2 \xi_\eta^2 \omega^2$, the energy per unit volume transferred to the medium can be estimated as

$$W^* \simeq \rho_e \omega^2 \int g(\eta) \xi_\eta^2 d\eta \quad (6.17)$$

Near the resonance we have

$$W^* \simeq \rho_e \omega^2 \zeta_\perp^2 (\zeta_\perp k_z)^{-2/3} g(\eta_0) \quad (6.18)$$

or

$$\frac{W^*}{W} \simeq \alpha \left(\frac{\rho_e c_{se}^2}{W} \right)^{1/3} \quad (6.19)$$

Here $W \sim \rho_e \omega^2 \zeta^2$ is the energy density of the incident sound wave. We used here the estimate $g(\eta_0) \sim \alpha$.

This result solves the problem of damping of a finite-amplitude wave, which may proceed in two major ways:

1. When $W/c_{se}^2 > \alpha^3$ the maximum energy which can be transferred by the flux tube is small compared to the energy of the sound wave, that is, the wave transfers only an insignificant fraction of its initial energy to flux tubes, after which the damping stops.
2. At $W/c_{se}^2 < \alpha^3$, the energy of flux tubes remains small even when the sound wave is completely absorbed; in this case, nonlinear effects, and in particular, a nonlinear frequency shift, are unimportant, and damping is determined by the linear theory.

The condition for the applicability of the linear approximation in the problem of damping of a monochromatic sound wave with initial amplitude ζ thus has the form

$$k\zeta < \alpha^{3/2} \quad (6.20)$$

Consider now the example of the case opposite to (6.20), i.e. when

$$k\zeta > \alpha^{3/2} \quad (6.21)$$

In this case the sound wave is ultimately damped to extinction due to radiation damping of the flux tube oscillations. The damping time turns out to be much larger than ν_L^{-1} . In this case the dissipation rate of the acoustic energy can be estimated as $-Q \sim \nu_{\text{rad}} W^*$, where W^* is given by (6.19) and ν_{rad} is the radiative damping rate. Now, instead of the estimate (6.19) we have

$$-\frac{\partial W}{\partial t} \simeq \nu_{\text{rad}} W \alpha \left(\frac{\rho_e c_{\text{se}}^2}{W} \right)^{1/3}, \quad (6.22)$$

which gives the characteristic damping time of the acoustic wave as

$$\tau \simeq \frac{1}{\nu_{\text{rad}} W \alpha} \left(\frac{\rho_e c_{\text{se}}^2}{W} \right)^{-1/3} \gg \nu_{\text{rad}}^{-1} \quad (6.23)$$

Note that we have kept the assumption that $\nu_{\text{rad}} \ll \Delta \omega_{\text{nl}}$, otherwise the nonlinear effects become unimportant.

To compare the contribution of linear and nonlinear processes let us directly find the dependence of the flux tube oscillation amplitude on the initial amplitude of the sound wave in both cases.

In the linear case we have

$$\xi_\eta \sim \frac{\zeta_\perp}{k_z^2 R^2} \quad (6.24)$$

For a nonlinear estimate of the oscillation amplitude can be obtained from (6.15)

$$\xi_\eta \simeq \left| \frac{\zeta_\perp}{\Delta - \Omega k_z^2 \xi_\eta^2 - i \nu_{\text{rad}}} \right|, \quad (6.25)$$

where ν_{rad} is the small imaginary part of the radiative damping of tube oscillations, and instead of the expansion of Ω in powers of $|\eta - \eta_0|$ we have retained $\Delta = |\omega - \Omega|$. Now with (6.14) we can rewrite (6.25) in the form

$$\xi_\eta \simeq \left| \frac{\zeta_\perp}{\Delta - \Delta \omega_{\text{nl}} - i \nu_{\text{rad}}} \right|. \quad (6.26)$$

In the case of an exact linear resonance we have

$$|\Delta| - |\omega - \Omega| = 0 \quad (6.27)$$

which, in fact, is the basic Cherenkov condition in Landau resonance, $c_s = v_{\text{ph}} \cos \theta$. Indeed, since $\omega = c_s k_z$ and $\Omega = c_{\text{ph}} k_z \cos \theta$, the condition $\omega - \Omega = 0$ gives $c_s = v_{\text{ph}} \cos \theta$.

Now, from (6.26), (6.14), and (3.50, Chap. 3) we find

$$\xi_\eta \simeq \left| \frac{\zeta_\perp \omega}{\omega(k_z \xi_\eta)^2 + i\omega(k_z R)^2} \right|. \quad (6.28)$$

This gives the simple dependence of ξ_η on the initial amplitude of the sound wave

$$\xi_\eta \sim \zeta_\perp \frac{1}{k_z^2 \sqrt{\xi_\eta^4 + R^4}} \quad (6.29)$$

Figure 6.3 contains plots of the function $\xi_\eta(\zeta_\perp)$ for both cases, the linear, dashed line (6.24) and nonlinear, solid line (6.29).

These plots show that, for large amplitudes, ζ_\perp , i.e. in nonlinear regime the scattering cross section considerably decreases with respect to the linear case. Thus the process of the energy transfer to the medium and its efficiency is totally governed by the wave packet parameters, the properties of individual flux tubes, and on their relationship. In other words on the character of oscillations excited in the flux tube ensembles.

Although the most contribution comes from the kink modes, the axisymmetric oscillations may also contribute to the dynamics and energy exchange in an ensemble of magnetic flux tubes (Komm et al. 2000; Tirry 2000; Fujimura and Tsuneta 2009). In the next section we describe the collective phenomena associated with the excitation of the $m = 0$ mode.

6.3 Axisymmetric Oscillation in Flux Tube Ensembles

6.3.1 Equations of Motion

Of three types of axisymmetric modes the most efficient one is a width phase velocity ((3.67), Chap. 3):

$$c_T = \frac{\omega}{k} = \frac{c_{\text{si}} v_A}{\sqrt{c_{\text{si}}^2 + v_A^2}} \quad (6.30)$$

The fact that the total pressure in the sausage oscillations remains unperturbed, $\delta P = \delta p + B\delta B/(4\pi) = 0$, allows us to write down the r -component of the displacement vector as

$$\bar{\xi}_r = \xi_0 \frac{r}{R} \quad (6.31)$$

Note that expression (6.31) is, in fact, a solution of the linearized MHD equations for $m = 0$, namely, the first term in the expansion of the resulting Bessel function.

In terms of displacement vector the linearized MHD equations for perturbations of the form $\exp(-i\omega t + im\phi + ikz)$ with $m = 0$ then are

$$\begin{aligned} -\rho_i \omega^2 \xi_z &= -ik_z \delta p \\ b_r &= ik_z \xi_r B_0, \quad b_z = -B_0 \frac{1}{r} \frac{\partial}{\partial r} r \xi_r \\ \delta \rho + \rho_i \frac{1}{r} \frac{\partial}{\partial r} r \xi_r + ik_z \xi_z & \\ \delta p_i &= c_{si}^2 \delta \rho \end{aligned} \quad (6.32)$$

From this set and expression (6.31) for ξ_r we can find the total pressure perturbation

$$\delta P = -2\rho_i \frac{\xi_0}{R} \left(\frac{2\rho_i c_{si}^2}{1 - c_{si}^2 k_z^2 / \omega^2} + v_A^2 \right) \quad (6.33)$$

Each flux tube that performs such oscillations pushes the surrounding plasma with a force proportional to δP . The boundary condition

$$\delta P = -\delta p \quad (6.34)$$

gives a connection between the response of the external bulk plasma and the volume force with which the ensemble of flux tubes act on the plasma.

Let us find this connection. First of all, note that (6.34) gives the dependence of the flux tube displacement on the external pressure. Indeed, substituting (6.33) into (6.34) we have

$$2\rho_i \frac{\xi_0}{R} \left(\frac{c_{si}^2}{1 - c_{si}^2 k_z^2 / \omega^2} + v_A^2 \right) = \delta p_e, \quad (6.35)$$

which gives for ξ_0 the following expression

$$\xi_0 = R \frac{\delta p_e}{\rho_i v_A^2} \frac{\omega^2 - k_z^2 c_{si}^2}{\omega^2 - k_z^2 c_T^2} \frac{c_T^2}{c_{si}^2} \quad (6.36)$$

Now we have to write the equation describing the propagation of sound waves in the medium containing the ensemble of random flux tubes. We assume that outside the flux tubes plasma is unmagnetized. Then the continuity equations become as

$$\rho_e \omega^2 \xi = -ik \delta p \quad (6.37)$$

$$\delta p_e = c_{si}^2 \delta \rho_e \quad (6.38)$$

and, instead of $\delta\rho_e = -\rho_e \operatorname{div}\xi$, we have

$$\delta\rho_e = -\rho_e \operatorname{div}\xi + \rho_e \frac{\langle \delta V \rangle}{L^3}, \quad (6.39)$$

where V is the volume occupied by flux tubes within the large volume L^3 , such that $V \ll L^3$, i.e. the flux tubes form a rarefied ensemble with small filling factor, $\alpha \ll 1$.

The presence of the second term on the right-hand side of (6.39) is very important and its meaning can be easily understood: this is the natural contribution of the expansion and compression of the oscillating flux tubes to the density perturbation of the surrounding plasma.

For flux tubes that are collinear but random in their other parameters the volume V can be written as $V = L \sum_j \pi R_j^2$, and for its perturbation we have

$$\delta V = 2v \sum_j \pi R_j \delta R_j, \quad (6.40)$$

It is obvious that

$$\delta R_j = \xi_{0j} \quad (6.41)$$

where the displacement ξ_{0j} of the individual flux tube's boundary is defined by (6.36). Thus, we have

$$\delta R_j = \xi_{0j} = R_j \frac{\delta p_{ej}}{2\rho_i v_{Aj}^2} \frac{\omega^2 - k_z^2 c_{sj}^2 c_{Tj}^2}{\omega^2 - k_z^2 c_{Tj}^2 c_{sj}^2} \quad (6.42)$$

When considering kink oscillations of flux tubes we neglected the plasma pressure inside the flux tubes. This assumption does not affect the phenomenological results. For sausage oscillations, however, we cannot neglect p_i , and unlike the previous case, the distribution function now contains one more parameter.

6.3.2 Dispersion Relation: Resonance and Frequency Shift

Let us introduce a broad distribution function of flux tubes $f(\mathcal{E})$ over the set \mathcal{E} of all their parameters, radius R , gas-kinetic pressure inside, p_i , and outside flux tube, p_e , density ratio, $\eta = \rho_i/\rho_e$, and magnetic field B . Normalization of the distribution function gives the magnetic filling factor of the medium:

$$\int f(\mathcal{E}) d\mathcal{E} dR = \alpha \quad (6.43)$$

where $d\mathcal{E} = d\eta dp_i dp_e dB$, and $\alpha \ll 1$.

With the help of the distribution function we can find the average of the perturbed value $\langle \delta V \rangle$ in (6.39), which allows one to find the volume force with which oscillating flux tubes act on the medium. To do this, we use first the traditional procedure and suppose that we have large number $N \gg 1$ of flux tubes occupying the volume V . The volume dV occupied by flux tubes whose parameters are in the intervals $\mathcal{E} + d\mathcal{E}$, $R + dR$ in a total volume L^3 is

$$dV = L^3 f(\mathcal{E}) d\mathcal{E} dR \quad (6.44)$$

The corresponding number of flux tubes in a volume L^3 then

$$dN = \frac{L^3}{\pi R^2} f(\mathcal{E}) d\mathcal{E} \quad (6.45)$$

The contribution of dN flux tubes in the perturbation δV of the volume (6.40) equals

$$\frac{d\delta V}{L^3} = \frac{2}{L^2} \pi R \delta R dN \quad (6.46)$$

Integrating this expression and, taking into account (6.45), we find

$$\frac{\delta V}{L^3} = 2 \int \frac{\delta R(\mathcal{E})}{R(\mathcal{E})} f(\mathcal{E}) d\mathcal{E}. \quad (6.47)$$

Substituting (6.42) for δR into (6.47), we obtain the perturbed volume averaged over the flux tube ensemble:

$$\frac{\delta V}{L^3} = \delta p_e \int \frac{1}{\rho_i v_A^2} \frac{\omega^2 - k_z^2 c_{si}^2}{\omega^2 - k_z^2 c_T^2} \frac{c_T^2}{c_{si}^2} f(\mathcal{E}) d\mathcal{E}. \quad (6.48)$$

With this expression (6.39) becomes

$$\delta \rho_e = -\rho_e \operatorname{div} \xi + \frac{\delta p_e}{c_{se}^2} I(\omega, \mathbf{k}), \quad (6.49)$$

where

$$I(\omega, \mathbf{k}) = \gamma p_e \int \frac{1}{\rho_i v_A^2} \frac{\omega^2 - k_z^2 c_{si}^2}{\omega^2 - k_z^2 c_T^2} \frac{c_T^2}{c_{si}^2} f(\mathcal{E}) d\mathcal{E}. \quad (6.50)$$

Equations (6.37), (6.38), (6.49), and (6.50) form a closed set which describes the response of the medium containing a random ensemble of flux tubes to the propagation of sound waves provided by the resonant excitation of sausage oscillations of the flux tubes.

For plane wave propagating in an arbitrary direction (6.37) and (6.49) give the straightforward dispersion relation:

$$\omega^2[1 - I(\omega, \mathbf{k})] = kc_{se}^2. \quad (6.51)$$

Since $I(\omega, \mathbf{k}) \sim \alpha \ll 1$, we can rewrite (6.51) as

$$\omega = kc_{se}[1 + \frac{1}{2}I(\omega, \mathbf{k})]. \quad (6.52)$$

To perform the integration in (6.50) we have to specify the set of parameters \mathcal{E} . In the whole set of parameters there are only a few independent ones. We will show that by adequate transformation and choice we can reduce their number to two. We will choose as independent variables the sound speed inside flux tube, c_{si} , and sausage oscillation phase velocity, c_T . Let us write the pressure equilibrium for a flux tube in the form

$$\rho_i c_{si}^2 + \frac{\gamma}{2} \rho_i v_A^2 = \rho_e c_{se}^2 \quad (6.53)$$

This gives for the plasma density inside the flux tube

$$\rho_i = \frac{\rho_e c_{se}^2}{c_{si}^2 + (\gamma/2)v_A^2}. \quad (6.54)$$

Using the expression for phase velocity (6.30) and (6.54), we can express $(\rho_i v_A^2)^{-1}$ in terms of c_{si} and c_T as

$$\frac{1}{\rho_i v_A^2} = \frac{1}{c_{se}^2} \left(\frac{c_{si}^2}{c_T^2} - 1 + \frac{\gamma}{2} \right). \quad (6.55)$$

Substituting this expression into the integral (6.50) we have

$$I(\omega, \mathbf{k}) = \gamma p_e \int \frac{1}{c_{se}^2} \left(\frac{c_{si}^2}{c_T^2} - 1 + \frac{\gamma}{2} \right) \frac{\omega^2 - k_z^2 c_{se}^2 c_T^2}{\omega^2 - k_z^2 c_T^2 c_{si}^2} f(\mathcal{E}) d\mathcal{E}. \quad (6.56)$$

Here γp_e cancels with $\rho_e c_{se}^2$, and so the integrand becomes a function of only c_{si} and c_T . Now putting $d\mathcal{E} = d\tilde{c}_{si} d\tilde{c}_T$, where \tilde{c}_{si} and \tilde{c}_T are nondimensionalized in terms of the sound speed outside the flux tubes ($\tilde{c}_T = c_T/c_{se}$ and $\tilde{c}_{si} = c_{si}/c_{se}$), with the use of (6.52) we arrive to the dispersion relation:

$$\omega = kc_{se} \left[1 + \frac{1}{2} \int \left(1 - \frac{2 - \gamma}{2} \frac{c_T^2}{c_{si}^2} \right) \frac{\omega^2 - k_z^2 c_{se}^2 \tilde{c}_{si}^2}{\omega^2 - k_z^2 c_{se}^2 \tilde{c}_T^2} f(\tilde{c}_{si}, \tilde{c}_T) d\tilde{c}_{si} d\tilde{c}_T \right]. \quad (6.57)$$

The real part of the integral gives a linear frequency shift for the acoustic waves interacting with the ensemble of flux tubes, while imaginary part reflects the resonant absorption of sound waves due to the excitation of flux tube oscillations. The corresponding damping rate and frequency shift are

$$\nu = -\text{Im}\omega = -\frac{kc_{se}}{2}\text{Im}I(\omega, \mathbf{k}). \quad (6.58)$$

and

$$\Delta\omega = \frac{kc_{se}}{2}\text{Re}I(\omega, \mathbf{k}). \quad (6.59)$$

For illustrative purposes let us calculate the damping rate. To find $\text{Im}I(\omega, \mathbf{k})$ it is useful to rewrite the integral (6.56) in the form

$$\text{Im}I(\omega, \mathbf{k}) = \text{Im} \int \left(1 - \frac{2 - \gamma}{2} \frac{c_T^2}{c_{si}^2}\right) \frac{[\omega^2 - k_z^2 c_{se}^2 \tilde{c}_{si}^2] f(\tilde{c}_{si}, \tilde{c}_T) d\tilde{c}_{si} d\tilde{c}_T}{(\omega - k_z c_{se} \tilde{c}_T + i0)(\omega + k_z c_{se} \tilde{c}_T)}. \quad (6.60)$$

where we have added a vanishing imaginary part in the resonance denominator in order to choose the correct integration path. Using the standard identity we can write

$$\text{Im} \frac{1}{\omega - k_z c_{se} \tilde{c}_T + i0} = -i\pi \delta(\omega - k_z c_{se} \tilde{c}_T), \quad (6.61)$$

The resonance condition is $\omega = k_z \tilde{c}_T$, has the form of the usual Cherenkov condition. Indeed, as $k = k_z \cos\theta$, and $\tilde{c}_T = c_T/c_{se}$, we have

$$c_{se} = c_T \cos\theta. \quad (6.62)$$

Now, integrating (6.60) over $d\tilde{c}_T$ we obtain

$$\text{Im}I(\omega, \mathbf{k}) = \frac{\pi}{k_z c_{se}} \int_0^\infty \left[1 - \frac{2 - \gamma}{2} \frac{(\omega/k_z c_{se})^2}{\tilde{c}_{si}^2}\right] f(\omega/k_z, \tilde{c}_{si}) d\tilde{c}_{si} \quad (6.63)$$

Bearing in mind that $\omega/(k_z c_{se}) = 1/\cos\theta$, we can rewrite (6.63) in the form

$$\text{Im}I(\omega, \mathbf{k}) = \frac{\pi}{2\cos^2\theta} \int_0^\infty \left[1 - \frac{2 - \gamma}{2} \frac{1}{x^2}\right] (1 - x^2) f(x) dx, \quad (6.64)$$

where we have introduced the variable

$$x = \tilde{c}_{se} \cos\theta \quad (6.65)$$

The integral (6.64) for a given distribution function is equal in order of magnitude to the magnetic filling factor of the medium. Thus, an estimate for the Landau damping rate is

$$\nu \simeq \alpha \frac{\pi k c_{se}}{4 \cos^2 \theta} \quad (6.66)$$

Note that the integrand contains a product of two terms $(1 - x^2)$ and $[1 - (2 - \gamma)/2x^2]$, which for a proper sign of the damping rate have to be positive. Since always $(1 - x^2) > 0$ (because $\tilde{c}_{si} = c_{si}/c_{se} < 1$, from (6.53)), we have to satisfy also the condition

$$\left(1 - \frac{2 - \gamma}{2} \frac{1}{x^2}\right) > 0 \quad (6.67)$$

which is automatically satisfied since $1/x^2 < 2/(2 - \gamma)$. Using the definition of x , and the resonance condition (6.62), we have

$$c_T^2 < \frac{2}{2 - \gamma} c_{si}^2, \quad (6.68)$$

which also always holds ($c_T < c_{si}$ and $2/(2 - \gamma) > 1$).

In the same way one can find the frequency shift (6.59). Given that $I(\omega, \mathbf{k}) \sim \alpha$, it is obvious that

$$\Delta\omega \simeq \alpha \frac{k c_{se}}{2} \quad (6.69)$$

Thus, under the resonance condition (6.62), the flux tubes absorb the energy of sound waves which remains in the form of natural oscillations of the flux tubes until it turns into one or the other form of energy depending on the particular dissipation mechanism.

The first effect which turns on is the radiative damping of sausage oscillations. The corresponding damping rate is (cf. (3.101), Chap. 3):

$$\nu_{\text{rad}}^{m=0} = \frac{\pi \omega}{2} \frac{k^2 R^2}{2} \frac{c_{si}^6}{c_{se}^2 (c_{ci}^2 + v_A^2)^2} \quad (6.70)$$

In this case the energy transfer scenario can be described as follows. If the Landau damping rate determined by (6.66),

$$\nu_L \equiv \nu > \nu_{\text{rad}}^{m=0}, \quad (6.71)$$

the resonant flux tubes absorb the energy of the sound wave in a time $t_L = \nu_L^{-1}$, and accumulate it during a time ν_{rad}^{-1} , after which the oscillating flux tubes radiate

secondary acoustic or MHD waves. In the case opposite to (6.71) when

$$\nu_L \equiv \nu < \nu_{\text{rad}}^{m=0}, \quad (6.72)$$

the energy of the incident acoustic waves goes directly to the energy of secondary waves, that is, a direct resonance scattering of sound waves takes place.

6.4 The Interaction of Unsteady Wave Packets with an Ensemble of Flux Tubes

In this section we consider the interaction of an unsteady wave packets of acoustic waves with plasma containing random ensembles of magnetic flux tubes. We focus mainly on the physical mechanisms of energy transfer to the plasma. We shall see, for example, that the propagation of an acoustic wave packets in randomly magnetized solar atmosphere is accompanied by clear morphological effects which include the spreading of the energy absorption region over scales much larger than the size of the initial wave packet. From observational point of view this is one of the ordinary events observed in chromosphere and corona above the quiet sun regions (see Fig. 6.1).

The regions of an efficient energy input and their localization depend on the distribution of magnetic flux tubes in space and over their physical parameters, including their noncollinearity, which plays important role here. The appearance of clouds of energy above the rarefied ensembles of flux tubes is determined by the fact that the solar atmosphere is *randomly* magnetized, and magnetic flux tubes covering the solar surface are essentially nonidentical.

We start with a brief summary of the acoustic wave propagation through the random ensembles of magnetic flux tubes. As was shown, the interaction of an acoustic wave with an ensemble of flux tubes results in the excitation of oscillations propagating along those *particular* flux tubes for which the Cherenkov resonance condition is satisfied:

$$\omega = (\mathbf{k} \cdot \mathbf{n})v_{\text{ph}} \quad (6.73)$$

where v_{ph} is the phase speed either of a kink mode ($m = \pm 1$) or an axisymmetric mode ($m = 0$). It is important that v_{ph} carries the required information on flux tube parameters and completely determines its individuality.

We shall operate again with a broad distribution function over flux tube parameters with the mean width $\Delta\eta \gg \alpha$, where α is the total fraction of the volume occupied by flux tubes in given area (see Fig. 3.2, Chap. 3). At the same time, it is only natural that the interval $\delta\eta$ of the parameters of those tubes that are close to resonance with a particular sound wave is small:

$$\delta\eta \simeq \alpha \ll \Delta\eta \quad (6.74)$$

The width of the interval of phase velocities of excited flux tube oscillations is $\delta v_{\text{ph}} \simeq \text{Im}\omega/k \simeq \alpha\omega/k$, so that

$$\delta v_{\text{ph}}/v_{\text{ph}} \simeq \alpha \quad (6.75)$$

The Landau damping rates due to the excitation of kink and sausage modes are, respectively,

$$v^{m=\pm 1} = g(\eta_0)\pi k c_{\text{se}} \sin^2\theta, \quad \eta_0 = \frac{2\cos^2\theta}{\gamma} - 1, \quad (6.76)$$

and

$$v^{m=0} \simeq \alpha \frac{\pi k c_{\text{se}}}{4\cos^2\theta} \quad (6.77)$$

Hereafter we will denote the damping rates (6.76) and (6.77) by ν_L , remembering that a Landau resonance occurs for both kinds of modes; which mode should be considered in a particular case is determined by the Cherenkov condition (6.73).

Once excited the flux tube oscillations are subject to radiative damping with the following damping rates:

$$v_{\text{rad}}^{m=\pm 1} = \frac{\pi\omega}{1+\gamma} \left(\frac{k_z R}{2}\right)^2 \left[\frac{2}{\gamma(1+\gamma)} - 1 \right] \quad (6.78)$$

and

$$v_{\text{rad}}^{m=0} = \frac{\pi\omega}{2} \frac{(kR)^2}{2} \frac{c_{\text{si}}^6}{c_{\text{se}}^2 (c_{\text{si}}^2 + v_A^2)^2} \quad (6.79)$$

For convenience let us overview the major steps in the process of the interaction of a sound wave with the magnetic flux tubes.

Under the Cherenkov condition (6.73) the resonant flux tubes absorb the energy of the sound wave in a time

$$\tau_L = \nu_L^{-1} \quad (6.80)$$

Excited oscillations then propagate along the flux tubes (Fig. 6.4). In a time

$$\tau_{\text{rad}} = v_{\text{rad}}^{-1} \quad (6.81)$$

the absorbed energy is re-radiated as secondary acoustic or MHD waves. The time for radiation of secondary waves is estimated as

$$\tau_{\text{rad}} \simeq \frac{1}{\omega(kR)^2}, \quad (6.82)$$

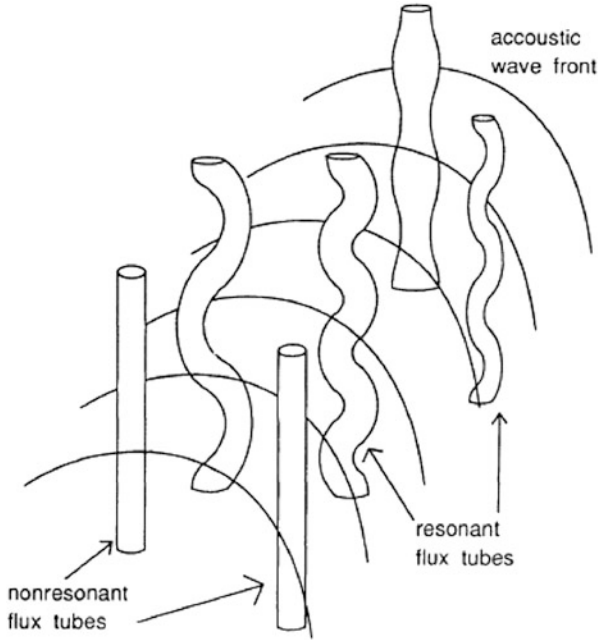


Fig. 6.4 Propagation of an acoustic wave through an ensemble of flux tubes, some of which are nonresonant, while others are resonant with respect to kink or sausage modes

For those regions of the solar atmosphere where the magnetic filling factor, α , is small, i.e. $R \ll l \ll k^{-1}$, expression (6.82) is much larger than the Landau damping time:

$$\tau_{\text{rad}} \gg \tau_L \quad (6.83)$$

Thus the energy of the incident acoustic wave remains for a long time in the form of flux tube oscillation energy.

From expression (6.82) it is obvious that the different flux tubes radiate secondary waves over different times and at different heights: thicker flux tubes, for example, radiate sooner than the thinner ones; and, of course, the radiated waves have random phases

$$\Delta\omega \simeq \nu_L \quad (6.84)$$

This process is illustrated in Fig. 6.5. These phenomena manifest themselves in clear morphological effects, namely in the appearance of clouds of energy overlying the rarefied ensembles of flux tubes. In other words, the energy absorption region spreads over the area that is much larger than the size of the initial wave packet. The amount of the energy input and its location determined by physical parameters of a system will be discussed in the next section.

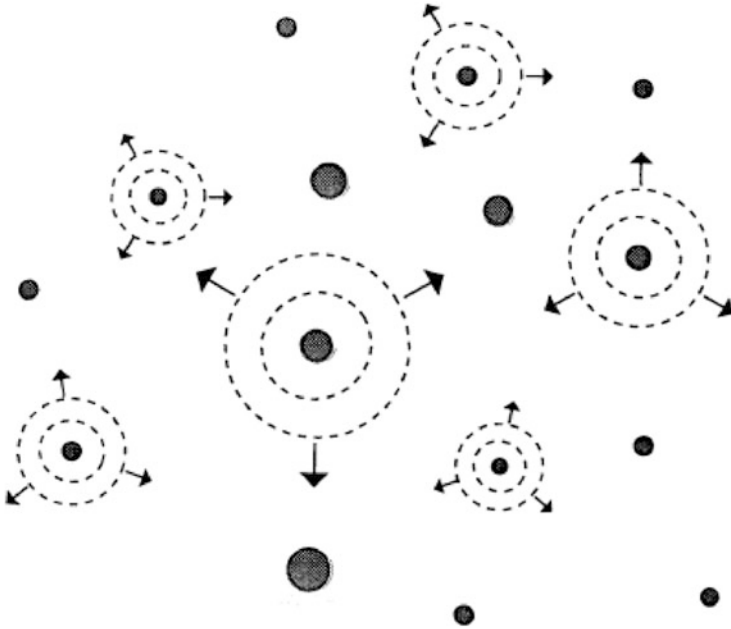


Fig. 6.5 Radiation of secondary acoustic or MHD waves by resonant flux tubes. Different flux tubes radiate secondary waves in different times and at different heights

6.5 Spreading of the Energy Absorption Region: “Clouds of Energy”

The processes described above by (6.78)–(6.83) and illustrated in Figs. 6.4 and 6.5 represent the initial stage of the interaction between acoustic wave-trains and ensembles of flux tubes. The process may continue farther due to the fact that the secondary acoustic or MHD waves are also subject to absorption or scattering by the randomly magnetized medium.

Specifically, the secondary waves are again reabsorbed after a length scale L_L which is of the order of c_{se}/ν_L , or

$$L_L = \frac{c_{se}}{\nu_L} \simeq \frac{\lambda}{\alpha}, \quad (6.85)$$

This process cascades farther until a reradiated waves get finally absorbed due to the action of some dissipative effects. In other words, process of the resonant absorption and re-radiation of the waves proceeds until final extinction of the wave energy. The duration and character of these processes depend, again, on the parameters of the acoustic wave packets and the properties flux tube ensembles.

To visualize clearly these effects let us start with the following criteria:

$$\nu_L \gg \nu_{\text{rad}} \gg \nu_{\text{diss}}, \quad (6.86)$$

where ν_{diss} is a damping rate due to the usual dissipative mechanisms, thermal conductivity, viscosity, Ohmic losses. These conditions are appropriate for the solar atmosphere, but the analysis can be reproduced with minor changes for other relationships between the acting damping rates.

Let us introduce the damping lengths corresponding to Landau damping, L_L , radiation, L_{rad} and dissipative processes L_{diss} :

$$L_L = \frac{c_{\text{se}}}{\nu_L}, \quad L_{\text{rad}} = \frac{v_{\text{ph}}}{\nu_{\text{rad}}}, \quad L_{\text{diss}} = \frac{v_{\text{ph}}}{\nu_{\text{diss}}}, \quad (6.87)$$

In accordance with criteria (6.86) we have

$$L_L \ll L_{\text{rad}} \ll L_{\text{diss}}. \quad (6.88)$$

Consider two limiting cases:

1. The case of a large wave packet, whose size D is larger than the Landau damping length L_L

$$D \gg L_L, \quad (6.89)$$

2. The case of a short wave packet when D is much smaller than L_L

$$D \ll L_L, \quad (6.90)$$

At the same time for both cases the following inequality holds with a good margin:

$$D \gg \lambda \gg d, \quad (6.91)$$

where d , as earlier, is the mean distance between flux tubes.

6.5.1 Large Wave Packets

Under the condition (6.89) a wave packet interacting with an ensemble of flux tubes is damped away without a considerable displacement: since the Landau damping length is much less than the size of the wave packet, all the resonant flux tubes are excited in the initial area of the wave packet. In Fig. 6.6 a schematic of a large wave packet which covers the space containing the ensemble of widely spaced flux tubes is shown. At the initial moment of time $t = 0$ flux tubes are not excited.

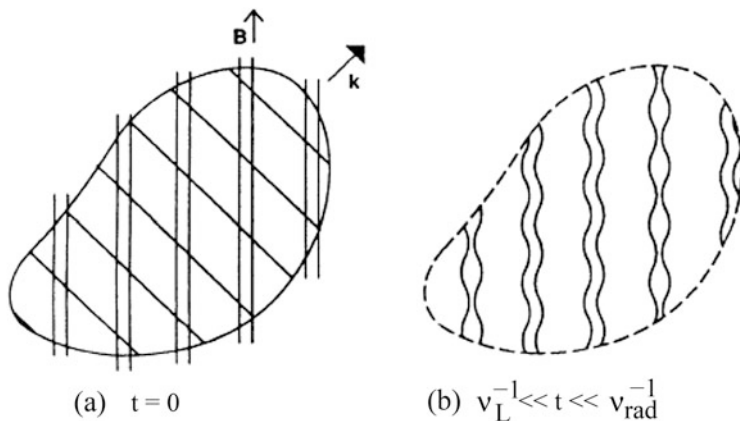


Fig. 6.6 Propagation of a large wave packet through an ensemble of flux tubes: (a) Initial location of a wave packet with no flux tubes yet excited; (b) At an intermediate time, $v_L^{-1} \ll t \ll v_{\text{rad}}^{-1}$, the wave packet has damped away, but the energy remains in the form of natural oscillations of flux tubes which have not yet radiated secondary waves. \mathbf{k} is the direction of the propagation of the wave packet

At a time which is larger than the Landau damping time but less than the time of the radiation of secondary waves

$$\frac{L_L}{c_{\text{se}}} \ll t \ll \frac{L_{\text{rad}}}{v_{\text{ph}}}, \tag{6.92}$$

the wave packet is already damped away, but the excited flux tubes have not yet radiated secondary waves. In other words, at the time t such that

$$v_L^{-1} \ll t \ll v_{\text{rad}}^{-1}, \tag{6.93}$$

the wave packet is damped away, but its energy remains in the form of natural oscillations of resonant flux tubes *imitating* the initial area of the wave packet. This stage is shown in Fig. 6.6b.

The excited perturbations, kink or sausage modes, propagate along the flux tubes carrying the accumulated energy of wave packet to higher layers of the atmosphere with a speed whose projection on the direction of the wave packet propagation is approximately c_{se} .

After a time

$$t \simeq v_{\text{rad}}^{-1}, \tag{6.94}$$

secondary waves are radiated. Since v_{rad} depends on the radius of the flux tube ((6.78) and (6.79)), different flux tubes radiate in different times. Respectively, the height of the energy input is different for different flux tubes. This fact leads to a

significant spreading of the region where the energy of the initial wave packet is transferred to the medium, so that the region of energy input becomes larger than the initial size of the wave packet. Note that noncollinearity of flux tubes enhances the spreading of energy input region. It is also important that the location of energy input, or in other words, the location of reappearance of the wave packet image differs from the expected position of the wave packet in the absence of random flux tubes.

The sketch of the process is shown in Fig. 6.7. In the absence of flux tubes the wave packet would travel along its initial direction spreading out diffusively. On the other hand, when passing through the random ensembles of flux tubes, the wave packet loses in fact its identity and reappears as a product of flux tube oscillations in different location and of different sizes. The most typical coronal emission above the rarefied ensembles of flux tubes forming quiet sun regions shown in Fig. 6.1 is in a striking agreement with the process described above.

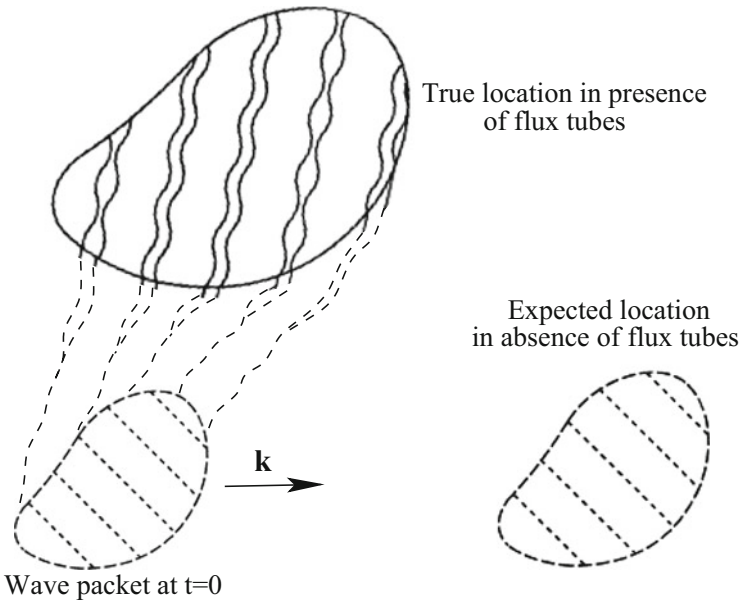


Fig. 6.7 Initial location and size of a wave packet shown at $t = 0$. In a time $t = v_{\text{rad}}^{-1}$ the final location of wave packet carrying the energy will be observed at the expected location if there are magnetic flux tubes, and on a true location when passing through the ensemble of flux tubes

6.5.2 Short Wave Packets: Energy Absorption and Release

For a short wave packet, with size $D \ll L_L$, we have

$$D \ll \frac{c_{se}}{\alpha\omega} \simeq \frac{\lambda}{\alpha} \quad (6.95)$$

where we have taken into account that $L_L \simeq c_{se}/\nu_L$ (see Eq. (6.87)), and thus

$$\nu_L \simeq \alpha\omega. \quad (6.96)$$

The condition (6.95) means that, during the traveling of the wave packet through the ensemble of flux tubes, both excited and non-excited flux tubes exist simultaneously.

Indeed, the wave packet traverses any particular flux tube within a time

$$T \simeq D/c_{se} \ll \nu_L^{-1} \quad (6.97)$$

which is short compared to Landau damping time. Thus the wave packet excites resonant flux tubes on its way and propagates further, leaving a trace of excited flux tubes, which in turn radiate secondary waves. In principle, the first excited flux tubes can already radiate their energy before the wave packet is finally damped away. In this case secondary acoustic waves coexist with the initial wave packet.

The particular scenario of wave packet dynamics and the final region of the energy input depend on the specifics of the flux tube distribution. In other words, the shape of the “new image” of the wave packet is determined by the memory of the system.

Now we proceed to quantitative analysis. Conditions (6.97) allow to write the pressure perturbation, and other perturbed quantities, through the slowly varying envelope:

$$\delta p_e = \frac{1}{2} \delta p_0 F \left(\mathbf{r} - \frac{\mathbf{k}}{k} c_{se} t \right) e^{-i\omega t + i\mathbf{k}\mathbf{r}} + \text{c.c.} \quad (6.98)$$

where $\omega = c_{se}k$, and $F(\mathbf{r} - (\mathbf{k}/kc_{se})t)$ is the slowly varying envelope. No damping is taken into account in this expression because of the condition (6.97). For definiteness, we consider δp_0 and F as real functions, i.e. $\delta p_0 = \delta p_0^*$ and $F = F^*$.

Let us first consider the response of a certain flux tube to the action of the external perturbation in the form (6.98). Consider as an example the kink oscillations of flux tube and recall the equation for the displacement vector ξ of a flux tube ((3.8), Chap. 3):

$$\frac{\partial^2 \xi_\eta}{\partial t^2} - v_{\text{ph}}^2 \frac{\partial^2 \xi_\eta}{\partial \zeta^2} = \frac{2}{1 + \eta} \frac{\partial \mathbf{v}_\perp}{\partial t} \quad (6.99)$$

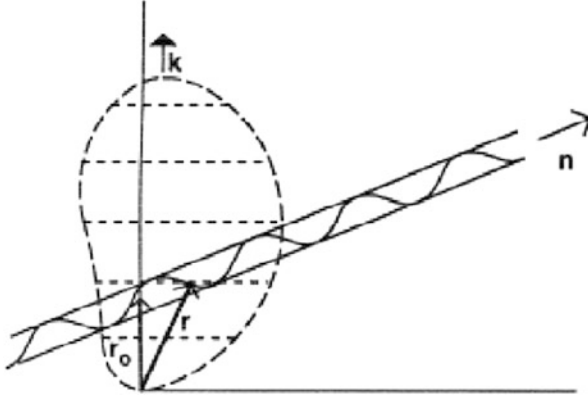


Fig. 6.8 A wave packet moving in the direction \mathbf{k} . While \mathbf{n} is the direction of a flux tube and \mathbf{r} is the coordinate of a point on the flux tube surface

where \mathbf{v}_\perp is the normal component of the macroscopic velocity of plasma outside the flux tubes, and ζ is the coordinate along the flux tubes.

Without the external motions, when $\mathbf{v}_\perp = 0$, (6.99) describes the $m = \pm 1$ eigenoscillations of a flux tube, whereas the right-hand side of (6.99) with nonzero $\mathbf{v}_\perp \neq 0$ represents the interaction force between flux tube and its environment.

Consider the wave packet traveling in the \mathbf{k} direction as sketched in Fig. 6.8, and let \mathbf{n} be a unit vector along the flux tube. The coordinate of any point at the flux tube surface can be written as $\mathbf{r} = \mathbf{r}_0 + \mathbf{n}\zeta$.

The absolute value of the macroscopic plasma velocity outside the flux tube, \mathbf{v} , can be written as $\mathbf{v} = (\mathbf{k}/k)v$, so that its component, normal to the vector \mathbf{n} , is

$$\mathbf{v}_\perp = v \frac{\mathbf{k} - \mathbf{n}(\mathbf{k} \cdot \mathbf{n})}{k} \quad (6.100)$$

In the external region, which we assume to be magnetic free, we have

$$-i\omega\rho_e v = -ik\delta p_e \quad (6.101)$$

which gives $v = k\delta p_e/\omega\rho_e$ or $v = \delta p_e/(c_{se}\rho_e)$, so that

$$\frac{\partial v}{\partial t} = \frac{1}{c_{se}\rho_e} \frac{\partial \delta p_e}{\partial t} \quad (6.102)$$

For the slowly varying envelope, given by (6.98), we therefore have

$$\frac{\partial v}{\partial t} \simeq -i\omega \frac{\delta p_0}{c_{se}\rho_e} F \left(\mathbf{r} - \frac{\mathbf{k}}{k} c_{se} t \right) e^{-i\omega t + i\mathbf{k}\mathbf{r}} + \text{c.c.} \quad (6.103)$$

and the force on the right-hand side of (6.99) can be written as

$$\frac{\partial \mathbf{v}_\perp}{\partial t} = -\frac{\mathbf{k} - \mathbf{n}(\mathbf{k} \cdot \mathbf{n})}{k} \left[\omega \frac{\delta p_0}{c_{se} \rho_e} F \left(\mathbf{r} - \frac{\mathbf{k}}{k} c_{se} t \right) e^{-i\omega t + i\mathbf{k}\mathbf{r}} + \text{c.c.} \right] \quad (6.104)$$

Introducing the notations

$$\tilde{v} \equiv \frac{2\delta p_0}{(1 + \eta)c_{se}\rho_e}, \quad \tilde{\xi}_\perp = \tilde{\xi} \frac{\mathbf{k} - \mathbf{n}(\mathbf{k} \cdot \mathbf{n})}{k}, \quad (6.105)$$

and using expression (6.104) for the interaction force we have instead of (6.99):

$$\frac{\partial^2 \tilde{\xi}_\eta}{\partial t^2} - v_{ph}^2 \frac{\partial^2 \tilde{\xi}_\eta}{\partial \zeta^2} = -i\omega \tilde{v} F \left(\mathbf{r} - \frac{\mathbf{k}}{k} c_{se} t \right) e^{-i\omega t + i\mathbf{k}\mathbf{r}} + \text{c.c.} \quad (6.106)$$

Since F is slowly varying function, we seek the solution of (6.106) in the form

$$\tilde{\xi} = \frac{1}{2} \xi_0(\zeta, t) e^{-i\omega t + ik_\parallel \zeta} + \text{c.c.} \quad (6.107)$$

where $\xi_0(\zeta, t)$ is also slowly varying function, and $k_\parallel = (\mathbf{k} \cdot \mathbf{n}) \equiv k \cos \theta$.

Taking second derivatives of function (6.107) over time and coordinate, substituting them into (6.106) we obtain

$$\frac{1}{2} (\omega^2 - k_\parallel^2 v_{ph}^2) \xi_0(\zeta, t) + i\omega \xi_{0t} + ik_\parallel v_{ph}^2 \xi_{0\zeta} = i\omega \tilde{v} F. \quad (6.108)$$

For flux tubes that are close to resonance the following conditions are fulfilled:

$$|\omega - k_\parallel v_{ph}| \ll \omega \quad (6.109)$$

For exact resonance we have the Cherenkov condition: $\omega = k_\parallel v_{ph}$. Denote the deviation from exact resonance by

$$\delta\omega = |\omega - k_\parallel v_{ph}| \quad (6.110)$$

Then the coefficient of the first term on the left of (6.108) can be written

$$\frac{1}{2} (\omega^2 - k_\parallel^2 v_{ph}^2) = \frac{1}{2} (\omega + k_\parallel v_{ph})(\omega - k_\parallel v_{ph}) \simeq \omega \delta\omega \quad (6.111)$$

With this we can rewrite (6.108) in the form

$$\xi_{0t} + v_{ph} \xi_{0\zeta} - i\delta\omega \xi_0 = \tilde{v} F(\zeta, t), \quad (6.112)$$

and for the complex conjugate

$$\xi_{0t}^* + v_{\text{ph}}\xi_{0\zeta}^* + i\delta\omega\xi_0^* = \tilde{v}F(\zeta, t), \quad (6.113)$$

Multiplying (6.112) by ξ_{0t}^* , (6.113) by ξ_{0t} , and integrating the sum we get the energy density of flux tube oscillations:

$$\frac{\partial}{\partial t} \int_{-\infty}^{\infty} |\xi_0|^2 d\zeta' = \tilde{v} \int_{-\infty}^{\infty} F(\zeta', t)[\xi_0(\zeta', t) + \xi_0^*(\zeta', t)] d\zeta' \quad (6.114)$$

The next important step is to average expression (6.114) over the large volume containing many tubes. This way we can find the energy input in this volume provided by the interaction of the acoustic wave packet with the ensemble of flux tubes.

Let us first find the energy density of a single magnetic flux tube. The energy of a flux tube per unit length is

$$\langle W \rangle = \left\langle \pi R^2 (\rho_i + \rho_e) \sin^2 \theta \left(\frac{\partial \tilde{\xi}_{\perp}}{\partial t} \right)^2 \right\rangle \quad (6.115)$$

Taking into account (6.107) we have for the averaged energy per unit length:

$$\langle W \rangle = \pi R^2 (\rho_i + \rho_e) \sin^2 \theta \omega^2 |\xi_0|^2. \quad (6.116)$$

The total energy of the flux tube is then

$$W = \int_{-\infty}^{\infty} \langle W \rangle d\zeta' = \pi R^2 (\rho_i + \rho_e) \sin^2 \theta \omega^2 \int_{-\infty}^{\infty} |\xi_0|^2 d\zeta'. \quad (6.117)$$

Taking the time derivative of (6.117) and comparing it with (6.114) we get an expression for the temporal variation of the flux tube energy:

$$\frac{\partial W}{\partial t} = \tilde{v} \pi \omega^2 R^2 (\rho_i + \rho_e) \sin^2 \theta \int_{-\infty}^{\infty} F(\zeta', t) \text{Re} \xi_0(\zeta', t) d\zeta'. \quad (6.118)$$

where we took into account that $\xi_0 + \xi_0^* = 2\text{Re} \xi_0$; $\xi_0(\zeta, t)$ is governed by (6.112).

To solve the problem qualitatively we have to find an explicit expression for $\xi_0(\zeta, t)$, that is, to solve (6.106). To do so we introduce new variables

$$s \equiv \zeta - v_{\text{ph}} t, \quad x \equiv \zeta \quad (6.119)$$

such that

$$\frac{\partial}{\partial t} \equiv -v_{\text{ph}} \frac{\partial}{\partial s}, \quad \frac{\partial}{\partial \zeta} \equiv \frac{\partial}{\partial s} + \frac{\partial}{\partial x}. \quad (6.120)$$

In these variables (6.112) becomes

$$-v_{\text{ph}} \frac{\partial \xi_0}{\partial s} + v_{\text{ph}} \left(\frac{\partial \xi_0}{\partial s} + \frac{\partial \xi_0}{\partial x} \right) - i \delta \omega \xi_0 = \tilde{v} F \left(x, \frac{x-s}{v_{\text{ph}}} \right) \quad (6.121)$$

or, finally,

$$\frac{\partial \xi_0}{\partial s} - i \delta \omega \xi_0 = \frac{\tilde{v}}{v_{\text{ph}}} F \left(x, \frac{x-s}{v_{\text{ph}}} \right). \quad (6.122)$$

The solution of this equation is of the form

$$\xi_0 = \frac{\tilde{v}}{v_{\text{ph}}} \exp \left(i \frac{\delta \omega}{v_{\text{ph}}} x \right) \int_{-\infty}^x \exp \left(-i \frac{\delta \omega}{v_{\text{ph}}} x' \right) F \left(x', \frac{x'-s}{v_{\text{ph}}} \right) dx'. \quad (6.123)$$

In the original variables (see (6.119)) this solution is

$$\xi_0(\zeta, t) = \frac{\tilde{v}}{v_{\text{ph}}} \int_{-\infty}^{\zeta} \exp \left[-i \frac{\delta \omega}{v_{\text{ph}}} (\zeta - \zeta') \right] F \left(\zeta', \frac{\zeta' - \zeta}{v_{\text{ph}}} + t \right) d\zeta', \quad (6.124)$$

and for temporal variation of the energy of flux tube oscillations (6.118) we have

$$\frac{\partial W}{\partial t} = \tilde{v} \pi \omega^2 R^2 (\rho_i + \rho_e) \sin^2 \theta \text{Re} \int_{-\infty}^{\infty} F(\zeta, t) d\zeta \cdot \xi_0(\zeta, t) \quad (6.125)$$

where $\xi_0(\zeta, t)$ is given by (6.124).

Averaging this expression over the large volume containing many flux tubes we can find the energy deposition to the medium from the ensemble of flux tubes interacting with the acoustic wave packets. This will be done in the next section.

6.6 The Energy Transfer from Unsteady Wave Packets to the Medium

Let us consider a large volume with a cross section of dimensions \mathcal{L} by \mathcal{L} , such that $d \ll \mathcal{L} \ll \lambda$, where d is, as earlier, a mean distance between the flux tubes.

The energy deposition into the volume with the cross section $\mathcal{L} \times \mathcal{L}$ has the form

$$\begin{aligned} \frac{1}{\mathcal{L}^2} \frac{\partial W_{\mathcal{L}}}{\partial t} &= \text{Re} \frac{\omega^2 \tilde{v}^2}{v_{\text{ph}}} \sin^2 \theta \int_0^{\infty} (\rho_i + \rho_e) g(\eta) d\eta \int_{-\infty}^{\infty} F(\zeta, t) d\zeta \\ &\quad \times \int_{-\infty}^{\zeta} \exp \left[-i \frac{\delta \omega}{v_{\text{ph}}} (\zeta - \zeta') \right] F \left(\zeta', \frac{\zeta' - \zeta}{v_{\text{ph}}} + t \right) d\zeta' \quad (6.126) \end{aligned}$$

As discussed, for a broad distribution function the estimate for the parameter range of resonance is quite small $\delta\eta \simeq \alpha \ll 1$. This condition implies that the main contribution in the expression (6.126) comes from a narrow resonance region of width $\delta\eta$ near the resonance value of $\eta = \eta_0$, ($\eta_0 = 2\cos^2\theta/\gamma - 1$).

The first integral in (6.126) can be written as

$$\int_{\eta}^{\infty} (\rho_i + \rho_e)g(\eta)d(\eta - \eta_0) \quad (6.127)$$

Since the function $g(\eta)$ is strongly peaked near the η_0 , the lower limit in this integral can be replaced by $-\infty$ and $(\rho_i + \rho_e)g(\eta)$ by its value at exact resonance, $[(\rho_i + \rho_e)g(\eta)]_{\eta_0}$. Then the triple integral in (6.126) can be written as

$$I_3 = \int_{-\infty}^{\infty} F(\zeta, t)d\zeta \cdot I_2(\zeta), \quad (6.128)$$

where

$$\begin{aligned} I_2 &= (\rho_i + \rho_e)g(\eta)|_{\eta_0} \quad (6.129) \\ &\times \int_{-\infty}^{\zeta} \int_{-\infty}^{\infty} \exp\left[-i\frac{\delta\omega}{v_{\text{ph}}}(\zeta - \zeta')\right] F\left(\zeta', \frac{\zeta' - \zeta}{v_{\text{ph}}} + t\right) d\zeta' d(\eta - \eta_0) \end{aligned}$$

The real part of (6.129) determines the energy dissipation (6.126) in the medium. After performing the double integration in (6.129) we find

$$\text{Re}I_2(\zeta) = \pi \frac{1}{|(d/d\eta)(\delta\omega/v_{\text{ph}})|_{\eta_0}} (\rho_i + \rho_e)g(\eta)|_{\eta_0} F(\zeta, t). \quad (6.130)$$

The evaluation of this double integral is detailed in the Appendix.

Using now (6.126) and (6.130) we can write the energy deposition into the ensemble of flux tubes from the acoustic wave packet as

$$\frac{\partial W_{\mathcal{L}}}{\partial t} = \frac{2\pi \mathcal{L}^2 \omega^2 v^2 \sin^2\theta}{v_{\text{ph}} |(d/d\eta)(\delta\omega/v_{\text{ph}})|_{\eta_0}} [(\rho_i + \rho_e)g(\eta)]_{\eta_0} \int_{-\infty}^{\infty} F^2(\zeta, t)d\zeta. \quad (6.131)$$

This gives the value of the energy dissipation in a volume with cross section $\mathcal{L} \times \mathcal{L}$ containing the ensemble of flux tubes with distribution function $g(\eta)$.

The energy dissipation per unit volume according to (6.131) will be

$$\frac{\partial W_{\mathcal{L}}}{\partial t} = \frac{2\pi \rho_e \omega^2 \tilde{v}^2 \sin^2\theta}{v_{\text{ph}} |(d/d\eta)(\delta\omega/v_{\text{ph}})|_{\eta_0}} (1 + \eta)g(\eta)|_{\eta_0} F^2(\zeta, t), \quad (6.132)$$

or, after substituting here \tilde{v} from (6.105),

$$\frac{\partial W_{\mathcal{L}}}{\partial t} = \frac{8\pi\omega^2 g(\eta_0)\sin^2\theta}{v_{\text{ph}} |(d/d\eta)(\delta\omega/v_{\text{ph}})|_{\eta_0}(1+\eta_0)} \frac{\delta p_0^2}{\rho_e c_{\text{se}}^2} F^2. \quad (6.133)$$

From this equation we can find the damping rate of the acoustic packet. To do so, we first find the energy density of the acoustic wave packet itself, namely, $W = \rho \overline{v^2}$, where the velocity v is

$$\overline{v^2} = \frac{\overline{\delta p_e^2}}{\rho_e^2 c_{\text{se}}^2} F^2. \quad (6.134)$$

Averaging the expression (6.98) representing the form of the wave packet we obtain

$$\overline{v^2} = \frac{1}{2\rho_e^2 c_{\text{se}}^2} \delta p_0^2 F^2, \quad (6.135)$$

and for the energy density of the acoustic wave packet we have:

$$W_{\text{ac}} = \frac{\delta p_0^2}{2\rho_e c_{\text{se}}^2} F^2. \quad (6.136)$$

Comparing (6.133) and (6.136) one can see that Eq. (6.133) can be written as follows:

$$\frac{\partial W_{\mathcal{L}}}{\partial t} = \frac{16\pi\omega^2 g(\eta_0)}{v_{\text{ph}} |(d/d\eta)(\delta\omega/v_{\text{ph}})|_{\eta_0}} \frac{\sin^2\theta}{1+\eta_0} W_{\text{ac}}, \quad (6.137)$$

which implies the damping rate of

$$\Gamma = \frac{16\pi\omega^2 g(\eta_0)}{v_{\text{ph}} |(d/d\eta)(\delta\omega/v_{\text{ph}})|_{\eta_0}} \frac{\sin^2\theta}{1+\eta_0}. \quad (6.138)$$

Now recall that v_{ph} is the phase velocity of the kink mode in the flux tube, and $\delta\omega$ is determined by (6.110). Then for the derivative in the denominator of (6.138) we have

$$\frac{d}{d\eta} \frac{\delta\omega}{v_{\text{ph}}} = \frac{d}{d\eta} \frac{\omega - k_{\parallel} v_{\text{ph}}}{v_{\text{ph}}} = -\frac{\omega}{v_{\text{ph}}^2} \frac{dv_{\text{ph}}}{d\eta} \quad (6.139)$$

And so

$$v_{\text{ph}} \left| \frac{d}{d\eta} \frac{\delta\omega}{v_{\text{ph}}} \right|_{\eta_0} = \frac{1}{2} \frac{\omega}{1+\eta_0} \quad (6.140)$$

After substituting (6.140) into (6.138) we have for the damping rate

$$\Gamma = 32\pi\omega g(\eta_0) \sin^2\theta. \quad (6.141)$$

Comparing (6.141) with the damping rate of a monochromatic wave (6.76), we see that qualitatively the damping rate of an unsteady wave packet is determined exactly by the same physical parameters, but it is almost an order of magnitude larger than that of a monochromatic wave. It is important to note, however, that the essential difference between these two cases is that the propagation of unsteady wave packet is accompanied by spreading of energy input region and its specific location.

Modern space instruments allow nowadays to observe and measure large-scale disturbances, like, e.g., so-called “EIT” waves (Delaboudiniere et al. 1995; Chen et al. 2005; Gopalswamy et al. 2009; Chen and Wu 2011; Long et al. 2013). Obviously these waves are hardly a local phenomena and are directly connected with the energy absorbed by the ensembles of photospheric flux tubes and transferred in form of various clouds of energy and high frequency waves into the corona.

6.7 Problems

6.1 The waves and wave packets in the vicinity of the solar surface may well be associated with the parametric excitation. Consider a sample problem of one-dimensional oscillator

$$\frac{\partial^2 x}{\partial t^2} + \omega_0^2(1 + \alpha \cos 2\omega t)x = 0 \quad (6.142)$$

with $\alpha \ll 1$ and $|\omega - \omega_0| \ll \omega_0$ (Kadomtsev 1968).

Describe the character of oscillations

- (a) in the region of parametric resonance, and
- (b) under the condition of instability.

6.2 The instability described above for beat waves (Fig. 24.2b) falls into a class of modulation instabilities (Lighthill 1965). This instability plays a major role in the systems of solitons, rogue waves, formation of chaos and other nonlinear phenomena. Find the criterion of instability for a plane wave packet with slowly varying amplitude and phase (Kadomtsev and Karpman 1971).

Appendix

To perform the integration in (6.129) we introduce the function

$$\kappa(\eta) = \frac{\delta\omega}{v_{\text{ph}}} \quad (6.143)$$

and change the variable $\zeta - \zeta' = x$. Then the double integral in (6.129) becomes (we need only its real part):

$$\text{Re } I(\zeta) = \text{Re} \int_0^\infty \int_{-\infty}^\infty d(\eta - \eta_0) e^{i\kappa(\eta)x} F\left(\zeta - x, t - \frac{x}{v_{\text{ph}}}\right) dx. \quad (6.144)$$

Now, the shortest way to integrate (6.144) is to use the definition of the δ -function, namely

$$\delta(x) = \frac{1}{2\pi} \int_{-\infty}^\infty e^{ikx} dk, \quad \delta[f(x)] = \frac{1}{|df/dx|_0} \delta(x). \quad (6.145)$$

Therefore, (6.144) can be written as

$$\text{Re } I(\zeta) = \text{Re} \int_0^\infty 2\pi \frac{1}{|df/dx|_0} \delta(x) F\left(\zeta - x, t - \frac{x}{v_{\text{ph}}}\right) dx. \quad (6.146)$$

which gives immediately

$$\text{Re } I(\zeta) = \frac{\pi}{|df/dx|_0} F(\zeta, t). \quad (6.147)$$

Substituting (6.147) into (6.144) we come to expression (6.130)

$$\text{Re } I_2(\zeta) = (\rho_i + \rho_e) g(\eta)|_{\eta_0} \frac{\pi}{|(d/d\eta)(\delta\omega/v_{\text{ph}})|_{\eta_0}} F(\zeta, t). \quad (6.148)$$

References

- T. Bogdan, E. Zweibel, *Astrophys. J.* **676**, L89 (1987)
 L. Chen, A.A. Hasegawa, *J. Geophys. Res.* **79**, 1033 (1974)
 P.F. Chen, Y. Wu, *Astrophys. J.* **732**, L20 (2011)
 P.F. Chen, C. Fang, K. Shibata, *Astrophys. J.* **622**, 1202 (2005)
 J.P. Delaboudiniere et al., *Sol. Phys.* **162**, 291 (1995)
 D. Fujimura, S. Tsuneta, *Astrophys. J.* **702**, 1443 (2009)
 N. Gopalswamy et al., *Astrophys. J.* **691**, L123 (2009)
 B.B. Kadomtsev, *Sov. Phys. Usp.* **11**, 328 (1968)
 B.B. Kadomtsev, V.I. Karpman, *Sov. Phys. Usp.* **14**, 40 (1971)

- R.W. Komm, R. Howe, F. Hill, *Astrophys. J.* **543**, 472 (2000)
L.D. Landau, *Sov. Phys. JETP* **16**, 574 (1946)
M.J. Lighthill, *J. Inst. Math. Appl.* **1**, 269 (1965)
D.M. Long et al., *Sol. Phys.* **288**, 567 (2013)
M. Lontano, E. Lazzaro, D. Ryutov, *Phys. Scr.* **T84**, 52 (2000)
D.D. Ryutov, M.P. Ryutova, *Sov. Phys. JETP* **43**, 491 (1976)
M.P. Ryutova, E.R. Priest, *Astrophys. J.* **419**, 349 (1993a)
M.P. Ryutova, E.R. Priest, *Astrophys. J.* **419**, 371 (1993b)
A. Timofeev, *Sov. Phys. Usp.* **13**, 632 (1970)
W.J. Tirry, *Astrophys. J.* **528**, 493 (2000)

Chapter 7

Effects of Magnetic Flux Tubes in Helioseismology



Abstract In the previous chapter we studied the response of rarefied ensembles of random magnetic flux tubes to the propagation of acoustic waves and unsteady wave packets. In this chapter we shall study how the properties of acoustic wave packets at the photospheric level, modified by presence of magnetic flux tubes, can be used for diagnostics goals. In particular, we shall study effects of flux tubes on local helioseismology based on the time-distance analysis (Duvall et al., *Nature* 362:430, 1993; Duvall et al., *Nature* 379:235, 1996). We shall see that flux tubes strongly affect the standard methods of time-distance tomography, and allow more realistic inference of physical parameters, including flows, magnetic fields, and their nonuniformities. Besides, one can study the structure of solar atmosphere by spectral features of acoustic waves using an approach in the data analysis called “Raman spectroscopy of p-modes.”

7.1 The Time-Distance Tomography

The time-distance tomography is based on the measurement of travel time of an acoustic wave between any point on the solar surface and a surrounding annulus (Duvall et al. 1993, 1996). An acoustic wave propagating through the near-surface envelope interacts with its random magnetic fields and mass flows and is exposed to the density and temperature perturbations. The alterations in travel time of acoustic waves due to these interactions carry the information on the surface and subsurface structures. In the original approach the travel times were measured by calculating the temporal cross correlation function between the data at some point of given area and the data within an annulus at large distance from the point. For each of chosen annuli the travel times were measured for both forward and backward propagation, i.e. from the central point of the annulus ($\tau^{(+)}$) and back ($\tau^{(-)}$). However, this approach, even though later extended to measurements of travel times in the north-south and east-west directions separately (Duvall et al. 1997) did not allow to detect the presence of magnetic fields.

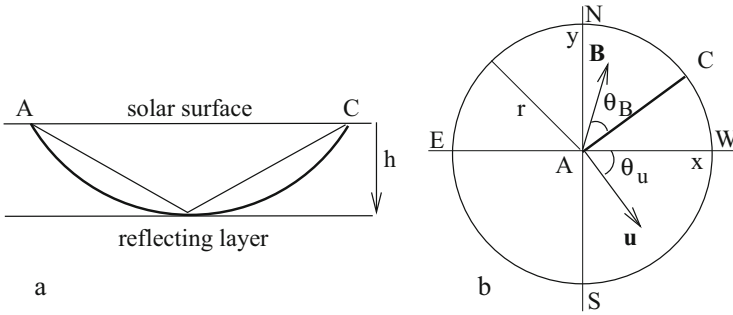


Fig. 7.1 Geometry of the problem: (a) ray trajectory in the model of uniform slab; $AC = r$ (b) annulus on the solar surface; the x -axis is parallel to solar equator, while the y -axis is directed along the local meridian

The situation has changed with development of the procedure based on the angular dependence of travel times. An advantage of such an approach is in its intrinsic invariance with respect to the choice of the coordinate frame and sensitivity to the presence of magnetic elements. The method provides an automatic rule of assigning proper weights to every observational points and its magnetic status.

7.1.1 Key Points of Time-Distance Analysis with Magnetic Fields

Consider a typical geometry of time-distance analysis in local helioseismology, but let the magnetic field be present (Ryutova and Scherrer 1998). Figure 7.1b shows the geometry of the problem: acoustic wave propagating from the point A on the solar surface downward is reflected at the depth of h and propagates back to certain point C on the surface. Flow velocity is denoted by u , its direction is characterized by the angle θ_u ; the magnetic field, B forms the angle θ_B with the axis x . The angle θ is counted, say, from west at the solar surface.

In ray approximation the averaged value of the propagation time can be expressed as

$$\bar{\tau} = \frac{1}{2\pi} \int_0^{2\pi} \tau(\theta) d\theta \quad (7.1)$$

The key point of the approach that reflects the presence of magnetic flux tubes is that in addition to the average (7.1) one must also take $\sin n\theta$ and $\cos n\theta$ transforms

of the propagation time

$$\bar{\tau}_c^{(n)} = \frac{1}{2\pi} \int_0^{2\pi} \tau(\theta) \cos n\theta d\theta \quad (7.2)$$

$$\bar{\tau}_s^{(n)} = \frac{1}{2\pi} \int_0^{2\pi} \tau(\theta) \sin n\theta d\theta \quad (7.3)$$

We will use the approximation of geometrical acoustics and assume that the magnetic effects are small. We will discuss only averages corresponding to the first two harmonics, $n = 1, 2$. It is remarkable that the first harmonics and their various combinations give amazingly rich information when used with the observational data. In particular, the first harmonics alone ($n = 1$) give information on the direction and absolute value of the horizontal flow velocity.

Combinations of the second harmonics ($n = 2$) of the inward ($\tau^{(-)}$) and outward ($\tau^{(+)}$) times give information on the orientation and absolute value of horizontal magnetic fields and the spatial gradients of flow velocity. Namely the sum of forward and backward propagating times $\tau^{(+)} + \tau^{(-)}$ carries information on the magnetic field distribution, while the difference $\tau^{(+)} - \tau^{(-)}$ on the magnitude and orientation of shear flows.

Besides, the method allows to separate the contributions of mass flows from the contribution of the magnetic fields and find the alteration of the travel time provided by flow field and magnetic field independently. One can also single out the horizontal components from vertical components of the magnetic field and mass flows. Higher order harmonics carry information on the finer structures of the medium and require high resolution data.

To illustrate the kind of information that is contained in $\bar{\tau}_{c,s}^{(1,2)}$, first we consider a simple model of acoustic wave propagation: we assume that “unperturbed” plasma parameters (i.e., parameters in the absence of flows and magnetic field) are uniform in the slab of thickness h corresponding to the lower reflection point for the acoustic wave. Then we present the corrections to the propagation time in a vertically stratified atmosphere and show that in this much more general case the alterations in the travel time still manifest the same $\cos n\theta - \sin n\theta$ dependence on the azimuthal angle.

We assume that the wavelength of acoustic waves is small compared to all other spatial scales and use the ray approximation. Typically, near the surface flow velocities, u , and Alfvén speed, v_A are much less than the sound speed, c_s

$$u, v_A \ll c_s, \quad (7.4)$$

Thus effects of flow and magnetic field enter into the propagation time $\tau(\theta)$ as small additions proportional to u/c_s , and v_A^2/c_s^2 , respectively. Since the conditions (7.4) are believed to be held for subsurface layers, one can consider the effects of flow and magnetic field separately. We will follow this line of reasoning throughout the chapter.

7.1.2 The Travel Times

The travel time of the wave propagating with the group velocity $\mathbf{v}_{gr} = \partial\omega/\partial\mathbf{k}$ in the ray approximation is

$$\tau = \int_l \frac{1}{v_{gr}} dl \quad (7.5)$$

where dl is an element of a ray trajectory. The dispersion relation for acoustic waves in the first approximation with respect to magnetic effects and mass flow, \mathbf{u} , has the form

$$\omega = kc_s + \mathbf{k}\mathbf{u} + \frac{v_A^2}{2kc_s} [\mathbf{k} - (\mathbf{k}\mathbf{b})\mathbf{b}]^2 \quad (7.6)$$

where \mathbf{b} is a unit vector along the magnetic field, and $k = \sqrt{k_x^2 + k_y^2 + k_z^2}$. The group velocity is

$$\mathbf{v}_{gr} = \frac{\partial\omega}{\partial\mathbf{k}} = \frac{\mathbf{k}}{k}c_s + \mathbf{u} + \frac{v_A^2}{2c_s} \frac{\mathbf{k}}{k} - \frac{v_A^2}{c_s} \frac{\mathbf{b}(\mathbf{k}\mathbf{b})}{k} + \frac{v_A^2}{2c_s} \frac{\mathbf{k}(\mathbf{k}\mathbf{b})^2}{k^2} \quad (7.7)$$

The absolute value of the group velocity up to the terms linear in \mathbf{u} and quadratic in v_A is

$$v_{gr} = c_s + \mathbf{n}\mathbf{u} + \frac{v_A^2}{2c_s} [1 - (\mathbf{n}\mathbf{b})^2] \quad (7.8)$$

where $\mathbf{n} = \mathbf{k}/k$.

Note that in the presence of a weak ($v_A \ll c_s$) magnetic field, in addition to the modified acoustic mode (fast-mode solution of the wave equation) that we have considered, there appear two more modes, the pure Alfvén mode, with

$$\omega = \mathbf{k}\mathbf{u} + (\mathbf{k}\mathbf{b})v_A \quad (7.9)$$

and a slow magnetosonic mode with

$$\omega = \mathbf{k}\mathbf{u} + (\mathbf{k}\mathbf{b})v_A - (\mathbf{n}\mathbf{b})^2 \frac{kv_A^2}{2c_s} \quad (7.10)$$

Modes (7.9), (7.10) have much slower group and phase velocities than the modified acoustic mode (7.6). These modes would correspond to much longer propagation times (c_s/v_A times longer) and may give large errors in the frame of the time-distance analysis.

It must be noted that in future one can study a domain of much longer propagation times. Despite some difficulties that may appear at small enough flow speed when group velocity of low-frequency modes (7.9), (7.10) closely follows the direction of the magnetic field, extension of the time-distance analysis to the domain of the propagation times

$$\tau \simeq \frac{r}{v_A} \quad (7.11)$$

may prove to be feasible and will then provide direct information about magnetic fields.

In the first approximation with respect to magnetic and flow effects (cf. the conditions (7.4)) travel time can be written as follows:

$$\tau = \int_l \left(\frac{1}{c_s} - \frac{\delta c_s}{c_s^2} - \frac{\mathbf{n}\mathbf{u}}{c_s^2} - \frac{v_A^2}{2c_s^3} [1 - (\mathbf{n}\mathbf{b})^2] \right) dl \quad (7.12)$$

Thus, the variation of sound speed, flows, and magnetic field have different angular dependence. Therefore, taking Fourier sine and cosine transforms (different harmonics!) of travel time one can see that the parity properties of the contribution of mass flows, magnetic effects, and variation in sound speed with respect to forward and backward propagation are different.

Additional and rich information can be obtained from the analysis of parity properties (with respect to forward and backward propagation) of the various contributions, including the spatial inhomogeneities of background parameters of medium, which can be distinguished by the Fourier sine and cosine transforms of the propagation time (7.12). The Fourier transform should be performed for the forward and backward propagation times, and also for some combinations of their differences. Finally, applying an inversion procedure to the transformed times one can reconstruct the depth-dependent flow and magnetic fields below the solar surface.

7.2 The Effects of Horizontal Flows

In the unperturbed state the propagation time from point A to the point C (Fig. 7.1) on the ring of radius r is obviously

$$\tau = \tau_0 = \frac{\sqrt{r^2 + 4h^2}}{c_s}, \quad (7.13)$$

and is the same for the waves traveling in the “forward” (from the point A to point C) and “backward” directions (from C to A). In the presence of plasma flows, these

times are different: the “upstream” group velocity of the acoustic wave is greater than that of “downstream.”

Let the direction of flow u form an angle θ_u with the axis x as shown in Fig. 7.1a. Then from (7.12) elementary calculations (in the linear approximation) show that

$$\tau = \tau_0 - \frac{ur}{c_s^2} \cos(\theta - \theta_u) \quad (7.14)$$

Integrating these expressions with $\cos \theta$ and $\sin \theta$ we obtain

$$\tau_s^{(1)} = -\frac{ur}{2c_s^2} \sin \theta_u, \quad \tau_c^{(1)} = -\frac{ur}{2c_s^2} \cos \theta_u \quad (7.15)$$

while $\tau_s^{(2)} = \tau_c^{(2)} = 0$.

The absolute value of the velocity can be found from the relationship

$$u = \frac{2c_s^2}{r} \sqrt{[\tau_s^{(1)}]^2 + [\tau_c^{(1)}]^2} \quad (7.16)$$

and the direction of propagation may be determined from

$$\sin \theta_u = -\frac{\tau_s^{(1)}}{\sqrt{[\tau_s^{(1)}]^2 + [\tau_c^{(1)}]^2}}, \quad \cos \theta_u = -\frac{\tau_c^{(1)}}{\sqrt{[\tau_s^{(1)}]^2 + [\tau_c^{(1)}]^2}} \quad (7.17)$$

or

$$u_x = \frac{2c_s^2}{r} \tau_c^{(1)}, \quad u_y = \frac{2c_s^2}{r} \tau_s^{(1)} \quad (7.18)$$

Note that the presence of a uniform vertical flow does not affect (7.16) and (7.17). As to the forward ($\tau_{s,c}^{(1)+}$) and backward ($\tau_{s,c}^{(1)-}$) propagation times, in the case of the uniform flow we have

$$\tau_{s,c}^{(1)+} = -\tau_{s,c}^{(1)-}. \quad (7.19)$$

Therefore, the “homogeneous” flow field may be found through (7.16) and (7.18), using for $\tau_{s,c}^{(1)}$ either of the transforms, forward propagation times, $\tau_{s,c}^{(1)+}$, backward propagation times, $\tau_{s,c}^{(1)-}$, or their average, $[\tau_{s,c}^{(1)+} + (-\tau_{s,c}^{(1)-})]/2$. For pure homogeneous flows all three results should be identical. Obviously such situation is far from reality. The stronger are inhomogeneities, the larger will be the discrepancies between the three velocity maps. The main discrepancies will be caused by those effects that have the opposite parity properties, i.e. nonuniformities in sound speed and horizontal magnetic field.

7.3 Effects of Horizontal Magnetic Field

First we derive expression for the propagation time $\tau(\theta)$ in a case when a magnetic field is parallel to x -axis, and then, we take into account the fact that θ_B is a finite angle.

For a simple model of the magnetic field parallel to the x -axis the dispersion relation (7.6) in the first approximation with respect to magnetic effects has a form:

$$\omega = kc_s + \frac{v_A^2}{2kc_s}(k_y^2 + k_z^2) \quad (7.20)$$

Using the equation for the ray trajectory, (7.5) yields:

$$\tau = \tau_0 - \frac{\tau_0 v_A^2}{2c_s^2} \left(1 - \frac{r^2}{2(4h^2 + r^2)}\right) + \frac{\tau_0 v_A^2}{4c_s^2} \frac{r^2}{4h^2 + r^2} \cos 2(\theta - \theta_B) \quad (7.21)$$

In this case, $\tau_s^{(1)} = \tau_c^{(1)} = 0$, while

$$\tau_s^{(2)} = \tau_0 \frac{v_A^2}{4c_s^2} \frac{r^2}{4h^2 + r^2} \sin 2\theta_B \quad (7.22)$$

and

$$\tau_c^{(2)} = \tau_0 \frac{v_A^2}{4c_s^2} \frac{r^2}{4h^2 + r^2} \cos 2\theta_B \quad (7.23)$$

The magnetic field strength (actually, the inverse plasma beta) can be easily determined from the expressions (7.22) and (7.23):

$$\frac{v_A^2}{c_s^2} = 4 \frac{4h^2 + r^2}{r^2} \frac{\sqrt{[\tau_s^{(2)}]^2 + [\tau_c^{(2)}]^2}}{\tau_0} \quad (7.24)$$

The orientation of the magnetic field can be determined from the following relations:

$$\sin 2\theta_B = \frac{\tau_s^{(2)}}{\sqrt{[\tau_s^{(2)}]^2 + [\tau_c^{(2)}]^2}}, \quad \cos 2\theta_B = \frac{\tau_c^{(2)}}{\sqrt{[\tau_s^{(2)}]^2 + [\tau_c^{(2)}]^2}} \quad (7.25)$$

Now, using (7.24) and (7.25) we have for $B_x = B \cos \theta_B$ and $B_y = B \sin \theta_B$:

$$B_{x,y} = \left(\frac{8\pi\rho c_s^2 \sqrt{[\tau_s^{(2)}]^2 + [\tau_c^{(2)}]^2}}{\tau_0 r^2 / (4h^2 + r^2)} \right)^{1/2} \left(1 \pm \frac{\tau_c^{(2)}}{\sqrt{[\tau_s^{(2)}]^2 + [\tau_c^{(2)}]^2}} \right)^{1/2} \quad (7.26)$$

It is important to note that forward ($\tau_{s,c}^{(2)+}$) and backward ($\tau_{s,c}^{(1)-}$) propagation times are the same

$$\tau_{s,c}^{(2)+} = \tau_{s,c}^{(2)-}. \quad (7.27)$$

This means that the half-sum of measured values of forward and backward propagation times, $(1/2)(\tau_{s,c}^{(2)+} + \tau_{s,c}^{(2)-})_{\text{obs}}$ will determine the orientation and magnitude of magnetic field (see Eq. (7.32)); while the difference of these values carries information about the gradients of mass flows. Thus, $\tau_{s,c}^{(2)}$ in (7.24) should be taken as

$$\tau_{s,c}^{(2)} = (1/2)(\tau_{s,c}^{(2)+} + \tau_{s,c}^{(2)-})_{\text{obs}} \quad (7.28)$$

The presence of vertical component of a uniform magnetic field will not give a contribution to $\tau_s^{(2)}$ and $\tau_c^{(2)}$ (as well as to $\tau_s^{(1)}$ and $\tau_c^{(1)}$). This fact is one of the merits of this approach that allows one to single out the influence of plasma flows from those of magnetic field on one hand, and explore the orientation and magnitude of horizontal components independently from the vertical projection, on the other.

7.4 Effects of Background Inhomogeneities

7.4.1 Weak Inhomogeneities

So far we were considering the simplest situation when the sound speed c_s , the flow velocity \mathbf{u} , and magnetic field \mathbf{B} do not depend on coordinates over the space comparable with radii of annuli where the measurements are taken.

Now we discuss a modification of the earlier results in a case when c_s , \mathbf{u} and \mathbf{B} weakly depend on coordinates x and y , such that they change insignificantly over the radius of annulus; then they can be described linearly over x and y additions to otherwise constant c_s , \mathbf{u} and \mathbf{B} .

As corrections to the propagation times caused by the presence of mass flow, magnetic field, and inhomogeneity of sound speed are small, they can be taken into account separately, i.e., cross terms can be neglected.

Now, instead of a uniform slab of thickness h with a bottom perfectly reflecting acoustic waves, we consider linear corrections (in x , y , z) to c_s , \mathbf{u} and \mathbf{B} , in other words, we assume that

$$c_s = c_{s0} + \boldsymbol{\sigma} \cdot \mathbf{r}, \quad (7.29)$$

$$u_\alpha = u_{0\alpha} + v_{\alpha\beta} \cdot r_\beta, \quad (7.30)$$

$$B_\alpha = B_{0\alpha} + b_{\alpha\beta} \cdot r_\beta \quad (7.31)$$

where σ is a constant (independent of coordinates) vector and $v_{\alpha\beta}$ and $b_{\alpha\beta}$ are constant tensors.

Let us consider the effects of the inhomogeneities of these three physical parameters on the *sine* and *cosine* transforms of the propagation times.

Nonuniformities of c_s : The vertical nonuniformity (dependence on z) does not break the cylindrical symmetry of the problem and does not contribute to $\tau_{s,c}^{(n)}$ ($n = 1, 2, \dots$) at all. The horizontal nonuniformity (nonvanishing σ_x and/or σ_y) gives rise to the appearance of finite contributions to $\tau_{s,c}^{(1)}$. These contributions, obviously, will be identical for $\tau_{s,c}^{(1)+}$ and $\tau_{s,c}^{(1)-}$.

Variation of horizontal magnetic field: The contribution of magnetic field effects to the group velocity scales as B^2 and, therefore, magnetic contributions to $\tau^{(n)}$ are even ($\tau^{(n)+} = \tau^{(n)-}$). The nonuniformity causes the appearance of the term of the type $B_{0x}b_{xy}yn_x^2$, $B_{0x}b_{xy}yn_y^2$, and $B_{0y}b_{yx}xn_y^2$. As n_x^2 and n_y^2 contain terms proportional to $\sin 2\theta$, $\cos 2\theta$, the propagation time will now contain terms proportional to $\sin \theta$, $\cos \theta$ and $\sin 3\theta$, $\cos 3\theta$.

Variation of horizontal velocity: The presence of the terms linear in x and y gives rise to a contribution to $\tau_{s,c}^{(2)}$. The change of the sign in \mathbf{u} is equivalent to mutual replacement of the emission source and detection points. On the other hand, the change of sign in velocity changes the sign in $\tau_{s,c}^{(2)}$. Therefore, we conclude that

$$\tau_{s,c}^{(2)+} = -\tau_{s,c}^{(2)-} \quad (7.32)$$

This particular case is considered in the next section, where we use (7.32) to find the spatial distribution of mass flows through the observed propagation times.

7.4.2 Variations of Flow Velocities

We use the model described by (7.30). Denoting the variable part of the velocity vector by $\Delta\mathbf{u}$, we can write:

$$\Delta u_x = u_{xx}x + u_{xy}y, \quad (7.33)$$

$$\Delta u_y = u_{yx}x + u_{yy}y \quad (7.34)$$

The horizontal component of the group velocity in the case shown in Fig. 7.1, for the ray propagating in the direction forming an angle θ with x -axis, is

$$\frac{c_s r}{\sqrt{r^2 + 4h^2}} + \Delta u_x \cos \theta + \Delta u_y \sin \theta, \quad (7.35)$$

or

$$\frac{c_s r}{\sqrt{r^2 + 4h^2}} + \rho \left(\frac{u_{xx} - u_{yy}}{2} \cos 2\theta + \frac{u_{xy} + u_{yx}}{2} \sin 2\theta \right) \quad (7.36)$$

where ρ is a polar radius, $x = \rho \cos \theta$, $y = \rho \sin \theta$.

The propagation time up to the terms linear in $u_{\alpha\beta}$ is then (see (7.14))

$$\tau = \tau_0 - \frac{ur \cos \theta}{c_s^2} - \frac{1}{c_s^2} \left(\frac{u_{xx} - u_{yy}}{2} \cos 2\theta + \frac{u_{xy} + u_{yx}}{2} \sin 2\theta \right) \int_0^r \rho d\rho \quad (7.37)$$

or

$$\tau = \tau_0 - \frac{ur \cos \theta}{c_s^2} - \frac{r^2}{2c_s^2} \left(\frac{u_{xx} - u_{yy}}{2} \cos 2\theta + \frac{u_{xy} + u_{yx}}{2} \sin 2\theta \right) \quad (7.38)$$

The first harmonics give the expressions for the horizontal components of uniform flow, while second harmonics include the effects of possible shear flows in the horizontal plane:

$$\tau_s^{(2)} = -\frac{u_{xy} + u_{yx}}{8c_s^2} r^2 \quad (7.39)$$

$$\tau_c^{(2)} = -\frac{u_{xx} - u_{yy}}{8c_s^2} r^2 \quad (7.40)$$

7.5 Practical Use of the Forward-Backward Information

We summarize here the symmetry properties of various contributions to the propagation time and use the results to find the general pattern of magnetic field and flow distribution at two different layers using the observational data.

7.5.1 Symmetry Properties

The symmetry properties and in particular parities of the forward-backward propagation times are shown in Table 7.1. As mentioned earlier, the parity properties give an additional mean to split various effects.

For example, if we take a half-sum of measured times, $\tau_{s,c}^{(2)+}$ and $\tau_{s,c}^{(2)-}$, we obtain the quantity that eliminates the contribution of the flow and by (7.24)–(7.28) gives directly the magnetic field strength. At the same time, the difference, $(1/2)(\tau_{s,c}^{(2)+} - \tau_{s,c}^{(2)-})$, gives the flow nonuniformities. Thus, when computing, for example

Table 7.1 Symmetry properties of various contributions to the propagation times

Effect	$\tau_{s,c}^{(1)}$	$\tau_{s,c}^{(2)}$	Parity property
Horizontal variation of sound speed	Yes	No	$\tau_{s,c}^{(1)+} = \tau_{s,c}^{(1)-}$
Uniform horizontal flow	Yes	No	$\tau_{s,c}^{(1)+} = -\tau_{s,c}^{(1)-}$
Variation in horizontal mass flow ($v_{\alpha\beta} \neq 0$)	No	Yes	$\tau_{s,c}^{(2)+} = -\tau_{s,c}^{(2)-}$
Uniform horizontal magnetic field	No	Yes	$\tau_{s,c}^{(2)+} = \tau_{s,c}^{(2)-}$
Variation in horizontal magnetic field ($b_{\alpha\beta} \neq 0$)	Yes	No	$\tau_{s,c}^{(1)+} = \tau_{s,c}^{(1)-}$
Uniform vertical flow	No	No	
Variation in vertical flow	Yes	No	$\tau_{s,c}^{(1)+} = -\tau_{s,c}^{(1)-}$
Variation in vertical magnetic field ($b_{z\alpha}$)	Yes	No	$\tau_{s,c}^{(1)+} = \tau_{s,c}^{(1)-}$

$u_{xy} + u_{yx}$, we use the expression (7.39) in a form:

$$\frac{\partial u_x}{\partial y} + \frac{\partial u_y}{\partial x} = -\frac{4c_s^2}{r^2} (\tau_s^{(2)+} - \tau_s^{(2)-}) \tag{7.41}$$

Note that although the *variation* in the horizontal magnetic fields contribute to the first harmonics (last row in Table 7.1), the alteration in travel time would be masked by the effects of a uniform mass flows (second row in Table 7.1) and may be ignored.

7.5.2 Reconstruction of Subsurface Flow and Magnetic Fields from Observations

For illustrative purposes we use here results of travel-time measurements obtained from the data sets taken by the MDI instrument on SOHO, and perform their *sine* and *cosine* transforms for reconstruction the subsurface flow and magnetic fields. The data were taken from the 8 h observation of line-of-sight velocity in the MDI high resolution field on January 27, 1996. The object of the observation is very quiet sun region. In other words, we deal with the helioseismology effects in the rarefied ensemble of flux tubes.

Figure 7.2 (top) shows magnetogram of the region with magnetic field shown in blue. The travel times have been measured for sets of ray paths on a grid of 30×40 points on the observed area of 175×130 Mm. The *sine* and *cosine* transforms have been made for two sets of short distance ray paths. Each set contains the data

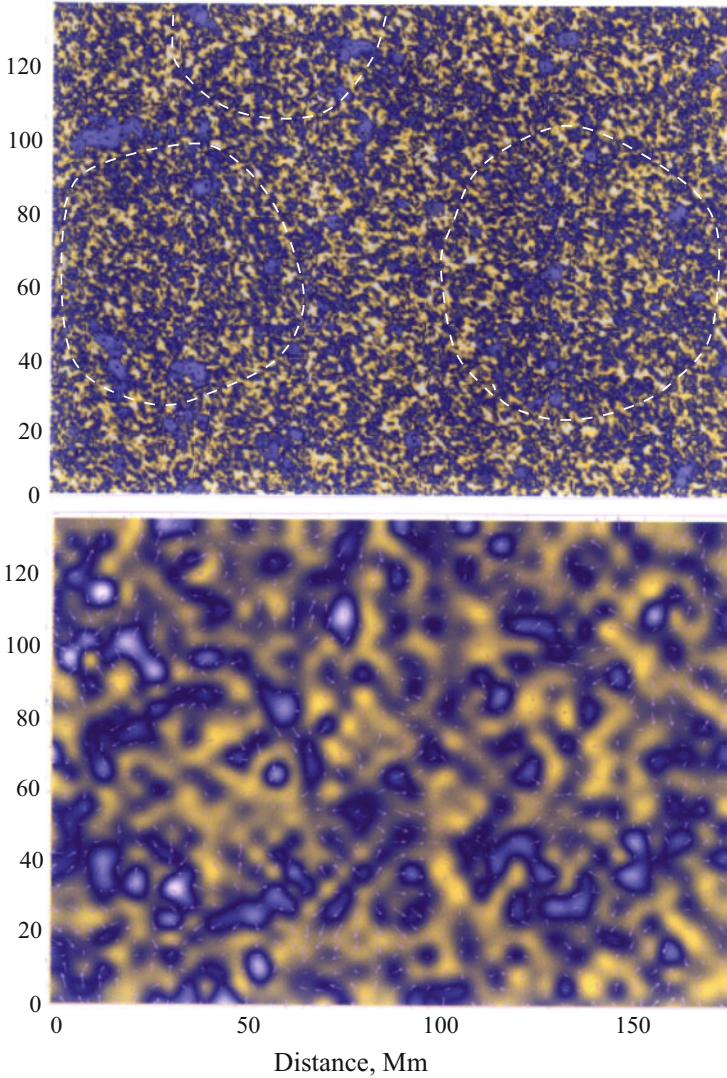


Fig. 7.2 Top: high-resolution magnetogram of a quiet sun region, taken by the MDI/SOHO instruments January 27, 1996. Bottom: The reconstructed subsurface horizontal magnetic field in terms of inverse plasma beta, v_A^2/c_s^2 at 1.2 Mm below the visible surface, $(v_A^2/c_s^2)_{\max} = 0.11$. Arrows show the subsurface velocity field. White dashed circles outline supergranular pattern populated by the magnetic field concentrations, which are especially well recognizable on the reconstructed map below the surface

averaged over the three sets of annuli with the radial distance ranges of $\Delta = 0.225\text{--}0.625^\circ$ and $\Delta = 0.625\text{--}1.025^\circ$.

For the reconstructed flow and magnetic fields the mean depths drop at $h_1 \simeq 1.2\text{ Mm}$ and $h_2 \simeq 2.8\text{ Mm}$ below the solar surface. Thus, for the first set of measured travel times and their *sine* and *cosine* transforms we prescribe the mean depth $h = 1.2\text{ Mm}$ and mean annulus radius $r = 5.2\text{ Mm}$, respectively, for the second set of measured travel times we have $h = 2.8\text{ Mm}$ and $r = 10\text{ Mm}$.

Figure 7.2 (bottom) shows a pattern of the reconstructed magnetic field, more precisely, v_A^2/c_s^2 at the depth $h = 1.2\text{ Mm}$ (blue color). One can see a strong correlation between the measured magnetic field on the solar surface and the underlying horizontal field. Note that although the procedure does not allow to resolve the scale less than the ray path, much larger scale of reconstructed local elements compared to elements on magnetogram is consistent with both ray approximation and observational data which also are restricted by the size of annuli. It is remarkable how well the reconstructed magnetic field pattern mimics a supergranular geometry (marked by white dashed circles in Fig. 7.2a).

Figure 7.3 shows the computed map of velocity field for the depths of 1.2 Mm . This map also clearly shows the supergranular pattern in the flow field. Maximum velocity at this depth is $v_{\max} = 2.3\text{ km/s}$. The flow map reconstructed at 2.8 Mm depth (not shown) also mimics the magnetic pattern, but the velocities are lower, e.g., $v_{\max} = 1.7\text{ km/s}$.

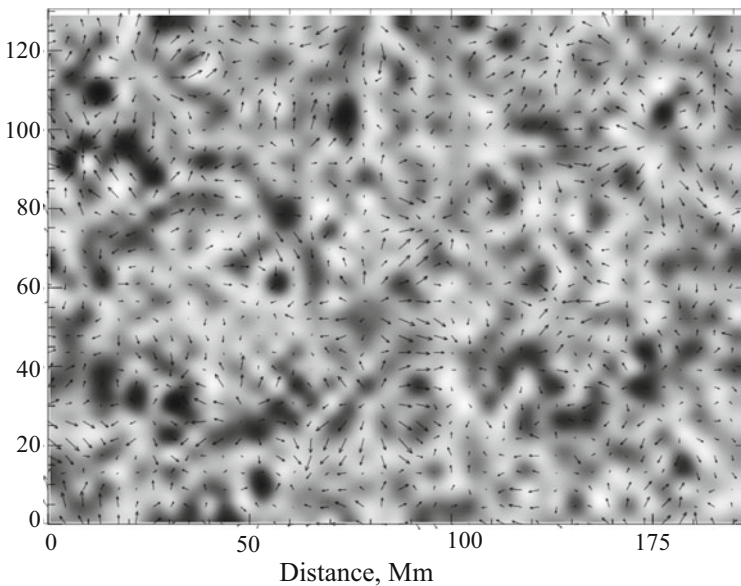


Fig. 7.3 The reconstructed velocity field at 1.2 Mm below the visible surface, $v_{\max} = 2.3\text{ km/s}$. One can see that at the location of strong magnetic field the mass flows are inhibited

In the absence of local inhomogeneities the velocity field reconstructed from the measurements of backward propagation times and forward propagation times should be the same. However, presence of the local inhomogeneities of medium violates the exact relationship (7.32) and causes discrepancies in the maps obtained from $\tau_{s,c}^{(1)+}$ and $\tau_{s,c}^{(1)-}$. These discrepancies are associated with those effects that have different parity properties, such as the variation in sound speed and nonuniform magnetic fields.

It is important that, although the effect of “uniform” mass flows in $\tau_{s,c}$ is much stronger than that of the magnetic field inhomogeneities, there is a significant difference between the velocity field reconstructed from the forward and backward propagation times. This difference shows the location of magnetic field inhomogeneities or/and variation in sound speed. Figure 7.4 shows the map of velocity vectors which represent the difference between the velocities obtained from $\tau_{s,c}^{(1)+}$ and $\tau_{s,c}^{(1)-}$. One can see a clear correlation between the location of largest discrepancies in reconstructed velocity field and the locations of strongest magnetic field (cf. Fig. 7.2).

For quantitative estimates of the magnetic field strength we need to adopt some model parameters for plasma density below the surface. Let us try, e.g., the parameters given in the model of the convection zone by Spruit (1974): at the depth $h = 1.2$ Mm, $\rho = 0.38 \times 10^{-5}$ g/cm³, which gives the estimate for sound speed $c_s = 14.8$ km/s; at $h = 2.8$ Mm, $\rho = 0.36 \times 10^{-4}$ g/cm³, and $c_s = 18.4$ km/s

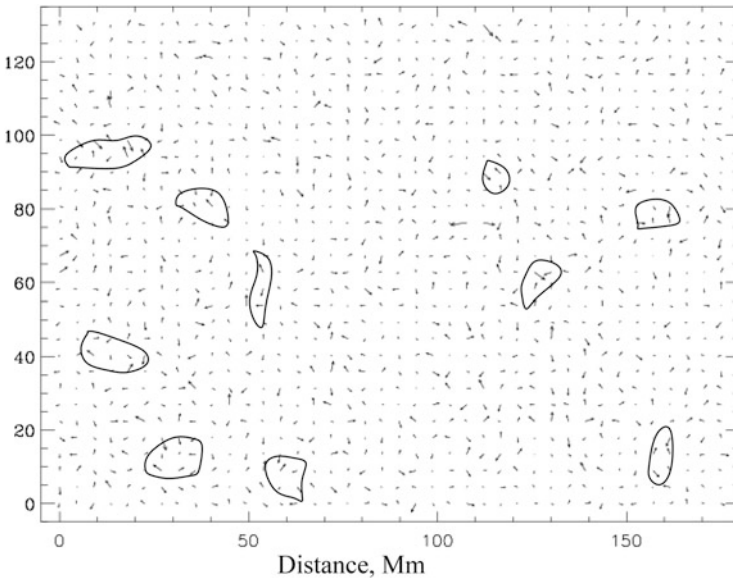


Fig. 7.4 Discrepancies between the velocity maps obtained from forward and backward propagation times at 1.2 Mm below the visible surface. Some of the largest discrepancies are outlined to show their correlation with strongest magnetic field concentrations

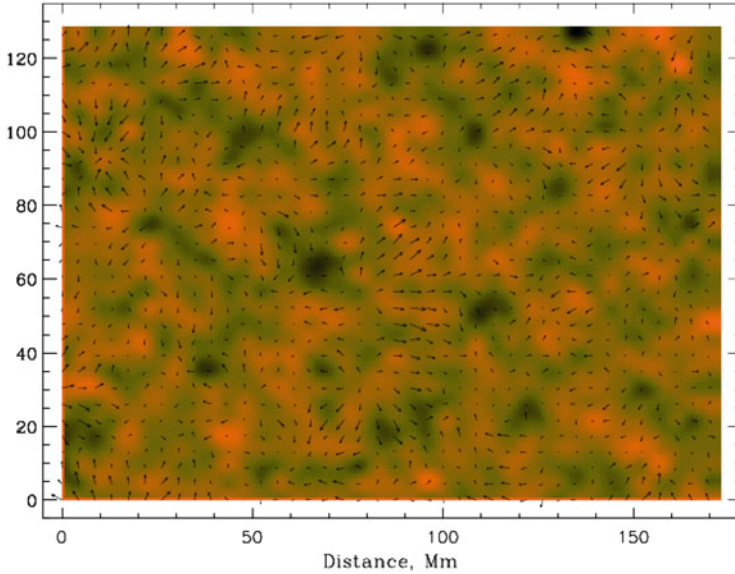


Fig. 7.5 The velocity field and the velocity shear at the depth 2.8 Mm, $D_{hz,max} \simeq 0.29 \times 10^{-3} s^{-1}$

(see also Hill 1995, and the references therein). For these parameters at $h = 1.2$ Mm, the upper bound value of magnetic field strength is $B_{max} = 3480$ Gs; at $h = 2.8$ Mm, $B_{max} = 10,760$ Gs.

As already mentioned, the method allows to obtain the information about the velocity gradients and construct the velocity shear maps. The example of such computation, i.e. the maps of velocity field and the intensity of shear flows, $D_{hz} = \partial u_x / \partial x - \partial u_y / \partial y$, at the depth 2.8 Mm is shown in Fig. 7.5. Note that at the depth 1.2 Mm, the maximum velocity shear is even higher, $D_{hz,max} \simeq 0.67 \times 10^{-3} s^{-1}$.

So far we were computing the velocity and magnetic field maps assuming that sound speed and other parameters depend on vertical coordinate in a stepwise manner. In the next section we consider more general case and take into account effects of gravity.

7.6 Magnetic Corrections in a Vertically Stratified Atmosphere

In this section we generalize the method to the case of a vertically stratified atmosphere. We start from expression for the correction to the propagation time:

$$\delta\tau = - \int_l \frac{dl}{v_{gr}} \frac{\delta v_g}{v_g} \quad (7.42)$$

where integration is carried out along the unperturbed ray trajectory. From (7.8) we have $v_g = c_s$, $\delta v_{gr} = v_A^2/(2c_s)[1 - (\mathbf{nb})^2]$. By noting that $ds/v_g = dz/v_{gz}$, where v_{gz} is the vertical component of the group velocity, one finds that

$$\delta\tau = -2 \int_0^h \frac{dz}{v_{gz}} \frac{\delta v_g}{v_g} = - \int_0^h \frac{v_A^2 [1 - (\mathbf{nb})^2] dz}{c_s^3 n_z} \quad (7.43)$$

As earlier, h is the depth of a layer where reflection of the ray occurs ($k_z = 0$). The factor “2” in (7.43) takes into account two branches of the ray trajectory, descending and ascending. From the condition $\omega = \text{const}$ we have:

$$c_s^2(h)(k_x^2 + k_y^2) = c_s^2(z)(k_x^2 + k_y^2 + k_z^2) \quad (7.44)$$

In the system where x and y are ignorable coordinates, k_x and k_y are conserved quantities. We have therefore

$$k_z = \sqrt{k_x^2 + k_y^2} \sqrt{1 - \frac{c_s^2(z)}{c_s^2(h)}} \quad (7.45)$$

and

$$n_z = \sqrt{1 - \frac{c_s^2(z)}{c_s^2(h)}}; \quad n_x = \frac{c_s(z)}{c_s(h)} \cos \theta; \quad n_y = \frac{c_s(z)}{c_s(h)} \sin \theta \quad (7.46)$$

We will take into account both vertical variation of the Alfvén velocity, $v_A = v_A(z)$, and the direction of the horizontal magnetic field, $\theta_B = \theta_B(z)$. We have:

$$(\mathbf{vb})^2 = \cos^2(\theta - \theta_B) \frac{c_s^2(z)}{c_s^2(h)} \quad (7.47)$$

Taking into account relations (7.43), (7.46) and (7.47) one finds that

$$\delta\tau = - \int_0^h \frac{v_A^2(z) c_s^2(h) [1 - \cos^2(\theta - \theta_B(z))]}{c_s^4(z) \sqrt{c_s^2(h) - c_s^2(z)}} dz \quad (7.48)$$

or

$$\delta\tau = - \int_0^h \frac{v_A^2(z) c_s^2(h) [1 - \cos 2\theta \cos 2\theta_B(z) - \sin 2\theta \sin 2\theta_B(z)]}{c_s^4(z) \sqrt{c_s^2(h) - c_s^2(z)}} dz \quad (7.49)$$

Remarkably, in this much more general case, $\delta\tau$ still manifests the same $\cos 2\theta$ and $\sin 2\theta$ dependence on the azimuthal angle as in the model of a uniform slab.

Recall that in the case of a uniform slab $(\mathbf{nb})^2 = (r^2/4h^2 r^+) \cos^2(\theta - \theta_B)$, $n_z = 2h/\sqrt{4h^2 r^+}$, and one recovers (7.21).

For *cosine* and *sine* transforms now, instead of (7.23), we have:

$$\tau_s^{(2)} = \frac{1}{4} \int_0^h \frac{v_A^2(z) c_s^2(h) \sin 2\theta_B(z)}{c_s^4(z) \sqrt{c_s^2(h) - c_s^2(z)}} dz \quad (7.50)$$

$$\tau_c^{(2)} = \frac{1}{4} \int_0^h \frac{v_A^2(z) c_s^2(h) \cos 2\theta_B(z)}{c_s^4(z) \sqrt{c_s^2(h) - c_s^2(z)}} dz \quad (7.51)$$

Probing different annuli, i.e., different reflection depths, and using a standard inversion procedure, one can find by virtue of (7.21) and (7.22) distribution of horizontal magnetic field and its depth dependence.

For known $c_s(z)$ one can apply Abel inversion $\tau_s^{(2)}$ and $\tau_c^{(2)}$ and obtain in this way both magnitude and direction of the horizontal magnetic field.

Note that one can also solve the problem of the accuracy of reconstruction of sub-surface flows over annular distances which become comparable with characteristic scale of convective motions, granular, mezogranular, and supergranular (Ryutova and Scherrer 1998).

7.7 Estimate of the Energy Flux from Time-Distance Analysis

Time-distance measurements in helioseismology can be used to estimate the energy flux on the solar surface (Ryutova 1997). Nonreciprocity of travel times along the ray path and different parity properties of sound speed, flow velocity, and magnetic field allow one to obtain information on large-scale distribution of plasma flows and magnetic fields and their energetics. We shall see that the covariance of sum and difference of the reciprocal travel times is a measure of large-scale, climatological heat flux and that the covariance of sum and difference of their departures from the mean gives an estimate for the magnetic energy flux. Using the reciprocal travel times measured in north-south and west-east directions, one can estimate the latitude- and longitude-dependent energy fluxes.

The procedure is based on the fact that the space-time average of the products, $\overline{\langle \mathbf{u} c_s^2 \rangle}$ and $\overline{\langle \mathbf{u} v_A^2 \rangle}$, which are related, respectively, to large-scale heat flux and magnetic energy flux, can be directly found from time-distance measurements. Indeed, the covariance of sum, $s = \tau^{(+)} + \tau^{(-)}$ and difference, $d = \tau^{(+)} - \tau^{(-)}$ is related to the heat flux, while covariance of their departure from the mean, $\overline{(\Delta s)^2} - \overline{(\Delta d)^2}$ is a measure of the magnetic energy flux.

We shall consider large-scale energy fluxes associated with the motions and magnetic field transport over spatial scales comparable to the size of annuli where the measurements are taken and over a time period that is much larger than the characteristic time of magnetic field fluctuations. This is somewhat similar to climatological heat flux measured in ocean tomography (see, e.g., Munk 1986). As

in the acoustic monitoring of ocean gyres, solar tomographic measurements can also be used to measure the eddy fluxes: the heat and magnetic energy transport associated with the small-scale flux tubes and rapid motion.

7.7.1 Heat and Magnetic Energy Fluxes

Recall that in the approximation of geometrical acoustics the group velocity (7.5) has a form

$$v_{gr} = c_s + \mathbf{n}\mathbf{u} + \frac{v_A^2}{2kc_s}[1 - (\mathbf{n}\mathbf{b})^2] \quad (7.52)$$

We have already mentioned that the flow velocity and Alfvén speed are much less than the sound speed (7.4), and enter the propagation time $\tau(\theta)$ as small additions proportional to u/c_s , and v_A^2/c_s^2 , respectively.

If the duration of observations, T , is much larger than the period of measured oscillations, $2\pi/\omega$, i.e. if

$$\omega T \gg 1, \quad (7.53)$$

one can define the averages over T , as

$$\begin{aligned} c_s(\mathbf{r}, t) &= \overline{c_{s0}(\mathbf{r})} + \delta c_s(\mathbf{r}, t) \\ u(\mathbf{r}, t) &= \overline{u_0(\mathbf{r})} + \delta u(\mathbf{r}, t) \\ B(\mathbf{r}, t) &= \overline{B_0(\mathbf{r})} + \delta B(\mathbf{r}, t) \end{aligned} \quad (7.54)$$

Time average of the fluctuating parts, δc_s , δu , and δB are zero:

$$\overline{\delta c_s} = 0, \quad \overline{\delta u} = 0, \quad \overline{\delta B} = 0 \quad (7.55)$$

In the first approximation with respect to magnetic and flow effects, the travel time is given by

$$\tau(t) = \int_l \left(\frac{1}{c_{s0}(l)} - \frac{\delta c_s(l, t)}{c_{s0}^2} - \frac{\mathbf{n}[\mathbf{u}_0(l) + \delta \mathbf{u}(l, t)]}{c_{s0}^2} - \frac{v_{A0}^2}{2c_{s0}^3}[1 - (\mathbf{n}\mathbf{b})^2] \right) dl \quad (7.56)$$

To separate the contribution of magnetic field from the velocity, one needs to perform the inversion of the difference, $d = \tau^+ - \tau^-$, which yields the simulation of the flow field, and the sum, $s = \tau^+ + \tau^-$, that gives the distribution of the temperature. In principle, heat fluxes can be determined through point-by-point

multiplication of the inverted flow and temperature fields with the subsequent averaging in space and time, which would be exactly the same as calculating a covariance of d and s : $sd = (\tau^+)^2 - (\tau^-)^2$, just like in the reconstruction of the flow field by using the first Fourier harmonics of travel times measured as a function of direction and distribution magnetic field patterns using the second harmonics.

Point-by-point multiplication of the two fields would give the average magnetic energy flux. This simply means that if one uses the measured travel times to calculate the covariance of sum and difference of reciprocal travel times and their departures from the mean, one obtains the estimate of heat and magnetic energy fluxes.

To illustrate how the method works, we assume that unperturbed plasma parameters are uniform along the ray path and that the measured ray averages may be considered the range averages. Then travel times in the forward and backward directions can be written as

$$\tau^\pm(t) = \frac{l}{c_{s0}} \left(1 \mp \frac{u_0}{c_{s0}} - \frac{v_{A0}^2}{2c_{s0}^2} [1 - (\mathbf{nb})^2] + \left\langle -\frac{\delta c_s(l, t)}{c_{s0}} \mp \frac{\delta u}{c_{s0}} \right\rangle \right) \quad (7.57)$$

Taking into account that the mean travel time is $\tau_0 = 1/c_{s0}$, the deviation of the travel time from the mean value due to the temperature inhomogeneities and presence of mass flows and magnetic fields is obviously

$$\Delta\tau^\pm(t) = \frac{l}{c_{s0}} \left(\mp \frac{u_0}{c_{s0}} - \frac{v_{A0}^2}{2c_{s0}^2} [1 - (\mathbf{nb})^2] + \left\langle -\frac{\delta c_s(l, t)}{c_{s0}} \mp \frac{\delta u}{c_{s0}} \right\rangle \right) \quad (7.58)$$

The time average $F_B = \overline{uv_A^2}$ is then the measure of the magnetic energy flux over the region where measurements are taken. Bearing in mind that c_s^2 is almost a linear function of temperature, the average $F_T = \overline{uc_s^2}$ may be considered a measure of the heat flux, \overline{uT} .

The time average of the above expression is

$$\overline{\Delta\tau^\pm(t)} = \frac{l}{c_{s0}^2} \left(\mp u_0 - \frac{v_{A0}^2}{2c_{s0}^2} [1 - (\mathbf{nb})^2] \right) \quad (7.59)$$

Note that $\overline{\delta c_s}$ and $\overline{\delta u}$ vanish due to (7.55). Now we can find the expression for the measure of the magnetic energy flux:

$$F_B = u_0 v_A^2 [1 - (\mathbf{nb})^2] = \frac{c_{s0}^3}{2\tau_0^2} (\overline{\Delta\tau^{+2}} - \overline{\Delta\tau^{-2}}) \quad (7.60)$$

Similarly, from (7.57) we obtain the expression for the measure of a heat flux. The time average of (7.57) is:

$$\overline{\tau^\pm(t)} = \frac{l}{c_{s0}^2} (c_{s0} \mp u_0 - \frac{v_{A0}^2}{2c_{s0}} [1 - (\mathbf{nb})^2]), \quad (7.61)$$

The difference of squares of the forward and backward propagation times is then

$$\overline{\tau^+(t)}^2 - \overline{\tau^-(t)}^2 = \tau_0^2 \left(-4 \frac{u_0 c_{s0}}{c_{s0}^2} + 2 \frac{u_0 v_A^2}{c_{s0}^3} \right) \quad (7.62)$$

The last term on the right-hand side is a measure of the magnetic energy flux. Using (7.60), we obtain the expression for a heat flux:

$$F_T = \overline{uc_s^2} = -\frac{c_{s0}^3}{4} \frac{(\overline{\tau^+}^2 - \overline{\Delta\tau^+}^2) - (\overline{\tau^-}^2 - \overline{\Delta\tau^-}^2)}{\tau_0^2} \quad (7.63)$$

Data averaged over the time of observations should represent the natural spatial scales of energy transport over the time comparable to the time of observations. There is, though, the limitation “from below”: the spatial scales cannot be less than the characteristic scale of annuli where measurements are taken. This restriction stems from the ray approximation. The method, however, is quite universal and can be used in future improved techniques.

7.7.2 Contribution of Eddy Fluxes

The eddy fluxes, which are related to the dynamics of the energy transport at small-scales, can be calculated by constructing the spatial mean product $\langle \delta u \delta c_s^2 \rangle$. For this we use the departure from the time mean:

$$\delta \tau^\pm(t) = \int_l \left(-\frac{\delta c_s^2(l, t)}{2c_{s0}^3} \mp \frac{\delta u}{c_{s0}^2} \right) dl \quad (7.64)$$

The mean square is

$$\overline{(\delta \tau^\pm)^2} = \frac{1}{4c_{s0}^4} \int dl \int ds \overline{[\delta f(l)][\delta f(l+s)]} \quad (7.65)$$

where $f(l) = \delta c_s^2(l) \pm 2c_{s0} \delta u(l)$. Introducing a correlation length, $r = \int_{-\infty}^{\infty} ds \rho(s)$, where $\rho(s) = \overline{f(l)f(l+s)}/f^2$ we obtain for the mean square

$$\overline{(\delta \tau^\pm)^2} = \frac{\overline{[\delta c_s^2 \pm 2c_{s0} \delta u]^2}}{4c_{s0}^6} lr \quad (7.66)$$

The estimate for the eddy heat flux along a particular ray is then

$$F_{\text{eddy}} = \overline{\langle \delta u \delta c_s^2 \rangle} = \frac{c_s^5}{lr} [\overline{(\delta \tau^+)^2} - \overline{(\delta \tau^-)^2}]. \quad (7.67)$$

The same approach can be applied to the travel times measured as a function of direction. In this case, taking sine and cosine convolutions of travel time, we can find the magnetic energy flux provided by small-scale motions, $F_{\text{eddy}}^B = \langle \delta u \delta v_A^2 \rangle$, as well.

The merit of this application is that although small-scale granular and mezo-granular motions are beyond the resolution of time-distance analysis, their contribution to heat flux can be determined.

7.7.3 *Reconstruction of Energy Fluxes from Observational Data*

In this section we estimate magnetic energy and heat fluxes (7.60)–(7.63) using the observational data described in previous section. For the estimate of the energy flux, we use the data sets for westward-eastward (WE) and north-south (NS) times (for observational details, see Duvall et al. (1997)). It is important to note that these time sets that are measured in quadrants cannot be used directly for detecting magnetic fields: according to their parity properties, magnetic fields contribute to the second Fourier harmonics of travel times, and nonconvoluted times are not directly related to magnetic field topology. So that for magnetic field and velocity field measurement one should apply the method described in the previous section. However, although WE and NS times do not give the distribution of the magnetic field, they can be directly used for estimating magnetic energy flux. This is shown in Fig. 7.6. The two upper panels show the intensity of a heat flux in the west-east (a) and north-south (b) directions. Two lower panels are the intensity of the magnetic energy flux in the west-east (c) and north-south (d) directions. The small arrows on all four panels correspond to the computed velocity field for the depths of 1.2 Mm obtained in Sect. 7.5.

One can see strong correlation between the intensity of a convective heat flux and magnetic energy transport with the direction of mass flows. Note that travel time measurements used for the reconstructed velocity fields and for the energy fluxes are different: the heat and magnetic energy fluxes are computed using both backward and forward propagation times and their departures from the mean; the velocity map is reconstructed from sine and cosine convolutions of travel times measured as a function of direction.

There is also good correlation between the magnetic energy flux and reconstructed magnetic field shown in Fig. 7.2b. In all four panels, the brightest yellow patches correspond to the highest flux in the west-east/north-south direction, while the white areas correspond to the strongest flux in the east-west/south-north

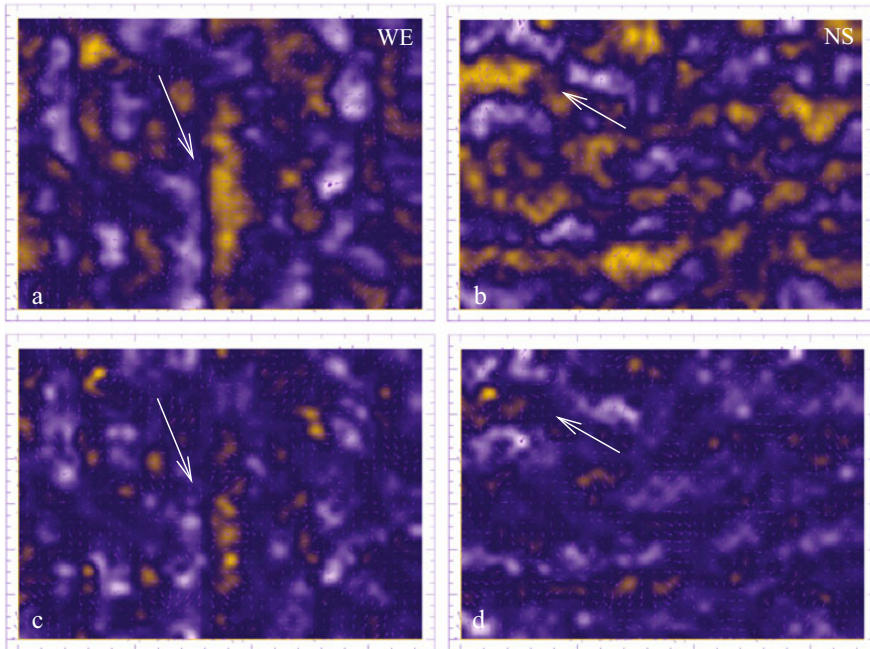


Fig. 7.6 Reconstruction of the energy flux from observations. (a) Heat flux in the west-east direction, $|F_T| = 1.84 \times 10^{12} \text{ erg/cm}^2 \text{ s}$; (b) Heat flux in the north-south direction, $|F_T| = 1.6 \times 10^{12} \text{ erg/cm}^2 \text{ s}$; (c) Magnetic energy flux in the west-east direction, $|F_B| = 9.5 \times 10^{10} \text{ erg/cm}^2 \text{ s}$; (d) Magnetic energy flux in the north-south direction, $|F_B| = 10.5 \times 10^{10} \text{ erg/cm}^2 \text{ s}$. Field of view is the same as in Fig. 7.2

direction. The white arrows in Fig. 7.6 highlight the essential difference between heat flux (top panels) and magnetic energy flux (bottom panels). Note that the mean of the maximum heat flux, $\langle F_T \rangle = 1.7 \cdot 10^{12} \text{ erg/cm}^2 \text{ s}$, is larger by an order of magnitude than the magnetic energy flux, $\langle F_B \rangle = 10^{11} \text{ erg/cm}^2 \text{ s}$.

7.8 Raman Spectroscopy of Solar Oscillations

Presence of magnetic flux tubes and their interaction with the acoustic waves can form a basis for a new approach in the analysis of helioseismic data. This quite useful analysis can be called “Raman spectroscopy of solar p-modes” (Ryutova 1998). It is based on the fact that interference of oscillating flux tubes with the incoming acoustic wave may result in the generation of beat wave with combination frequency: the power spectra of scattered waves in addition to main peak will have Stokes and anti-Stokes satellites. The amplitude and frequency shift of these satellites reflect the properties and the structure of the observed region.

7.8.1 Stokes and Anti-Stokes Satellites

The presence of the constant level of the solar p-mode fluctuations is a reflection of the dynamic balance between two processes: generation of p-modes by turbulent motions, and their damping by classical and/or anomalous dissipation mechanisms. Observational studies of the acoustic wave properties show that the sources and sinks are distributed nonuniformly over the solar surface. The sources exciting the p-modes (on the average level) are more likely connected with the turbulent motions in the convective zone and, according to the conjecture that was put forward by Brown (1991), may be isolated and thus sources and sinks may well be separated from one another in space and time.

Localized sources of the acoustic waves and excess of the acoustic emission compared to the average were observed in the quiet sun regions with the enhanced network of small-scale magnetic flux tubes (Brown 1991; Braun et al. 1992; Braun 1995).

A physical mechanism that may explain the excess of the emission in the quiet Sun is associated with the interaction of p-modes with nonsteady motions, and in particular with the oscillating magnetic flux tubes (see Chap. 3). Note that only nonsteady motions can give rise to the increase in the energy of outgoing waves: the steady-state nonuniformities may cause scattering but not a significant energy increase.

As discussed in Chap. 3, there are two major effects that contribute to this process. One is a *resonance scattering*, when the energy of p-modes propagating in the random ensembles of flux tubes damps out due to the resonance excitation of natural oscillations of magnetic flux tubes. It was shown that transformed energy of p-modes remains for a “long time” in a form of flux tube oscillations. Then, in a time $\tau_{\text{rad}} \simeq 1/\omega(kR)^2$ the resonant flux tubes radiate the accumulated energy into surrounding plasma. The radiation occurs only if the phase velocity of flux tubes oscillations exceeds the sound speed in the ambient plasma: $v_{gr} > c_{se}$ (Chap. 6).

Another effect works in the opposite case when $v_{gr} < c_s$, and is connected with nonlinear coupling of flux tubes oscillations and acoustic waves, which in turn leads to generation of beat waves with combination frequencies and wavenumbers (Fig. 7.7):

$$\omega_{\text{out}} = \omega_{\text{in}} \pm \Omega, \quad k_{\text{out}} = k_{\text{in}} \pm K \quad (7.68)$$

The frequency shift, Ω , does not necessarily correspond to any of the eigenfrequencies of the p-modes. Both, Ω and K are perturbations determined by a local properties of medium, and may correspond, for example, to eigenfrequency (and eigenvector) of a scattering centers. It is just this process that facilitates appearance of Stokes and anti-Stokes satellites.

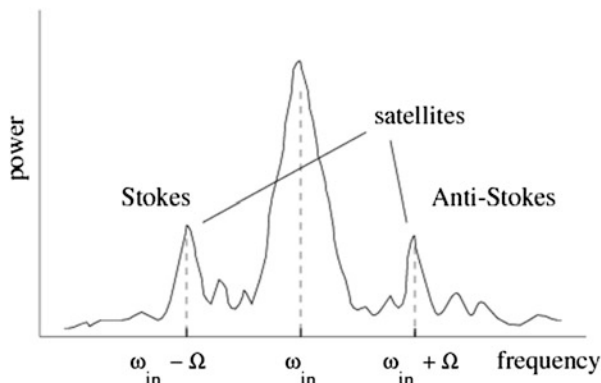


Fig. 7.7 Sketch of a power spectrum for outgoing wave in Raman scattering. In addition to main peak at the incident frequency, there appear equidistant Stokes and anti-Stokes satellites

The effective distance at which acoustic waves interact with a particular flux tube is of the order of flux tube radius, R . The main component of pressure perturbation in the vicinity of the magnetic flux is axisymmetric:

$$\delta p \simeq k \xi_{ac} p; \quad \delta v \simeq \xi_{ac} k R; \quad \frac{\delta R}{R} \simeq \frac{\delta p}{p} \quad (7.69)$$

This is coupled with $m = \pm 1$ flux tube motions. The resulting nonlinear drive exists at the scale $\simeq R$, has $m = \pm 1$ symmetry, and can be expressed as the following equivalent displacement

$$\delta x \simeq \xi_{\text{kink}} k \xi_{ac} \quad (7.70)$$

Here δx can be conceived as a forcing term for generating the secondary emission.

Assuming that $\omega = \omega_{\text{in}} \simeq \Omega$, $k_z^{\text{in}} \simeq K_z$, one finds the following estimate for the power radiated per unit length of flux tube:

$$P_{\text{Raman}} \simeq \frac{\rho c_{\text{se}}^2}{\omega} \left(\frac{R\omega}{c_{\text{se}}} \right)^4 \xi_{\text{kink}}^2 \omega^2 (k \xi_{ac})^2 \quad (7.71)$$

If the filling factor of the area is f , then the power scattered by the volume of the size $L \times L^2$ is $f P_{\text{Raman}} L^3$. Incident acoustic energy flow into the same volume is $\xi_{ac}^2 k^2 \rho c_{\text{se}}^3 L^2$. The ratio of the two is a measure of the excess of the emitted acoustic power:

$$\zeta = f L \left(\frac{R\omega}{c_{\text{se}}} \right)^5 \frac{\xi_{\text{kink}}^2}{R} \quad (7.72)$$

Obviously, a quantity ζ has a meaning of the optical depth with respect to the scattering process. Even more power may be emitted by the Raman scattering

of acoustic waves in association with the sausage oscillations. In this case the equivalent displacement is

$$\delta x \simeq \frac{R\omega}{c_{se}} \xi_{\text{sausage}} \xi_{ac}^- \quad (7.73)$$

Energy radiated per unit length is

$$P_{\text{Raman}} \simeq \frac{\rho c_{se}^2}{\omega} \left(\frac{R\omega}{c_{se}} \right)^2 \xi_{\text{sausage}}^2 \xi_{ac}^2 \omega^2 \quad (7.74)$$

and the optical depth is

$$\zeta = \sigma L \left(\frac{R\omega}{c_{se}} \right)^3 \frac{\xi_{\text{sausage}}^2}{R} \quad (7.75)$$

Using the amplitude of satellites and frequency shift one can infer a typical physical parameters of “scattering centers,” and, generally speaking, develop the analysis for the study of the structure of atmosphere through the spectroscopic features of p-modes.

7.8.2 Using Raman Spectroscopy in Observations

In this section we give some examples of measured power spectra of incoming and outgoing waves and their possible interpretation, only to demonstrate the principle of the method.

The MDI/SOHO high resolution data were used to compute the series of incoming and outgoing acoustic power for different spherical harmonics by employing the Hankel decomposition method (Braun 1995). Some 512 Dopplergrams contributed to this series. The target region was a very quiet sun on the disk center. The annulus had inner and outer radii of 2.5 and 11.25 heliocentric degrees (1 degree = 12.151 Mm length-of-arc). The power was computed up to $L = \sqrt{l(l+1)} = 2016$.

Figure 7.8 shows example of measured power spectra for incoming (solid line) and outgoing (dashed line) wave for the spherical degree $l = 452.6$. The equidistant Stokes and anti-Stokes satellites clearly exceed their counterparts in the incoming power spectrum.

To distinguish a true Stokes and anti-Stokes peaks from closely situated neighboring p-mode ridges, one needs, except fulfillment of equality $\nu_0 - \nu_- = \nu_0 - \nu_+$, additional facts which are associated *only* with the Raman scattering and are not related to neighboring acoustic ridges. Most important here is that Stokes frequency shift is determined by physical parameters of a local “scattering centers,” and, in particular is directly associated with an eigen-frequency of oscillating flux tubes. This means that the frequency shifts must not only be equidistant, but should give a reasonable estimate for the Alfvén velocity. For given spherical degree ℓ and

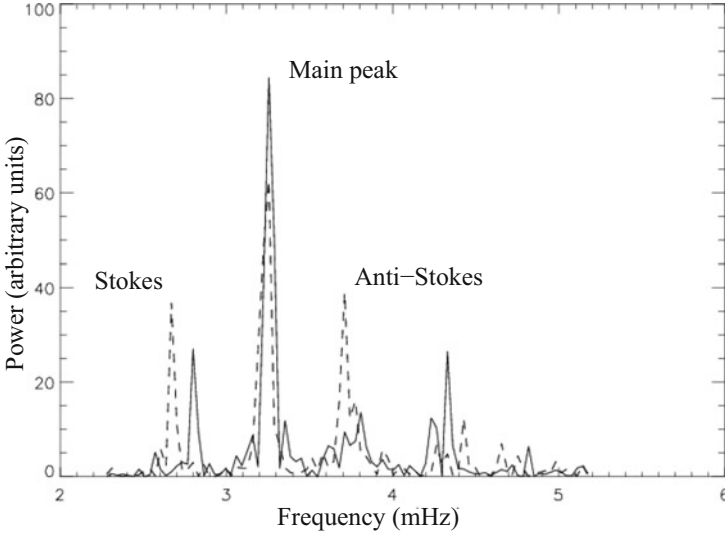


Fig. 7.8 The measured power spectra for incoming (solid line) and outgoing (dashed line) wave for the spherical degree $l = 452.6$. The equidistant Stokes and anti-Stokes satellites clearly exceed their counterparts in the incoming power spectrum

frequency ν the local sound speed is roughly estimated as (e.g., Hill 1995)

$$c_s(l, \nu) = 2\pi R_\odot \frac{\nu}{l} \quad (7.76)$$

In the subsurface layers Alfvén velocity is small compared to sound speed, therefore the phase velocities of both kink and sausage mode of flux tube oscillations is close to the Alfvén speed, i.e.

$$v_{gr} = \frac{\Omega}{k} \simeq v_A \quad (7.77)$$

Assuming that the wave number is approximately the same as that of incident acoustic wave we can express it through sound speed from (7.76):

$$v_A \simeq \frac{\Omega}{\omega_{in}} c_s(l, \nu) \quad (7.78)$$

Examples of the parameters of power spectra, calculated sound speed and inferred Alfvén velocity are given in Table 7.2. P_{in} and P_{out} are values of net averaged powers (in arbitrary units). The averaging is done over a narrow frequency interval (0.23 mHz) near the peaks in outgoing power spectrum for first three cases, $\ell = 452.6, 699.4$ and 740.6 . In all three cases the satellite peaks in outgoing power spectra which exceed their counterparts in the incoming power spectra, are shifted,

Table 7.2 The parameters of power spectra and estimates for inferred Alfvén speed

	P_{in}	P_{out}	ν (mHz)	$\nu_0 - \nu_-$	$\nu_0 - \nu_+$	c_s	v_A
$\ell = 452.6$	2.14×10^3	1.44×10^4	$\nu_- = 2.67$	0.55	-0.55	31.1	5.30
	3.46×10^4	2.72×10^4	$\nu_0 = 3.22$				
	1.31×10^4	3.1×10^4	$\nu_+ = 3.77$				
$\ell = 699.4$	4.96×10^3	9.9×10^3	$\nu_- = 2.6$	0.60	-0.60	20.0	3.75
	3.52×10^4	3.51×10^4	$\nu_0 = 3.20$				
	2.75×10^4	4.48×10^4	$\nu_+ = 3.8$				
$\ell = 740.6$	1.54×10^4	1.69×10^4	$\nu_- = 2.7$	0.62	-0.62	19.6	3.66
	2.32×10^4	5.9×10^4	$\nu_0 = 3.32$				
	2.78×10^4	3.25×10^4	$\nu_+ = 3.94$				

equally from the central peak. Peak at incident frequency, must contain *equidistant* Stokes and anti-Stokes satellites. The emitted power is proportional to magnetic filling factor and *size* of the observed area. It is more sensitive to small parameter $(kR)^2$ than the power radiated, for example, by resonant flux tubes, which in addition may have incoherent character. Besides, in contrast to the resonance case where the condition $(kR)^2 \ll 1$ is required, here the parameter $(kR)^2$ may be finite. Therefore, large regions of flux tubes, comparable with the acoustic wavelength, will contribute the Raman scattering most readily, and will be easier to analyze. Good candidates here are the quiet photospheric network near plages and regions containing small pores.

Finally, it must be noted that the methods of time-distance analysis have proved to be very useful instrument in reconstructing the observational data to test the conditions under the solar surface, and, as we discussed above, to perform additional analysis of the atmospheric structure.

During the last decades the helioseismic approach has been generalized in many ways (Gizon and Birch 2005; Couvidat et al. 2006; Schad et al. 2013). One can apply its methods to various problems from probing the subsurface filamentary structure of sunspots and field inclination (Schunker et al. 2005; Cameron et al. 2011; Felipe et al. 2014) to testing the far-side helioseismic maps (Lindsey and Braun 2000; Zhao 2007; Gonzalez-Hernandez et al. 2013).

It must be noted again that this chapter deals only with the role of small-scale magnetic flux tubes in helioseismology.

7.9 Problem

7.1 In the actual data analysis one usually deals with the discrete points. The discreteness of data cause, obviously the errors. Develop the approach that can minimize these errors in time-distance helioseismology analysis (Ryutova 1997).

References

- D.C. Braun, *Astrophys. J.* **451**, 859 (1995)
D.C. Braun, C. Lindsey, Y. Fan, S.M. Jefferies, *Astrophys. J.* **392**, 739 (1992)
T.M. Brown, *Astrophys. J.* **371**, 396 (1991)
R.H. Cameron, L. Gizon, H. Schunker, A. Pietarila, *Solar Phys.* **268**, 293 (2011)
S. Couvidat, A.C. Birch, A.G. Kosovichev, *Astrophys. J.* **640**, 516 (2006)
T.L. Duvall, Jr., S.M. Jefferies, J.W. Harvey, M.A. Pomerantz, *Nature* **362**, 430 (1993)
T.L. Duvall, Jr., S. D'Silva, S.M. Jefferies, J.W. Harvey, J. Schou, *Nature* **379**, 235 (1996)
T.L. Duvall, Jr., et al., *Solar Phys.* **170**, 63 (1997)
T. Felipe, A.D. Crouch, A.C. Birch, *Astrophys. J.* **788**, 136 (2014)
L. Gizon, A.C. Birch, Local helioseismology. *Living Rev. Sol. Phys.* **2**, 6 (2005)
I. Gonzalez-Hernandez, et al., *J. Phys. Conf. Ser.* **440a**, 2029 (2013)
F. Hill, *Helioseismology, 4th SOHO Workshop*, ESA, vol. 63 (1995)
C. Lindsey, D.C. Braun, *Science* **287**, 1799 (2000)
W. Munk, *J. Fluid Mech.* **173**, 43 (1986)
M. Ryutova, *Astrophys. J.* **490L**, 111 (1997)
M. Ryutova, *IAUS* **185**, 213 (1998)
M. Ryutova, P. Scherrer, *Astrophys. J.* **494**, 438 (1998)
A. Schad, J. Timmer, M. Roth, *Astrophys. J.* **78**, L38 (2013)
H. Schunker, et al., *Astrophys. J.* **621**, L149 (2005)
H.C. Spruit, *Solar Phys.* **34**, 277 (1974)
J. Zhao, *Astrophys. J.* **664**, L139 (2007)

Chapter 8

Wave Phenomena in Dense Conglomerate of Flux Tubes



Abstract In this chapter we shall consider the properties of strongly magnetized regions of the sun such as sunspots, pores, and active regions, where random magnetic flux tubes form a dense conglomerates. Physical processes and, in particular, the wave phenomena in closely packed flux tubes exhibit some distinct features that are observable and can be used for testing the structure and energetics of these regions. One of the most pronounced effects is the strong enhancement of the dissipation of the incoming wave energy, caused by large local gradients of velocity, temperature, and pressure arising at borders of neighboring small-scale inhomogeneities.

8.1 Propagation of MHD Waves in an Ensemble of Closely Packed Flux Tubes

In the previous chapters we studied response of a rarefied ensembles of random magnetic flux tubes to the propagation of acoustic waves and unsteady wave packets, typical to quiet Sun areas (Fig. 8.1a). Unlike quiet photosphere, sunspots and active regions represent a dense conglomerate of flux tubes (Fig. 8.1b) where all the parameters of the medium (magnetic field, plasma density, temperature, etc.) change from one domain to another by an order of magnitude (see, e.g., Livingston 1991). The dynamics of these two different types of ensemble and, in particular, their response to propagation of acoustic and MHD waves are very different. The dispersion properties and the observational spectroscopy of these regions, as well as the mechanisms of energy transfer from photosphere to upper layers of atmosphere are also very different.

The most striking effect here is that sunspots, pores, and active regions act as a sink of incoming wave energy. This phenomenon is similar to the enhanced dissipation in poly-crystals considered many years ago by Zener (1937) and Isakovich (1948), and widely used in modern buildings by use of a porous materials in order to reduce the noise. For sunspots and other densely magnetized regions the effect of enhanced absorption of incoming wave power has been first described by Ryutova and Persson (1984) and measured independently by Braun et al. (1987,

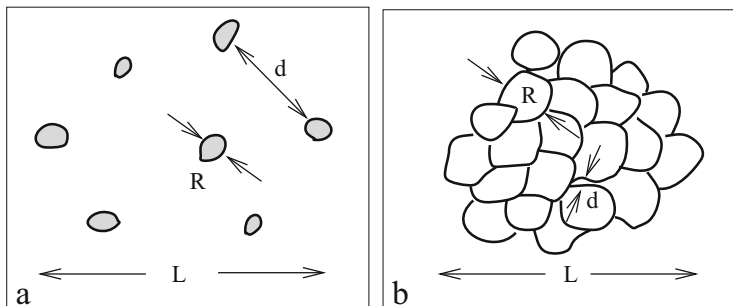


Fig. 8.1 Classes of ensembles of magnetic flux tubes: (a) Widely spaced flux tubes with small magnetic filling factor typical to quiet sun; (b) Dense conglomerate of random flux tubes with magnetic filling factor on the order of unity typical to sunspots

1988, 1990). The theory later was extended and complemented by numerical analysis (Ryutova et al. 1991).

Strong enhancement of the wave dissipation occurs due to the presence of closely packed random flux tubes with characteristic radius, R , much smaller than the wavelength:

$$d \ll R \ll \lambda \quad (8.1)$$

where d is a small gap between the flux tube comprising the sunspot. The efficiency of enhanced dissipation is of the order of $\lambda/R \gg 1$.

The physical reason for this effect can be easily understood. Since all the plasma parameters change from tube to tube, and tubes have common boundaries, the velocity amplitude of perturbations as well as all other perturbed quantities are different in different flux tubes. This results in appearance of *strong local gradients* of all the plasma parameters at much smaller scales. In other words, the MHD equations now contain a *vortex part* of these parameters leading to much stronger dissipation of the wave energy compared to homogeneous medium.

The characteristic scale of *local gradients* is naturally of the order of the tube radius—the scale of the inhomogeneities, at which the dissipative effects are enhanced. The damping rate, and the very process of absorption, can be quite different in different regions, and is largely determined by the level of the fluctuations of the background plasma parameters and their time and spatial scales. Inside the sunspot physical parameters, as already was mentioned, change from one small domain to another by the order of unity. Figure 8.2 shows high resolution image of a typical well-shaped sunspot. Excellent contrast achieved in Fe I 6302 Å line shows densely packed individual flux tubes inside the umbra (white arrows) surrounded by a beautiful penumbra.

Another example of highly heterogeneous nature of the sunspot umbra is taken from studies of photometric properties of sunspot umbra (Fig. 8.3). Using a color index analysis (Beckers and Schröter 1968) high temperature umbral dots densely

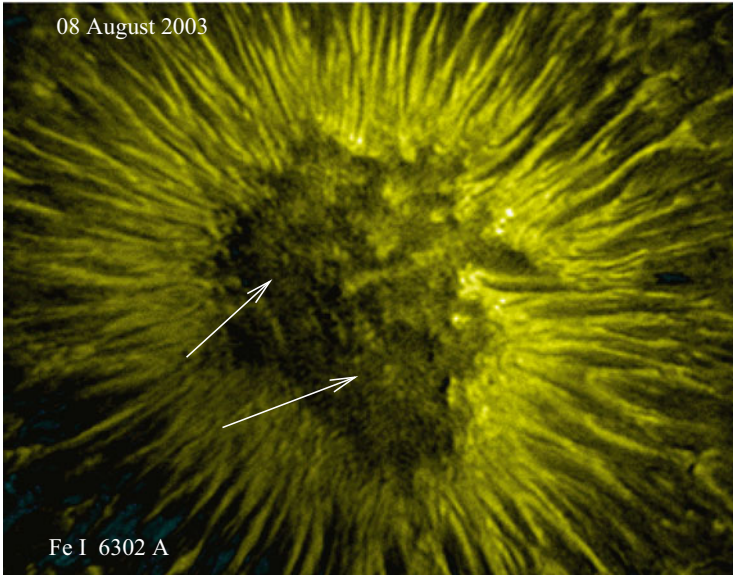


Fig. 8.2 Sunspot umbra densely packed by small scale magnetic flux tubes (white arrows, e.g.) is surrounded by filamentary penumbra. Magnetogram of the sunspot AR 425 is taken with the Swedish 1-m Solar Telescope (SST) in Fe I 6302 Å line. Reprinted from <http://www.isf.astro.su.se>. Credit G. Scharmer and K. Langhans, ISP, Sweden

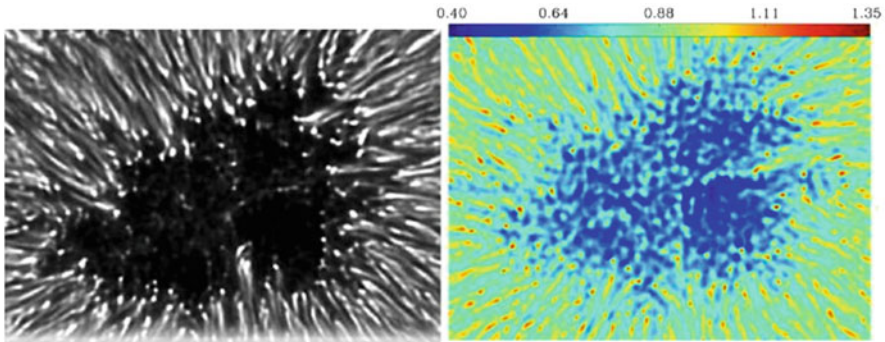


Fig. 8.3 Left: the deconvoluted image of the central part of sunspot taken by Hinode/SOT with the blue filter (Goodarzi et al. 2015); Right: Image of umbra, highly populated by umbral dots, is taken with the blue and the green filters to compute the ratio of intensities (normalized to quite photosphere); the color bar shows value of the color index. Image size is 4.2×3 Mm. Reprinted from <http://www.isf.astro.su.se>. Credit H. Goodarzi and K. Langhans, ISP, Sweden

populating the umbra were studied in great details (Goodarzi et al. 2016). It was shown, for example, that umbral dots can reach photospheric temperatures and even higher at the periphery (the average background temperature of umbra is 3100 K).

It was found that they are distributed more or less similar to quiet sun network forming minute bright and dark round or elongated cells with a spacing of order of 0.35 arcsec. Possible formation of umbral dots and flushes may be associated with the nonlinear phenomena in dense conglomerate of flux tubes providing natural inhomogeneity of sunspots.

8.1.1 Basic Equations and Dispersion Relation

We begin with the linear theory following the original approach by Ryutova and Persson (1984), and describe a formalism that allows to study the propagation of long MHD waves in an inhomogeneous plasma. We consider the case where unperturbed magnetic field is concentrated in vertical flux tubes with z -axis directed along the field, and consider the MHD waves propagating *across* the system of magnetic flux tubes.

The unperturbed parameters of plasma, $B_0(x, y)$, and $\rho_0(x, y)$ $p_0(x, y)$ are assumed to be stationary. This means that the inhomogeneities belong to the class of the so-called entropy inhomogeneities, in which the total pressure P_0 is constant

$$P_0 = p_0(x, y) + \frac{B_0^2(x, y)}{8\pi} = \text{const} \quad (8.2)$$

But local temperature, density, and magnetic field vary each by the order of unity.

The lifetime of such inhomogeneities is determined by the thermal conductivity and the diffusion, which are quite slow varying quantities in a photospheric plasma.

Consider small linear perturbations of all physical parameters, including the entropy, $S(x, y, t)$, i.e, assume that

$$\begin{aligned} p &= p_0(x, y) + \delta p(x, y, t) \\ B &= B_0(x, y) + \delta B(x, y, t) \\ \rho &= \rho_0(x, y) + \delta \rho(x, y, t) \\ S &= S_0(x, y) + \delta S(x, y, t) \\ \mathbf{v} &= \delta \mathbf{v}(x, y, t) \end{aligned} \quad (8.3)$$

It is convenient to introduce the displacement vector:

$$\mathbf{v} = \frac{\partial \boldsymbol{\xi}}{\partial t} \quad (8.4)$$

Substituting these into the 2D ideal MHD system and neglecting terms of higher than the first order perturbations we obtain

$$\rho_0 \frac{\partial^2 \delta \xi}{\partial t^2} = -\nabla \left(\delta p + \frac{B_0 \delta B}{4\pi} \right) \tag{8.5}$$

$$\delta \rho + \text{div}(\rho_0 \xi) = 0 \tag{8.6}$$

$$\delta B + \text{div}(B_0 \xi) = 0 \tag{8.7}$$

$$\frac{\delta p}{p_0} - \gamma \frac{\delta \rho}{\rho_0} + \xi \left(\frac{\nabla p_0}{p_0} - \gamma \frac{\nabla \rho_0}{\rho_0} \right) = 0 \tag{8.8}$$

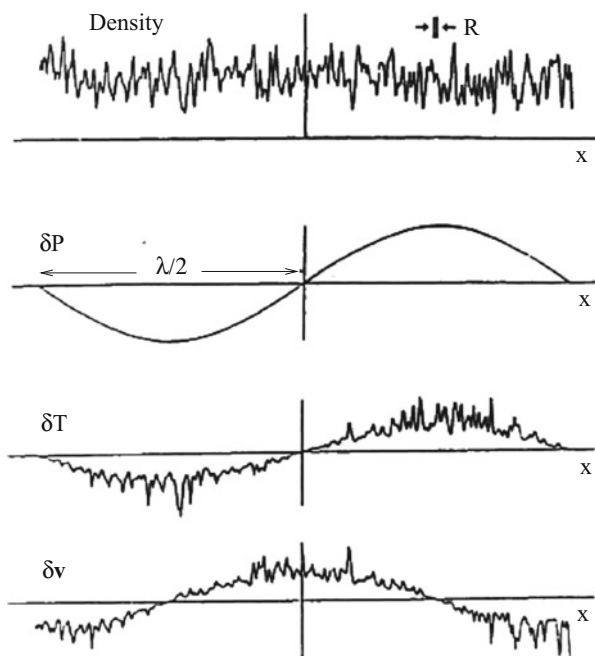
The last equation describes the entropy perturbations. We consider harmonic oscillations, proportional to $\exp(-i\omega t)$, and replace $\partial/\partial t$ by $-i\omega$.

We are considering a motion with a scale $\lambda \gg R$. At the same time, the scale over which we average the equations of motion, l , is much larger than R , i.e.

$$R \ll l \ll \lambda. \tag{8.9}$$

This means that at the scale l the compression of the plasma may be considered as a quasi-stationary one, that is, δP is almost a constant, even though ρ_0 and ξ change by the order of unity at even smaller scale $R \ll l$. Figure 8.4 shows the basic

Fig. 8.4 Sketch of the spatial variation of plasma parameters in the presence of the long wave. The initial state of the sunspot (or any other dense conglomerate of magnetic elements) has large amplitude density and magnetic field variation on the scale of flux tubes, R . The incident wave sets up a total pressure perturbations δP on the much larger scale λ . The temperature and velocity respond to the wave with amplitude δT and δv that depend on small-scale structure and thus have many small regions of high gradients (cf. Fig. 8.2)



approach in spatial variations of plasma parameters in field of wave with $\lambda \gg R$. Indeed, as one can see from (8.5), the change of δP at the scale l is of the order of $\rho_0 |\xi| \omega^2 l$, where $\omega \sim c_s \lambda$ is characteristic frequency of oscillations, c_s being the sound speed. In other words, the change of δP at the smallest possible averaging $l \sim R$ is as small as $\rho_0 |\xi| \omega^2 R$, while the change of δP at a scale λ is much larger:

$$\delta P \sim \rho_0 |\xi| \omega^2 \lambda. \quad (8.10)$$

Using the equilibrium condition (8.2), from (8.5)–(8.8) we have

$$\delta p = \gamma p_0 \operatorname{div} \xi - \xi \nabla p_0 \quad (8.11)$$

$$\delta B = -B_0 \operatorname{div} \xi - \xi \nabla B_0 \quad (8.12)$$

$$\delta P = -2 \left[\left(\frac{\gamma}{2} - 1 \right) p_0 + P_0 \right] \operatorname{div} \xi \quad (8.13)$$

Taking into account estimate (8.10), it is obvious from (8.13) that

$$\operatorname{div} \xi \sim \frac{|\xi|}{\lambda} \quad (8.14)$$

and there are *no large terms* of the order of $|\xi|/R$ in $\operatorname{div} \xi$.

It is, however, important that from (8.13) one can not say anything about the magnitude of the divergence-free part of ξ . On the other hand, from (8.5) we have

$$\nabla \times \xi = \frac{1}{\omega^2 \rho_0^2} [\nabla \rho_0 \times \nabla \delta P] \quad (8.15)$$

For $\nabla \delta P$ (8.10) gives the estimate $|\nabla \delta P| \sim \omega^2 |\xi| \rho_0$. As for an inhomogeneous plasma $|\nabla \rho_0| \sim \rho_0/R$, we find from (8.15) that

$$|\nabla \times \xi| \simeq \frac{|\xi|}{R}, \quad (8.16)$$

This estimate shows that, unlike the case of a homogeneous plasma, in the dense conglomerate of flux tubes the *divergence-free part* (vortex) is very important.

Let us now proceed to the derivation of averaged equations. By expressing $\operatorname{div} \xi$ in terms of δP from (8.13), and taking the average, we obtain:

$$\operatorname{div} \langle \xi \rangle = \frac{\langle \delta P \rangle}{2} \left\langle \frac{1}{(\gamma/2 - 1) p_0 + P_0} \right\rangle, \quad (8.17)$$

where angular brackets denote averaging over the volume with characteristic size l ($R \ll l \ll \lambda$). While deriving (8.17) we have taken into account that, up to the small terms of order $R\lambda$, we can put $\langle \delta P \rangle = \delta P$.

In order to obtain a closed system of equations describing self-consistently large-scale oscillations in an inhomogeneous plasma, in addition to (8.17) we need to add another equation expressing $\langle \xi \rangle$ in terms of $\langle \delta P \rangle$. From (8.5) we have

$$\xi = \frac{1}{\omega^2 \rho_0} \nabla \delta P \quad (8.18)$$

As shown above, $\text{div} \xi \ll |\nabla \times \xi|$. This means that taking the divergence of (8.18), we can neglect the left-hand side of resulting equation and write the following approximate relation

$$\text{div} \left(\frac{\nabla \delta P}{\rho_0} \right) \simeq 0 \quad (8.19)$$

Let us introduce the notations:

$$\delta \tilde{P} = \delta P - \langle \delta P \rangle, \quad \tilde{q} = q - \langle q \rangle \quad (8.20)$$

where $q = 1/\rho$. It follows from (8.19) that

$$\text{div}(q \delta \tilde{P}) = \nabla \langle \delta P \rangle \cdot \nabla q \quad (8.21)$$

This equation together with the condition $\langle \delta \tilde{P} \rangle = 0$ uniquely determines $\delta \tilde{P}$.

By averaging (8.18), we obtain:

$$\langle \xi \rangle = \frac{1}{\omega^2} \left[\langle q \nabla \delta P \rangle + \langle \tilde{q} \rangle \langle \nabla \delta \tilde{P} \rangle \right]. \quad (8.22)$$

Since in (8.21), which is linear, the right-hand side is proportional to $\nabla \langle \delta P \rangle$, we can write

$$\langle \tilde{q} \nabla \delta \tilde{P} \rangle_\alpha = Q_{\alpha\beta} \nabla_\beta \langle \delta P \rangle \quad (8.23)$$

where $Q_{\alpha\beta}$ is a tensor whose symmetry is determined by the symmetry of the fluctuations of $q = 1/\rho_0$. For example, if statically, there is not any selected direction in the xy -plane, then obviously, $Q_{\alpha\beta} = q \delta_{\alpha\beta}$, where Q is constant. If the level of fluctuations is of the order of unity, i.e. $\langle \tilde{q}^2 \rangle \sim \langle q \rangle^2$, then Q is of the order $\langle q \rangle$.

Finally, using (8.22) and (8.23) we obtain

$$\langle \xi \rangle_\alpha = \frac{1}{\omega^2} \left[\langle q \rangle \delta_{\alpha\beta} + Q_{\alpha\beta} \right] \cdot \nabla_\beta \langle \delta P \rangle. \quad (8.24)$$

Equation (8.24), together with (8.17), forms closed system which defines all the properties of the linear long-wave oscillations propagating through the dense

conglomerate of random flux tubes. For spatially harmonic wave proportional to $\exp(i\mathbf{k} \cdot \mathbf{r})$, these equations lead directly to the dispersion relation:

$$\omega^2 = 2 \left\langle \frac{1}{(\gamma/2 - 1)p_0 + P_0} \right\rangle^{-1} \left[\left\langle \frac{1}{\rho_0} \right\rangle k^2 + Q_{\alpha\beta} k_\alpha k_\beta \right]. \quad (8.25)$$

It must be noted that this dispersion relation can be directly used for the diagnostic goals when measuring $\omega(k_x, k_y)$ diagrams, which allows to reconstruct the morphological map of studied region.

The normalized phase velocity corresponding to this dispersion relation (8.25) can be represented as follows:

$$v_{\text{ph}} = \frac{\omega}{k} = \left\langle \frac{1}{\rho(c_s^2 + v_A^2)} \right\rangle^{-1/2} \left(\left\langle \frac{1}{\rho} \right\rangle + Q_{\alpha\beta} \frac{k_\alpha k_\beta}{k^2} \right)^{1/2} \quad (8.26)$$

To find $Q_{\alpha\beta}$, one needs to solve (8.21), which, in most cases, cannot be done analytically. Example of two-dimensional case where analytical solution is possible is given in the next section.

8.1.2 Spacial Cases

In a two-dimensional case (8.21) can be analytically solved if we assume that density inhomogeneities are small, i.e. $\tilde{q} \ll q$. Then (8.21) can be written as

$$\langle q \rangle \Delta \delta \tilde{P} = -\nabla \langle \delta P \rangle \cdot \nabla \tilde{q} \quad (8.27)$$

where we have neglected the term $\langle \tilde{q} \nabla \delta \tilde{P} \rangle \sim \tilde{q}^2$.

Using the Fourier-transformation

$$\tilde{q} = \frac{1}{2\pi} \int e^{i\mathbf{k} \cdot \mathbf{x}} \tilde{q}_{\mathbf{k}} d^2 \mathbf{k}, \quad (8.28)$$

we find that

$$\delta \tilde{P}_{\mathbf{k}} = \frac{i\mathbf{k}}{\langle q \rangle k^2} \nabla \langle \delta P \rangle \cdot \tilde{q}_{\mathbf{k}}, \quad (8.29)$$

then

$$\langle \tilde{q} \nabla \delta \tilde{P} \rangle = \frac{1}{(2\pi)^2} \left\langle \int \int d^2 \mathbf{k}_1 d^2 \mathbf{k}_2 e^{i(\mathbf{k}_1 + \mathbf{k}_2) \cdot \mathbf{r}} \cdot \tilde{q}_{\mathbf{k}_1} \tilde{q}_{\mathbf{k}_2} \frac{\mathbf{k}_2 (\mathbf{k}_2 \cdot \nabla \langle \delta P \rangle)}{\langle q \rangle k_2} \right\rangle \quad (8.30)$$

Using the formula

$$\langle e^{i(\mathbf{k}_1+\mathbf{k}_2)\cdot\mathbf{r}} \rangle = \frac{4\pi^2}{L^2} \delta(\mathbf{k}_1 + \mathbf{k}_2) \quad (8.31)$$

where L is normalization length, we obtain

$$\langle \tilde{q} \nabla \delta \tilde{P} \rangle = - \int d^2\mathbf{k} (\tilde{q}^2)_{\mathbf{k}} \frac{\mathbf{k}(\mathbf{k} \cdot \nabla \langle \delta P \rangle)}{\langle q \rangle_{\mathbf{k}}} \quad (8.32)$$

here

$$(\tilde{q}^2)_{\mathbf{k}} \equiv \frac{1}{L^2} |\tilde{q}_{\mathbf{k}}|^2 \quad (8.33)$$

is the spectral density of fluctuations. We used here the identity $q_{\mathbf{k}} \equiv q_{-\mathbf{k}}^*$, as $q(\mathbf{r})$ is a real function.

Using now relation $(\tilde{q}^2)_{\mathbf{k}} \simeq [(\tilde{\rho}^2)_{\mathbf{k}}/\langle \rho_0 \rangle^4]$, we obtain the following expression for the correlation function

$$\langle \tilde{q} \nabla \delta \tilde{P} \rangle = - \frac{1}{\langle \rho_0 \rangle^4} \int d^2\mathbf{k} (\tilde{\rho}_0^2)_{\mathbf{k}} \frac{\mathbf{k}(\mathbf{k} \cdot \nabla \langle \delta P \rangle)}{\langle q \rangle_{\mathbf{k}^2}} \quad (8.34)$$

Thus, up to the terms of the order of $\tilde{\rho}_0^2$,

$$Q_{\alpha\beta} = - \frac{1}{\langle \rho_0 \rangle^3} \int d^2\mathbf{k} (\tilde{\rho}_0^2)_{\mathbf{k}} k_{\alpha} k_{\beta} \quad (8.35)$$

Finally, we need an expression for the fluctuating part of the displacement vector $\tilde{\xi} = \xi - \langle \xi \rangle$. With accuracy up to the terms linear in $\tilde{\rho}$ we have (see (8.18):

$$\tilde{\xi} = \frac{1}{\omega^2 \tilde{\rho}_0} \left[\nabla \delta \tilde{P} - \frac{\tilde{\rho}_0}{\langle \rho_0 \rangle} \nabla \langle \delta P \rangle \right], \quad (8.36)$$

where $\delta \tilde{P}$ is related to $\tilde{\rho}_0$ by (8.29).

For isotropic fluctuations $Q_{\alpha\beta} = 0$, and the dispersion relation (8.25) acquires an especially simple form:

$$\omega^2 = 2 \left\langle \frac{1}{(\gamma/2 - 1)P_0 + P_0} \right\rangle^{-1} \left\langle \frac{1}{\rho_0} \right\rangle k^2. \quad (8.37)$$

8.2 Dissipative Processes

In the MHD approximation, there are three major sources of damping of magnetoacoustic waves in plasma: viscosity, thermal conductivity, and Ohmic losses. In most cases the damping is slow, i.e. the damping rate Γ is much smaller than the frequency of oscillations. Thus, we can write

$$\Gamma = \frac{\bar{Q}_{\text{visc}} + \bar{Q}_{\text{therm}} + \bar{Q}_{\text{ohm}}}{2W} \quad (8.38)$$

where W is the energy density of oscillations and \bar{Q} is the energy dissipated per unit time and averaged over the space period of the wave.

To be more specific, we will perform the calculations for the case, which is characteristic to solar atmosphere, where $\omega_i \tau_i \gg 1$, τ_i and $\omega_i = eB/m_i c$ being ion collision time and ion gyro-frequency.

We therefore can use a standard relations (Braginskii 1965):

$$Q_{\text{visc}} = Q_{\text{visc}}^{(1)} + Q_{\text{visc}}^{(2)} \quad (8.39)$$

with

$$Q_{\text{visc}}^{(1)} = \left(\frac{1}{3} \eta_0 - \eta_1 \right) (\text{div } \delta \mathbf{v})^2 \quad (8.40)$$

$$Q_{\text{visc}}^{(2)} = \frac{1}{2} \eta_1 \left(\frac{\partial v_\alpha}{\partial x_\beta} + \frac{\partial v_\beta}{\partial x_\alpha} \right)^2 \quad (8.41)$$

where

$$\eta_0 = 0.96nT\tau_i, \quad \eta_1 = \frac{\eta_0}{3} \frac{1}{2(\omega_i \tau_i)^2}, \quad \tau_i = \frac{3}{4} \sqrt{\frac{m_i}{\pi}} \frac{T^{3/2}}{\Lambda e^4 n} \quad (8.42)$$

and Λ is a Coulomb logarithm. Further

$$Q_{\text{therm}} = \frac{\chi}{T} (\nabla \delta T)^2; \quad \chi = \frac{2nT}{m_i \omega_i^2 \tau_i} \quad (8.43)$$

with χ being the thermal conductivity. Here we have assumed that in an unperturbed state the temperature is homogeneous and one can neglect terms of the type $(\delta \chi / T) \nabla \delta T \cdot \nabla T_0$ in Q_{therm} .

8.2.1 Weakly Inhomogeneous Medium

We start with the estimate of the damping rate for a homogeneous plasma. We shall see that the terms with small or no effect on the damping rate in homogeneous plasma become very large in presence of closely packed flux tubes.

The main contribution to damping rate Γ in homogeneous plasma comes from the first term in (8.40), since it does not contain a small parameter $(\omega_i \tau_i)^{-2}$, and can be estimated as

$$Q_{\text{visc}}^{(1)} \simeq nT \tau_i \frac{\delta v^2}{\lambda^2} \quad (8.44)$$

while the contribution from the second term in (8.40) is $(\omega_i \tau_i)^2$ times smaller:

$$Q_{\text{visc}}^{(2)} \simeq \frac{nT \tau_i}{(\omega_i \tau_i)^2} \frac{\delta v^2}{\lambda^2} \quad (8.45)$$

Since δT is of the order of $T_0(\delta v/\omega\lambda)$, Q_{therm} is of the same order as $Q_{\text{visc}}^{(2)}$, i.e. $(\omega_i \tau_i)^2$ times smaller than the viscous dissipation due to η_0 , and also can be ignored.

The Ohmic dissipation is estimated as follows:

$$Q_{\text{ohm}} \simeq \left(\frac{c}{4\pi}\right)^2 \frac{\delta B^2}{\sigma \lambda^2} \quad (8.46)$$

where $\sigma \sim \omega_{pe}^2 \tau_e / 4\pi$ is the plasma conductivity.

Now we can estimate the ratio of Q_{ohm} to $Q_{\text{visc}}^{(2)}$, bearing in mind that δB is of the order of $(B_0/\omega\lambda)$:

$$\frac{Q_{\text{ohm}}}{Q_{\text{visc}}^{(2)}} \simeq \sqrt{\frac{m_e}{m_i}} \frac{1}{\beta_0} \quad (8.47)$$

where $\beta_0 = 8\pi p_0/B_0^2$ is plasma β in the unperturbed state. That is, for not too small β_0 , Q_{ohm} is much smaller than $Q_{\text{visc}}^{(2)}$ and Q_{therm} , and even more so with respect to $Q_{\text{visc}}^{(1)}$.

Consequently, the damping rate is essentially determined only by $Q_{\text{visc}}^{(1)}$:

$$\Gamma \simeq \frac{Q_{\text{visc}}^{(1)}}{W} \quad (8.48)$$

As the estimate for the energy density is

$$W \simeq m_i n \delta v^2, \quad (8.49)$$

we obtain the following estimate for Γ :

$$\Gamma \simeq \frac{T \tau_i}{m_i \lambda}. \quad (8.50)$$

The reason why the damping rate in a plasma with small scale inhomogeneities may become much larger than that given by (8.50) is that in such a case all perturbed quantities ($\delta \tilde{v}$, $\delta \tilde{B}$, $\delta \tilde{T}$ etc.) have a component that changes *not at a scale* λ , but at a scale R , so that all the spatial derivatives in (8.39)–(8.43) become much larger than for waves traveling in a homogeneous plasma.

Assuming that inhomogeneities are of the order of unity, $\tilde{\rho} \simeq \rho$, one can expect that all dissipative terms increase by the factor $(\lambda/R)^2 \gg 1$.

Note, however, that the main dissipative term, $Q_{\text{visc}}^{(1)}$, does not increase in the inhomogeneous case. This happens because it is proportional to $(\text{div} \delta v)^2$ and, $(\text{div} \delta v)$ is of the order of $\delta v/\lambda$ even in the case of an inhomogeneous plasma. Therefore, the enhancement of dissipation comes only from terms $Q_{\text{visc}}^{(2)}$ and $Q_{\text{therm}}^{(1)}$.

Although the dissipation in homogeneous case, caused by $Q_{\text{visc}}^{(2)}$ and $Q_{\text{therm}}^{(1)}$ is much less than by $Q_{\text{visc}}^{(1)}$, in some cases of an inhomogeneous plasma it can be quite large, resulting in a much faster damping than that determined by (8.50). This will be discussed in the next section.

8.2.2 Medium with Moderate and Strong Inhomogeneities

Even though the main dissipation term does not increase, the terms $Q_{\text{visc}}^{(2)}$ and $Q_{\text{therm}}^{(1)}$ increase by a factor $(\lambda/R)^2 \tilde{\rho}_0/\rho_0$, where $\tilde{\rho}_0$ is the characteristic amplitude of the inhomogeneities (see Eq. (8.20)). Thus, if

$$\frac{\lambda}{R} \frac{\tilde{\rho}_0}{\rho_0} > \omega_i \tau_i, \quad (8.51)$$

$Q_{\text{visc}}^{(2)}$ and $Q_{\text{therm}}^{(1)}$ become much larger than $Q_{\text{visc}}^{(1)}$, resulting in the significant enhanced dissipation of an incoming wave power.

Thus, under condition (8.51), the energy dissipation is determined by the sum $Q_{\text{visc}}^{(2)} + Q_{\text{therm}}^{(1)}$, and can be estimated as

$$Q_{\text{visc}}^{(2)} + Q_{\text{therm}}^{(1)} \simeq \frac{nT \tau_i}{(\omega_i \tau_i)^2} \frac{\delta v^2}{R^2} \left(\frac{\tilde{\rho}_0}{\rho_0} \right)^2 \quad (8.52)$$

Q_{ohm} remains related to $Q_{\text{visc}}^{(2)}$ by the estimate (8.47) and is thus much smaller than $Q_{\text{visc}}^{(2)}$. The damping rate can be found from (8.49) and (8.52):

$$\Gamma \simeq \frac{T \tau_i}{m_i R^2} \frac{1}{(\omega_i \tau_i)^2} \left(\frac{\tilde{\rho}_0}{\rho_0} \right)^2 \quad (8.53)$$

In previous calculations we assumed that initially the plasma was stationary. However, in an inhomogeneous plasma there are processes of thermal conductivity and magnetic field diffusion that tend to reduce inhomogeneities. The shorter of the two is the thermal conductivity time,

$$\tau_{\text{therm}} \simeq \frac{R^2 n}{\chi} \simeq \left[\frac{T \tau_i}{m_i R^2} \frac{1}{(\omega_i \tau_i)^2} \right]^{-1} \quad (8.54)$$

Consideration of a stationary background in the problem of the absorption of the wave power requires the condition $\Gamma \tau_{\text{therm}} \gg 1$ to be satisfied. However, from (8.53) and (8.54) it is obvious that τ_{therm} is always much smaller than Γ^{-1} , which means that the background temperature becomes homogeneous much earlier than the wave is damped. This is just the reason why we assumed that the plasma in the initial state has a homogeneous temperature (see discussion following (8.43)).

The diffusion of the magnetic field occurs over a time scale

$$\tau_{\text{diff}} \simeq \frac{4\pi R^2 \sigma}{c^2} \simeq \tau_{\text{therm}} \sqrt{\frac{m_i}{m_e}}, \quad (8.55)$$

(we consider the case when plasma $\beta \simeq 1$).

From the condition $\Gamma \tau_{\text{diff}} \gg 1$, we obtain the following restriction on plasma parameters:

$$\left(\frac{\tilde{\rho}_0}{\rho_0} \right)^2 \gg \sqrt{\frac{m_e}{m_i}}. \quad (8.56)$$

Assuming that the condition (8.56) is satisfied, we calculate the enhanced damping rate for the plasma with a moderate level of inhomogeneities, $\tilde{\rho}_0/\langle \rho_0 \rangle < 1$. In the initial stationary state we have a regular equation of state $p_0(x, y) = (2/m_p) \rho_0(x, y) \cdot T_0(x, y)$.

Using (8.6)–(8.8) we can express δT through the displacement vector

$$\delta T = -T_0(\gamma - 1) \text{div} \xi \quad (8.57)$$

Now from Eqs. (8.11)–(8.13) we have:

$$\frac{\delta T}{T} = (\gamma - 1) \frac{\delta \rho}{\rho} = \frac{\delta P}{P} \frac{\gamma - 1}{\gamma + (2 - \gamma)(P_m/P)}, \quad (8.58)$$

and, using the adiabatic relation, we have for $\delta\rho$:

$$\frac{\delta\rho}{\rho} = \frac{\delta P}{P} \frac{1}{\gamma + (2 - \gamma)(P_m/P)}. \quad (8.59)$$

Thus, when the acoustic or MHD waves propagate in the dense conglomerate of flux tubes, there are always temperature and density perturbation with a scale R which is much less than λ . The enhanced dissipation of incoming waves is caused just by these steep temperature and density gradients.

8.2.3 Dissipation by Thermal Conduction

The dissipation caused by thermal conductivity is described by the expression

$$Q_{\text{therm}} = \frac{\chi}{T} \langle (\nabla \delta T)^2 \rangle \quad (8.60)$$

The average is taken over a scale which is much larger than R . For δT given by (8.58) we obtain

$$Q_{\text{therm}} = \frac{\chi}{T} \left(\frac{\gamma - 1}{\gamma} \right)^2 \frac{\delta P_0^2}{[P + (2/\gamma - 1)P_m]^2} \times \left\{ k^2 + \left\langle \frac{(2/\gamma - 1)^2 (\nabla P_m)^2}{[P + (2/\gamma - 1)P_m]^2} \right\rangle \right\} \quad (8.61)$$

where we have taken into account that $k \ll 1/R$ and have assumed the sinusoidal dependence of δP on x : $\delta P = \delta P_0 \sin(kx - \omega t)$.

The first term in the curly brackets corresponds to the usual dissipation of p-modes in a homogeneous medium while the second term describes the additional damping associated with strong inhomogeneities.

The spatial damping rate $\text{Im } k_T$ caused by thermal dissipation (see, e.g., Landau and Lifshitz 1984) is

$$\text{Im } k_T = \frac{Q_{\text{therm}}}{2c_s E_0} \quad (8.62)$$

where $E_0 = \rho(\delta v)^2/2$ is the energy density of the initial acoustic wave.

Let us express now the velocity perturbations in terms of the total pressure perturbations

$$\delta v = \frac{\delta P}{\rho v_{\text{ph}}} \quad (8.63)$$

where v_{ph} is determined by (8.26).

As an example, let us choose an isotropic distribution of inhomogeneities. In this case in (8.26), $Q_{\alpha\beta} = 0$ and

$$v_{\text{ph}}^2 = \frac{\gamma}{\rho} \left[P = \left(\frac{\gamma}{2} - 1 \right) P_m \right]. \quad (8.64)$$

Using (8.26) and (8.61)–(8.64) we can write for the damping rate

$$\text{Im } k_T = \frac{\chi}{2c_s} \frac{T(\gamma - 1)^2}{\gamma[P + (2/\gamma - 1)P_m]} \left\{ k^2 + \left\langle \frac{(2/\gamma - 1)^2 (\nabla P_m)^2}{[P + (2/\gamma - 1)P_m]^2} \right\rangle \right\} \quad (8.65)$$

From (8.58)

$$\frac{T(\gamma - 1)^2}{\gamma[P + (2/\gamma - 1)P_m]} = \frac{\delta T}{\delta P}. \quad (8.66)$$

The equation of state and an adiabatic relation of the temperature and gas pressure give

$$\frac{\delta T}{\delta p} \simeq \frac{\delta T}{\delta P} = \frac{1}{\gamma c_V}, \quad (8.67)$$

where instead of the number density n we used the specific heat at constant volume, $c_V = n/(\gamma - 1)$. Combining (8.64), (8.65), and (8.67), for the spatial damping rate we obtain

$$\text{Im } k_T = \frac{\kappa}{2c_s} \frac{\gamma - 1}{\gamma} \left\{ k^2 + \left\langle \frac{(2/\gamma - 1)^2 (\nabla P_m)^2}{[P + (2/\gamma - 1)P_m]^2} \right\rangle \right\} \quad (8.68)$$

where $\kappa = \chi/c_V$ is the thermal diffusivity.

Note that in denominator of the second term in (8.68) the last term is numerically small compared to the first term; for $\gamma = 5/3$, it is only 0.2 of the first term even when $p/P = 1$ (i.e., in nonmagnetic medium, while in sunspots $p/P < 1$ always). This allows us to use the expansion

$$\frac{1}{[P + (2/\gamma - 1)P_m]^2} \simeq \frac{1}{P^2} \left[P - 2 \left(\frac{2}{\gamma} - 1 \right) \frac{P_m}{P} \right], \quad (8.69)$$

and write

$$\text{Im } k_T = \frac{\kappa}{2c_s} \frac{\gamma - 1}{\gamma} \left\{ k^2 + \left\langle \frac{(2/\gamma - 1)^2 (\nabla P_m)^2}{P^2} \right\rangle \right\}. \quad (8.70)$$

For flux tubes with known internal structure we can easily take the average of $\langle (\nabla P)^2 \rangle$. As an example, suppose the magnetic field decreases from axis according

to, say, a Gaussian law,

$$B = B_{\max} \exp(-r^2/R^2). \quad (8.71)$$

With the characteristic distance between flux tubes' centers d and the flux tube areal filling factor to be $f = R^2/d^2$, we have

$$\left\langle \frac{(\nabla P_m)^2}{P^2} \right\rangle = \frac{f}{R^2} \left\langle \frac{P_{m,\max}^2}{P^2} \right\rangle \quad (8.72)$$

In what follows we omit the angle brackets and bear in mind that the ratio $P_{m,\max}^2/P^2$ is averaged over the ensemble of flux tubes. Note that we use here adiabatic approach which is valid for wavenumbers

$$k > k_T \equiv \frac{\kappa}{R^2 c_s} \quad (8.73)$$

Finally, for the spatial damping rate caused by thermal losses we have:

$$\text{Im } k_T = \frac{\kappa}{2c_s} \frac{\gamma - 1}{\gamma} \left[k^2 + \left(\frac{2}{\gamma} - 1 \right)^2 \frac{f}{R^2} \frac{P_{m,\max}^2}{P^2} \right] \quad (8.74)$$

For Gaussian magnetic field profile in a flux tube, the average magnetic pressure of the flux tube is $\langle P_m \rangle = f P_{m,\max}^2/2$. Even in the case of closely packed flux tubes, with $f \simeq 1$, the average magnetic pressure will be reduced below its maximum value, which should be taken into account in constructing equilibrium sunspot models.

8.2.4 Dissipation by Viscosity

A very similar mechanism leads to enhancement of the viscous dissipation. The plasma densities inside and outside the individual flux tube are usually different and the total pressure perturbation δP gives rise to a relative motion of flux tube and the external plasma. The characteristic scale of these motions is of the order of R . The viscous dissipation

$$Q_v = \frac{\eta}{2} \left(\frac{\partial v_i}{\partial x_k} + \frac{\partial v_k}{\partial x_i} - \frac{2}{3} \delta_{ik} \text{div} \mathbf{v} \right)^2 + \zeta (\text{div} \mathbf{v})^2 \quad (8.75)$$

can greatly exceed its homogeneous value. Calculations similar to those made in previous section, give

$$Q_v = \frac{c_s^2}{2} \left(\frac{4}{3} \eta + \zeta \right) \frac{\delta P^2}{P^2} \left\{ k^2 + \frac{\eta}{(4/3)\eta + \zeta} \left\langle \left[\nabla \left(1 - \frac{\rho}{\langle \rho \rangle} \right) \right]^2 \right\rangle \right\} \quad (8.76)$$

Assuming that the temperature of the plasma in the unperturbed state (in absence of the wave) is more or less uniform, we can write that $[1 - \rho/\langle \rho \rangle] = p + p_m/P$. With this, for the spatial damping rate $\text{Im } k_v$, caused by viscous dissipation, we obtain

$$\text{Im } k_v = \frac{7}{6} \frac{\nu}{c_s} \left(k^2 + \frac{3}{7} \frac{f}{R^2} \frac{P_{m,\max}^2}{P^2} \right), \quad (8.77)$$

where we assumed that $\zeta \sim \eta$ and have introduced a kinematic viscosity $\nu = \eta/\rho$.

Equation (8.76) has been obtained under the assumption that the viscous forces have a weak influence on the velocity field which is determined by the inertial forces. This is true for time scales ω^{-1} of the perturbations less than the time of establishing of viscous flows over the scale R , $\omega^{-1} \leq R^2\nu$. Thus, the damping rate (8.77) is valid if the condition analogous to condition (8.73) is satisfied, that is, if

$$k > k_{cv} \equiv \frac{\nu}{R^2 c_s}. \quad (8.78)$$

8.2.5 Total Dissipation Rate

The total damping rate which includes both thermal and viscous losses is simply the sum of expressions (8.74) and (8.77). Both these expressions contain two parts: the usual absorption of sound waves in medium with finite viscosity and thermal conductivity, and the absorption caused by the presence of small-scale inhomogeneities.

Let us denote the spatial damping rate corresponding to the usual losses (i.e., in homogeneous medium) as $\text{Im } k_1$ and the damping rate caused by the strong local gradients by $\text{Im } k_2$. Then the total damping rate is

$$\text{Im } k = \text{Im } k_1 + \text{Im } k_2, \quad (8.79)$$

where

$$\text{Im } k_1 = \frac{k^2}{2c_s} \left[\frac{7}{3} \nu + \left(1 - \frac{1}{\gamma} \right) \kappa \right] \quad (8.80)$$

and

$$\text{Im } k_2 = \frac{f}{2c_s R^2} \frac{P_{m,\max}^2}{P^2} \left[\nu + \left(1 - \frac{1}{\gamma}\right) \left(1 - \frac{2}{\gamma}\right)^2 \kappa \right]. \quad (8.81)$$

For pure molecular transport, the kinematic viscosity ν and the thermal diffusivity κ are of the same order of magnitude. In this case, because of the small numerical factor in the second term in (8.81), the enhanced dissipation is dominated by viscosity. The same conclusion holds in the case of a turbulent viscosity and thermal conductivity, when

$$\nu \sim \kappa \sim \tilde{v} \tilde{l} \quad (8.82)$$

with \tilde{v} being a characteristic velocity of turbulent elements and \tilde{l} their characteristic scale. Thermal dissipation may become more important in the case of a large radiative heat transfer where $\kappa \gg \nu$.

It is important that, although formally $\text{Im } k$ contains k^2 through $\text{Im } k_1$, the damping rate does not depend on k : according to our basic assumption the scale of inhomogeneities R is much less than the acoustic wavelength, $k^2 R^2 \ll 1$, and, respectively,

$$\text{Im } k_1 \ll \text{Im } k_2. \quad (8.83)$$

So that the absorption is completely determined by the anomalous damping rate $\text{Im } k_2$:

$$\text{Im } k_2 = \frac{1}{2} \frac{f P_{m,\max}^2}{P^2} \frac{\nu}{c_s R^2}. \quad (8.84)$$

We neglected here the second term in square brackets in (8.81), and have taken into account the condition (8.82).

Respectively, the enhancement factor

$$\text{EF} = \text{Im } k_1 / \text{Im } k_2 \quad (8.85)$$

is

$$\text{EF} = \frac{3f}{7k^2 R^2} \frac{P_{m,\max}^2}{P^2}, \quad (8.86)$$

which because of $k^2 R^2 \ll 1$ is quite large.

We see that the expression for $\text{Im } k_2$ contains the critical wavenumber:

$$k_{\text{cr}} = \frac{\nu}{R^2 c_s}. \quad (8.87)$$

This quantity plays a significant role in the interaction of the wave with the inhomogeneous medium.

Finally, taking into account the condition (8.81) we can neglect $\text{Im } k_1$ in (8.79) and represent the total damping rate as follows:

$$\text{Im } k = \frac{1}{2} \frac{f P_{m,\max}^2}{P^2} k_{\text{cr}} \quad (8.88)$$

This expression shows, first of all, that the damping of acoustic waves does not depend on the wavenumber and is determined by the physical properties of absorption region: magnetic filling factor, the scale of inhomogeneities, dissipative coefficients, sound speed, and the average magnetic field.

The dependence of the absorption on the magnetic field is quite specific and needs separate comments. Namely, according to (8.88) the damping rate is proportional to B^4 . At large values of magnetic field, when $P_{m,\max}^2$ becomes of the order of P^2 the damping rate does not depend on magnetic field any more and there occurs a saturation of the absorption enhancement over the magnetic field strength.

So that, for high enough magnetic field, such that $P_{m,\max}^2 \simeq P^2$ we have

$$\text{Im } k = \frac{f}{2} k_{\text{cr}}. \quad (8.89)$$

The other important meaning which carries the expression (8.88) is that it allows us to introduce the specific parameter μ which actually determines the acoustic opacity of the region:

$$\mu = \frac{\text{Im } k}{k} = \frac{1}{2} \frac{f P_{m,\max}^2}{P^2}. \quad (8.90)$$

An important feature of the parameter μ is that it does not depend on the assumptions on the particular value of viscosity ν and, in this respect, is independent on the particular model of viscous transport.

It is also important that the local damping rate has no dependence on the sunspot size; the total absorption of a spot then scales simply with the path length through the spot, that is, the sunspot dimension L . We will see below that these features are totally consistent with the observations.

If α is the total absorption of the wave propagating through the sunspot, the spatial damping rate can be evaluated as

$$\text{Im } k = \frac{1}{L} \ln \left(\frac{1}{1 - \alpha} \right). \quad (8.91)$$

So that the total damping coefficient, $\alpha = 1 - \exp(-\text{Im } kL)$ depends only on the size of sunspot (or/and plage) and on the physical parameters of medium:

$$\alpha = 1 - \exp\left(-\frac{1}{2} \frac{f P_{m,\max}^2}{P^2} k_{\text{cr}} L\right). \quad (8.92)$$

8.3 Anomalous Damping at Small Wavevectors

In the previous sections, to find the dissipation rate of p-modes, we concentrated on the region of wave vectors higher than some critical value k_{cr} . In this section we extend the analysis to the region of low wavenumbers (low frequencies) when conditions (8.73) and (8.78) break, and

$$k < k_{\text{cr}} \quad (8.93)$$

We will see that the picture of anomalous damping of p-modes described above considerably changes at smaller wave vectors. First of all, the viscous forces inhibit the relative motions of the flux tubes and the ambient gas (“sloshing mode”), thus reducing the dissipation enhancement: there appears a strong dependence of the damping rate on the wavevector (and frequency), and $\text{Im } k$ decreases with decreasing wave number. The same happens with the damping process provided by thermoconductivity. In what follows, we, as before, assume that $\nu \sim \kappa$.

We start from the description of the dissipation caused by the thermal losses. At $k < \kappa/(R^2 c_s)$, the temperature and density perturbations become nonadiabatic and their relation should be estimated from the full thermoconductivity equation:

$$\frac{d}{dt} \left[\delta T - (\gamma - 1) \frac{T \delta \rho}{\rho} \right] = \kappa \Delta \delta T. \quad (8.94)$$

Evaluating for estimation $d\delta T/dt$ as $\omega \delta T$, and $\kappa \Delta \delta T$ as $\kappa \delta T/R^2$, we obtain that at $k < k_{\text{cr}}$ the first term in the left-hand side of (8.94) becomes negligibly small as compared to the right-hand side. Hence, the relation between the temperature and density perturbation is determined by the expression

$$\left| \frac{\delta T}{T} \right| \simeq k c_s (\gamma - 1) \frac{R^2 \delta \rho}{\kappa \rho} \quad (8.95)$$

Using here the definition for k_{cr} analogous to (8.87), instead of (8.58), we have

$$\left| \frac{\delta T}{T} \right| \simeq \frac{k}{k_{\text{cr}}} (\gamma - 1) \frac{\delta \rho}{\rho} = \frac{k}{k_{\text{cr}}} \left| \frac{\delta P}{P} \right| \frac{\gamma - 1}{\gamma + (2 - \gamma)(P_m/P)}. \quad (8.96)$$

The factor k/k_{cr} that appears in (8.96) obviously gives rise to the dependence of the dissipation rate on the wavenumber, and, respectively, on frequency. After the substitution of (8.96) in (8.60) the same procedure described in Sect. 8.2.2 leads to the following expression for damping rate at $k < k_{\text{cr}}$ (cf. (8.74)):

$$\text{Im } k_T \simeq \frac{k_{\text{cr}} \gamma - 1}{2 \gamma} \left[k^2 R^2 + \left(\frac{2}{\gamma} - 1 \right)^2 \frac{k^2 f P_{m,\text{max}}^2}{k_{\text{cr}}^2 P^2} \right] \quad (8.97)$$

We see that the contribution provided by the presence of small-scale inhomogeneities of magnetic field (the second term in square brackets) is still larger than the homogeneous one:

$$f \frac{P_{m,\text{max}}^2}{P^2} > k_{\text{cr}}^2 R^2. \quad (8.98)$$

As was mentioned above, at $k < v/(R^2 c_s)$ the relative motions of flux tubes and ambient plasma is inhibited by viscous forces. Indeed, one can see from Navier-Stokes equation that the Archimedean force is now balanced by the viscous friction and the velocity δv of relative motions of fluid elements with different unperturbed densities should be determined from the condition

$$\frac{v}{R^2} \left| \frac{\delta v}{v} \right| \simeq \omega \frac{\delta \rho}{\rho} \quad (8.99)$$

with $\omega = k c_s$, this estimate becomes as

$$\left| \frac{\delta v}{v} \right| \simeq \frac{k}{k_{\text{cr}}}, \frac{\delta \rho}{\rho} \quad (8.100)$$

and, finally, the damping rate for $k < k_{\text{cr}}$ becomes as follows (cf. (8.77)):

$$\text{Im } k_v \simeq k_{\text{cr}} \left(\frac{7}{6} k^2 R^2 + \frac{1}{2} \frac{k^2 f P_{m,\text{max}}^2}{k_{\text{cr}}^2 P^2} \right), \quad (8.101)$$

Exactly as in the case of thermal losses, here we have that the anomalous damping caused by the presence of small-scale inhomogeneities even at small wavenumbers is still larger than the dissipation in a uniform medium. Although both expressions, (8.77) and (8.101), are the order-of-magnitude estimates, they allow us to perform qualitative, and at some degree, quantitative analysis of observational data of p-mode absorption by sunspots. This is done in the next section.

8.4 Absorption of p-Modes by Sunspots and Active Regions—Observations

By analyzing the velocity field inside and outside a sunspot, one can directly detect the difference between the radially propagating components of the incident and outgoing waves. The most natural way to perform this analysis is to use a polar coordinate system centered on the sunspot (Braun et al. 1987). The general procedure is analogous to the partial wave analysis in classical mechanics.

The general solution of the two-dimensional wave equation in polar coordinates, (r, ϕ) , is given by the two kinds of Hankel functions, representing incoming, $H_m^{(1)}(k, r)$, and outgoing, $H_m^{(2)}(k, r)$, waves

$$\Psi_m(r, \theta, t) = e^{(i\omega t + im\phi)} [A_m(\omega, k)H_m^{(1)}(k, r) + B_m(\omega, k)H_m^{(2)}(k, r)] \quad (8.102)$$

Here, m is the azimuthal wave number, k is the horizontal wavenumber, and A_m and B_m are complex coefficients. Both are determined by power and phase of the waves; A_m corresponds to the wave traveling radially inward and B_m to outward wave.

If there is no absorption of incoming waves, then $A_m = B_m$, and radial component of the wave amplitude can be expressed by Bessel function of the first kind. If, however, there is a sink of wave power, then $|A_m| \neq |B_m|$, and there appears a net flow of power either toward or away from the center of sunspot.

Long-run temporal sequences of two-dimensional longitudinal velocity fields were recorded in the vicinity of several sunspots, pore, and a region of quiet sun. A summary of the observational parameters is given in Table 8.1. First column is the date of the observation. The second column is the object of the observation. Following columns list the total duration of the run, the interval between the successive scans, the spatial extent of the object of the observation and resolution of each scan.

A refined data reduction method which was employed by Braun et al. (1987, 1988) for the analysis of each time series showed that unlike quiet sun region, for each studied sunspot, there was a significant deficit of outgoing power in comparison with incoming power.

Figure 8.5 shows example of the 1986 October run. $|A_m|^2$ and $|B_m|^2$, i.e. power of incoming and outgoing waves summed over all computed azimuthal orders are

Table 8.1 1983, 1986 observing parameters

Date	Activity	Duration (h)	Time interval	Size (arcsec)	Resolution (arcsec)
1983 January 18	Spot	4.1	90.8	512 × 240	1 × 1
1983 February 23	Spot	6.0	90.8	512 × 240	1 × 1
1983 April 26	Quiet	6.4	91.0	512 × 240	1 × 1
1986 October 24	Spot	7.8	96.1	512 × 480	1 × 2
1986 October 25	Spot	5.8	96.3	512 × 480	1 × 2
1986 November 20	Pore	8.4	93.1	512 × 460	1 × 2

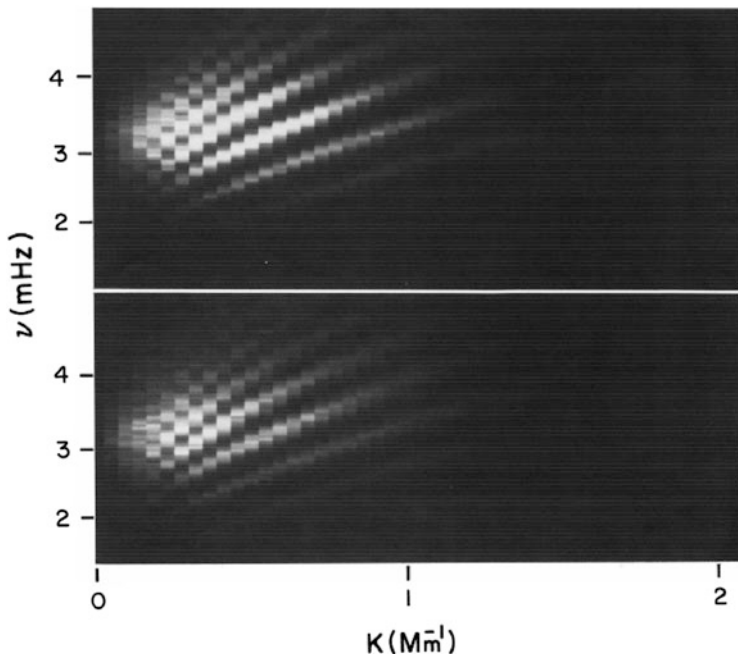


Fig. 8.5 The power spectrum computed in the $k - \omega$ plane for the 1986 October time series, summed over all azimuthal orders. Power spectra were computed individually for the October 24 and 25 observing runs and combined for the purposes of this illustration. The top and bottom halves of the diagram indicate the power present in inward and outward propagating waves, respectively. A deficit of outward traveling waves is clearly seen in all of the ridges. Reprint from Braun et al. (1988) by permission from IOP copyright AAS

plotted in the $k - \omega$ plane. The structure of the p-mode ridges in this diagram is identical to that determined by analysis of quiet sun oscillations with difference that instead of, e.g., spherical harmonic degree ℓ , the radial wavenumber has been used in the present analysis. The top and bottom panels show the amplitude of incoming and outgoing waves, respectively. Note that both, $|A_m|$ and $|B_m|$, are each summed over the interval of azimuthal wavenumbers of $-5 \leq m \leq 5$. A deficit of outward traveling waves is clearly seen in all of the p-mode ridges.

In all studies, it was found that for each of the sunspot observations there was a substantial deficit of outgoing power relative to incoming power. This power deficit can be characterized by an absorption coefficient defined as

$$\alpha = \frac{\mathcal{P}_{in} - \mathcal{P}_{out}}{\mathcal{P}_{in}} \tag{8.103}$$

where \mathcal{P}_{in} and \mathcal{P}_{out} are the total power in the incoming and outgoing p-modes summed over all azimuthal orders and over the frequency interval of $1.5 \text{ mHz} \leq$

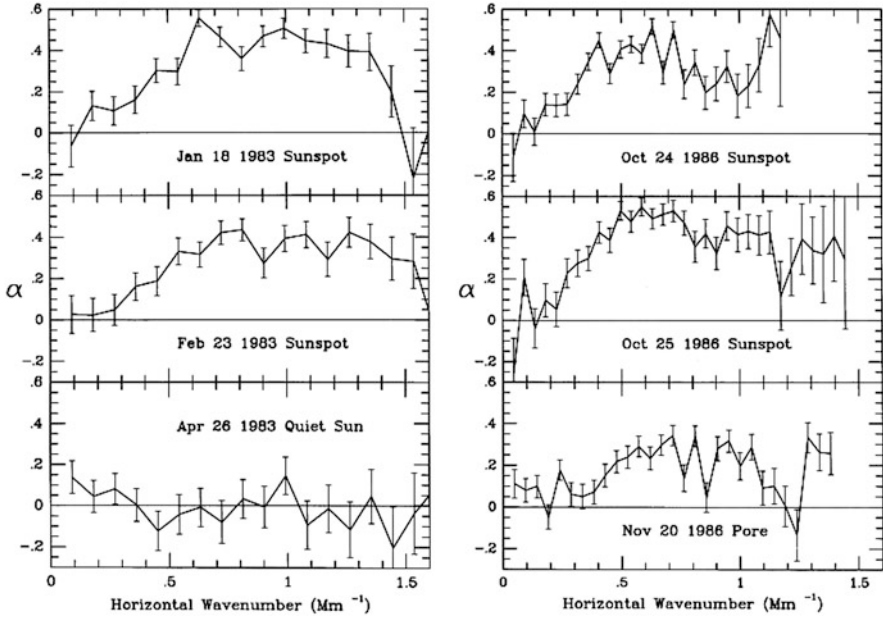


Fig. 8.6 The absorption coefficient α vs. horizontal wavenumber for sunspots, pore and the quiet sun. In all cases α is shown up to the horizontal wavenumber where p-mode power could still be discerned from the background noise. The errors were calculated from the statistical properties of the power spectra and a standard treatment of the error propagation. Reprint from Braun et al. (1988) by permission from IOP copyright AAS

$\nu \leq 5$ mHz. The background noise visible outside of the p-mode ridges has been estimated and subtracted from the total power before calculating α .

Figure 8.6 shows the dependence of α on horizontal wavenumber where the incoming and outgoing wave power has been summed over azimuthal orders $-5 \leq m \leq 5$. Every sunspot and even a pore show significant absorption of p-mode oscillations. In the case of the January 1983 and October 1986 sunspots as much as 50% of incoming power has been absorbed. It is important to note that the amount of absorption is constant at the higher wavenumbers ($k \geq 0.5 \text{ Mm}^{-1}$), but noticeably drops as k approaches 0. For comparison with sunspot behavior the measurements were performed over the quiet sun region (see panel marked April 26, 1983). One can see that the quiet sun observations, as expected, show no significant difference between incoming and outgoing power.

In the subsequent studies, a significant improvement in the measurements of p-mode absorption and scattering amplitudes, and in particular, the increased temporal frequency resolution, provided a greater details in the interaction of p-modes with sunspots, active regions and quiet sun (see, e.g., Gizon et al. 2009 and literature therein).

The observed regularities can be summarized as follows.

1. The absorbing regions are spatial coincident with sunspots and plages seen on the solar surface, with some differences in detail.
2. The fraction of the incident p-mode power absorbed is zero at low wavenumbers, $k \leq 0.1 \text{ Mm}^{-1}$, then rises to a high value at higher wavenumbers, $k > 0.4 \text{ Mm}^{-1}$. The absorbed fraction remains constant at the high value to the observational limit at $k \sim 1 \text{ Mm}^{-1}$.
3. The onset of absorption occurs at lower wavenumbers and the absorbed fraction is higher in larger sunspots than in smaller sunspots and pores. Typical isolated sunspots absorb 40% of p-mode power at high wavenumber ($k > 0.4 \text{ Mm}^{-1}$). Giant sunspots absorb up to 70%, while small ones absorb only 20%.
4. The absorbed fraction is larger in sunspots than in plages, but the acoustic opacity, the absorption per unit magnetic field, appears to be saturated in sunspots, whereas in plages this effect was not observed.
5. The dependence on the temporal frequency shows a broad peak in p-mode absorption centered approximately at 3 mHz.

Understanding the direct interaction of p-modes with sunspots and plages is a powerful tool in probing inhomogeneities in sunspot interior and for developing the helioseismology methods. It is remarkable that the mechanism of the enhanced absorption of acoustic wave power by sunspots, described earlier in this chapter has been developed before the observational data became available (Ryutova and Persson 1984). The comparison of theory and observations turned out to be remarkably good (LaBonte and Ryutova 1993). In the next section we overview these results.

8.5 The Interpolation Formula and Comparison with Observations

The qualitative analysis of the p-mode absorption (LaBonte and Ryutova 1993) shows that at low wavenumbers the damping rate depends on the magnitude of wavenumbers and increases quadratically with the increasing wavenumbers. The total damping rate provided by both, viscosity and thermal conductivity (in sunspot environment $\nu \simeq \kappa$) according to (8.97) and (8.101), is

$$\begin{aligned} \frac{\text{Im } k}{k_{\text{cr}}} &\simeq \left(\frac{7}{6} + \frac{\gamma - 1}{2\gamma} \right) k^2 R^2 \\ &+ \left[1 + \left(1 - \frac{1}{\gamma} \right) \left(1 - \frac{2}{\gamma} \right)^2 \kappa \right] \frac{k^2 f P_{m,\text{max}}^2}{k_{\text{cr}}^2 2P^2} \end{aligned} \quad (8.104)$$

This expression for the damping rate is valid up to the critical values of $k \simeq k_{\text{cr}}$, above which the enhancement of the absorption becomes more efficient and reaches its saturation.

The damping rate corresponding to the saturation regime is given by (8.88), and, obviously, does not depend on the wavenumber any more.

To unify the description of both limiting cases, $k < k_{cr}$, (8.104), and $k \geq k_{cr}$, (8.88), we will use the following interpolation formula

$$\text{Im } k = q_0 \frac{k^2}{k^2 + k_{cr}^2}, \quad (8.105)$$

where according to (8.88), q_0 is the damping rate corresponding to the saturation over the wavenumber

$$q_0 = \frac{1}{2} \frac{f P_{m,\max}^2}{2P^2} k_{cr}. \quad (8.106)$$

The interpolation formula for the total absorption coefficient (8.92) then is

$$\alpha = 1 - \exp\left(-q_0 L \frac{k^2}{k^2 + k_{cr}^2}\right). \quad (8.107)$$

Using the least squares approximation we can match the curve (8.107) with the observational dependence of the total damping rate α on k .

To do this, we choose six sunspots observed in different times (Braun et al. 1988, 1992; Braun and Duvall 1989). Dates and parameters of the observed objects are shown in Table 8.2. These examples cover the cases from the very small sunspot of November 20, up to the giant active region of March 10.

Using the observational data for α and k in (8.107) we obtain the values of q_0 and k_{cr} for chosen sunspots. The observed and calculated values of α_{\max} are shown in the last two columns in Table 8.2.

The interpolation curves calculated with (8.107) together with the observed absorption seen in all six sunspots are shown in Figs. 8.7, 8.8 and 8.9. The cross indicates the values of critical wave number k_{cr} . Note a remarkably good *qualitative* and *quantitative* matching of observations and theory in *all cases*. This includes the theoretical dependence of the absorption on the wave number and size of sunspot.

Table 8.2 Comparison of the observed and calculated absorption coefficients for six different sunspots

Date	Diameter (Mm)	q_0	k_{cr} (Mm ⁻¹)	$\mu = \text{Im}k/k_{cr}$	α_{\max}	
					Observed	Calculated
1983 January 18	40	0.017	0.44	0.0386	0.50	0.44
1988 February 23	30	0.02	0.516	0.0387	0.45	0.40
1986 October 25	32	0.022	0.33	0.066	0.50	0.45
1986 November 20	8	0.047	0.43	0.11	0.31	0.30
1989 March 10	120	0.013	0.37	0.35	0.78	0.70
1988 November 29	36	0.024	0.445	0.054	0.58	0.45

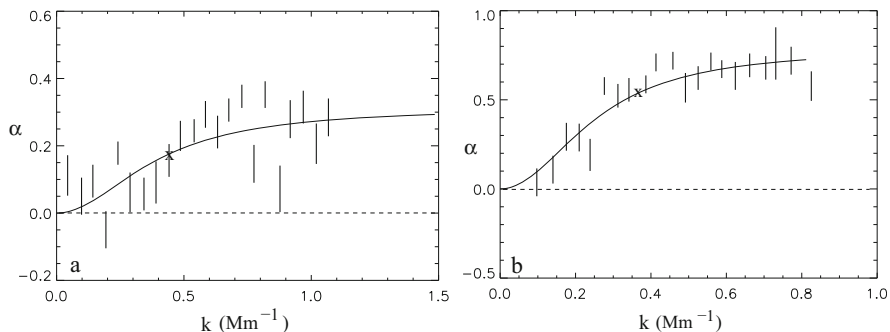


Fig. 8.7 The absorption coefficient α vs. horizontal wavenumber k calculated from theoretical model (solid lines) are compared with the observational data: (a) the 1986 November 20 pore (8 Mm), and (b) the 1989 March 10 giant active region (120 Mm)

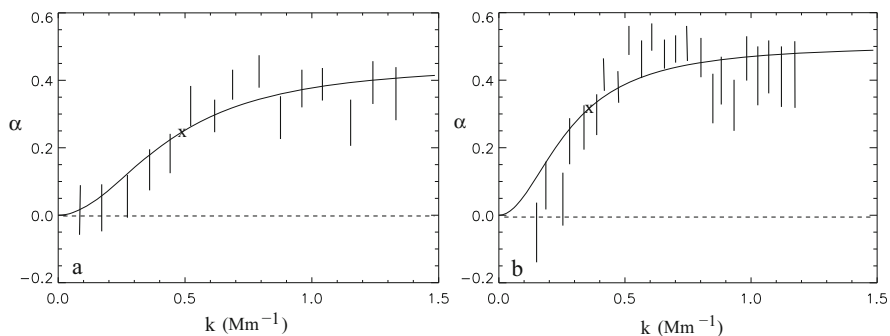


Fig. 8.8 The same as in Fig. 8.7, but two other similar sunspots that are similar in size and properties: (a) the 1983 February 23 sunspot (30 Mm), and (b) the 1986 October 25 sunspot (32 Mm)

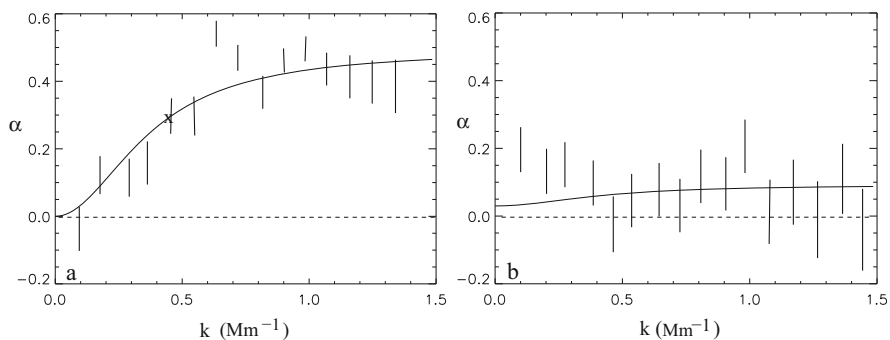


Fig. 8.9 Comparison of the absorption coefficients for (a) a regular sunspot of 1983 January 18 (a) and (b) the quiet sun region taken on 1983 April 26

Recall that at large wavenumbers,

$$k_{\text{cr}} \leq k < 1/\ell, \quad (8.108)$$

where k_{cr} (for $\nu \simeq \kappa$) is given by (8.87), the damping rate is almost constant and by the enhancement factor (EF) larger than in uniformly magnetized plasma (see Eq. (8.86)). Note that in this regime (i.e. $k > k_{\text{cr}}$), the viscous effects and thermal conductivity have less influence on the sloshing mode, and the enhancement of the wave dissipation becomes more efficient, which is reflected in steepening of the theoretical curve in agreement with observational points.

At smaller wavenumbers,

$$k < k_{\text{cr}}, \quad (8.109)$$

the viscosity and thermal conductivity reduce the velocity and temperature fluctuations, and the damping rate $\text{Im}k$ gets proportional to k^2 (and respectively, to ω^2). The enhancement factor in this interval of wave numbers is

$$\text{EF} = \frac{3}{7} \frac{1}{k_{\text{cr}}^2 R^2} \frac{f P_{m,\text{max}}^2}{2P^2}. \quad (8.110)$$

The saturation regime, the very fact of its natural appearance in theory, and the corresponding maximum value of the total absorption coefficient is also in a good agreement with observations.

In conclusion, we overview the basic points of agreements between the theory and the observed properties of the p-mode absorption. For the general estimates we adopt the following typical values: flux tube radius, $R = 50 \text{ km}$; p-mode frequency $\omega/2\pi \times 3 \text{ s}^{-1}$; p-mode wavenumber $k = 0.5 \text{ Mm}^{-1}$; sunspot radius $L = 25 \text{ Mm}$; sound speed $c_s = 10 \text{ km s}^{-1}$.

1. Acoustic absorption is co-spatial with magnetic field locations. In the situation where viscous processes are dominant, we conclude that $\text{Im}k$ in a nonuniform medium increases with respect to the uniform medium by the enhancement factor EF, given by (8.86) at $k \geq k_{\text{cr}}$, and by (8.110) at $k < k_{\text{cr}}$.

For a quantitative estimate, we use the observed quantities for k and R , take the filling factor $f \simeq 1$ as appropriate to a sunspot, and assume that $P_{m,\text{max}}^2/2P^2 = 1/2$, a value consistent with the models of Maltby et al. (1986) for a sunspot with a photospheric magnetic field of $\simeq 2 \text{ kG}$. This gives an enhancement factor of

$$\text{EF} \simeq 3 \times 10^2 \quad (8.111)$$

Thus, the enhancement of absorption is quite large. The absorbing regions should be distinct from the background. The lower filling factor f in plages compared to sunspots explains the reduced absorption seen in the observations, despite the larger size of the plage.

2. The absorbed fraction of the acoustic power rises with increasing wavenumber at low wavenumbers but then levels off and remains constant at high wavenumbers.

From (8.104) we see that at wavenumbers below the critical value k_{cr} which is determined by the thermal and viscous diffusion time scales ((8.73) and (8.78)), $\text{Im}k$ is proportional to k^2 . Soon above the critical value, the absorption saturates and at large enough wavenumbers ($k \simeq 1 \text{ Mm}^{-1}$) becomes constant.

A plot of absorption coefficient versus wavenumber k as calculated from theory for six different sunspots is compared with the observational data (Figs. 8.7, 8.8 and 8.9). The calculated curves adequately describe the observed behavior; this includes the saturation regime, the corresponding maximum values of the total absorption coefficient for each sunspot, and the region of wavenumbers below k_{cr} . The theory clearly indicates that soon after k_{cr} the plot must steepen because at $k \geq k_{\text{cr}}$, and the enhancement of wave dissipation becomes more efficient, which is also in agreement with observational points.

3. The absorption level increases with sunspot size. Theoretically indeed the local damping rate (8.88) has no dependence on sunspot size, and the total absorption of the wave power by a spot scales simply with the path length of the wave through the spot (8.91).

Table 8.2 shows calculated values for the local damping rate $q_0 = \text{Im}k$, critical wavenumber k_{cr} , and the total absorption coefficient α , covering the case of a small sunspot saturating at 30% (1986 November 20) to the giant active region of 1989 March 10 saturating at 70%. The typical isolated sunspots absorb 40–50% of incident acoustic wave power (e.g., 1983 January 18, 1983 February 23), in agreement with observations.

Note that the deviation of critical wavenumbers for different spots from the mean value of $k_{\text{cr}} = 0.4 \text{ Mm}^{-1}$, both in theory and observations, is quite small. This means that, generally speaking, the physical parameters of the medium (mean viscosity ν , sound speed c_s , and scale of inhomogeneities R) are quite similar in different sunspots. In order to explain the typical value of k_{cr} , the kinematic viscosity (neglecting the thermal conductivity contribution) should be of the order of $10 \text{ km}^2 \text{ s}^{-1}$. This is much larger than the kinematic viscosity caused by “molecular” transport (the thermal diffusivity would also be larger than provided by radiative transport). Therefore, we have to assume that within the sunspot some turbulent viscosity is present, which is only natural. If one uses (8.82), then, to fit the calculated value ν , one can use the observed limit on turbulent velocities in sunspots of $\tilde{v} = 2 \text{ km s}^{-1}$ to find the length scale of the turbulence $\tilde{l} \sim 5 \text{ km}$, much smaller than flux tube radius but consistent with Becker’s observed limit on turbulent scales.

A very important parameter for future diagnostic goals is the acoustic opacity coefficient μ , (8.90), the parameter which is determined only by the magnetic field and plasma density distribution over the region and is independent on the particular model of viscous transport.

4. The absorption per unit magnetic field (acoustic opacity) appears to saturate in sunspots compared to plagues. The dependence of the enhancement factor (8.86) on the magnetic field strength is $\text{EF} \sim B^4$ for weak magnetic fields; at large

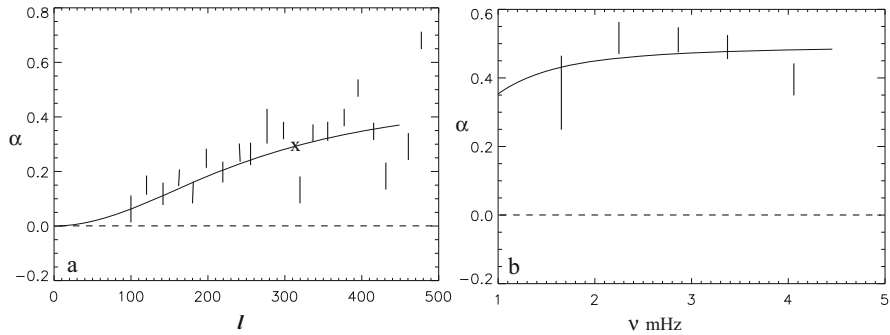


Fig. 8.10 The theoretical curve and the observed absorption coefficient for the 1988 November sunspot (November 27–30 run): (a) vs. spherical harmonic degree of the mode 1, and (b) vs. the wave frequency

values of B , when $P_{m,\max}^2$ becomes of the order of P^2 , the enhancement factor saturates. The same holds with the acoustic opacity, (8.90).

There is no observed saturation over magnetic fields in plages, which is quite natural from theoretical point of view: the average magnetic field strength in plages is hundreds of Gauss (and less); the magnetic filling factor is less than unity ($\simeq 0.3$) which means that magnetic elements are separated by almost magnetic free plasma, and the condition $P_{m,\max}^2 \simeq P^2$ can hardly be reached.

5. In a frame of linear theory, frequency scales linearly with the wavenumber, and we should expect the dependence of the absorption on frequency similar to those on wavenumber. Example of the dependence of the absorption coefficient on frequency is given Fig. 8.10. Shown are the theoretical curve and the observed absorption coefficient for the November 1988 spot. Left panel is dependence on the absorption coefficient of spherical harmonic degree of the mode 1, and right panel dependence on the wave frequency. The theoretical curve is calculated for the saturation regime over the wavenumber which corresponds to the critical wavenumber $k_{\text{cr}} = 0.44 \text{ Mm}^{-1}$, or $\ell_{\text{cr}} = 309.73$. The observational points correspond to $\ell_{\text{cr}} = 308$ (Braun et al. 1992). Thus for frequency dependence comparison of theory with observations shows good qualitative and the order-of-magnitude quantitative agreement, and as we are dealing here with the saturation regime, the calculated curve is smooth.

It must be noted finally that the dispersion relation (8.26) contains much more information on the structure of medium than those inferred above. In particular, it carries information on the statistical properties of the medium providing the dependence of the phase velocities on the angle of the propagation in a plane perpendicular to magnetic field. At the same time, there is always the dependence on the angle between the magnetic field and the direction of the wave propagation, i.e., $v_{\text{ph}} = v_{\text{ph}}^{\parallel} / \cos\theta$. These and other details give wider opportunity for topographical studies of randomly magnetized atmosphere.

8.6 Problem

8.1 Find the pressure fluctuations in a turbulent nonstationary stream in the presence of random fluctuations of velocity.

References

- J.M. Beckers, E.H. Schröter, *Sol. Phys.* **4**, 142 (1968)
S.I. Braginskii, in *Reviews of Plasma Physics*, vol. 1, ed. by M.A. Leontovich (Consultants Bureau, New York, 1965)
D.C. Braun, T.L. Duvall Jr., *Sol. Phys.* **129**, 83 (1989)
D.C. Braun, T.L. Duvall Jr., B.J. LaBonte, *Astrophys. J.* **319**, L27 (1987)
D.C. Braun, T.L. Duvall Jr., B.J. LaBonte, *Astrophys. J.* **335**, 1017 (1988)
D.C. Braun, B.J. LaBonte, T.J. Duvall Jr., *Astrophys. J.* **354**, 372 (1990)
D.C. Braun et al., *Astrophys. J.* **391**, L113 (1992)
L. Gizon Jr. et al., *SSRv* **144**, 249 (2009); *Astrophys. J.* **354**, 372 (1990)
H. Goodarzi et al., *Astrophys. Space Sci.* **358**, 25 (2015)
H. Goodarzi et al., *Astrophys. Space Sci.* **361**, 366 (2016)
M.A. Isakovich, *Sov. Phys. JETP* **18**, 386 (1948)
B. LaBonte, R. Ryutova, *Astrophys. J.* **419**, 388 (1993)
L. Landau, M. Lifshitz, *Fluid Mechanics* (Pergamon Press, Oxford)
W. Livingston, *Nature* **350**, 45 (1991)
P. Maltby, E.H. Avrett, M. Carlsson, O. Kjeldseth-Moe, R.L. Kurucz, R. Loeser, *Astrophys. J.* **306**, 284 (1986)
M. Ryutova, M. Persson, *Phys. Scr.* **29**, 353 (1984)
M. Ryutova, M. Kaisig, T. Tajima, *Astrophys. J.* **380**, 268 (1991)
C. Zener, *Phys. Rev.* **52**, 230 (1937); *Astrophys. J.* **380**, 268 (1991)

Chapter 9

Nonlinear Wave Phenomena in Dense Conglomerate of Flux Tubes



Abstract Nonlinear wave phenomena in strongly inhomogeneous media have a number of specific features that are important for various physical objects where the parameters of medium change by an order of unity over the scales small compared to the wavelength. Generally, one would expect that the presence of strong inhomogeneities may “cut” the steepening of the wave front, and thus prevent formation of shocks. We shall see that this is not always the case. In this chapter, we address this problem based on properties of sunspots and describe the procedure that allows one to obtain nonlinear equations in the presence of strong inhomogeneities. The approach involves dispersion properties of a system, and dissipative effects. The equation itself takes a form similar to KdV–Bürgers equation and thus describes corresponding scenarios of the system evolution. For example, the predominance of dissipative effects leads to damping of the primary wave at linear stage causing direct heating, or, depending on the interplay between nonlinear and dispersion effects, the process of heating may proceed either through the formation of shocks or through the storing of wave energy in a system of solitons which are later damped away. In any case, the presence of inhomogeneities results in strongly enhanced heating compared to that in homogeneous medium.

9.1 Nonlinear Equations in Strongly Inhomogeneous Medium

In the previous chapter, we saw that strongly inhomogeneous areas such as sunspots and active region consisting of tightly settled flux tubes with varying parameters behave as a sink of incoming wave energy. There are however the observed effects, such as strong local brightenings in sunspots, light bridges, explosive events, and others that cannot be described in the frame of linear theory. Besides, the analysis of the enhanced dissipation of the incoming wave energy by dense conglomerate of magnetic domains becomes more complete in nonlinear studies. First of all, we will see that even in the presence of small-scale inhomogeneities the magnetosonic waves of arbitrary (and finite) amplitude can split into two simple (Riemann) waves

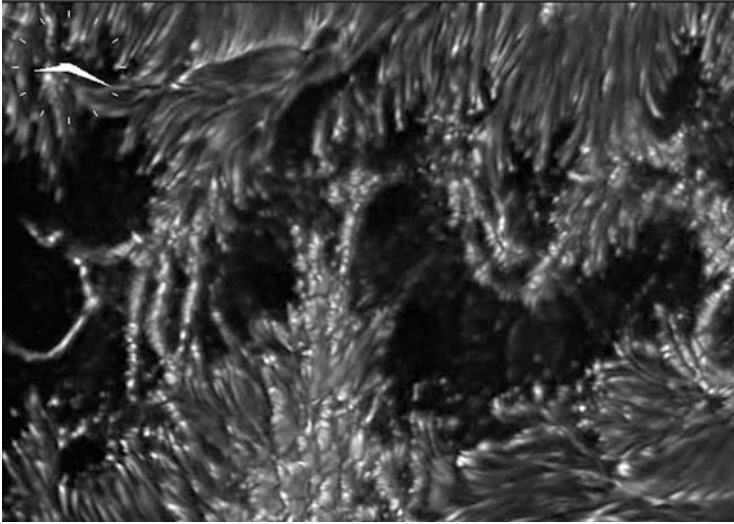


Fig. 9.1 Image of the active region (AR 10375) in G-band covering 80×56 Mm area. One can see spectacular families of local brightenings all over the active region. The image is taken by the DOT on September 9, 2000. Reprinted from <http://www.staff.science.uu.nl>, courtesy of Rob Rutten

traveling in the opposite directions. Each wave has a tendency of steepening and overturning with the subsequent formation of shocks.

The presence of inhomogeneities leads also to the finite dispersion of the wave, having the cubic dependence on wavenumber, and thus to the frequency shift of incident wave.

$$\omega = v_{\text{ph}} \cdot k(1 + \delta^2 k^2) \quad (9.1)$$

The final form of the averaged equations for the finite amplitude wave acquires the form of KdV–Bürgers’ type equations containing the nonlinear, dispersive, and dissipative terms. These terms along their “direct functions” carry the information on statistical properties of the system.

To illustrate small-scale energetic events in magnetic cluster, we show in Fig. 9.1 a captivating image of the active region (AR 09169) in G-band taken by the DOT. One can see ubiquitous small-scale brightenings all over the active region, and, as expected, highly filamentary structure of umbrae (seen as faint white dots).

We start with a semi-two-dimensional analysis and assume that all plasma parameters are random functions of coordinate x : $\rho_0(x)$, $p_0(x)$, $B_0(x)$, $T_0(x)$. The dependence on coordinate y is assumed to be weak so that $\partial/\partial y \ll \partial/\partial x$, and the magnetic field is directed along the z -axis.

The lifetime of such inhomogeneities is determined by the thermal conductivity and diffusion which are small in a strongly magnetized plasma in the direction x perpendicular to the flux tube direction. The inhomogeneities can be considered as

stationary, providing at the same time the total pressure being constant:

$$P_0 = p_0(x) + \frac{B_0^2(x)}{8\pi} = \text{const} \quad (9.2)$$

It is important that we make *no* assumption that inhomogeneities are small: all parameters can change from one domain to another by an order of magnitude.

To describe the magnetosonic wave, we use the ideal MHD equations:

$$\rho \frac{dv}{dt} = -\frac{\partial P}{\partial x}, \quad \frac{d\rho}{dt} + \rho \frac{\partial v}{\partial x} = 0, \quad \frac{dB}{dt} + B \frac{\partial v}{\partial x} = 0, \quad \frac{dp}{dt} + \frac{p}{\gamma} \frac{\partial v}{\partial x} = 0, \quad (9.3)$$

where $d/dt = \partial/\partial t + v(\partial/\partial x)$. From the second and the third equations of the system (9.3), there follows the frozen in flux condition:

$$\frac{B(x)}{\rho} = \frac{B_0(x)}{\rho_0(x)}, \quad (9.4)$$

where $B(x)_0$ and $\rho(x)_0$ are the values of $B(x)$ and $\rho(x)$ at the point where a given element of the medium was located at the initial moment of time, $t = 0$. Similarly, from the entropy equation:

$$p(x)\rho(x)^{-\gamma} = p_0\rho_0^{-\gamma}. \quad (9.5)$$

We average the first and second equations of the system (9.3) over the scale L that is much larger than the size of inhomogeneities R , but much smaller than the length of magnetosonic wave λ : $R \ll L \ll \lambda$. Denoting this averaging by angular brackets, we have

$$\left\langle \rho \frac{dv}{dt} \right\rangle = -\frac{\partial}{\partial x} \langle P \rangle \quad (9.6)$$

and

$$\frac{d\langle \rho \rangle}{dt} + \frac{\partial}{\partial x} \langle \rho v \rangle \frac{\partial v}{\partial x} = 0 \quad (9.7)$$

Now, because of the averages $\langle \rho dv/dt \rangle$ and $\langle \rho v \rangle$, the system (9.6) and (9.7) is not a closed one anymore. This means that one needs to find a way to split the averages and bring the system of equations to the closed form.

To do this, we use the following considerations, which are valid for large-scale slow motions with a timescale $T \equiv (2\pi/\omega) \gg R/c_s$ (c_s being the sound speed) and spatial scale $\lambda \gg R$. For these kinds of motions, the changes in any characteristics of the system (density, pressure, frozen-in magnetic field, etc.) in the frame moving with the fluid element are slow, for example, changing the time of the order of \mathcal{T} . To avoid misunderstanding, it must be emphasized that at the same time, the *partial*

derivative $\partial/\partial t$ can be large, $\partial/\partial t \sim v/R$. Now, we can rewrite the continuity equations from the system (9.3) in the form:

$$\frac{\partial v}{\partial x} = -\frac{d \ln \rho}{dt}, \quad \frac{\partial v}{\partial x} = -\frac{d \ln B}{dt}, \quad \frac{\partial v}{\partial x} = -\frac{1}{\gamma} \frac{d \ln p}{dt} \quad (9.8)$$

It is clear that $\partial v/\partial x$ is a small quantity estimated as:

$$\frac{\partial v}{\partial x} \sim \frac{1}{\mathcal{T}} \sim \frac{v}{\lambda} \ll \frac{v}{R} \quad (9.9)$$

That is, despite the presence of inhomogeneities of density, pressure, and magnetic field which have the scale R , velocity is a “smooth” function, changing only over the scale $\lambda \gg R$. This allows us to write the following relations:

$$\left\langle \rho \frac{dv}{dt} \right\rangle \simeq \langle \rho \rangle \frac{d\langle v \rangle}{dt}, \quad \langle \rho v \rangle \simeq \langle \rho \rangle \langle v \rangle \quad (9.10)$$

these relations are valid with the accuracy of the order $R/\lambda \ll 1$. Recall that the scale L over which the averaging is made is small compared to λ and large compared to R . As a result, we obtain instead of Eqs. (9.6) and (9.7) the following equations:

$$\langle \rho \rangle \frac{d\langle v \rangle}{dt} = -\frac{\partial}{\partial x} \langle P \rangle, \quad (9.11)$$

$$\frac{\partial \langle \rho \rangle}{\partial t} + \left(\frac{\partial}{\partial x} \langle \rho \rangle \right) \langle v \rangle = 0 \quad (9.12)$$

The form of (9.11) and (9.12) is similar to the equations for one-dimensional gas-dynamics. The analogy will become complete when we find the closure relationship between the averaged quantities $\langle \rho \rangle$ and $\langle P \rangle$.

Note that the density ρ of each plasma element can be expressed in terms of its initial density $\rho_0(x)$, pressure $p_0(x)$, and total pressure P at a given point. Thus, using the definition of P and relationships (9.2), (9.4), and (9.5), we obtain

$$P = p_0 \left(\frac{\rho}{\rho_0} \right)^\gamma + \frac{P_0 - p_0}{\rho_0^2} \rho^2. \quad (9.13)$$

This relationship determines implicitly the dependence of ρ on P , ρ_0 , and p_0 (P_0 is assumed to be known),

$$\rho = \rho(P, \rho_0, p_0). \quad (9.14)$$

In what follows, it is convenient to introduce the distribution function $f(\rho_0, p_0)$ of the random quantities ρ_0 and p_0 , which we define as follows: the fraction of those

segments of the axis x , where ρ_0 and p_0 take the values in the intervals $(\rho_0, \rho_0 + d\rho_0)$, $(p_0, p_0 + dp_0)$, is proportional to $f(\rho_0, p_0)d\rho_0dp_0$:

$$dx_0 \sim f(\rho_0, p_0)d\rho_0dp_0. \tag{9.15}$$

Let us choose now two Lagrangian planes with the distance L ($R \ll L \ll \lambda$). The amount of the matter between the Lagrangian planes, which by definition are “affixed” to plasma particles, is constant:

$$M = \int_L \rho(x)dx = \int_{L_0} \rho_0(x_0)dx_0 = \text{const} \tag{9.16}$$

This condition leads to the connection of the segment dx in MHD wave with its initial value dx_0

$$dx = dx_0 \frac{\rho_0(x_0)}{\rho(P, p_0, \rho_0)} \tag{9.17}$$

Note that the total pressure P is slowly varying function with the characteristic scale of the order of λ . Since the distance L is much less than λ , the change of P between Lagrangian planes is small, and we can substitute P by its average value $\langle P \rangle$.

With the help of (9.14), we can find the density of each element of plasma, which can be written as $\rho = \rho(\langle P \rangle, \rho_0, p_0)$. Then, instead of Eq. (9.17) we have

$$dx = dx_0 \frac{\rho_0(x_0)}{\rho(\langle P \rangle, p_0, \rho_0)}. \tag{9.18}$$

Taking into account that $dx_0 \sim L_0 f(p_0, \rho_0)d\rho_0dp_0$, from (9.18) we obtain

$$L = L_0 \frac{1}{\int f(p_0, \rho_0)d\rho_0dp_0} \int \frac{\rho_0(x_0)}{\rho(\langle P \rangle, p_0, \rho_0)} f(p_0, \rho_0)d\rho_0dp_0. \tag{9.19}$$

The whole mass of substance between the Lagrangian planes is obviously the following:

$$M = L_0 \frac{\int \rho_0 f(p_0, \rho_0)d\rho_0dp_0}{\int f(p_0, \rho_0)d\rho_0dp_0} \tag{9.20}$$

Dividing this mass by the distance defined by (9.19), we obtain the expression for the average density,

$$\begin{aligned} \langle \rho \rangle &= \int \rho_0 f(p_0, \rho_0)d\rho_0dp_0 \left[\int \frac{\rho_0(x_0)}{\rho(\langle P \rangle, p_0, \rho_0)} f(p_0, \rho_0)d\rho_0dp_0 \right]^{-1} \\ &\equiv F(\langle P \rangle). \end{aligned} \tag{9.21}$$

In this way, one can find the relationship between $\langle \rho \rangle$ and $\langle P \rangle$ for any distribution function $f(p_0, \rho_0)$. Now, together with (9.21), Eqs. (9.11) and (9.12) form a closed system of dynamical equations describing self-consistently the propagation of long-wave magnetosonic oscillations of a finite amplitude in an inhomogeneous plasma. The specific features of the system are determined by its statistical properties, and in particular, by the function $f(p_0, \rho_0)$.

9.2 Formation of Shocks Across Small-Scale Inhomogeneities

The problem of the finite amplitude wave propagation, and in particular the process of the steepening of a wave front and its overturning is largely determined by the dependence of ρ on P , i.e., by the specific form of a function $\rho = F(P)$.

For ordinary gas, the $\rho = F(P)$ dependence, which is $\rho \sim p^{1/\gamma}$ (and $\gamma > 1$), automatically satisfies the condition of overturning:

$$\frac{du}{d\rho} > 0 \quad (9.22)$$

where $u = v + c_s$, and $v = \int (c_s/\rho)d\rho$.

It must be noted that the analysis of the shock formation in case of a strongly inhomogeneous plasma requires several clarifying steps. First of all, we have to represent the condition (9.22) in a more general form, namely through the relationship (9.21), and then verify whether a particular $\rho = F(P)$ satisfies the overturning condition or not.

Let us rewrite the (9.11) and (9.12) in the form

$$\rho \frac{dv}{dt} = -\frac{dP}{d\rho} \frac{d\rho}{dv} \frac{dv}{dx}, \quad (9.23)$$

$$\frac{d\rho}{dv} \frac{dv}{dt} = -\rho \frac{\partial v}{\partial x}. \quad (9.24)$$

We omit herewith the averaging brackets and bear in mind that we deal with the averaged quantities. Eliminating dv/dt in these equations, we find

$$\frac{dP}{d\rho} \frac{d\rho}{dv} \frac{dv}{dx} = \rho^2 \frac{\partial v/\partial x}{d\rho/dv}. \quad (9.25)$$

Substituting this expression in the right-hand side of (9.23), we obtain the general form of nonlinear equation:

$$\frac{\partial v}{\partial t} + \left(v + \rho \frac{dv}{d\rho} \right) \frac{\partial v}{\partial x} = 0. \quad (9.26)$$

If we introduce the notation $u = v + c_s$, the analogy with an ideal compressible gas becomes complete, and the condition for overturning of the wave front, (9.22), remains the same:

$$\frac{dv}{d\rho} + \frac{d}{d\rho} \left(\rho \frac{dv}{d\rho} \right) > 0. \tag{9.27}$$

We now have to express all terms in this condition through the function $\rho = \rho(P)$. From (9.25), it follows that

$$\rho \frac{dv}{d\rho} = \frac{1}{\sqrt{d\rho/dP}} \tag{9.28}$$

For the first term in condition (9.27), this expression yields simply

$$\frac{dv}{d\rho} = \frac{1}{\rho(P)\sqrt{d\rho/dP}} \tag{9.29}$$

The second term in Eq. (9.27) can be written as

$$\frac{d}{d\rho} \left(\rho \frac{dv}{d\rho} \right) = \frac{dP}{d\rho} \frac{\partial}{\partial P} \frac{1}{\sqrt{d\rho/dP}}, \tag{9.30}$$

or, performing the differentiation, we have

$$\frac{d}{d\rho} \left(\rho \frac{dv}{d\rho} \right) = -\frac{1}{2} \frac{d^2\rho/dP^2}{(d\rho/dP)^{5/2}}, \tag{9.31}$$

Using now (9.27), (9.29), and (9.31), we obtain the most general form of the condition of steepening of a wave front in a medium with an arbitrary relationship between the density and pressure:

$$2 \left(\frac{d\rho}{dP} \right)^2 > \rho(P) \frac{d^2\rho}{dP^2}. \tag{9.32}$$

9.2.1 Validation of the Overturning Condition

We need to clarify now that the condition (9.32) is indeed satisfied when the dependence $\rho = F(\langle P \rangle)$ is defined by the expression (9.21):

$$F(\langle P \rangle) = \int \rho_0 d\Gamma \left[\int \frac{\rho_0(x_0)}{\rho(\langle P \rangle, p_0, \rho_0)} d\Gamma \right]^{-1} \tag{9.33}$$

where $d\Gamma = f(\rho_0, p_0) d\rho_0$.

The first and second derivatives of this function are

$$\frac{dF}{d\langle P \rangle} = \int \rho_0 d\Gamma \int \frac{\rho_0}{\rho^2} \frac{d\rho}{d\langle P \rangle} d\Gamma \left[\int \frac{\rho_0}{\rho(\langle P \rangle)} d\Gamma \right]^{-2} \quad (9.34)$$

and

$$\begin{aligned} \frac{d^2 F}{d\langle P \rangle^2} &= \frac{2 \int \rho_0 d\Gamma}{\left(\int (\rho_0/\rho) d\Gamma \right)^{-3}} \left(\int \frac{\rho_0}{\rho^2} \frac{d\rho}{d\langle P \rangle} d\Gamma \right)^2 \\ &+ \frac{\int \rho_0 d\Gamma}{\left(\int (\rho_0/\rho) d\Gamma \right)^{-2}} \int \left[\frac{\rho_0}{\rho^2} \frac{d^2 \rho}{d\langle P \rangle^2} - 2 \frac{\rho_0}{\rho^3} \left(\frac{d\rho}{d\langle P \rangle} \right)^2 \right] d\Gamma \end{aligned} \quad (9.35)$$

Combining the condition (9.32) with (9.21), (9.34), and (9.35) after some algebra, we obtain

$$\left(\int \rho_0 d\Gamma \right)^2 \left(\int \frac{\rho_0}{\rho} d\Gamma \right)^{-3} \int \left[\frac{\rho_0}{\rho^2} \frac{d^2 \rho}{d\langle P \rangle^2} - 2 \frac{\rho_0}{\rho^3} \left(\frac{d\rho}{d\langle P \rangle} \right)^2 \right] d\Gamma < 0 \quad (9.36)$$

It is obvious that $\int \rho_0 d\Gamma > 0$ and $\int \rho_0/\rho d\Gamma > 0$.

The first and second derivatives in (9.36) can be easily found from (9.13) where P is substituted by its average value $\langle P \rangle$ (see the explanations after (9.17)):

$$\frac{d\rho}{d\langle P \rangle} = \frac{\rho}{\gamma\langle P \rangle + (2-\gamma)(P_0 - p_0)(\rho^2/\rho_0^2)}, \quad (9.37)$$

$$\frac{d^2 \rho}{d\langle P \rangle^2} = \frac{(d\rho/d\langle P \rangle)[\gamma\langle P \rangle - (2-\gamma)(P_0 - p_0)\rho^2/\rho_0^2] - \gamma\rho}{[\gamma\langle P \rangle + (2-\gamma)(P_0 - p_0)(\rho^2/\rho_0^2)]^2}, \quad (9.38)$$

these derivatives, taken in the point $\langle P \rangle = P_0$, become

$$\left. \frac{d\rho}{d\langle P \rangle} \right|_{P_0, \rho_0} = \frac{\rho_0}{\gamma P_0 + 2(P_0 - p_0)}, \quad (9.39)$$

$$\left. \frac{d^2 \rho}{d\langle P \rangle^2} \right|_{P_0, \rho_0} = \frac{\rho_0[\gamma P_0 - \gamma^2 p_0 - 2(P_0 - p_0)]}{[\gamma P_0 + 2(P_0 - p_0)]^3}. \quad (9.40)$$

Substituting expressions (9.39) and (9.40) into the condition (9.36), we obtain

$$\int f(p_0, \rho_0) \frac{\gamma(\gamma+1)p_0 + 6(P_0 - p_0)}{[\gamma P_0 + 2(P_0 - p_0)]^3} d\rho_0 dp_0 > 0. \quad (9.41)$$

In accordance with the equilibrium condition, the magnitude $P_0 - p_0$ is always positive, $P_0 - p_0 = B^2/8\pi > 0$. This means that the integrand in expression (9.41) is positive definite.

Thus, the condition (9.41) as well as its general form, Eq. (9.32), is satisfied for any distribution function $f(p_0, \rho_0)$. It is therefore only natural that the magnetosonic wave of finite amplitude propagating in a plasma with random inhomogeneities can split into two simple waves with subsequent steepening and overturning.

Note however that when the width of the wave front becomes comparable with the characteristic scale of inhomogeneities, this conclusion becomes invalid. In this case, the dispersion effects play essential role; since at $\lambda \sim R$ the dispersion of MHD waves becomes nonlinear, a steepening of the wave front may be inhibited.

9.3 Effect of Inhomogeneities on the Dispersion Properties of the System

In this section, we consider the dispersion properties of a dense conglomerate of flux tubes and find nonlinear dependence of the frequency on the wavenumber.

9.3.1 Basic Equations

Consider again the one-dimensional problem and start with the linearizing of the MHD equations (9.3) introducing small perturbations, remembering that unperturbed quantities are random functions of coordinate x :

$$\begin{aligned} p &= p_0(x) + \delta p(x, t), & \rho &= \rho_0(x) + \delta \rho(x, t), \\ p &= B_0(x) + \delta B(x, t), & v &= \delta v(x, t). \end{aligned} \quad (9.42)$$

Using the resulted equations and equilibrium condition $\delta P = \delta p + (B_0 \delta B)/4\pi$, we can write for δP :

$$\frac{\partial \delta P}{\partial t} = -2 \left[\left(\frac{\gamma}{2} - 1 \right) p_0 + P_0 \right] \frac{\partial \delta v}{\partial x}. \quad (9.43)$$

This equation together with the momentum equation,

$$\rho(x) \frac{\partial \delta v}{\partial t} = -\frac{\partial \delta P}{\partial x}, \quad (9.44)$$

forms a closed set describing linear perturbations in an inhomogeneous plasma.

All perturbed quantities can be represented in the following way:

$$\delta P = \langle \delta P^{(0)} \rangle + \delta P^{(1)}, \quad \delta v = \langle \delta v^{(0)} \rangle + \delta v^{(1)}, \quad \text{etc.}, \quad (9.45)$$

where $\langle \delta P^{(0)} \rangle$, $\langle \delta v^{(0)} \rangle$, etc., are linear perturbations averaged over the distance L : $R \ll L \ll \lambda$, and $\delta P^{(1)}$, $\delta v^{(1)}$, etc., are fluctuating parts of perturbations caused by the presence of inhomogeneities.

For slow motions, $\partial/\partial t \sim \epsilon \ll 1$, we have from (9.43) and (9.44)

$$\frac{\partial \delta v^{(0)}}{\partial x} \sim \epsilon \ll 1, \quad \frac{\partial \delta P^{(0)}}{\partial x} \sim \epsilon \ll 1. \quad (9.46)$$

therefore $\delta P^{(0)} \simeq \langle \delta P^{(0)} \rangle$ and $\delta v^{(0)} \simeq \langle \delta v^{(0)} \rangle$. At the same time, by definition $\langle \delta P^{(1)} \rangle = 0$ and $\langle \delta v^{(1)} \rangle = 0$.

Since we deal with inhomogeneities that are initially stationary, we can consider a harmonic wave in time and replace $\partial/\partial t$ by $-i\omega$. It is convenient to introduce the notation:

$$\phi_0(x) = \frac{1}{2} \left[\left(\frac{\gamma}{2} - 1 \right) p_0(x) + P_0 \right]^{-1} \quad (9.47)$$

Now, Eqs. (9.43) and (9.44) acquire a form:

$$i\omega \rho_0(x) \delta v = \frac{\partial \delta P}{\partial x}, \quad i\omega \phi_0(x) \delta P = \frac{\partial \delta v}{\partial x}. \quad (9.48)$$

Let us represent $\rho_0(x)$ and $\phi_0(x)$ as follows:

$$\rho_0(x) = \langle \rho_0(x) \rangle + \rho_1(x), \quad \phi_0(x) = \langle \phi_0(x) \rangle + \phi_1(x) \quad (9.49)$$

Note that the fluctuations of plasma parameters of the background medium and the average values of these parameters are of the same order: $\rho_1(x) \sim \langle \rho_0(x) \rangle$ and $\phi_1(x) \sim \langle \phi_0(x) \rangle$, which reflects the fact that the inhomogeneities are strong, and in particular that all unperturbed quantities change from one flux tube to another by an order of magnitude. At the same time, $\langle \rho_1(x) \rangle = 0$ and $\langle \phi_1(x) \rangle = 0$.

Introducing into the system (9.48) a fluctuating part of perturbations and of background inhomogeneities, we have

$$i\omega(\langle \rho_0(x) \rangle + \rho_1)(\delta v^{(0)} + \delta v^{(1)}) = \frac{\partial}{\partial x}[\delta P^{(0)} + \delta P^{(1)}], \quad (9.50)$$

$$i\omega(\langle \phi_0(x) \rangle + \phi_1)(\delta P^{(0)} + \delta P^{(1)}) = \frac{\partial}{\partial x}[\delta v^{(0)} + \delta v^{(1)}]$$

After averaging, (9.50) become

$$i\omega[\langle\rho_0(x)\rangle\delta v^{(0)} + \langle\rho_1\delta v^{(1)}\rangle] = \frac{\partial\delta P^{(0)}}{\partial x}, \quad (9.51)$$

$$i\omega[\langle\phi_0(x)\rangle\delta P^{(0)} + \langle\phi_1\delta P^{(1)}\rangle] = \frac{\partial\delta v^{(0)}}{\partial x}$$

The second terms in the left-hand side of (9.51) are those that determine the dispersion of the wave due to the presence of inhomogeneities.

9.3.2 Dispersion Relation

To solve the system (9.51), we have to express $\delta v^{(1)}$ and $\delta P^{(1)}$ through unperturbed quantities. The equations describing $\delta v^{(1)}$ and $\delta P^{(1)}$ can be obtained by subtraction from the system (9.50) of the corresponding equations of system (9.51):

$$i\omega[\rho_1\delta v^{(0)} + \langle\rho_0(x)\rangle\delta v^{(1)} + \langle\rho_1\delta v^{(1)}\rangle] = \frac{\partial\delta P^{(1)}}{\partial x}, \quad (9.52)$$

$$i\omega[\phi_1\delta P^{(0)} + \langle\phi_0(x)\rangle\delta P^{(1)} + \langle\phi_1\delta P^{(1)}\rangle] = \frac{\partial\delta v^{(1)}}{\partial x}$$

Since we are looking for the first-order corrections, we can omit in (9.52) second and third terms in the left-hand side; these terms give the next-order corrections in $\delta P^{(1)}$ and $\delta v^{(1)}$. Then, the system (9.52) becomes

$$i\omega\rho_1\delta v^{(0)} = \frac{\partial\delta P^{(1)}}{\partial x}, \quad i\omega\phi_1\delta P^{(0)} = \frac{\partial\delta v^{(1)}}{\partial x}. \quad (9.53)$$

Now, we introduce the following definitions:

$$\rho_1(x) = \frac{d\psi(x)}{dx}, \quad \phi_1(x) = \frac{d\zeta(x)}{dx}. \quad (9.54)$$

Naturally, $\langle\psi\rangle = 0$ and $\langle\zeta\rangle = 0$. With these definitions, the (9.53) are

$$\delta P^{(1)} \equiv i\omega\psi(x)\delta v^{(0)}, \quad \delta v^{(1)} \equiv i\omega\zeta(x)\delta P^{(0)}. \quad (9.55)$$

Substituting (9.55) into (9.51), we obtain the final set of equations containing the corrections that determine the dispersion of the wave due to the presence of

inhomogeneities:

$$i\omega[\langle\rho_0(x)\rangle\delta v^{(0)} + i\omega\langle\rho_1\xi\rangle\delta P^{(0)}] = \frac{\partial\delta P^{(0)}}{\partial x}, \quad (9.56)$$

$$i\omega[\langle\phi_0(x)\rangle\delta P^{(0)} + i\omega\langle\phi_1\psi\rangle\delta v^{(0)}] = \frac{\partial\delta v^{(0)}}{\partial x}$$

Since the coefficients in the system (9.56) do not depend on coordinates, we can put $\partial/\partial x = ik$ and obtain the dispersion relation:

$$\langle\phi_0\rangle\langle\rho_0\rangle\omega^2 + \langle\rho_1\xi\rangle\langle\phi_1\psi\rangle\omega^4 + ik\omega^2[\langle\rho_1\xi\rangle + \langle\phi_1\psi\rangle] = k^2. \quad (9.57)$$

Using the definitions (9.55), we see that the third term in the left-hand side of (9.57) is a full derivative whose average is evidently zero

$$\langle\rho_1\xi\rangle + \langle\phi_1\psi\rangle = \left\langle\frac{d\psi}{dx}\xi + \frac{d\xi}{dx}\psi\right\rangle = \left\langle\frac{d\xi\psi}{dx}\right\rangle \equiv 0 \quad (9.58)$$

On the other hand, the square of this expression, $\langle\rho_1\xi\rangle + \langle\phi_1\psi\rangle$, determines the coefficient of ω^4 in the dispersion relation, and, because of (9.58), evidently has a negative definite quadratic form:

$$\langle\rho_1\xi\rangle\langle\phi_1\psi\rangle = -\frac{1}{2}\left[\left\langle\frac{d\psi}{dx}\xi\right\rangle^2 + \left\langle\psi\frac{d\xi}{dx}\right\rangle^2\right] \equiv -a^2 \quad (9.59)$$

Taking this into account, the dispersion relation (9.57) becomes

$$\langle\phi_0\rangle\langle\rho_0\rangle\omega^2 - a^2\omega^4 = k^2 \quad (9.60)$$

In the zeroth-order approximation (neglecting the dispersion of the wave), ω scales linearly with k :

$$\omega = \tilde{c}_s(\rho_0, p_0, B_0)k \quad (9.61)$$

where modified sound speed $\tilde{c}_s(\rho_0, p_0, B_0)$ has a form:

$$\tilde{c}_s(\rho_0, p_0, B_0) = \frac{1}{\sqrt{\langle\phi_0\rangle\langle\rho_0\rangle}} = \frac{1}{\sqrt{\langle\phi_0\rangle}} \left\langle\frac{1}{\gamma p_0 + B^2/4\pi}\right\rangle^{-1/2}. \quad (9.62)$$

Using linear approximation (9.61), from (9.60) we obtain the next approximation in the wave vector

$$\omega^2 = k^2\tilde{c}_s^2 + a^2k^4\tilde{c}_s^6 \quad (9.63)$$

or, finally,

$$\omega = k\tilde{c}_s(1 + \delta^2 k^2). \quad (9.64)$$

Here, δ^2 is a coefficient that determines the dispersion of the wave due to the presence of inhomogeneities:

$$\delta^2 = \frac{1}{2}a^2\tilde{c}_s^4. \quad (9.65)$$

9.3.3 *KdV–Bürgers' Equation with Strong Inhomogeneities*

For a wave of a small but finite amplitude, along a finite dispersion, one should take into account the effects of a weak nonlinearity described by (9.26). Note first that the dispersion relation (9.64), if written in the velocity frame moving with the modified sound speed \tilde{c}_s , corresponds to the dynamic equation of the form:

$$\frac{\partial v}{\partial t} = \tilde{c}_s \delta^2 \frac{\partial^3 v}{\partial x^3}. \quad (9.66)$$

Respectively, the desired nonlinear equation, in the reference frame moving with \tilde{c}_s , can be written in the form:

$$\frac{\partial v}{\partial t} + \alpha v \frac{\partial v}{\partial x} = \tilde{c}_s \delta^2 \frac{\partial^3 v}{\partial x^3}. \quad (9.67)$$

where α is coefficient of nonlinearity. This is a typical KdV equation.

Now, we can conclude that the evolution of the initial magnetosonic perturbation in a plasma with random density and magnetic field inhomogeneities can be described by a KdV equation whose coefficients are uniquely determined by the statistical properties of these inhomogeneities (see (9.21) and (9.59)). It must be noted that the coefficient δ that determines the dispersion differs from zero only in an inhomogeneous plasma, whereas in homogeneous case $\delta = 0$.

Obviously, (9.67) implies that depending on the interplay between the dispersion and nonlinearity, the system is subject to a soliton formation. In this case, the width ΔX of leading (the largest) soliton may be estimated in a standard way as:

$$\Delta X \sim \sqrt{\frac{\tilde{c}_s \delta^2}{\alpha \tilde{v}_0}}, \quad (9.68)$$

where \tilde{v}_0 is the amplitude of the initial perturbation. In order for the soliton to be formed (and the approach to be valid), the width ΔX must be larger than the characteristic scale of inhomogeneities R . Since, according to (9.59), at large

enough inhomogeneities ($\rho_1 \sim \rho$, $p_1 \sim p_0$), δ is of the order R , and α is of the order of unity, we conclude that the above description is adequate under the condition when $\tilde{v}_0 \ll \tilde{c}_s$, which is relatively weak constraint.

As already mentioned, a plasma with strong inhomogeneities exhibits an important feature: dissipative effects caused by thermal conductivity and viscosity are significantly enhanced. For the complete description of nonlinear wave propagation in such a media, (9.67) has to contain the dissipative terms as well. This leads to KdV–Bürgers’ equation (Ryutova et al. 1991):

$$\frac{\partial v}{\partial t} + \alpha v \frac{\partial v}{\partial x} = \tilde{c}_s \delta^2 \frac{\partial^3 v}{\partial x^3} + \mu \frac{\partial^2 v}{\partial x^2} \quad (9.69)$$

where coefficients $\mu(\rho, p_0, B_0) = \mu_{\text{visc}} + \mu_{\text{therm}}$ are again determined by statistical properties of inhomogeneities and contain parts connected with viscous and thermal losses (Ohmic losses as already discussed, remain the same as in homogeneous medium and are much less than those two). The procedure that allows to find μ is described in the previous chapter (Sect. 8.2, Eq. (8.53), see also Ryutova and Persson 1984). By the order of magnitude, μ can be estimated as follows:

$$\mu \simeq \lambda^2 \Gamma = \lambda^2 \frac{T \tau_i}{m_i R^2} \frac{1}{(\omega_i \tau_i)^2} \left(\frac{\tilde{\rho}_0}{\rho_0} \right)^2 \quad (9.70)$$

where Γ is the damping rate (Eq. (8.53)) determined by the level of inhomogeneities and mainly by the viscous losses (τ_i and $\omega_i = eB/m_i c$ being ion collision time and ion gyro-frequency).

Equation (9.69) allows us to make general comments. This equation describes the evolution of the arbitrary initial perturbation: depending on the interplay of the nonlinear, dissipative, and dispersive effects, it can evolve either to weak shocks or be split into a train of some number of independent solitons which then will be damped away, or in the case of predominance of dissipative effects, the primary perturbation can be damped away in a linear stage (Karpman 1975).

9.4 Numerical Analysis

In this section, we study numerically the influence of strong background inhomogeneities with small-scale spatial on the propagation and evolution of long-wavelength perturbations using a one-dimensional code of ideal magnetohydrodynamics. The set of the ideal MHD equations (9.3) is solved by numerical simulations as given in Ryutova et al. (1991).

9.4.1 The Model

As the initial state, consider an isothermal plasma with temperature T and assume the gas to be a polytrope of index $\gamma = 1.5$. The distribution of magnetic field is given by:

$$B(x) = \sqrt{\frac{8\pi p(x)}{\beta(x)}} \quad (9.71)$$

where plasma beta

$$\beta(x) = \beta_0 f(x) \quad (9.72)$$

and β_0 is the maximum value of the plasma beta, $f(x) = f(\rho_0, p_0)$ describes the randomly distributed small-scale inhomogeneities of the background. In what follows, we use $\beta_0 = 1.0$.

The initial density and pressure distributions are calculated using the equation of state $p(x) = \rho(x)T$, and the equation of magnetostatic equilibrium (9.2).

Long-wavelength perturbations of the form:

$$\delta v_x(x) = A \sin\left(2\pi \frac{x}{\lambda}\right), \quad \delta \rho(x) = \frac{\rho_0}{c_s} \delta v_x, \quad \delta p(x) = \rho_0 c \delta v_x, \quad (9.73)$$

are initially imposed, where A is the amplitude of the initial perturbation and λ is its wavelength.

We assume periodic boundaries for $x = 0$ and $x = X_{\max}$, where X_{\max} is the size of computational domain. The set of MHD equations (9.3) is nondimensionalized using the following normalizing constants: the atmospheric scale height H , sound speed c_s , and density ρ_0 .

Equation (9.3) are solved numerically using a modified Lax–Wendroff scheme (Rubin and Burstein 1967) with an artificial viscosity according to Richtmyer and Morton (1967). The test and accuracy of MHD code in such a scheme were described by Shibata (1983), Matsumoto et al. (1988), and Tajima (1989). The mesh size is $\Delta x = X_{\max}/(N_x - 1)$, where N_x is the number of mesh points in the x direction.

We shall see that the numerical analysis presented below supports the theoretical results derived in the previous sections and extends the studies to the case when $\lambda \sim R$. In particular, it will be shown that long-wavelength perturbations steepen and form shock waves even in the presence of small-scale background fluctuations of basic physical parameters, and that the energy dissipation due to the small-scale inhomogeneities is strongly enhanced with respect to the case of a homogeneous medium. Although theory assumes the characteristic wavelength is greater than the characteristic scale of inhomogeneities, $\lambda \gg R$, numerical computation allows us to remove such a restriction and generalize the dissipation effect regardless of the characteristic wavelength.

9.4.2 Formation of Shock Waves

Assume that $A = 0.5$, $N_x = 1001$, $X_{\max} = 100$, and $\lambda = X_{\max}$. Since the length scale of the background fluctuations is Δx , our theoretical assumption $\lambda \gg R$ is amply fulfilled. The magnitude A of the initial pressure perturbation is too large to be realistic. However, our simulations with different values of A show that the amplitude of the perturbation within the regime of $0.1 < A < 0.5$ does not qualitatively affect the overall evolution. Since the timescale for the steepening of the initial wave with wavelength λ is of the order of λ/v , its quantitative effect is that the smaller A is, the larger is the computational time. Thus, this high value of the initial perturbation is chosen simply for computational convenience.

Figure 9.2 shows the time variation of the velocity field V_x in the strongly nonuniform plasma. The initially sinusoidal perturbation becomes more and more asymmetric ($t \sim 22$), steepens, and forms strong shock waves at $t \sim 42$. The characteristic Burgers' sawtooth shock formation is apparent. Note that the "discontinuities" of shocks are more than several grid spacings so that they are not beyond the numerical resolution.

Figure 9.3 contains the velocity V_x , the total pressure P_{tot} , the plasma density ρ , and the vertical magnetic field B_z in the final state at $t = 76$. The shocks

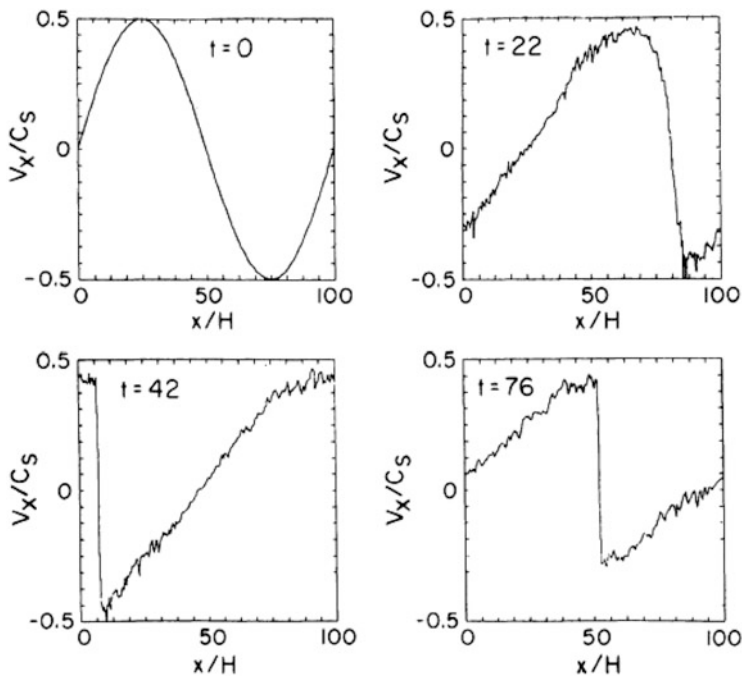


Fig. 9.2 The case of small-scale inhomogeneities: distribution in x of the velocity V_x at $t = 0$ (upper left panel), and its evolution at $t = 22$, 42, and $t = 76$

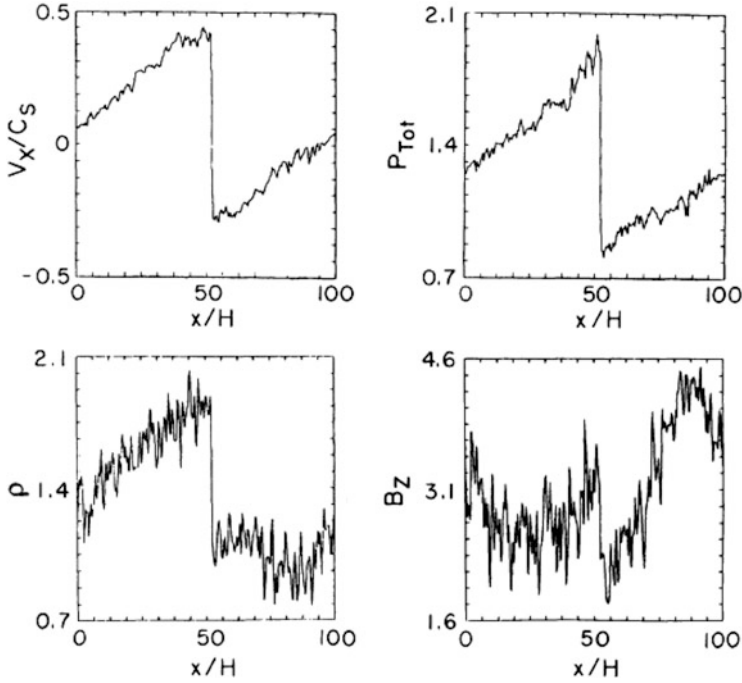


Fig. 9.3 Plots of the velocity V_x , the total pressure $P = p + B^2/8\pi$, the density ρ , and the magnetic field strength B_z at $t = 76$ for the case shown in Fig. 9.2

are best resolved in V_x , ρ , and P_{tot} . The profiles of the density and magnetic field are strongly modulated by the small-scale background fluctuations. At this point, we summarize that even in the presence of strong, small-scale background inhomogeneities the propagation of acoustic waves with wavelengths $\lambda \gg R$ is characterized by steepening of the wave front and the formations of shocks.

9.4.3 Energy Dissipation

We now discuss the energetics of the system and compare the case of inhomogeneous background fluctuations with that of a homogeneous medium. We assume the same amplitude of the initial perturbation, $A = 0.5$, as in the previous calculations, but use $X_{max} = 20$. The smaller wavelength of the initial perturbation reduces the timescale for steepening of the wave front by a factor of 5 compared to the case of $X_{max} = 100$.

Consider first the case of a homogeneous medium. Figure 9.4 shows the time variation of magnetic, thermal, and kinetic energies in a system. It should be noted that $\Delta E = E(t) - E(0)$. The kinetic energy E_k strongly decreases within the first

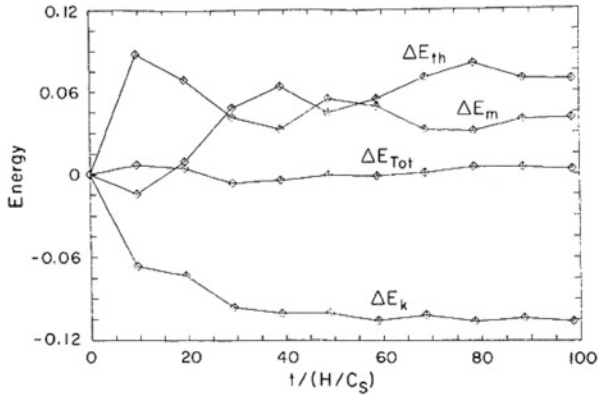


Fig. 9.4 Time variation of magnetic (ΔE_m), thermal (ΔE_{th}), kinetic (ΔE_k), and total (ΔE_{Tot}) energies, where $\Delta E = E(t) - E(0)$, for the case of homogeneous background

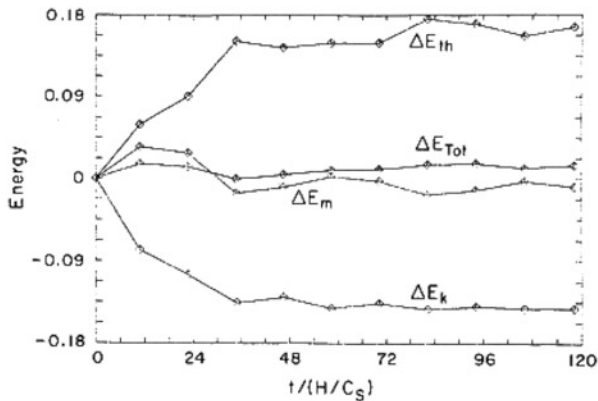


Fig. 9.5 Time variation of magnetic (ΔE_m), thermal (ΔE_{th}), kinetic (ΔE_k), and total (ΔE_{Tot}) energies for the case of dense conglomerate of inhomogeneities

10 time intervals. In this period, the waves steepen and form shocks. Within the next 30 time intervals, 10% of the kinetic energy dissipates and is converted mostly into thermal energy through compressional shock heating, and partly into magnetic energy. The total energy in this numerical analysis is conserved within less than 1% of its initial value.

Figure 9.5 shows the evolution of the energy flow for the case of an inhomogeneous plasma. The kinetic energy decreases more drastically compared to homogeneous cases. Within the first period ($t \sim 30$), the thermal energy strongly increases partly due to damping of the kinetic energy and partly due to the dissipation of the magnetic energy. The heating effect is gauged by the increase of thermal energy ΔE_{th} , or lack of it. For example, ΔE_{th} in Fig. 9.5 in the

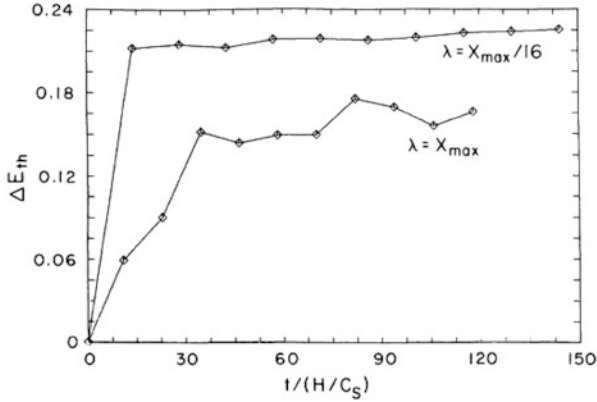


Fig. 9.6 Time variation of thermal energy, ΔE_{th} , for different wavelengths of the initial perturbation in the case of an inhomogeneous medium

inhomogeneous case is ~ 0.18 , while ΔE_{th} shown in Fig. 9.5 for homogeneous case is ~ 0.09 .

An interesting difference between the homogeneous and the inhomogeneous case is that in the latter one the magnetic field also releases its energy which is converted into thermal energy of medium through formation and dissipation of compressional shocks.

Very useful are results of the limiting case when $\lambda \sim R$, in which the wavelength of the initial perturbation is of the same order as the length scale of the inhomogeneities (characteristic scale of flux tube). This case is beyond the reach of analytical studies that do not allow to make any predictions.

In solving this problem, the following set of parameters are taken: $A = 0.5$, $X_{max} = 20$, and $\lambda = X_{max}/16$. Results of the calculation show again the strong dissipation of kinetic and magnetic energies in the early stage of the wave front evolution.

Figure 9.6 shows the time evolution of the thermal energy ΔE_{th} . Compared to the case when $\lambda \simeq X_{max}$, which is also shown in Fig. 9.6, the heating of the plasma is even more efficient. Due to strong dissipation from the very beginning, the initial perturbations are rapidly damped before the wave steepens and reaches the shock regime.

Thus, the presence of small-scale background inhomogeneities, in case a dense conglomerate of random flux tubes, results in a much stronger dissipation of incoming wave power and a stronger heating of the medium compared to the case of a homogeneous plasma. Qualitatively, this result is independent of the amplitude A of the initial wave, but the higher is the amplitude the larger the amount of heating. In the limiting case of $\lambda \sim R$, the numerical analysis indicates that the waves *do not steepen* to form shocks but rather are rapidly damped out. Compared to the case of long-wave perturbations, the heating in this case is more efficient.

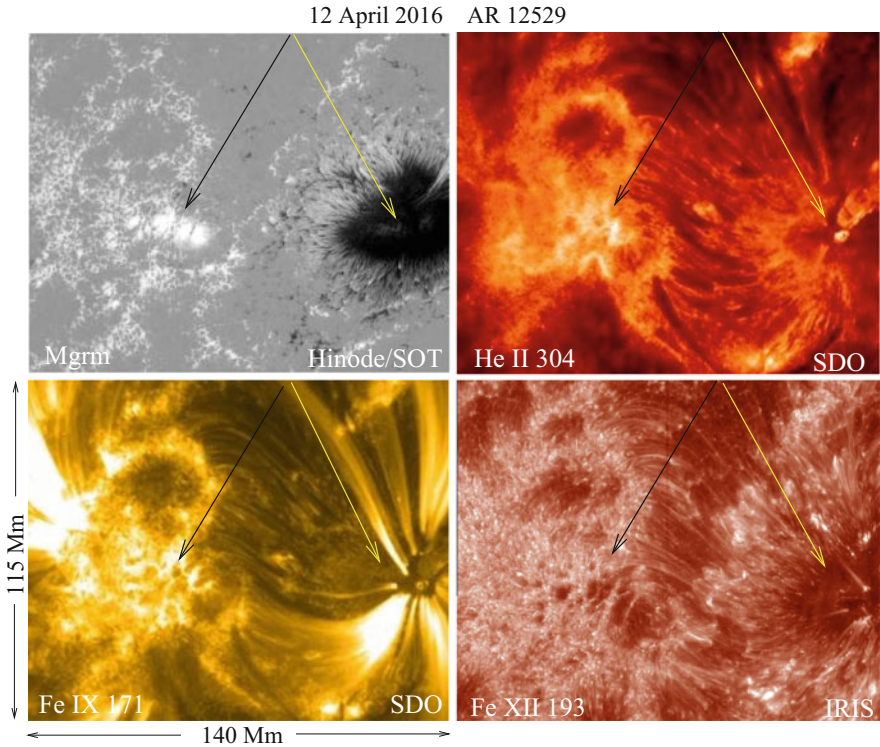


Fig. 9.7 The Hinode magnetogram of active region 12529 is shown with aligned images of the overlying chromosphere in SOT He II 304, low corona in SOT Fe IX 171 line, and hot corona in IRIS Fe XII 193 line. Black and yellow arrows indicate the different response of the overlying atmosphere to the activity in tattered and dense sunspots. Courtesy of Hinode, NASA/SDO, and NASA/IRIS

Note again that energy deposition due to the generation of shocks and solitons should manifest itself in strong *local* brightenings, chains of bright points, and light bridges (if solitons are involved). The size of bright points is naturally comparable with the thickness of wave front. Thus, possibility of shock and soliton formation may play an essential role in the widespread appearance of local brightenings and their chains observed in sunspots and active regions (Aballe Villero et al. 1993; Anastasiadis and Vlahos 1994; Berger and Berdyugina 2003; Schleicher et al. 2003; Lagg et al. 2014).

It is important to compare the energy production and its supply to overlying chromosphere/corona provided by the young sunspot where flux tubes are tightly settled and the decaying tattered sunspot with magnetic filling factor less than unity. Figure 9.7 shows active region 12529 consisting of young leading sunspot of negative polarity and the following sunspot of positive polarity in its decaying phase. One can see a clear difference between the response of the atmosphere overlying

these two sunspots. The pattern of hot plasma in the chromosphere and corona above the dense negative sunspot is very different from that of the positive tattered sunspot “compound.” Above the negative sunspot we see typical large-scale coronal loops and chromospheric umbral dots, while above the tattered compound the entire atmosphere is the conglomerate of densely packed brightenings. Indeed, less dense is the conglomerate of magnetic flux tubes (but still with the filling factor close to unity), the more space have the shocks to be enhanced, and interact with higher efficiency.

9.5 Problems

9.1 Obtain the traveling wave-type solution of KdV equation for shallow water. Assume that the wave propagates along the x -axis, so that the pressure p and the velocity u do not depend on y (Kadomtsev and Karpman 1971).

9.2 Find the conditions for shock formation in dispersive media with dissipation. Describe specific features of such shocks. Consider a traveling wave solution of KdV–Bürgers equation (Sagdeev 1966).

9.3 Under the conditions of previous problem, determine μ_{cr} , i.e., find the critical value of the dissipation coefficient corresponding to monotonic and oscillating shock profiles.

References

- M.A. Aballe Villero et al., *Astron. Astrophys.* **267**, 275 (1993)
 A. Anastasiadis, L. Vlahos, *Astrophys. J.* **428**, 819 (1994)
 T.E. Berger, S.V. Berdyugina, *Astrophys. J.* **589L**, 117 (2003)
 B.B. Kadomtsev, V.I. Karpman, *Sov. Phys. Usp.* **14**, 40 (1971)
 V.I. Karpman, *Nonlinear Waves in Dispersive Media* (Pergamon Press, London, 1975)
 A. Lagg et al., *Astron. Astrophys.* **568**, 60 (2014)
 R. Matsumoto et al., *Publ. Astron. Soc. Jpn.* **40**, 171 (1988)
 R.D. Richtmayer, K.W. Morton, *Difference Methods for Initial Value Problems*, 2nd edn. (Interscience, New York, 1967)
 E. Rubin, S.Z. Burstein, *J. Comput. Phys.* **2**, 178 (1967)
 M. Ryutova, M. Persson, *Phys. Scr.* **29**, 353 (1984)
 M. Ryutova, M. Kaisig, T. Tajima, *Astrophys. J.* **380**, 268 (1991)
 R.Z. Sagdeev, *Reviews of Plasma Physics* (Consultants Bureau, New York, 1966), p. 23
 H. Schleicher et al., *Solar Phys.* **215**, 261 (2003)
 K. Shibata, *Publ. Astron. Soc. Jpn.* **35**, 263 (1983)
 T. Tajima, *Computational Plasma Physics* (Addison-Wesley, Redwood City, 1989)

Chapter 10

Magnetosonic Streaming



Abstract The Faraday effect in gas dynamics called acoustic streaming and its accompanying nonlinear phenomena is found to have analogies in plasma magnetohydrodynamics. A natural place where these effects occur is the solar atmosphere covered by random ensembles of magnetic flux tubes. Unlike acoustic streaming, magnetosonic streaming consisting of the generation of plasma flows by an oscillating flux tube, is accompanied by a current drive, and results in a specific evolution of magnetic structures. Depending on the physical parameters of a system, a single magnetic flux tube may be either split into thinner flux tubes or be diffusively dissolved into the ambient plasma. The effect of the magnetosonic streaming, on the one hand, is an obvious candidate for the generation of electric currents and mass flows at magnetic flux tube sites, and, on the other hand, it determines the evolution of magnetic structures, like, e.g., their fragmentation processes, and ultimately their lifetimes. In this chapter, we shall describe the nature and origin of the magnetosonic streaming and then use the theory to explain observed regularities in the evolution of photospheric flux tubes. Some regimes will be also verified in numerical simulation. Application of these results to observed properties of photospheric flux tubes will be given both in the qualitative and quantitative analysis.

10.1 Secondary Flows—Boundary Layer Effects

10.1.1 *Acoustic Streaming—History and Nature of Faraday’s Effect*

The effect of the acoustic streaming was first observed by Faraday in one of his simple trials while assisting the lectures of Professor Devi. Young Faraday found that above the oscillating membrane there appears a well-directed, perpendicular to the face of membrane, air streaming. Much later, Lord Rayleigh was involved in the problem of a musical organ seemingly out of tune without an evident reason. He found that for each tube there must be a threshold with respect to the intensity of sound above which some physical effects turn on and lead to discord of organ. Soon,

he found that these effects are related to viscosity of the air in the vicinity of solid surface of the tube and gave an analytical description (Rayleigh 1884) considering the stationary sound waves in a space between two plain parallel walls. He found that gas flows must appear due to the viscosity of medium in a thin boundary layer along the tube walls. Moreover, he found similar to air streaming generated by the vibrating membrane. Lord Rayleigh wrote in his paper:

“Experiments in acoustics have discovered more than one set of phenomena, apparently depending for their explanation upon existence of regular *currents of air* resulting from vibratory motion. . . Such currents, involving as they do *circulation of the fluid*, could not arise in the absence of friction. . .

. . . The more important of the problems relates to flows generated over vibrating plate. . . This was traced by Faraday (1831) to the action of currents of air, rising from the plate at the place of maximum vibration, and falling back to it at the nodes.”

The acoustic streaming is connected with the viscosity of the medium and with the presence of a solid obstacle or solid boundary walls in a field of sound wave, or other kind of oscillations: near the obstacle or a boundary, sound waves result in the tangential motion and in additional stresses that give rise due the absorption of the energy of oscillations in a thin boundary layer; this energy is transformed into the energy of stationary mass flows. The effect is nonlinear and appears in the second order in the wave amplitude. Although the effect is provided by the presence of viscosity, the velocity of established stationary flows actually does not depend on the viscosity coefficient. However, the time required to set up the steady flows is inversely proportional to the coefficients of viscosity.

Fascinated by the effect, Rayleigh tried to perform different experiments to further explore it. For example, he found strong air streaming as a result of the oscillation of a fork at the mouth of Helmholtz resonator. After the studies of Lord Rayleigh, almost half of a century passed before the renewal of the problem of the acoustic streaming.

Acoustic streaming was rediscovered in the experiments on piezoelectric generators and named Quartz wind: a strong mass flow was observed in front of an oscillating surface of quartz crystal in liquid (Meissner 1926). The flows of liquid generated by an ultrasonic source turned out to be so strong that they were enough to disturb the crystal face.

Soon, a new manifestation of acoustic streaming was found. Andrade (1931) experimentally studied flows generated by induced *standing sound waves* about a circular cylinder and found four stationary vortices visible by injection of smoke.

Similar results were obtained by Schlichting (1932), who performed also the calculation of the boundary layer on the cylinder oscillating in viscid fluid. In Fig. 10.1, the calculated streamlines of secondary flow and an experiment by Schlichting visualizing the four vortices generated by the oscillating (solid) cylinder are shown.

However, understanding that Andrade’s and Schlichting’s experiments demonstrate the same effect as quartz wind was reached only when a complete theory of acoustic streaming was built up by Eckart (1948). Since then, acoustic streaming is often referred to as Eckart flows. These studies invoked an activity exploring the

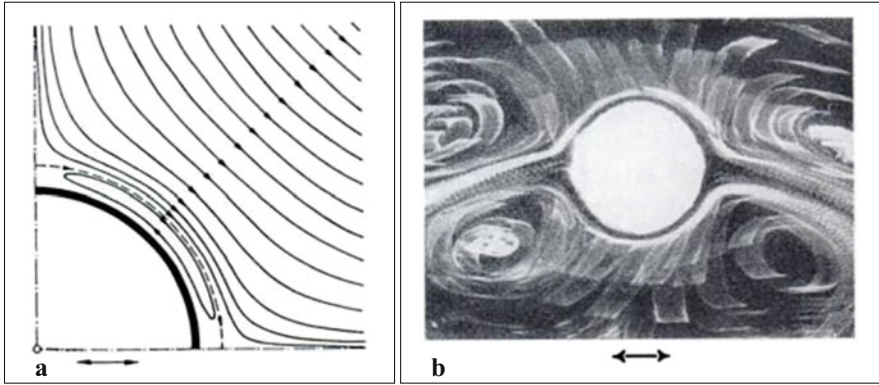


Fig. 10.1 Schlichting's results: (a) Flow portrait of the secondary flow (streaming) close to an oscillating circular cylinder; (b) experimental results on generation of secondary flow (streaming) close to an oscillating circular cylinder. After Schlichting (1932). Copyright Springer Science and Business Media

acoustic streaming in a wide range of media including the cell membrane in biology (Nyborg 1965). It is interesting that Faraday's effect explains creation of fountains in Tibetan singing bowls.

10.1.2 Secondary Flows in Magnetohydrodynamics

Especially, rich effects analogous to the acoustics streaming were found in studies of nonlinear effects in the interaction of magnetic flux tubes with acoustic wave (p -modes) in solar atmosphere (Ryutova 1986; Ryutova et al. 1996). It was found that at the site of an oscillating magnetic flux tube there appear qualitatively new effects that are absent in usual gas- and hydrodynamics. These are briefly described below.

1. First of all, the Reynolds stresses appear only *outside* the solid-body cylinder; in case of a magnetic cylinder, the additional magnetic stresses appear both *outside* and *inside* of the flux tube. This causes generation of plasma flows *outside* as well as *inside* magnetic structure. Of these two, *the inner flow* (that is absent in case of solid obstacles) plays a crucial role in the evolution of flux tube and its dynamics.

As a result, the magnetic field and plasma density are leveled along the field lines of the induced flow. Depending on the ratio of the duration of wave train (in particular p -modes) to the time of establishing viscous flow, the magnetic flux tube may be either split into smaller flux tubes (in case of coherent wave train, for example) or be diffusively dissolved into the ambient plasma (in the case of convective motions or incoherent wave train).

If in the splitting regime the same conditions are fulfilled for newborn flux tubes, each of the newborn flux tube experiences further splitting. This process of filamentation of magnetic structure proceeds until fragmentation products meet conditions corresponding to diffusive dissolution. Outer fragments are dissolved first. Note that higher-order nonlinear effects can also stop the fragmentation process.

The very process of fragmentation obviously determines the lifetime of magnetic structure.

2. Unlike the acoustic streaming, the magnetosonic streaming is accompanied by the current generation: if the absorption of oscillation energy is provided mostly by one of the plasma species electron or ion (the specific situation depends on the damping mechanism), current drive occurs along the plasma flow. This current leads to distortion and redistribution of the initial magnetic field, and, thus, to changing of the equilibrium. Geometry of the currents corresponds to that of the generated mass flows.
3. The most remarkable feature of the effect in the case of magnetic flux tube is that there are two different mechanisms leading to magnetosonic streaming, while for the acoustic streaming *only the absorption* of oscillation energy in a thin boundary layer is responsible:
 - (a) One mechanism is associated with the ponderomotive force which naturally arises if the force acting on plasma contains a nonzero vortex part. This mechanism is not connected with the direct absorption of oscillations, i.e., dissipative process, but requires radial inhomogeneity of magnetic field and plasma density across the magnetic flux tube. This condition holds always for solar flux tubes. In hydrodynamics, it is quite problematic, as it would require the inhomogeneous compressibility of medium.
 - (b) The other mechanism is similar to those in gas dynamics and is connected with the absorption of the momentum and angular momentum of flux tube oscillations.

Absorption of the momentum leads to the generation of *upward* and *downward* mass flows. Absorption of angular momentum causes the rotational mass flows across the flux tube axis.

4. In solar magnetic flux tubes, there are two major *nondissipative* mechanisms of the absorption of flux tube oscillations (see Chaps. 3 and 4). One is the anomalous damping in the resonance point, where the phase velocity of oscillations becomes equal to local meaning of Alfvén velocity. The second is the radiative damping of flux tube oscillations due to the radiation of secondary acoustic waves. This means that even in the absence of dissipative effects, the flux tube itself is able to provide and sustain the generation of plasma streaming and current drive inside and outside it.

10.2 Magnetosonic Streaming Due to the Action of Ponderomotive Force

We start with the generation of plasma streaming in and around magnetic flux tube resulted by action of ponderomotive force which naturally arises in the oscillating electromagnetic field at nonlinear stage.

Consider the flux tube performing a kink oscillations (with z -axis directed along the magnetic field):

$$m = \pm 1 \quad (10.1)$$

and having a long wavelength:

$$\lambda \gg R \quad (10.2)$$

To visualize the nature of magnetosonic streaming, we choose the kink mode as it is an exact analogue to periodic vibration of a solid cylinder in Schlichting's experiment shown in Fig. 10.1. The analogy is especially complete with the experiment of Andrade who placed a circular cylinder in a field of acoustic waves.

We will see that there are conditions under which an oscillating magnetic flux tube generates four vortices similar to those in the experiments of Andrade and Schlichting. Furthermore, as mentioned above, the force responsible for the generation of vortices *outside* the flux tube affects the plasma *inside* the flux tube as well and leads to generation of *inner* plasma flows and electric currents.

Plasma density and magnetic field are leveled along the streamlines of the induced flows and initially smooth magnetic flux tube splits into four independent flux tubes. The process of splitting continues until "newborn" flux tubes reach the regime when they diffusively dissolve.

The linearized system of MHD equations describing kink oscillations of a flux tube with radial dependence of background parameters has a form:

$$\rho \frac{\partial \tilde{\mathbf{v}}}{\partial t} = -\nabla \tilde{p} + \frac{1}{4\pi} (\nabla \times \tilde{\mathbf{B}}) \times \mathbf{B} + \frac{1}{4\pi} (\nabla \times \mathbf{B}) \times \tilde{\mathbf{B}} \quad (10.3)$$

$$\frac{\partial \tilde{\mathbf{B}}}{\partial t} = \nabla \times (\tilde{\mathbf{v}} \times \mathbf{B}) \quad (10.4)$$

where tilde marks perturbed quantities.

For long-wavelength oscillations under the condition (10.2), incompressibility is maintained with good accuracy:

$$\operatorname{div} \tilde{\mathbf{v}} = 0. \quad (10.5)$$

Since in the linear regime the z -component of velocity of kink oscillations is negligibly small (flux tube performs a periodic transverse motion), velocity perturbations $\tilde{\mathbf{v}}(\tilde{v}_r, \tilde{v}_\phi, 0)$ can be expressed through the stream function ψ :

$$\tilde{v}_r = -\frac{1}{r} \frac{\partial \psi}{\partial \phi}, \quad \tilde{v}_\phi = \frac{\partial \psi}{\partial r}. \quad (10.6)$$

Obviously, the ponderomotive force appearing in the second order has only components in the plane perpendicular to the z -axis, and the problem becomes two-dimensional. Then, the equation of motion for plasma in the second order has a form:

$$\rho(r) \frac{\partial \mathbf{V}}{\partial t} = -\nabla \left[p(r) + \frac{B^2(r)}{8\pi} \right] + \mathbf{f} + \nu \Delta \mathbf{V} \quad (10.7)$$

All quantities here have a standard meaning; ν is the kinematic viscosity, and \mathbf{f} is the ponderomotive force acting on a unit volume of plasma:

$$\mathbf{f} = -\left\langle \tilde{\rho} \frac{d\tilde{\mathbf{v}}}{dt} \right\rangle + \frac{1}{c} \langle \tilde{\mathbf{j}} \times \tilde{\mathbf{B}} \rangle \quad (10.8)$$

The averaging is performed over the wave period. Under the condition that the inertial term, the first term in left-hand side of (10.7), is small, Eq. (10.7) becomes stationary, describing a velocity field of steady flow:

$$\rho \nu \Delta \mathbf{V} = -\nabla \left[p + \frac{B^2}{8\pi} \right] + \mathbf{f} \quad (10.9)$$

This equation determines *existence* or *nonexistence* of magnetosonic streaming: the streaming can be generated by the oscillation flux tube only if *the force is nonpotential*. In other words, for generation of secondary flows it is necessary that

$$\nabla \times \mathbf{f} \neq 0. \quad (10.10)$$

Otherwise, the ponderomotive force leads to an insignificant redistribution of the plasma and magnetic field.

We will see below that the nonzero vortex part in the ponderomotive force is provided by the radial dependence of magnetic field and plasma density across the flux tube. The magnitude of the force is, therefore, determined by the gradient of magnetic field and plasma density.

The magnitude of \mathbf{f} becomes large in the resonance layer where the phase velocity of kink oscillations becomes close to the local Alfvén velocity. Although the generated flow is of the second-order effect, a strong plasma streaming can arise in a thin resonance layer.

Let us rewrite (10.9) through the angular velocity $\boldsymbol{\Omega} = \nabla \times \mathbf{V}$:

$$\rho v \Delta \Omega = \nabla \times \mathbf{f} \quad (10.11)$$

Equation (10.11) uniquely describes the velocity field of generated steady flows.

To carry out a quantitative analysis, we solve linear equations for kink oscillations and through linear solution find the ponderomotive force.

We assume that all perturbed quantities are proportional to $\exp(i\omega t - ikz)$ and their dependence on ϕ has a form (linearly polarized wave):

$$\psi(r, \phi) = \chi(r) \cos \phi \quad (10.12)$$

With (10.6) and (10.12), the linearized system of MHD equations for the kink mode is reduced to a single equation for χ :

$$\frac{\partial}{\partial r} \left[\rho(r) - \frac{k^2 B^2(r)}{4\pi\omega^2} \right] r \frac{\partial \chi}{\partial r} - \left[\rho(r) - \frac{k^2 B^2(r)}{4\pi\omega^2} \right] \chi(r) = 0 \quad (10.13)$$

The important feature of (10.13) is that it has the classical form of the Rayleigh equation with a singularity: the coefficient of higher derivative at some point across the tube becomes zero. In our case, this is just the same point where the phase velocity of kink oscillations (ω/k) becomes equal to the local Alfvén velocity. As considered in Chap. 4 strong absorption of oscillations, the anomalous damping, takes place at this point. The analytical solution of (10.13) and corresponding damping rate are given in Chap. 4, Sect. 4.1.

Having solutions of (10.13),

$$\tilde{v}_r = \frac{\chi(r)}{r} \sin \phi, \quad \tilde{v}_\phi = \frac{\partial \chi(r)}{\partial r} \cos \phi \quad (10.14)$$

and

$$\tilde{B}_r = -\frac{kB}{\omega} \frac{\chi(r)}{r} \sin \phi, \quad \tilde{B}_\phi = -\frac{kB}{\omega} \frac{\chi(r)}{r} \cos \phi \quad (10.15)$$

we can find the expression for ponderomotive (nonlinear) force (10.8).

The averaged force has only stationary terms and can be written as follows:

$$\mathbf{f} = -\langle [\tilde{\mathbf{v}} \operatorname{div}(\rho \tilde{\mathbf{v}}) + \rho(\tilde{\mathbf{v}} \nabla) \tilde{\mathbf{v}}] \rangle + \frac{1}{4\pi} \langle (\nabla \times \tilde{\mathbf{B}}) \times \tilde{\mathbf{B}} \rangle \quad (10.16)$$

After some algebra, we get the following expressions for components of the ponderomotive force:

$$f_r = G(r) \cos 2\phi, \quad f_\phi = H(r) \sin 2\phi \quad (10.17)$$

where

$$f_r = \frac{\rho}{2} \cos 2\phi \left\{ \frac{\chi^2}{r^3} - \frac{\chi'^2}{r} - \frac{\chi^2}{r^2} \frac{\partial \ln \rho}{\partial r} - \frac{k^2 v_A^2}{\omega^2} \left[\chi' \left(\frac{1}{r} \frac{\partial}{\partial r} r \chi' - \frac{\chi}{r^2} \right) + \chi'^2 \frac{\partial \ln B}{\partial r} \right] \right\} \quad (10.18)$$

and

$$f_\phi = \frac{\rho}{2} \sin 2\phi \left\{ \frac{\chi}{r} \chi'' + \frac{\chi}{r^2} \chi' - \frac{\chi'^2}{r} + \frac{\chi \chi'}{r} \frac{\partial \ln \rho}{\partial r} - \frac{k^2 v_A^2}{\omega^2} \left[\frac{\chi}{r} \left(\frac{\chi}{r^2} - \frac{1}{r} \frac{\partial}{\partial r} r \chi' \right) + \frac{\chi \chi'}{r} \frac{\partial \ln B}{\partial r} \right] \right\} \quad (10.19)$$

Here, $\chi(r)$ is the solution of (10.13) and the prime stands for derivative over r .

Equations (10.17)–(10.19) immediately show that streamlines of the field of ponderomotive force are closed in each quarter of the circle at a given radius of the magnetic flux tube. Sketch of streamlines of generated flow is shown in Fig. 10.2. It is important that plasma particles frozen in magnetic field follow the streamlines and ultimately end up with the same geometry as the generated flows (Fig. 10.2). It must be emphasized that the flow is generated *inside* the flux tube as well as *outside* it.

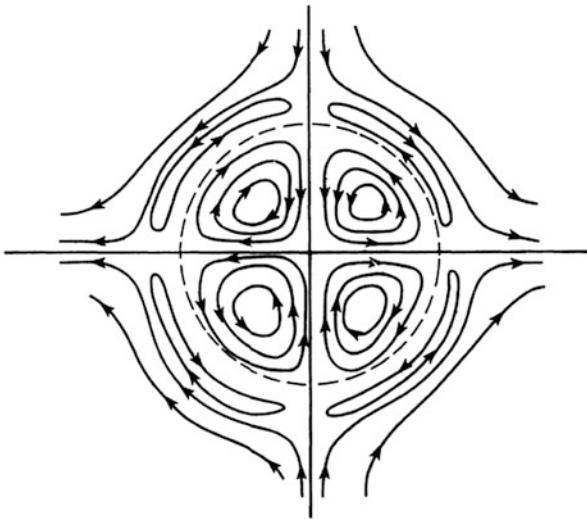


Fig. 10.2 Field of ponderomotive forces. The dashed line is an effective radius of flux tube

It is interesting to compare (10.11) with the classical equation describing the streaming generated by sound waves in a liquid (Equation (25) in Eckart 1948):

$$\frac{\partial \mathbf{R}_1}{\partial t} - v_0 \nabla^2 \mathbf{R}_1 = b \frac{v_0}{\rho_0} \nabla \rho_1 \times \nabla \left(\frac{\partial \rho_1}{\partial t} \right) \quad (10.20)$$

where $\mathbf{R}_1 = \nabla \times \mathbf{u}_1$ is rotation of the secondary flow, and the coefficient $b = 4/3 + v'/v_0$ is the abbreviation containing v , which is the ordinary coefficient of shear viscosity measured in cm^2/s , and v' which is the bulk viscosity. Although in fluid dynamics the generation of flow is provided by the viscous stresses and thus by the *absorption* of oscillation energy, the velocity amplitude of secondary flow turns out to be *independent* of the magnitude of viscous coefficients unless the bulk viscosity is nonzero.

There is a principal difference between the amplitude of generated flow in the case of acoustic streaming and that in the magnetosonic streaming. In the case of flux tube oscillations, we have two different means for generation of secondary flows and electric currents. One is associated with the *dissipative effects*. In this case, the amplitude of plasma flow is proportional to the ratio of the damping rate to the coefficient of plasma viscosity. The magnitude of the damping rate is determined by the specific mechanism of absorption, which can be provided by the resonance absorption, by radiation of secondary acoustic waves, or by the usual dissipative mechanisms of absorption such as viscosity, thermoconductivity, and Ohmic losses. And yet, like in the acoustic streaming, the amplitude of secondary flow also turns out to be *independent* of the dissipative coefficients. But, the time required to set up the steady state depends on the plasma resistance and is inversely proportional to the coefficient of viscosity or other dissipative coefficients. This is discussed in Sect. 10.4.

Another cause of secondary flows is the action of ponderomotive force, considered above. Here, the situation is quite different because ponderomotive force is not dissipative and the amplitude of generated flow is no longer *independent* of the viscous coefficient (or other dissipative coefficients) but is inversely proportional to it. This means that, at the applicability limit, flow generated by the action of ponderomotive force can reach a significant value.

In the following sections, we discuss a qualitative picture of the effect of ponderomotive force, and, thus, of the induced flow on the evolution of magnetic flux tubes with the initially smooth radial profile of background parameters.

10.3 Process of Filamentation and Diffusive Vanishing of Magnetic Flux Tubes

The evolution of a flux tube due to the generated plasma flow strongly depends on the physical parameters of the flux tube and surrounding plasma, in particular, on the initial size (radius) of the tube, and on the relationship between the time of

establishing of viscous flows and the duration of acoustic wave trains interacting with the flux tube. One can see from (10.7) that for large enough flux tubes the viscous term is small and its evolution is determined by the inertial term $\rho \partial V / \partial t$.

In this section, we give qualitative analysis of the case when the viscous term is essential and secondary streaming can be described by the averaged stationary equation (10.9). At the end of this section, we compare these results with an estimate of the lifetime of flux tube for which viscous effects are negligible.

We start with qualitative analysis of the field of forces defined by (10.18) and (10.19).

Denote the amplitude of flux tube displacement in kink oscillations by $\xi = \sqrt{\xi_r^2 + \xi_\phi^2}$ ($\tilde{\mathbf{v}} = \partial \xi / \partial t$). From (10.3) and (10.4), we can estimate the magnitude of magnetic field perturbation \tilde{B} as:

$$\tilde{B} \sim B \frac{\xi \omega}{v_A} \quad (10.21)$$

The magnitude of ponderomotive force is of the order of (\tilde{B}^2/R) , that is,

$$f \sim \frac{B^2 \xi^2 \omega^2}{8\pi v_A^2 R} \quad (10.22)$$

The velocity amplitude of generated flow is estimated from (10.11):

$$\rho v V \frac{1}{R} \sim f \quad (10.23)$$

or

$$V \sim \frac{f R^2}{\rho v} \quad (10.24)$$

As discussed above, the amplitude of plasma streaming under the action of ponderomotive force does *depend* on the coefficient of viscosity and is inversely proportional to it. This assertion is valid until the last term in (10.18) is larger than the inertial term.

The quantity (R^2/ρ) entering estimate (10.24) is proportional to the time of establishing of viscous flow:

$$\tau_v \sim \frac{R^2}{\nu}, \quad (10.25)$$

and determines the time required for magnetic structure to reach a new state provided by generated plasma flows.

The field of forces and, therefore, the character of generated flows depend on the relation between τ_v and the duration, T , of the acoustic wave train interacting with the flux tube.

We discuss here two cases, those of “*coherent*” and “*incoherent*” wave trains.

In the case of a long “*coherent*” wave train when

$$T > \tau_v \quad (10.26)$$

the estimate (10.24) becomes as follows:

$$V \sim \frac{f \tau_v}{\rho} \quad (10.27)$$

The plasma density and magnetic field are gradually equilibrating along the streamlines of induced flow and obtain the same symmetry as those of ponderomotive force. This process leads to splitting of magnetic flux into four independent flux tubes. This symmetry is a result of the specific kink oscillations whose azimuthal number, (10.1), provides the corresponding symmetry of the force:

$$\mathbf{f} = \mathbf{i}G(r)\cos 2\phi + \mathbf{j}H(r)\sin 2\phi \quad (10.28)$$

Farther evolution of the system depends on the behavior of newborn flux tubes. Analytical description of the next stage is difficult, because newborn flux tubes form an ensemble of closely spaced structures with complicated flows inside them. They can interact with each other or/and be influenced by acoustic waves as their predecessors. If newborn flux tubes (or some of them) are influenced mostly by coherent acoustic waves, the filamentation process goes further, and those flux tubes experience further splitting. The behavior in this regime is confirmed by numerical simulation (Sect. 10.5). In this case, the lifetime of the magnetic structure is determined by the length of the time required to complete the filamentation process and by the subsequent diffusive vanishing of the smallest flux tubes.

10.3.1 Diffusive Broadening of Flux Tube

In the opposite case of short “*incoherent*” wave train or convective motions, when

$$T < \tau_v \quad (10.29)$$

the generated flows have a character of stochastic motions. These motions result in a diffusive broadening of a flux tube: the plasma density and magnetic field are smoothed out gradually until the flux tube disappears.

In Fig. 10.3, the schematic change in time of squared magnetic field squared and gas kinetic pressure is shown: the decrease of magnetic field and the leveling of gas

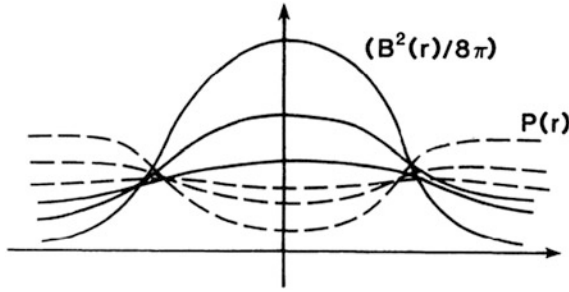


Fig. 10.3 Schematic change in time of squared magnetic field and gas kinetic pressure: the decreasing of magnetic field and the leveling of gas kinetic pressures inside and outside flux tube ends up by diffusive dissolving of flux tube

kinetic pressures inside and outside flux tube lead ultimately to complete dissolving of a flux tube.

The “diffusion coefficient,” defining a speed of this process, is

$$D \sim \frac{\Delta x^2}{T} \tag{10.30}$$

where Δx is the displacement of an element of a tube estimated as

$$\Delta x \sim VT \tag{10.31}$$

The velocity amplitude of generated flow, in this case, is of the order of

$$V \sim \frac{f}{\rho} T, \tag{10.32}$$

and for the diffusion coefficient, we have

$$D \sim \frac{\xi^4 \omega^4}{R^2} T^3 \tag{10.33}$$

The lifetime of a magnetic flux tube can be estimated in terms of the diffusion coefficient as:

$$t_D \sim \frac{R^4}{\xi^4 \omega^4 T^3} \tag{10.34}$$

This estimate is valid for flux tubes that interact with the acoustic waves with the period T less than τ_v or with the convective motions with turnout time $T < \tau_v$. At the same time, the radius of flux tubes should be small enough to satisfy the

condition when the inertial term is small compared with the viscous term:

$$\rho \left| \frac{\partial \mathbf{V}}{\partial t} \right| < |\nu \Delta \mathbf{V}| \quad (10.35)$$

As mentioned above for thick flux tubes, the term $|\nu \Delta \mathbf{V}|$ is negligibly small and their evolution is determined by the inertial term. In this case, the generated flow is estimated as:

$$V \sim \frac{f t_V}{\rho}, \quad (10.36)$$

where t_V is the time of the establishing of the generated flow. If this time is less or comparable with the duration of acoustic wave trains, the flux tube experiences the splitting into thinner tubes. The time of splitting is of the order of t_V :

$$t_{\text{split}} \sim t_V \sim \frac{R}{V} \sim \frac{\rho R}{f t_{\text{split}}} \quad (10.37)$$

or

$$t_{\text{split}} \sim \sqrt{\frac{\rho R}{f}} \sim \frac{R}{\omega \xi} \quad (10.38)$$

Transition from the case (10.34) to (10.38) occurs when these timescales become comparable, i.e., for a tube radius exceeding the estimate

$$R \sim \xi \omega T. \quad (10.39)$$

In the next section, we give order-of-magnitude estimate of generated flows and corresponding lifetimes for photospheric flux tubes interacting with the convective motions and acoustic wave trains.

10.3.2 *Quantitative Estimates—Lifetimes and Spatial Scales of Flux Tubes*

For quantitative estimates, we adopt the following typical values: the period of acoustic waves $T_p = 300\text{--}180$ s, duration of acoustic wave train $T_{\text{wtr}} = 25$ min, and lifetime of convective granule $T_{\text{conv}} = 8$ min. Consider flux tubes with $R = 100$ km and less. For the effective viscosity at magnetic flux site, we use the observed limit on turbulent velocities, \tilde{v} , and characteristic length scale of the turbulence, \tilde{l} , consistent with observations (Beckers 1976; Title et al. 1992; Yi and Engvold 1993): $\tilde{v} = 0.4 \text{ km s}^{-1}$ and $\tilde{l} = 20$ km. This gives for the effective viscosity $\nu = 8 \text{ km}^2/\text{s}$.

For the chosen parameters $\tau_\nu = R^2/\nu \simeq 21$ min, and the necessary condition (10.26) is fulfilled. Obviously, the duration of the splitting process is comparable with the time of the establishing of viscous flows, e.g., τ_ν . So that in time $t_{\text{split}} \simeq 21$ min flux tube with radius $R = 100$ km splits into four newborn flux tubes each with radius roughly of $R = 50$ km.

To estimate the amplitude of corresponding flows generated across the flux tube, we use (10.24) which with (10.22) becomes as follows:

$$V \simeq \frac{1}{2} \frac{\xi^2 \omega^2}{\nu} R \quad (10.40)$$

We assume that transverse displacement of a flux tube ξ is not less than $R/2\pi$. This assumption may be justified from the condition (10.39) where, for periodic motions replacing ωT by 2π , we come to above estimate.

For the velocity of transverse displacement of a flux tube, $\tilde{v} = \omega\xi$, this estimate gives $\tilde{v} = \omega\xi = R/T_p$. And for tubes of radius $R = 100$ km, we have $\tilde{v} = 0.33 \text{ km s}^{-1}$ which is consistent with the observed values. From (10.40), we find the amplitude of generated flows: $V = 0.7 \text{ km s}^{-1}$.

Newborn flux tubes having radius 50 km may experience farther splitting. This time either again due to the interaction with the acoustic wave trains or, more likely, due to the action of convective motions: for these flux tubes $\tau_\nu = 5.21 \text{ min} < T_{\text{conv}}$. Duration of this process is of the order of 5.21 min. The amplitude of generated flows is $V \simeq 0.1 \text{ km s}^{-1}$. In the third generation, flux tubes whose radius is now about 25 km are too thin to experience farther splitting and should vanish diffusively in time $\simeq 1.3$ min. The total lifetime of a flux tube with $R = 100$ km is thus roughly 27 min.

It is important to note that the condition (10.39) determines the lower limit of flux tube size (its radius) below which flux tubes do not experience fragmentation and vanish diffusively. To estimate the critical radius given by (10.39) note that diffusive regime requires the condition (10.29). This means that at given timescale T , flux tubes with radius $R \leq \sqrt{\nu T}$ are subject to diffusive vanishing with $t_D \simeq T$ (with $T \leq \tau_\nu$!). If we assume that the minimum effective timescale is that of 3 min oscillations, the minimum critical radius is then $R_{\text{min}} = \sqrt{\nu T_p} = 38$ km. Of course, this estimate is the order-of-magnitude one, and the value of critical radius may be smaller or larger than 40 km. For example, convective motions also can terminate the fragmentation process in flux tubes with radius about 60–70 km. In this case, the flux tube vanishes diffusively in time of $\simeq 7$ –9 min.

The estimated timescales, the range of velocities, and the dynamics of photospheric flux tubes are in a good agreement with the observed regularities found in sub-arcsecond measurements (Berger et al. 1995; Schrijver et al. 1997; Kubo et al. 2010).

It is important to note that plasma flows are also generated *outside* flux tube. In a case of kink oscillations under the conditions close to (10.26), four stationary vortices are generated outside a flux tube. These vortices, shown in Fig. 10.2 outside dotted line (representing the flux tube effective radius), are similar to those

generated in the experiments of Andrade and Schlichting shown in Fig. 10.1 (see also Holtzmark et al. 1954). In these experiments, as well as in any manifestation of an acoustic streaming, the only mechanism leading to the generation of flows is the *absorption* of the energy of oscillation in a thin boundary layer. Whereas the mechanism of generation of mass flows inside and outside oscillating magnetic flux tubes is associated with “always present” intrinsic properties of flux tubes.

10.4 Generation of Mass Flows Due to the Absorption Mechanisms

In the presence of dissipative effects just like in the case of acoustic streaming, the energy of oscillating flux tube may be converted into secondary flows within a thin boundary layer. This mechanism leads to additional and much richer effects in magnetohydrodynamics of flux tubes which in some aspects have no analogy in hydrodynamics.

As discussed throughout the book, along with the usual dissipative effects, the energy of flux tube oscillations is intrinsically damped out due to the nondissipative damping mechanisms: (1) Radiative damping when an oscillating flux tube gives off its energy through emission of secondary acoustic or MHD waves; and (2) Anomalous damping in the resonance layer, where the phase velocity of flux tube oscillations becomes close to the local meaning of Alfvén velocity.

In particular, the anomalous damping of kink oscillations in the resonant layer leads to especially strong effect of magnetosonic streaming.

Recall that physically, the nature of this mechanism is the pumping of oscillation energy into the resonance layer where the dissipation occurs. The whole *momentum* or/and *angular momentum* of flux tube oscillations is transferred to the plasma in a thin layer, causing in nonlinear stage generation of a strong mass flows.

Formally, the expression for the force inducing the secondary streaming has the same form as (10.8), but now the terms that are directly connected with the resonant absorption are taken into account.

Absorption of the *momentum* of oscillations leads to the generation of *upward* or *downward* mass flows. Absorption of *angular momentum* of oscillations causes the *rotational* mass flows in a plane perpendicular to tube axis. Nonzero angular momentum can be transmitted, for example, by circularly polarized kink oscillations.

The solution of (10.13) for a smooth dependence of plasma density and magnetic field on the tube radius (Chap. 4, Eq. (4.12)) leads to the following dispersion relation:

$$\omega \simeq \frac{kB}{\sqrt{4\pi(\rho + \rho_e)}} \left(1 + \frac{i\pi}{4} \frac{\rho}{\rho + \rho_e} \frac{l}{R} \right) \quad (10.41)$$

One can see that it contains a large imaginary part corresponding to strong absorption of kink oscillations in the resonance layer. For smooth radial profile of magnetic field and density, when $l \simeq R$, the damping rate becomes comparable with eigenfrequency $\gamma = \text{Im}\omega \sim \text{Re}\omega$, and the effect is quite strong.

From (10.41), we have for the spatial damping rate $\alpha = \text{Im}k$:

$$\alpha = \frac{\pi}{4} \frac{\omega}{v_A} \sqrt{\frac{\rho}{\rho + \rho_e}} \frac{l}{R} \quad (10.42)$$

The energy of kink oscillations per unit length of a tube is $W = \rho \tilde{v}^2 \pi R^2$; \tilde{v} is the magnitude of linear velocity perturbation (see (10.6)). The momentum of oscillation is

$$\mathcal{P} = \frac{k_z}{\omega} W \quad (10.43)$$

The force F_z appearing due to the absorption of momentum \mathcal{P} is proportional to

$$F_z \sim \alpha \frac{k_z}{\omega} \mathcal{P} \quad (10.44)$$

The force acting on a unit volume of a tube is then

$$f_z = \frac{F_z}{2\pi Rl} \quad (10.45)$$

From (10.42), (10.44) and (10.45), we have

$$f_z \simeq \frac{\pi}{8} \frac{\omega}{v_A} \sqrt{\frac{\rho}{\rho + \rho_e}} \rho \tilde{v}^2 \quad (10.46)$$

As we see, the “model” parameter (l/R) does not enter in the final expression for the force responsible for the generation of mass flows. The magnitude of generated flows which is proportional to f_z is completely determined by the basic physical parameters and assumes their radial dependence to be arbitrary.

Let us now estimate the flow velocities generated along magnetic flux tubes under a real conditions typical to solar atmosphere. In particular, we consider two examples, flux tubes in the chromosphere and low corona.

For these estimates, it is convenient to rewrite expression (10.46) through plasma beta. The pressure equilibrium condition gives that $\rho/\rho_e = \beta/(1 + \beta)$, and (10.46) becomes

$$f_z \simeq \frac{\pi}{8} \frac{\omega}{v_A} \sqrt{\frac{\beta}{1 + 2\beta}} \rho \tilde{v}^2 \quad (10.47)$$

The amplitude of generated flows, (10.24), is then

$$V_z \simeq \frac{\pi}{8} \frac{\omega}{v_A} \sqrt{\frac{\beta}{1+2\beta}} \tilde{v}^2 \frac{R^2}{v} \quad (10.48)$$

In chromosphere and corona, i.e., in the magnetic dominant case ($\beta \ll 1$), viscosity is estimated by Braginsky's kinetic coefficients:

$$\rho\nu = 2.21 \times 10^{-15} \frac{T^{5/2}}{\ln\Lambda} \text{ g cm}^{-1} \text{ s}^{-1} \quad (10.49)$$

For quantitative estimate, we use the following parameters.

For chromosphere: temperature $T = 10^4$ K, Coulomb logarithm $\Lambda = 10$, density $n = 10^{11} \text{ cm}^{-3}$ ($\rho = 1.67 \times 10^{-13} \text{ g cm}^{-3}$), magnetic field $B = 50$ G (Alfvén velocity is then $v_A = 345$ km/s), characteristic radius of magnetic structure $R = 100$ km, and wave period $T_p = 180$ s.

For low corona: temperature $T = 10^5$ K, $\Lambda = 20$, density $n = 3 \times 10^9 \text{ cm}^{-3}$ ($\rho = 5 \times 10^{-15} \text{ g cm}^{-3}$), weaker magnetic field of $B = 10$ G (Alfvén velocity $v_A = 399$ km/s), and wider structure of radius $R = 200$ km; for the wave period, we accept a typical period of Alfvén waves $T_p = 100$ s.

We assume that the velocity of transverse displacement of a flux tube in chromosphere and corona is proportional to the radius of the structure and wave frequency. This gives in chromosphere $\tilde{v} \simeq 3$ km/s, and in corona $\tilde{v} \simeq 12$ km/s.

For the chosen set of parameters, (10.48) gives the following estimates for the amplitude of mass flows generated along the flux tube: in chromosphere $V_z \simeq 23$ km/s and in corona $V_z \simeq 2.5$ km/s. It is remarkable that the range of velocities in the chromosphere are close to those observed in spicules.

Thus, in the application to chromospheric magnetic structures “magnetosonic streaming” can be considered as a promising candidate for more detailed studies of the origin of spicules and their dynamics. It is important to note that the secondary flows generated along and/or across the magnetic flux tube should not be confused with short-living strong sporadic jets observed throughout the solar atmosphere. The secondary flows belong rather to the flux tubes themselves, the feature that is “always there.”

In the same way as above, we can estimate the magnitude of the force appearing due to the absorption of angular momentum of oscillations which is responsible for generation of azimuthal flows and electric currents. The angular momentum directed along the tube axis is estimated as:

$$M_z \sim \frac{W}{\omega} \quad (10.50)$$

The angular momentum absorbed per unit length of a tube is proportional to $(\alpha k_z / \omega) M_z$. An estimate for force acting on plasma in the azimuthal direction may

be obtained from the following relation:

$$2\pi Rl \sim \frac{\alpha k_z}{\omega} M_z \omega \quad (10.51)$$

or

$$f_\phi \sim \frac{\alpha k_z}{\omega} \frac{W}{2\pi Rl}, \quad (10.52)$$

These are the same order-of-magnitude force as in the case of the absorption of the momentum of oscillation.

As mentioned above, if the oscillation energy is mostly absorbed by one of the plasma components (electron or ion), mass flows are accompanied by current drive. In this case, imaginary part of (10.41) contains additional terms connected with the specific damping mechanism.

If the absorption is associated mostly with the electron component of plasma, the damping may be a result of one of the two major damping mechanisms:

1. Electron–ion collision with collisional damping rate

$$\delta_e \sim v_{ei} \frac{v_A}{k_z v_{Te}^2} \quad (10.53)$$

2. Landau damping with

$$\delta_L \sim \frac{\omega}{k_z v_{Te}}, \quad (10.54)$$

v_{Te} being the electron thermal speed.

For example, in a case of Landau damping for spatial damping rate α_L , we have

$$\alpha_L \sim \frac{\sqrt{\pi}}{2} \frac{r_i^2}{l^2} \frac{T_e}{T_i} \frac{kv_A}{v_{Te}} \quad (10.55)$$

Here, r_i is the ion Larmor radius, T_e and T_i are the electron and ion temperatures, respectively.

Let us estimate, for example, the magnitude of the azimuthal electric current generated by the absorption of angular momentum. The force (Eq. (10.52)) causes the motion of electrons with the velocity

$$u_{e\phi} \sim \frac{f_\phi \tau}{n_e m_e}, \quad (10.56)$$

And, thus, leads to the appearance of azimuthal current $j_\phi = en_e u_\phi$ of the order of

$$j_\phi \sim \frac{\alpha_L}{v_{ei}} \frac{e}{m_e} \frac{\rho \tilde{v}^2}{2} \frac{R}{l} \quad (10.57)$$

In the same way, we can estimate the currents generated along the magnetic field due to the action of the z -component of the force (Eq. (10.46)).

Although the generated currents are of the second-order effect, they play an essential role in the dynamics of the magnetic flux tube and may lead to the distortion of the initial magnetic field, changing its equilibrium conditions.

10.5 Numerical Analysis

In this section, numerical simulations of magnetosonic streaming and current drive are performed for the regime corresponding to the filamentation process, i.e., to the generation of the azimuthal flows and electric currents.

10.5.1 Basic Equations and Numerical Method

For numerical simulations, the following assumptions are adopted: (1) the medium is an ideal gas, (2) the gas is a polytrope of index $\gamma = 1.5$, (3) the magnetic field is frozen in the gas and is vertical, and (4) gravity is neglected. Cartesian coordinates (x, y, z) are adopted so that the z -direction is parallel to the magnetic field. It is assumed that the evolution is two-dimensional with $\partial/\partial z = 0$. Thus, the basic equations are as follows:

$$\frac{\partial \rho}{\partial t} + \frac{\partial}{\partial x}(\rho V_x) + \frac{\partial}{\partial y}(\rho V_y) = 0, \quad (10.58)$$

$$\frac{\partial}{\partial t}(\rho V_x) + \frac{\partial}{\partial y}(\rho V_x V_y) + \frac{\partial}{\partial x} \left(\rho V_x^2 + p + \frac{B_z^2}{8\pi} \right) = \delta_x, \quad (10.59)$$

$$\frac{\partial}{\partial t}(\rho V_y) + \frac{\partial}{\partial x}(\rho V_x V_y) + \frac{\partial}{\partial y} \left(\rho V_y^2 + p + \frac{B_z^2}{8\pi} \right) = \delta_y, \quad (10.60)$$

$$\frac{\partial B_z}{\partial t} + \frac{\partial}{\partial x}(V_x B_z) + \frac{\partial}{\partial y}(V_y B_z) = 0, \quad (10.61)$$

$$\begin{aligned}
& \frac{\partial}{\partial t} \left[\frac{p}{\gamma - 1} + \frac{1}{2} \rho (V_x^2 + V_y^2) + \frac{B_z^2}{8\pi} \right] \\
& + \frac{\partial}{\partial x} \left[\frac{\gamma}{\gamma - 1} p V_x + \frac{1}{2} \rho V_x (V_x^2 + V_y^2) + \frac{B_z^2}{4\pi} V_x \right] \\
& + \frac{\partial}{\partial y} \left[\frac{\gamma}{\gamma - 1} p V_y + \frac{1}{2} \rho V_y (V_x^2 + V_y^2) + \frac{B_z^2}{4\pi} V_y \right] = \delta_x V_x + \delta_y V_y,
\end{aligned} \tag{10.62}$$

where δ_x and δ_y describe the interaction of a flux tube with acoustic waves. All other symbols have their standard meaning.

The distribution of the initial magnetic field strength $B_z(x, y)$ is given by:

$$B_z(x, y) = [8\pi p(x, y)/\beta(x, y)]^{1/2} \tag{10.63}$$

where

$$\beta(x, y) = \beta_0/f(x, y), \tag{10.64}$$

$$f(x, y) = \frac{1}{2} \left[-\tanh\left(\frac{r - r_0}{w_0}\right) + 1 \right], \tag{10.65}$$

$$r = [(x - x_0)^2 + (y - y_0)^2]^{1/2}, \tag{10.66}$$

and where β_0 is the plasma beta at the center of the flux tube, x_0 and y_0 are the coordinates of the center of the flux tube, r_0 is its radius, and w_0 is the width of the boundary layer between the flux tube and the unmagnetized plasma. In these calculations, we use $\beta_0 = 0.2$ and $w_0 = 1.0H$, where H is the characteristic length scale.

The initial density and pressure distributions are calculated by using (10.63)–(10.66), the equation of the state and the equation of magnetostatic equilibrium

$$p(x, y) + \frac{B_z^2}{8\pi} = \text{const.} \tag{10.67}$$

An incompressible velocity field is initially imposed on the magnetic flux tube. We assume a velocity potential of the form:

$$\Phi(x, y) = A \sin\pi x \cdot \sin\pi y, \tag{10.68}$$

and consider resulting velocity field:

$$V_x = -f(x, y) \frac{\partial \Phi}{\partial y}, \quad V_y = -f(x, y) \frac{\partial \Phi}{\partial x}, \tag{10.69}$$

Time-dependent acoustic perturbations are imposed on the magnetic flux tube via interaction terms in the equations of motion ((10.59) and (10.60)) of the following form:

$$\delta_x = Af(x, y) \cdot \sin \omega t, \quad \delta_y = Af(x, y) \cdot \cos \omega t. \quad (10.70)$$

We assume free boundaries for $x = 0, x = X_{\max}, y = 0,$ and $y = Y_{\max}$. Equations (10.58)–(10.65) are nondimensionalized by using a characteristic length scale H , the sound speed c_s , and the density ρ_0 outside the flux tube. The system is solved numerically by using a modified Lax–Wendroff scheme with an artificial viscosity according to Richtmyer and Morton (1967). The tests and accuracy of such an MHD code have been described, for example, in Tajima (1989). The mesh sizes are $\Delta x = X_{\max}/(N_x - 1)$ and $\Delta y = Y_{\max}/(N_y - 1)$, where N_x and N_y are the numbers of mesh points in the x - and y -directions. The total number of mesh points is $(N_x \times N_y) = (203 \times 203)$, and the total area is $(X_{\max} \times Y_{\max}) = (20 \times 20)$ in a typical model in units of the characteristic length scale.

10.5.2 Numerical Results

We will discuss here two examples (models 1–2) of numerical simulation of the filamentation process in the interaction of magnetic flux tube with acoustic waves. The main parameters of simulation models are the interaction terms, δ_x and δ_y , the initial radius of flux tube, r_0 , the frequency, ω , and the artificial viscosity parameter, q . Model 1 represents the case where the interaction term has only an x -component, $\delta_x = 0.05$. In model 2, we allow a nonzero y -component of the interaction term, $\delta_y = 0.05$. The artificial viscosity is $q = 3.0$. By varying radius and frequency, we also study the dependence of the evolution of flux tube on these parameters. Two other regimes will be discussed in Chap. 22 as an illustration of what can be observed.

Figure 10.4 shows the initial ($t = 1$) and final ($t = 52$) states of the contour lines of the magnetic field B_z , the density distribution ($\log \rho$), the velocity field $\mathbf{V} = (V_x, V_y)$, and the current density $\mathbf{j} = (j_x, j_y)$ for model 1. The radius of unperturbed flux tube in this model is $r_0 = 2H$, and temporal frequency of the wave is $\omega = 2\pi/5$. Initially, the vertical magnetic field with a smooth radial profile is concentrated in a flux tube with radius r_0 , the plasma density inside the flux tube (also having a smooth radial dependence) is lower than outside for pressure equilibrium (isothermal plasma), and the velocity field shows the potential, incompressible flow imposed on magnetic flux tube according to (10.69). In the course of the evolution, the magnetic flux tube breaks down into four different magnetic structures ($t = 52$).

The magnetic field of the final configuration is distributed into two major and two minor, nearly symmetrical, tubes. The density distribution and generated current density show the filamentation process as well. It is remarkable that magnetic field lines and plasma density lines in the “final” state are no longer collinear—a fact

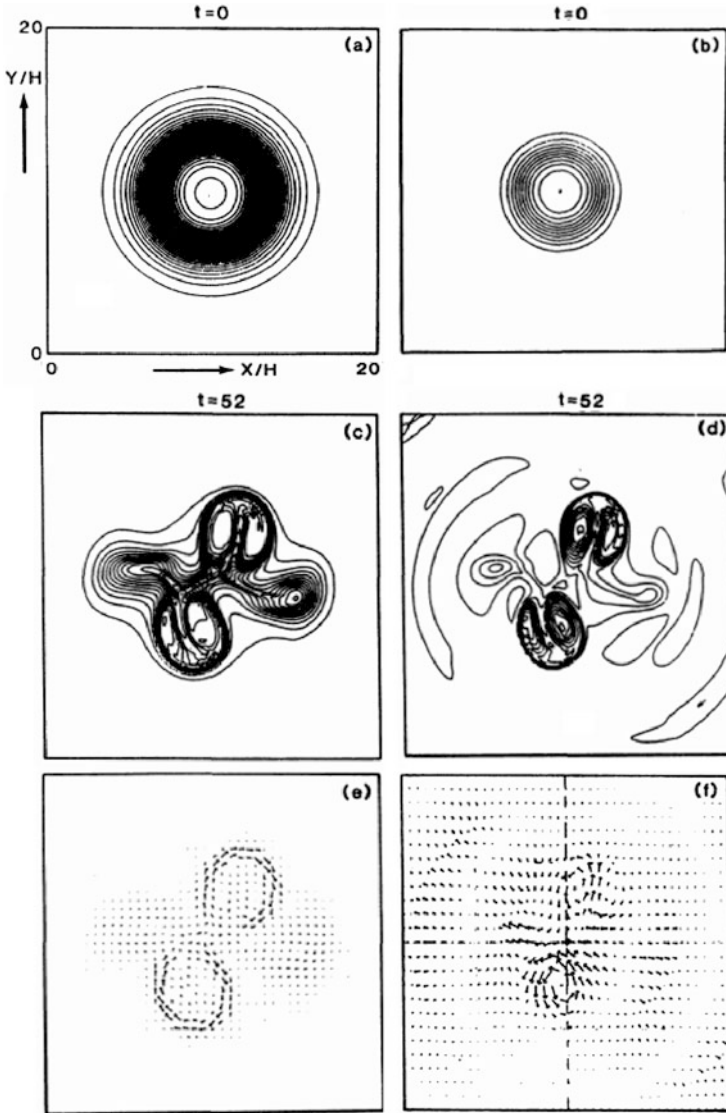


Fig. 10.4 Results for model 1. Shown are: (a) the contour lines of B_z and (b) the density contours ($\log \rho$) of undisturbed flux tube. (c)–(f) Results at $t = 52$: (c) the contour lines of magnetic field, (d) the density contours, (e) the current density $\mathbf{j} = (j_x, j_y)$, and (f) the velocity field $\mathbf{V} = (V_x, V_y)$. Total illustrated area is (20×20) in units of H . The contour level step width is 1.5 for (a) in the unit of linear scale and 0.2 for (b) in the unit of logarithmic scale. The maximum values of the current density and velocity vectors shown in panels (e) and (f) are in units of $(\rho c_s^2/H)^{1/2}$ and sound speed c_s , respectively. Numbers on top of each frame represent the time in units of H/c_s .

important for further evolution of a conglomerate of newborn flux tubes as well as for observed properties of magnetic structures.

It is important to emphasize that in all cases the generation of flows and fragmentation of magnetic flux tubes accompanied by redistribution of electric currents, occurs according newly acquired topology determined by system parameters. To understand the influence of the artificial viscosity on the numerical code showed that within the regime of $q = 3$ to $q = 6$, the evolution of flux tube is not sensitive to the magnitude of the artificial viscosity, except may be for the fact that higher viscosity, as predicted by theory, leads to more pronounced effect of filamentation (see example in Sect. 22.2).

Now, we investigate the case where the interaction terms have nonzero x and y components (model 2). This case is close to the theoretical analysis with the difference that theory assumes both components of the force equal to each other. The advantage of the numerical result compared with the analytical one is that here the evolution of the flux tube can be traced further into later stages: the filamentation process does not stop at the formation of the first four newborn flux tubes but goes further, showing the formation of a complex structure with many magnetic elements of different strength and size (Fig. 10.5).

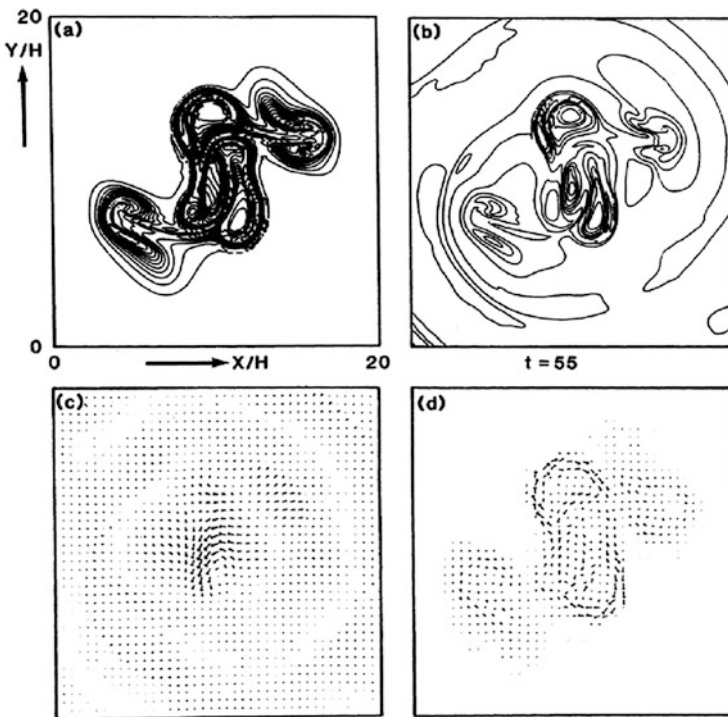


Fig. 10.5 Results at $t = 55$ for model 2, where the generated force has both x - and y -components. The formation of a complex structure with many magnetic elements of different strength and size is shown. As earlier, (a) is the magnetic field, (b) shows density contours, (c) is the velocity field and (d) is the current density

10.6 Intrinsic Nature of Flux Tube Fragmentation

Time series of high-resolution observations show that continuous fragmentation, merging, and dissolution of small-scale magnetic flux tubes is the fundamental process in the photosphere and overlying atmosphere (Yi and Engvold 1993; Berger et al. 1995; Berger and Title 1996; de Wijn et al. 2009; Bellot Rubio et al. 2001). The timescale of splitting and merging processes spans from tens of second to minutes. In each individual case, the process persists to the limit of resolution. The resolved elements vary in shape from circular points as small in diameter as 70 km to elongated filaments with lengths of the order of 500–1000 km which in high resolution consist of *chains of circular magnetic elements*. They are located predominantly in the intergranular lanes constantly buffeted by convective motions and wave trains.

The flux tubes are associated with intergranular bright points whose intensity structure consists of a bright core with dark surroundings. The best proxy of the small-scale flux tubes are G-band images taken through a 12-Å bandpass filter centered at 4305 Å line. Example of the G-band image of a small quiet sun area is shown at four instances of time in Fig. 10.6.

Boxes 1 and 2 highlight examples of two groups of small-scale flux tubes that quickly break into smaller and smaller elements. First, three snapshots show the evolution of flux tubes with 1-min interval. The group in the box 1 consisting roughly of four elements in 2-min breaks into about 7–8 smaller elements. In another 4 min shown at UT 09:02, every flux tube has been “dissolved.” The fragmentation of flux tubes in box 2 is longer process: at UT 09:02, a beautiful chain of tiny flux tubes have been spread along the intergranular lane. The average cross section of these elements is less than 100 km. In a few minutes, they will be dissolved as well.

It is interesting that the fragmentation process even in the case of photospheric magnetic flux tubes can end up with quite vigorous nonlinear dynamics. In other words, diffusive vanishing is only one possibility of the final stage of life of flux tube. Given that generated flows are accompanied by current drive with quite complicated geometry, strong distortion of the topology of magnetic field takes place. This may lead to such a situation that is favorable for *local reconnections*. This process will manifest itself in a strong localized brightening and plasma jets well above the photosphere, i.e., in the chromosphere/transition region including corona. These effects will be considered in Chaps. 12 and 13.

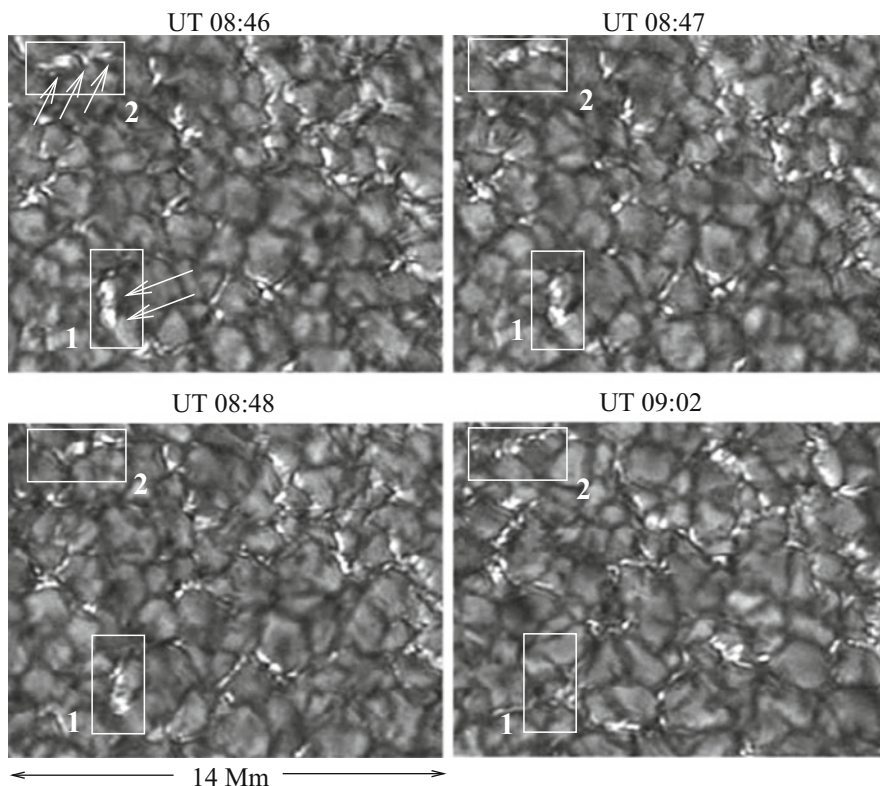


Fig. 10.6 Snapshots of quiet sun region in G-band showing evolution of small-scale magnetic elements buffeted by convective motions. Examples of breaking of magnetic flux tubes in smaller and smaller satellites are highlighted by boxes 1 and 2. The image is taken by the DOT on 13 April, 2005. Reprinted from <http://www.staff.science.uu.nl>, courtesy of Rob Rutten

10.7 Problems

10.1 Find the velocity profile of a wave generated at a viscous boundary layer near an oscillating infinite plate. Let the plate lying in xy plane performs harmonic oscillations in x direction (Stokes first problem), i.e., the velocity components on the surface of plate are

$$v_x|_{z=0} = v_0 \exp(-i\omega t), \quad v_y|_{z=0} = v_z|_{z=0} = 0 \tag{10.71}$$

10.2 The acoustic streaming, one of the most beautiful nonlinear effects, consists in generation of unsteady mass flows by the sound waves propagating near the solid obstacles and is originated by the near-wall viscous stresses. Consider the acoustic boundary layer at a plane solid wall (in the xz -plane) assuming two-dimensional

flow in the xy -plane. Find the velocity of the streaming generated by the oscillating wall (Schlichting 1932).

10.3 Determine the acoustic streaming in the space between two plane parallel walls ($y = 0$ and $y = h$) in the presence of a stationary sound wave (24.153). The distance h between the plates satisfies the condition $\lambda \gg l \gg \delta_p$ Rayleigh (1883).

References

- E.N. Andrade, Proc. Roy. Soc. **A134**, 445 (1931)
 J.M. Beckers, Astrophys. J. **203**, 739 (1976)
 L. Bellot Rubio et al., Astrophys. J. **560**, 101 (2001)
 T. Berger, A. Title, Astrophys. J. **463**, 365 (1996)
 T. Berger et al., Astrophys. J. **454**, 531 (1995)
 A.G. de Wijn et al., SSRv **144**, 275 (2009)
 C. Eckart, Phys. Rev. **73**, 68 (1948)
 M. Faraday, Philos. Trans. R. Soc. Lond. **121**, 229 (1831)
 J. Holtzmark et al., J. Acoust. Soc. Am. **26**, 26 (1954)
 M. Kubo, B.C. Low, B.W. Lites, Astrophys. J. **712**, 1321 (2010)
 A. Meissner, Z. Tech. Phys. **7**, 585 (1926)
 W.L. Nyborg, *Properties of Polymers and Nonlinear Acoustics*. Physical Acoustics, vol. 2, part B (Academic, Cambridge, 1965)
 L. Rayleigh, Proc. Lond. Math. Soc. **14**, 170 (1883)
 L. Rayleigh, Philos. Trans. R. Soc. Lond. **175**, 1 (1884)
 R.O. Richtmyer, K.W. Morton, *Difference Methods for Initial Value Problems*, 2nd edn. (Interscience, New York, 1967), Chap. 13
 M.P. Ryutova, *Proceedings of the Joint Varenna-Abastumani International School on Plasma Astrophysics* (ESA, Noordwijk, 1986), p. 71
 M.P. Ryutova, M. Kaisig, T. Tajima, Astrophys. J. **459**, 744 (1996)
 H. Schlichting, Phys. Z. **33**, 327 (1932)
 C.J. Schrijver et al., Solar Phys. **175**, 329 (1997)
 T. Tajima, *Computational Plasma Physics* (Addison- Wesley, Redwood City, 1989)
 A.M. Title et al., Astrophys. J. **393**, 782 (1992)
 Zh. Yi, O. Engvold, Solar Phys. **144**, 1 (1993)

Chapter 11

Moving Magnetic Features (MMFs)



Abstract In highly dynamic environment of sunspot areas with various sources and sink of energy, small-scale flux tubes do not in general obey the local conservation laws nor do the ensembles of flux tubes that exhibit a complex collective phenomena. Some of the most spectacular phenomena are associated with the so-called Moving Magnetic Features, MMFs, small bipoles streaming radially outward the sunspot penumbra and exhibiting various mysterious properties. For example, they are observed to propagate faster than background mass flows and sometimes even upstream. Altogether, the properties of the MMFs are inconsistent with the energy and momentum conservation laws and require the approach of a non-conservative, energetically open systems. In this chapter, we shall study these amazing features, their observed characteristics, and their impact on the overlying atmosphere. We shall apply the methods of non-conservative systems to understand their behavior. We will also see the negative energy waves in action, and associated formation of shocks and solitons.

11.1 Types of MMFs and Their Observed Properties

The regular outward motions of bright points around sunspots observed by Sheeley (1967) and Vrabec (1971) were named by Harvey and Harvey (1973) moving magnetic features, MMFs. They were first to give a detailed description of the MMF properties by using simultaneous magnetic and $H\alpha$ observations of 37 sunspots (during about 1-year time span). Since then, the MMFs were extensively studied both with ground-based and space observations (Brickhouse and LaBonte 1988; Lee 1992; Ryutova et al. 1998; Yurchyshyn et al. 2001; Bernasconi et al. 2003; Ryutova and Hagenaar 2007; Ryutova et al. 2007; Zuccarello et al. 2009).

It was found that on the very edge of the penumbra along the systematic outflow of $0.5\text{--}1\text{ km s}^{-1}$, the small magnetic features, $1\text{--}2''$ in size, are observed to move outward from the penumbra with velocities higher than the background flows. They eventually form the outer boundary of the moat where they vanish or begin to reside in the network. During their lifetime, MMFs exhibit some clear and well-established

properties that are listed below:

1. MMFs tend to appear in opposite-polarity pairs. The pairs may not be equally visible.
2. The emerging phase takes about 10 min.
3. Pairs can emerge anywhere in the moat but most are near the outer edge of the penumbra.
4. They frequently appear along the continuation of dark filaments; a substantial fraction of the magnetic field is horizontal from the mid to outer penumbra and is confined to dark filaments; the Evershed flow occurs in the regions of horizontal fields.
5. MMFs move with (almost) the constant velocity, and may slow down gradually; nearby MMFs may have quite different speeds.
6. The inner foot predominantly shares the sunspots polarity for pair emergence; there are also opposite-polarity structures, some might appear *Nonpaired*, emitted from the edge.
7. There is a trend for the short-living MMFs to have higher than average velocities.
8. Shorter-lived MMFs seem to be smaller in size.
9. The outer foot moves slightly faster than the inner one; the opposite-polarity footpoints are gradually separating at perhaps 100 m s^{-1} .
10. There are other structures that move faster than 2 km s^{-1} .
11. Several MMFs seen at the very moment of emergence have initial velocities up to 8 km s^{-1} .
12. After the emerging phase, MMFs appear as bright areas in the upper photosphere and chromosphere with excess emission in the Ca II K line.
13. They appear to carry a total magnetic flux several times larger than the total flux of the sunspot.
14. There are bipolar features that move *inward*, i.e., from the edge of penumbra toward the sunspot umbra.

Having some common properties, MMFs are quite distinct from each other. As a result, they were formally divided into classes (Shine and Title 2001).

Type I MMFs are opposite-polarity pairs seen as a compact bipoles. Their initial velocities (at the moment of emergence) may be quite high, $3\text{--}8 \text{ km s}^{-1}$. Moving outward from the sunspot, they gradually slow down; at this stage, the separation between the footpoints gradually increases at about 100 m s^{-1} . During their lifetime, which may be hours, they still move with velocities higher than background plasma flows. Nearby MMFs may have quite different speeds. The inner footpoint shares the sunspot's polarity.

Type II MMFs appear as seemingly unipolar features emitted from the edge of a sunspot and having another footpoint partially or totally hidden. They share the sunspot's polarity, and have properties similar to those of the inner footpoint of the type I MMFs. Footpoints of type I MMFs are often not equally visible with well-pronounced inner footpoint and diffuse outer footpoint.

Type III MMFs also appear either as unipolar features, or opposite-polarity pairs with one footpoint barely visible. Unlike type II, these MMFs have the polarity (of a strong footpoint) opposite to parental sunspot. They are of smaller size, travel with higher velocities than the other MMFs ($2\text{--}3\text{ km s}^{-1}$), and are associated with bright points in the continuum.

Type I* MMFs are outflowing opposite-polarity pairs with the inner footpoint having the polarity opposite to the sunspot (Yurchyshyn et al. 2001; Zhang et al. 2003). To distinguish them from regular type I MMFs, we use the notation of a “complex conjugate.”

Type IV MMFs, called MDFs, moving dipolar features, were found in an emerging sunspot region (Bernasconi et al. 2003). They have the remarkable property of moving *inward*, i.e., toward the sunspot umbra. These are slowly migrating bipoles ($0.3\text{--}0.8\text{ km s}^{-1}$) with the inner footpoint having a polarity opposite to the sunspot.

11.2 Impossibility of the Origin of MMF's in Conservative Systems

Harvey and Harvey in their original observational paper proposed a graphic scenario in which some flux tube becomes detached (!) from the sunspot trunk at the surface where it is nearly horizontal. The supergranular or granular motions then twist this detached part of flux tube into kinks that then are carried outward by the systematic Evershed outflow. This “sea-serpent” sketch by Harvey and Harvey became the basis for subsequent models. Copy of the original Harvey and Harvey's cartoon is incorporated in the combined sketch shown in Fig. 11.1, right. Left side of the cartoon shows the sketch of Wilson's (1986) model. Figure 11.2 is a sketch by

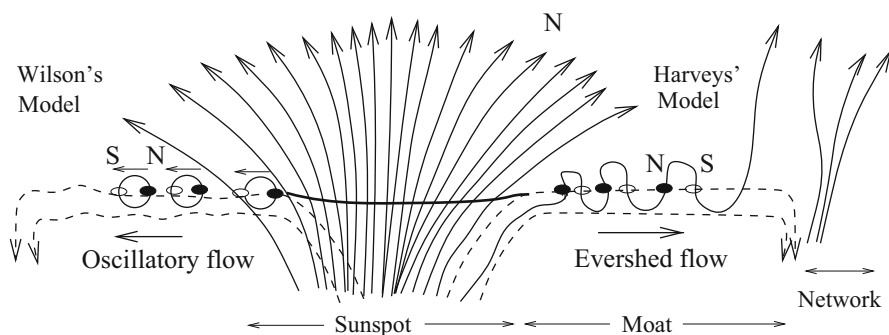


Fig. 11.1 Cartoon visualizing a possible creation and motion of MMFs: right side of cartoon shows a sketch given by Harvey and Harvey showing how twisted magnetic flux tube may be separated from the main body of sunspot and swept to the network by flows; left side of cartoon is Wilson's (1986) sketch showing a possible formation of MMFs in form of the new flux loops generated by an oscillatory velocity field

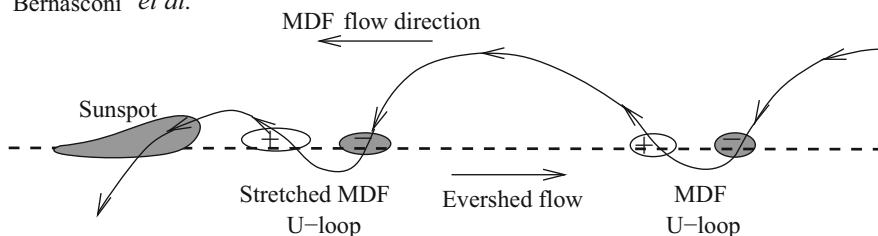
Bernasconi *et al.*

Fig. 11.2 Cartoon visualizing even more mysterious magnetic features—MDFs, moving *toward* parental sunspot against the main stream of Evershed flow directed from sunspot to its periphery. Reprinted from Bernasconi *et al.* (2003) with permission from Springer Copyright 2002, Kluwer Academic Publishers

Bernasconi *et al.* showing a possible motion of MDF's (type IV MMFs) moving against the background flow toward the sunspot.

Wilson (1986) suggested that new flux loops may be generated by suitable oscillatory velocity field near the boundaries of existing magnetic structures with subsequent detachment (!) of loops, which may appear as compact bipoles. Wilson, however, objects the Harvey and Harvey's cartoon mainly on the basis of energy disbalance: comparison of magnetic energy density (for a 1500 G flux tube) and the energy density of granular motions shows that energy density of granular motions is smaller than the former one by two orders of magnitude.

Finally, Wilson justly concludes: "It is hard to see how the motions could deform such a flux tube into the required kink, far less maintain the tube in this form during the passage across the moat." Indeed, if flux tubes and outer motions are considered as a conservative system, origin of MMFs, moving faster than background flows and even upstream, is impossible to explain.

And yet, most of the subsequent attempts to visualize MMFs were somehow or other connected with the Harvey and Harvey's "sea-serpent" picture. For example, it was tempting to represent type I MMF as a \cap -shaped kink formed along a thin horizontal filament, which would indeed have the appearance of a bipolar formation with the inner footpoint of the same polarity as the sunspot. Similarly, \cup -shaped kinks would appear as MDF or MMF with the inner footpoint having opposite to sunspot polarity.

The fundamental problem here is that either kind of kink is highly unstable: under the action of magnetic tension and buoyancy forces, a \cup -shaped kink straightens in 1–2 min, while a \cap -shaped kink may at best first oscillate and survive only for several minutes longer (Ryutova, Tarbell, and Shine 2003).

But, the problem goes even deeper. One needs to not only overcome the stability issue but also find the forces that push MMFs to travel faster than the background flows with lifetimes from tens of minutes to hours. In case of MDF's (Fig. 11.2), mysterious forces make the kink to travel even upstream, against the background flows.

In other words, the properties of the MMFs are inconsistent with energy and momentum conservation laws and require approach of non-conservative, energetically open systems. We will see below that the mechanism that operates in an energetically open system describes all the observed types of MMFs and their properties.

11.2.1 *The Mechanism*

The mechanism that explains the origin of MMFs and their observed properties is based on a natural coexistence of flux tubes and adjacent shear flows, that form non-conservative system, and must be considered as such. The system with unbalanced sources and sinks of energy cannot maintain (locally) conservation laws and, as open energetically, becomes the subject to vigorous nonlinear dynamics (Kadomtzev et al. 1964; Dikasov et al. 1965; Coppi et al. 1969; Ostrovsky et al. 1986; Ryutova 1988). In our case, an unaccounted energy source comes from mass flows, sinks are played by any dissipative effects.

As shown in Chap. 5, the exchange of energy and momentum between magnetic flux and outer motions results in the development of two kinds of shear flow instabilities. The onset of the instabilities occurs respectively at two thresholds with respect to velocity: (1) Kelvin–Helmholtz instability (KHI) which develops at a linear stage and leads to the excitation of natural oscillations propagating along the magnetic flux tube; and (2) instability of negative energy waves (NEW) which leads to nonlinear growth of oscillations excited along the flux tubes.

Recall that the dispersion relation for linear kink oscillation in the presence of flow, u , has a form (cf. Eq. (5.12), Chap. 5):

$$\omega_{\pm} = \frac{k}{1 + \eta} \left[u \pm \sqrt{\eta[(1 + \eta), v_A^2 - u^2]} \right] \quad (11.1)$$

and that super-Alfvénic velocities, $u > v_A \sqrt{1 + \eta}$, correspond to the KHI threshold, whereas dissipative instabilities of NEWs develop at sub-Alfvénic shear velocities. Namely, when the shear velocity, u , drops into the interval:

$$v_A \sqrt{\eta} \leq u < v_A \sqrt{1 + \eta} \quad (11.2)$$

Thus, dissipative instabilities require weaker flows to trigger the energy and momentum exchange between the magnetic flux and outer motions. In other words, under the condition (11.2), the kink along flux tube not only becomes stable but may also grow under the action of any dissipative effect, including the action of non-dissipative damping mechanisms specific for the flux tubes, i.e., due to anomalous damping in the Alfvén resonance layer, or due to radiative damping. First mechanism is provided by the smooth radial profiles of flux tube, while the second mechanism is provided by the radiation of secondary acoustic or MHD waves. Both

mechanisms are inherent for the photospheric flux tubes, making thus formation of a kink and its further behavior unrestricted.

It must be noted that the range of the flow velocities observed in sunspot region are enough to “deform” a flux tube and generate a stable kink, that later may evolve into the shock, traveling soliton, or series of solitons.

11.3 Nonlinear Kink and Its Evolution in the Presence of Shear Flows

To describe the evolution of a kink mode in the presence of shear flow, we use nonlinear equations obtained in Chap. 4 (Eq. 4.114), complemented by the additional dissipative terms that represent the intrinsic dissipative features of flux tube:

$$\begin{aligned} \frac{\partial \psi}{\partial t} + \alpha \psi \frac{\partial \psi}{\partial x} + \beta_{\text{disp}} \frac{\partial^3 \psi}{\partial x^3} = & v \frac{\partial^2 \psi}{\partial x^2} - \frac{\gamma}{\pi} \mathcal{P} \int_{-\infty}^{\infty} \frac{\partial \psi}{\partial s} \frac{ds}{x-s} \\ & + \frac{\mu}{\pi} \mathcal{P} \int_{-\infty}^{\infty} \frac{\partial^3 \psi}{\partial s^3} \frac{ds}{x-s} \end{aligned} \quad (11.3)$$

Here, $\psi = B_y^2 + B_z^2$, $\alpha \simeq 3c_k/4B^2$ is the coefficient of nonlinearity, β_{disp} is the dispersion coefficient, v is the dissipative coefficient provided by usual dissipative losses (viscous, thermal, and Ohmic), γ corresponds to anomalous damping of kink oscillations in the Alfvén resonance layer, and μ represents the radiative damping of oscillations. \mathcal{P} denotes the principal value of the integral. The equation is written in a frame moving with the group velocity of linear kink oscillation $c_k = v_A \sqrt{\eta/(1+\eta)}$.

Although (11.3) in the presence of mass flows formally remains the same as without flows, coefficients α , β_{disp} , γ , and μ are now the functions of the shear velocity u :

$$\alpha \simeq \frac{3}{4} \frac{c_k^\pm}{B^2} \quad (11.4)$$

$$\beta_{\text{disp}}^\pm = \mp \frac{R^2}{2\eta v_A^2} \frac{(c_k^\pm - u)^4}{\sqrt{\eta[(1+\eta)v_A^2 - u^2]}} \quad (11.5)$$

$$\gamma = \pm \frac{\pi \epsilon}{4 \eta} \frac{(c_k^\pm - u)^2}{\sqrt{\eta[(1+\eta)v_A^2 - u^2]}} \quad (11.6)$$

Here, $c_k^\pm = [(1/(1 + \eta))] \left[u \pm \sqrt{\eta[(1 + \eta)v_A^2 - u^2]} \right]$ is the group velocity of linear kink oscillations in the presence of shear flow, u , and ϵ is a measure of the diffused boundary of a magnetic flux. We assume that the initial magnetic field is constant across the effective radius, R , and then drops to zero linearly in thin boundary layer of thickness l , thus $\epsilon = l/R$. In the analytical approach, we assume that $\epsilon \ll 1$ and consider magnetic field well concentrated in the effective radius R . In the numerical studies (see Sect. 11.4 below), this restriction will be removed, and a more realistic situation with smooth radial dependence of flux tube parameters and velocities on radius will be considered.

Equation (11.3), as a typical KdV–Bürgers, describes several scenarios of the evolution of the initial kink perturbation depending on the interplay of the nonlinear, dissipative, and dispersive effects. Besides, the sign of dispersion plays a crucial role in the properties of the equation and its solution.

For example, if nonlinear and dispersion effects are in balance, the steepening of the amplitude gets compensated by dispersive stretching and leads to formation of a long-lived soliton, which travels with its own velocity that is higher than the shear-flow velocity. In observations, such a formation appears along the line of sight as a compact bipole.

If nonlinearity prevails over dispersion, the soliton becomes asymmetric and acquires shocklike form, i.e., one side of the soliton becomes steeper than the other. Such a formation appears along the line of sight either as a single-polarity element or as a bipole with one sharp and one diffuse footpoint. Its velocity may be even higher than that of a soliton.

It is important that in case of a *positive* dispersion of medium there appears a *bright* soliton, i.e., nonlinear kink is \cap -shaped. If the dispersion changes sign, the soliton becomes *dark*, negative soliton, acquiring \cup -shape (Karpman 1975).

First, we shall discuss in detail the case of the soliton formation and its evolution in medium with positive dispersion. In other words, we choose the lower branch of the dispersion relation (11.1), and lower signs of all parameters given by (11.4)–(11.6).

The right-hand side of (11.3) is assumed to be small compared to each term in the left-hand side. In this case, one can use a well-developed technique (e.g., Whitham 1974, Ostrovsky et al. 1986) to find quasi-stationary solutions of (11.3). This technique consists mainly of two steps. First, we find solution of a stationary KdV equation, and then assuming that the amplitude and other parameters of the system are slowly varying functions of time, we find the evolutionary equation for the amplitude.

In the absence of dissipative terms, a stationary solution of (11.3) is a solitary wave with amplitude A (in our case $A \simeq B_\perp^2$), width Δ and travel velocity of soliton, v_s ,

$$\psi = A \operatorname{sech}^2 \frac{x - v_s t}{\Delta} \quad (11.7)$$

$$\Delta = \sqrt{\frac{12\beta_{\text{disp}}}{\alpha A}}, \quad (11.8)$$

$$v_s = c_k + \frac{\alpha A}{3} \quad (11.9)$$

Now, to obtain a solution of (11.3) for the dissipative system (with nonzero, but small right-hand side) one assumes that the amplitude, width, and the speed of a soliton are slowly varying functions of time.

The time dependence of these parameters is determined by the energy equation that can be obtained by multiplying (11.3) by ψ and integrating over a distance large compared with the size of a soliton. This procedure leads to the evolutionary equation for the amplitude:

$$\frac{dA}{dt} = \frac{2.92}{\pi} \gamma \left(\frac{\alpha}{12\beta_{\text{disp}}} \right)^{1/2} A^{3/2} - \frac{16}{15} \frac{\alpha}{12\beta_{\text{disp}}} \nu A^2 \quad (11.10)$$

By analyzing this equation, we can conceive the nature of its solution. First, in the beginning of soliton evolution, when its amplitude is small enough, the first term in the right-hand side of (11.10) is leading one; the amplitude in this case experiences an explosive growth:

$$A \simeq \frac{A_0}{(1 - t/t_{\text{expl}})^2} \quad (11.11)$$

with the explosion time $t_{\text{expl}} = \pi \sqrt{12\beta_{\text{disp}}/\alpha A_0}/2.92\gamma$. Under photospheric conditions, this time is quite large; that is, the phase of the explosive growth is short: after several inverse growth rates, the amplitude gets stabilized by higher nonlinear effects (Coppi et al. 1969; Ryutova 1988). At about this time, the second term in (11.10) becomes more important, and the amplitude of soliton decays as follows:

$$A(t) = \frac{A_0}{1 + t/t_{\text{diss}}}, \quad (11.12)$$

where $t_{\text{diss}} \simeq 12\beta_{\text{disp}}/\nu\alpha A_0$. With (11.11)–(11.12) and basic relationships between the parameters of soliton, (11.7)–(11.9), one can easily draw a qualitative picture of the formation of magnetic soliton and its further behavior. Moreover, these relations, containing directly observable parameters, allow one to perform the quantitative analysis and comparison with the observations.

Thus, at flow velocities in the range defined by condition (11.2), one should expect the formation of a stable soliton with the properties described by the simple relationships between the soliton parameters, (11.7)–(11.9). The simplicity of these relations makes the conclusion regarding the validity of soliton solution quite rigorous. One can see that all three relations are *interdependent*: the amplitude,

the width of the soliton, and its velocity are all functions of each other. So that, for the kinked formation to be a soliton, these parameters must obey all three conditions simultaneously. In other words, if one of these conditions breaks, the kinked formation cannot be considered as a solitary wave.

In the solar photosphere, and in particular in the sunspot area, two of the abovementioned parameters, the travel velocity, v_s , and width of the soliton, Δ , are directly measured quantities. The amplitude, A , which is proportional to magnetic field strength, B^2 , is also well-measurable parameter. In this sense, (11.8) and (11.9) are the first to be checked. We will perform the quantitative analysis and comparison with the observations to Sect. 11.5. Before doing this, in the next section we present numerical studies of soliton-like and shocklike formations, which extend the analytical studies and allow, for example, to study temperature distribution inside a kinked formation.

11.4 Soliton and Shocklike Formations Along the Flux Tube: Numerical Studies

Numerical studies are based on a three-dimensional simulation code of a normalized set of MHD equations in which the numerical scheme is the modified 2-step Lax–Wendorff method (Fushiki and Sakai 1995; Suzuki and Sakai 1996). The region of calculation or the system sizes in the x , y , and z directions are, respectively, $0 < x < 4\pi L_0$, $0 < y, z < 2\pi L_0$. The density, the magnetic field, and the pressure are normalized by ρ_0 , B_0 , and p_0 ; the velocity is normalized by the Alfvén velocity, v_A . The space and time are normalized by L_0 and $\tau_A = L_0/v_A$. Thus, the normalized set of MHD equations is as follows:

$$\frac{\partial \rho}{\partial t} + \text{div}(\rho \mathbf{v}) = 0 \quad (11.13)$$

$$\rho \left(\frac{\partial \mathbf{v}}{\partial t} + \mathbf{v} \nabla \mathbf{v} \right) = -\beta \nabla p + \nabla \times \mathbf{B} \times \mathbf{B} + \rho \tilde{g} \mathbf{e}_z \quad (11.14)$$

$$\frac{\partial \mathbf{B}}{\partial t} = \nabla \times \mathbf{v} \times \mathbf{B} + \frac{1}{R_m} \nabla^2 \mathbf{B} + A_D \nabla \times \left(\frac{1}{\rho} \mathbf{B} \times \mathbf{B} \times \nabla \times \mathbf{B} \right) \quad (11.15)$$

$$\frac{\partial \rho}{\partial t} + \mathbf{v} \nabla \rho + \Gamma p \text{div} \mathbf{v} = \frac{\Gamma - 1}{\beta R_m} (\nabla \times \mathbf{B})^2 \quad (11.16)$$

where the plasma beta is $\beta = c_s^2/v_A^2$, R_m is the magnetic Reynolds number defined by $R_m = \tau_B/\tau_A$, where $\tau_B = 4\pi\sigma L_0^2/c^2$ is the magnetic diffusion time, $\tilde{g} = g\tau_A/v_A$ is normalized gravitational acceleration, and the coefficient of ambipolar diffusion A_D is defined as $A_D = B_0^2\tau_A/4\pi\Gamma\rho_e\rho L_0^2$.

The system sizes are $0 \leq x \leq 4\pi L$, and $0 \leq y = z \leq 2\pi L$ in the x , y , and z directions, respectively. The mesh points are $N_x = 80$, $N_y = 50$, and $N_z = 50$ in the x , y , and z directions, respectively. Free boundary conditions (first derivatives of all physical quantities are continuous) are used for the y and z directions, while a periodic boundary condition is used in the x direction.

The flux tube (containing the current) initially is placed along the x direction and satisfies an equilibrium. The flux tube magnetic fields are given by:

$$B_\theta = \frac{B_m r/R}{1 + (r/R)^2}, \quad (11.17)$$

$$B_z = \frac{B_{z0}}{1 + (r/R)^2} \quad (11.18)$$

For computations, the radius of a flux tube is taken as $R = 0.5$, and $B_m = 1.2$, $B_z = 1.0$. r means the distance from the center line of a flux tube. The initial density is $\rho = p$ and the initial pressure p is taken to satisfy an equilibrium as follows:

$$p = \rho = \exp(-\tilde{g}z/\beta) + \frac{B_m^2 - B_{z0}^2}{2\beta(1 + r^2/a^2)^2} \quad (11.19)$$

where the first term shows the balance with gravity, and the second is the pressure needed to balance the Lorentz force. Plasma flow outside the flux tube is assumed to be directed along the flux tube (i.e., along x -axis), and with r -dependence of the form: $u(r) = u_0(1 - 0.8/(1 + (r/R)^2))$. The velocity perturbations, v_z , are imposed at $x = \pi L$ as $v_z = v_m \exp[-(x - \pi)^2/(1 + (r/R)^2)]$. The parameters used here are as follows: $\Gamma = 5/3$, $\beta = 1.0$, $R_m = 10^4$, $A_D = 10^{-3}$, $\tilde{g} = 0.05$, $u_0 = 0.2-1.0$, and $v_m = 1.2$.

Numerical simulations were performed in several regimes, changing mainly the external flow velocity, u_0 . It was found that depending on the shear flow velocity there are two different and well-distinguishable regimes of the evolution of a kink perturbation, which can be identified as shocklike and soliton-like cases.

The shocklike regime requires lower-amplitude shear velocities. It is remarkable, however, that the propagation velocity of shocklike kinks is larger than shear velocity. From the observational point of view, the shocklike regime may correspond to either a unipolar MMF (if the front of a shock is much more pronounced than its tail) or to those MMFs whose legs have different propagation velocities: the outer (leading) leg should be faster than the trailing one.

Soliton-like kinks always appear as a bipole features. Their propagation velocity may be both lower or higher than the speed of the shear flow.

In Fig. 11.3a, b, the evolution of kinks into the (a) shocklike and (b) soliton-like events at time $t = 8\tau_A$ are shown. In Fig. 11.3c, the relation between the velocity of shear flow and the propagation velocity of the generated kink is shown. At the velocities less than $0.6v_A$, the generated kink shows shocklike behavior. Region of flow velocities $\simeq 0.6v_A$ for chosen parameters of magnetic flux tube and its

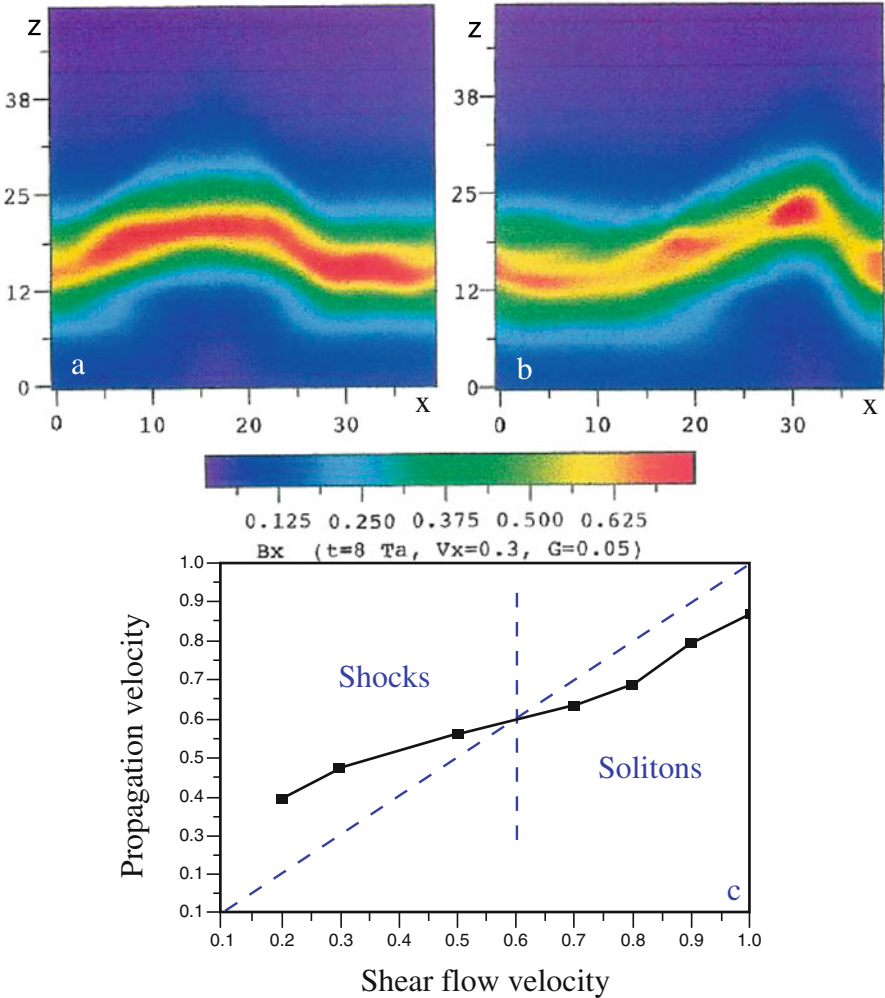


Fig. 11.3 Two different regimes of the evolution of a magnetic kink. Top: snapshots of the shocklike event at $t = 8\tau_A$ (a), and the soliton-like event at $t = 8\tau_A$ (b); bottom (c) the relation between the velocity of shear flow, $u(r)$, which facilitates the generation of a magnetic kink, and the propagation velocity of a new-born kink; dashed lines demarcate the approximate regions of the shocklike and soliton-like formations

environment corresponds to the bifurcation point. At the shear velocities higher than these velocities, the generated kink acquires the properties of a stable solitary wave.

In Fig. 11.4, the time history of the soliton-like kink is shown for a shear velocity $v_x = 0.8v_A$. One can see that with a “decreasing” of the “amplitude” (which corresponds to decreasing the magnetic field strength), the width of the soliton—the separation between the “two legs” increases (cf. (11.8)). The last panel in this figure corresponds to time $t = 3\tau_A$ and shows three-dimensional view of the same event along the tube axis.

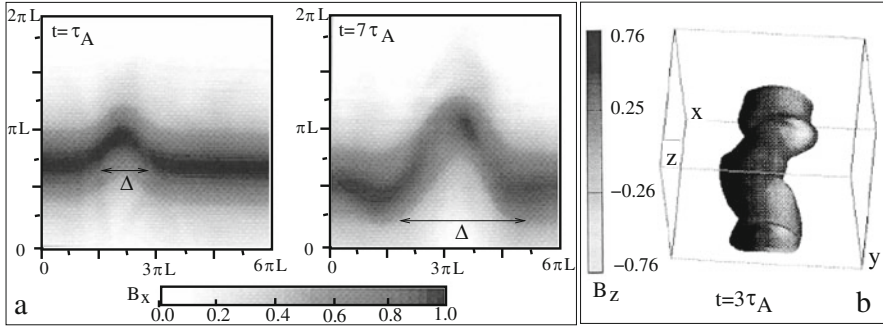


Fig. 11.4 Soliton-like kink at the shear velocity $v_x = 0.8v_A$: **(a)** The time history of the soliton evolution at two time steps; note how weakening of magnetic field is accompanied by the increasing of the separation between the two legs, i.e., the width of the soliton, and growth of its kink; a bar shows the magnetic field scale along the flux tube, B_x . **(b)** The snapshot of three-dimensional view of magnetic field, B_z at $t = 3\tau_A$ with the scale bar showing one of the a transverse component of magnetic field, B_z

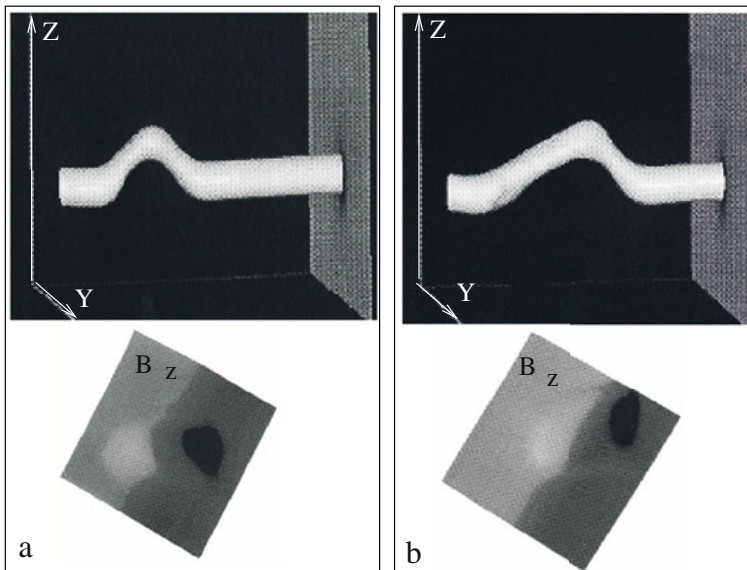


Fig. 11.5 The three-dimensional view (upper panels) and line-of-sight magnetic field (lower panels) **(a)** for a stable propagating soliton corresponding to type I MMFs, and **(b)** for the shocklike MMF. Note that in case of soliton both footpoints are equally well pronounced, while in case of the shocklike formation one footpoint along the line of sight is sharp and compact, while its pair is weaker and diffuse

Figure 11.5 shows well-developed three-dimensional view of soliton and shock-like formations and their line-of-sight magnetic field. Figure 11.5a is a stable propagating soliton—a typical bipole, with both positive and negative footpoints

clearly seen. Figure 11.5b is shocklike formation whose line-of-sight magnetic field differs from the soliton case: its leading footpoint is sharp and compact, while the trailing one is diffuse (cf. Fig. 11.3a, b). From observational point of view this means, that shocklike MMF may appear as bipolar feature with uneven emission from its legs, or even as a single-polarity MMF.

It is important to discuss the change of the temperature distribution inside the magnetic flux during the formation and propagation of a kink. Note that the analytical theory does not allow us to include the temperature distribution in the nonlinear dynamics of magnetic flux tube, but the numerical calculations proved to be very helpful.

In both cases, shocklike and soliton-like kink formation, quite uneven redistribution of the temperature takes place. A numerical modeling clearly shows the regions with some energy excess in the new-born magnetic features. For example, in the case of a soliton both legs have higher temperature than the surrounding plasma. The temperature in the following leg is slightly higher than in the leading one (Fig. 11.6a). In the case of a shocklike formation, the temperature behind the shock-front is, as it should be, significantly higher than in the rest of medium (Fig. 11.6b). The described temperature distribution may explain the excess of the emission in the Ca II K line that almost exactly mimics the path of the MMFs in the photosphere.

The animated process of the magnetic kink propagation shows several remarkable features, such as the shredding of the magnetic field at the late stage of its evolution. These kind of events are usually well seen in the high cadence movies obtained from observations.

11.5 Observations and Comparison with Theory

In this section, when discussing and comparing the theoretical results with the observed properties of moving magnetic features, we use several examples from the set of observations taken on June 14 1994 at the Swedish Vacuum Solar Telescope (SVST) on La Palma. The observations include simultaneous images in Ca II K-line, G-band, and magnetograms. The 0.3-nm bandpass Ca II K filter has some contribution from the chromosphere but in non-active areas most of the intensity is from the inner wings of the line profile which originate in the upper photosphere.

Hence, the images show dark patches during the early stages of flux emergence and the movies show many examples of emerging flux in the moat area, especially near the outer edge of the penumbra. These appear as dark elongated features which expand and develop bright points at opposite ends which then continue to separate while traveling outward. Each end becomes an MMF. The long axis of the emergence is generally in the radial direction.

The time series for the magnetograms, K-line filtergrams, and G-band filtergrams have been co-aligned. The observing time is 175 min.

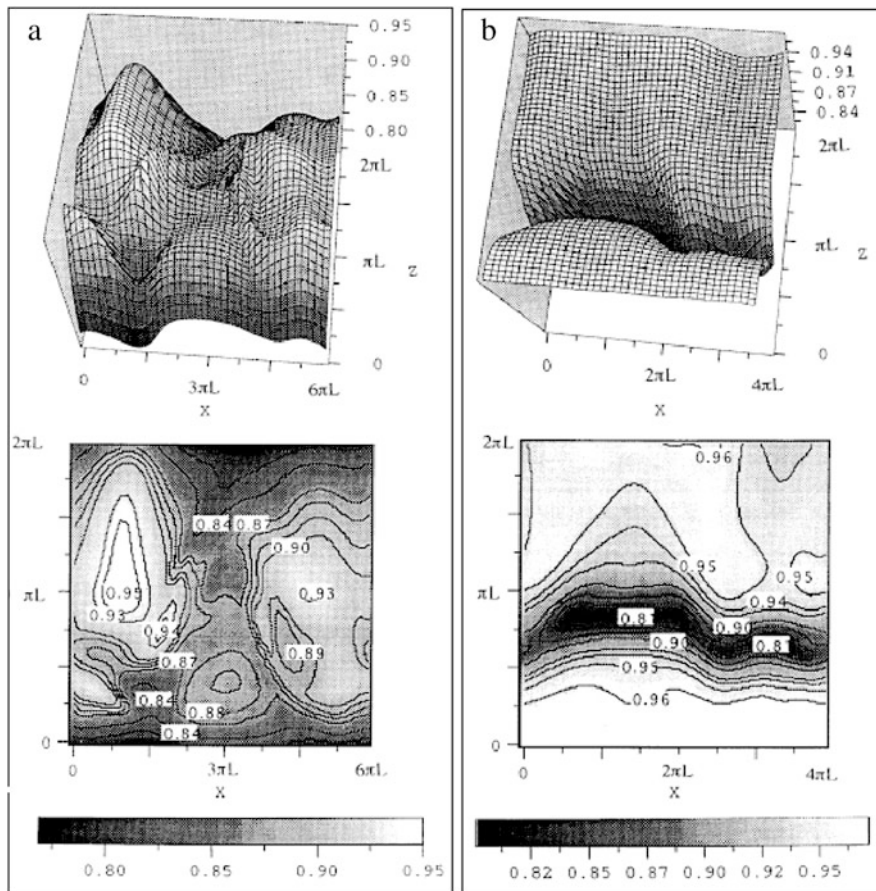


Fig. 11.6 The temperature distribution in the well-developed nonlinear kink: **(a)** The soliton-like kink at $t = 7\tau_A$, and the shear velocity is $v_x = 0.8v_A$; **(b)** The shocklike kink at $t = 7\tau_A$, and the shear velocity is $v_x = 0.2v_A$. Note the elevated temperature level in the soliton legs **(a)**, and strong behind-shock heating at shocklike formation **(b)**

To display their time evolution, the space–time images were constructed for several of these MMFs using the long axis of the emergence as the space dimension. These are shown in Fig. 11.7.

For detailed analysis, we choose three examples, namely space–time slices 1, 3, and 4. The space–time images resulted from cuts 1 and 3 are shown in Figs. 11.8 and 11.9, respectively, and those resulted from cut 4 is shown in Fig. 11.10.

Each of the paths corresponding to 1 and 3 slices shows the appearance of two quite similar MMFs. All four events have high velocities in the initial phase, about 4 km s^{-1} . In the region where a well-defined darkening is seen in the Ca II K images, indicating the emergence of magnetic field, the separation between two legs, the width of soliton, gets stabilized and becomes almost constant; after this, the travel

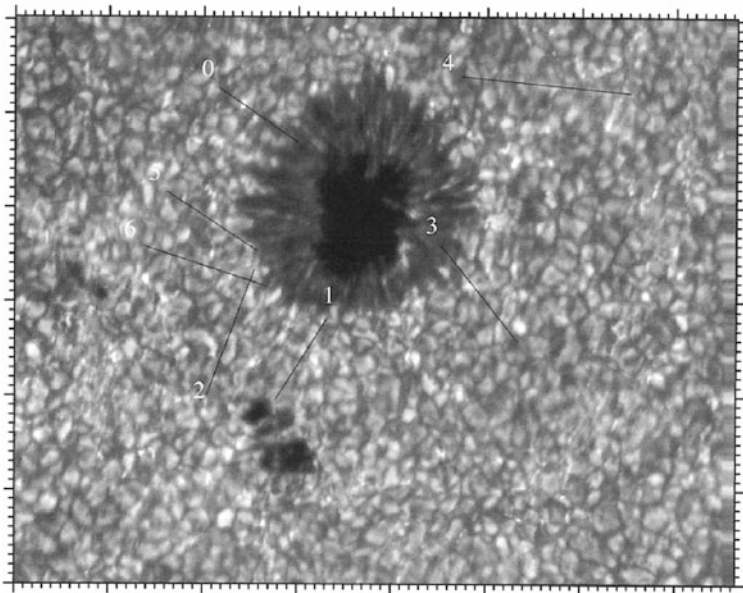


Fig. 11.7 A G-band image of the sunspot area taken on June 14 1994 at the SVST on La Palma. The labeled lines represent the spatial component of space–time images made from the movies to follow various emerging flux events and their variation in time

velocities of the MMFs drop to $1.0\text{--}0.7\text{ km s}^{-1}$, after which all four events show a slow evolution: their width gradually increases, while the propagation velocity gradually decreases.

The most spectacular MMF which can be interpreted as an exemplary solitary wave is revealed by cut 4 and is shown in Fig. 11.10. The evolution of all the observed MMFs fits amazingly well the analytical description given by (11.7)–(11.12). Besides, their appearance and location where they emerge can be also well understood in the frame of theory. For example, we will see below that the 1 and 3 events are most likely shallow events, while the MMF shown on the slice 4 should have been originated at some depth below the visible surface. This can be explained along the following line of reasoning.

If the stable kink (a kink soliton) is formed close to the surface, the buoyancy force may be neglected. From the observational point of view, such events should be seen both in their initial phase which corresponds to fast growth and fast propagation (in accordance with Figs. 11.13 and 11.14), and in the second stage, which corresponds to their slow evolution after the moment of stabilization. The four MMFs shown in Figs. 11.8 and 11.9 are good candidates to be considered shallow kinks formed on or slightly below the surface. Their proximity to the edge of the penumbra is also consistent with a shallow origin, since at least some of the nearly horizontal field at the outer penumbra boundary may extend just below the visible surface.

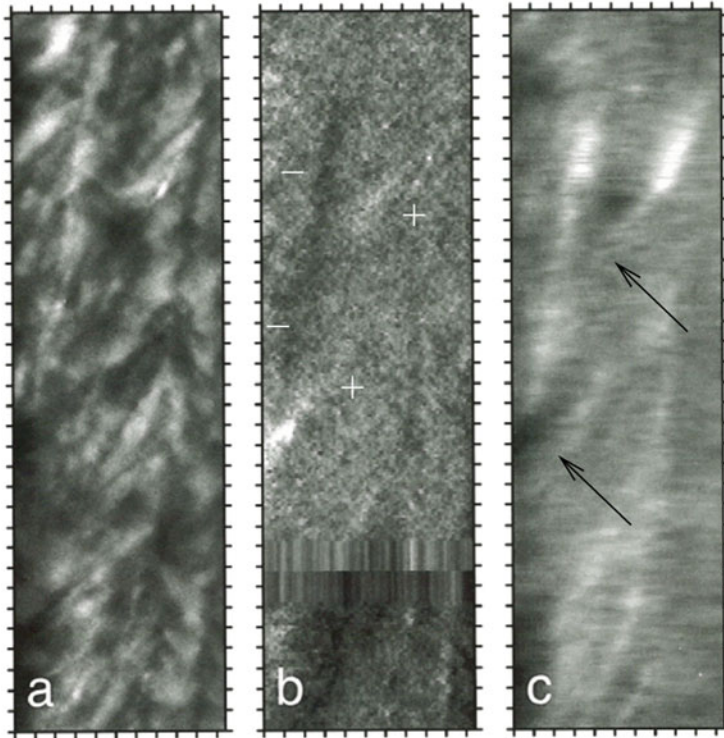


Fig. 11.8 Space–time slices along the line labeled 1 in Fig. 11.7 for: (a) the G band filtergrams movie, (b) the magnetogram movie, and (c) the K-line filtergram movie. Time is along the vertical axis increasing upwards with tick marks every 5 min. Observation period is 175 min. The horizontal axis is distance along the line with tick marks every arc second (about 726 km). One can see two beautiful MMFs especially well recognizable in the magnetogram and Ca II K-line movies (marked by black arrows)

If the MMF is formed well below the surface, then its initial fast phase develops below the surface and the MMF may appear while in its second phase of slow evolution. This type of event may be more likely to appear further from the penumbra as is the case for event 4 shown in Fig. 11.10.

During the initial stage of soliton formation while the amplitude is small (so that the first term in (11.10) is a leading one), its growth is governed by (11.11). This phase is accompanied by the fast emergence of magnetic flux and may start below the visible surface. The emerging kink appears as closely spaced, opposite-polarity couple moving with relatively high velocity (see all four MMFs shown in Figs. 11.8 and 11.9).

When the amplitude of a kink becomes such that both terms in the right-hand side of (11.10) are comparable, the soliton becomes stabilized. Its amplitude remains constant until some other dissipative processes make the second term in (11.10) more important. At this stage, the amplitude of the soliton decreases slowly in

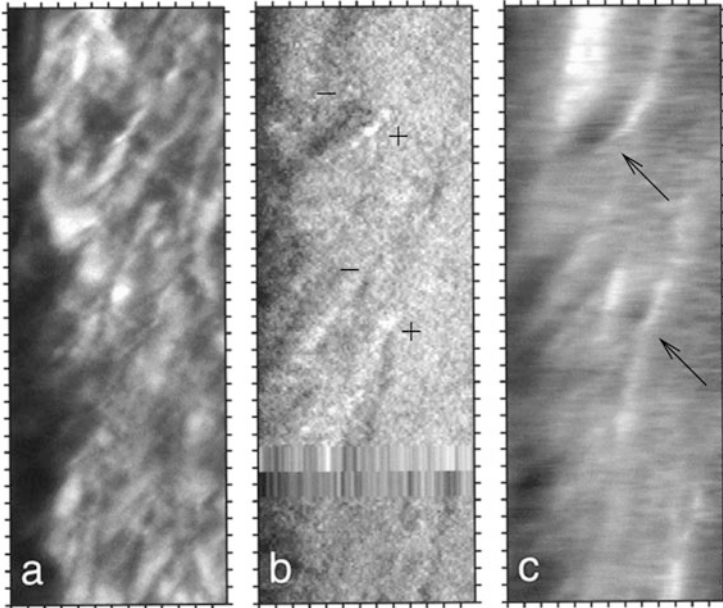


Fig. 11.9 Same as Fig. 11.8 but for the line labeled 3 in Fig. 11.7

accordance with (11.12). Its travel velocity (see (11.9)) also decreases, and its width, or the separation between the opposite-polarity legs (11.8), gradually increases. This stage can be easily identified in all four events shown in Figs. 11.8 and 11.9. As the dark structure seen in the Ca II K images expands and fades, the propagation velocity drops to values of $1.0\text{--}0.7\text{ km s}^{-1}$, after which their behavior is described by (11.12).

Thus, we may conclude that qualitatively, these MMFs show both phases of the evolution: the fast, explosive phase, and the phase of a gradual decay.

The exemplary event shown in Fig. 11.9 may be an excellent demonstration of an observed solitary kink formed well below the visible surface. It is seen only in the second stage and from the period of about $t = 20\text{--}60\text{ min}$ the width of a soliton remains almost constant and then very gradually decreases.

The moment of the transition from one phase to another (i.e., the moment when the amplitude A reaches its stationary value, A_{st}) carries some additional information about the nature of the effect and, also, about the physical parameters of the medium. Roughly, at this moment

$$\frac{2.92}{\pi} \gamma \left(\frac{\alpha}{12\beta_{\text{disp}}} \right)^{1/2} A^{3/2} \simeq \frac{16}{15} \frac{\alpha}{12\beta_{\text{disp}}} v A^2 \quad (11.20)$$

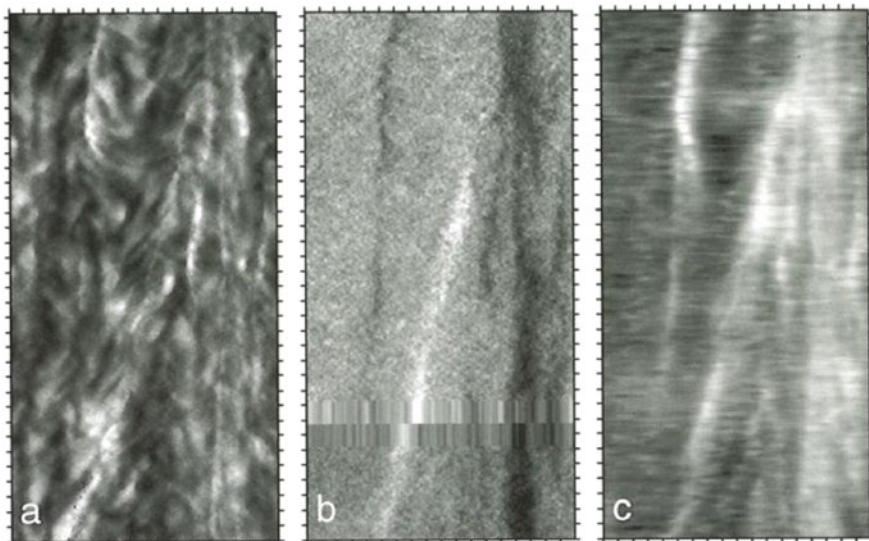


Fig. 11.10 An exemplary magnetic soliton. This body has emerged obviously before the start of the observations. Its behavior, growth of the separation between the legs, slowing down, etc., strictly obey the laws of evolutionary soliton

that is,

$$A_{st}^{1/2} \simeq 0.87 \sqrt{\frac{12\beta_{\text{disp}}}{\alpha}} \frac{\gamma}{\nu} \quad (11.21)$$

or, taking into account (11.8), we can estimate the stationary value of the width,

$$\Delta_{st} \simeq 1.15 \frac{\nu}{\gamma} \quad (11.22)$$

This result is analogous to a well-known fact in the theory of solitary waves: after some time, the “memory” of soliton weakens and soliton “forgets” its initial conditions. As noted earlier, ν represents any kind of dissipative losses. If the soliton formation occurs close to visible surface, we may suggest that dissipation is provided mostly by the viscous losses. If the formation of soliton occurs in deeper layers, say at $h = -1000$ km, then thermal and radiative losses become more important.

11.6 Quantitative Analysis

For quantitative estimates, we consider two examples: (1) the formation of a soliton on or slightly below the surface, and (2) the formation of a soliton at a depth $h = -1000$ km.

For the first case of a shallow soliton, we adopt the following typical values: mass density (outside the magnetic flux tube), $\rho_e = 3.4 \times 10^{-7}$ g/cm³; temperature $T = 0.94 \times 10^4$ K; sound speed, respectively, is $c_s = 10.2$ km s⁻¹ (see e.g., Maltby et al. 1986); the ratio of mass densities $\eta = \rho_i/\rho_e = 0.9$; the flux tube radius $R = 500$ km; $\epsilon = l/R = 0.05$; and magnetic field strength (for analytical estimates, the unperturbed value of the field along the tube axis) $B_x = 500$ G.

With these parameters, we may find the Alfvén velocity, the range of shear velocities corresponding to dissipative instabilities, Eq. (11.2), and, choosing some critical value for the shear velocity, compute the width, the amplitude, and the speed of the propagation of a soliton.

At the Alfvén velocity $v_A = 2.6$ km s⁻¹, the range of shear velocities that would generate a kink is then 2.45 km s⁻¹ $< u < 3.55$ km s⁻¹. This is higher than the usual outflow velocities seen in the sunspot moat (Shine et al. 1987) by about a factor of 2 but lower than the maximum Evershed velocities seen at the outer edge of the penumbra. Localized and perhaps transitory shear velocities between the magnetic flux tube and the surrounding medium of this magnitude seem likely in this environment. Taking a value of $u = 3$ km s⁻¹, we then have a phase velocity of $c_k = 0.63$ km s⁻¹ and $\gamma = 0.12$ km s⁻¹. At this depth, dissipative losses may be provided both by the effective viscosity and thermal diffusivity. The estimate for the dissipative coefficient, assuming kinematic viscosity, may be taken as $\nu \simeq 10^2$ – 10^3 km² s⁻¹.

In accordance with expression (11.22), we should expect the stabilization of a soliton when its width reaches the value of $\Delta_{st} = 1.15\nu/\gamma$. At this moment, the travel velocity of a soliton, Eq. (11.9), should approach its stationary value, $v_{st} = c_k + \alpha A_{st}/3$, which corresponds to changing the regime of the evolution of a soliton in time. We can write this estimate through the directly observed parameter, the width of a soliton, Δ (separation between the opposite-polarity legs):

$$v_{st} = c_k + \frac{4\beta_{\text{disp}}}{\Delta_{st}^2} \quad (11.23)$$

After this moment, according to (11.10) the evolution of a soliton is governed by (11.12): Its amplitude gradually decreases, which means that its width increases gradually, resulting in the slowing down of its propagation velocity. Equation (11.12) rewritten for the width of a soliton has a form:

$$\Delta = \Delta_{st} \sqrt{1 + \frac{t}{t_{\text{diss}}}} \quad (11.24)$$

where $t_{\text{diss}} \simeq 12\beta_{\text{disp}}/\nu\alpha A_{st}$, or $t_{\text{diss}} \simeq \Delta^2/\nu$.

If we adopt $v \simeq 100 \text{ km}^2 \text{ s}^{-1}$, for the chosen example, we get: $\Delta_{st} \simeq 960 \text{ km} = 1.3''$, which is less than Δ_{st} for given observed MMFs in Figs. 11.7, 11.8, and 11.9. If we take $v \simeq 200 \text{ km}^2 \text{ s}^{-1}$, $\Delta_{st} \simeq 2.6''$, which is very close to observed values. We can estimate the velocity of a soliton in both fast (emerging) and slow phases. For this, let us estimate the dispersion coefficient: $\beta_{\text{disp}} = 3.6 \times 10^5 \text{ km}^3 \text{ s}^{-1}$. The theory does not allow us to estimate the initial width of a soliton, but if we make a natural suggestion that is well justified by the observational data, that the initial width of a solitary kink is of the order of a flux tube radius or slightly larger, say, $\Delta_0 \simeq 1''$, then for the speed of a soliton in the fast phase we get the soliton propagation speed $v_{0A} = c_k + 4\beta_{\text{disp}}/\Delta_0^2 \simeq 0.63 + 2.74 = 3.4 \text{ km s}^{-1}$. This is very close to the observed values of 4 km s^{-1} .

After the bifurcation point (at the moment of stabilization), the propagation velocity drops to the values determined by Δ_{st} , so that in a slow phase the speed of a soliton is $v_s \simeq c_k + 4\beta_{\text{disp}}/\Delta_{st}^2 \simeq 0.63 + 1.59 = 2.2 \text{ km s}^{-1}$ with $v = 100 \text{ km}^2 \text{ s}^{-1}$. At $v = 200 \text{ km}^2 \text{ s}^{-1}$, $v_s \simeq 0.63 + 0.4 = 1.0 \text{ km s}^{-1}$. This result shows that as the “resistance” of the medium (the effective viscosity or thermal diffusivity) becomes higher, the propagation speed of the soliton decreases.

Given the wealth of the observational data, this simple approach may be used for the estimation of the effective viscosity of the medium. The estimate for t_{diss} for $v = 100 \text{ km}^2 \text{ s}^{-1}$ is $t_{\text{diss}} \simeq 156 \text{ min}$, which means, in accordance with (11.24), that the width of a solitary kink remains almost constant for a long time. This is one of the main observed features of MMFs.

Let us consider now the event shown in Fig. 11.10. This MMF is seen only in its slow phase and its evolution in time should be governed by (11.24). Our goal here is to find out if the observed separation between the bipoles fits the time dependence given by (11.24) and then to compare the most crucial parameter in this expression, t_{diss} found from the observations and theory.

Comparison of the measured separations as a function of time with the theoretical curve is shown in Fig. 11.11. The squares are the observed values. Times are just from the beginning of the series; the transition time is unclear here, and we adopt an offset below to fit the observations. Independent of the start time, it follows from (11.12) that for different moments of time, $t_{k,i}$, the separation between the legs of the MMF, $\Delta_{k,i}$, should satisfy the relationship

$$a_{ki} = \frac{\Delta_k^2 - \Delta_i^2}{t_k - t_i} = \frac{\Delta_{st}^2}{t_{\text{diss}}}, \quad (11.25)$$

which should be constant. The observed separations show an average value for a of 0.17. We can then make a reasonable fit to the data with $\Delta_{st} = 1.0''$ and a start time at 2 min.

The resulting curve is displayed as the solid line in Fig. 11.11 and shows that the observed temporal behavior of the separations is indeed totally consistent with (11.24).

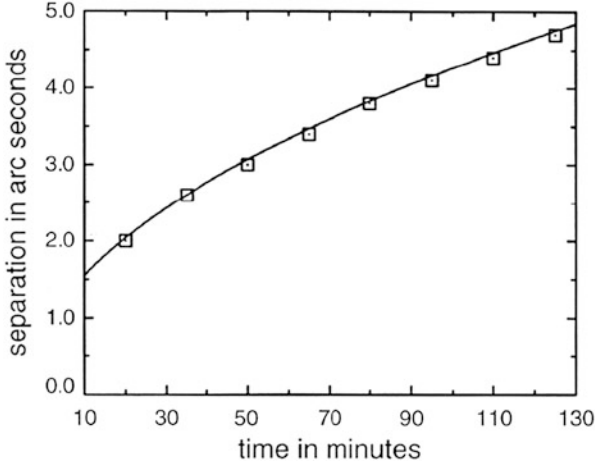


Fig. 11.11 The time dependence of the width of a solitary kink. Squares indicate the observed values for the event shown in Fig. 11.10. The solid line is a fit using (11.24) showing a perfect match of theory and observations

Comparison of the observations with theory allows one to develop quite reliable diagnostic tool For example, from the above example follows the estimate for t_{diss} which is $t_{\text{diss}} = \Delta_{st}/a = 1.0/0.17 \text{ min} = 5.88 \text{ min}$. To compare this value with the theoretical one, we have to take into account the effect gravity. In this case, the dispersion caused by the force of gravity is much stronger than the cubic dispersion caused by the compressibility of the medium. The linear dispersion relation for the incompressible kink perturbations of the horizontal magnetic slab in a stratified atmosphere has a form:

$$\eta[(\omega - ku)^2 - k^2 v_A^2] + \omega \sqrt{\omega^2 - N^2} \tanh kR - (1 - \eta)gk \tanh kR = 0 \quad (11.26)$$

where N is a Brünt-Väisälä frequency,

$$N^2 = -g \frac{1}{\rho} \frac{d\rho}{dz} \quad (11.27)$$

In a long-wavelength approximation (thin magnetic flux tube), $kR \ll 1$, for the phase velocity we have

$$c_k = u \pm \sqrt{\frac{(1 - \eta)}{\eta} gR + v_A^2}, \quad (11.28)$$

and the lower threshold for the KH instability is

$$u_{c1} = \sqrt{\frac{(1-\eta)}{\eta} g R + v_A^2} \quad (11.29)$$

Therefore, the growth rate of the negative energy kink (at $u > u_{c1}$) is

$$\gamma = -NR \frac{u - u_{c1}}{u_{c1}} \quad (11.30)$$

Note that this case, i.e., the effect of gravity on nonlinear kink oscillations described by (11.26–11.28), is quite general and may be applied to the magnetic flux emerging elsewhere at the solar surface and not necessarily in the vicinity of a sunspot.

Returning now to the quantitative analysis of the exemplary soliton shown in Fig. 11.10, we need to use the dispersion relation (11.26). Let us assume that the instability of a negative energy kink occurs at $h = -1000$ km below the surface. At this depth, we adopt the following parameters: the mass density (outside the magnetic field), $\rho_e = 0.27 \times 10^{-5}$ g cm³, temperature, $T = 1.5 \times 10^4$, sound speed, $c_s = 14$ km s⁻¹, and the ratio of mass densities, $\eta = \rho_i/\rho_e = 0.8$. We choose the magnetic field strength as $B = 1000$ Gs, which gives an Alfvén velocity of $v_A = 1.92$ km s⁻¹. The lower limit of a critical shear velocity for the instability is then $u_{c1} = 6.16$ km s⁻¹. We have no direct evidence of local shear velocities at this depth, but values of such magnitude are plausible. If we take $u = 8$ km s⁻¹, then the phase speed is $c_k = 0.84$ km s⁻¹. Now, we can calculate the first dissipative coefficient, γ , responsible for the growth rate of the negative energy kink:

$$\gamma = -NR \frac{c_k}{u_c} = 1.96 \text{ km s}^{-1} \quad (11.31)$$

where the Brünt-Väisälä frequency $N = 0.013$ s⁻¹. With $v = 10^3$ km s⁻¹, we obtain, for the width of a solitary kink in the moment of stabilization, a value $\Delta_{st} = 587$ km, and for $t_{\text{diss}} = \Delta_{st}^2/v$, we have $t_{\text{diss}} = 5.7$ min, which is in good agreement with the fitted values of 725 km and 5.88 min.

11.7 Unification of Known Types of Moving Magnetic Features

As we have seen throughout this chapter, the general problems associated with the MMFs are their great variety and their nonconformity with conservation laws. It is just the second point, i.e., their energetically open character that explains all the observed types of MMFs and different scenarios of their evolution. The variety of MMFs is determined by a great variety of flux tube themselves, their adjacent sheared mass flows, and dispersion and dissipative properties of a whole system.

The most attractive point here is that the most parameters that enter the theory are directly observable. This fact itself not only serves as tools for understanding the nature of the MMFs but may also serve as a powerful tool to infer physical parameters that are not directly observable.

Thus, (11.7)–(11.12) must carry the information about all “five” types of MMFs, their lifetimes, and behavior. Besides, as there are clear differences in the observed properties of MMFs, that have lead to their classification listed in Sect. 11.1, the theory must provide the means to put a particular MMF into its own class.

According to general theory, the MMFs may be either soliton-like or shocklike formation. Now, we need to find out, for example, why one soliton may behave as type I MMF, i.e., move outward from parental sunspot with velocity higher than background flows, and the other soliton may behave as the MDF, i.e., move slowly upstream toward parental sunspot.

To describe different properties of all five types of MMFs, we need to analyze various combinations of the system parameters.

First, we need to emphasize how important role is played by the dispersion of the medium. If the dispersion is positive, the generated kink is a *bright* soliton propagating as a \cap -shaped kink (Fig. 11.12a). If the dispersion is negative, the solution is a *dark* soliton forming a \cup -shaped kink (Fig. 11.12b). Properties of these solitons are very different. Before we come to the main differences, note, e.g., that the propagation velocity of a bright soliton is higher than that of a dark soliton. This is obvious from (11.9) representing the soliton velocity. Written through the dispersion and the width of a soliton, it gives: $v_{\text{sol}}^{\pm} = c_k \pm 4\beta_{\text{disp}}/\Delta^2$. Respectively, lifetime of a bright soliton is longer and it travels farther from sunspot than that of the dark soliton. But the main difference, as one can see from Fig. 11.12, is that the bipoles formed by the kinked flux tube are mirror opposite.

Indeed, in case of positive dispersion, the observer sees along the line of sight a bipole whose leading footpoint has a polarity opposite to that of the parental sunspot, while the trailing footpoint (the one that is closer to sunspot) has the same polarity

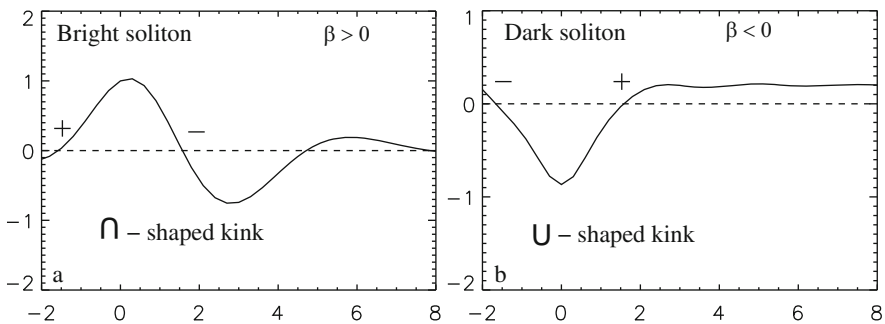


Fig. 11.12 Analytical solutions for nonlinear kink: (a) a bright soliton at positive dispersion; (b) a dark soliton at negative dispersion. Vertical axes are ψ normalized by B^2 , and horizontal axes are x normalized by flux tube radius

as the sunspot (Fig. 11.12a). In case of negative dispersion, it is vice versa, and the observer sees a bipole with a leading footpoint having the same polarity as the sunspot, and the trailing footpoint of the opposite polarity (Fig. 11.12b).

Two other major conditions that further determine the character and properties of generated kink are in the first place, whether the nonlinearity is balanced by the dispersion or not. And then, it is a relation between the phase velocity of a kink and its propagation velocity determined by (11.32). Note that the solutions shown in Fig. 11.12 correspond to a solitary wave when the nonlinearity is balanced by the dispersion effects.

Breaking down the classes of the solution with respect to above three conditions we arrive to all five types of moving magnetic features. These are illustrated in Fig. 11.13 and described below.

Type I At the positive dispersion, $\beta_{\text{disp}} > 0$, when the nonlinearity is balanced by the dispersion, the solution correspond type I MMFs that are observed as a compact bipoles with the inner footpoint sharing the sunspot's polarity. Moving outward from the sunspot, they gradually slow down. During their lifetime, which may be hours, they still move with velocities higher than background plasma flows (Fig. 11.13a, c—balance).

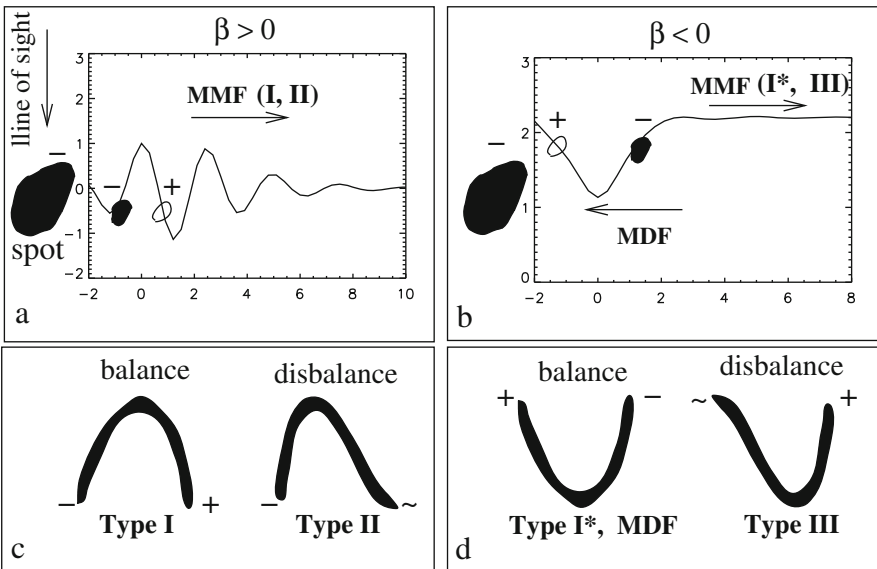


Fig. 11.13 Analytical solutions for nonlinear kink (upper panels), and cartoons depicting all types of MMFs. Balance means that nonlinearity is balanced by dispersion, and disbalance that nonlinearity prevails over dispersion. If at negative dispersion, $\beta_{\text{disp}} < 0$, the phase velocity is such that $c_k < \alpha A/3$, and a moving magnetic feature has negative velocity, it will travel upstream toward sunspot

Type II If under above conditions (i.e., at positive dispersion, $\beta_{\text{disp}} > 0$) nonlinearity prevails over dispersion, the soliton becomes asymmetric and acquires shocklike form, i.e., one side of the soliton becomes steeper than the other. In this case, the observer sees either a bipole with one footpoint clearly and another being diffuse, or only one footpoint. This solution corresponds to type II MMFs which appear as unipolar features emitted from the edge of a sunspot. They share the sunspot's polarity. Often, type II MMFs may have two footpoints: well-pronounced inner one having the same polarity as the parental sunspot, and a diffuse outer footpoint having opposite polarity (Fig. 11.13a, c—disbalance).

Type I* At the negative dispersion, $\beta_{\text{disp}} < 0$, when the nonlinearity is balanced by the dispersion, the solution corresponds to type I* MMFs that are outflowing as opposite-polarity pairs with the inner footpoint having the polarity opposite to the sunspot (Fig. 11.13b, d—balance).

Type III If at $\beta_{\text{disp}} < 0$, nonlinearity prevails over dispersion, just like in the case of positive dispersion, the soliton becomes asymmetric: one side of the soliton becomes steeper than the other, so that the observer sees either a bipole with one footpoint clearly or another being diffuse, or only one-footpoint. This solution corresponds to type III MMFs which appear as a unipolar features emitted from the edge of a sunspot and having the same polarity as sunspot (Fig. 11.13b, d—disbalance).

Type IV The most mysterious magnetic bipoles dubbed moving dipolar features (MDFs), unlike all other MMFs travel *toward* the sunspot against background mass flows. But, even these remarkable features are part of the general scheme: they require a negative dispersion, and flux tube parameters such that the condition $c_k < \alpha A/3$ be fulfilled. In this case, according to (11.9), the soliton propagation velocity becomes negative. According the same equation, their propagation velocity is always less than that of other types of MMFs, and less than the background flows. Indeed, the MDFs were observed as slowly migrating bipoles with velocities ranging $0.3\text{--}0.8 \text{ km s}^{-1}$ (Fig. 11.13b, d—balance).

It must be noted again that observations of MMFs during their long passage across the penumbra and moat may provide a reliable tool for inference of physical parameters of the photosphere that are not directly observable. Simple relations, (11.7)–(11.9), between its size (separation between the footpoints), velocity, and line-of-sight magnetic field (with new satellite the vector magnetic fields are also readily available), allow one to infer such parameters as dispersive properties of a system, dissipative effects and others. These parameters then may be used for the evaluation of their dissipative properties, which determine coupling with the upper atmosphere.

11.8 Impact of MMFs on the Overlying Atmosphere

In the above section, we saw that all types of MMFs, often having conflicting properties, can be described on a unified basis. Note that MMFs may appear in any other magnetized regions where magnetic flux tubes interact with shear mass flows and are subject to gravity forces.

In this section, we will study the response of the upper atmosphere to individual MMFs, i.e., how dynamics and energetics of MMFs affect the upper layers of atmosphere. We must expect, of course, that these effects depend on the type of MMFs. For example, the soliton-type bipolar MMFs, being quite sturdy, should mainly participate in the formation of a moat, unless conditions for explosive instability turn on. The shocklike MMFs, however, being the subject to gravity acceleration may trigger the energetic events in the chromosphere, such as jets and microflares.

We use here several data sets of multi-wavelength observations of the photosphere and its overlying chromosphere and corona to demonstrate the response of the upper atmosphere to dynamics of MMFs.

We start with the data taken on 10 June 1999 (N18.5W5.0), which consist of time series of high-resolution MDI magnetograms co-aligned with the TRACE chromospheric and coronal time series in 1600 Å, Fe IX/X 171 Å and Fe XII 195 Å lines complemented by time series of H α filtergrams obtained from the Swedish Vacuum Solar Telescope (SVST) on La Palma.

Figure 11.14 shows a sample MDI magnetogram (panel (a)) of the central sunspot co-aligned with the image of overlying atmosphere in the ± 700 mÅ wings of H α (panel (b)). To study temporal variability of small magnetic features, we use again the procedure of space–time cuts. Three examples of such cuts in both wavelengths are shown in the upper- and lower-right panels (1a,b); (2a,b); and (3a,b). The population of MMFs and their association with mass flows around the sunspot are well seen in the ± 700 mÅ wings of H α showing the motions at somewhat elevated photospheric level.

More than three quarters of the moat area is well populated by MMFs. The paths of corresponding cuts and their directions are shown, respectively, in panels (a) and (b). The left sides of cuts 1 and 2 and the entire cut 3 through the diameter of a moat pass through the region well populated by MMFs. One can see different types of MMFs on the left sides of panels (1a,b) and (2a,b), and at both sides of panel (3a,b), streaming outward from sunspot; whereas the right ends of cuts 1a,b and 2a,b pass through the moat region devoid of MMFs (curved arrows in the left panels mark the region depleted of MMFs). We will see below that regions with a deficit of MMFs usually serve as a preferred site for coronal loop formation (Ryutova et al. 2007).

Features of individual MMFs as well as expected response of overlying atmosphere are consistent with the predictions of the theory.

The processes of energy transfer and release by soliton (type I,I*, MDF) and shocklike kinks (type II and III), and therefore their impact on the dynamics of the overlying atmosphere, are quite different.

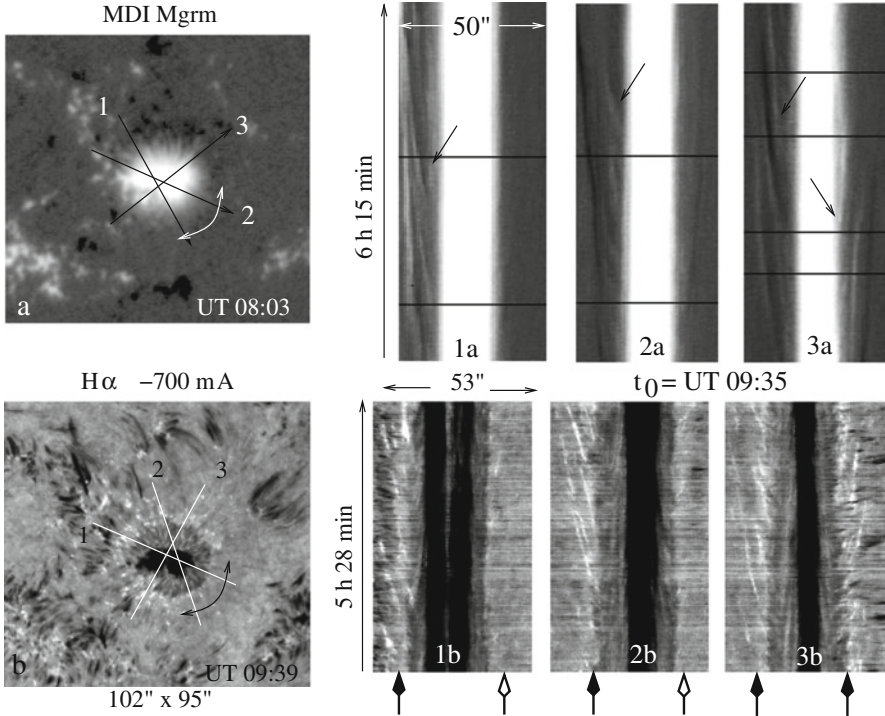


Fig. 11.14 The sunspot observed on 10 June 1999. (a) MDI magnetogram scaled from -1000 to 1000 G; (b) co-aligned image of the same area in the -700 mÅ wing of H α ; upper-right panels: three cuts made over the central sunspot showing propagation of negative (black) and positive (white) magnetic footpoints lying along these cuts; small arrows show some long-living MMFs; lower panels: As in the magnetogram movie, left sides of cuts 1 and 2, and the entire cut 3 pass through the region well populated by MMFs (thick black arrows); the right ends of cuts 1 and 2 reveal very little activity of small-scale bipoles (thick white arrows)

Solitons, once formed, remain “self-contained” and sturdy for a long time. Their amplitude slowly decays as $1/(1 + t/t_{\text{diss}})$. During the passage of a soliton through the moat, it gradually slows down, separation between the footpoints increases, and a kink straightens out. The slow process of energy loss by a traveling soliton may produce a faint emission in chromospheric lines, which may end up at the moat boundary by the appearance of bright points. Under certain and rare conditions, though, solitons may experience an explosive growth, as $1/(1 - t/t_{\text{expl}})^2$. This corresponds to quick and violent energy release which may produce well-concentrated jets and microflares even at coronal temperatures.

A shocklike kink is a more unsteady state than a soliton. Its lifetime may be as long as that of a soliton, but to remain in a quasi-stable state, it requires an intense process of energy supply and release.

One should bear in mind that the very existence of evolutionary soliton- and shocklike kinks is possible only in energetically open systems, i.e., in systems with

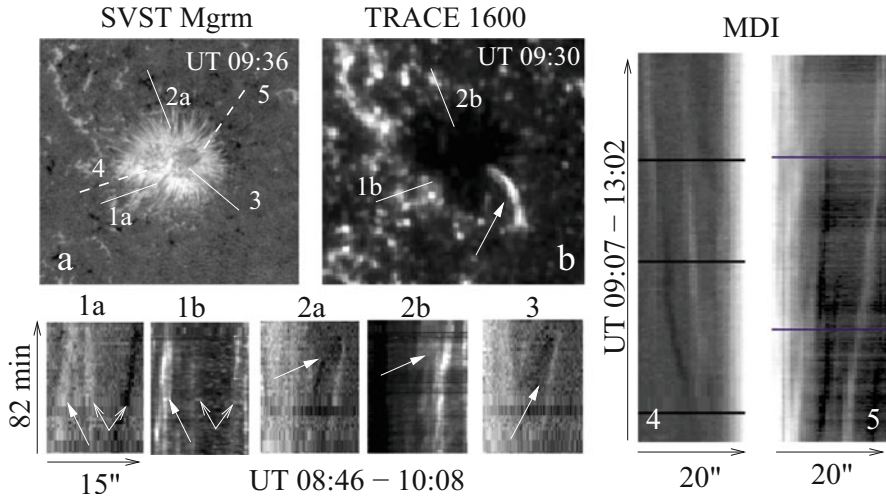


Fig. 11.15 Examples of different types of MMFs and their counterparts in the transition region. Upper panels: (a) SVST magnetogram of the central sunspot from Fig. 11.14 with resolution $0.2''$, (b) the same region in TRACE 1600 at $T \sim 6 \times 10^4$ – 2.5×10^5 K; three straight lines show corresponding space–time cuts in the lower panels. Cut 1 contains two most typical MMFs, type I (double arrow) and type II (single arrows); Stable soliton (type I) leaves a very faint trace at high temperatures, while type II which has shocklike properties produces strongly enhanced emission in the TR. Cut 2 shows type I MMF (with the inner footpoint of polarity opposite the sunspot’s), which after about an hour of a steady state starts to shrink and quickly disappears; this process is accompanied by the extended brightening (2b). Cut 3 shows another type I MMF under the condition when it experiences an “explosive” collapse, which results in the intense, but short-lived microflare (snapshot in panel (b) shows its maximum phase). Panel (4) shows a long-lived Type I MMF at the MDI resolution with the inner footpoint of the same polarity as parental sunspot (type I, bright soliton), and panel (5) shows type I MMF with the inner footpoint of the opposite to sunspot polarity (type I*, dark soliton)

continuous energy inflow and outflow (sources and sinks). Therefore, the intensified process of the absorption and release of energy by shocklike formation should be accompanied by the enhanced emission in the upper layers of atmosphere during most of its lifetime. The energy of a shocklike kink is concentrated in a small volume. When this volume decreases, the kink quickly dissipates its energy, and may cause the appearance of jets and microflares.

Examples of different types of MMFs and their counterparts in the overlying atmosphere are shown in Fig. 11.15. Cuts 1a,b contain two MMFs, type I, marked by double arrows, and type II, marked by a single arrow. The size of the footpoints is about 1 – $1.3''$. This type I feature was born obviously long before the SVST data were taken; its footpoints are already far apart exceeding a separation of $4''$. It continues a steady motion with further gradual spreading, typically seen in the numerous long-lived MMFs. At transition region temperatures, as expected, this MMF is barely noticeable. Its neighbor, a type II MMF with shocklike properties, on

the contrary, produces strongly enhanced emission at the temperatures $T \sim 6 \times 10^4 - 2.5 \times 10^5$ K during its passage throughout the moat.

The third example is quite rare. This is a type I MMF born during the SVST observations. Its short path resembling the Greek λ is consistent with the explosive behavior leading to collapse and violent energy release. Indeed, the collapse of this MMF was accompanied by a strong and short-lived (~ 6 min) microflare seen in its maximum phase on the TRACE 1600 image (panel b).

To obtain more information about the influence of MMFs on an overlying atmosphere, a high cadence (≤ 30 s) movies in G-band 4305 Å were compiled together with co-spatial Dopplergrams.

In Fig. 11.16, we compare space–time slices made along cuts 1–3 using Dopplergram and G-band movies. Cut 1 lies in the region of a significant deficit of the MMFs. The corresponding Dopplergram image (Fig. 11.16a, upper panel), shows characteristic umbral oscillations and running penumbral waves. The left vertical lines in these panels mark the umbra/penumbra boundary, and the right lines the approximate boundary of the penumbra. The rest is the moat region. One can see how regular umbra/penumbra plane waves smooth out in the moat and leave a place

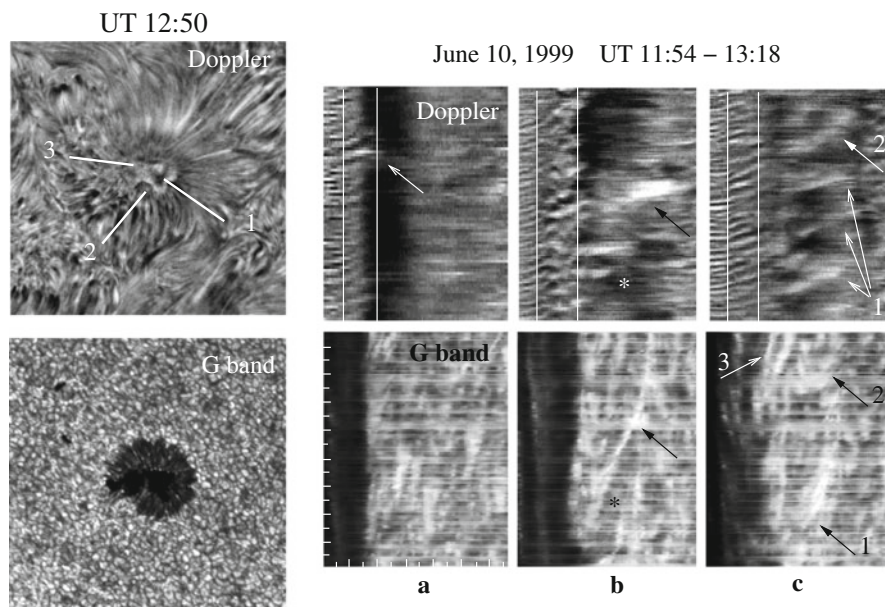


Fig. 11.16 Computed Dopplergram in $H\alpha \pm 0.350 \text{ \AA}$ and SVST G-band images of a target area (left panels). Corresponding space–time images for three cuts shown in the right panels (upper row is from a Dopplergram movie, lower row is from G-band movie): (a) Cut 1 is made over the region devoid of MMFs; (b) cut 2 reveals “unipolar” type II MMF and its imprint on overlying chromosphere; and (c) cut 3 shows two MMFs of type II marked by black arrows, 1 and 2, and one MMF of type I marked by white arrow, 3. See text for details. Tick marks in the x -axis correspond to $2.5''$ and tick marks in the y -axis to 5 min

to a vague pattern of granular motions. Note here that a short-lived chromospheric transient appeared at UT 12:50.

The bottom-left panel is a G-band image at 4305 \AA . This line has been commonly used to track the small-scale magnetic elements that appear as G-band bright points. The space–time slice in the G-band passing through region devoid of MMFs (lower panel a) shows irregular motions, appearance, and disappearance of small-scale network magnetic elements.

The other two cuts, 2 and 3, corresponding to images in panels (b) and (c), lie in regions dominated by type II MMFs having shocklike properties. Cut 2 reveals a typical example of such an MMF. Its emergence is accompanied by the strongly enhanced up-flows seen in Dopplergram image (marked by stars). Traveling with high velocity, $\simeq 6 \text{ km s}^{-1}$, the MMF generates along its path strong disturbances that culminate at about the time when the MMF “settles down” and starts to migrate slowly toward the moat boundary (black arrows in panels (b)). Note that a lateral motion of the $H\alpha$ disturbance at this time is about 14 km s^{-1} , which at $T \simeq 10^4 \text{ K}$ is already (but slightly) supersonic.

Cut 3 reveals three features, two MMFs of type II marked by black arrows in lower panel (c), and one MMF of type I, marked by white arrow. During the passage of the MMF # 1 through the moat, Dopplergram movie shows how a regular pattern of oscillations disintegrates into two distinct velocity fields associated with the ridges of up-flow material followed by the post-ridge downflows, marked by white arrows in the upper panel (c). The velocity of the ridges associated with the first MMF is over 16 km s^{-1} , and is clearly supersonic, while the lateral motion of a ridge 2 is about 9 km s^{-1} and seems to be subsonic.

As already mentioned, simple relations between the width of a soliton, its velocity, amplitude (B_z^2), and lifetime, expressed in directly observable quantities allow detailed analysis of the data and inference of such parameters as dissipative coefficients (which determine the lifetime of MMFs), dispersion, the slope of a soliton, etc. Most importantly, these parameters may be used to study observational signatures of dissipation processes which are associated with the energy transfer and release by MMFs.

11.9 Anticorrelation Between Population of MMF’s and Coronal Loop Formation

So far, we were discussing the properties of individual MMFs and their observed signatures. It is interesting that as an ensemble, the families of MMFs have an essential influence on the dynamics of solar atmosphere from its visible surface to corona.

It was found that very intense formation of an ensemble of MMFs as a collective phenomenon is strictly correlated with the absence of large-scale “stable” coronal loops (Ryutova et al. 2007). Such loops are usually rooted at the side of the sunspot

with no or few MMFs. We will discuss below possible reasons that may cause the observed anticorrelation. For these studies, several sets of multi-wavelength observations of different sunspot areas from the photosphere to the corona have been used.

Hagenaar and Shine (2005) studied statistical properties of MMFs using time sequences of high-resolution magnetograms of eight sunspots. They have developed an automated algorithm to find and track unipolar magnetic field concentrations, and derived flow-maps around the spots to compare plasma flow patterns with the tracks of moving magnetic features. These results were compared with the corresponding images of overlying corona.

The examples of the data taken on 3 November 1998 and 9 April 2003 are shown in Fig. 11.17. Figure 11.17a, b is a co-aligned MDI magnetogram and the overlying corona in the TRACE 171 Å line. Figure 11.17c shows tracks of unipolar magnetic elements obtained from the time sequence covering a 19-hr period. In all studied cases, the number and distribution of MMFs around sunspots is uneven: one side of a sunspot may show a much higher population of MMFs than the other. The side of the sunspot with a small population of MMFs is indicated by black arrows, and as in all studied cases, it is just this side where large-scale coronal loops are rooted.

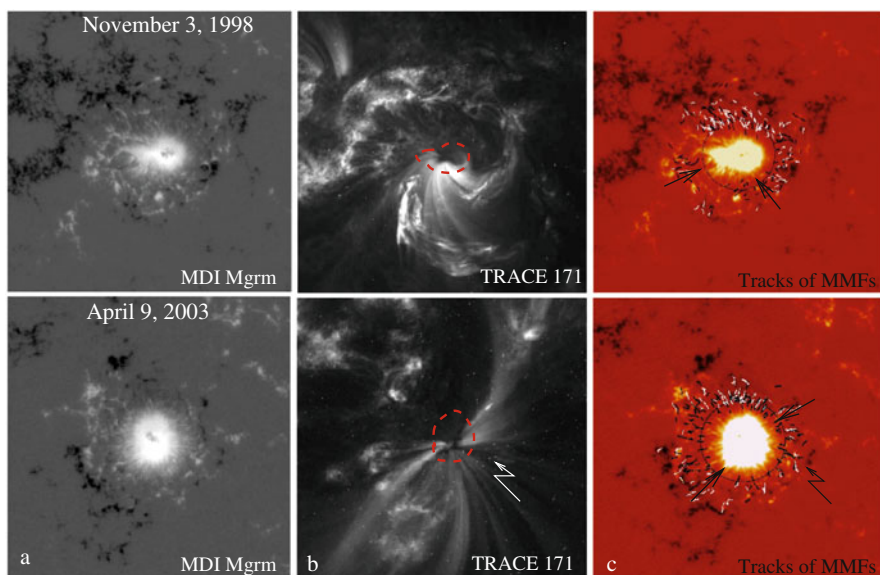


Fig. 11.17 Connection between the number of MMFs and the preferable site for the formation of coronal loops. Left and middle panels: co-aligned MDI magnetogram and overlying corona. Right panels: paths of outflowing unipolar magnetic features obtained from the MDI movies covering a 19-h period. Black arrows show the side of the sunspot where the population of MMFs is low and where large-scale coronal loops are originated. The zigzag arrows indicate a tiny region with quite sturdy MMFs and, respectively, a gap in the coronal loops rooting. Red dashed curves outline the position of the umbrae, and black circles the approximate penumbrae radii

It is important to note, however, that only intense MMF production strictly correlates with the absence of loops. Moderate MMF production may or may not prevent coronal loop formation, and prominent loop bundles do not necessarily mean the absence of MMFs. And yet, in a long-term period a dynamic ensemble of a large number of MMFs seems to create physical conditions unfavorable for the formation of long-lived coronal loops. The correlation between the deficiency of MMFs and the preferable location of coronal footpoints definitely calls for further studies.

For the time being, it is obvious that whatever is the reason for coronal loops to avoid regions highly populated by MMFs, it should be sought in the nature of MMFs as a collective phenomenon. Below, we discuss two possible reasons that may cause the observed anticorrelation:

1. According to the observations, MMFs appear along horizontal magnetic filaments usually located in areas of strong horizontal flows. From the theoretical point of view, as well, a primary condition for the soliton formation is a horizontal magnetic flux tube (with gravity force perpendicular to its axis) in the presence of aligned shear flow (Ryutova et al. 1998). Some part of the sunspot penumbra, however, may be dominated by elevated magnetic filaments that cannot support formation of MMFs but may well serve as a base for coronal loops. The key element here seems to be the natural coexistence and uneven distribution of horizontal and elevated filaments in the penumbra: an intense MMF formation and the lack of loops correspond to strong predominance of horizontal filaments, while regions with a preference to more elevated filaments produce coronal loops. The coexistence of horizontal and vertical filaments explains the emergence of a few MMFs in the presence of coronal loops.
2. The other effect that may cause a lack of MMFs around sunspots with horizontal penumbral filaments and co-aligned flows (i.e., under satisfactory primary conditions) is deviation of local physical parameters of a system from values adequate for the formation of MMFs. To discuss this effect, we first briefly address some key properties of MMFs and conditions for their formation based on (11.3)–(11.9).

As we know, the solution of (11.3) has several branches, determined by the phase velocity, (11.1), the sign of dispersion, and the interplay of nonlinear, dispersion, and dissipative effects. If dispersion is balanced by nonlinearity, stationary solution of (11.3) is known to be a stable solitary kink with a simple relation between the width of a soliton, Δ (separation between MMF footpoints), its velocity, v_{sol} , and amplitude, $A \simeq B_z^2$ (B_z is the line-of-sight magnetic field at the MMF footpoint) given by (11.7)–(11.9).

Order-of-magnitude comparison of the two last terms in the left-hand side of (11.3) gives a condition for balance between nonlinear and dispersive terms, $\alpha\psi \sim \beta_{\text{disp}}/\Delta^2$; for positive dispersion, we have

$$\frac{3}{4} \frac{B_z^2}{B^2} c_k \simeq \frac{R^2}{\Delta^2} \frac{1}{2\eta v_A^2} \frac{(c_k - u)^4}{\sqrt{\eta[(1 + \eta)v_A^2 - u^2]}} \quad (11.32)$$

Table 11.1 Measured and estimated parameters of MMFs

Directly observed parameters						Estimated parameters		
MMF	B_z (G)	R	Φ (10^{18} Mx)	Δ	v_{sol} (km s $^{-1}$)	c_k (km s $^{-1}$)	v_A (km s $^{-1}$)	$c_k^{(\text{th})}$ (km s $^{-1}$)
1	480	1.2''	3.6	4''	1.2	0.48	3.8	0.42
2	230	2.2''	5.1	8''	0.8	0.32	1.8	0.32

By slight violation of the equivalence (11.32) toward increasing dispersion, roughly for thicker flux tubes, solitons become flat, their width increases, and their velocity drops. Thus, if the penumbral filament is thick enough, the kink produced by the shear flow instability will not survive. Finally, when the nonlinear term in (11.3) can be neglected, i.e., the problem becomes linear, a kink generated by shear flow after few undulations will disappear as usual wave. This will also happen if the dispersion term exceeds the nonlinearity by one or two orders of magnitude.

To estimate the radius of the flux tube at which in otherwise suitable conditions solitons do not form, we use two examples of a long-lived type I MMFs shown in Fig. 11.15 (panels 4 and 5).

The observed and estimated parameters are shown in Table 11.1. The first five columns are directly observed parameters. The two next columns containing v_A and c_k are values of Alfvén and phase velocities deduced from observations. The value $c_k^{(\text{th})}$ is calculated with (11.1). We must to add this table the values of an angle and radii that at given physical conditions *are not suitable* for the formation of MMFs. These are: for MMF 1, $\theta = 10\text{--}15^\circ$, $R_\theta = 7\text{--}4.6''$, and for MMF 2, $\theta = 16\text{--}27^\circ$, $R_\theta = 8\text{--}4.8''$.

We adopt the following values: the plasma density outside the flux tube $\rho_e = 2.8 \times 10^{-7}$ g cm $^{-3}$, the ratio of mass densities, $\eta = \rho_i / \rho_e = 0.9$, and the flux tube inclination in the developed soliton, $\theta = 45^\circ$, so that $B_z = B \sin \theta$.

Using condition (11.32), and the soliton velocity, from (11.7)–(11.9), we may exclude a quantity $\beta_{\text{disp}} / \Delta^2$ and estimate the phase velocity directly through the observed speed of a soliton. This gives $c_k \simeq 0.4 v_{\text{sol}}$. For the lower sign in Eq. (11.1), the shear flow velocity should be taken in the range of $\sqrt{\eta} v_A \leq u \leq \sqrt{1 + \eta} v_A$. Taking a value of $u = 4$ km s $^{-1}$ for MMF # 1, and $u = 2$ km s $^{-1}$ for MMF # 2, we obtain, respectively, $c_k^{(\text{th})} = 0.42$ km s $^{-1}$, and $c_k^{(\text{th})} = 0.38$ km s $^{-1}$. Both values are close to values estimated from observations.

If the slope of the kink legs levels down, nonlinearity becomes negligible, and conditions for the formation of MMFs are no longer satisfied. For small enough angles ranging over interval $15\text{--}10^\circ$, the right-hand side of (11.32) exceeds the left-hand side by a factor of 15–33. This means that if under the condition of MMF 1, with a radius of 1.2'', a flux tube with a radius of about 4.6–7'' (and higher) cannot form a stable kink. For a comparable size of flux tubes, under conditions allowing formation of “thicker” kinks, such as MMF # 2, “unfavorable” angles may be as high as 16–27°.

Most probably, it is a combination of both effects, uneven coexistence of elevated and horizontal magnetic filaments in the penumbra and the presence of thick

horizontal filaments, that causes the observed correlation between coronal loops and the deficiency of MMFs. The effects of MMFs in the dynamics of the upper atmosphere seem to be quite pronounced and call for further studies. An analysis of flow maps in and around the sunspot together with the vector magnetograms may provide reliable information on the nature of the photosphere–corona coupling.

11.10 Problems

11.1 Obtain conservation laws for the KdV equation,

$$\frac{\partial u}{\partial t} + u \frac{\partial u}{\partial x} + \beta \frac{\partial^3 u}{\partial x^3} = 0. \quad (11.33)$$

Here, the equation is given in normalized form, β is dimensionless dispersion coefficient.

11.2 Analyze solutions of Gardner equation which is known as the combination of KdV and modified KdV (MKdV) equations:

$$\overline{u}_t + 6\overline{u}\overline{u}_x + 6\alpha\overline{u}^2\overline{u}_x + \overline{u}_{xxx} = 0 \quad (11.34)$$

Show that depending on the sign of α , the Gardner equation describes either bright (\cap -shaped kink) or dark (\cup -shaped kink) solitons.

11.3 In one-wave approximation (for nondimensionalized amplitude u), solitons in non-equilibrium media may be described by the generalized KdV-Bürgers equation which includes dispersion of medium, $\beta \neq 0$:

$$\frac{\partial u}{\partial t} + u \frac{\partial u}{\partial x} + \beta \frac{\partial^3 u}{\partial x^3} = \gamma u + \nu \frac{\partial^2 u}{\partial x^2} \quad (11.35)$$

Analyze behavior of solitons in case of a strong dispersion.

References

- P.N. Bernasconi et al., *Solar Phys.* **209**, 119 (2003)
 N. Brickhouse, B. LaBonte, *Solar Phys.* **115**, 43 (1988)
 B. Coppi, M.N. Rosenbluth, R. Sudan, *Ann. Phys.* **55**, 201 (1969)
 V.M. Dikasov, L.I. Rudakov, D.D. Ryutov, *Sov. Phys. JETP* **21**, 608 (1965)
 I. Fushiki, J.I. Sakai, *Solar Phys.* **161**, 317 (1995)
 H. Hagenaar, R. Shine, *Astrophys. J.* **635**, 659 (2005)
 K. Harvey, J. Harvey, *Solar Phys.* **28**, 61 (1973)
 B.B. Kadomtzev et al., *Sov. Phys. JETP* **20**, 1517 (1964)
 V.I. Karpman, *Nonlinear Waves in Dispersive Media* (Pergamon Press, London 1975)

- J.W. Lee, *Solar Phys.* **139**, 267 (1992)
- P. Maltby et al., *ApJ* **306**, 284 (1986)
- L.A. Ostrovsky, S.A. Rybak, L.S. Tsimring, *Sov. Phys. Uspekhi* **29**, 1040 (1986)
- M.P. Ryutova, *Sov. Phys. JETP* **67**(8), 1594 (1988)
- M. Ryutova, H. Hagennar, *Solar Phys.* **246**, 281 (2007)
- M. Ryutova, R. Shine, A. Title, J.I. Sakai, *Astrophys. J.* **492**, 402 (1998)
- M. Ryutova, T. Tarbell, R. Shine, *Solar Phys.* **213**, 231 (2003)
- M. Ryutova, H. Hagennar, A. Title, *Astrophys. J.* **656**, L45 (2007)
- N.R. Sheeley, *Solar Phys.* **1**, 171 (1967)
- R. Shine, A. Title, in *Encyclopedia of Astronomy and Astrophysics*, ed. by P. Murdin (IOP, Bristol, 2001), p. 3209
- R.A. Shine, A.M. Title, T.D. Tarbell, K.P. Topka, *Science* **238**, 1203 (1987)
- M. Suzuki, J.I. Sakai, *Astrophys. J.* **465**, 393 (1996)
- D. Vrabec, in *Solar Magnetic Fields*, ed. by R. Howard. IAU Symposium, vol. 43 (Reidel, Dordrecht, 1971), p. 329
- G.B. Whitham, *Linear and Nonlinear Waves* (Wiley, New York, 1974)
- P.R. Wilson, *Solar Phys.* **106**, 1 (1986)
- V.B. Yurchyshyn, H. Wang, P. Goode, *Astrophys. J.* **550**, 470 (2001)
- J. Zhang, S.K. Solanki, J. Wang, *AandA* **399**, 755 (2003)
- F. Zuccarello et al., *AA* **500**, 5 (2009)

Chapter 12

Reconnection of Flux Tubes: Specifics of High Plasma β



Abstract Two fundamental mechanisms of magnetic reconnection worked out by Sweet–Parker tandem (Parker, *J Geophys Res* 62:509, 1957; Sweet, IAU symposium on electromagnetic phenomena in cosmic plasmas, Stockholm, 1956 (1958), p 123) and Petschek (The physics of solar flares, ed. by W.N. Hess. Proceedings of the AAS-NASA symposium on physics (NASA, Washington, 1964), pp 425–439) were both aimed to explain an enormous amount of energy produced by coronal flares. Since then, extensive studies of a topological change of magnetic field resulted in a huge body of refined reconnection theories, beautiful laboratory experiments, and numerical modeling. One thing, however, remained for a long time unchanged: the subject of studies, magnetized plasma, has been a priori considered magnetically dominated, i.e., having very low plasma beta, $\beta = 8\pi p/B^2 \ll 1$. It is just this condition that provides release of a huge amount of energy stored in magnetic fields due to their topological change. This simple fact dominated so strongly that during almost six decades there was no attempt to investigate the opposite situation, i.e., when topologically favorable conditions for reconnection appear in gas-dominated plasma with finite or even larger than unity plasma beta, $\beta = 8\pi p/B^2 \geq 1$. As quest was for large amount of magnetic energy, the case of high-beta plasma (with magnetic energy less than gas-kinetic energy) did not seem promising. This, however, proved to be wrong. It turned out that in case of small-scale magnetic flux tubes under real conditions of solar photosphere, high β reconnection is unavoidable process. In the photosphere, magnetic flux tubes buffeted by convective motions collide and reconnect. True that the photospheric reconnection does not give the immediate gain in energy, but it sets the system in strongly unstable state. Now, the central problem becomes to understand how the post-reconnection products evolve. In this chapter, we shall study the peculiarities of high β reconnection, and what is more important, the post-reconnection processes. We shall see that high-beta reconnection triggers various nonlinear processes that are responsible for wide range of observed phenomena.

12.1 Basics of Magnetic Reconnection

It all started with trying to solve a mystery of chromospheric flares. Back in the 1940s, there were accumulated quite a rich observational data in Ca H and K lines and in $H\alpha$ showing clear association of chromospheric flares with underlying sunspot groups.

Giovanelli (1946), who involved himself in these observations, in a short note on a theory of chromospheric flares pointed out that the changing magnetic flux of ever-evolving sunspot groups leads to formation of an X-type neutral points in the magnetic field lines and to formation of at least two types of current systems, whose evolution eventually leads to electrical discharges along neutral lines. Figure 12.1a shows Giovanelli's sketch of currents flowing in a system of a bipolar sunspot group. Magnetic field lines are shown in a "dividing" plane containing the sun's general magnetic field, and intersecting the two sunspots. A current filament, one in the neutral point current sheet (j_1), and two others flowing into sunspots (j_2) are shown by dashed lines. Arrows show their relative direction. The line AB is the locus of points where the dividing plane meets the surface of the sunspot. The line CDE is the locus of points where lines of force from near the neutral point meet the sun's surface. This line serves as a base of the neutral point current sheet.

The most remarkable fact in Giovanelli's studies is that his model of magnetic field reorganization is essentially *three dimensional*. Although Giovanelli does not talk about "breaking" and "rejoining" lines of forces, the very idea and accompanying drawing form the bases of all types of future reconnection models.

The very first statement that "lines of force can be regarded as being broken and rejoined" belongs to Dungey (1953), who suggested that near-neutral point magnetic

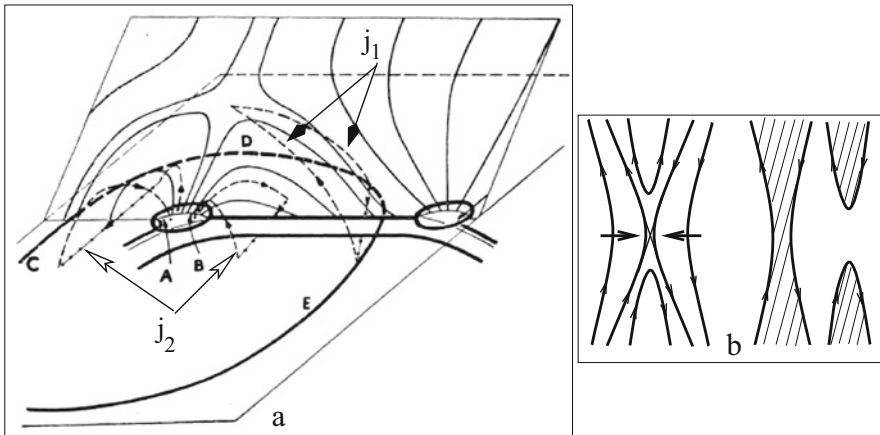


Fig. 12.1 Earliest representation of magnetic energy release: (a) Three-dimensional (!) cartoon by Giovanelli (1948), showing *currents* near a growing bipolar spot group (see details in text); (b) Dungey's (1953) "lines of force" that "can be regarded as being broken and rejoined"

field may go unstable and result in the reconfiguration of magnetic field and the fast dissipation of magnetic energy. Figure 12.1b illustrates Dungey's examples which he describes as follows. When "two parts of a loop of force are close together with their fields in opposite directions, the result is that the loop of force breaks into two loops, whose total length is less than that of the original loop." And, Dungey concludes that "the field energy from relatively large region is concentrated on particles in the neighborhood of the neutral point, and that part of energy is released."

Bumba (1958) was first to observe that the $H\alpha$ emission in the largest flares begins over a series of small-scale magnetic elements, dubbed at that time as flare knots, that form to strips on either side of the polarity inversion boundary. It was found that the flare knots are associated with strong electric currents (Moreton and Severny 1968).

Simple and appealing, Dungey's two-dimensional cartoon took a long journey. And, reconnection theories became two dimensional for decades.

Sweet (1958) presented a talk at the 1956 IAU Symposium in Stockholm on theory of solar (chromospheric) flares based on formation of a neutral collision layer as a result of merging of opposite-polarity magnetic field systems, with subsequent change in their topology leading to strong radiation of energy and production of high-energy particles.

Parker (1957), impressed by Sweet's presentation, derived scaling laws of the process and coined the term "reconnection." When two oppositely directed magnetic fields approach each other (Fig. 12.1b), the field gradient steepens and the electric current density $(c/4\pi)\nabla\times\mathbf{B}$ becomes large. At the same time, at small characteristic distance, the dissipative effects turn on and strong dissipation occurs.

To be consistent with Sweet's hydrodynamic analogy of expelling gas occupying a space between two rigid plates forced to move toward each other, Parker derives the rate of steady-state reconnection from the basic conservation laws. The total pressure, $p + B^2/8\pi$, is uniform across the current sheet, so the gas pressure is highest on the neutral plane where B goes through zero (Fig. 12.2a). This excess pressure ejects the gas from the mid-plane region along the lines of force in the $\pm x$ directions with the velocity v . For irrotational and steady motion, Bernoulli's equation is

$$\rho v \frac{\partial v}{\partial x} + \frac{\partial p}{\partial x} = 0 \quad (12.1)$$

Integrating along x -axis from the origin at the center, where $v = 0$, to a point outside the fields, one obtains $\rho v^2 = 2\Delta p$, where Δp is the pressure excess $B^2/8\pi$. Thus, the velocity of expulsions is just the Alfvén velocity, $v_A = B/\sqrt{4\pi\rho}$.

If l is the characteristic length of the gradient of \mathbf{B} across the neutral plane, then the characteristic rate of the net expulsion of gas out of both ends is $4lv$. If the two magnetic fields approach each other with velocity w , then the mass conservation of

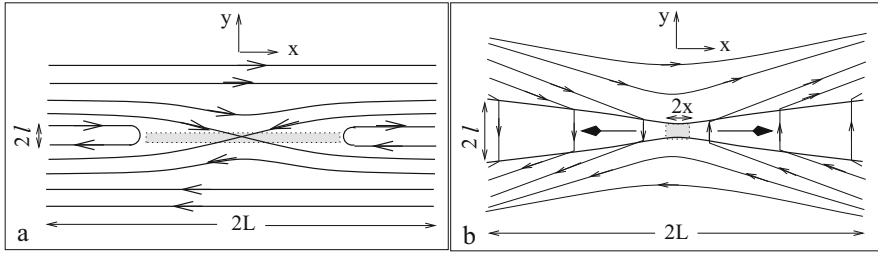


Fig. 12.2 Magnetic field and flow configuration in the reconnection process. (a) Diffusion-dominant mechanism by Sweet-Parker: the plasma moves toward boundary from both sides and after field lines reconnect at the x -point due to finite conductivity, is ejected along it; (b) Petschek's mechanism includes standing waves, shown by vertical arrows off the x -type neutral point. Flow geometry is the same as in previous case, but now it is independent of the diffusivity and is controlled by Alfvén waves

gas requires that

$$wL = v_A l. \quad (12.2)$$

As the field changes by $2B$, across the thickness $2l$, the current density (perpendicular to the xy -plane) is $j = cB/4\pi l$. The Ohmic dissipation across the width l is lj^2/σ which, in fact, equals the magnetic energy influx $wB^2/8\pi$. Hence, the velocity with which the opposite fields move toward each other is $w = (2/l)(c^2/4\pi\sigma)$, or

$$w = \frac{2\eta}{l} \quad (12.3)$$

where $\eta = c^2/4\pi\sigma$ is the resistive diffusion coefficient. Thus, w has a simple meaning of the characteristic diffusion velocity over a scale l . Solving for w and l , (12.2) and (12.3) give

$$w = \frac{2v_A}{\sqrt{R_m}}, \quad l = \frac{2L}{\sqrt{R_m}} \quad (12.4)$$

where R_m is magnetic Reynolds number $R_m = 2Lv_A/\eta$. Thus, the rate (12.4) is larger by $\sqrt{R_m}$ than pure diffusion, but it is still too small compared to the Alfvén speed. In the solar atmosphere, magnetic Reynolds number is of the range 10^6 – 10^{12} , and reconnection rates are then 10^{-3} – 10^{-6} of the Alfvén speed. In other words, the rate at which magnetic energy can be released by Sweet-Parker mechanism is by several orders of magnitudes less than the observed one.

At AAS-NASA Symposium on Physics of Solar Flares, (Petschek 1964) gave a talk on “Magnetic Field Annihilation” and showed that the rate of magnetic energy release due to the merging of opposite polarity magnetic fields can be made comparable with that observed in solar flares.

Petschek pointed out that on the basis of resistive instability analysis of Furth et al. (1963) the boundary in the Sweet–Parker model would be unstable. However, the linearized instability analysis is not sufficient for estimate of the actual reconnection rate. Petschek showed that the two opposite fields could meet and form much shorter current sheet than that assumed by Sweet and Parker. The Petschek’s drawing is shown in Fig. 12.2b. Once the field lines in this small region ($2l \times 2x$) are reconnected, their tension ejects the plasma vigorously generating the Alfvén waves that accelerate further to form slow magnetosonic shocks. The reconnection rate in this process depends strongly on system parameters and may be arbitrary. Sweet–Parker’s solution is one of the special cases. Petschek, deriving the maximum reconnection rate which can be presented as

$$w = \frac{v_A}{\ln R_m} \quad (12.5)$$

comments: “It is a fortunate circumstance that this answer depends only logarithmically on the magnetic Reynold’s number and is therefore rather insensitive to our ignorance of the effective conductivity of plasma.”

Sweet, during discussion after Petschek’s presentation said: “Dr. Parker and I have been living with this problem for several years and have got the feel of it. Your solution struck me at once as the solution for which we have been seeking.”

Petschek’s work was prophetic in that simple way which gives extremely wide range of the reconnection outcome depending on the physical parameters of medium. Nature, from laboratory plasma devices, near earth magnetosphere, the Sun and outer space consists of plasma which never is at rest. This means that any moving plasma is magnetized and, naturally, is strongly inhomogeneous. Thus, magnetic fields are permanently subject of topological changes. This is exactly what the reconnection is, but the outcome, depending on physical parameters of a particular system, has many faces.

Since those early days, all studies of magnetic reconnection were focused exclusively on those areas where the reconnection would lead to a strong *in situ* heating and particle acceleration (Rosenau 1979; Syrovatskii 1981; Axford 1984; Biskamp 1986). And, the requirement of plasma beta to be much smaller than unity became an imperative.

Highly improved solar observations made the marsh of reconnection mechanism triumphant: favorable magnetic configuration (such as shown in Fig. 12.3), rearrangement of overlying coronal loops, and subsequent flare became regularly observed. The observed timescales, however, are still too far from those estimated theoretically. And refining of reconnection models, their study in laboratory experiments that allows to change and control the system parameters, continues to this day (Parker 1991; Somov 1992; Priest and Forbes 2000; Yamada et al. 2010; Kulsrud 2011).

This concludes our brief look at the “orthodox,” $\beta \ll 1$, magnetic reconnection. In this and in subsequent chapters, we shall study the opposite case, the reconnection and post-reconnection processes in high-beta plasma containing magnetic flux

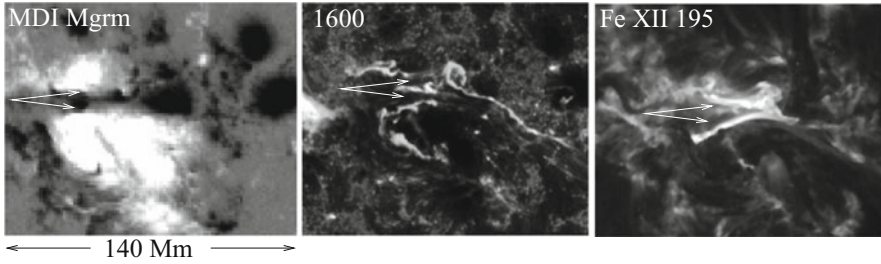


Fig. 12.3 Magnetogram of a huge active region AR 10486 taken on 28 October 2003 by the MDI instrument on SOHO. (a) White arrows show two parallel regions with possibly two separate current sheets. (b) The same region in the chromospheric 1600 Å line, and (c) in the coronal Fe XII 195 Å line. Enhanced emission at chromospheric and coronal temperatures mimic the possible current sheets

tubes, i.e., the case when magnetic energy stored in flux tubes is less than gas-kinetic energy of medium.

Odd enough, but during almost six decades of reconnection studies the case of high-beta reconnection was not questioned until late 1990s. The problem of high-beta reconnection was first considered in series of papers by Tarbell et al. (1999, 2000), and Ryutova et al. (2000, 2001, 2003). These studies originated from the attempts to explain new regularities established in simultaneous multi-wavelength observations of the photosphere and its overlying chromosphere/transition region.

12.2 Photospheric Reconnections: No Immediate Gain in Energy

Throughout this book, we talked and will come back to the fact that small-scale magnetic flux tubes in the photospheric network are the subject of a complex dynamics that includes continuous emergence of new flux tubes, total or partial cancellation of opposite-polarity elements, merging and splitting processes, the appearance of bright points in their vicinity, etc.

An exemplary set of magnetograms illustrating various processes in a very quiet sun is given in Fig. 12.4. Shown are the magnetograms of $90'' \times 90''$ area at six instances of time with 20-min intervals taken by the MDI/SOHO instrument on January 22, 1997. Three white boxes identify the most typical events.

The box 1 is a region of newly emerging flux: at UT 17:08, the box is almost empty, in 20 min newly emerged bipole shows up, and in another hour the box is full of mixed polarity “pairs.” This region produces strongly enhanced emission at the transition region temperatures.

The box 2 contains two bipolar objects. Both bipoles during a given time get strongly reduced, which also coincides with strongly enhanced emission in the chromosphere/transition region temperatures.

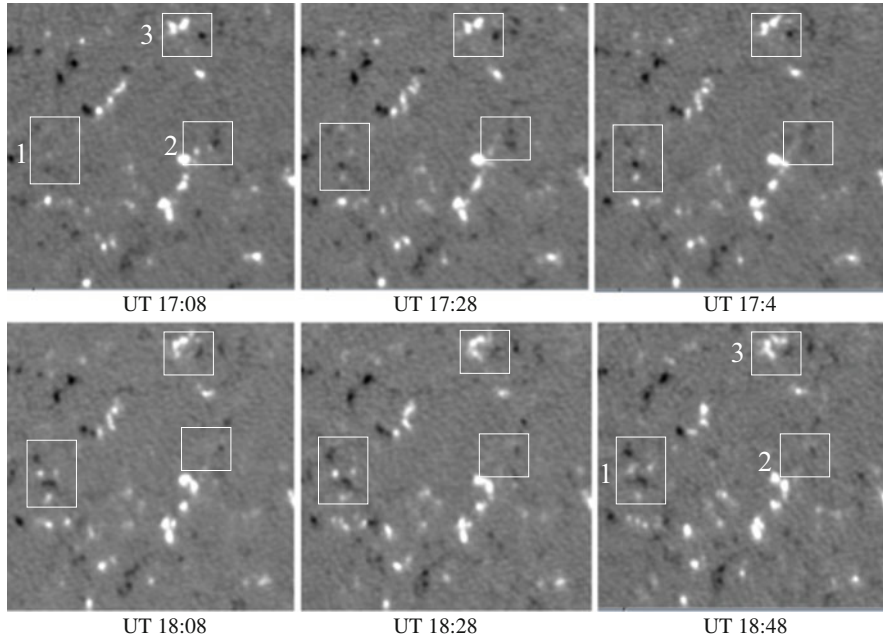


Fig. 12.4 Magnetograms of a quiet sun region taken by the MDI instrument on SOHO at six instances of time with 20-min intervals. Field of view is $90'' \times 90''$. Three most typical events are marked by boxes: the emergence of new magnetic flux (box 1), cancellation of opposite-polarity magnetic elements (box 2), and fragmentation process in the system of one polarity fluxes (box 3)

Region inside the box 3 is dominated by magnetic elements of a single (positive) polarity. It shows a distinct fragmentation which at the given resolution ($\simeq 1.2''$) roughly may be described as two “thick” magnetic concentrations (UT 17:08) breaking eventually into six “thinner” elements (UT 18:28).

Multi-wavelength observations taken simultaneously at different heights of the solar atmosphere reveal a clear connection between dynamic changes in the photospheric magnetic fields and the energetic events in the overlying atmosphere (Harrison et al. 1997; Brekke et al. 1997; Benz 1999; Tarbell et al. 1999). These observations provided the basis for studies of reconnection processes between the photospheric magnetic flux tubes (Tarbell et al. 1999, 2000; Ryutova and Tarbell 2000; Ryutova et al. 2001).

12.2.1 Specifics of Photospheric Reconnections

Brought together by convective or other motions, flux tubes collide and *must* reconnect. The reconnection of photospheric flux tubes proceeds and results in

essentially different effects than that in the coronal plasma. Unlike the low-beta corona where the reconnection process liberates a large amount of energy stored in the magnetic field ($B^2 \gg 8\pi p$) and deposits it “on the spot,” in the photosphere with much smaller magnetic energy than the gas-kinetic energy of environment, the reconnection does not give an immediate gain in the energy. But, it puts the system in strongly nonlinear unsteady state whose further evolution is determined by physical parameters of the post-reconnection products.

The key elements of photospheric reconnection, that, in fact, are absent in low-beta corona, are provided by the specific conditions near the solar surface. The most important of which are following:

1. Photospheric magnetic fields are concentrated in well-defined flux tubes embedded in an almost non-magnetic environment; that is, the plasma beta in the surrounding medium is very large,

$$\beta = \frac{8\pi p_{\text{ext}}}{B_{\text{ext}}^2} \gg 1 \quad (12.6)$$

2. At the same time, because of the pressure equilibrium, the ratio of external gas-dynamic pressure and magnetic pressure inside flux tubes is finite:

$$\beta^* = \frac{8\pi p_{\text{ext}}}{B^2} \geq 1 \quad (12.7)$$

3. Flux tubes are *always* noncollinear, i.e., approaching each other always make some angle.
4. The low atmosphere is sharply stratified.

The first and second conditions ensure that after reconnection, the post-reconnection products that acquire strongly curved shape are kept in dynamic equilibrium by external gas kinetic pressure. Under such conditions, the post-reconnection products behave like elastic bands: straightening and shortening they create a sling-shot effect triggering strongly nonlinear processes in the external plasma.

The third condition, i.e., the fact that photospheric flux tubes are noncollinear, is extremely important: reconnection occurs not only between the opposite-polarity flux tubes but between the same-polarity flux tubes as well.

The fourth condition, strong stratification of low atmosphere, plays a decisive role in development of strongly nonlinear processes. When the kick produced by the sling-shot effect generates acoustic or MHD waves, those waves that propagate upward against gravity quickly steepen and become shocks. Further evolution of shocks leads to a wide class of phenomena that are directly observable higher in the transition region and corona.

Before we consider these phenomena in detail and put in practical use, let us discuss some general properties of flux tube reconnections. Consider first an interaction of two noncollinear flux tubes containing equal magnetic fluxes as shown

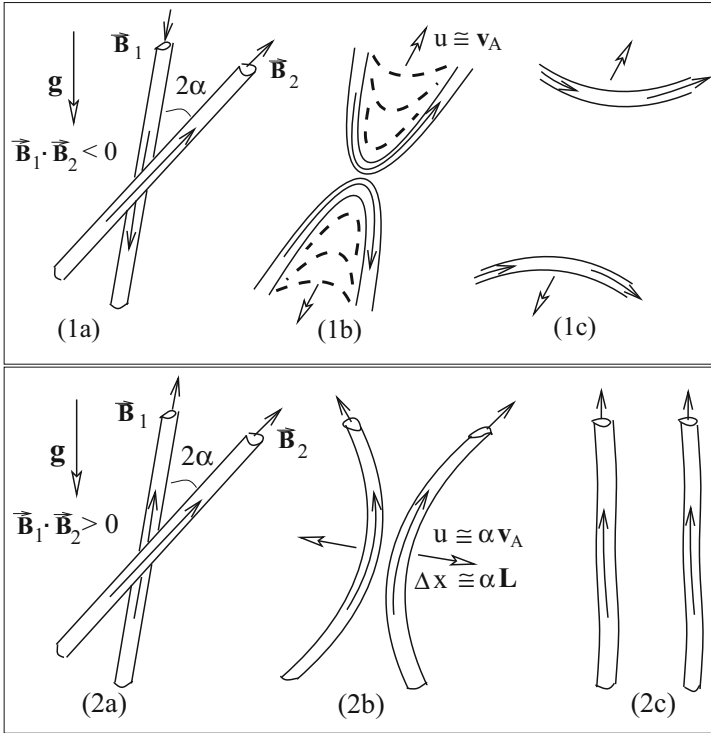


Fig. 12.5 Reconnection of noncollinear flux tubes. Top: opposite-polarity flux tubes; bottom: same-polarity flux tubes. Inside panels: (1a)–(2a) just before the collision; (1b)–(2b) post-reconnection sling-shot effect; (1c)–(2c) the reconnection products in the final moment of action of a restoring magnetic force. Δx in panel 2b is the displacement of the flux tube tip in the time interval between the reconnection and the straightening

in Fig. 12.5. When two slender (noncollinear) flux tubes with magnetic fields \mathbf{B}_1 and \mathbf{B}_2 collide, they overlap only in a short region. Along line of sight, these flux tubes may be seen as opposite polarity elements if they approach each other in such way that the smaller angle, α , is formed between the opposite-polarity ends. If the smaller angle, α , is formed between the same-polarity ends, the observer sees the same-polarity pairs.

Reconnection occurs in both cases creating a sling-shot effect due to the straightening of reconnected flux tubes. Depending on the relative amount of flux and whether the colliding fluxes are the same or opposite polarities, the magnetic reconnection leads to different scenarios of the evolution of post-reconnection products and their observational signatures. In principle, orientation of colliding flux tubes making an angle 2α may be arbitrary. We will assume for convenience that the bisector of the angle 2α is oriented along the line of sight.

Thus, in case of the opposite-polarity flux tubes (Fig. 12.5 top), immediately after reconnection, the new flux tubes are strongly curved. Magnetic tension in

this strongly curved state causes a fast shortening and straightening of post-reconnection flux tubes. The energy release in this process is approximately $W_{\text{magn}} \sim (B^2/8\pi)SL$, where B is the absolute value of the magnetic field strength, S is the cross section of interacting area and L is the effective length of a flux tube participating in the reconnection process.

In case of the same-polarity flux tubes (Fig. 12.5 bottom), the reconnection creates an illusion of scattering of flux tubes. Soon after reconnection, the restoring magnetic force acting on the reconnection products straightens and drags them away from each other. The change of flux tube half-length in this process is proportional to $\delta L \simeq \alpha^2 L$. The magnetic energy content in this process is $\delta W_M \simeq \delta LS(B^2/8\pi) \simeq \alpha^2 LS(B^2/8\pi)$.

The velocity of post-reconnection flux tube motion can be estimated from the released energy: $LS(\rho v^2/2) \simeq \delta W_M$, which gives $v \simeq \alpha v_A$. The time for the flux tube straightening is:

$$\Delta t = \frac{\Delta x}{v} \simeq \frac{\alpha L}{v} \simeq \frac{L}{v_A} \quad (12.8)$$

For the flux tube to participate in the reconnection process over its whole cross section, the characteristic reconnection time should be less than the straightening time. This condition sets the limit on the flux tube radius R_{max} at which the whole flux tube reconnects and behaves as a single elastic band in a sling-shot effect. The maximum rate in the fast reconnection process is estimated as $w_{\text{max}} \simeq v_A/(\ln Re_m)$, where $Re_m = Lv_A/D_m$ is magnetic Reynolds number and D_m is a magnetic diffusivity (Petschek 1964). The reconnection time is, therefore:

$$\tau_{\text{rec}} \simeq \frac{R}{w_{\text{max}}} = \frac{R \ln Re_m}{v_A} \quad (12.9)$$

From (12.8) and (12.9), one gets the estimate for a maximum radius of the flux tube participating in elemental act of reconnection:

$$R_{\text{max}} < \frac{L}{2 \ln Re_m} \quad (12.10)$$

At the photospheric conditions, the Reynolds number is between 10^3 – 10^6 , so that the condition for the flux tube to be thin enough to participate in the reconnection process “as a whole” (i.e., over a whole flux tube radius) is $R_{\text{max}} < L/6$ – $L/13$.

The same estimate is valid for the reconnection between the opposite-polarity elements. In this case, the straightening time is $\simeq L/u$, where the ascending/descending velocity of flux tube $u \simeq v_A$ (see below). If we take the half-length of the flux tube as $L = 500$ km, the estimate for the radius drops into the interval $R_{\text{max}} \sim 36$ – 70 km.

Thus, in either case magnetic flux concentrations having as small radius as 150–200 km may be the sites of multiple reconnection processes. Moreover, the

straightened segments of post-reconnection products may participate further in similar processes, creating a cascade of shocks in case of the opposite polarity pairs, and continuous fragmentation in case of the same-polarity pairs.

12.2.2 Flux Tubes Carrying Different Amount of Magnetic Flux

The fact that under photospheric conditions magnetic flux concentrations having a radius larger than $R_{\max} \sim 36\text{--}70\text{ km}$ may participate in multiple reconnection processes that result in flux tube shredding is totally consistent with the observations (see e.g., Berger and Title 1996). It is important, therefore, to consider the reconnection of flux tubes carrying different amount of magnetic flux and having different radii. We consider the most typical scenarios shown in Figs. 12.6 and 12.7.

Consider first the case shown in Fig. 12.6 depicting the interaction of opposite-polarity flux tubes. Top left: “thick” and “thin” flux tubes reconnect resulting total cancellation of thin flux tube. Bottom left: the initial stage of two “thick” flux tube interaction when they only *partially* cancel each other.

The timescale and energetics of the reconnection and post-reconnection processes are governed mainly by the parameters of the thinner flux tube. From the observational point of view, if a bisector of collision angle is directed along the line of sight, this process corresponds to the apparent cancellation of the smaller magnetic flux and shrinking of the thicker flux tubes. It is accompanied by possible acoustic emission and shock formation caused by the U-shaped part of the reconnection product. The shocks may produce a bright point in overlying chromosphere/transition region.

The four right panels in Fig. 12.6 are the MDI magnetograms of $10'' \times 10''$ area marked by box 2 in Fig. 12.4. Sequence of snapshots at four instances of time show the interaction of mixed polarity elements where partial cancellation of “thick” negative-polarity flux and total cancellation of “thin” positive-polarity flux occurs. One can follow the process of reconnection until almost total disappearance of both fluxes.

Consider now the interaction of same-polarity flux tubes having different parameters. Figure 12.7 is constructed in the same way as Fig. 12.6. Top-left panel shows the interaction of “thick” and “thin” flux tubes which results in splitting of the thicker flux tube, while the reconnection products move away from the remnants of the thicker flux tube. Thus, the observer should see three dynamic objects instead of initial two.

Bottom-left panel shows the interaction of two “thick” flux tubes. In its initial stage, this event is a fragmentation process. Next, the new-born fragments, accelerated by the sling-shot effect, will inevitably hit other magnetic flux tubes. In any case, the process of apparent cancellation (the opposite-polarity fluxes) or fragmentation and scattering (the same-polarity fluxes) will repeatedly take place down to the smallest possible scales until the magnetic flux disappears diffusively.

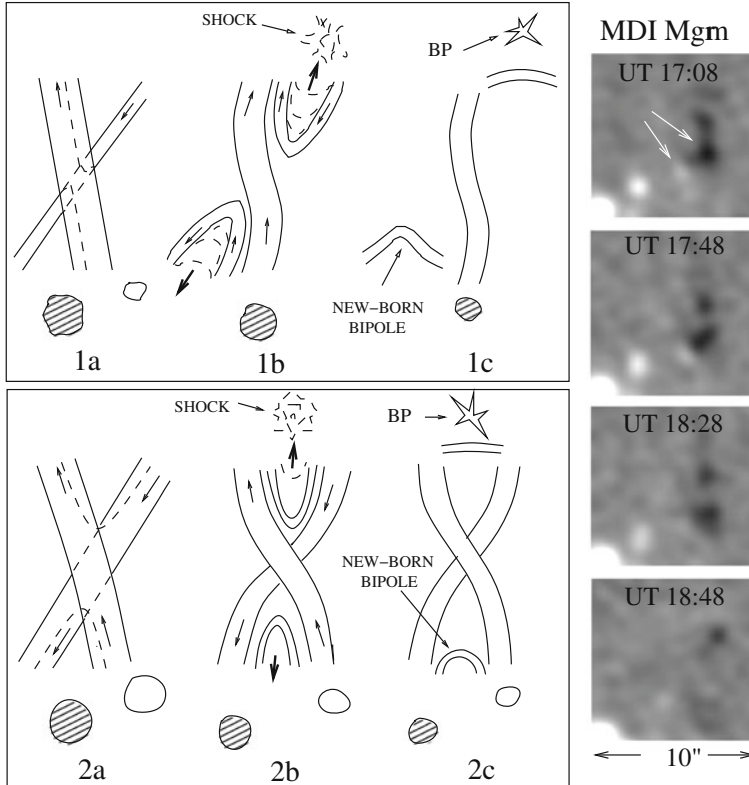


Fig. 12.6 Reconnection of opposite-polarity flux tubes carrying different amount of magnetic flux. Top left: opposite-polarity “thick” and “thin” (elementary) magnetic flux tubes showing total cancellation of thin and partial cancellation of thick flux; bottom left: partial cancellation in the collision of thick flux tubes; right panels give an observational example; the MDI magnetograms of $10'' \times 10''$ area at four instances of time show the interaction of “thick” negative (black) polarity flux and total cancellation of “thin” positive (white) polarity flux. After Ryutova et al. (2003)

Observational example of the interaction of the same-polarity thick flux tubes is shown in right panels in Fig. 12.7. The $10'' \times 10''$ area (box 3 in Fig. 12.4) initially contained two large positive flux tubes that approached each other. Subsequently, flux tubes experience multiple reconnections ending up with whole string of smaller flux tubes.

A simple general conclusion here is that the most pronounced effects in the regions of mixed polarity are partial or total cancellation of magnetic fluxes and frequent appearance of photospheric and chromospheric bright points, while in the regions dominated by a single polarity the most typical event is fragmentation of neighboring fluxes into smaller elements and an illusion of a scattering process.

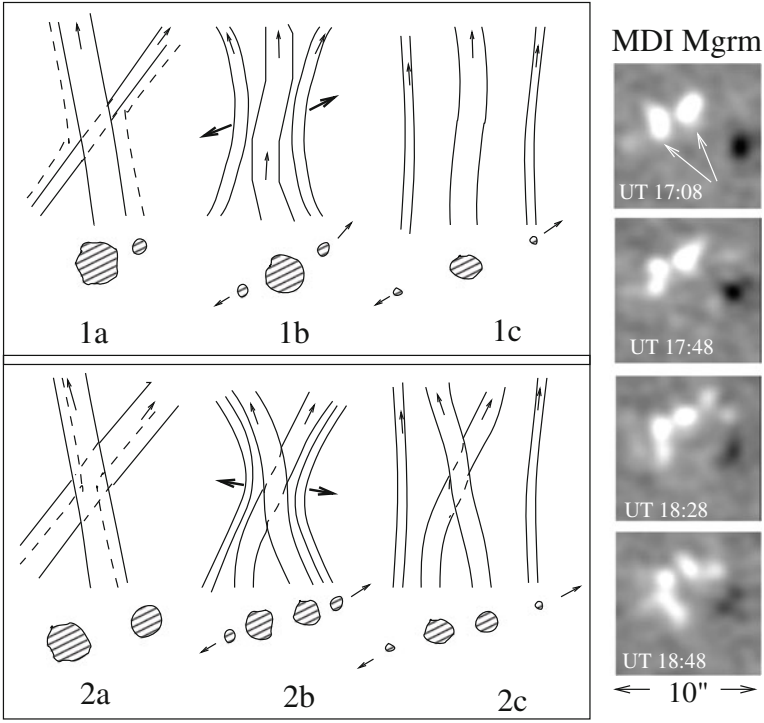


Fig. 12.7 The same as in Fig. 12.6 but now the reconnection occurs between the same-polarity flux tubes. See text for details

12.2.3 Number of Events: Importance of Noncollinearity of Flux Tubes

The frequency of events shown in Figs. 12.5, 12.6, and 12.7 depends on the magnetic filling factor of a given area and the velocity of surface motions, u . Let us denote the characteristic distance between two neighboring flux tubes at the surface by l , and the characteristic flux tube radius by R . Obviously, the number of flux tubes intersecting the unit area, σ , is $\sigma \sim 1/l^2$. The filling factor is $f \sim R^2\sigma \simeq R^2/l^2$, and for the quiet Sun $f \ll 1$.

Let us evaluate the number of collisions, n , per unit time, experienced by a particular flux tube, in both cases, collinear flux tubes and noncollinear flux tubes with the degree of noncollinearity ~ 1 .

In the first case, the collision rate n_{\parallel} can be estimated analogously to the estimate of gas-kinetic theory:

$$n_{\parallel} \simeq R\sigma u \tag{12.11}$$

Note that in case of collinear flux tubes two of them merge together if they come to a distance comparable with flux tube radius over the whole length of the flux tube. For any particular flux tube, the number of such events per unit time is estimated by (12.11). One can see that in the case of collinear fluxes n_{\parallel} scales as σ .

In the case of noncollinear flux tubes, the collision rate does not explicitly depend on the radius of flux tube, R , because two noncollinear flux tubes inevitably intersect even at $R \Rightarrow 0$. Therefore, $n_{\Psi} \simeq (u/l) \simeq u\sqrt{\sigma}$. The ratio of number of events in the case of noncollinear and collinear flux tubes is, thus, $n_{\Psi}/n_{\parallel} \simeq (1/R\sqrt{\sigma}) \gg 1$. So, in the case of noncollinear flux concentrations, the frequency of collisions is much higher than in the collinear case.

The total number of collisions occurring per unit area is given by:

$$N_{\Psi} = n_{\Psi}\sigma \simeq u\sigma^{3/2} \quad (12.12)$$

Since the filling factor is $f \simeq R^2\sigma$, the number of events *per unit time* occurring with every particular flux concentration, n_t equals to n_{Ψ} , that is: $n_t = u\sqrt{\sigma}$. To estimate the number of particular events, we need to introduce a probability of the “proper” geometry of the collision, ν . Then, the number of particular events N_{ν} per unit area of the solar surface is $N_{\nu} = \nu u\sigma^{3/2}$. In fact, no flux tube seems to be left without colliding with its neighbor.

The outcome of flux tube interaction, depending on the specifics of the process, produces its own impact on the overlying atmosphere. It is therefore not surprising that at any height (and temperatures), the solar atmosphere mimics the pattern of small-scale elements in the photosphere. Before we discuss details of the response of the atmosphere to reconnection events among the ensembles of small-scale magnetic fields (which will be done in the next chapters), it is useful to investigate the dynamics of post-reconnection product immediately after reconnection occurs.

12.3 Dynamics of Post-reconnection Products

Here, we consider the dynamics of a flux tube motion after the reconnection has occurred, starting from the configuration shown in Fig. 12.8. We assume that the flux tube radius R is small compared to the other dimensions of the problem, in particular, the characteristic length L of the flux tube involved in the post-reconnection motion. The upper points of the flux tube merging the asymptotes of magnetic field lines at $B \rightarrow B_{\infty}$ are supposed to remain at rest.

In the further discussions, to reduce the number of parameters entering the problem, we assume that the flux tube is empty, i.e., the pressure of the ambient plasma is counterbalanced by the magnetic pressure inside the tube, $p_e = B^2/8\pi$. In other words, we assume that the internal plasma beta is very small, $\beta_i = 8\pi p_i/B^2 \ll 1$. This approach is quite reasonable for regions close to surface (Sánchez Almeida 2001).

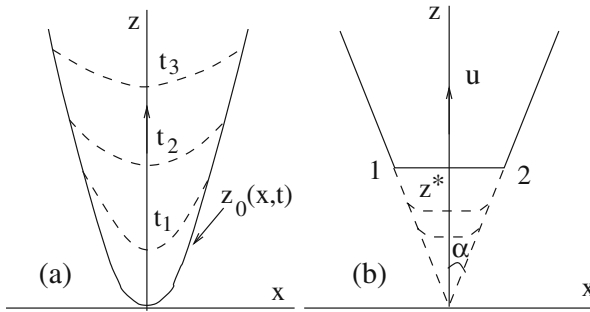


Fig. 12.8 The shape of magnetic field lines, $z(x, t)$. (a) Solid line, $z_0(x, t)$ —just after reconnection; the dashed lines—time sequence of the straightening and shortening of the flux tube due to the action of the magnetic field tension. (b) Simplified shape of the reconnection product

We describe the shape of the flux tube by a curve $z = z_0(x, t)$ (sketched in Fig. 12.8). After reconnection occurs, the magnetic tension inside the flux tube tends to straighten it and the initial configuration begins to evolve along a sequence of states $1 \rightarrow 2 \rightarrow 3 \dots$

In the case of an empty flux tube, the inertia is determined by the added-mass effect, i.e., by the inertia of the external fluid that gets involved into the motion as soon as the flux tube begins to move (Ryutov and Ryutova 1976).

At large Reynolds numbers typical even for solar photosphere, the is relatively small at sub-sonic motions of the flux tube. Per unit length of the flux tube, it can be evaluated as (Parker 1979):

$$F_{\text{drag}} = C_D \rho u^2 2R \tag{12.13}$$

where C_D is a dimensionless drag coefficient, which, in the parameter domain $Re \geq 10^3$, $u < c_s$, is $\simeq 0.1\text{--}0.2$. When u exceeds the sound speed, c_s , a bow shock is formed in front of the flux tube, and a friction force increases abruptly. For a flow with $u \simeq 2c_s$, C_D becomes of the order of unity (Landau and Lifshitz 1987). We approximate it by the step function. When evaluating the friction force for transsonic motions of the flux tube, we discuss constraints imposed by this approximation.

12.3.1 Self-similarity of Solution

In this section, we consider the dynamics of post-reconnection flux tube in absence of gravity, assuming that the scale L satisfies the condition:

$$\rho g L < \frac{B^2}{8\pi} \tag{12.14}$$

This is equivalent to the condition of L being smaller than the scale height, $L < \Lambda$, which is usually satisfied in upper layers of atmosphere.

The case without the effects of gravity is directly applicable to the flux tube dynamics when the reconnection occurs between the same-polarity magnetic elements and reconnection products move across the gravity force (Fig. 12.7). In this case, the magnetic tension is almost perpendicular to the gravitational acceleration and gravity does not play a role. Therefore, the xz plane of Fig. 12.8 should not necessarily be perceived as a vertical plane. Besides, the non-gravity situation is also valid for upper layers of atmosphere where the atmospheric stratification strongly weakens.

We begin the analysis with an incompressible case. In other words, we assume that the velocity of a flux tube is much less than c_s , and the drag force may be neglected. The other forces acting on a certain small segment of the flux tube are the magnetic tension acting through the ends of the segment, and the gas pressure acting through the side surface. Simple calculations give the following expression for the net force acting on a curved segment of the flux tube (per unit length):

$$F_{\text{net}} = \frac{B^2}{4\pi} \frac{\pi R^2}{r} \quad (12.15)$$

where r is the curvature radius. Note that there are two degrees of freedom in the problem: the minor radius of the flux tube, R , and the major radius of curvature, r . With respect to R the flux tube is in equilibrium, while with respect to r the flux tube is straightening. Let the shape of the flux tube be described by $z = z_0(x, t)$.

Consider a shape of the flux tube at the time $t + \Delta t$. Let ξ be a normal displacement of a certain point to its new position. Obviously, $(\partial z_0 / \partial t) = (1/n_z)(\partial \xi / \partial t)$, where n_z is a z -projection of a unit vector normal to the tube: $n_z = [1 + (\partial z_0 / \partial x)^2]^{-1/2}$. Therefore,

$$\frac{\partial \xi}{\partial t} = \frac{\partial z_0}{\partial t} [1 + (\partial z_0 / \partial x)^2]^{-1/2} \quad (12.16)$$

We take the second derivative of ξ over the time and multiply it by the added mass per unit length, which in the case of a cylinder is $\pi R^2 \rho$. Equating this to the normal component of the force acting on a certain segment of the flux tube, we obtain

$$\pi R^2 \rho \frac{\partial}{\partial t} \left(\frac{\partial z_0}{\partial t} [1 + (\partial z_0 / \partial x)^2]^{-1/2} \right) = F \quad (12.17)$$

According to (12.15),

$$\rho \frac{\partial}{\partial t} \left(\frac{\partial z_0}{\partial t} [1 + (\partial z_0 / \partial x)^2]^{-1/2} \right) = \frac{B^2}{4\pi} \frac{1}{r} \quad (12.18)$$

From the equations of differential geometry for the radius of curvature, r , we have

$$\frac{1}{r} = \frac{\partial^2 z_0}{\partial x^2} \left[1 + (\partial z_0 / \partial x)^2 \right]^{-3/2} \quad (12.19)$$

and the equation of motion of the flux tube acquires the form:

$$\frac{\partial}{\partial t} \left(\frac{\partial z_0}{\partial t} \left[1 + (\partial z_0 / \partial x)^2 \right]^{-1/2} \right) = v_A^2 \frac{\partial^2 z_0}{\partial x^2} \left[1 + (\partial z_0 / \partial x)^2 \right]^{-3/2} \quad (12.20)$$

One can see that the parameter R does not enter the problem and (12.20) looks like the equation for an infinitesimally thin “string.” Note that, in the limit of small curvature, (12.20) coincides with the linear equation of motion for magnetic flux tube (Ryutov and Ryutova 1976; Spruit 1981).

We present a solution where after reconnection the flux tubes arms are asymptotically straight lines. Hence, there is no parameter of the dimension of the length in the system and the solution can depend on the variable z only in the combination $\beta = x/v_A t$. This solution is *self-similar*. Moreover, it corresponds to a motion with a constant velocity. We can check this property by presenting z_0 in the form: $z_0 = v_A t f(\beta)$. For space and time derivatives, we have

$$\frac{\partial z_0}{\partial t} = -v_A \beta^2 \frac{d}{d\beta} \left(\frac{f}{\beta} \right); \quad \frac{\partial z_0}{\partial x} = \frac{df}{d\beta}, \quad (12.21)$$

and similarly for the higher-order derivatives. With these, (12.20) acquires the form of an ordinary differential equation for $f(\beta)$:

$$\beta \frac{d}{d\beta} \left\{ \beta^2 \frac{d}{d\beta} \left(\frac{f}{\beta} \right) \left[1 + (df/d\beta)^2 \right]^{-1/2} \right\} = \frac{d^2 f}{d\beta^2} \left[1 + (df/d\beta)^2 \right]^{-3/2} \quad (12.22)$$

Thus, the self-similar solution does exist. Taking derivatives, we find

$$f_{\beta\beta} [\beta f_{\beta} f + \beta^2 - 1] = 0 \quad (12.23)$$

The motion described by this equation is an ascent with a constant velocity. Note that a constant velocity motion corresponds to a zero inertial force, and, therefore, to a zero magnetic tension. This means that the part of the flux tube involved in the motion should be a straight line, i.e., the flux tube has the shape shown in Fig. 12.8b.

The presence of the multiplier $f_{\beta\beta}$ in (12.23) means that the evolving flux tube consists of straight segments for which $f_{\beta\beta} = 0$. The initially resting material begins an ascending motion near the points 1 and 2 (Fig. 12.8b), where the magnetic curvature is large. We do not resolve this region in the asymptotic solution, but realistic velocity u of ascending flux tube can be found using energy analysis.

12.3.2 Energy Analysis

We start with the energy conservation law:

$$W_{\text{kin}} = -\Delta W_{\text{pot}} \quad (12.24)$$

where ΔW_{pot} is the change in potential energy. The kinetic energy for the segment 1–2 (Fig. 12.8b) is:

$$W_{\text{kin}} = 2z^* \tan\alpha \frac{\rho u^2}{2} S \quad (12.25)$$

The change in potential energy consists of the change in the magnetic energy plus the $p dV$ work associated with the change of flux tube volume. If gravity is neglected, the external pressure is constant and, therefore, due to pressure equilibrium, the magnetic field is also constant, leading to:

$$\Delta W_{\text{pot}} = \left(2z^* \tan\alpha - \frac{2z^*}{\cos\alpha} \right) \frac{B^2}{4\pi} S \quad (12.26)$$

Where we have used the fact that the $p dV$ work, according to the analysis related to (12.15), is equal to the release of the magnetic energy. From (12.24)–(12.26), one finds

$$u = v_A \sqrt{2(1 - \sin\alpha)/\sin\alpha} \quad (12.27)$$

The model neglecting dissipation is good for sub-sonic velocities u . From the pressure balance, $p_e = B^2/8\pi$, and the expression for sound speed, $c_s^2 = \gamma p/\rho$, the condition for the sub-sonic motion of flux tubes is

$$\sin\alpha > 4/(4 + \gamma) \quad (12.28)$$

which for $\gamma = 5/3$ gives $\alpha \geq 45^\circ$. Hence, for a wide range of angles $\leq 45^\circ$, the motion of flux tube may be trans- and super-sonic which we discuss in the next section.

12.3.3 Transsonic Motion

At smaller intersection angles ($\leq 45^\circ$), the segment 1–2 (Fig. 12.8b) reaches the sound speed and the drag caused by the formation of a bow shock enters the problem. We first evaluate the drag force for the case where the velocity u exceeds the sound speed by the order of unity.

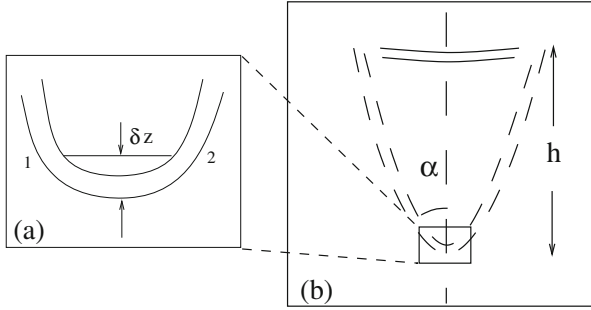


Fig. 12.9 A straightening flux tube: (a) moving segment of flux tube with finite curvature; (b) sketch for the estimate of a total energy release

From (12.13), we find that the drag force F_{drag}^* acting on the segment 1–2 is approximately (for $\alpha \simeq 1$) $F_{\text{drag}}^* \simeq 2R\pi\rho c_s^2 z^*$. On the other hand, the lifting force produced by the magnetic tension is $F_{\text{magn}} \simeq 2\pi R^2(B^2/4\pi)$. Taking the ratio, one finds: $(F_{\text{magn}}/F_{\text{drag}}^*) \simeq (R/z^*)$. For $z^* \gg R$, the magnetic force is much less than the drag force. This will restrict the upward velocity to values only slightly above the sound speed and the drag coefficient, C_D in (12.13) becomes much less than unity ($\simeq R/z^*$). Note that a step-wise approximation of the friction force as used above does not allow one to find a complete solution in the domain of velocities of about $(2/3)c_s \leq u \leq c_s$, where a transition from small values of C_D to $C_D \simeq 1$ occurs.

If friction is present, the flux tube will have a finite curvature at the segment 1–2. This deviation from a straight line gives only a second-order (in δz) correction to the length of a segment 1–2 and, in the evaluation of the energy release W_{therm} , we will assume that the segment 1–2 is straight (Fig. 12.9). From the balance equation:

$$W_{\text{therm}} = -\Delta W_{\text{pot}} - W_{\text{kin}}, \tag{12.29}$$

after substituting $u = c_s$ into (12.25) and (12.29), we have

$$W_{\text{therm}} = S \frac{\rho c_s^2}{2} 2z^* \frac{4 - (\gamma + 4)\sin\alpha}{\gamma \cos\alpha} \tag{12.30}$$

Here, we must assume that $\sin\alpha < 4/(4 + \gamma)$ (otherwise, the motion is sub-sonic). When the flux tube finally straightens out (Fig. 12.5b), the energy released per unit length of the final state is

$$\tilde{W} = \frac{\Delta W_{\text{pot}}}{2htan\alpha} = S \frac{B^2}{4\pi} \frac{1 - \sin\alpha}{\sin\alpha} \tag{12.31}$$

At small α 's, the energy release diverges, indicating the significance of a sling-shot effect for almost antiparallel flux tubes.

12.4 Dynamics of U-Shaped Flux Tubes

Consider now the motion of post-reconnection flux tubes in the presence of gravity. For simplicity, we adopt an isothermal model, $\rho = \rho_0 \exp(-z/\Lambda)$, with a constant scale height, $\Lambda = p/\rho g$. The subscript “0” refers to the region where intersection of flux tubes occurred.

The pressure balance condition in the initial state is

$$\frac{B^2}{8\pi} = p_0 \exp(-z/\Lambda) \quad (12.32)$$

From (12.32) and the magnetic flux conservation, $B_0 S_0 = BS$, we find the initial magnetic energy of a flux tube, W_{mag}^0 :

$$W_{\text{mag}}^0 = \frac{2}{\cos\alpha} \int_0^h \frac{B^2}{8\pi} S dz \quad (12.33)$$

or,

$$W_{\text{mag}}^0 = \frac{1}{\cos\alpha} \frac{B_0^2 S_0}{4\pi} 2\Lambda (1 - \exp(-h/2\Lambda)) \quad (12.34)$$

The final magnetic energy is

$$W_{\text{mag}}^f = 2h \tan\alpha \frac{B^2}{8\pi} S = 2h \tan\alpha \frac{B_0^2}{8\pi} S_0 \exp(-h/2\Lambda), \quad (12.35)$$

and the change of the magnetic energy, $\Delta W_{\text{mag}} \equiv W_{\text{mag}}^f - W_{\text{mag}}^0$, is:

$$\Delta W_{\text{mag}} = -\frac{B_0^2 S_0 \Lambda}{2\pi \cos\alpha} \exp(-h/2\Lambda) \left[\exp(h/2\Lambda) - 1 - \frac{h}{2\Lambda} \sin\alpha \right] < 0 \quad (12.36)$$

Now, we evaluate the work of the gravity force over the ascending (straight) segment of the flux tube. At some height z above the reconnection point, the length of the segment is $2z \tan\alpha$, and its cross section is $S = S_0 \exp(z/2\Lambda)$, so that the gravity force acting upward is:

$$F_{gr} = 2\rho g S_0 z \exp(z/2\Lambda) \tan\alpha \equiv 2\rho_0 g S_0 z \exp(-z/2\Lambda) \tan\alpha \quad (12.37)$$

Accordingly, the change of the gravitational energy between the final and initial state is negative, $\Delta W_{\text{gr}} = -\int_0^h F_{gr} dz$:

$$\Delta W_{\text{gr}} = \frac{\Lambda S_0 B_0^2}{\pi \exp(h/2\Lambda)} \tan\alpha \left[1 + \frac{h}{2\Lambda} - \exp(h/2\Lambda) \right] < 0 \quad (12.38)$$

We used here the pressure equilibrium condition. In addition to the variation of the magnetic energy, ΔW_{mg} , the pdV work makes an equal contribution to the total variation of a potential energy of the system, that is:

$$\Delta W_{\text{pot}} = 2\Delta W_{\text{mg}} + \Delta W_{\text{gr}} \quad (12.39)$$

The kinetic energy of the flux tube in the final state can be found from the energy conservation law:

$$W_{\text{kin}} = -\Delta W_{\text{pot}} \quad (12.40)$$

Collecting (12.36)–(12.40), we find

$$W_{\text{kin}} = \frac{S_0 B_0^2}{4\pi \cos\alpha} \exp(-h/2\Lambda) [4\Lambda(1 + \sin\alpha)(\exp(h/2\Lambda) - 1) - 4h\sin\alpha] \quad (12.41)$$

The kinetic energy of the fluid in the final state is (12.25), with $z^* = h$, $\rho = \rho_0 \exp(-h/\Lambda)$ and $S = S_0 \exp(h/2\Lambda)$ we have

$$W_{\text{kin}}^f = 2htan\alpha \frac{\rho_0 u^2}{2} S_0 \exp(-h/2\Lambda) \quad (12.42)$$

From (12.41) and (12.42), one finds the velocity of a tip at the moment when U-shaped tube gets straightened:

$$u^{(f)} = v_A \sqrt{2 \frac{(\exp(h/2\Lambda) - 1)(1 + \sin\alpha) - 2(h/2\Lambda)\sin\alpha}{(h/2\Lambda)\sin\alpha}} \quad (12.43)$$

In the limit where gravity may be neglected, i.e., at $\Lambda \rightarrow \infty$, this expression naturally coincides with (12.27).

When the velocity of flux tube exceeds the sound speed, a bow shock is formed in front of ascending segment of flux tube. At the same time, the velocity of the flux tube still increases which leads to an increase of the friction force and thus to dissipation of energy. This keeps the final velocity of the flux tube close to c_s , and the excess of the potential energy will be spent on plasma heating. The threshold for sub-/transsonic motion, unlike the simplified estimate (12.28) for “empty” flux tube, now depends on the height where the reconnection occurs.

Using (12.43), we can roughly estimate the height where transsonic motions set in. In Fig. 12.10, the plots of the ascending velocity (actually the Mach number) vs the normalized height are shown for an “empty” flux tube, i.e., in virtue of pressure

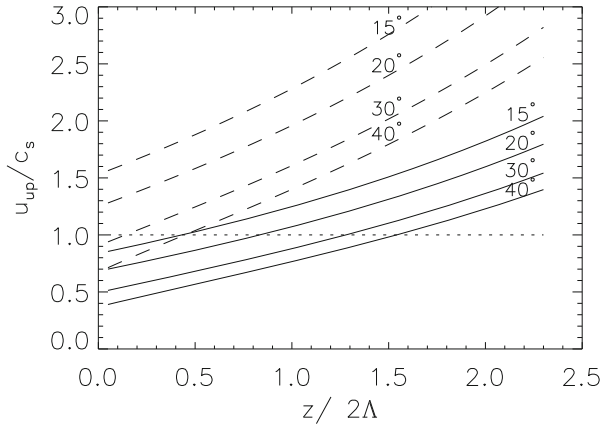


Fig. 12.10 The velocity of the ascending portion of a flux tube as a function of height for several angles of collision; solid lines correspond to the ratio $v_A/c_s = 0.35$, and dashed lines to $v_A/c_s = 0.64$. The dotted line shows the $M = 1$ level

equilibrium condition. Several qualitative conclusions can be drawn here. A smaller collision angle results in faster upward motion of flux tubes, so that its motion becomes transsonic at lower altitudes. At very small angles of collision (almost antiparallel flux tube), the reconnection process leads mainly to the conversion of magnetic energy into thermal energy in the immediate vicinity of the collision region.

With increasing angle of collision, the shock formation and the dissipation of the energy occurs at higher altitudes. As the initial velocity of a tip is proportional to Alfvén velocity, the stronger is the magnetic field the higher are the regions of the shock formation (the dashed lines in Fig. 12.10).

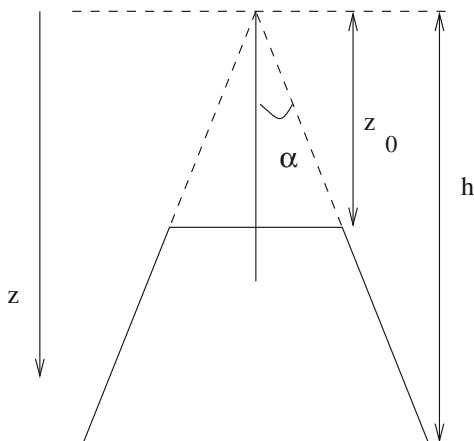
12.5 Dynamics of \cap -Shaped Flux Tube

Here, we consider the motion of the lower, \cap -shaped part of flux tube formed after reconnection. If the magnetic field is strong enough, the \cap -shaped part of the reconnection product starts moving in the downward direction against the gravity force. We again use the piece-wise model of the flux tube (Fig. 12.11), and perform an energy analysis to find the character of the motion of flux tube and its velocity.

The gravitational energy increase caused by the deformation of flux tube shown in Fig. 12.11, similarly to (12.37) and (12.38), is

$$\Delta W_{\text{gr}} = -8\Lambda S_0 \frac{B^2}{8\pi} \tan\alpha \left[\exp\left(\frac{z_0}{2\Lambda}\right) - \frac{z_0}{2\Lambda} \exp\left(\frac{z_0}{2\Lambda}\right) - 1 \right] \quad (12.44)$$

Fig. 12.11 Sketch for the motion of the \cap -shaped part of the reconnection product



Integration has been carried here downward from the point of reconnection. In the downward motion of a curved flux tube (forced by sling-shot effect), the change of potential energy is positive as the final state has higher gravitational energy. The change of the magnetic energy, plus pdV work, is $2\Delta W_{mg}$:

$$2\Delta W_{mg} = -\frac{B_0^2 S_0}{\pi \cos\alpha} \left[\exp\left(\frac{z_0}{2\Lambda}\right) - 1 - \frac{z_0}{2\Lambda} \exp\left(\frac{z_0}{2\Lambda}\right) \sin\alpha \right] \tag{12.45}$$

It is remarkable that the function:

$$\Delta W_{pot} = \Delta W_{gr} + 2\Delta W_{mg} \tag{12.46}$$

may have a minimum at some height z^* less than h . The flux tube will then evolve to reach an equilibrium state in which the buoyancy force is balanced by the magnetic tension.

Note that immediately after reconnection the top of the \cap -shaped flux tube will always move downward, because of a high curvature the magnetic tension acting on the tip is universally dominant over the buoyancy force. Besides, the gravitational energy variation scales as z^2 , whereas the magnetic energy variation scales as z , which can be easily verified by expansion of (12.44) and (12.45) with respect to $z_0/2\Lambda$. Therefore, magnetic energy is always dominant at the beginning.

There are a variety of possibilities for how the flux tube reaches equilibrium state depending on physical parameters of a system and, in particular, on the angle α .

For example, the flux tube may reach an equilibrium state with sub-sonic motion. Then, because of inertia, it overshoots the equilibrium state and oscillates around it, gradually dissipating the energy. The repercussions of these oscillations may be visible as periodic bright transients on the solar surface. Figure 12.12 shows plots of the potential energy vs height for different angles of collision. The energy is normalized by the factor $8\Lambda S_0(B^2/8\pi)$ and the height by 2Λ .

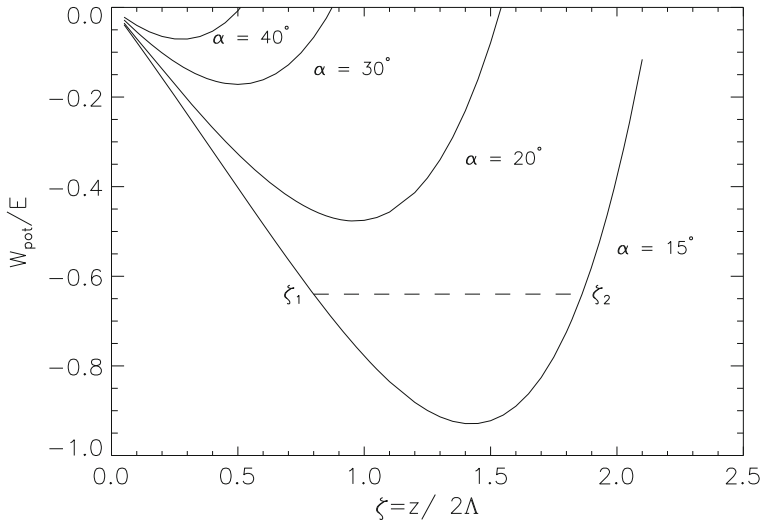


Fig. 12.12 A plot of the potential energy normalized by the factor $8\Lambda S_0(B^2/8\pi)$ vs height for different angles of collision. The dashed line shows the energy level where oscillation periods are estimated (see text for details)

At smaller half-angles, $\alpha = 15^\circ, 20^\circ$, the potential well is deep enough for the flux tube to oscillate about some equilibrium height, gradually dissipating its energy. The period of the oscillations can be found through the velocity of downward motion, $u(z)$:

$$T = \oint \frac{dz}{u(z)} \tag{12.47}$$

The velocity of downward motion, on the other hand, can be derived from the energy conservation law $W_{kin}^{seg} = -\Delta W_{pot}$, where now the kinetic energy of a segment is is

$$W_{kin}^{seg} = 2z \tan \alpha \frac{\rho_0 u^2}{2} S_0 \exp\left(\frac{z}{2\Lambda}\right) \tag{12.48}$$

and,

$$\Delta W_{pot} = \frac{B^2}{\pi} \frac{\Lambda S_0}{\cos \alpha} \left[(1 + \sin \alpha) \left(1 - \exp\left(\frac{z}{2\Lambda}\right) \right) - \frac{z}{\Lambda} \sin \alpha \exp\left(\frac{z}{2\Lambda}\right) \right] \tag{12.49}$$

Finally, for the velocity of the downward motion, we obtain

$$u = v_A \sqrt{2 \frac{(1 + \sin \alpha)(1 - e^{-\zeta}) - 2\zeta \sin \alpha}{\zeta \sin \alpha}} \tag{12.50}$$

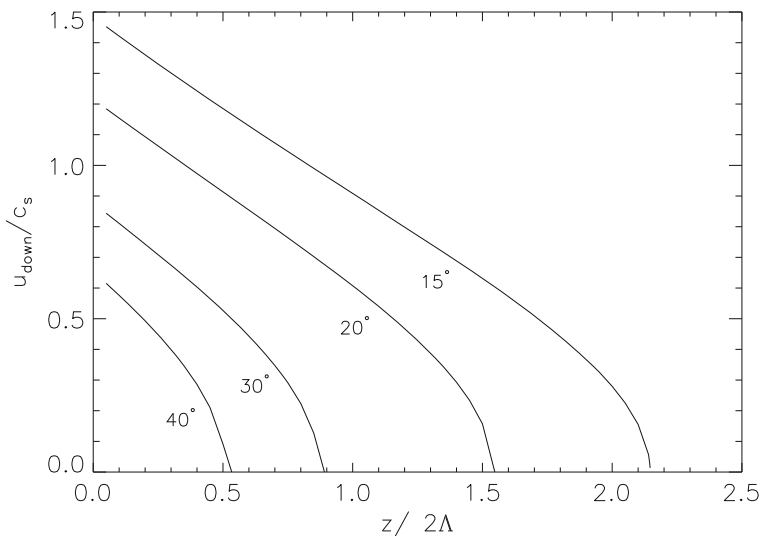


Fig. 12.13 The velocity of downward motion of the apex of a \cap -shaped part of a flux tube as a function of depth (measured from the reconnection point)

In the limit of $\zeta = (z/2\Lambda) \rightarrow 0$, i.e., $\Lambda \rightarrow \infty$, this expression, just like (12.43) for the upward motion, coincides with expression (12.27) for unstratified media.

From observational point of view, this analysis is very useful because allows direct measurements of some parameters and, in particular, the velocities. Figure 12.13 shows plots of the velocity of downward motion of the flux tube normalized by the atmospheric sound speed. One must bear in mind that these velocities are sub-sonic.

If immediately after reconnection the downward motion is supersonic (see velocity plots for $\alpha = 15^\circ, 20^\circ$, in Fig. 12.13), the energy of the flux tube is converted quickly into thermal energy. At some height, when its motion slows down to sub-sonic velocity, the flux tube approaches equilibrium in the oscillatory regime. Thus, at sufficiently small angles of collision, a sling-shot effect produced by the \cap -shaped part of flux tubes results in a multi-step process of energy release. Initially, the straightening flux tube pushes surrounding plasma to move with the transsonic velocity leading to local heating. Then, the flux tube oscillates gradually releasing its energy.

At larger collision angles and/or weaker magnetic field, the oscillatory regime is reached without a preliminary heating of surrounding plasma.

Finally, with increasing angle of collision (e.g., at half-angle $\alpha = 40^\circ$), the potential well becomes so shallow that buoyancy quickly overcomes the magnetic force and the flux tube stops its downward motion and reaches equilibrium. Note that in all cases described above, the equilibrium is a priori marginal: any fluctuations in the medium will trigger the *upward* motion of flux under the action the buoyancy, and possible appearance of a next-generation bipole.

Consider a quantitative example of flux tubes colliding, say at half-angle $\alpha = 15^\circ$. Immediately after collision, a flux tube moves with transsonic velocity. This motion is accompanied by an energy release estimated from the difference between the potential energy (12.49) and the kinetic energy of the flux tube at height z^* where the velocity of the flux tube becomes equal to sound speed:

$$W_{\text{therm}} = -\Delta W_{\text{pot}}(z^*) - 2z^* \tan \alpha \frac{\rho c_s^2}{2} S_0 \exp\left(\frac{z^*}{2\Lambda}\right) \quad (12.51)$$

For $\alpha = 15^\circ$, $z^* \simeq 1.6 \Lambda$. This corresponds to an energy level $W_{\text{pot}}/E = -0.64$ (Fig. 12.12, dashed line). At this level, the flux tube will oscillate in the interval $z_1 - z_2 = 1.6 \Lambda - 3.72 \Lambda$.

The oscillation period is easily estimated. Using (12.47) and (12.50), we have

$$T = \frac{2\Lambda}{v_A} \int_{\zeta_1}^{\zeta_2} \frac{\zeta \sin \alpha \, d\zeta}{(1 + \sin \alpha)(1 - e^{-\zeta}) - 2\zeta \sin \alpha} \equiv \frac{4\Lambda}{v_A} I \quad (12.52)$$

where I is the integral:

$$I = \frac{1}{2} \int_{\zeta_1}^{\zeta_2} \frac{\zeta \sin \alpha \, d\zeta}{(1 + \sin \alpha)(1 - e^{-\zeta}) - 2\zeta \sin \alpha} \quad (12.53)$$

For this example with end points $\zeta_1=0.8$ and $\zeta_2 = 1.86$, numerical integration gives $I = 0.98$. Assuming a collision close to the surface, we take $\rho = 2.7 \cdot 10^{-7} \text{ g cm}^{-3}$ and scale height $\Lambda = 150 \text{ km}$ (Maltby et al. 1986). The Alfvén velocities for magnetic field values $B = 300, 500, \text{ and } 1000 \text{ G}$ are $v_A = 1.6, 2.7, \text{ and } 5.4 \text{ km s}^{-1}$, respectively. Periods of oscillation are, respectively, $T \simeq 5.2, 3.1, \text{ and } 1.6 \text{ min}$.

Note again that if the velocity of flux tube reaches the acoustic velocity, the dissipation rate becomes large, and the flux tube will approach the equilibrium state in an essentially aperiodic fashion. Acoustic waves will be generated running in front of the flux tube, but they will not be enhanced to strong shocks because the density grows in the direction of their propagation. Eventually, all the potential energy is converted to thermal energy of plasma. The loss of energy in the case of transsonic motion will make the oscillatory regime possible again.

With high-resolution and high-cadence data, all the processes described in Sects. 12.3–12.5 are, in principle, directly observable. Simple analytical relations can be used for developing the diagnostic tools.

12.6 Problems

12.1 Estimate the rate of energy flux produced in the upper atmosphere by the reconnection of flux tubes, assuming that in the photosphere flux tubes, randomly distributed within supergranular cells, are carried out to the network and reconnect there with elements of opposite polarity.

12.2 Compare the speed and efficiency of the Sweet–Parker and Petschek reconnection models under the chromospheric conditions.

References

- W.I. Axford, in *Magnetic Reconnection in Space and Laboratory Plasmas*, ed. by E.W. Hones Jr., Geophysical Monograph Series, vol. 30 (AGU, Washington, 1984), pp. 1–8
- A.O. Benz, S. Krucker, *Astron. Astrophys.* **341**, 286 (1999)
- T. Berger, *A. Title ApJ* **463**, 365 (1996)
- D. Biskamp, *Phys. Fluids* **29**, 1520 (1986)
- P. Brekke, D.M. Hassler, K. Wilhelm, *Solar Phys.* **175**, 349 (1997)
- V. Bumba, *Publ. Crim. Ap. Obs.* **19**, 105, (1958)
- J.W. Dungey, *Phil. Mag.* **44**, 725 (1953)
- H.P. Furth, J. Killeen, M.N. Rosenbluth, *Phys. Fluids* **6**, 459 (1963)
- R. Giovanelli, *Nature* **158**, 81 (1946)
- R. Giovanelli, *Mon. Not. R. Astron. Soc.* **108**, 163 (1948)
- R.A. Harrison et al., *Solar Phys.* **170**, 123 (1997)
- R. Kulsrud, *Phys. Plasmas* **18**, 111201 (2011)
- L.D. Landau, E.M. Lifshitz, *Fluid Mechanics* (Pergamon Press, Oxford, 1987)
- P. Maltby et al. *ApJ* **306**, 284 (1986)
- G. E. Moreton, A. B. Severny, *Solar Phys.* **3**, 282 (1968)
- E.N. Parker, *J. Geophys. Res.* **62**, 509 (1957)
- E.N. Parker, *Cosmical Magnetic Fields* (Clarendon Pres, Oxford, 1979)
- E.N. Parker, *ApJ* **376**, 355 (1991)
- E. Petschek, in *The Physics of Solar Flares*, ed. by W.N. Hess. Proceedings of the AAS-NASA Symposium on Physics (NASA, Washington, 1964), pp. 425–439
- E. Priest, T. Forbes, *Magnetic Reconnection-MHD Theory and Applications* (Cambridge University Press, Cambridge, 2000)
- P. Rosenau, Three dimensional flow with Neutral Points. *Phys. Fluids* **22**, 5 (1979)
- D.D. Ryutov, M.P. Ryutova, *Sov. Phys. JETP* **43**, 491 (1976)
- M.P. Ryutova, T.D. Tarbell, *ApJ* **541**, L29 (2000)
- M. Ryutova, S. Habbal, R. Woo, T. Tarbell, *Solar Phys.* **200**, 213 (2001)
- M. Ryutova, T. Tarbell, R. Shine, *Solar Phys.* **213**, 231 (2003)
- J. Sánchez Almeida, *ApJ* **556**, 928 (2001)
- B.V. Somov, *Physical Processes in Solar Flares* (Kluwer Academic Publishers, Dordrecht, 1992)
- H.C. Spruit, *AA* **98**, 155 (1981)
- P.A. Sweet, in *IAU Symposium on Electromagnetic Phenomena in Cosmic Plasmas, Stockholm, 1956* (1958), p. 123
- S. I. Syrovatskii *Ann. Rev. Astron. Astrophys.* **19**, 163 (1981)
- T. Tarbell, M. Ryutova, J. Covington, A. Fludra, *ApJ* **514**, L47 (1999)
- T. Tarbell, M. Ryutova, R. Shine, *Solar Phys.* **193**, 195 (2000)
- M. Yamada, R. Kulsrud, H. Ji, *Rev. Mod. Phys.* **82**, 603–664 (2010)

Chapter 13

Post-reconnection Processes: Shocks, Jets, and Microflares



Abstract In the previous chapter, we began to study the reconnection of magnetic flux tubes under the photospheric conditions where magnetic energy is less than the gas-kinetic energy of surrounding plasma ($\beta \geq 1$). We saw that unlike a low β reconnection that liberates large amount of magnetic energy leading to an in situ heating, high β reconnection does not give an immediate gain in energy, but it sets the system in a highly dynamic state triggering strongly nonlinear processes. These processes, determined by the evolution of post-reconnection products, occur higher in the atmosphere at a considerable distance from the reconnection area. In this chapter, we shall study how the post-reconnection products evolve and what determines the form and energetics of their impact on the overlying atmosphere. We will see that there are three major forms of the post-reconnection outcome: (1) generation of supersonic plasma jets, (2) formation of microflares, and (3) various combinations of jets and microflares. These were found to be in a perfect agreement with observations. Moreover, multiwavelength observations show details and interrelation of a ubiquitous sequence of events that start from cancellation of photospheric magnetic fields, pass through shock formation, and result in appearance of supersonic jets, microflares, and their combinations in the overlying atmosphere.

13.1 Key Regularities Observed in the Photosphere/Transition Region

The uninterrupted time series shows distinctive properties in the response of the chromosphere and transition region to dynamic changes in the photospheric network. It was found that appearance of sporadic bright transients and mass flows in the upper atmosphere strongly correlates with the cancellation (total or partial) of opposite polarity network magnetic fields in the photosphere. The observed plasma flows are found to have a steady, nonsteady, or explosive character, with amplitudes varying from a few km s^{-1} up to hundreds of km s^{-1} . Hot localized regions (emitting soft X-rays) often correlate with lower velocity regions of 40 km s^{-1} rather than with the high-velocity explosive events (Dere 1994; Harrison et al.

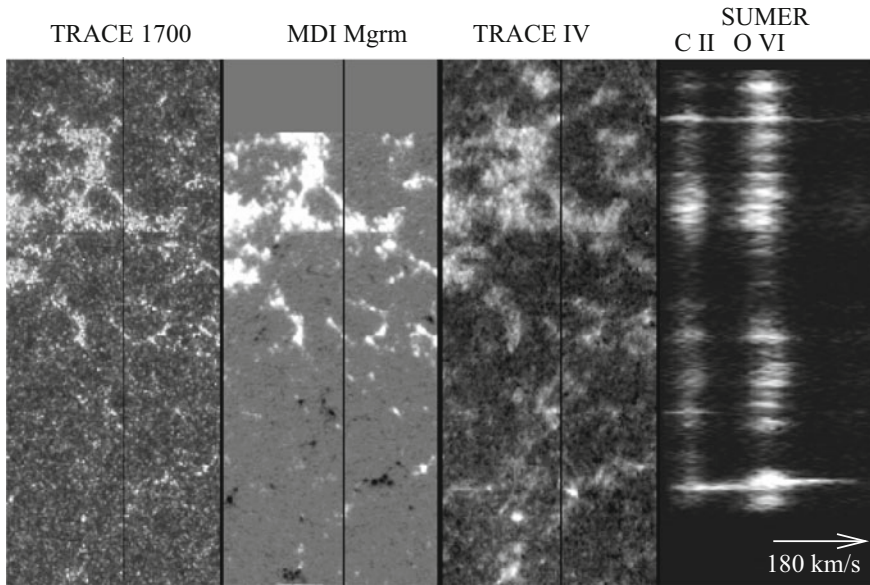


Fig. 13.1 Snapshots of the 90×230 Mm region: first and third panels are the TRACE images in UV continuum ($\sim 5 \times 10^3$ K) and C IV line ($\sim 10^5$ K); the second panel is the MDI magnetogram; the fourth panel shows SUMER spectra in two lines: C II 1037.0 Å corresponding to $\sim 2.5 \times 10^4$ K (left) and O VI 1037.6 Å corresponding to $\sim 3 \times 10^5$ K (right). The SUMER slit position is indicated on three images by vertical line

1997; Brekke 1999; Tarbell et al. 1999, 2000; Ryutova and Tarbell 2000; Ryutova et al. 2003). New generation of space-based instruments allow to study the jets and explosive events in higher cadence time series that add more details to their behavior (Mendoza-Torres et al. 2005; Fludra and Warren 2010; Curdt and Tian 2011; Innes and Teriaca 2013).

Example of the key elements in the observed regularities in the quiet sun atmosphere is shown in Fig. 13.1, which contains snapshots from an uninterrupted time series taken by several instruments on SOHO and TRACE on May 16, 1999. High-resolution magnetograms taken by MDI compiled in the 2.2-h movie show changes in small scale magnetic flux concentrations. TRACE images in the C IV lines and UV continuum are taken simultaneously with 15 s cadence and co-aligned with the MDI magnetograms and SUMER data. The field of view is 128×320 arcsec near disk center. The time series of C IV images shows the appearance and evolution of bright transient phenomena. The SUMER spectra allow one to study mass flows along the slit position. The far right panel in Fig. 13.1 shows C II and O VI lines which correspond to chromospheric ($\sim 2.5 \times 10^4$ K) and transition region ($\sim 3 \times 10^5$ K) temperatures. The imprint of the magnetic field pattern in the photosphere is clearly seen in the 1700 Å continuum and C IV images showing the unambiguous connection between the photospheric magnetic fields and significant emission in the chromosphere and transition region.

The most persistent regularities in the photosphere/transition region coupling can be described as follows:

1. At any moment of time the enhanced emission in the continuum (1700 Å) and C IV line mimics the magnetic pattern.
2. The appearance of bright transients usually correlates with reduction of magnetic flux in the photosphere, observed in canceling mixed polarity elements.
3. Microflares and other bright transients are often accompanied by two-directional plasma jets. Supersonic jets associated with bright transients and observed over the canceling magnetic features may appear several thousands of kilometers away from the center of a C IV transient.
4. If the radiative transient is accompanied by plasma flows, the energy is distributed between the two: usually the stronger localized emissions correspond to lower velocity jets and vice versa.
5. Plasma flows are always seen whenever the slit crosses the site of magnetic flux tubes or a region of converging supergranules, a vertex.
6. If the magnetic flux concentrations in the vicinity of a “vertex” are weak or even below the MDI resolution, multiple flows are seen in cooler (C II) lines without much activity in the transition region.
7. Multiple flows and explosive events occurring repeatedly are seen in the O VI line above the converging supergranules if they harbor significant number of magnetic flux concentrations.
8. Explosive events may appear in both SUMER lines or in only one. Events seen in both lines, i.e., both in chromosphere and transition region, are also accompanied by C IV microflares, as would be expected from the temperatures of formation. In the events seen only in one of SUMER lines, C IV microflares are usually very weak or even absent.

There are a lot of works devoted to explanation and modeling of the transition region jets and microflares. As a rule, the explanations are based on the low β magnetic reconnection, as indeed, in upper chromosphere and transition region $\beta \ll 1$. But unresolvable problem here is that the reconnection theories do not have the specific conditions that would correspond to one or the other form of released energy. In other words, even the most sophisticated reconnection theories cannot explain why the observed energetic events take the form of either only a supersonic jet, or that of pure microflare (heating), or their various combinations.

Contrary to this, the photospheric reconnection serving as a triggering mechanism, and being only an initial phase of a long chain of upcoming events, may explain not only the fact that the pattern of energetic events in the upper atmosphere mimics exactly the magnetic pattern in the photosphere, but allows to follow the process of energy transfer and its release that may develop in very different ways depending on the behavior of post-reconnection products.

Thus, at the photosphere, flux tubes collide and reconnect at any given moment of time and at any place. Post-reconnection products begin their “own life” and the system soon “forgets” about the reconnection. The farther evolution of a system is the subject of simple laws determined by the specific conditions that allow

to distinguish the final form of the energy release. These conditions not only predict formation of jets, microflares, and their diverse combinations, but allow the quantitative analysis as well. This will be discussed below.

13.2 Post-reconnection Shocks and Hydromagnetic Cumulation of Energy

The nature of photospheric reconnection and, most importantly, the nature of post-reconnection processes are determined by specific conditions in the photosphere (Tarbell et al. 1999; Ryutova et al. 2001). As discussed in the previous chapter, the most important of which are:

1. The property of network magnetic fields to be concentrated in isolated flux tubes and being in pressure equilibrium with almost non-magnetic high plasma beta environment ($\beta = 8\pi p_{\text{ext}}/B_{\text{ext}}^2 \gg 1$).
2. The property of flux tubes to be essentially noncollinear.
3. Sharp stratification of the low atmosphere.

The first condition implies that after reconnection strongly curved magnetic field lines, due to pressure equilibrium, $p_{\text{ext}} = p_{\text{in}} + B_{\text{tube}}^2/8\pi$, still remain confined in thin flux tubes. The magnetic tension results in fast straightening and shortening of the reconnection products creating a slingshot effect (Fig. 13.2a, b).

The initial velocity of tips, u_0 is proportional to Alfvén speed, $u_0 \simeq v_A$, but is less than the sound speed $u_0 < c_s$. The tip of the U-shaped part of flux tube that is moving upward accelerates quickly under the magnetic tension and the buoyancy force that are acting in the same direction. Depending on the angle of collision α between the flux tubes, the velocity of a tip itself reaches the velocity of ambient sound speed in 1–2 scale heights (see Fig. 12.10, Chap. 12).

At transonic velocities, the slingshot effect generates acoustic shocks. Most importantly, the shock front itself, because of the inhomogeneity of the medium, has an uneven curved surface. So that some elements of the shock front may move faster than others. Propagating upward in a stratified atmosphere, the front of a shock will become more uneven: faster elements of the shock front lead, and slower elements lag (Fig. 13.2c, d).

The stability analysis shows that the perturbation of the shock front displacement, ξ , evolves in time as $\partial\xi/\partial t = \xi(\partial u/\partial z)|_{z=H}$, where $u(z)$ is the velocity and H is a position of the unperturbed shock front (Gurevich and Rumyantsev 1969; Luo and Chevalier 1994). Note that perturbations grow with the increment proportional to $\partial u/\partial z > 0$.

In those regions where a shock front has a concave form, self-focusing and the collision of the advanced shock fronts occur (Fig. 13.2d, e). This leads to hydrodynamic cumulation, i.e., the concentration of the kinetic energy in a small volume (Stanyukovich 1960; Landau and Lifshitz 1987; Zababakhin and Zababakhin 1988).

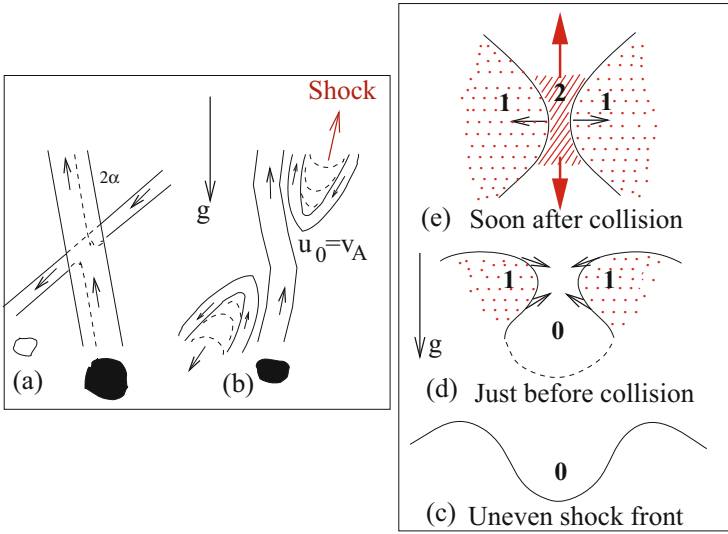


Fig. 13.2 Reconnection of photospheric flux tubes and post-reconnection outcome. Left: (a) noncollinear flux tubes approaching each other at a half-angle α ; (b) the post-reconnection slingshot causing straightening of reconnection products and generating shock; Right: (c) uneven shock front in gravitational field becomes more uneven: faster elements accelerate faster and slower elements lag; (d) converging shock fronts just before the self-focusing; (e) reflection of shocks immediately after collision

The form and amount of released energy depends on the angle at which shock fronts collide. We will see below that the head-on shock front convergence leads to deposit of entire energy of a system in the kinetic energy of plasma, whereas the shock convergence at some angle leads to deposit of the energy either into supersonic jets or to the distribution of energy between the plasma jets and microflares.

13.2.1 Head-On Convergence of Shock Fronts

Thus shocks generated by post-reconnection slingshot effect and propagating in strongly inhomogeneous atmosphere must have an uneven form and may experience self-focusing in upper layers of atmosphere (Fig. 13.2). Besides, the shocks resulted from neighboring reconnections are also the subject of collision as well. These effects are as ubiquitous as the reconnection of flux tubes in the photosphere. Obviously, a great variety of shock–shock collision implies that shock fronts may approach each other at an arbitrary angle, including head-on collision when shock fronts are almost parallel to each other.

Fig. 13.3 Wave front configuration in case of head-on collision: **(a)** shock fronts approaching each other with the velocity u with respect to laboratory system, $u \simeq v_A(\rho_0/\rho)$; **(b)** reflection of shock fronts after a head-on collision ($\theta = 0$)

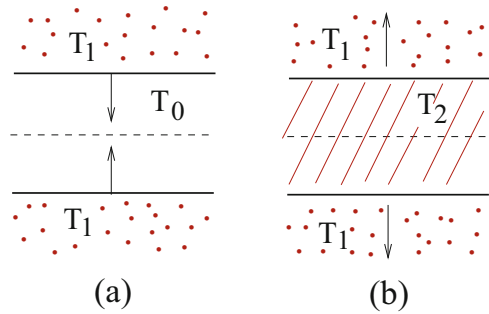


Figure 13.3 shows shock front configurations corresponding to head-on collision. In a small vicinity of the collision region, shock fronts may be considered as planar.

Figure 13.3a shows two parallel segments of shock front approaching each other in the unperturbed region with temperature T_0 (zone 0). Behind the shocks (zone 1) the temperature increases to the value T_1 (e.g., Landau and Lifshitz 1987):

$$T_1 = \frac{2\gamma(\gamma - 1)}{\gamma + 1} M^2 T_0 \quad (13.1)$$

After collision, behind reflected shocks (Fig. 13.3b) the temperature increases farther and becomes:

$$T_2 = \frac{3\gamma - 1}{\gamma} T_1 \quad (13.2)$$

If shocks are of about equal Mach numbers, the matter in zone 2 with temperature T_2 (behind reflected shocks) immediately after collision is at rest. Therefore, all the initial kinetic energy is converted entirely into the thermal energy of plasma. It must be emphasized that this is *additional*, 2.4 times more heating of a region which was already heated behind the shocks prior to their collision.

Some quantitative estimates are shown in Table 13.1. We consider two examples, one when the reconnection of flux tubes occurs at the photospheric level, and the other, when flux tubes reconnect slightly above the surface, near the temperature minimum region. At the surface $\rho_0 \simeq 2.8 \times 10^{-7} \text{ g cm}^{-3}$, and for magnetic field strength of $B = 1000 \text{ G}$, $v_A = 5.35 \text{ km s}^{-1}$. Thus, the initial velocity of plasma pushed by slingshot is $u_0 \simeq 5.35 \text{ km s}^{-1}$. The wave propagating against gravity accelerates according to a power law as (e.g. Whitham 1958):

$$u(z) = u_0 \left(\frac{\rho_0}{\rho(z)} \right)^\sigma \quad (13.3)$$

Table 13.1 Examples of the heating of the chromosphere at height $h = 1100$ km by the head-on collision of shocks resulted from reconnection of flux tubes at two different heights: (1) at the surface, $h_0 = 0$, and at the temperature minimum, $h_0 = 200$. $M = u/c_s$ being Mach number

h_0 (km)	T_0 (K)	ρ_0 (g cm^{-3})	B (G)	$u_0 = v_A$ (km s^{-1})	u (km s^{-1})	M	T_1 (K)	T_2 (K)
0	6520	2.8×10^{-7}	1000	5.35	41.4	5	5.1×10^4	1.2×10^5
200	4990	8.2×10^{-8}	500	4.9	28.4	3.5	2.4×10^4	6.0×10^4

where u_0 and ρ_0 are the velocity and density of a preshock plasma at the reference point, and

$$\sigma = \left[2 + \sqrt{\frac{2\gamma}{\gamma - 1}} \right]^{-1} \quad (13.4)$$

with $\gamma = 5/3$, $u = u_0(\rho_0/\rho)^{0.236}$.

At the height $h = 1100$ km, $\rho = 4.8 \times 10^{-11}$ g cm^{-3} , and the shock is accelerated up to the velocity $u = 41.4$ km s^{-1} . At this height $T_0 = 6100$ K, $c_s = 8.2$ km s^{-1} , and Mach number $M = 5$. Therefore, the temperature *behind* the shock *prior* to the collision becomes $T_1 = 5.1 \times 10^4$ K. Additional heating *after* the collision gives $T_2 \simeq 2.4 T_1 = 1.2 \times 10^5$ K.

In the region of temperature minimum at about $h = 200$ km, where $\rho_0 = 8.20 \times 10^{-8}$ g cm^{-3} , and the temperature is lower than at the surface, $T = 4990$ K. The magnetic field in flux tube drops and we may take for $B = 500$ G. The initial velocity is then $u_0 \simeq v_A = 4.9$ km s^{-1} . Note that the parameter $\beta^* = 2.66$. At the same height as above ($h = 1100$ km), $M \simeq 3.6$, and the temperature *behind* the shock will be $T_1 = 2.4 \times 10^4$ K, and the *after*-collision additional heating gives $T_2 \simeq 6.0 \times 10^4$ K. For atmospheric parameters a reference model by Maltby et al. (1986) is used.

13.2.2 Energy Distribution Between Heat, Jet, and Their Combinations

If the shock fronts intersect at some angle $\theta \neq 0$ (Fig. 13.4a), the temperature increase occurs in a larger volume and will be less than in the case of head-on collision. At the same time, a finite angle between the reflected shock fronts, 2ϕ , gives the plasma space to escape (Fig. 13.4b). Therefore, only a part of the kinetic energy of a system is converted into heat. The other part is converted into directed flows of plasma or cumulative jets.

With increasing collision angle, the velocity of the jet increases at the expense of local heating. At some critical angle, there is no reflected wave, and most of the energy is concentrated in the hot and dense plasma jets. The main characteristics of

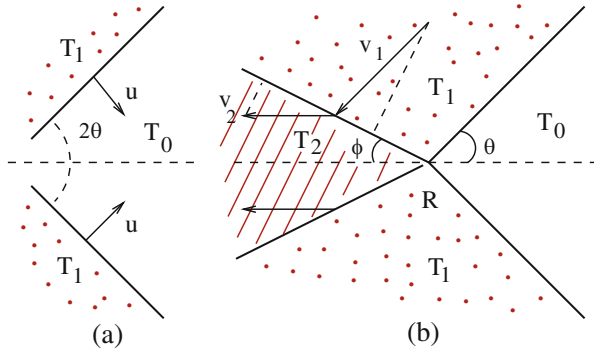


Fig. 13.4 Wave front configuration for converging shocks: (a) shock fronts moving with the velocity u with respect to laboratory system at the angle 2θ ; (b) collision and reflection of shock fronts in the coordinate system moving with the velocity $u/\sin \theta$

this process may be obtained from general theory of shock reflection (Stanyukovich 1960; Landau and Lifshitz 1987).

Let us take a closer look on the process shown in Fig. 13.4b. When shock fronts collide, a preshock plasma is at rest, i.e., the velocity in zone 1 is zero, and in the laboratory system, the intersection line, R , moves to the left with the velocity $v_R = u/\sin \theta$. We will carry out analysis in the coordinate system moving with the v_R , where the process is stationary.

The relations across the reflected shocks, i.e., conservation of mass, normal momentum, tangential velocity, and energy, respectively, are

$$\rho_2 v_2 \sin \phi = \rho_1 v_1 \sin (\theta + \phi) \quad (13.5)$$

$$p_2 + \rho_2 v_2^2 \sin^2 \phi = p_1 + \rho_2 v_1^2 \sin^2 (\theta + \phi) \quad (13.6)$$

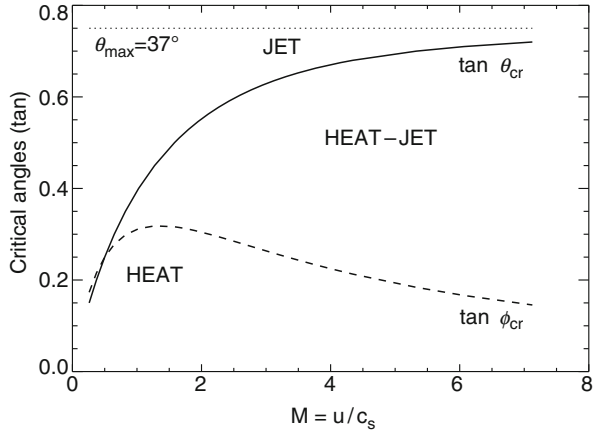
$$v_2 \cos \phi = v_1 \cos (\theta + \phi) \quad (13.7)$$

$$h_2 + \frac{1}{2} v_2^2 \sin^2 \phi = h_1 + \frac{1}{2} v_1^2 \sin^2 (\theta + \phi) \quad (13.8)$$

where $h_i = \gamma/(\gamma - 1)(p_i/\rho_i)$ is the enthalpy. Excluding v_2 , p_2 , and ρ_2 , this system reduces to a single equation of the form

$$\begin{aligned} & 2 \left[(1 - \tau_1 \tau_2)^2 + (\tau_1 + \tau_2)^2 \right] \\ & = \tilde{M}^2 (\tau_1 + \tau_2) \left[(\gamma + 1) \tau_2 (1 - \tau_1 \tau_2) - (\gamma - 1) (\tau_1 + \tau_2) \right] \end{aligned} \quad (13.9)$$

Fig. 13.5 Critical angles of shock front convergence, θ_{cr} , and reflection, ϕ_{cr} , vs the Mach number defining regions of predominant heating (HEAT), jet formation (JET), and the distribution of energy between the two (HEAT-JET). The dotted line shows a limiting angle corresponding to maximum jet velocity



where we used notations: $\tilde{M} = v_1/c_s$, $\tau_1 = \tan \theta$ and $\tau_2 = \tan \phi$. (13.9) is a quadratic equation for τ_1 , and may be written as

$$A\tau_1^2 + B\tau_1 + C = 0 \tag{13.10}$$

For each value of incident angle, τ_1 , there is a maximum value of τ_2 at a given Mach number beyond which this equation has imaginary roots; i.e., there is no reflected wave in the process. This regime corresponds to *pure jet formation*.

Thus, the condition of the vanishing of the discriminant

$$\Delta = B^2 - 4AC = 0 \tag{13.11}$$

determines the regions of varying energy release: dominant heating, jet formation, and distribution of energy between the two.

Solving (13.9) with $\Delta = 0$, one obtains critical angles vs Mach number. Results are shown in Fig. 13.5. We took into account that $M = M/\tan \theta$. In the region below dashed curve (the plot of the critical reflection angle), the energy of a system is converted entirely into heat. The region between the two curves corresponds to the distribution of energy between the thermal energy and cumulative jets. Above the solid curve, the parameters of colliding shock fronts correspond to jet formation. The critical incident angle, θ_{cr} , approaches a limit and, at large Mach numbers, becomes independent of M .

The maximum value of θ_{cr} can be found directly from Eq. (13.9) setting $M \gg 1$. This gives a simple equation:

$$(\gamma + 1)\tau_1\tau_2^2 - \tau_2 + (\gamma - 1)\tau_1 = 0. \tag{13.12}$$

The discriminant of this equation, $\Delta = 1 - (\gamma^2 - 1)\tau_1^2$, gives $\tau_1^{\max} = 1/\sqrt{\gamma^2 - 1}$ for limiting value of incident angle, or $\theta_{\max} = \tan^{-1}(1/\sqrt{\gamma^2 - 1})$, which coincides

with the classical result of $\theta_{\max} = \sin^{-1}(1/\gamma)$ (Stanyukovich 1960; Landau and Lifshitz 1987). In our case, for $\gamma = 5/3$, $\theta_{\max} = 36.87^\circ$.

The jet velocity ($v_{\text{jet}} = v_2$) can be found from (13.5)–(13.8). In the laboratory system, one obtains:

$$v_{\text{jet}} = u \left(\frac{1}{\tan \theta} - \frac{2 \tan^2 \theta}{M^2} \right) \left(1 + \frac{2 \tan^2 \theta}{M^2} \right)^{-1/2} \quad (13.13)$$

At large Mach numbers this reduces to $v_{\text{jet}} \simeq u \cot(\theta/2)$, which is also in agreement with classical theory (Stanyukovich 1960). Here θ should be understood as its limiting value $\theta_{\max} = \tan^{-1}(1/\sqrt{\gamma^2 - 1})$, so that $v_{\text{jet}}^{\max} = u(\gamma + \sqrt{\gamma^2 - 1})$. For $\gamma = 5/3$, $v_{\text{jet}}^{\max} = 3u$. Thus, even at moderate Mach numbers, $M \simeq 2$, at the collision angles close to 37° , most of the kinetic energy of a system is concentrated into the hot and dense plasma jets. The density of jet is estimated as $\rho_{\text{jet}} \simeq \rho_1 \gamma / (\gamma - 1)$.

Using above quantitative examples (Table 13.1), and suggesting that shock fronts collide at the angle close to 37° , we find that the usual after-shock heating (T_1) is accompanied by strong cumulative jets with high velocities; in the first example, $v_{\text{jet}} \simeq 124 \text{ km s}^{-1}$ ($T_1 = 5.1 \times 10^4 \text{ K}$), and in the second example, $v_{\text{jet}} \simeq 103 \text{ km s}^{-1}$ ($T_1 = 3.4 \times 10^4 \text{ K}$).

In three-dimensional geometry, there may occur rare but violent event of cylindrical focusing. This happens when the initial shock front is close to the figure of revolution. In this case, a cylindrical cumulation similar to Guderley's effect will occur, and strong two-directional hot jets of material will be formed in the intersection point (Guderley 1942; Landau and Lifshitz 1987). This will be addressed in the subsequent sections.

Note again that the above consideration applies to the case where the magnetic pressure is small everywhere, except *inside* the flux tubes. So that the slingshot generates almost purely acoustic waves, and the magnetic effects are not involved in further dynamics. On the other hand, even if the magnetic pressure in the ambient plasma is non-negligible, all the essential features of the phenomena will remain in place. In the same manner as above, the MHD waves will be driven by the slingshot effect, and the waves will steepen when propagating upward, leading to the formation of MHD shocks and to the cumulation in the areas of the appropriate curvature of shock fronts (Whitham 1958; Pai Shih-I 1962; Sokolov 1991).

A great variety of the quiet sun magnetic network that covers 90% of the solar surface ensures all possible combinations of the process that starts from magnetic flux reduction in the photosphere, passes through shock formation, and ends up in the various forms of energy release. Accordingly, the recycling time of the magnetic network is very short (Schrijver et al. 1997): in about 40 h magnetic field in the entire network replaces itself providing continuous energy supply to the upper atmosphere. The energy flux estimated on the basis of this time scale is enough to explain the observed UV/EUV radiation of the order of $5\text{--}10 \times 10^5 \text{ erg cm}^{-2} \text{ s}^{-1}$. The height of the most intensive shock formation and subsequent appearance of the impulsive

phenomena corresponds to the empirical height of the sharp temperature jump. The high rate of emergence of new fluxes and diversity of their parameters result in the cascade of shock waves, thus creating a magnetic energy avalanche and “steady” energy input into higher layers of atmosphere. This is an on-going process which works all the time and is independent of the phase of magnetic activity of the sun.

13.3 Observation of Photospheric Reconnections and Their Impact on Overlying Atmosphere

To demonstrate relation between the reconnecting flux tubes and subsequent energy transfer and release in overlying atmosphere we shall compare high-resolution magnetograms with the observational data taken simultaneously for the chromosphere and transition region.

We start with data taken on January 22, 1997. High-resolution MDI magnetograms of a very quiet region were co-aligned with the simultaneous CDS/SOHO images taken in the O V line (629 \AA), which shows plasma at $2.5 \times 10^5 \text{ K}$. The data were compiled in the 2.5 h movie that shows motions and changes in the photospheric magnetic fields and the response of the transition region to these changes. At any moment of time, the enhanced intensity in the O V line mimics the magnetic pattern of the photosphere. The appearance of bright transients is correlated with the flux reduction in the colliding opposite-polarity magnetic elements. Two examples of such events are shown in Figs. 13.6 and 13.7.

Figure 13.6, left four panels, show magnetograms of a small region with reconnecting flux tubes (marked by red arrow) and the same area at the transition

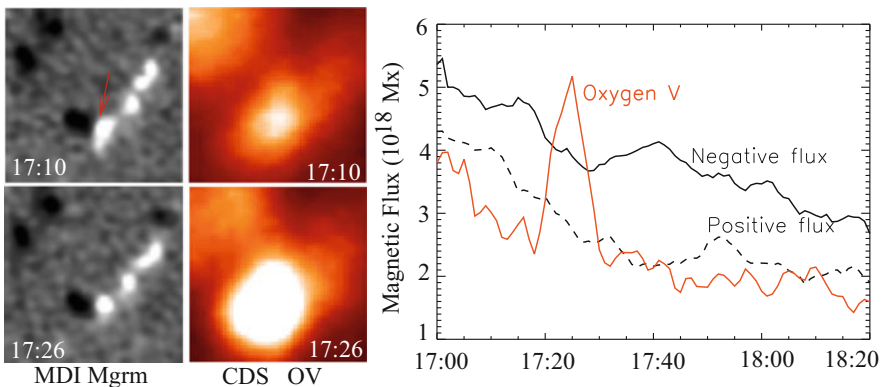


Fig. 13.6 Magnetic flux cancellation and subsequent appearances of bright transient in the transition region at $2.5 \times 10^5 \text{ K}$. Left four panels are magnetograms of a small, $30 \times 30 \text{ arcsec}$ region of quiet sun at two instances of time together with the same area in the Oxygen V 629 \AA . The right panel shows a quantitative picture of this process in time. Magnetic flux is in 10^{18} Mx , UT time is minutes, and the O V intensity is in arbitrary units

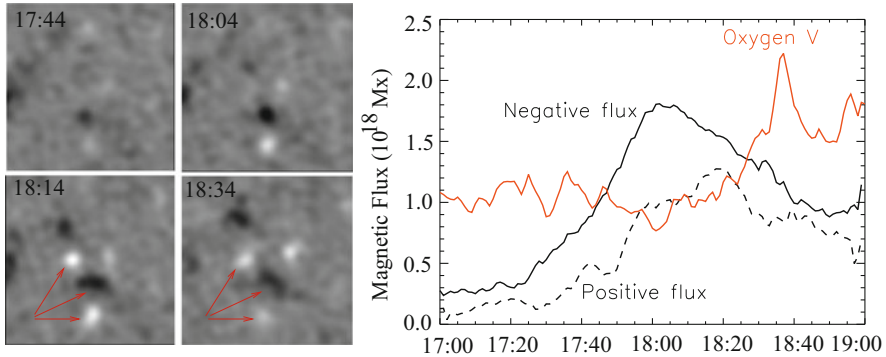


Fig. 13.7 Time variation of negative (solid line) and positive (dashed line) fluxes in region of newly emerging bipole, and corresponding intensity curves. The reconnection starts at about UT 18:10 and proceeds with several steps. The microflare peaks up at UT 18:40

region temperature (2.5×10^5 K) at two instances of time. Right panel shows time history of this process before and after the reconnection occurred. A black solid curve is the time variation of measured negative flux (black spots in left panels) and dashed curve is that of positive flux (white spot in left panels). The corresponding intensity variation is shown by the red curve. The reconnection started at UT 17:15, and in about 5 min when magnetic flux reduced by 30–40% a strong microflare appeared in the transition region.

Another example of the reconnection process and its impact to overlying transition region is shown in Fig. 13.7. Left four panels are magnetograms showing a newly emerging bipoles and their interaction. The right panel contains measured magnetic flux and the Oxygen V intensity. The reconnection process begins at about UT 18:10 and continues with several steps until UT 18:30. Soon after that the microflare appears and reaches its maximum at UT 18:40.

The events shown in Figs. 13.6 and 13.7 represent the most typical pattern for the majority of the observed mixed polarity neighbors. Several flux tubes show such pattern repeatedly during the time of observation. In particular, the above examples come from quite a short (2.2 h) data set, and the $128'' \times 320''$ area of a quiet sun region. There were observed over 200 different events of bright radiative transients in the transition region, and appearance of each event was preceded by reduction of the photospheric magnetic field.

13.3.1 Microflares, Jets, and Their Combinations

The picture becomes more complete when complimented by the observation of mass flows. Now one can observe not only time history of microflares resulted from the photospheric reconnections, but whether these microflares are accompanied by

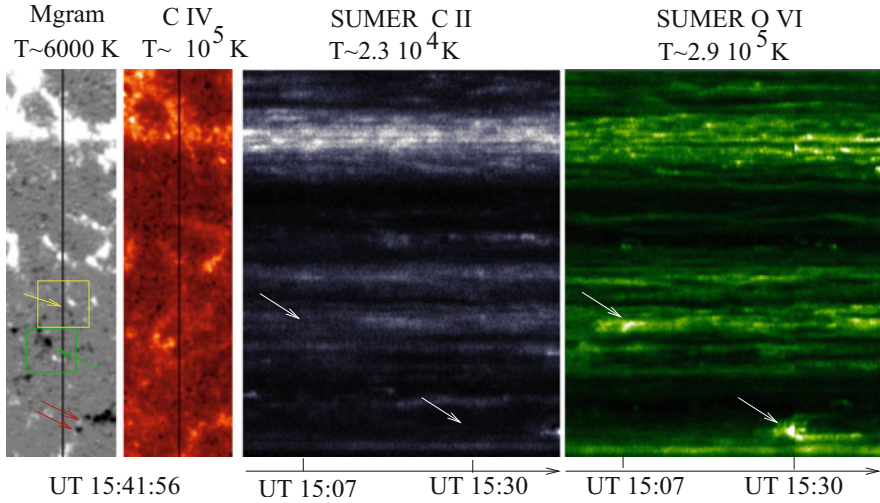


Fig. 13.8 Left Panel: The MDI magnetogram of the $66'' \times 220''$ region shows small scale network magnetic elements of positive (white) and negative (black) polarities that outline the regular set of supergranules; Middle panel: The same region at transition region temperatures showing the enhanced emission in C IV line that mimics the network magnetic pattern. Solid lines on these images show the SUMER slit position (slit width is $1''$); Left panels: The time variation of C II chromospheric and O VI transition region line intensities at each position of the slit during a 45-min (out of 2.2 h) time sequence. Each bright dot on this image corresponds to the enhanced plasma flows. Their occurrence also traces closely the sites of magnetic elements

generation of mass flows or not. To demonstrate these processes we will use the data sets shown in Fig. 13.1.

Figure 13.8 is an example from these observations. The MDI magnetogram of the target region is shown in left panel, the second panel is the TRACE image of the same region in C IV transition region line. Two right panels show time variation of C II (chromospheric) O VI line (transition region) intensities at each position of the slit during about 45 min (out of 2.2 h) time sequence.

A well-distinguished normal set of supergranules in the magnetogram is outlined by small-scale network magnetic elements. The hot plasma in the transition region (C IV line) mimics exactly the photospheric magnetic pattern. The SUMER slit that captures flows extends over about 10 supergranules crossing several vertices and a short, ~ 15 arcsec, section of a plage highly populated by positive (white) magnetic concentrations. The enhanced intensities in the C II and O VI lines clearly reflect the topology of the photosphere as well. For example, the SUMER spectra above the plage region with dense conglomerate of magnetic fluxes (in the upper part of image) show continuing enhanced emission, while above the cell interiors with little magnetic field there are only rare sporadic events.

The enhanced emission in the cooler C II line traces the magnetic field sites more closely than the O VI line and has a more diffuse character. While the enhanced emission in the O VI line is more discrete. This difference is quite remarkable, and

reflects the evolution of post-reconnection shocks: at low chromosphere there are much more shocks that provide a regular behind shock heating, while higher in the atmosphere, where the cumulative effects, and cylindrical focusing turn on (not all the shocks are subject to cylindrical focusing!) and lead to more concentrated sporadic events. Note that the explosive events accompanied by a strong jets such as those marked by white arrows on the O VI image (the velocity of these jets exceed 100 km s^{-1}) do not usually appear in C II images. This again means that cumulative effects associated with shock front convergence occur higher in the atmosphere.

Thus, the usual behind-shock heating is continuously sustained above the magnetic flux concentrations and should appear as diffuse “clouds” with the temperatures higher than that of unshocked material. This particular stage of the energy production is what the enhanced emission in the C II line shows. Higher in the atmosphere, shocks experience either self-focusing or collision with other shocks leading to hydrodynamic cumulation, i.e., concentration of energy into a small volume. These events are strongly localized and appear as small-scale isolated features with significantly enhanced emission. Note again that the enhanced emission in a hot O VI line is much more discrete than corresponding emission in underlying chromosphere (C II line).

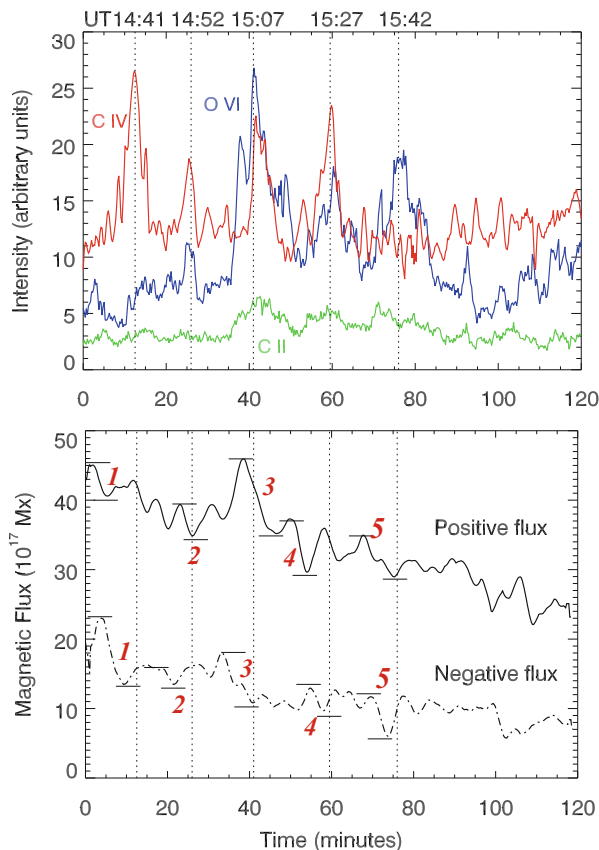
Each bright grain (i.e., enhanced emission) in a hot C IV and O VI lines has its own character and may represent one of three forms of energy release:

1. microflare alone corresponding to pure C IV emission;
2. a strong jet corresponding mainly to O VI emission; and
3. combination of two. To see these regularities in detail and distinguish three type of events from each other we plot measured positive and negative magnetic fluxes in time and compare them with time evolution of CDS and SUMER intensities. Example of such procedure is shown in Fig. 13.9.

Lower panel here shows time variation of positive and negative magnetic fluxes of a bipole inside the yellow box in Fig. 13.8. The upper panel shows the response of the chromosphere and transition region to magnetic field variations. Green and red lines are C II and C IV microflare intensities and blue line shows strength of generated flows. The numbers 1–5 on the magnetic curves mark changes of magnetic fields in the most prominent events produced by on-going reconnection in this bipole during 2-h period.

The flux reduction marked by “1” resulted in appearance of microflare alone without significant flows (a pure “HEAT” regime). The next three events, 2–4, correspond to the “HEAT-JET” regime: microflares are accompanied by supersonic jets, the most spectacular of which is # 3 event. In this particular case a multistep reduction of magnetic fluxes, i.e., multiple reconnection processes, lasted almost 10 min, generating enough energy to trigger appearance of a strong microflare and supersonic jet with velocity of about 120 km s^{-1} (see also below). Note that a significant energy was deposited even in low chromosphere (C II green line in upper panel). Finally, case 5 corresponds to pure “JET” regime.

Fig. 13.9 Time variation of positive and negative magnetic fluxes in the compact bipole inside the yellow box in Fig. 13.8, and corresponding changes in the C IV (the red line in the upper panel), C II (green line), and O VI (blue line) intensities over this area. The flux reduction marked by “1” in lower panel caused appearance of microflare alone without significant flows (a pure “HEAT” regime); the next three events correspond to the “HEAT-JET” regime when microflares are accompanied by the O VI plasma jets, and the event marked by “5” is the example of a pure “JET” regime



13.3.2 Effects of Converging Supergranular Flows

The supergranular topology and convective flows in general play very important role in electro-mechanical coupling between the photosphere and chromosphere/transition region. Converging flows attract all possible magnetic elements, which then float along the supergranular lanes, collide, and reconnect. Vertices where three supergranules meet are the most populated areas, and thus the most active energy production sites.

Figure 13.10 shows examples of energy release in the chromosphere and transition region along the SUMER slit passing through differently magnetized and topologically distinct regions. The left panel is a magnetogram, with uneven circles marking the supergranular pattern. Numbers with arrows indicate several areas along the SUMER slit to be discussed. We will also discuss event overlying a strong magnetic concentration marked as # 13, which lies in the intergranular lane off the SUMER slit, but supersonic jets generated by post-reconnection shocks were so strong that they reached the slit and were well detectable.

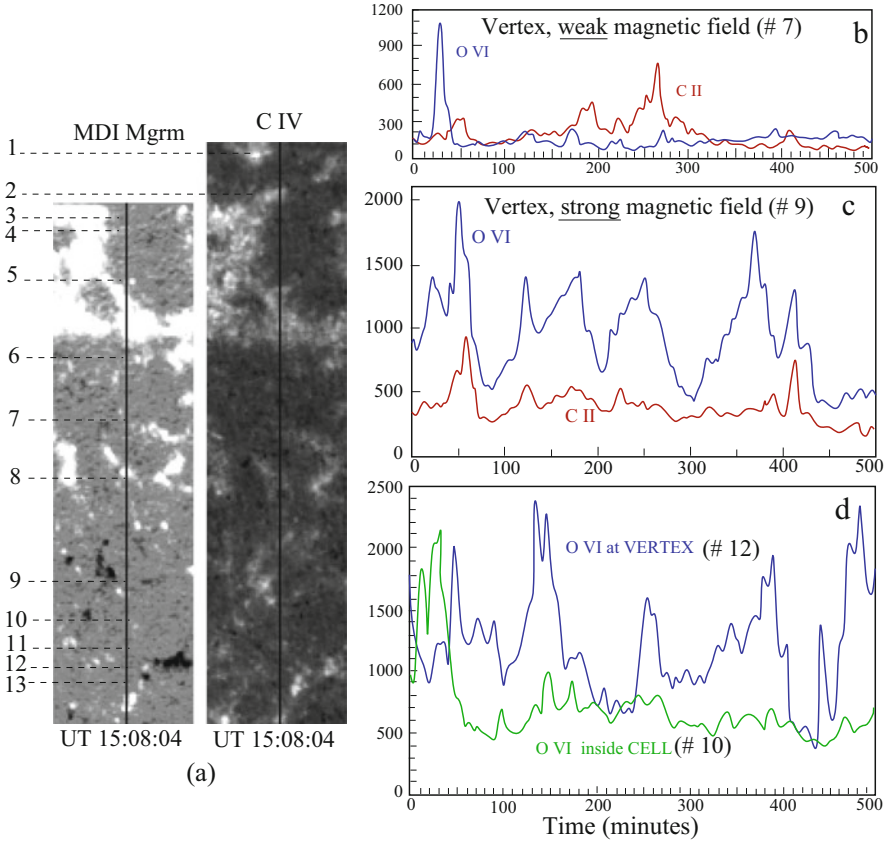


Fig. 13.10 Illustration of the influence of supergranular motions on the energy production. Panel **a**: The magnetogram of the $66'' \times 190''$ region together with overlying chromosphere/transition region in C IV line. Numbers 1–13 correspond to differently magnetized and topologically distinct regions; Panels **b** and **c** show O VI and C II intensities (in arbitrary units) above vertices # 7 and # 9: vertex # 7 contains weak magnetic concentrations while # 9 vertex is site of a strong magnetic concentrations; Panel **d** compares intense energetic events occurring above strongly magnetized vertex # 12 with the cell interior # 10 depleted of magnetic elements

We choose four examples, vertices marked as # 7, # 9, and # 12, where supergranules converge, and #10 which represents the cell interior. The right panels in Fig. 13.10 are computed intensity curves in SUMER O VI and C II lines for chosen examples.

The process of energy production, transfer and release is very sensitive to local conditions. There are also clear differences in the outcome depending on whether magnetic flux tubes near the vertex are weak (like region # 7) or strong (like regions # 9 and # 12).

At vertices, converging flows will attract neighboring magnetic elements, including the smallest. High-resolution observations show that cancellation, merging and splitting processes among the tiny flux tubes persist to the limit of resolution.

The process of heating and jet formation caused by reconnection of the smallest possible elements should have two general features: (1) The shock convergence and formation of jets may occur at lower altitude (because of small magnetic fluxes), i.e., in cooler emission lines; and (2) The re-occurrence of generated flows will happen frequently in the same place, because the long lifetime of supergranules makes long-lived attracting centers. On the other hand, if there is a strong magnetic flux concentration near the attracting center, the multiple flows may be observed at higher altitudes and in hotter emission lines.

Example of a vertex with very weak magnetic field is region # 7 shown in Fig. 13.10b. Generated flows, as expected, are seen predominantly in the C II line. The strong explosive event seen in O VI at $t = 30$ may have an origin associated with the strong downflows observed a few moments earlier in C II line (not shown). This type of event is quite common: appearance of sporadic explosive events and complex dynamical structures with multiple velocities in regions of maximum downflows is ubiquitous.

If in the region of converging supergranules strong magnetic flux concentrations are present, the series of reconnections releases energy at higher altitudes which manifests itself in hot and dense multiple flows observable in the hotter O V I line. Example of such event is shown in Fig. 13.10c. One can see the appearance of series of hot plasma flows and some explosive events during the entire time span, just as expected due to the supergranular converging flows that provide continuous supply of small scale magnetic elements which interact with longer-lived strong magnetic field.

To illustrate one more time the effect of a vertex, we superimpose the O VI intensities for the vertex region # 12 and cell interior region # 10, which is quite distant from the supergranular lane (Fig. 13.10d). One can see that during more than 2 h nothing spectacular happens in region # 10. While the repetitive explosive events seen, e.g., at $t = 140$, $t = 390$, and $t = 480$ above the vertex (# 12) are quite natural.

In each case one can estimate the energy content in the radiative events and compare it with magnetic energy, reduced during reconnection. One should bear in mind, however, that this energy is not a direct deposit, but triggers multistep process of shock formation and shock–shock interaction.

Now the question is do the observations show formation shocks and their possible association with the reconnection of flux tubes. The answer is yes, and we address this question in the next section.

13.4 Key Elements of Energy Production and Observation of Shocks

Let us first overview key elements of energy production and its release in the chromosphere/transition region. As discussed throughout this chapter, the process starts with reconnection of *opposite polarity* photospheric flux tubes, passes through shock formation and ends up with one of the forms of energy release determined by the system parameters and evolution of shocks. The main steps of this process are shown again in Fig. 13.11. Left panels are the MDI magnetogram of $30'' \times 30''$ region marked by green box in Fig. 13.8 together with radiative events in the chromosphere/transition region (Trace C IV and SUMER O VI lines). Time history of negative and positive magnetic fluxes and corresponding changes in C IV and O VI intensities are shown in upper right panel. The lower panel shows line profiles of SUMER spectra as function of wavelength extracted at two instances of time, $t = 15:26:53$ and $t = 15:26:40$ (solid lines). The approximate moment of the maximum flux reduction is marked by $t_1 = 15:23$. High velocity jets appear about 6 min later ($t_3 = 15:29:03$). The peak intensity in C IV slightly precedes the appearance of the jet. Before the maximum of intensities about 2 min earlier at $t_2 = 15:26:53$ (also at $t = 15:26:40$) SUMER spectra showed clear shock signatures (lower right panel): the left intensity peak is significantly stronger than the right one. The difference between the two peaks, $\Delta\lambda^*$, is a measure of the shock velocity. Indeed, $\Delta\lambda^*$ is a difference between the Doppler shifted lines resulted from mass motions, v_2 (left peak) and v_1 (right peak). The velocity difference $v^* = v_2 - v_1$ is

$$v^* \cos\theta = \frac{\Delta\lambda^*}{\lambda_0} c \quad (13.14)$$

where θ is the angle between the direction of flow and line of sight, λ_0 is the wavelength of unshifted line (e.g., $\lambda_0 = 1037.656 \text{ \AA}$). The velocity in front of the shock v_1 and behind the shock velocity v_2 are related by (e.g., Landau and Lifshitz 1987):

$$v_2 - v_1 = c_s \frac{2(M^2 - 1)}{(\gamma + 1)M} = v^* \quad (13.15)$$

This expression can be used to estimate the Mach number $M = v_{\text{sh}}/c_s$. For strong shocks ($M \gg 1$) Eq. (13.15) gives $v_{\text{sh}} = (\gamma + 1)v^*/2$.

The estimate for a shock velocity in the example shown in Fig. 13.11 with $\Delta\lambda^* = 0.135 \text{ \AA}$ is $v_{\text{sh}} = 60 \text{ km s}^{-1}$ (we took $\theta = 30^\circ$).

Note that usually the first generation shocks appear predominantly in the C II, and occasionally in the O VI line (including the above example). This fact is quite natural: shock formation is the earlier stage of the energy production that occurs shortly after the flux tubes reconnect. Therefore, the average enhancement in the C II and even C IV lines can be explained by the direct behind-shock heating and behind-

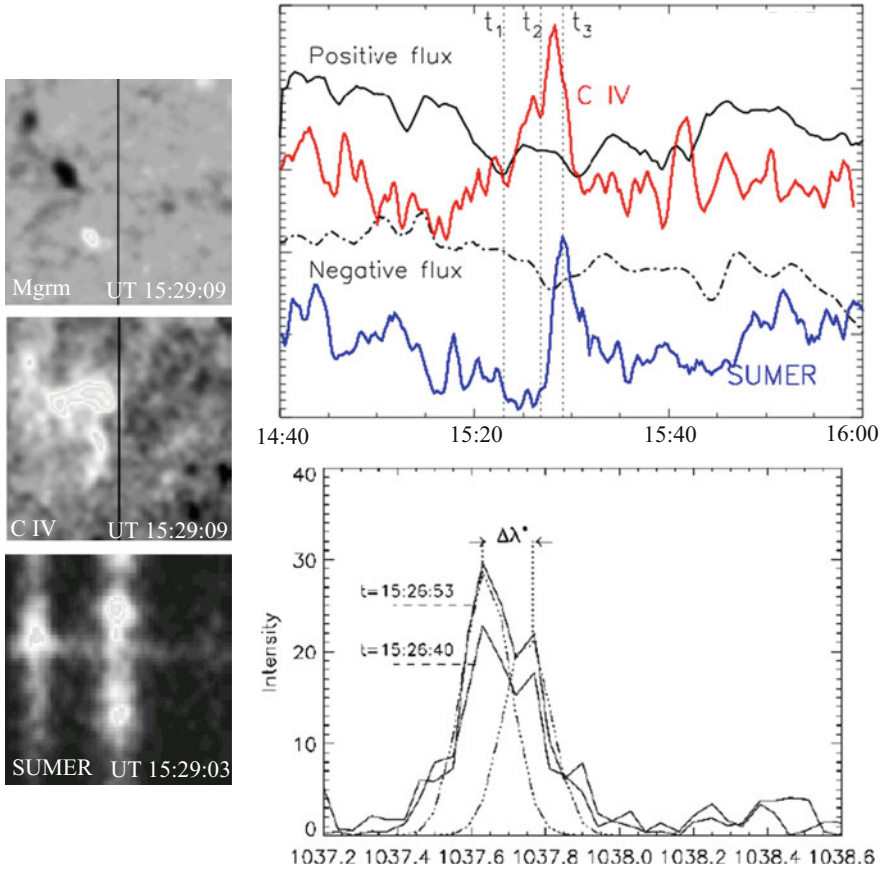


Fig. 13.11 Key elements of energy production and its release associated with the photospheric reconnection. The left three panels are snapshots of the $30'' \times 30''$ region, marked by green box in Fig. 13.8, at the moment of the intensity maximum in the O VI line. The upper right panel shows time history of positive and negative magnetic fluxes and corresponding changes in the intensities of C IV (red) and O VI (blue) lines. The lower right panel contains line profiles vs wavelength (\AA) extracted from exposures at $t = 15:26:40$ and $t = 15:26:53$ (solid lines). Dash-dotted line is Gaussian fit

shock flows, while strong radiative events (blinkers, microflares) and explosively growing flows are consequences of further evolution of shocks.

It is remarkable that high cadence data compiled in movies show not only shock signatures, but allow to see and measure step by step evolution of shocks. Figure 13.12 shows a typical example of the evolution of shock triggered by reconnection of opposite polarity flux tubes (marked by the white arrow in panel a). As mentioned above the C II ($T \simeq 10^4$ K) shocks appear soon after the reconnection but before the enhanced emission in hotter C IV and O VI lines appear (panels b and c, respectively).

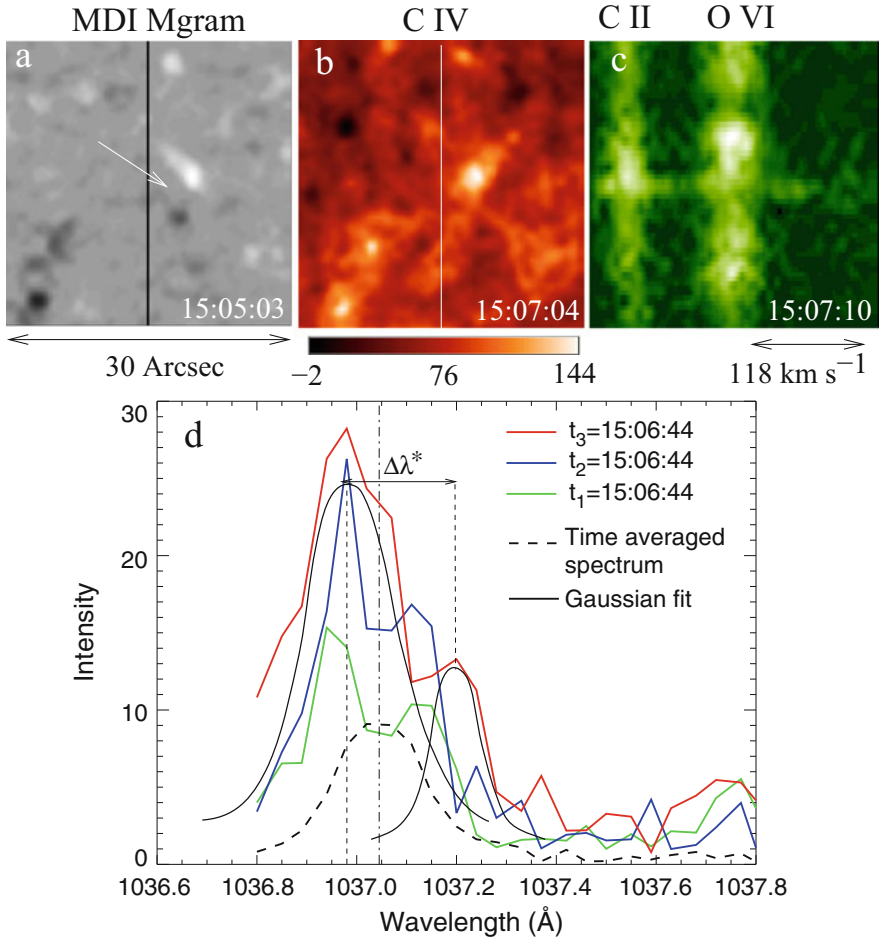


Fig. 13.12 Example of a step by step evolution of shock and its accompanying phenomena. Panel **a**: Magnetogram of $30'' \times 30''$ area (yellow box in Fig. 13.8) with compact bipole near the SUMER slit just before the reconnection occurred; Panels **b** and **c**: appearance C IV microflare and a strong O VI jet with velocity $v_{\text{jet}} = 118 \text{ km s}^{-1}$. Panel **d**: Line profiles of C II SUMER spectra extracted from exposures with 13 s time step; from $t_1 = 15:06:19$ (green line) a double-humped profile typical of shocks rapidly evolves into a strong shock (blue line, $t_2 = 15:06:32$), and at $t_3 = 15:06:44$ (red lines) reaches its maximum resulting strong radiative transient in less than 20 s

Line profiles of C II SUMER spectra at 13 s time steps are shown in Fig. 13.12d. From $t_1 = 15:06:19$ (green line) a double-humped profile typical of shocks rapidly evolves into a strong shock (blue and red lines). At $t_3 = 15:06:44$, when peaks reach maximum, the difference between the two peaks is $\Delta\lambda^* = 0.18 \text{ \AA}$. This gives for the shock velocity $v_{\text{sh}} = 0.5(\gamma + 1)(v_2 - v_1) = 69 \text{ km s}^{-1}$. At C II temperature ($2.3 \cdot 10^4 \text{ K}$, sound speed $c_s = 24 \text{ km s}^{-1}$) this corresponds to Mach number $M =$

$v_{sh}/c_s \simeq 3$. At transition region heights such a shock may generate jets in the HEAT-JET regime, with velocities ranging from 105 km s^{-1} to 170 km s^{-1} . Indeed, fast evolution of the shock (shown in panel d in three instances of time) is followed by the appearance of a bright transient in C IV line and a hot O VI plasma jet. The measured velocity of the jet at $t = 15:07:10$ is 118 km s^{-1} . This is a typical explosive event—one of the main features observed in the transition region. In the next section we address this issue in more detail.

13.5 Explosive Events

There are basically two major classes of explosive events in the chromosphere/transition region (coronal mass ejection, CMEs, and polar plumes belong to totally different classes of high velocity events and are not discussed here):

1. those that may be generated by post-reconnection shocks, and
2. those that are associated with the nonlinear explosive instability of Negative Energy Waves (NEWs). Naturally, the explosive events produced by these two different mechanisms *must and have* different signatures.

Consider first the mechanism associated with post-reconnection shocks. As we have discussed earlier, shocks produced by the post-reconnection slingshot effect, propagating upward and having uneven surface, may experience self-focusing (Guderley's effect), in which the entire energy of a system, squeezed in a small volume, gets violently released in form of a hot bi-directional jets. Similar effects may occur when two different shocks produced by two independent reconnections collide. This effect is universal and well observable.

Figure 13.13 shows an example demonstrating shock–shock interaction and subsequent generation of strong explosive event. Reconnections occurring in close bipoles marked by double red arrows in Fig. 13.8 (#13 in Fig. 13.10) cause a series of upward propagating shocks (Fig. 13.13a): left peaks are higher than right peaks corresponding to higher intensity behind the shock than in front of it. These shocks result in two close microflares and strong bi-directional jets in O VI (right panels in Fig. 13.13a).

The jet generates the downward shock in O VI line: now the double-humped spectrum has its right peak higher than the left one, which interacts with the upward propagating C II shock at $t = 15:30:45$ UT (blue line in Fig. 13.13b). This results in the immediate appearance of the O VI explosive event (marked by yellow arrows in lower right panel of Fig. 13.13b) and a strong C II jet.

Prior to the collision temperature increases only due to regular, behind-shock heating, $T_1 = 2\gamma(\gamma - 1)(\gamma + 1)^{-2}M^2T_0$ (subscripts “0” and “1” denote the unperturbed and behind-shock plasma, respectively). In this example the shock velocity (before the collision) is $v_{sh} \simeq 88 \text{ km s}^{-1}$, and $T_1 = 8.5 \times 10^4 \text{ K}$. After the collision behind the reflected shocks the temperature increases further and becomes: $T_2/T_1 = (3\gamma - 1)\gamma^{-1}$, $T_2 = 2.46 \times 10^5 \text{ K}$. This is accompanied by strong

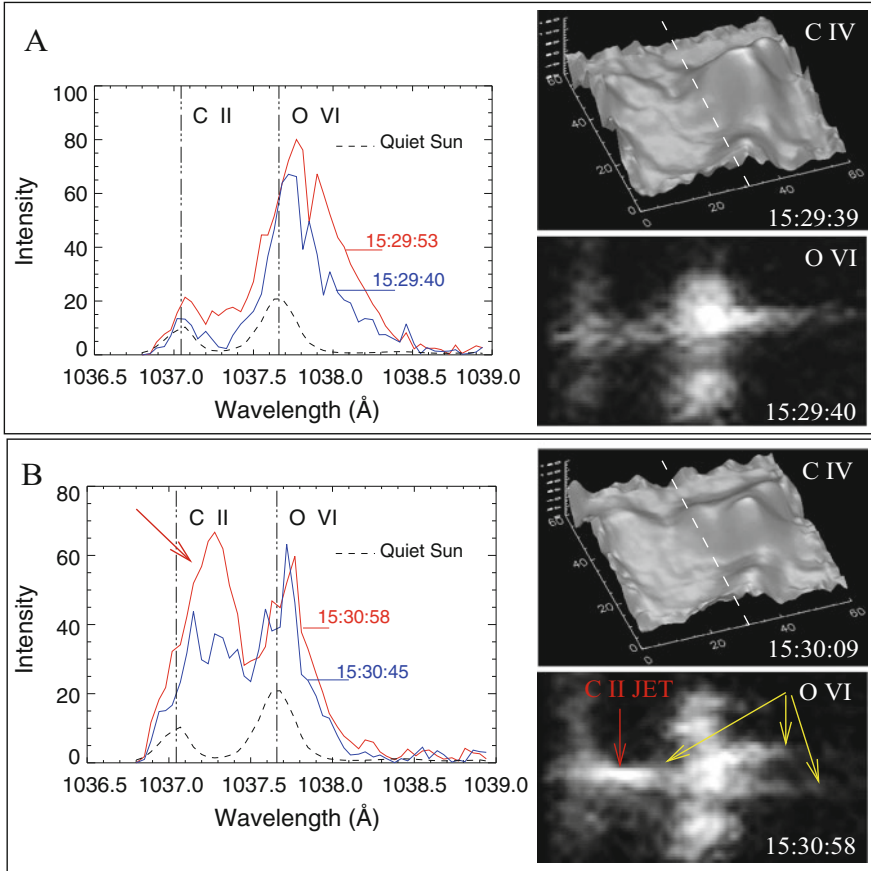


Fig. 13.13 Example of the observed shock–shock interaction and the resulting sporadic events. (a) A series of strong shocks continuing to occur during and after the double microflare at C IV temperature accompanied by the downward propagating O VI jet (peaks are significantly redshifted) with velocity exceeding 180 km s^{-1} ; (b) Downward propagating shocks (O VI line profiles show the right peaks exceeding the left peaks) interact with a series of upward propagating C II shocks at $t = 15:30:45$; The right panels show 3D plots of C IV emission together with the jet images taken by SUMER; the approaching shocks cause a triple humps seen at $t = 15:30:09$ in the C IV line; immediately after the shock collision, at $t = 15:30:58$ a strong C II jet and the explosive event in O VI line (marked by yellow arrows) appear. The field of view in panels and scales of the SUMER spectra are the same as in Fig. 13.13

plasma jets. The jet velocities are in the range of $115\text{--}220 \text{ km s}^{-1}$. These are typical observed parameters in the transition region explosive events.

The probability of the explosive events produced by collision of neighboring shocks is quite high and can be observed everywhere from quiet sun regions to plages where shocks produced by *non-collinear* flux tubes may reach each

other when accelerating and expanding in overlying chromosphere. Typically these explosive events are accompanied by a strong microflares as well (cf. Fig. 13.13).

In case of self-focusing of a single shock front when the entire cumulative energy goes into the strong bi-directional jets, there is usually little energy left for microflare. Strong support for such events is the absence or weakness of a transient microflares (the cylindrical focusing corresponds to a pure “jet” regime). The probability of such events, in principle, is also quite high. But in those regions where shock production is high, cylindrical convergence can be easily destroyed by the cascade of shocks produced by neighboring reconnection processes. Therefore, cylindrical focusing and resulted pure “JET” regime must be expected at least above the regions that are magnetically underpopulated, such as cell interior and magnetically poor vertices. Besides, as these events have the character of impulsive phenomena, their lifetimes must be short.

Thus we have two sub-classes in class of explosive events associated with post-reconnection shocks. From observational point of view the observed signatures of these two sub-classes of explosive events are well distinguishable.

Another, totally different class of explosive events is associated with the instability of negative energy waves. These explosive events, having totally different origin, may look quite similar to those associated with the shock convergence, and yet have their own signatures.

In the first place the instability of NEWs requires the presence of downflows in a system of structured magnetic field and can develop in a wide interval of velocities (Ryutova 1988):

$$40 \text{ km s}^{-1} \leq u \leq 220 \text{ km s}^{-1} \quad (13.16)$$

These conditions are easily met in the chromosphere, and we should expect this class of events to be quite common. Among the observed signatures of this kind of explosive events, we should expect (1) downflows with velocities of about 40 km s^{-1} and higher; (2) microflares, since such downflows correspond to the heat-jet regime in shock–shock collision; and (3) a high birthrate.

Note that the lifetimes of the explosive events caused by the instability may vary from a few seconds to minutes depending on the physical conditions of the instability, which may be realized in a wide range of parameters.

Most of the chromosphere/transition region explosive events fall into one of two classes and have the properties listed above. These properties are summarized in Table 13.2.

Numbers in the first column correspond to chosen examples along the slit shown in Fig. 13.10. The second column shows the photospheric features at a given position along the slit; e.g., “Vertex, B” denotes a supergranular vertex with a strong magnetic field. The third column shows recurrence of the explosive events during the entire observed interval (2.2 h). Column 4th shows the reduction of magnetic flux before the appearance of the explosive event. Column 5th shows the intensity of the C IV transient. The velocities and lifetimes in columns 6 through 8 are approximate. Column 9 reflects the mechanism causing an explosive event: “instability” stands

Table 13.2 Examples of explosive events and their properties

Case	Location	Recurr.	$\Delta\Phi$ (Mx)	C IV (Intensity)	C II (km s^{-1})	O VI (km s^{-1})	Lifetime	Class
1	Cell	Rare	n/a	Strg	40	80	~ 120 s	Instb
2	Vertex(B)	Multi	n/a	Strg	30	120	≥ 180 s	Instb
2	Vertex(B)	Multi	n/a	Strg	40	180	$\simeq 90$ s	Instb
3	Cell	Rare	$> 10^{18}$	Weak	20	80	~ 100 s	Gudrl
4	Edge B	Multi	10^{18}	Weak	20	60	~ 3 min	Instb
5	Edge B	Multi	$2 \cdot 10^{18}$	Med	20	60	~ 6 min	Instb
6	Cell	Rare	$3 \cdot 10^{17}$	Weak	20	80	~ 4 min	Instb
7	Vertex	Rare	$4 \cdot 10^{17}$	None	20	110	~ 90 s	Gudrl
8	Vertex, B	Multi	10^{18}	Med	20	80	~ 3 min	Instb
9	Vertex, B	Multi	$2 \cdot 10^{18}$	Strg	40	180	≤ 120 s	Instb
10	Cell	Rare	$< 10^{17}$	Weak	10	120	≥ 70 s	Gudrl
11	Vertex	Rare	$2 \cdot 10^{17}$	Weak	40	80	≥ 120 s	Instb
12	n/a	Few	$6 \cdot 10^{18}$	Strg	50	200	≥ 5 min	Instb
13	n/a	Few	$2 \cdot 10^{18}$	Med	10	80	~ 90 s	Instb

for the explosive instability of NEWs, and ‘‘Gudereley’’ for a cylindrical focusing of shock waves or shock-shock collision.

Among more than 40 analyzed events, only a few cases (10%) could be explained by cylindrical focusing. Some examples shown in Table 13.2 are: case 7 which is above the vertex with no magnetic field (below the MDI resolution), and cases 3 and 10 that are both above the cell interiors. In all cases, the peak velocities are more than 100 km s^{-1} , the C IV event is absent, and lifetimes are quite short (90 s). Examples of the explosive events in cases 7 and 10 are shown in left four panels in Fig. 13.14. One can see that C IV emission that would represent microflare is absent, while SUMER O VI jet is quite prominent.

The properties of strong jets generated by the explosive instability of NEWs are more diverse. This is quite natural because the interval of the critical velocities (13.16) is quite wide. For example, downflows close to the lower critical limit lead to long-lasting explosive events and are often accompanied by a medium or weak microflares. Stronger downflows lead to explosive events of shorter duration and are usually accompanied by a strong microflares. Examples of this type of jets are shown in right panels, Fig. 13.14. In both cases 1 and 2, strong microflares occur first and are accompanied by downflows. Then very quickly the explosive events appear. The time interval corresponding to the development of the explosive instability is roughly estimated as $t_{\text{expl}} \sim 30\text{--}100$ s. This means that as soon as cumulative effects create the microflare and downflows, in a few tens of seconds the explosive instability develops, leading to extremely fast acceleration of jets.

The examples in Fig. 13.14 show that explosive events can be detected by SUMER even when the main emission is located in several arcseconds from the slit. The overall birthrate for explosive events can be roughly estimated

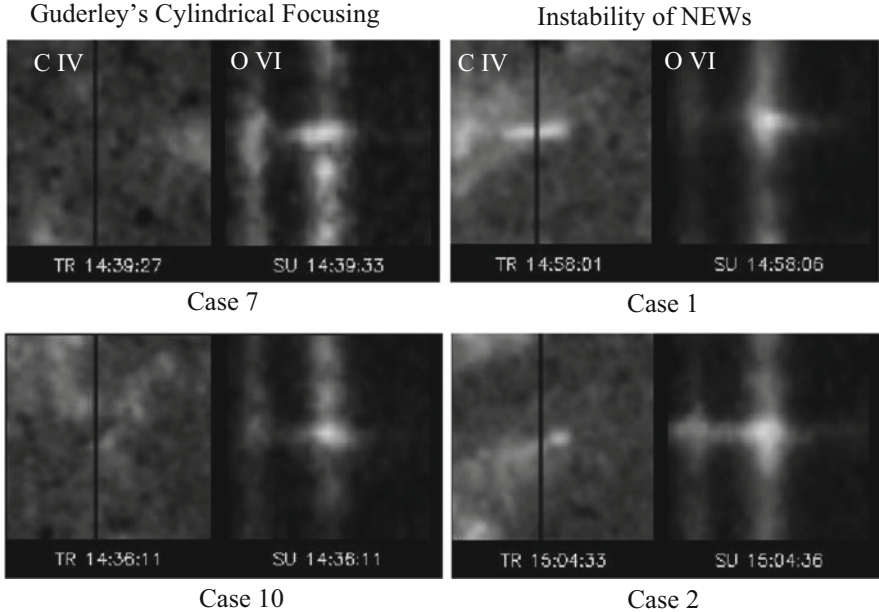


Fig. 13.14 Four examples of explosive events shown in TRACE C IV and SUMER O VI lines. Left panels are events driven by the cylindrical focusing of shock fronts; the remarkable feature of this class of explosive events is the absence of emission in the C IV line. Right panels are the explosive events driven by the explosive instability of NEWs; the necessary attribute here is the appearance of a prominent microflare accompanying the strong jets

as $f = N/(ST)$, where the number of events $N = 40$, the “effective” area $S = 5'' \times 360'' = 9.5 \times 10^{18} \text{ cm}^2$, and the time of observation $T = 7800 \text{ s}$. This gives $f = 5.4 \times 10^{-20} \text{ cm}^{-2} \text{ s}^{-1}$, which is consistent with the earlier estimates, $f = 4 \times 10^{-21} \text{ cm}^{-2} \text{ s}^{-1}$ for coronal holes and 10^{-20} for the quiet Sun (e.g., Dere 1994).

13.6 Response of the Upper Atmosphere to Reconnection of Unipolar Flux Tubes

We saw that the reconnection processes occur both in the system of the opposite polarity flux tubes and the same polarity flux tubes. The post-reconnection processes, however, are quite different, and response of the overlying atmosphere is quite different as well.

Figure 13.15 shows an example of the response of the upper layers of atmosphere to dynamic changes in the photospheric magnetic field. Three left images in both panels are the SUMER spectra in N II (corresponding to chromosphere at temperature $\simeq 2.7 \times 10^4 \text{ K}$), N IV (transition region at $T \simeq 1.4 \times 10^5 \text{ K}$), and

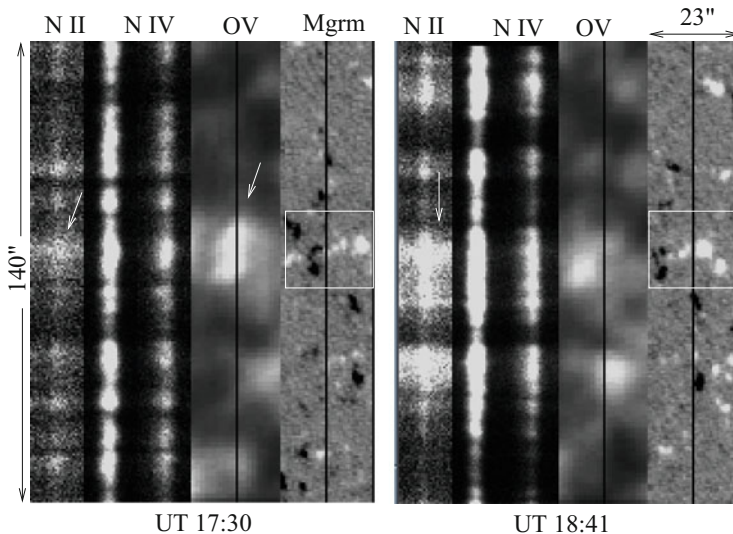


Fig. 13.15 Response of the chromosphere (N II and N IV SUMER spectra) and transition region (SUMER O V and CDS O V images) to reconnections of the photospheric flux tubes. Left panels: example of opposite polarity magnetic flux tubes; Right panels: the reconnection between the same polarity flux tubes. Solid line is a SUMER slit

O V (transition region at $T \simeq 2.3 \times 10^5$ K). Two right images in both panels are the O V emission taken by the CDS, and high-resolution magnetogram taken by the MDI.

One can see that when slit crosses the center of the mixed polarity group (Fig. 13.15, left panels), strongly enhanced transient emission in CDS O V line is detected. This is a typical example of the hydrodynamic cumulation of upward propagating shock produced by the post-reconnection slingshot.

When the slit crosses the region dominated by one polarity elements (Fig. 13.15, right panels), the slingshot effect must be tilted, or be perpendicular to gravity, so that in this case the lateral motions dominate over the upward propagating shocks. As a result, the motions are detected in lower chromosphere (N II line is significantly broadened), while upward propagating shocks are suppressed. The enhanced emission on the CDS image is still seen over the mixed polarity group, now left from the slit.

Concluding this chapter we must say that the energy supply for highly energetic events at all temperature levels from chromosphere to corona overlying the small scale magnetic network lies in the continuous hydromagnetic activity of small scale magnetic flux tubes.

The fact that the atmosphere above the quiet sun is far from quiet is, therefore, only natural. It is just here, within a narrow transition region, the sharp temperature jump from 6000 K to the million degree corona occurs. We saw that the chromosphere and transition region are the first to amass the energy coming from below and

transport it into the corona. And it is also only natural the chromosphere/transition region are the sites of continuous radiative transients, microflares, plasma jets, and explosive events. Indeed, localization of all these events in the transition region is co-spatial with the photospheric magnetic pattern, and their appearance correlates with canceling mixed polarity magnetic elements. Moreover, each observed event, be it just a microflare, supersonic jet, or combination of two can only be explained by various conditions for generation of post-reconnection shocks and their interaction. Theoretical solution for the parameter range gives a simple set of physical parameters that corresponds to all three regimes. Of which the largest range of parameters is release of the energy in form of combined microflares and jets. Naturally, just like it is observed, stronger microflare assumes the weaker jet and vice versa. A simple theory allows to easily perform quantitative analysis.

13.7 Problems

13.1 A strong magnetosonic shock wave propagating across the magnetic field may be subject of corrugation instability, when there appear a small oscillations on the shock front. Find conditions for the instability of shock front in the presence of Ohmic and viscous losses. Take the magnetic field directed along the z -axis and, respectively, electric field and current along the y -axis (Landau and Lifshitz 1987).

13.2 In case of a strong shock under certain conditions there may occur a radiative transfer of energy that drastically changes the after shock temperature. Find the condition for radiant heat exchange at a shock front and describe its phenomenology (Zeldovich and Raizer 1967).

13.3 A point blast explosion idealized as the sudden release of energy concentrated in a small volume generates a strong shock. This is one of the best known problem described by similarity solution (Sedov 1959).

- (a) Reproduce so-called Sedov-Taylor solution,
- (b) Describe the same solution by the rough estimates.

References

- P. Brekke, *Solar Phys.* **190**, 379 (1999)
 W. Curdt, H. Tian, *AandA* **532**, L9 (2011)
 K.P. Dere, Explosive events, magnetic reconnection, and coronal heating. *Adv. Space Res.* **14**, 13–22 (1994)
 A. Fludra, H. Warren, *AandA* **523**, 47 (2010)
 G. Guderley, *Luftfahrtforschung* **19**, 302–312 (1942)
 L.E. Gurevich, A.A. Romyantsev, *AJ* **13**, 908 (1969)
 R.A. Harrison et al., *Solar Phys.* **170**, 123 (1997)
 D.E. Innes, L. Teriaca, *Solar Phys.* **282**, 453 (2013)

- L.D. Landau, E.M. Lifshitz, *Fluid Mechanics* (Pergamon Press, Oxford, 1987)
- D. Luo, R. A. Chevalier, *ApJ* **435**, 815 (1994)
- P. Maltby et al., *ApJ* **6**, 284 (1986)
- J. E. Mendoza-Torres, J.P. Torres-Papaqui, K. Wilhelm, *AandA* **431**, 339 (2005)
- S.-I. Pai, *Magnetogasdynamics and Plasma Dynamics* (Springer, Berlin, 1962)
- M. P. Ryutova, *Sov. Phys. JETP* **67**(8), 1594 (1988)
- M.P. Ryutova, T.D. Tarbell, *ApJ* **541**, L29 (2000)
- M. Ryutova, S. Habbal, R. Woo, T. Tarbell, *Solar Phys.* **200**, 213 (2001)
- M. Ryutova, T. Tarbell, R. Shine, *Solar Phys.* **213**, 231 (2003)
- C.J. Schrijver et al., *ApJ* **487**, 424 (1997)
- L.I. Sedov, *Similarity and Dimensional Methods in Mechanics* (Academic Press, London, 1959)
- I.V. Sokolov, *Sov. Phys. Uspekhi* **33**, 960 (1991)
- K.P. Stanyukovich, *Unsteady Motion of Continuous Media* (Pergamon Press, Oxford, 1960)
- T. Tarbell, M. Ryutova, J. Covington, A. Fludra, *ApJ* **514**, L47 (1999)
- T. Tarbell, M. Ryutova, R. Shine, *Solar Phys.* **193**, 195 (2000)
- G.B. Whitham, *J. Fluid Mech.* **3**, 337 (1958)
- E.I. Zababakhin, I.E. Zababakhin, *Unboundad Cumulative Phenomena* (Nauka, Moscow, 1988)
- Ya.B. Zeldovich, Yu.P. Raizer, *Physics of Shock Waves and High-Temperature Hydrodynamic Phenomena* (Academic Press, New York, 1967)

Chapter 14

Photospheric Network as Energy Source for Quiet Sun Corona



Abstract In previous chapters, we studied post-reconnection processes resulted from interaction of photospheric flux tubes, embedded predominantly in non-magnetic environment. Higher in the atmosphere, magnetic field preserves its filamentary structures, but is surrounded by low beta-magnetized plasma. In this chapter, we will study post-reconnection processes occurring in the arbitrarily magnetized plasma. We will see that in this case a reconnection triggers various branches of MHD shocks, and cumulation of energy occurs higher in the atmosphere reaching coronal heights and beyond. We are still dealing here with the atmosphere above the rarefied ensembles of flux tubes. Thus imprint of quiet sun at coronal heights is the most expected outcome of post-reconnection processes occurring at all levels. Moreover, these processes seem to be the reliable energy source to fuel the fast solar wind which is rooted in coronal holes outside sunspots and active regions.

14.1 Post-reconnection Processes in Arbitrarily Magnetized Environment

In previous chapters, we studied post-reconnection processes resulted from constantly interacting photospheric flux tubes, and in particular, the evolutionary shocks that experience strong gradient acceleration in the sharply stratified photosphere/chromosphere region. We saw that a great variety of transition region radiative transients, microflares, jets, and their combinations can be explained by post-reconnection processes that evolve along many different ways depending on local physical parameters. Although all these processes occur far from the reconnection region, and in time when the system has long “forgot” the flux tube reconnection itself, the fact that the reconnection occurred at the photospheric level, i.e., in predominantly magnetic free environment, determines the range of parameters for radiative transients observed in the chromosphere/transition region.

In this chapter, we will see that similar processes occur when reconnection occurs above the surface in arbitrarily magnetized environment. In this case the post-reconnection shocks and their further evolution follow the same path as those

triggered by the photospheric reconnection, but final energy release occurs higher in the atmosphere, and the process itself fits different range of parameters.

14.1.1 Magnetic Loop Arcades in the Chromosphere

One of the key elements of the entire mechanism of energy production by reconnection of individual flux tubes is the *very existence* of intermittent magnetic structures, which implies that parameter β^* is finite:

$$\beta^* = \frac{P_{\text{ext}}}{B^2/8\pi} \geq 1 \quad (14.1)$$

This condition, which is always true for the photospheric flux tubes, also holds in highly inhomogeneous chromosphere and even corona. Let us estimate heights at which the condition (14.1) can still be applied. We use the reference model of the solar atmosphere given by Maltby et al. (1986). For example, the gas pressure at heights $h = 200, 500, \text{ and } 800 \text{ km}$, respectively, is: $p_e \simeq 2.65 \times 10^4 \text{ dyn cm}^{-2}$, $\simeq 1.77 \times 10^3 \text{ dyn cm}^{-2}$, $\simeq 18.9 \text{ dyn cm}^{-2}$. At $h = 200 \text{ km}$ $\beta^* \geq 1$ for magnetic field strength $B \leq 800 \text{ G}$, at $h = 500 \text{ km}$, $\beta^* \geq 1$ for $B \leq 160 \text{ G}$, and at $h = 800 \text{ km}$ for the magnetic field $\leq 60 \text{ G}$ $\beta^* \geq 1$ and there still will be an interface between the magnetic flux and the external plasma.

Figure 14.1 shows example of the chromosphere/transition region magnetic loop arcades taken by AIA instrument on the SDO on August 2, 2010. The well-defined thin magnetic loops forming such arcades is the most typical form of magnetic field at all heights of solar atmosphere. In other words, the filamentary structure of magnetic field is an intrinsic property of the solar atmosphere. This means that as far as the magnetic loops preserve their identity and have their well-defined boundaries with the environment, the post-reconnection processes will have qualitatively similar character as those under the photospheric conditions.

As the very first step, just like in the photosphere, magnetic field forming thin loops and being in equilibrium with environment after reconnection will still be confined in loops but now in strongly curved form. This as we know immediately leads to slingshot effect. As mentioned above, the parameter range for the initial stage of the process, and for subsequent steps, is of course different than those for photospheric reconnections.

The system of loops is usually long-living. It lives as long as photospheric magnetic flux concentrations serving as footpoints, last. The individual loops, however, are in constant motion, changing their shape and orientation. At any moment of time the neighboring loops may come close to each other at some point and reconnect. This is obviously a continuous process providing a continuous generation of post-reconnection shocks and subsequent energy release in various forms. In other words, ever evolving magnetic loop arcades are sites of cascades of shocks and appearance of microflares, supersonic jets, and their combinations.

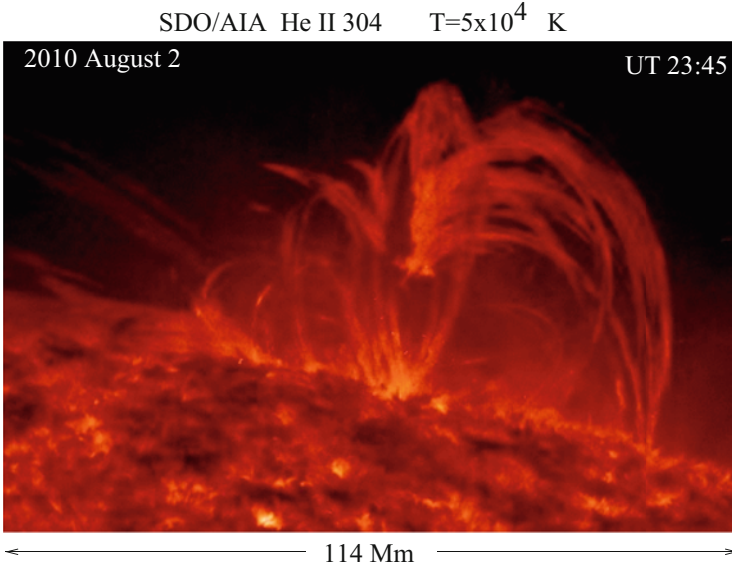


Fig. 14.1 Image of the magnetic loop systems at chromosphere/transition region temperatures taken by the SDO/AIA instrument in the He II 304 Å line. The very existence and dynamic stability of chromospheric loops implies the pressure equilibrium across the loops and favorable conditions for post-reconnection slingshot that generates microflares and jets

Figure 14.2 shows snapshots of the “same” arcade of loops as in Fig. 14.1 (i.e., loops rooted in the same magnetic region at the photosphere). These are different images made by subtracting the subsequent movie frames with 60 s interval to increase the contrast. Three instances of time show the system in different phases. At UT 19:19 a nice shaped arcade looks quite peaceful, but harbors several strong microflares (marked by arrows). White frame in this panel is the area occupied by loop system shown in Fig. 14.1. At UT 19:27 (middle panel) a well-developed supersonic jet continues to raise. The right panel shows the maximum phase of the jet. The loop system has been significantly reorganized.

Thus, rooted in the photospheric small-scale network magnetic elements, magnetic loops form arcades of different sizes in the chromosphere/transition region. In these ever evolving arcades magnetic loops may reconnect at any time at any given height. And, of course, the reconnection occurs in various environments. The most typical cases are shown in Fig. 14.3. Dark crosses mark the reconnection regions. Numbers correspond to different magnetic status of environmental plasma in the vicinity of reconnection region. Reconnections marked by #1 occur in magnetic free environment. #2 corresponds to reconnections occurring in vicinity of vertical magnetic field. In cases marked by #3 the neighboring magnetic field makes some angle with gravity force, and #4 is when external magnetic field is almost horizontal.

The post-reconnection waves generated in these different cases will have different properties depending on the magnetic status of the environmental plasma. The

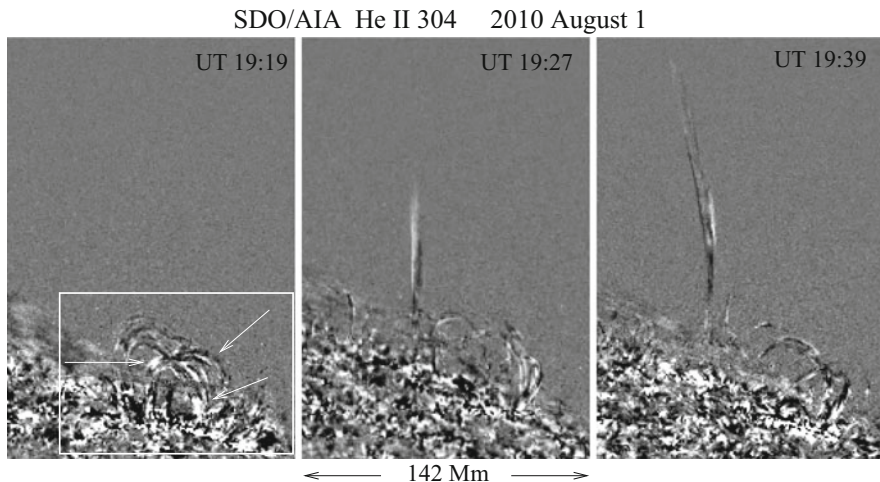


Fig. 14.2 Example of microflares and strong supersonic jet originated in the magnetic loop arcades at the chromosphere/transition region temperatures. To increase a contrast, the images were obtained by subtracting the subsequent movie frames with 60 s interval. The left panel shows one of “quiet” moments of the arcade exhibiting a few microflares (marked by arrows); white frame is the area occupied by loop system shown in Fig. 14.1. At UT 19:27 (middle panel) a well-developed jet reaches a projection height of about 100 Mm. The right panel shows the maximum phase of the jet

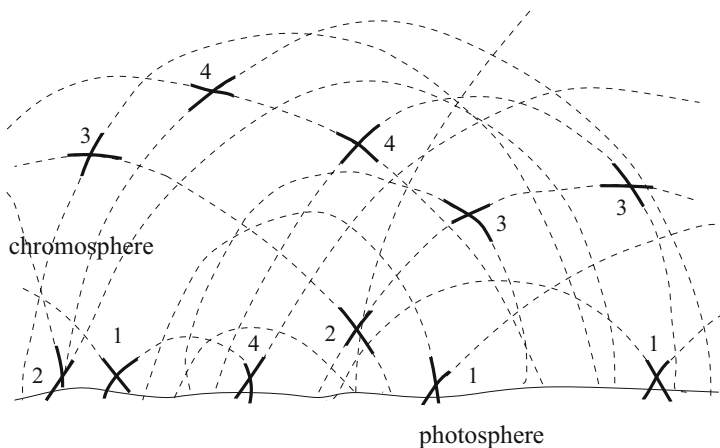


Fig. 14.3 Sketch of magnetic structures above the photosphere and examples of reconnection regions in different magnetic environments. Numbers correspond to different magnetic status of plasma in the vicinity of reconnection region: #1 is magnetic free case; #2 corresponds to vertical magnetic field near reconnection region (i.e., parallel to gravity force); #3 is when magnetic field makes some angle with gravity force, and #4 is when external magnetic field is almost horizontal

evolution of shocks and final energy release will be also different. Detailed analysis of each case will be considered below. Before doing this we need to emphasize the direction of energy transport.

It is important that in any case, whether the environment is nonmagnetic or there is a magnetic field having parallel, oblique, or perpendicular direction with respect to the gravity force, the most efficient energy transfer provided by the post-reconnection shocks occurs in the direction of decreasing density, i.e., *always radially outward* from solar surface.

The fact that the energy released due to the post-reconnection processes in the environment of arbitrary magnetic topology is carried out radially outward is extremely important for understanding one of the puzzles associated with the fast solar wind. It was found (Woo 1996; Woo and Habbal 1999) that the fast solar wind is organized in a form of small-scale filamentary ray-like structures.

Observations of density and velocity distribution in the outer corona obtained from radio occultation measurements (Woo 1996; Woo and Habbal 1999) showed, for example, that the density profile closest to the Sun at $1.15 R_{\odot}$, representing the imprint of the Sun, is carried radially into interplanetary space by small-scale ray-like structures that pervade the entire solar corona. Moreover, a significant fraction of mass fluxes which extend into interplanetary space originate from the quiet sun and the coronal hole areas (Cranmer 2009; Nistico et al. 2011; Zhao et al. 2014).

Hassler et al. (1999) have also reported on the connection between the fast solar wind outflow and the chromospheric magnetic network. This means that the mechanism responsible for the formation of fast solar wind must not only connect the roots of the wind with the chromospheric network, but also explain how generated flows are guided through strongly inhomogeneous atmosphere radially outward. From this perspective the post-reconnection processes occurring in very different magnetic regions, but always carrying energy radially outward, seem to be the most reliable mechanism.

14.1.2 *Post-reconnection Shocks in Upper Atmosphere: Types and Characters*

To illustrate the basic properties of post-reconnection processes in arbitrarily magnetized environment, characteristic to upper atmosphere, we consider a two-dimensional problem with $\mathbf{B}_0 = (B_{0x}, B_{0z})$, and assume that all the equilibrium parameters depend only on the coordinate z , directed along the gravity force, $\mathbf{f}_g = -gz$.

2D nonlinear MHD equations, in Riemannian coordinates (method of characteristics, see, e.g., Landau and Lifshits 1987, Whitham 1974) reduce to a single equation for z -component of the velocity $u(z)$ which, for homogeneous medium, has a form of the simple wave:

$$\frac{\partial u}{\partial t} + [v + \alpha u] \frac{\partial u}{\partial z} = 0, \quad (14.2)$$

whose parameters are constant at fixed characteristics

$$\frac{dz}{dt} = v + c_s, \quad (14.3)$$

where $c_s = (\partial p / \partial \rho)$ is a sound speed, and v is characteristic velocity (Jeffrey and Taniuti 1964):

$$v_{\pm}^2 = \frac{1}{2} \left\{ c_s^2 + \frac{B^2}{4\pi\rho} \pm \sqrt{\left(c_s^2 + \frac{B^2}{4\pi\rho} \right)^2 - \frac{c_s^2 B_z^2}{\pi\rho}} \right\} \quad (14.4)$$

$B^2 = B_x^2 + B_z^2$, and α is a coefficient of nonlinearity:

$$\alpha = \frac{1}{v} \left[\frac{\partial(v\rho)}{\partial\rho} + \frac{4\pi\rho(v^2 - c_s^2)}{B_x} \frac{\partial v}{\partial B_x} \right] \quad (14.5)$$

Note that other quantities, e.g., transverse velocity $u_x(z)$ and the magnetic field $B_x(z)$ evolve according to linear equations: in these quantities nonlinearity appears in higher order (Sagdeev 1966; Sokolov 1991; Ryutova and Sakai 1993).

In the stratified medium, nonlinear distortions of the wave profile can still be described by a Riemann equation if the spatial scale of nonlinear perturbations is assumed to be small compared to the scale height. In this case all the wave parameters vary slowly on characteristics, and (14.2) acquires a form of a quasi-simple wave with non-zero body force, $F(\rho, B, v)$ in its right-hand side (Asano and Taniuti 1969; Ostrovskii and Rubakha 1974):

$$F(z) = v^2(z) \frac{1}{W(z)} \frac{dW(z)}{dz} \quad (14.6)$$

where

$$W(z) \simeq \left[\frac{\rho(z)v(z)}{\rho_0 v_0} \right]^{-1/2} \quad (14.7)$$

with $\rho(z)$ and $v(z)$ being the values of density and characteristic velocity in the undisturbed gas ahead of the shock front; subscript "0" marks their initial values. The solution of (14.2) with the body force (14.6) is a quasi-simple wave (Landau and Lifshits 1987; Ostrovskii and Rubakha 1974):

$$t - \int_0^z \frac{dz'}{v_{\pm}(z')} + \frac{u}{W(z)} \int_0^z \frac{\alpha W}{v_{\pm}^2(z')} dz' = \Phi \left(\frac{u}{W} \right), \quad (14.8)$$

where Φ is a function determined by the boundary conditions.

The height of shock formation and its amplitude are determined by simultaneous conditions on the derivatives of (14.8) (Landau and Lifshits 1987):

$$\frac{\partial t}{\partial u} = 0, \quad \frac{\partial^2 t}{\partial u^2} = 0 \quad (14.9)$$

For a given magnetic field geometry two branches of the velocity $v_{\pm}(z)$ ((14.4)) determine two independent characteristics along which nonlinear MHD waves evolve.

We know that thin magnetic loops forming canopy-shaped arcades of different sizes is an intrinsic property of the solar atmosphere from the chromosphere to corona. In these arcades magnetic flux tubes may collide and reconnect. Notably, the reconnections may occur in the differently magnetized environment. As shown in Fig. 14.3 there are basically four most typical cases marked by numbers 1–4.

Below we describe these four cases in more detail, and illustrate them in Fig. 14.4. Case numbers 1–4 correspond to cases marked by the same numbers in Fig. 14.3.

No. 1 corresponds to the case when intense magnetic flux tubes collide at the photosphere level in totally magnetic free environment (the external plasma $\beta \gg 1$). Therefore, a slingshot effect generates pure acoustic waves,

$$v_{\pm} = c_s \quad (14.10)$$

Propagating upward these waves steepen and become shocks with complex wavy surfaces, whose further evolution leads to strong hydrodynamic cumulation and production of high-energetic events as we have seen in the previous chapter.

No. 2 is the process when flux tubes collide and reconnect in the vicinity of some vertical magnetic field, $B_x \ll B_z$. This case is typical for areas at or slightly above the surface where magnetic field tends to be vertical. It may be realized as well in higher layers of the atmosphere underlying coronal hole regions where the “background” magnetic field is predominantly vertical. In this case the slingshot effect generates MHD waves, and characteristic velocity (14.4) has two branches: the upper branch is a pure acoustic wave, while the lower branch corresponds to the Alfvén wave, propagating along the vertical magnetic field:

$$v_+ = c_s, \quad v_- = \frac{B_z}{\sqrt{4\pi\rho}} \quad (14.11)$$

No. 3 corresponds to the case when the slingshot effect operates in an arbitrarily oriented magnetic field which is typical of magnetic canopies, i.e. throughout entire solar atmosphere. Two branches of (14.4) correspond to the fast and slow MHD waves with phase velocities (respectively, v_+ and v_-):

$$v_+ = \frac{B}{\sqrt{4\pi\rho}}, \quad v_- = c_s \cos\theta \quad (14.12)$$




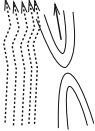
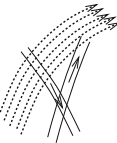

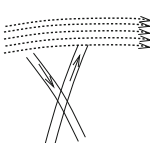
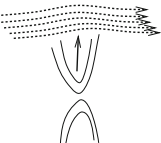
Case No.	External Magnetic field	Characteristic Velocities	Flux Tubes Prior Reconnection	Sling-shot Effect	Aftereffect
1	$\vec{B} = 0$ (Non-magnetic environment)	$v_{\pm}^2 = c_s^2$			Acoustic Shocks Jets Microflares
2	$B_x \ll B_z$ (Vertical field)	$v_+^2 = c_s^2$ $v_-^2 = \frac{B_z^2}{4\pi\rho}$			Acoustic Shocks & HF Alfvén Waves Jets Microflares
3	$B_x = B \sin\theta$ $B_z = B \cos\theta$	$v_+^2 = \frac{B^2}{4\pi\rho}$ $v_-^2 = c_s^2 \cos^2\theta$			Acoustic & MHD Shocks; HF Alfvén Waves Jets Flares
4	$B_x \gg B_z$ (Horizontal field)	$v_{\pm}^2 = c_s^2 + v_A^2$			Fast MHD Shocks Jets Flares

Fig. 14.4 Reconnection of magnetic flux concentrations in nonmagnetic (case No. 1) and magnetic (cases No. 3–No. 4) environments. The second column shows external magnetic field, the next column shows the characteristic velocities; the fourth and fifth columns depict the flux tubes prior and after the reconnection, and the last column contains a slingshot outcome

where θ is the angle between the z -axis and the magnetic field ($B_x = B\sin\theta$, $B_z = B\cos\theta$). Only for this case we assume that plasma beta is small (actually, $\beta \leq 0.1$ is already a good approximation).

No. 4 is the case when the shock is formed in the presence of a predominantly horizontal magnetic field. In this case ($B_z = 0$), the characteristic velocity (14.4) then has only one root corresponding to fast magnetosonic waves:

$$v_+ = \sqrt{c_{s0}^2 + v_{A0}^2} \tag{14.13}$$

This situation is readily realized in upper chromosphere where magnetic fields form a hierarchy of canopies. It is also often met in lower atmosphere, especially in regions occupied by compact bipoles. In high-beta plasma the process is similar to that of the acoustic shocks, while in low-beta plasma the process is dominated by the properties of nonlinear Alfvén waves.

In all cases considered above it is the acoustic component that provides the action of strong hydrodynamic cumulation, i.e., transport of energy by post-reconnection acoustic shocks, and subsequent formation of radiative transients and collimated jets. As we will see below, formation of shocks associated with the Alfvén component occurs in a restricted range of parameters, but frequency of these waves may be quite high.

14.2 Heights of Shock Formation

To find the height of shock formation and the shock amplitude, we use (14.8) and (14.9) and specify boundary conditions by assuming that the kick produced by slingshot effect has a form of sinusoidal pulse with the initial velocity v_A :

$$u(0, t) = \begin{cases} v_A \sin \omega t & 0 \leq t \leq \pi/\omega \\ 0 & t > \pi/\omega \end{cases} \quad (14.14)$$

where $\omega \simeq v_A/R$ (R being a characteristic radius of reconnecting flux tubes). Then the function Φ in (14.8) acquires a form:

$$\Phi(u, W) = \frac{1}{\omega} \sin^{-1} \left(\frac{u}{v_A W} \right) \quad (14.15)$$

With this function the first of two conditions (14.9) gives:

$$- \int_0^z \frac{\alpha(z') W(z')}{v_{\pm}^2(z')} dz' + \frac{1}{\omega \sqrt{v_A^2 - (u/W)^2}} = 0 \quad (14.16)$$

The second condition, $\partial^2 t / \partial \alpha^2 = 0$, gives

$$\frac{1}{\omega [v_A^2 - (u/W)^2]^{3/2}} = 0 \quad (14.17)$$

Thus, the shock formation occurs at the height z_{sh} , determined by the integral (14.16), with $u = 0$:

$$\int_0^{z_{sh}} \frac{\alpha W(z')}{v_{\pm}^2(z')} dz' = \frac{R}{v_A^2} \quad (14.18)$$

The shock amplitude, $u(z)$ as a function of height, can be found from (14.16).

A crucial role in the height of shock formation and the amplitude of the shock is played by parameters $\alpha(z)$ and $W(z)$, which in fact reflects thermodynamic properties of medium and its magnetic status.

To solve (14.16) and (14.18) one needs to use a specific model of the atmosphere, and, in principle, take into account a back reaction of the temperature on the propagation of shock waves. Here we restrict ourselves by description of basic properties of the energy transfer process associated with the post-reconnection shocks produced at different heights and in differently magnetized regions of a low atmosphere. For this we assume that the equilibrium atmosphere is an ideal gas ($p = (k/m)\rho T$) and the temperature gradient is adiabatic, $(dT/dz) = [(\gamma - 1)/\gamma](gm/k)$. For γ we will use below $\gamma = 5/3$ and a harmonic mean value $\gamma = 1.29$.

As shown in Fig. 14.4, pure acoustic branch is a necessary component in almost all cases (even the case No. 4 for a weak external field drops into this category). This means that in any magnetic field geometry one of the channels of the energy transport and its release is governed by properties of the acoustic shocks.

To illustrate the general properties of the shock formation, first we consider the acoustic branch and then discuss the fast MHD wave associated with $v_+ = B/\sqrt{4\pi\rho}$ ($B = \sqrt{B_x^2 + B_z^2}$).

For the acoustic waves the parameters $\alpha(z)$ and $W(z)$ are as follows:

$$\alpha_+ = \frac{\gamma + 1}{2}, \quad W = \exp\left(\frac{\gamma + 1}{4} \frac{z}{\Lambda}\right) \quad (14.19)$$

Equation (14.18), determining the height of the shock formation becomes as follows:

$$\frac{\gamma + 1}{2c_{s0}^2(0)} \int_0^{z_{\text{sh}}} \exp\left(\frac{5\gamma - 3}{4} \frac{z'}{\Lambda}\right) dz' = \frac{R}{v_A^2}, \quad (14.20)$$

Integrating this equation yields:

$$\frac{1}{z_{\text{sh}}^{(0)}} \frac{4\Lambda}{(5\gamma - 3)} \left[\exp\left(\frac{5\gamma - 3}{4} \frac{z}{\Lambda}\right) - 1 \right] = 1 \quad (14.21)$$

where $z_{\text{sh}}^{(0)}$ is the height of shock formation in an unstratified atmosphere ($\Lambda \rightarrow \infty$):

$$z_{\text{sh}}^{(0)} = \frac{2}{\gamma + 1} \frac{c_{s0}^2}{v_{A0}^2} R \quad (14.22)$$

(14.21) immediately gives the expression for the height of the shock formation in the stratified atmosphere:

$$z_{\text{sh}} = \frac{4}{5\gamma - 3} \Lambda \ln \left(1 + \frac{5\gamma - 3}{4} \frac{z_{\text{sh}}^{(0)}}{\Lambda} \right) \quad (14.23)$$

For the Alfvén branch out of (14.12) the height of shock formation is as follows (Asano and Taniuti 1969; Ostrovskii and Rubakha 1974):

$$z_{sh} = \frac{4}{3} \Lambda \ln \left[1 - \frac{3}{4} \frac{z_{sh}^{(0)}}{\Lambda} \right]^{-1} \tag{14.24}$$

with $z_{sh}^{(0)} \simeq (2/3)R$.

Figure 14.5 shows the height of the shock formation in stratified atmosphere z_{sh} , normalized to its value in the unstratified medium, $z_{sh}^{(0)}$: solid and dashed lines correspond to the acoustic branch, while dash-dotted line to Alfvén waves. Naturally, the acoustic shock formation in the stratified atmosphere for upward propagating waves occurs at lower heights than in the homogeneous medium, as always $z_{sh} < z_{sh}^{(0)}$. At the same time, for essentially different specific heat ratios there is a little difference between the corresponding values of z_{sh} . In both cases it decreases monotonically with decreasing scale height and remains almost the same for $\gamma = 1.29$ and $\gamma = 5/3$. We will see below that the shock amplitude, on the contrary, is very sensitive to thermodynamic properties of medium.

Unlike the acoustic waves, the shocks associated with the Alfvén waves are formed in the stratified atmosphere at much higher altitudes than in the homogeneous medium. The height of their formation quickly increases with decreasing scale height, and if the parameters of medium and magnetic field are such that $z_{sh}^{(0)} > (4/3)\Lambda$, the shocks associated with Alfvén waves do not develop at all (see (14.17)). This threshold is marked by dotted line in Fig. 14.5. Physically this

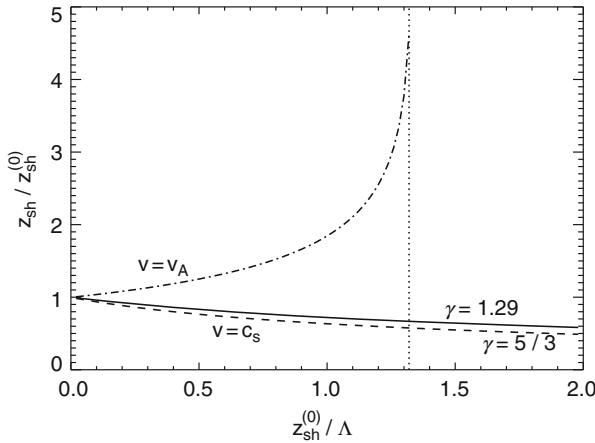


Fig. 14.5 Height of the shock formation in stratified atmosphere, z_{sh} , vs its value in the unstratified medium, $z_{sh}^{(0)}$: *solid and dashed* lines correspond to the acoustic branch, while *dash-dotted* line to Alfvén waves. The *dotted* line is a boundary beyond which (to the right) the shocks associated with Alfvén waves do not develop

means that in photosphere/chromosphere region where scale height is small, the formation of Alfvén shocks is not favorable even in the presence of strong magnetic fields, i.e., in low atmosphere (or in any other height where $z_{\text{sh}}^{(0)} > (4/3)\Lambda$) the generated Alfvén waves will rather participate in other nonlinear processes. For example, they may release the energy through the strong phase mixing or evolve into solitary waves.

It is important to note that the frequency of these waves may be quite high—the fact consistent with observations. The theoretical value of characteristic frequency can be estimated as $\omega \simeq 2\pi w/R$, where w is the reconnection rate,

$$w = v_A / \ln Re_m, \quad (14.25)$$

Re_m being a magnetic Reynolds number (Petschek 1964). R is a characteristic size of reconnection area. Remember that we deal with the post-reconnection processes, and that the waves are generated by post-reconnection slingshot. For the photosphere and low chromosphere, the characteristic radius of magnetic flux participating in one act of reconnection is $R \sim 35 - 70$ km (Tarbell et al. 1999, 2000; Ryutova and Tarbell 2000). Quantitative estimates are as follows. Magnetic Reynolds number in these regions is $Re_m \sim 10^3 - 10^6$. If we take $R \sim 40$ km, then in the photosphere region for $v_A \simeq 10$ km s⁻¹, $\omega \sim 0.11 - 0.23$ s⁻¹, in low chromosphere, for $v_A \simeq 50$ km s⁻¹, $\omega \sim 0.6 - 1.14$ s⁻¹; at $v_A \simeq 100$ km s⁻¹, $\omega \sim 1.14 - 2.27$ s⁻¹.

The shock amplitude immediately after the shock formation, $u_{\text{sh}}(z)$ as a function of altitude and scale height can be found by evaluating the integral in (14.16) for given parameters α , $W(z)$ and $z_{\text{sh}}^{(0)}$, and resolving the equation with respect to $u(z)$. The results of these calculations for the acoustic and Alfvén waves are shown in Figs. 14.6 and 14.7, respectively. Two values of $z_{\text{sh}}^{(0)}/\Lambda = 0.6, 1.0$, have been used.

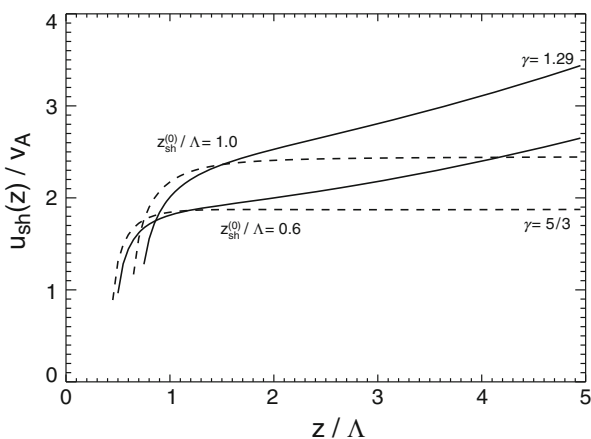


Fig. 14.6 The shock amplitudes at the moment of the shock formation as a function of height for the acoustic branch. Solid lines correspond to $\gamma = 1.29$, and dashed lines to $\gamma = 5/3$

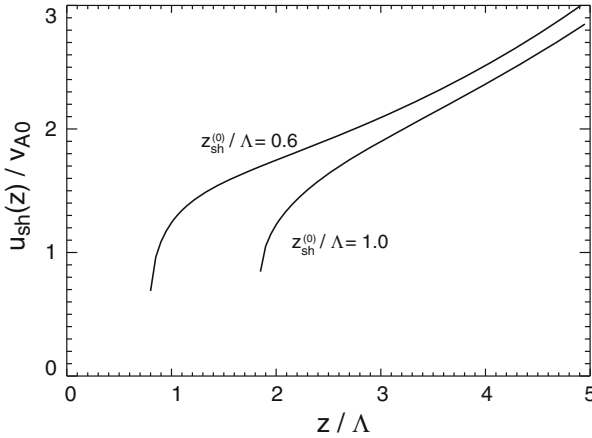


Fig. 14.7 The same as in Fig. 14.6 but for the Alfvén waves. Unlike the acoustic waves the amplitude of the Alfvén waves grows exponentially at high altitudes

One can see that immediately after the shock is formed, its amplitude sharply increases in all cases whether it is acoustic or Alfvén wave. At large heights the amplitude of the acoustic shock is proportional to $\exp[(5 - 3\gamma)/8]$, and for monatomic gas it reaches some constant value (at about Mach numbers $M \simeq 2$). For medium with $\gamma = 1.29$, the shock amplitude grows exponentially as $\sim \exp(0.14z/\Lambda)$. The amplitude of the Alfvén shocks at large distances is proportional to $\exp(z/4\Lambda)$, providing their fast exponential growth with height (Fig. 14.7). Such a behavior of the shock amplitude, however, is valid only up to the altitudes of $2.5\text{--}3\Lambda$ from the height of shock formation or up to the heights where Mach number reaches quite moderate values of $1.5\text{--}2$ (which is earlier). As one can see from Figs. 14.6 and 14.7, in all cases this happens approximately at about the same time. After which the shock amplitude becomes independent of the Mach number and being subject to gradient acceleration, increases in accordance with the power law (Whitham 1974; Landau and Lifshits 1987):

$$u_{\text{sh}} = u_0(\rho_0/\rho)^\kappa \tag{14.26}$$

where u_0 and ρ_0 are shock velocity and pre-shock plasma density at the reference point, and $\kappa = [2 + \sqrt{2\gamma/(\gamma - 1)}]^{-1}$. For $\gamma = 5/3$, $\kappa = 0.236$ and for $\gamma = 1.29$, $\kappa = 0.201$. Below we will use the results of this section for some quantitative estimates.

14.3 Energy Release in the Chromosphere-Transition Region

The universal character of the mechanism which works in wide range of physical parameters and in any place where magnetic flux tubes or loops collide and reconnect makes the after-shock jets and radiative transients ubiquitous throughout the entire atmosphere overlying the quiet sun. To look into the mechanism deeper and use it in practice let us make some quantitative estimates based on the observational data.

14.3.1 Quantitative Analysis

Consider again example demonstrating direct connection between the changes of the photospheric fields and their association with the transition region plasma flows and bright radiative transients (Fig. 14.8). The upper panels are the MDI magnetogram of the $66'' \times 85''$ area at some instance of time and C IV image of the same region together with the SUMER spectra showing how the enhanced emission in the chromosphere/transition region mimics the photospheric magnetic pattern. The middle panel shows the time variation of positive and negative magnetic fluxes in the area marked by red square in the MDI magnetogram, and corresponding changes in the C IV intensity over this area (red line). The lower panel is the co-aligned time variation of SUMER spectra in C II (green) and O VI (blue) lines. The most prominent radiative transients produced above chosen area are marked by numbers 1, 2a, 2b, and 3.

The radiative transients highlighted in (Fig. 14.8) have very characteristic features and precursors that are most typical of the majority of the observed bright and high velocity events. The event marked by “1” corresponds to energy release in a form of a microflare alone without significant flows. Two similar events marked by “2a” and “2b” are typical to the “HEAT-JET” regime when highly concentrated cumulative energy is distributed between the radiative transient (having the enhanced intensity in the C IV line) and plasma jets (cf. Fig. 14.5, Chap. 13). The event marked by “3” corresponds to pure jet regime. It is remarkable that before this event quite significant portion of negative magnetic flux has been moved into the marked area. Simultaneous reduction of this newly emerged negative and pre-existed positive fluxes resulted in the series of events, the strongest of which are marked by “3” and “2b.”

As discussed throughout the book, these regularities are universal features of the energy build up process that starts from the reconnection of opposite polarity elements passes through shock formation, then through shock-shock interaction that results in the release of energy in upper layers of atmosphere in one of the three forms:

1. microflare;
2. microflare accompanied by plasma jets; and
3. only plasma jets.

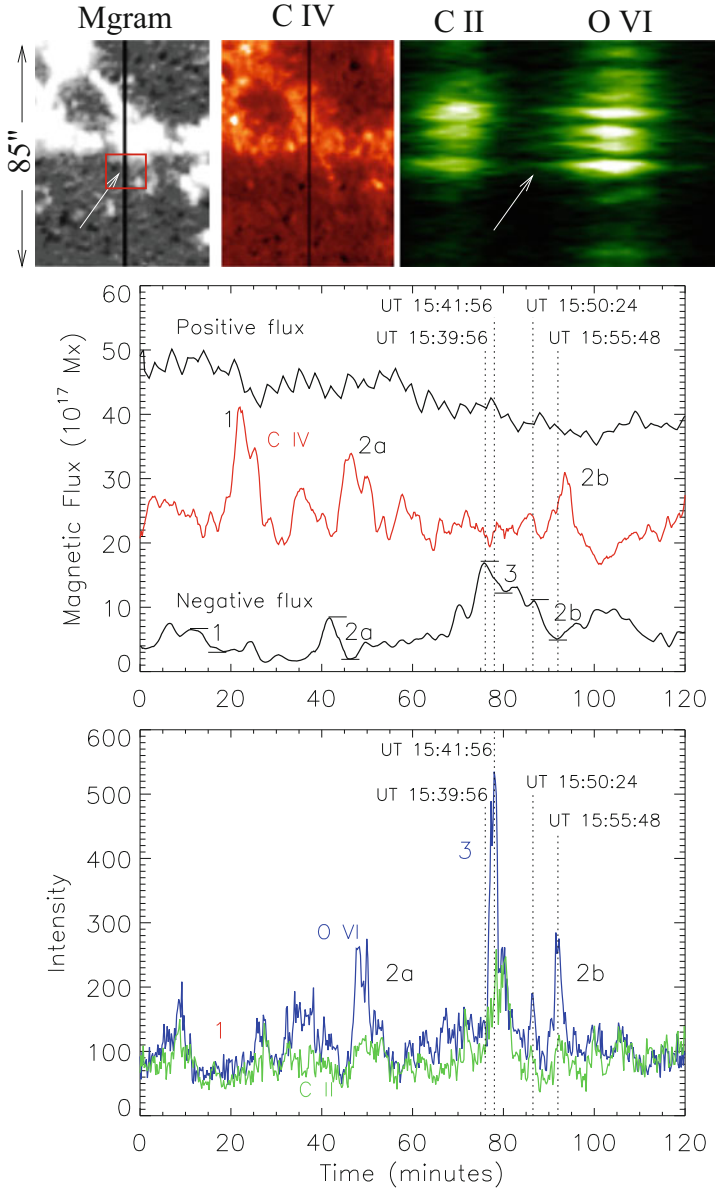


Fig. 14.8 Microflares and jets produced by reconnecting flux tubes. Upper panels are the magnetogram, chromosphere in C IV line and corresponding SUMER spectra with mass flows in lower chromosphere (C II line) and transition region (O VI line); a small region marked by a red square in the MDI magnetogram is where the studied reconnection occurred. Middle panel shows the time variation of positive and negative magnetic fluxes in the marked area, and corresponding changes in the C IV intensity over this area (the red line); Lower panel is time variation of SUMER spectra in C II (green) and O VI (blue) lines; Numbers 1, 2a, 2b, and 3 label the events used for quantitative estimates

The largest range of physical parameters corresponds to energy distribution between the radiative transients and plasma flows. Usually weaker microflare is accompanied by a stronger jets and v.v.

The time history of the photospheric magnetic fluxes (Fig. 14.8, middle panel) shows, as always, a clear connection between the magnetic flux reduction and subsequent appearance of energetic events in the chromosphere-transition region. Before we discuss these particular events in detail, let us recall that in each reconnection process only a limited portion of the magnetic flux is involved. For typical magnetic flux tubes in the photosphere a characteristic radius of magnetic flux tube participating in one elemental act of reconnection is $\sim 40\text{--}100$ km (Tarbell et al. 2000). Usually, colliding flux tubes are of different sizes, but each reconnection reduces the magnetic flux of either polarity by equal amounts. In our example the positive magnetic flux belongs to a large magnetic flux concentration while the negative flux is small and isolated. Although the positive flux decreases with time, its sawtooth character caused by the measurements taken at the edge of magnetic conglomerate is not as informative as time variation of the negative flux.

For quantitative estimates we will use the measurements of the negative magnetic flux (lower curve in Fig. 14.8, middle panel). For the background photospheric parameters we adopt a reference model by Maltby et al. (1986) where at “zero” level, ($z = 0$) the plasma density $\rho \simeq 2.8 \times 10^{-7}$ g cm $^{-3}$ and the temperature $T = 6500$ K; the sound speed $c_s = 8.5$ km s $^{-1}$, and the scale-height $\Lambda \simeq 160$ km.

First, we need to estimate the height of the shock formation, z_{sh} , Eq. (14.23), and the shock amplitude at this height which can be obtained from (14.16):

$$u_{\text{sh}}(z) = v_{A0} + v_{A0} \exp\left(\frac{\gamma + 1}{4} \frac{z}{\Lambda}\right) \frac{\sqrt{[\mathcal{I}(z) - 1]}}{\mathcal{I}(z)} \quad (14.27)$$

where $\mathcal{I}(z)$ is the left-hand side expression of (14.21) with the running coordinate z instead of the fixed one z_{sh} :

$$\mathcal{I}(z) = \frac{4\Lambda}{(5\gamma - 3)z_{\text{sh}}^{(0)}} \left[\exp\left(\frac{5\gamma - 3}{4} \frac{z}{\Lambda}\right) - 1 \right] \quad (14.28)$$

Note that at $z = z_{\text{sh}}$, $\mathcal{I}(z_{\text{sh}}) = 1$, by definition. v_{A0} is the pre-shock velocity of the wave generated initially by the post-reconnection slingshot effect. This velocity is determined by the magnetic flux participating in the reconnection process, $\Delta\Phi = \pi R^2 B$, and the reconnection rate, (14.16), or time, $\tau = R \ln Re_m / v_A$. For the quantitative estimates we will use for $\Delta\Phi$ the measured drops of the magnetic flux and for τ the corresponding observed times in which these drops occur.

Excluding from $\Delta\Phi$ and τ the radius of the magnetic flux, we obtain an estimate for the Alfvén velocity:

$$v_A^3 = \frac{\Delta\Phi}{\pi\sqrt{4\pi\rho}} \left[\frac{\ln Re_m}{\tau} \right]^2 \quad (14.29)$$

With the magnetic Reynolds number $Re_m \simeq 10^3$ typical to the photosphere (cf. Parker 1979), measured times and corresponding magnetic flux changes give for the events 1, 2a, 2b, and 3, respectively, $v_A = 3.61 \text{ km s}^{-1}$; 4.18 km s^{-1} ; 4.12 km s^{-1} and 4.5 km s^{-1} . These are typical values for the Alfvén velocities in the photospheric flux tubes with magnetic field strength ranging from 500 to 1000 G: $v_A = 2.7\text{--}5.3 \text{ km s}^{-1}$.

The radius of the magnetic flux participating in the reconnection process is estimated as $R = \tau v_A / \ln Re_m$, which gives for these four events the values: 132, 163, 161, and 137 km. Now we can find the height of shock formation corresponding to given parameters in the homogeneous atmosphere, $z_{sh}^{(0)}$, using (14.22), and respectively, the height of the shock formation in the stratified atmosphere, z_{sh} , using Eq. (14.27). We then find the shock amplitude, $u_{sh}(z)$. Results of these calculations are shown in Table 14.1 and Fig. 14.9.

One can see that height of the shock formation u_{sh} is very close to the solar surface: from these heights shock wave quickly accelerates, and in a few scale

Table 14.1 Parameters and results of quantitative estimates

Events	1	2a	2b	3
$\Delta\Phi$ (10^{17} Mx)	3.7	6.6	6.3	5.0
τ (s)	252	270	270	120
v_{A0} (km s^{-1})	3.61	4.18	4.12	4.5
\tilde{R} (km)	132	163	161	137
$z_{sh}^{(0)}$ (km)	549	505	514	370
z_{sh} (km)	206	198	199	169
z_{sh}^{sat} (km)	750	780	780	800
u_{sh}^{sat} (km s^{-1})	14.5	16.0	16.2	19.3
M_0	1.7	1.9	1.9	2.3

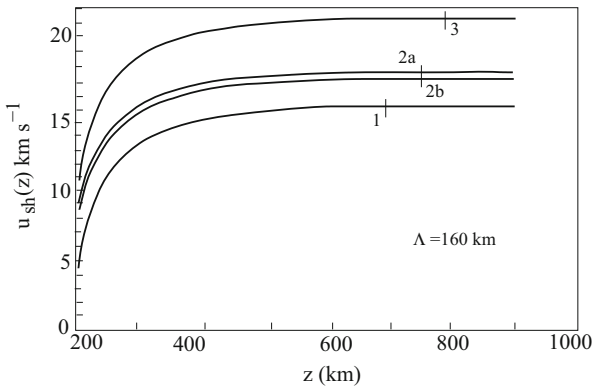


Fig. 14.9 The shock velocity for chosen events as a function of height. The vertical bars indicate the approximate height at which the shock amplitude saturates

heights gets saturated. Figure 14.9 shows the shock velocity as a function of the atmospheric height ($z=0$ corresponds to $\rho \simeq 2.8 \times 10^{-7} \text{ g cm}^{-3}$ and $T = 6500 \text{ K}$). The vertical bars indicate the height at which the shock amplitude saturates: from there the velocity of shock, which becomes independent of the Mach number and scale height, increases in accordance with the power law, (14.26), i.e., as

$$u_{\text{sh}}(z) = u_{\text{sh}}^{\text{sat}} \left[\frac{\rho(z)}{\rho_{\text{sat}}} \right]^{0.236} \quad (14.30)$$

As expected, the shock amplitude saturates at Mach numbers $M_0 \sim 1.5\text{--}2$ (see last line in Table 14.1). The corresponding heights are between 750–800 km. The mass density here is $\rho_{\text{sat}} \simeq 4 \times 10^{-10} \text{ g cm}^{-3}$. At height $z = 2000 \text{ km}$ ($\rho \simeq 3 \times 10^{-13} \text{ g cm}^{-3}$) (14.30) gives following estimates for the shock velocities produced, respectively, in the events 1, 2a, 2b, and 3: 79 km s^{-1} , 87 km s^{-1} , 88 km s^{-1} , and 105 km s^{-1} .

To estimate a behind shock temperature, $T_2 = M^2 T_1 (3\gamma - 1)\gamma^{-1}$, at this height we adopt for the sound speed the value 13 km s^{-1} and background temperature $T_1 = 7300 \text{ K}$. Then Mach numbers for each event are: $M^{(1)} = 6.1$; $M^{(2a)} = 6.7$; $M^{(2b)} = 6.8$; $M^{(3)} = 8$. Respectively, the behind shock temperatures are $T_2^{(1)} = 8.5 \times 10^4$; $T_2^{(2a)} = 10.2 \times 10^4$; $T_2^{(2b)} = 10.5 \times 10^4$; $T_2^{(3)} = 1.46 \times 10^5$.

The obtained estimates are the most typical for the measured and inferred physical parameters of the chromosphere and transition region.

14.3.2 Total Energy Flux in Quiet Sun Atmosphere

The total energy flux released by the entire quiet sun “magnetic carpet” is consistent with the observed UV/EUV radiation. It can be estimated on the basis of observed time scale ($\sim 40 \text{ h}$) in which the total magnetic field in the quiet sun network is replaced (Title and Schrijver 1997). The energy release in each event of the reconnection is on the order of

$$W_{\text{mag}} \simeq \frac{B^2}{8\pi} SL \quad (14.31)$$

where S is the cross section of the interacting area, $S = \pi R^2$, and L is a characteristic length of the flux tube. In the quiet sun the magnetic filling factor, $f \simeq (S/d^2) \ll 1$ (d being a characteristic distance between the flux tubes). Let the velocity of relative motion of colliding flux tubes be v_T , then a “collision” rate in the system of non-collinear flux tubes, n_{Ψ} , may be estimated as $n_{\Psi} \simeq v_T/d$. The number of events per unit area of solar surface per unit time is $N = n_{\Psi}/d^2$. The energy released per unit area of solar surface per unit time is:

$$E = \frac{B^2}{8\pi} S L \frac{1}{d^2} \frac{v_T}{d} \simeq \frac{B^2}{8\pi} f v_T \quad (14.32)$$

or in terms of a mean flux density $\bar{B} = B(S/d^2) = Bf$,

$$E = \frac{\bar{B}^2}{8\pi} \frac{v_T}{f} \quad (14.33)$$

The velocity v_T can be estimated as $v_T = d/\tau$, where τ is the time of the total replacement of the quiet sun magnetic flux, $\tau \simeq 40$ h (Title and Schrijver 1997). This gives:

$$E = \frac{\bar{B}^2}{8\pi} \frac{v_T}{f} = \frac{\bar{B}^2}{8\pi} \frac{d}{f\tau} = \frac{\bar{B}^2}{8\pi} \frac{\sqrt{S}}{f^{3/2}\tau} \quad (14.34)$$

Examples: for $\bar{B} \simeq 2$ G, $f \simeq 5 \times 10^{-3}$, $\bar{R} \simeq 200$ km, the energy flux $\simeq 10^5$ erg/(cm² s). For $\bar{B} \simeq 5$ G, $f 10^{-2}$, the energy flux $\simeq 2.5 \cdot 10^5$ erg/(cm² s).

This energy supply is maintained continuously by constant addition and replacement of newly emerging small-scale network magnetic fluxes, keeping thus the chromosphere/corona above the quiet sun warm and topologically imitating the pattern of small-scale magnetic elements.

14.4 Magnetic Energy Avalanche and the Fast Solar Wind

What we see within a few solar radii of the solar surface as a slow and fast wind seems to be a natural consequence of the two different types of magnetic field clusters observed on the solar surface:

1. the dense conglomerates of active regions, and
2. the rarefied ensembles of small scale magnetic flux tubes covering the rest, 90% of the solar surface.

The slow wind, flowing from the sun's equatorial belt with typical velocities below 500 km s⁻¹ and having highly variable physical properties, seems to be associated with the active regions which form the near-equatorial belt of active latitudes and exhibit a strong variability over the solar cycle.

The fast wind flowing on average at 750 km s⁻¹ fills the remaining vast regions of interplanetary space and consists of highly thin intermittent streamers. Although the small-scale structures are highly dynamic, the overall properties and background physical parameters of the fast wind appear to be almost constant (see, e.g., proceedings of the Solar Wind Eight conference, Gosling et al. 1996).

Intuitively, it is obvious that the slow wind is associated with the active regions and the fast wind with the quiet sun magnetic network. But how these two components of the solar wind are connected to their too far removed source regions and where are they actually rooted in the Sun were long-standing questions.

Earlier studies of the solar wind has been based mainly on remote in situ measurements conducted beyond 0.3 AU. Restricted by extrapolations, high speed streamers were related to coronal holes, and, respectively, the heating and acceleration mechanisms in the fast component of the wind were based on large scale open magnetic structures typical to coronal hole regions (Hundhausen 1977; Zirker 1977; Gosling et al. 1995). And it was *the corona* that has been unquestionably considered as the base of the solar wind.

Detailed observations of density and velocity structure in the outer corona obtained from radio occultation measurements (Woo 1996; Habbal et al. 1997; Woo and Habbal 1999) provided a link for understanding the connection between the Sun and interplanetary space by probing the solar wind before it evolves with heliocentric distance. These data combined with later ultraviolet and white-light measurements of solar atmosphere showed, for example, that the density profile closest to the Sun at $1.15 R_{\odot}$, representing the imprint of the Sun, is carried essentially *radially* into interplanetary space by small-scale ray-like structures that pervade the entire solar corona, and that a significant fraction of mass fluxes which extend into interplanetary space originate from the quiet Sun regions, and are indistinguishable in properties from those emanating from polar coronal holes. In other words, the primary energy source of the fast wind seems to be associated with small-scale magnetic flux tubes both in large quiet sun regions and regions underlying coronal holes. It was also found that there is a direct connection between the fast solar wind outflow and the chromospheric magnetic network (Hassler et al. 1999).

One of the most important details of the above observations is the fact the energy flow occurs *radially* outward from the sun. This means that no matter how complicated are the magnetic structures throughout the solar atmosphere from its surface, the energy that fuels the fast solar wind always finds its way vertically upward, which obviously requires action of some universal mechanism. Such a mechanism may well be associated with the post-reconnection shocks produced all over the quiet sun surface in arbitrarily magnetized environment as shown in Figs. 14.3 and 14.4. We saw that in any case, no matter what the environmental magnetic field is, even if it is horizontal (case # 4), the energy released due to the post-reconnection processes always flows radially outward along the gravity. The energy content in these processes (Sect. 14.3) is comparable with the energy estimated at the base of the solar wind.

We may conclude, therefore, that the fast solar wind can originate from the entire quiet sun surface supported by the following facts:

1. Intense hydro-magnetic activity resulting from interacting small-scale network magnetic elements in the quiet sun and regions underlying coronal holes creates the magnetic energy avalanche maintained by the continuous supply of emerging magnetic elements and their all-time reconnections;
2. Cumulative jet formation as an intrinsic feature of the post-reconnection dynamics of flux tubes in the arbitrary magnetic environment is always in place;

3. In the presence of vertical or near-vertical magnetic fields the jet formation is accompanied by the generation of high frequency Alfvén waves (Axford and McKenzie 1992);
4. The resulting energy flux estimated on the basis of observed time scale (~ 40 h) in which the total magnetic field in the quiet sun is replaced is enough to explain the observed UV/EUV radiation of the order of $5-10 \times 10^5 \text{ erg cm}^{-2} \text{ s}^{-1}$;
5. The high rate of the emergence of new fluxes and diversity of their parameters result in the cascade of shock waves, creating thus magnetic energy avalanche and relatively steady energy input into higher layers of atmosphere: short recycling time of total magnetic field in the quiet sun network ensures that produced energy flux will be uniformly felt in the corona. This in turn provides the observed steady character of the fast wind.
6. The most efficient energy transport provided by the gradient acceleration in strongly stratified photosphere/chromosphere region and occurring radially outward from solar surface strongly supports the observations showing that the fast solar wind may be organized in a form of small-scale filamentary ray-like structures diverging radially outward from the solar surface.

It is important to note that the purpose of this section is to address the problem of primary energy source that may originate the fast wind. A priori it is clear that there is no other energy than that stored in the convective zone and highly dynamic magnetic network that could produce the quiet sun corona and start the fast wind. This mechanism seems to provide a natural way of the energy transfer from a huge photosphere/convective zone energy reservoir to upper layers of atmosphere and is consistent with the observed properties of heating and high velocity events in the bottom of the fast wind. Obviously these processes occur at much earlier stages (and at much lower altitudes) than the body of the wind is formed and get accelerated. The link between these two stages is subject of future studies.

14.5 Problems

14.1 Consider a strong acoustic shocks and compare density compression for adiabatic and isothermal shocks.

14.2 Find the condition for unlimited cumulation of a cylindrically converging electromagnetic waves in a volume limited by radius R_{cyl} (Zababakhin and Nechaev 1958).

References

- N.I. Asano, T. Taniuti, J. Phys. Soc. Jpn. **29**, 209 (1969)
 W.I. Axford, J.F. McKenzie, in *Solar Wind Seven*, vol. 1 (Pergamon Press, Oxford, 1992)
 S.R. Cranmer, LRSP **6**, 3 (2009)

- J.T. Gosling, *Geophys. Res. Lett.* **22**, 3329 (1995)
- J.T. Gosling, S.R. Habbal, W.S. Kurth, M. Neugebauer (eds.), *Solar Wind Eight* (AIP, New York, 1996)
- S.R. Habbal, R. Woo, S. Fineschi, R. O'Neal, J. Kohl, G. Noci, C. Korendyke, *Ap. J. Lett.* **489**, 103 (1997)
- D.M. Hassler et al., *Science* **283**, 810 (1999)
- A.J. Hundhausen, in *Coronal Holes and High Speed Wind Streams*, ed. by J.B. Zirker (Colo. Assoc. Univ. Press, Boulder, 1977), p. 225
- A. Jeffrey, T. Taniuti, *Non-Linear Wave Propagation* (Academic, New York, 1964)
- L.D. Landau, E.M. Lifshits, *Fluid Mechanics* (Pergamon Press, Oxford, 1987)
- P. Maltby et al., *ApJ* **6**, 284 (1986)
- G. Nistico et al., *Adv. Space Res.* **48**, 1490 (2011)
- L.A. Ostrovskii, N.R. Rubakha, *Radiophys. Quantum Electron.* **15**, 986 (1974)
- E.N. Parker, *Cosmical Magnetic Fields* (Clarendon Pres, Oxford, 1979)
- H.E. Petschek, *NASA Spec. Pub. SP-50*, 425, 1964
- M. Ryutova, J. Sakai, *JETP Lett.* **58**, 507 (1993)
- M.P. Ryutova, T.D. Tarbell, *ApJ* **541**, L29 (2000)
- R.Z. Sagdeev, in *Review of Plasma Physics*, ed. by M.A. Leontovich, vol. 4 (Consultants Bureau, New York, 1966)
- I.V. Sokolov, *Sov. Phys. Uspekhi* **33**, 960 (1991)
- T. Tarbell, M. Ryutova, J. Covington, A. Fludra, *ApJ* **514**, L47 (1999)
- T. Tarbell, M. Ryutova, R. Shine, *Solar Phys.* **193**, 195 (2000)
- A.M. Title, C.J. Schrijver, in *Cool Stars, Steller Systems, and the Sun*, ed. by R. Donahue, J.A. Bookbinder, *Astronomical Society of the Pacific Conference Series* (1997)
- G.B. Whitham, *Linear and Nonlinear Waves* (Wiley, New York, 1974)
- R. Woo, *Nature* **379**, 321 (1996)
- R. Woo, S.R. Habbal, *ApJ* **510**, L69 (1999)
- E.I. Zababakhin, M.N. Nechaev, *JETP* **33**, 442 (1958)
- J.S. Zhao, D.J. Wu, J.Y. Lu, *Astrophys. J.* **735**, 114 (2014)
- J.B. Zirker (ed.), *Coronal Holes and High Speed Wind Streams* (Colo. Assoc. Univ. Press, Boulder, 1977)

Chapter 15

Response of the Corona to Magnetic Activity in Underlying Plage Regions



Abstract The fact that corona is strongly inhomogeneous in space and evolves in time in very different ways means that the processes of energy production, flow, and release have several branches. The processes of the extraction of energy stored in the photosphere strongly depend on the magnetic filling factor, i.e., whether we deal with the quiet sun network, plages or active regions. So far we were studying rarefied ensembles of flux tubes typical to quiet sun. In this chapter, we move to denser ensembles of flux tubes typical to plages and consider the response of the upper atmosphere to magnetic activity in underlying plage regions. We will see that the character of the EUV emission above plage regions that are dominated by single polarity magnetic elements, i.e., unipolar plages, always has an amorphous shape that topologically mimics the shape of the underlying plage. Contrary to this, the EUV emission above mixed polarity plages is highly discrete and consists of sporadic localized radiative transients. Such a different response of the chromosphere/corona to unipolar and mixed polarity plages obviously implies the action of different mechanisms for energy production, flow, and release. In all cases, however, the primary energy source lies in continuous hydromagnetic activity among the photospheric magnetic fields. It is just the character of this activity, different in differently magnetized regions, that determines the processes of the extraction of energy and its transport throughout the solar atmosphere.

15.1 Magnetic Imprint of Plage Regions in the Corona

A great variety of the coronal structures, from large-scale steady loops associated with active regions, amorphous structures seen above unipolar plages, all kinds of flares and microflares, evolve in time in different ways and have underneath (at the photosphere) very different patterns of magnetic fields and plasma flows. It is, however, obvious that despite of all the diversities of the observed phenomena, the primary energy source is associated with the photospheric magnetic fields.

The specifics of the photospheric magnetic fields and their interaction with highly dynamic environment determine in large the action of particular physical mechanism of energy production and its flow into upper layers of atmosphere. These mechanisms lead, in the first place, to formation of one or the other type of chromospheric and coronal structures, reflecting the composition of the underlying photosphere, and then to the release of incoming energy. It is important that along the filling factor, a decisive role in the energy production is played by the dominant polarity of the region. This is especially prominent in plages and quiet sun regions which may either consist of mixed polarity elements or be dominated by one polarity features. This is also true for sunspots and active regions where inclusions of opposite polarity elements are permanently observed.

Response of the chromosphere and corona to hydromagnetic activity in these largely different magnetic clusters is quite different. We have already seen that regions with mixed polarity flux tubes in quiet sun produce localized microflares and jets in the overlying chromosphere and corona. In this chapter, we will see that the EUV emission above unipolar plages has the amorphous structure and very peculiar braidlike behavior in time. As in case of mixed polarity regions, the chromosphere and corona above the unipolar regions also mimic magnetic topology of underlying photosphere.

Figure 15.1 represents a typical view of the sun's region containing various clusters of magnetic elements and its overlying chromosphere and corona. The images are taken on January 10, 2012 by the AIA and HMI instruments on the SDO. The top left panel is a magnetogram containing the active region (AR), unipolar plage (the red contour), mixed polarity plage (the blue contour), and quiet sun (QS). The top right panel is the overlying chromosphere at 5×10^4 K in the He II line. Two bottom panels are the corona at 6.5×10^5 and 1.3×10^6 K temperatures in Fe IX 171 and Fe XII 193 lines, respectively. The white arrows in the chromosphere and coronal images show a huge body of the amorphous emission that overlies and mimics the magnetic pattern of a unipolar plage. The blue arrows show sporadic events in the chromosphere and corona localized above mixed polarity plage. The hot coronal loops and sporadic events overlie the active region. Note that the chromospheric emission above the quiet sun has a discrete character, obviously associated with the isolated network elements. Higher in the corona the emission above the quiet sun becomes diffusive. It is interesting that this emission often looks "perforated," which is well seen in the Fe XII 193 line (bottom right). The dark lanes making the bushy pattern coincide with supergranular lanes. These are the sites of spicules whose cool material protrudes the hot coronal plasma.

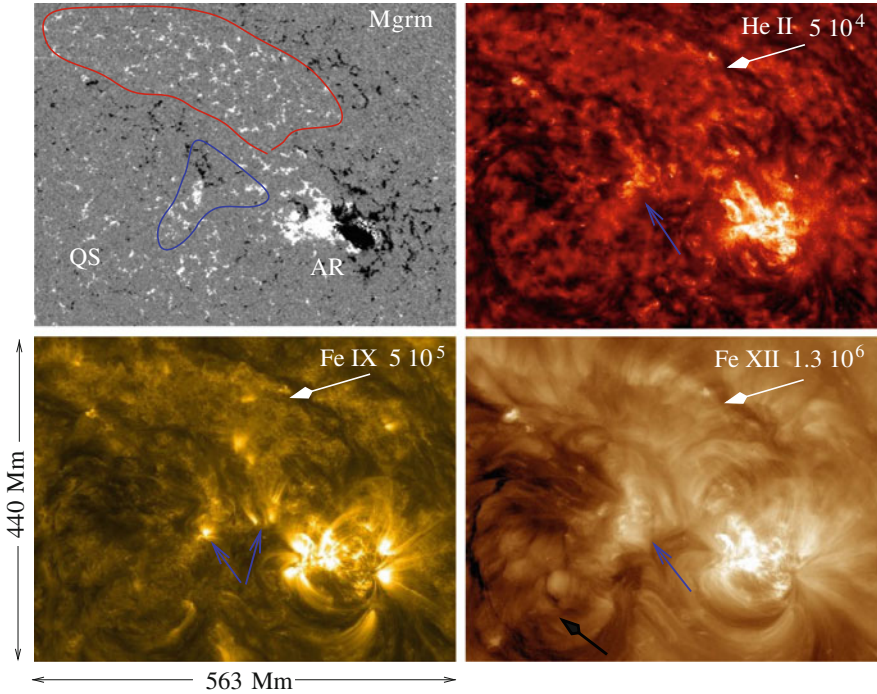


Fig. 15.1 Snapshots of an ordinary region of the sun containing various kinds of magnetic structures: the active region (AR), unipolar plage (demarcated by the red contour in the magnetogram), mixed polarity plage (demarcated by the blue contour), and quiet sun (QS). A huge body of a fuzzy emission in the chromosphere and corona overlying the unipolar plage region reflects the shape and location of the plage. The same is true for a sporadic events occurring above the mixed polarity plage (the blue arrows). The images are taken by the SDO instruments in four wavelengths on January 10, 2012. Field of view is 440 Mm \times 563 Mm

15.2 Coronal Dynamics Above Unipolar and Mixed Polarity Plages

To illustrate the details of the photosphere/corona coupling and see associated regularities between the coronal emission and the underlying chromosphere and photosphere, we use multiwavelength observations from the TRACE instruments and the MDI on SOHO.

The analyzed data sets, obtained on June 10, 1999, consist of time series of high-resolution MDI magnetograms co-aligned with the TRACE 1600 Å, Fe IX/X 171 Å, and Fe XII 195 Å lines. The data cover a 166'' \times 270'' area near disk center. There are several sunspot groups and both types of plages, unipolar and mixed polarity. The period of observation is over 10 h. Figure 15.2 shows a sample MDI magnetogram (top) and overlying corona in Fe IX/X 171 Å line (bottom). One can see three sunspots in the region and several plages. The region marked by a triangle is a

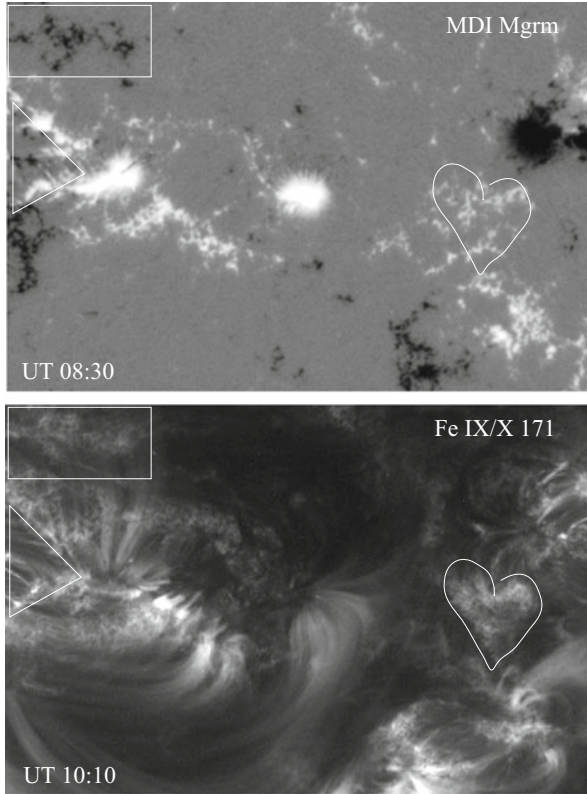


Fig. 15.2 Aligned MDI and TRACE images taken on June, 10 1999. MDI magnetogram is scaled from -1000 to 1000 G. Field of view $120 \text{ Mm} \times 196 \text{ Mm}$. The region demarcated by a triangle is an example of plage with mixed polarity magnetic elements; rectangular and heart-shaped regions are examples of unipolar plages

typical mixed polarity plage, rectangular- and heart-shaped regions are examples of unipolar plages.

The corona above the sunspots and plages shows all kinds of formations: steady large-scale loops, patchy amorphous structures, X-ray bright points, and various radiative transients. To study temporal variability of these formations, the data were compiled in co-aligned movies with a 15 s cadence to use again the procedure of space-time cuts, and follow the motions of various bright patches lying along the cut (Ryutova and Shine 2004). Simultaneous movies taken in the TRACE 171, 195, and 1600 \AA lines allow to study a character of temporal behavior of the enhanced emission at different heights and temperatures. Figure 15.3 shows snapshots of corona at two temperatures with five space-time cuts shown by straight lines and marked by numbers 1–5. The near horizontal slices are made from left to right; the vertical slices are made from top to bottom. Note that the difference between the

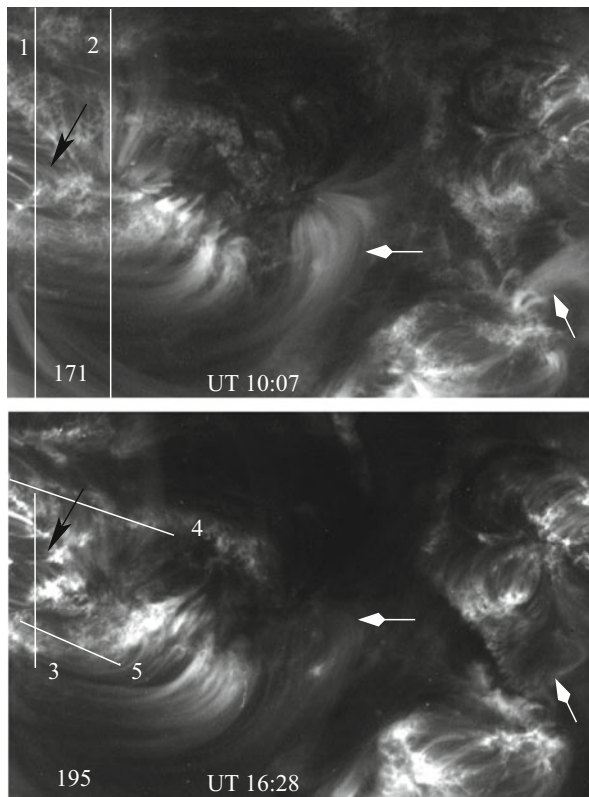


Fig. 15.3 Snapshots of the entire field of view at $T \simeq 10^6$ K (171 \AA) and $T \sim 2 \times 10^6$ K (Fe XII 195 \AA). The straight lines marked by numbers 1–5 are the space-time cuts unfolded in Fig. 15.4. It is remarkable that large-scale loops prominent in 171 \AA (white arrow) faded significantly in the Fe XII 195 \AA line, while all spongy structures seen in the 171 \AA emission remain in place at the higher temperatures. Note that time difference between 171 and 195 \AA snapshots is 6 h 20 min, and yet the amorphous emission in both coronal lines mimics closely the magnetic pattern of unipolar plages. Black arrows mark a mixed polarity plage

start times of these two sets is about 6 h, and yet the properties of the hotter $\lambda 195$ emission are remarkably similar to those of $\lambda 171$.

Space-time slices reveal clear differences in the properties of the emission at the coronal and chromospheric temperatures associated with the sunspot and plage regions.

Intersections through large-scale coronal loops (marked by curved arrows in Fig. 15.4) show a slow process of brightening up and dimming down. These are long-living quasi-steady loops showing transverse oscillations accompanied by merging and splitting processes.

The enhanced emission above the unipolar plages is *always* of amorphous texture. When observed in high cadence time series this fuzzy emission shows

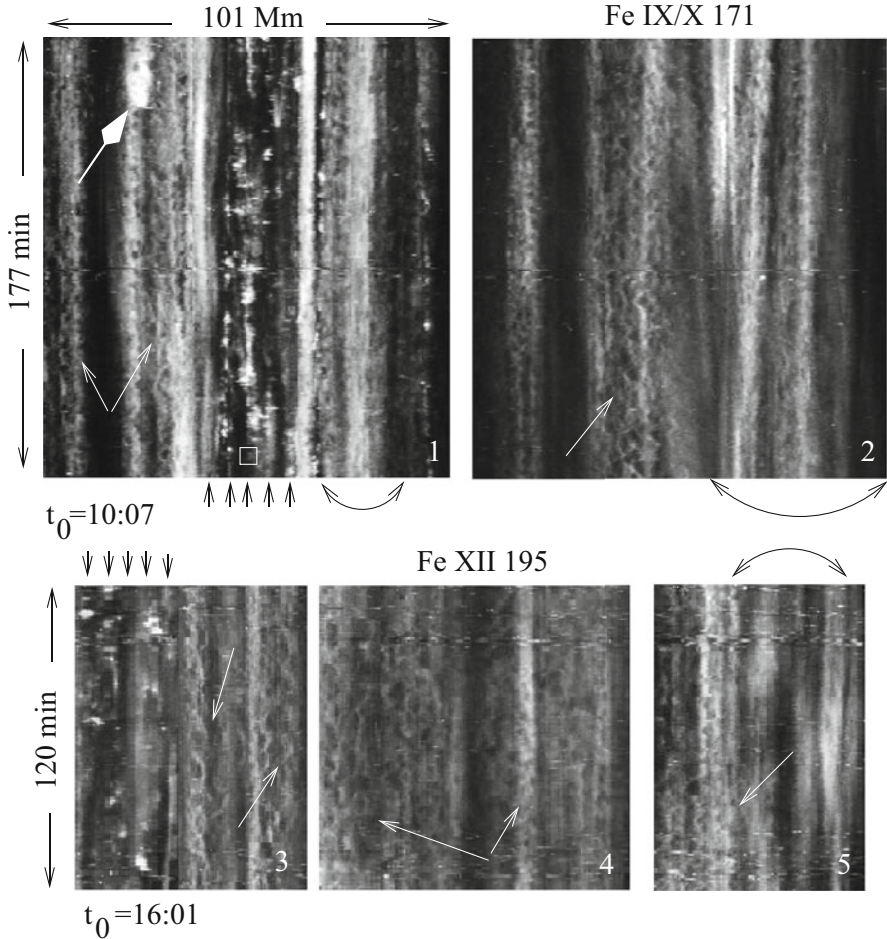


Fig. 15.4 Examples of the space-time tracks along lines 1–2 in Fe IX/X 171 images (upper panels) and along lines 3–5 in Fe XII 195 images (lower panels). All over the chosen area coherent braidlike structures are well seen above each unipolar plage (some are marked by thin white arrows); the mixed polarity plage produces a frequent radiative transients—jets and microflares, hot enough to be seen at 10^6 K (series of small arrows along slices 1 and 3). Thus, the response of corona to hydrodynamic activity in a unipolar and mixed polarity flux tubes is radically different. Curved arrows demarcate intersections through long-living quasi-steady coronal loops with their subtle motions and slow intensity variations

extremely sturdy well-organized coherent structures having braidlike appearance. These are indicated by thin white arrows in Fig. 15.4.

Braidlike coherent structures remain regular as long as the plage preserves its properties. They are not affected by overlying or neighboring coronal loops. Their destruction is associated only with the emergence of opposite polarity magnetic elements in the unipolar plage. Such an event is marked, for example, by the

thick white arrow in the top left panel of Fig. 15.4. Just before the appearance of a compact flare, additional magnetic flux of the opposite polarity has emerged in the underlying plage, and destroyed the braided coherent structure. This interesting phenomena were discovered by Shine et al. (1999). We will see below that the braidlike structures are ubiquitous for the corona overlying the unipolar plages and have very natural explanation (Ryutova and Shine 2004).

Contrary to long-living braidlike structures, coronal emission above mixed polarity plages is highly discrete and consists of frequent localized transients, resembling a continuous irregular firework.

The system of mixed polarity magnetic elements intrinsically prevents the formation of coherent structures. This is clearly seen in the space-time cut # 1 (Fig. 15.4). This cut (made from top to bottom) first crosses a negative polarity unipolar plage (see Fig. 15.3, upper panel), then enters the region of mixed polarity plage (black arrows in Fig. 15.3) and finally crosses the site of quasi-steady loops. Accordingly, the space-time image (Fig. 15.4 upper left panel) shows first a braided coherent structures, then frequent sporadic microflares (marked by the set of short arrows), and finally the “lazy” motions of quasi-steady loops. Another cut through this area is made in the hotter 195 Å line (cut # 3 in Fig. 15.3, lower panel). One can see that sporadic radiative transients produced by the mixed polarity plage are as frequent at 2×10^6 K temperatures as in lower corona. It is important that coherent structures are also formed at 2×10^6 K temperatures (cuts 3–5), and have the same properties and longevity as their counterparts in lower corona.

15.3 Properties of Braidlike Coronal Structures

The braidlike structures, being quite similar, still have quite distinguishable properties from one region to another. One of the main causes affecting them is magnetic filling factor of underlying plage. To see what can we learn from comparing the various regions, we choose the most typical cases that may characterized as *Rare*, *Medium*, and *Dense* plages. These are illustrated in Figs. 15.5a–d and 15.6e–h. Each figure contains the snapshots of the magnetogram and its overlying corona in Fe IX/X 171. Space-time slices made over the coronal emission are represented as always by white lines. The time interval is 177 min. Analyzing these figures we may summarize some general properties of the coherent structures as follows.

First of all, the braidlike structures have an isotropic nature. One can see that two parallel cuts, *a* and *b* in Fig. 15.5 made over a rarefied plage show similar space-time behavior. The same is true in case of *medium* plage, demonstrated by cuts *e* and *f* which are made under different angles, and in case of densely populated plage shown by cuts *g* and *h* (Fig. 15.6).

The next important feature of the coherent structures, as we have already mentioned, is their sturdy character. Once formed, they remain regular as long as their underlying plage remains unipolar, which may usually last for hours. Their destruction, sometimes only temporary, occurs if there is emergence of

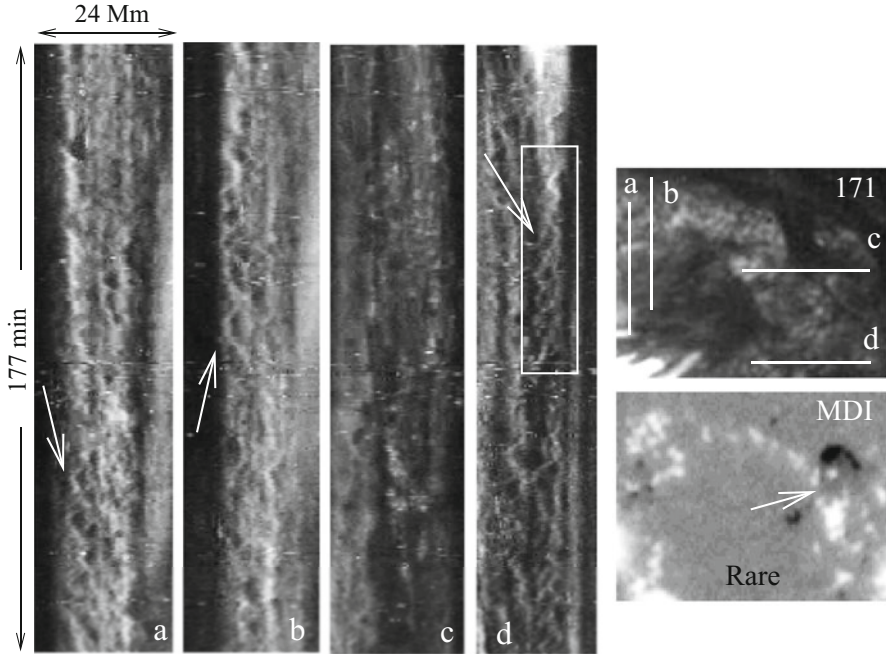


Fig. 15.5 Some properties of the coherent structures: (1) They have an isotropic nature (cuts *a*–*b*); (2) The braid period depends on the plage magnetic filling factor; (3) Emergence of opposite polarity fluxes destroys the well-organized structures (space-time image *c*), and (4) The braidlike structure along cut *d* remain quite regular until the appearance of a “mini-flare” caused by emergence of an opposite polarity flux tube in the photosphere. White boxes are used for quantitative analysis

opposite polarity magnetic flux. This is shown in panel *c*, Fig. 15.5 and panels *g* and *h*, Fig. 15.6. In the first case, along the cut *c* a group of negative polarity elements emerged (around the region marked by white arrow in the magnetogram). Interaction of opposite polarity flux tubes totally destroyed the braidlike structures replacing them by frequent sporadic microflares. Note that neighboring coherent structures are not affected by the whole series of radiative transients (cut *d*). In two other cases, along the cuts *g* and *h* (Fig. 15.6) a single opposite polarity element emerged around UT 12:27 and caused appearance of a mini-flare that temporarily destroyed coherent structure. This is also seen in space-time images *g* and *h*. A flare that appeared at UT 12:27 (cf. Fig. 15.4, panel 1, thick white arrow) destroys only its “own” structures while neighboring structures (to the right) remain unaffected.

The braid period depends mainly on the magnetic filling factor of the underlying plage. The braid period is in fact, a time interval between two neighboring peaks of intensity, and thus is directly measurable. As a result, one finds that the denser the plage, the shorter is the braid period. Using the above observation one gets the following. The rarefied plage with a magnetic filling factor, $f \simeq 0.2$, produces a

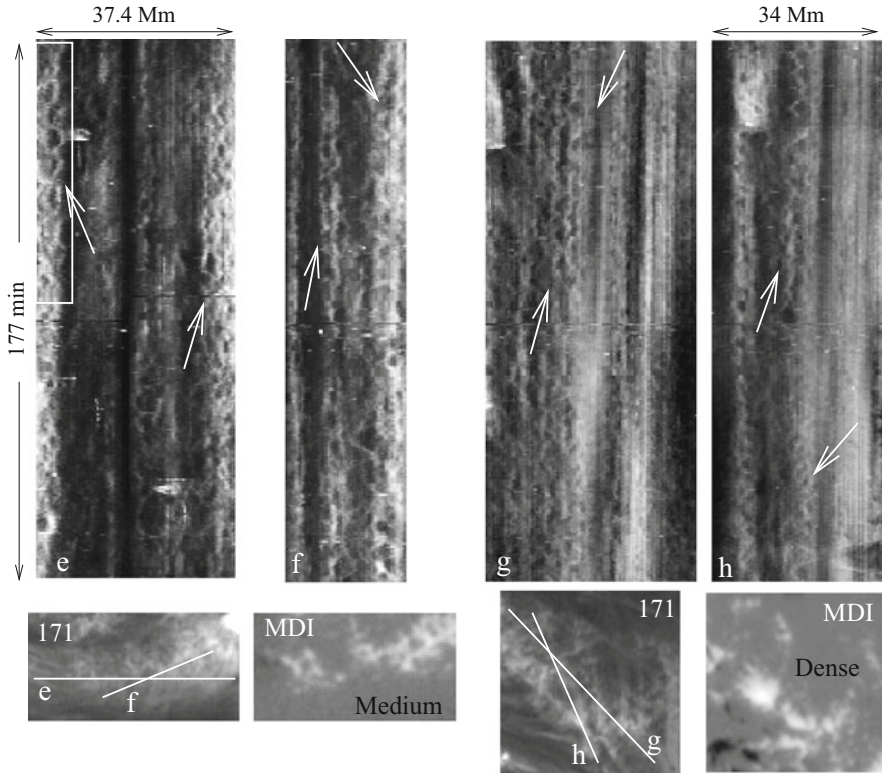


Fig. 15.6 Properties of the coherent structures (cont.) over medium and densely populated plages showing a ubiquitous nature of a spectacular braidlike structure

coronal emission with a braid period $T \simeq 20$ min. For a denser, *medium* plage with $f \simeq 0.3$, $T \sim 10$ min. Above the dense plage *Dense* with $f > 0.4$, the braid period is $T \sim 6$ min. The filling factors were computed from the MDI magnetograms as a fraction of a plage area covered by magnetic field.

To better understand the properties and nature of the coronal emissions above the unipolar and mixed polarity plages, it is important to examine the properties of the underlying chromosphere/transition region, which is the first to respond to magnetic activity in the photosphere. As expected, there is a clear difference between the response of the chromosphere to dynamic changes in the unipolar and mixed polarity plages.

Figure 15.7 is an example of the analyzed data sets. Shown is the eastern part of the studied region in TRACE 1600 Å, corresponding to a range of temperatures in the interval $T \sim 6 \times 10^4 - 2.5 \times 10^5$ K. Space-time cuts 1 and 2, made over the unipolar plages, show the typical pancakes—regular chromospheric oscillations with periods 3–6 min. Cuts 3 and 4 made over the mixed polarity plages show all kinds of sporadic brightening from quite strong and long lasting ones (marked by

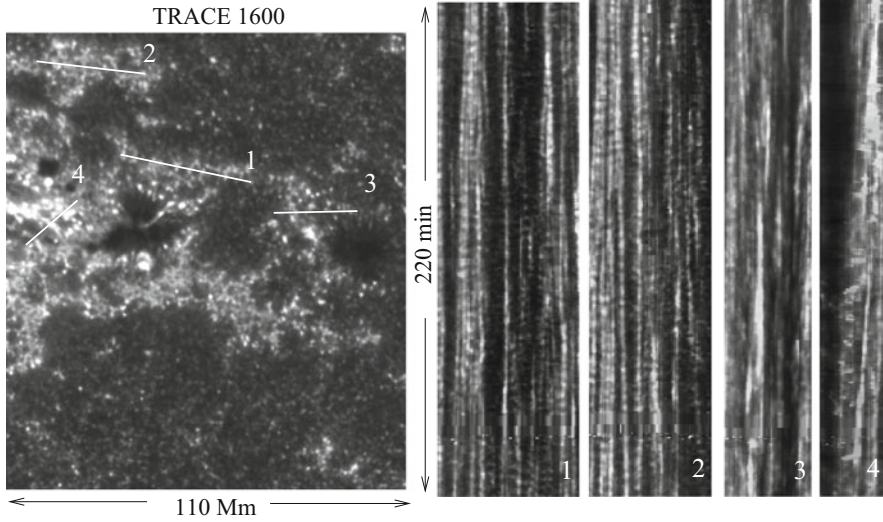


Fig. 15.7 Space-time images in the chromosphere. Cuts 1 and 2 are made over the unipolar plages, while cuts 3 and 4 are made over the mixed polarity plages. Panels 1 and 2 show a regular oscillations of intensity corresponding to waves with 3–6 min period; Panels 3 and 4 show both, long lasting and brief sporadic brightenings typical to chromosphere overlying mixed polarity plage

white arrow on the image (3), to whole series of short-living UV flashes (see image (4)). These brightenings turned out to be precursors of coronal radiative transients.

15.4 Comparison of Coronal Emission Above Mixed Polarity and Unipolar Plages

Long lifetime and sturdy character of the coronal emission above plage regions allow to perform quantitative analysis of the observations. For example, the space-time images, which themselves carry valuable information for diagnostics, may be complimented by the intensity variation over a particular area. To demonstrate such an approach, let us allocate several small regions with the area size of some $S \simeq 2.2 \text{ Mm} \times 2.2 \text{ Mm}$, and, using the movies, compute the time variation of intensities in these areas. Three examples of such a procedure are shown in Figs. 15.8, 15.9, and 15.10.

Figure 15.8 represents the coherent emission above the unipolar plage, marked by white rectangle in Fig. 15.6e. A blown up view of this region and a corresponding sketch are shown in Fig. 15.8, left. Small white squares in these images demarcate locations corresponding to the apex of the emission and knots over which the intensity curves are computed. These are shown in the right panel of Fig. 15.8. As

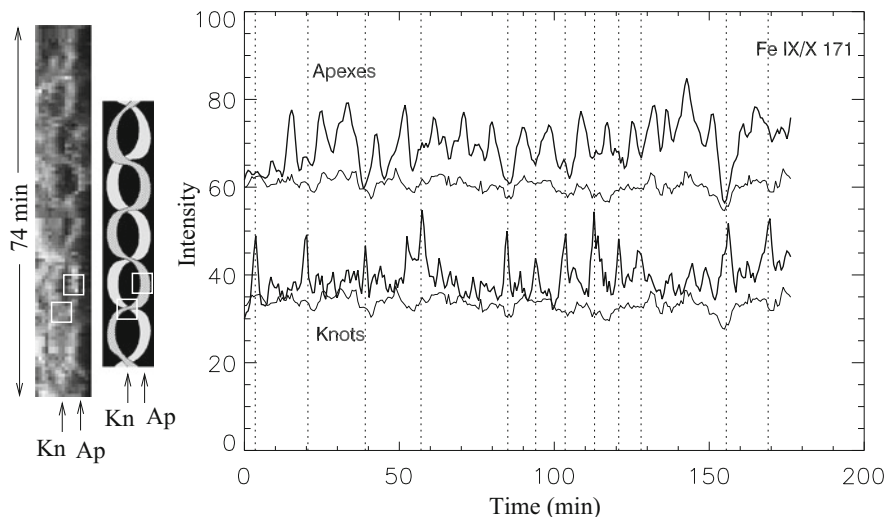


Fig. 15.8 Intensity curves of the Fe IX/X 171 emission radiated from two $2.2\text{ Mm} \times 2.2\text{ Mm}$ regions located in the apex and in the knot of the braidlike emission. Left: Space-time slice of the exemplary region (elongated box in Fig. 15.6e) and its sketch; white squares indicate the apex (Ap) and knot (Kn) regions where the intensities are measured. Right: Thick lines show the intensity variation in the knot and apex regions during the 177 min period, and thin curves represent an average background intensity. Maximums in the knot region correlate with minimums in the apex region, and appear with about 10 min periodicity

expected, maximums of intensity in the knot region coincide with minimums of intensity in the apex region, and vice versa. The braid period here is about 10 min. The intensities are in arbitrary units. To emphasize the significance of signal of the enhanced emission, we plot the integrated background intensity curves, which are shown for comparison by thin solid lines.

Figure 15.9 also represents the temporal variation of spongy emission above the unipolar plage. The left panel is the space-time sample marked by white box in Fig. 15.5d. One can see an unmistakable braidlike structure of the emission. To enhance the visual effect we made a sketch of a segment marked by box in left panel, trying to follow the intensity borders as they look. One can notice that in this case, “left” and “right” apexes are slightly shifted with respect to each other. The measured intensity variations over these areas are shown in the right panel of Fig. 15.9. Both peaks appear with about 15 min periodicity. A longer period of these braided structures (compared to previous example) is consistent with the fact that underlying plage region in this case is more rarefied.

Note also that in this case toward the end of observations coronal emission gets strongly enhanced, but still preserves its oscillatory pattern. The enhancement is caused by emergence of small-scale opposite polarity flux tubes, which by interacting with the existing magnetic flux tubes supply enough energy to enhance the emission, but not destroy the structure itself.

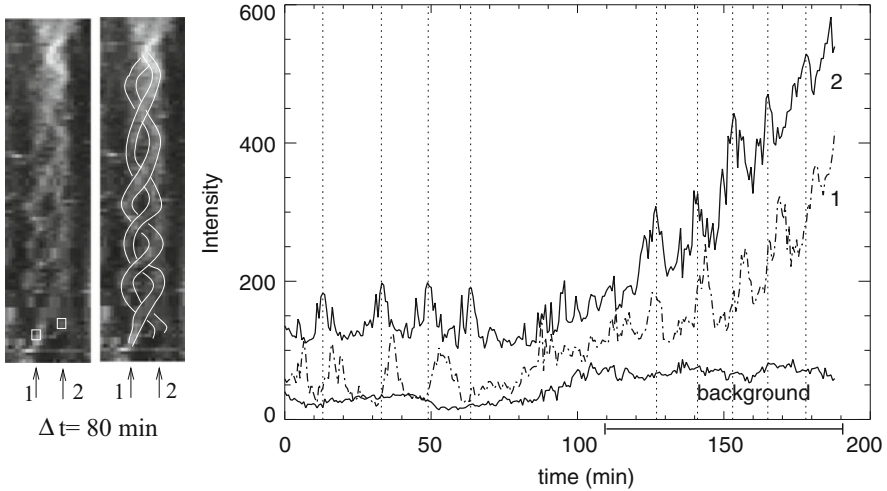


Fig. 15.9 Temporal behavior of the Fe IX/X 171 emission radiated above the rarefied plage region along the slice d (Fig. 15.5d, white box). Two left panels show a braided behavior of the emission. The right panel contains the intensity curves measured for $2.2 \text{ Mm} \times 2.2 \text{ Mm}$ regions confined in small white boxes: (1) the “left” apex and (2) the “right” apex. Maximums in the “left” and “right” apices are slightly shifted with respect to each other enhancing the visual impression of braidlike appearance. Period is about 15 min. Thin lower curve represents an integrated background intensity. A strongly enhanced emission during last 70 min is caused by the emergence of the opposite polarity flux and its interaction with the existing magnetic elements

Totally different is the behavior of coronal emission above the mixed polarity plage. Examples of the intensity curves for the Fe IX/X 171 emission line above mixed polarity plage ($2.2 \text{ Mm} \times 2.2 \text{ Mm}$ white square above the short arrows in the upper left panel of Fig. 15.4) are shown in Fig. 15.10 together with the intensity curve measured for TRACE 1600 above the unipolar plage (Fig. 15.7, cut 2). The upper, Fe IX/X 171 emission curve is measured above $2.2 \text{ Mm} \times 2.2 \text{ Mm}$ area marked by white square above the short arrows in the upper left panel of Fig. 15.4. The lower, 1600 emission curve is measured over the region marked with cut 2 in Fig. 15.7. Thin curves represent corresponding background intensities.

A series of million degree radiative transients of various duration are clearly seen in the upper curve of Fig. 15.10. Contrary to this, UV emission above the unipolar plage (“pancakes”) shows regular oscillations with about 270 s period. Generally period of these oscillations ranges between 3 and 6 min. Note that in most cases 1600 oscillations are modulated. One can see that in this particular case the modulation period is about 120 min.

Obviously, the physical processes behind the observed regularities in the chromosphere/coronal emission are directly associated with the mechanisms of the energy extraction from the photospheric magnetic fields, and must be different for differently magnetized regions. Phenomenology of these processes is a subject of

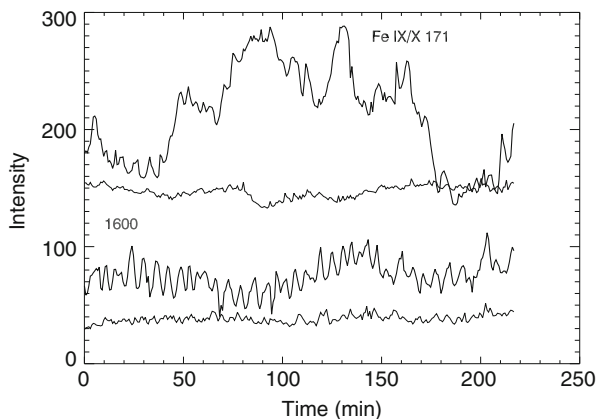


Fig. 15.10 Intensity curves measured for 3×3 arc sec regions: upper curve in Fe IX/X 171 emission line is computed above the mixed polarity plage (short arrows in Fig. 15.4), and shows series of significant flares and microflares of various duration; lower curve in the chromospheric 1600 emission line is computed above unipolar plage (Fig. 15.7, cut 2), and shows regular oscillations with period less than 5 min. Thin curves represent corresponding background intensities

the next section. Before we turn to this, it is useful to briefly summarize the results of this section.

Plage dominated by unipolar magnetic flux tubes:

1. The enhanced emission in TRACE 1600 ($T \sim 6 \times 10^4 - 2.5 \times 10^5$ K), Fe IX/X 171 Å, and Fe XII 195 Å ($T \sim 10^6$ and $T \sim 2 \times 10^6$) lines mimic the plage magnetic pattern.
2. The emissions in Fe IX/X 171 Å and Fe XII 195 Å lines exhibit coherent braidlike structures in space-time images, and have an isotropic character. The structures remain regular as long as an underlying plage preserves its general properties. The braid period depends on the magnetic filling factor of plage: the denser the plage, the shorter the braid period.
3. There is no direct connection between the *coronal* emission and individual magnetic elements. Moreover, the actual distribution of individual magnetic elements inside the plage does not play a role. Whatever irregular pattern they form inside the plage, the coherent structures are regular and occupy an area somewhat larger than the plage but with boundaries which follow closely the demarcation line of the plage region.
4. The only factor observed to disrupt these structures was the emergence of the opposite polarity magnetic field in the plage dominated by one polarity magnetic elements.
5. The emission in TRACE 1600 Å, corresponding to chromosphere and transition region temperatures, not only mimics the general shape of underlying plage, but also traces the individual magnetic flux tubes to the limit of their resolution.

6. The space-time images in TRACE 1600 Å show typical regular oscillations with 3–6 min period seen in space-time images as pancake structures.

Mixed polarity plage:

1. The enhanced emission in TRACE 1600 ($T \sim 6 \times 10^4$ – 2.5×10^5 K), Fe IX/X 171 Å, and Fe XII 195 Å ($T \sim 10^6$ and $T \sim 2 \times 10^6$) always exists above the mixed polarity plages, but has a discrete nature.
2. The emission in Fe IX/X 171 and 195 Å lines shows a random set of sporadic radiative transients in the region confined by boundaries which coincide with the general boundaries of the underlying plage.
3. There is a correlation between the numbers of radiative transients and the density of mixed polarity flux tubes.
4. Mixed polarity plages intrinsically prevent formation of any kind of a stable structures and fill the coronal space by randomly distributed frequent flares and microflares.
5. The emission in TRACE 1600 Å is quite irregular and dynamic, but traces closely the magnetic pattern of underlying plage.
6. The space-time images in TRACE 1600 Å show random “flashes”—localized, sporadic brightening which may be attributed as precursors for the coronal radiative transients.

15.5 Energy Extraction Mechanisms from the Ensembles of Photospheric Flux Tubes

In this section, we discuss a phenomenology of physical processes that may extract the energy stored in the plages and provide the transport of this energy into upper layers of atmosphere. These processes include the formation of a million degree plasma exhibiting regular structures observed above the unipolar plages, and sporadic radiative transients above the mixed polarity regions. It is important, that in the first case, the mechanism should explain not only the fact that the regular coronal structures are observed only above the unipolar plages, but also two different characteristic timescales: the short period of braiding and the longevity of their duration. As to the second case, i.e., energy production and transfer in mixed polarity plages, the physical processes here must be similar to those in the quiet sun region where mixed polarity flux tubes form rarefied ensembles and sustain ubiquitous reconnection events. The main difference, however, is that the reconnection and post-reconnection processes that occur in the quiet sun regions are strongly intensified in plages due to higher magnetic filling factor. This will be discussed below before we turn to the problem of unipolar plages.

15.5.1 *Mixed Polarity Plage*

In the previous chapters we saw that the photospheric reconnections between the opposite polarity flux tubes lead to multi-step process of energy buildup that involves the formation of post-reconnection shocks and their further evolution. As a result, the final energy release falls into three main classes of radiative transients: (1) strong localized emissions, just microflares, not exhibiting significant flows of material; (2) microflares with lesser intensities, but accompanied by one or two directional plasma jets: as a rule, stronger microflare correspond to lower velocity jets, and vice versa; and (3) strong supersonic jets and explosive events not associated with microflares. The appearance of any kind of radiative transients usually correlates with canceling mixed polarity magnetic elements. Moreover, the observations clearly show that the sequence of events that start with cancellation of the photospheric magnetic fields, pass through shock formation, and result in the transition region radiative transients—microflares, jets, and their combinations—have a universal character and are ubiquitous.

It is important to emphasize again that the photospheric reconnection is only a triggering mechanism for multi-step processes of post-reconnection shocks and their subsequent interaction. These processes, as we saw, occur higher in the atmosphere at a large distance from the reconnection area where post-reconnection shocks are already well developed and lead to hydrodynamic cumulation of energy.

The similar processes occur obviously, in mixed polarity plage regions. Here, however, magnetic filling factor is much higher than in the quiet sun regions, and shock production is strongly enhanced. Respectively, the rate of appearance of jets and microflares significantly increases. Besides, unlike a quiet sun where flux tubes reconnect in almost nonmagnetic environment, in plage regions with higher magnetic filling factor flux tubes may collide and reconnect in the environment of arbitrarily oriented magnetic fields (see Figs. 14.3 and 14.4, Chap. 14). In this case, along the acoustic branch, there are MHD and Alfvén waves which propagate much higher into the atmosphere and result in the generation of million degree coronal jets and microflares.

In the case of the acoustic branch, as we have seen, the shock amplitudes saturate at heights where the Mach number reaches quite moderate values of 1.5–2 (this corresponds to 2–4 scale heights). After that the shock amplitude becomes independent of the Mach number and being subjected to gradient acceleration, increases in accordance with the power law (Whitham 1958; Stanyukovich 1960; Landau and Lifshitz 1987).

In the case of the MHD and Alfvén branches, their steepening starts at much higher altitudes, and their shock amplitudes do not saturate, but rather increase exponentially from heights where their Mach numbers reach values of 1.5–2 (Jeffrey and Taniuti 1964; Ryutova et al. 2001).

Figure 15.11 shows the shock amplitude for the acoustic and Alfvén waves as a function of height for two sets of initial parameters of flux tubes. Plots for acoustic shocks are produced with the parameters taken from the observations of a very quiet

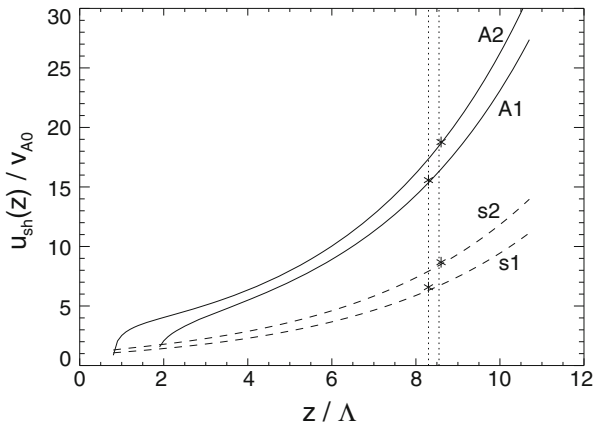


Fig. 15.11 Comparison of the shock amplitudes as a function of height: dotted lines correspond to the acoustic shocks generated by reconnection of magnetic flux tubes in nonmagnetic environment; solid lines are the amplitudes (actually Mach numbers) of the Alfvénic shocks generated by the reconnection of flux tubes in the neighborhood of other magnetic structures. Lines s1–A1 correspond to shock resulted from the magnetic flux reduction of $\Delta\Phi = 3.7 \times 10^{17}$, and lines s2–A2 are obtained for flux reduction of $\Phi = 5.0 \times 10^{17}$. Alfvén shocks accelerate faster and dissipate their energy with much more efficiency than the acoustic shocks, producing temperatures close to 1 MK

sun region presented in Ryutova et al. (2001). In particular, line 1 in Fig. 15.11 corresponds to a magnetic flux reduction of $\Delta\Phi = 3.7 \times 10^{17}$ and reconnection time $\tau = 252$ s; line 2 corresponds to $\Delta\Phi = 5.0 \times 10^{17}$ and $\tau = 120$ s (cf. Fig. 15.6 and Table 1 in Ryutova et al. (2001)). The calculated temperatures produced in these cases are, respectively, $T^{(s1)} = 8.5 \times 10^4$; $T^{(s2)} = 1.46 \times 10^5$, and are consistent with the transition region temperatures. Plots for the Alfvén shocks are obtained assuming that the similar flux tubes collide and reconnect in the vicinity of the external magnetic field. If the Alfvén shocks dissipate at the same height as their acoustic counterparts (as shown by stars in Fig. 15.11), the plasma temperature would increase up to the values $T^{(A1)} = 5.1 \times 10^5$ and $T^{(A2)} = 7.5 \times 10^5$, respectively. These are already close to coronal temperatures. In two more scale heights these temperatures would be $T^{(A1)} = 8.2 \times 10^5$ and $T^{(A2)} = 1.3 \times 10^6$.

It is important to emphasize that this is an ongoing process and requires only the existence of the opposite polarity magnetic flux tubes. It has a random character giving the appearance of sporadic radiative transients in a wide range of temperatures from chromospheric flashes to million degree mini-flares. The wide range of temperatures in these radiative transients is ensured by various heights of the shock formation and their energy release.

15.5.2 Unipolar Plage

In contrast to mixed polarity plagues, the unipolar plagues heat the corona more uniformly, and, what is most important, the *heated* corona not only mimics the general shape of an underlying plague, but also exhibits an extremely stable braidlike oscillatory pattern. These million degree structures, as we saw, remain regular as long as the unipolar plague preserves its general properties. It must be noted that although reconnections between the same polarity magnetic flux tubes are as ubiquitous as between the opposite polarity flux tubes, the post-reconnection dynamics is completely different. As discussed in Chap. 12, the post-reconnection sling shot in this case works mainly across the tube axis and leads to fragmentation of the magnetic flux tubes. This may be accompanied by possible excitation of waves propagating along the flux tubes (Tarbell et al. 2000; Ryutova et al. 2003a; Ryutova and Tarbell 2003b). Therefore, the mechanism for heating corona by small-scale flux tube ensembles that works so well in the mixed polarity plagues is not that efficient in the unipolar regions.

What is then the dominant process in the ensemble of unipolar magnetic flux tubes? How does this process extract the energy stored in the dynamic plague, and how does this energy flow into corona? One thing is clear, whatever are the mechanisms causing these processes, they must be associated with collective phenomena in the entire ensemble of flux tubes. In other words, the problem requires consideration of a plague as a whole, i.e., as an ensemble of magnetic flux tubes randomly distributed in space and over their physical parameters.

In Fig. 15.6 we have studied the interaction of acoustic waves and unsteady wave packets with an ensemble of random magnetic flux tubes. It was shown, for example, that the physical processes of energy transfer to the medium, as well as the maximum available energy input, crucially depend on the distribution of the random flux tubes in space and over their parameters (see also Ryutova and Priest 1993a,b).

The remarkable feature of these processes is that they are accompanied by specific morphological effects occurring in overlying atmosphere. The most important role in these processes is played by resonant interaction. Recall that due to Landau damping the energy of an acoustic wave (of wave vector \mathbf{k} and sound speed c_{se}) damps out at a rate

$$\nu_L \sim fkc_{se} \quad (15.1)$$

and remains for a long time in the form of flux tube oscillations. $f = R^2/d^2$ being a magnetic filling factor of the medium. The corresponding resonance condition is:

$$\omega = (\mathbf{kn})v_{ph}^m, \quad (15.2)$$

where \mathbf{n} is a unit vector along the flux tube axis. v_{ph}^m is the phase velocity of the flux tube oscillation:

$$\begin{aligned} v_{\text{ph}}^{m=\pm 1} &= c_k = \frac{\sqrt{\eta} v_A}{\sqrt{1 + \eta}} \\ v_{\text{ph}}^{m=0} &= c_T = \frac{c_{\text{si}} v_A}{\sqrt{c_{\text{si}}^2 + v_A^2}} \end{aligned} \quad (15.3)$$

with $\eta = \rho_i / \rho_e$ being the ratio of plasma densities inside and outside flux tube.

Thus, under the condition (15.1) the resonant flux tubes absorb the energy of the sound wave in a time $\tau_L = v_L^{-1}$, and carry it into upper layers of atmosphere in the form of a kink or sausage oscillations propagating along the flux tubes. This is sketched in Fig. 15.12, left (see also Figs. 6.4, 6.5, 6.6, and 6.7 of Chap. 6). Then, in a time $\tau_{\text{rad}} = v_{\text{rad}}^{-1}$ the resonant flux tubes radiate the accumulated energy as secondary acoustic or MHD waves. The radiative damping rate is:

$$v_{\text{rad}} \sim \omega k^2 R^2 \quad (15.4)$$

Since τ_{rad} depends on the tube radius R , different tubes radiate secondary waves in different times and at different heights (Fig. 15.12, right panel), e.g., thicker flux tubes give off their energy earlier than thinner ones. This leads to the energy release in a form of patchy EUV emission that fills the region of a finite thickness spread over the entire space occupied by a given ensemble of flux tubes.

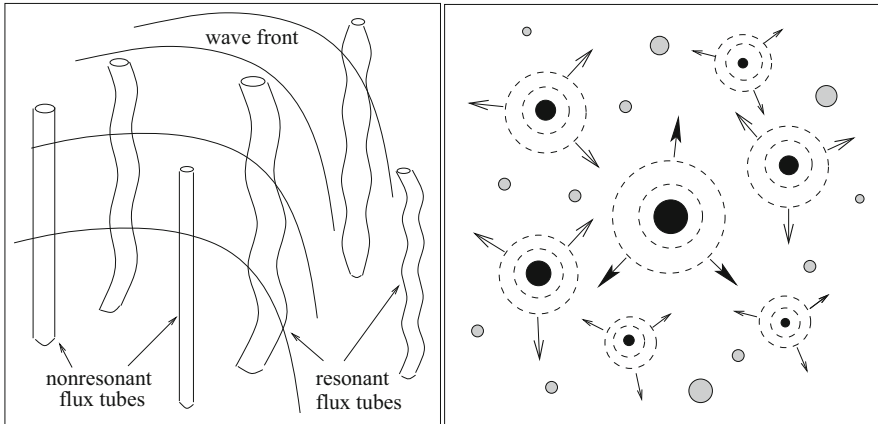


Fig. 15.12 Interaction of a wave packet with the random ensemble of flux tubes. Left: Energy of wave packet is transferred to flux tubes, some of which are nonresonant, while others are resonant with respect to excitation either of kink or sausage oscillations. Right: Radiation of secondary acoustic or MHD waves by oscillating flux tubes. After Rytova and Priest (1993b)

15.5.3 *N-Solitons*

Most importantly, as flux tube oscillations propagate upward into a more rarefied atmosphere, many of them reach the nonlinear regime. These waves are subject to modulation instabilities which may lead to the formation of regular coherent structures (Zakharov and Shabat 1972; Mjølhus 1976).

Consider example of nonlinear kink oscillations. The analysis presented below may also be performed for the sausage modes. Nonlinear kink oscillations of flux tubes are described by the MKdV-Burgers equation for $\mathbf{B}_\perp = (B_x, B_y)$ and can written as an energy equation for $\psi = B_x^2 + B_y^2$ (see Chap. 11, Eq. (11.3), of three dissipative terms we retain below only the term associated with radiative damping):

$$\frac{\partial \psi}{\partial t} + \alpha \psi \frac{\partial \psi}{\partial z} + \beta \frac{\partial^3 \psi}{\partial z^3} = \frac{\mu}{\pi} v \cdot p \cdot \int_{-\infty}^{\infty} \frac{\partial^3 \psi}{\partial s^3} \frac{ds}{z-s} \quad (15.5)$$

The coefficients α , β , and μ are, respectively, those of nonlinearity, dispersion, and radiative damping:

$$\alpha \simeq \frac{3}{4} \frac{c_k}{B_0^2}, \quad \beta = \frac{c_k R^2}{8(1+\eta)^2}, \quad \mu = \frac{\pi c_k R^2}{4} \frac{c_k^2 - c_s^2}{(1+\eta)c_s^2} \quad (15.6)$$

c_k is the phase velocity of the kink mode (15.3).

In the absence of dissipation a stationary solution of (15.5) is a solitary wave with the amplitude $A \simeq B_\perp^2$, width Δ , and travel velocity of the soliton, v_{sol} :

$$\psi = A \operatorname{sech}^2 \left(\frac{z - v_s t}{\Delta} \right) \\ \Delta = \sqrt{\frac{12\beta}{\alpha A}}, \quad v_{\text{sol}} = c_k + \frac{\alpha A}{3} \quad (15.7)$$

To obtain a nonstationary solution one has to derive the evolutionary equation for the amplitude, suggesting that all the parameters of soliton, its amplitude, A , width, Δ , and velocity, v_{sol} , are slowly varying functions of time. Using a standard procedure of fast and slow variables (Mjølhus 1976), we obtain the evolutionary equation for slowly varying amplitude for the modulated MKdV soliton, $\tilde{A}(\zeta, \tau)$, which is known to be a Schrödinger equation with cubic nonlinearity (Dodd et al. 1982):

$$i \frac{\partial \tilde{A}}{\partial \tau} + 3k \frac{\partial^2 \tilde{A}}{\partial \zeta^2} + \left(\frac{3}{4} - \frac{c_k^2}{4c_s^2(1+\eta)} \right) |\tilde{A}|^2 \tilde{A} = 0 \quad (15.8)$$

Here $\tilde{A} = A(\zeta, \tau)/A_0$ (A_0 being a soliton amplitude in the initial moment of time), and τ and ζ are slow time and space (dimensionless) variables:

$$\tau = (c_k^3/\beta)^{1/2}t, \quad \zeta = \tilde{z} - (1 - 3k^2)\tau \quad (15.9)$$

$\tilde{z} = (c_k/\beta)^{1/2}z$, and k is the wavenumber of a carrier wave, normalized by the inverse radius.

Equation (15.8) has two different solutions depending on the sign of the cubic term. If this term is negative, then (15.5) together with the Schrödinger (evolutionary) equation describes a soliton with slowly decaying amplitude.

The situation changes dramatically if this term is positive. At

$$\epsilon = \frac{3}{4} - \frac{c_k^2}{4c_s^2(1 + \eta)} > 0 \quad (15.10)$$

Equations (15.5) and (15.8) describe the interaction in the soliton gas which results in self-focusing (and self-modulation) of solitons. This is a well-known N-soliton solution in the exact theory of two-dimensional self-focusing of waves in nonlinear media pioneered by Zakharov and Shabat (1972).

It was shown that only pair interactions of solitons can occur. Therefore, since in the self-focusing problem the soliton has the meaning of a homogeneous waveguide, the N-soliton solution describes the intersection of N “homogeneous” channels with a bound state having a form of a “complicated” oscillating channel (Zakharov and Shabat 1972; Kuznetsov et al. 1995). Examples of the corresponding solution as applied to our problem are shown in Fig. 15.13. For background atmospheric parameters we adopt the reference model of the solar atmosphere (Maltby et al. 1986).

Solutions shown in Fig. 15.13 are obtained for height $h = 2200$ km. The background temperature at this height is $T = 2.1 \times 10^4$ K. The temperature in the self-focused structures, i.e., in the oscillating “energy” channel, is about 10^6 K. We adopted a flux tube radius at the surface of $R = 500$ km. The top panel shows the solution for a plage filling factor $f = 0.35$, and average magnetic field in flux tubes, $\langle B \rangle = 30$ G. The bottom panel corresponds to a solution for $f = 0.28$ and $\langle B \rangle = 20$ G. As expected from the observations, the braid period increases with decreasing filling factor of the flux tubes ensemble.

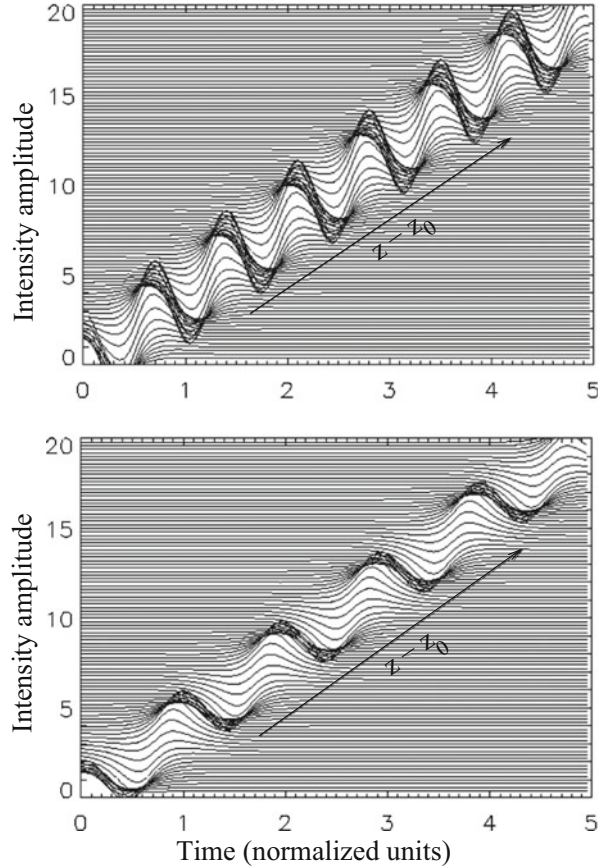
It is important to emphasize that there are two necessary conditions for the formation of these structures. First, the Schrödinger equation must have an N-soliton solution, i.e., condition (15.10) must be satisfied, i.e.:

$$c_k < \sqrt{3(1 + \eta)}c_s \quad (15.11)$$

Second, for solitons to interact through radiation, their velocity must be higher than the environmental (background) sound speed:

$$v_{\text{sol}} = c_k + \frac{\alpha A}{3} > c_s \quad (15.12)$$

Fig. 15.13 Visualization of N-soliton solution with radiation for two slightly different regimes. Top: Magnetic filling factor of plage is $f = 0.35$; Bottom: $f = 0.28$



These two conditions determine a finite thickness of self-organized structures and the optimal height of their formation. Quantitative estimates for the above examples give heights of formation $h \simeq 2\text{--}4\text{ Mm}$.

The mechanism described above may serve as a natural basis for models of coronal heating above the unipolar plages. Moreover, as the braided structures are easy to observe, they may serve as a valuable tool for the inference of physical parameters that are not directly observable.

It must be noted that the theoretical problem is treatable in a frame of energetically open turbulence and structure formation. Here again, a starting process is the one shown in Fig. 15.12: random flux tubes absorb the energy of the waves and convective motions; because of the randomness of flux tubes, the accumulated energy is transferred and released by the individual flux tubes at different times and different heights; the reradiated waves have random phases. Such a process most naturally generates plasma turbulence. Given a permanent energy supply and radiative losses, this is an energetically open turbulence that has a tendency for self-organization and structure formation.

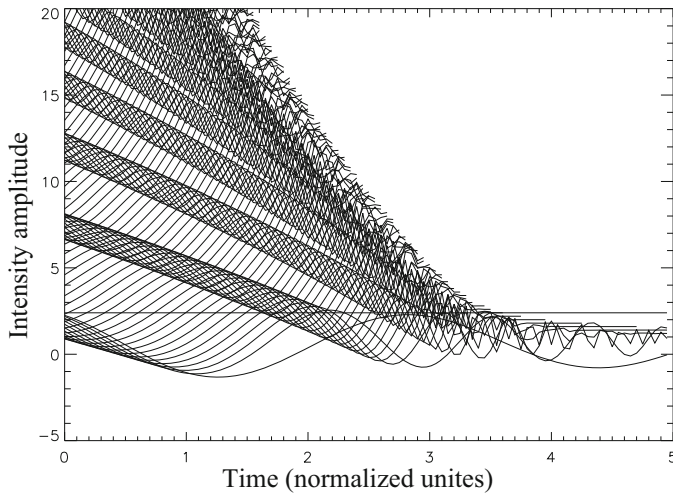


Fig. 15.14 Visualization of a collapse in soliton gas that leads to concentration of energy in a small volume and thus to the dramatic increase of the temperature in a squeezed volume. Due to self-focusing the system of solitons bifurcates into the state of a hot loops that should overlie the spongy structures

As a next step, one can study coupling processes between the coherent braided emission and the overlying hotter corona. If the observed structures above the unipolar plages have similar properties as “moss” (Berger et al. 1999), then above these structures $3\text{--}5 \times 10^6$ K coronal loops should be observed (Berger et al. 1999). In the frame of the present theoretical model this seems quite natural and may be attributed to well-studied phenomena of collapse in soliton gases and in energetically open turbulence (Grimshaw et al. 2001). Collapse in the system of solitons (as well as in turbulence) leads to concentration of energy in a small volume and thus to a dramatic increase of temperature in this volume. As a result of self-focusing in the coherent coronal emission, the system will bifurcate into the state of a much hotter loops. Qualitative picture of the N -soliton collapse is shown in Fig. 15.14.

Concluding this chapter, we must emphasize that strong inhomogeneity of the EUV emission at $1\text{--}2 \times 10^6$ K temperatures, and the fact that it evolves in time in very different ways, is largely determined by the “magnetic status” of underlying photosphere.

In particular, the EUV emission above plage regions dominated by single polarity magnetic elements always has an amorphous structure spread over the region that topologically mimics the shape of the underlying plage. Space-time slices of the amorphous EUV emission show coherent braidlike structures with almost constant period for a given area. The braid period depends mainly on the magnetic filling factor of the underlying plage. The denser the plage, the shorter is the braid period. The structures remain regular as long as the plage preserves its general

properties. The only factor observed to disrupt these structures was the emergence of opposite polarity magnetic field in the otherwise unipolar plage (Fig. 15.14, see also Fig. 15.4).

Contrary to the case of unipolar plages, coronal emission above the mixed polarity plages is highly discrete and consists of sporadic localized radiative transients—jets, microflares, and their combinations.

Although physical mechanisms that may explain the observed properties of the coronal emission are different for the mixed polarity plages and plages dominated by a single polarity magnetic elements, the primary energy source in either case is associated with hydromagnetic activity among the photospheric magnetic flux tubes. Thus, sporadic radiative transients observed in the corona above the mixed polarity plages are produced by the cumulative effects triggered by post-reconnections processes among the opposite polarity photospheric flux tubes.

On the other hand, the corona above plages dominated by single polarity elements is heated by the energy flux resulting from collective phenomena in the interaction of a random ensemble of flux tubes with the acoustic or MHD waves and unsteady wave packets. This energy flux is released in the corona over the finite region that mimics the underlying plage and has the properties of energetically open turbulence with a tendency to self-organization. These properties manifest themselves as periodically spaced regions of enhanced brightening forming braidlike structures in time similar to those obtained from observations. The observed coherent structures are extremely sturdy which characteristic to any self-organized state.

15.6 Problems

15.1 Consider finite amplitude Alfvén waves propagating along the magnetic field and analyze the conditions for the formation of Alfvén solitons and their properties.

15.2 Magnetic braiding and its accompanying phenomena have been a subject of intensive studies and accumulated a huge body of literature related to magnetic confinement experiments as well as solar and space plasmas. The equilibrium of twisted magnetic braid depends on the radius of curvature of a magnetic body, R , and the degree of twisting, $\kappa = B_\phi/B_z$. Find conditions for stability of the equilibrium state of magnetic braids in two cases:

- (a) $R \simeq \infty$;
- (b) for finite radius of curvature R .

References

- T.E. Berger et al., *Astrophys. J.* **519**, L97 (1999)
- R.K. Dodd et al., *Solitons and Nonlinear Wave Equations* (Academic, London, 1982)
- R.H.J. Grimshaw, E.A. Kuznetsov, E.G. Shapiro, *Physica D* **152**, 325 (2001)
- A. Jeffrey, T. Taniuti, *Non-linear Wave Propagation* (Academic, New York, 1964)
- E.A. Kuznetsov, A.V. Mikhailov, I.A. Shimokhin, *Physica D* **87**, 201 (1995)
- L.D. Landau, E.M. Lifshitz, *Fluid Mechanics* (Pergamon Press, Oxford, 1988)
- P. Maltby et al., *Astrophys. J.* **306**, 284 (1986)
- E. Mjølhus, *J. Plasma Phys.* **16**, 321 (1976)
- M.P. Ryutova, E. Priest, *Astrophys. J.* **419**, 349 (1993)
- M.P. Ryutova, E. Priest, *Astrophys. J.* **419**, 371 (1993)
- M.P. Ryutova, R. Shine, *Astrophys. J.* **606**, 571 (2004)
- M.P. Ryutova, T.D. Tarbell, MHD shocks and the origin of the solar transition region. *Phys. Rev. Lett.* **90**, 191101 (2003)
- M. Ryutova, S. Habbal, R. Woo, T. Tarbell, *Solar Phys.* **200**, 213 (2001)
- M. Ryutova, T. Tarbell, R. Shine, Interaction and dynamics of the photospheric network magnetic elements. *Solar Phys.* **213**(2), 231 (2003)
- R. Shine et al., *1999 Fall AGU Meeting*, SH41A-06 (1999)
- K.P. Stanyukovich, *Unsteady Motion of Continuous Media* (Pergamon Press, Oxford, 1960)
- T. Tarbell, M. Ryutova, R. Shine, Electro-mechanical coupling between the photosphere and transition region. *Solar Phys.* **193**, 195 (2000)
- G.B. Whitham, *J. Fluid Mech.* **3**, 337 (1958)
- V.E. Zakharov, A.B. Shabat, *Soviet Phys.-JETP* **34**, 62 (1972)

Chapter 16

Electrodynamic Coupling of Active Region Corona with the Photosphere



Abstract In the previous chapters we studied response of the chromosphere and corona to magnetic activity in the underlying quiet sun regions and both types of plagues, unipolar, and mixed-polarity ones. In this chapter we turn to the question how the chromosphere and corona respond to magnetic activity in the active regions where filling factor is close to unity. Our consideration will be based on a specific case favorably caught in multiwavelength observations, showing the entire process from the birth and evolution of a compact active region to formation and dynamics of coronal structures above it. We then discuss a general theory based on energetically open systems of currents that may be driven into various dynamic forms via nonlinear processes with continuous flow of matter and energy. Depending on the system parameters these may be long-living steady loops showing subtle oscillations, loops in the relaxation regime, and the periodically flaring and exploding loop systems. The theory also predicts that the EUV loops must have a filamentary structure and allows one to estimate the limiting currents and critical radii of elemental filaments associated with the stability criteria.

16.1 The Problem of Multi-Face Corona

The problem of energy production, transfer, and release throughout the solar atmosphere not only involves ambiguous mechanisms of the magnetic energy dissipation but also includes a wide range of phenomena that shape the upper layers of atmosphere and link their structure and dynamics to photospheric motions and magnetic fields. Especially rich in its diversity is the active region chromosphere and corona. Note that studies of active region corona were strongly dominated by attempts to explain coronal flares. However, observations show a great variety of coronal structures that do not produce the major flares. Most long-living coronal loop may slowly decay, oscillate, periodically result in flare-like events, produce a series of microflares, and even show spatio-temporal periodicity of microflares resembling the echo effects. In other words, the question why the solar flare *occurs* is, of course, important but no less important is the question why, under seemingly equal conditions, the flare *does not occur*. The answer to this question is closely

related to the very basic question: how the coronal structures are formed and what makes them to take one or the other form.

To look into this problem we shall consider some characteristic features of electromagnetic coupling throughout the solar atmosphere, and in particular, we shall study links between the photospheric driver and structure formation in the overlying chromosphere/corona. Special attention will be paid to the fact that the magnetic structures rooted in an unsteady photosphere/convective zone are necessarily the current carrying system. This fact plays a crucial role in the formation, evolution, and disruption of any magnetic structure throughout the solar atmosphere. As a first step one needs to investigate how the observed hydromagnetic effects may generate electric currents.

Generation of electric currents and their role in the astrophysical plasma is a long-standing problem and has been studied by many authors (see, e.g., Alfvén 1981, and the references therein). In applications to the solar atmosphere it was, for example, shown that plasma pressure at the base of magnetic flux tubes can drive large currents along the entire length of flux tube (Boozer 1988). In the nonlinear regime (when the interaction of flux tubes with convective motions is included) this effect leads to the generation of both longitudinal and azimuthal currents in flux tubes (Ryutova et al. 1996). Elfmov et al. (1996) showed that Alfvén waves can drive significant currents in solar coronal loops that may support loops in a quasi-stationary state.

Alfvén and Carlqvist (1967) suggested that the coronal loops and storage of flare energy can be represented by force-free currents analogous to the circuit currents and even performed laboratory experiment on current limitation and disruption. Because an inductive circuit has a general tendency to “explode,” it was supposed that it also may explain the coronal flares.

The advantage of the circuit approach is quite clear, as it naturally consolidates many different aspects of electrodynamics into a simple scheme. The concept of the electric circuit has been further exploited by several authors in application to a wide range of phenomena from the solar flares to ionospheric substorms (see monograph by Alfvén (1981) and the literature therein). Ionson (1982), addressing the problem of stellar coronal heating, emphasized that all the proposed mechanisms that were thought as a unique in their own right “are based upon a unifying foundation of electrodynamics whose principal ingredients are capacitance C (the ability of a magnetoplasma to store electric and kinetic energy), inductance L (the ability to store magnetic energy), resistance R (the ability to convert the above electrodynamic energy into thermodynamic end products such as heat). Extending the LRC circuit analogue to a continuously driven system with a $\beta \leq 1$ velocity field as a secondary voltage generator, Ionson established coupling between the solar surface driver and coronal dissipation region. The model gives scaling laws that are in a good agreement with the observations. These are, however, valid only for large-scale, long-living (stable) coronal loops.

In fact, due to flexibility of the equivalent circuit parameters that reflect the physical properties of a system both at macroscales and microscales, the LRC circuit approach has a great potential in studying an overall behavior of coronal structures.

The main point here is that the formation of a current system, storage and dissipation of electromagnetic energy, is ongoing and energetically unbalanced process. In other words this is a typical dissipative, energetically open system, driven into various dynamic forms via internal processes and sustained by a continuous flow of matter and energy.

The main properties of a system are determined by several key factors, such as (1) character of the photospheric driver; (2) magnetic field that interconnects the $\beta \geq 1$ energy source region with the $\beta \ll 1$ dissipation region; (3) local height of the chromosphere/transition region where the most efficient generation of currents occurs (Ryutova and Shine 2006; Ryutova 2006); (4) feedback between the current generation and dissipation regions; and (5) characteristic spatial scales and timescales of a system. A theory is quite transparent, and containing directly measurable parameters, allows quantitative analysis and comparison with the observations.

To clarify theoretical analysis by comparing them with observations we use here a specific event associated with the birth, formation, and evolution of compact coronal structures caused by strong localized motions generated by emerging magnetic flux in the photosphere. Multiwavelength observations show that long before the magnetic pore is formed, the chromosphere and transition region show a high activity above the future site of pore formation: rising but not yet visible magnetic flux exerts a strong pressure on the overlying plasma generating highly collimated plasma flows seen in the $H\alpha$ images. About the time when the magnetic pores are formed and the $H\alpha$ surges bifurcate into the established arc-like flows, a system of compact coronal loops is formed, showing direct connection between the motions associated with the evolving magnetic fields and the coronal structure formation.

16.2 Emerging Magnetic Flux and Structure Formation in Overlying Atmosphere

The primary data sets that we will use in this section are observations from the Swedish Vacuum Solar Telescope (SVST) on La Palma, complemented by the TRACE data sets, used in the previous chapter to describe the response of corona to magnetic activity in underlying plage regions. A target region now is a central sunspot and its nearby environment.

Figure 16.1 shows snapshots of the sunspot area and its overlying corona made at two instances of time several hours apart. The white arrow in Fig. 16.1a shows a part of a unipolar plage, and in particular, a group of the positive polarity flux tubes that form in the beginning of the observation, a pattern resembling a *kitten paw*. The corona above this region (panel b) shows an amorphous emission typical of regions overlying unipolar magnetic plages. Figure 16.1c, d taken hours later shows a fully developed pores of opposite polarities, and a completely different shape of

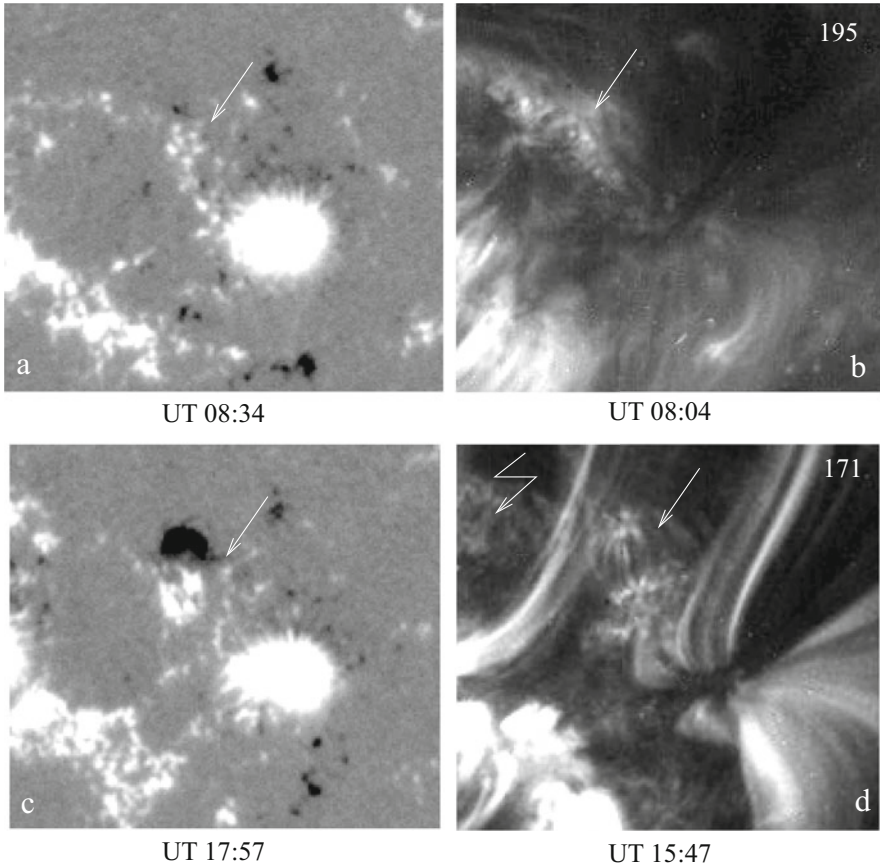


Fig. 16.1 Snapshots of the studied region. Aligned MDI and TRACE 171 and 195 images of the $56'' \times 51''$ area. MDI magnetogram is scaled from -500 to 500 G. Thin arrows show a future site of flux emergence and pore formation. (a) Positive polarity magnetic flux tubes form a “kitten paw” in the beginning of the observation. (b) 2.0×10^6 K emission in Fe XII 195 \AA has amorphous structure typical of unipolar plages. (c) Hours later, MDI magnetogram shows fully developed bipolar pores; (d) 10^6 K emission in Fe IX/X 171 \AA line shows well-established system of compact loops overlying the pore and large-scale “open” loops rooted in the central sunspot; broken arrow shows a sturdy character of the amorphous structure above the unipolar plage

the coronal emission. Part of the spongy emission seen before the pore formation is replaced by the system of compact loops overlying and “connecting” two opposite polarity pores.

It is remarkable that part of the amorphous emission outside newborn pores has preserved its unipolar properties and remains amorphous (panel c, broken arrow). As discussed in previous chapter, space-time slices of the amorphous EUV emission show coherent braid-like structures that remain regular as long as the plage preserves

its general properties. The only factor observed to disrupt these structures is the emergence of opposite polarity magnetic field in the unipolar plage.

In what follows we describe the evolution of coronal structures from the amorphous stage shown in Fig. 16.1b to much more complicated picture shown in Fig. 16.1d that includes compact loop structures overlying newly formed pores and prominent open structures rooted in the north side of the central sunspot.

Initially, there are few changes in the magnetic field configuration in and around the central sunspot. But, gradually, during the first 2 h, a group of positive polarity magnetic flux tubes that form the kitten paw move out and form a circle (Fig. 16.2, upper row). We know from the observations that this is a future site of a large-scale magnetic pore in form of a double compact sunspot. It is therefore natural to suggest that upward moving but not yet surfaced large magnetic flux generates plasma motions that sweep out the small scale flux tubes. This suggestion indeed

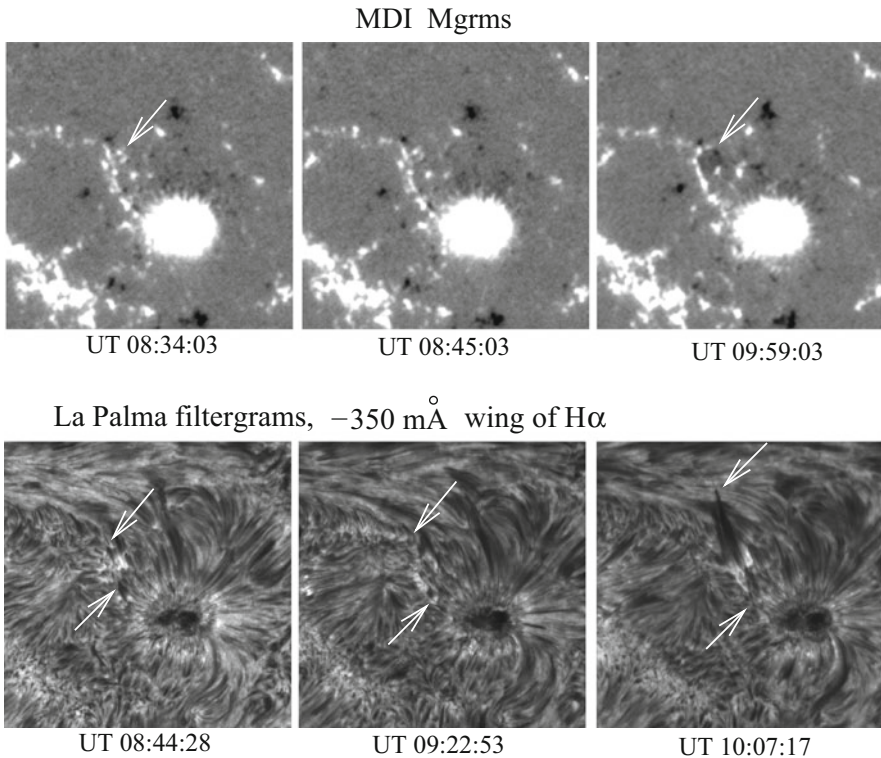


Fig. 16.2 Time sequence of snapshots showing changes in the configuration of the photospheric magnetic field and response of the chromosphere to this changes. During about 1 h 25 min positive polarity flux tubes forming the kitten paw, gradually move out and arrange into a circle with inclusions of a few negative magnetic flux tubes; Lower panels show the origination and evolution of an accelerating mass flow in the chromosphere

is readily supported by the chromospheric data: overlying chromosphere and even corona respond to these motions at very early stage.

Snapshots taken in a blue wing of $H\alpha$ (lower row in Fig. 16.2) show piercing plasma flow directed upward from *kitten paw* area, and their evolution in time. As early as about UT 08:45 when positive polarity magnetic flux tubes are still arranged in a kitten paw pattern, coronal plasma above this region is already significantly disturbed, and acquires a form of a dagger shaped upward flow. A primary coronal emission having an amorphous structure still remains amorphous but now is pierced by these flows. The appearance of a few negative polarity magnetic flux tubes before the large-scale magnetic flux surfaces causes in the transition region appearance of sporadic brightening. In the kitten paw region, the number of sporadic events increases with emergence of more and more of negative polarity inclusions.

It is important to note that the newly generated plasma flows themselves do not heat the surrounding coronal plasma. But they play an essential role in the final rearrangement of a hot coronal plasma and its additional heating, as we will see below. During the maximum activity of $H\alpha$ surges, the “damaged” corona still remains amorphous. Only when the $H\alpha$ surges abruptly decay does the coronal emission gets enhanced, suggesting that the energy of these flows somehow is converted into the heat.

The maximum activity of the $H\alpha$ surges and their decay phase are shown in Fig. 16.3, upper row. Lower row shows corresponding images during the decay phase. The former amorphous emission at the maximum phase in the 171 Å line

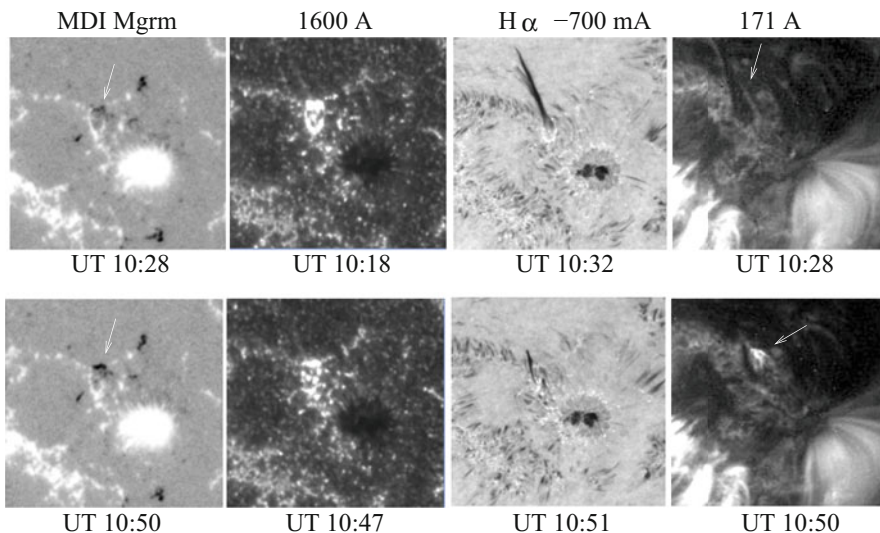


Fig. 16.3 Target region around the time of maximum activity of $H\alpha$ surges (upper row) and around the decay phase (lower row). The pores are not yet formed, but unipolar kitten paw pattern is replaced by mixed polarity magnetic fields resulting in significant energy input and release in the transition region (e.g., 1600 Å images)

(black dagger in upper image) is replaced by the appearance of the “first light”—a new enhanced emission (right panel in lower row).

At about the time when both positive and negative polarity pores are formed, two different types of formations develop in the overlying corona. One may be characterized as a system of “stable” loops rooted at the North edge of the sunspot and overlying unipolar region (marked by arrow “st” in Fig. 16.4). The other formation, also resembling a loop system, consists of frequent X-ray microflares, appearing at different places along the virtual lines that eventually become loops (marked by arrow “fl” in Fig. 16.4). Shortly after this stage, taken around UT 12:00, a seemingly unstable structure overlying the bipolar pore region forms a very regular loop system; from now on (e.g., after UT 13:03), this system keeps its identity for many hours (to the end of available data sets). Its persistent character is supported by a well-established flow system seen in H_{α} images.

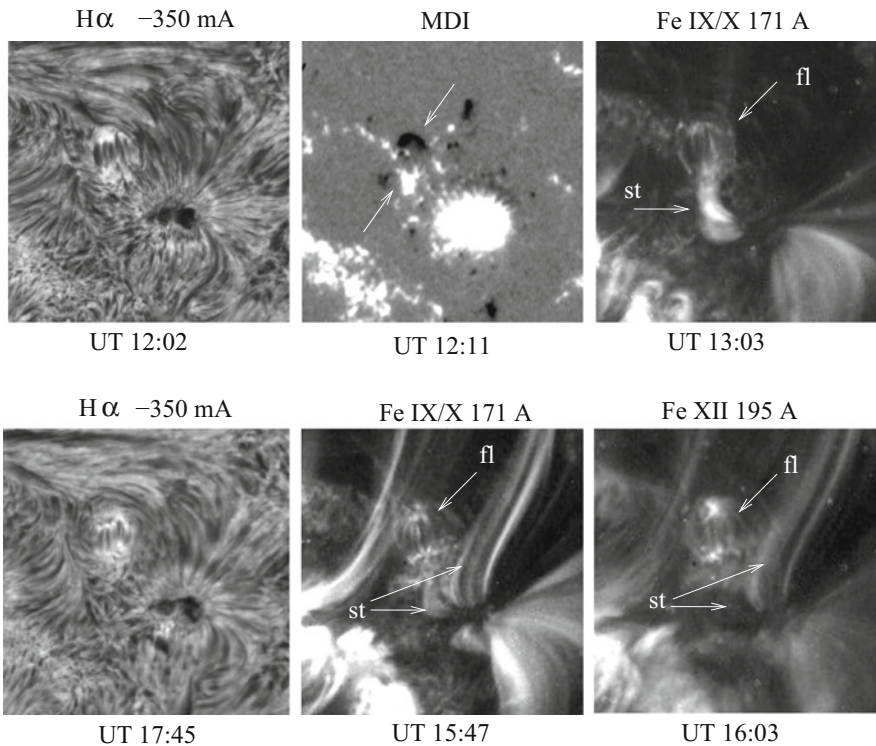


Fig. 16.4 Formation of compact coronal structures and their evolution. White arrow marked by “st” shows the compact loops that remain stable for over 2 h (upper row). In lower row these compact “stable” loops are shown disrupted and replaced by large-scale open spurs. The unstable structures consisting of sporadic microflares (marked by arrow “fl”), on the contrary, become stabilized. H_{α} images corresponding to these structures show a well-established flow pattern; a clear arc system formed by flows mimics the tiny arc system of loops seen in both coronal lines, 171 and 195 Å

The loop system marked by arrow “st” from the moment of its formation up to some time around UT 13:03 (period that lasted over 2 h) remained “quiet” and showed neither changes nor any microflare activity. At around UT 13:03 these loops seem to be gained some energy, and in couple of hours (at about UT 15:22), the compact loop system was gone, and in place of it large-scale open structures were formed. These structures are quite prominent in hotter 195 Å line as well (lower row in Fig. 16.4).

Obviously, their stable period was provided by the monotonic polarity of underlying region. In other words, the lack of opposite polarity magnetic elements ensured the lack of sporadic injection of energy into system. The appearance of additional energy and its source can be traced in space-time cuts shown in Fig. 16.5. Cuts made along lines 1 and 2 on the MDI image show motions of magnetic fluxes (horizontal panels 1 and 2) and cut 3 on the 1600 Å image. Two cuts made on the magnetogram show the motion of magnetic elements with slightly different orientations, and cut 3 shows a temporal variability of the enhanced emission in the transition region.

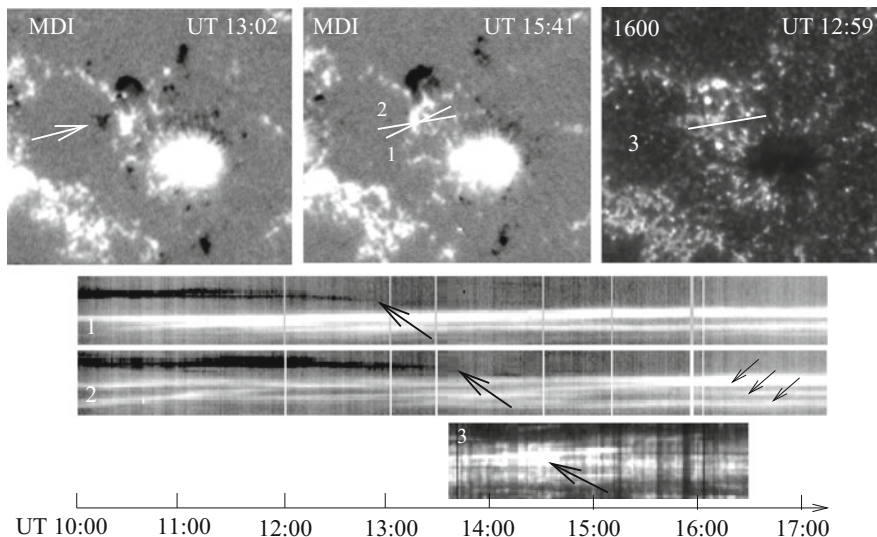


Fig. 16.5 Photospheric reconnections and chromospheric microflares preceding the structure formation in overlying corona. Left panel is the magnetogram showing a newborn negative and positive polarity pores at UT 13:02, with a negative satellite flux next to the positive pore (white arrow). It is this area where a continuous reconnection occurs. At the central panel showing magnetogram at UT 15:41, the satellite negative flux is already gone. The horizontal panels 1 and 2 are the space-time images made along the paths (1, 2) in the magnetogram, and 3 in the 1600 Å image. Space-time images 1–2 show the tracks of the motions of the magnetic elements, and 3 shows a temporal variability of the enhanced emission in the transition region. Large black arrows show photospheric reconnections; small black arrows show the splitting of the positive polarity flux into several flux tubes

One can see that during the period between UT 14:40 and UT 15:10 the negative polarity flux disappeared completely (shown by white arrow in the MDI snapshot at UT 13:02), and positive flux has been reduced and fragmented. There is a slight time lag between the final magnetic flux reduction and appearance of a strong chromospheric microflare of about 6 min. This is just the time needed to transfer and release the energy at the $T \simeq 10^5$ K in the transition region produced by the reconnection of the photospheric magnetic flux tubes (Tarbell et al. 1999; Ryutova and Tarbell 2003). Series of reconnection processes (black arrows in panels 1, 2 of Fig. 16.5) that provided the strong energy supply to previously stable loop system naturally lead to its destruction. This series of reconnection events could also trigger the processes along the entire North edge of the sunspot resulting the formation of large-scale open coronal loops (see 171 and 195 Å coronal images in Fig. 16.4).

Obviously, the mechanisms that may explain the observed regularities must, in the first place, link the formation of coronal structures with their *forerunner*, strong plasma motions generated by emerging but not yet visible magnetic flux. We will see below that such mechanisms are uniquely associated with the current drive, arising due to a strong disturbances propagating in the magnetized plasma. In the next section we will address these mechanisms and estimate possible values of generated currents.

16.3 Current Drive Mechanisms Associated with the Emerging Magnetic Flux

A strong disturbances confined in a limited surface area and propagating upward in the magnetized and sharply stratified atmosphere may provide several sources for efficient current drive. The kick produced by the large emerging flux generates acoustic and Alfvén waves. The exchange of energy and momentum between the induced waves and the electrons leads to an efficient generation of electric currents. Strong collimated flows (analog of a beam-plasma system) cause generation of currents as well. Finally, helical motions clearly seen in the generated H_α surges (see, e.g., Fig. 16.3) may also contribute to the current drive.

Non-inductive current drive is a fundamental process used for decades to generate and continuously sustain the toroidal currents in tokamak fusion devices (see, e.g., Fish 1987 and the literature therein). It can be studied as a natural process occurring in various space plasmas as well (Otani and Strauss 1988; Ryutov and Ryutova 1989; Block et al. 1998). Although there are a number of very different non-inductive methods of current generation, they all rely upon two basic principles: (i) beam–particle interactions (Ohkawa 1970), and (ii) wave–particle interactions (Wort 1971). In any case it is the energy and momentum exchange between the electrons and wave/particles that determines the efficiency of the current drive, $\eta = j/\mathcal{P}$. j is a current density, and $\mathcal{P}=dW/dt$ is work done by the “source”,

i.e. the induced power per unit volume of plasma:

$$\mathcal{P} = \frac{1}{2} m_p \frac{d(nu^2)}{dt} \quad (16.1)$$

In other words, the plasma electrons interacting with particles and/or waves gain a momentum $m_e nu$, where n is a plasma density and u is a longitudinal component of the injected beam (or wave) velocity; this momentum (and the electric current associated with it) is subject to losses due to electron ion collisions. Thus, the momentum balance is determined by the equation (Fish 1987):

$$\frac{dj}{dt} \simeq \frac{e}{m_e} m_p u \frac{dn}{dt} - v_{ei} j \quad (16.2)$$

where v_{ei} is electron-ion collision frequency, u is the velocity of the injected beam or the phase velocity of a source wave. Equation (16.2) gives a standard estimate for the efficiency of current drive in the stationary regime:

$$\eta = \frac{j}{\mathcal{P}} \simeq \frac{e}{m_e v_{ei} u} \quad (16.3)$$

The induced power depends on the specific mechanism of the current drive. We will consider three major cases.

16.3.1 Proper Motion

First we will estimate the currents that may be driven by strong collimated flows similar to those observed in our data set (cf. Fig. 16.3). As the hydrogen plasma is injected into the atmosphere, the streaming particles with velocity, u , interact with the background electrons. Induced power per unit volume of plasma may be estimated using the standard transport equations (Trubnikov 1965), which give:

$$\mathcal{P} \simeq m_p n \tilde{\nu}_{ie} u^2 \alpha \frac{u^2}{v_{Te}^2} \quad (16.4)$$

Here $\tilde{\nu}_{ie} = (m_e/m_p)v_{ie}$ is the inverse slowing-down time of particles via electron ion collisions; the factor $\alpha(u/v_{Te})^2$ is the cross-section of electron ion collisions, where α is a coefficient of the order of unity (Stanyukovich 1960), and v_{Te} is the electron thermal velocity. With this estimate and (16.3), the current density is estimated as $j \simeq neu(u/v_{Te})^2$.

The quantitative estimates for our observations are as follows. The average velocity of H_α surges is $u \simeq 2.0 \times 10^6$ cm/s. Low in the atmosphere, say at $T = 2.0 \times 10^5$ K and density $n = 4.0 \times 10^{10}$ cm⁻³ ($v_{Te} = 5.5 \times 10^8$ cm s⁻¹), generated

current density may be quite high, $j \simeq 0.17 \text{ A m}^{-2}$. Higher in the atmosphere, the efficiency drops. Thus, at $T = 10^5 \text{ K}$, $n = 4.0 \times 10^{10} \text{ cm}^{-3}$, and $T = 8.0 \times 10^5 \text{ K}$, $n = 2.0 \times 10^9 \text{ cm}^{-3}$, current densities become respectively, $j \simeq 8.5 \times 10^{-3} \text{ A m}^{-2}$ and $j \simeq 2.1 \times 10^{-4} \text{ A m}^{-2}$. These estimates are close to current densities in the EUV loops estimated from the analysis of vector magnetograms of active regions (Georgoulis et al. 2004).

16.3.2 Acoustic Waves

It was shown (Ryutov and Ryutova 1989) that strong disturbances generated in the solar atmosphere from a limited area and propagating upward against gravity may excite electric currents (and magnetic fields) in the transition region between the chromosphere and corona.

Two simple properties of the solar atmosphere provide the basis of the mechanism: (1) upward propagating waves quickly steepen due to sharp stratification and at the chromospheric height break into sequence of shocks, and (2) at these heights the plasma is strongly collisional. It was shown that in strongly collisional plasma for the perturbations emitted from a limited surface area, half of the wave momentum is transferred to electrons and half to ions. This means that the velocity of the electrons becomes m_i/m_e times higher than that of the ions providing the generation of currents. The mean force acting on the electron gas, F_e , has been evaluated in two cases, for purely sinusoidal wave (low atmosphere), and for a nonlinear wave that reaches the sawtooth, weak shocks regime. In the linear case F_e has a form:

$$F_e = \frac{4\pi^2}{15} \frac{m_p c_s \kappa_e}{\lambda^2 n} \xi \quad (16.5)$$

where $\kappa_e = nkT\tau_e/m_e$ is the electron thermal conductivity, λ is the wavelength, and $\xi = W/\rho c_s^2$ is actually a squared Mach number, W being an acoustic wave energy. In the second case the energy dissipation occurs at the front of a shock and no longer depends on κ_e (Landau and Lifshitz 1988). F_e then has the form:

$$F_e = \frac{8\sqrt{3}m_p c_s^2}{\lambda} \xi^{3/2} \quad (16.6)$$

In a stationary regime which is established in about time associated with skin-effect, the generated currents reach the value:

$$j = \frac{\sigma}{e} F_e \quad (16.7)$$

First we estimate the generated currents by the sinusoidal waves (linear regime). This regime may be valid only up to heights of a few hundred km above the surface. For example, let us take the temperature $T = 6.2 \times 10^3$ K, electron density $n_e = 10^{11} \text{ cm}^{-3}$, and the wavelength $\lambda = 3 \times 10^7$ cm. Sound speed is then $c_s \simeq 9.2$ km/s, the wave amplitude is about 8 km/s (assuming that the initial wave amplitude is 0.5 km/s, and the average scale height is 200 km), and $\xi \simeq 0.76$. With these parameters (16.5) and (16.7) give an estimate of the generated current density $j = 1.3 \times 10^{-8} \text{ A/m}^2$.

In weakly nonlinear, sawtooth regime ($\xi \geq 1$), the efficiency of current drive increases dramatically, in fact, by about 6 orders of magnitude. From (16.6) and (16.7) we have

$$j = 0.275 \frac{e}{m_e} \frac{T^{3/2}}{\ln \Lambda} \frac{8\sqrt{3} m_p c_s^2}{\lambda} \xi^{3/2} \quad (16.8)$$

Now, for example, at $T = 8 \times 10^3$ K ($h \simeq 2000$ km), $c_s \simeq 10.4$ km/s, $\ln \Lambda = 16$, $\lambda = 3 \times 10^7$ cm, and $\xi = 1.1$, we have $j = 2.1 \times 10^{-2} \text{ A/m}^2$. This is a typical current density for the EUV loops.

16.3.3 Alfvén Waves

To estimate the efficiency of current drive by Alfvén waves we need to find the power dissipated by the Alfvén waves in the presence of plasma flows. Current drive by Alfvén waves in coronal loops in the absence of mass flows was studied, e.g., by Elfilimov et al. (1996). The effects of mass flows on the dissipation of Alfvén waves in the solar atmosphere have, however, very characteristic features (Ryutova and Habbal 1995). It was found that in the approximation of geometrical optics the energy dissipation rate, \mathcal{P} , has a form:

$$\mathcal{P} \simeq v_* (\nabla_{\perp} S)^2 \frac{\rho_0 (v_{0A} + u_0)^2}{2} \exp \left(- \int^l v_* \frac{(\nabla_{\perp} S)^2}{v_A + u} d\ell \right) \quad (16.9)$$

Here $v_* = (\eta_0/\rho) + \eta_D$ is the combined dissipative coefficient; $\eta_0 = 0.96nkT\tau_i$ is the ion viscosity and $\eta_D = c^2/4\pi\sigma$ is the magnetic diffusivity, and τ_i is the ion collision time (Braginskii 1965). u is the flow velocity. $\nabla_{\perp} S$ is the gradient of eikonal across the magnetic field structure. The integration is performed along the ray trajectory. With the simplified magnetic field geometry $\mathbf{B} = \mathbf{B}(0, B_{\phi}(r), B_z)$, and plasma flow directed along the vertical B_z component, the dissipation rate at height z can be estimated as follows:

$$\mathcal{P} \simeq v_* \frac{\rho \omega^2}{2} \frac{(v'_{A} + u')^2}{(v_A + u)^2} z^2 \exp \left[- \frac{2}{3} v_* \frac{\omega^2 (v'_{A} + u')^2}{(v_A + u)^5} z^3 \right], \quad (16.10)$$

The height dependence of \mathcal{P} has a form $f(\zeta) = \zeta^2 e^{-\frac{2}{3}\zeta^3}$. This function has a maximum at $\zeta = 1$, which for given physical parameters determines maximum amount of the power absorption, \mathcal{P}_m , and its height, z_m . With the approximation $(v_A + u)/(d(v_A + u)/dr) \sim R$, where R is a radius of a separate filament in a magnetic structure, the estimates for these quantities are as follows:

$$z_m \simeq (v_A + u)\tau_\omega, \quad \mathcal{P}_m \simeq \frac{\rho(v_A + u)^2}{2\tau_\omega} e^{-2/3} \quad (16.11)$$

where we introduced notation

$$\tau_\omega = \left[\frac{R^2}{v_* \omega^2} \right]^{1/3} \quad (16.12)$$

τ_ω has a meaning of the inverse damping rate of the Alfvèn waves due to the phase mixing (Ryutova and Habbal 1995). Using (16.2) we can now estimate the maximum current density, $j_m = [e/m_p \tilde{v}_{ei}(v_A + u)]\mathcal{P}_m$ (the z-dependence of generated currents is the same as in (16.10)):

$$j_m \simeq 0.257ne(v_A + u) \frac{1}{\tilde{v}_{ei}\tau_\omega} \quad (16.13)$$

For quantitative estimates we choose some exemplary values for temperature, density, and the Alfvèn speed typical for the chromosphere and lower transition region. These are shown in Table 16.1 together with kinetic coefficients calculated via standard expressions:

$$v_* = 1.32 \times 10^9 \frac{T^{5/2}}{n \ln \Lambda} + 5.25 \times 10^{11} \frac{\ln \Lambda}{T^{3/2}}, \quad (16.14)$$

Table 16.1 Estimate of the generated current densities and corresponding heights

Parameter	Set 1	Set 2	Set 3
T (K)	2.0×10^4	10^5	3.0×10^5
n (cm^{-3})	4.0×10^{10}	2.0×10^{10}	10^{10}
\tilde{v}_{ei} (s^{-1})	4.4×10^2	25.0	2.4
v_* ($\text{cm}^2 \text{s}^{-1}$)	1.2×10^8	10^{10}	3.27×10^{11}
v_A (cm s^{-1})	6.5×10^6	9.2×10^6	1.3×10^7
R (cm)	2.0×10^6	4.0×10^6	10^7
$\omega = 0.1 \text{ s}^{-1}$			
z_m (cm)	1.3×10^9	6.13×10^8	4.73×10^8
j_m (A m^{-2})	2.1×10^{-3}	7.0×10^{-2}	0.82
$\omega = 0.3 \text{ s}^{-1}$			
z_m (cm)	6.13×10^8	2.93×10^8	2.33×10^8
j_m (A m^{-2})	4.4×10^{-2}	0.14	1.7

and $\tilde{v}_{ei} = 1.97 \times 10^{-3} n \ln \Lambda / T^{3/2}$. For the plasma flow we take again $u = 2.0 \times 10^6 \text{ cm s}^{-1}$, and for radius of a magnetic filament $R = 2.0 \times 10^6 - 10^7 \text{ cm}$.

The last six rows in Table 16.1 contain the height of the maximum absorption and corresponding maximum density of the generated currents estimated for Alfvén wave frequencies, 0.1 and 0.3 s^{-1} . The efficiency of the current drive is quite sensitive to the frequency of the Alfvén waves—higher frequency waves can generate stronger currents and at lower altitudes. Nonetheless, the variation of the basic physical parameters (corresponding to chromosphere/transition region) gives the range of current densities close to those shown in Table 16.1 and is consistent with observations.

The estimate of corresponding heights shows that generated currents mainly reach their maximum values at the transition region level. It is also important to also mention that the injection of a magnetic helicity, which is a necessary part of the emergence of complex magnetic fields, can also play an important role in the current drive.

Each effect or their combinations may contribute to generation of currents. The dominance of one or the other effect depends on the specific situation and the local physical parameters of the system.

16.4 Energy Flow Throughout Solar Atmosphere

In the previous sections, we studied formation and properties of the EUV structure formation associated with the emergence of a large-scale magnetic flux which eventually formed two opposite polarity pores. We saw that long before the magnetic pore is formed, chromosphere and corona show a high activity above the future site of pore formation: rising but not yet visible magnetic flux exerts a strong pressure on the overlying plasma generating highly collimated plasma flows seen in the $H\alpha$ images. About the time when the magnetic pores are formed and $H\alpha$ surges bifurcate into the established arc-like flows, a system of compact coronal loops are formed, showing direct connection between the plasma motions, the evolving magnetic fields and the coronal structure formation. It was suggested that the triggering mechanism for structure formation may be associated with generation of currents caused by strong disturbances propagating upward from a limited surface area.

The kick produced by highly concentrated emerging flux is not only accompanied by the observed $H\alpha$ flows but may also generate acoustic and Alfvén waves. Therefore, the efficiency of current drive has been analyzed for three main sources:

1. the proper motion of hydrogen plasma,
2. the acoustic waves, and
3. the Alfvén waves.

Quantitative estimates of current densities for each of these mechanisms are in the range of $j_m = 2.1 \times 10^{-3} - 2 \text{ A m}^{-2}$, which agrees with the reported range of measured current densities (Leka et al. 1996; Georgoulis et al. 2004; Georgoulis and LaBonte 2004). We saw that generated currents reach their maximum values mainly at the transition region heights. It should be emphasized again that the current drive is considered as the initial stage of the EUV structures formation.

Now we turn to the question how the structures evolve in time. We shall use the electric circuit analogue to address this problem focusing on major questions: what makes the coronal structures take one or the other observed form, and what are the conditions for their realization.

Once a current system is formed, its further evolution depends on the capacity of a system to store electromechanical and magnetic energies, on its dissipative properties and thus the ability to release the accumulated energy. These properties are determined by several key factors, such as:

1. character of the photospheric driver;
2. magnetic field that interconnects the $\beta \geq 1$ energy source region and $\beta \ll 1$ dissipation region;
3. local height of the chromosphere/transition region where the most efficient generation of currents occurs;
4. feedback between the current generation and dissipation regions; and
5. characteristic spatial and time scales of a system.

The key element of the present approach is the recognition of the fact that the transition region plays an essential role in the process of energy transfer throughout the atmosphere (see, e.g., Title 2000; Tarbell et al. 2000; Ryutova and Tarbell 2003; Ryutova and Shine 2004). On the one hand, this is a region where the most efficient generation of currents occurs, and on the other hand, it is where presumably the energy transfer from large- to small-scale culminates, thus providing interconnection between corona and its underlying atmosphere through the resistive stresses.

16.4.1 An Equivalent Circuit: Earlier Attempts

The evolution of newly formed current system may proceed in different ways depending on hydromagnetic activity of underlying photosphere and on physical and kinetic properties of a system, in other words on the nature of photospheric driver and the overlying region.

The equivalent LRC approach turned out to be very helpful to study not only coupling between the energy source and remote dissipation regions, but also to analyze the various scenarios and find conditions for their realization on a unified basis.

The circuit equation follows directly from the global electrodynamics, and has been derived by many authors in application to laboratory plasma (see, e.g., Lehnert 1963) and to various space objects (Alfvén and Falthammar 1963; Alfvén and Carlqvist 1967; Ionson 1982; Spicer 1982; Melrose 1995). Generally, the equation has a standard LRC form, but its coefficients obtained from the MHD equations written for a particular system reflect the specific parameters of this system.

For convenience, we will demonstrate here the equivalence of an LRC circuit and electrodynamic equations:

$$\frac{4\pi}{c^2} \frac{\partial \mathbf{j}}{\partial t} = \nabla \times (\nabla \times \mathbf{E}) \quad (16.15)$$

$$\nabla \cdot \mathbf{j} = 0 \quad (16.16)$$

$$\mathbf{j} = \sigma \left(\mathbf{E} + \frac{\mathbf{v} \times \mathbf{B}}{c} \right) \quad (16.17)$$

$$\rho \frac{d\mathbf{v}}{dt} = -\nabla P_e + \frac{\mathbf{j} \times \mathbf{B}}{c} \quad (16.18)$$

One can start from the equation of motion for the electron gas and arrive to the equation for the generation of the electric field (Spicer 1982; Melrose 1995). This approach leads to a simple circuit equation of a ‘transmission line.’ In this case, however, the physical mechanism of coupling which occurs at small resistive scales is obscured.

As it was pointed out by Ionson (1982), the electrodynamic coupling between the two regions occurs through the turbulent stressing of the common magnetic field in the photosphere that results in generation of a Poynting flux of energy that propagates upward and subsequently dissipates. This process is directly related to the dissipation of the surface Alfvén waves (and associated heating) where energy is transferred from large to small scales by phase mixing.

Indeed, because of high conductivity of coronal plasma, dissipative effects turn on at a small transverse scale, Δx_r , where the resonance absorption of the Alfvén waves occurs. In other words, Δx_r is a characteristic distance at which the dissipative terms link the perturbations at the magnetic field lines (Heyvaerts and Priest 1983; Ryutova and Habbal 1995):

$$\Delta x_r = \frac{a}{Re_m^{1/3}}, \quad (16.19)$$

$Re_m = v_A a / \eta_D$ is the magnetic Reynolds number with $\eta_D = c^2 / 4\pi\sigma$ being magnetic diffusivity, and $\sigma = 1.96ne^2 / (m_e v_{ei})$ plasma conductivity. Parameter a is the width of magnetic structure.

16.4.2 LRC Circuit with Mutual Inductance (Transition Region)

Thus physics of coupling is associated with the dissipative stresses that operate at small scales characterized by generalized skin depth, Δx_r , which is in fact the local cross-field shear length of the induced current.

Here we adopt the approach used by Ionson (1982, 1984). Figure 16.6a illustrates the prototype of physical system from subsurface layers to the corona and its equivalent electrodynamic circuit. The system comprises a $\beta < 1$ magnetic loop and an underlying region of $\beta \geq 1$ velocity fields which are electro-dynamically coupled via the interconnecting magnetic field. It is important to note, however, that Ionson’s model (as well as all other previous models) ignores the influence of the transition region. The points marked by the question marks and the straight line passing them in Fig. 16.6a is only a formal boundary between the two regions, and is not reflected in the circuit equation. On the other hand, Fig. 16.6b that illustrates the energetically open circuit includes the presence of the transition region and its influence. This will be discussed in the next section. Before doing this, we will continue Ionson’s (1982) line of reasoning.

Despite the above-mentioned disadvantage, the Ionson’s model is important to discuss. Let us choose a coordinate system with l directed along the magnetic field, and $x_{\perp} = (x_r, x_{\theta})$, where x_r represents the radial direction, with characteristic scale Δx_r , and x_{θ} —the azimuthal direction, with characteristic scale of the width of elemental loop, a . It is assumed that physical parameters vary only in the l and x_r directions. Using $(\nabla \times \mathbf{E})_l \simeq 0$, which follows from the condition that Poynting

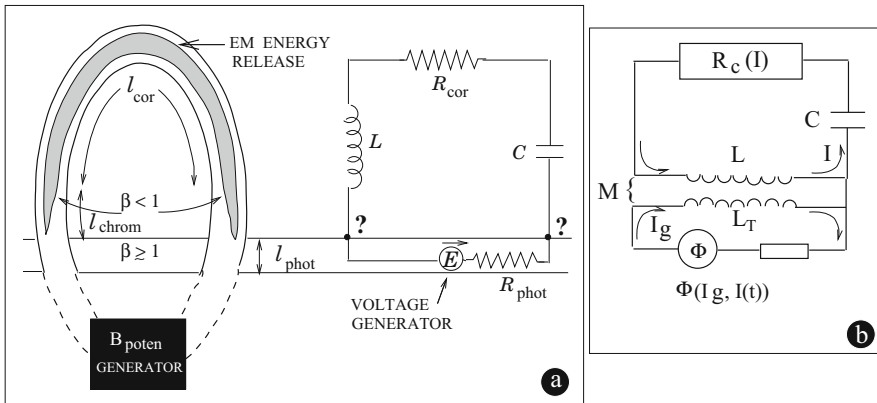


Fig. 16.6 Model of the equivalent LRC circuit for the coronal loops: (a) Prototype magnetic loops system proposed by Ionson (1982); question marks highlight the cloudy points on line dividing a $\beta \geq 1$ and $\beta < 1$ regions; (b) Energetically open LRC circuit (Rytova 2006); Chromosphere/transition region is reflected by the necessarily present mutual inductance, M

flux be directed along the loop, one has from (16.15):

$$\frac{4\pi}{c^2} \frac{\partial \mathbf{j}_\perp}{\partial t} + \nabla_\perp \left(\frac{\partial E_l}{\partial t} \right) - \frac{\partial^2 \mathbf{E}_\perp}{\partial l^2} = 0 \quad (16.20)$$

$$\frac{4\pi}{c^2} \frac{\partial j_l}{\partial t} + \frac{\partial}{\partial l} (\nabla_\perp \cdot \mathbf{E}_\perp) - \nabla_\perp^2 E_l = 0 \quad (16.21)$$

Obviously, $\partial/\partial x_r \gg \partial/\partial x \gg \partial/\partial l$. This implies that $E_\theta \ll E_r$, and since $\mathbf{j}_\perp \sim \partial \mathbf{E}_\perp/\partial t$, $j_\theta \ll j_r$. Taking into account that $\nabla \mathbf{j} = 0$, one can see that (16.20) and (16.21) are redundant.

Thus, formally it is sufficient to consider one of the above equations. But as will be discussed later choice of the equation is not only matter of convenience but may cause essential limitations. To demonstrate this we briefly describe below Ionson's derivation who has focused upon (16.21). Using Ohm's law, and taking time derivative of (16.21) one obtains:

$$\frac{4\pi}{c^2} \frac{\partial^2 j_l}{\partial t^2} + \frac{\partial^2}{\partial x_r \partial l} \left(\frac{1}{\sigma} \frac{\partial j_r}{\partial t} \right) - \nabla_\perp^2 \left(\frac{\partial j_l}{\partial t} \right) - \frac{1}{c} \frac{\partial^3 (v_\theta B)}{\partial x_r \partial l \partial t} = 0 \quad (16.22)$$

With the use of the Heaviside step function of plasma beta, $H(1 - \beta)$, this equation can be rewritten in the form that reflects the contribution of various terms of this equation in the $\beta \geq 1$ and $\beta < 1$ regions. Note that the second term in this equation can be neglected since it is small compared to the other terms. The last term has a meaning of the driving emf in the $\beta \geq 1$ region, which cannot be evaluated explicitly. In the $\beta < 1$ region this term represents the reactance of the overlying plasma to driving emf, and can be easily determined from the force balance, Eq. (16.18):

$$\rho \frac{\partial v_\theta}{\partial t} \simeq -\frac{j_r B}{c}, \quad (16.23)$$

Now (16.22) can be written as follows:

$$\frac{4\pi}{c^2} \frac{\partial^2 j_l}{\partial t^2} - H(1 - \beta) \frac{1}{\sigma} \frac{\partial^3 j_l}{\partial x_r^2 \partial t} - H(1 - \beta) \frac{4\pi v_A^2}{c^2} \frac{\partial^2 j_l}{\partial l^2} = H(\beta - 1) \frac{1}{c} \frac{\partial^3 (v B_0)}{\partial x_r \partial l \partial t} \quad (16.24)$$

This equation has already a form of a simple LRC equation: the first term is an inductive reactance, the second term is associated with the resistance, the third term is a capacitive reactance, and the term on the right-hand side is the external source of emf.

Using the equivalence $\partial/\partial x_r \rightarrow i\pi/\Delta x_r$, $\partial/\partial l \rightarrow i\pi/l$, (16.24) can be integrated over the total volume of the magnetic loop. Note that this integration is equivalent to averaging procedure in which Eq. (16.24) is multiplied by volume

of the elemental loop of the length l , i.e., by $la\Delta x_r$. One should bear in mind that j_l currents are localized within a cross-sectional area, $a\Delta x_r$.

Assuming that *most of the resistive load is associated with the $\beta < 1$ region*, the result of this integration is as follows:

$$L\frac{d^2I}{dt^2} + R\frac{dI}{dt} + \frac{I}{C} = \frac{d\Phi(t)}{dt}, \quad (16.25)$$

where the equivalent inductance L , capacitance C , and resistance R are given by

$$L = \frac{4l}{\pi c^2}, \quad C = \frac{lc^2}{4\pi v_A^2}, \quad R = \frac{1}{\sigma} \frac{l}{(\Delta x)^2}, \quad (16.26)$$

with the current and emf as

$$I = j_l a \Delta x_r = j_r a l \quad (16.27)$$

$$\Phi(t) = \frac{av_\theta B}{c} \quad (16.28)$$

(16.25)–(16.28) obtained by Ionson (1982, 1984) allowed him to perform detailed analysis and obtain several important results. In particular, the coupling between the photospheric driver and coronal loop features was established, and implicit equations for the maximum temperature and base pressure were found in a good agreement with observations. It was shown that coronal loops have a classic feature of high quality resonators, which allows, for example, to study the resonant properties of a system and make reasonable predictions.

This model, however, can be applied only to a “stable” (long living) coronal loops, and does not describe their *evolution*. The important restricting factor here is the assumption (highlighted above in italic) that the resistive load of a system is associated only with the $\beta \ll 1$ coronal region. But, as discussed earlier, the energy production and transfer necessarily involves the transition region where the resistive stresses already operate at the corresponding small scales. The coupling mechanism therefore must reflect connection between the resistive properties of both, corona and the transition region, as shown schematically by the mutual inductance, M in Fig. 16.1b.

16.5 Energetically Open Circuit

To represent transition between the chromosphere and corona, as discussed above, we take into account that the resistive load is associated not only with the corona, but with the chromosphere/transition region as well. This leads to appearance of an equivalent mutual resistance in the circuit equation, which in fact is equivalent

to appearance of mutual inductance. This element is crucial for stability of newly formed EUV structures and realization of different scenarios of the structure evolution. Besides, as the system has all the properties of energetically open, locally non-conservative system with source and sink of energy, we extend the analysis to nonlinear processes. Fully nonlinear treatment of the problem is hardly possible, but the advantage of circuit approach is that it allows quite a simple treatment of weakly nonlinear unsteady processes.

One of the basic principles of the circuits is that if Ohm's law, $\Phi = RI$, does not hold, the circuit must be considered *nonlinear*. There are many factors that brake Ohm's law in practice. First of all, if there is some functional relation between I and Φ , the circuit becomes intrinsically nonlinear. Among numerous so-called contingently nonlinear elements, one of the most important is thermally sensitive resistance. Even a weak dependence of the resistance on temperature leads to nonlinear functional of $I = I(\Phi)$ (see, e.g., Harnwell 1949). The present study will be restricted only by the intrinsic nonlinearity of a system.

As shown in Sect. 16.2, the triggering mechanism for the EUV structure formation is associated with electric currents generated by strong disturbances produced by the emerging flux. We have discussed the efficiency of current drive for three types of disturbances: proper motion of hydrogen plasma (the observed $H\alpha$), acoustic waves, and Alfvén waves.

It is hard to tell which of these mechanisms is dominant during the formation process. However, after the current system is formed, one can accept that its sustaining source of energy has a periodic or quasi-periodic character. It is therefore only natural to assume that during the entire process, the currents are voltage-dependent, $I = I(\Phi)$, and the sustaining photospheric driver is quasi-periodic. This, of course, does not exclude some sporadic injection of energy, caused, for example, by the reconnection processes.

We will distinguish three interconnected regions: (1) the photosphere with the quasi-periodic driving force, (2) chromosphere/transition region where the most efficient generation of currents occurs, and (3) corona.

Figure 16.7 illustrates a typical example of well-established system of coronal loops near the eastern limb of the Sun (the image is rotated by 90° so that north is to the right, upper panel) together with co-aligned MDI magnetogram of underlying region and its image at the transition region temperatures (lower panels). The average length of the coronal part of loops is about $l \simeq 280$ arcsec ($\simeq 2 \times 10^{10}$ cm), and width of elemental filament is in a range of $a \simeq 1\text{--}3$ arcsec ($\simeq 0.73\text{--}2.2 \times 10^8$ cm). The aspect ratio is of the order of $(a/l) \simeq 0.01$. This estimate will be used below for quantitative analysis.

Note that as longitudinal currents are localized within a cross-sectional area, $a\Delta x_r$, where Δx_r is determined by (16.19), each elemental loop resolved in TRACE 171 Å line consists of thousands of current carrying filaments.

The family of loops is rooted at relatively compact sunspots with well-defined boundaries (marked by large arrows). The enhanced emission at the transition region temperatures corresponding to these sunspots is spread over much larger area that mimics the bright conglomerate of coronal loop footpoints. Note that transition

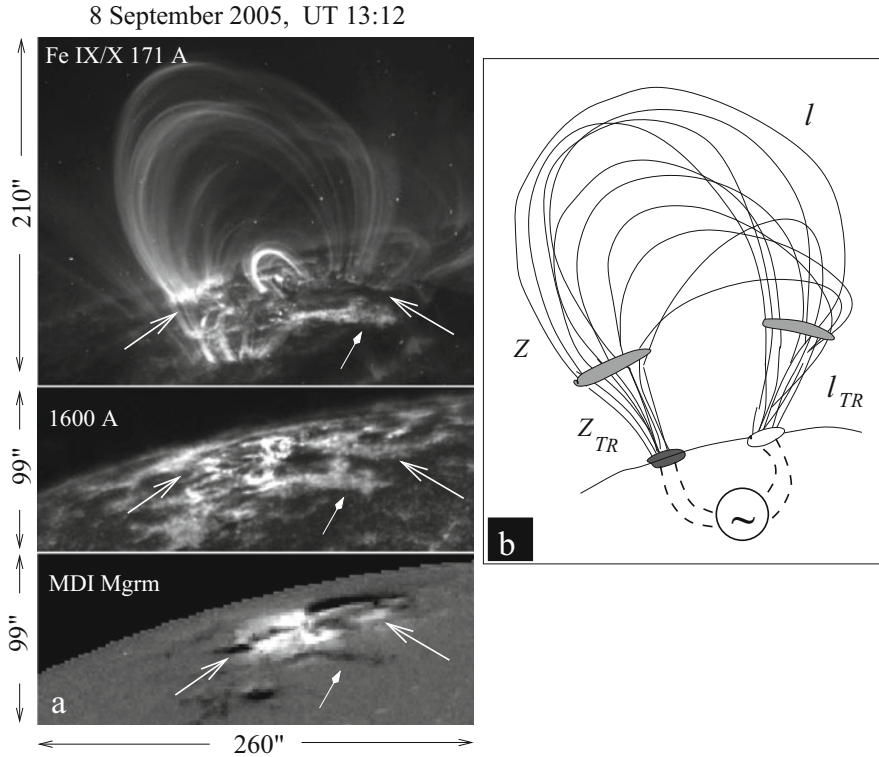


Fig. 16.7 Model of coronal loops for the equivalent circuit. **(a)** Example of well-established system of coronal loops close to limb, together with co-aligned MDI magnetogram of underlying region and its image at the transition region temperatures (TRACE 1600 Å). Note that the family of loops is rooted in the photosphere at compact sunspots with well-defined boundaries, while corresponding enhanced emission in 1600 and 171 Å lines is spread over much larger area (marked by large arrows). **(b)** Schematic of the model for the equivalent circuit with the photospheric driver, corona, and the transition region that links these regions through mutual resistance, $Z_M = \sqrt{ZZ_{TR}}$

region shows high activity above the entire active region, while response of the corona is quite selective: coronal loops appear at some preferable (and limited) sites, while rest of the corona is either covered by mossy emission (marked by small arrows) or seems intact (except a spectacular short living compact loops lying over the polarity inversion line).

A sketch in Fig. 16.7b illustrates the model studied here with the photospheric driver and overlying transition and coronal regions coupled through mutual resistance, $Z_M = \sqrt{ZZ_{TR}}$. This in fact is equivalent to mutual inductance, because $Z_i = \omega L_i$, and $M = \sqrt{LL_{TR}}$ (see below for details). Thus we take into account that the resistive load is associated not only with the corona, but with the chromosphere/transition region as well. To reflect this in the equivalent circuit equation, it is convenient to use (16.20) which with Ohm's law has a form (as

discussed above, $j_\theta \ll j_r$, and j_\perp is carried mostly by j_r):

$$\frac{4\pi}{c^2} \frac{\partial j_r}{\partial t} - \frac{\partial^2}{\partial r^2} \frac{1}{\sigma} j_r + \frac{1}{c} \frac{\partial^2 v_\phi B}{\partial l^2} = 0 \quad (16.29)$$

We use the Heaviside step function of plasma beta in the form: $H(\beta_{TR} - \beta)$, where β_{TR} denotes the plasma beta at about the transition region heights. We apply the same averaging procedure that established equivalence between (16.22) and (16.25).

It is convenient to represent the coronal part of (16.29) in terms of induced emf, $\Phi = (v_\theta Ba)/c$. Using Eq. (16.23) one obtains:

$$j_r = -\frac{c^2}{4\pi v_A^2} \frac{1}{a} \frac{\partial \Phi}{\partial t} \quad (16.30)$$

Now (16.22) can be written as follows:

$$H(\beta_{TR} - \beta) \left[\frac{1}{a} \frac{c^2}{4\pi v_A^2} \left(\frac{4\pi}{c^2} \frac{\partial^2 \Phi}{\partial t^2} - \frac{1}{\sigma} \frac{\partial^3 \Phi}{\partial x_r^2 \partial t} \right) - \frac{1}{a} \frac{\partial^2 \Phi}{\partial l^2} \right] = H(\beta - \beta_{TR}) \frac{4\pi}{c^2} \frac{\partial j_r(\Phi)}{\partial t} \quad (16.31)$$

The term on the right-hand side (kept in general form) includes dependence on the driving emf in the $\beta \geq 1$ region, and reactance of the transition region plasma. Integrating over the volume of the system gives:

$$LC \frac{d^2 \Phi}{dt^2} + RC \frac{d\Phi}{dt} + \Phi = \frac{4l}{\pi c^2} \frac{dI_g(\Phi)}{dt} \frac{\Delta x_{TR}}{\Delta x} \quad (16.32)$$

where we used (16.27), i.e., that $I_g = j_r a_{TR} l_{TR}$, and divided (16.32) by $\Delta x/l$. Using expression (16.26) for resistance, and assuming that R/R_{TR} is proportional to $(1/\sigma)/(1/\sigma_{TR})$, one obtains that $(\Delta x_{TR}/\Delta x) \simeq \sqrt{l_{TR}/l}$. With this, (16.32) takes the following form:

$$LC \frac{d^2 \Phi}{dt^2} + RC \frac{d\Phi}{dt} + \Phi = 4 \frac{\sqrt{ll_{TR}}}{\pi c^2} \frac{dI_g(\Phi)}{dt}, \quad (16.33)$$

or

$$LC \frac{d^2 \Phi}{dt^2} + RC \frac{d\Phi}{dt} + \Phi = M \frac{dI_g}{d\Phi} \frac{d\Phi}{dt}, \quad (16.34)$$

where M has a meaning of the equivalent mutual inductance determined by the resistive coupling between the corona and its underlying region:

$$M = \frac{4}{\pi c^2} \sqrt{ll_{TR}}, \quad (16.35)$$

Note that the spatial extent of the resistive coupling covers the cross-section area of the family of loops at the transition region heights (shaded area in Fig. 16.7b, marked by long arrows in Fe $IX/X171$ and 1600 \AA images in Fig. 16.7a).

The functional $I_g(\Phi)$ cannot be determined explicitly, but as a first step we may assume that the current is a weakly nonlinear function of the quasi-periodic emf. This can be treated with the perturbation theory, using the standard asymptotic methods of oscillation theory (Bogolubov and Mitropolsky 1961; Hagedorn 1988):

$$I_g = I_g(0) + \left. \frac{dI_g}{d\Phi} \right|_0 \Phi + \frac{1}{2} \left. \frac{d^2 I_g}{d\Phi^2} \right|_0 \Phi^2 + \frac{1}{6} \left. \frac{d^3 I_g}{d\Phi^3} \right|_0 \Phi^3 + \dots \quad (16.36)$$

In the first approximation $dI_g/d\Phi \simeq I_0/\Phi$ (where I_0 is the induced current in a stationary state), and the first expansion coefficient in (16.36) can be estimated as

$$\left. \frac{dI_g}{d\Phi} \right|_0 \simeq \frac{I_0}{\Phi} = C \frac{I_0}{\int Idt} = \Gamma_0 \quad (16.37)$$

The second expansion coefficient, $d^2 I_g/d\Phi^2$ corresponds to the inflection point, and can be put zero. This assumption is not essential, as it does not change the final result. The third expansion coefficient can be estimated using the assumption that at weak nonlinearity, Eq. (16.36) remains valid for maximum currents corresponding to saturation limit, $\Phi = \Phi_{\text{sat}}$, where $\Phi_{\text{sat}} \simeq v_\theta Ba/2c$ is coronal loop's capacitive emf (cf. (16.28)). Taking derivative of (16.36) at this limit and using maximum power balance, $I_g \Phi|_{\text{sat}} = RI_g^2|_{\text{sat}}$, we have

$$\left. \frac{1}{2} \frac{d^3 I_g}{d\Phi^3} \right|_0 \simeq -\frac{1}{R} \frac{1}{\Phi_{\text{sat}}^2} = -\Gamma_2, \quad (16.38)$$

and Eq. (16.36) becomes

$$I_g = I_g(0) + \Gamma_0 \Phi - \frac{1}{3} \Gamma_2 \Phi^3 \quad (16.39)$$

Note that this is analogous to sinusoidal volt-ampere characteristic at weak nonlinearity, $\sin x = x - (1/3!)x^3$. Respectively,

$$\frac{dI_g}{d\Phi} = \Gamma_0 - \Gamma_2 \Phi^2, \quad (16.40)$$

and Eq. (16.34) takes a form

$$L \frac{d^2 \Phi}{dt^2} + (R - M\Gamma_0 + M\Gamma_2 \Phi^2) \frac{d\Phi}{dt} + \frac{1}{C} \Phi = 0 \quad (16.41)$$

Taking into account that

$$I = C \frac{d\Phi}{dt}, \quad (16.42)$$

and using the balance of capacitive and inductive reactance, $(1/2)C\Phi^2 \simeq (1/2)MI^2$, for the third term in brackets, Eq. (16.41) reduces to the following electrodynamic equation having a form of the equivalent circuit equation with a weak nonlinearity:

$$LC \frac{d^2I}{dt^2} + (RC - MS_0 + MS_2I^2) \frac{dI}{dt} + I = 0 \quad (16.43)$$

where

$$S_0 = C\Gamma_0 = C \frac{I_0}{\int I(t)dt}, \quad (16.44)$$

and

$$S_2 = \frac{M}{RC} \frac{1}{\Phi_{\text{sat}}^2}. \quad (16.45)$$

Coefficients of nonlinear expansion, S_0 and S_2 have a natural physical meanings (Bogolubov and Mitropolsky 1961; Gaponov-Grekhov and Rabinovich 1992). MS_0 represents the excess of energy supply over the generation threshold. MS_2 reflects the nonlinear effect associated with the back-reaction of a circuit to the induced currents and is a measure of the amplitude of self-excited oscillations. Γ_0 is a measure of a current drive rate and can be estimated from the momentum balance (16.2):

$$\Gamma_0 = \frac{I_0}{\int I(t)dt} \simeq \tilde{\nu}_{ie}. \quad (16.46)$$

where $\tilde{\nu}_{ie} = (m_e/m_p)v_{ie}$ is the inverse slowing-down time of particles via electron ion collisions.

The presence of the new terms, $-MS_0 + MS_2I^2$, in Eq. (16.43) significantly changes the situation. First of all, as is well known, if the coefficients in the circuit equation are not of the *same sign*, the system is subject to instabilities. The evolution of the system strongly depends on the interplay between the coefficients, and most importantly, on the sign of parameter,

$$\mu = MS_0 - RC, \quad (16.47)$$

which determines the solution of the circuit (16.43), and thus the actual behavior of the current system. This parameter reflects the basic physical properties of the

current loops both, at micro-scales (skin depth, kinetic coefficients, density) and at large-scales (spatial dimensions, magnetic field).

Physically, $MS_0 - RC < 0$ corresponds to the situation when the energy supply is less than the current generation threshold; in other words, the characteristic current buildup time, $\sim M/R$, is less than the inverse current generation rate, $1/\tilde{\nu}_{ei}$.

At $MS_0 - RC > 0$ the additional energy supply exceeds the generation threshold, i.e., is analogous to high quality resonator.

Finally, proximity to $MS_0 - RC \simeq 0$ corresponds to a parameter range where the bifurcation of the system from one regime to another occurs.

Instabilities can develop in all three cases, including linear regime. But the character of the instability and conditions for its stabilization are different, providing thus realization of a wide range of coronal loop regimes from lengthy oscillatory states to flare-type disruption. In the next section we will present the solutions of Eq. (16.43), and discuss conditions for several basic regimes.

16.6 Evolution of Current Systems

16.6.1 Linear Regime

We start with the brief analysis of linear regime, i.e., when the term, $MS_2 I^2$ in Eq. (16.43) is negligibly small. There are two classes of the coronal loop evolution, determined, again by the sign of μ .

If $\mu < 0$, Eq. (16.43) is a standard circuit equation that describes three well-known types of behavior depending on the determinant $\Delta = \tilde{R}^2 - 4L/C$ (with $\tilde{R} = R - M_0 S_0 / C$):

1. $\Delta < 0$ gives a regime of underdamped oscillations of currents, with frequency $\omega = \omega_0 \sqrt{1 - \tilde{R}^2 C / 4L}$ and damping rate $\gamma_{\tilde{R}} = \tilde{R} / 2L$; this corresponds to long living “stable” loops showing the intensity oscillations with the above parameters.
2. $\Delta > 0$ corresponds to overdamped oscillations of currents with damping rate $\gamma_{\pm} = (\tilde{R} \pm \Delta^{1/2}) / 2L$.
3. $\Delta = 0$ corresponds to marginal state, critically damped oscillations, which can bifurcate into the weakly damped state or v.v. due to the external disturbances.

If $\mu = MS_0 - RC > 0$, i.e., when the energy supply exceeds the generation threshold, the system becomes unstable, and the damping rate $\gamma_{\tilde{R}}$ becomes a growth rate. As the instability is linear it may result in a not too violent and yet the flare-like energy release without disruption of the global loop system. This process may occur repeatedly as long as a particular loop system exists. At any time when the accumulated energy exceeds the threshold and gets released the system starts to gain energy back until it again reaches the critical conditions for the release of

the excess of energy. This regime corresponds to quasi-stable periodically flaring coronal loops.

16.6.2 Nonlinear Regime

To discuss the nonlinear regime, first we rewrite Eq. (16.43) in dimensionless form:

$$\frac{d^2 i}{d\tau^2} - \epsilon(1 - i^2) \frac{di}{d\tau} + i = 0 \quad (16.48)$$

Time is dimensionalized by $\omega_0^{-1} = \sqrt{LC}$, and current by the coefficient of nonlinearity:

$$\tau = t/\sqrt{LC}, \quad i = \sqrt{\frac{MS_2}{|\mu|}} I, \quad \epsilon = \mu/\sqrt{LC}. \quad (16.49)$$

Equation (16.48) is a typical Van der Pol equation for an energetically open oscillator with the dissipation and the driving force. The solution to this equation is known to be a modulated oscillations of the form:

$$i(\tau) = A(\tau) \cos(\tilde{\omega}\tau + \phi) - \frac{\epsilon}{32} A^3(\tau) \sin 3(\tilde{\omega}\tau + \phi) \quad (16.50)$$

with $\tilde{\omega} = 1 - \epsilon^2/16$, and slowly varying amplitude $A(\tau)$ satisfying the evolutionary equation (see Appendix):

$$\frac{dA(\tau)}{d\tau} = \frac{\epsilon}{2} \left\{ A(\tau) - \frac{A^3(\tau)}{4} \right\} \quad (16.51)$$

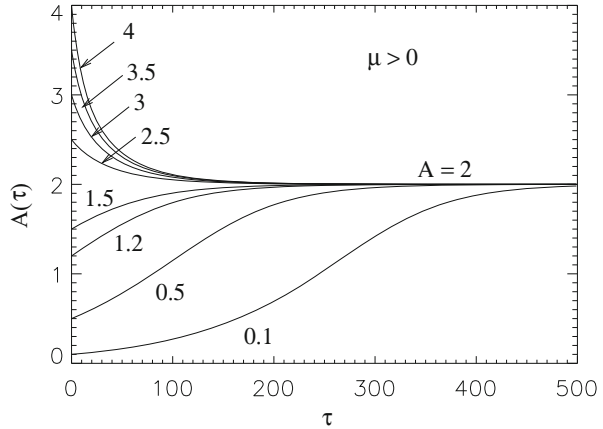
The solution to this equation is:

$$A(\tau) = \frac{2A_0}{\sqrt{A_0^2 + (4 - A_0^2) \exp(-\epsilon\tau)}} \quad (16.52)$$

As discussed above the time dependence of the current amplitude is determined by the sign of μ (i.e., on the sign of ϵ).

If $\mu > 0$, currents evolve in accordance with a typical Poincare limit cycle; i.e., whatever the initial amplitude of the generated currents is “large” ($A_0 > 2$) or “small” ($A_0 < 2$), asymptotically the currents tend to a stationary value of $A = 2$. In other words, currents with initial amplitude $A_0 > 2$ evolve in a decreasing regime, while currents with the initial amplitude $A_0 < 2$ increase until they reach the limiting value. The larger the initial amplitude the faster it drops (i.e., the shorter is

Fig. 16.8 Poincare limit cycle ($\mu > 0$ regime of the coronal loop evolution): Coronal loops with the initial current amplitude higher than $A = 2$ quickly approach the quasi-stable state releasing the excess of energy until currents drop to a limiting value. Loops with the initial current amplitude less than $A = 2$ gradually gain energy until currents reach a limiting value. The plots of the amplitudes are calculated for $\epsilon = 0.1$



its limiting cycle) and the faster is the release of excess energy. The opposite regime corresponds to longer living systems gradually accumulating energy until the system reaches a stationary regime. Note that any stationary regime may be destroyed by some additional source of energy like reconnection process or interaction of the system with neighboring loops.

Figure 16.8 shows the time dependence of the current amplitude for different values of the initial amplitude starting from $A_0 = 0.1$ to $A_0 = 4$. In all examples we used $\epsilon = 0.1$, i.e. we assumed that the energy supply exceeds the generation threshold by 10%. This solution describes a quasi-stationary oscillatory regime of coronal loops.

If $\mu < 0$ (i.e., $\epsilon < 0$), Eq. (16.51) describes two qualitatively different evolution of currents. For high enough initial amplitudes, i.e., for $A_0 > 2$, the system becomes subject to explosive instability. In a finite time the currents reach infinitely large values. To illustrate this we may drop the linear term in Eq. (16.51), and rewrite the equation in the form

$$\frac{d\tau}{dA} \simeq \frac{8}{|\epsilon|} \frac{1}{A^3} \tag{16.53}$$

Integration of τ gives a straightforward standard expression for explosively growing amplitude

$$A(\tau) = \frac{A_0}{\sqrt{1 - (\tau/\tau_{\text{expl}})}} \tag{16.54}$$

with the explosive time (in this approximation) $\tau_{\text{expl}} = 4/(|\epsilon|A_0^2)$. The actual explosive time is somewhat longer and follows from the general solution of Eq. (16.51) with $\epsilon = -|\epsilon|$.

Written in the form:

$$A(\tau) = \frac{2}{\sqrt{1 - \exp\{|\epsilon|(\tau - \tau_{\text{expl}})\}}}, \tag{16.55}$$

this solution clearly shows the explosive behavior with the characteristic time

$$\tau_{\text{expl}} = \frac{1}{|\epsilon|} \ln \frac{A_0^2}{A_0^2 - 4} \tag{16.56}$$

After the onset of the explosive instability, the system may develop in several different ways. This is determined by effects that may suppress or sustain the instability. Formally, in time τ_{expl} the currents indeed reach infinitely large values. This means that the system becomes strongly nonlinear, and other nonlinear effects turn on that may stabilize the instability (Weiland and Wilhelmsson 1977; Ryutova 1988).

There are two major regimes:

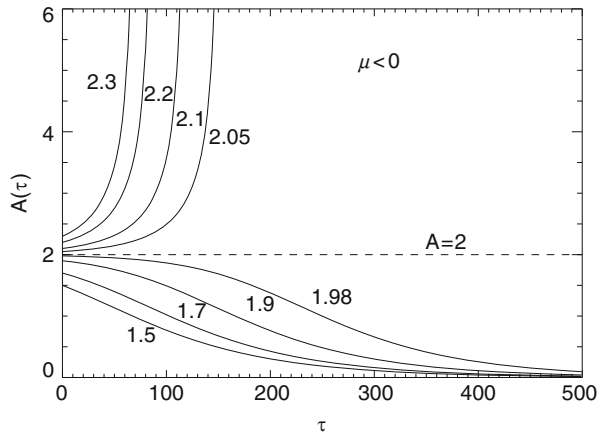
1. the disruption of the circuit occurs before the instability gets stabilized, and
2. higher nonlinear effects stabilize the explosive instability which leads to partial energy release.

The first case corresponds to strong flare event which may destroy the current system.

If at $\mu < 0$ the initial amplitude of the injected current is less than $A = 2$, the currents are in the decaying regime and loops gradually (and quite slowly) lose their energy.

The plots of the amplitude (16.55) for both regimes are shown in Fig. 16.9. The numbers next to plots are non-dimensionalized values of initial amplitude. In these

Fig. 16.9 The $\mu < 0$ regime of the coronal loop behavior. The numbers next to plots are the initial (nondimensional) amplitude A ; $\epsilon = 0.02$ for all cases. Loops with the initial current amplitude higher than $A = 2$ show the explosive growth of currents; higher are the initial currents, shorter is the explosive time. Loops with the initial current less than $A = 2$ are in a gradually decaying state



examples we used $\epsilon = 0.02$, i.e., the supplied energy is close to the generation threshold, but below it by 2%.

16.7 Quantitative Analysis

To perform quantitative analysis we need to represent solutions in the dimensional units:

$$I = i \sqrt{\frac{|\mu|}{MS_2}}, \quad t = \tau \sqrt{LC}, \quad \epsilon = \frac{|\mu|}{\sqrt{LC}}, \quad (16.57)$$

It is also useful to introduce a dimensional amplitude of current $\mathcal{I}(t)$:

$$\mathcal{I}(t) = \sqrt{\frac{|\mu|}{MS_2}} A(\tau) \quad (16.58)$$

Now we need to express the above quantities through the basic physical parameters including the specific parameters of coronal loops. For $\mu = MS_0 - RC$ using (16.26) and (16.35)–(16.46) we obtain:

$$\mu = CL \frac{m_e}{m_p} v_{ei} \left[\sqrt{\frac{l_{TR}}{l}} - \frac{\pi^2 m_p}{m_e} \frac{\delta^2}{(\Delta x_r)^2} \right] \quad (16.59)$$

where $\delta = c/\omega_{pe}$ is a plasma skin depth, $\delta = 5.3 \times 10^5 / \sqrt{n}$, and Δx_r is given by Eq. (16.19). Note that parameter μ is determined by the loop properties at micro-scales as well as at large-scales. With (16.19)–(16.26) μ takes a form:

$$\mu = \frac{\tilde{v}_{ei}}{\omega_0^2} \alpha \quad (16.60)$$

where we introduced parameter α , which determines the sign of μ :

$$\alpha = \sqrt{\frac{l_{TR}}{l}} - 1.06 \times 10^7 \frac{T}{n} \left(\frac{v_A}{a^2} \right)^{2/3} \quad (16.61)$$

Using (16.26) and (16.45) with $\Phi \simeq vBa/2c$ we have for S_2^{-1} :

$$S_2^{-1} = \frac{R}{4M} m_p v^2 n l a^2 = \frac{Re_m^{2/3}}{\sigma} \frac{m_p v^2 n l^2}{4M} \quad (16.62)$$

Now the normalization factor for dimensional current reduces to:

$$\sqrt{\frac{|\mu|}{MS_2}} = nev l \frac{\sqrt{|\alpha|}}{2M\omega_0} \frac{Re_m^{1/3}}{\sigma}, \quad (16.63)$$

and for the amplitude of current we have:

$$\mathcal{I}(t) = nev \sqrt{|\alpha| \frac{l}{l_{TR}} \frac{\pi}{2Re_m^{2/3}} a} |A| \quad (16.64)$$

It is also convenient to make quantitative estimates in terms of the current density. As $|I| = ja \Delta x_r$, the current density is given by:

$$j = nev \sqrt{|\alpha| \frac{l}{l_{TR}} \frac{\pi}{2Re_m^{1/3}} \frac{l}{a}} |A| \quad (16.65)$$

The velocity of the induced coronal flow, v , can be estimated by balancing the capacitive and inductive resistances (Ionson 1982):

$$v \simeq 5 \times 10^{-3} v_A Re_m^{1/6} \quad (16.66)$$

The above equations, containing the physical parameters simply associated with the observed quantities allow perform the quantitative analysis and use results both for diagnostic goals and prediction of the behavior of loop systems.

16.7.1 Examples

For quantitative estimates we will choose three temperature regimes: $T = 2 \times 10^6$ K, $T = 10^6$ K, and $T = 3 \times 10^5$ K. We will also assume that some million degree loops may be quite compact and reach only transition region heights. Therefore for each temperature regime we consider examples of the loop lengths of $l = 10^{10}$ cm, $l = 2 \times 10^9$ cm, and $l = 5 \times 10^8$ cm. We choose for the aspect ratio $a/l = 0.01$.

First we need to find values of α that define the regions with $\mu > 0$ and $\mu < 0$, and thus two basic groups of different regimes of the loop evolution. Using the dependence of the Alfvèn speed on the temperature and plasma beta as

$$v_A = 1.82 \times 10^4 \sqrt{T/\beta}, \quad (16.67)$$

we have:

$$\alpha = \sqrt{\frac{l_{TR}}{l}} - 7.3 \times 10^9 \frac{1}{n\beta^{1/3}} \left(\frac{T}{a}\right)^{4/3} \quad (16.68)$$

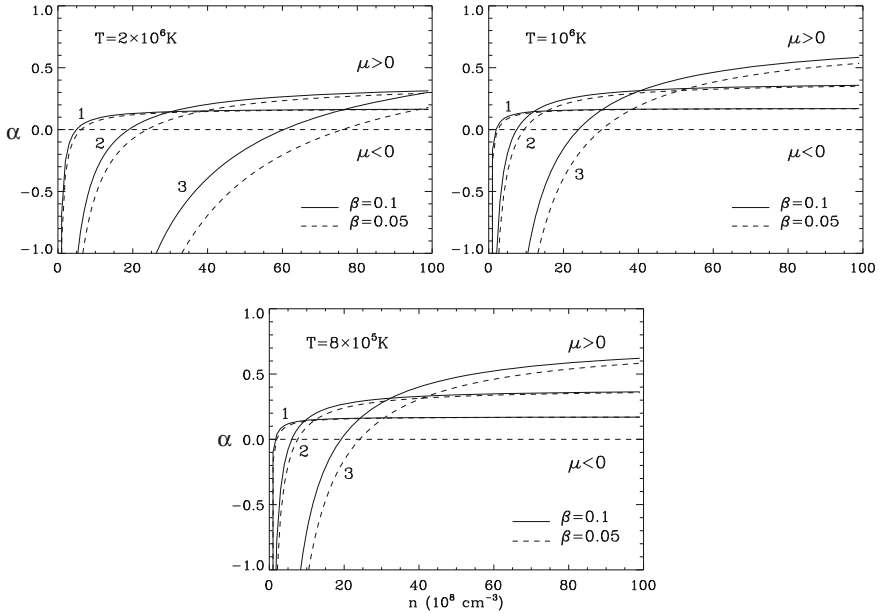


Fig. 16.10 Parameter α as a function of plasma density at three different temperatures. Numbers “1”, “2”, and “3” correspond to loop lengths of $l_1 = 10^{10}$ cm, $l_2 = 2 \times 10^9$ cm, and $l_3 = 5 \times 10^8$ cm, respectively. In all examples solid lines correspond to plasma beta $\beta = 0.1$ and dashed lines to $\beta = 0.05$. The range of parameters with $\alpha < 0$ ($\mu < 0$) corresponds to explosively unstable loops, whereas $\alpha > 0$ ($\mu > 0$) to loops evolving according to Poincaré limit cycle

Parameter α as a function of density is shown in Fig. 16.10. Three panels correspond to three temperature regimes. Each temperature regime contains plots for three different lengths of loops, reflecting the examples of the chromosphere and corona. Solid lines correspond to $\beta = 0.1$, and dashed lines to $\beta = 0.05$.

Some qualitative conclusions follow immediately from these plots. The regime with $\mu > 0$, which corresponds to dynamics of coronal loops evolving in accordance with the Poincaré limit cycle requires quite high densities for loops to be in a stable state. For example, for 2 MK loops with $l = 10^{10}$ cm to be in a stable regime, densities should be higher than 2×10^9 cm $^{-3}$. At lower temperatures, the density threshold slightly decreases. This result is consistent with recent observations showing that densities in large and hot loops are by the order of magnitude higher than those believed earlier (Aschwanden et al. 2000). It was also shown that not only the loops with moderate length $l \leq 10^9$ cm, but even long loops with $l > 10^{10}$ cm have densities higher than 10^9 cm $^{-3}$.

If the density drops below some critical value, and μ becomes negative (cf. (16.68)), the loop becomes either subject to explosive instability if the initial current density exceeds the critical values ($A_0 > 2$ in dimensionless units) or slowly decays if $A_0 < 2$.

Parameters close to $\mu \simeq 0$ ($\alpha \simeq 0$) correspond to the bifurcation region.

Table 16.2 Estimates of critical currents and current densities for loops of three different length at coronal temperatures

T (K)		2×10^6			10^6		8×10^5
η_D ($\text{cm}^2 \text{s}^{-1}$)		3.7×10^3			1.05×10^4		1.47×10^4
v_A (cm s^{-1})		8×10^7			5.7×10^7		5×10^7
l (10^8 cm)	100	20	5	100	20	5	5
Re_m (10^{10})	200	43	10	54	10	2.7	1.7
ω_0 (s^{-1})	0.025	0.13	0.5	0.02	0.1	0.36	0.31
α ($\mu < 0$)	-0.1	-0.15	-0.2	-0.1	-0.2	-0.3	-0.5
n (10^8 cm^{-3})	3.2	14	48	1.2	5	17	11
\tilde{v}_{ei} (10^{-2} s^{-1})	0.45	2	6.7	0.48	2	6.7	6.1
\mathcal{I}_{cr} (10^6 A)	76	17	3	42	10	2.6	2.4
$I_{\text{cr}}^{(a)}$ (10^{10} A)	96	12.8	1.33	34	4.4	0.77	0.63
j_{cr} (A/m^2)	0.96	3.2	5.4	0.34	1.1	3.1	2.5
α ($\mu > 0$)	0.1	0.15	0.2	0.1	0.2	0.3	0.5
n (10^8 cm^{-3})	12	31	82	5	16	40	57
\tilde{v}_{ei} (10^{-2} s^{-1})	0.17	4.3	0.12	2	6.3	0.16	0.32
\mathcal{I}_{lim} (10^6 A)	290	38	5	180	30	6.1	12
$I_{\text{lim}}^{(a)}$ (10^{10} A)	360	28.6	2.3	140	14	1.82	3.17
j_{lim} (A/m^2)	3.6	7.1	9.2	1.4	3.5	7.3	12.7

The range of parameters corresponding to negative values of μ also describes different regimes of loop behavior, which, again, depends on the initial energy supply. Thus, in the $\mu < 0$ regime the explosive instability may develop only if $A_0 > 2$; if $A_0 < 2$ loops just gradually lose their energy, as shown in Fig. 16.9.

As the normalized factor for currents contains the specific parameters of coronal loops, the limiting value is different for different loops. Some quantitative examples are shown in Table 16.2. The upper section has some basic parameters for chosen lengths of coronal loops at three temperatures. The middle part of the table contains the quantitative estimates of critical currents and current densities for loops in the $\mu < 0$ regime. The lower part of the table contains the estimates for limiting currents for loops in the $\mu > 0$ regime. We defined the $A = 2$ value in dimensional units for the $\mu < 0$ regime as \mathcal{I}_{cr} and for $\mu > 0$ as \mathcal{I}_{lim} to distinguish them from the initial current amplitude \mathcal{I}_0 .

The values of \mathcal{I}_{cr} and \mathcal{I}_{lim} are given by Eq. (16.64) with $A = 2$. To estimate these values we choose $\alpha = \pm 0.1, \pm 0.15$, and ± 0.2 for loops at $T = 2 \times 10^6 \text{ K}$; $\alpha = \pm 0.1, \pm 0.2$ and ± 0.3 for loops at $T = 10^6 \text{ K}$, and $\alpha = \pm 0.5$ at $T = 8 \times 10^5 \text{ K}$ for loop of $5 \times 10^8 \text{ cm}$ length. The choice of α determines the densities of loops (see Fig. 16.10).

It is important to note that \mathcal{I}_{cr} and \mathcal{I}_{lim} are calculated for elemental current filaments with cross-section $a \Delta x_r$ using (16.27). The total average current flowing through the visible loop with cross-section $\simeq a^2$ will be obviously $I^{(a)} = j_l a^2$ or $I^{(a)} = \mathcal{I} Re l / 3$. As measured currents in literature are related to visible loops (see, e.g., Leka et al. 1996), it is useful to calculate the critical values of these averaged

currents as well. These values are given in Table 16.2 as $I_{\text{cr}}^{(a)}$ and $I_{\text{lim}}^{(a)}$. Thus, e.g., for loop with $l = 10^{10}$ cm and $a = 10^8$ cm at $T = 2 \times 10^6$ K, the critical current is $I_{\text{cr}}^{(a)} = 9.6 \times 10^{11}$ A; for loop with $l = 2 \times 10^9$ cm at $T = 10^6$ K, $I_{\text{cr}}^{(a)} = 4.4 \times 10^{10}$ A.

Take, for example, a loop with $l = 10^{10}$ cm at $T = 2 \times 10^6$ K with $\alpha = -0.1$. The critical current for such a loop is $\mathcal{I}_{\text{cr}} = 7.6 \times 10^7$ A ($I_{\text{cr}}^{(a)} = 9.6 \times 10^{11}$ A). If the initial amplitude of injected current is, say $\mathcal{I}_0 \simeq 2 \times 10^7$ A, then the loop is subject to explosive instability. In dimensional units the explosive time is $t_{\text{expl}} = \tau_{\text{expl}} \sqrt{LC}$, where τ_{expl} is determined by (16.56). Using (16.57) and (16.60) we have

$$t_{\text{expl}} = \frac{1}{\tilde{v}_{ei} |\alpha|} \ln \frac{\mathcal{I}_{\text{cr}}^2}{\mathcal{I}_{\text{cr}}^2 - \mathcal{I}_0^2} \quad (16.69)$$

In the above example, currents with initial amplitude of 2×10^8 A will reach the “infinitely” large values in about 6 min. If the initial amplitude of the injected current is somewhat smaller (but still higher than the critical value), say 10^8 A, it will take about 32 min to bring the system to the regime of explosive instability. Obviously, the larger the injected currents the shorter the explosive time.

At $\mu > 0$ the initial current, $\mathcal{I}_0 = 2 \times 10^8$ A, for the same loop is less than $\mathcal{I}_{\text{lim}} = 2.9 \times 10^9$ A, and the loop will continue to accumulate energy until currents reach this limiting value. The ratio $\mathcal{I}_0/\mathcal{I}_{\text{lim}}$ in this case 0.069, so time for currents to reach the limiting value is longer than $\tau = 500$ (cf. curve “0.1” in Fig. 16.8).

In dimensional units for loop with $l = 10^{10}$ cm and $v_A = 8 \times 10^7$ cm/s, this time translates into $t = \tau \sqrt{LC} = 5.5$ h. Consider, for example, the loop with $l = 2 \times 10^9$ cm at $T = 2 \times 10^6$ K. The critical current with $\alpha = -0.15$ is $\mathcal{I}_{\text{cr}} = 1.7 \times 10^7$ A. If the initial amplitude of the injected current is only $\mathcal{I}_0 = 4 \times 10^7$ A ($A_0 = 2.3$), the explosive instability will develop in about 8 min. The same loop with the initial current $\mathcal{I}_0 = 2.5 \times 10^7$ A ($A_0 = 1.5$) will cool down in about 1.2 h.

It is important to emphasize again that the parameter $\mu = MS_0 - RC$ that defines two major groups for coronal loop conditions reflects the physical properties of a system both at large-scales (e.g., l , a , B) and at micro-scales (e.g., σ , \tilde{v}_{ie} , etc.).

Wide range of these parameters and their combinations provide various regimes for the coronal loop evolution. Within each of the major group, loops may behave in a very different ways. As seen in Fig. 16.8 ($\mu > 0$), loops with high initial currents cool down and quickly approach a quasi-stable state—this may well represent the post-flare cooling regime; loops with sub-limited currents gradually gain the energy until they reach a quasi-stable state. Figure 16.9 shows, e.g., that within the range of parameters defined by $\mu < 0$, loops with high initial currents are subject to the explosive instability that correspond to fast and violent energy release, while loops with sub-critical currents remain for a long time in slowly decaying phase.

16.8 Limiting Currents and Filamentary Structures

When plotting parameter α as a function of plasma density (Fig. 16.10), we fixed the aspect ratio $a/l = 0.01$. Clearly, one can fix any other parameter, say density or temperature, and plot α as a function of thickness, a , or aspect ratio. Character of these plots will be similar to those shown in Fig. 16.10, and will show the critical values of the structure dimensions at given density or temperature.

According to the recent observations coronal loops should indeed have a filamentary structure (see, e.g., Aschwanden et al. 2000; Winebarger et al. 2003). It is remarkable that in the circuit model *small-scales of current-carrying filaments arise automatically*. Radius of the filamentary structure is restricted from above roughly speaking by the Reynolds number (Ryutova and Habbal 1995). More precise estimate involve many factors which are the subject of future studies, whereas minimum, critical value of radius, a_{cr} follows directly from the parameter μ which determines regime of the loop dynamics (see (16.60) and (16.68)).

If density, temperature, and loop length are known from observations, Eq. (16.68) allows one to estimate the limiting current for a particular loop, and find critical radius of elemental filament, a_{cr} , below which the filament becomes unstable. Examples of such estimates are given in Table 16.3, where we used results of Winebarger et al. (2003) for 8 loops. w here is the observed loop width. One can see that it exceeds the calculated critical radius of filamentary structure in all cases except one (# 3 loops in Table 16.3). Indeed, the “stable” loops should have higher radii than a_{cr} . If the radius of some filament drops below this value, the filament becomes unstable.

In conclusion, it is useful to briefly overview the results of this chapter and make some additional remarks.

We started this chapter with consideration of the particular events associated with magnetic flux emergence that eventually forms two opposite polarity pores, and triggers formation of magnetic loop structures in the overlying chromo-

Table 16.3 Estimates of limiting currents, \mathcal{I}_{lim} , and critical radii of filamentary structures, a_{cr} , for the “stable” loops observed with TRACE and SXT

No	Observations				Estimates	
	l (10^8 cm)	w (10^8 cm)	T (MK)	n (10^8 cm $^{-3}$)	\mathcal{I}_{lim} (10^{10} A)	a_{cr} (10^8 cm)
1	4.0	1.9	1.2	12.2	2.11	0.91
2	10.0	2.3	1.2	14.7	6.99	1.1
3	17.0	1.5	1.2	9.1	5.94	1.9
4	18.0	2.2	1.2	15.2	12.7	1.4
5	26.2	9.9	6.7	40.6	44.4	4.2
6	28.1	10.3	6.0	25.5	32.2	5.4
7	28.7	21.1	5.8	18.5	34.8	6.7
8	29.5	19.5	5.1	17.3	34.3	6.3

sphere/corona. This is an ordinary event occurring in the solar atmosphere in any moment of time at various scales. Particular event considered in this chapter stands out only in virtue of the acquisition of a rich multiwavelength data that show step by step development of events that starts from detection of the subsurface motions and ends up with the formation of the EUV structures that outline well- established flows above the newly formed pores. Changes in the photospheric magnetic fields occur “hand in hand” with dynamic changes in EUV structures, and serve as evidence for unambiguous coupling of the photosphere, chromosphere and corona.

High cadence multiwavelength observations show how the emergence of a large scale magnetic flux is accompanied by strong collimated plasma flows which appear at coronal heights at the very early stage of the flux emergence. The corona and chromosphere quickly respond to these motions, and show a high activity above the future site of pore formation long before the pore is formed. Coronal structures acquire their “final” forms only after the strong H_{α} flows are significantly reduced and acquire a more or less stable shape of a compact arcades “connecting” two opposite pores. The EUV structures as well consist of an arcades of many thin loops of the same shape as the flow pattern.

These observations clearly indicate that the impulsive phenomena associated with strong magnetic flux emergence (whose visible manifestation is, e.g., a highly collimated plasma flows) are directly responsible for the EUV structure formation. Combination of magnetic fields and impulsive phenomena suggest the involvement of electric currents.

We have analyzed the efficiency of current drive associated with the photospheric drivers. In particular, we have concentrated on those mechanisms of current drive which are directly connected with strong disturbances produced by emerging magnetic flux. These are

1. the currents generated by the proper motion of hydrogen plasma,
2. the wave-induced currents, and
3. currents driven by the Alfvén waves in the presence of mass flows. Each of these mechanisms gives a reasonable range of parameters for generated currents.

The proper motion of plasma is quite efficient at all heights, and may generate currents from $j \simeq 2.0 \times 10^{-4} \text{ A m}^{-2}$ at high altitudes up to $j \simeq 0.17 \text{ A m}^{-2}$ at low altitudes. The acoustic waves in linear regime can be ignored, whereas in a weakly nonlinear regime they may drive currents on the order of $j \simeq 10^{-2} \text{ A m}^{-2}$. In case of the Alfvén waves, the efficiency of current drive is quite sensitive to wave frequency. For example, higher frequency waves can generate stronger currents and at lower altitudes. Quantitative estimates of current densities at different temperatures (and frequencies) give an interval ranging from $j \simeq 1.7 \text{ A m}^{-2}$ to $j \simeq 2.0 \times 10^{-3} \text{ A m}^{-2}$. The advantage of this mechanism is that it naturally combines the mechanical (flows) and magnetic effects in the process of current drive. Besides, the method itself allows to estimate both, the current densities and corresponding heights.

The effect of the current drive as a natural consequence of a photospheric driver allows to study further evolution of currents and coronal structures associated with

the dynamic changes in the photosphere. These processes may be described in terms of the equivalent electric circuit, that consolidates mechanical, magnetic, and electrical effects into one scheme, and establishes coupling between the surface driver and dissipation region in the overlying atmosphere.

Further evolution of currents and coronal structures associated with the dynamic changes in the photosphere is studied using the analogue of an energetically open circuit. This approach is quite general and may be applied to any current systems throughout the solar atmosphere. The system consists of the energy source (in our case a photospheric driver), dissipation region, and region where transition and feedback between the $\beta \geq 1$ and $\beta \ll 1$ regions occur (transition region between the chromosphere and corona). Such a system has obviously all the properties of energetically open, dissipative system which has a tendency to self-organization and formation of various forms of dynamic structures. We treated the system as such and extended analysis to nonlinear regime, which allows to study the various regimes of the EUV structures and conditions for their realization.

The major element of the approach is the inclusion of the transition region and its influence on coupling between the corona and photosphere/chromosphere region. Physics of coupling has the resistive character, and consists of the mechanical stressing of the common magnetic field in the photosphere that results in generation of electric currents and corresponding Poynting flux of energy that propagates upward and subsequently dissipates. Because of high conductivity of coronal plasma, dissipative effects turn on only at a small transverse scales of the order of generalized skin depth determined by kinetic coefficients of plasma. The generated currents reach their maximum values mainly at the transition region heights establishing conditions for coronal loop formation.

To reflect influence of transition region on the coupling process we take into account that the resistive load is associated not only with the corona, but with the chromosphere/transition region as well. This leads to appearance of an equivalent mutual resistance in the circuit equation derived from the global electrodynamics. This in fact is equivalent to appearance of mutual inductance (as $Z_i = \omega L_i$, cf. Figs. 16.6b and 16.7b).

The nonlinear circuit equation with mutual inductance acquires the form of the Van der Pol oscillator. Depending on the coefficients, determined by the loop parameters, this equation describes various regimes which include long living steady loops, periodically flaring and exploding loop systems. A crucial element of the problem is a measure of an energy supply and the capacitance of a loop, reflected by parameter $\mu = MS_0 - RC$. The sign of this coefficient determines the solution of the circuit equation, and thus the actual behavior of the loop. Physically, $\mu < 0$ corresponds to the situation when the energy supply is less than the current generation threshold. For $\mu > 0$ the additional energy supply exceeds the generation threshold; the range of parameters near $\mu \simeq 0$ corresponds to the state when the system bifurcates from one regime to another.

Table 16.4 briefly summarizes typical regimes of coronal loop evolution. A_0 is in dimensional units, and for individual loop system is given by (16.64) with $|A| = 2$.

Table 16.4 Linear and nonlinear regimes of the coronal loop dynamics

	$\mu = MS_0 - RC < 0$	$\mu = MS_0 - RC > 0$
Linear regime	Long living loops showing a weakly damped, over-damped, or critically damped oscillations of intensity	Long living loops gradually gain and then lose energy periodically resulting a flare-like events
Nonlinear regime, $A_0 < 2$	The oscillating loops gradually lose the energy (Fig. 16.8, solid curves)	Poincare limit cycle: currents grow until they reach a limiting value to establish a quasi-stable long living system
Nonlinear regime, $A_0 > 2$	Explosive instability leading to (1) a violent energy release and disruption of a system, or (2) repetitive flare-like events	Poincare limit cycle: currents drop to a limiting value releasing the excess of energy and approaching a quasi-stable state

Thus the physical parameters for realization of different scenarios of loop evolution form a simple system and most of them are directly observable. It is important to note that the circuit model also predicts that the EUV loops must have a small-scale filamentary structures. A critical radius of elemental filament for each individual structure is also a simple function of the observed parameters and can be used for diagnostic goals.

One can say that the equivalent circuit model is a very efficient tool to study the physical processes that couple the subsurface and photospheric energy reservoir with the energy dissipation region in the upper layers of atmosphere. The advantage and broadness of this approach is that it includes several important issues in the coronal dynamics and structure formation:

1. connection between the remote parts of energy production region and regions of energy flow and release,
2. combination of both, magnetic and electric current viewpoints,
3. the natural explanation of the diversity of a coronal loop's behavior from oscillatory to periodically flaring and exploding states,
4. simple relations between the physical parameters of a system, most of which are observable.

The model of energetically open circuit is quite general and can be applied to other astrophysical objects consisting of a dynamic magnetized plasma with continuous flow energy and its dissipation.

16.9 Problems

16.1 Establish the connection between current drive by plasma waves and helicity conservation in the presence of viscous and resistive losses.

16.2 Obtain nonlinear equation for electrical transmission line with variable-capacitance. Show that the equation has a solitary wave solution.

Appendix: Method of Slow Variables for Van der Pol Equation

In a real time Eq. (16.48) has a form

$$\frac{d^2i}{dt^2} - \mu(1 - i^2)\frac{di}{dt} + \omega_0^2i = 0 \quad (16.70)$$

and belongs to the class of nonlinear equations of the type

$$\frac{d^2i}{dt^2} + \omega_0^2i = f\left(i, \frac{di}{dt}\right) \quad (16.71)$$

with

$$f\left(i, \frac{di}{dt}\right) = -\mu(i^2 - 1)\frac{di}{dt} \quad (16.72)$$

The method of slowly varying phase and amplitude is based on the usage of transformation (see, e.g., Hagedorn 1988):

$$\begin{aligned} i &= A(t)\sin(\omega_0t + \psi), \\ \frac{di}{dt} &= A(t)\omega_0\cos(\omega_0t + \psi) \end{aligned} \quad (16.73)$$

which replaces Eq. (16.71) by the system of a simple integro-differential equations:

$$\begin{aligned} \frac{dA}{dt} &= \frac{1}{2\pi\omega_0} \int_0^{2\pi} f(A, \psi) \cos(\phi + \psi) d\phi, \\ \frac{d\psi}{dt} &= -\frac{1}{2\pi\omega_0A} \int_0^{2\pi} f(A, \psi) \sin(\phi + \psi) d\phi \end{aligned} \quad (16.74)$$

With Eq. (16.72) we have

$$\begin{aligned} \frac{dA}{dt} &= \frac{\mu A}{2\pi} \int_0^{2\pi} (1 - A^2\sin^2\phi) \cos^2\phi d\phi, \\ \frac{d\psi}{dt} &= -\frac{\mu}{2\pi} \int_0^{2\pi} (1 - A^2\sin^2\phi) \cos\phi \sin\phi d\phi \end{aligned} \quad (16.75)$$

or, equivalently,

$$\begin{aligned}\frac{dA}{dt} &= \mu \frac{A}{2} \left(1 - \frac{A^2}{4}\right), \\ \frac{d\psi}{dt} &= 0\end{aligned}\tag{16.76}$$

With the nondimensional time $\tau = t/\sqrt{LC}$ and $\epsilon = \mu/\sqrt{LC}$, Eq. (16.76) becomes Eq. (16.51).

References

- H. Alfvén, *Cosmic Plasma* (Springer, Berlin, 1981)
- H. Alfvén, J. Carlqvist, *Solar Phys.* **1**, 220 (1967)
- H. Alfvén, C.-G. Fälthammar, *Cosmical Electrodynamics. Fundamental Principles* (Clarendon Press, Oxford, 1963)
- M.J. Aschwanden, R.W. Nightingale, D. Alexander, *Astrophys. J.* **541**, 1059 (2000)
- L. Block, C.-G. Fälthammar, et al., *J. Geophys. Res.* **103**(A4), 6913 (1998)
- N.N. Bogolubov, Y. A. Mitropolsky, *Asymptotic Methods in the Theory of Non-Linear Oscillations* (Gordon and Breach, New York, 1961)
- A.H. Boozer, *Astrophys. J.* **325**, 891 (1988)
- S.I. Braginskii, in *Reviews of Plasma Physics*, Vol. 1 (Consultants Bureau, New York, 1965), p. 205
- A.G. Elfimov, C.A. de Azevedo, A.S. de Assis, *Solar Phys.* **167**, 203 (1996)
- N.J. Fish, Theory of current drive in plasmas. *Rev. Mod. Phys.* **59**, 175 (1987)
- A.V. Gaponov-Grekhov, M.I. Rabinovich, *Nonlinearities in Action* (Springer, New York, 1992)
- M.K. Georgoulis, B.J. LaBonte, *Astrophys. J.* **615**, 1029 (2004)
- M.K. Georgoulis, B.J. LaBonte, T.R. Metclaf, *Astrophys. J.* **602**, 446 (2004)
- P. Hagedorn, *Non-Linear Oscillations* (Clarendon Press, Oxford, 1988)
- G.P. Harnwell, *Principles of Electricity and Electromagnetism* (McGraw-Hill Book Co., New York, 1949)
- J. Heyvaerts, E.R. Priest, *Astron. Astrophys.* **117**, 220 (1983)
- J.A. Ionson, *Astrophys. J.* **254**, 318 (1982)
- J.A. Ionson, *Astrophys. J.* **276**, 357 (1984)
- L.D. Landau, E.M. Lifshitz, *Hydrodynamics* (Pergamon Press, Oxford, 1988)
- B. Lehnert, in *Plasma Physics and Thermonuclear Research*, ed. by J.L. Tuck (Macmillan Co., New York, 1963), p. 201.
- K.D. Leka, R.C. Canfield, A.N. McClymont, L. van Driel-Gesztelyi, *Astrophys. J.* **462**, 547 (1996)
- D.B. Melrose, *Astrophys. J.* **486**, 521 (1995)
- T. Ohkawa, *Nucl. Fusion* **10**, 185 (1970)
- N.F. Otani, H.R. Strauss, *Astrophys. J.* **325**, 468 (1988)
- D. Ryutov, M. Ryutova, *Sov. Phys. JETP*, **69**, 965 (1989)
- M.P. Ryutova, *Sov. Phys. JETP*, **67**(8), 1594 (1988)
- M.P. Ryutova, *JGR* **111**, A09102 (2006)
- M.P. Ryutova, S.R. Habbal, *Astrophys. J.* **451**, 381 (1995)
- M.P. Ryutova, R. Shine, *Astrophys. J.* **606**, 571 (2004)
- M.P. Ryutova, R. Shine, *JGR* **111**, A03101 (2006)
- M.P. Ryutova, T.D. Tarbell, *Phys. Rev. Lett.* **90**, 191101 (2003)

- M.P. Ryutova, M. Kaisig, T. Tajima, *Astrophys. J.* **459**, 744 (1996)
- D.S. Spicer, *Space Sci. Rev.* **31**, 351 (1982)
- K.P. Stanyukovich, *Unsteady Motion of Continuous Media* (Pergamon Press, Oxford, 1960)
- T. Tarbell, M. Ryutova, J. Covington, A. Fludra, *Astrophys. J.* **514**, L47 (1999)
- T. Tarbell, M. Ryutova, R. Shine, *Solar Phys.* **193**, 195 (2000)
- A. Title, *Philos. Trans. R. Soc. Lond.* **358**, 657 (2000)
- B.A. Trubnikov, Particle interactions in a fully ionized plasma, in *Reviews of Plasma Physics*, vol. 1 (Consultants Bureau, New York, 1965), p. 105
- J. Weiland, H. Wilhelmsson, *Coherent Nonlinear Interaction of Waves in Plasmas* (Pergamon Press, Oxford, 1977)
- A.R. Winebarger, H.P. Warren, J.T. Mariska, *Astrophys. J.* **587**, 439 (2003)
- D.J.M. Wort, *Plasma Phys.* **13**, 258 (1971)

Chapter 17

Fine Structure of Penumbrae: Formation and Dynamics



Abstract In this chapter we shall study amazing properties of sunspot penumbra—a beautiful “crown” surrounding mature sunspots and being one of the long-standing mysteries of solar magnetism. High-resolution observations with the Swedish 1-m Solar Telescope (SST) on La Palma revealed earlier unavailable features of penumbral filaments showing their fine substructure and new properties in their dynamics (Scharmer et al., *Nature* 420:151, 2002). We shall see that these properties are associated with the nature of umbra which itself is a dense conglomerate of twisted flux tubes. Being more or less vertical in the center of sunspots, twisted and interlaced flux tubes branch out at the periphery from the “trunk” due to an ongoing reconnection processes, and arc downward to the photosphere forming the penumbral “umbrella.” The twist of individual filaments, and resulted distribution of magnetic fields and temperature inside them are consistent with the onset of screw pinch instability, which in large explains the properties and behavior of penumbral filaments.

17.1 Peculiarities of Sunspot Penumbrae: Observations

Penumbrae consist of an uncombed system of thin magnetic filaments arcing radially outward from the umbra and terminating in the photosphere. The inclination of the magnetic field is found to vary across the penumbra from 45° to 90° to the sunspot normal (Title et al. 1993). There are also strong intensity inhomogeneities across the penumbra, resulting in a visual effect of interlaced dark and bright filaments.

The Evershed flow (unsteady plasma outflow at the photospheric level) is also found to be structured on the scale of the penumbral filaments. The flow is more horizontal than the mean magnetic field at all radii in the penumbra and has a spatial correlation with dark penumbral filaments (Shine et al. 1994). The bright filaments are usually less horizontal making thus some angle with the direction of Evershed flows.

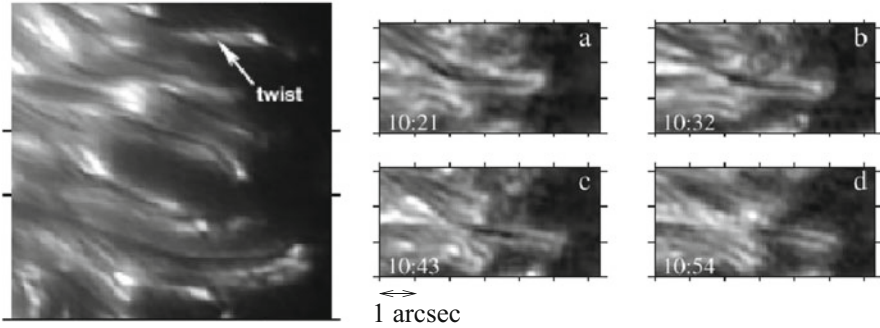


Fig. 17.1 Left: Dark-cored filaments first reported by Scharmer et al. (2002); Right: Temporal evolution of a dark-cored filaments, that includes splitting of filaments. Credit: Sütterlin et al. (2004), reproduced with permission copyright ESO

Livingston (1991), comparing images of sunspot with different exposures, came to the conclusion that the sunspot umbra also has a filamentary structure, and may exhibit presence of vertical, diverging, and horizontal filaments.

Observations with the 1-m Swedish Solar Telescope (Scharmer et al. 2002) in the different wavelength bands (e.g., 4305 Å G-band and 4368 Å continuum) have revealed unprecedented details in the penumbral structure and dynamics. It was found that many of individual filaments show dark cores surrounded by bright walls. The footpoints of the dark cores are mostly adjacent to the bright dots or grains. Filament often looks twisted. High cadence movies show continuous filament branching into several filaments which also have dark cores. Figure 17.1 shows an example of a typical appearance of penumbral filaments at the highest possible resolution of about 70 km. Left panel is one of the first reported images showing dark-cored filaments of different shapes that include twisted configuration as well (Scharmer et al. 2002). Four right panels show temporal evolution of a system of an exemplary dark-cored filaments showing their growth, merging and splitting processes (Sütterlin et al. 2004). After the first results all the persistent features were confirmed and complemented in subsequent observations with the SST (Berger et al. 2004; Rouppe van der Voort et al. 2005; Bellot Rubio et al. 2005; Langhans et al. 2005; Rimmele and Marino 2006). These may be summarized as follows:

1. The widths of filaments close to their point of origin are 150–180 km.
2. The width of dark cores may be below the resolution (≤ 70 km).
3. Filament lengths range from 300 to 3000 km.
4. The average lifetime of individual filaments is 1–2 h.
5. The inclination of the dark-cored filaments with respect to the normal varies from 35° in the inner penumbra to about 60° toward the outer penumbra.
6. The magnetic signal is lower in the dark (cooler) cores than in the lateral (warmer) brightenings.

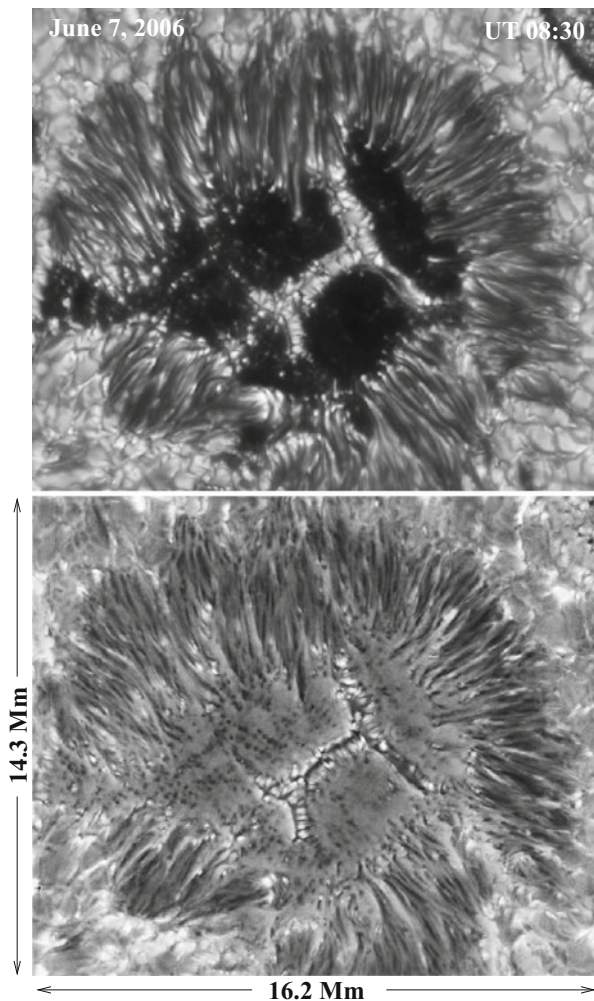


Fig. 17.2 Images of the 2006 June 6 sunspot. Top: G-band filtergram in the beginning of the observation. Bottom: Simultaneous G-band/4396 Å continuum difference image. Along the filamentary penumbra one can see well-defined small scale structures in the middle of the umbra, which are especially prominent in the difference image. These tiny black dots are the individual flux tubes forming the sunspot umbra

The SST observations of a sunspot obtained on 2006 June 6, in 4305 Å G-band and 4364 Å continuum lines confirmed the basic properties of penumbral filaments listed above and extended the analysis to their temporal evolution (Ryutova et al. 2008a).

Figure 17.2 shows two simultaneous images of the studied sunspot. The observations covered a $23.8 \times 16.8 \text{ Mm}^2$ area of active region (AR 10892) near the

disk center with the period of observation of 1 h 25 min. The data were taken simultaneously every 5–7 s in the 4305 Å G-band and a nearby “pseudo-continuum” bandpass centered at 4364 Å. The G-band, commonly used to trace small scale photospheric magnetic elements, is excellent bandpass to reveal high contrast (and brightness) in penumbral filaments. Continuum images also show bright contrast in the observation of penumbral filaments continuum.

The fact that continuum images show a contrast by a factor of 10 less than in the G-band turns out to be quite useful. Given the precise alignment of the G-band and continuum images and a contrast difference, a subtraction of the two images intensifies the structures having the magnetic origin. The top panel in Fig. 17.2 shows the sunspot in the 4305 Å G-band. The bottom panel shows the result of subtraction of the 4364 Å continuum image from the G-band. Note that the umbral dots show up in the difference image with reversed contrast. The typical size of the umbral dots is ~ 70 km and may be below the resolution limit.

A closer look from these observations is shown in Fig. 17.3.

In addition to already established properties (listed above) these observations revealed new properties of penumbral filaments. Most important of them are illustrated in Fig. 17.3 and listed below:

1. All filaments, whether or not they show obvious dark cores, are associated with a bright point which may be found *anywhere* along their length, and often inside umbra.
2. The umbral end of the filaments often splits into a series of bright dots, each having its own tails (left panel, thick arrow).
3. Filaments with or without dark core may branch into several filaments anywhere in the penumbra. The branching region is always brighter than the filament itself (small vertical arrows).
4. Several filaments may twist around each other into a bunch resembling multiwire cable. When unwinding, the individual filaments often keep their identity, but the process itself is accompanied by localized sporadic brightenings (right panel, thick arrow).
5. Many filaments exhibit twist along their lengths, resembling cylindrical helices having various pitch (thin long arrows). Strongly twisted filaments are usually short-lived.
6. The ratio of filament radius and pitch is about the same for the majority of the long-lived filaments.

The temporal variability of penumbral filaments studied by space-time procedure shows the motions of various bright and dark patches revealing the true nature of an apparent twisting of filaments. It was found that the twisting motion is an intrinsic property of penumbral filaments. Screw-type motion is well observed in the majority of filaments, including those which do not show a clear twist in single snapshots. This property of penumbral filaments determines in large the observed peculiarities of penumbral filaments.

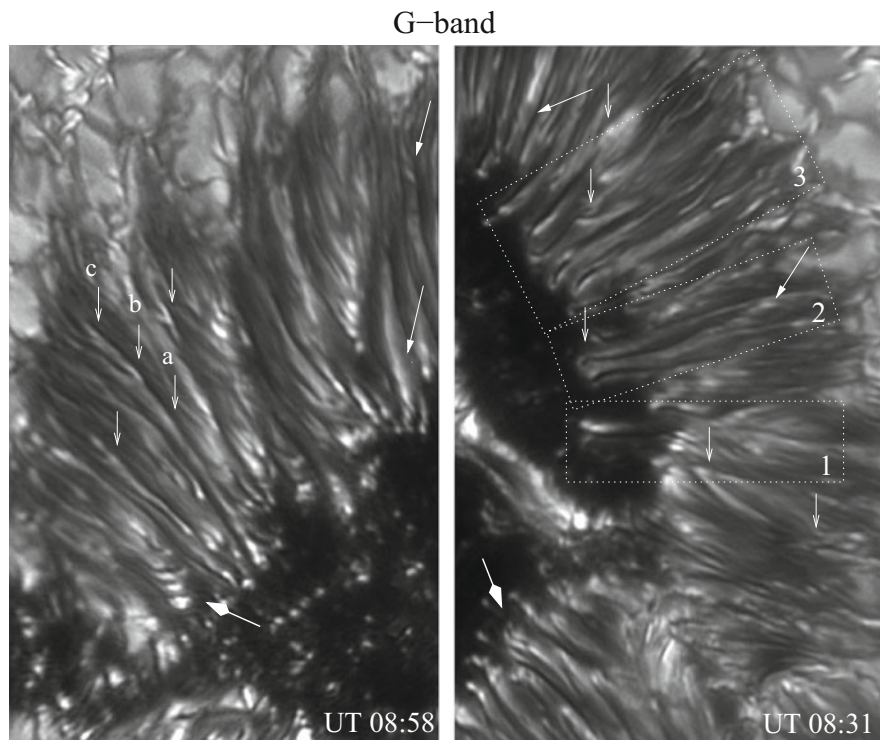


Fig. 17.3 Eastward and westward parts of the sunspot showing various topological structures in penumbral filaments. Small downward arrows show the apparent splitting of filaments. Note that all the branching points show enhanced brightening. Three arrows marked by a, b, and c show multiple branching of one filament. Although the snapshot caught them together, the branching occurred in different times. The thick arrow in the left panel shows a regular series of intense bright points that may represent a strongly twisted individual filament or branching points of several filament below the surface; In the right panel the thick arrow shows multiwire view of filaments. The westward part of the penumbra (right) is center-side and therefore shows more dark-cored filaments than the eastward part of the penumbra. See text for discussion of dotted boxes marking several ubiquitous events

17.2 Dynamics of Penumbral Filaments and Ongoing Reconnections

Before we discuss the details of the observed regularities in the temporal behavior of penumbral filaments, let us recall a well-known fact from basic plasma physics: long, cylindrical magnetic structures are subject to helical instabilities, and a long magnetic flux tube with both azimuthal and axial components twists into a kinked helical shape, forming the screw pinch configuration (Shafranov 1956; Kruskal and Kulsrud 1958; Kadomtsev 1966; Parker 1979).

In other words, long penumbral filaments, as any other long magnetic flux tubes, are intrinsically unstable unless they wind into a helical shape with nonzero field-aligned current components that provide their dynamic stability in twisted shape. The magnetic field lines are therefore helices of some radius r . The pitch angle $\theta(R)$, i.e., the angle between a line of force and the direction of flux tube axis (z -direction) is: $\tan \theta(R) = B_\phi/B_z$, where B_z and B_ϕ are axial and azimuthal components of magnetic field. The pitch of the helices, i.e., the distance in which the field line makes one revolution around the flux tube is:

$$h(R) \equiv \frac{2\pi R}{\tan\theta} = \frac{2\pi R B_z}{B_\phi} \quad (17.1)$$

The twisted state is characterized by the safety factor defined as follows:

$$q = \frac{2\pi R B_z}{L B_\phi} \equiv \frac{h}{L} \quad (17.2)$$

where R is the radius of the flux tube, L is its length. The screw pinch instability turns on when the safety factor becomes less than one:

$$q \equiv \frac{h}{L} < 1 \quad (17.3)$$

The most readily excited configuration is usually the kink mode ($m = 1$), when the flux tube winds along the screw direction together with the axis. It is interesting that in the case of penumbral filaments the safety factor is observed directly, and it is such that (17.3) is applicable virtually to all the penumbral filaments.

Examples of space-time slices made in the G-band and G-band/4364 Å continuum difference movies are shown in Fig. 17.4. The top panels are snapshots of penumbra segments, where the space time cuts are made. The paths of these cuts are marked by numbers 1–4. The corresponding space-time images are shown in the lower panels. One can see that the twists seen in the snapshots indicate “cork screw” motions, which may be either right-handed or left-handed. In any case, twisting motion remains regular for a long time, probably during the entire lifetimes of filaments. Duration of these observations is 85 min.

Not all the filaments show a helical shape in single snapshots, while movies reveal the twisting motions much more readily. In any case the pitch of the helical structure is directly measurable.

To measure the pitch using the movies, one needs to make at least two nearby cuts over a filament at some distance from each other, Δx . A pitch, h , will be then $h = \Delta x(T/\Delta t)$, where T is a period, e.g., time between maxima of intensity in the space-time image, and Δt is the time shift between the maxima in the neighboring cuts.

Examples of such a procedure are shown in Fig. 17.4. Cuts 1a and 1b are made in the G-band movie, and cuts 1c and 1d in the G-band/Continuum difference

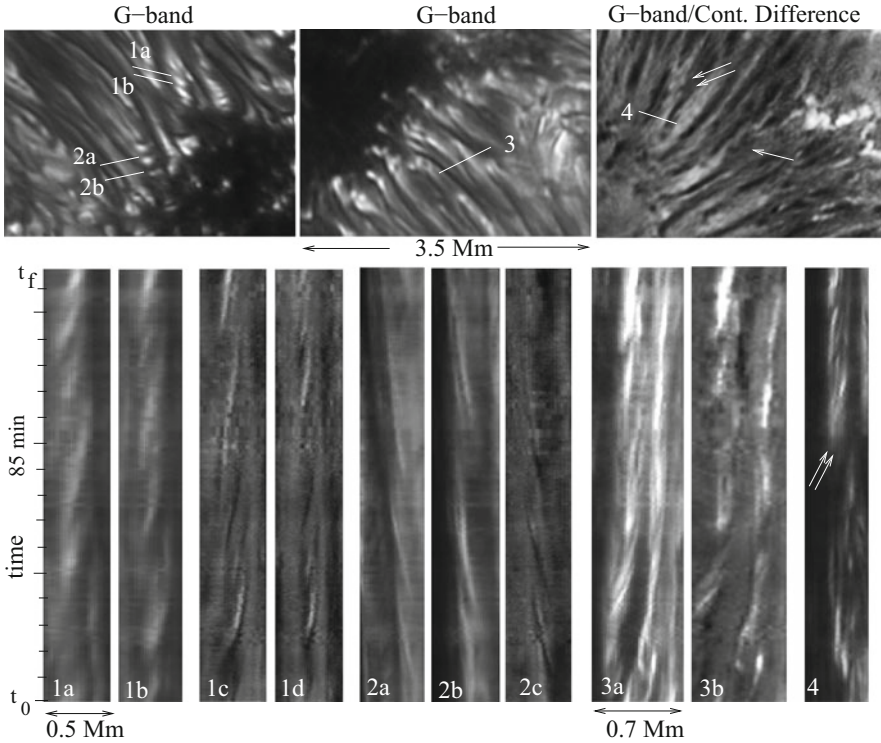


Fig. 17.4 Space-time images revealing helical structure and corkscrew motions of the penumbral filaments (see text for details). The tick marks on the time axis have 5 min spacing, $t_0 = \text{UT } 08:30:05$, $t_f = \text{UT } 09:55:05$

movie (the corresponding snapshot is not shown). One can see immediately that the maximum intensities in cuts $1a$ and $1b$ are phase shifted, while in cuts $1c$ and $1d$ they are in phase. The distance between cuts $1a$ and $1b$ is $\Delta x \simeq 300 \text{ km}$, measured times are $T \simeq 22$ and $\Delta t \simeq 12 \text{ min}$. For the pitch, we have then $h \simeq 550 \text{ km}$. To confirm this result we made cuts $1c$ and $1d$ about 550 km apart. Indeed, the corresponding space-time images are perfectly synchronous. The same is true for cuts $2a$ and $2b$ (cut $2c$ made in the G-band/Continuum difference movie is located in the same place as $2a$). All three twists are in phase. In this case, $T = 20 \text{ min}$, and $\Delta x \simeq 700 \text{ km}$. Thus the pitch $h \simeq 700 \text{ km}$.

Cuts $3a$ and $3b$ made in the G-band and G-band/Continuum difference movies in the same place over the multiwired filaments show the coexistence of closely located filaments. This cluster of filaments remains quite sturdy during the observation period. One can see, however, signs of interaction between the individual filaments accompanied by the enhanced brightening.

Signs of interaction are also seen in panel 4 of Fig. 17.4. Cut 4, made in the G-band/Continuum difference movie shows the birth of a strong twist occurring

at about 09:20 UT (double arrows). The newly generated twist is quite strong and oriented in such a way that is well recognized even in the snapshot (marked by double arrows in upper third panel). One should bear in mind that different orientations of a cut show different patterns in motions of bright and dark patches lying along this cut. Cut 4 is made to reveal a birth of twist but does not clearly show interaction of filaments which could result in it. One can see several interlaced filaments in the first half of observing period before the appearance of a twist, changing their locations and intensities.

The most pervasive kind of interaction seen in high-cadence movies, is apparent splitting of filaments. Most importantly, this process is always accompanied by the enhanced brightening of splitting region. Some examples are highlighted by small arrows in Fig. 17.3.

To see more details we selected three regions marked by dotted boxes in right panel, Fig. 17.3. Boxes 1 and 2 contain filaments that are protruding deep into umbra and are therefore well seen on its background. The third box represents bunch of dark-cored filaments. All three groups of filaments are shown in Fig. 17.5 in three instances of time.

Panels 1a–c in Fig. 17.5 are simultaneous G-band and G-band/Continuum difference images of the “first couple” of filaments. One can clearly see that at UT 08:30:05 longer (“upper”) filament overlays the shorter one. This is especially well noticeable in the G-band/Continuum difference image. At this instant of time (beginning of the observations) an enhanced brightening is quite prominent in the small region marked by arrows. This region becomes the place where left parts of two filaments “exchange” their places, now the longer filament is overlaid by the shorter one. This process is sketched in white boxes embedded in the G-band images, 1a–c. By its nature such a process can obviously be understood as reconnection of filaments.

Panels 2a–c show another example of filament interaction. The beginning of this process has occurred before the observations started. The enhanced brightening of the region of intersection (marked by arrow in panel 2a and 2c) is still visible. As in the previous case, this region becomes the place where filaments separate from each other. Note that in about 20 min filaments seem to disappear (panel 2c). There might be several reasons for this: one is that orientation of filaments has changes, or that they indeed started to decay.

Panels 3a–d show the complex behavior of the filaments as a dense conglomerate. Here we highlight two splitting processes, marked by arrows a and b. In both cases, after splitting, the filaments acquire a twisted shape. In case a splitting is seen in both G-band and difference images, while the arrow b splitting is noticeable only in the difference image. The dashed line in panel 3a is the cut passing through several dark-cored filaments. The corresponding space time image (panel 4) shows several splitting events during the time of observation, as well as the major “survival”: the filament strongly protruding into the umbra, marked by arrow c in panels 3c and 4.

Obviously, the apparent splitting of penumbral filaments, helical shape, and enhanced brightening of the region of splitting are caused by ongoing reconnections.

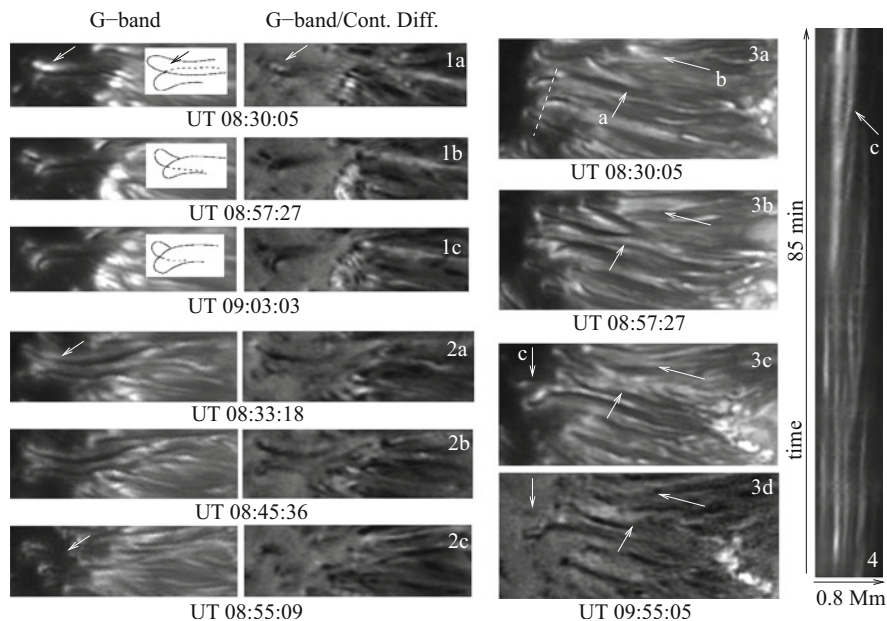


Fig. 17.5 Examples of interacting filaments in three instances of time. Panels **1a–1c** show simultaneous G-band and G-band/Continuum difference images of two neighboring filaments; initially, the longer filament overlays the shorter one. In subsequent instances it seems that filaments have exchanged their left ends. This process is sketched in the white boxes. Panels **2a–2c** show another example of filaments in the later stage of their interaction. In both cases the interaction is accompanied by enhanced brightening (marked by arrows). Panels **3a–3d** show the evolution of the system of filaments. Arrows *a* and *b* show the regions where filaments possibly reconnect, and acquire the twisting shape. The dotted line in panel **3a** is the cut passing through several filaments. Corresponding space time image (panel **4**) shows several splitting events

In the next section, we discuss specifics of the reconnection and post-reconnection processes in the penumbra and their relevance to the observed regularities.

17.3 Formation of Filamentary Penumbrae

Fine structures seen at the visible surface suggest that physical processes in deeper layers also occur at small spatial scales: the nature of the surface umbra-penumbra is determined by the sub-photospheric structures. One of the ways to visualize a sunspot (in a vertical cut) is a tree-trunk analogue with branches of tree running along the length of a trunk and gradually deviating outward, forming an umbrella-like ensemble of thin magnetic filaments.

It is important to emphasize that not only penumbra, but the umbra itself is highly inhomogeneous (Fig. 17.2). Observations of filamentary structure of

umbrae go back to 50s, leading to studies of an umbral fine structures long before the recent high-resolution observations became available. For example, Papathanasoglou (1971) showed that widths of umbral filaments are $< 1''$, and dark spacing between them is about $0.6''$. As mentioned in the Introduction (Livingston 1991), a filamentary structure of umbrae is quite complex, and may exhibit presence of vertical, diverging, and horizontal filaments. Such random alternation of magnetic fluxes and almost nonmagnetic spacing between them is indicative that the umbrae consist of a dense conglomerate of noncollinear flux tubes that are in constant motion relative to one another. Among fundamental processes in such a conglomerate are reconnection and post-reconnection processes.

17.3.1 Phenomenology of Basic Mechanism

The penumbral filaments are obviously of the same polarity as the parental sunspot. However, they are strongly noncollinear, and being in such vicinity to each other, they are subject of frequent reconnections.

The reconnection and post-reconnection processes in penumbra, as well as their observed signatures strongly depend on the orientation of filaments and the bisector of the collision angle between the interacting flux tubes.

If the bisector is close to vertical, situation most typical to the sunspot center (Fig. 17.6a), the magnetic force acting in the plane perpendicular to the bisector, straightens the reconnection products and drags them away from each other (see Chap. 12). Line-of-sight picture will show a fragmentation process. Toward

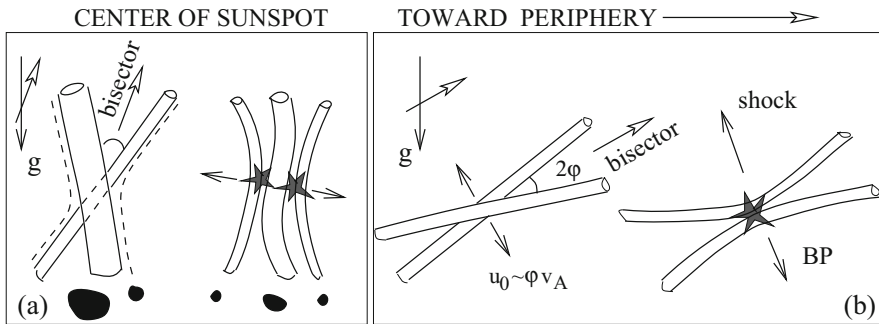


Fig. 17.6 Visualization of photospheric and sub-photospheric reconnections between the same polarity flux tubes: (a) Reconnection between the umbral (almost vertical) flux tubes colliding at the angle with the bisector close to the line of sight; in this case, the post-reconnection slingshot drags away the fragmented parts; (b) Reconnection between the peripheral filaments when the bisector of the collision angle strongly deviates from the vertical; in this case, the upper slingshot generations shocks and subsequent jets; the appearance of the bright point in the reconnection region is always in place

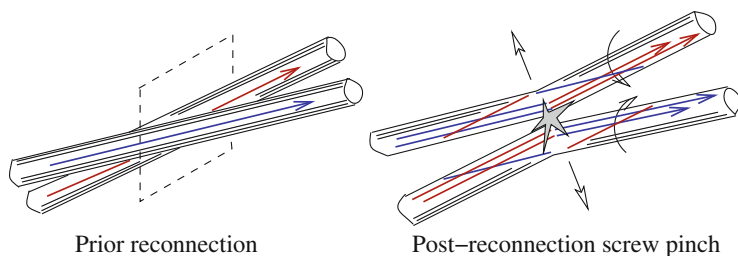


Fig. 17.7 The post-reconnection screw pinch resulted from an inevitable twist inherited by the reconnection products

periphery, penumbral filaments deviate from vertical, so does the bisector of their collision angle. In this case along the magnetic tension the reconnection products experience action of the buoyancy force. For upper part of the reconnection product (Fig. 17.6b) the magnetic tension and buoyancy force are acting in the same, upward direction, which leads to the generation of shocks, and eventually the appearance of lateral jets (Tarbell et al. 1999; Ryutova et al. 2003; Ryutova and Tarbell 2003; Katsukawa et al. 2007; Ryutova et al. 2008b). Besides, region of reconnection always has some excess of energy, which manifests itself in enhanced brightening, usually observed as bright points (BP).

Most importantly, the reconnection generates an inevitable twist (Fig. 17.7). This fact plays a crucial role in the topological features of penumbral filaments, and in particular, in the appearance of dark cores along their axes, first observed by Scharmer et al. (2002).

It is important that only a limited portion of flux participates in each elemental reconnection. Recall (Chaps. 12–13) that the effective radius is determined mainly by the magnetic Reynolds number, $R_{\max} < L/2\ln Re_m$. With $Re_m \simeq 10^3\text{--}10^6$, and a typical length of $L \simeq 10^3$ km, we have $R_{\max} \sim 36\text{--}70$ km. As discussed earlier, this means that magnetic flux tubes having a radius as small as 150–200 km may be the sites of multiple reconnection processes. Good illustration of such a process is an example of multiple branching of penumbral filament shown, e.g., by vertical arrows in Fig. 17.3. As mentioned in the figure caption, although the snapshot caught all these branching together, they did not appear simultaneously, i.e., interaction of a given filament occurred with different neighbors in different times. This process is ubiquitous and is well observed both in G-band and G-band/continuum difference movies, suggesting that it just these continuous reconnections, fragmentation, and branching are responsible for the formation of filamentary structure of penumbra and the sunspot as a whole.

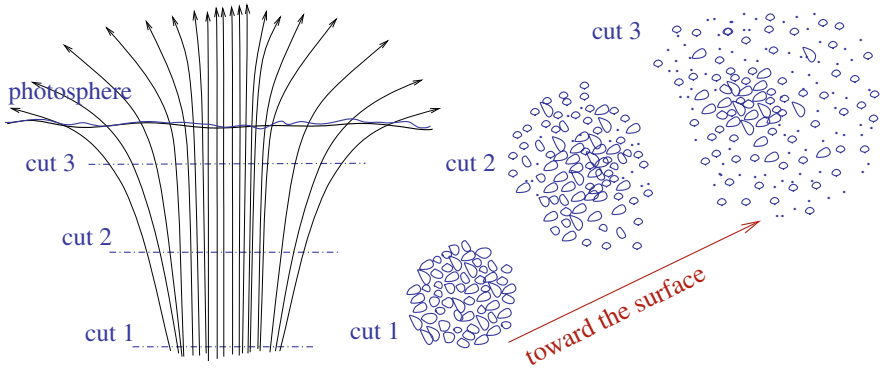


Fig. 17.8 Schematic of the sunspot illustrating the formation of a filamentary umbra/penumbra

17.3.2 *Filamentary Structure of Sunspot*

A schematic of the formation of the fine structures of the sunspot and the branching out of the peripheral flux tubes that form the penumbra is shown in Fig. 17.8.

Thus the process of fragmentation in the sunspot, and branching out of the newborn flux tubes will occur repeatedly until the reconnection products reach their critical radii. As flux tubes have different parameters, branching occurs at different heights. In the central region of sunspot fragmented flux tubes remain mostly vertical, but may also diverge (Livingston 1991).

Toward the edge of the umbra flux tubes deviate more and more from the vertical. So does the bisector of the collision angle between the interacting flux tubes. In this case, the upward slingshot generates oblique shocks and leads to the appearance of a lateral jets. Note that the reconnection region is always marked by enhanced brightening corresponding to the bright points seen throughout the penumbra. The larger the deviation, the stronger the shocks leading to stronger jets. In addition, the reconnection of noncollinear flux tubes leads naturally to a twist in the reconnected filaments. This twist as already mentioned plays a crucial role in stability, dynamics, and properties of penumbral filaments. This will be discussed in the next section.

17.3.3 *Properties of Individual Filaments*

Thus, the ongoing reconnection and fragmentation processes that determine the morphology and properties of a sunspot, shape as well the penumbral filaments. All the observed properties of the penumbral filaments listed in Sect. 17.2, are natural consequences of these processes: the very formation of the filamentary penumbra, the multiple splitting of individual filaments and their footpoints, the enhanced brightening of the footpoints (region of reconnection), a twist of filaments, and as we will see below, the presence of dark cores in most of the filaments.

A simple phenomenological approach allows one to make a reasonable quantitative analysis.

We start with the most readily excited, a kink mode configuration ($m = 1$). The condition (17.3) for safety factor, defined by (17.2), puts a constraint on the azimuthal electric current known as the Kruskal-Shafranov limit:

$$I_\phi > I_{KS} = \frac{2\pi Rc}{L} B_z, \quad (17.4)$$

where I_{KS} is the Kruskal-Shafranov current below which the magnetic field is supposed to be stable with respect to screw pinch instability. Laboratory experiments, however, show that the screw pinch configuration is surprisingly stable far below the Kruskal-Shafranov limit. Theoretical studies show that there are indeed many factors (such as finite plasma β , nonzero resistivity, the finite length of the plasma column, the presence of plasma flows, field reversal, and others) that provide realization and stability of a screw pinch configuration far below the expected limit (Schuurman et al. 1968; Goedbloed and Zwart 1975; Miyamoto 1988; Lehnert and Scheffel 1992; Martynov and Medvedev 2003; Ryutov et al. 2006; Bergerson et al. 2006).

In case of the penumbral filaments, the safety factor, $q = h/L$, is observed directly and allows infer B_ϕ from the direct measurements of the pitch and B_z . As we know, along the most common $m = 1$ kink mode, the current-carrying magnetic flux tubes are subject to higher modes of MHD instabilities, $\sim \exp(im\phi)$. The mode m determines the entry of helical perturbations (Fig. 17.9, left; cf. Fig. 3.3). For qualitative comparison, we illustrate possible high azimuthal modes of twisted filaments in Fig. 17.9, right panels. The next step in observations is obtaining vector field maps with high spatial resolution that became available with spectropolarimetric measurements with the SOT aboard the Hinode satellite and

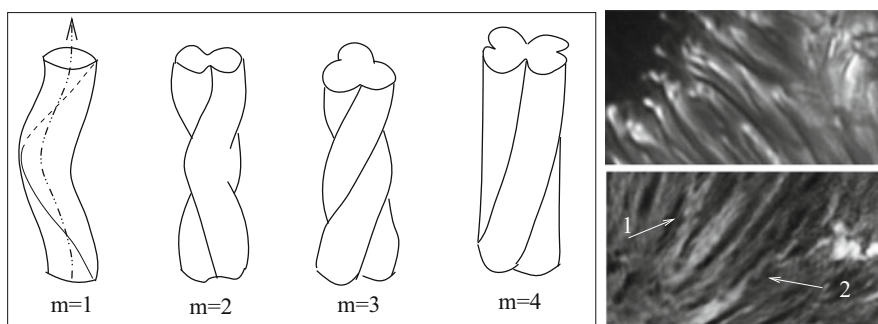


Fig. 17.9 Screw pinch configurations. Left panel: Various modes of helical perturbations. Right panel: Possible observational evidence for various modes shown in the fragments of penumbra—G-band (top), and G-band/4396 Å continuum difference image (bottom). The arrows show strongly twisted filaments; pitch/radius ratio for the first helical structure is slightly larger than unity, and for the second structure it is between 1.5 and 2

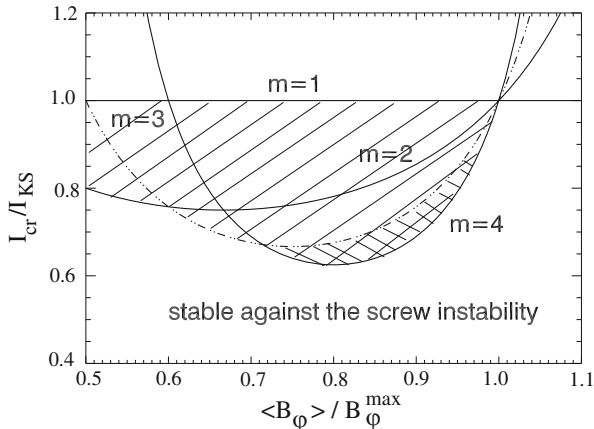


Fig. 17.10 Stability boundary determined by the critical current and azimuthal magnetic field. There is a significant range of parameters below the line $m = 1$ where the screw pinch configuration with one of the higher modes may be formed (after Ryutov et al. 2004)

the SDO instruments. Detection of higher modes in the observations, which will allow a direct measurement of the basic parameters in the screw pinch provides an additional means to infer the electric currents and other physical parameters.

Theoretically, it is shown that there is a considerable range of parameters for higher modes of the screw pinch configuration (Ryutov et al. 2004). We use here their calculations to plot the stability boundary for various magnetic field profiles (Fig. 17.10). The ratio $I_{cr} \geq I_{KS}$ demarcates the stability boundary as a function of the azimuthal component of the magnetic field. The kink mode, $m = \pm 1$, e.g., develops for $I_{cr} \geq I_{KS}$, i.e., above the straight line $m = 1$ in Fig. 17.10 (see (17.4)). Below this line, there is a significant range of parameters where screw pinch configuration with one of the higher modes may be formed.

The excitation of other modes, as well as the manifestation of the individual properties of a given filament, depends on the actual distribution of the magnetic fields and currents inside it. It is important that the helical shape of the magnetic field has a significant effect on the temperature distribution inside a magnetic flux tube that naturally accounts for the appearance of dark-cored filaments.

17.4 Screw Pinch Instability and Dark Cores

To see how the screw pinched flux tube acquires the dark cores, let us find profiles of the temperature, magnetic fields, and currents in a twisted flux tube. We start with a stationary form of the energy balance equation, which can be written as:

$$\kappa_{\parallel} \frac{\partial^2 T}{\partial z^2} = -\frac{j^2}{\sigma} + Q_{rad} - H_{visc} \quad (17.5)$$

where κ_{\parallel} is the parallel thermal conductivity, j is a current density, σ is the electric conductivity, and Q_{rad} and H_{visc} are the radiative loss function and viscous heating, respectively.

In order to isolate the effect of the helical structure on the temperature and electric current distributions, we assume that the filament is kept in radiative equilibrium by viscous heating. Roughly, this can be justified by estimating the two last terms in Eq. (17.5).

The radiative cooling time, τ_{rad} (Spiegel 1957), calculated for a photospheric magnetic flux tube of radius $R = 50$ km, plasma density $\rho = 2 \times 10^{-7} \text{ g cm}^{-3}$, and temperature change from 12,000 to 4800 K is about $\tau_{rad} = 200$ s (Schlichtenmaier 1999). The estimate for radiative heat flux at $T = 4800$ K is $Q_{rad} \simeq (3/2)nkT/\tau_{rad} = 413 \text{ erg cm}^{-3}\text{s}^{-1}$. Viscous heating is provided mostly by turbulent motions, and may be estimated as $H_{visc} \simeq \eta_{turb} e_{ij}^2$, where $e_{ij} = [(\partial v_i/\partial r_j) + (\partial v_j/\partial r_i)]$, and $\eta_{turb} \simeq \rho v R$. For the above parameters with a turbulent velocity $v \simeq 2 \text{ km s}^{-1}$, we have $H_{visc} \simeq 320 \text{ erg cm}^{-3}\text{s}^{-1}$.

Profiles of equilibrium magnetic fields and currents in twisted magnetic flux tubes are calculated by balancing the Lorentz force and the pressure gradient:

$$\frac{1}{c} \mathbf{j} \times \mathbf{B} = \nabla p \quad (17.6)$$

where p , \mathbf{j} , and \mathbf{B} are the pressure, current density, and magnetic field. For a simple axisymmetric state, magnetic field profiles can be expressed through a generating function $f(r)$ defined as the total pressure, $f(r) = p + (B_{\phi}^2 + B_z^2)/8\pi$ (see, e.g., Parker 1979):

$$p(r) + \frac{B_z^2}{8\pi} = f(r) + \frac{1}{2} \frac{df}{dr}, \quad \frac{B_{\phi}^2}{8\pi} = -\frac{1}{2} r \frac{df}{dr} \quad (17.7)$$

The generating function is arbitrary except that in order that B_{ϕ} and B_z are real, $f(r)$ should decline monotonically with r , but not faster than $1/r^2$, i.e., $0 \geq df/dr \geq -2f(r)/r$. For illustrative purpose we consider a force-free field, $\mathbf{j} \times \mathbf{B} = 0$ ($p = \text{constant}$), with a simple generating function:

$$f(r) = P_0 \frac{1 + R^2 \mu^2}{1 + r^2 \mu^2}, \quad (17.8)$$

where μ is the inverse pitch of a helical flux tube,

$$\mu \equiv \frac{2\pi}{h} \quad (17.9)$$

Corresponding solutions for magnetic fields and currents are shown in Fig. 17.11. We use here typical observed parameters of penumbral filaments, e.g., $R = 4 \times 10^1$ km, $h = 5 \times 10^2$ km, $B_z = 1500$ G.

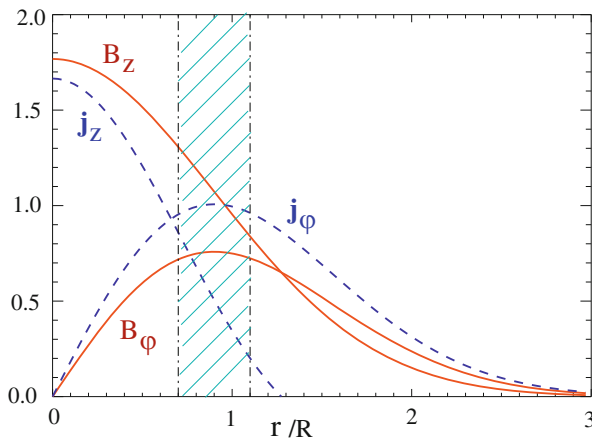


Fig. 17.11 Magnetic field and current profiles. The shaded area is where the enhanced heating occurs providing a cooler interior of the flux tube compared to its hotter walls

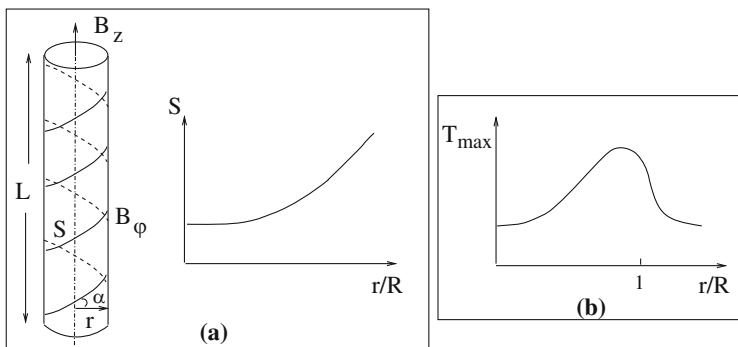


Fig. 17.12 A helical flux tube: (a) Flux tube and a plot of length of helix, $S(r)$. (b) Sketch of the temperature profile across the flux tube

The individual magnetic lines of force are helices of radius r . The entire length of the helix, S (the connection length between the ends of flux tube), depends on the pitch angle, $\theta(r)$, defined as $\tan \theta(r) = B_z/B_\phi$ at a given flux surface. Simple geometrical considerations show that the length of the helix, S considerably exceeds the physical length of a tube, L :

$$S = L\sqrt{1 + B_z^2/B_\phi^2} \tag{17.10}$$

For the magnetic field distribution shown in Fig. 17.11, S is minimum at the axis (where $B_\phi = 0$), and rapidly grows toward periphery (Fig. 17.12a).

If according to the above estimates the filament is kept in radiative equilibrium by the viscous heating, the effect of helical structure on the temperature distribution

can be evaluated by the approximate equation for the temperature in the middle of the flux tube (along the axis) determined by the balance of the Joule heating and parallel thermal conductivity. Then along the field line we have:

$$\kappa_{\parallel} \frac{\partial^2 T}{\partial z^2} = -\frac{J^2}{\sigma} \quad (17.11)$$

This gives an estimate

$$T \simeq T_{\max}(1 - 4z^2/S^2), \quad (17.12)$$

with T_{\max} as

$$T_{\max}(r) \simeq \frac{j^2(r)S^2(r)}{8\sigma\kappa_{\parallel}}, \quad (17.13)$$

The presence of the factor $S^2(r)$ makes the hollow temperature profiles a natural occurrence (Fig. 17.12b). The fact that these are rotating, axially flowing plasma fluid structures (i.e., plasma vortex tubes) means that the density profile increases from its minimum along the tube axis to a maximum at the walls. This fact again supports the occurrence of the dark cores and their consistency with the optically thin radiative transfer.

17.4.1 More on Substructures of Filaments

Now we turn to a more general solution of (17.6). The simplest solution in cylindrical geometry is known to be a Lundquist field (Lundquist 1951), having form of Bessel functions (Fig. 17.13):

$$\begin{aligned} B_z(r) &= B_0 J_0(\mu r), & B_\phi(r) &= B_0 J_1(\mu r) \\ j_z(r) &= \frac{B_0 c}{2\pi} \mu J_0(\mu r), & j_\phi(r) &= \frac{B_0 c}{2\pi} \mu J_1(\mu r) \end{aligned} \quad (17.14)$$

where μ is the inverse pitch of a helix, defined by (17.9). Note that the solution shown in Fig. 17.11 is qualitatively the same if μr is less than the first zero of $J_0(\mu r)$. The above field configuration, often met in laboratory plasmas, has been extensively studied both theoretically and in advanced experiments. Similar studies of solar and space magnetic fields with helical configurations have been carried out (Van Hoven et al. 1977; Parker 1979; Lothian and Hood 1989; Rust and Kumar 1994; Linton et al. 1996; Li 2000; Wissink et al. 2000).

A characteristic feature of the Lundquist solution is the reversal of the magnetic field and electric currents (Fig. 17.13), first emphasized by Taylor (1974) and later

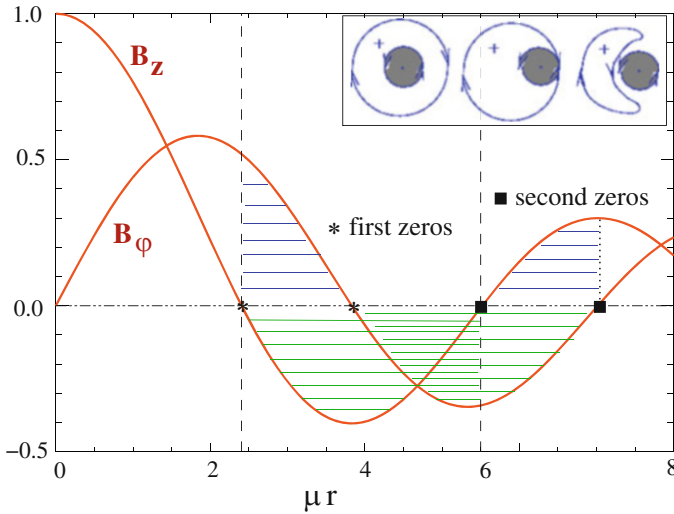


Fig. 17.13 Oscillatory character of the Bessel functions. Shown are several regimes determined by the critical current and azimuthal magnetic field. The inset shows the cross-section of the reversed pinch in the interval $3.85 < 2\pi R/h < 5.5$ with formation of a reversed core and its dynamics (after Miyamoto 1988)

observed in numerous laboratory experiments. The oscillatory character of the Bessel functions provides several regimes of magnetic field distribution inside flux tubes. Depending on the magnetic field geometry inside flux tubes represented by parameter μR , and the degree of twist, there are several regimes of magnetic field configuration:

1. The parameter μR is below the first zero of $J_0(\mu R)$, i.e., $2\pi R/h < 2.4$, which translates into a condition for a pitch/radius ratio, $(h/R) > 2.62$. In this case the magnetic field components preserve their initial direction and chirality.
2. The parameter μR exceeds the first zero of $J_0(\mu R)$ but is below the first zero of $J_1(\mu R)$, i.e., $2.4 < 2\pi R/h < 3.85$, or $1.63 < (h/R) < 2.62$. In this case the axial magnetic field reverses, but the chirality of the filament remains the same.
3. In the interval $3.85 < 2\pi R/h < 5.5$ ($1.14 < (h/R) < 1.63$) the axial magnetic field reversal is accompanied by reversed chirality. The interval with higher zeros is unlikely, as it leads to strong twist and a likely disruption of the filament.

Field reversal configurations, well studied in laboratory plasmas, have clear morphological effects that can be observed. For example, the internal reconnections lead to a typical magnetic field rearrangement, shown in the inset of Fig. 17.13. This corresponds to a pitch/radius ratio in the interval $3.85 < 2\pi R/h < 5.5$. With high-resolution observations, such multicomponent configurations of the magnetic field can be observed as local reversals in the direction of the field in the penumbra. If the filament twist is very strong (see filaments marked by white arrows in Fig. 17.9,

bottom right), the core per se may not be visible, but the effect of the small-scale local field reversals may be observationally detectable.

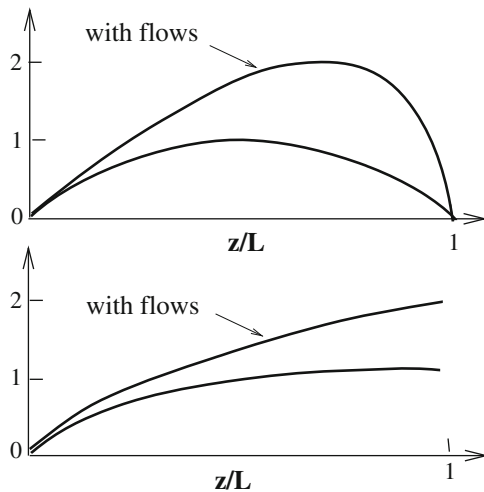
In many cases, the force-free approximation gives a reasonable qualitative picture. However, for most of the problems associated with the solar atmosphere, especially in the lower layers with high plasma β and nonzero resistivity, the equilibrium magnetic field must depart from the force-free configuration. And yet, under reasonable conditions, a modified non-force-free magnetic field is still described by the Bessel functions of the Lundquist solution (Chiuderi et al. 1977; Rust and Kumar 1994).

17.4.2 Effects of Axial Flows

Here we briefly discuss the effects of axial flows on the twisted flux tubes. This problem is extremely important for solar flux tubes, and, in particular, for umbra/penumbral filaments where mass flows are the necessary accomplice of their dynamics. However, this problem did not receive much attention, and yet there are some specific effects that can be directly observed. These will be described below.

Laboratory studies (Ryutov et al. 2006; Furno et al. 2006) show that the presence of an axial flow causes rotation of the kink in the flux tube, and the perturbation amplitude increases in the flow direction. An axial flow causes the advection of perturbations and results in a *skewing* and *wreathing* of the eigenfunction toward the outer edges of filaments (Fig. 17.14). If both ends of the filament are line-tied (Fig. 17.14, top), skewing occurs in such a way that the line-of-sight magnetic field will be observed to be opposite to the parental sunspot polarity. This may explain

Fig. 17.14 Revolution over which the axis of filament is wound. Top: Both ends of a filament are line-tied. Bottom: Only the inner foot is line-tied (after Ryutov et al. 2006)



why the majority of penumbral filaments dive into the moat region at the outer edge of the penumbra, naturally showing an opposite polarity.

We may conclude that all the observed properties of the penumbral filaments, and the formation of the penumbra itself, are natural consequences of the ongoing reconnection processes in a conglomerate of random, interlaced flux tubes forming the sunspot.

In the central umbra, the flux tubes are close to vertical, and thus the bisector of their collision angle is also close to vertical. Therefore in the central region of sunspot fragmenting flux tubes remain mostly vertical. Toward the periphery, flux tubes deviate more and more from the vertical, and branch out from the parental sunspot. As flux tubes have different parameters, branching occurs at different heights thus forming the observed uncombed penumbra. Most importantly, the bisector of the collision angle between the interacting flux tubes deviates from the vertical as well providing conditions for shock formation and their subsequent evolution.

The process of fragmentation in the sunspot, and branching out of the newborn flux tubes occurs repeatedly until the reconnection products reach their critical radii $\sim 20\text{--}40$ km), determined by the local Reynolds number.

The reconnection processes that take place continually in sunspot penumbra lead to twisting of the post-reconnection flux tubes. The inherent twist of individual filament facilitates the onset of a screw pinch instability, which determines the distribution of electric currents and temperature inside the filaments. These in turn lead to the appearance of dark cores surrounded by bright walls. Moreover, all the observed properties are not only qualitatively understood but may be used for quantitative estimates. These again, are:

1. The sunspot umbra is a dense conglomerate of random flux tubes where the reconnection of same polarity neighbors leads to their further fragmentation accompanied by bright points.
2. The formation of filamentary penumbra by means of peripheral flux tubes continuously reconnecting and branching out from the "trunk."
3. Occurrence of multiple splitting of individual filaments and their footpoints.
4. Enhanced brightening of footpoints (region of reconnection).
5. Generation of post-reconnection twist of filaments.
6. Occurrence of dark cores associated with the redistribution of magnetic field and temperatures inside filaments due to the onset of screw pinch configuration.
7. The fact that filaments with or without dark core may branch into several filaments anywhere in penumbra, with branching region being always brighter than the filament itself.
8. The visual effect that not all filaments show the dark-cored structure is pure geometrical one.
9. The fact that several filaments may spin around each other into a bunch resembling multiwire cable (high azimuthal modes). When unwinding the individual filaments often keep their identity, but the process itself is accompanied by the localized sporadic brightenings.

It is important to note that the simplicity of screw pinch physics, based on directly measurable parameters, such as pitch, radius, and magnetic field, allows quantitative analysis of the penumbral properties.

The next obvious question is: what is the impact of the penumbral dynamics on the overlying atmosphere. We shall address this problem in the next chapter, and see that the reconnection between the penumbral filaments leads to expected post-reconnection jets and sporadic brightenings in the overlying chromosphere.

17.5 Problems

17.1 Find the equilibrium condition for the infinitely long current carrying cylinder embedded in the external magnetic field. Assume that all quantities vary in the r direction only, i.e., $\partial/\partial z = \partial/\partial \theta = 0$. Current flowing through a plasma tends to squeeze the plasma causing a pinch effect. Specify conditions of a pinch effect for a long magnetic flux tube.

17.2 Obtain the equilibrium conditions when magnetic field has only z -component.

17.3 The same for the flux tube having only θ component of magnetic field, $B_\theta \neq 0$. The current then has z -component and nonzero $\mathbf{j} \times \mathbf{B}$ force must be balanced by the pressure gradient. Such configuration is known as z -pinch.

17.4 The same for the case when both B_z and B_θ components are nonzero.

References

- L. Bellot Rubio, K. Langhans, R. Schlichenmaier, *Astron. Astrophys.* **443**, L7 (2005)
 T. Berger, et al., *Astron. Astrophys.* **428**, 613 (2004)
 W.F. Bergerson, et al., *Phys. Rev. Lett.* **96**, 015004 (2006)
 C. Chiuderi, R. Giachetti, G. Van Hoven, *Solar Phys.* **54**, 107 (1977)
 I. Furno, et al., *Phys. Rev. Lett.* **97**, 015002 (2006)
 J.P. Goedbloed, J.W.A. Zwart, *Plasma Phys.* **17**, 45 (1975)
 B.B. Kadomtsev, *Reviews of Plasma Physics*, Vol. 2, ed. by M.A. Leontovich (Consultants Bureau, New York, 1966), p. 153
 Y. Katsukawa, T. Berger, K. Ichimoto, et al., *Science* **318**, 1594 (2007)
 M.D. Kruskal, R.M. Kulsrud, *Phys. Fluids* **1**, 265 (1958)
 K. Langhans, et al., *Astron. Astrophys.* **436**, 1087 (2005)
 B. Lehnert, J. Scheffel, *Plasma Phys. Controlled Fusion* **34**, 1113 (1992)
 L.-X. Li, *Astrophys. J.* **531**, L111 (2000)
 M.G. Linton, D.W. Longcope, G.H. Fisher, *Astrophys. J.* **469**, 954 (1996)
 W. Livingston, *Nature* **350**, 45 (1991)
 R.M. Lothian, A.W. Hood, *Solar Phys.* **122**, 227 (1989)
 S. Lundquist, *Phys. Rev.* **83**, 307 (1951)
 A.A. Martynov, S. Yu. Medvedev, *Phys. Rev. Lett.* **91**, 085004 (2003)
 K. Miyamoto, *Plasma Phys. Contr. Fusion* **30**, 1493 (1988)
 D. Papathanasoglou, *Solar Phys.* **21**, 113 (1971)

- E.N. Parker, *Cosmical Magnetic Fields* (Clarendon Press, Oxford, 1979)
- T. Rimmele, J. Marino, *Astrophys. J.* **646**, 593 (2006)
- L. Rouppe van der Voort, et al., *Astron. Astrophys.* **435**, 327 (2005)
- D.M. Rust, A. Kumar, *Solar Phys.* **155**, 69 (1994)
- D.D. Ryutov, R.H. Cohen, L.D. Pearlstein, *Phys. Plasmas*, **11**, 4740 (2004)
- D.D. Ryutov, et al., *Phys. Plasmas*, **13**, 032105 (2006)
- M. Ryutova, T. Tarbell, *Phys. Rev Lett.* **90**, 191101 (2003)
- M. Ryutova, T. Tarbell, R. Shine, *Solar Phys.* **213**, 231 (2003)
- M. Ryutova, T. Berger, A. Title, *Astrophys. J.* **676**, 1356 (2008a)
- M. Ryutova, T. Berger, Z. Frank, A. Title, *Astrophys. J.* **686**, 1404 (2008b)
- G. Scharmer, et al., *Nature* **420**, 151 (2002)
- R. Schlichenmaier, J.H.M.J. Bruls, M. Schüssler, *Astron. Astrophys.* **349**, 961 (1999)
- W. Schuurman, C. Bobeldjik, R.F. de Vries, *Plasma Phys.* **11**, 495 (1968)
- V.D. Shafranov, *At. Energy* **30**, 38 (1956)
- R.A. Shine, A.M. Title, T.D. Tarbell, K. Smith, Z.A. Frank, *Astrophys. J.* **430**, 413 (1994)
- E.A. Spiegel, *Astrophys. J.* **126**, 202 (1957)
- P. Sütterlin, et al., *Astron. Astrophys.* **424**, 1049 (2004)
- J.B. Taylor, *Phys. Rev. Lett.* **33**, 1139 (1974)
- T. Tarbell, M. Ryutova, J. Covington, A. Fludra, *Astrophys. J.* **514**, L47 (1999)
- A. Title, et al. *Astrophys. J.* **403**, 780 (1993)
- G. Van Hoven, C. Chiuderi, R. Giachetti, *Astrophys. J.* **213**, 869 (1977)
- J.G. Wissink, P.M. Matthews, D.W. Hughes, M.R.E. Proctor, *Astrophys. J.* **536**, 982 (2000)

Chapter 18

Bow Shocks and Plasma Jetting over Penumbrae



Abstract Penumbral filaments being in constant motion, reconnecting, splitting, and twisting, strongly affect the overlying atmosphere. In this chapter we shall study the response of the chromosphere to penumbral dynamics, which shows spectacular cascades of bow shocks and plasma jetting. These spectacular events are produced by the ongoing reconnection processes between neighboring penumbral filaments, basically at the periphery of sunspot where penumbral filaments become more and more horizontal. There post-reconnection products moving upward quickly accelerate. At transonic velocities a bow(detached) shock is formed in front of the accelerated flux tube, as it usually occurs in cases of blunt bodies moving with supersonic velocities. In the chromosphere bow shocks are seen in the form of elongated transients moving as a whole in a direction almost perpendicular to their long axes. On some much more rare occasions compared to “drifting” bow shock-type transients, there appear compact “true” microjets moving in the radial direction, and having much higher velocities compared to bow shocks.

18.1 Response of the Overlying Atmosphere to Penumbral Dynamics

High cadence observations with the Solar Optical Telescope (SOT) on Hinode have led to the discovery of frequent transient brightenings in the penumbral chromosphere with lifetimes of ~ 1 min (Katsukawa et al. 2007), referred to as penumbral microjets. They are seen in Ca II H line observations in the form of bright strokes abundantly covering the entire chromosphere above penumbra. Their typical length is found to be between 1000 and 4000 km, some may reach 10,000 km. Their width is ~ 400 km. It was found also that microjets are almost parallel to the penumbral filaments in the radial direction (which makes them difficult to identify when the sunspot is close to disk center), but are more vertical to the surface than penumbral filaments. The estimated elevation angles range from 20° to 60° . Katsukawa et al. (2007) suggested that the observed microjets could be associated with magnetic reconnection in the penumbra. As the physical nature of

these phenomena at time of their discovery was not clear, the authors left room for two possible, but different explanations:

1. One is that “the jetlike brightenings are a signature of plasma transiently heated to much higher temperatures.”
2. The other is that transients represent true mass motion with supersonic velocities, i.e., microjets.

We will see below that both explanations are true, but are related to two different classes of events. One class includes bright elongated transients drifting as a whole in a direction almost perpendicular to their long axes. Their properties are well represented by bow shocks and we classify them as bow shock-type transients. The other class includes compact, short lived, and much faster bright transients exhibiting true plasma motion “along” their axes. We classify these events as microjets. The triggering mechanism for either kind of transient is the reconnection between the neighboring penumbral filaments but it is the post-reconnection processes and local physical conditions that determine their specific nature.

18.1.1 Penumbral Transients: Double Structures and Jets

To demonstrate the observed properties of radiative transients above sunspot penumbrae, we present the observations obtained during the disk passage of active region (AR 10923) on November 10–20, 2006. The data were taken with the SOT instrument on Hinode in 4305 Å G-band and 3968 Å Ca II H line (Ryutova et al. 2008). Movies taken at 8 s cadence show detailed dynamics of jetlike phenomena under different angles as sunspot takes various positions when it passes the solar disk from limb to limb. Such a favorable circumstance allowed to perform detailed analysis of observation and reveal the nature of the impact of penumbral dynamics to the overlying atmosphere.

Figure 18.1 shows the target region on November 10 when sunspot was located at a heliospheric angle of 55° toward the east of the disk center. At any moment of time, the penumbra is covered with bright elongated transients that last from 30 s to several minutes. Their appearance always correlates with the appearance of bright points in the corresponding G-band image. Some examples are marked with white arrows in Fig. 18.1. White boxes demarcate two regions whose time sequences are shown in Figs. 18.2 and 18.3. Transients marked by broken arrows are in the decay phase, while their parental bright points in G-band are still prominent.

Figure 18.2 shows evolution of three well-shaped transients during a 4 min 30 s period. The first frame at UT 13:13:36 shows when transient 1 has just appeared. Transient 2 appeared 30 s earlier. Transient 3 is seen here during its entire lifetime (UT 13:15:06–13:16:37). Note that all three transients are quite similar. They have the same position angle in the plane of the sky. Their intensity increases in time, and then either gradually decreases (as in cases 1 and 2), or vanishes abruptly, as in case

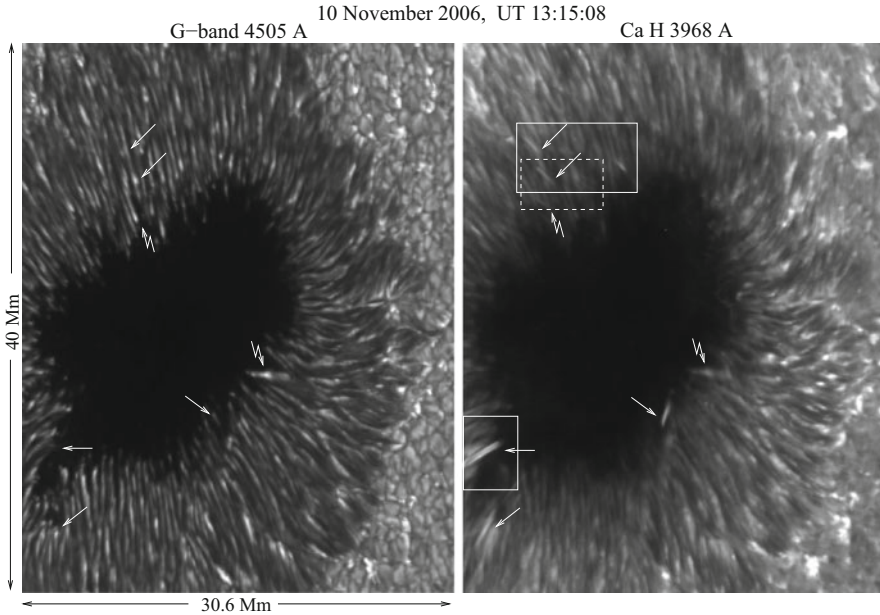


Fig. 18.1 Snapshots of the sunspot on November 10, 2006. Left: G-band filtergram. Right: 3968 Å Ca II H line. Usually, transients (seen in the Ca II H line) are closely related to bright points seen in the G-band image (some are marked by arrows). Transients marked by broken arrows are decaying, while their “parental” bright points in G-band are still prominent. White boxes demarcate regions shown in Figs. 18.2, 18.3, and 18.4 at several instances in time. Note that event shown in Fig. 18.3 occurred about 45 min earlier (its area is marked by a dashed box)

3. Lifetimes are ≥ 6 min (transient 1), 2 min (transient 2), and 90 s (transient 3). All three transients seem to be almost motionless. In fact, they are slowly drifting in the direction perpendicular to their long axes, with velocities $v_1 = 0.6 \text{ km s}^{-1}$, $v_2 = -1.3 \text{ km s}^{-1}$ (a minus sign formally means that, unlike the other two transients, transient 2 is drifting “downward”), and $v_3 = 3.3 \text{ km s}^{-1}$, indices correspond to prescribed numbers. This is, however, a visual effect associated with the angle between the line of sight and the direction of motion of the transients. So that the true velocities of transients must be considerably higher.

These three examples represent the vast majority of the transient brightenings that always move as a whole in the direction perpendicular to their long axes. Their visual velocities range from $\leq 1 \text{ km s}^{-1}$ to 20 km s^{-1} . We shall see below that this type of transient have all the properties of bow shocks.

Another set of slowly drifting transients is shown in Fig. 18.3. We focus on two of them marked as 1 and 2 in a middle frame (UT 12:38:05). The lifetime of both transients is about 5 min. The black dashed arrow in lower left panel shows the spacetime cut. The corresponding spacetime image is shown in the vertical panel. The cut is made from top to bottom, which together with the vertical panel indicates

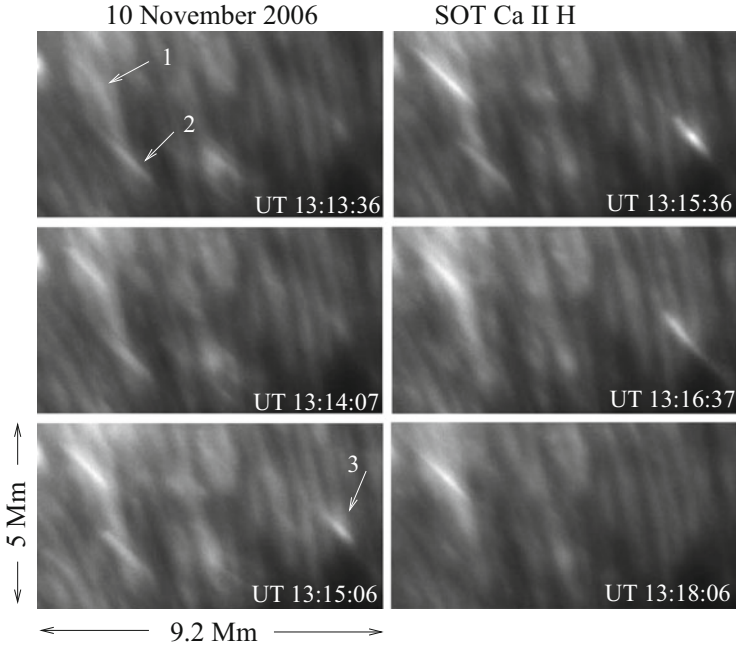


Fig. 18.2 Examples of three transients, from the upper white box in Fig. 18.1, slowly drifting in a direction perpendicular to their long axes

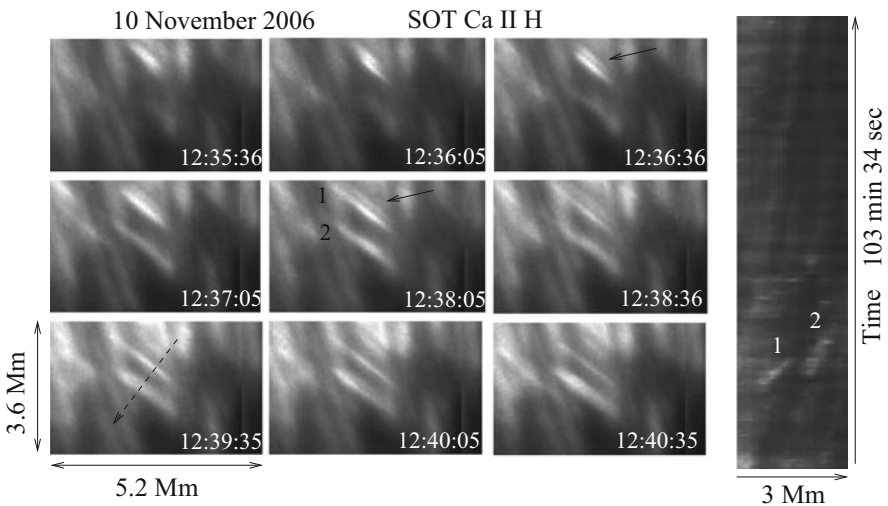


Fig. 18.3 Slowly drifting transients with specific feature showing a double structure. The black dashed arrow in the lower left panel shows the path along which a spacetime cut is made. The vertical panel is the corresponding spacetime image. The velocities in the direction of the cut are $v_1 = 3.9 \text{ km s}^{-1}$, $v_2 = 3.1 \text{ km s}^{-1}$. Black solid arrows show a new feature found in these observations: the double structure of chromospheric transients

that transients are moving downward. Measured velocities are $v_1 = 3.9 \text{ km s}^{-1}$ and $v_2 = 3.1 \text{ km s}^{-1}$.

A remarkable new feature revealed in these observations is that some transients, in particular, the transient 1 in Fig. 18.3, have a double structure. This structure starts to develop soon after the transient has appeared (i.e., just 30 s after its “first light”) and, in this particular example, is easily visible during its maximum phase. This important feature turned out to be quite pervasive: many elongated transients show a double structure and patterns similar to those seen in Fig. 18.3.

Hence, a double structure turns out to be a basic property of drifting transients and, in fact, has a natural explanation in the frame of the theory based on post-reconnection processes. Before we discuss the details of the theory, it is useful to study other observed properties of chromospheric transients that show up under different viewing angles, namely when sunspot is located at the disk center, and then when it moves toward the west limb.

18.1.2 Viewing Under Different Angles

The main feature of transients described in previous section is that their direction of motion is perpendicular to their long axis. This fact makes them easily observable. There are other types of transients whose behavior is similar to jets, i.e., when a collimated plasma moves along its axis. Such transients oriented in radial directions usually coincide with underlying penumbral filaments and are barely detectable. On some occasions though, if the transient exhibits proper motion, it can be observed. An example of such event is shown in Fig. 18.4.

The same sunspot, AR 10923, is now shown on November 14, 2006 when it moved closer to the disk center. Shown are a G-band and Ca II H line images of the chromosphere above the sunspot. A tiny microjet with proper motion is shown in a Ca II H line image. It originates at the base of the fork (marked by black arrows in the upper images) and first appears as an enhanced brightening in the Ca II H line at about UT 10:22:34 (bottom left panel). It slowly accelerates and moves during the first 5 min with an average velocity $\simeq 9 \text{ km s}^{-1}$. Starting from UT 10:27:55, it quickly accelerates reaching a velocity of $\simeq 30 \text{ km s}^{-1}$, and then suddenly disappears. This is one of the examples of collimated plasma streaming which can be classified as a true microjet. Generation of collimated plasma flows requires special conditions (Tarbell et al. 1999; Ryutova et al. 2003; Ryutova and Tarbell 2003). The key elements, as we have discussed throughout the book, are associated with the geometry of a shock profile and environmental magnetic fields, which may provide conditions for self-focusing of the shock, and generation of microjets.

As the sunspot moves toward the limb, the transients become clearly visible and appear elevated with respect to penumbral filaments with angles ranging from 30° to 50° . Figure 18.5 shows the same sunspot (approaching the West limb) at two heliographic locations: 42° W , 6° S on November 17, 2006 (left) and 85° W , 6° S

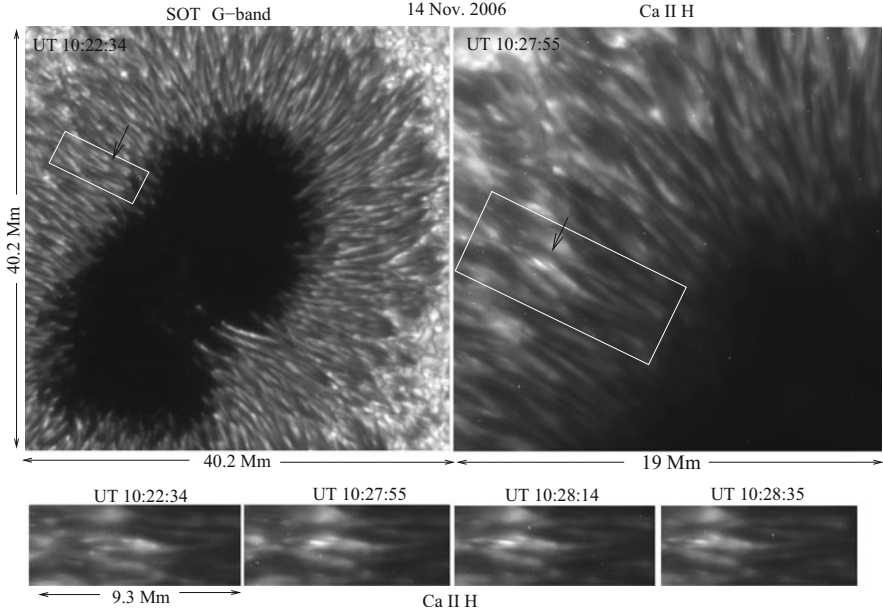


Fig. 18.4 Same sunspot, AR 10923, near the disk center. Shown are a G-band image of the sunspot and the enlarged Ca II H image of its upper east quarter. The birth and evolution of a supersonic microjet is shown in Ca II H images at four instances of time. The microjet originated at the base of a fork made by penumbral filaments (marked by black arrows). Its average velocity during the first 5 min is $\simeq 9 \text{ km s}^{-1}$ reaching $\simeq 30 \text{ km s}^{-1}$ during the last minute

on November, 20 2006 (right). White arrows imitate the azimuthal direction of some transients showing their fan-like distribution with quite regular position angles. All of the marked examples belong to bow shock-type transients drifting as a whole in a direction perpendicular to their long axes. As already mentioned, the overwhelming majority of bright transients seen at any given instance of time belong to this class of events. On some occasions there appear true “microjets”—collimated plasma streaming. White boxes in Fig. 18.5 are drawn in solid and dotted lines to emphasize that the events shown in these boxes occur at different times.

Figure 18.6 shows the evolution of two transients during about a 3 min period. The area with these events is demarcated by a solid box “a” in the snapshot of 17 November 2006 (Fig. 18.5 left panel). The transient marked by a black arrow is oriented in quite a favorable way to show the formation of a double structure. This is a very typical process that starts with an enhanced brightening already having an elongated form. Soon after formation, the double structure gets quickly stretched until the dissipation process turns on.

This example is a good illustration of the process associated with the post-reconnection flux tube moving upward with supersonic velocity. Note that the flux tube, still being cold inside, is not visible in Ca II H, but the shock, generated by a slingshot effect resulting from its straightening, heats the plasma. This is a regular

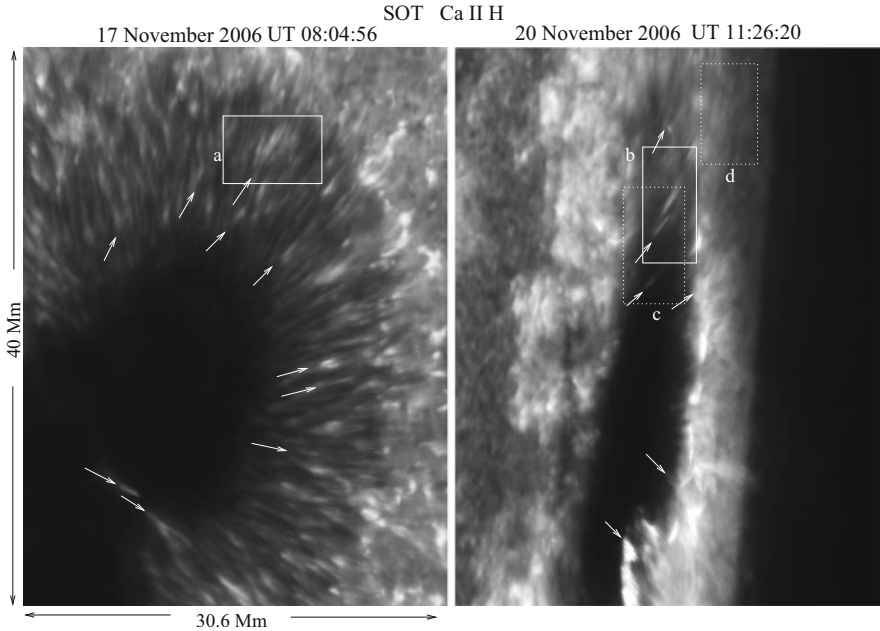


Fig. 18.5 Sunspot at two Western hemisphere locations: $42^{\circ}\text{W } 6^{\circ}\text{S}$ on November 17, 2006 (left) and $85^{\circ}\text{W } 6^{\circ}\text{S}$ on November 20, 2006 (right). White arrows imitate a position angle of some transients showing their fan-like distribution in the plane of the sky. White boxes a, b, c, and d demarcate regions shown in the subsequent figures

occurrence of behind-shock heating which appears as a “first light,” and should manifest itself in a way similar to that shown in the upper left frame, including its elongated form (at UT 08:03:26).

It is important to note that the flux tube is still a “body” which continues to travel with supersonic velocity. As such, it creates a *bow shock* in front of it, as any solid object that moves with supersonic velocity. Indeed, soon after the appearance of the first behind-shock brightening, the double structure starts to form and becomes visible at UT 08:04:14. In this particular case, the bow shock appears in about 48 s after the behind-shock brightening.

As the original shock propagates faster than the flux tube, the bow shock always appears *after* the regular behind-shock heating. This pattern, with various time delays, is confirmed in all the observed cases of double structures. We will return to this process in the next section and present quantitative analysis.

It must be noted that a standoff distance, i.e., the space between the bow shock and the object created it, which is necessary attribute of bow shocks, is clearly visible during entire evolution of the bow shock until the whole structure starts to dissipate. The velocity of the structure in the plane at a given orientation is 5.6 km s^{-1} (directed from top-left to bottom-right). A true velocity of the transient, however, should be transonic. If the measured velocity of a transient is v_{obs} , then its

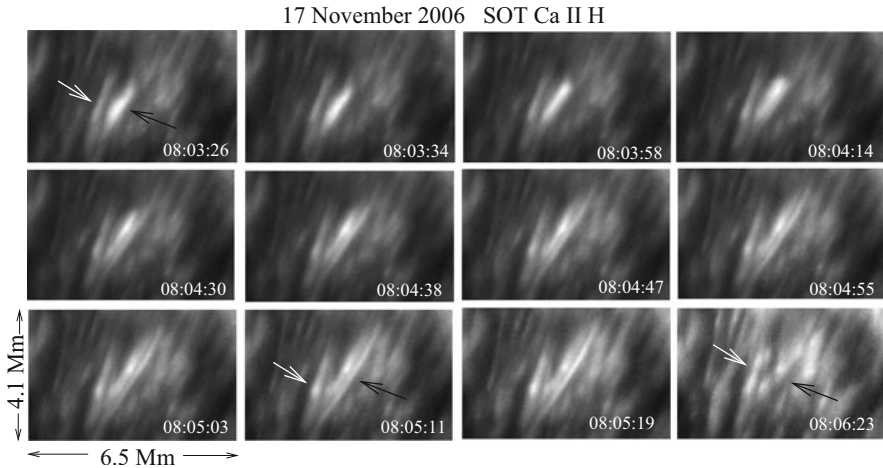


Fig. 18.6 Formation and evolution of a bow shock

true velocity can be estimated as $v \simeq v_{\text{obs}}/\sin\theta$, where θ is an angle between the line of sight and the trajectory plane of the transient. For example, if angle $\theta = 20 - 40^\circ$, $v \simeq 16.4 - 10.1 \text{ km s}^{-1}$.

Another transient in Fig. 18.6, marked with a white arrow, shows only its “thermal” evolution, and slow drifting with velocity 1.5 km s^{-1} . The velocity component of the apparent motion of the transient in the plane of the sky is only 2.24 km s^{-1} . To be supersonic, the angle between the plane of motion and line of sight should be $\leq 16^\circ$. Nothing contradicts such an orientation; the plane may be parallel to the line of sight, in which case the transient will appear motionless and will only exhibit its thermal evolution. Given their abundance, quite a large number of transients, however, have a favorable orientation to show their double structure.

Some other examples of transients differently orientated and having thus different velocities are shown in Fig. 18.7. These were taken on November 20, 2006 when the sunspot moved quite close to the western limb. The first column (the area marked by a solid white box b in Fig. 18.5 right panel) shows the most typical occurrence of several transients (marked 1–8); they are appearing, evolving, and disappearing in time intervals less than 3 min. In this orientation none of the transients barely show a double structure and the highest drift velocity measured (transient 2) is 4.2 km s^{-1} . This time series shows transient 2 during its entire life ($\simeq 2 \text{ min } 15 \text{ s}$). At UT 11:24:51, the transient 1 is in its final stage. Transient 3, which seems practically motionless, shows its thermal evolution, reaching maximum brightness at UT 11:26:51. From this moment on, it quickly dissipates energy and disappears. Its lifetime is about 3 min. At the end of this time sequence (UT 11:26:51) a strong transient appears (transient 4), which quickly gains energy and disappears in 2 min. About this time (UT 11:27:23), in the small area of a given frame, four new transients appear almost simultaneously, showing a typical abundance of “one type” of transients.

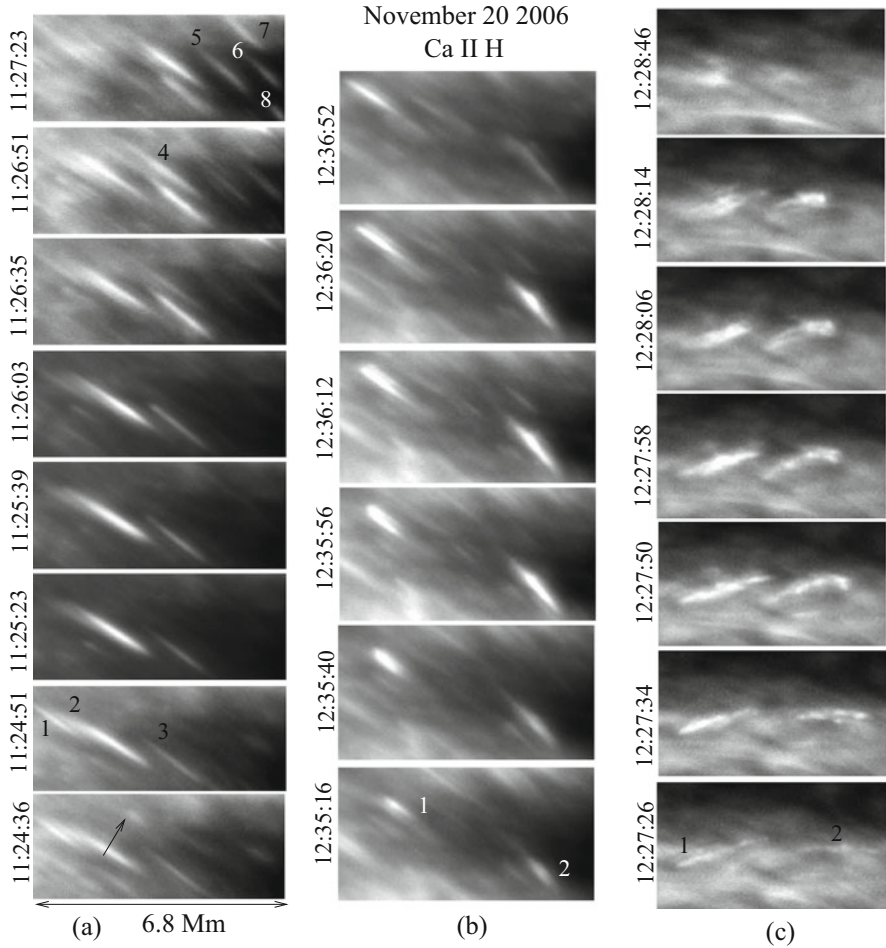


Fig. 18.7 Examples of three bright transients under different viewing angles. See text for details. The images are rotated by 90°

The central column (the area marked by dotted white box c in Fig. 18.5) shows evolution of two fast “conveniently” oriented transients. In other words, their orientation is such that their measured velocities are, indeed, supersonic, $v_1 = 16.8 \text{ km s}^{-1}$ (transient 1), and $v_2 = 8.8 \text{ km s}^{-1}$ (transient 2), and a double structure of transient 1 is well observable.

The right column (the area marked by dotted white box d in Fig. 18.5ad and located on the farther side of the penumbra) shows the evolution of two other supersonic transients. Their measured velocities exceed $v_1 = 14 \text{ km s}^{-1}$. Both transients show vague but recognizable double structures. Their lifetimes are less than 1 min. Again, all the events shown in Fig. 18.7, as well as an overwhelming majority of transients at any moment of time, belong to the bow shock class.

Contrary to this, events that may be classified as true microjets—collimated plasma streaming (cf. Fig. 18.4)—are much more rare. For comparison of their observed signatures, we show one more example seen in the November 20 data set.

Figure 18.8 shows snapshots of the upper penumbra at two instances of times, with a $10.2 \times 16.2 \text{ Mm}^2$ field of view. The white box at UT 12:06:12 demarcates the region with a fast transient that clearly exhibits proper, jetlike motion. A time series of the microjet is shown in a middle row. Its lifetime is a little over 30 s and velocity exceeds 50 km s^{-1} . Its motion is directed *along* its axis unlike the “transverse” motion of bow shock-type transients. For comparison, the lower row shows an example of a “favorably” oriented bow shock-type transient. Its measured velocity is $\simeq 20 \text{ km s}^{-1}$, lifetime about 2 min, and its double structure is clearly visible.

The white dotted box in Fig. 18.8 (upper right panel) and three arrows marked by asterisks are related to Fig. 18.9 which is used to illustrate the process of bow shock formation (see next section). The position of the bow shock is marked by a white dashed arc. It appears around UT 13:29:26 (half an hour earlier than the snapshot shown in Fig. 18.8). Similar events under less favorable angles showing only bright arcs are marked by arrows with a star.

18.1.3 *Brief Summary of Properties*

Briefly, the above observational results can be summarized as follows.

1. The chromosphere above penumbrae is highly dynamic and shows an abundance of bright, elongated transients at any given moment of time.
2. Transients are always associated with bright points seen in G-band images.
3. Bright points are usually located at the Y-shaped fork made by neighboring penumbral filaments but may be found anywhere in the penumbra.
4. There are two different types of chromospheric transients. One type shows strongly elongated brightenings that move almost perpendicular to their long axes. Their measured velocities range from $\leq 1.5 \text{ km s}^{-1}$ to $\simeq 20 \text{ km s}^{-1}$. They have clear properties of bow shocks. The other type is collimated plasma motion directed along their long axis. These are true mass motions representing supersonic microjets. Their measured velocities are well above 20 km s^{-1} .
5. The bow shock-type transient makes the vast majority of chromospheric brightenings above the penumbra. Many of them exhibit a double structure.
6. The lifetime of bow shocks ranges from $\leq 40 \text{ s}$ to $\geq 6 \text{ min}$. Their apparent length is between 2000 and 10,000 km and their width is 300–600 km. The lifetime of microjets is usually $\leq 1 \text{ min}$, and their length is $\leq 1000 \text{ km}$.
7. The appearance of bow shocks (from the observers point of view), whether or not their double structure is seen, their spatial scale, and apparent (measurable) velocities strongly depend on their location, the position of the sunspot, and the orientation of their trajectory planes with respect to the line of sight.



Fig. 18.8 Comparison of true microjet and bow shock. Top: snapshots of the upper part of the penumbra at two instances of time. Middle row: a true microjet with a lifetime of about 30 s, traveling in the radial direction with velocity $\geq 50 \text{ km s}^{-1}$. Bottom: more favorably oriented transient of a bow shock nature—its measured velocity is $\simeq 20 \text{ km s}^{-1}$, lifetime about 2 min, and its double structure is quite visible. The meaning of the dotted box and white arrows marked by stars in the upper right panel is explained in the text

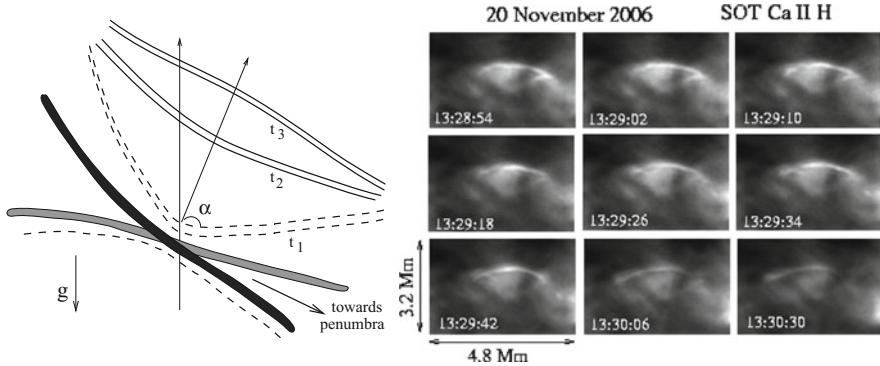


Fig. 18.9 Bow shock formation. Left: Sketch of the straightening \cup -shaped reconnection product with an opening angle 2α . Right: A possible observational analogy. The image, rotated by 90° , is located on the side of penumbra closest to disk center and marked by the dotted box in Fig. 18.8 (top right). Similar events are marked in the same snapshot by white arrows and asterisks

In the next section, we address the phenomenology of post-reconnection processes in penumbral filaments and associated mechanism of formation of the bow shocks and microjets.

18.2 Phenomenology and Quantitative Analysis

As discussed in Chaps. 12 and 13, the specific character of post-reconnection dynamics at the photospheric level is determined basically by finite plasma β and sharp stratification of the low atmosphere. Pressure equilibrium in a high plasma β environment implies that, after reconnection, magnetic field lines remain confined in thin flux tubes. Straightening, the reconnection products create a slingshot effect. At the periphery of a sunspot, flux tubes strongly deviate from the vertical as does the bisector of their collision angle (see Fig. 17.6, Chap. 17). In this case, the reconnection products acquire \cup - and \cap -shaped forms with respect to gravity.

We focus here on further dynamics of the \cup -shaped reconnection product. In this case, two major forces, the magnetic tension and buoyancy force, both act in the upward direction leading to shock formation. Also, under specific conditions, this leads to the appearance of lateral jets (Tarbell et al. 1999; Ryutova et al. 2003). The process is always accompanied by an enhanced brightening of a small reconnection region.

One more important effect associated with finite plasma β and sharp stratification occurs when a \cup -shaped post-reconnection product straightens and accelerates upward *itself*, exceeding the sound speed, i.e., moving with transonic velocity. In this case, a bow shock is formed in front of the flux tube, as it behaves as a usual

blunt body moving with supersonic velocity. It is just this macroscopic effect which is observed in the form of bright, elongated transients all over penumbrae.

The formation of bow shocks is as ubiquitous as the ongoing reconnection processes between penumbral filaments. More importantly, unlike special conditions required for the generation of true plasma jetting, the formation of bow shocks requires only that flux tube, still having well-defined boundaries, reaches transonic velocities. This simple condition makes bow shocks appear easily and densely occupy the chromosphere above penumbrae.

Below we detail some basic calculations of the formation of bow shocks and perform quantitative analysis.

18.2.1 Dynamics of U-Shaped Filaments

We follow the energy analysis carried out by Ryutova et al. (2003) and evaluate major forces acting on the U-shaped reconnection product (see Chap. 12). As mentioned above, magnetic and buoyancy forces act in the same, upward direction accelerating the straightening segment of a flux tube. On the other hand, the flux tube, as well-defined body moving with velocity u in the ambient plasma, experiences the action of a frictional force, $F_{\text{drag}} = (1/2)C_D\rho u^2 S_{\text{srf}}$, where C_D is drag coefficient, and S_{srf} is the flux tube area transverse to the direction of motion.

It is important that the drag force is negligibly small at large Reynolds numbers (small C_D) and small velocities, e.g., in the parameter domain $\text{Re} \geq 10^3$, $u < c_s$, is $C_D \simeq 0.1 - 0.2$ (see, e.g., Parker 1979). However, when u exceeds the sound speed, the frictional force increases abruptly. At the velocity $u \simeq 1.5 - 2c_s$, C_D becomes the order of unity (Landau and Lifshits 1987) and the drag force becomes strong enough to restrict the upward motion of the flux tube to values not exceeding $M = u/c_s \simeq 1.5 - 2.5$. At the same time, conditions for bow shock formation are met.

In the following, we adopt an isothermal model of the atmosphere, $\rho = \rho_0 \exp(-z/\Lambda)$, with a constant scale height, $\Lambda = p/\rho g$. The subscript “0” refers to the point where reconnection occurred. Consider first, a U-shaped flux tube with vertical axis of symmetry as shown in the left panel of Fig. 18.9. The right panel of the figure contains snapshots of Ca II H brightenings whose configuration may illustrate the process shown in the left sketch. It should be noted that such a configuration is seen repeatedly in the observations. Some examples are marked by asterisks in Fig. 18.8. Dashed box in this figure is the area shown in Fig. 18.9, right panel. The location of the bow shock itself is marked by the dashed arc: at UT 13:59:10 it was already gone.

At some height, z , above the reconnection level, the length of the straightened segment is $2z \tan \alpha$ (Fig. 18.9 left). Its cross-section is $S = S_0 \exp(z/2\Lambda)$. Recall that the upward motion of U-shaped reconnection product is governed by action of magnetic tension and gravity forces. Using results of energy consideration, from Eqs. (12.36)–(12.39), Chap. 12, we have the following expression for the total

variation of the potential energy of the system, $\Delta W_{\text{pot}} = 2\Delta W_{\text{mag}} + \Delta W_{\text{gr}}$,

$$\Delta W_{\text{pot}} = -\rho_0 v_{A0}^2 \frac{4\Lambda S_0}{\cos \alpha} \exp(-h/2\Lambda) \quad (18.1)$$

$$\times \{(1 + \sin \alpha)[\exp(h/\Lambda) - 1] - (h/\Lambda) \sin \alpha\}$$

Respectively, a total force acting upward on the ascending segment at height h is:

$$F_{\text{up}} = \rho_0 v_{A0}^2 \frac{4\Lambda S_0}{h \cos \alpha} \exp(-h/2\Lambda) \quad (18.2)$$

$$\times \{(1 + \sin \alpha)[\exp(h/\Lambda) - 1] - (h/\Lambda) \sin \alpha\}$$

It is important to note that, when the velocity of the ascending flux tube, u , exceeds the sound speed, the friction coefficient, C_D , becomes the order of unity, and the drag force increases abruptly restricting the upward motion of the flux tube. The tip of the straightening segment reaches transonic velocities quite quickly, only in a few scale heights. From then on, the motion of the flux tube is determined by the balance of upward acting forces, (18.2) and the drag force:

$$F_{\text{drag}} = \frac{1}{2} C_D \rho u^2 S_{\text{srf}} \quad (18.3)$$

where $S_{\text{srf}} = \pi R \, 2h \tan \alpha = S(2h/R) \tan \alpha$ is the flux tube area transverse to the direction of motion, $S = \pi R^2$. With this, the drag force at height h becomes

$$F_{\text{drag}} = \frac{1}{2} C_D \rho_0 u^2 S_0 \exp\left(-\frac{3h}{4\Lambda}\right) \frac{2h \tan \alpha}{R_0} \quad (18.4)$$

From Eqs. (18.2) and (18.4), we find the velocity at the tip where these forces are balanced (which implies $C_D \simeq 1$) to be:

$$u_f = v_{A0} \left\{ \frac{4\Lambda R_0 \exp(h/4\Lambda)}{h^2 \sin \alpha} [(1 + \sin \alpha)[\exp(h/\Lambda) - 1] - (h/\Lambda) \sin \alpha] \right\}^{1/2} \quad (18.5)$$

The height where the bow shock is expected to form corresponds to a final velocity of the flux tube of the order of $u_f \simeq 1.5 - 2 c_s$.

For quantitative estimates, assuming the reconnection occurs close to the surface, we take $\rho_0 = 2.25 \cdot 10^{-7} \text{ g cm}^{-3}$, scale height $\Lambda = 150 \text{ km}$, and sound speed $c_s = 8 \text{ km s}^{-1}$. We assume a filament radius of $R_0 = 40 \text{ km}$. The Alfvén velocity in a magnetic field of $B = 1000 \text{ G}$ is $v_A = 6 \text{ km s}^{-1}$. For these parameters, Table 18.1 shows estimated heights where the Mach number, $M = u_f/c_s$, reaches values of 1.5–2 for different angles of collision, and corresponding opening angles, 2α .

Table 18.1 Final velocity of a shock at different heights and angles

α	$h = 800$ km			$h = 1000$ km			$h = 1100$ km		
	60°	50°	40°	60°	50°	40°	60°	50°	40°
M	1.35	1.42	1.5	1.9	2	2.1	2.3	2.4	2.5
u_f (km s ⁻¹)	10.8	11.36	12	16.2	16	16.8	18.4	19.2	20

18.2.2 Nature of Double Structures

Let us now return to the phenomenology of the observed double structure and, in particular, look at the connection between the regular behind-shock heating and bow shock. As mentioned earlier, a regular shock produced by a slingshot effect propagates faster than the flux tube, and must therefore appear before the straightened flux tube reaches transonic velocities, and becomes able to generate a bow shock.

In Chap. 14 we have studied photospheric reconnections and shock formation in various magnetic environments, and calculated corresponding heights of shock formation and shock velocities. In case of the chromospheric transients, shocks evolve in the magnetic environment, i.e., correspond to the case 3 shown in Figs. 4.3 and 4.4, Chap. 14. Now we need to compare the shock velocity from expression (14.16), Chap. 14, with velocity of ascending flux tube (18.5). The expression for the shock velocity (solution of Eq. (14.16), Chap. 14) has the form:

$$u_{\text{sh}}(z) = v_{A0} \frac{\sqrt{(3z_0/\Lambda) \exp(z/2\Lambda)[1 - \exp(-3z/4\Lambda) - 3z_0/4\Lambda]}}{1 - \exp(-3z/4\Lambda)} \quad (18.6)$$

where z_0 is the height of shock formation in an homogeneous atmosphere:

$$z_0 = \frac{2}{\gamma + 1} \frac{c_{s0}^2}{v_{A0}^2} R \quad (18.7)$$

Plots of u_{sh} and u_f , Eq. (18.5), for three opening angles, are shown in Fig. 18.10. We use the same parameters as those used above for construction of Table 18.1.

One can see that the regular shock reaches the transonic region earlier than the bow shock is formed. Note that for chosen parameters, $c_s = 8$ km s⁻¹, $v_{A0} = 6$ km s⁻¹, Mach one, $M = u/c_s = 1$, corresponds to $u/v_{A0} = 1.5$ (Fig. 18.10).

To estimate times needed for regular shocks and bow shocks to reach approximately the same height, we need to integrate (18.5) and (18.6), i.e., evaluate the integral $t = \int_a^b dz/u(z)$. Vertical dashed lines in Fig. 18.10 intersecting the plots mark end points for numerical integration. We choose for lower limit of integrals $a_1 = 0.5$, i.e., $z \simeq 75$ km (half of the scale length, Λ) above the reconnection point. $b_1 = 1.1$ corresponds to the height of a regular shock formation, $M = 1$ ($u/v_{A0} = 1.5$). Corresponding heights for bow shock are $c_1 = 4$ at $\alpha = 40^\circ$, and

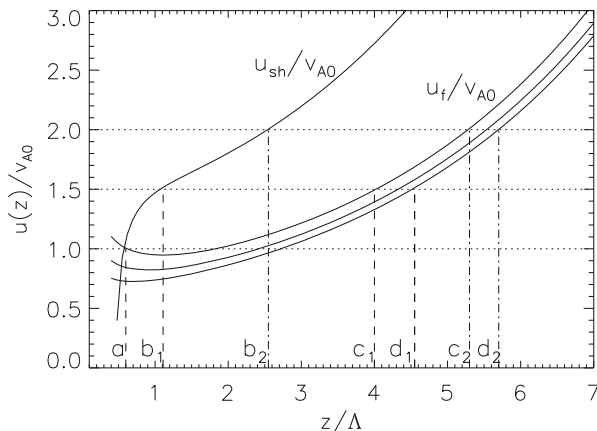


Fig. 18.10 Shock amplitudes as a function of height: the upper curve, marked as u_{sh}/v_{A0} , corresponds to the shock resulting from post-reconnection slingshot. Three lower curves, marked as u_f/v_{A0} , correspond to the velocity of the ascending flux tube for three opening angles, 40° , 50° , 60° —from top to bottom. For the meaning of dashed lines and letter marks see the text

$d_1 = 4.55$ at $\alpha = 60^\circ$. Numerical integration of u_{sh} (18.6) between a_1 and b_1 , gives a time of $t_{b1} = 16.5$ s.

Numerical integration of u_f (18.5) with end points $a_1 = 0.5$ and $c_1 = 4$, $a_1 = 0.5$ and $d_1 = 4.55$ gives the estimates of time when the velocity of the ascending portion of flux tubes reaches $M = 1$: $t_{c1} = 65.5$ s ($\alpha = 40^\circ$), $t_{d1} = 74$ s ($\alpha = 60^\circ$). These estimates show that there is a finite time interval, Δt between the appearance of a regular shock and following bow shock. Thus, for $M = 1$, the delay times are, respectively, $\Delta t = 49$ s ($\alpha = 40^\circ$) and $\Delta t = 57.5$ s ($\alpha = 60^\circ$).

For higher Mach numbers, the delay times slightly drop. A similar procedure for $M = 1.5$ ($u/v_{A0} = 2$) gives the following estimates. The regular shock reaches this level in $t_{b2} = 39$ s. The flux tube reaches this velocity in $t_{b2} = 83.5$ s, for $\alpha = 40^\circ$, and in $t_{b2} = 88.7$ s, for $\alpha = 60^\circ$. Respectively, “delay times” are $\Delta t = 44.5$ s and $\Delta t = 49.7$ s.

The observed delay times for the appearance of a bow shock range from tens of seconds to minutes. For the examples given above, we have the following numbers. The bow shock shown in Fig. 18.3 appears in 29 s after a regular behind-shock heating. The time delay in the case of the bow shock shown in Fig. 18.4 is about 1 min. In the case shown in Fig. 18.6, the time delay is 48 s. In the example shown in Fig. 18.7a, the bow shock appears in about 40 s and, in the last example (Fig. 18.8 bottom), time delay is only 24 s. Thus, the observed and estimated time delays are in good agreement.

18.3 Bow Shocks

Thus, formation of bow (*detached*) shocks in front of accelerating flux tubes is a natural occurrence. Parameters of bow shock are determined by Mach number and relation between pressure, p , density, ρ , and temperature, T relations across the shock (Landau and Lifshits 1987):

$$\frac{p_2}{p_1} = \frac{2\gamma M^2 - (\gamma - 1)}{\gamma + 1}, \quad \frac{\rho_2}{\rho_1} = \frac{(\gamma + 1)M^2}{2 + (\gamma - 1)M^2} \quad (18.8)$$

$$v_2 = v_1 \frac{2 + (\gamma - 1)M^2}{(\gamma + 1)M^2} \quad (18.9)$$

$$T_2 = T_1 \frac{[2\gamma M^2 - (\gamma - 1)][2 + (\gamma - 1)M^2]}{(\gamma + 1)^2 M^2} \quad (18.10)$$

Subscript “2” refers to the region behind the bow shock and subscript “1” denotes parameters of the incident stream associated with the flux tube; γ is a specific heat ratio. These are determined by the standard expressions for the variation of quantities along the streamline (Landau and Lifshits 1987, Par. 83), e.g., $T_1 = T_0[1 + (1/2)(\gamma - 1)M^2]$.

A standoff distance of the bow shock, Δ (distance between the bow shock and the body creating it) is known to be proportional to the inverse density ratio across the shock, $\Delta \sim h(\rho_1/\rho_2)$:

$$\frac{\Delta}{h} = \zeta \frac{2 + (\gamma - 1)M^2}{(\gamma + 1)M^2} \quad (18.11)$$

Coefficient of proportionality, ζ , is usually of the order of unity. For cylindrical objects it can be approximated as (see, e.g., Hayes and Probstein 1966):

$$\zeta = \ln \frac{4}{3\epsilon}, \quad \epsilon = \frac{2 + (\gamma - 1)M^2}{(\gamma + 1)M^2} \quad (18.12)$$

With (18.8)–(18.12) one can estimate the position of the bow shock, $h_{\text{bow}} = h + \Delta$, temperature, and velocity. In addition, given that the lateral extension of the bow shock is of the same order of magnitude as the straightened segment of the flux tube, the “length” of the bow shock, L_{bow} , can be estimated as $2h \tan\alpha$, and its thickness should be on the order of the standoff distance, $d_{\text{bow}} \simeq \Delta$.

In Table 18.2 we estimate bow shock parameters at different Mach numbers for three different angles. In principle, most of the transient parameters are observable. The observed length of transients (ranging from 2000 to 10,000 km), their width (300–600 km), and lifetime are in good order of magnitude agreement with the calculated quantities given in Table 18.2. There are of course uncertainties in

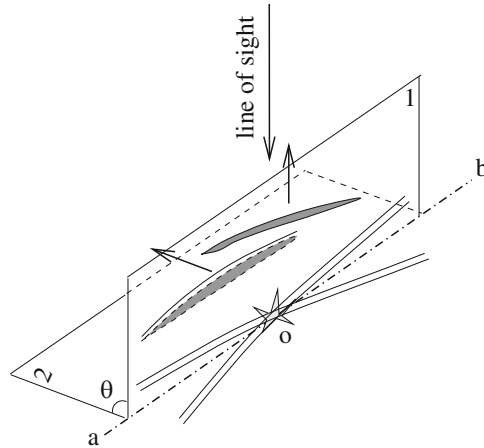


Fig. 18.11 Orientation of the plane in which the bow shock travels depends on the orientation of the upper post-reconnection flux tube producing a slingshot effect and may be arbitrary. This in turn determines the appearance, velocity, and dimensions of the bow shock from the observer's point of view. Point "o" is a reconnection region, "ab" is bisector of a collision angle between interacting penumbral filaments. If the plane is in position 1, the transient appears as a single elongated brightening; but, with increasing angle θ , the double structure of the transient becomes visible

measuring velocities and linear scales of transients which are largely due to the uncertainty of their true orientation with respect to the line of sight. This is illustrated in Fig. 18.11.

Thus, when penumbral filaments reconnect, the reconnection region may have arbitrary orientation with respect to observer, depending on the heliographic location of sunspot and the azimuthal location of the reconnecting filaments in the penumbra. The orientation and location of the penumbral bisector is also essential. If the final orientation of the plane in which the bow shock moves is similar to plane "1" in Fig. 18.11, i.e., if the line of sight lies almost in the same plane, the transient will appear almost motionless, as is often seen in observations.

With arbitrary angle θ , the velocity of the transient from the observer's point of view may range from almost zero to its maximum value. In these data sets (showing the sunspot traveling from limb to limb) the maximum measured velocities, perpendicular to the transient long axis, are found to be $19\text{--}20\text{ km s}^{-1}$. Calculated velocities show a strong dependence on height of the transient formation and range from 11 km s^{-1} to 20 km s^{-1} .

The image of the transient, in addition to the direction of motion, is also affected by its orientation. When the line of sight is parallel to the plane of transient motion, ($\theta = 90^\circ$), the transient appears as a single elongated brightening. With a finite angle θ , the double structure of the transient becomes visible and may appear to be moving either away from or toward the observer (Fig. 18.11). Obviously, the longer and more horizontal are penumbral filaments, the more chance they have

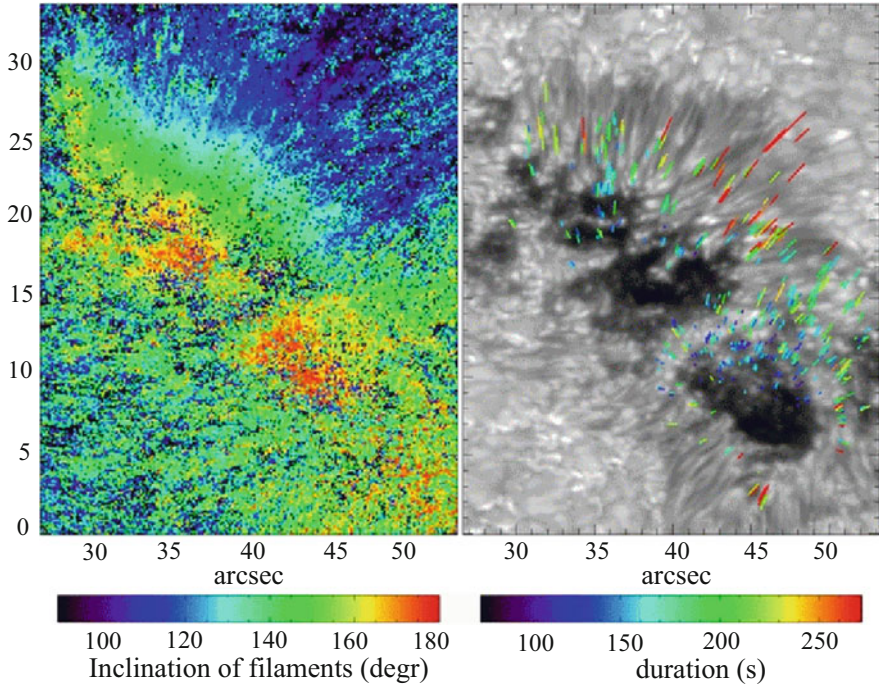


Fig. 18.12 Relation between magnetic field inclination and filament lifetime and length. The left panel shows a map of the magnetic field inclination from LTE inversion of the Ca II 8542 Stokes data. 180° is a vertical, negative polarity field; 90° is a horizontal field. The right panel shows a continuum Ca II 8542 image with the paths drawn on the top of 460 filaments. The color of the paths indicates the duration of the filaments. Reprinted from Rouppe van der Voort and de la Cruz Rodriguez (2013) by permission from IOP, copyright AAS

to produce multiple shocks and multiple bright transients in the chromosphere. Luckily, the penumbra is organized in such a way that shocks are abundantly observed. Figure 18.12 shows example of the relation between the magnetic field inclination in filaments and filament parameters (Rouppe van der Voort and de la Cruz Rodriguez 2013).

For theoretical estimates of the lifetimes, we shall consider shock-related dissipation as the dominant process at this spatial scales. First, we find the released thermal energy, and then the corresponding dissipation rate. This is done in the next section.

18.4 Energy Release and Lifetime of Bright Transients

In this section we perform the energy analysis and estimate the lifetime of transients. In fact, one of the most accurate parameters for comparison with observations is just the lifetime of transients.

For theoretical estimates of the lifetimes, we shall consider shock-related dissipation as the dominant process. First, we find the released thermal energy, and then the corresponding dissipation rate.

Energy release during the final stage of the straightening flux tube, when its velocity reaches u_f , can be estimated from the difference between the potential energy (18.1) and the kinetic energy of the flux tube at the corresponding height h :

$$\Delta W_{\text{therm}} = -\Delta W_{\text{pot}} - \frac{\rho_0 u_f^2}{2} 2h \tan \alpha S_0 \exp\left(-\frac{h}{2\Lambda}\right). \quad (18.13)$$

Using (18.1) and (18.5) one obtains

$$\begin{aligned} \Delta W_{\text{therm}} &= \delta \rho_0 v_{A0}^2 \frac{4\Lambda S_0}{\cos \alpha} \exp\left(-\frac{h}{2\Lambda}\right) \\ &\times \left[(1 + \sin \alpha) \left(\exp\left(\frac{h}{2\Lambda}\right) - 1 \right) - \frac{h}{\Lambda} \sin \alpha \right] \delta \end{aligned} \quad (18.14)$$

here

$$\delta = \left[1 - \frac{R_0}{h} \exp\left(\frac{h}{4\Lambda}\right) \right] \quad (18.15)$$

Using the same parameters as above ($\rho_0 = 2.25 \cdot 10^{-7} \text{ g cm}^{-3}$, $\Lambda = 150 \text{ km}$, $R_0 = 40 \text{ km}$, $v_A = 6 \text{ km s}^{-1}$), for the chosen heights (or equivalently, Mach numbers), and angles, (18.14) gives the estimates for thermal energy shown in Table 18.3. One can see that the released energy is in range of $3 \times 10^{26} - 6 \times 10^{26} \text{ erg}$. This is comparable with the energy of blinkers, microflares, and other short-lived transients observed in the chromosphere/transition region.

To calculate the lifetimes of bow shocks, we recall the fact that the strength of a weak shock and its energy, $E(t)$, are known to diminish as $1/t^2$ (Landau and Lifshits 1987) namely,

$$E(t) = \frac{E_0}{(1 + \alpha_n u t / h)^2} \quad (18.16)$$

Table 18.3 Thermal energy at different heights and angles

α	60°	50°	40°	60°	50°	40°	60°	50°	40°
$M = u_{\text{bow}}/c_s$	1.35	1.42	1.5	1.9	2	2.1	2.3	2.4	2.5
$W_{\text{therm}}(10^{26} \text{ erg})$	5.5	6.0	6.13	4.12	4.48	4.56	3.26	3.53	3.57

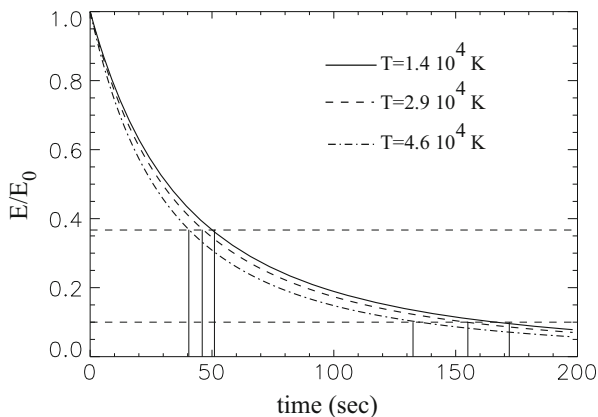


Fig. 18.13 Decay of bow shock energy. Characteristic lifetimes range from 40 s to 3 min

where $\alpha_n = (1/2)(\gamma + 1)$ is a coefficient of nonlinearity for a polytropic gas, $\alpha_n = 4/3$. Plots of $E(t)$ normalized by the initial energy carried by a shock are shown in Fig. 18.13.

For illustrative purposes, we use an example with $\alpha = 50^\circ$. The solid line corresponds to a bow shock at $h \simeq 1200$ km, velocity $u_{\text{bow}} = 11.36$ km s $^{-1}$, and temperature $T = 1.4 \times 10^4$ K. The dashed line corresponds to $h \simeq 1500$ km, $u_{\text{bow}} = 16$ km s $^{-1}$, and $T = 2.9 \times 10^4$ K. The dash-dotted line to $h = 1625$ km, velocity $u_{\text{bow}} = 19.2$ km s $^{-1}$, and $T = 4.6 \times 10^4$ K. The characteristic time in which the energy of the bow shock drops by factor of $e = 2.7$ is in range of 40–50 s. For the chosen example, the average thermal energy is $W_{\text{therm}} = 4 \times 10^{26}$ erg, which drops to $\simeq 1.5 \times 10^{26}$ erg in about 1 min. A more significant order of magnitude decay occurs in 130–180 s. Thus, roughly, the lifetime of the bow shock may be from 40 s to 3 min. This is the time interval corresponding to the observed lifetimes of transient brightenings.

Concluding this chapter it is useful to summarize the observational results and their interpretation. These results represent one of the clear picture of a particular phenomena in the solar atmosphere that are well observed and quite well understood. Moreover, as other events that are quantitatively interpretable, they can be used for diagnostic goals.

Thus, high-resolution and high cadence observations of sunspot penumbrae reveal an abundant population of highly dynamic transient phenomena in the overlying chromosphere and show clear regularities in their properties. Very useful details in chromospheric dynamics were obtained, thanks to observations of the sunspot at different locations during its passage from the east to west limb, showing the penumbra at various angles.

There are basically two different classes of bright elongated transients above penumbrae. The first discriminator that stands out is a difference in the direction of their motion with respect to their long axes.

One class includes the transients that move as a whole in a direction almost perpendicular to their long axes. These are classified as bow shocks. It is just this type of transients that make up the vast majority of all observed transients over the penumbrae.

Their measured velocities range from $\leq 1.5 \text{ km s}^{-1}$ to $\simeq 20 \text{ km s}^{-1}$. As the orientation of the plane of the transient motion may be arbitrary, measured velocities may range from almost zero (when the plane of transient motion is parallel to the line of sight) to their maximum values (when the plane of transient motion is normal to line of sight). This explains a wide range of velocities measured when the sunspot was in various locations on the disk.

A remarkable property of the bow shock-type transients is their double structure, which usually develops soon after the appearance of the “first light” at a characteristic standoff distance from it. The double system then travels as a whole until it starts to dissipate. This feature strongly supports the bow shock nature of transients. The fact that not all the transients show a double structure is, like apparent velocities, affected by the orientation of the plane of the transient motion with respect to the line of sight.

Lifetimes of bow shock-type transients range from $\leq 40 \text{ s}$ to $\geq 6 \text{ min}$. Their apparent length is between 2000–10,000 km and their width is 300–600 km. In double structures, the standoff distance is on the order of, or less than, the width of the “secondary” transient (the bow shock itself).

The other type, representing the minority of chromospheric transients, falls into class of microjets. They have properties of collimated plasma streaming directed along their axes.

Their measured velocities range from 20 km s^{-1} to 50 km s^{-1} . Lifetimes of microjets are $\leq 1 \text{ min}$. Their apparent length hardly exceeds 1000 km. As already mentioned, the number of microjets is significantly less than the ubiquitous bow shock-type transients covering the entire penumbra at any instance of time.

The observed properties of chromospheric transients can be well understood in the framework of penumbral model based on the filamentary structure of sunspots where the most natural processes are the ongoing reconnections among interlaced filaments (Ryutova et al. 2008). The specific character of photospheric reconnection and post-reconnection processes (provided by high plasma β and strong stratification of the low atmosphere) lead to macroscopic effects that are consistent with all observed properties of individual filaments, and explain the very formation of penumbrae.

The most striking and well-observed effects produced by reconnecting filaments are shocks resulting from a slingshot effect associated with the straightening U-shaped reconnection product. Besides, under the action of magnetic tension and a buoyancy force acting in the same upward direction, a U-shaped flux tube itself quickly accelerates. At transonic velocities in front of it a bow (detached) shock is formed as it usually occurs in cases of blunt bodies moving with supersonic velocities (Fig. 18.14).

In case of the flux tubes moving with supersonic velocities, i.e., reaching Mach numbers $\simeq 1.5 - 2$, the bow shock, once formed, tends to remain at the initial

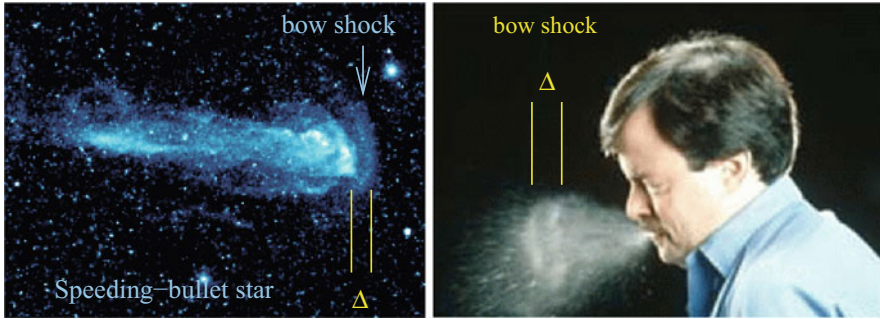


Fig. 18.14 Bow shocks in front of blunt objects moving with supersonic velocities. Left: Reprinted from <http://www.galex.caltech.edu>. Credit NASA/JPL-Caltech/C. Martin/M. Seibert(OCIW); Right: Reprinted from <http://www.gettyimages.com>. Credit: R. Grapes-Michaud

standoff distance until the whole system starts to dissipate. The lifetimes, spatial scales, velocities, and even temperatures of bow shocks are directly observable quantities. This fact allows to verify the validity of theory of entire process, and use the observed quantities for parameter studies.

For the time being, bright radiative transients and jets in the sunspot chromospheres were studied from various points of view (Louis et al. 2009; Katsukawa and Jurcak 2010; Nishizuka et al. 2011; Reardon et al. 2013; Rouppe van der Voort and de la Cruz Rodriguez 2013; Anan et al. 2014).

It was found, for example, that transients propagating upward above penumbrae are associated with supersonic downflows close to umbra–penumbra boundary, detected in high-resolution spectropolarimetric observations (Louis et al. 2011). The orientation of the penumbral filaments at the site of the downflows was found to be consistent with those resulted from the post-reconnection process in penumbral filaments (Ryutova et al. 2008). It is interesting that some observations show that outer penumbra filaments are associated with running waves. Moreover the redshift ridges seen in the time-distance plots of velocity often merge, forming a fork-like pattern (Chae et al. 2014). Extremely rich picture of penumbral dynamics, shocks, jets, and evolutionary waves that became well observable opens rich possibilities to study farther the sunspot dynamics and energy production sources.

18.5 Problems

18.1 Consider the bow shock formed in front of the body having a cylindrical form. Calculate the standoff distance (cf. (18.11)–(18.12)) (Hayes and Probstein 1966).

18.2 We have already discussed properties of cumulative jets that are relative to shaped charges capable to pierce the armor. It is interesting that mathematically even a real armor-piercing problem is modeled by collision of two liquid jets. In solar

atmosphere ubiquitous plasma jets can hardly avoid mutual collisions. Consider here a classical problem of formation of cumulative jets and their characteristics.

References

- T. Anan, R. Casini, K. Ichimoto, *Astrophys. J.* **786**, 94 (2014)
J. Chae et al., *Astrophys. J.* **789**, 108 (2014)
W.D. Hayes, R.F. Probstein, *Hypersonic Flow Theory* (Academic, New York, 1987)
Y. Katsukawa, J. Jurcak, *Astron. Astrophys.* **524**, 20 (2010)
Y. Katsukawa, T. Berger, K. Ichimoto et al., *Science* **318**, 1594 (2007)
L.D. Landau, E.M. Lifshitz, *Fluid Mechanics* (Pergamon Press, Oxford, 1987), p. 390
R.E. Louis et al., *Astrophys. J.* **704**, L29 (2009)
R.E. Louis et al., *Astrophys. J.* **727**, 49 (2009)
N. Nishizuka et al., *Astrophys. J.* **731**, 43 (2011)
E.N. Parker, *Cosmical Magnetic Fields* (Clarendon Press, Oxford, 1979)
K. Reardon, A. Tritschler, Y. Katsukawa, *Astrophys. J.* **779**, 143 (2013)
L. Rouppe van der Voort, J. de la Cruz Rodriguez, *Astrophys. J.* **776**, 56 (2013)
M. Ryutova, T. Tarbell, *Phys. Rev. Lett.* **90**, 191101 (2003)
M. Ryutova, T. Tarbell, R. Shine, *Solar Phys.* **213**, 231 (2003)
M. Ryutova, T. Berger, A. Title, *Astrophys. J.* **676**, 1356 (2008)
M. Ryutova, T. Berger, Z. Frank, A. Title, *Astrophys. J.* **686**, 1404 (2008)
T. Tarbell, M. Ryutova, J. Covington, A. Fludra, *Astrophys. J.* **514**, L47 (1999)

Chapter 19

Self-organization in the Corona and Flare Precursors



Abstract Exploding loop systems producing X-ray flares often, but not always, bifurcate into a long-living, well-organized system of multithreaded loop arcades resembling solenoidal slinkies. The subject of this chapter is to look into the physical conditions that cause or prevent this process. We shall see that the X-class flares that bifurcate into long-living slinky arcades have different signatures than those which do not produce such structures. The most striking difference is that, in all cases of slinky formation, a high-energy proton (HEP) flux becomes significantly enhanced 10–40 h before the flare occurs. No such effect was found prior to the “non-slinky” flares. This fact is found to be associated with the difference between energy production by a given active region and the amount of energy required to bring the entire system into the form of self-organized loop arcades. One of the important features is that post-flare coronal slinky formation is preceded by scale-invariant structure formation in the underlying chromosphere/transition region. The observed regularities may serve as long-term precursors of strong flares and may help to study predictability of system behavior, and in particular, flare occurrence. We shall also discuss some aspects of recurrence of coronal microflares and flares which have signatures consistent with spatial and temporal plasma echoes.

19.1 Well-Organized Multithreaded Coronal Arcades: Slinkies

We have discussed throughout this book that coronal structures above the Sun’s active regions appear in various forms, have lifetimes ranging from days to minutes, and show different behaviors from subtle oscillations of large-scale quasi-steady loops to exploding loop systems producing strong EUV flares. In this chapter we shall study some systematic peculiarities in major X-ray flares that often bifurcate into a long-living, well-organized system of multithreaded loop arcades resembling the winding in a curved solenoid or a funnel. Due to this resemblance, these solenoidal structures were dubbed slinkies. Examples of two different slinkies one at 6.4×10^5 K and other at $0.2\text{--}1.6 \times 10^6$ K are shown in Fig. 19.1. Slinkies are usually

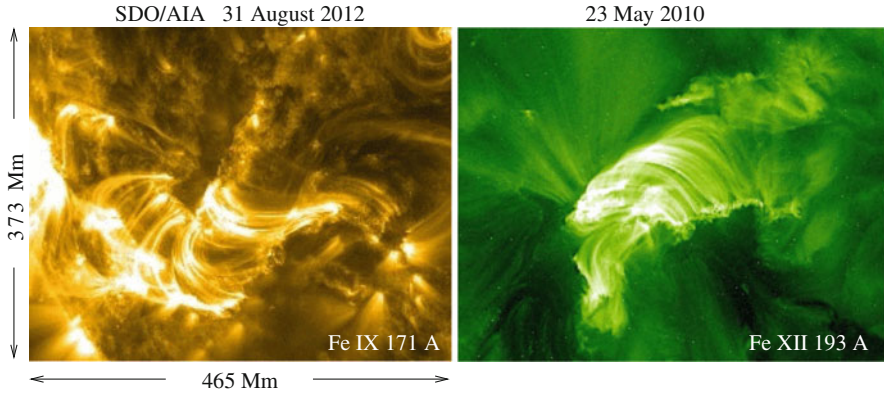


Fig. 19.1 Snapshots of the most typical post-flare slinkies at two different temperatures. Left: The SDO/AIA image of corona in Fe IX line at 6.4×10^5 K taken on August 31, 2012; Right: The image of a slinky at a temperature range of $0.2\text{--}1.6 \times 10^6$ K taken by TRACE. A regular filamentary structure of slinkies turns out to be a backbone of their long-term dynamic stability

associated with X-class flares, but they may well be produced by the M-class and even by C-class flares.

High-resolution and high cadence observations show coronal structures and dynamics in great details (Gibson et al. 2002; Ryutova and Shine 2006; Kosugi et al. 2007; Aschwanden and Aschwanden 2008; Cirtain et al. 2013; Brooks et al. 2013; Winebarger et al. 2014). One of the most important facts revealed in recent observations is that *all coronal formations*, regardless of their size, shape, and lifetime, have filamentary structure. Individual filaments and their clusters are in constant motion reflecting various stages of coronal activity.

Figure 19.2 shows an example of three stages in the evolution of corona overlying a large active region (AR 10792 on July 30, 2005). Figure 19.2a is a typical picture of a strongly inhomogeneous conglomerate of coronal loops in its “regular” state, characterized by the quasi-steady behavior of long-living loops (marked by green and blue arrows), periodic brightening and dimming of individual filaments, and the appearance of frequent microflares (marked by small white arrows). No matter how complicated an inhomogeneous conglomerate is, it may remain for h and days in such a chaotic state until some sudden increase in activity causes an explosive release of energy, leading to a major flare.

Figure 19.2b shows a pre-flare phase of the coronal system around the time of its growing activity accompanied by the appearance of a strong coronal mass ejection, CME (marked by the thick white arrow), and several moderate flares, such as the one that occurred at UT 05:29 (highlighted by the white box). The major X1.3 flare occurs at UT 06:35, in the location marked by the white star (not shown, note the time difference). When this happens, within a few minutes of the explosive phase/flare, the “messy” corona bifurcates into dynamically stable, well-organized

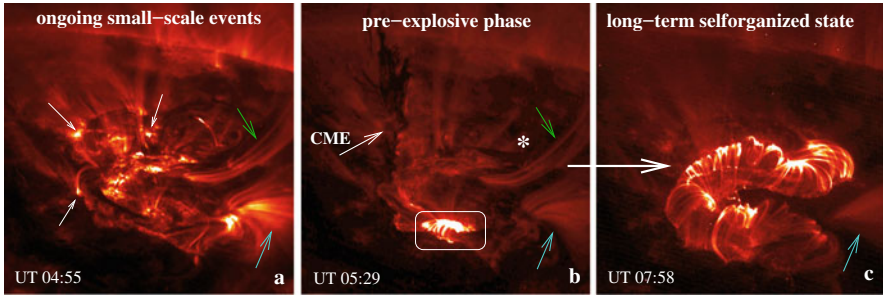


Fig. 19.2 Image of the corona in the TRACE Fe IX/X ($0.2\text{--}1.6 \times 10^6$ K), overlying a large active region. Field of view is $230 \times 230 \text{ Mm}^2$. (a) Large and small-scale loops of different forms show well-defined filamentary structure. Snapshots represent a long-term dynamic state of coronal structures being in constant motion and harboring numerous microflares that appear continuously in different places. (b) At some point, the corona shows a sudden increase in pre-flare activity including several moderate flares (one of them occurring around UT 05:29 is highlighted by the white box) and strong CME (marked by the white arrow). The major X1.3 flare occurs at UT 06:35, in the location marked by the white star. (c) Within a few minutes after the major flare, a huge “chaotic” conglomerate of coronal structures bifurcates into a well-organized dynamic state having the form of a multithread solenoid and remains in this state for many h

arcades of thin flux tubes (Fig. 19.2c). This regime usually lasts for many h or/and days, signifying the self-organized character of the state.

This pattern, i.e., when a long-lasting chaotic state that turns into a well-organized system of self-similar loop arcades due to the increased activity and flare, being quite typical, is not, however, universal. Not all of the major X-class flares end up with the formation of long-living, well-organized structures. In many cases, post-flare loops quickly cool down and disappear from the EUV images. The physical conditions that determine or prevent the formation of long-living, well-organized structures are to be addressed in this chapter.

Our goal here is twofold. One objective is to investigate the nature of well-organized systems of self-similar loops and their formation. The other is to look into the question of why, among seemingly similar flares, some may bifurcate into a long-living, well-organized slinky stage and others not. These problems also include an important fact: the regularities observed in the corona must have their precursors in the underlying chromosphere/transition region whose topological and functional relations need to be also identified.

To address these problems we follow studies of the most prominent (major X-class and some C-class) flares occurred in about a decade period (Ryutova et al. 2011). It was found that the flares that bifurcate into long-living slinky arcades differ significantly from those that do not produce such structures. As mentioned above, the most striking difference is that, in all cases of slinky formation, the GOES high-energy proton (HEP) flux becomes significantly enhanced many h before the flare occurs. There is also a correlation between the occurrence of slinky formation and an active region size.

To illustrate the process of post-flare slinky formation, first, we use Hinode observations of a large active region (NOAA AR 10930) during the time period of December 5–13, 2006. Events associated with this active region show extremely well a time sequence of pre-flare and flare activity, and the formation of dynamically stable, well-organized structures. These observations have also provided a unique opportunity to compare data taken simultaneously at different heights of the solar atmosphere. As a result, it was revealed that post-flare coronal slinky formation is preceded by scale-invariant structure formation in the underlying chromosphere/transition region. Such a pattern is characteristic to process of self-organization that takes place simultaneously at several special and timescales (Prigogine 1961; Gaponov-Grekhov and Rabinovich 1992). This will be discussed in more details in subsequent sections.

It must be emphasized that any system that is potentially subject of self-organization need to be treated as an energetically open, dissipative system. In case of slinky formation, the system must include coupling between photospheric energy reservoir and the overlying chromosphere/corona, assuming also the back-reaction of coronal activity on the underlying atmosphere. In previous chapters, we have already encountered the necessity of applying the method of energetically open systems (see, e.g., in Chap. 16). In electrodynamics such a system, as we saw, may be driven into various dynamic forms that include the Poincare limit cycle, and a spontaneous process of self-organization, characterized by scale-invariant structure formation. It must be noted that small-scale, current-carrying filaments arise automatically in the model (Ryutova and Shine 2006; Ryutova 2006).

19.2 Essential Difference Between “Regular” and Slinky-Producing Flares

One of the established classifications of solar flares is their arrangement into B, C, M, and X classes, which is based on their X-ray output measured by the GOES spacecraft. Although flares in general exhibit common physical phenomena such as particle acceleration, radiation of electromagnetic waves, association with shocks and others, individual flares are quite unique and may exhibit their own set of specific events.

Many individual flares have been studied in great detail, especially with the opportunity given during the last decades by excellent satellite data sets. These were complemented by several survey works that have brought together some general properties of flares (Bai and Sturrock 1989; Battaglia et al. 2005; LaBonte et al. 2007). The existence of common properties naturally indicates common sources and origins of flares, thus facilitating the search for possible predictability criteria.

In this chapter, our primary goal is to study the nature and formation of post-flare well-organized loop arcades by analyzing general signatures observed in the major flares that occurred during a decade period (1998–2007). These analysis revealed

quite puzzling fact indicating that among quite congruent flares, some bifurcate into self-organized state, while others do not.

A search for the observational properties distinguishing flares producing long-living slinkies from “non-slinky” flares led to several well-defined differences. For example, the non-slinky flares are usually characterized by short post-flare relaxation period, while post-flare slinky configuration has long lifetime. The enhancement of high-energy proton flux, typical to pre-flare period of slinky-producing flares, is absent in case of non-slinky flares.

Several examples of slinky and non-slinky flares together with their specific properties are shown in Table 19.1. The first column contains dates of the chosen examples; second and third columns are the start and peak times of the flare. The fourth column shows the scale of the event in GOES X-ray classification; fifth column contains the enhancement factor of particle fluxes long before the flare occurs. The approximate duration of these precursors is given in the next, sixth column. The enhancement of particle fluxes only occurs for those flares that bifurcate into self-organized slinkies. This is reflected in the seventh column, where “Yes” designates a slinky structure formation. Once the post-flare self-similar loop arcades are formed, they remain in this dynamically stable state for h. The approximate lifetime of the self-organized loop arcade is shown in the eighth column. The last column represents parental active region and its size. By size we mean a gross estimate of a visual area occupied by the active region, roughly defined as small (S, $\sim 100\text{--}500\text{ Mm}^2$), medium (M, $\sim 600\text{--}10^3\text{ Mm}^2$), large (L, $\sim 2 \times 10^3\text{--}10^4\text{ Mm}^2$), and extra large (XL, $\sim 2 \times 10^4\text{--}10^5\text{ Mm}^2$).

Four examples in Table 19.1 have “No” in the seventh column meaning that, soon after the flare, coronal loops quickly cool down without forming a long-living, self-similar loop arcades. In other words, after a short relaxation regime, the system returns almost to its pre-flare chaotic state. One can immediately see two major differences between this type of flares and slinky-producing ones: (1) they are not preceded by the early enhancement of high-energy proton fluxes and (2) they are usually associated with large, or super-large active regions.

To visualize more details of these differences and reveal others, we show three examples of the evolution of flares in Figs. 19.3, 19.4, and 19.5. It is interesting to note that although the 2004/03/30 UT 22:53 event *was* preceded by the enhancement of >1 Mev protons, the energy liberated by the flare was not enough to bring the system into the self-organized state. One can hardly determine why, but there are several factors that could be involved here: (1) the higher energy proton fluxes remain normal, (2) the active region is too large, and (3) the fact that >1 Mev proton flux may not be relevant here because usually the cutoff energy at geostationary orbit is typically of the order of several Mev, and therefore the response of >1 Mev protons may be primarily due to trapped protons of the outer zone of the magnetosphere (<http://www.swpc.noaa.gov/>).

We now turn to the description of figures listed above. Figure 19.3 shows two neighboring active regions, AR 10581 and AR 10582, and their overlying corona in the TRACE 195 Å line. Of these active regions the much larger and much more complicated AR 10582 has produced seventeen C-class flares in the 24 h interval

Table 19.1 Examples of the flares and their signatures

(1)	(2)	(3)	(4)	(5)			(6)	(7)	(8)	(9)
				Enhancement factor						
Event year/day	Start time (UT)	Peak time (UT)	GOES class	Protons 1 Mev	5 Mev	10 Mev	Electrons 2 Mev			
2000/07/14	10:03	10:24	X5.7	$>10^3$	10^2	50	$>10^2$	Yes	18 h	09077 (L)
2001/04/10	05:06	05:26	X2.3	$>10^3$	$>10^2$	>80	$>10^3$	Yes	8 h	09415 (S)
2003/05/28	00:17	00:27	X3.6	10^2	40	60	10^4	Yes	4 h	10365 (S)
2003/06/11	20:01	20:14	X1.6	20	Normal	Normal	$\sim 10^4$	No	N/A	10375 (XL)
2003/10/28	09:51	11:10	X17	10^4	10^4	10^4	8×10^2	Yes	4 h	10486 (XL)
2003/11/04	19:29	19:44	X18+	10^4	10^5	10^4	No data	Yes	>5 h	10486 (XL)
2004/03/30	22:53	23:01	C8.3	10^3	Normal	Normal	10^4	No	N/A	10582 (L)
2004/03/30	23:20	23:28	C3.2	10^3	Normal	Normal	10^4	Yes	10 h	10581 (S)
2004/07/15	01:30	01:40	X1.8	Normal	Normal	Normal	10^2	No	N/A	10649 (XL)
2004/07/16	13:49	13:55	X1.7	Normal	Normal	Normal	$<10^2$	No	N/A	10649 (XL)
2005/07/30	06:17	06:35	X1.3	4×10^2	80	3	No data	Yes	10 h	10792 (M)
2005/09/07	17:17	17:40	X17	$<10^2$	Normal	Normal	$>10^4$	Yes	~ 30 h	10808 (M)
2005/09/09	19:13	20:04	X6.2	$>10^4$	10^3	10^2	No data	Yes	8 h	10808 (M)
2005/09/13	23:15	23:22	X1.7	$\sim 10^3$	50	~ 6	$>10^4$	Yes	11 h	10808 (M)
2006/12/13	02:14	02:40	X3.4	$>10^4$	6×10^2	60	$>10^4$	Yes	~ 11 h	10930 (S)

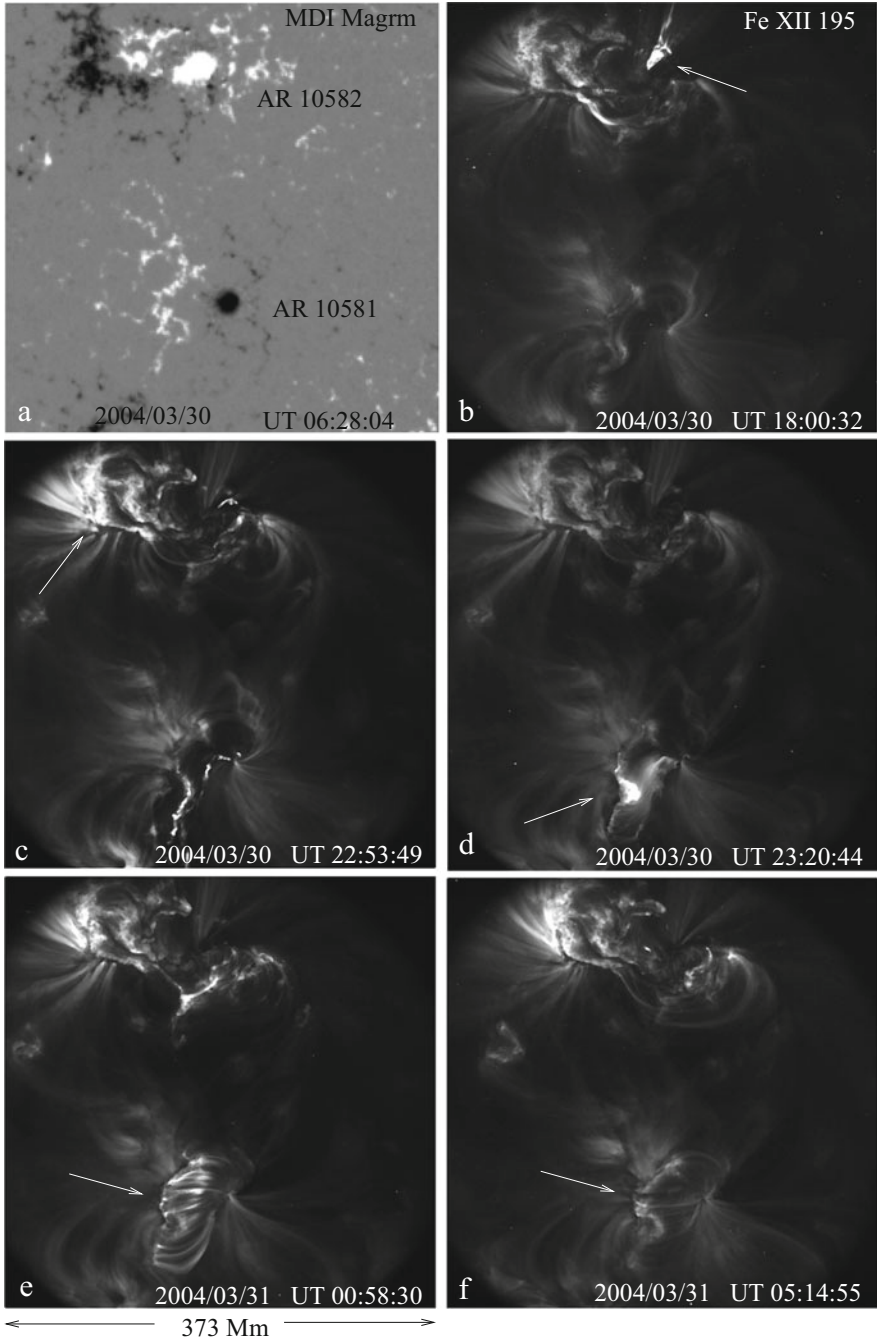


Fig. 19.3 Two neighboring active regions, AR 10581 and AR 10582, give an excellent example of absolutely different patterns in their coronal dynamics. Explanation of images shown in panels (a)–(f) is given in text

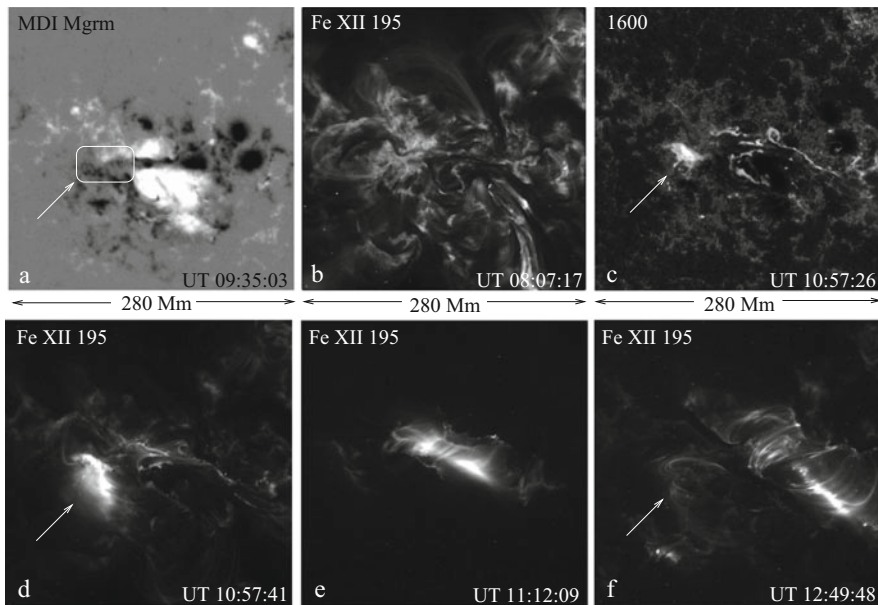


Fig. 19.4 A major, Oct 28, 2003 X17-class flare originating at the periphery of a large active region, AR 10486, synchronizes the entire active region, and causes bifurcation of a large chaotic conglomerate of coronal loops into a huge regular solenoid with a lifetime exceeding 4 h. Note that the flare kernel first appears in the chromosphere (panel c). The events shown in panels a–f are described in text

(from UT 05:30, 2004/03/30 to UT 05:30, 2004/03/31). One of these flares is marked by white arrows in Fig. 19.3b, c. Each of these flares has been followed by a short relaxation regime, after which the system of coronal loops returned approximately to the same, pre-flare chaotic configuration.

A totally different situation eventuates in the southern AR 10581 which, by its topology and size, is far more simple and smaller than AR 10582. Besides these visual properties, AR 10581 had been inactive for many h. It is remarkable, however, that a single flare of a C3.2 class, occurring during the same 24 h time interval (Fig. 19.3d, white arrow), resulted in an abrupt bifurcation of the entire system of coronal loops into a self-organized loop arcade (Fig. 19.3e, white arrow). The lifetime of this arcade exceeded 10 h. Figure 19.3f shows the corona in the TRACE Fe XII line at 2004/03/31 UT 05:14:55. At this time, the corona above AR 10582 which produced seventeen C-class flares remains as complex as it was before all of these flares occurred. Contrary to this, the post-flare loop arcades above AR 10581, formed after a single C3.2 class flare, once acquired, keep their well-organized form.

These observed regularities clearly agree with the difference between energy production by a given active region and the amount of energy required to bring the entire system into a self-organized form (cf. Table 19.1). Obviously, none of the seventeen C-class flares have produced enough energy to unify the huge

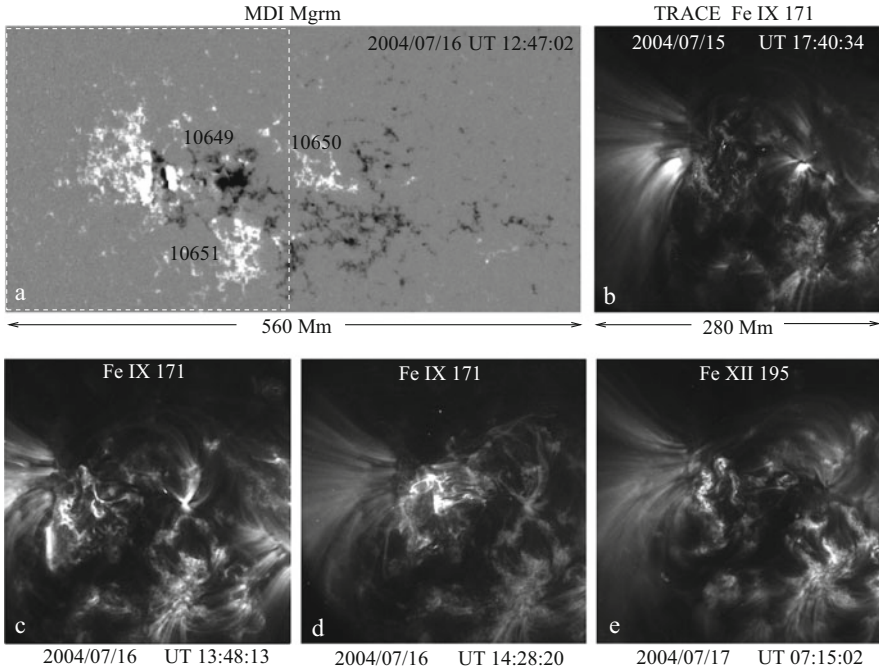


Fig. 19.5 Coronal activity above a huge conglomerate of three active regions. White dashed box in panel **a** shows the TRACE field of view. Numerous flares occurring during the disk passage of this active region conglomerate were not able to synchronize the system, leaving the coronal loops in their chaotic state. Panels **a–e** containing the image of magnetogram (**a**) and time sequence of associated corona (**b**)–(**e**) are described in text

conglomerate of coronal loops above the large active region 10582, and bring it to a self-organized stage; whereas, the energy accumulated before and released after the C3.2 class flare was enough to reorganize the loop system above the compact active region 10581.

Similar regularities were observed in all studied cases (see Table 19.1). Figures 19.4 and 19.5 show two other examples of totally different outcome. Figure 19.4a, b shows a large and complex active region, AR 10486, with a very irregular and complicated system of coronal loops overlying it. During about a 24 h period before UT 11:00 on Oct 28, 2003 several top C-class, M-class, and low X-class flares were continuously shaking the system. None of these flares, however, was able to change the intricate shape of the huge coronal system (Fig. 19.4b) until before UT 11:00 when the system was struck by a super-major X17 class flare (the famous Halloween flare). The Halloween event started with energy release first recorded in the TRACE 1600 chromospheric line (Fig. 19.4c) and escalated quickly to produce a rare X17-class flare (Fig. 19.4d). A few minutes after the X-ray intensity peak, the huge disarranged system of loops bifurcated into a well-organized, self-similar loop system having the form of a beautiful solenoid (panels

e and f in Fig. 19.4). It is remarkable that the energy release, in the form of a major flare and its photospheric counterpart, is associated with a magnetically rarefied peripheral region marked by a white box in Fig. 19.4a and by arrows in panels a, c, d, and e. The shortest distance between the region of flare energy release and the solenoid axis exceeds 80 Mm; yet, the blow produced by the X17 flare and the amount of associated energy were enough to synchronize the entire active region, and cause bifurcation of a large chaotic conglomerate of coronal loops into a huge regular solenoid with a lifetime exceeding 4 h.

Figure 19.5 shows an example of a post-flare outcome opposite to that of the Oct 28, 2003 flare. This case, dated July 16, 2004, also involves an extra large active region stretched over $360 \times 162 \text{ Mm}^2$ area, consisting of three “subdivisions,” AR 10649, AR 10650, and AR 10651. The complexity of the overlying corona is, therefore, not surprising. The TRACE field of view of the corona is restricted by the $280 \times 280 \text{ Mm}^2$ area (marked by the white dashed square in panel a). This huge ensemble of active regions produced during its disk passage numerous flares of all calibers.

For example, during 3 days, from 2004 July 15 UT 01:00 to July 17 UT 21:00, there were 12 low and mid X-class flares recorded, plus many more C-class and M-class events. Neither individual nor sequences of flares were able to synchronize the huge conglomerate of coronal loops to bring them into a self-organized state. After each and every one of the flares, the corona quickly relaxed back to its chaotic state. Panels b, c, d, and e in Fig. 19.5 show the corona soon after some of the X-class flares. The general character of the corona did not appear to change much from July 15 to July 17. This pattern was held throughout the disk passage of the active region.

19.3 Precursors and Predictability

The fact that high-energy proton (HEP) flux gets enhanced before the slinky-producing flares and vice versa is obviously associated with the ratio between energy production by a given active region and the amount of energy required to bring the entire system into the self-organized form.

Figure 19.6 shows example of the GOES high-energy proton fluxes around the 2003 October 28 X17-class flare (panel a) and series of flares during 2004 July 13–15 associated with AR 10649 (panel b). For the GOES plots we use a collection at the web site <http://goes.ngdc.noaa.gov/data/plots/> and also the SolarSoft GOES Data available at <http://www.lmsal.com/SXT/> (developed by S. Freeland).

One can see a striking difference between the two cases shown in Fig. 19.6: in the case of the 2003 Oct 28 flare, high-energy proton fluxes are strongly enhanced. More than 40 h prior to the flare, the fluxes of protons with energy higher than 1, 5, and 10 Mev are close to the post-flare level; moreover, even protons with energy higher than 50–100 Mev are significantly enhanced.

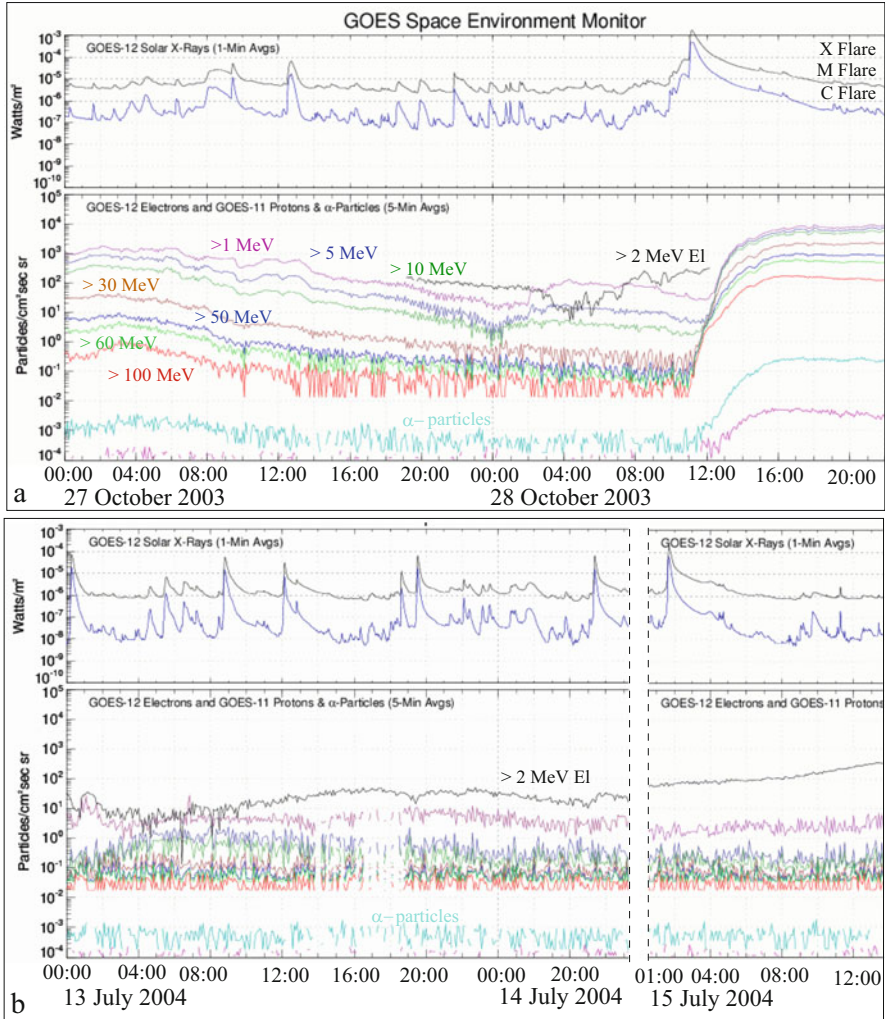


Fig. 19.6 Comparison of GOES high-energy proton fluxes for two cases. Panel **a**: 2003 Oct 28 X17 flare occurrence that peaked at UT 11:10. High-energy proton fluxes are strongly enhanced more than 40 h prior to the flare. Protons with energy higher than 1, 5, and 10 MeV are close to the post-flare level and even protons with energy higher than 50–100 MeV are significantly enhanced. Panel **b**: Series of X-class and M-class flares during a limited time interval. The level of high energy particles remained normal throughout the chosen time interval

A totally different picture is seen in the case of the long series of 2004 July 13–15 flares: throughout this time period, the level of high-energy proton fluxes remained normal. Obviously, there was no preliminary accumulation of energy associated with AR 10649 and its neighbors. Therefore, even a long series of X- and M-class flares could not reorganize their associated corona. Contrary to this, the energy

content and its earlier accumulation in AR 10486 was so high that, despite its huge size, a single X17-class flare was enough to reorganize the entire system and bring it to a self-organized state (Fig. 19.4f).

It should be emphasized again that the enhancement of particle fluxes only occurs for those flares that bifurcate into self-organized slinkies. The beginning of the enhancement process, or in other words, the first signs of the precursors develop from several h to several days prior to the flare, as is shown, for the given examples listed in the sixth column of Table 19.1.

For illustrative purposes, we show in Fig. 19.7 the transition from a normal level of particle fluxes to their enhanced state for the October 28, 2003 flare (the fifth example in Table 19.1). The precursor appears at about UT 18:00 on October 26, i.e., over 40 h before the start of the flare at UT 09:51 on October 28. These instances of time are shown by arrows on the lower panel in Fig. 19.7. During many days prior to the appearance of the precursor, the level of high-energy particle fluxes remained

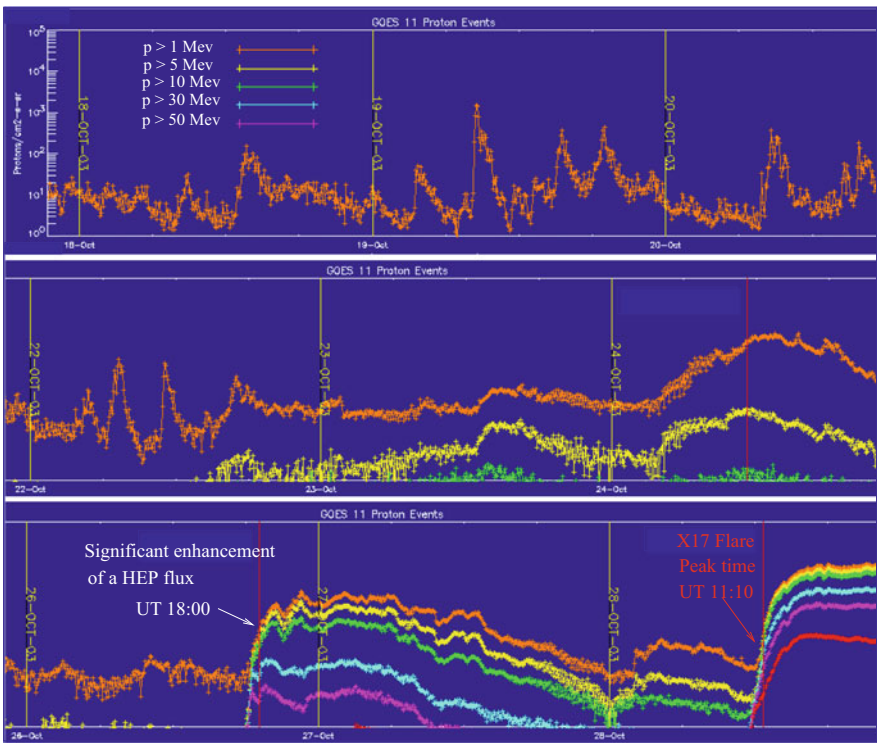


Fig. 19.7 Plots of high-energy proton (HEP) fluxes 10 days prior to the flare that started at UT 09:51 on October 28, 2003. High-energy particle fluxes (>5 MeV and higher) stay at low level. Precursor shows up at about UT 18:00 on October 26, i.e., about 40 h prior the flare, and appears as a sudden elevation of all channels including even the >50 MeV protons (purple line). The >1 MeV proton flux is shown to emphasize the absence of higher energy proton fluxes during several days prior to the precursor and flare (see the text for more details)

normal. It should be noted, however, that the elevated level of the >1 Mev protons (light brown curve) can hardly be considered as a precursor, because this channel is mainly due to trapped protons of the outer zone of the magnetosphere. This channel is shown in Fig. 19.7 to emphasize the absence of higher energy proton fluxes prior to the precursor.

The two major components of regularities were observed in all cases of major flares during the last decade, i.e.: (1) The occurrence of an early enhancement of high-energy particle flux was inevitably followed by the bifurcation of pre-flare chaotic loop systems into post-flare self-organized loop arcades; (2) When early enhancement of high-energy particle flux was absent, the pre-flare and post-flare corona remained in its chaotic state divided only by a short post-flare relaxation period.

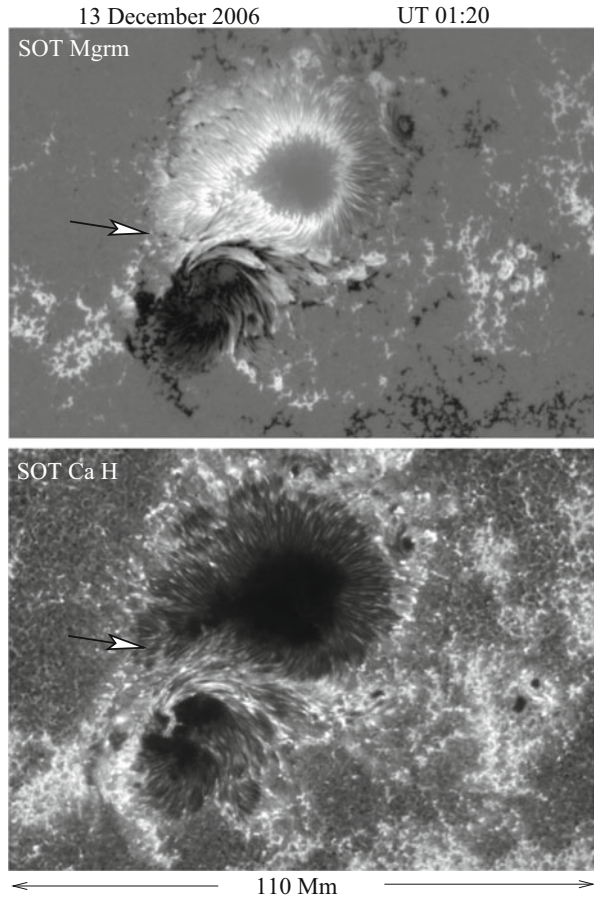
These regularities indicate that any system must be characterized by some critical parameters and, in particular, by some critical energy level above which the system must undergo a phase transition from one energetic and morphological state to another. In our case, spontaneous transition of a dynamic system of coronal loops from a chaotic state to a state characterized by coherent structure formation is a typical process of self-organization observed in all *dynamic systems* in nature (Mandelbrot 1967; Gaponov-Grekhov and Rabinovich 1992), including the solar atmosphere (Mogilevsky and Shilova 2006; Golovko et al. 2009; Nishizuka et al. 2009).

Additional strong support for identifying the spontaneous formation of slinkies as a process of self-organization is the observation of a scale invariance associated with it. This became possible with simultaneous multiwave observations taken by the Hinode spacecraft. Hinode shows the formation of self-organized structures not only at two levels of temperature in the corona (Fe IX 171 and Fe XI 195), but also at chromospheric and transition region temperatures. In the next section, we give an example of a corresponding case study and show that post-flare coronal structure formation is preceded by scale-invariant structure formation in the underlying chromosphere/transition region.

19.4 Exemplary Case of X-Class Flare and Formation of Slinkies

In this section, we will show step by step process that starts from energy production in the photosphere, passes through pre-flare stage, resulting a strong flare, and ends up with the formation of long-living well-organized multithread arcades of coronal loops. We will address here the following questions: (1) How the multithread arcades are formed; (2) Why they live so long; (3) What determines energy *inflow* and *outflow*; (4) What role is played by photospheric activity; and (5) How the energy release by coronal flare affects the lower layers of atmosphere.

Fig. 19.8 SOT magnetogram of an exemplary active region (top) and its overlying chromosphere in Ca H line at $\sim 10^4$ K (bottom). The arrow points to the polarity inversion line surrounded by the most active clusters of opposite polarity elements



For this purpose we use the uninterrupted sets of the SOT magnetograms and chromospheric images in Ca II λ 3968 H line ($\simeq 10^4$ K) combined with simultaneous images of the corona taken with the TRACE spacecraft in Fe XII λ 195 line ($1.2\text{--}2.6 \times 10^6$ K), showing the step by step evolution of the entire system.

The target is a complex active region consisting of closely located opposite polarity sunspots surrounded by a mixed polarity plage. Figure 19.8 shows the SOT magnetogram of the region and chromosphere above it in Ca H line. While the sunspots do not show a drastic changes with time, the clusters of small-scale magnetic concentrations around the polarity inversion line (marked by arrows in Fig. 19.8) are extremely dynamic.

A continuous energy supply coming from permanent interactions among small-scale mixed polarity elements in the polarity inversion region is uniquely felt by the overlying chromosphere. As we saw throughout this book, every small region of mixed polarity elements is reflected in Ca H line in the form of enhanced brightenings. The magnetogram movies showing the ubiquitous disappearance of small-scale opposite polarity neighbors obviously represent the ongoing reconnection processes.

The co-aligned Ca II and TRACE Fe XII 195 movies show, as expected, that the disappearance of opposite polarity couples uniquely precedes the appearance of chromospheric bright transients, frequently followed by coronal microflares. Note that, during this long-term stage, the general topology of the active region does not vary noticeably.

The situation changes when significantly larger elongated magnetic structures of opposite polarities emerge in the polarity inversion region. This newly emerged magnetic fluxes provide a significant supply of additional energy. This energy soon shows up as a strong chromospheric flare (Fig. 19.9). A hot overlying corona remains for a while in a “modest” shape compared to raging chromosphere/transition region. In other words, a strong chromospheric flare develops earlier than and independently of upcoming coronal flare.

Energy released in the chromosphere affects significantly both, the underlying low atmosphere and the overlying corona. In low atmosphere the chromospheric flare generates a huge blast wave which first appears in the Ca H line, then at lower temperatures in the G-band, and finally it reaches the photosphere.

In chosen case, the process starts at about UT 02:20 and reaches its maximum at UT 02:30. Figure 19.10 shows the impact of the chromospheric flare on the underlying layers of atmosphere at UT 02:28, with well-developed shock front of finite thickness seen in the south segment of umbra (marked by arrows in Fig. 19.10).

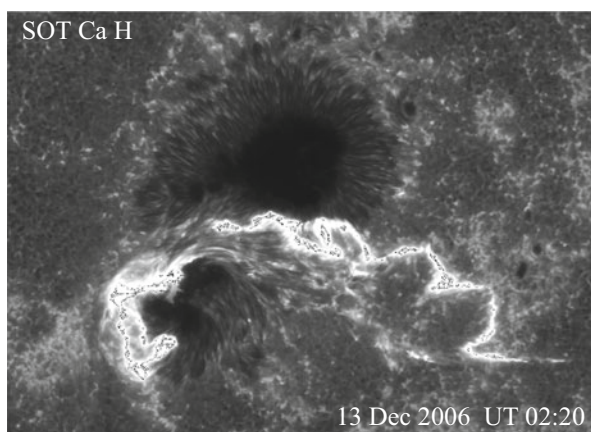


Fig. 19.9 Snapshot of Ca H developing flare at UT 02:20. The maximum phase will peak at UT 02:32. Field of view is 79×110 Mm

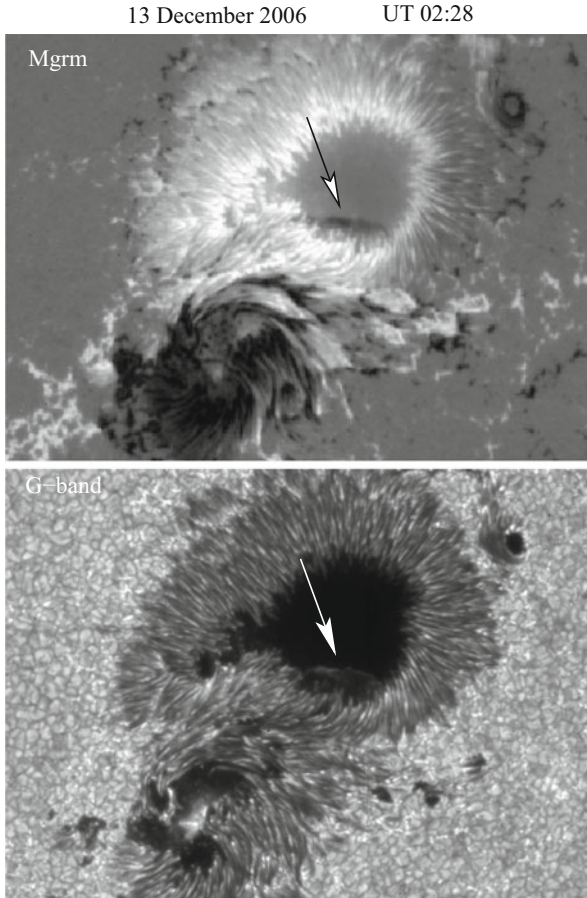


Fig. 19.10 The impact of the chromospheric flare to underlying photosphere and lower chromosphere regions. The arrows point to the shock front, part of which is clearly seen at the south segment of umbra

In the corona the blast wave triggers explosive release of energy lasting from UT 02:16 to UT 02:28.

Here we come across very important event: the explosive growth of energy is directly associated with the blast wave adding more power to *energy production region* located at the photospheric level. Thus due to this “last drop,” the explosive growth of energy quickly evolves into a major coronal flare that reaches its maximum at UT 02:40. Figure 19.11 shows GOES X-ray intensity curves for the 1.8 keV (upper curve) and for 3.1 keV (lower curve) particles.

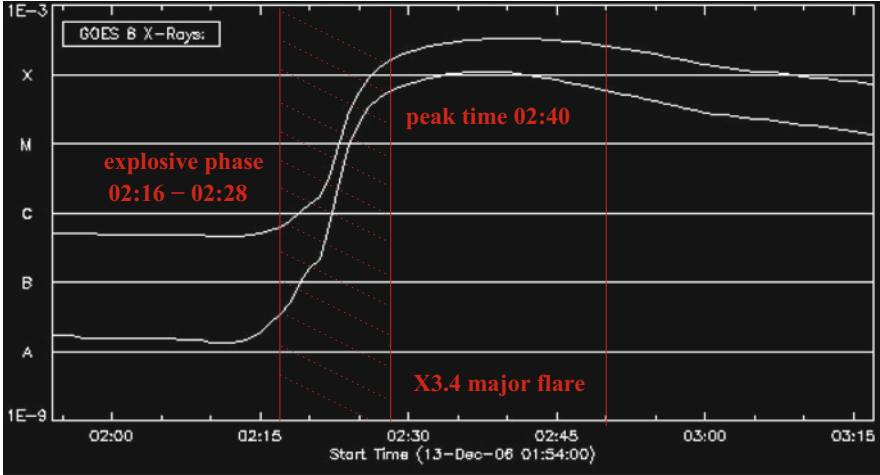


Fig. 19.11 GOES X-ray intensity curves for the 1.8 keV (upper curve) and for 3.1 keV (lower curve) particles. Peak time of a major (X3.4) flare is UT 02:40. The red dashed time interval corresponds to pre-flare explosive energy release

Thus the main steps of the process of energy production, transfer, and release can be briefly described as follows. The energy supply coming from reconnection between small-scale mixed polarity elements continues to accumulate and grow. At some point cumulative effects lead to the explosive release of energy. We see it to happen first in the chromosphere. Starting at about UT 01:40, the Ca H flare becomes so strong that, at UT 02:26, it generates a blast wave and triggers the explosive phase at coronal temperatures (Fig. 19.10). This additional supply of energy leads to further enhancement of explosive release of energy characterized as a major flare of X3.4 class.

After a short phase of flare maximum, the system bifurcates into a well-organized arcade of thin flux tubes at all chromospheric and coronal temperatures (Fig. 19.12). The self-organized regime lasts in the corona over 5 h, until a new flare destroys the structure at about UT 08:02. The chromospheric structures, however, remain in this state only about an hour. In other words, the higher the energy content, the longer the lifetime of the self-organized structures.

It must be emphasized that the peak of energy release in the corona *lags* the peak in the chromosphere by about 8 min, as does the bifurcation of the system into the self-organized state (Fig. 19.13). This uniquely indicates that the energy supply and its flow occurs from the photosphere throughout the chromosphere/transition region.

It is also important to note that the magnetic shear of the whole active region and accompanying helicity injection rate started to increase long before the flare occurred; moreover, the energy and helicity injection rates reached a saturation level

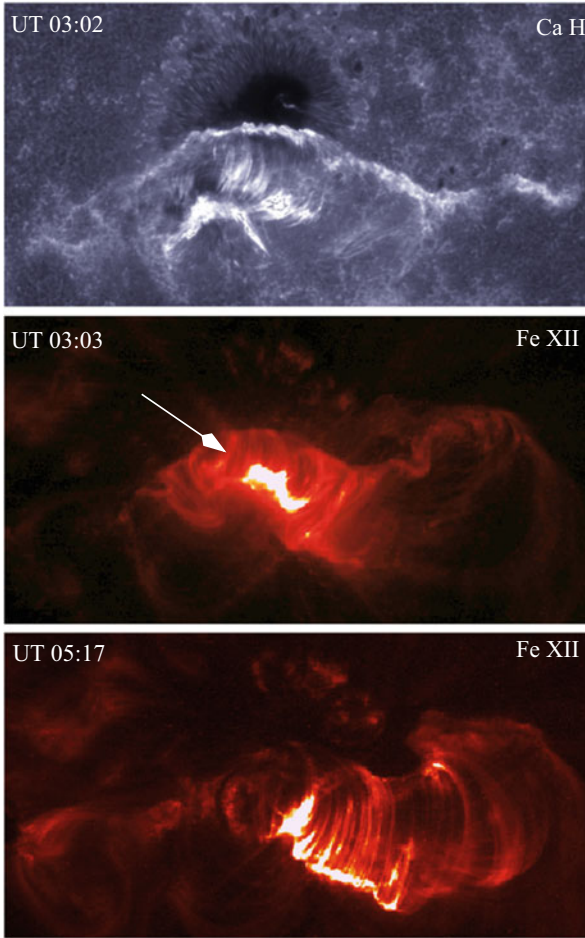


Fig. 19.12 Upper panel: Well-developed multithread system in the chromosphere at 10^4 K; Lower panels: Self-organized arcade in the corona in the initial stage of its formation (UT 03:03) and in the “mature” stage at UT 05:15. The coronal self-organized arcades outlive its chromospheric counterpart by more than 5 h. The white arrow in a middle panel indicates still flaring heart of the system

almost 24 h prior to the flare (Kubo et al. 2007; Harra et al. 2009). As these processes are directly connected with the energy injection into the system, the observed facts are consistent with the expected enhancement of high-energy proton flux long before the flare occurs.

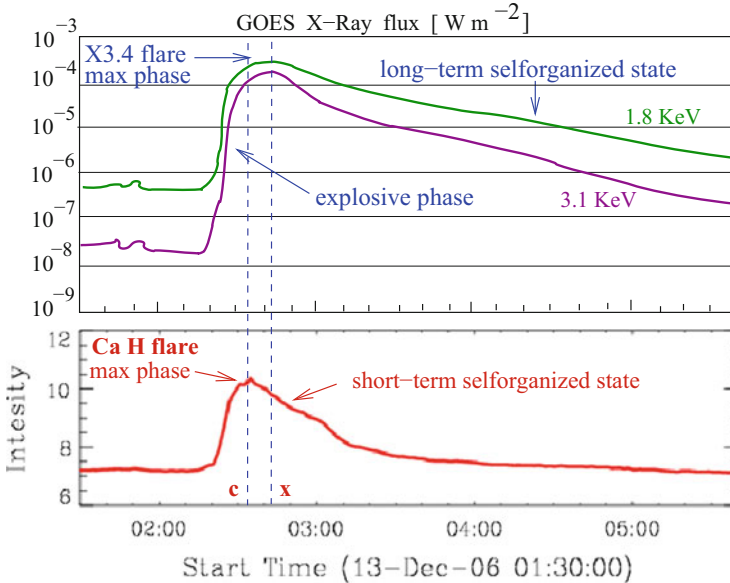


Fig. 19.13 GOES X-ray curves co-aligned with the SOT Ca H intensity curve. Top: The explosive phase and long-term, self-organized state of coronal plasma; Bottom: Ca H intensity curve which shows that the peak of energy release in the chromosphere (line *c*) precedes the peak in the corona (line *x*) by about 8 min. Post-flare regime is significantly shorter in the chromosphere than in the corona

19.5 Phenomenology of Energy Buildup and Quantitative Analysis

The mechanisms governing such a diverse observed regularities as ongoing small-scale sporadic events, the explosively growing pre-flare activity ending with a major flare, and bifurcation of systems into a self-organized state must have a common origin, and need to be explained by unified model. The theory that may unify description of various forms of coronal activity must also explain a ubiquitous filamentary structure of the coronal formations. Such a theory and its quantitative application is the subject of this section.

At all the diversity of coronal structures, they have several properties in common, e.g.,

1. the energy source lies in an intense hydromagnetic activity of photospheric magnetic fields,
2. any coronal formation has a small-scale filamentary structure, and
3. elemental filaments must carry electric currents.

Together, these properties indicate *modus operandi* is a typical energetically open, dissipative system. Therefore, various processes in formation and evolution

of coronal structures can be consolidated and understood by employing a method of dissipative systems based on global electrodynamics with source and sink of energy as discussed in Chap. 16.

Thus, the system consists of current-carrying magnetic loops that interconnect the photosphere—a high β energy-production region with an overlying low β dissipation region. Source is photospheric driver associated with the turbulent and electromagnetic stresses which generate a Poynting flux of energy and magnetic helicity that propagate upward, *get accumulated*, and subsequently dissipate.

The high conductivity of the chromosphere/coronal plasma causes dissipative effects to turn on at small transverse scales, $\Delta x_r = a/Re_m^{1/3}$, where a is the width of an elemental loop, $Re_m = v_A a / \eta_D$ is the magnetic Reynolds number ($\eta_D = c^2 / 4\pi\sigma$ is magnetic diffusivity, with $\sigma = 1.96ne^2 / (m_e v_{ei})$ being the plasma conductivity (Ionson 1982; Ryutova and Habbal 1995)).

The dissipative stresses that operate at very small scales of generalized skin depth, Δx_r , determine the width of a local cross-field shear and cause a filamentation process in magnetic structures.

The system of electrodynamic equations, i.e., Maxwell's equations together with the generalized Ohm's law fully represent the ability of a magneto-plasma to produce the energy, represented by driving electromotive force (e.m.f.), the ability to store electric and kinetic energy (system capacitance), the ability to store magnetic energy (system inductance), and the ability to release the accumulated energy (resistive loads). Below we follow analysis of an energetically open circuit presented in Chap. 16, and reproduce here a logic and some equations for convenience.

As shown in Chap. 16, with the use of the Heaviside step function of plasma beta, $H(1 - \beta)$, the set of electrodynamic equations describing the system of current-carrying magnetic loops that interconnect a high β energy-production region, with an overlying low β corona, is reducible to a single 3D equation for longitudinal electric current, j_l (cf. Eq. (16.24), Chap. 16):

$$\frac{4\pi}{c^2} \frac{\partial^2 j_l}{\partial t^2} - H(1 - \beta) \frac{1}{\sigma} \frac{\partial^3 j_l}{\partial x_r^2 \partial t} - H(1 - \beta) \frac{4\pi v_A^2}{c^2} \frac{\partial^2 j_l}{\partial l^2} = H(\beta - 1) \frac{1}{c} \frac{\partial^3 (vB)}{\partial x_r \partial l \partial t} \quad (19.1)$$

The first term in this equation is, indeed, an inductive reactance of a system, the second term is associated with the resistance, the third term is a capacitive reactance of the overlying plasma, and the term on the right-hand side is the source of driving electromotive force (e.m.f.), with v being a turbulent velocity. The competition, balance and imbalance of these parts in an active region and its coronal counterparts determine the system behavior.

For an adequate description of the energy flow, it is necessary to take into account the resistive losses that are associated not only with the corona, but also with the chromosphere/transition region which is the first to amass the energy coming from below and “transport” it into the corona (Kjeldseth-Moe et al. 1988; Dere et al. 1989; Golub et al. 1999; Ryutova and Tarbell 2000, 2003).

The feedback between the corona and the underlying atmosphere is also transmitted through the transition region. This leads to the appearance of nonlinear terms in the equation for the electric current. With this in mind, integrating (19.1) over the volume of elemental loop, $la\Delta x_r$, one obtains the equation for a total longitudinal current flowing along the elemental loop, $I = ja\Delta x_r$, which after some algebra (Ryutova 2006), acquires the form of the forced Van der Pol equation (Van der Pol 1927):

$$\frac{1}{\omega_0^2} \frac{d^2 I}{dt^2} - (\mu - Z_M Q I^2) \frac{dI}{dt} + I = 0 \tag{19.2}$$

Here $\omega_0 = \pi v_A/l$ is the natural frequency of the elemental loop, l being the length of the loop, and $Z_M = (4v_A/c^2)\sqrt{l_{TR}/l}$ is mutual resistance, with l_{TR} being the height of the transition region. The parameter $Z_M Q$ reflects the nonlinear effects associated with the back-reaction of a system to the induced currents, $Q \sim \tau_j \Phi^{-2}$, where τ_j is the characteristic current buildup time, and $\Phi = (vBa)/c$ is the driving e.m.f.

The evolution of the system is determined by the interplay between the coefficients in (19.2), i.e., by the amount of energy supply and its accumulation (associated with the driving e.m.f. and capacitive reactance), and ability of the system to build up the electric currents.

The important role in the realization of various scenarios of the current loop evolution is played by the sign of parameter μ (16.59),

$$\mu = \frac{v_{ei}}{\omega_0^2} \frac{m_e}{m_p} \left[\sqrt{\frac{l_{TR}}{l}} - 1.06 \times 10^7 \frac{T}{n} \left(\frac{v_A}{a^2} \right)^{2/3} \right] \tag{19.3}$$

which is a measure of the excess of energy supply or its deficiency with respect to the current generation threshold. It is important to note that (19.2), along the ‘‘individual’’ loops, contains parameters that interconnect the entire system in the photosphere (e.g., via e.m.f.), and realize the interpenetration of elemental loops and their environment through the cross-field share (Δx_r). As Δx_r is very small, the signal quickly propagates throughout the entire system of loops united by a common active region.

The solution to (19.2) for time varying current amplitude $I(\tau)$ is:

$$I(\tau) = \frac{2I_0}{\sqrt{I_0^2 + (4I_{cr} - I_0^2)\exp(-\epsilon\tau)}}, \tag{19.4}$$

where $\tau = t\omega_0$ is dimensionless time, $\epsilon = \mu\omega_0$, and I_{cr} a critical current threshold, at which the system may bifurcate to one or another regime depending on the initial current amplitude, i.e., whether $I_0 > 2I_{cr}$ or $I_0 < 2I_{cr}$.

$$I_{cr} = 5 \times 10^{-3} \frac{nev_A}{Re_m^{1/6}} \sqrt{\frac{|\mu|\omega_0^2}{\tilde{v}_{ei}} \frac{l}{l_{TR}}} \pi a l \tag{19.5}$$

It is important that the (19.4) acquires different forms depending on the parameter ϵ and the sign and value of coefficient in front of the exponent in the denominator. In fact, the way how the system approaches a quasi-stationary state is especially sensitive to ϵ , or in other words, to the sign and value of μ . Depending on the system parameters, μ may be positive, negative, or close to zero. In each case, the solution of the Van der Pol equation (19.4) describes different regimes of system behavior, including the Poincare limit cycle and a spontaneous process of self-organization.

In Chap. 16 we have studied in detail the behavior of currents in different regimes determined by the sign of μ . It is useful to recall some basic properties of system evolution here.

If $\mu > 0$, the current loops evolve in accordance with a typical Poincare limit cycle, approaching a quasi-stationary regime characterized by a critical current, I_{cr} . There are two major subregimes across the “border line” defined by $I_{cr}/I_0 = 2$ (see Figs. 16.8 and 16.9, Chap. 16). In the case of $I_0 > 2I_{cr}$, the system periodically releases the energy excess in the form of microflares (e.g., numerous bright “dots” in Fig. 19.2a) or moderate flares (boxed area in Figs. 19.2b and 19.5) approaching a quasi-stationary regime. The opposite regime, $I_0 < 2I_{cr}$, corresponds to long-living systems that gradually accumulate energy approaching a stationary regime. In this case, coronal loops can even survive the neighboring flares (such as blue and green arrows in Fig. 19.2 and white arrows in Fig. 19.4).

In other words, at $\mu > 0$, regardless of the initial current amplitude, the currents asymptotically tend to a stationary value of I_{cr} : currents with initial amplitude $I_0/I_{cr} < 2$ increase until they reach the limiting value, while currents with initial amplitude $I_0/I_{cr} > 2$ evolve in a decreasing regime. The larger the initial amplitude, the faster it drops, i.e., the shorter its limiting cycle, and the excess energy gets faster released. Several solutions for both subregimes at $\mu > 0$ are shown in Fig. 16.8 (Chap. 16). Numbers correspond to the ratio I_0/I_{cr} .

If $\mu < 0$, (19.2) describes several qualitatively different regimes of current evolution depending, again, on the amount of the initial energy supply. If the initial energy supply provides the value of injected currents below their critical values, $I_0 < 2I_{cr}$, the currents are in the decay regime and loops gradually (and very slowly) lose their energy. This regime corresponds to last stage of diffusively disappearing loop systems. The plots of corresponding currents are shown in Fig. 16.9 (Chap. 16), for several factors (1.5–1.98 I_0/I_{cr}).

On the other hand, in the case when the energy supply exceeds the generation threshold and $I_0 > 2I_{cr}$, the system becomes subject to explosive instability. In finite time, the currents reach infinitely large values, growing explosively in time, $I(t) = I_0/\sqrt{1 - (t/t_{expl})}$, with

$$t_{expl} = \frac{1}{|\mu|\omega_0^2} \ln \frac{I_{cr}^2}{I_0^2 - I_{cr}^2}. \quad (19.6)$$

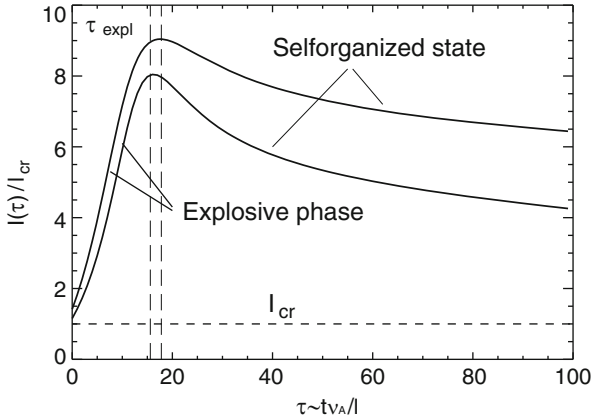


Fig. 19.14 Evolution of coronal loop currents for the explosive and post-explosive regime at $\mu \approx 0$ (μ approaching to zero from *negative* values). The upper curve corresponds to $I_0 = 2.2I_{cr}$ and lower curve is for $I_0 = 2.4I_{cr}$; the higher the initial current, the shorter is the “explosive” time (cf. Fig. 19.13)

Table 19.2 Estimates of critical currents

T (10^4 K)	n (10^9 cm^{-3})	v_A (cm s^{-1})	l (10^8 cm)	a_{cr} (10^6 cm)	ω_0 (s^{-1})	$ \mu $	I_{cr} (A m^{-2})
200	1.4	8×10^7	20	21	0.13	0.12	3.2
2	23	9.1×10^6	2	1.9	0.143	0.15	1.1

In the vicinity of $t = t_{expl}$, the system quickly releases energy producing a major flare. The corresponding plots for factors, 2.05–2.3, are shown in Fig. 16.9 (Chap. 16).

At this strongly nonlinear stage, higher nonlinear effects turn on and stabilize the further growth of the currents leading to the bifurcation of a system into a self-organized state. This process is illustrated by the theoretical curve shown in Fig. 19.14, which is well representing the observed HEP curve shown in Fig. 19.13. A parameter range where the system bifurcates from one regime to another corresponds to proximity of $\mu \simeq 0$, or to proximity of the critical current to value, determined by condition, $\mu - Z_M Q I_{cr}^2 \simeq 0$ (coefficient of the first derivative in (19.2)).

It is important, that parameter μ , which reflects the physical properties of a system both at macro- and microscales, and determines the actual behavior of a system, is expressed through the physical quantities most of which are observable, e.g., temperature, density, magnetic field, and spatial scales of coronal loops. This allows quantitative analysis and usage of observational data for modeling and studies the predictability of different regimes.

Table 19.2 contains the quantitative estimates of critical current densities for loops at coronal and chromospheric temperatures. Alfvén velocity here is calculated through the temperature and plasma β , $v_A = 1.82 \times 10^4 \sqrt{T/\beta}$. We adopt $\beta = 0.1$

and $l_{TR} = 2.2 \times 10^8$ cm. The aspect ratio (for the critical value of a loop radius, a_{cr}) is of the order of $(a_{cr}/l) \simeq 0.01$ at both temperatures, consistent with the scale invariance typical of self-organization. Now we can estimate the explosive times for the two regimes shown in Fig. 19.11.

In the first case, when $j_0 = 1.1 j_{cr}$, $t_{expl}^{cor} \simeq 19$ min, for coronal loops, and $t_{expl}^{chr} = 12$ min 23 s for the chromospheric ones. In the second case, when $j_0 = 1.2 j_{cr}$, we have respectively, $t_{expl}^{cor} \simeq 13$ min and $t_{expl}^{chr} = 8$ min 30 s. Thus, in agreement with observations, the onset of the explosive phase and bifurcation of a system into a self-organized state occurs in the corona later than in the chromosphere (Figs. 19.12 and 19.13). The measured explosive times and duration of the explosive phase also agree well with the observations.

Due to flexibility of the system parameters and wide range of their combinations various scales, this approach has a great potential in studying the overall behavior of coronal structures.

19.6 Recurrent Flares and Echoes

Highly intermittent corona consisting of a regular ensemble of a thin magnetic loops and harboring frequent impulsive bursts is the most natural place for the occurrence of plasma echoes. Before we discuss this spectacular echo-like phenomena seen in the high-resolution observations of corona, let us recall the features of echo effect.

Along the familiar sound echo, sonic navigation, and a Greek legend about a nymph echo, there are many echo-like phenomena in macro- and microworlds. Some were discovered and put in practical use long, some only in modern times.

In microworlds, first was a spin echo observed by Hahn (1950) in nuclear magnetic resonance experiment. Two short radiofrequency pulses satisfying the resonance condition and separated by a time interval τ were applied to an ensemble of spins in a liquid placed in a static magnetic field. After removal of the pulses (τ being much larger than the duration of a pulse), in the same time interval τ after the second pulse, when the ensemble of spins relaxed to thermal equilibrium, a spontaneous nuclear induction signal has been observed. The effect was dubbed spin echo. Soon after first results, Hahn performed experiments with multiple echoes and using the Bloch theory explained the effect. Hahn concluded that the echo technique appears to be highly suitable as a fast and stable method in searching for unknown resonances, and suggested that it is of technical interest to consider the possibility of applying echo pattern as a type of memory device. This modest prediction turned out to be shortly a key element in biomedical nuclear resonance diagnostics and a computer technology.

Most importantly, any physical system with the “memory” and hidden resonances may produce the echo effect, and thus be a subject of reliable diagnostics.

Along the diagnostics, the echo may be used in many different ways. For example, the echo effect provides a unique opportunity for electromagnetic field to

overpass the skin depth and penetrate through a metal (Kemoklidze and Pitaevskii 1970a). Consider this example for illustrative purpose. Let the thickness of the metal plate, d , be much larger than the skin depth, δ , $d \gg \delta$. By the definition an electromagnetic field cannot penetrate a metal deeper than δ . If, however, the electron mean free path, l , in the metal is $l \gg d$, then by applying two electromagnetic fields at both sides of a plate, the echo effect arises and generates the third signal inside the metal. Namely, let an electromagnetic field E_1 of frequency ω_1 is applied to the left side of metal. If now a field E_2 of frequency ω_2 is applied at both sides of the plate, the much stronger echo field will appear with the amplitude $E_e \sim E_1 E_2^2$, at $\omega_2 = 3\omega_1$ inside the metal. The key role here, as in all cases of echo effect, is played by the memory of electrons flying through the metal. Note, that the amplitude of echo field E_e does not decrease with increasing plate thickness, but increases. The example of the penetration of the electromagnetic field into the metal is a *spatial* echo, while the Hahn's echo effect is a *temporal*.

Very rich echo-like phenomena were found in plasmas. There were identified and experimentally verified conditions for a temporal, spatial, and spatiotemporal echoes. The main condition for realization of a plasma echo is the ability of a system to maintain the *reversible* processes for which the medium having filamentary structure is extremely favorable. First plasma echoes were described and tested in collisionless plasmas, where the Landau damping operates and provides the necessary attributes of "memory" (O'Neal 65; Gould 1965; Gould et al. 1967; Malmberg et al. 1968a,b; Kemoklidze and Pitaevskii 1970b).

19.6.1 Landau Damping, Memory, and Spatiotemporal Echoes

By its nature, the Landau damping occurs in collisionless plasma due to the phase memory of particles resonantly interacting with the wave (Landau 1946). As Landau damping is not connected directly with dissipative effects, it may be considered as a *reversible* process. In other words, although the macroscopic quantities such as an amplitude of the wave pulse (e.g., electric field) and mass density are damped exponentially, the distribution function becomes only distorted, and may oscillate indefinitely, i.e., a damped wave in a collisionless plasma retains the "memory" of the preceding oscillatory motion. This means that the direction of the phase evolution of the perturbed distribution function can be reversed by the application of a second wave pulse. As a result, a macroscopic field subsequently reappears after both the previously applied fields have Landau damped away.

The basic mechanism of the plasma echo can be easily understood (O'Neal and Gould 1968; Malmberg et al. 1968a,b; Kadomtsev 1968).

When an electric field of *spatial* dependence $\exp(-ik_1x)$ is excited in a plasma and then Landau damps away, it modulates the distribution function leaving a perturbation of the form $f_1(v)\exp(-ik_1x + ik_1vt)$. For large time, t , there is no electric field associated with this perturbation, since an integral over velocity will phasemix to zero. If after a time τ a wave $\sim \exp(-ik_2x)$ is excited and then damps

away, it will modulate the unperturbed part of the distribution function leaving a first-order term of the form $f_2(v)\exp[-ik_2x + ik_2v(t - \tau)]$, but it also modulates the perturbation leaving a second-order term of the form $f_1(v)f_2(v)\exp[-i(k_2 - k_1)x + ik_2v\tau - i(k_2 - k_1vt)]$. The coefficient of v in the exponent will vanish when

$$t = \tau \frac{k_2}{k_2 - k_1}. \quad (19.7)$$

At this time an integral over velocity will not phasemix to zero, and an electric field reappears in the plasma. This is a *temporal* second-order echo. In addition to this, higher order echoes can also be observed. For example, a third-order echo is produced when the velocity space perturbation from the first pulse is modulated by the second spatial harmonic of the electric field. The echo then occurs at $t = \tau[2k_2/(2k_2 - k_1)]$.

The mechanism of the spatial echo is quite similar to the temporal echo. In this case if an electric field of frequency ω_1 is continuously excited at one point in a plasma and an electric field of frequency $\omega_2 > \omega_1$ is continuously excited at a distance l from this point, then a second-order spatial echo of frequency $\omega_2 - \omega_1$ will be produced at a distance $l\omega_2/(\omega_2 - \omega_1)$. Higher order spatial echoes are also easily produced and observed. For example, the spatial echo of frequency (O'Neal and Gould 1968)

$$\omega_3 = m\omega_2 - n\omega_1. \quad (19.8)$$

will appear at a distance

$$l^* = l \frac{n\omega_1}{\omega_3} \quad (19.9)$$

provided that

$$m\omega_2 > n\omega_1 \quad (19.10)$$

Here integers m and n ($m > n$) correspond to the order of an echo in the perturbation theory, namely $m + n = 2, 3, 4, 5$ correspond to second-, third-, fourth-, and fifth-order echoes. For small-amplitude initial waves, the amplitude of the echo A_{echo} is estimated as

$$A_{\text{echo}} \sim A_1^n A_2^m. \quad (19.11)$$

The existence of various echos, associated with second-, third-, and higher order perturbation theory, has been demonstrated experimentally (Malmberg et al. 1968a,b; Ikezi and Takahashi 1968; Yugami et al. 1994). The echoes always appear at the predicted positions. The frequency and wavelength of the echo wave and the

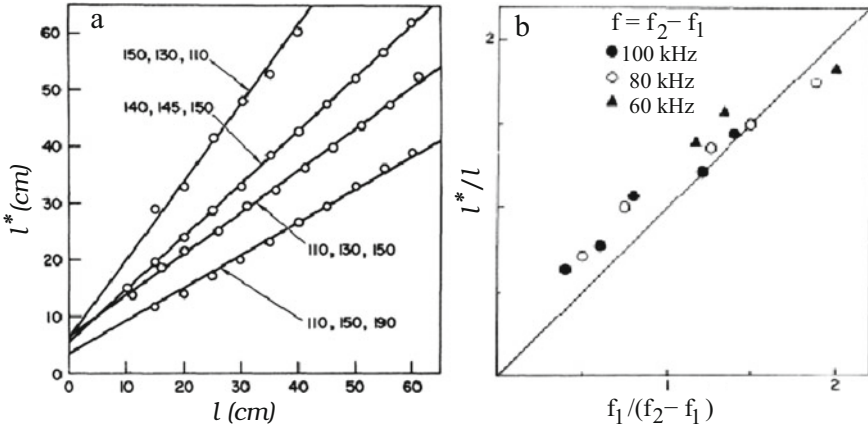


Fig. 19.15 Experimental results on a plasma wave echo. (a) Echo position versus transmitter separation obtained by Malmberg et al. (1968a): the slope of the curves is theory (19.9), the circle are experimental measurements; the numbers on the curves are frequencies f_1, f_2 , and f_3 in MHz. (b) Relation between the position of the echo and the frequencies f_1 and f_2 obtained by Ikezi and Takahashi (1968); the solid line is theoretical slope $x = l f_1 / (f_2 - f_1)$; the echo frequencies $f = f_2 - f_1$ are given for three sets of experiment. Reprinted with permission, copyright APS

dependence of its amplitude on the amplitude of the initial waves are totally consistent with theory.

Figure 19.15 shows examples of earliest experiments on plasma echoes. Figure 19.15a is a plot of the position of a third-order ($m = 2, n = 1$) echo as function of the separation of the two Transmitters obtained for several values of frequency ratio f_1/f_3 (Malmberg et al. 1968a). The slopes of the straight lines are computed with (19.9). For small signals, as expected from (19.11), the echo amplitude is $A_{\text{echo}} \sim A_1^n A_2^m$. At large signal levels the echo amplitude saturates. Figure 19.15b shows results obtained by Ikezi and Takahashi (1968) also for the third-order plasma echo. Shown are the experimental values of the echo position l^* for several sets of frequencies $f_2 > f_1$.

Since the pioneering works on the plasma echoes, the subject obtained a great attention for various diagnostics. For example, the diffusion of plasma electrons in velocity space has been measured using the plasma wave echo as an experimental tool (Jensen et al. 1969). The study of spatial-temporal echoes generated in a magnetized plasma by low frequency external perturbations led to temperature diagnostics of the electrons and ions, and allowed to diagnose their distribution over longitudinal velocities in thermonuclear devices (Gromov and Revenchuk 1990). Plasma echo as diagnostic tool is used in wide range of near-earth and space instruments as well (Fung et al. 2003; Benson and Osherovich 2004; Mahmoudian et al. 2011).

The plasma echoes in the solar atmosphere, where they are the most anticipated phenomena, did not get much attention (Frank and Rytova 2007). Although there

were some attempts made before the sun's "space era" when only the ground-based observations were available. For example, Erokhin et al. (1975) explained a series of small-scale mottles—sporadic brightenings, observed to appear during a chromospheric flare almost simultaneously in different places, as an effect of plasma echo. They also suggested that plasma echo may operate in an often observed phenomena when a coronal flare above one active region triggers a new flare above another active region. Today, having excellent solar missions, the similar studies may open great diagnostic facilities.

19.6.2 *Echo Effects in Slinkies*

The solar atmosphere, in general, with its ubiquitous filamentary magnetic fields, and well-organized coronal arcades of thin magnetic filaments, in particular, are indeed the most natural places where the realization of Landau damping and subsequent appearance of plasma echoes must be expected.

Elemental filaments in arcades being in highly dynamic state show not only subtle oscillations, but also are harboring frequent microflares. These microflares, having various intensities, often appear simultaneously in different places, i.e., several elemental filaments far removed from each other show synchronous lighting up.

Figure 19.16 shows snapshots of the corona at four instances of time taken by the TRACE in the Fe XII 195 line at 2×10^6 K. The upper left panel is the July 14, 2000 flare at its maximum phase (UT 10:23). In several minutes (around UT 10:31) the system of loops relaxes to well-shaped state. Note that in this stage no threads at given resolution are yet seen. By UT 10:49 the system bifurcates into fully developed self-organized slinky consisting of slim self-similar filaments. A frequent sporadic brightenings appearing soon after formation of arcades (marked by arrows) have a clear properties of both, spatial and temporal echoes. The echoes occur continuously in various places in the system until the arcades preserve their filamentary structures.

Time intervals between the first two brightenings and their successors follow a pattern typical to either temporal or spatiotemporal echos. Besides, many individual filaments produce homologous microflares, i.e., strong localized brightenings may occur repetitively along the same elemental flux tube. It is also important that the larger the system the longer it lives, and respectively harbors larger number of echoes.

Another example of self-organized slinky that may used to observe the echo effects is shown in Fig. 19.17. We have already encountered this slinky as an exemplary evidence of post-flare self-organization (see Fig. 19.2).

Before the first major flare the system of coronal loops represents a huge chaotic conglomerate. The flare occurred at UT 05:29 which generated a powerful CME brought the system into a "quasi"-organized state (Fig. 19.17a). Already at this stage, the system consists of enough filamentary structure to support series of echoes. Recall that the energy released in the first major flare did not lead to

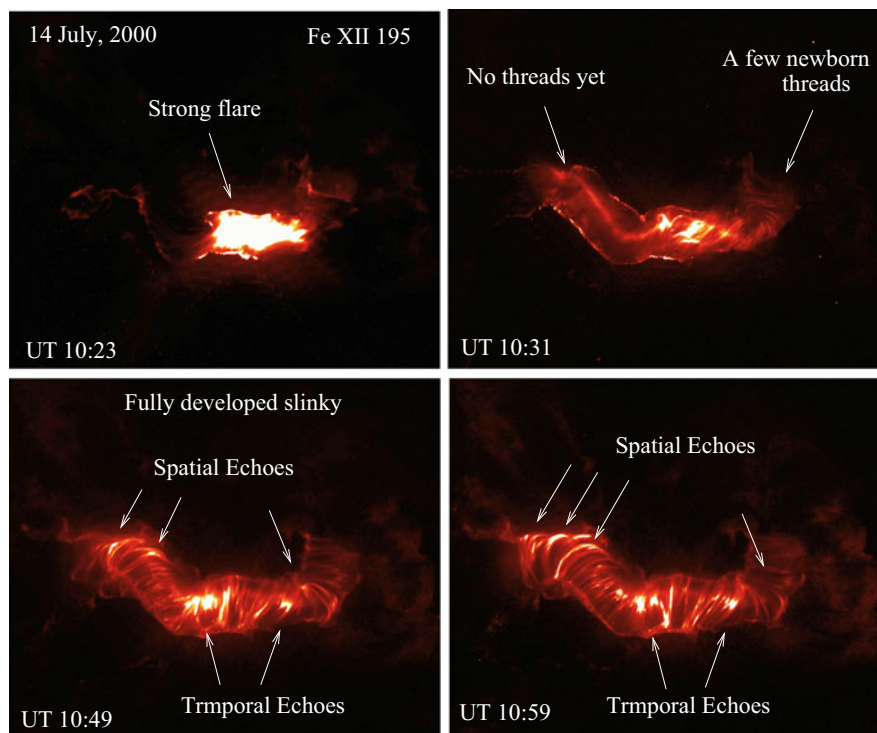


Fig. 19.16 Snapshots of the active region corona of 14 July, 2000 at four instances of time. The major flare that occurred at UT 10:23 relaxes to well-shaped confined state (e.g., UT 10:31) and by UT 10:49 bifurcates into fully developed self-organized system of thin filaments harboring numerous microflares with the spatial and temporal echo pattern

formation of a solenoid, but has been clearly distributed between the loop system and a powerful CME (cf. Fig. 19.2b). In other words, part of energy coming from the first flare was not enough for the system to bifurcate into self-organized state. This job was done by the second major flare (Fig. 19.17b). Soon after this flare the system acquired a form of fully developed solenoid of self-organized loops and remained in this state for many h. During the entire period of existence, the observations showed a multiple echoes traveling back and forth along the solenoid. It must be noted again that timescales of these events are fraction of minutes while lifetime of the entire dynamic system may be h and days.

The observation of the systematic echoes in slinkies is quite a straightforward matter. One only needs to observe and measure times of their occurrence and distances between different events. This makes the echo observations very promising for development of diagnostic tools and an important addition to verify basic physics of plasma echoes in action.

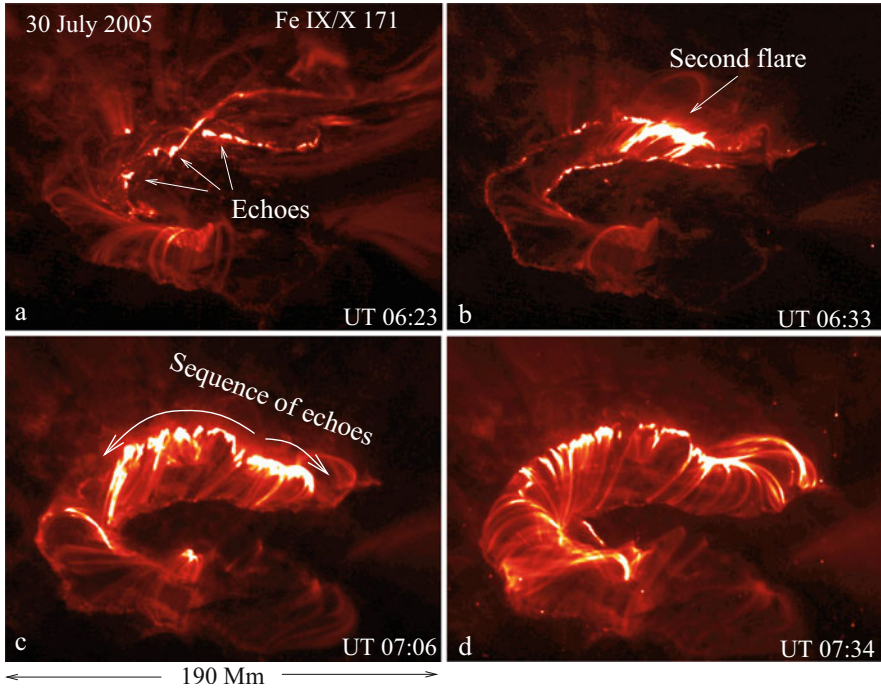


Fig. 19.17 Snapshots of an active region corona taken on July 30, 2005 in Fe IX/X 171 line. Panel **a** shows the system of coronal loops after the first major flare which occurred at UT 05:29 (see Fig. 19.2); at this stage the system already harbors multiple echoes; at UT 06:33 a second flare (panel **b**) brings the system in a long-living well-organized system with sequences of echoes traveling back and forth along the solenoid; the series of echoes generated soon after UT 06:33 flare, propagate in both directions from the flare kernel (panel **c**) during the mature state of slinky, echoes are seen all over the slinky (panel **d**)

19.6.3 Spatial and Temporal Recurrences in Flares

The echo effects may occur, of course, at much larger spatial and temporal scales. These are usually characteristic of coronal flares that include all the classes, from the weakest C-class flares to largest X-class flares. As a rule, the larger are the flares the larger are the times between the successive flares and larger are the distances between them.

Figure 19.18 contains additional evidence of echo occurrence in large flares. Shown are GOES X-ray plots of 24 h duration measured during the occurrence of two sets of recurrent flares. One was produced by the active region AR 10718 on Jan 13, 2005 (top panel) and the other by the AR 11882 on Oct 25, 2013. In both cases we deal with the temporal echoes. The case of 13 Jan 2005 shows multiple echoes producing C-class flares. The characteristic time interval between the repetitive bursts is about 3 h. In case of 25 Oct 2013, the M2.9-class flare occurring at UT

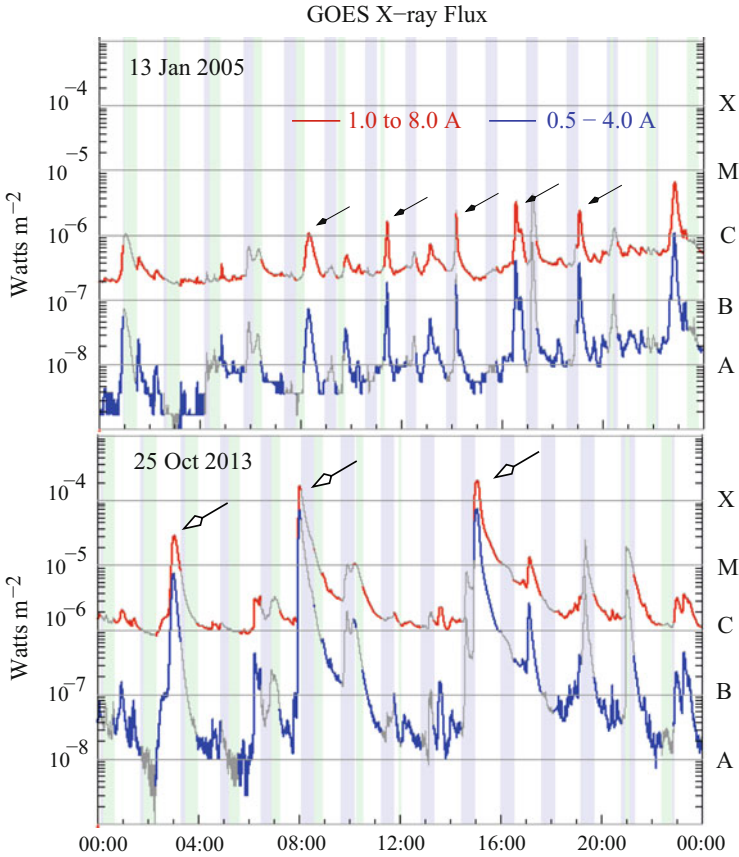


Fig. 19.18 Occurrence of temporal echoes in coronal flares illustrated by the GOES X-ray flux. Top: Multiple echoes in a C-class flares occurring in a characteristic time interval of about 3 h (small arrows); the recurrent flares were produced by the same active region AR 10718 on Jan 13, 2005; Bottom: The temporal echo (large arrows) in large M2.9 (UT 02:48), X1.7 (UT 08:03), and X2.1 (UT 14:51) flares produced by the active region 11882 on Oct 25, 2013

02:48 and the X1.7 occurring at UT 08:03 with third X2.1-class flare appearing in about 7 h (UT 14:51) show a typical pattern of the temporal echo. Note that, as expected, the time interval between the successive flares is significantly larger in case of a stronger X-class flares than in weaker C-class flares.

The fact that the flares show recurrence has been realized decades ago. Richardson (1951), classifying solar flares and their characteristics, describes the pattern in flare occurrence which is consistent with a spatial and temporal echo phenomena. He writes: “A region has been called “recurrent” if 5 or more distinct flares are observed at one station in one transit time” (temporal recurrence). The analogue of a spatial echo is presented as follows: “The question has been investigated of whether two or more flares occur nearly simultaneously over widely separated spot

groups more often than would be expected by chance. The number of multiple flares observed was found to be higher than the number calculated, if they occurred at random, from Poisson's law." Since then number of authors studied recurrent flares, where the recurrent flares were called "sympathetic," "simultaneous," and "homologous" (Fritzova-Svestkova et al. 1976; Cheng and Pallavicini 1987; Zhang and Wang 2002; Wheatland and Craig 2006; Chandra et al. 2011).

The subject of solar echoes requires farther studies and development of unified basis for their description and utilization. Using the simple relations in spatiotemporal echoes based on directly measurable quantities opens broad opportunities in understanding not only flare characteristics but also their precursors and outcome. And, again, due to the "arithmetically" simple relations between the spatial and timescales of simultaneous and homologous flares, it must not be a distant future when solid diagnostic tools will be developed.

Concluding this chapter it is useful to overview some key elements of its subject. A survey of major X-ray flares shows that a complex pre-flare system of coronal loops often, but not always, bifurcate into a long-living, well-organized system of multithreaded loop arcades having a fundamental scale. Analyzing physical conditions that cause or prevent this process, it was found that those flares which bifurcate into long-living slinky arcades, and those that do not produce such structures, have very different signatures. The most striking difference is that, in all cases of slinky formation, the GOES high-energy proton flux becomes significantly enhanced 10–40h before the flare occurs. No such effect was found prior to the "non-slinky" flares. One of the important features revealed is that post-flare coronal slinky formation is preceded by scale-invariant structure formation in the underlying chromosphere/transition region.

The formation of well-organized loop structures, having a fundamental scale, and occurring subsequently at different temperatures, is consistent with a spontaneous process of self-organization that naturally follows from general electrodynamics of nonlinear energetically open systems. Thus, a method of an energetically open, dissipative system, which describes coupling of the photospheric energy reservoir with the overlying chromosphere and corona, and includes the back-reaction of coronal activity to the underlying atmosphere, proved to be very reliable tool for understanding a wide range of observed regularities. The set of electrodynamic equations reduces to a single equation having the form of a Van der Pol oscillator, which, depending on the system parameters, describes various dynamic forms of the system evolution. This includes, in particular, two major regimes studied in this chapter: (1) the Poincare limit cycle, when systems experience the explosive release of energy, returning to a physically similar state in a short relaxation time; this regime corresponds to "regular" flares that do not produce slinkies, and (2) a spontaneous process of self-organization, characterized by scale-invariant structure formation, usually having form of solenoidal slinkies.

The observations show a clear pattern of continuously appearing microflares traveling back and forth throughout the body of the solenoidal system of filaments. The timing and spatial distribution of microflares are consistent with multiple spatial and temporal plasma echoes. The echo pattern is also a regular appearance

in recurrent (simultaneous and homologous) flares. These observations may be used for reliable “micro” diagnostic of physical parameters, such as electron and ion temperatures and their anisotropies, local electric currents and velocities, and microturbulence associated with them.

Simple relationships between the physical parameters of a system, most of which are observable, may provide reliable diagnostic tools. The observed regularities may serve as a long-term precursor of strong flares. Future observations of precursory events may allow the study of the predictability of system behavior.

19.7 Problems

19.1 Using the model of two combs describe the echo effect.

19.2 Consider the basic mechanism for the temporal plasma echo in the case of one-dimensional electrostatic perturbations in a collisionless plasma.

19.3 As discussed earlier, a solar flare in one active region will often triggers a new flare in another active region. It has also been observed that the initial phase of a chromospheric flares is associated with small “mottles” appearing almost simultaneously at different places. This phenomena can be interpreted as a plasma echo effect. Describe phenomenology of plasma-echo effect in the repetitive flare phenomena (Erokhin et al. 1975).

References

- M.J. Aschwanden, P.D. Aschwanden, *Astrophys. J.* **674**, 530 (2008)
 T. Bai, P.A. Sturrock, *Annu. Rev. Astron. Astrophys.* **27**, 421 (1989)
 M. Battaglia, P.C. Grigis, A.O. Benz, *Astron. Astrophys.* **439**, 737 (2005)
 R. Benson, V.A. Osherovich, *Radio Sci.* **39**, RS1S28 (2004)
 D.H. Brooks et al., *Astrophys. J.* **772L**, 19 (2013)
 R. Chandra et al., *Sol. Phys.* **269**, 83 (2011)
 C. Cheng, R. Pallavicini, *Astrophys. J.* **318**, 459 (1987)
 J.W. Cirtain et al., *Nature* **493**, 501 (2013)
 K.P. Dere, J.-D.F. Bartoe, G.E. Brueckner, *Sol. Phys.* **123**, 41 (1989)
 N.S. Erokhin, S.A. Kaplan, S.S. Moiseev, *Sov. Astron.* **18**, 524 (1975)
 Z. Frank, M. Ryutova, AGU, FMSH22A0842F (2007)
 L. Fritzoza-Svestkova, R.C. Chase, Z. Svestka, *Sol. Phys.* **48**, 275 (1976)
 S.F. Fung et al., *Geophys. Res. Lett.* **30**, 110000-1 (2003)
 A.V. Gaponov-Grekhov, M.I. Rabinovich, *Nonlinearities in Action* (Springer, New York, 1992)
 S.E. Gibson et al., *Astrophys. J.* **574**, 1021 (2002)
 A.A. Golovko, I.I. Salakhutdinova, A.I. Khlystova, *Geomagn. Aeron.* **49**, 907 (2009)
 L. Golub et al., *Phys. Plasmas* **6**, 2205 (1999)
 R.W. Gould, *Phys. Lett.* **19**, 477 (1965)
 R.W. Gould, T.M. O’Neal, J.H. Malmberg, *Phys. Rev. Lett.* **19**, 219 (1967)
 S.N. Gromov, S.M. Revenchuk, *Plasma Phys. Controlled Fusion* **32**, 1257 (1990)

- E.L. Hahn, Phys. Rev. **80**, 580 (1950)
L.K. Harra et al., Astrophys. J. **691**, L99 (2009)
H. Ikezi, N. Takahashi, Phys. Rev. Lett. **20**, 140 (1968)
J.A. Isonson, Astrophys. J. **254**, 318 (1982)
T.H. Jensen, J.H. Malmberg, T.M. O'Neil, Phys. Fluids **12**, 1728 (1969)
B.B. Kadomtsev, Sov. Phys. Usp. **11**, 328 (1968)
M.P. Kemoklidze, L.P. Pitaevskii, JETP Lett. **11**, 548 (1970a)
M.P. Kemoklidze, L.P. Pitaevskii, JETP **31**, 994 (1970b)
O. Kjeldseth-Moe et al., Astrophys. J. **334**, 1066 (1988)
T. Kosugi et al., Sol. Phys. **243**, 3 (2007)
M. Kubo et al., Publ. Astron. Soc. Jpn. **59**, S779 (2007)
B.J. LaBonte, M.K. Georgoulis, D.M. Rust, Astrophys. J. **671**, 955 (2007)
L. Landau, Sov. Phys. - JETP **16**, 574 (1946)
A. Mahmoudian et al., Ann. Geophys. **29**, 2169 (2011)
J.H. Malmberg, C.B. Wharton, R.W. Gould, T.M. O'Neil, Phys. Rev. Lett. **20**, 95 (1968a)
J.H. Malmberg, C.B. Wharton, R.W. Gould, T.M. O'Neil, Phys. Fluids **11**, 1147 (1968b)
A.B. Mandelbrot, Science **135**, 63 (1967)
E.I. Mogilevsky, N.S. Shilova, Geomagn. Aeron. **46**, 303 (2006)
N. Nishizuka, A. Asai, H. Takasaki, H. Kurokawa, K. Shibata, Astrophys. J. **694L**, 74 (2009)
T.M. O'Neal, Phys. Fluids **8**, 2255 (1965)
T.M. O'Neal, R.W. Gould, Phys. Fluids **11**, 134 (1968)
I. Prigogine, *Introduction to Thermodynamics of Irreversible Processes* (Interscience, New York, 1961)
R.S. Richardson, Astrophys. J. **114**, 356 (1951)
M. Ryutova, J. Geophys. Res. **111**, A09102 (2006)
M.P. Ryutova, S.R. Habbal, Astrophys. J. **451**, 381 (1995)
M. Ryutova, R. Shine, J. Geophys. Res. **111**, A03101 (2006)
M. Ryutova, T. Tarbell, Astrophys. J. **541**, L29 (2000)
M. Ryutova, T. Tarbell, Phys. Rev. Lett. **90**, 191101 (2003)
M.P. Ryutova, Z. Frank, H. Hagenaar, T. Berger, Astrophys. J. **733**, 125 (2011)
B. van der Pol, Philos. Mag. **3**, 65 (1927)
M.S. Wheatland, I.J.D. Craig, Sol. Phys. **238**, 73 (2006)
A.R. Winebarger et al., Astrophys. J. **787L**, 10 (2014)
N. Yugami, S. Kusaka, Y. Nishida, Phys. Rev. E **49**, 2276 (1994)
J. Zhang, J. Wang, Astrophys. J. **566**, L117 (2002)

Chapter 20

Quiescent Prominences



Abstract In this chapter we shall consider dynamics of quiescent prominences. These amazing phenomena offer excellent opportunity to study fundamental properties of various plasma instabilities, and also address to some of the most enigmatic features of solar atmosphere. We shall combine the observational evidence and theory to identify such instabilities as: (1) prominence cavity formation and its evolution, associated with a screw pinch instability; (2) development of regular series of plumes and spikes typical to the Rayleigh-Taylor (RT) instability; and (3) the appearance of growing ripples at the prominence/corona interface, often followed by a sudden collimated mass up- and downflows, attributed to the Kelvin-Helmholtz instability. We shall specify the conditions for transition from a linear, rippling mode to nonlinear stage of the KH instability, known to have an explosive character. We show examples of a practical use of direct measurements of the instability parameters and also briefly discuss the natural occurrence of greenhouse-like effect under prominence body.

20.1 Background: Problem of Stability

A great astronomer and photographer Ferdinand Ellerman said: “He who has never seen a solar prominence has missed one of the most fascinating objects in the Heavens’.

Quiescent prominences are clouds of *cool dense* plasma, suspended over a hot rarefied plasma of corona, akin to heavy dumbbells floating in a thin air or Kellar’s Princess Karnac beautifully levitating (Fig. 20.1).

The prominence enigma includes not only their stability, i.e., the questions what keeps such a heavy material on top of much lighter substance of coronal plasma and why their lifetime, reaching sometimes several solar rotations, is so long, but the very formation of prominences and their highly dynamic behavior. During their lifetimes, prominences show all kinds of irregular motions, changes, and structure formations on a wide range of spatial and timescales, from small-scale downflows and oscillatory motions to the formation of large-scale prominence



Fig. 20.1 Miracle of power. Reprinted from <http://www.loc.gov> Credit Library of Congress

cavities, characterized by sudden disruptions of large portions of the prominence body leading to explosive coronal mass ejections (CMEs).

Projected on the sky, the prominences appear in so many faces that people began to call them names, like Hedgerow, Loop-kind, Twirl, Fan, etc. (Fig. 20.2). Simplest of them were chosen to guess at least the magnetic field geometry that could support heavy prominence material.

Extensive studies of prominences have been roughly centered on two classes of closely related problems, their stability and disruption. Work done on the first problem leads to general understanding of the magnetic field topology able, in principle, to support the heavy plasma against gravity (Kippenhahn and Schlueter 1957; Kuperus and Raadu 1974; Vrsnak et al. 1988; Priest 1988; van Ballegooijen and Martens 1990; Low 1993; Kuperus 1996), providing a basis and requirements for improving or reconsidering prominence models. A key issue of the magnetic field topology and a major stumbling block is the fact that the magnetic field embodied by quiescent prominences overlies the neutral (polarity inversion) line. Experiencing the action of photospheric shear motions, it must have a helical structure and carry electric currents. Signs of helical structures, direct or indirect,

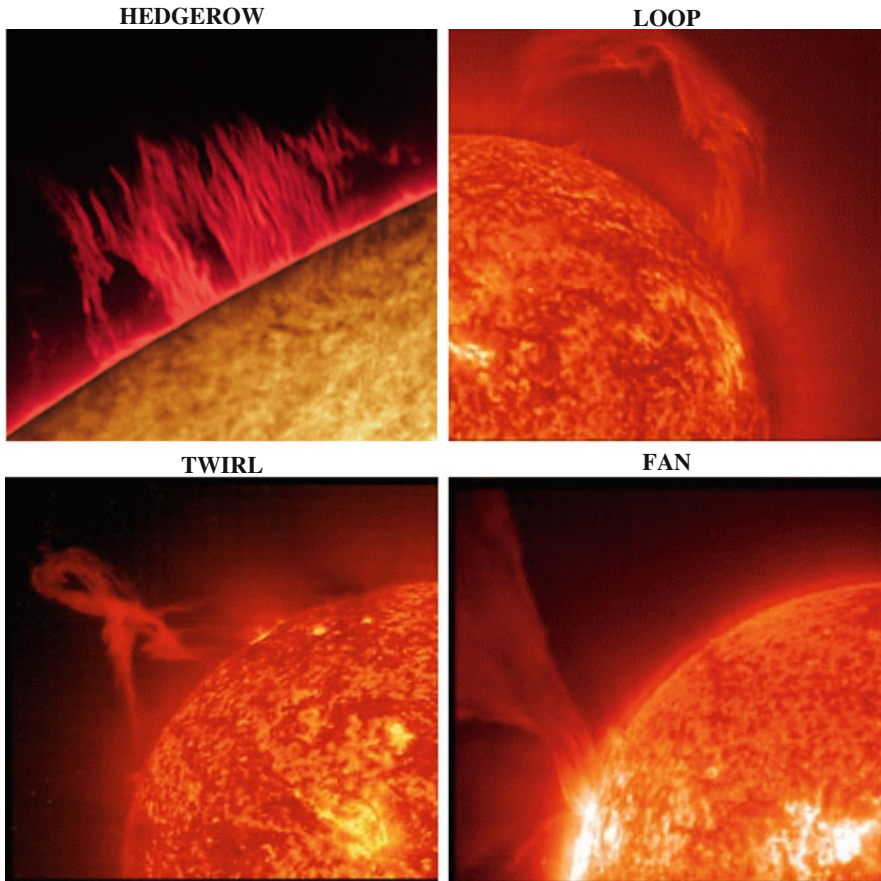


Fig. 20.2 A few examples of many faces of quiescent prominences as seen at chromospheric temperatures ($\sim 5 \times 10^4$ K)

have been observed decades ago (Severny and Khokhlova 1953; Rothschild et al. 1955; Sakurai 1976; Tandberg-Hanssen 1995).

Severny and Khokhlova (1953) reported that one of the most prominent features of quiescent prominences are persistent irregular motions. With frozen-in magnetic field, this was obviously indicative of a complex magnetic field and current topology.

Rothschild et al. (1955) directly measured motions of 47 knots on a limb prominence. They found knots moving “downward” with an acceleration that was much smaller than gravitational acceleration and a tendency for the acceleration to reverse at a certain point in the trajectory. The authors cautiously concluded that this could be explained by helical motions. They also refer to earlier findings indicating that “accelerations are smaller than gravitational, with little or no relationship even to the direction of gravity.”

Rotational motions have been observed in prominences by Ohman (1972) who also reported the possibility of “ring shaped” objects with helical motions ejected from prominences.

Rust and Kumar (1994) re-examining the Kippenhahn-Schlueter and the Kuperus-Raadu models conclude: “All models known to us, even those with helical fields, rely on some initial distortion of the bordering fields. . . They predict either normal or inverted cross-filament components, but the axial component is always incorrect. We conclude that such models are defective’.” They propose a model based on observations which clearly indicated that magnetic fields have helical nature, the mass in the filament is supplied during the emergence of helical flux ropes, and that the prominence is lifted bodily out of the chromosphere. To further describe the dynamics and stability of prominences, Rust and Kumar also invoked the screw pinch instability. This provided criteria for a stable helical configuration, determined the distribution of magnetic fields and currents, and resulted in quite a good agreement with observations.

The problem of disruption of prominences, directly related to their stability conditions, includes a wide range of plasma instabilities that must arise in such an environment. To consolidate the problems of prominence equilibrium and stability with respect to various MHD modes, Fong et al. (2001) studied prominence equilibria with respect to pressure- and gravity-driven instabilities using ballooning formalism and found conditions and growth rates for these instabilities. Under prominence conditions, this formalism includes the Rayleigh-Taylor instability, Parker instability, and any unstable modes characterized by long parallel and short cross-field dependencies. For the time being many aspects of plasma instabilities associated with prominence dynamics have been revealed and clarified in analytical and numerical studies (Dolginov and Ostryakov 1980; Matsumoto et al. 1993; De Bruyne and Hood 1993; Strauss and Longcope 1994; Magara 2001; Low and Petrie 2005; Mackay and van Ballegoijen 2009).

New data obtained from space observations (Berger et al. 2010; Ryutova et al. 2010; Xing et al. 2012; Dudík et al. 2012; Feng et al. 2013; Druckmüller et al. 2014; Carlyle et al. 2014) offer a unique opportunity to study fundamental plasma instabilities in more detail. Here we address this problem and investigate the occurrence and evolution of various instabilities to reveal their role in the dynamics of quiescent prominences. Our approach is twofold. First, we use the observational data to identify a particular kind of instability and its observed signatures. These data allow direct measurements of spatial and temporal parameters of various events. We then compare the measured spatiotemporal characteristics of particular event with corresponding results given by basic plasma theory. We will see that the fundamental plasma instabilities, expected and predicted earlier, continuously develop during the prominence lifetime. Quantitative analysis not only allows reliable identification of plasma instabilities, but may also be used for inference of physical parameters that are not directly measurable.

20.2 Large-Scale Observed Regularities

The necessary conditions for prominence formation is accumulation of opposite polarity small-scale magnetic elements each forming unipolar ensembles with clear boundary between the areas of their population. Such a process naturally occurs when dispersed magnetic elements drift toward high latitudes in course of the solar cycle evolution, and encounter the opposite polarity remnants from the previous cycle. This is a regular process and serves as a basis for the majority of the quiescent prominences to encircle near-polar latitudes and endure for several solar rotations.

The focal point of the observations of quiescent prominences has always been the time when part of prominence body passes through the limb, displaying its structure and dynamics at the best viewing angle (Fig. 20.2). Obviously, the portion of prominence positioned at the limb and projected on the sky is only a two-dimensional picture of small part of a huge solenoidal body of prominence.

Wrapped by 3D magnetic field and currents, the body of prominence is usually stretched over the entire polarity inversion line. Figure 20.3 shows example of quiescent prominence taken by the SDO at three temperatures. Lower panel is the magnetogram showing northern high latitude part of solar surface covered by ensembles of opposite polarity small-scale flux tubes. One can see a clear polarity inversion line made between near pole region dominated by negative polarity magnetic elements and southern adjusted region dominated by positive polarity elements. Middle panel is the same area in He II 304 at 5×10^4 K. Chromosphere shows here a huge quiescent prominence overlying entire polarity inversion line with its beautiful limb portion on the East. Top panel is overlying corona in Fe IX at 6.3×10^5 K. A hot corona seems to be intact by presence of prominence. In fact, one can see darkened 171 Å emission on the disk caused by the presence of prominence *shadowing* EUV emission. Usually, the prominence shadow is seen throughout entire corona up to temperatures exceeding 10^7 K. This is shown in Fig. 20.4. One can see how the prominence following exactly the polarity inversion line blocks the hot EUV emission up to the outermost corona.

Global three-dimensional magnetic field and currents ($\mathbf{j} \times \mathbf{B} \neq 0$), overlying the highly inhomogeneous photosphere with crooked polarity inversion line, acquire the shape of quite uneven solenoid. With solar rotation a prominence projection on the sky varies quite significantly. The shape and character of its *limb portion* depends on the orientation of a solenoidal body of prominence approaching the limb.

Figure 20.5 shows a cartoon illustrating several different possibilities. If the prominence approaches the limb with such an orientation as shown by dashed arrows that portion of prominence will appear as hedgerow shaped. In case of the prominence orientation as shown by a solid arrow, the limb portion will appear as a system of loops, which may simply arched, or form the dips and rings.

Accordingly, the details of prominence behavior observed on the limb may vary to a great degree depending on the orientation of a limb portion of prominence. The same is true for manifestation of fundamental plasma instabilities. These limitations

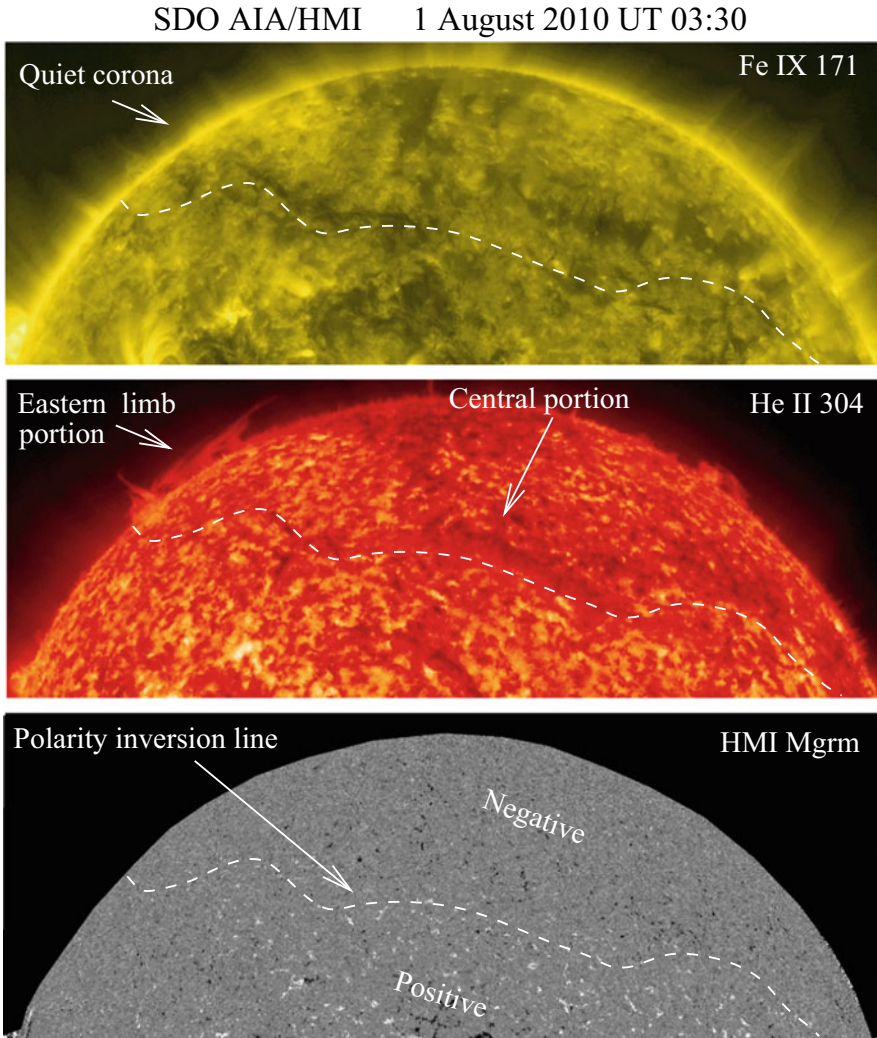


Fig. 20.3 Example of quiescent prominence taken by AIA instrument in He II 304 line (middle panel), simultaneously with underlying photosphere (lower panel) and overlying corona in Fe IX line (upper panel). Dashed line highlights the polarity inversion line which serves as a path to a gigantic solenoid with twisted axis and skewed body. Eastern portion of prominence projected on the sky appears in He II 304 line as a typical loop-type prominence

however do not hinder the regularity of certain events which makes them an intrinsic attribute of prominence dynamics.

Thus, as the prominences survive several solar rotations, experiencing permanent changes, gaining and losing the energy, their projection on the sky may acquire infinitely diverse, never duplicating forms. Often the prominence projection on sky

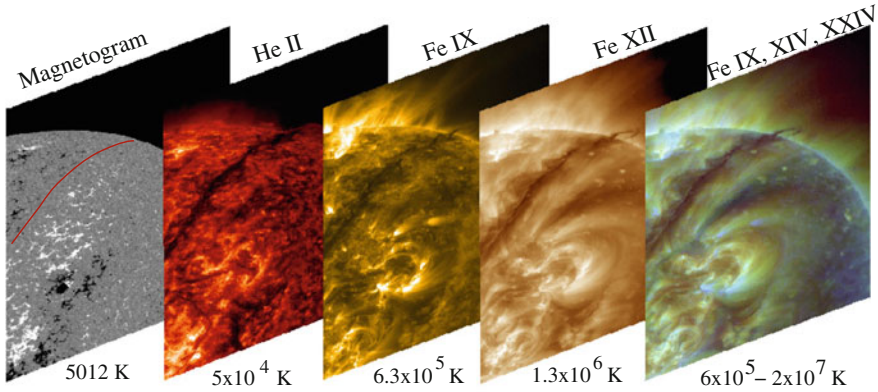


Fig. 20.4 Note how diligently the prominence demarcates the magnetic shear between two opposite polarity quiet regions. Red curve in the magnetogram demarcates the polarity inversion line. The fact that the prominence shadow is seen throughout entire corona up to its highest temperatures shows its enormous body and height

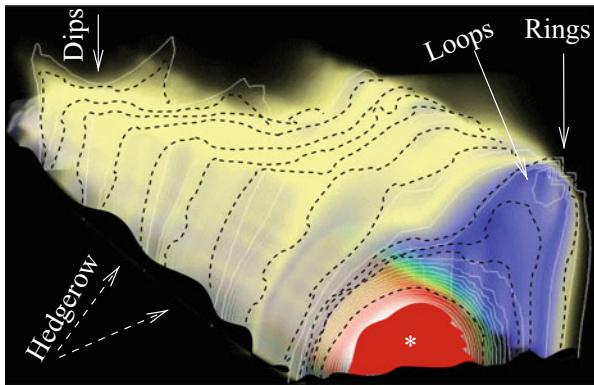


Fig. 20.5 Cartoon illustrating different forms of the visible portion of prominence situated near the limb. Depending on the orientation of the prominence body at the moment of time when it passes through the limb, the observer may see either the hedgerow shape (dashed arrows), or loop shaped prominence (solid arrow), or their combination. White star indicates the prominence cavity filled by a hot coronal plasma

combines several named shapes simultaneously (cf. Fig. 20.2). Example of such prominence is shown in Fig. 20.6. This is a huge prominence observed on November 30, 2006 by the Hinode. One can see a hedgerow-type body in the middle, a loop-like system on the northern part, and twisted structures in the southern part that overlies a hot corona represented by black “cavities” under the prominence body. These are marked by white stars. To distinguish these “cavities,” i.e., *hollow space* under prominence body filled by a hot coronal plasma from coronal cavities which are usually understood as a coronal voids *above* the prominences, we shall call them

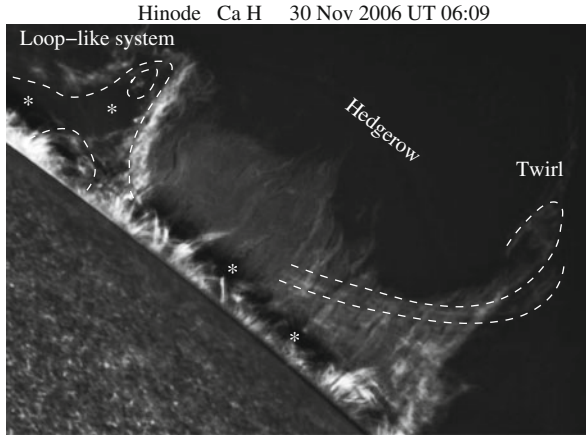


Fig. 20.6 Limb portion of prominence at $N 50^\circ$ latitude, observed on November 30, 2006 showing a complex twisted form which has a loop-like system on the northern part, a hedgerow-type body in the middle, and twisted structures in the southern part. White stars indicate location of a hot prominence cavities filled by coronal plasma

prominence cavities or just *cavities*. It is important to bare in mind that plasma in these cavities is at coronal temperatures and has much lower densities than those in the prominence body.

To demonstrate some basic properties of quiescent prominences, we use the data sets for six prominences taken with the SOT instrument on Hinode. The images are taken with 10–30 s cadence with the spatial resolution corresponding to a pixel size of $0''.16$ in H_α , and $0''.108$ in Ca II H line. The advanced procedures were used to highly improve the row data (Berger et al. 2008, 2010; Ryutova et al. 2010).

Data were compiled in movies to study temporal variation of chosen events. Duration of the observation usually exceeded 4 h, that allowed to study both, slow processes and short-living events including their possible long-term recurrences. There were found several persistent features that occur at different stages of the prominence evolution and that are common for all the chosen cases. Here we discuss three classes of events.

- I. Formation of large-scale arch-shaped prominence cavities expanding up to 30–50 Mm, and lifting the body of prominence to these heights and beyond. Interior of growing cavity consists of coronal material, and may be characterized as growing hot bulbs *under* the prominence body. Observed regularities in growth and collapse of such cavities can be well understood as a result of screw pinch instability in their early phase of formation (Sakurai 1976; Rust and Kumar 1994), and as a cavity dynamics under the influence of gravity and magnetic field during their further evolution.
- II. Development of a regular series of plumes and spikes seen at any moment of time at any possible orientation of a limb portion of prominence. This

ubiquitous phenomena have all the attributes of Rayleigh-Taylor (RT) instability (Rayleigh 1883; Taylor 1950; Chandrasekhar 1981). Using the above-mentioned data sets allowed for the first time to identify several branches of RT instability, and measure their spatiotemporal characteristics. These are: (a) Single mode regime which in its nonlinear stage may produce jets or be stabilized by formation of a mushroom cap analogous to explosive instability; (b) Multimode regime characterized by formation of regular series of plumes and spikes; (c) Two plume competition. Hinode data allowed also to verify the influence of magnetic field on the RT instability.

- III. Development of growing ripples at the lower prominence/corona interface often followed by a sudden appearance of a collimated mass upflows, which can be attributed to the Kelvin-Helmholtz (KH) instability; high cadence data have provided the means to determine conditions for transition of a linear phase (rippling mode) to nonlinear stage of KH instability which is known to have an explosive character.

20.3 Formation of Prominence Cavity and Helical Structures

Formation of cavities under prominence body filled by the coronal plasma is an integral part of the 3D helical structure of the prominence and its evolution. It is only natural to expect that quiescent prominences stretched below the polar cap are indeed supported by solenoidal magnetic field composed of a thin arcades formed over the opposite polarity small scale magnetic fragments dispersed at high latitudes.

Uneven distribution of magnetic elements provides quite uneven shape of magnetic solenoid. This, on the other hand, causes various shapes of the limb portion of prominence. In most cases, i.e., almost at any orientation of a limb portion of prominence, cavity formation is a regular phenomenon. Their dynamics and lifetime, however, may be very different. This is determined by the set of local physical parameters. The very fact of a cavity formation, however, is a natural consequence of a solenoidal shape of a twisted prominence body, which, as mentioned above, approaching the limb may appear in various shapes.

In Chap. 17 we have already used the basic property of magnetized plasma associated with Kruskal-Shafranov law (Shafranov 1956; Kruskal and Kulsrud 1958; Kadomtsev 1966). According to this law long magnetic field configurations having low aspect ratio, i.e., with radius of a magnetic tube being much smaller than its length, are intrinsically unstable unless they wind into a helical shape with nonzero field-aligned current. Accordingly, screw-pinch configuration acquired by long magnetic filament is dynamically stable if a pitch angle of a kinked helical structure, $\theta = B_\phi/B_z$, is such that the safety factor; see (17.1)–(17.3),

$$q \equiv h/L < 1 \quad (20.1)$$

Here L is the length of the structure, and h is the pitch, i.e., a distance in which the field line at running radius R makes one revolution around the axis of filament:

$$h(R) \equiv \frac{2\pi R}{\tan\theta} = \frac{2\pi R B_z}{B_\phi} \quad (20.2)$$

It is important to note that Kruskal-Shafranov condition and Eqs. (20.1) and (20.2) hold on wide range of scales from the Tokamak devices and penumbral filaments to a huge body of prominence. For high latitude quiescent prominences safety factor is always less than unity, i.e., condition for long magnetic configuration to acquire the skewed shape and remain in it is always satisfied. This explains longevity of quiescent prominences. If, however, structure becomes short, i.e., the aspect ratio R/L increases, or B_ϕ weakens, safety factor approaches unity, $q \simeq 1$, and the prominence loses its global stability. This may occur if the prominence body brakes, which may be caused by disappearance of underlying photospheric magnetic elements, served as roots of given portion of prominence. Or, by some reason, the radius of structure (or large part of prominence) increases and reaches a critical point. Global shape of quiescent prominences as a skewed helical solenoid has been captured as early as in 1950s (Severny and Khokhlova 1953; Rothschild et al. 1955).

Sakurai (1976) has measured transverse and line of sight velocity distribution in the prominence observed on 30 August 1971 (Fig. 20.7). These measurements clearly showed a three-dimensional helical structure of prominence body.

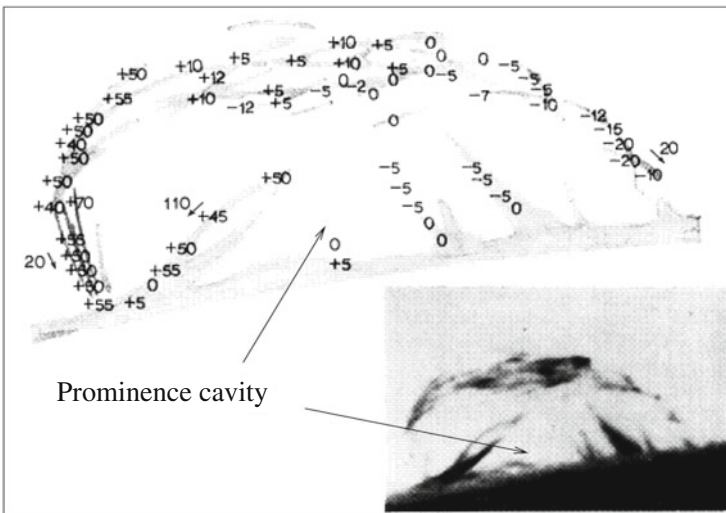


Fig. 20.7 Velocity distribution in the prominence of August 30, 1971 in its remnant loop-system phase. Unit is km s^{-1} and arrows indicate the direction of transverse velocities. This distribution of velocities suggests a three-dimensional helical structure of the prominence. Reprinted from Sakurai (1976) by permission of Oxford University Press/on behalf of the PASJ

Especially prominent signs were seen near the top of the prominence where the upper part exhibited red shifts, while the lower part exhibited violet shifts. He also observed large-scale ascending motions of prominences and, making a direct connection between the ascending motion and rotational motions, interpreted them unilaterally as a result of a screw-pinch instability. In particular, to explain the observed ascending motion of the semi-spherical cavity and its growth, he performed numerical analysis and found a good qualitative agreement with observations. Quantitatively, the range of physical parameters was found also very reasonable.

For illustrative purposes we show some results of Sakurai's numerical calculations in Fig. 20.8, which contains examples of three values of a safety factor, $q = 0.08; 0.14; 0.31$. The unit of time is R/v_A . As expected, the growth of cavity formed by the skewed kink depends on the safety factor, q : a smaller safety factor corresponds to a longer lifetime of the cavity, and respectively the kink may reach higher altitudes.

To address the problem of prominence dynamics and structure formation using high resolution observations, we choose here several exemplary prominences. Some of them are shown in Fig. 20.9. During the observations (of about 5–6 h), each prominence showed various types of cavities, from long-living cavities that reach significant heights (Fig. 20.9 panels a, c, d), to very low lying shallow cavities (panel b). Recall also a huge prominence shown in Fig. 20.6 with series of cavities under its stretched body (marked by white stars).

Despite quite different spatial and temporal characteristics, the dynamics of each cavity's growth and collapse obey simple laws imposed by screw pinch dynamics, providing solid ground for solenoidal helical structures. Note how prominent is a filamentary structure of prominence in all shown cases.

20.3.1 *The Case of the August 16 2007 Prominence*

In order to follow typical regularities seen in all studied cases, we consider the detailed dynamics of the cavity formation and evolution observed on August 16, 2007 prominence. The duration of the observation was about 6 h, cadence 25 s.

Figure 20.10 shows the location of the cavity formation at six intervals. The first panel at UT 16:16 shows the growth phase of the prominence, already noticeable at the beginning of the observation at UT 16:04. The cavity retained its semi-spherical shape as it grew (panel b), until about UT 18:50 when small scale ripples started to appear at the western edge of the prominence/cavity boundary (arrow on panel c shows already well-developed ripples). These quite regular ripples turned out to be an unstable mode that evolved into growing disturbances, resulting in an explosive collapse of the cavity. A full-scale avalanche and collapse of the cavity is shown in panel d. Within about 80 min, a new cavity started to form in about the same area (panel e). Panel f shows the new cavity in its mature phase. The dynamics of new cavity was amazingly similar to its predecessor's behavior.

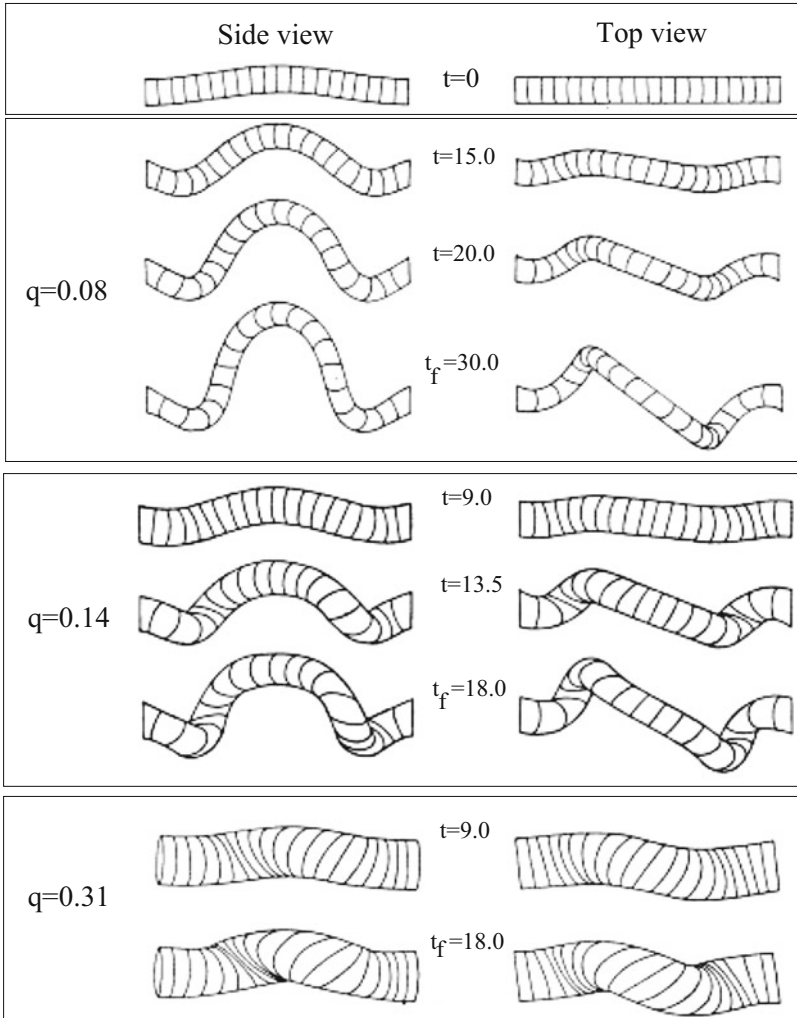


Fig. 20.8 Computed motion of magnetic flux tube with a uniform pinch and no gravity force. The top panel shows a portion of flux tube in the initial time, t_0 . The growth of a kinked helical structure depends on the safety factor, q . A smaller safety factor corresponds to a higher tip of the kinked flux tube (i.e., to a larger cavity). t_f is the time when the cavity stops growing. The unit of time R/v_A . Reprinted from Sakurai (1976) by permission of Oxford University Press/on behalf of the PASJ

To study the temporal variability of the cavity, as a first step, we measure the velocity of a tip of the cavity using the space-time procedure. Figure 20.11 shows August 16, 2007 cavity in its well-developed stage. The red line in panel a is the path and direction of a cut. The lower panel b shows space-time image of the motion of the cavity apex. The cavity grew almost linearly during the first 2 h and then

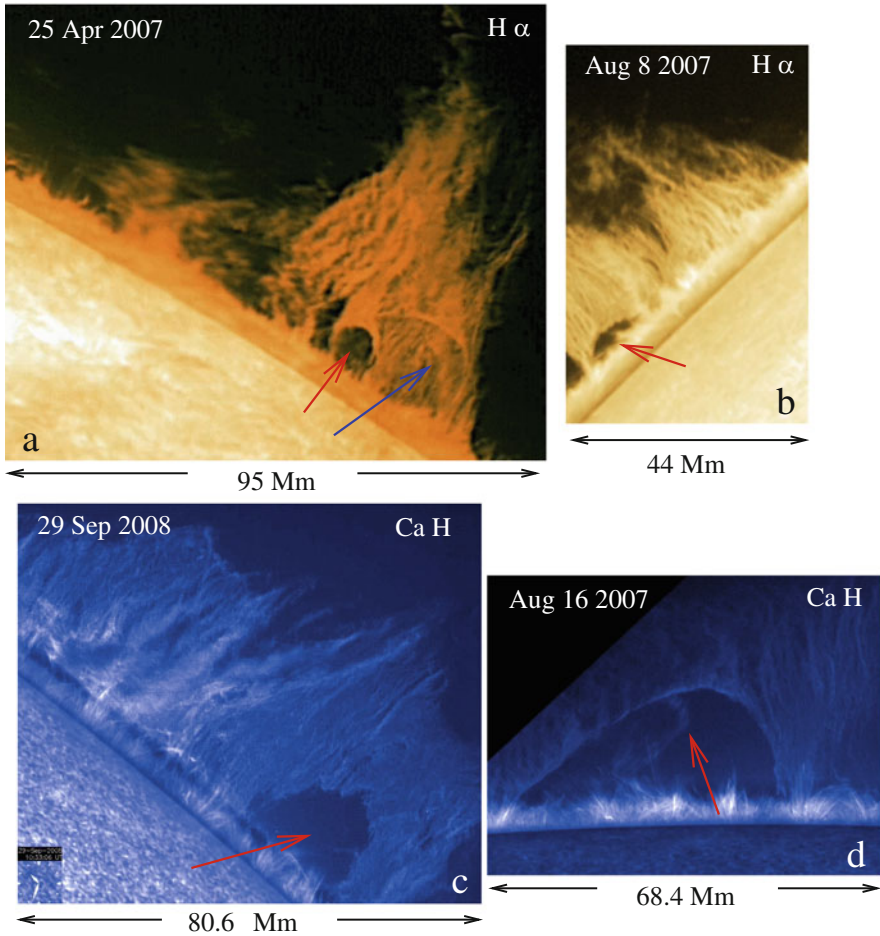


Fig. 20.9 Snapshots of exemplary prominences with various bubble/cavity formations. **(a)** Limb portion of the 25 April 2007 prominence located at the West limb, S 36°; to the south of the well-defined cavity (red arrow) there is another cavity hindered by the frontal hedgerow part of the prominence body (blue arrow); **(b)** Small cavity on the East limb, N 49° having a much shorter lifetime due to the sudden development of an explosive instability; **(c)** Highly dynamic cavity having an almost circular shape observed on 29 September 2008 at the West limb, N 56°; **(d)** Long-lived, “classical” recurring cavity, observed on 16 August 2008 at the West limb, N 54°

started to accelerate. The dotted line corresponds to UT 17:47, the moment when quasilinear growth of the cavity moves into a nonlinear regime.

At about UT 18:48 the height of the cavity apex reaches a maximum and the cavity collapses. In other words, when a semi-spherical cavity with growing radius, R , reaches its maximum, R_{\max} , and its velocity reaches the so-called terminal velocity, \dot{R}_{term} , the cavity quickly collapses. The velocity of the ascending motion in the linear regime is $v_1 \simeq 2.1 \text{ km s}^{-1}$, average velocity during the acceleration phase

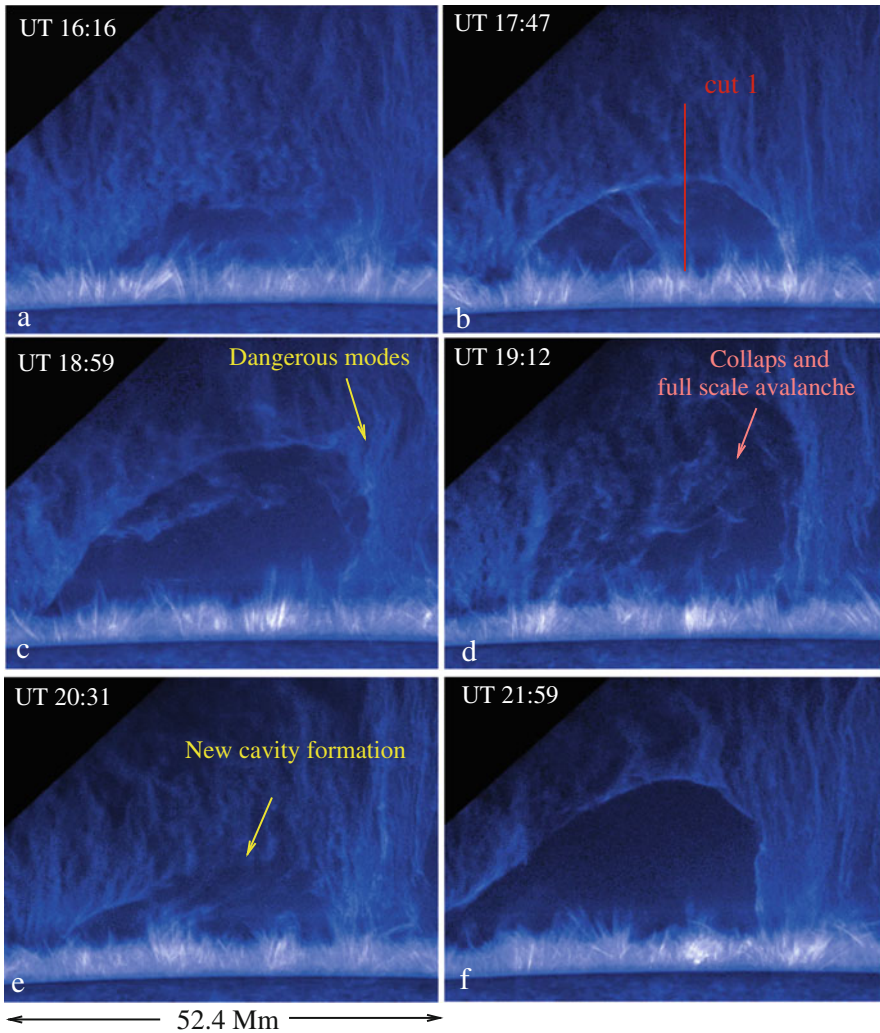


Fig. 20.10 Classical example of cavity formation, dynamics and recurrences, observed on 16 August 2007. The duration of the observation was about 6 h, cadence 25 s. Meaning of images shown in panels from **a** through **f** is explained in text

is $v_2 \simeq 15 \text{ km s}^{-1}$, and collapsing velocity is $v_3 \simeq -25.6 \text{ km s}^{-1}$. As mentioned above, about 90 min after the total collapse a new cavity started to form at the same place (see Fig. 20.10e, f). Recurrence of cavities is quite common and, as we will see below, has a natural explanation.

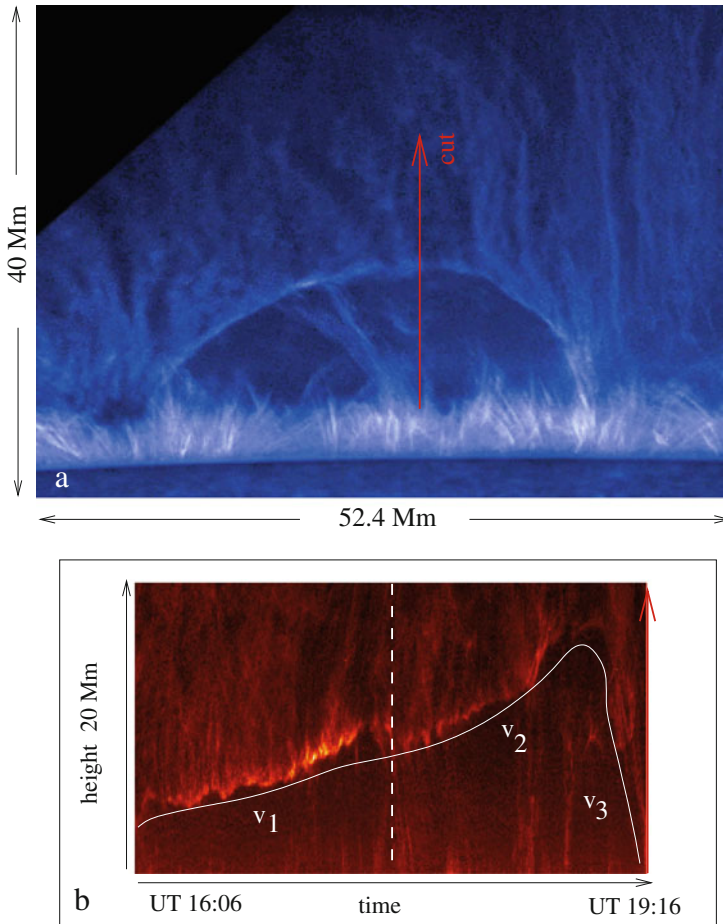


Fig. 20.11 Dynamics of a 16 August 2007 long-lived cavity: **(a)** Snapshot of a well-developed stage just before a linear growth of cavity turned into the accelerated phase; **(b)** Space-time image of the motion of the cavity apex. Dotted line corresponds to UT 17:47, the start of acceleration. Velocity of ascending motion is $v_1 \simeq 2.1 \text{ km s}^{-1}$, average velocity during the acceleration phase is $v_2 \simeq 15 \text{ km s}^{-1}$, and collapsing velocity is $v_3 \simeq -25.6 \text{ km s}^{-1}$

20.3.2 Phenomenology of Cavity Formation

To describe the later stages of an already established semi-spherical cavity and its unsteady motions, we need to consider gravitational forces, nonlinearity, and dissipative effects. Since the semi-spherical shape of the cavity is persistent, even during unsteady motion, it may be described in terms of the Rayleigh-Plesset equation (Rayleigh 1917; Plesset 1949).

The Rayleigh-Plesset equation is the most common nonlinear equation describing the cavitation and bubble dynamics in diverse media including hydrodynamics, laboratory and space plasmas, nuclear reactions and biology. It follows from the compressible Navier-Stokes equations and, being universal, is applicable to various types of cavities, from spherical and semi-spherical bubbles to cavities of very different forms, requiring only minor adjustments mainly related to system parameters (Brennen 1995; Franc and Michel 2004).

Modified for magnetized plasma the Rayleigh-Plesset equation reads as follows:

$$R\ddot{R} + \frac{3}{2}\dot{R}^2 = gR - \frac{2\sigma}{\rho R} - \frac{4\nu}{R}\dot{R}, \quad (20.3)$$

here R is variable radius of cavity (Fig. 20.12a), ρ is the density of the prominence plasma, σ is the surface tension dominated by the magnetic field, $\sigma \simeq (B^2/8\pi^2)hq$, and $\nu = \eta/\rho$ is the viscosity. As earlier, h is the pitch and q is the safety factor. Together they represent a combination of poloidal and toroidal components of magnetic field and the aspect ratio of a solenoidal structure, (20.1) and (20.2).

To see the meaning of the terms in (20.3) as they stand in the Navier-Stokes equation, one can multiply it by a factor ρ/R :

$$\rho\ddot{R} + \frac{3}{2}\rho\frac{\dot{R}^2}{R} = \rho g - \frac{2\sigma}{R^2} - \frac{4\rho\nu}{R^2}\dot{R}, \quad (20.4)$$

it is now evident that the two terms on the left-hand side represent acceleration and inertia, and the three terms on the right-hand side are the gravity force, surface tension, and viscous forces, respectively.

Neglecting the viscosity and using the identity,

$$R\ddot{R} + \frac{3}{2}\dot{R}^2 \equiv \frac{1}{2}\frac{1}{R^2}\frac{d}{dt}(R^3\dot{R}^2), \quad (20.5)$$

(20.3) reduces to a directly integrable form:

$$\frac{d}{dt}(R^3\dot{R}^2) = \frac{1}{2}g\frac{dR^4}{dt} - \frac{2\sigma}{\rho}\frac{dR^2}{dt}, \quad (20.6)$$

or

$$R^3\dot{R}^2 = \frac{1}{2}gR^4 - \frac{2\sigma}{\rho}R^2 + \text{const} \quad (20.7)$$

The integration constant is determined by the initial conditions of the cavity provided by the initial screw pinch configuration and corresponding safety factor.

Equation (20.7) can be further integrated to obtain $R(t)$. Plots of $R(t)$ for two values of safety factor, $q = 0.12$ and $q = 0.14$ are shown in Fig. 20.12b.

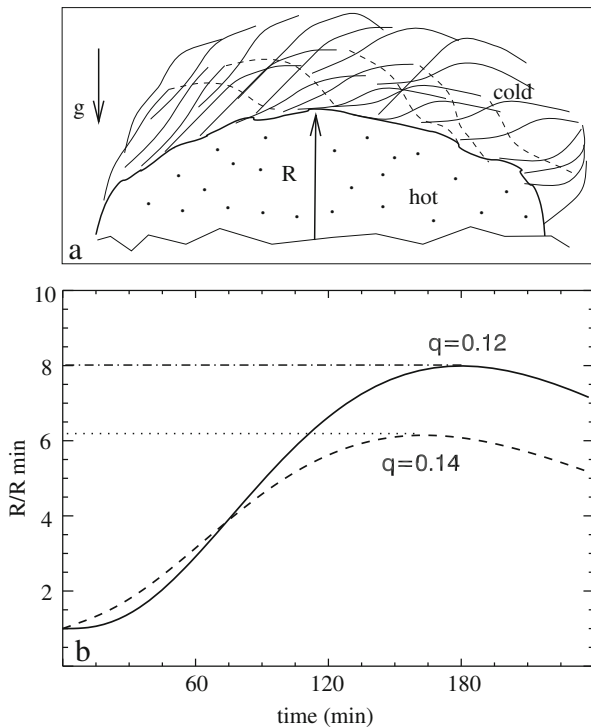


Fig. 20.12 (a) Sketch of the kinked shape of a solenoidal prominence; (b) Solution of the Rayleigh-Plesset equation for the prominence Parameters. R is the radius of a semi-spherical cavity, q is the safety factor

It is important to emphasize that one can estimate the minimum radius of a cavity, R_{\min} , necessary for the cavity to grow. The point is that the appearance of kinks is an integral part of the dynamics of the prominence body but, in order to survive and grow the initial radius must be above some critical value, $R_{\min} \simeq \sqrt{\sigma/\rho g}$. Taking, e.g., $B = 6 \text{ G}$, $h = 20 \text{ Mm}$, $q = 0.12$, $\rho = 8.5 \times 10^{-14} \text{ g cm}^{-3}$, we get $v_A = 58 \text{ km s}^{-1}$, and $R_{\min} \simeq 2.17 \text{ Mm}$. Using the plot corresponding to $q = 0.12$ we see that a cavity with an initial radius of 2.17 Mm would reach terminal velocity and a maximum radius of 17.36 Mm in about 3 h, which agrees well with the measured parameters of August 16, 2007 cavity dynamics.

Note that the presence of $d^2R(t)/dt^2$ in (20.3) is responsible for the recurrent nature of cavity formation.

20.4 Regular Series of Plumes: Multimode Regime of Rayleigh-Taylor Instability

The Rayleigh-Taylor (RT) instability develops when two fluids of different densities accelerating toward each other come into contact (Rayleigh 1883; Taylor 1950). The exemplary case is when a heavy substance with mass density ρ_H lies in a gravity field over a lighter substance with $\rho_L < \rho_H$. The interface between the two media becomes unstable with respect to perturbation with a wave vector $k = 2\pi/\lambda$, such that the growth rate of the instability is

$$v = \sqrt{gk \left[A - \frac{k\sigma}{g(\rho_H + \rho_L)} \right]} \quad (20.8)$$

Here σ is the surface tension, and A is the Atwood number:

$$A = \frac{\rho_H - \rho_L}{\rho_H + \rho_L} \quad (20.9)$$

The RT instability is ubiquitous in a wide range of media from the Earth's atmosphere and soil to laboratory and space plasmas. It is especially evident in quiescent prominences.

The specifics of the RT instability in prominences as in magnetized plasmas are influenced by supporting three-dimensional magnetic fields. Magnetic field effects can be briefly described as follows (Chandrasekhar 1981):

- I. The magnetic field parallel to gravity ($\mathbf{B} \parallel g$) has different effects on long and short wavelengths. Long wavelengths are unaffected. The growth rate is

$$v = \sqrt{Agk} \quad (20.10)$$

Short wavelengths are restricted by the following growth rate:

$$v = (g/V_A) [\sqrt{\rho_H/(\rho_H + \rho_L)} - \sqrt{\rho_L/(\rho_H + \rho_L)}] \quad (20.11)$$

- II. The magnetic field transverse to gravity ($\mathbf{B} \perp g$) has a strong effect on the RT instability and may well stabilize it. The growth rate is as follows:

$$v^2 = gk \left[\frac{\rho_H - \rho_L}{\rho_H + \rho_L} - \frac{B^2 k_x^2}{2\pi(\rho_H + \rho_L)gk} \right], \quad k^2 = k_x^2 + k_y^2 \quad (20.12)$$

In this case, the magnetic field creates a “surface tension” and limits the instability ($v^2 > 0$) at a critical wavelength, λ_c :

$$\lambda_c^2 = \frac{B^2}{g(\rho_H - \rho_L)} \cos\theta \quad (20.13)$$

where θ is the inclination of the wave vector $\mathbf{k}(k_x, k_y)$ to the direction of \mathbf{B} , $k_x = k\cos\theta$, $k_y = k\sin\theta$. Note that the orientation of the x, y plane was chosen in such a way that the uniform magnetic field be along the x -axis (Chandrasekhar 1981).

Thus, perturbations with wavelengths $\lambda < \lambda_c$ are stable with respect to the RT instability. Instability on a scale L parallel to the field thus requires that magnetic field be below some critical value:

$$B < B_c \equiv \sqrt{Lg(\rho_H - \rho_L)/\cos\theta} \tag{20.14}$$

A magnetic field component stronger than B_c that is transverse to gravity suppresses the RT instability. This fact is very useful to estimate the magnetic field in cases when the RT instability is fully developed.

Depending on system parameters, the instability may evolve in several branches, most typically in a multimode regime where the interface between the heavy and light components breaks into a series of plumes and spikes separated by the characteristic wavelength. Examples of a multimode regime are shown in Fig. 20.13

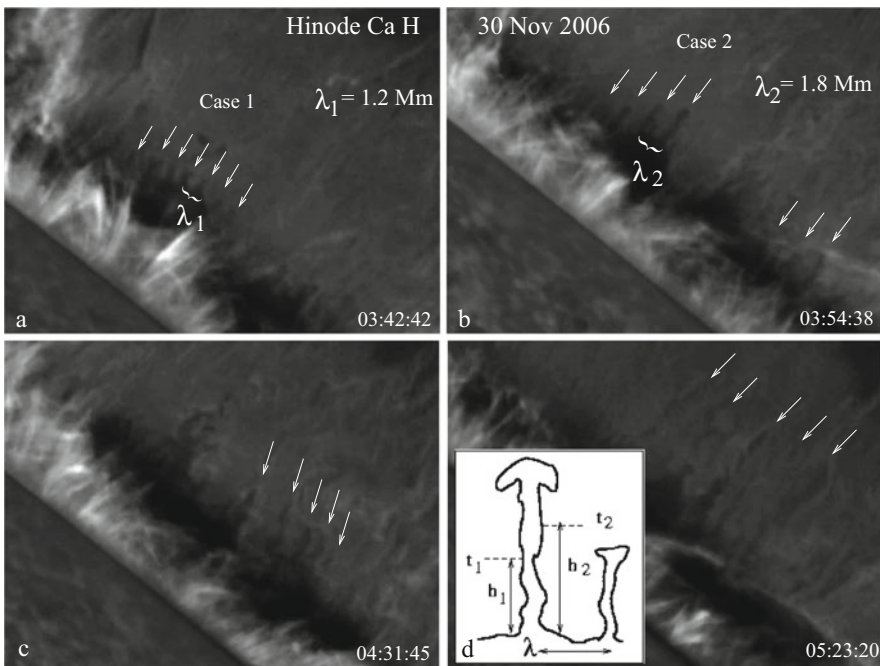


Fig. 20.13 Examples of Rayleigh-Taylor instability with necessary attributes: self-similarity of plumes in family, similarity of the wavelength/height ratio in different families. Inset in last panel shows a way to directly measure the growth rate from observations. Meaning and notations presented in panels a through d are explained in text

(see also Fig. 20.14 below). One can see that all of the necessary features of a classical RT instability are in place:

1. A multimode front (seen in all four panels, a–d in Fig. 20.13 and marked by arrays of small arrows);
2. Self-similarity of plumes in one family;
3. Similarity ratio of wavelength/height in different families (i.e., larger wavelength, higher plumes);
4. Suppression of the regular oscillations of filaments comprising the prominence (see Fig. 20.14).

20.4.1 Practical Use

The universality of the RT instability in prominences allows direct comparison of observations and theory. The most reliable parameter is the growth rate. The height of the plume during its linear and quasilinear growth changes with time as

$$h(t) = h_0 \exp[-\nu_{\text{obs}}(t - t_0)] \tag{20.15}$$

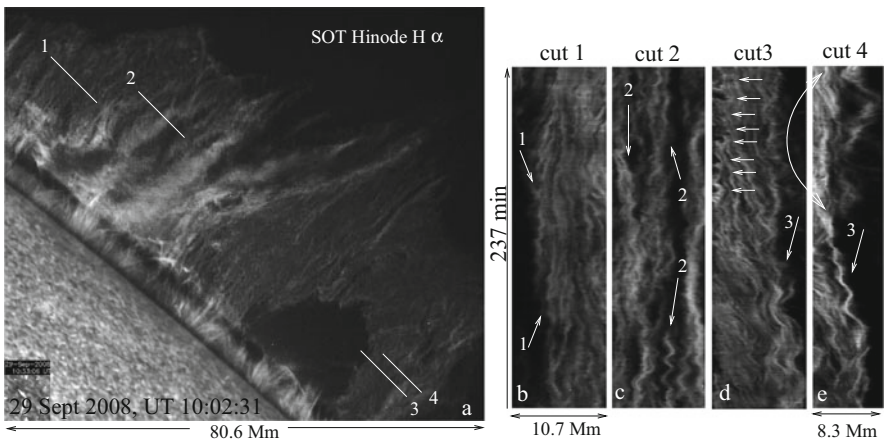


Fig. 20.14 Effect of Rayleigh-Taylor instability on regular oscillatory motions of filaments comprising prominences. (a) Sept. 2008 prominence with space-time cuts. (b), (c) Cuts 1 and 2 show a regular oscillatory pattern seen in all observed prominences. (d), (e) Cuts 3 and 4 show the region where the RT instability broke into plumes (array of small arrows) and destroyed the regular oscillatory pattern (curved arrow)

Measuring the heights of the plume, h_i , at an arbitrary times, t_i , one finds the growth rate:

$$v_{\text{obs}} = \frac{1}{t_2 - t_1} \ln(h_2/h_1) \quad (20.16)$$

The inset in Fig. 20.13 illustrates this simple procedure. High cadence data easily allow to measure dozens of (h_i, t_i) pairs in each family of plumes and accurately calculate growth rates.

The beauty of this procedure is that one can do these measurements many times during the lifetime of a regular array of finger-like plumes, and compare the calculated growth rates. As a result, one may easily find when the linear or quasilinear regime ends and the system goes to a weak nonlinear regime. This happens when the growth rate, being quite constant during the linear regime, starts to change. If a strong nonlinear regime develops, this will correspond to turbulence in the medium and the disappearance of the vertical, finger-like structures from the plasma.

In order to compare the measured value of v_{obs} with the theoretical growth rate, one can use (20.12) written in the form

$$v_{\text{th}} = \sqrt{\frac{2\pi g}{\lambda} A \left[1 - \frac{B^2 \cos^2 \theta}{(\rho_H - \rho_L) g \lambda} \right]} \quad (20.17)$$

where the magnetic field is perpendicular to the gravity force. It is important to note that v_{th} itself contains directly measurable parameters, primarily the wavelength, λ . Also, the Atwood number, A , can be quite accurately estimated as it only varies between 0.8–0.96.

Consider two examples shown in Fig. 20.13a, b. Empirical measurements for case 1 give $v_1 = 8.06 \times 10^{-3} \text{ s}^{-1}$ and for case 2 $v_2 = 6.07 \times 10^{-3} \text{ s}^{-1}$. For theoretical estimates, we take $\rho_H = 8.5 \times 10^{-14} \text{ g cm}^{-3}$, $\rho_L = 1.7 \times 10^{-15} \text{ g cm}^{-3}$, $|B| = 6 \text{ G}$, and $\theta = 85^\circ$; then, for $\lambda_1 = 1.2 \text{ Mm}$, $v_{\text{th}} \simeq 9.2 \times 10^{-3} \text{ s}^{-1}$, and for $\lambda_2 = 1.8 \text{ Mm}$, $v_{\text{th}} \simeq 7.5 \times 10^{-3} \text{ s}^{-1}$, which are in good agreement with the measured values.

Note that, as measurements of the growth rate are simple and reliable, comparison of v_{obs} and v_{th} may be used to infer magnetic field and its direction.

The relationship between the RT plumes and the regular oscillatory pattern observed in the body of a prominence can also be used for quantitative analysis. This approach has a wide and very rich applications for prominence studies. Here we only demonstrate the relationship between the RT plumes and the regular oscillatory pattern. Figure 20.14 shows a typical example, represented by a prominence observed on September 29, 2008 (panel a). Panels b and c and the lower parts of panels d and e show typical oscillations of thin filaments comprising the prominence body.

Prominences with a large projection on the sky show filament oscillations in a wide range of frequencies. In this particular example periods are as follows: $T_1 \simeq 380 \text{ s}$ (panel b), $T_2 \simeq 680 \text{ s}$ (panel c), and $T_3 \simeq 1040 \text{ s}$ (panels d and e).

Note that in all cases, the period of oscillations in one “neighborhood” is nearly constant reflecting more or less uniform physical conditions in a given area (arrows 1, 2, 3). The last two panels show the effect of the RT instability on the long-lasting oscillations of the filamentary medium: the appearance of RT plumes quickly destroys the regular oscillatory pattern (curved arrow in panel e).

20.5 Fast-Growing Plumes: Nonlinear Regime

The Kelvin-Helmholtz (KH) instability develops in the presence of shear flows at the interface of two media with different densities and has several branches depending on the dispersion, dissipation, and other physical parameters of the medium (see Chap. 5). Obviously, the highly dynamic cavity/prominence interface as border line between two very different media must be a subject of shear flows and thus various instabilities. The cavity/prominence interface therefore is a natural place to expect, in particular, a manifestation of the KH instability. The most readily excitable mode that may lead to a KH instability is a kink mode, $m = \pm 1$. The corresponding dispersion relation in presence of shear flows with velocity u has a form:

$$D(\omega, k) \equiv \omega_{\pm} - \frac{k}{1 + \eta} \left[u \pm \sqrt{\eta[(1 + \eta)v_A^2 - u^2]} \right] = 0 \quad (20.18)$$

Here $\eta = \rho_L/\rho_H$, with indices L and H indicating “light” and “heavy” plasmas. Note that in the corona, the scale height is $\Lambda \geq 50$ Mm and the linear amplitude of oscillations is $\simeq 0.5$ – 1 Mm. This means that the effect of gravity is negligible.

A gross, linear KH instability, when the square root term in the dispersion relation (20.18) becomes imaginary, requires super-Alfvénic shear flows:

$$u > u_c^{(2)} = v_A \sqrt{1 + \eta} \quad (20.19)$$

A much more dangerous branch of the KH instability produces negative energy waves (see Chap. 5). NEWs occur when the system is stable with respect to a linear KH instability, i.e., at sub-Alfvénic velocities when $u < v_A \sqrt{1 + \eta}$, but $\partial D/\partial \omega < 0$. In this case, the energy of kinked perturbations becomes negative and the damping rate turns into a growth rate.

Indeed, the energy density of kink perturbations in the presence of flows has a form:

$$W = \frac{1}{2} \rho_H \zeta^2 k^2 \left[(1 + \eta) \frac{\omega^2}{k^2} + \eta v_A^2 - u^2 \right] \frac{v^2 \pm uv}{1 + \eta} \quad (20.20)$$

where ζ is the amplitude of perturbations. For convenience, we have defined $v = \sqrt{\eta[(1 + \eta)v_A^2 - u^2]}$. Substituting the expression ω^2/k^2 from the dispersion

relation into this equation and taking the lower sign, i.e., considering the case when the system is stable with respect to the linear KH instability, we have:

$$W = \rho_H \zeta^2 k^2 (\eta v_A^2 - u^2) \frac{v}{v + u} \tag{20.21}$$

Obviously, the energy of the wave becomes negative as soon as $u > v_A \sqrt{\eta}$; thus, the interval of shear flow velocities, $v_A \sqrt{\eta} < u < v_A \sqrt{1 + \eta}$, corresponds to a branch of NEWs that are subject to explosive growth (Ryutova 1988).

Recall that the most remarkable property of NEWs is that the action of any dissipative mechanism which provides an energy loss leads to growth of their amplitudes (Coppi et al. 1969; Ryutova 1988, 2006). In this regime, any dissipative effects turn linear perturbations into explosively growing disturbances. In a few inverse growth rates of explosive instability, higher nonlinear effects are initiated and provide stability. This competition often leads to the formation of a classical mushroom cap.

20.5.1 Mushroom Formation

An example of this regime is shown in Hinode $H\alpha$ data of the August 8, 2007 prominence (Fig. 20.15). The perturbed cavity/prominence boundary shows a regular rippling mode that lasts over 3 min. In general, the duration of the linear regime is arbitrary and may last much longer. In this particular case at about UT 20:02:33, a strong distortion of the interface appears. The distortion starts to grow while still remaining close to the quasilinear regime. At UT 20:03:04, enhanced disturbances become dominant, suppressing the rippling mode (shown by arrows a

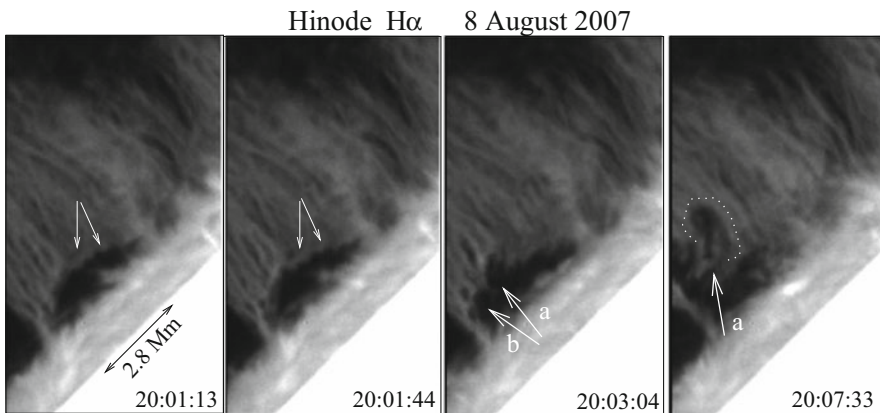


Fig. 20.15 Growth of ripples into explosively growing disturbances and their stabilization phase taking a typical mushroom form

and b in Fig. 20.15). Just before UT 20:06:04, slowly growing disturbances show explosive growth and, in about 90 s, acquires a mushroom form, typical to the explosive phase of the KH instability (UT 20:07:33).

The growth rate of the explosive instability is (Ryutova 1988, 2006):

$$v_{\text{expl}} \simeq \alpha \frac{\tilde{v}_{ei}}{\ln(|W|/|W_0|)} \quad (20.22)$$

where α is a parameter of the order of unity, $\alpha(T, l, n) \simeq 1$, and $\tilde{v}_{ie} = (m_e/m_p)v_{ie}$ is the inverse slowing-down time of particles via electron-ion collisions. For $T = 10^6$ K, and $n = 5 \times 10^{10} \text{ cm}^{-3}$, $\tilde{v}_{ie} = 2.7 \times 10^{-2} \text{ s}^{-1}$. The logarithmic energy increase may be estimated by measuring the initial (linear) and final (explosive) amplitudes of the perturbation: $\ln(|W|/|W_0|) \simeq \ln(\zeta^2/\zeta_0^2)$ (cf. Eq. (20.21)). For our chosen example, $\zeta_0 \simeq 0.5 \text{ Mm}$ (Fig. 20.15, UT 20:01:44), $\zeta \simeq 2.2 \text{ Mm}$ (UT 20:07:33). This gives:

$$v_{\text{expl}} \simeq 9.07 \times 10^{-3} \text{ s}^{-1}, \quad (20.23)$$

and the characteristic time of the explosive growth of a single plume acquiring e -times amplitude is 110 s, very close to the observed times in general and to the measured time of August 8, 2007 explosive event, in particular. We can also estimate ranges of shear velocities leading to the development of the explosive phase:

$$v_A \sqrt{\eta} < u < v_A \sqrt{1 + \eta} \quad (20.24)$$

With $n_L = 5 \times 10^{10} \text{ cm}^{-3}$, $n_H = 10^9 \text{ cm}^{-3}$, $\eta = n_L/n_H = 0.02$, and for magnetic field values such that $B = 4; 6; 10 \text{ G}$, $v_A = 39; 58.6; 97.7 \text{ km s}^{-1}$, we find at any $u_c^{(1)} = v_A \sqrt{\eta} = 5.5, 8.3, 13.8 \text{ km s}^{-1}$, rippling modes are subject to the explosive branch of the KH instability.

One must bear in mind that there are several important differences between the KH (both linear and explosive branches) and RT instabilities. The main feature of the RT instability is the development of a *series of self-similar plumes*, characterized by the specific wavelength, that corresponds to the distance between family “members.” The KH instability, especially in its nonlinear explosive phase is characterized by the dominance of a *single plume*, breaking through the prominence body. Another typical example of this is shown in Fig. 20.16.

The growth rates of such single disturbances, as well as their dimensions, significantly exceed those formed by the RT instability. Their energy content as well is much higher than the energy content of individual plumes in the RT case. We believe that under some extreme conditions, an explosive phase of the KH instability may be responsible for triggering CMEs associated with quiescent prominences.

It is important that the observation of prominence dynamics offers one of the most efficient and reliable diagnostic tools. This is provided by the fact that the details of the prominence dynamics is easy to distinguish and analyze them, using

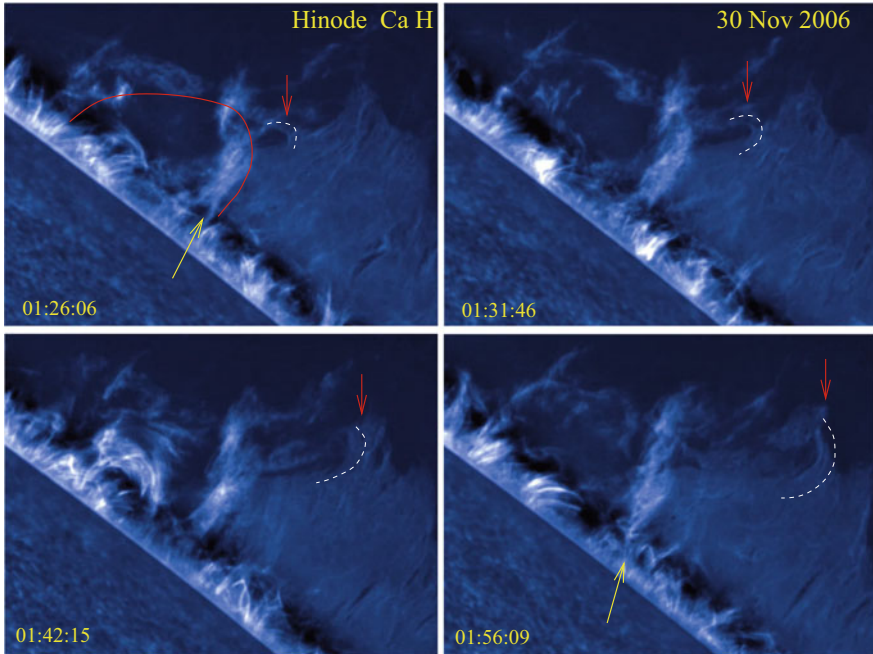


Fig. 20.16 One of the 30-Nov-2006 prominence cavities, partially blocked by the bright gable (shown by thick yellow arrows). The linear growth of a single plume lasted over 10 min. At about UT 01:40:06, it started to accelerate taking the form of a post-explosion mushroom cap (denoted by red arrows)

directly measurable parameters. It is interesting that determination of prominence plasma β from the dynamics of plumes is also possible (Hill et al. 2012).

20.5.2 Bubble Competition

Neighboring bubbles being at close vicinity must inevitably interact. Competition between the neighboring bubbles is natural process and can also serve as a diagnostic tool. Example of such an event is shown in Fig. 20.17. One can see in fact three neighboring bubbles, but their life history shows that interaction between two of them (marked by solid arrows, 1 and 2) turns out to be dominant and eventually destroys the lower bubble (marked by dashed arrow, 3). The measured (average) velocities of bubbles 1 and 2 are, respectively, $u^{(1)} \simeq 5.1 \text{ km s}^{-1}$ and $u^{(2)} \simeq 14.8 \text{ km s}^{-1}$. The merging time, $\tau = 5 \text{ min } 54 \text{ s}$.

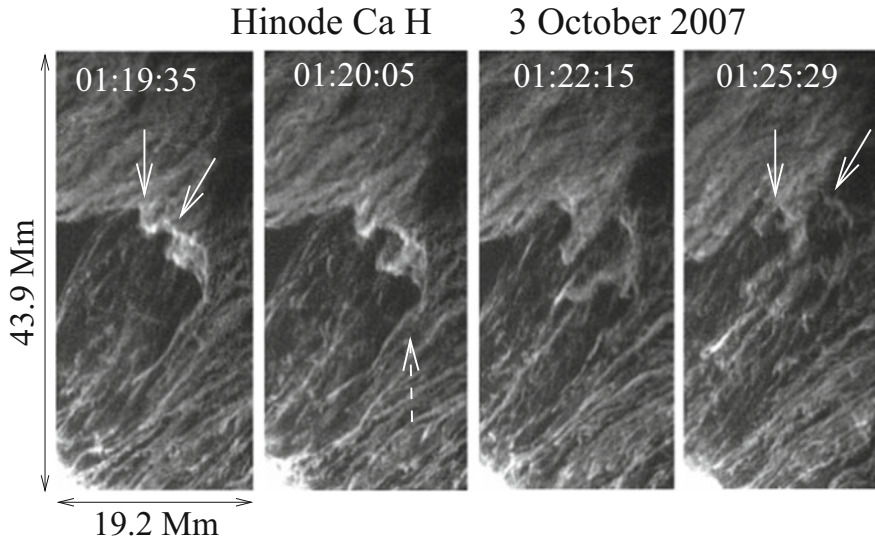


Fig. 20.17 Two bubble competition captured by Hinode on 3 September 2007. Bubbles 1 and 2 eventually merge destroying the third neighbor bubble 3. See details in text

Theoretical merger time is

$$\tau_{\text{merg}} = \frac{\Delta u}{0.1Ag} \quad (20.25)$$

where Δu is the velocity difference of the neighboring bubbles, A is an Atwood number (20.9), and g is the gravitational constant. Using measured difference of velocities, $\Delta u = 9.7 \text{ km s}^{-1}$, for $A = 0.9$, we get for the merging time $\tau = 6 \text{ min } 33 \text{ s}$ which is reasonably close to observed time.

20.6 Greenhouse-Like Effect

Unlike previous observations limited by the two-dimensional view of the prominence projection on the sky, new space missions opened the opportunity to observe the central portion of prominence body, located on the disk, in high resolution and contrast. These observations give unprecedented information on the prominence nature and dynamics.

Figure 20.18 shows the prominence body stretched across the disk at two instances of time: in its initial raising phase at UT 06:50:03 (top), and at UT 08:46:03, when prominence material is high enough to create a huge cavity underneath (bottom, dotted area, see also Fig. 20.3). Formation of cavities under

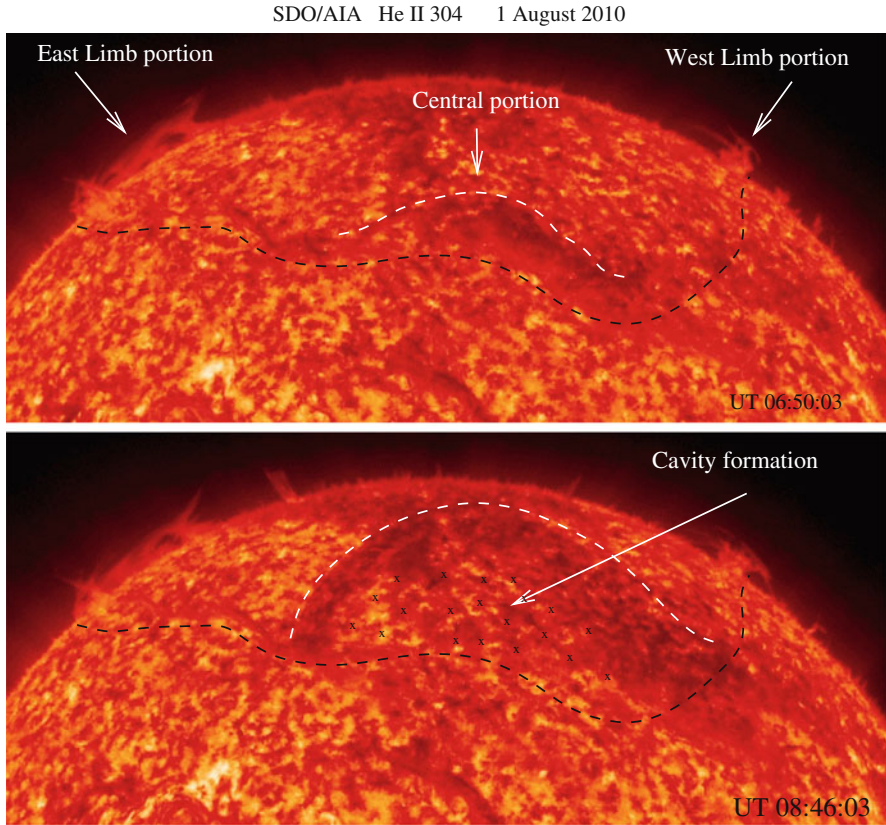


Fig. 20.18 Snapshots of 1 August 2010 prominence at two instances of time: in its initial raising phase at UT 06:50:03 (top), and at UT 08:46:03, when prominence material is high enough to create a huge cavity underneath (bottom, dotted area)

the prominence body filled by the coronal plasma is an integral part of the three-dimensional helical structure of the prominence.

To reveal the true helical structure of the prominence body, it is useful to make a difference movie subtracting images taken at different time intervals. Figure 20.19 shows examples extracted from the movie made in the AIA 171 Å with 120 s difference between the consequent images. The fragments of two snapshots are shown at UT 08:14:13 and UT 08:54:13. At UT 08:14:13 the prominence has been already lifted high enough to leave underneath a well-developed cavity.

Strongly curved prominence body clearly shows a well-preserved three-dimensional helical structure. Raising higher, the prominence solenoid grows further with enhanced twist of its solenoidal body (cf. a sketch shown in Fig. 20.12a).

At about UT 11:38:13 the prominence disappears from 171 wavelength (Fig. 20.20 bottom), which means that plasma with temperatures around 6.3×10^5 K

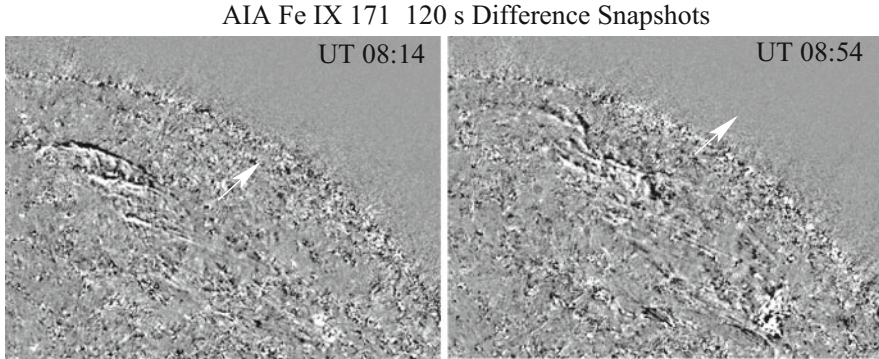


Fig. 20.19 Three-dimensional picture of the prominence clearly exhibiting a solenoidal filamentary structure. The snapshots are obtained from AIA 171 Å movie made with 120 s difference between the consequent frames

is replaced by the plasma having much higher temperatures. This is seen in the top panel of Fig. 20.20. Here, in a huge cavity left behind, the plasma, concentrated *under* the prominence body, has the temperature in the range of $1.26 \times 10^6 - 2 \times 10^7$ K. Thus, the prominence body covering the cavity works as a lid over the boiling substance.

In other words, when the space where cavity is formed gets quickly filled by the surrounding coronal plasma, the prominence body acting as a lid, and producing the effect similar to greenhouse effect, leads to significant increase of the temperature of the captured plasma. Note that a compact coronal loop arcades overlying the polarity inversion line (black dashed line in Fig. 20.18) are clearly seen in whole range of temperatures from 6.5×10^5 to $1.26 \times 10^6 - 2 \times 10^7$ K.

Concluding this chapter we note again that high-resolution and high cadence data from satellites allow to study the dynamics of quiescent prominences and, in particular, to identify manifestation of fundamental plasma instabilities. Data compiled in movies of several hours duration show both slow processes and short-lived events and their possible long-term recurrences. Many processes occurring at different stages of prominence evolution are found to be common for all studied cases. Having universal character, these processes can be related to fundamental plasma instabilities. One can combine the observational evidence and theory to identify these instabilities and perform quantitative analysis.

A fundamental puzzle associated with the dynamic stability of quiescent prominences suspended in rarefied coronal plasma seems to be only natural occurrence. If we consider, however, only the part of the prominence projected on the sky when observed at the limb, this puzzle can hardly be solved. On the other hand, if we look at the problem as being part of the global structure of the prominence body stretched along the entire latitude over the polarity inversion line, we immediately come to a simple solution. Indeed, in accordance with well-known facts from basic plasma physics, a three-dimensional magnetic field configurations with small aspect

1 August 2010 UT 11:38:13

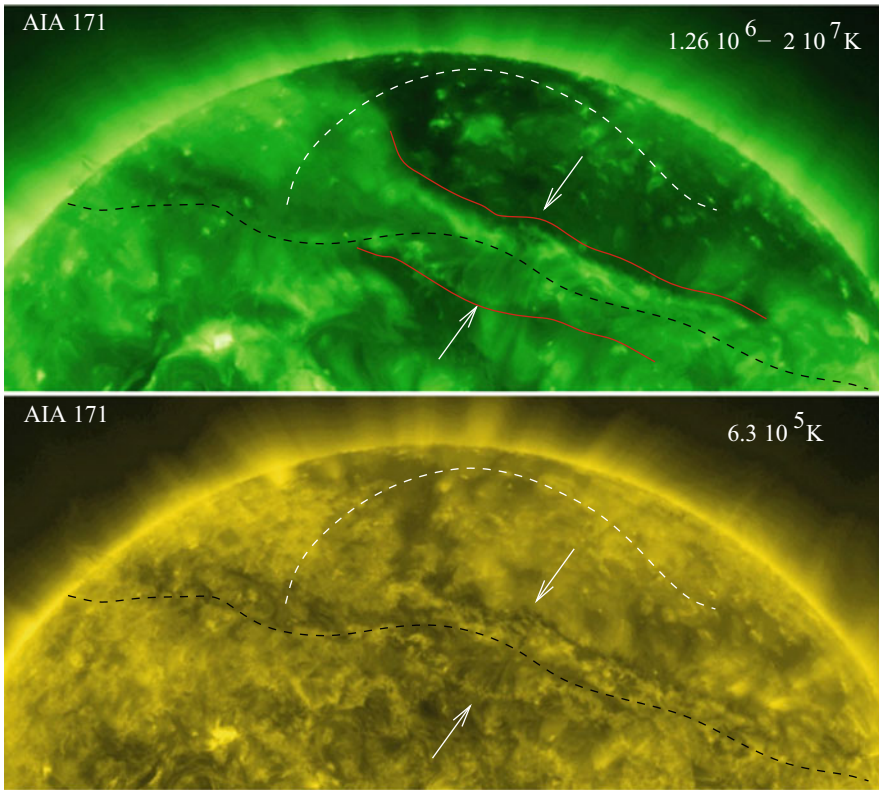


Fig. 20.20 Greenhouse-like effect: A curved prominence body moving upward (white dashed curves) leaves behind a cavity which is quickly filled by the surrounding coronal plasma. But the prominence body acts as a lid to captured plasma whose temperature quickly raises. Top panel shows a million degree plasma under cavity (read lines), while cooler, 171 Å plasma fills the entire disk more or less evenly (bottom). Black dashed line is a polarity inversion line. The white dashed line shows earlier location of lifted prominence

ratios ($R/L \ll 1$) are intrinsically unstable with respect to screw pinch instabilities, and, to survive, must wind into a helical shape with pitch angle determined by the aspect ratio, and magnetic field components.

Once the helical shape is acquired, the screw pinch configuration is dynamically stable and long-lived as long as a safety factor $q < 1$. Most importantly, a skewed helical structure in a gravitational field is subject to kinking. The process of skewing leads to formation of prominence cavities under the prominence body which are quickly filled by hot coronal plasma. This creates the illusion of levitation of a heavy prominence material above the rarefied coronal plasma. In other words, formation of kinks observed as under-prominence cavity formation is only natural occurrence. The maximum height of a kink is, again, determined by a safety factor: the smaller

the safety factor, the “taller” the kink grows. Note this process does not contradict previous models of prominences based on arcades of three-dimensional magnetic field supporting prominence material.

Process of cavity formation and raising motion of prominence body is also associated with phenomenon similar to greenhouse effect: when the space where cavity is formed gets quickly filled by the surrounding coronal plasma, the prominence body “sitting” over the cavity holds additional energy coming from below acting as a stopper and leading to further increase of the temperature of underlying, already hot plasma.

20.7 Problems

20.1 Derive Rayleigh-Plesset equation for spherical bubble pulsating in the field of sound. Consider the case of an incompressible fluid. Use the bubble radius $R(t)$ as the dynamic parameter. The temperature and pressure far from the bubble being T_∞ and $p_\infty(t)$. The fluid temperature, density, ρ_L . and the dynamic viscosity, μ_L are assumed to be constant. The temperature, $T_B(t)$, and pressure, $p_B(t)$, within the bubble are uniform (Brennen 1995).

20.2 Consider an analogy between the prominence levitating over much hotter coronal plasma and the liquid droplets levitating on their own vapor over extremely hot surface (Leidenfrost drops).

References

- T.E. Berger et al., *Astrophys. J.* **676**, L89 (2008)
 T.E. Berger et al., *Astrophys. J.* **716**, 1288 (2010)
 C.E. Brennen, *Cavitation and Cavity Dynamics* (Oxford University Press, Oxford, 1995)
 J. Carlyle et al., *Astrophys. J.* **782**, 87 (2014)
 S. Chandrasekhar, *Hydrodynamic and Hydromagnetic Stability* (Dover Publications, Inc. New York, 1981)
 B. Coppi, M.N. Rosenbluth, R. Sudan, *Ann. Phys.* **55**, 201 (1969)
 P. De Bruyne, A.W. Hood, *Sol. Phys.* **147**, 97 (1993)
 A.Z. Dolginov, V.M. Ostryakov, *Astron. Zh.* **57**, 1302 (1980)
 M. Druckmüller et al., *Astrophys. J.* **785**, 14 (2014)
 J. Dudík et al., *Astrophys. J.* **761**, 9 (2012)
 L. Feng, B. Inhester, W.Q. Gan, *Astrophys. J.* **774**, 141 (2013)
 B.H. Fong, O.A. Hurricane, S.C. Cowley, *Sol. Phys.* **201**, 93 (2001)
 J.-P. Franc, J.-M. Michel, *Fundamentals of Cavitation* (Kluwer, Dordrecht, 2004)
 A. Hillier, R. Hillier, D. Tripathi, *Astrophys. J.* **761**, 106 (2012)
 B.B. Kadomtsev, in *Reviews of Plasma Physics*, vol. 2, ed. by M.A. Leontovich (Consultants Bureau, New York, 1966), p. 153
 R. Kippenhahn, A. Schlüter, *Z. Astrophys.* **43**, 36 (1957)
 M.D. Kruskal, R.M. Kulsrud, *Phys. Fluids* **1**, 265 (1958)
 M. Kuperus, *Sol. Phys.* **169**, 349 (1996)

- M. Kuperus, M. Raadu, *Astron. Astrophys.* **31**, 189 (1974)
B.C. Low, *Astrophys. J.* **408**, 689 (1993)
B.C. Low, G.J.D. Petrie, *Astrophys. J.* **626**, 551 (2005)
D.H. Mackay, A.A. van Ballegoijen, *Sol. Phys.* **260**, 321 (2009)
T. Magara, *Astrophys. J.* **549**, 608 (2001)
R. Matsumoto, T. Tajima, K. Shibata, M. Kaisig, *Astrophys. J.* **414**, 357 (1993)
Y. Ohman, *Sol. Phys.* **23**, 134 (1972)
M.S. Plesset, *J. Appl. Mech.* **16**, 277 (1949)
E.R. Priest, *Dynamics and Structure of Quiescent Solar Prominences* (Kluwer, Dordrecht, 1988)
L. Rayleigh, *Proc. Lond. Math. Soc.* **14**, 170 (1883)
L. Rayleigh, *Philos. Mag.* **34**, 94 (1917)
K. Rothschild, J.C. Pecker, W.O. Roberts, *Astrophys. J.* **121**, 224 (1955)
D. Rust, A. Kumar, *Sol. Phys.* **155**, 69 (1994)
M.P. Ryutova, *Sov. Phys. JETP* **67**(8), 1594 (1988)
M.P. Ryutova, *J. Geophys. Res.* **111**, A09102 (2006)
M.P. Ryutova et al., *Sol. Phys.* **267**, 75 (2010)
T. Sakurai, *Publ. Astron. Soc. Jpn.* **28**, 177 (1976)
A.B. Severny, V.L. Khokhlova, *Publ. Crimean Astrophys. Obs.* **10**, 9 (1953)
V.D. Shafranov, *At. Energy* **30**, 38 (1956)
H.R. Strauss, D.W. Longcope, *Sol. Phys.* **149**, 63 (1994)
E. Tandberg-Hanssen, *The Nature of Solar Prominences* (Kluwer, Dordrecht, 1995)
G.I. Taylor, *Proc. R. Soc. Lond. Ser. A* **201**, 192 (1950)
A. van Ballegoijen, P. Martens, *Astrophys. J.* **361**, 283 (1990)
B. Vrsnak, V. Ruzdjak, R. Brajsa, A. Dzibur, *Sol. Phys.* **116**, 45 (1988)
L. Xing et al., *Astrophys. J.* **752**, L22 (2012)

Chapter 21

Laboratory Experiments Scaled to Solar and Space Plasmas



Abstract Modern experimental facilities with their precision diagnostic tools and ability to accurately control the system parameters may be used to mimic various astrophysical processes and applying high repetitive rate, change parameters of a system, and identify missing elements in physics of studied phenomena. In order to apply laboratory results to astrophysical phenomena one needs to satisfy similarity criteria (Ryutov et al., *Plasma Phys Control Fusion* 54:105021, 2012). In this chapter we first describe the MHD type similarities and then briefly discuss several exemplary experiments, such as studies of magnetically driven plasma jets, bow shocks, magnetic field generation and self-organization, instabilities, and formation of solar tadpoles. The main goal of this chapter is to bring attention of solar physicists to excellent results obtained in laboratory astrophysics and, using simple scaling criteria, apply these results to observational data.

21.1 Criteria for Scaled Laboratory Experiments of Astrophysical MHD Phenomena

Similarity theory has many aspects and uses, such as dynamical Euler similarity for hydrodynamics and Euler-Alfvén similarity for MHD processes, Sedov-Taylor similarity, self-similarity, and others. In laboratory experiments, the spatial and temporal scales are 10–20 orders of magnitude less than that in the astrophysical objects. An important question arises about the degree of confidence with which one can apply the laboratory results to astrophysical phenomena (Ryutov et al. 2000, 2001, 2012; Remington et al. 2006). There are two main conditions that need to be satisfied for reliable similarity criteria. First, dissipative processes such as viscosity, thermal conductivity, and radiative cooling should be unimportant (although the presence of shocks is allowed). Second, regarding thermodynamics, the gas in both systems should be polytropic, that is, the internal energy should be proportional to the pressure. This is so-called Euler similarity, as it directly follows from the Euler equations for the polytropic gas (Ryutov et al. 1999). The similarity between two systems can be established also within the framework of ideal MHD,

i.e., Euler-Alfvén similarity given the same limitations on the thermodynamic properties of the systems hold.

21.1.1 Similarity Criteria in the Ideal MHD

For convenience we bring here again the ideal MHD equations

$$\frac{\partial \rho}{\partial t} + \nabla \cdot \rho \mathbf{v} = 0 \quad (21.1)$$

$$\rho \left(\frac{\partial \mathbf{v}}{\partial t} + \mathbf{v} \cdot \nabla \mathbf{v} \right) = -\nabla p + \frac{1}{4\pi} (\nabla \times \mathbf{B}) \times \mathbf{B} \quad (21.2)$$

$$\frac{\partial \mathbf{B}}{\partial t} = \nabla \times (\mathbf{v} \times \mathbf{B}) \quad (21.3)$$

and the energy equation for the polytropic gas,

$$\frac{\partial p}{\partial t} + \mathbf{v} \cdot \nabla p = -\gamma p \nabla \cdot \mathbf{v} \quad (21.4)$$

It is easy to verify that the set of (21.1)–(21.4) remains invariant under the following transformation of variables (transformed quantities are marked with the subscript “1”):

$$\begin{aligned} \mathbf{r} &= a\mathbf{r}_1, & \rho &= b\rho_1, & p &= cp_1, \\ \mathbf{B} &= \sqrt{c}\mathbf{B}_1, & t &= a\sqrt{\frac{b}{c}}t_1 & \mathbf{v} &= \sqrt{\frac{c}{b}}\mathbf{v}_1 \end{aligned} \quad (21.5)$$

Consider the initial value problem for some MHD system with initial state:

$$\begin{aligned} \rho|_{t=0} &= F(\mathbf{r}), & p|_{t=0} &= G(\mathbf{r}) \\ \mathbf{v}|_{t=0} &= \mathbf{H}(\mathbf{r}), & \mathbf{B}|_{t=0} &= \mathbf{K}(\mathbf{r}) \end{aligned} \quad (21.6)$$

where the functions in the right-hand side are known. Consider now another system, where the initial state is geometrically similar to the first system, and the initial distributions of the density, pressure, velocity, and the magnetic field satisfy transformations (21.5), i.e.

$$\begin{aligned} \rho_1|_{t=0} &= \frac{1}{b}F(a\mathbf{r}_1), & p_1|_{t=0} &= \frac{1}{c}G(a\mathbf{r}_1) \\ \mathbf{v}_1|_{t=0} &= \sqrt{\frac{b}{c}}\mathbf{H}(a\mathbf{r}_1), & \mathbf{B}_1|_{t=0} &= \frac{1}{\sqrt{c}}\mathbf{K}(a\mathbf{r}_1) \end{aligned} \quad (21.7)$$

The geometrical similarity means that the functions F , G , etc., are the same as in (21.6). The invariance of MHD equations with respect to the transformation presented by (21.5) means that the second system will evolve similarly to the first one, with a time changed by the scale factor $a\sqrt{b/c}$. More explicitly, if the evolution of the density in the first system is described by some function $\rho(\mathbf{r}, t)$, the density in the second system will be

$$\rho(\mathbf{r}, t) \implies \frac{1}{b}\rho(a\mathbf{r}_1, a\sqrt{b/c}t_1), \quad (21.8)$$

and similarly for the other functions.

Hence, we can indeed establish a direct correspondence between two MHD systems, no matter how different the spatial scales of the problems are, provided the initial conditions match one another in the sense of (21.6)–(21.7). The timescale of the evolution of the two systems is then uniquely related to each other. This understanding provides the basis for comparison of MHD phenomena in astrophysics and in laboratory experiments.

21.1.2 Invariance of Shock Boundary Conditions

One of the important questions in scaling of laboratory experiment to astrophysical plasma is whether the invariance can be established between the systems when they contain shocks. As dissipative structures, shocks connect regions of adiabatic flows by shock boundary conditions. If these boundary conditions “survive” the transformation described by Eq. (21.5), the similarity between the two systems will exist and can be used.

The Rankine-Hugoniot conditions in the MHD are (see, e.g., Landau and Lifshitz 1987):

$$\{\rho v_n\} = 0 \quad (21.9)$$

$$\left\{ v_n \left(\frac{\rho v^2}{2} + \frac{\gamma p}{\gamma - 1} \right) + \frac{1}{4\pi} [(v_n B^2 - B_n(\mathbf{v} \cdot \mathbf{B}))] \right\} = 0 \quad (21.10)$$

$$\left\{ p + \rho v_n^2 + \frac{1}{8\pi} \mathbf{B}_t^2 \right\} = 0 \quad (21.11)$$

$$\left\{ \rho v_n \mathbf{v}_t - \frac{1}{4\pi} B_n \mathbf{B}_t \right\} = 0 \quad (21.12)$$

$$\{B_n \mathbf{v}_t - \mathbf{B}_t v_n\} = 0, \quad \{B_n\} = 0 \quad (21.13)$$

where the curled brackets denote the difference of the corresponding quantities between two sides of the shock discontinuity, and the subscripts “ n ” and “ t ” mean the normal and tangential components of the vector with respect to the shock front. Equations (21.9) and (21.10) are the continuity of the mass and energy flux, (21.11) and (21.12) describe the continuity of the normal and tangential components of the momentum flux, and (21.13) are electrodynamic conditions of the continuity of the tangential component of the electric field and the normal component of the magnetic field.

The invariance of the conditions (21.9) and (21.13) under the transformation (21.5) is obvious, because the left-hand sides of these conditions are homogeneous functions of vectors \mathbf{v} and \mathbf{B} . With regard to conditions (21.10)–(21.11), one can check their invariance by direct substitution of transformation (21.5). Let us, for example, check the invariance of the condition (21.10). According to (21.5), one has

$$v_n \left(\frac{\rho v^2}{2} + \frac{\gamma p}{\gamma - 1} \right) = \frac{c^{3/2}}{b^{1/2}} v_{n1} \left(\frac{\rho_1 v_1^2}{2} + \frac{\gamma p_1}{\gamma - 1} \right), \quad (21.14)$$

and

$$(v_n B^2 - B_n(\mathbf{v} \cdot \mathbf{B})) = \frac{c^{3/2}}{b^{1/2}} (v_{n1} B_1^2 - B_{n1}(\mathbf{v}_{n1} \cdot \mathbf{B}_{11})) \quad (21.15)$$

As the right-hand side of (21.10) is zero, this means that it is invariant under the transformation. In the same fashion one can prove the invariance of (21.11) and (21.12).

21.1.3 Applicability Conditions for the MHD Similarity

In above sections, the analysis was set for the equations of nondissipative MHD. In order for the hydrodynamic approach to be valid, the particles must be well localized on the length scale of the problem. This localization may be produced either by collisions or by some combination of magnetic fields and turbulence. In addition, the applicability of (21.1)–(21.4) requires that dissipative processes, the heat sources and/or sinks be negligible. The quantitative criteria can be formulated in terms of dimensionless parameters like the Reynolds number and the Peclet number. As an example let us briefly discuss conditions under which Ohmic dissipation can be neglected.

The role of Ohmic dissipation can be conveniently characterized by the magnetic Reynolds number :

$$Re_m = \frac{uL}{D_m}, \quad D_m = \frac{c^2}{4\pi\sigma} \quad (21.16)$$

A large magnetic Reynolds number (high electrical conductivity) corresponds to small dissipation. Typically, in the astrophysical environment the magnetic Reynolds number is large and, hence the Ohmic dissipation can be neglected.

Take, for example astrophysical processes where the hot plasma is produced by the shock compression, and where a natural measure of the characteristic velocity u is the sound speed c_s . Then (21.16) can be rewritten as $Re_m \simeq c_s L / D_m$. For solar corona, e.g., $Re_m \simeq 10^{12}$.

In laboratory experiments, as a result of smaller length scales, the magnetic Reynolds number is typically much smaller. Still, at high enough plasma temperatures it can be much higher than 1. Taking as an example a fully ionized plasma of an element with the atomic number A and the charge of the nucleus Z , one has

$$c_s = \sqrt{\frac{5(Z+1) T}{3A m_p}} \quad (21.17)$$

or with the temperature in eV

$$c_s \simeq 1.3 \times 10^6 \sqrt{\frac{Z+1}{A}} \sqrt{T} \quad (21.18)$$

The magnetic diffusivity for such a plasma is given by

$$D_m \simeq 1.5 \times 10^7 \frac{Z}{T^{3/2}}, \quad (21.19)$$

and the expression for Re_m becomes

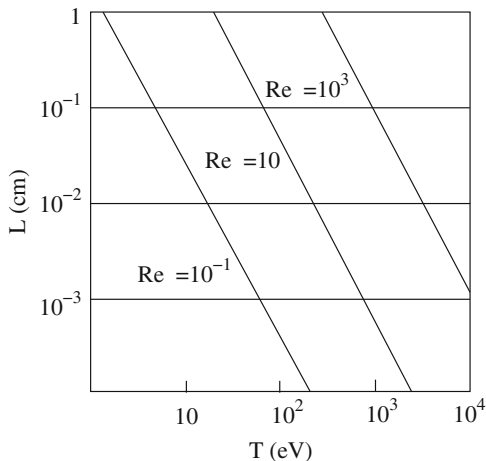
$$Re_m \simeq 0.08 \sqrt{\frac{Z+1}{Z^2 A}} L T^2 \quad (21.20)$$

As an example, the lines $Re_m = \text{const}$ are shown in Fig. 21.1 for a fully stripped carbon in the range of parameters potentially achievable in laboratory experiments.

21.2 Jets, Bow Shocks, and Instabilities

Magnetically driven plasma jets of various speeds and characteristics are observed throughout the universe, from large-scale galactic jets to solar outflows and explosive events. The relevance of laboratory experiments to astrophysics rests on the capability of reproducing in the laboratory both the dynamics of the astrophysical system and, more importantly, a valid set of dimensionless scaled parameters. Various laboratory experiments have been performed in recent years using high-intensity lasers (Remington et al. 1997; Keilty et al. 2000; Foster et al. 2005; Park et al. 2012; Ryutov et al. 2013), pulsed power facilities (Lebedev et al. 2002, 2005;

Fig. 21.1 Lines $Re_m = \text{const}$ for a fully stripped carbon in the $L - T$ plane (Ryutov et al. 2001). Courtesy of D. Ryutov



Ciardi et al. 2009), spheromacs (Stenson and Bellan 2012), and others. This list is only a small part of laboratory experiments successfully studying the astrophysical jets and their underlying physics. In what follows we will give some examples of a laboratory representation of astrophysical jets.

21.2.1 Magnetically Driven Plasma Jets

The exemplary results were obtained in a series of experiments using the pulsed power machine (MAGPIE) in the Blackett Laboratory, Imperial College (Suzuki-Vidal et al. 2013, 2009; Lebedev et al. 2005).

To create jets whose properties can be scaled to real astrophysical systems, in accordance with similarity criteria, it is required in the first place that the Reynolds numbers Re , Re_m , and Peclet Pe number be much larger than unity. This implies that the transport of momentum, magnetic fields, and thermal energy occurs predominantly through advection with the flow. In addition, the dimensionless parameters that describe a flow need to be similar between both systems, i.e., the Mach number M , the density ratio of the jet and the ambient medium $\eta = n_j/n_e$, and the cooling parameter, the ratio of the radiative cooling time and a characteristic time scale of jet, $\chi = \epsilon_{\text{th}}/P_r \tau_j$ (ϵ_{th} and P_r being the thermal energy density and the power radiated per unit volume, respectively).

In one series of experiments the plasma jets are produced by the ablation of aluminium plasma from a radial foil, which is subjected to a 1.4 MA, 250 ns current pulse from the MAGPIE pulsed-power generator. The ablated plasma converges on axis, producing a collimated plasma flow. Example of the experimental setup is shown in Fig. 21.2a. The morphology of a plasma jet in the absence of an ambient

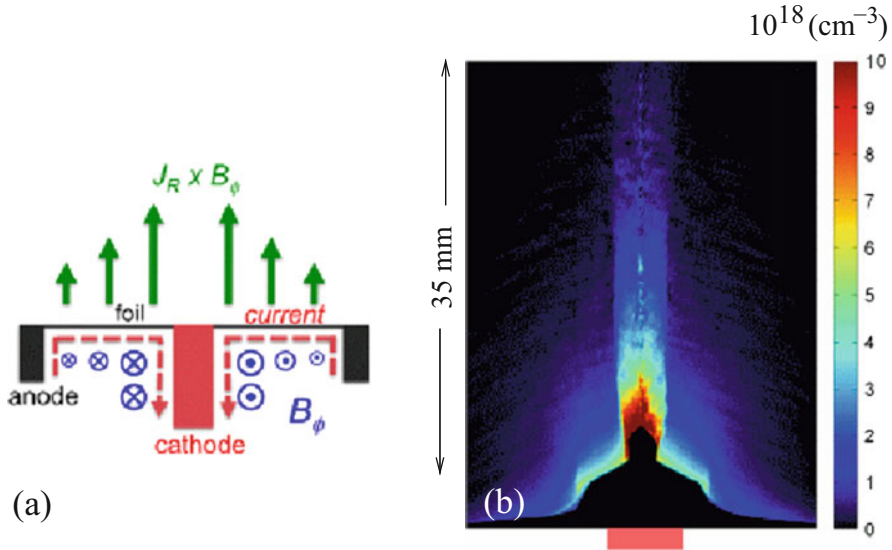


Fig. 21.2 Generation of a tower jet in vacuum: (a) Schematic of the experimental setup: the radial foil setup showing the current path through the foil (J_R), toroidal magnetic field (B_ϕ), and the net $J_R \times B_\phi$ force acting on the plasma produced from the foil; (b) Electron density distribution measured by interferometry (Suzuki-Vidal et al. 2009, 2013). Reprinted with permissions from Springer Science and Business Media and Elsevier

gas is illustrated in Fig. 21.2b by the map of electron density obtained from laser interferometry.

The jet is highly collimated and the flow is sustained for 450 ns. The tip of the jet reaches a height of 35 mm above the foil, which corresponds to an aspect ratio of the jet L/R exceeding 20. The jet has a well-defined smooth boundary and a high degree of collimation with a half-opening angle of $\sim 2^\circ$. Although the degree of jet collimation does not decrease with time, the measurements show a slow increase of the jet's diameter employing a characteristic radial expansion velocity of $v_r \sim 5 \text{ km s}^{-1}$. The axial velocity of the tip of the jet is estimated as $v_z > 100 \text{ km s}^{-1}$. The measured electron temperature in the jet body is $T_e \sim 15\text{--}20 \text{ eV}$ (with $Z \sim 4$), and an internal Mach number is in the range $M = v_z/c_s \sim 2.5\text{--}3$.

The parameters of the jet, its velocity, $\sim 100 \text{ km s}^{-1}$, estimated Mach number $M \sim 10\text{--}30$, and the aspect ratio, $L/R \sim 20$ are comparable to those of the astrophysical jets, where often $v > 100 \text{ km s}^{-1}$, $M > 20$ and $L/R \sim 20$. Conditions on Re , Re_m , and Pe to be much larger than unity are valid for both systems. These studies were extended to more sophisticated scaled experiments, aiming, in particular, to evolution of supersonic jets under conditions when radiative cooling is playing a significant role (Suzuki-Vidal et al. 2012, 2013).

21.2.2 Bow Shocks

A great number of plasma jets observed throughout the solar atmosphere at any moment of time, as well as various galactic jets often lead to development of bow shocks and may be associated with some irregular structures (see, e.g., Chap. 18). The characteristics of bow shocks and associated clumpy features can be attributed to interaction of jet with the ambient medium. In order to vary critical dimensionless parameters for astrophysical applications and study these phenomena, in the above mentioned experiments the jet–ambient plasma interaction has been performed in two different geometries for different gases. First, gas was injected by the nozzle placed above the foil, and, second, gas was injected transverse to the direction of the jet propagation at a certain height from the foil. The ambient medium was created by injection of cold, neutral gas into the region above the foil.

Figure 21.3 shows example of the jet interaction with medium in case when gas was injected above the foil. Left panel is 2D map of electron density in the plasma at 430 ns obtained with optical laser interferometry. A well-collimated jet was observed to have several new features compared to the case without ambient gas.

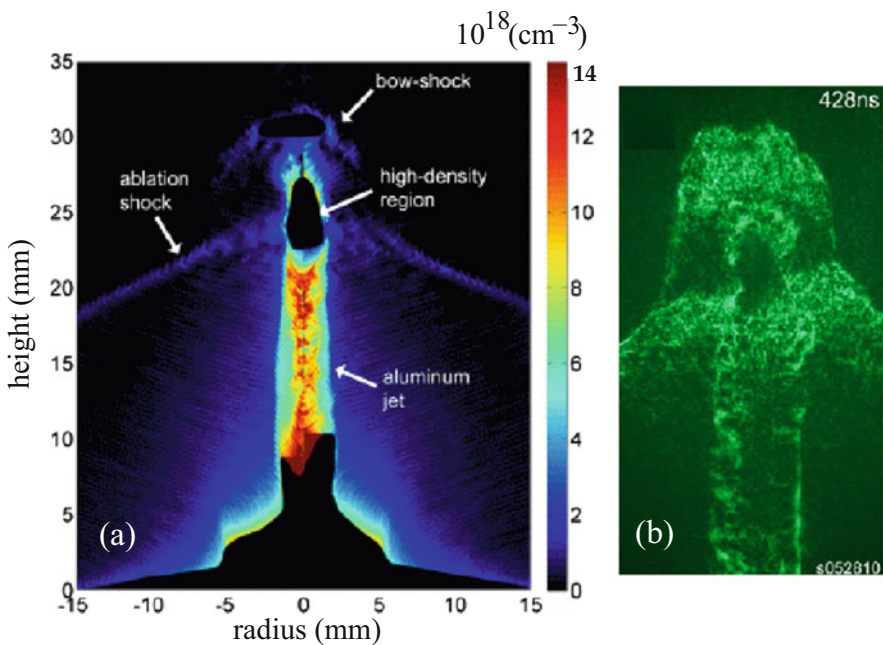


Fig. 21.3 Results of jet–ambient argon gas interaction in case when ambient gas is released in the same direction as the jet (the ambient gas velocity is much smaller than that of the jet and it can be considered as static): **(a)** Electron density at $t = 430$ ns (fully developed bow-shock); **(b)** Optical dark-field laser schlieren imaging revealing the formation of small-scale structures on the bow-shock front (Suzuki-Vidal et al. 2013). Reprinted with permission from Elsevier

The interaction of the plasma ablated from the surface of the foil with the ambient argon forms a shock extending from the tip of the jet towards large radii (labeled as ablation shock).

The numerical calculations indicate that a toroidal magnetic field is generated between the foil and the ablation shock. This produces a radial component of the Lorentz force near the shock, redirecting the plasma flow towards the axis and converging into the tip of the jet resulting in the formation of a dense, highly emitting region at the tip of the jet. The accumulation of plasma in this region leads to a local increase of pressure and acceleration of the flow, which starts propagating into undisturbed ambient argon leading to the formation of a bow-shock. Figure 21.3b shows the optical dark-field laser schlieren revealing the presence of small scale structures at the front of the bow shock.

Example of jet–ambient interaction dynamics for the second case, when gas is injected transverse to the direction of the jet propagation is given in Fig. 21.4. Shown is an optical dark-field laser schlieren of a jet propagating into argon at 420 ns (the view of this diagnostic is perpendicular to the direction of the gas injection). This time, the jet is formed below the gas cloud in the same way as in the absence of ambient gas. As the jet and the halo plasma surrounding the jet, reach the region where gas is present, an ablation shock is formed. Unlike the previous case, now the ablation shock is asymmetric with respect to the axis of the jet. The formation of a

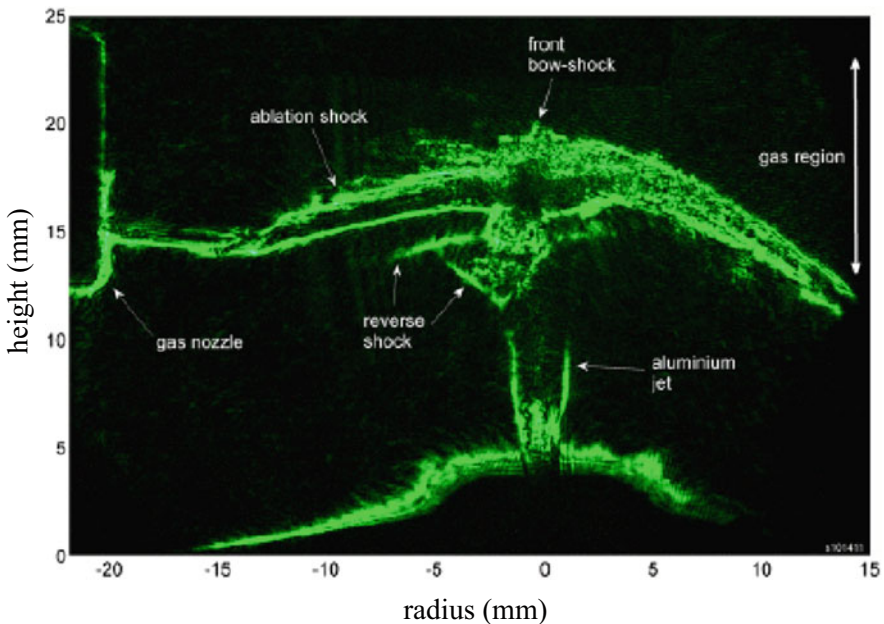


Fig. 21.4 Results from the interaction of the jet with a localized gas ambient cloud (argon), transverse to the direction of propagation of the jet. Optical dark-field laser schlieren image (Suzuki-Vidal et al. 2013). Reprinted with permission from Elsevier

high density region at the tip of the jet is still present. However its formation does not appear on the axis of the jet and instead is shifted towards the nozzle, i.e., where the gas density is higher. In addition, with this configuration the formation of a bow shock ahead of the jet is less evident. Instead a propagating against the jet is formed.

Experimental studies of bow shock formation and properties in presence of the arrays of cylindrical obstacles (very useful for solar applications!) also showed that the orientation of the embedded field with respect to cylindrical obstacles has a dramatic effect on the bow shock structure (Burdiak et al. 2017). When the field is aligned with the cylinders, a sharp bow shock is formed with a structure determined by the fast magnetosonic Mach number. When the field is orthogonal to the cylinders, magnetic draping occurs. This leads to the growth of a magnetic precursor and the subsequent development of a magnetized bow shock that is mediated by two-fluid effects, with an opening angle and a stand-off distance, that are both many times larger than in the parallel geometry. By changing the field orientation, one can change the regime in a system and, thus, physical mechanisms that are responsible for the development of the bow shocks.

Given that the jet formations, shocks, bow shocks, and reverse shocks are only natural occurrence throughout the solar atmosphere, these results are extremely useful to analyze and, using the scaling laws, study their characteristics. These studies can also be used for developing the diagnostic tools.

21.3 Shock–Shock Interaction, Magnetic Field Generation and Self-organization

Shocks, supersonic, and super-alfvénic flows and their interactions are ubiquitous in solar atmosphere and space plasma. Because of the low density of astrophysical plasmas the particle mean free path is typically very large, and, therefore, shock waves are collisionless. Of the nonlinear plasma processes involved in the collisionless shock formation and their properties, a crucial role is played by plasma instabilities and self-generated magnetic fields. A series of experiments at the Omega and Omega-EP laser facilities (Boehly et al. 1995; Maywar et al. 2008) revealed an important features of the shock–shock interactions, allowing to clarify the role of the filamentation, Weibel instabilities in collisionless shock formation, the self-generation of magnetic fields in shocks, the influence of external magnetic fields on shock formation, as well as conditions for the onset of self-organization process (Gregori et al. 2012; Kugland et al. 2012; Park et al. 2012; Ross et al. 2012; Huntington1 et al. 2015).

21.3.1 *Weibel Instability and Filamentation*

Weibel instability operates in unmagnetized plasma with an electron velocity space anisotropy. In the process of restoration of plasma isotropy it leads to the exponential growth filamentation of electromagnetic fields. In astrophysical plasmas, there is no way to directly measure the key quantities to investigate the shock dynamics and particle acceleration by collisionless shocks, whereas scaled laboratory experiments allow to reach the collisionless plasma regime and study the instability dynamics.

In experiments performed at the Omega Laser Facility, one can directly image the magnetic fields associated with the Weibel instability in counter-streaming plasma flows. The flows were established by laser ablation of opposing foils, as shown in Fig. 21.5a. The foils were oriented opposite to each other and irradiated simultaneously, such that the expanding plasma flows interacted near the mid-plane between the foils. The plasma density in the counter-propagating flows increased by the factor of two, whereas the electron and ion temperatures increased rapidly mainly due to ion two-stream instability, which quickly stabilizes. The ions remain directed throughout the process, allowing to develop the Weibel instability and grow due to the energy supplied by the flows. Magnetic fields were detected by using proton imaging. An isotropically emitting proton source is generated by the implosion of a capsule filled with mixture of deuterium (D) and ^3He . The protons that pass through the plasma interaction region are deflected by the electric and magnetic fields in the system, and are recorded using a nuclear track detector at a magnification of approximately 30.

The proton radiography data, taken at three different times during the interaction of the flows, are shown in side panels of Fig. 21.5b, d. One can see a clear pattern of filamentary structures, oriented along the flow direction, and consistent with Weibel filamentation in the counter-propagating flows. In addition to the filaments, horizontal “plate” features are seen near the mid-plane of the drive plasmas. These large-scale magnetic features are presumably the magnetic fields generated by the Biermann battery effect ($\partial\mathbf{B}/\partial t \sim \nabla n_e \times \nabla T_e$).

Note that the battery mechanism leads to generation of quite a weak magnetic fields. However, unlike all the dynamo mechanisms that require some initial magnetic field which then gets amplified by plasma motions, the Biermann battery does not require presence of magnetic field providing generation of a seed field, which depending on the environmental dynamics can be further amplified by the appropriate dynamo mechanisms.

21.3.2 *Magnetic Field Generation by Biermann Battery Effect*

Magnetic field generation by the Biermann battery effect has been successfully demonstrated in an experiment with the laser-produced shocks (Gregori et al. 2012). Using scaling relations these results were successfully applied to the intergalactic

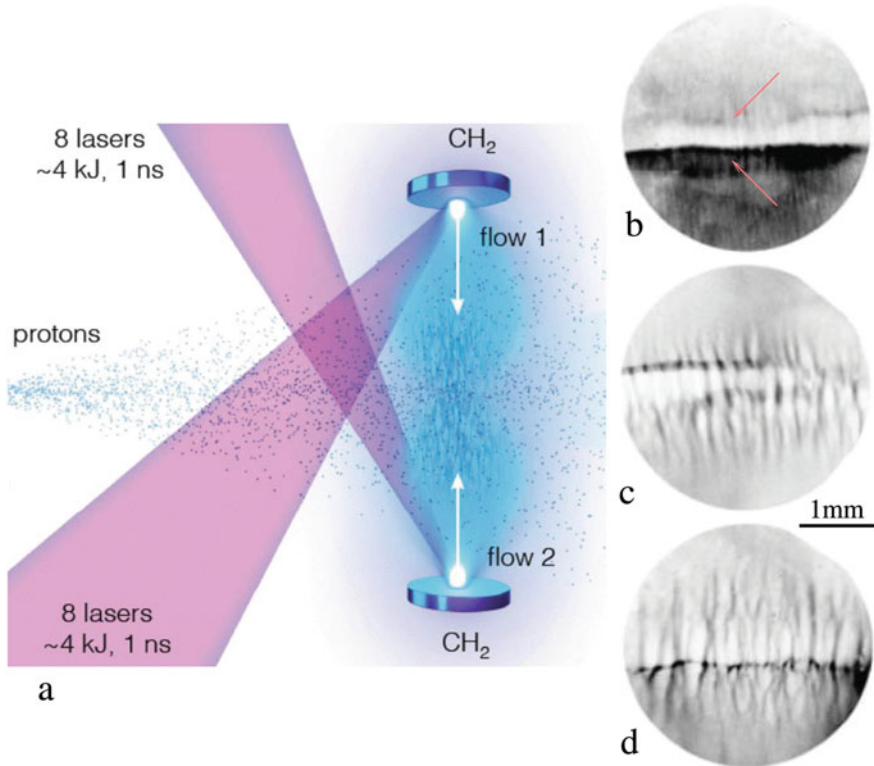


Fig. 21.5 Schematic for generation of counter-streaming plasma flows and example of generated magnetic field structures. **(a)** A pair of CH₂ plastic foils of diameter 2 mm and thickness 500 μm , oriented face-on and separated by 8 mm were irradiated with eight overlapped laser beams. Protons produced at energies of 3.0 and 14.7 MeV were detected by a nuclear track detector positioned on the mid-plane of the CH₂ target foils, such that the protons traverse the central interaction region as shown; **(b)–(d)** 14.7 MeV D-³He proton images of plasma interaction region. In each case the plasma flows enter the frame from the top and bottom. At early time (about 3 ns after the drive begins, panel **b**), only initial traces of filamentation are observed. At later times (panels **c** and **d**) the filaments become more coherent and increase in extent along the flow direction. In each case extended magnetic “plates” are formed above and below the mid-plane as a result of the large-scale Biermann battery fields generated in the laser-ablation process (shown by pink arrows in panel **b**). The persistence and evolution of these fields perforated by the Weibel filaments are clearly seen in panel **c–d** (Huntington1 et al. 2015). Reprinted with permission from Springer Science and Business Media

medium, to produce a seed magnetic field which can then be amplified by turbulence.

The intense laser was used to illuminate a small carbon rod inside a low-pressure gas-filled interaction chamber. Schematic of the experimental setup is shown in Fig. 21.6a. The large energy density accumulated on the carbon target over the relatively short laser pulse duration caused a ballistic expansion of the heated solid

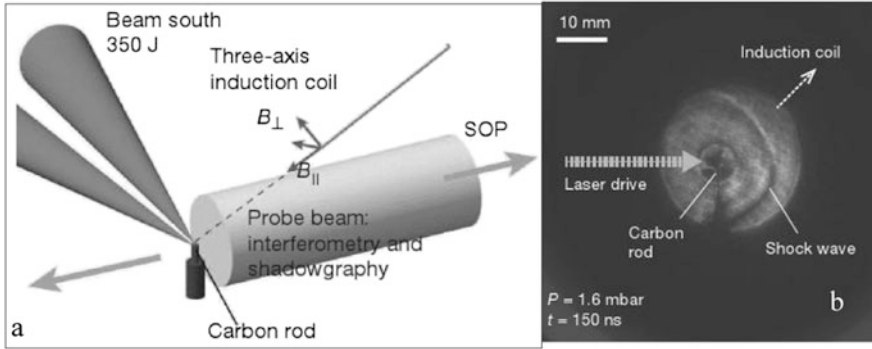


Fig. 21.6 Experimental setup showing (a) The laser beams and diagnostics configuration. Either one or two frequency-doubled (527 nm), 1.5 ns long laser beams are focused on the tip of a 500 mm diameter carbon rod. At focus, each laser beam has a 400 mm flat-top distribution, achieving a peak intensity of $2 \times 10^{14} \text{ W cm}^{-2}$, delivering around 350 J. The interaction chamber is filled with helium gas. The shock wave evolution was monitored using transverse interferometry and Schlieren shadowgraphy with an optical probe and (b) The Schlieren image showing laser and magnetic pick-up coil configuration as well as the shock position (Gregori et al. 2012). Reprinted with permission from Springer Science and Business Media

matter. When the shocked mass was roughly equal to the ejected mass, the shock evolved into to a Sedov-Taylor blast wave.

The shock evolution over time was monitored using transverse interferometry and Schlieren shadowgraphy with an optical probe. In Fig. 21.6b, the Schlieren image shows laser and magnetic pick-up coil configuration as well as the shock position. The Schlieren image indicates when the refractive index of the plasma changes rapidly, thus tracking the position of the shock.

The measurement of the magnetic field was performed with three-axis magnetic induction coils, giving both the magnetic field components along the shock, B_{\parallel} , and perpendicular to the shock, B_{\perp} (Fig. 21.7). At a radius $r \simeq 3 \text{ cm}$ from the initial blast, peak values of B_{\perp} were in the range 10–30 G.

Magnetic field generated through vorticity by Biermann’s battery effect is estimated as:

$$B_{\text{vort}} = \frac{m_i}{e} \Omega \simeq \frac{(\rho_{\text{cmp}} - 1)^2}{\rho_{\text{cmp}}} \frac{m_i}{e} \left| \frac{\partial \mathbf{v}_{sh}}{\partial S} \right| \quad (21.21)$$

where $\Omega = \nabla \times \mathbf{v}$ is the vorticity, $\rho_{\text{cmp}} \simeq 3$ is the shock compression ratio and $\partial \mathbf{v}_{sh} / \partial S \simeq \kappa v_{sh} / r$, where κ is the tangential gradient scale coefficient. The approximate value for κ was obtained from the asymmetry in the shape of the shock wave, $\kappa \simeq 0.1\text{--}0.3$. Estimates obtained with (21.21) give at $r \simeq 3 \text{ cm}$, $B_{\text{vort}} \simeq 10\text{--}30 \text{ G}$, which is in agreement with the measured values.

Note that the vorticity-generated magnetic field is perpendicular to the shock normal, which is consistent with the experimental traces shown in Fig. 21.7, $B_{\perp} \gg$

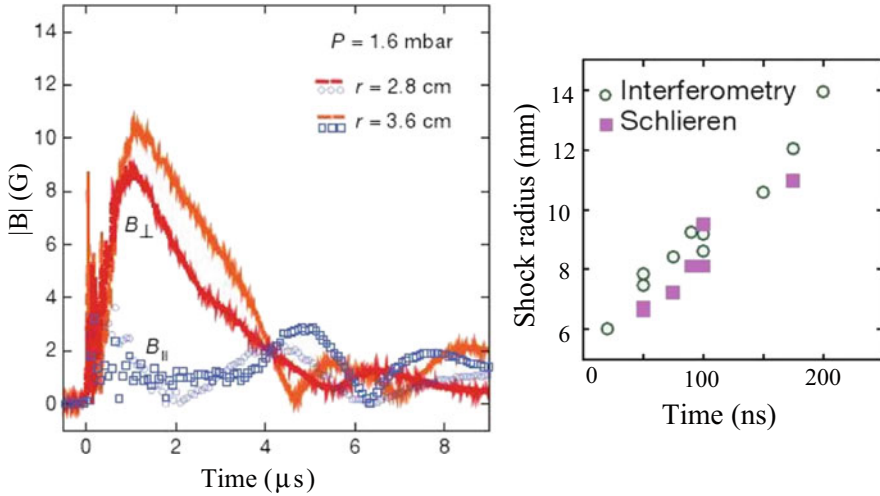


Fig. 21.7 Example of Biermann-generated magnetic-field measurements from induction coils. Left: B_{\perp} (lines) and B_{\parallel} (symbols) traces taken at $P = 0.8$ mbar. The rise and gradual decay of B_{\perp} was consistent with the shock front crossing the coil and the subsequent evolution of the shocked material; Right: The measured shock radius along the laser axis for $P = 0.8$ mbar (Gregori et al. 2012). Reprinted with permission from Springer Science and Business Media

B_{\parallel} . In a perfectly spherical shock no magnetic field can be produced because in this case $\partial \mathbf{v}_{sh} / \partial S = 0$. Magnetic fields can thus only be generated in non-spherical shock expansions, which are expected to occur during structure formation under spatially inhomogeneous astrophysical conditions.

21.3.3 Self-organization in Laser-Produced Counter-Streaming Plasmas

Long living well-organized structures that emerge in dynamic systems and show all the properties of self-organization can be studied in laboratory and scaled to astrophysical environment. The experiments performed at the OMEGA EP laser facility have demonstrated that stable magnetic structures can arise within counter-streaming supersonic plasmas. These structures were predominantly oriented transverse to the primary flow direction, extended for much larger distances than the intrinsic plasma spatial scales and persisted for much longer than the plasma kinetic timescales.

The schematic of the experiment is shown in Fig. 21.8a (for more detailed experimental setup, see Fig. 21.5). Two kilojoule-class lasers irradiated two polyethylene (CH_2) plastic discs that faced each other at a distance of 8 mm, creating a system of high-velocity laser-ablated counter-streaming plasma flows.

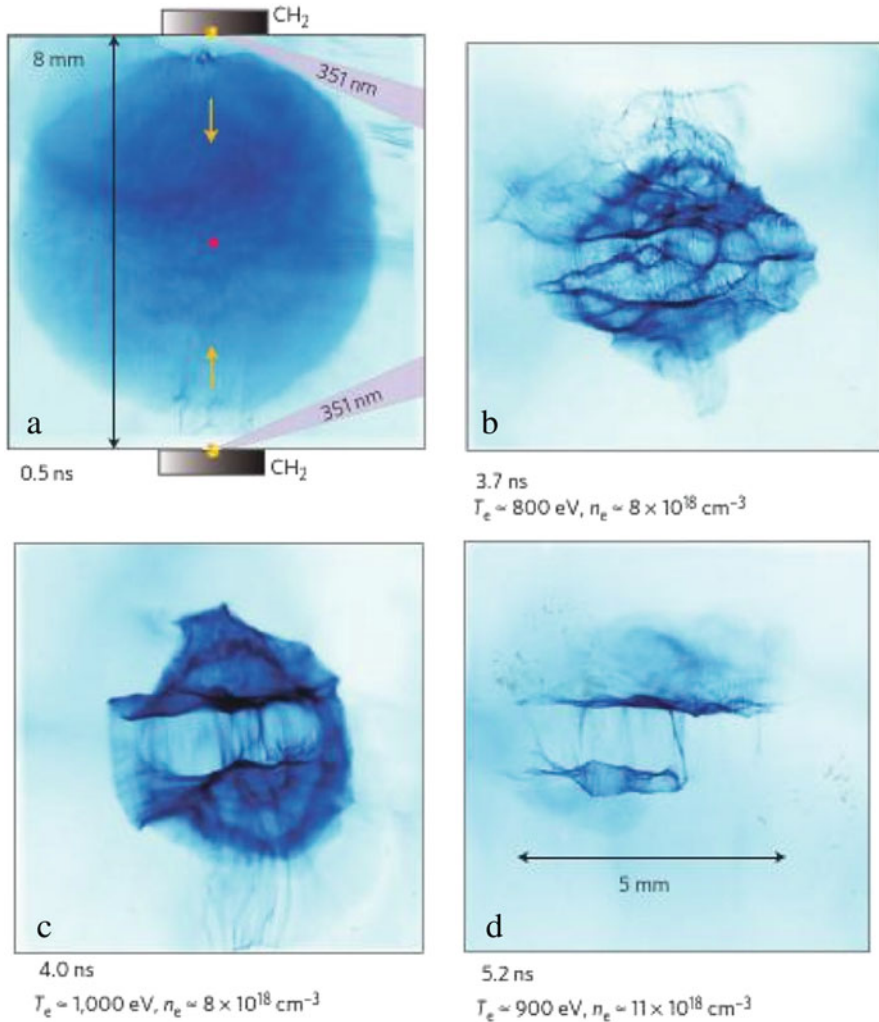


Fig. 21.8 Time sequence of proton images showing the evolution of self-organized electromagnetic field structures (side-view): (a) Two long-pulse lasers (purple) created counter-streaming plasmas from CH₂ disc targets. The orange arrows show the direction of counter-streaming flows. The magenta dot marks the target chamber center. At this early time the plasmas are still close to the targets; (b) By 3.7 ns well-developed caustics appear; (c) Transition to large-scale caustics and appearance of two horizontal large swaths; (d) Nearly closed caustic contours connecting the two horizontal features, suggesting a cellular field structure (Kugland et al. 2012). Reprinted with permission from Springer Science and Business Media

The electric and magnetic field structures have been visualized with short-pulse laser-generated proton beam imaging. After about 3 ns (Fig. 21.8b), proton images showed development of well-defined caustics (large-intensity variations), indicating

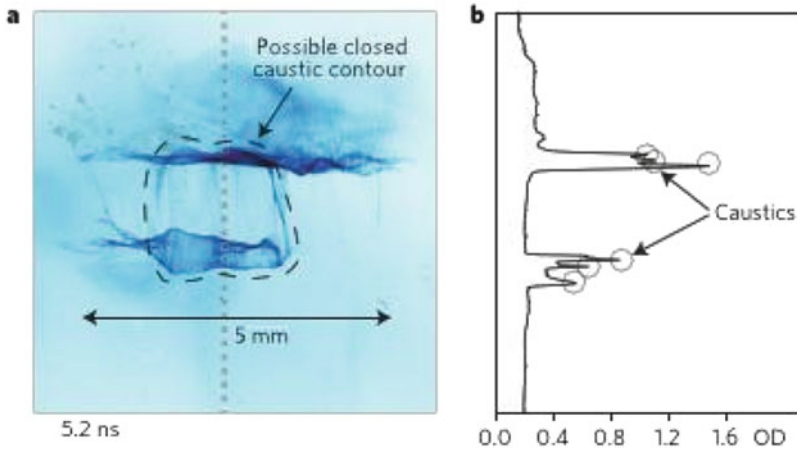


Fig. 21.9 Caustic detail: (a) A detail of the proton image from Fig. 21.8d, with the dashed line indicating a nearly closed contour suggestive of a cellular field structure; (b) A line profile (in units of optical density, OD) taken along the dotted line in (a), from a separate scan of the film with a photometric densitometer. The sharp features, circled, are caustics made by self-organized field structures (Kugland et al. 2012). Reprinted with permission from Springer Science and Business Media

the formation of strong field zones within the plasma. By 4 ns (Fig. 21.8c, d), the features have changed markedly into two large swaths of straight transverse caustics that extend for up to 5 mm.

Here we arrive to very important point: the swaths extent is large compared with the fundamental scale lengths of the plasma, e.g., it is 50,000 times larger than the Debye length, and nearly 100 times larger than the ion inertial length. The structures show a high degree of stability. Their lifetime was found to be much longer than fundamental plasma timescales: 75,000 times longer than the electron plasma period, nearly 3000 times longer than the ion plasma period indicating a high degree of self-organization.

It is interesting that in the established state (Fig. 21.8d) there are nearly closed caustic contours connecting the two horizontal features, suggesting a cellular field structure. Details of this caustics are shown in Fig. 21.9. The horizontal swaths themselves consist of multiple caustics clustered together (Fig. 21.9b). The positions of the caustics remain the same for different proton energies. The main caustic features are summarized in Table 21.1.

The origin of the fields that create the horizontal swaths of caustics is still unknown. These swaths of caustics could be from planar field structures, or the rims of conical or cylindrical discontinuities. Detailed analysis of proton imaging suggests that two widely separated layers of fields are required to create two widely separated swaths of caustics.

Table 21.1 Proton image features, properties and possible origins

Caustic feature	Spatial scale	Most visible	Possible origins
Striation	10 μm	2 ns	Shocks in a sheared flow
Turbulent circular caustics	0.5 mm	2–3 ns	Hydrodynamic instabilities (e.g., laser ablative or Rayleigh-Taylor)
Dual swaths of horizontal caustics	1 mm	4–7 ns	Requires a highly self-organizing inverse cascade mechanism. The field structure could be dual planar, cylindrical/conical or a single wavy blob
Nearly closed contours	1 mm	4–7 ns	Cellular field structures

21.4 Rayleigh-Taylor Instability and Self-generated Magnetic Fields

The Rayleigh-Taylor instability and its influence on dynamic properties of a system is subject of intense experimental and theoretical studies which span from pure hydrodynamic problems in laboratory and nature to inertial confinement fusion and astrophysics. In this section, we discuss some results obtained on OMEGA Laser System. We mention here some experiments that seem to be of particular interest for solar physics. One series of experiments were devoted to studies of the RT unstable (laser-seeded) 3D perturbations that resulted nonlinear regime of bubble formation and evolution. Next, as the RT instability in plasmas can produce seed vorticity that generates magnetic fields, the experiments were performed to study magnetic field generation during RT instability growth (Smalyuk et al. 2005; Sadot et al. 2005; Gao et al. 2013; Nilson et al. 2015).

21.4.1 Nonlinear Rayleigh-Taylor Instability

In linear regime of classical RT instability, small initial perturbations develop independently of each other and grow exponentially with growth rates of $\nu = \sqrt{Agk}$ (cf. (20.8)). For ablatively driven RT instability, the growth rate is reduced to $\nu = a_1\sqrt{gk} - a_2kV_{ab}$. Here k is the modulation wave number, g is the target acceleration, A is the Atwood number, V_{ab} is the ablation velocity, a_1 and a_2 are constants. The growth rate can be stabilized by the ablation term a_2kV_{ab} . The first indication of nonlinear RT effects appear when the mode amplitude becomes comparable to its wavelength, the modulations develop into bubbles and spikes, where lighter material rises through heavier material and heavier material falls through light material.

In fully nonlinear regime, bubbles merge and evolve self-similarly prior to more complex behavior, where the interaction between neighboring bubbles governs

the modulation evolution. In this regime smaller bubbles (with smaller nonlinear velocities) are overcome by larger bubbles (with higher nonlinear velocities) through bubble competition and bubble merger processes. At the same time the average size of modulations is expected to be shifted to longer wavelengths as the modulations grow.

These regularities were successfully studied in the experiments on the OMEGA Laser Facility where a high-energy laser ablates a solid target (Boehly et al. 1995; Sadot et al. 2005). Initial 3D, broadband modulations were created by the nonuniformities of the individual laser drive beams. As the hot, light plasma, created by laser ablation, accelerates, the interface between the light and dense plasma (the ablation surface) becomes unstable and the modulations on this interface grow due to RT instability. The growing target modulations were measured using X-ray face-on radiography.

Figure 21.10 shows the central portions of the recorded images of the target modulations at different times and different target distances. The light areas

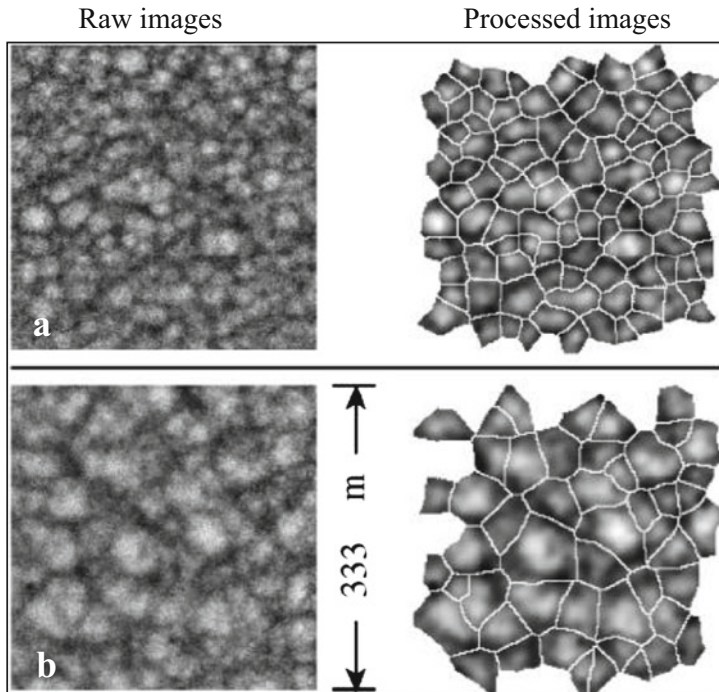


Fig. 21.10 X-ray radiographs of growing 3D broadband modulations (left panels) with distributions of the bubble sizes and their rms amplitudes (right panels). Growing modulation was measured with X-ray radiography at traveled distances of $18\ \mu\text{m}$ (a) and $67\ \mu\text{m}$ (b). The corresponding Wiener-filtered images with imposed bubble borders (found using the watershed algorithm) are shown on the right-hand side. The light areas (more X-ray transmission) represent bubbles, while dark areas (less X-ray transmission) represent spikes (Sadot et al. 2005). Reproduced with permission from AAS

(higher X-ray transmission) represent bubbles, while the dark areas (lower X-ray transmission) represent spikes. As the modulations grow, the average bubble size shifts to longer wavelengths, big bubbles become bigger, and small bubbles eventually disappear.

To measure bubble characteristics such as size and amplitude, the images were processed with the watershed algorithm to determine the bubble edges. Examples of this procedure are shown in the right-hand side of Fig. 21.10 where the bubble borders are superimposed on the Weiner-filtered images. Studies of the distribution of bubble sizes in time showed that as modulations grow, the number of bubbles decreases while their average size and average rms amplitude increase. Both bubble size and amplitude distributions are in the self-similar regime because the normalized distributions do not change in time.

As the modulations grow, new bubbles are born as a result of the bubble competition and merger processes. Because the measured bubble sizes and rms amplitude distributions are in a self-similar regime, their evolution can be described by a very simple form based on their measured normal distributions. The number of bubbles N evolves as $N(t) \simeq (wt\sqrt{g} + 2C)^{-4}$, where w is the scaled average merging rate, and constant $C = 2\sqrt{\langle \lambda \rangle_0}$ is related to the initial average bubble size $\langle \lambda \rangle_0$. Both, the average bubble size and average rms amplitude grow proportionally to gt^2 , as predicted by the self-similar growth and scaling theory. These results and possible scaling to such a diverse regions as solar convective zone and quiescent prominences could be very useful.

21.4.2 Self-generation of Magnetic Field by RT Instability

In this section, we will discuss another experimental result obtained at OMEGA EP Laser Facility devoted to generation of magnetic field in plasmas that is subjected to RT instability (Stamper et al. 1971; Gao et al. 2012, 2013).

Magnetic fields generated during the nonlinear growth phase of the RT instability in an ablatively driven plasma were observed using ultrafast laser-driven proton radiography. Thin plastic foils were irradiated with ~ 4 kJ, 2 ns laser pulses focused to an intensity of $\sim 10^{14}$ W/cm². Target modulations were seeded by laser nonuniformities that were amplified during target acceleration by the RT instability.

Figure 21.11 shows a schematic of the experimental setup. Two long-pulse beams irradiated a 15 or 25 μm thick CH foil. Each laser beam delivered ~ 2 kJ pulse with a wavelength of 351 nm at 23° to the target normal. The laser beams were focused to ~ 850 μm diameter focal spots. The CH foil was probed in a direction orthogonal to the main interaction with an ultrafast proton beam. The proton source was generated by irradiating a planar, 20 μm thick Cu foil. The laser pulse was focused with a 1 m focal length parabolic mirror onto the Cu foil at normal incidence, providing an intensity of $\sim 5 \times 10^{18}$ W/cm².

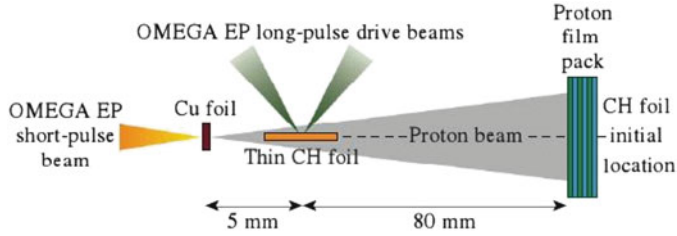


Fig. 21.11 Experimental setup (Gao et al. 2012). Reproduced with permission from AAS

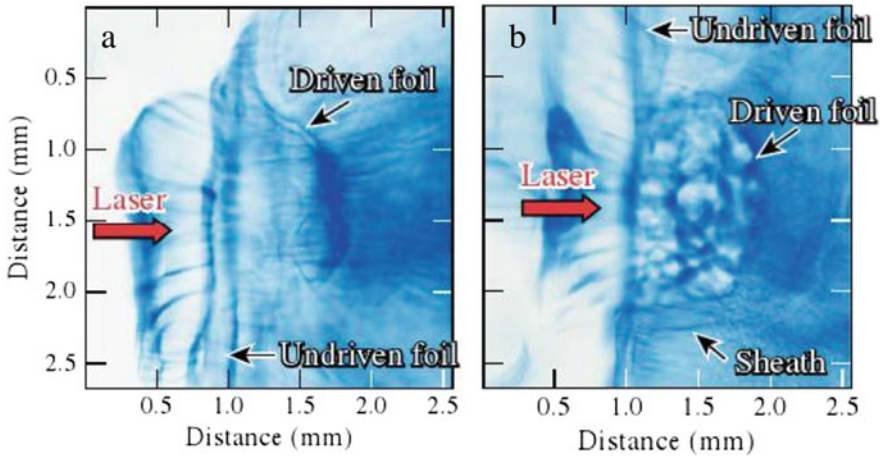


Fig. 21.12 Proton radiographs of a CH foil taken with 13 MeV protons at $t = t_0 + 2.56$ ns. The laser drive and the undriven foil horizon are indicated: (a) Proton radiograph of a $25\ \mu\text{m}$ thick CH foil which is unbroken by the RT instability formation; (b) Proton radiograph of a $15\ \mu\text{m}$ thick CH foil showing development of RT instability and the formation of sheath field (Gao et al. 2012). Reproduced with permission from AAS

The high-energy protons that passed through the driven CH target were detected with a stack of radiochromic film interleaved with aluminum filters. Soft X-rays were filtered with an additional aluminum foil on the front surface of the stack.

Figure 21.12 shows a typical proton radiograph of a $25\ \mu\text{m}$ thick CH foil (panel a) and $15\ \mu\text{m}$ thick CH foil (panel b). The radiographs were obtained with 13 MeV protons at time $t = t_0 + 2.56$ ns, where t_0 is the arrival time of the long-pulse beams at the target surface. The location of the undriven foil horizon is indicated.

The long-pulse beams irradiated the target from the left and the blowoff plasma accelerated the central part of the foil toward the right. The foil had a velocity of $(3 \pm 1) \times 10^7$ cm/s. Left panel shows proton radiograph of a $25\ \mu\text{m}$ thick CH foil, right panel shows proton radiography for a $15\ \mu\text{m}$ thick CH foil. Unlike the “thick” foil, thinner-foil targets were broken by instability formation during the acceleration phase. Besides, in this case, one can clearly see that the target has broken apart and bubble-like structures, growing in time are formed.

Further evidence for the broken foil is provided by the appearance of plasma beyond the driven target. Figure 21.12 right panel shows a sheath ahead electric field formed at the plasma–vacuum interface, indicating that the electromagnetic fields are generated during the RT instability growth.

Estimates for the magnitude of the generated magnetic field is made by measuring the angular deflection of protons from their original trajectory while passing through the field region. The proton path-integrated magnetic field field caused by the Lorentz force acting upon the proton probe beam is

$$\int \mathbf{B} \times d\mathbf{l} = \frac{m_p v}{e} \sin\theta, \quad (21.22)$$

where v and m_p are the proton velocity and mass. In the experiments, the protons are deflected by azimuthal magnetic fields generated around the RT spikes. Assuming an integration path length slightly larger than the target thickness gives a magnetic field strength of 1.4 MG.

Hence, at the RT–unstable interface, narrow spikes are formed where the dense matter falls through the light matter, and bubbles are generated when the light material rises into the dense material. This process generates magnetic fields wrapping around the troughs of the spikes. The growth of the spatial scale length of the perturbed features is caused by magnetic field evolution as the RT instability develops.

21.5 Arched Magnetic Flux Tubes and Plasma Flows

In this section, we will discuss an exemplary laboratory experiment aimed to study the formation and properties of arched magnetic flux tubes (loops) typical to solar atmosphere and other astrophysical objects (Stenson and Bellan 2012). In particular, solar coronal loops rooted in the photosphere exhibit well-defined collimated shape. And the question is how magnetic flux supplied by the photosphere/subphotosphere regions is transported into the corona and being confined in flux tubes with axial uniformity even as they lengthen and kink.

The experimental setup is a pulsed, magnetized plasma gun mounted on the end of a vacuum chamber (Hsu and Bellan 2003; Hansen et al. 2004). The chamber is much larger than the plasma thus simulating a half-infinite space. Two magnetic field coils are pulsed to produce an arched vacuum potential magnetic field. The field strength has a temporal FWHM of 7 ms and spatially varies from 3.5×10^3 G near the footpoints to 10^2 G near the apex of the loop. At each footpoint is a gas nozzle, connected to a fast gas valve. Shortly after the fast gas valve is pulsed, a strongly divergent flow of neutral gas (sound speed 3×10^5 – 1.3×10^6 cm s⁻¹) enters the chamber. At this time high voltage from a 59 μF capacitor is applied to the electrodes, thereby ionizing the gas to form an initial low density plasma. This quickly evolves into a current-carrying flux rope (Fig. 21.13).

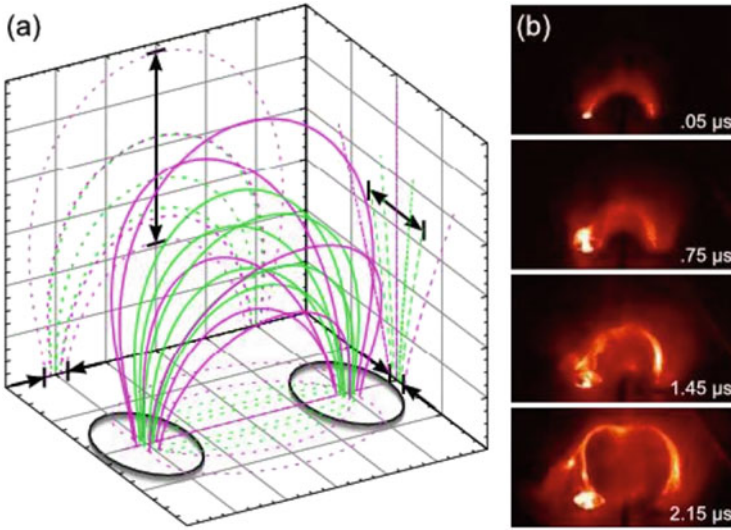


Fig. 21.13 (a) Two sets of vacuum magnetic field lines link a pair of solenoids (only the last few coils of which are drawn). Dashed lines show the projection of the magnetic field lines onto the three orthogonal planes; arrows indicate lines' separation, which is 5–8 times greater at the top of the arch than at the footpoints. (b) A hydrogen flux tube (shown with a red temperature color table) exhibits a comparatively narrow, uniform cross section both shortly after its formation (0:05 s) and even as its axis lengthens and kinks at later times (0:75; 1:45; 2:15 s) (Stenson and Bellan 2012). Reproduced with permission from AAS

The measurements show that about one tenth of the total current output flows through the flux tube and that the magnetic field peaks at 10^3 – 2×10^3 G. Plasma densities inside the flux tube are 10^{14} – 10^{15} cm^{-3} , corresponding to $\beta \simeq 0.01$ – 0.1 . The configuration evolves over 3–5 μs .

Although the plasma-filled loop is semi-toroidal when it forms, magnetic forces drive a rapid evolution toward more complex structures. Two parameters characterize the loop geometry: the flux tube minor radius and the locus of the flux tube axis. Plasma is confined inside the minor radius, corresponding to a force balance condition. By contrast, the axis is observed to evolve dramatically, increasing to as much as 10 times its initial length and undergoing a kink instability. Note that the flux tube volume increases substantially while the brightness remains approximately constant. This means that there must be inflow of plasma into the structure. If this were not the case, the tenfold increase in loop length would produce a tenfold decrease in loop density, and the brightness would significantly drop.

To determine the source of material entering the plasma loop, experiments are performed using a different gas at each of the two footpoint nozzles. High repetitive rate of the experiment allows to take the shots with optical filters chosen to transmit only the optical line emission of one species. The images can then be combined digitally. The typical images produced by this color-coding technique are shown

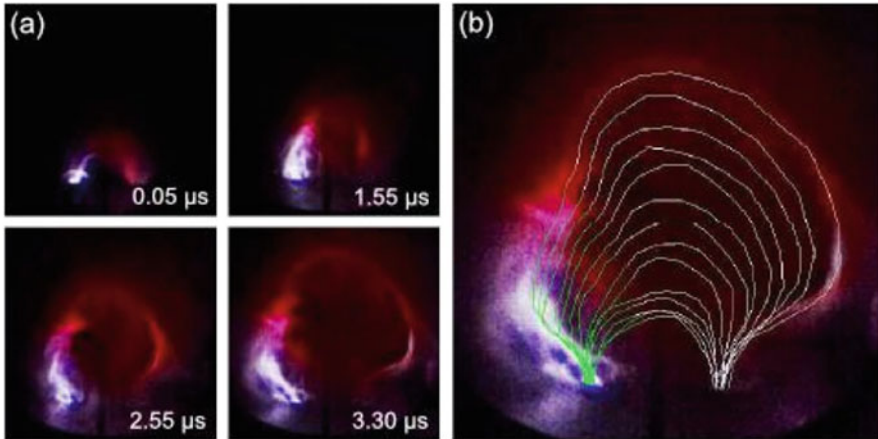


Fig. 21.14 (a) A nitrogen-hydrogen plasma loop at four consecutive times. Color pictures were produced by combining images from three different shots; two of the images were taken through optical filters, then used to color the third, unfiltered image. Nitrogen sections of the plasma (originating from the left footpoint) are tinted blue and hydrogen sections of the plasma (originating from the right footpoint) are tinted red. (b) Locus of the loop axis at 14 different times, all overlaid on top of the 3:30 s frame. Thin green and white contours indicate the nitrogen and hydrogen sections of the loop, respectively (Stenson and Bellan 2012). Reproduced with permission from AAS

in Fig. 21.14a. These images show that plasma flows into the loop from both footpoints, and that the flow dynamics depends strongly on the mass density.

To quantify the flow dynamics, image sequences were made for various combinations of gas species. The locus of the flux tube axis was manually traced out in each frame, as was the fraction of the loop length occupied by each species. Example of the resulting sets of traces for a nitrogen-hydrogen plasma loop is shown in Fig. 21.14b.

The measurements of the time-dependent loop length made from plasma shots taken at different times and with different gas species combinations show that the length of each subsection (i.e., filled with different species) of the loop is independent of the other subsection. It was found that each species flows from a footpoint into the flux tube at a particular rate.

The experiment has also allowed to determine relationship between loop dynamics and electric current. Increasing the capacitor charge voltage increases both the electric current and the rate at which the plasma loop expands. At all charging voltages, the expansion of loop was found to be as time squared. The constant acceleration of each loop is directly proportional to the initial rate at which the electrical current increases, with the same proportionality for all loops of a given species. The described laboratory processes are governed by the MHD, and thus may be scaled to various astrophysical processes and, in particular, to well-collimated solar loops from low atmosphere to solar corona.

21.6 On the Magnetic Reconnection

Magnetic reconnection per se and its role in various astrophysical phenomena have been broadly studied for decades in many laboratories, from early simple devices (Syrovatskii et al. 1973, 1981; Stenzel and Gekelman 1981; Gekelman et al. 1982) to highly sophisticated ones (Bergerson 2006; Fiksel et al. 2014; Forest et al. 2015; Frank et al. 2006; Furno et al. 2007; Yamada et al. 1997). Excellent reviews on the fundamental physics of magnetic reconnection in laboratory and space plasmas and literature therein provide a rich source to study the subject for both theorists, observers and experimenters (Yamada et al. 2010; Shibata and Takasao 2016; Zweibel and Yamada 2016; Myers et al. 2015).

Here we consider an example of well-scaled laboratory experiment aimed to reproduce a magnetic reconnection topology similar to that observed in solar flares, namely a loop-top reconnection (Masuda et al. 1994; Nitta et al. 2001). The experiment was performed at the Shenguang (SG) II laser facility (Zhong et al. 2010, 2016). Eight laser beams, with wavelength of $\lambda_L = 0.351 \mu\text{m}$, are divided into four bunches with each bunch consisting of two laser beams. The configuration is designed to be similar to the scheme of a loop-top X-ray source in the solar flares depicted in Fig. 21.15a.

Two synchronized laser bunches separated by 400–600 μm are focused onto one side of the aluminium foil with the other two laser bunches simultaneously irradiating the other side. Each bunch is focused to a focal spot diameter, giving an incident laser intensity of $\sim 5 \times 10^{15} \text{ W cm}^{-2}$. A copper target is set 250 μm away from one foil edge. The X-ray emission is measured using three X-ray pinhole cameras in the forward, side and reverse directions, to investigate the reconnection jets as well as their impact on the copper target.

Two bright X-ray spots resulted from the laser heating of the Al foil are clearly seen in Fig. 21.15b. The spontaneous magnetic field has an estimated MG strength. When two plasma bubbles expand on the Al foil surface, toroidal MG magnetic fields merge resulting appearance of a diffusion region which can be clearly seen with two significant X-ray patterns signifying the release of magnetic energy. In this region electrons and ions are decoupled, and magnetic reconnection takes place.

A similar experiment was carried out with two imbalanced laser beams separated by 400 μm . The result is shown in Fig. 21.15c. One can see that the upflow is not vertical. The measured inclination is about 10° . This kind of effect is quite typical to the plasma jets associated with the solar coronal flares. At the same time, the X-ray intensity in this setting is greatly enhanced in comparison with the previous case shown in Fig. 21.15b. Note also that in both experiments a bright X-ray spot at the center of the Cu target is observed just below the downward outflow.

The position and the arc shape of the spot is clearly resembling the loop-top X-ray source in solar flare observations. Moreover, for example, the inclined upflow seen in Fig. 21.15c extends more than for 2 mm and has an average width 300 μm ,

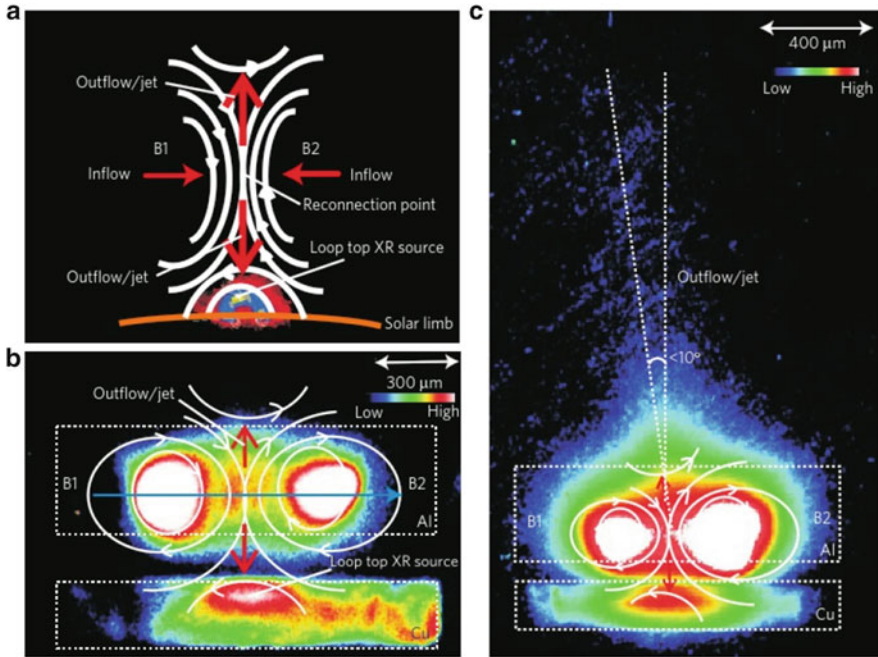


Fig. 21.15 The X-ray source and outflows similar to the solar coronal loop-top case observed in the laboratory. (a) Sketch of magnetic reconnection and the loop-top X-ray source in a compact solar flare; (b) The pinhole X-ray image observed forward of the Al foil target. Magnetic field lines are illustrated based on the flux surface of the plasma bubbles. The Al and Cu targets are the rectangles enclosed by white dotted lines. The red arrows indicate directions of outflow; (c) X-ray image with two laser spots separated by $400\ \mu\text{m}$ and with a foil thickness of $10\ \mu\text{m}$. The asymmetry of the laser intensity on the Al target causes an imbalance of the laser spots as well as of the magnetic fields $B1$ and $B2$, and further induces the inclination of the upward outflow. The downward outflow impinges on the Cu target and results in a hot X-ray source (Zhong et al. 2010). Reprinted with permission from Springer Science and Business Media

which translates to $2 \times 10^5\ \text{km}$ in length and $3 \times 10^4\ \text{km}$ in width when scaled to a solar parameters, which are on the order of the typical lengths and widths of X-ray jets observed in solar flares. The measured flow velocity in the experiment, $400(\pm 50)\ \text{km s}^{-1}$, agrees well with the typical Alfvén speed of $v_A \simeq 400\ \text{km s}^{-1}$, in a magnetic field of $10^6\ \text{G}$ for the experiment. A similarity criteria hold also well for the transverse velocity for bi-directional plasma jets of $\simeq 150\text{--}300\ \text{km s}^{-1}$.

The MHD similarity in solar flares and laser-produced plasmas is shown in Table 21.2, with the transformation coefficients $a = 10^{-11}$, $b = 10^8$ and $c = 10^{10}$. The scaled parameters of the solar coronal plasmas in the third column are very similar to those of the laser-produced plasmas in the second column.

Table 21.2 The similarity of solar flares and laser-produced plasmas, with $a = 10^{-11}$, $b = 10^8$, $c = 10^{10}$

Parameters	Flare plasma	Laser plasma	Scaled for flare plasma
Length (cm)	$\sim 10^9-10^{10}$	$\sim 10^{-1}$	$\sim 10^{-2}-10^{-1}$
Times (s)	$\sim 10^2-10^3$	$\sim 10^{-9}$	$\sim 10^{-9}-10^{-10}$
Pressure (Pa)	$\sim 10^{-3}-10$	$\sim 10^7$	$\sim 10^7-10^{11}$
Density (cm^{-3})	$\sim 10^9-10^{11}$	$\sim 10^{19}-10^{20}$	$\sim 10^{19}-10^{21}$
Velocity (km s^{-1})	$\sim 10-100$	~ 100	$\sim 100-1000$
Magnetic field (G)	$\sim 10-100$	$\sim 10^6$	$\sim 10^6-10^7$

21.7 Laboratory Simulation of Solar Coronal Plasmoids

The small-scale (sub-arcsec) coronal mass ejection (CME) phenomena, plasmoids, often having the shape of tadpoles are believed to play an important role in the coronal dynamics. The observations of small plasmoids propagating in the solar corona (Koutchmy et al. 1994; Alexander and Fletcher 1999) revealed details of dynamic behavior of plasmoid and lead authors to the plausible model of plasmoid as a toroidal vortex. A tadpole-shaped jets in galactic clusters have been observed for decades.

Figure 21.16 shows examples of a classical tadpole-shaped galactic clusters (left) and solar coronal plasmoid which, in a few minutes, develops the thick head and a weak tail (right). The origin of coronal plasmoids was successfully associated with the coronal reconnections (Yokoyama and Shibata 1995; Shibata et al. 1995).

Formation and evolution of solar plasmoids can be simulated in the scaled laboratory experiment using an accelerated spheromak-like compact toroid (CT) injected into a tokamak magnetized target region. The UC Davis Compact Toroid accelerator (CTIX) is designed to study the formation and acceleration of a compact toroid under repetitive operation, with well-developed diagnostics of interaction and thermalization of the plasmoid as it is injected into a target region (Hwang et al. 1999, 2000, 2002).

The CT is excited by a combination of dynamo action and externally produced static magnetic field in a magnetized coaxial plasma gun. The resultant magnetic field structure is in a nearly force free state (i.e., $\nabla \times \mathbf{B} = \lambda \mathbf{B}$). The accelerator consists of two sections, the formation section and the acceleration section (Fig. 21.17).

In the coaxial (injection) region the accelerated CT interacts with the pre-existing magnetic field, generated by the solenoidal coils. The coils are also used to change the geometry of the ambient magnetic field. The accelerating force is the magnetic field pressure gradient generated across the CT. The plasma and poloidal field are driven into an expansion region. During the motion of the accelerated CT, its internal magnetic field can be measured using magnetic probes based on the Faraday induction effect. Once the CT has detached from the central accelerating electrode, magnetic probes can measure the tilting of the CT in the azimuthal direction.

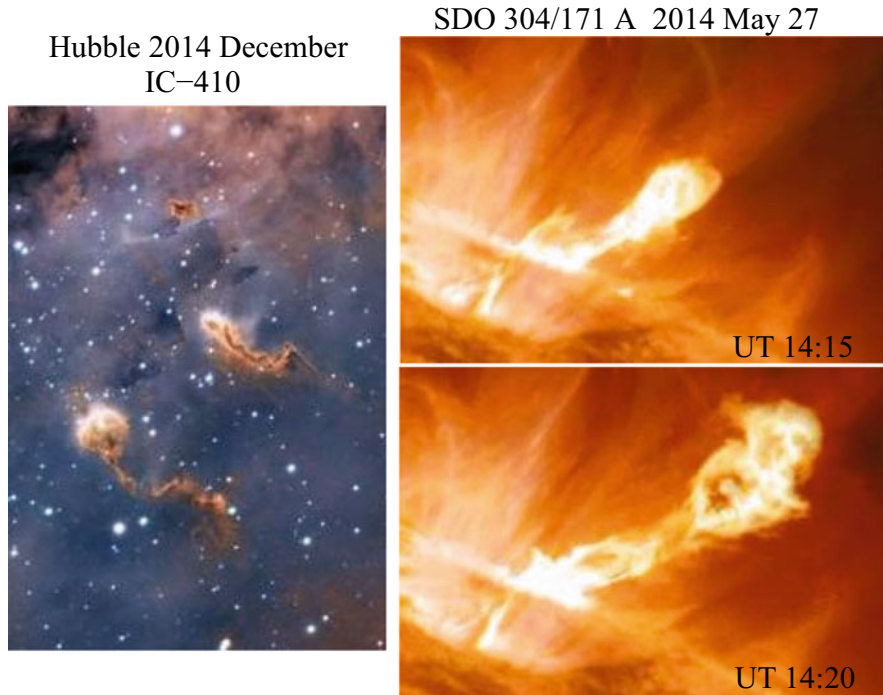


Fig. 21.16 Cosmic tadpoles: Galactic clusters observed by the Hubble in the IC-410 nebula (left) Courtesy of NASA; a tadpole originated in the solar chromosphere/corona in two instances of time observed with the SDO/AIA (right)

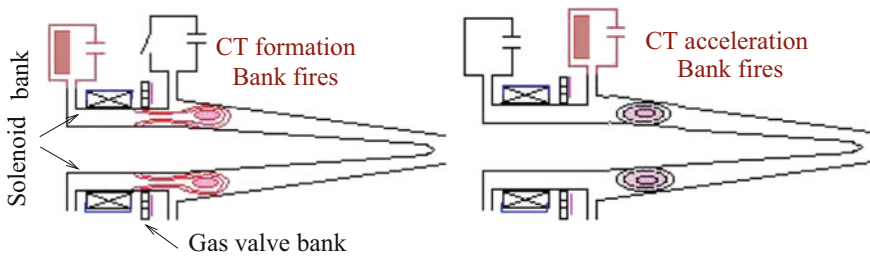


Fig. 21.17 Stages of CT formation and acceleration (Hwang et al. 1999). Courtesy of D. Hwang

Figure 21.18 shows a sample 2D images of the CT as it is accelerated towards the mirror. The different range of parameters and geometries of the external magnetic field allows to reproduce the various conditions of the propagation of the compact toroid in the target chamber.

In most cases the field reversal in the shell between the compact toroid and ambient field occurs, suggesting a strong coupling between the toroid and the ambient field that may eventually lead to the reconnection and “braking” of the CT.

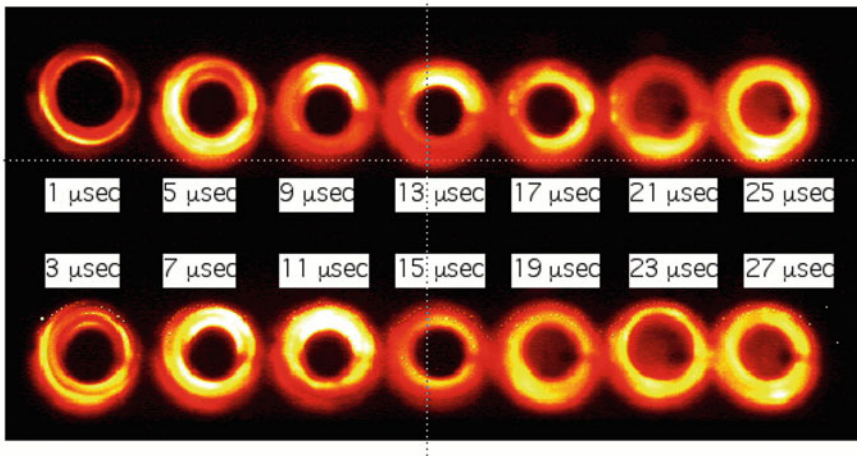


Fig. 21.18 Sample 2D images of the CT as it is accelerated towards the mirror. Time sequence of the SCT images shows the dynamic changes in its magnetic field and density during acceleration (variation of the intensity) (Hwang et al. 1999). Reprinted with permission from IOP

In this case, the “broken” CT acquires the shape of tadpole having a strong head and weak tail.

Examples of such process is shown in Fig. 21.19. The CT interacting with the weak external magnetic field of 280G acquires the shape of a tadpole. Panel **a** shows the CT evolution in case when its poloidal field is antiparallel to the external magnetic field, and panel **b** shows the evolution of CT when its magnetic field is parallel to external field. One can see that in the second case the effect is more pronounced. The outcome also depends on the electric currents. Inlets in panels a-b show color codes for five sets of electric current ranging from zero (red lines with circles) to $j = 200$ A (red dashed lines with plus signs). One can see that the stronger is current the stronger becomes the tail of tadpole and weaker is its head and v.v.

Physical conditions in the CTIX experiment can be reliably scaled to solar conditions: the main requirements for a proper scalings are well achievable. Indeed, thermodynamically both systems, the solar photosphere and tokamak plasma, are polytropic with $\gamma = 5/3$. The Lundquist number, $S = \tau_R/\tau_A$, the ratio of the resistive diffusion time $\tau_R = L^2/D_m$ and the Alfvèn time, τ_A , are much larger than unity.

In the laboratory, along the condition $S \gg 1$, the duration of the experiment, t_{exp} , on the one hand must be short compared to resistive time, and, on the other hand it must be much larger than the Alfvèn time, providing the force-free equilibrium of the plasma, i.e.

$$\tau_A \ll t_{\text{exp}} \ll \tau_R, \quad S \gg 1 \quad (21.23)$$

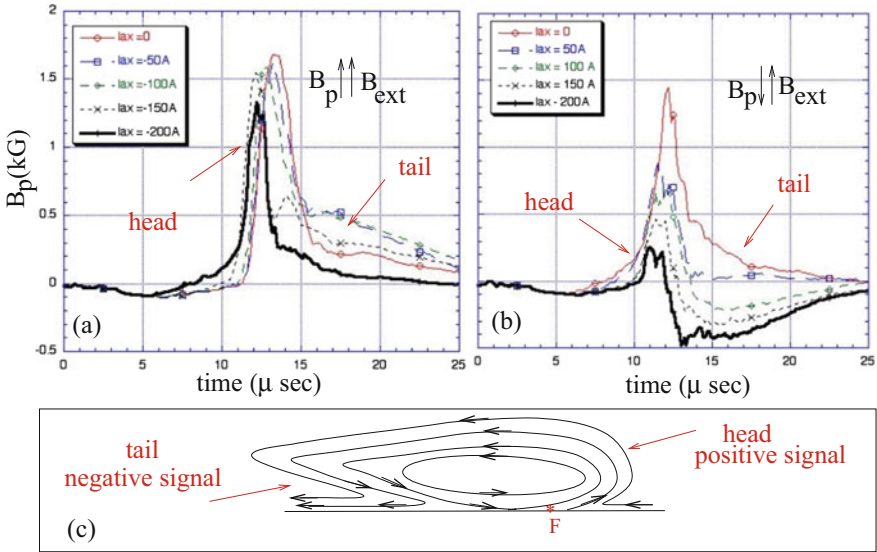


Fig. 21.19 Interaction of the CT with external magnetic field. (a) The CT evolution in case when its poloidal magnetic field is antiparallel to the external magnetic field; (b) the case when the poloidal magnetic field of CT is parallel to the external field. In both cases there appears negative signal in the CTs magnetic field indicating change of its shape into the tadpole shape; (c) schematic of a tadpole (Hwang et al. 2002). Courtesy of D. Hwang

For the CT $L = 20$ cm, density $n = 10^{15} \text{ cm}^{-3}$, and the temperature $T = 10$ eV. Then for the resistive diffusion time, $\tau_R = L^2/D_m$, where $D_m = 0.824 \times 10^6 \lambda/t^{3/2} \text{ cm}^2 \text{ s}^{-1}$, we have $\tau_R = 1.54 \times 10^{-3} \text{ s}$ (with $\lambda = 10$). The Alfvén time, $\tau_A = 5.8 \times 10^{-7} \text{ s}$, while the duration of the experiment is $t_{exp} = 20 \mu\text{s}$, much longer than τ_A providing the force-free equilibrium of the plasma. The Lundquist number $S = \tau_R/\tau_A$ for this particular example is 2.6×10^3 . For the coronal plasmoid $L = 1.4 \times 10^9$ cm, $n = 10^9 \text{ cm}^{-3}$, $B = 2\text{--}4$ G, average lifetime $\tau_{obs} = 250$ s. And we arrive to the following estimates: $\tau_R = 3.7 \times 10^{10} \text{ s}$, $\tau_A = 17.5 \text{ s}$. Hence, $\tau_A \ll \tau_{obs} \ll \tau_R$ and $S = 2 \times 10^9$.

Thus, the conditions (21.3) are well satisfied for both, laboratory and coronal plasmoids. Now, and, most importantly, we need to find the scaling parameters, determined by relations (21.5). Note that the parameters a , b , and c are interdependent, ensuring thus the reliability of the scaling. Using the physical parameters of the CT and solar plasmoid, we get $a = 3 \times 10^{-8}$, $b = 5 \times 10^5$, $c = 2.9 \times 10^5$. The similarity of the CT and solar tadpole-like plasmoid is shown in Table 21.3.

The similar procedure can be applied to the tadpoles observed in the sunspot penumbra. Observations of magnetic fields and flows in sunspot penumbrae at a spatial resolution of $0.1\text{--}0.2''$ revealed amazing details in the fine structure of penumbral filaments and their dynamics (Scharmer et al. 2002; Langhans et al. 2005). Some properties the fine structure of penumbrae briefly may be characterized

Table 21.3 The similarity of the CT and solar tadpole-like plasmoid, with $a = 3 \times 10^{-8}$, $b = 5 \times 10^5$, $c = 2.9 \times 10^5$

Parameters	Solar tadpole	Lab plasmoid	Scaled for sun
Length (cm)	5×10^8 – 10^9	20	15–30
Pressure (Pa)	5.5×10^{-2} – 10^{-1}	1.6×10^4	$(1.6$ – $2.9) \times 10^4$
Density (cm^{-3})	2×10^9 – 10^{10}	10^{15}	$(1.1$ – $5.5) \times 10^{15}$
Velocity (km s^{-1})	150–300	200	115–230
Magnetic field (G)	2–4	1.5×10^3	$(1.2$ – $2.15) \times 10^3$

as a dense ensemble of dark-cored and bright magnetic filaments, highly dynamic at short time scales and preserving their general properties for hours. Topologically, dark-cored filaments surrounded by bright walls have a peculiar shape of penumbral tadpoles with a thick head “diving” into the umbra and a long tail reaching the outer edge of penumbra. It was found (Ryutova and Hagenaar 2005) that differences in the inclination of magnetic fields and sheared velocities result in the nonlinear instabilities associated with the vortex motion and interaction of the poloidal and toroidal components of magnetic fields. This, in turn, leads to a filamentation process, as well as formation of the structures having the appearance of tadpoles.

References

- D. Alexander, L. Fletcher, *Sol. Phys.* **190**, 167 (1999)
W. Bergerson, C. Forest, G. Fiksel et al., *Phys. Rev. Lett.* **96**, 015004 (2006)
T.R. Boehly et al., *Rev. Sci. Instrum.* **66**, 508 (1995)
G.C. Burdiak et al., *Ph. Pl.* **24**, 2713 (2017)
A. Ciardi, S.V. Lebedev, A. Frank et al., *Astrophys. J.* **691**, L147 (2009)
G. Fiksel, W. Fox, A. Bhattacharjee et al., *Phys. Rev. Lett.* **113**, 105003 (2014)
C.B. Forest et al., *J. Plasma Phys.* **81**, 345810501 (2015)
J.M. Foster, B.H. Wilde, P.A. Rosen et al., *Astrophys. J.* **634**, L77 (2005)
A.G. Frank, S.Y. Bogdanov, G.V. Dreiden et al., *Phys. Lett. A* **348**, 318 (2006)
I. Furno, T.P. Intrator, G. Lapenta et al., *Phys. Plasmas* **14**, 022103 (2007)
L. Gao et al., *Phys. Rev. Lett.* **109**, 115001 (2012)
L. Gao et al., *Phys. Rev. Lett.* **110**, 185003 (2013)
W. Gekelman, R. Stenzel, N. Wild, *J. Geophys. Res. Space Phys.* **87**, 101 (1982)
G. Gregori et al., *Nature* **481**, 480 (2012)
J.F. Hansen, S.K.P. Tripathi, P.M. Bellan, *Phys. Plasmas* **11**, 3177 (2004)
S.C. Hsu, P.M. Bellan, *Phys. Rev. Lett.* **90**, 215002 (2003)
C.M. Huntington et al., *Nat. Phys.* **11**, 173 (2015)
D.Q. Hwang et al., *Phys. Plasmas* **6**(5), 1 (1999)
D.Q. Hwang et al., *Nucl. Fusion* **40**, 897 (2000)
D.Q. Hwang et al., AGU, SSM32D (2002)
K. Keilty, E.P. Liang, T. Ditmire et al., *Astrophys. J.* **538**, 645 (2000)
S. Koutchmy et al., *Astron. Astrophys.* **281**, 249 (1994)
N. Kugland et al., *Nat. Phys.* **8**, 809 (2012)
L.D. Landau, E.M. Lifshitz, *Fluid Mechanics* (Pergamon Press, Oxford, 1987)
K. Langhans et al., *Astron. Astrophys.* **436**, 1087–1101 (2005)

- S.V. Lebedev, J.P. Chittenden, F.N. Beg et al., *Astrophys. J.* **564**, 113 (2002)
- S.V. Lebedev, A. Ciardi, D.J. Ampleford et al., *Mon. Not. R. Astron. Soc.* **361**, 97 (2005)
- S. Masuda et al., *Nature* **371**, 495 (1994)
- D.N. Maywar et al., *J. Phys.* **112**, 032007 (2008)
- C.E. Myers, M. Yamada, H. Ji et al., *Nature* **528**, 526 (2015)
- P.M. Nilson et al., *J. Plasma Phys.* **81**, 365810201 (2015)
- N.V. Nitta, J. Sato, H.S. Hudson, *Astrophys. J.* **552**, 821 (2001)
- H.-S. Park, D.D. Ryutov, J.S. Ross et al., *High Energy Density Phys.* **8**, 38 (2012)
- B.A. Remington, J. Kane, R.P. Drake et al., *Phys. Plasmas* **4**, 1994 (1997)
- B.A. Remington, R.P. Drake, D.D. Ryutov, *Rev. Mod. Phys.* **78**, 755 (2006)
- J.S. Ross et al., *Phys. Plasmas* **19**, 056501 (2012)
- D.D. Ryutov et al., *Astrophys. J.* **518**, 821 (1999)
- D.D. Ryutov, R.P. Drake, B.A. Remington, *Astrophys. J. Suppl.* **127**, 465 (2000)
- D.D. Ryutov, B.A. Remington, H.F. Robey, R.P. Drake, *Phys. Plasmas* **8**, 1804 (2001)
- D.D. Ryutov et al., *Plasma Phys. Control. Fusion* **54**, 105021 (2012)
- D.D. Ryutov et al., *Phys. Plasmas* **20**, 032703 (2013)
- M. Ryutova, H. Hagenaar, AGU FMSH11A 0239R (2005)
- O. Sadot et al., *Phys. Rev. Lett.* **95**, 265001 (2005)
- G. Scharmer et al., *Nature* **420**, 151 (2002)
- K. Shibata, S. Takasao, in *Magnetic Reconnection, ASSL*, vol. 427, ed. by W. Gonzalez, E. Parker (Springer, Berlin, 2016), p. 373
- K. Shibata et al., *Astrophys. J.* **451**, L83 (1995)
- V.A. Smalyuk et al., *Phys. Rev. Lett.* **95**, 21500 (2005)
- J.A. Stamper et al., *Phys. Rev. Lett.* **26**, 1012 (1971)
- E.V. Stenson, P.M. Bellan, *Phys. Rev. Lett.* **109**, 075001 (2012)
- R. Stenzel, W. Gekeleman, *J. Geophys. Res.* **86**, 649 (1981)
- F. Suzuki-Vidal et al., *Astrophys. Space Sci.* **322**, 19 (2009)
- F. Suzuki-Vidal, M. Bocchi, S.V. Lebedev et al., *Phys. Plasmas* **19**, 022708 (2012)
- F. Suzuki-Vidal, S.V. Lebedev, M. Krishnan et al., *High Energy Density Phys.* **9**, 141 (2013)
- S.I. Syrovatskii, *Annu. Rev. Astron. Astrophys.* **19**, 163 (1981)
- S.I. Syrovatskii, A.G. Frank, A.Z. Khodzhaev, *Sov. Phys. Tech. Phys.* **18**, 580 (1973)
- M. Yamada, H. Ji, S. Hsu et al., *Phys. Rev. Lett.* **78**, 3117 (1997)
- M. Yamada, R. Kulsrud, H. Ji, *Rev. Mod. Phys.* **82**, 603 (2010)
- T. Yokoyama, K. Shibata, *Nature* **375**, 42 (1995)
- J.Y. Zhong, Y. Li, X. Wang et al., *Nat. Phys.* **6**, 984 (2010)
- J.Y. Zhong, J. Lin, Y.T. Li et al., *Astrophys. J. Suppl.* **225**, 30 (2016)
- E.G. Zweibel, Yamada M., *Proc. R. Soc. A* **472**, 20160479 (2016). <https://doi.org/10.1098>

Chapter 22

What to Observe in Low Atmosphere



Abstract In this chapter, we shall discuss some aspects of solar phenomena that can be described as “what to observe in low atmosphere.” New space and ground based instruments with ever increasing spatial resolution and time cadence allow to observe amazing details of solar phenomena. Examples of the observational results will be presented in about the same order as the content of the book. When possible, the frames for quantitative analysis discussed throughout the book will be given.

22.1 Wave Phenomena

We start with the sunspots. Before 1990s there were only a few observational papers arguing that the sunspot umbra has a filamentary structure (Papathanasoglou 1971; Livingston 1991). By now, high resolution data revealed not only filamentary structure of umbra but also show the infrastructure of various small-scale elements in sunspots. As discussed throughout the book, it is just this highly intermittent nature of sunspots that provides occurrence of physical effects that would not be there had the sunspot a monolithic nature (Ryutova and Persson 1984). Here we mention a few of them and, in particular, the wave phenomena. Even in linear stage, filamentary structure of sunspot leads to strong absorption of the wave power, just like perforated sealing and wall make the room quieter (Chap. 8). In nonlinear stage, not only shocks and solitons may develop, but they have their own specifics associated with highly inhomogeneous nature of sunspots (Chap. 9). With modern instruments details of the wave phenomena in sunspots and their impact on the overlying atmosphere can be studied in detail.

Figure 22.1 shows an example of umbral oscillations studied by chromospheric imaging of a sunspot with the NST instrument at BBSO. The images were acquired every 23 s by scanning of the $H\alpha$ spectral line from the blue wing -1 \AA to the red wing $+1 \text{ \AA}$ with a step of 0.2 \AA . Images in the TiO 7057 \AA line, that forms at temperatures below 4000 K, were used to identify the boundary between umbra and penumbra. The propagating velocities of umbral and penumbral waves are shown in Fig. 22.2. The space-time image corresponds to the vertical slit marked in Fig. 22.1.

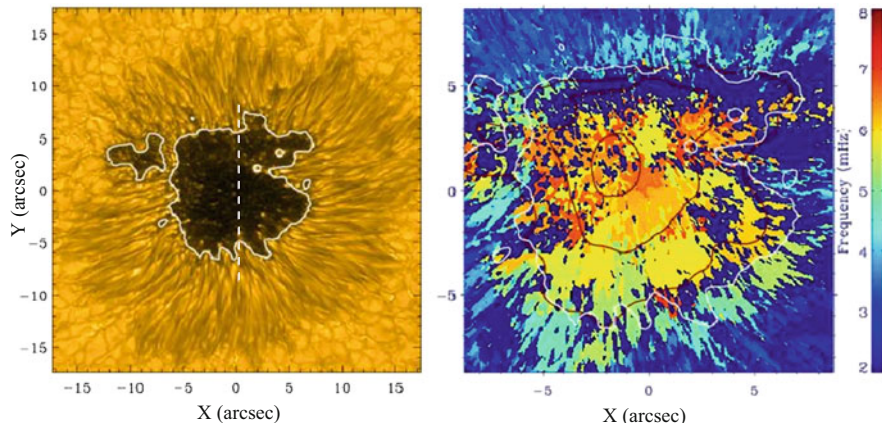


Fig. 22.1 Left: Image of the sunspot NOAA 12132 taken with TiO filter at 7075 \AA on Aug. 5 2014. Right: the power map of the dominant oscillation frequencies in the umbra. The red contours show the cosines of magnetic field inclinations with levels of 0.85, 0.95, and 0.99. The dotted line marks a slit position for the space-time analysis (see Fig. 22.2 below). The white contour outlines the umbral boundaries (Su et al. 2016). Reproduced with permission of the AAS

Calculating the gradient of the ridges, one obtains the wave velocities. In these observations the velocity distribution for umbral waves was found to range from ~ 15 to 50 km s^{-1} , and for the penumbral waves from 6 to 20 km s^{-1} . It is interesting that these observations allowed to study a global rotation of wavefronts having a spiral nature. Besides, the shock waves in the central part of umbra were clearly identified.

Temporal pattern of shock waves are well observed in space-time images as well as in temporal series of spectropolarimetric observations. Figure 22.3 shows an example of the shock velocity observations in sunspot umbra simultaneously in two spectral lines: Si I 1082.7 \AA (photosphere) and He I 1083 \AA line multiplet (chromosphere). The observations were carried out at the VTT, the Observatory del Teide on October 1, 2000, using the Tenerife Infrared Polarimeter (TIP).

Temporal evolution of Stokes V inside the umbra having a saw-tooth shape is a clear evidence of shock formation above the umbra. This pattern has been observed on a regular basis with different instruments (see, e.g., also earlier (Christopoulou et al. 2001; Chae et al. 2015; Madsen et al. 2015; Yurchyshyn et al. 2015)). Note that observations of the small-scale umbral brightenings were also found to be directly associated with shock formation above the sunspot umbrae (Roupe van der Voort et al. 2003; Yang et al. 2015; Zhang et al. 2017; Song et al. 2017; Nelson et al. 2017). These shocks may cause a surge-like oscillations in the overlying chromosphere and transition region. Example of such event is shown in Fig. 22.4. It was found, for example, that the Si IV 1402.77 \AA ($T \sim 10^5 \text{ K}$, middle of the transition region) is generally enhanced and broadened in the bright front, and the oscillation period stays almost unchanged over a long time, indicating that the surge-like oscillations

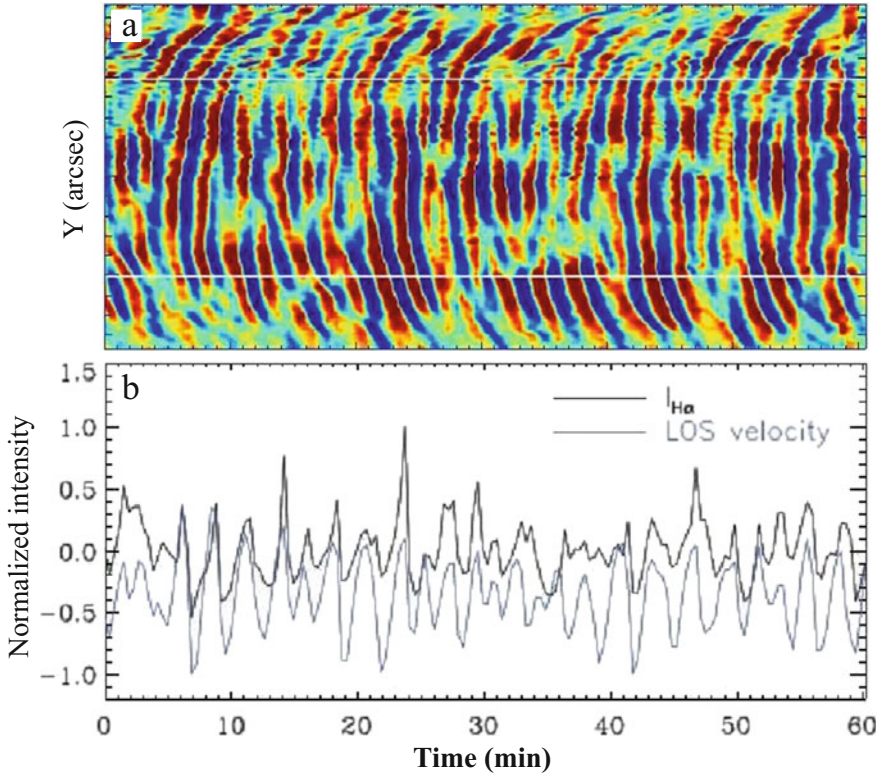


Fig. 22.2 The space-time map showing the mass motions with a clear wave pattern in the umbra and penumbra. The solid lines mark the umbral/penumbral boundary (Su et al. 2016). Reproduced with permission of the AAS

above light bridges are caused by shocks produced in underlying photosphere. It is interesting that in the chromosphere, the Mg II K 2796 Å line first shows a large blueshift, and then gradually decreases to zero before increasing to a redshift of comparable magnitude. Such a behavior suggests that the oscillations are highly nonlinear.

When studying shocks, one of the necessary thing is to measure the intensity of spectral line vs wavelength, especially for several consecutive time steps, e.g., in Figs. 13.11, 13.12 and 13.13. Such measurements allow a simple quantitative analysis described in Chap. 13 (based on Eqs. (13.14)–(13.15)).

The IRIS instrument allows to make such measurements directly. Example is shown in Fig. 22.5. Upper panels show a regular saw-tooth shock pattern. Lower panels depict the intensity profiles vs wavelength. A double-humped profiles typical of shocks are well seen in the transition region (Si IV 1393.76 Å) and in the chromosphere (Mg II 2796.35 Å). Most importantly, the left peak of chromospheric line is higher than the right one, which means that the shock is *upward* propagating. In case of the transition region line, at $t = 33.4$ min (blue curve), the left peak

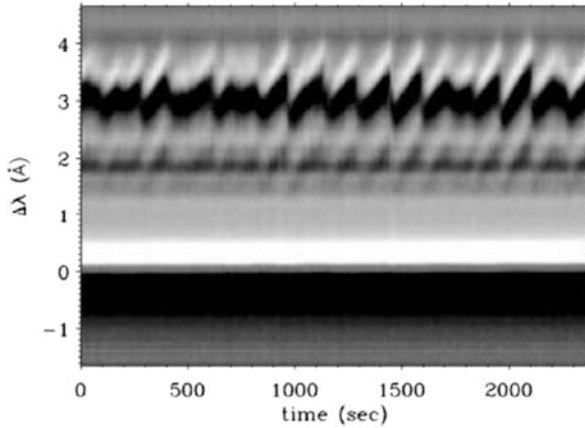


Fig. 22.3 Temporal evolution of Stokes V inside the umbra. The Si I profile (lower part of the figure) shows no apparent change with time, while He profiles (upper part) show periodic Doppler shifts with a clear saw-tooth shape (Centeno et al. 2006). Reproduced with permission of the AAS

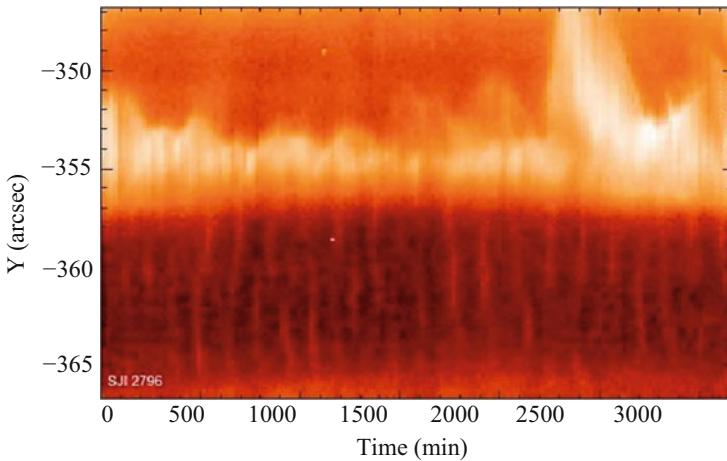


Fig. 22.4 Space-time image of the IRIS 2796 Å SJI images along the slit crossing the center of umbra and light bridge. The upper part shows the surge-like activities and light wall oscillations. The lower part shows umbral oscillations (Zhang et al. 2017). Reproduced with permission of the AAS

is also higher than the right peak, i.e., around this time the shock is propagating upward, whereas at $t = 33.7$ min (red) line, the left peak is lower than the right one indicating appearance of a reverse shock.

As described in Chap. 13, this kind of data allow full quantitative analysis and estimate of the energetics of the event. To study further the stochasticity of umbral oscillations and upward-downward propagating shocks, it is important to investigate

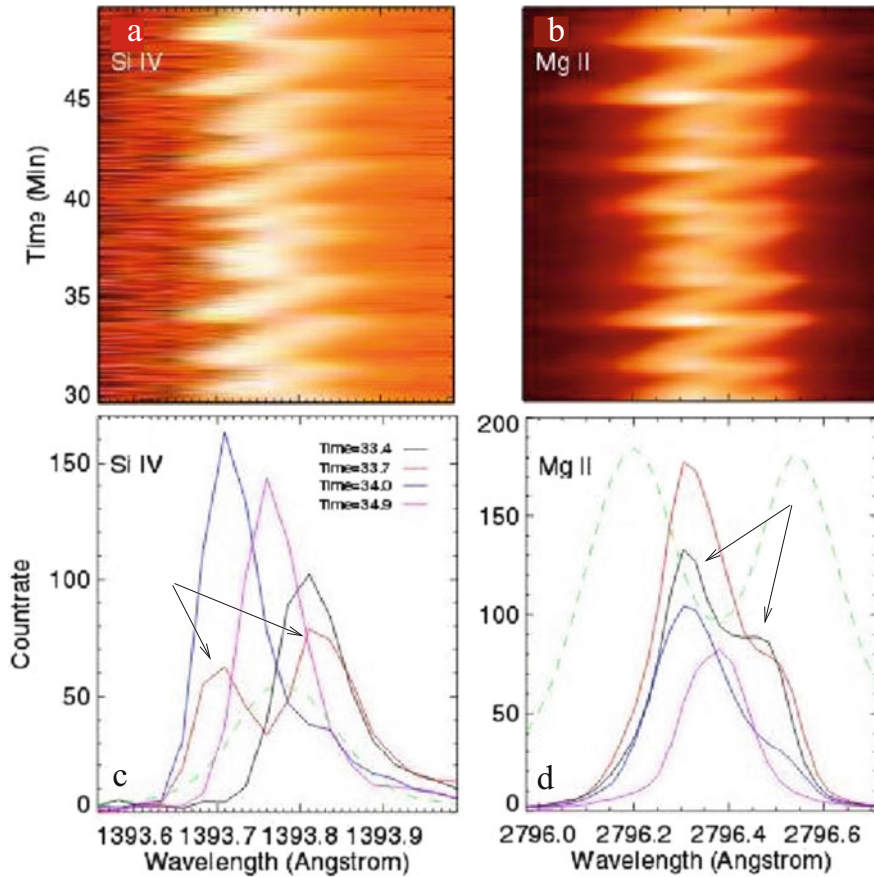


Fig. 22.5 Upper panels: Wavelength-time plots for Si IV 1393.76 Å and Mg II 2796.35 Å at the slit crossing the center of the umbra (shown is part of the time range). Lower panels: Profiles of the two line intensities vs wavelength. Colors are related to different time. Typical profiles in the plate are shown as the dashed lines. Courtesy of H. Tian

their dependence on several factors and compare results obtained under various conditions such as: (1) character of the sunspot: whether the sunspot is isolated or it is a part of active region; (2) how strong is activity of MMFs and, by contrast, are there long-living coronal loops rooted; (3) what is the activity in the overlying chromosphere/transition region which are the first to respond to the sunspot activity.

One can also search for appearance of solitons in accordance with Eq. (9.67) that predicts both regimes, generation of shock waves in case of prevailing nonlinearity and solitons in case of the balanced non-linearity and dispersion. From the observational point of view the solitons may be less bright but will have much longer lifetimes, and their propagation velocities may be close but below the local sound speed.

22.2 Magnetosonic Streaming and Fragmentation of Magnetic Flux Tubes

Photospheric flux tubes buffeted by convective motions undergo a complex evolution. In particular, nonlinear coupling of surrounding motions and flux tube resulting in magnetosonic streaming causes fragmentation of a flux tube which continues until the individual fragments reach the critical radii and get diffusively dissolved into the ambient plasma. At the same time, the process of fragmentation is accompanied by the generation of secondary mass flows and current drive. In Chap. 10 we have discussed these effects in detail. Below, we will demonstrate for convenience results of some more numerical experiments (for description of numerical experiment and theory, see Sect. 10.5).

Figures 22.6 and 22.7 show two regimes of flux tube evolution. Figure 22.6 shows a final stage of flux tube evolution that first splits into two major elements still surrounded by the peripheral magnetic field (cf. Figs. 10.4 and 10.5, Chap. 10)

Note that in the experiment shown in Fig. 22.6 the perturbation frequency is twice as high as in the experiment shown in Fig. 10.4, Chap. 10 (Model 1). Although we again witness the splitting of the initial flux tube, but this time into two major satellites, while in Model 1 along two major newborn flux tubes there were two weaker elements. In both cases, the process, of course, proceeds further until the structure disappears, but it is important to investigate dependence of the process of fragmentation on the oscillation frequency.

Another example of the flux tube evolution, showing dependence on the viscosity, is given in Fig. 22.7 (only magnetic field evolution is shown). In this experiment we deal with higher viscosity of medium.

One can see that at the time step $t = 38$ (i.e., much earlier than in previous cases), flux tube acquires quite complicated shape that could be seen in the observation as several satellites and a sigmoidal magnetic structure. Let us see how experimental parameters translate into solar scales. The area of the frame is $20/H \times 20/H$. The scale height in the photosphere is about 130 km, then we deal with the area of 2600×2600 km. The small satellites marked by arrows 1 and 2 in the fourth panel have roughly diameters $D_1 = 2.3H \simeq 300$ km and $D_2 = 2.7H \simeq 350$ km. This means that with the resolution of about 100–200 km not only these satellites will be well resolved, but their further evolution will be seen as well.

It is important to emphasize that the fragmentation process described above may also be accompanied by generation of the upflow/downflows and aligned them currents (see Sect. 10.4). The corresponding equations are quite simple, and contain mostly directly observable parameters. With modern instruments one can verify many aspects of these phenomena, and using simple theoretical estimates perform quantitative analysis. High resolution data allow to better resolve the small-scale magnetic elements and, making high cadence movies reveals more details of their evolution (Vargas Dominguez et al. 2015; Martinez Gonzalez et al. 2016; Park et al. 2016; Requerey et al. 2017; Ermolli et al. 2017). For example, individual flux tubes

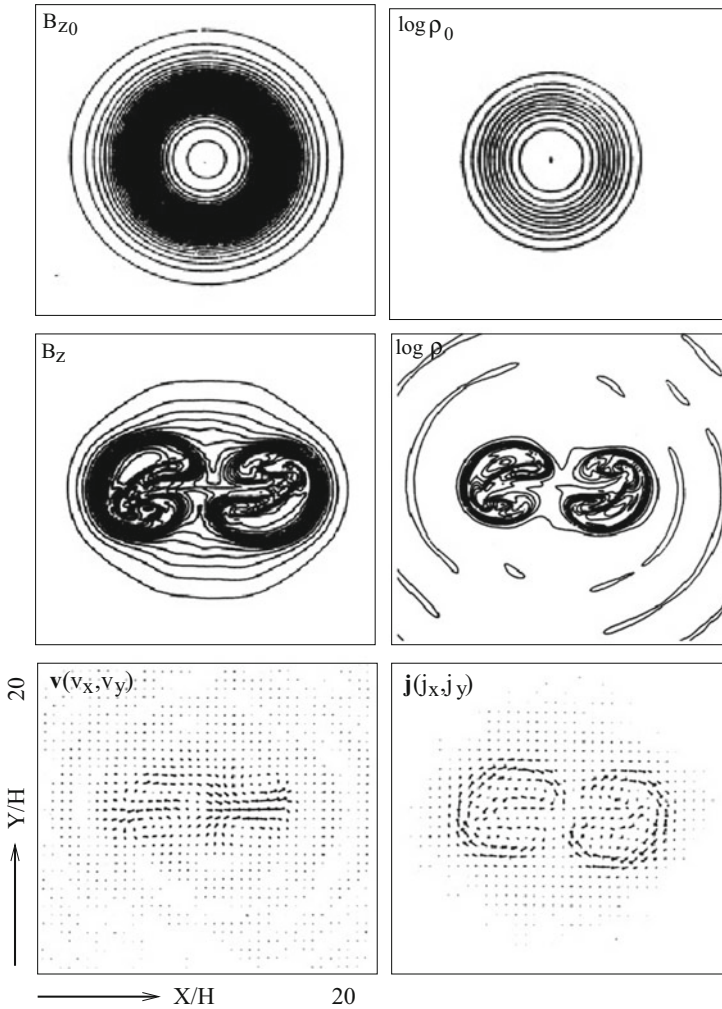


Fig. 22.6 Nonlinear evolution of flux tube buffeted by acoustic field and convective motions (Rytova et al. 1996). Upper panels ($t = 0$): undisturbed contour lines of longitudinal magnetic field, $B_z(r)$, and the density $[\log \rho(r)]$. Four lower panels show results of final time step of the experiment: the contour lines of magnetic field, the density contours, the generated current density $\mathbf{j} = (j_x, j_y)$, and the velocity field $\mathbf{V} = (V_x, V_y)$. Total illustrated area is (20×20) in units of photospheric scale height H . The maximum values of the current density and velocity vectors are in units of $(\rho c_s^2/H)^{1/2}$ and sound speed c_s , respectively. The time is in units of H/c_s .

seen at the resolution of, say $1''$, show at the resolution of $0''.15$ – $0''.18$ continuously evolving complex internal structure in compliance with physics described above. Recall that flux tubes may experience fragmentation until they reach a diffusively vanishing limit which is about 40–70 km, i.e., $0''.06$ – $0''.1$.

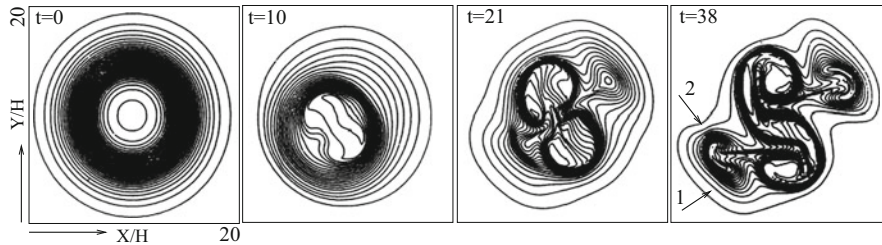


Fig. 22.7 Time evolution of flux tube in case of higher viscosity of medium: multiple fragmentation process proceeds faster and satellites acquire quite a complex shape

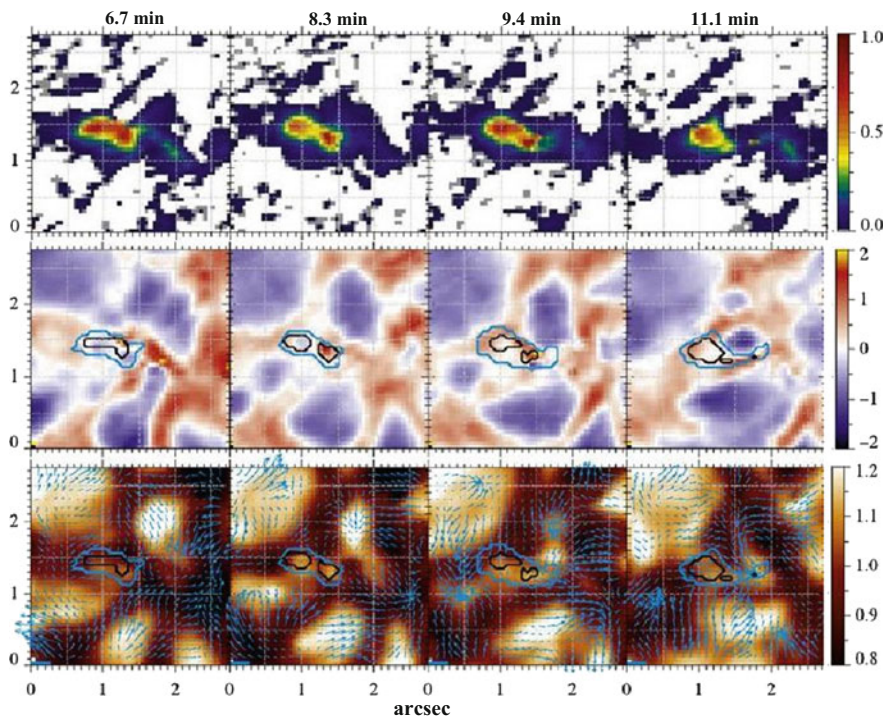


Fig. 22.8 Evolution of a multi-cored magnetic structure. First row: Longitudinal magnetic field, B_z in kG; second row: line-of-sight velocity, v_z in within the black contours remains equal to 2.9×10^{17} Mx. Overplotted blue arrows outline the horizontal flow field. The length of the blue bar at the origin corresponds to 1.8 km s^{-1} . Blue contours mark the periphery of the multi-cored magnetic structure (Requerey et al. 2015). Reproduced with permission of the AAS

Figure 22.8 shows an example of the observations of flux tube evolution obtained with the SUNRISE instrument (Solanki et al. 2010). This instrument allows to study the dynamics of solar convection and magnetic fields in the quiet sun at a resolution of about 110–130 km. The above example comes from high cadence (33 s) time series of data obtained for a quiet Sun region close to disk center. A

group of individual flux tubes having a common canopy in the upper photosphere and behaving as a multi-cored entity evolves in a complex way: the individual flux tubes continually intensify, fragment, and disappear during the observing interval of about 23 min. Figure 22.8 shows an example of an uneven shaped magnetic structure which during a short interval of time (shown only 4.4 min) fragments, intensifies, and almost loses the smallest fragments, just in a way described by theory and numerical experiments.

Note that along the horizontal velocity field (third row in Fig. 22.8) the appearance of a significant line-of-sight (LOS) velocities was observed during the evolution of “multi-cored” structures. It was found that LOS velocities could grow from nearly 0 to 1.1 km s^{-1} , reaching sometimes 3 km s^{-1} .

It is interesting that the observed evolution of magnetic structures is accompanied by the oscillatory behavior of a magnetic flux area (black contours in Fig. 22.8), as well as of the magnetic field strength, LOS velocities and, the intensity. Figure 22.9 shows the oscillatory character of the evolution of magnetic field

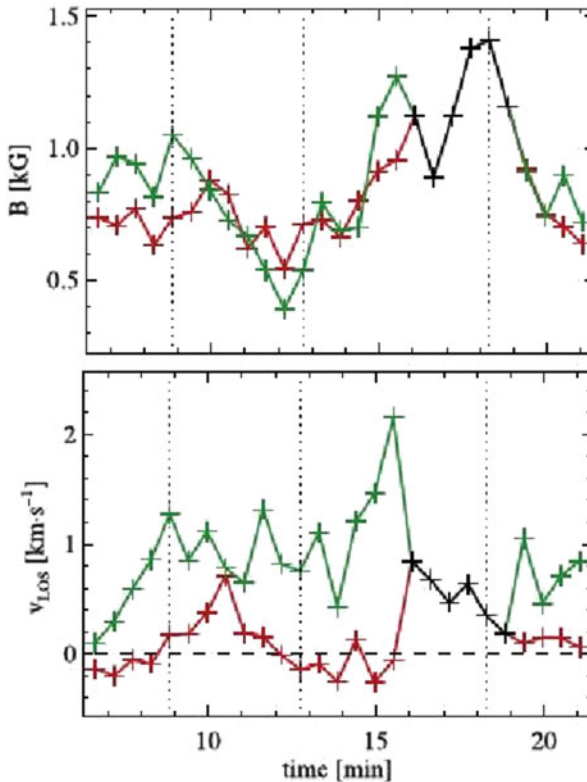


Fig. 22.9 Evolution of the magnetic field and line-of-sight velocities during the 23 min observing time. Red and green lines stand for the leftmost and rightmost magnetic cores, respectively; the black line is used when a single magnetic core is observed (Requerey et al. 2015). Reproduced with permission of the AAS

and LOS velocities. The observed oscillations are most probably associated with the action of nonlinear oscillatory ponderomotive force which leads eventually to nonlinear fragmentation process and generation of mass flows accompanied by the current drive.

These studies complemented with newly developed feature-tracking algorithm used for a statistical study of flux emergence, splitting, merging, and disappearance (Anusha et al. 2017) would provide deeper insight into the fundamental processes of magnetic flux evolution.

22.3 Penumbra and Moving Magnetic Features

In this section, we will discuss some developing aspects of moving magnetic features (MMFs) and their impact to overlying atmosphere. Before doing this, it is important to emphasize that the MMFs by their nature manifest the properties of an energetically open system, i.e., dynamic system with unbalanced sources and sinks of energy, so that locally their energy is not conserved. In the frame of conservative systems it is impossible to understand their basic properties that include their stability (and longevity), various forms that they make take, the fact that they travel faster than the background flows, and that they can travel even upstream. As discussed in Chap. 11, all their diverse properties are well explained in the frame of nonconservative system sustaining the origin evolutionary kink that acquires the properties of traveling solitons and/or shock-like formations. This theory not only explains the origin and behavior of all types of MMFs, but allows very simple quantitative analysis and comparison of the observations with theory (Ryutova et al. 1998; Ryutova and Hagenaar 2007). What is studied less is the impact of the MMFs on the overlying atmosphere.

In what follows we will discuss the observed correlation between the MMF population and formation of large-scale coronal loops. In Sect. 11.9 we have already discussed that as an ensemble, the families of MMFs have an essential influence on the dynamics of the overlying atmosphere from nearest layers of the chromosphere to corona. One of the essential findings was that an intense formation of a large number of MMFs strictly correlates with the absence of large-scale “stable” coronal loops (Ryutova et al. 2007). Such loops are usually rooted at the side of the sunspot with no or few MMFs.

Multiwave observations of MMFs in and above the photosphere performed with the Hinode/SOT instrument revealed more details in coupling of the MMFs and overlying atmosphere (Hagenaar et al. 2012). The SOT observations of the large sunspot, in NOAA AR 10933 (2007, Jan 4), in G-band, Ca II H, and Fe 6302 Å, were complemented by the TRACE images in 171 Å (Fig. 22.10). An automatic object recognition method (Hagenaar et al. 1999) revealed more than 200 MMFs. The population of MMFs on the East side of the sunspot was found to be much higher than on the opposite side Fig. 22.10 (dashed white semi-circle). Accordingly, the chromosphere shows *strongly enhanced brightenings* with a clear pattern: enhanced

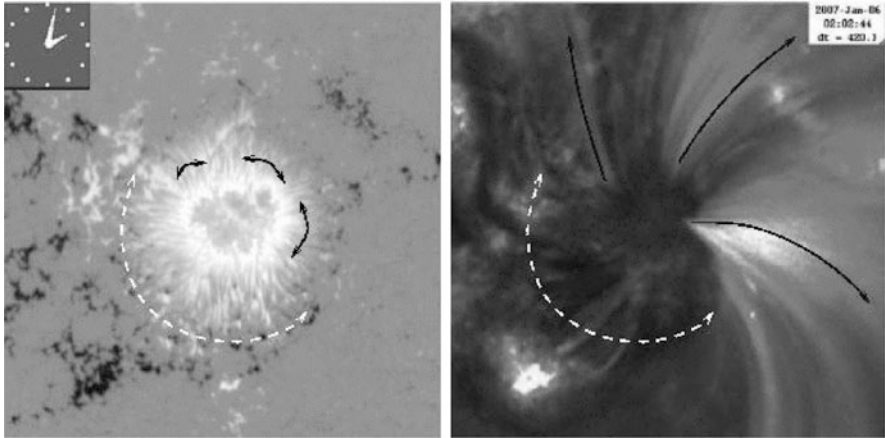


Fig. 22.10 The SOT magnetogram (left) aligned with TRACE 171 Å corona (right). White dashed semicircle demarcates the region of an intense MMF formation, while short black arrows outline the regions of MMF deficiency. Accordingly, the corona (right panel) shows the systems of large-scale loops rooted in “quasi-calm” regions with the deficit of MMFs and their absence at the side of strong MMF activity (Hagenaar et al. 2012). Courtesy of H. Hagenaar

brightenings in Ca H outline the locations where opposite polarity MMFs meet, suggesting their possible reconnections and subsequent shocks leading to enhanced brightenings. The other side, with MMF deficiency, shows rooted there long living “open” coronal loops.

The reasons that may cause the observed correlation between the preferable site of coronal loops and the deficiency of MMFs were discussed in Chap. 11. The model allows quantitative analysis and comparison with observations. In particular, one can use high cadence movies to study (1) appearance of brightenings when the opposite polarity MMFs meet, and (2) the brightenings that may appear above unipolar MMFs. In the first case, the most probable effect is the reconnection and subsequent post-reconnection processes that involve shocks and shock–shock interactions (Chap. 13). In the second case, we deal with unipolar MMFs akin the shock-like formation that in the overlying atmosphere result in strong behind-shock heating (cf. Fig. 11.6). One can easily distinguish the brightening triggered by these two different mechanisms. In the first case brightenings may take form of microflares and their associated jets, whereas in the second case the brightenings should be weaker.

The very fact of different response of the corona to the population of MMFs is not clear. Most probably, the interaction of MMFs with each other producing elevated activity in the overlying atmosphere may prevent formation of the long-living coronal loops. This subject calls for further studies and may shed light on the basic phenomena associated with sunspots.

More aspects of the MMFs coupling with overlying atmosphere can be studied observing details of magnetic flux emergence around active regions and response of

the overlying atmosphere to their activity. Example of such studies showed a correlation between the activity among the MMFs and occurrence of the homologous flares that triggered coronal mass ejections (Zhang and Wang 2002). Time-series of high-resolution MDI magnetograms of the AR 9236 (November 24–26, 2000) were used to follow the evolution of hundreds of MMFs from their birth to death. It was found that the most visible magnetic changes around one of the sunspots (positive) in the AR was the high rate of emergence of the MMFs. Three major peaks in their number were clearly identified. Comparison with the subsequent homologous flares and associated CMEs lead to conclusion that they were triggered in about the same sequence as peaks of the MMF's activity. This kind of observations are absolutely "must" given an ample opportunities of modern instruments.

Interesting results were obtained by the observations of the MMFs interaction with the larger scale emerging flux showing the generation of surges (Brooks et al. 2007). Studies of coronal jets associated with the MMFs and other small-scale magnetic activity at the umbra/penumbra region were performed with the most advanced solar instruments as well. Part of such works is systematized in Innes et al. (2016).

Here we mention one more important aspect of the MMF's signatures in the overlying transition region/corona. Time series of data taken simultaneously by the MDI on SOHO, TRACE 1600 Å and EIT He II 304 Å and the Normal Incidence Spectrometer (NIS) of CDS/SOHO were aligned to study oscillatory behavior of the transition region counterpart of the MMF (Lin et al. 2006). The wavelet analysis was used to examine and compare the periodicities of time-series signals in different regions. It was found that the chromospheric and transition region brightenings associated with the MMFs exhibit the oscillations with a multitude of frequencies. The region of the brightenings shows a tendency to be blue-shifted when compared to the average motion of the entire field of view.

Figure 22.11 shows the correlation between the MMFs and the dynamics of the transition region brightening. In the intensity time series (left panels) there is a strong brightening above the MMFs area marked by the white box. Here, the detrended intensity variations clearly show a periodic oscillatory pattern. The dotted horizontal line marks 0 km s^{-1} . The bright patch over the MMF is between 35 min and 60 min marks. One can see that this 35–60 min region is relatively blue-shifted at $y = 0$ and $y = 3$.

These results indicate the presence of waves and/or flows associated the MMFs that carry energy to the higher atmosphere. Recall that Type II MMFs that appear as unipolar features have a shock-like nature. On the other hand, the other types of MMFs representing a stable solitary features traveling in an inhomogeneous environment may also evolve into the shock. Any shock in strongly stratified solar atmosphere quickly reaches the transition region and coronal heights depositing their energy at heights determined by the shock properties. The energy release of along a strong brightening by shocks, as discussed throughout this book, may be accompanied by generation of flows and oscillatory motions. The corresponding theory contains directly observable parameters, and can be used for quantitative analysis.

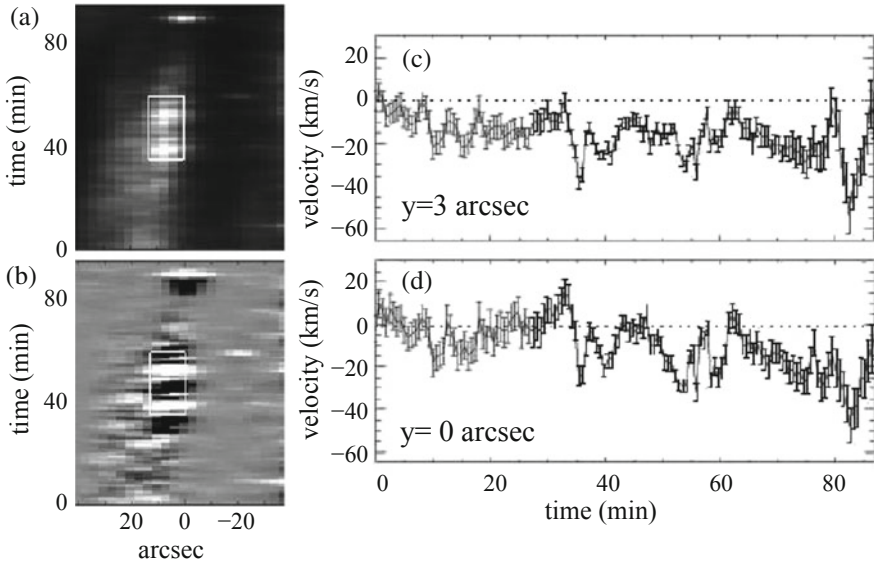


Fig. 22.11 The O V 629.7 Å time series of the intensity variation (left), and the Doppler velocities in the same line along the slit passing the region over the MMF (right): (a) the intensity variation; (b) the de-trended intensity variation, the white rectangle marks the location of the MMF. The y axis corresponds to coordinates of the pixels along the detector slit. Panels (c) and (d) show the blue shift represented by negative velocities (Lin et al. 2006). Reproduced with permission from A&A, Copyright ESO

Finally, as far as the MMFs are concerned, we mention here that to be born the MMFs do not at all require the fully developed penumbra. They may appear around the “naked” sunspot as well. These were observed during the analysis of the short-lived sunspot group NOAA 10977, consisting of a following polarity pore, that emerged first and then followed by the formation of a preceding polarity naked spot depleted of penumbra. The observations were performed using G-band and H_{α} visible lines co-aligned with the MDI and SOT magnetograms, the SOT/HINODE Ca II, and the TRACE Fe 171 Å coronal line.

While measuring a moat flow around the naked spot, there appeared several MMFs streaming out from it during the decay phase. According to their characteristics, these MMFs were classified as type I (U-shaped) MMFs. It is important that all the MMFs were found to be co-spatial with sites of increased brightness both in the photosphere and in the chromosphere. Figure 22.12 shows four bipolar MMFs around the naked spot. It is interesting that the SOT G-band images show brightening spatially coincident with MMFs A and B only, while in the Ca II H line images, all the MMFs are co-spatial with brightness enhancements. Even this fact may be used in quantitative analysis in identification of MMF properties and for the inference of the system parameters (see below).

Why the naked sunspot, not having a penumbral filaments, may give birth to MMFs. The thing is that any sunspot, regular or naked has an internal filamentary

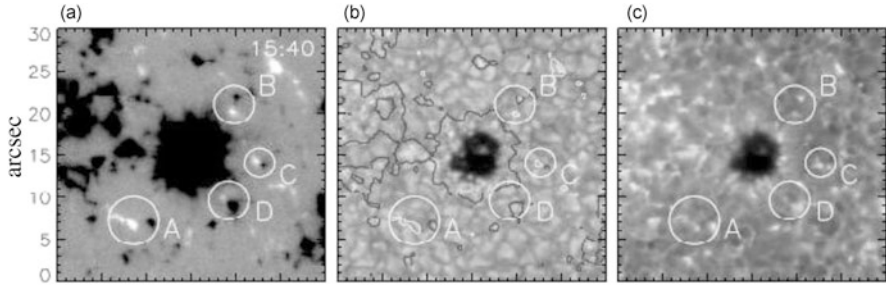


Fig. 22.12 From left to right: (a) Hinode magnetogram showing the MMFs flowing out of the negative polarity sunspot associated with the preceding naked spot. The circles indicate the locations of MMFs A, B, C, and D. (b) Hinode G-band image showing the position of the MMFs; MMFs A and B coincide with sites of brightness increase; black (white) contours indicate negative (positive) polarities. (c) Hinode Ca ii H line image, showing that at this wavelength all the observed MMFs are associated with an increased emission. The FoV field of view is 30×30 arcsec (Zuccarello et al. 2009). Reproduced with permission from A&A, Copyright ESO

structure (see, e.g., Fig. 17.8). Any kind of filamentation of magnetic field under the appropriate conditions may generate solitary kink. It is important that the birth of the MMFs is not limited by the penumbral filaments. All is needed is the existence of magnetic filaments and associated mass flows such that dispersion properties of the system and nonlinear effects balance each other. Presence of gravity provides additional properties, but even in case of a weak or no gravity, e.g., corona and solar wind, conditions for solitons can be easily met. Hence, the observation of the MMFs and measurements of their properties may be used to infer physical parameters of the medium that are not directly observable. For quantitative analysis of the MMFs, see Sect. 11.6.

22.4 Post-reconnection Processes

Now we turn to discussion of post-reconnection processes associated with the photospheric reconnections. As we already know, 90% of solar magnetic field is concentrated in small-scale magnetic flux tubes, and the entire supply of the “pepper and salt” magnetic flux, forming quiet sun magnetic carpet, is replaced in about 40 h (Title and Schrijver 1997; Schrijver et al. 1997). This estimate has been obtained for network elements (NE) at scales of more than a few supergranules using a sequence of early MDI magnetograms.

The next generations of solar instruments with higher spatial resolution opened a platform for further improvement to investigate the behavior of small-scale flux tubes and their ensembles.

The important contribution into studies of the appearance and disappearance rates of flux tubes and the estimate of the recycling time of quiet sun magnetic carpet was done by using high resolution Hinode magnetograms (see, e.g., Gošić et al.

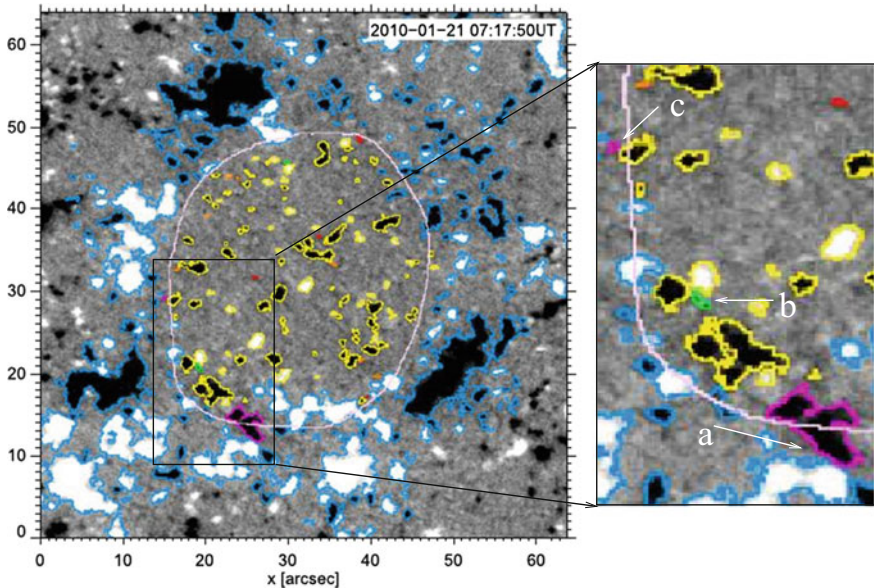


Fig. 22.13 Example of individual supergranular cell from 20–21 January 2010 data sets (left). Left: The cell and its surrounding network; interior is outlined by pink contours and the surrounding NE flux features are marked with blue contours. Red contours show IN elements that appear in situ. Fading elements are marked by orange contours, apparently canceling elements by green contours, those that enter the NE and interact with NE features by purple contours. IN patches that do not undergo any of those processes are indicated with yellow contours; Right: inlet shows zoomed out portion of network/inter-network boundary for further discussion (see text) (Gošić et al. 2016). Reproduced with permission of the AAS

2014, 2016). The new aspect here was consideration of the inter-network magnetic elements (IN) and their role in the total replacement of the quiet sun magnetic carpet. Note that the internetwork magnetic elements are mostly less than $1''$ and therefore were beyond the MDI resolution. Example of a target region is shown in Fig. 22.13.

All the elements were counted individually, regardless of their nature. In tracking magnetic elements, 5 major processes were taken into account: (1) In-situ appearance; (2) The coalescence of two or more elements of the same polarity into a larger structure; (3) Fragmentation, when an element splits into two or more smaller features; (4) Cancellation of a magnetic element in the vicinity of an opposite-polarity feature; (5) In-situ disappearance, the process whereby magnetic elements disappear from the solar surface without an obvious interaction with any other feature.

It was found that the IN magnetic elements modify the flux budget of the network, either by adding flux through *merging* processes or by removing it through *cancellations*. Merging was found to be dominant, thus increasing the net magnetic flux.

Our goal here is not to go into more details of the above-mentioned results, but clarify the processes occurring during lifetime of magnetic elements and what could be observed next. Each of the processes listed above, i.e., appearance of magnetic elements, their merging, fragmentation, cancellation, and in-situ disappearance, is accompanied by the physical processes that can be identified and observed.

One of the major processes is the reconnection, which occurs inevitably, be the magnetic elements of the opposite or the same polarities (see Figs. 12.6 and 12.7). As discussed in Chap. 12, the outcome of photospheric reconnection in high plasma β environment is totally different than that in the low β plasma. The most important difference is that in low atmosphere the reconnection does not lead to the immediate heating like in corona, but sets the system in strongly nonlinear stage, triggering at later stage appearance of jets, microflares, and their combinations (Tarbell et al. 2000).

The strongest activity in the photospheric reconnection is observed, as expected, at the network boundaries and especially at the vertices where several supergranules converge (see, e.g., Fig. 13.9). As described in Chap. 13, in case of “merging” or “cancellation” of the opposite polarity fluxes, in the overlying chromosphere and transition region one systematically observes appearance of blinkers/microflares and plasma jets. Example similar to those discussed in Chap. 13 is shown in Fig. 22.14. Hence, both, in cell interior and at the boundaries reduction of magnetic flux accompanied by appearance of bright transients in the chromosphere/transition region, thus providing a permanent energy supply to the upper layers of atmosphere. Although the expectation of jets and microflares above the network/internetwork boundary is much higher than above the cell interior, it is not at all negligible. Note that in case of coalescence of the same polarity fluxes, the reconnection leads to fragmentation process (cf. Fig. 12.7).

Such studies complemented by the statistical analysis of network and internetwork magnetic elements and associated energetic events will provide better understanding of the processes of energy production and its transport. Some steps have been already done in the direction of an automatic detection of small-scale brightenings in the corona and evolution of their underlying magnetic elements in the photosphere. For example, tracing of photospheric flux tubes and corresponding appearance of soft X-ray brightenings that could be blinkers, microflares or jets were performed simultaneously using time series of high resolution HMI magnetograms and the SDO/AIA Fe IX line (Honarbakhsh et al. 2016). Snapshots of the corona and its underlying magnetogram are shown in Fig. 22.15. Green asterisks in the upper panel correspond to 85 detected microflare/jets. Lower panel is the snapshot of the tracking of the photospheric magnetic elements. It was found that 27% of the events had slight changes and 73% showed considerable changes in magnetic flux. Note that most of the brightenings/dimming took place above the supergranular boundaries.

A direct connection of the $H\alpha$ surges with cancellation of photospheric magnetic fields and subsequent appearance of UV jets and compact flares have been observed in quite regular basis (see e.g. Young and Muglach 2014). For example, the $H\alpha$ surges were found to appear repeatedly in those locations where the photospheric longitudinal fluxes of opposite magnetic polarities emerged and were canceled

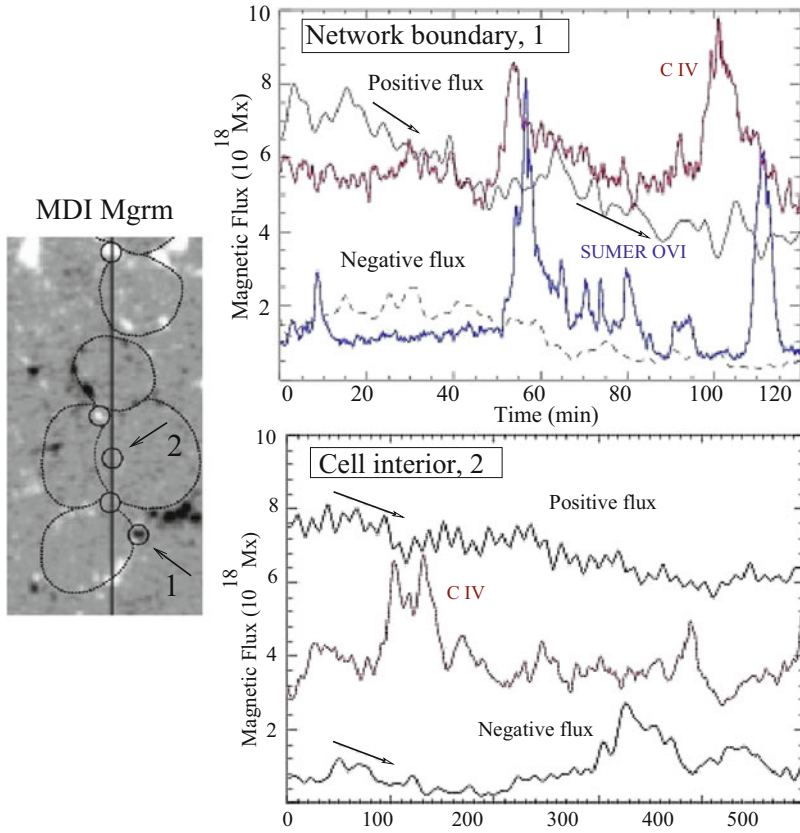


Fig. 22.14 Examples of magnetic activity in the cell interior and at the network/internetwork boundary. Left: the $60'' \times 120''$ MDI magnetogram with uneven circles marking the supergranular pattern; Upper right: The evolution of magnetic flux and intensities in the TRACE C IV and SUMER OVI at the network/internetwork boundary—reduction of magnetic flux is followed by appearance of a strong transition region microflares ($T \simeq 10^5$ K, red line) and jets ($T \simeq 3 \times 10^5$ K, blue line). Bottom right: reduction of magnetic flux here is also followed by microflares, that is significantly weaker than their counterparts located at the boundaries

by each other (Chen et al. 2008). The dynamic properties of surges were found to vary in wide ranges, as well as the intensities of their associated microflares and corresponding energy release. In 1600 \AA , some surges showed the composite structures of bright jets and nearby small flaring loops (Fig. 22.16). A projected maximum lengths of surges range from 38 to 220 Mm, and their transverse velocities are $30\text{--}200 \text{ km s}^{-1}$ with lifetimes from several to tens of minutes. It was found that each surge was accompanied by an $H\alpha$ brightening. These observations indicate that origin of the surges is the direct result of photospheric magnetic reconnection.

Photospheric reconnection in complex active regions and their accompanied phenomena were also studied using high-quality $H\alpha$ imaging spectrometry from

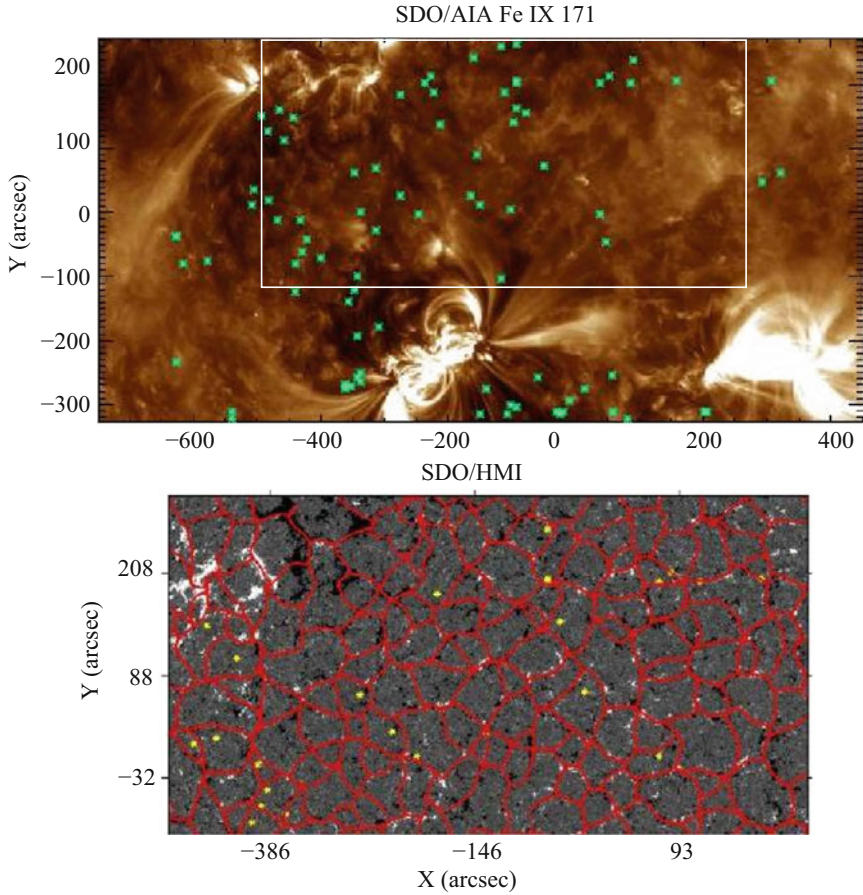


Fig. 22.15 Snapshots of the soft X-ray corona (upper panel) and its underlying quiet sun (lower panel). Green asterisks show location of coronal brightenings associated with a dimming or wave-like features traveling with velocities of tens of km s^{-1} . Yellow asterisks in lower panel are the locations where a significant reduction of photospheric magnetic fluxes has been observed. Inlet in the upper panel corresponds to the field of view of the underlying magnetogram (lower panel) (Honarbaksh et al. 2016). Reproduced with permission from Springer Science and Business Media

the Swedish 1-m Solar Telescope (SST). The observed transient brightenings in the wings of the Balmer $H\alpha$ line were found to mark strong-field reconnections in the photosphere. These brightenings are similar but smaller and less intense than those occurring in quiet areas away from active regions. Their typical lifetimes are less than a minute. The authors emphasize that in lesser-quality data they cannot be distinguished from more ubiquitous facular brightenings, nor in the ultraviolet diagnostics currently available from space platforms.

The appearance and morphology of these small bright $H\alpha$ flames is illustrated in Fig. 22.17, including comparison with larger and brighter Elerman Bombs flames.

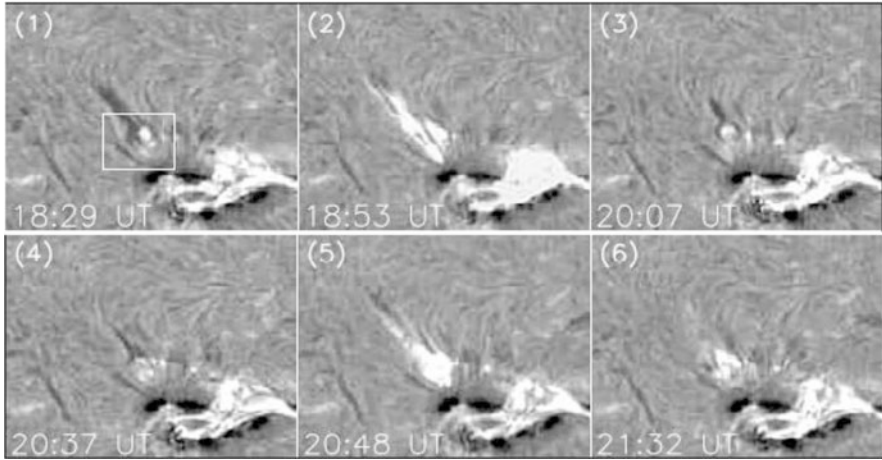


Fig. 22.16 BBSO full-disk $H\alpha$ images of the surges occurred at the same location in different times (shown in each frame) (Chen et al. 2008). Reproduced with permission from Springer Science and Business Media

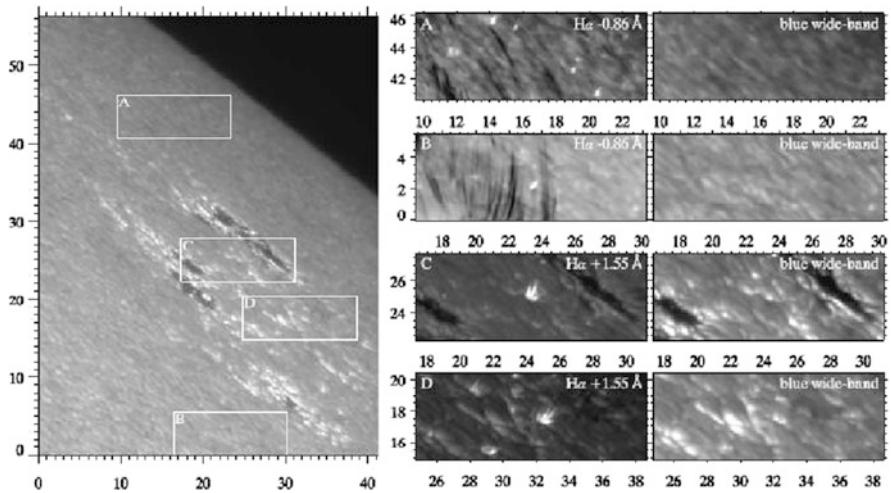


Fig. 22.17 Examples of Elerman Bombs and quiet sun brightenings around the active region AR 11778 near the limb. The axis are in arc secs. Right panels contain examples of a quiet sun, A and B, and inlets C and D sample the active region. Quiet sun brightenings are visible as bright flames in the $H\alpha$ wings, as smaller and weaker features in A and B, and as larger and brighter Elerman Bombs in C and D (Roupe van der Voort et al. 2016). Reproduced with permission from Springer Science and Business Media

The right panels show enlarged cutouts in quiet areas (A and B) and, for comparison, two areas in the active region (C and D). It was clearly shown that there is an extended range of small reconnection events in the low atmosphere, with variation in magnetic topography, released energy, and penetration into the higher atmosphere.

Observation and statistical analysis of events occurring above the internetwork and network regions paying special attention to the boundary region can give reliable estimate for the energy supply provided by photospheric small-scale magnetic network to overlying atmosphere.

22.5 Misuse of Reconnection Physics

Now it is useful to discuss the problem associated with misuse of reconnection physics. The word “reconnection” is now used in most observational papers describing high energetic events that include chromospheric and coronal jets, CMEs, bursts in the active regions, violent eruption of quiescent prominences, etc.

Important: the reconnection itself cannot explain a great variety of active phenomena observed throughout the solar atmosphere. But careful insight into the time steps of a particular event may provide better understanding of the process and even its quantitative picture.

The process of magnetic reconnection in the solar atmosphere from its visible surface to solar wind occurs everywhere at any moment of time. Intrinsic filamentary structure of solar magnetic field at all scales ensures the universality of the reconnection process that occurs both, between the opposite and the same polarity fluxes (see Figs. 12.6 and 12.7). Hence, the reconnection can be called atmospheric breathing of the Sun. But despite its pervasive nature, the reconnection alone cannot explain the majority of large-scale burst, eruptions and flares. By its nature, the reconnection is quite a local process with its characteristic spatial and time scale. For example, under the photospheric conditions cross section of magnetic flux participating in one elemental act of reconnection is about 40 km. On the other end of extremes is the time scale of coronal reconnection that is too large, for example, the time scales are too large to rely on the reconnection process alone. For example, Fig. 22.18 shows quite an ordinary environment and its activity. Two neighboring active regions, the decaying AR 12030 and still young AR 12027, are covered by permanent brightenings and jets in the overlying chromosphere. A large area of quiet sun (scattered white arrows) and plage (black arrow) are covered by permanent brightenings. Because of the smaller filling factor in the quiet sun area, chromospheric brightenings here are less intense than over the plage region.

Higher magnetic filling factor of active regions and, respectively, large supply of magnetic field provide larger energy supply to overlying chromosphere. Here, one requires continuous elemental acts of reconnections that occur until “supplies last.” Accordingly, bright patches and jets remain in place, again, as long as “supplies last.” Now the spatial and time scale of reconnection is only a constituent part of many spatial and time steps determined by the amount of magnetic flux.

Using the above example, it is instructive to discuss some details and obvious differences in the chromospheric brightening above the young (AR 12027) and decaying active region (AR 12030). The chromosphere above AR 12027 is less brighter than above the AR 12030. Moreover, during 24 h the AR 12030 produced five C1 flares, whereas the AR 12027 gave off the accumulated energy in form of

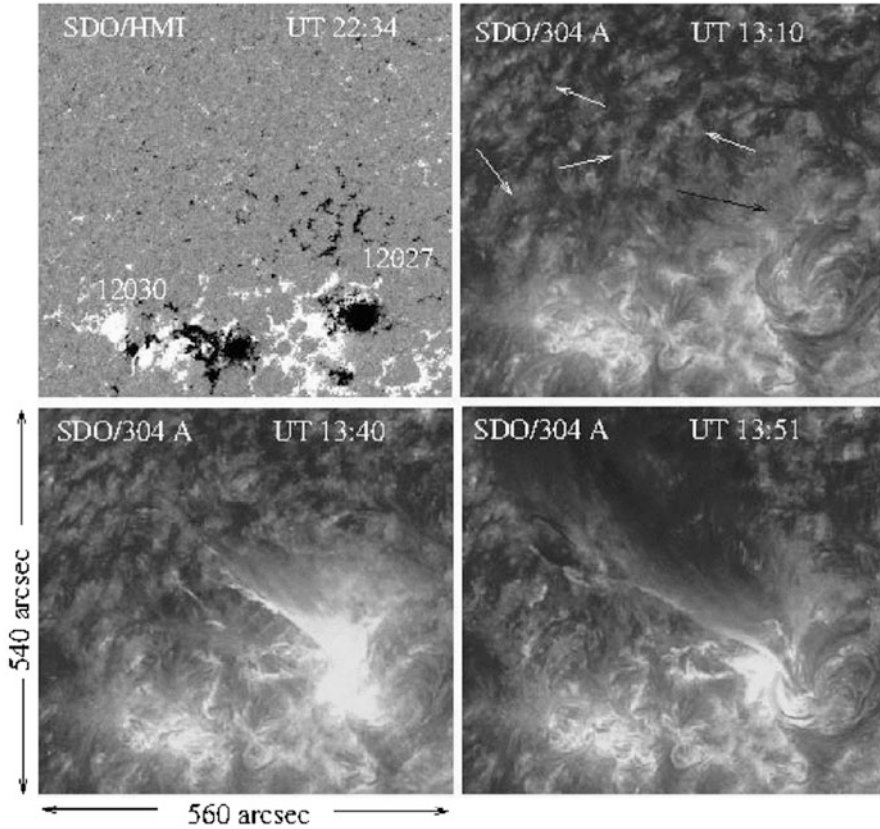


Fig. 22.18 Chromospheric activity above the active regions 12027 and 12030 on April 04, 2014, taken by SDO/HMI (upper panel showing a magnetogram) and SDO/AIA in 304 Å at three instances of time. Credit: SDO/NASA

a single C8 flare accompanied by a strong post-flare mass ejection (lower panels in Fig. 22.18). This kind of regularities are quite natural. The young AR 12027, which is much less “wearing out” than the decaying active region can withstand to more reconnection events and accumulate more energy until it reaches the saturation limit and bifurcates into the lower energy state releasing the energy excess.

Here we come to the most important conclusion: it is the post-reconnection processes *triggered* by multiple-reconnections that are responsible for a great variety of solar energetic phenomena. Hence, when analyzing the data, it is important to study *details* of the process with highest possible resolution and time steps.

22.6 Explosive Instability and Post-reconnection Jets

Now we turn to one of the major processes associated with the post-reconnection processes: the explosive instability that quickly develops in energetically open dynamic system like solar atmosphere. Such systems are usually subject of non-linear evolution associated with continuous pump of energy into them. When the system reaches the saturation regime, it explosively releases the accumulated energy and bifurcates into the lower energy state.

Explosive instability of multiple erupting flux tubes in a magnetized plasma has been proposed as a mechanism for fast (at Alfvénic timescales) energy release (Cowley et al. 2015). It was shown that just above their linear stability threshold all fine scale pressure and gravitational instabilities obey a generic equation that yields explosive dynamics. Studying a particular mechanism that leads to explosive release of stored magnetic and gravitational energy in a slowly evolving system that suddenly erupts, the authors leave several questions that are still without quantitative answers. Such as:

1. What triggers the instability?
2. What sets the timescale? How much energy is released?
3. How much energy is converted into heat and energetic particles?

These questions call for detailed studies both in theory and by observations.

Now we move to the problem of energy supply provided by the photospheric network. We start with the practical use of high cadence multi-wavelength data compiled in movies that show the entire process from the reconnection of photospheric flux tubes, shock formation, their evolution and resulted generation of microflares and jets in the overlying chromosphere/transition region (cf. Sect. 13.4). Recall that a double-humped peak in the spectra is the signature of a shock. If the higher peak is on the left of the shorter one (i.e., on the shorter wavelength), the shock is propagating upward towards higher temperatures, and $v.v$.

Using the spectra obtained from observations, and applying shock relations one can infer physical parameters, such as Mach number, direction of the shock propagation, shock velocities, and others. In particular, as discussed in Sect. 13.4, the difference $\Delta\lambda^*$ is a measure of shock velocity. Indeed, $\Delta\lambda^*$ is a difference between the Doppler shifted spectral lines resulted from mass motions, v_2 (left peak) and v_1 (right peak). The velocity difference is

$$v^* \cos\theta = \frac{\Delta\lambda^*}{\lambda_0} c \quad (22.1)$$

where θ is the angle between the direction of flow and line of sight, λ_0 is the wavelength of unshifted line. For example, for SUMER CII, $\lambda_0 = 1037.06 \text{ \AA}$ and for O VI, $\lambda_0 = 1037.656 \text{ \AA}$.

The velocity in front of the shock v_1 and behind the shock velocity v_2 are related by Mach number:

$$v_2 - v_1 = c_s \frac{2(M^2 - 1)}{(\gamma + 1)M} \quad (22.2)$$

which can be used to estimate first the Mach number $M = v_{\text{sh}}/c_s$, and then the shock velocity:

$$v_{\text{sh}} \simeq \frac{\gamma + 1}{2}(v_2 - v_1) \quad (22.3)$$

For usage of these simple calculations, see Fig. 13.12 and its accompanying text. Below we show one more time that even shock–shock collision is easy to observe and using above equations perform quantitative analysis Fig. 22.19.

As discussed in Sect. 13.5, explosive events are usually preceded by the shock–shock collision. It is instructive to show how easily such an event can be observed (see Fig. 13.12). Quantitative analysis of such data would not only provide the physical parameters of the process but will also make possible to estimate the energy content of such events.

The explosive events are readily observable over the photosphere covered by the mixed polarity flux tube and form basis to study an avalanches of post-reconnection shocks. As already discussed, especially rich are of such events the vertex regions where the supergranular boundaries meet. For the same reason, frequent events can be observed at the coronal hole boundaries. Here, the presence of opposite polarity magnetic field concentrations and co-existence of closed and open magnetic

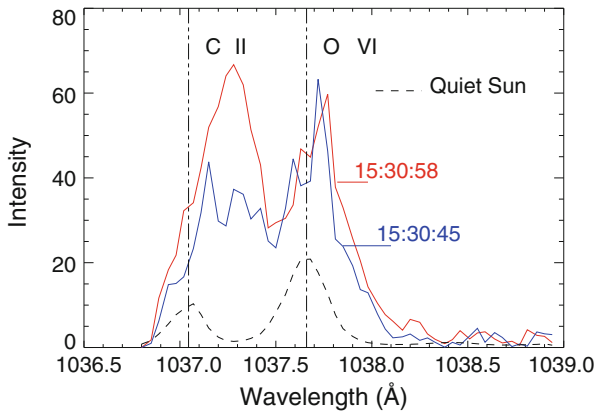


Fig. 22.19 Example of the observed shock–shock collision. Red is the chromospheric C II spectral line and blue is the transition region O VI line. Shock O VI line profile shows the right peak exceeding the left peak signifying that the shock is propagating downward (only one line for each temperature is shown). In fact the O VI shocks interact with a series of upward propagating C II shocks leading to generation of strong explosive events (Ryutova and Tarbell 2003)

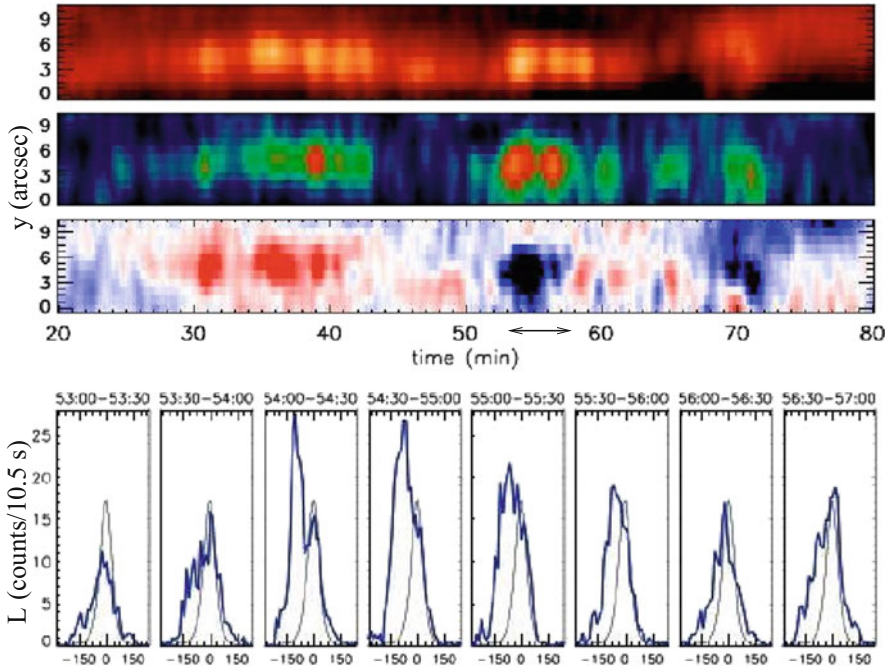


Fig. 22.20 Sequence of the explosive events in SUMER O VI line observed at a coronal hole boundary. Upper panels from top to bottom are the O VI integrated flux (logarithmic scale), line widths (logarithmic scale), and the Doppler velocity (linear scale, 20 km s^{-1}). The bottom panel shows the spectral radiance, L , integrated over 30 s for an interval of 5 min, showing how rapidly it changes during the sequence of explosive events. The thin black contour on these images represents the average spectral radiance in a quiet sun (Doyle et al. 2006). Reproduced with permission from A&A, Copyright ESO

fields provide favorable conditions for frequent reconnections at various heights, and hence for generation of post-reconnection shocks and explosive events.

Figure 22.20 shows an example of recurrent explosive events observed at a coronal hole boundary (Doyle et al. 2006). The SUMER O VI 1032 \AA data with spatial resolution of 1 arcsec and an exposure time of about 10.5 s were taken during several hours. When slit passed coronal hole boundary the sequence of recurrent explosive events were detected. The space-time map of biggest concentration of explosive events is shown in three upper panels of Fig. 22.20 which includes the O VI integrated flux, FWHM, and the Doppler velocity. The Doppler map is however only an indication of excess blue/red wings in the line. Single line profiles of spectra are shown, as an example, for a short period time of 5 min (lower panel). The spectra clearly show double humped profiles typical to shocks and accompanying them explosive events.

It is important to emphasize that jets and explosive events resulted from the post-reconnection process have an obvious tendency to recurring: recall that when flux tubes reconnect, only a small part of each flux tube participates in one elemental

act of reconnection (see Chap. 12, e.g., Figs. 12.6 and 12.7). Maximum radius participating in the elemental act of reconnection is estimated as

$$R_{\max} < \frac{L}{2\ln Re_m} \tag{22.4}$$

where L is the characteristic length of the system, and Re_m is the magnetic Reynolds number. For the photospheric flux tubes we get the estimate $R_{\max} \sim 40\text{--}70$ km. Hence, the flux tubes having radii of several hundred km are the subject of multiple reconnections. Thus, it is only natural to expect the appearance of the avalanche of shocks and subsequent generation of recurrent jets and explosive events.

Observation of the recurrent jets can provide additional information about the system parameters (see e.g. Mulay et al. 2017; Sterling et al. 2016). For example, the periodicity of their recurrence may be associated with reconnection time, which is

$$\tau_{\text{rec}} \simeq \frac{R}{w_{\max}} = \frac{R\ln Re_m}{v_A} \tag{22.5}$$

One could say that the solar atmosphere from its visible surface to outer corona and winds is pierced by plasma jets, just like it is pierced by threaded magnetic fields. As discussed in Chap. 14, the jets must be generated continuously over the entire small-scale network as a result of post-reconnection processes occurring from the bottom of the photosphere to the upper chromosphere (Fig. 14.3).

Figure 22.21 shows example of the chromosphere/transition region jetting above the quiet sun observed with IRIS (Tian et al. 2014). These data reveal the

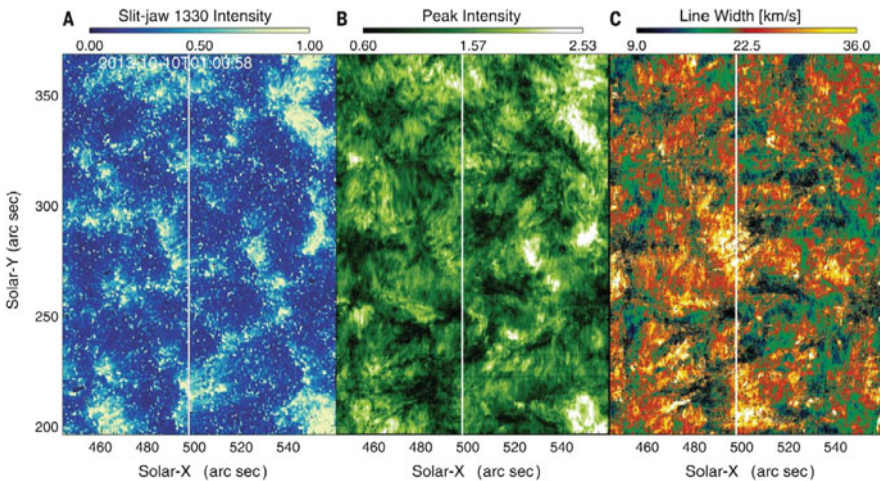


Fig. 22.21 An unsharp masked 1330 Å slit-jaw image (a); Maps of intensity and line width from a Gaussian fit to Si IV 1393.77 Å line profiles. The vertical line indicates the slit location (b and c) (Tian et al. 2014). Reproduced by permission of the AAS

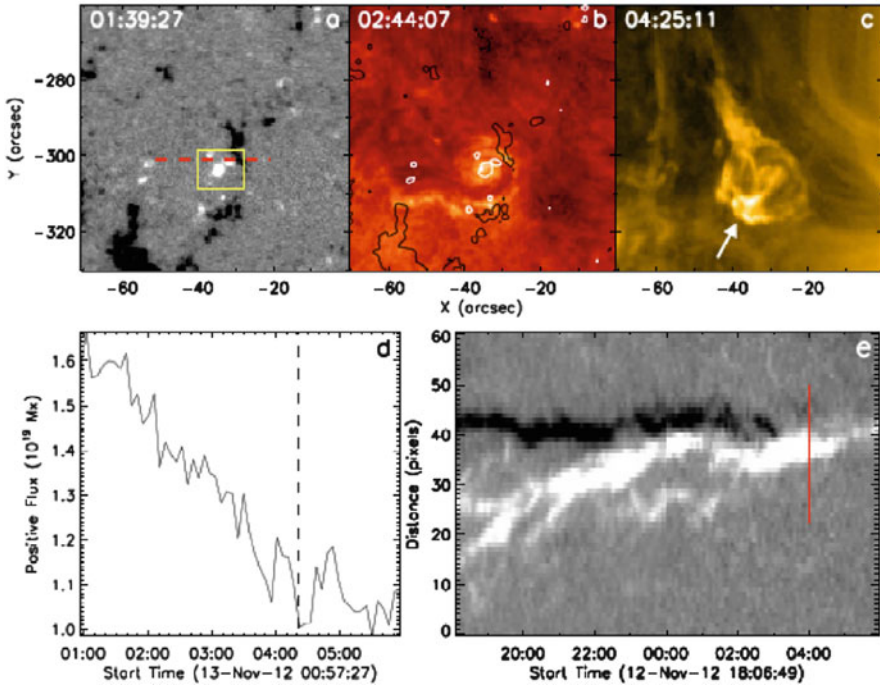


Fig. 22.22 Photospheric reconnection and post-reconnection jets observed on 13 Nov 2012 in the quiet sun region. Panel (a): The yellow box shows the area of reconnection; the red dashed line shows the space-time cut shown in panel (e); Panel (b): A pre-jet microflare in AIA 304 Å; Overlaid black and white contours represent negative and positive polarities; Panel (c) Developed jet in AIA 171 Å; Panel (d) “Consumption” of positive flux with the dashed line showing onset of the jet eruption; Panel (e): The space-time cut showing the tracks of positive and negative fluxes; the red line marks the moment shown in Panel (c) (Panesar et al. 2016). Reproduced by permission of the AAS

ubiquitous nature of small-scale jets with speeds of $80\text{--}250\text{ km s}^{-1}$ associated with the narrow bright network lanes of the chromosphere/transition region. These jets have lifetimes of 20–80 s and widths of about 300 km. They originate from small-scale bright regions, often preceded by footpoint brightenings. Many jets reach temperatures of at least $\sim 10^5\text{ K}$.

High resolution observation shows also the direct connection between the photospheric reconnection and formation of strong coronal jets. Example of the coronal jets associated with the photospheric reconnections is shown in Fig. 22.22. It is only natural that in this case the process of multiple reconnections takes much longer time than for generation of ubiquitous chromospheric jets. During this time, i.e., from the significant cancellation of photospheric magnetic fluxes to appearance of coronal jets, that took several hours, there were continuous brightenings over the future location of coronal jet. One can use quantitative analysis described above to all the steps of the process that starts with reconnection of photospheric flux tubes and proceeds to formation of jets and microflares.

References

- L.S. Anusha et al., *Astron. Astrophys.* **598**, A47 (2017)
- D.H. Brooks et al., *Astrophys. J.* **656**, 1197 (2007)
- R. Centeno et al., *Astrophys. J.* **640**, 1153 (2006)
- J.C. Chae et al., *Astrophys. J.* **805**, L21 (2015)
- H.D. Chen et al., *Astron. Astrophys.* **478**, 907 (2008)
- E.B. Christopoulou et al., *Astron. Astrophys.* **375**, 617 (2001)
- S.C. Cowley et al., *Proc. R. Soc.* **471**, 2180 (2015)
- J.D. Doyle et al., *Astron. Astrophys.* **446**, 327 (2006)
- I. Ermolli et al., *Astron. Astrophys.* **600**, A102 (2017)
- M. Gošić et al., *Astrophys. J.* **797**, 49 (2014)
- M. Gošić et al., *Astrophys. J.* **820**, 35 (2016)
- H. Hagennar et al., *Astrophys. J.* **511**, 932 (1999)
- H. Hagennar et al., *ASPC* 454, 181H (2012)
- L. Honarbakhsh, N. Alipour, H. Safari, *Sol. Phys.* **291**, 941 (2016)
- D.E. Innes et al., *Astron. Nachr.* **10**, 1024 (2016)
- C.-H. Lin et al., *Astron. Astrophys.* **560**, 597 (2006)
- W. Livingston, *Nature* **350**, 45 (1991)
- C.A. Madsen et al., *Astrophys. J.* **800**, 1129 (2015)
- M.J. Martínez González et al., *Astron. Astrophys.* **596**, A5 (2016)
- S.M. Mulay et al., *Astron. Astrophys.* **598**, A11 (2017)
- C.J. Nelson et al., *Astron. Astrophys.* **605**, A14 (2017)
- N.K. Panesar et al., *Astrophys. J.* **832**, L7 (2016)
- D. Papathanasoglou, *Sol. Phys.* **21**, 113 (1971)
- S.-H. Park et al., *Astron. Astrophys.* **586**, A25 (2016)
- I.S. Requerey et al., *Astrophys. J.* **810**, 79 (2015)
- I.S. Requerey et al., *Astrophys. J. Suppl.* **229**, 14 (2017)
- L.H.M. Rouppe van der Voort et al., *Astron. Astrophys.* **403**, 277 (2003)
- L.H.M. Rouppe van der Voort et al., *Astron. Astrophys.* **592**, A100 (2016)
- M. Ryutova, H. Hagennar, *Sol. Phys.* **246**, 281 (2007)
- M. Ryutova, M. Persson, *Phys. Scr.* **29**, 353 (1984)
- M. Ryutova, T. Tarbell, *Phys. Rev Lett.* **90**, 191101 (2003)
- M.P. Ryutova, M. Kaisig, T. Tajima, *Astrophys. J.* **459**, 744 (1996)
- M. Ryutova, R. Shine, A. Title, J.I. Sakai, *Astrophys. J.* **492**, 402 (1998)
- M. Ryutova, H. Hagennar, A. Title, *Astrophys. J.* **656**, L45 (2007)
- C.J. Schrijver, A.M. Title, H. J. Hagenaar et al., *Astrophys. J.* **487**, 424 (1997)
- S. Solanki et al., *Astrophys. J.* **723**, L127 (2010)
- D. Song et al., *Astrophys. J.* **835**, 240 (2017)
- A.C. Sterling et al., *Astrophys. J.* **821**, 100 (2016)
- J.T. Su et al., *Astrophys. J.* **817**, 117 (2016)
- T. Tarbell, M. Ryutova, R. Shine, *Sol. Phys.* **193**, 195 (2000)
- H. Tian et al., *Astrophys. J.* **786**, 137 (2014)
- A.M. Title, C.J. Schrijver, in *Cool Stars, Stellar Systems, and the Sun*, ed. by R. Donahue, J.A. Bookbinder. *Astronomical Society of the Pacific Conference Series* (1997)
- S. Vargas Domínguez et al., *Sol. Phys.* **290**, 301 (2015)
- S. Yang et al., *Astrophys. J.* **804**, L27 (2015)
- P. Young, K. Muglach, *Publ. Astron. Soc. Jpn.* **66**, S12 (2014)
- V. Yurchyshyn et al., *Astrophys. J.* **798**, 136 (2015)
- J. Zhang, J. Wang, *Astrophys. J.* **566**, L117 (2002)
- J. Zhang et al., *Astrophys. J.* **838**, 2 (2017)
- F. Zuccarello et al., *Astron. Astrophys.* **500**, L5 (2009)

Chapter 23

What to Observe in the Upper Atmosphere



Abstract In this chapter, we shall discuss some aspects of solar phenomena that can be described as “what to observe in upper atmosphere.” As in the previous chapter, examples of the observational results will follow the content of the book. And, again, when possible, quantitative analysis based on theoretical aspects presented in the book will be discussed.

23.1 Braided Magnetic Structures and Screw Pinch Instability

We start with the amazing phenomena of braidlike structures observed in the corona. Braidlike structures in the X-ray emission were discovered by Richard Shine (Shine et al. 1999) while studying the photosphere/corona coupling using the data taken simultaneously by the TRACE, MDI/SOHO, and the Swedish Vacuum Solar Tower (SVST) at La Palma. Eventually, like in laboratory plasmas, magnetic braiding turned out to be ubiquitous for solar atmosphere, from sunspot penumbrae to outer corona. As the magnetic braiding is described by the basic physical parameters of a system and, in principle, allows quantitative analysis, its observation is extremely useful.

For convenience we will show below one of the episodes from those discussed in Chap. 15. Figure 23.1 shows an exemplary event of the coronal braiding seen above the unipolar plage. It is important to emphasize that it is a true braiding structure and not the X-ray emission of *twisted flux tubes*. In other words, it consists of two independent interlaced “bodies” forming a long zigzagging structure. For clarity, small square segments marked by “1” and “2” in left panel are made in order to follow intensity borders of two “ropes” aligned with their apexes. One can see that “left” and “right” apexes are shifted with respect to each other. The measured intensity variations over these areas are shown in the right panel of Fig. 23.1. Both peaks appear with about 15 min periodicity. Eventually the coronal emission strongly intensifies presumably due to the collapse of self-organized braidlike structures that leads to concentration of energy in a small volume and thus to the dramatic increase of the temperature in squeezed volume (cf. Fig. 15.14).

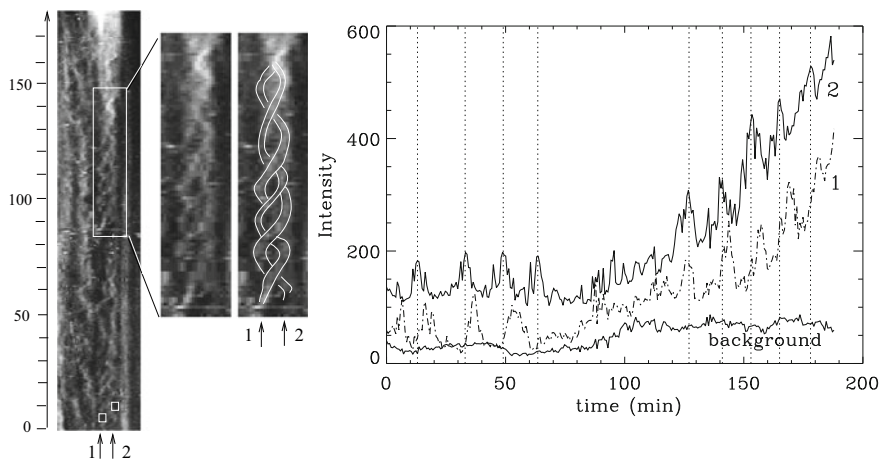


Fig. 23.1 Space-time behavior along the cut made over a spongy coronal emission in TRACE Fe IX/X 171 line above the rarefied plage region (see Chap. 15). The vertical scale marks 177 min time interval. Tiny white boxes of $2.2 \text{ Mm} \times 2.2 \text{ Mm}$ area are aligned along “left” (1) and “right” (2) apices of braids and will serve for the measurement of the intensities of braids. Two middle panels show a blown up image of marked segment with lines that follow the emission pattern. Last panel contains the intensity curves measured for regions of the “left” (1) and “right” (2) apex. The coronal emission strongly intensifies leading to explosive growth of energy (right panel). Thin curve represents an integrated background intensity (Ryutova and Shine 2004)

Note that, although line-of-sight snapshots of the corona show only a spongy emission, under a favorable angle, the braids can be observable in space as well. A spatiotemporal braids are naturally formed by twisted flux tubes that often wrap around each other. High-resolution observations reveal the ubiquitous nature of twisted shape of magnetic flux tubes that wrap around each other. Excellent examples were given, from sub-arcsec observations of penumbral filaments (Scharmer et al. 2002; Sutterlin et al. 2004; Rimmele and Marino 2006; Ryutova et al. 2008) to coronal structures (Ravindra et al. 2011; Cirtain et al. 2013; Pant et al. 2015; Wang et al. 2017). Figure 23.2 shows high resolution (of about 70 km) image of penumbra where majority of filaments are clearly twisted (Ryutova et al. 2008) and some show braiding (see Chap. 17). Left panel is taken in G-band and the right panel is G-band/4396 Å continuum difference. On the G-band image among number of twisted filaments, the filament marked by arrow “1” does not show a clear twist whereas G-band/4396 Å continuum difference image clearly reveals a screw pinch configuration with easily measurable pitch. Moreover, the space-time cut made close to the “bottom” of the filament shows a twisted motion with well kept period. Such measurements allow full quantitative analysis and comparison with theory.

Note that, as discussed in Chap. 17, screw pinch instability is often facilitated by reconnection (Ryutova et al. 2008). Thereby, when observing the twisted structures they must be accompanied by the energy release that can be observed in form of

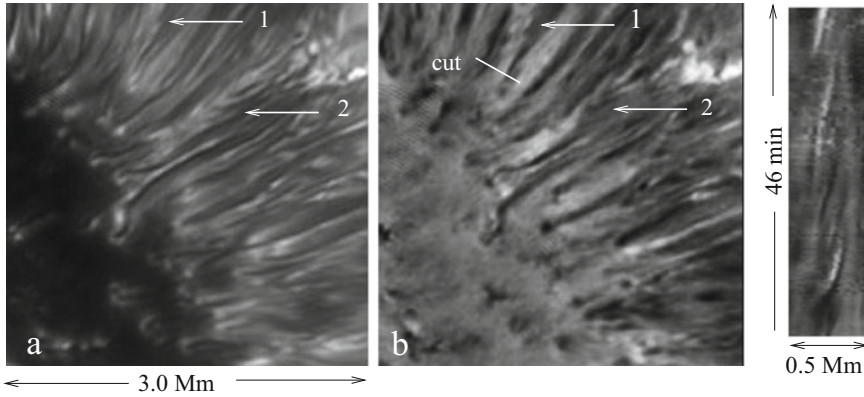


Fig. 23.2 Screw pinch configuration of penumbral filaments: (a) G-band and (b) G-band/4396 Å continuum difference image of 3 Mm area of penumbra, arrows 1 and 2 show clearly twisted filament and filaments braiding, respectively; (c) Space-time image along the cut on the G-band/4396 Å continuum difference image showing cork-screw motion of a filament 1 (not in scale)

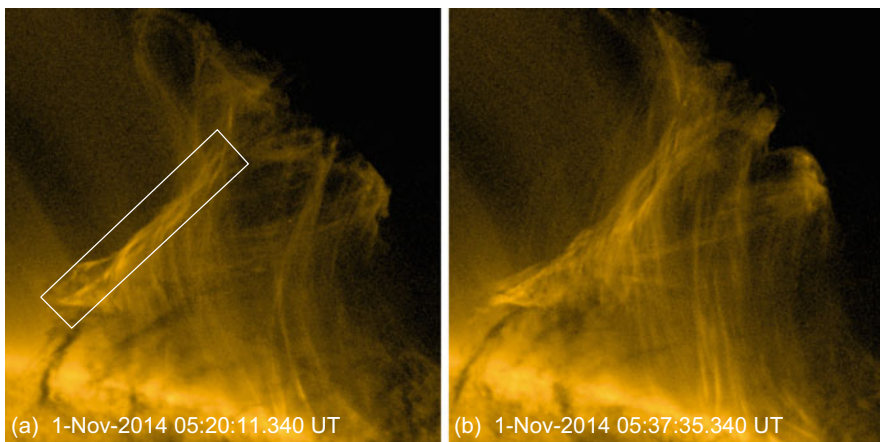


Fig. 23.3 The braidlike structure (marked by a rectangle in left panel) and its unraveling phase (right panel) (Wang et al. 2017). Courtesy of W. Wang

microflares, jets, or their combinations. This process is quite general and may occur at any height and at any temperatures in system of structured magnetic fields.

For example, the appearance of braidlike structure has been reported while observing the formation and evolution of a quiescent prominence (Wang et al. 2017). In time, the prominence body rose upward and formed an arch-shaped structure which then writhed in counterclockwise direction. At some point a braidlike structure appeared at the edge of the skewed arch (Fig. 23.3). Figure 23.4 shows

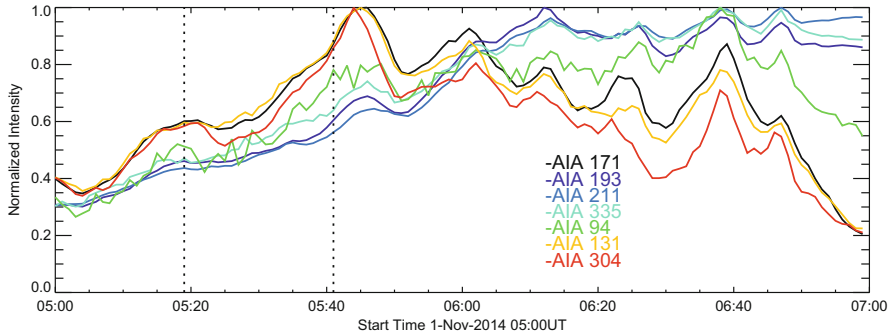


Fig. 23.4 Transient brightening associated with the unraveling of the braidlike structure. The plot shows temporal variation of the normalized average intensity from the rectangle in left panel of Fig. 23.3 with the seven AIA EUV passbands. The vertical dotted lines indicate the time interval during which the braidlike structure was clearly visible (Wang et al. 2017). Courtesy of W. Wang

the process of unraveling that was observed to be accompanied by the brightening of the prominence material in 304, 171, and 131 Å.

Note again that it is important to distinguish between the temporal braidlike behavior which, among other properties, allows to follow independent ropes forming the braids (like in Fig. 23.1), from the screw pinched ropes performing the corkscrew motion (like in Fig. 23.1). One of the major difference of these visually similar phenomena is that the “true” braiding is a long process that may last hours, and has clear properties of self-organized state. Such self-organized structures are long-living and carry a significant amount of energy. Collapse in the system will produce strong heating and violent energy release.

The ropes and flux tubes subjected to screw pinch instability have shorter lifetimes and may be accompanied by the axial mass flows leading skewing of the twisted ropes. The most reliable tool in studying these phenomena is space-time analysis and quantitative estimates. Note that in the above-mentioned examples (Wang et al. 2017), several very clear signs indicate that the part of the prominence experienced the action of screw pinch instability. These are, e.g., a short spatial twist, the axis of twisted structure showed skewing, and enhanced brightening was most probably associated with reconnection (cf. Fig. 17.7).

The dynamic braiding, as natural phenomena in energetically open systems, may be observed in wide range of spatial scales. For example, a large-scale braiding in the erupting prominence is shown in Fig. 23.5.

Fine-scale coronal loop braiding, practically unresolved by the SDO instruments having 1.0 arcsec resolution, is well detected by the High-resolution Coronal Imager (Hi-C) having ~ 0.2 arcsec resolution. Figure 23.6 shows snapshots of a narrow coronal loop braided along its length (Cirtain et al. 2013). Observation of the intensity of emission in a loop at several AIA wavelengths revealed that the twist in the braided structures increased with time. At some moment, a small flare, accompanied by strong (150 km s^{-1}) outflows, was observed at the intersection of

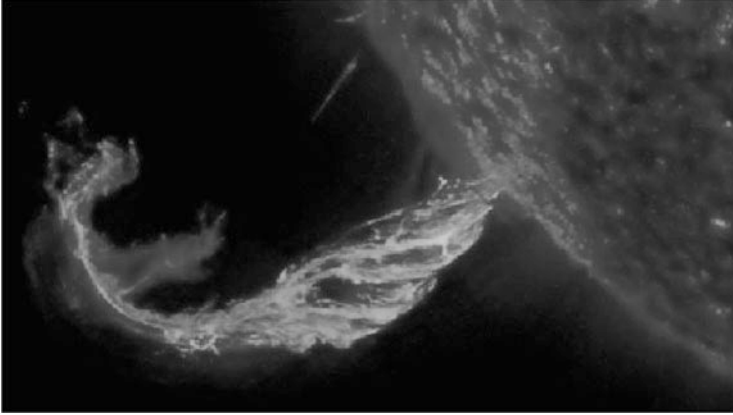


Fig. 23.5 A violent coronal mass ejection observed on 2015, Feb 24, UT 10:17. The prominence mass started to lift at about UT 08:30, showing during its active phase showed a clear braided structure. At about UT 10:35 the structure started to collapse. Field of view is $3.2 \times 4.0 \text{ Mm}^2$. Courtesy of NASA/SDO

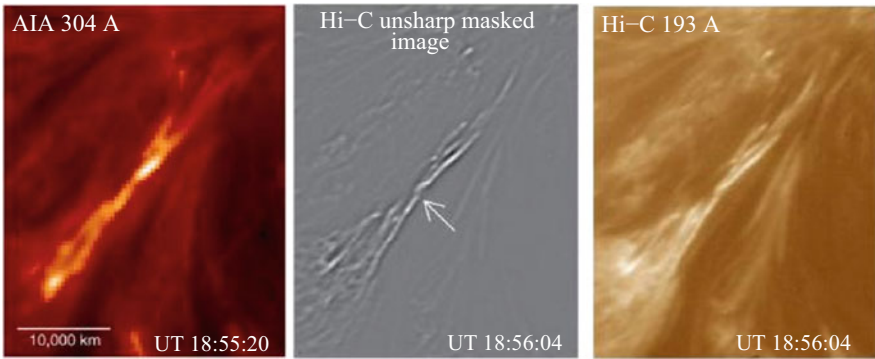


Fig. 23.6 A coronal loop at several temperatures. Left: the AIA image in 304 \AA ; Middle: “unsharp mask” version of Hi-C data constructed by smoothing the original image and subtracting the processed image to enhance the shapes of fine-scale structures; Right: the Hi-C image in 193 \AA (Cirtain et al. 2013). Reprinted with permission from Springer Science and Business Media

the converging strands. AIA data in several passbands showed repeated impulsive events. This braided bundle of loops were observed for over 12 h and with repeated brightening occurring during the entire observation period.

Note that (Parker 1972) put forward a coronal heating mechanism associated with magnetic braiding assuming that the corona responds quasi-statically to the footpoint motions, and due to the random walk of the footpoints the coronal field lines become tangled and braided. Then, in ideal MHD the magnetic free energy builds quadratically with time (see also Berger 1993). Comparison with

observations lead to establishing the role of the reconnection between the tangled magnetic threads (Berger et al. 2015). It was shown that the reconnected field lines evolve to a self-organized critical state. In this state, the frequency distributions of coherent braid sequences as well as flare energies follow power law distributions. Theory of self-organization is quite well developed for quantitative analysis and can be effectively applied to high-resolution data.

23.2 Electrodynamic Coupling of Corona and Underlying Photosphere

Energetically open systems of currents may be driven into various dynamic forms via nonlinear processes with continuous flow of matter and energy. Depending on the system parameters these may be long-living steady loops showing subtle oscillations, loops in the, and the periodically flaring and exploding loop systems. The theory predicts that the EUV loops must have a filamentary structure and allows one to estimate the limiting currents and critical radii of elemental filaments associated with the stability criteria. Addressing these problems in Chap. 16, we paid special attention to the following issues:

1. How do the coronal loops formed.
2. What determines their shape, size, and lifetime.
3. Why one loop system produces X-ray flares and relaxes to long-living system of self-organized slinky structure, while other loop systems gradually decay producing only occasional weak flares or no flares at all.
4. What determines the filamentary structure of coronal loops and their physical parameters. Are there some critical parameters like the radius of elemental loop, electric currents, etc.

Figure 23.7 shows snapshots of the “initial” and “developed” states of the target region. One can see a group of the positive polarity flux tubes that form in the beginning of the observation, a pattern resembling a kitten paw. The corona above this region shows a quiet amorphous emission typical of regions overlying unipolar magnetic plages. A global changes start with strong subsurface disturbances that grow fast and pierce a whole overlying atmosphere including corona. What we learn in a few minutes is that this surge was a precursor of emerging magnetic field that eventually formed a bipolar pore. By that time a surge flows “calm down” and a system of small coronal loops was formed. This example shows the birth of the coronal loop systems. In the same way, studying the emergence of surges one can predict and observe the formation of coronal loops.

Farther, it was shown that various regimes of the evolution of coronal loops can be described by the Van der Pol equation. Depending on the system parameters the Van der Pol equation describes a long-living steady loops showing subtle oscillations, loops in the relaxation regime, and the periodically flaring and exploding

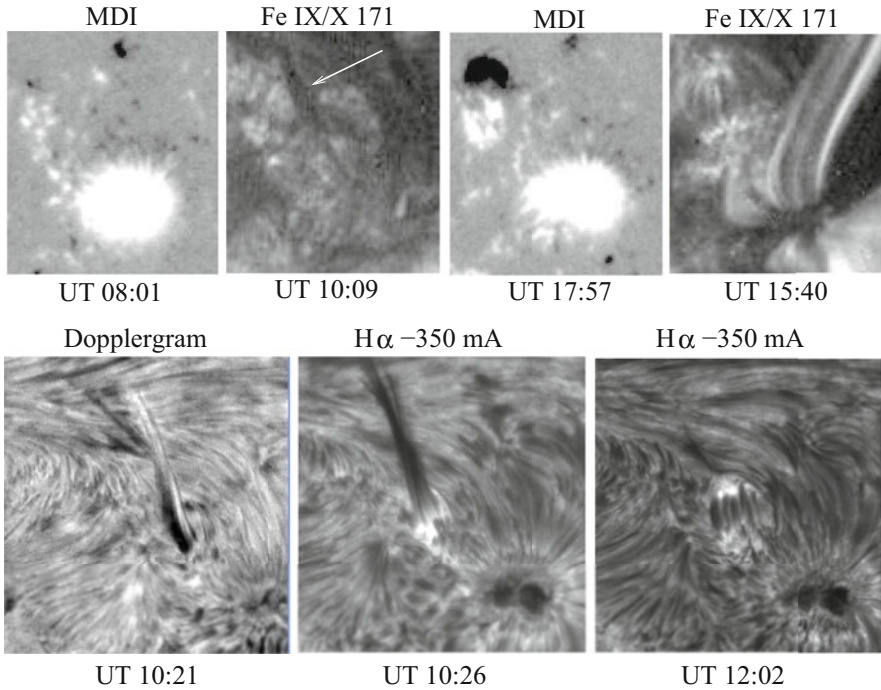


Fig. 23.7 Emergence of a strong surge and loop formation (Rytova and Shine 2004)

loop systems. Most importantly, solutions of equation are expressed through directly observable parameters, allowing thus quantitative analysis.

The theory also predicts that the EUV loops must have a filamentary structure and allows one to estimate the limiting currents and critical radii of elemental filaments associated with the stability criteria. A critical radius of elemental filament for each individual structure is also a simple function of the observed parameters and can be used for diagnostic goals. Comparing the observed radius of elemental coronal loops and using other observed parameters, one can predict the behavior of the loop systems.

The same procedure can be applied to observations similar to those that study post-flare coronal loops which become filled with evaporated chromosphere plasma and become detectable in $H\alpha$. It was found, for example, that post-flare loops have multi-thermal, multi-stranded substructures (Scullion et al. 2014). Many cool strands were found to fully extend intact from loop-top to footpoint. The estimate of the strand number density versus cross-sectional width was found to peak at well below 100 km.

The flare studied with the 1.6 m New Solar Telescope (NST) equipped with high order adaptive optics at Big Bear Solar Observatory (BBSO) also revealed unprecedented details, coronal rain streaming down along the post-flare loops, and

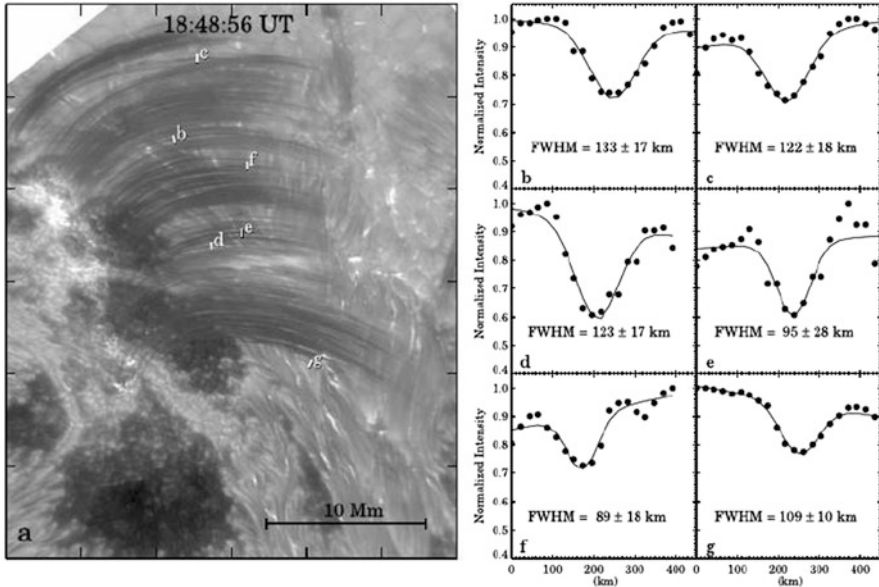


Fig. 23.8 Panel (a) a snapshot of $H\alpha + 1.0 \text{ \AA}$ image taken in the decay phase of the flare. Six short slits show where the cross-section of six loops were measured. Panels (b–g): the normalized $H\alpha + 1.0 \text{ \AA}$ intensity profiles (black dots) along the slits and the Gaussian fits (black curves). The Gaussian FWHM and its $\pm 3\sigma$ are provided in each panel (Jing et al. 2016). Reprinted with permission from Springer Science and Business Media

the response of the chromosphere to the impact of coronal rain, showing fine-scale brightenings at the footpoints of the falling plasma (Jing et al. 2016). The measured cross-sectional widths of flare ribbons, post-flare loops, and footpoint brightenings were found in the range of 80–200 km.

Figure 23.8a shows a $H\alpha + 1.0 \text{ \AA}$ snapshot of the post-flare loop system. Six short cross-cut slits in Fig. 23.8a single out the loops (marked by letters b–d) for which the cross-sectional Gaussian FWHM has been measured. These were found to be within a range of 89–133 km (Fig. 23.8b–g).

Note that the analysis of the same data sets (Wang et al. 2017) showed that the M6.5 flare that occurred in the system had precursors observed as small pre-flare brightenings in various wavelengths. These precursors were also found to be associated with small-scale magnetic configurations such as opposite-polarity fluxes.

The observed regularities fit well the scheme described by Van der Pol oscillator that includes the photospheric driver, magnetic field that interconnects the $\beta \geq 1$ energy source region with the $\beta \ll 1$ dissipation region, feedback between the current generation and dissipation regions, and formation of small-scale threads comprising coronal structures.

A useful example of application of the Van der Pol equation is given in connection of weakly damping kink oscillations of coronal loops observed in non-

flaring active regions (Wang et al. 2012; Anfinogentov et al. 2015; Nakariakov et al. 2016; Liu et al. 2016). The oscillations of multi-stranded loops with growing amplitudes and internal coupling observed with the SDO/AIA revealed the presence of multi-thermal strands, whose dynamic behavior showed differences in their oscillation amplitudes, phases, and emission. Most importantly these oscillations not only kept their amplitude undamped but at some point showed growing pattern (Wang et al. 2012).

Figure 23.9 shows the magnetic flux evolution of the three bands along a cut at the loop's apex. During the first 20 min, the loop in 171 Å already shows a weakly damped oscillations that become more prominent and gradually split into two strands that continue the undamped oscillating behavior. The loops in 193 and 211 Å, composed of several close strands, also show the oscillations with no clear change in amplitude in each strand.

Studies of low amplitude weakly damped coronal loop oscillations performed for dozens of sunspots showed their common character. The oscillation periods were found to lie in the range from 1.5 to 10 min with the apparent increase of periods with the length of the oscillating loops (Anfinogentov et al. 2015).

More detailed view of undamped oscillations in 171 Å of the same data set is shown in Fig. 23.10.

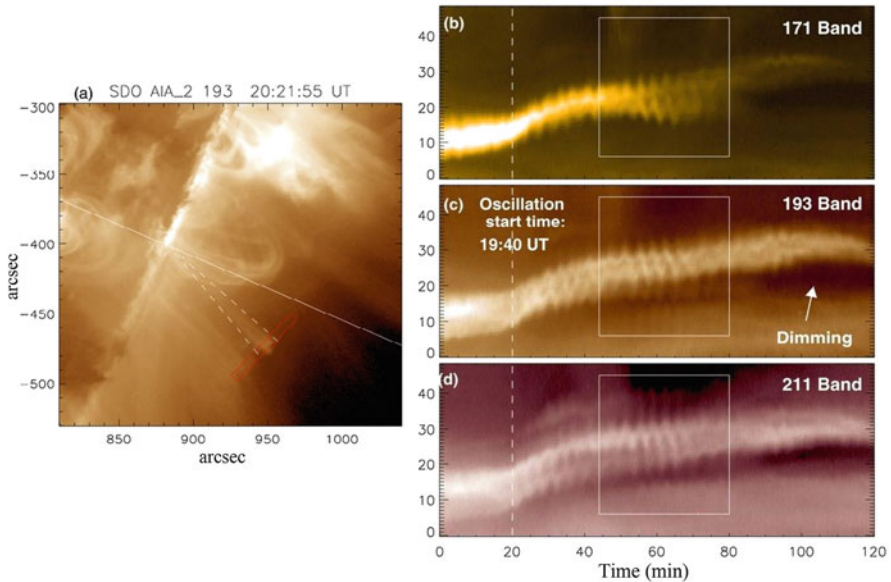


Fig. 23.9 Observations of the transverse loop oscillation event on 2011 March 8, with SDO/AIA. Left panel: the object of the observations in 193 Å, the red narrow box marks the space-time cut; Right panels: Space-time images along a cut at the loop apex as shown in Panel (a) (averaged over the narrow width) in three bands: (b) 171 Å, (c) 193 Å, and (d) 211 Å (Wang et al. 2012). Reprinted with permission of the AAS

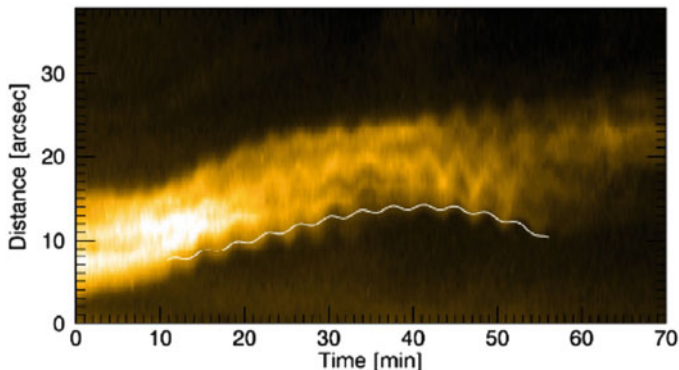


Fig. 23.10 Example of undamped oscillations of coronal loops, illustrated by a time-distance map made for a slit directed across the oscillating loop. The oscillation was measured on the 8th of March 2011, beginning at 19:40 UT in AR 11165 at 171 \AA with SDO/AIA (Nakariakov et al. 2016). Reproduced with permission from A&A, Copyright ESO

As discussed earlier, undamped and/or growing oscillations are natural occurrence in dissipative, energetically open systems with the source and sink of energy. One of the equations arising in such system (Chap. 16) is Van der Pol oscillator.

Hence undamped oscillations in coronal loops in order to exist require continuous energy supply and any kind of dissipation. One of the most natural sources of energy supply is the appearance of surges that are observed at footpoints of coronal loops. Association of the photosphere/chromosphere surges reaching in the corona the velocities up to $200\text{--}300 \text{ km s}^{-1}$ has been reported in various papers (Tian et al. 2014; Doschek et al. 2015). It is important to note, however, that the conditions on magnetic field, electric currents and kinetic coefficients, and other parameters of a system, determined, e.g., by the Van der Pol equation and boundary conditions, must be met. Most of the parameters are directly observable or can be calculated using the model description.

As an example, let us estimate electric currents generated by the upward propagating waves from a limited surface area, S . In strongly stratified atmosphere, as we know, these waves quickly evolve into a sequence of shocks.

At the transition region heights plasma is strongly collisional and the particle mean free path is small:

$$l \sim \frac{(kT)^2}{ne^4 \ln \Lambda} \quad (23.1)$$

Thus, for $T = 10^5 \text{ K}$ and $n = 10^{10} \text{ cm}^{-3}$, we have $l \sim 2.19 \cdot 10^4 \text{ cm}$. Under these conditions half of the mechanical momentum carried by the waves is transferred to electrons and a half to the ions, which leads to the generation of currents (Ryutov and Ryutova 1990).

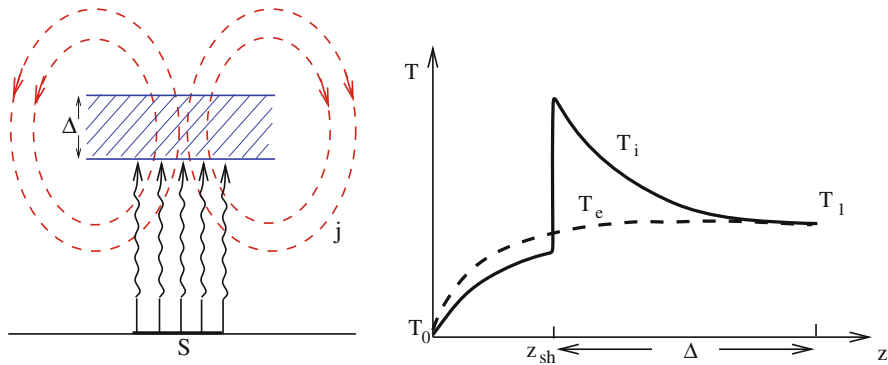


Fig. 23.11 Current drive by the acoustic or MHD waves. Left: The upward motions generated from a limited surface area, S , quickly accelerate in the upper layers of atmosphere and generate a sequence of shocks and create a strong absorption region at shock front discontinuity, Δ (blue shaded area); Right: Ion and electron temperature profiles at the shock front, z_{sh} is the height of shock formation (Ryutov and Ryutova 1990)

The mean force acting on the electron gas, \mathbf{F}_e . When the wave acquires the saw tooth profile, the mean force acting on the electron gas, \mathbf{F}_e , becomes nonpotential. Therefore, it will have a large (of the order of unity) solenoidal component due to the spatial variations in the intensity, the plasma density, and temperature. The schematic of absorption region and current lines is shown in Fig. 23.11, left panel.

At the shock front hot ions remain behind the shock, while hot electrons move ahead as their velocity is $(m_i/m_e)^{1/2}$ times higher than the ion and shock front velocities. Ion and electron temperature profiles at a shock front are shown in Fig. 23.11, right panel. The thickness of the relaxation region where T_i and T_e equilibrate is $\delta \sim \sqrt{m_i/m_e}l$, where l is the particle mean free path. Detailed estimate of current generation has been already discussed in Sect. 16.3. It was shown that acoustic wave flux from the photosphere reaching as small Mach numbers as $M \simeq 1.2 - 1.4$ may generate currents at transition region with $T = 10^5$ K and $n = 10^{10} \text{ cm}^{-3}$ of the order of $j \simeq 10^{-2} \text{ A/cm}^2$. The governing equations given in Sect. 16.3.2 can be used for quantitative analysis. Besides, as currents generated by the oscillations are associated with the ion temperature jump, this fact can also be observed.

23.3 Evolution of Rudimentary Penumbra and Response of the Overlying Atmosphere

We have discussed throughout the book that filamentary structure of sunspot and the umbra itself yield numerous unsteady phenomena in wide range of physical parameters. Most of which are triggered by continuous multiple reconnections

between the neighboring filaments (Alissandrakis et al. 2017; Kirk et al. 2017). In particular, the very formation of penumbra and shredding of umbra are directly associated with these reconnections, as illustrated in Fig. 17.8.

The question arises, what could be reason of the fact that some pores and compact sunspots do not develop penumbra or loose it quickly.

Figure 23.12 shows Hinode magnetogram of the pore (NOAA 10940) and the temporal evolution of its overlying atmosphere in the G-band and Ca II H lines

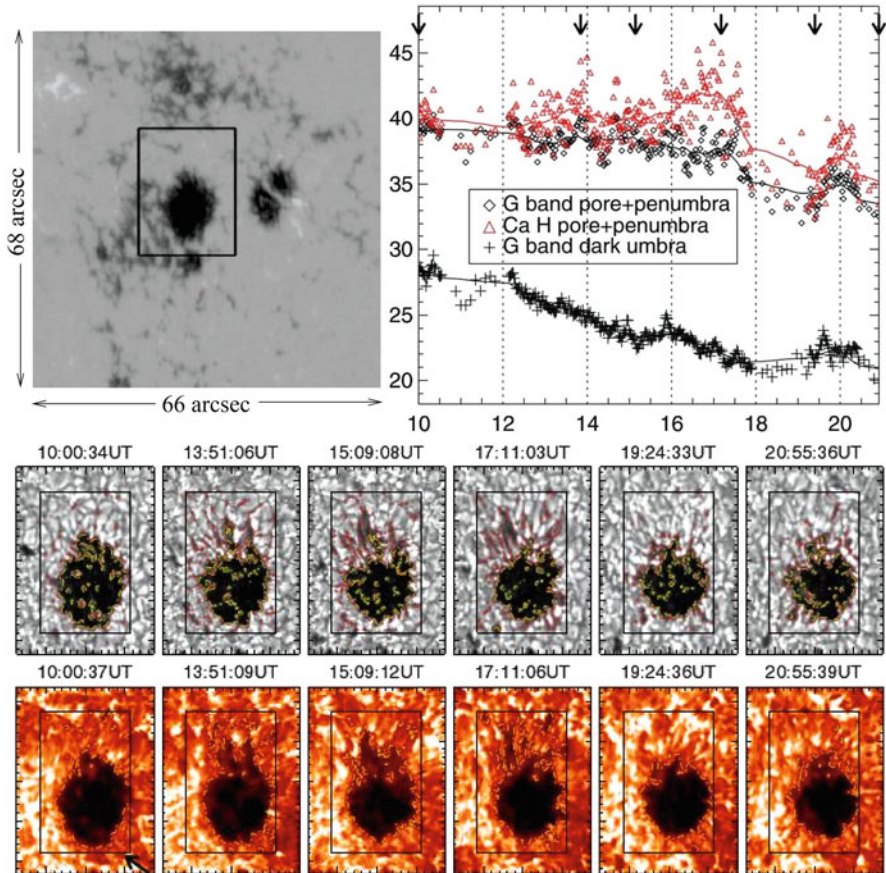


Fig. 23.12 Evolution of the pore and formation of penumbra. Upper left: Hinode magnetogram of NOAA 10940; the black rectangle shows the cropped $18'' \times 24''$ FOV of area displayed in the bottom images. Upper right: Temporal variation of the area (in Mm^2) of pore + penumbra in the G-band (black diamond), pore + penumbra in Ca II H (red triangle), and dark umbra in the G-band (black plus). The solid lines show smoothed variation with about a 1 h width. The black arrows at the top of the plot indicate the timing of the frames shown in the bottom panels. Bottom: time sequence of the pore in the G-band (upper row) and Ca II H (lower row). The yellow and red contours on the G-band images show the thresholding for the pore/penumbra of $0.4I_{qs}$ and $0.7I_{qs}$. The yellow contours on the Ca II H images show the chromospheric penumbral thresholding of $0.1I_{qs}$ (Watanabe et al. 2014). Reproduced with permission of the AAS

(Watanabe et al. 2014). At some point, the rudimentary penumbra to the north of the pore started to form. The apparent speed of the elongation of a single penumbral filament reached $2\text{--}3\text{ km s}^{-1}$, while the overall penumbral structure extended its boundary with a speed of about 0.5 km s^{-1} . In the chromosphere, frequent brightenings at the outer edge of the penumbra were observed. In the decay phase, multiple opposite polarity patches were observed to appear outside the pore void of newborn penumbra and, simultaneously, many small-scale fragmented patterns were seen in the intensity images.

All the details of this process fit well the model of filamentary structure of sunspot and continuous reconnection processes. Depending on the angle at which neighboring filaments reconnect, in post-reconnection phase they may be either scattered or produce shocks and subsequent brightenings. This process in young developing pore may stop formation of penumbra and destabilize the farther growth of sunspot.

Penumbral sub-arcsecond penumbral brightening and shocks observed simultaneously with the NST, IRIS, and SDO showed that the brightening, whose thermal energy is in the range of nanoflares, have signatures from the chromosphere to the corona.

Figure 23.13 shows the snapshots of an exemplary event near the maxima. NST's $H\alpha$ channel reveals the fine structure of the event of about 101 km. The transient brightening can be characterized as a “doublet” with two maxima at UT 17:16:14 and UT 17:19:20, lasting for about 3 min, as seen in significantly enhanced and broadened chromosphere and transition region lines. Moreover, the event is seen in all the extreme-ultraviolet passbands of the AIA. The $H\alpha$ images in Fig. 23.13b reveal the same order fine structures of the brightening event, as penumbral filaments with widths as small as 101 km.

The transient appeared at the outside edge of the penumbra and then moved toward the sunspot umbra with a speed of about 87 km s^{-1} . The maximum brightening was seen almost simultaneously at all coronal temperatures. It was also found to be associated with a redshift of about 17 km s^{-1} , as seen in the Si IV 1402.77 Å line.

Figure 23.14 shows the IRIS spectra before and during the event. One can see that the TR line profiles, both C II 1334.53 Å and Si IV 1402.77 Å, are enhanced by a factor of about 3, and more than 20 during the event and significantly broadened relative to the average penumbral profiles. Besides, in the Si IV 1402.77 Å line a redshift of about 17 km s^{-1} averaged along the line of sight was found during the brightening. Before the appearance of the chromospheric transient, at 17:00 UT, a negative magnetic feature has been emerged at near location of the upcoming transient brightening that was observed to move outward and decay at UT 17:36:00.

What we witness here is a clear demonstration of the effects described in Chaps. 13 and 14 and elsewhere throughout the book: reconnections in low atmosphere, due to the finite plasma β , do not give an immediate release of energy. It is a post-reconnection sling shot created by straightening flux tubes first generate upward and downward shocks. Farther interaction of shocks as shown in Fig. 13.5 leads to appearance of either microflare (brightening), or plasma jets or the combination of brightenings and jets.

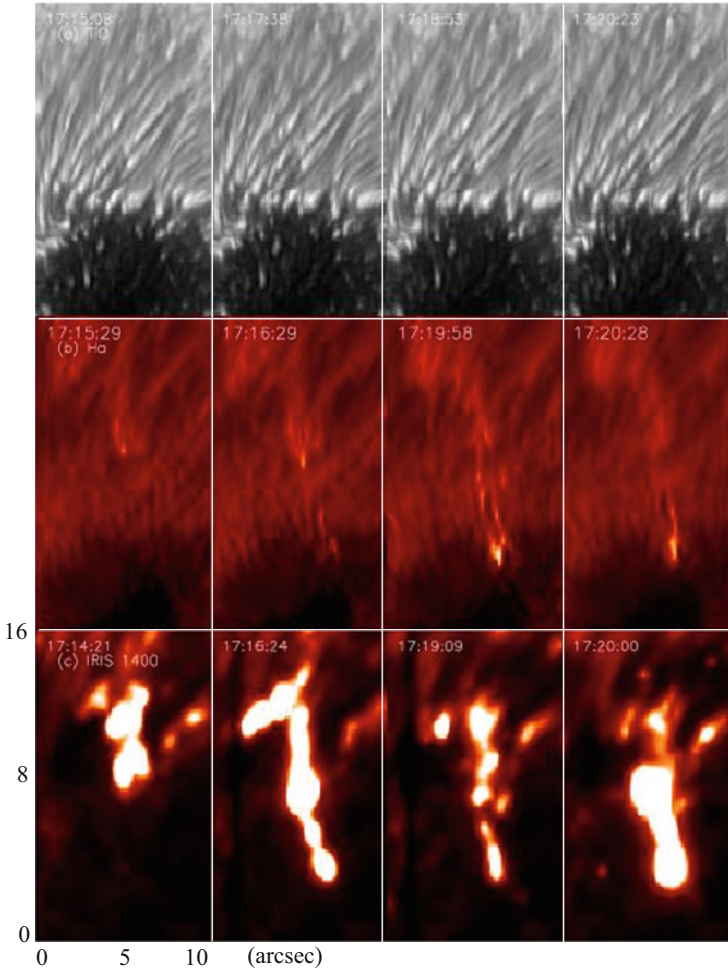


Fig. 23.13 Temporal evolution of the penumbral transient brightening in NST/TiO (a), NST/H α (b), and IRIS 1400 Å (c) images (Bai et al. 2016). Reproduced with permission of the AAS

Let us now look at Mg II k 2796.35 Å images in panels a–b, Fig. 23.14, and the plot in panel c. At UT 17:14:52 not long before the brightening occurred, the chromospheric line already shows enhancement and brightening. At the same time, line profiles show clear signatures of shocks in the shape of double humped peaks. The red and blue lines show downward propagating shocks: higher peaks are on the right, toward longer wave-length. The green and orange lines show the signatures of upward propagating shocks. A symmetric broadening in Mg II k line corresponds to behind-shock heating accompanied later by symmetric up and down mass flows. In the hotter, C II 1334.53 Å shock signatures are less distinguishable, except the peak time at UT 17:16:14 when a strong shock signatures and broad widening of

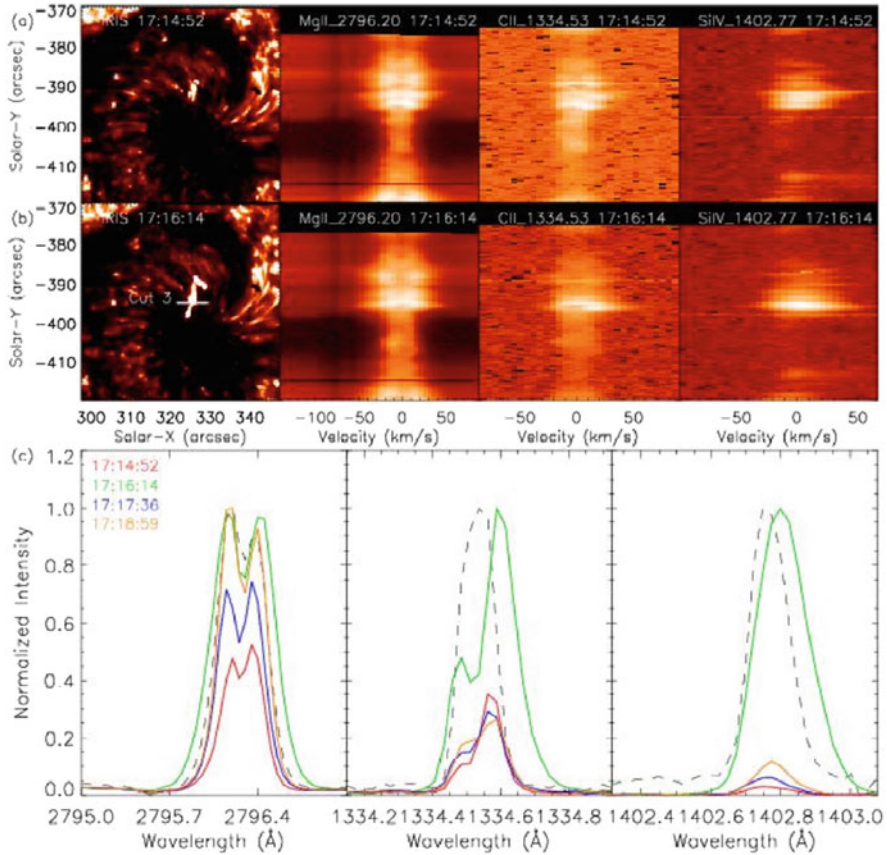


Fig. 23.14 Spectral characteristics of the penumbral transient. (a) The position of the slit in IRIS 1400 Å images; (b) Spectra of Mg II K 2796.35 Å, C II 1334.53 Å and Si IV 1402.77 Å, along the slit before and after the enhanced brightening; (c) Line profiles at four different times at the cross point between cut 3 and the brightening region. The normalized average line profiles in the penumbra before the event are represented by the dashed lines (Bai et al. 2016). Reproduced with permission of the AAS

the peak appear. Corresponding velocities and Mach numbers are quite easy to estimate (see Eqs. (13.3)–(13.15)). The entire picture would be more complete with the measurement of underlying magnetic field changes in time.

Of many properties of penumbral filaments, observation of their twisting motions provides very rich information. Thus, penumbral filaments, along the twisting motion, show also a chirality change. Besides, in the presence of mass flows that are always observed in penumbra, body of filament is subject writhing and skewing (see Sect. 17.4.2). Example of such observations is shown in Fig. 23.15 (Su et al. 2010). It was found, for example, that penumbral filaments often showing unwinding motions are associated with the decrease of their, say, right-handed twists. After unwinding, they get twisted again but now with the left-handed chirality, and vice versa. This process is a natural occurrence during screw pinch instability.

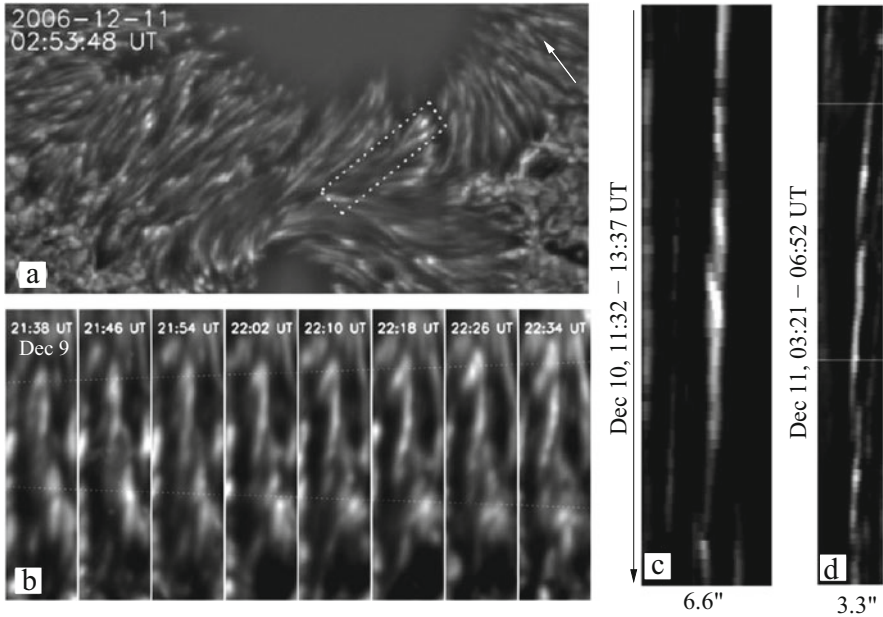


Fig. 23.15 The part of the AR NOAA 10930 in the G-band (a). White arrow singles out an exemplary penumbral filament whose evolution is shown in panel (b); The dotted rectangle in panel (a) highlights the area where the filaments with a right-handed chirality disappear and new filaments with left-handed chirality appear; Examples of space-time images of left-handed and right-handed chirality filaments from this box are shown in panels (c) and (d) (Su et al. 2010). Reproduced with permission of the AAS

Chirality injection into the overlying atmosphere and its variation may have well-observed effects in the chromosphere and corona, as well as skewing and writhing which must occur in the presence of axial flows (see Fig. 17.14). These effects are well described by the basic plasma theory and allow quantitative estimates.

It is important to emphasize that physical effects described in application to penumbral filaments are universal for any magnetic filamentary structure. In other words, if the safety factor, q , is less than unity (Eqs. 17.2–17.3) the magnetic structure is subject to screw pinch instability and necessarily acquires the twisted shape with further development of specific internal structure (e.g., dark cores), skewing, writhing and chirality change, and other accompanying phenomena.

23.4 Plasma Jetting and Bow Shocks

In Chap. 18 we have discussed the observed properties of bow shocks and their associated bright transients above penumbrae. We have emphasized that the “true” microjets, i.e., the bright transients moving *along* their “body” as do projectiles, are

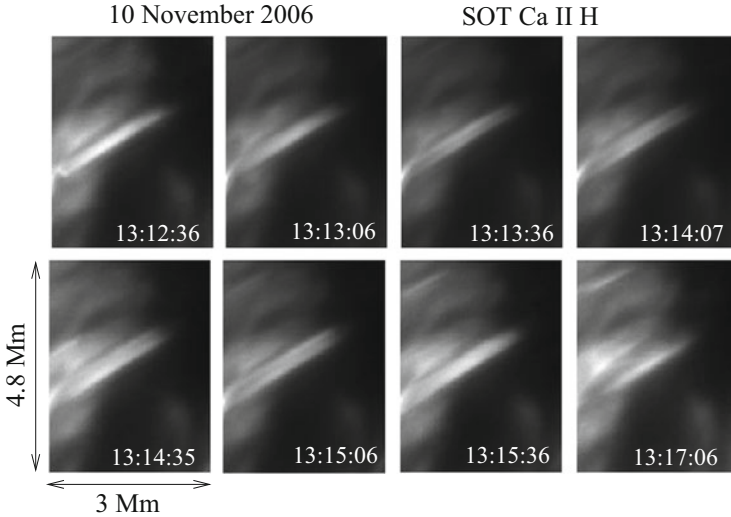


Fig. 23.16 Double structure of the elongated transient drifting with velocity $\sim 1.5 \text{ km s}^{-1}$. Its true motion, if measured in its trajectory plane, may well be supersonic (Ryutova et al. 2008)

essentially different from the bright transients associated with bow shocks. Unlike microjets/projectiles these transients move rather in the transverse direction or under some angle to their body, and they have double structure as it usually occurs in case of bow shocks. For convenience, example of transient associated with bow shocks and exhibiting double structure is shown in Fig. 23.16.

One can see that at UT 13:13:36 the transient seen as a single bright stroke soon develops a clear double structure. The transient is drifting from top-left to bottom-right with velocity $\sim 1.5 \text{ km s}^{-1}$ preserving its double structure during the most of its lifetime ($\geq 5 \text{ min}$). As discussed in Chap. 18, a double structure turns out to be a basic property of drifting transients and has a natural explanation in the frame of post-reconnection theory.

Very useful proved to be spectroscopic observations of penumbral transients with a high cadence co-temporal data taken with the SOT instrument on Hinode and the IBIS (Imaging by Interferometric Survey) on DOT (Reardon et al. 2013).

Spectroscopic data, in addition to studies of character and temporal evolution of transients, allow to estimate the height of their formation. It was found, e.g., that the enhanced emission of brightenings was coming from the wings of the Ca II 8542 Å line, indicating that the energy deposition could occur in the lower layers of atmosphere, around the temperature minimum. Examples of two type of transients are shown in Fig. 23.17. Both events show a greater blue-shifted wing, while no strong Doppler shifts are seen in the core of the Ca II 8542 Å line. In both cases there occurred a pre-event brightening that triggered the impulsive brightening of the transient that occurred uniformly over the length of a structure. These precursors are the most probably associated with the bow shocks. The evolution of the precursor

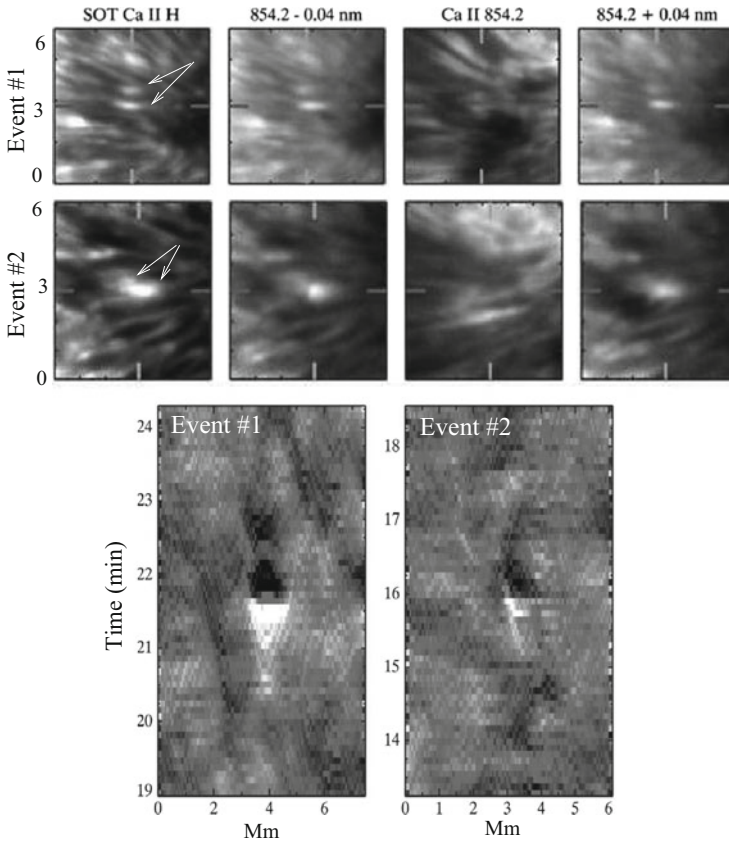


Fig. 23.17 Spatio-temporal behavior of two events (#1 and #2). Upper panels: images at four different wavelengths (SOT Ca II H, blue line wing, line core, and red line wing of the IBIS Ca II 8542.1 Å line) at the peak time of the event. The event location is indicated by the intersection point of the red and orange tick marks. Lower panels: Space-time plots of the running difference of the blue-wing intensity along the length of Events #1 and #2 around the time of peak brightening. The enhanced spreading of enhanced emission begins 1 min prior to the peak intensity (Reardon et al. 2013). Reproduced with permission of the AAS

brightening can be more clearly seen by making space-time slices from the running difference images in the blue wing Ca II 8542 Å line, as shown in two lower panels in Fig. 23.17.

Rich data can be obtained from high cadence spectroscopic observations of drifting transients and penumbral jets, especially under various viewing angles, i.e., observing penumbrae at various locations from disc center to peripheries. With such observations it will be easier to perform classification of various types of transients like drifting transients and their precursors in form of bow shocks, true plasma jets, Ellerman bombs, and other. Most importantly, all these features can be put in the frame of quantitative analysis described in Sect. 18.2.

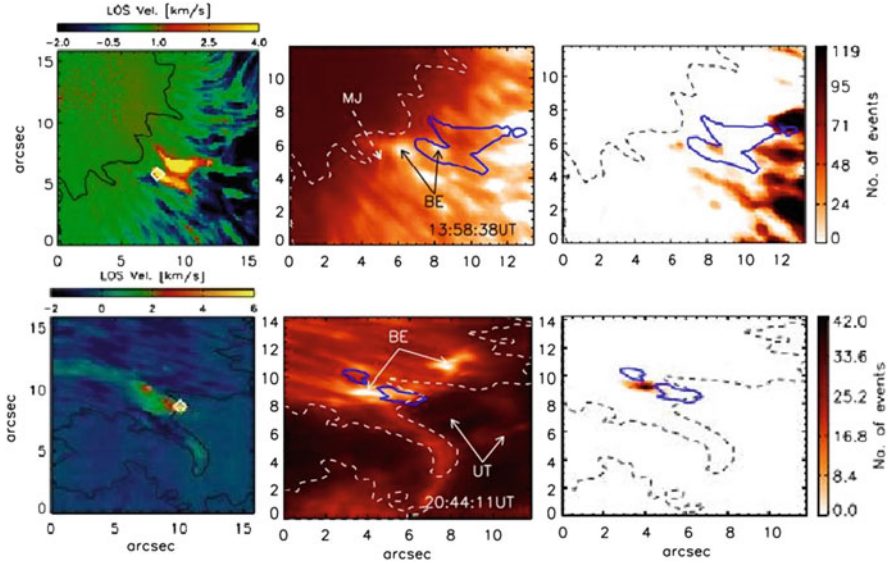


Fig. 23.18 Examples of two active regions NOAA 10923 (upper row) and NOAA 10955 (bottom). Left panels: Line-of-sight velocities derived from the SIR inversion. The diamonds represent regions of strong downflows. Middle panels: Ca II H filtergrams with blue contours showing regions of the LOS velocity greater than 2 km s^{-1} . The white dashed contours correspond to the continuum intensity at 6300 \AA . BE is brightness enhancement, MJ is penumbral microjet, and UT is bright umbral thread. Right panels: Ca II H maps with the bar showing number of events (Louis et al. 2011). Reproduced with permission of the AAS

High-resolution spectropolarimetric observations have also revealed the existence of supersonic downflows at or close to the umbra–penumbra boundary (Louis et al. 2011). Figure 23.18 shows example of two active regions showing strong, long-lived brightenings in the neighborhood of the downflows. In Ca II H filtergrams (middle panels) one can identify penumbral microjets as well as brightness enhancements in the vicinity of the strong downflow areas according to the process shown in Figs. 17.6 and 17.7. The right panels of Fig. 23.18 show the number of events for both active regions. The counts for two large patches in the AR 10923 indicate that brightness enhancements persisted for nearly one-third of the 1 h sequence. The strongest chromospheric brightenings observed in AR 10953 was confined to a region between the two downflow patches. These kind of observations can be directly used for quantitative analysis using the models described in Chaps. 13 and 18.

The important work was done on the statistical analysis of penumbral microjets using observations in the Ca II 8542 \AA line obtained with the SST (Drews and Rouppe van der Voort 2017). In this work in all over the penumbra a total of 453 tracked microjets were detected, with peak downward velocities of -10.4 km s^{-1} and upward velocities of 10.2 km s^{-1} . Their lifetimes ranged in 90–117 s. It was found that there are regions of penumbra with significantly higher occurrence rates of penumbral microjets than in other parts of penumbra.

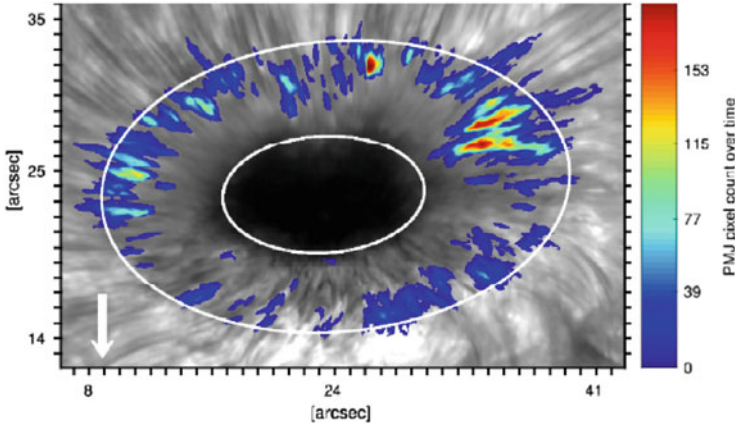


Fig. 23.19 Penumbral microjet densities, with all pixel detection summed over 202 time frames, overlain a frame at the midpoint in time of the observations, at an offset of -275 m\AA in the Ca II 8542 \AA line. The arrow indicates the direction toward disk-center (Drews and Roupe van der Voort 2017). Reproduced with permission from A&A, Copyright ESO

Figure 23.19 shows a density map of all the individual microjets detection-pixels, summed over all time frames. One can see a clear clustering of penumbral microjets in certain regions, and two distinct regions in the upper right corner in particular.

There are two most probable reasons for increased density of microjets at some particular site of penumbra. One is associated with inclination of the neighboring penumbral filaments with respect to each other: the more filaments intersect with sharper angle the better is condition for generation of post-reconnection jets (see Fig. 17.6b, Chap. 17). The other obvious reason is associated with the number of magnetic elements with the opposite to the parental sunspot polarity, such as unipolar or even bipolar moving magnetic features. The more such elements wander around the sunspot, the higher is probability of reconnections between the opposite polarity elements and direct generation of jets. Both these processes are easily observable and could be done in future observations of the penumbrae.

23.5 Self-organization and Recurrent Flares

We have discussed throughout the book that the solar atmosphere is intrinsically nonlinear dynamic system with unbalanced sources and sinks of energy. As such, it exhibits a chaotic behavior, practically at all scales. This includes, for example, fractals, energetically open periodic processes and bifurcation, limit cycles, and self-organization (see e.g. Aschwanden 2011). Moreover, these processes are not only observed on a regular basis, but most of them can quantitatively analyzed. Figures 23.20 and 23.21 illustrate the self-organized states in the solar atmosphere from its surface through the corona.

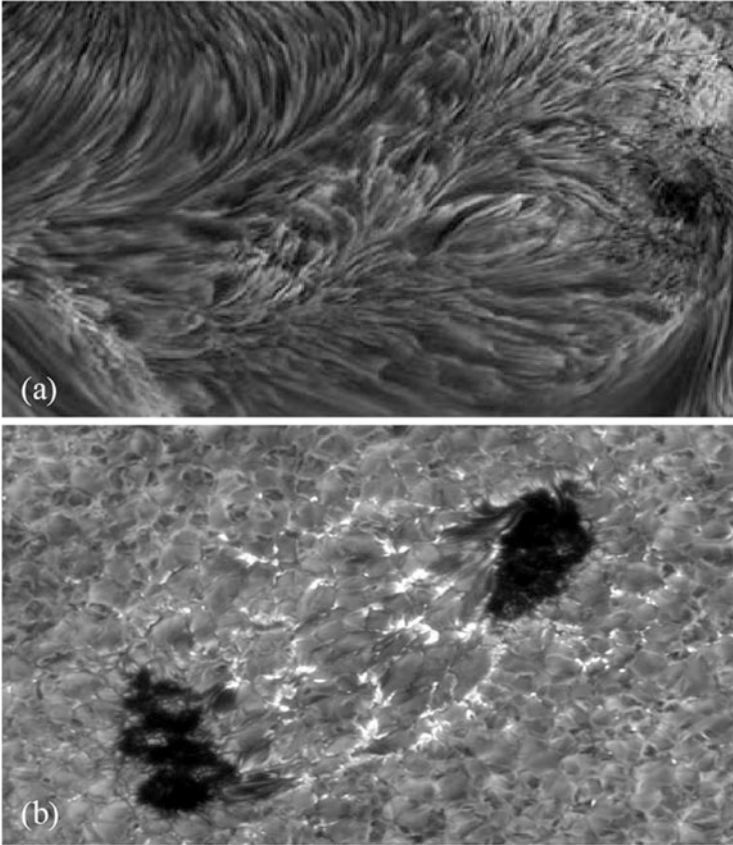


Fig. 23.20 Self-organization in low atmosphere. (a) Just like an ice pattern on window: solar chromosphere in $H\alpha$ taken by the DOT, field of view is about 700×400 Mm (courtesy of R Rutten); (b) The SST/CRISP image of solar photosphere in 5100 \AA (courtesy of G. Sharmer)

Spectacular example of self-organization is the formation of long-living post-flare arcades, slinkies. As discussed in Chap. 19, when the energy supplied to a system reaches its limiting value, the system experiences the explosive release of energy and may bifurcate into self-organized state. The example of such process is the formation of long living slinkies after the solar flare. In Figs. 23.22 and 23.23 we show two more examples of this process. Figure 23.22 shows a typical slinky-producing flare. Hours before the major flare, the system exhibits series of homologous flares in a strict time periodicity corresponding to evolution of system approaching a limit cycle (cf. Chap. 16). At about UT 20:10 the system releases the accumulation energy and relaxes to previous state. From this moment the system gains energy again and at UT 21:50 releases it again. The process repeats with the same ~ 300 min periodicity: at about UT 23:30 new burst puts the system back. This time, supposedly more energy is pumped into the system which releases it at

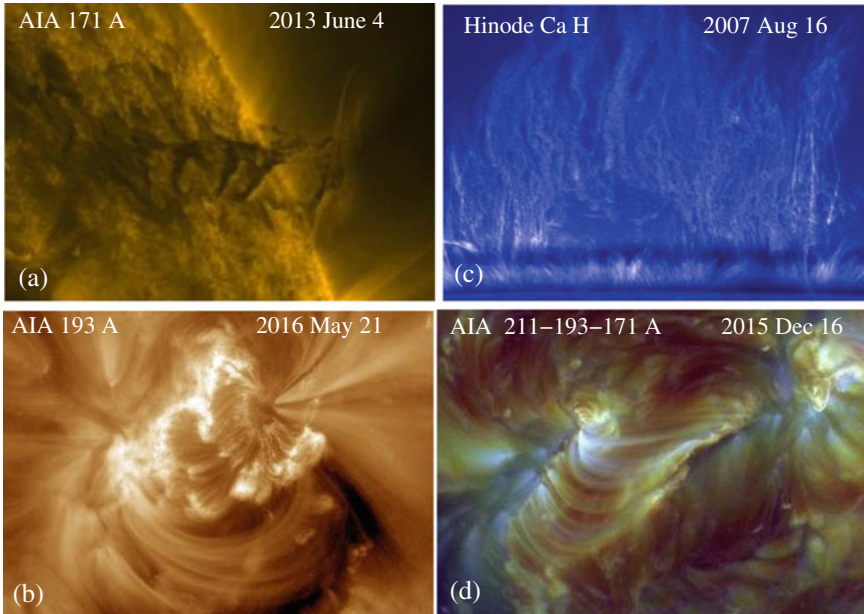
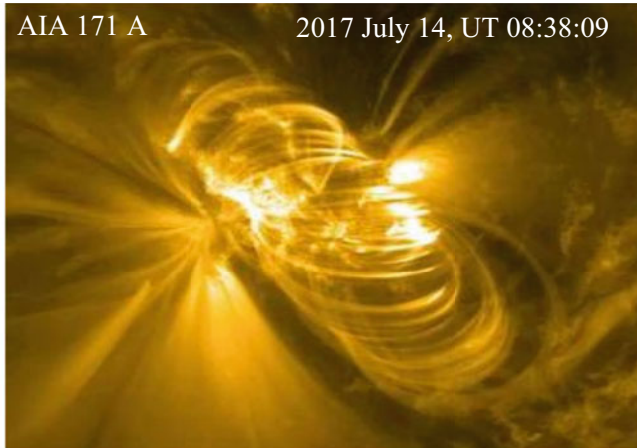


Fig. 23.21 Self-organization in the upper atmosphere. (a) Very regular long-living tornado-like prominences like solders move and live in harmony for tens of hours; (b) 10^6 K coronal loops having a peacock-style of self-organized pattern, harbors numerous microflares during more than 4 days; (c) Quiescent prominence, harboring all kind of plasma instabilities also lives for days; (d) Post-flare slinky in combined wavelength of 211-193-171 Å courtesy of NASA/SDO

UT 01:07, July 14 in form of M 2.4 flare, reaching its limit cycle, approaching to bifurcation into the self-organized state. Self-organized state lasts about 19 h until the new cycle begins.

Similar process is shown in Fig. 23.23 with some differences in detail. This time we face much stronger, X 4.9 flare and its bifurcation into the self-organized slinky. The main difference here is that the homologous precursor flares occur in this case with significantly longer intervals (shown is only the last pre-flare energy release at UT 21:40 Feb 23). A strict periodicity of the process and possibility to measure intensities allows to perform reliable quantitative analysis of these processes. Besides, these periodicities can be used for prediction of upcoming flare events.

Time series of date taken for slinkies can provide the information regarding the echo effects as well. In Sect. 19.6 we have discussed nonlinear plasma wave echoes that can be harbored by post-flare slinkies. By their amazing regularity, slinkies are the perfect system to observe the echo effects, which may be temporal, spatial, and spatio-temporal. As an example we show four snapshots of slinky exhibiting the plasma wave echoes (Fig. 23.24). The lifetime of the slinky is about 8 h. In four consecutive snapshots we see, e.g., that enhanced brightening



GOES X-Ray Flux, 2017 July 13–15

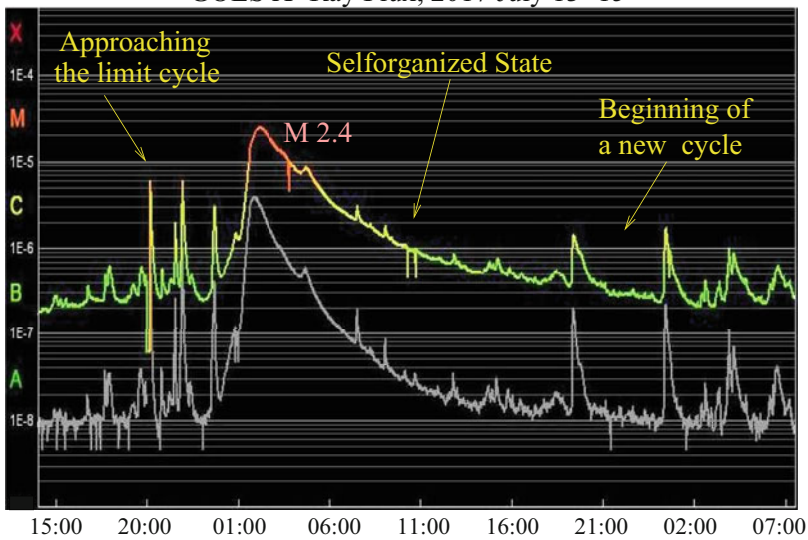


Fig. 23.22 M 2.1 flare and post-flare self-organized slinky. Upper panel: Fe 171 Å emission of the post-flare loops already bifurcated into long-living self-organized arcades. Start time: UT 01:07, peak time: UT 02:09. Lower panel: GOES X-ray curves from July 13, 15:00 UT to July 15, UT 07:00, showing intense pre-flare recurrent flushes organized in a regular echo pattern and post-flare echoes started at about UT 18:30 that lead to spatio-temporal scale-invariance. GOES curves are reprinted from Andreas Möller

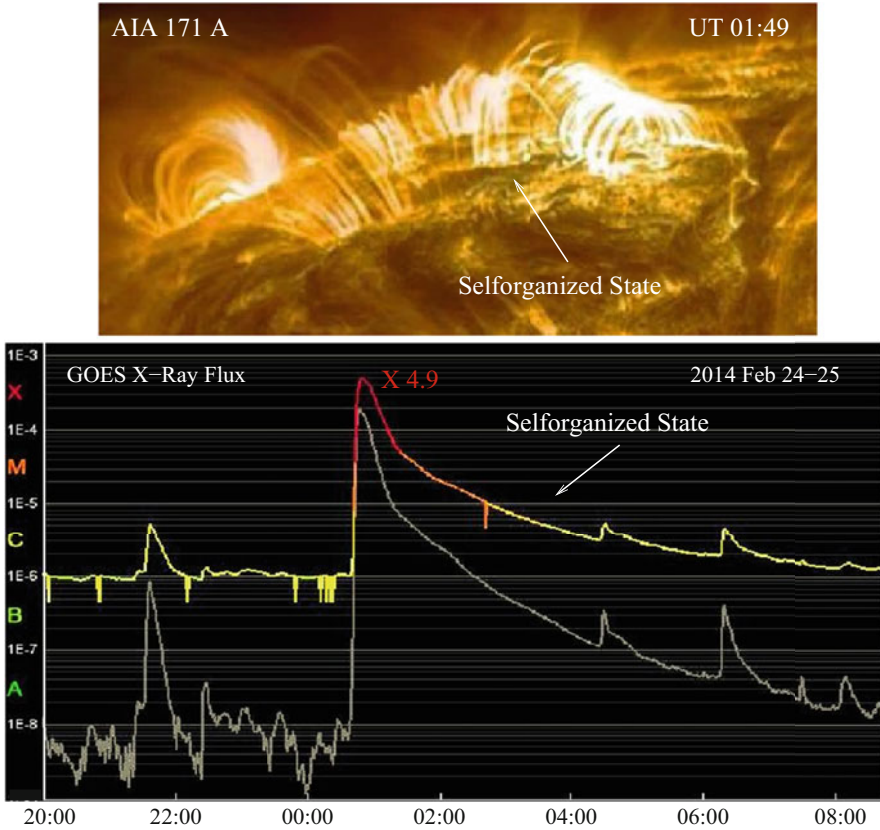


Fig. 23.23 X 4.9 flare and post-flare self-organized slinky. Upper panel: Fe 171 Å emission of the post-flare loops bifurcated into the state of self-organized slinky. Start time: 01:07 UT, peak time: 02:09 UT. Lower panel: GOES X-ray curves from Feb 24, UT 20:00 to Feb.25, UT 08:50. GOES curves courtesy of Andreas Möller

of loops 1 and 2 (panel **a**) excites (clockwise) the enhanced brightening in loops 3, 4, 5, and 6 (panel **b**). It is important that these loops are evenly spaced, which is one of the characteristics of the echo effect. Example of similar process, now in counterclockwise direction is shown in panels **c–d**: now loops 5 and 6, dimming down, pump energy into loops 4 (panel **c**), and 7–8 (panel **d**).

A natural and frequent occurrence of echo effect can be observed everywhere through the solar atmosphere and at all possible spatial and timescales. For years the solar physics vocabulary contains such term as “sympathetic” and sequential flares and mass ejections meaning the events occurring in nearby locations, during a short period of time (see e.g. Romano et al. 2015; Polito et al. 2017). These effects were observed for decades but they were not association with simple regularities of plasma echoes. And yet, looking on the spatial and timescales of an event, it is easy to distinguish the echo pattern from seemingly regular sequential pattern.

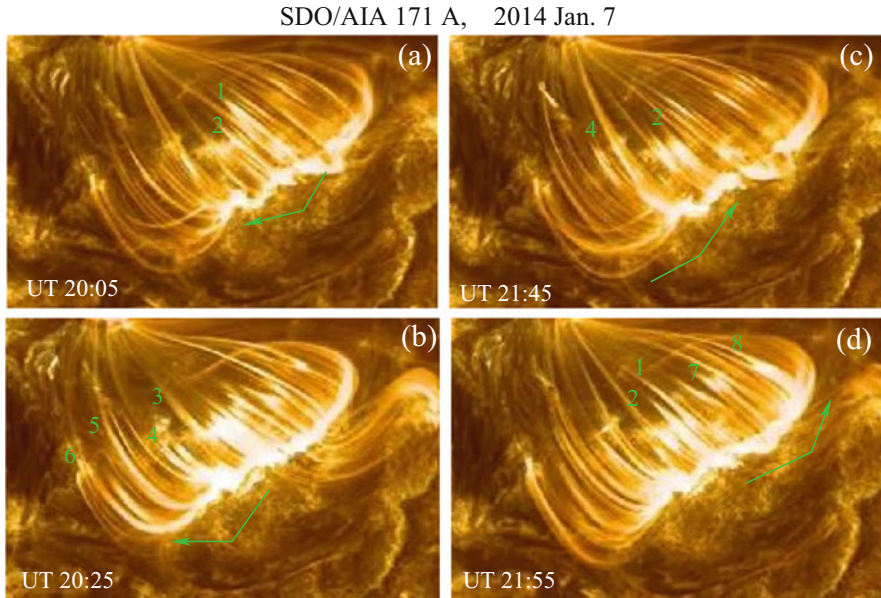


Fig. 23.24 Plasma wave echoes in post-flare self-organized arcade formed after a major X1.2 class flare on January 7, 2014. Shown are four examples of echo propagation. (a)–(b): Multiple echoes travel from right to left igniting loops 1–6; (c)–(d): Wave echo travels back igniting again 4 and 2, and then 7 and 8

Figure 23.25 shows snapshots of the active regions producing M-class flares and filament eruptions on Feb 17, 2000 (Wang et al. 2001). Two successive flares occurred first in the AR 08869 and shortly after that in the AR 8872. Upper right panel shows the filaments F1, F2, and F3 associated with active regions and dense plage at a pre-flare stage. At UT 18:51 in place of F1 the M2.5 flare is in progress. This flare generated a surge that was observed to quickly turn into a set of disturbances that propagated at a speed of about 80 km s^{-1} . These disturbances first caused appearance of brightenings in the loop structures above F3 filaments and then triggered the M1.3 flare in the AR 8872. The observed regularities clearly fall into the spatio-temporal echo pattern.

The nonlinear wave echoes can be observed even at larger scales than that discussed above. Figure 23.26 shows an example of three active regions at large but equal distances from each other. The AR 12445 approaching the NW limb exhibited two successive short-duration C1 and M1.9-class flares, associated with spray-like eruptions of filament material. Following the first such eruption, a small trailing AR 12441 destabilizes producing the flare, which in turn ignites a flare-like brightenings in the AR 12446. A strong flares can ignite sequential flares almost at the distances comparable with the solar disc.

These regularities are often explained as consequence of shocks generated by explosive behavior of flares. Such effects undoubtedly exist. However, there is

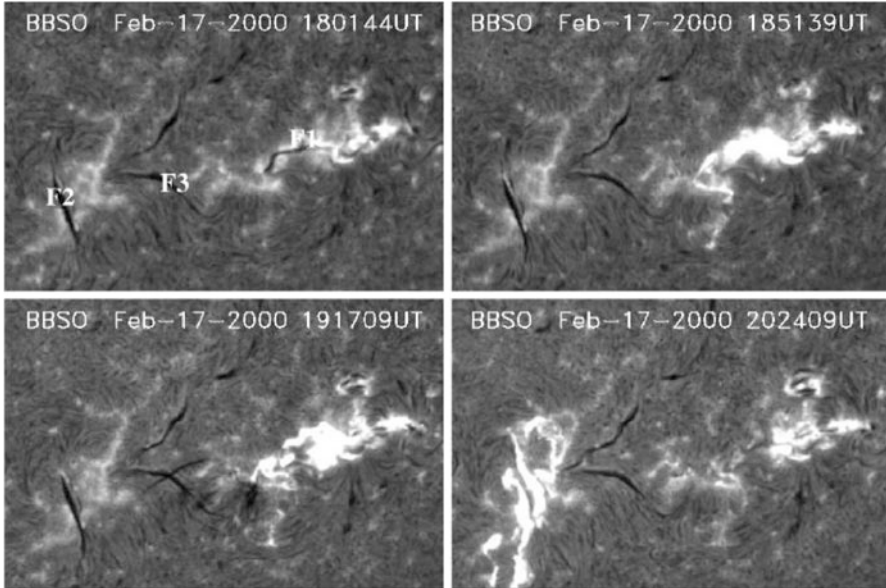


Fig. 23.25 Sequence of $H\alpha$ images from BBSO showing the evolution of the active regions producing sympathetic flares. Filaments F1 and F2 are associated with active regions 08869 and 08872, respectively. Filament F3 is located at dense unipolar plage between two ARs. The field of view is 600×400 arcsec (Wang et al. 2001). Reproduced with permission of the AAS

essential difference between the event produced by shocks and nonlinear wave echoes. The echo effects, spatial or/and temporal, exhibit a strict spatial and temporal regularities and there must be at least *two* sequential events. One can say that the echo effects, often and naturally occurring in solar atmosphere, are the easiest to observe and quantitatively analyze.

23.6 Exotics in Prominences

Quiescent prominences, named thus because of their long lifetimes, are, by all means, far from quiescent. Subjected to gravity, ever evolving, they are highly dynamic and harbor a wide range of gravitational and plasma instabilities. Combination and competition of different instabilities leads to various spectacular events in the evolution of prominences. Especially fascinating are the events associated with the bifurcation of the “quiescent” state into a violent and explosive state, leading to an abrupt prominence body crush, explosive mass ejections, appearance of tornado-like formations, and others. All these events are not only well observed, but they can be quantitatively analyzed. Most importantly, the prominences provide excellent illustration of fundamental physical processes (Ryutova et al. 2010).

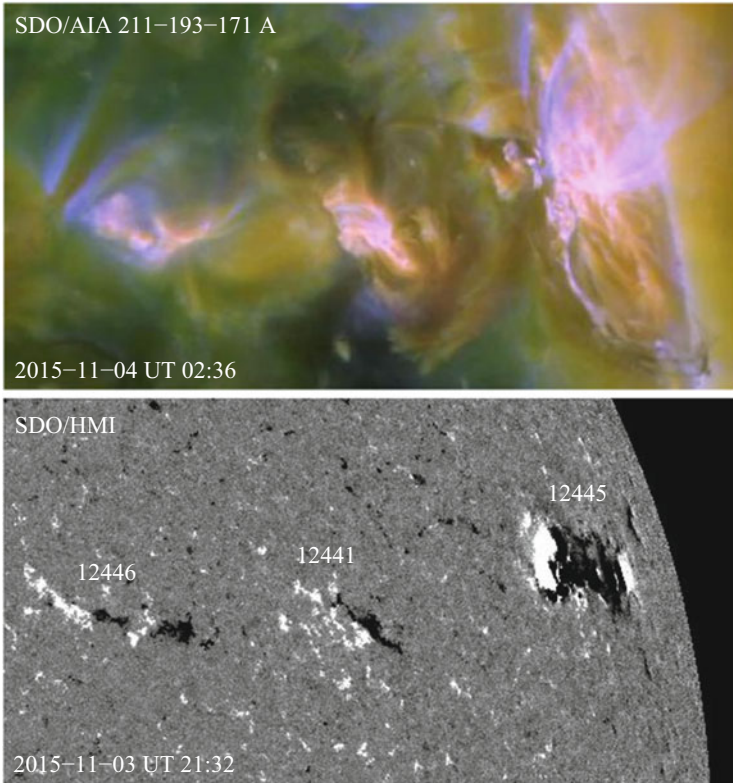


Fig. 23.26 Three active regions at large but equal distances from each other. The AR 12445 was first to exhibit two successive flares which resulted destabilization of the trailing AR 12441. This in turn ignites a loop brightening in the AR 12446 and associated with flare. The field of view is 1000×550 arcsec

Figures 23.27 and 23.28 show example of twisted prominence threads in natural accordance with Kruskal-Shafranov theorem, that any elongated magnetic structure with safety factor $q > 1$, in order to **exist**, must acquire the twisted shape. This is a universal property valid for all spatial scales from laboratory to space plasmas.

A huge prominence shown in Fig. 23.27 exhibits continuous motions of threads and their brightenings. The motion of threads appeared as sinusoidal space-time trajectories with a typical period of ~ 390 s, which is consistent with plane-of-sky projections of rotational motions (Fig. 23.28). Phase delays at different locations suggest propagation of twists along the threads at phase speeds of $90\text{--}270$ km s^{-1} . Of about 15 episodes of such motions observed during two days, none was found to be associated with any eruption. This means that the twisting shape and motions are intrinsic properties of magnetic threads and necessary condition for their dynamic stability lasting as long as strong instabilities take over and lead to violent disruption of prominences.

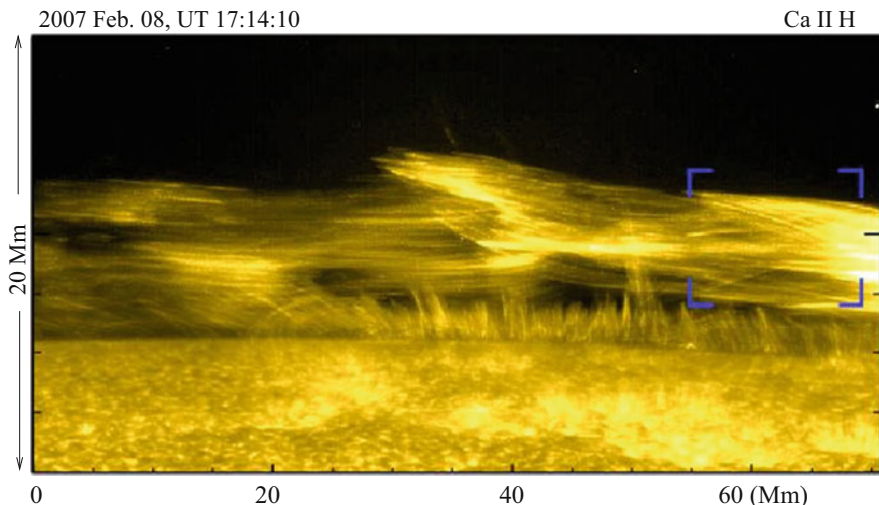


Fig. 23.27 Snapshot of the prominence observed in the Ca II H line by Hinode/SOT at 17:14:10 UT. The solar north is to the left and the west is up. The blue brackets mark the region for rotational motions shown in Fig. 23.27 (Okamoto et al. 2016). Reproduced with permission of the AAS

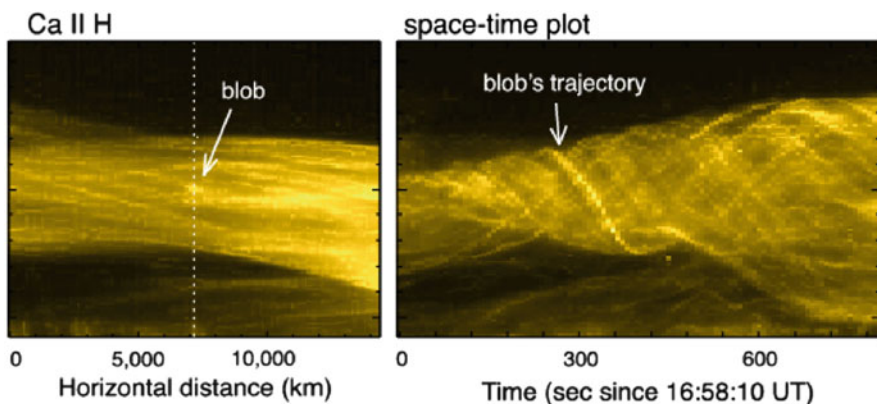


Fig. 23.28 Snapshot (left panel) showing prominence threads in the blue box of figure 2 and space-time plots (right panel) obtained from a vertical cut (dashed line on the left) located on a bright blob. A bundle of threads expands radially at a rate of 4.5 km s^{-1} , its rotation period is about 390 s (Okamoto et al. 2016). Reproduced with permission of the AAS

Of many instabilities, as discussed in Chap. 20, the Rayleigh-Taylor instability is one of the most frequent to observe. We saw that in magnetized plasma the RT instability has its own specifics described by the Rayleigh-Plesset equation (Eq. 20.3). Recall that it naturally reflects the intrinsic helical structure of the prominence and that its nonlinear character ensures the description of both, explosive growth of the prominence and its violent collapse. Above all, the Rayleigh-Plesset equation allows reliable quantitative analysis.

In case of “classical” RT instability, the main driving force is expected to be gravity, leading to appearance of “ripples.” In addition to gravity, given that the prominence magnetic field has a complex curved shape, there arises a *centrifugal* force on the plasma due to the particle motions along the curved field-lines, that acts like a gravitational force. Theoretical and laboratory studies of the RT instabilities driven *only* by field curvature showed that centrifugal instability is the most aggressive type of MHD instabilities in nonuniform plasmas (Lehnart 1974). The main approach here is based on the equilibrium and stability studies of a fully ionized rotating magnetized plasma in terms of plasma beta and basic measurable plasma parameters (Lehnart 1974). The obtained results have been directly applied to laboratory plasma for quantitative estimates and, interestingly, to solar prominences as well.

Obviously, the action of centrifugal force together with gravity should result in a strong rotation of the prominence body that may exhibit even tornado-like behavior. This kind of behavior has been observed back in 1920s when (Pettit 1925) making amazingly full classification of types of prominences, assigned rotating prominences a separate tornado-like class. Ohman (1969) added a smoke ring prominence class. Liggett and Zirin (1984) studying motions in quiescent prominences found that along the proper motion of prominence material, in some cases part of prominence showed rotation. In any case, dynamics and disruption of prominences occurs either in balance between the gravity and centrifugal forces or in prevalence of gravity over centrifugal force and vice versa. In those cases when the centrifugal force takes over the gravity, the prominence develops centrifugal instability and acquires tornado-like behavior. We have already encountered tornado type behavior that shows multi-tornado self-organized behavior (Fig. 23.21a).

One of the studies of tornado-like prominences showed that a total number of 201 giant tornadoes were detected in a period of 25 days, suggesting that, on average, about 30 events must be present across the whole Sun at a time close to solar maximum (Wedemeyer et al. 2013, see also Li et al. 2012).

Modern instruments allow to observe amazing details of prominence behavior, its Evolution, and disruption. Figure 23.29 shows two snapshots from the life of tornado prominence at chromospheric temperature. This tornado has been acquiring various rotational shapes for hours, until about UT 03:21:25 when bullwhip, fire hose instability turned on and caused disruption of prominence and mass ejection.

Figure 23.30 shows another example of tornado prominence and its bullwhip behavior. Using the approach described in Sect. 4.3 one can perform qualitative analysis and some cases make quantitative estimates.

We will conclude this chapter by one more amazing phenomena in outer corona which, in fact, belongs to class of quite ordinary events in hydro- and gas dynamics: vortex rings. They were observed in white light during eclipse observations. Figure 23.31 shows examples of beautifully shaped vortex rings captured during three eclipses (Druckmüller et al. 2014). Studies on prominence-corona dynamic interface not only reveal the extraordinary dynamics of corona but also allow to study input of the coronal dynamics into the solar wind.

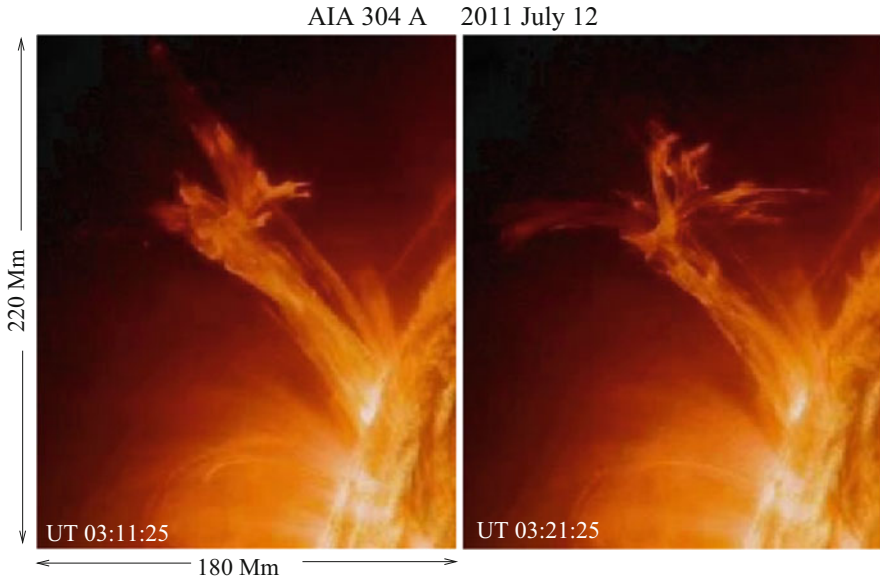


Fig. 23.29 Images of tornado type prominence at two instances of time, behaving in a bullwhip manner. Courtesy of NASA/SDO



Fig. 23.30 SDO/AIA composite image from 171 Å emission (green), 193 Å (blue), and 304 Å (red) of the northeast section of the corona on 2010 July 11 at 15:49 UT showing a snapshot of the whipping prominence past the “elbow-shaped” projection (Habbal et al. 2014). Courtesy of Shadia Habbal

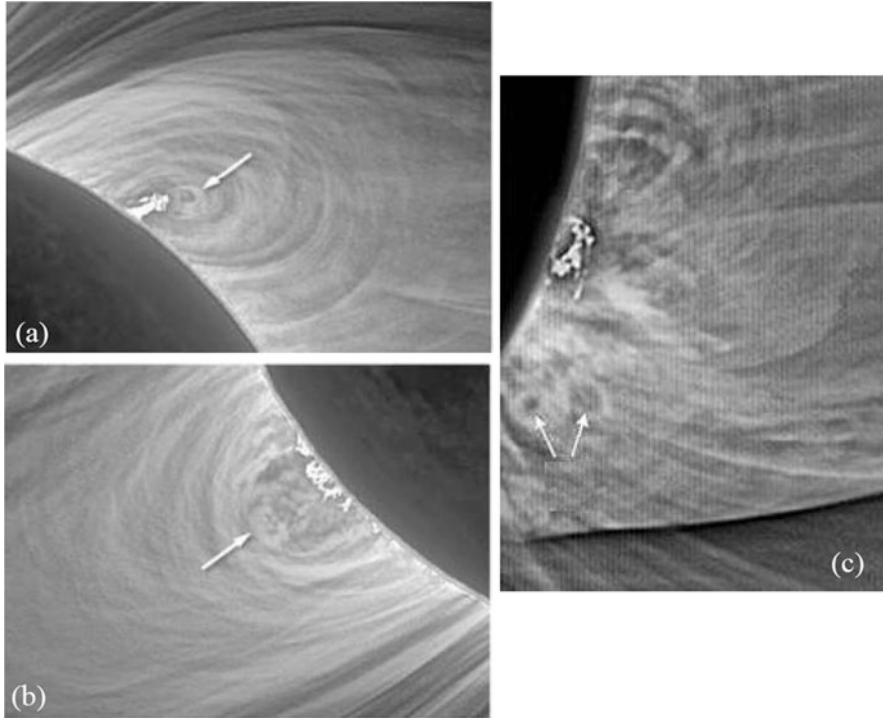


Fig. 23.31 Vortex rings detected during eclipse observations: White light images of 2008 August 1 showing the northwest prominence (a) and the southeast prominence complex (b), (c) Neighboring vortex rings captured during the 2010 July 11 (Habbal et al. 2014; Druckmüller et al. 2014). Courtesy of M. Druckmüller

References

- C.E. Alissandrakis et al., *Astron. Astrophys.* **603**, 95A (2017)
 S.A. Anfinogentov et al., *Astron. Astrophys.* **583**, A136 (2015)
 M.J. Aschwanden *Self-Organized Criticality in Astrophysics. The Statistics of Nonlinear Processes in the Universe* (Springer, Heidelberg, 2011)
 X.Y. Bai et al., *Astrophys. J.* **823**, 60 (2016)
 M. Berger, *Phys. Rev. Lett.* **70**, 705 (1993)
 M. Berger, M. Asgari-TarghiPant, A. DeLuca, *Astrophys. J.* **705**, 347 (2015)
 J.W. Cirtain et al., *Nature* **493**, 501 (2013)
 G.A. Doschek et al., *Astrophys. J.* **813**, 32 (2015)
 A. Drews, L. Rouppe van der Voort, *Astron. Astrophys.* **602**, 80D (2017)
 M. Druckmüller et al., *Astrophys. J.* **785**, 14 (2014)
 S. Habbal et al., *Astrophys. J.* **793**, 119 (2014)
 J. Jing et al., *NatSR* 624319J (2016)
 M.S. Kirk et al., *Solar Phys.* **292**, 72 (2017)
 B. Lehnart, *Phys. Scr.* **9**, 229 (1974)
 X. Li et al., *Astrophys. J.* **752**, 22 (2012)
 M. Liggett, H. Zirin, *Solar Phys.* **91**, 259 (1984)

- R. Liu et al., *NatSR* **6**, 34021 (2016)
- R.E. Louis et al., *Astrophys. J.* **727**, 49 (2011)
- V.M. Nakariakov et al., *Astron. Astrophys.* **797**, 36 (2016)
- Y. Ohman, *Solar Phys.* **9**, 427 (1969)
- J. Okamoto et al., *Astrophys. J.* **831**, 126 (2016)
- V. Pant et al., *Astrophys. J.* **801**, L2 (2015)
- E. Parker, *Astrophys. J.* **174**, 499 (1972)
- E. Pettit, *Publ. Yerkes Obs.* **111**, 205 (1925)
- V. Polito et al., *Astron. Astrophys.* **601**, 39 (2017)
- B. Ravindra et al., *Astrophys. J.* **743**, 33 (2011)
- K. Reardon et al., *Astrophys. J.* **779**, 143 (2013)
- T. Rimmele, J. Marino, *Astrophys. J.* **646**, 593 (2006)
- P. Romano et al., *Astron. Astrophys.* **582**, A55 (2015)
- D. Ryutov, M. Ryutova, *Geophys. Monogr.* **58**, 167 (1990)
- M.P. Ryutova, R. Shine, *Astrophys. J.* **606**, 571 (2004)
- M. Ryutova, T. Berger, Z. Frank, A. Title, *Astrophys. J.* **686**, 1404 (2008)
- M. Ryutova, T. Berger, A. Title, *Astrophys. J.* **676**, 1356 (2008)
- M. Ryutova et al., *SoPh* **267**, 75 (2010)
- G. Scharmer et al., *Nature* **420**, 151 (2002)
- E. Scullion et al., *Astrophys. J.* **797**, 36 (2014)
- R. Shine et al., *1999 Fall AGU Meeting*, SH41A-06 (1999)
- J. Su et al., *Astrophys. J.* **710**, 170 (2010)
- P. Sütterlin et al., *Astron. Astrophys.* **424**, 1049 (2004)
- H. Tian, G. Li, K.K. Reeves et al., *Astrophys. J. Lett.* **797**, L14 (2014)
- H. Wang et al., *Astrophys. J.* **559**, 1171 (2001)
- W. Wang, R. Liu, Y. Wang, *Astrophys. J.* **834**, 38 (2017)
- T. Wang et al., *Astrophys. J.* **751**, L27 (2012)
- H. Watanabe et al., *Astrophys. J.* **796**, 77 (2010)
- S. Wedemeyer et al., *Astrophys. J.* **774**, 123 (2013)

Chapter 24

Solutions



Abstract This chapter contains solutions of problems covering subjects of Chaps. 2–20. The problems and their solutions can be used as tools for further studies of related topics. Most problems are made out of original papers containing fundamental results. This way, practical use of these results and their application for quantitative analysis becomes easier. At the same time reader can always go back to a full version of the paper and fill the gap if necessary. The problems are arranged in the same order as book chapters.

24.1 Problems of Chap. 2

2.1 The plasma equilibrium conditions expressed through the energy-momentum tensor have a form:

$$\frac{\partial}{\partial x_i} T_{ik} = 0 \quad (24.1)$$

with

$$T_{ik} = P_{\perp} \left(\delta_{ik} - \frac{B_i B_k}{B^2} \right) + P_{\parallel} \frac{B_i B_k}{B^2} \quad (24.2)$$

where

$$P_{\perp} = p + \frac{B^2}{8\pi}, \quad P_{\parallel} = p - \frac{B^2}{8\pi} \quad (24.3)$$

Let us use the identity

$$\frac{\partial}{\partial x_i} (x_k T_{ik}) = T_{ik} \delta_{ik} + x_k \frac{\partial}{\partial x_i} T_{ik} \quad (24.4)$$

According to (24.1) the second term on r.h.s, of this equation must vanish. Integrating the remaining expression over the volume V bounded by the surface S , we obtain

$$\int_V T_{ii} dV = \oint_S T_{ik} x_k dS_i \quad (24.5)$$

On the other hand, for the tensor (24.2) we can write

$$\int (2P_{\perp} + P_{\parallel}) dV = \oint \left[P_{\perp} (\mathbf{r} d\mathbf{S}) + (P_{\parallel} - P_{\perp}) \frac{(\mathbf{B}\mathbf{r})}{B^2} (\mathbf{r} d\mathbf{S}) \right] \quad (24.6)$$

or, taking into account (24.3), we can write

$$\int \left(3p + \frac{B^2}{8\pi} \right) dV = \oint \left[\left(p + \frac{B^2}{8\pi} \right) \mathbf{r} d\mathbf{S} - \frac{(\mathbf{B}\mathbf{r})}{4\pi} (\mathbf{B} d\mathbf{S}) \right] \quad (24.7)$$

Let us apply this relation to a plasma occupying a bounded volume outside of which the pressure $p = 0$. If there are no current-carrying conductors inside or outside the plasma, we may put the surface of integration to infinity. Since $B \sim 1/r^3$, the surface integral vanishes. Thus, relation (24.7) cannot hold. This means that any bounded equilibrium plasma configuration with a magnetic field can exist only in the presence of current-carrying conductors. The r.h.s. of (24.7) then reduces to an integral over the surfaces of these conductors.

This is well known Shafranov's virial theorem implying that nontrivial MHD equilibrium configurations must be supported by externally supplied currents.

2.2 For the variation of H_m we have

$$\frac{dH_m}{dt} = \int_V \left(\frac{\partial \mathbf{A}}{\partial t} \cdot \delta \mathbf{B} + \mathbf{A} \cdot \frac{\partial \mathbf{B}}{\partial t} \right) dV \quad (24.8)$$

or

$$\frac{dH_m}{dt} = \int_V \left[\frac{\partial \mathbf{A}}{\partial t} \cdot (\nabla \times \mathbf{A}) + \mathbf{A} \cdot \left(\nabla \times \frac{\partial \mathbf{A}}{\partial t} \right) \right] dV \quad (24.9)$$

This immediately reduces to

$$\frac{dH_m}{dt} = \int_V \nabla \cdot \left(\frac{\partial \mathbf{A}}{\partial t} \cdot \times \mathbf{A} \right) dV = \oint \mathbf{n} \cdot \left(\frac{\partial \mathbf{A}}{\partial t} \cdot \times \mathbf{A} \right) dS \quad (24.10)$$

As $(\partial \mathbf{A} / \partial t) \perp \mathbf{B}$, and, in our case $\mathbf{B} \cdot \mathbf{n} = 0$, then $\partial \mathbf{A} / \partial t \parallel \mathbf{n}$, and from (24.10) we have $dH_m / dt = 0$. If $\mathbf{B} \cdot \mathbf{n} \neq 0$, the local helicity is not conserved.

2.3 For thin flux tubes $\mathbf{B} = \nabla \times \mathbf{A}$ is approximately normal to the cross section of flux tube, S . Helicity of tube 1 is:

$$H_1 = \int \mathbf{A} \cdot \mathbf{B} dV = \oint d\mathbf{s} \cdot \mathbf{A} \int \mathbf{n} \cdot \nabla \times \mathbf{A} ds \quad (24.11)$$

Here, by their physical meaning,

$$\Phi_1 = \int \mathbf{n} \cdot \nabla \times \mathbf{A} ds \quad \Phi_2 = \oint d\mathbf{s} \cdot \mathbf{A} \quad (24.12)$$

Thus, $H_1 = \Phi_1 \Phi_2$. Similarly $H_2 = \Phi_1 \Phi_2$. And the total helicity is $H = 2\Phi_1 \Phi_2$. If the tubes are wound N times around each other, $H = N\Phi_1 \Phi_2$.

2.4 From the Faraday's law, $\nabla \mathbf{B} = 0$, we have

$$\frac{1}{r} \frac{\partial}{\partial r} r B_r(r, z) + \frac{\partial B_z(r, z)}{\partial z} = 0 \quad (24.13)$$

Assuming that field configuration inside flux tube remains potential, the flux tube may be considered almost uniform across its cross section. Then we can put $B_z(r, z) = B_z(0, z)$ and perform series expansion of r -component around axis of symmetry

$$B_r(r, z) = B_r(0, z) + r \left. \frac{\partial B_r(r, z)}{\partial r} \right|_{r=0} \quad (24.14)$$

At the axis $B_r(0, z) = 0$, so that

$$B_r(r, z) = r \frac{\partial B_r(0, z)}{\partial r} \quad (24.15)$$

Combining this with (2.16) we obtain

$$2 \frac{B_r}{r} = - \frac{\partial B_z}{\partial z}, \quad (24.16)$$

Taking now into account that $B_z = B \exp(-z/2\Lambda)$, we obtain

$$\frac{B_r}{B} = \frac{R}{4\Lambda}, \quad (24.17)$$

where R is the effective radius of flux tube. Thus, thin flux tube approximation in a simplest case of a static flux tube requires that its effective radius be significantly smaller than the scale height: $R < 4\Lambda$.

24.2 Problems of Chap. 3

3.1 The fluid equations describing the flow around the sphere in linear approximation are

$$\rho \frac{\partial \mathbf{v}}{\partial t} = -\nabla \delta p, \quad \nabla \cdot \mathbf{v} = 0 \quad (24.18)$$

Let us denote the velocity of sphere by $v_s(t)$. In spherical coordinates, the points on the surface of the sphere (of radius R) will have only two velocity components, r and θ ,

$$v_{sr}|_{r=R} = -v_s \cos\theta, \quad v_{s\theta}|_{r=R} = v_s \sin\theta \quad (24.19)$$

On the other hand, at the solid surface the normal component of fluid velocity must equal to the normal component of the surface velocity, i.e.,

$$v_r|_{r=R} = v_{sR}|_{r=R} = -v_s \cos\theta \quad (24.20)$$

As the fluid velocity is curl-free, it can be represented via scalar potential, $\mathbf{v} = -\nabla\psi$. The second equation of (24.18) then becomes

$$\nabla^2 \psi = \frac{1}{r^2} \frac{\partial}{\partial r} r^2 \frac{\partial \psi}{\partial r} + \frac{1}{r^2 \sin\theta} \frac{\partial}{\partial \theta} \sin\theta \frac{\partial \psi}{\partial \theta} = 0 \quad (24.21)$$

The boundary condition (24.20) in terms of ψ is:

$$\frac{\partial \psi}{\partial r} \Big|_{r=R} = v_s \cos\theta \quad (24.22)$$

The solution can be found by the separation of variables, with dependence on θ specified by (24.22): $\psi = f(r)\cos\theta$, where function $f(r)$ satisfies the equation:

$$\frac{d}{dr} r^2 \frac{df}{dr} - 2f = 0 \quad (24.23)$$

There are two solutions to this equation: $f = \text{const}/r^2$ and $f = \text{const } r^2$, of which the second solution corresponds to perturbations diverging at large r and can be dropped. For the first solution, we can determine a constant, using (24.22):

$$\psi(r, \theta) = v_s R^3 \cos\theta / 2r^2 \quad (24.24)$$

For the pressure perturbation from the first equation of (24.18) we have:

$$\delta p = \rho \frac{\partial v_s}{\partial t} \frac{R^3}{2r^3} \cos\theta \quad (24.25)$$

On the surface of sphere the pressure perturbation is then

$$\delta p|_{r=R} = \frac{1}{2}\rho \frac{\partial v_s}{\partial t} \cos\theta \quad (24.26)$$

The net pressure force F_p acting on the sphere can be found by multiplying δp by $-\cos\theta$ and integrating over the surface of the sphere:

$$F_p = -2\pi R^2 \int_0^\pi \sin\theta \cos\theta \delta p|_{r=R} d\theta = -\frac{2\pi R^3}{3} \rho \frac{\partial v_s}{\partial t} \quad (24.27)$$

The equation of motion of the sphere under the action of the external force F is then $M(\partial v_s/\partial t) = F + F_p$, or taking into account (24.27), we have

$$(M + m) \frac{\partial v_s}{\partial t} = F, \quad (24.28)$$

where m is a half of the mass of the liquid displaced by the sphere:

$$m = \frac{2\pi R^3 \rho}{3} \quad (24.29)$$

Thus we obtained expression for the added mass that appears due to the inertia added to the system executing unsteady motions. Now, using (24.29) we find the velocity of the established oscillations

$$v_s = \frac{F_0}{(M + m)\omega} \cos\omega t \quad (24.30)$$

3.2 The (24.18) are now to be solved in cylindrical coordinates r, ϕ with the z axis directed along the cylinder. The points on the surface of the cylinder will have two velocity components

$$v_{sr}|_{r=R} = v_s \cos\phi, \quad v_{s\phi}|_{r=R} = -v_s \sin\phi \quad (24.31)$$

where the subscript s , as earlier, refers to the surface. The boundary condition for the fluid velocity is

$$v_r|_{r=R} = v_{sR}|_{r=R} = -v_s \cos\phi \quad (24.32)$$

And, with scalar potential, $\mathbf{v} = -\nabla\psi$, we have the equation:

$$\nabla^2\psi = \frac{1}{r} \frac{\partial}{\partial r} r \frac{\partial\psi}{\partial r} + \frac{1}{r^2} \frac{\partial^2\psi}{\partial\phi^2} = 0 \quad (24.33)$$

with boundary condition (24.32), written in terms of ψ :

$$\frac{\partial \psi}{\partial r} \Big|_{r=R} = v_s \cos \phi \quad (24.34)$$

As earlier, we take $\psi = f(r) \cos \phi$, where $f(r)$ satisfies the equation:

$$\frac{d}{dr} r \frac{df}{dr} - \frac{f}{r} = 0 \quad (24.35)$$

Out of two solutions of this equation, $f = \text{const}/r$ and $f = \text{const } r$, only nondiverging one is valid. Using now (24.34) we obtain

$$\psi(r, \phi) = v_s R^2 \cos \phi / r \quad (24.36)$$

For the pressure perturbation the first equation of (24.18) gives:

$$\delta p = \rho \frac{\partial v_s}{\partial t} \frac{R^2}{r} \cos \phi \quad (24.37)$$

On the surface of the cylinder

$$\delta p|_{r=R} = \rho \frac{\partial v_s}{\partial t} R \cos \phi \quad (24.38)$$

As in the previous problem, we find the net perpendicular force F_p acting on the surface of the cylinder:

$$F_p = -R \int_0^{2\pi} \cos \phi \delta p|_{r=R} d\phi = -\pi R^2 \rho \frac{\partial v_s}{\partial t} \quad (24.39)$$

Now, the equation of motion of the cylinder under the action of the force F is $M(\partial v_s / \partial t) = F + F_p$, or with (24.39),

$$(M + m) \frac{\partial v_s}{\partial t} = F, \quad (24.40)$$

where m is a mass of the liquid displaced by the cylinder:

$$m = \pi R^2 \rho \quad (24.41)$$

Hence, we arrived to the expression for the added mass of cylinder: the cylinder is reacting to the external force as if its mass were $M + m$ (per unit length), and for the established oscillations we have:

$$v_s = \frac{F_0}{(M + m)\omega} \cos \omega t \quad (24.42)$$

3.3 With z -axis directed along the gravity, the density and gas pressure in the blob raised at small height, $\delta z > 0$ is

$$\begin{aligned}\rho_{i,e}(z + \delta z) &= \rho_0(z) + \delta\rho_{i,e} \\ p_{i,e}(z + \delta z) &= p_0(z) + \delta p_{i,e}\end{aligned}\quad (24.43)$$

Initially, pressure and density inside blob are the same as outside, and are determined by the balance between a pressure gradient and gravity:

$$\frac{dp_0}{dz} = -\rho_0 g \quad (24.44)$$

Thus, outside the blob,

$$\delta p_e = -\rho_0 g \delta z, \quad \delta \rho_e = \frac{d\rho_0}{dz} \delta z \quad (24.45)$$

Inside the blob, from the entropy conservation, $S \simeq p\rho^{-\gamma} = \text{const}$, we have

$$\frac{\delta p_i}{p_i} = \gamma \frac{\delta \rho_i}{\rho_i} \quad (24.46)$$

Taking into account the pressure balance, $\delta p_i = \delta p_e$, from (24.45) and (24.46) we obtain

$$\delta \rho_i = \frac{\delta p_i}{c_s^2} = -\frac{1}{c_s^2} g \rho_0 \delta z \quad (24.47)$$

Since at new height the density inside the blob differs from that of outside, the blob experiences the action of buoyancy force, $g(\delta \rho_e - \delta \rho_i)$,

$$\rho_0 \frac{d^2 \delta z}{dt^2} = g(\delta \rho_e - \delta \rho_i) \quad (24.48)$$

Substituting here $\delta \rho_i$ and $\delta \rho_e$, we arrive to the following equation:

$$\frac{d^2 \delta z}{dt^2} = -N^2 \delta z \quad (24.49)$$

where N is known as Brünt-Väisälä frequency,

$$N^2 = -g \left(\frac{1}{\rho_0} \frac{d\rho_0}{dz} + \frac{g}{c_s^2} \right) \quad (24.50)$$

It is useful to express it in terms of temperature. Using (24.44) and the equation of state, one gets

$$N^2 = \frac{g}{T_0} \left(\frac{dT_0}{dz} + (\gamma - 1) \frac{T_0 g}{c_s^2} \right) \quad (24.51)$$

Thus, if $N^2 > 0$, the plasma blob experiences harmonic oscillations with frequency N , generating internal gravity waves, $\sim \exp(-iNt)$. If the temperature is uniform,

$$N^2 = \frac{(\gamma - 1)g^2}{c_s^2} \quad (24.52)$$

On the other hand, if $N^2 < 0$, $\delta z \sim \exp(iNt)$, and we have an instability.

3.4 When flux tube rises into rarefied atmosphere, it expands. With

$$\frac{\delta B_i}{B_i} = \frac{\delta \rho_i}{\rho_i}, \quad (24.53)$$

pressure balance equation becomes:

$$\delta p_i + \frac{B_i \delta B_i}{4\pi} = \delta p_e + \frac{B_e \delta B_e}{4\pi} \quad (24.54)$$

With (24.53)–(24.54) and the entropy conservation, $\delta p_i / p_i = \gamma \delta \rho_i / \rho_i$, we obtain

$$\left(\frac{\gamma p_i}{\rho_i} + \frac{B_i^2}{4\pi \rho_i} \right) \delta \rho_i = \delta p_e + \frac{B_e \delta B_e}{4\pi} \quad (24.55)$$

Taking into account that $\delta p_e + B_e \delta B_e / 4\pi = -\rho_e g \delta z$ we have from (24.54)

$$\delta \rho_i = \frac{\rho_e g}{c_s^2 + v_A^2} \delta z \quad (24.56)$$

The equation of motion for magnetized blob takes the form similar to (24.48)–(24.49):

$$\frac{d^2 \delta z}{dt^2} = -N^2 \delta z \quad (24.57)$$

with the modified expression for Brünt-Väisälä frequency

$$N^2 = -g \left(\frac{1}{\rho_0} \frac{d\rho_0}{dz} + \frac{g}{c_s^2 + v_A^2} \right) \quad (24.58)$$

In case of a uniform temperature,

$$N^2 = \frac{g^2}{c_s^2} \left(\gamma - \frac{c_s^2}{c_s^2 + v_A^2} \right) \quad (24.59)$$

It is interesting that in this particular case, for $\gamma = 5/3$, there is no parameter range for instability, and magnetic flux tube executes the oscillatory motions.

24.3 Problems of Chap. 4

4.1 The MHD equations for Alfvén waves can be reduced to a single equation of motion

$$\frac{\partial^2 v_y}{\partial t^2} - (\eta + \nu) \left(\frac{\partial^2}{\partial x^2} + \frac{\partial^2}{\partial z^2} \right) \frac{\partial v_y}{\partial t} + \omega_A^2(x) v_y = A(x) e^{i(k_z z - \omega_d t)} \quad (24.60)$$

where $\omega_A = k_z B_0 / \sqrt{4\pi \rho_0(x)}$ is the Alfvén frequency. The second term in (24.60) reflects the fact that the resonance occurs at small scales where the dissipative effects turn on and must be taken into account. Seeking a solution for the form $v_y = V_0 \exp[i(k_x x + k_z z - \omega_d t)]$, one obtains

$$V_0 = \frac{A(x)}{[\omega_A^2(x) - \omega_d^2] - i\omega_d(\eta + \nu)(k_x^2 + k_z^2)} \quad (24.61)$$

Thus, the resonance occurs at the location x_{res} where $\omega_A(x) = \omega_d$. In the steady state, $\partial/\partial z \ll \partial/\partial x$ and a Taylor expansion of $\omega_A(x)$ about x_{res} in (24.60) yields a length-scale and time-scale for resonant absorption as follows:

$$l_{\text{res}} \sim \left(\frac{\eta + \nu}{2\omega'} \right)^{1/3}, \quad \tau_{\text{res}} = \frac{l_{\text{res}}^2}{\eta + \nu} \sim \frac{1}{(\eta + \nu)^{1/3} \omega_{A0}^{\prime 2/3}} \quad (24.62)$$

where $\omega'_{A0} \equiv (d\omega_A/dx)_{x=x_0}$. Note that in the photosphere the driving frequencies have a broad range for each field line, but on each field line, only the energy associated with its particular resonant frequency is dissipated. This is much less than the total energy input and so it is unlikely to be a reliable coronal heating mechanism by itself.

4.2 In case of a short coronal loop, standing waves have their wavenumber, k_z , fixed by the geometry (Priest 2014). Hence, each magnetic surface with $x = \text{const}$ oscillates independently of its neighbor with a frequency $\omega(x) = k_z v_A(x) \equiv \omega_A(x)$ and a velocity

$$v_y(x, z, t) = V(x) e^{i[k_z z - \omega_A(x)t]} \quad (24.63)$$

With time the field lines become more and more out of phase, thus causing phase mixing. At the same time the x -gradients grow

$$\frac{\partial v_y(x, z, t)}{\partial x} = i \frac{d\omega_A}{dx} t v_y \quad (24.64)$$

and the phase mixing results in an effective wavenumber $k_{k,\text{eff}} = (d\omega_A/dx)t$, which grows in time. The effective wavelength becomes smaller and smaller until dissipative effects turn on and convert the wave energy into heat. This as earlier is described by phase-mixed solution of visco-resistive equation

$$\frac{\partial^2 v_y}{\partial t^2} - v_A^2(x) \frac{\partial^2 v_y}{\partial z^2} - (\eta + \nu) \frac{\partial^2}{\partial x^2} \frac{\partial v_y}{\partial t} = 0, \quad (24.65)$$

having the form $v_y = V(x, z, t) \exp[i(k_z z - \omega_A(x)t)]$. Here, the amplitude $V(x, t)$ is slowly varying function. Thus, for $V(x, t)$ (retaining the dominant terms) we arrive to the following equation

$$-2i\omega_A \frac{\partial V}{\partial t} = i(\eta + \nu)\omega_A \left(\frac{d\omega_A}{dx}\right)^2 t^2 V, \quad (24.66)$$

Solution of this equation gives the amplitude which decays in time as

$$V(x, t) = V(x, 0) \exp\left[-\frac{\eta + \nu}{6} \left(\frac{d\omega_A}{dx}\right)^2 t^3\right] \quad (24.67)$$

Hence, the time-scale for dissipation by phase-mixing is

$$\tau_{\text{phase}} = \frac{1}{\omega_A} \left(12\pi Re_m \frac{a}{\lambda}\right)^{1/3}, \quad (24.68)$$

where ω_A^{-1} is the Alfvén time, and $Re_m = av_A/(\eta + \nu)$ is the magnetic Reynolds number. At this phase-mixing time, the x -scale becomes a fraction of the original scale of magnetic structure, a :

$$\frac{1}{k_{x,\text{eff}} a} = \left(12\pi Re_m \frac{a}{\lambda}\right)^{1/3}. \quad (24.69)$$

4.3 Let the lash move with velocity u . The energy conservation requires that

$$\frac{1}{2}(M + m)u^2 = \frac{1}{2}\left(M\frac{L+x}{2L} + m\right)v^2 \quad (24.70)$$

This gives for the velocity of the lash-tip

$$v(x) = u \frac{\sqrt{M/(m+1)}}{\sqrt{(M/m)(L+x)/2L+1}} \quad (24.71)$$

At the beginning, the cracker is positioned at $x = +L$, and the whip-tip has the same translation velocity as the lash, i.e., $v = u$. However, with increasing propagation in the x -direction $v(x)$ grows and, approaching the free end at $x \rightarrow -L$, reaches the maximum velocity

$$v_{\max} = u \sqrt{\frac{M+m}{m}} \quad (24.72)$$

which increases without limit for an infinitesimal mass of cracker, $m \rightarrow 0$. Note that the real model of bullwhip effect requires much more sophisticated approach that includes drag and gravity forces, and, of course, the variable mass density of a whip as function of its length. This simple approach only shows that the tempered shape of magnetic or any other whip causes the unlimited growth of the tip velocity. See Krehl et al. (1998).

24.4 Problems of Chap. 5

5.1 Let an incompressible fluid of density ρ_1 in the region $z > 0$ move with velocity U in x -direction, and the fluid with density ρ_2 in the region $z < 0$ is at rest. The gravity force acts in the negative z -direction. For the perturbations of the form

$$\xi(x, t) = A(t) \cos(kx - \omega t), \quad (24.73)$$

the hydrodynamic equations, including the effect of surface tension τ , give the following dispersion relation:

$$D(\omega, k) = (\rho_1 - \rho_2)g - k^2\tau + (\omega - kU)^2 \frac{\rho_1}{k} + \omega^2 \frac{\rho_2}{k} \quad (24.74)$$

The wave energy per unit area is

$$W = \frac{1}{4} \omega \frac{\partial D(\omega, k)}{\partial \omega} A^2 \quad (24.75)$$

The derivative of dispersion relation by ω is

$$\frac{\partial D(\omega, k)}{\partial \omega} = 2(\omega - kU) \frac{\rho_1}{k} + 2\omega \frac{\rho_2}{k} \quad (24.76)$$

and the wave energy, respectively, is

$$W = \frac{\omega}{2} \left[\frac{\omega \rho_2}{k} + \frac{\rho_1}{k} (\omega - kU) \right] A^2 \quad (24.77)$$

The solution of the dispersion relation (24.74) gives for frequencies the following expression

$$\omega = \frac{\rho_1 k U}{\rho_1 + \rho_2} \pm \left\{ \frac{C_0^2}{u^2} - \frac{\rho_1 \rho_2}{(\rho_1 + \rho_2)^2} \right\}^{1/2} k U \quad (24.78)$$

where

$$C_0^2 = \frac{\rho_2 - \rho_1}{\rho_2 + \rho_1} \frac{g}{k} + \frac{k\tau}{\rho_2 + \rho_1} \quad (24.79)$$

The usual KH instability occurs when square root in (24.78) becomes imaginary, i.e., when

$$U > \frac{C_0(\rho_1 + \rho_2)}{\sqrt{\rho_1 \rho_2}} \quad (24.80)$$

On the other hand, one can see that when $\omega < ku(\rho_1/\rho_1 + \rho_2)$, $\partial D(\omega, k)/\partial \omega < 0$, and the energy of the wave for positive frequencies becomes negative. Hence, the instability of negative energy waves occurs at frequencies corresponding to *lower* sign in (24.78).

Hence, at the critical velocity

$$U_{\text{cr}} = \frac{C_0(\rho_1 + \rho_2)}{\sqrt{\rho_1 \rho_2}}, \quad (24.81)$$

and the frequency,

$$\omega_{\text{cr}} = \frac{\rho_1 k U}{\rho_1 + \rho_2}, \quad (24.82)$$

for which the wave energy, $W = 0$, the coalescence of a positive energy root with a negative energy root occurs. Thus, relations (24.81) and (24.82) determine a bifurcation point. See e.g. Cairns (1979).

5.2 A three-wave interaction where one of the waves has negative energy can be described by the following set:

$$\frac{\partial u_1}{\partial t} = c_1 u_2 u_3 \cos \phi, \quad \frac{\partial u_2}{\partial t} = c_2 u_1 u_3 \cos \phi, \quad \frac{\partial u_3}{\partial t} = c_3 u_1 u_2 \cos \phi \quad (24.83)$$

where u_i are normalized velocities, c_{ik} are the matrix elements of three-wave interactions, and ϕ is determined by mutual phase relations of the interacting waves. The conditions (5.76) are automatically satisfied. The constant of motion corresponding to the above set has a form

$$u_1 u_2 u_3 \sin\phi + \frac{1}{4}(\alpha_1 u_1^4 + \alpha_2 u_2^4 + \alpha_3 u_3^4) = \Gamma \quad (24.84)$$

where $\alpha_i = \text{const}$ and Γ are parameters associated with the frequency relations and nonlinear phase shifts.

Consider the simplest case when initially all three waves have the same amplitude, i.e., when $u_i(x, 0) = u(x, 0)$ and, therefore, $c_{ik} = c$ and $\alpha_i = \alpha$, and $\Gamma = 0$. Then the system (24.83)–(24.84) reduces to the well-known Rate equation

$$\frac{\partial u(x, t)}{\partial t} = cu^2(x, t)\cos\phi \quad (24.85)$$

with the constant of motion having a form

$$\Gamma = u^3 \sin\phi + \frac{3}{4}\alpha u^4 \quad (24.86)$$

Substituting (24.86) into (24.85) we get

$$\frac{\partial u(x, t)}{\partial t} = \pm u^2(x, t)\sqrt{1 - \alpha^2 u^2} \quad (24.87)$$

One can see that at $u = 1/\alpha$, $\partial u/\partial t = 0$, i.e., $|u|_{\max} = 1/\alpha$ is the maximum amplitude, and the distribution acquires the hump-shaped form. The solution of (24.87) (integrating $\partial t/\partial u$ over u) is

$$u(x, t) = \frac{1}{\sqrt{\alpha^2 + (t_m - t)^2}} \quad (24.88)$$

The plus and minus signs in (24.87) correspond to $t < t_m$ and $t > t_m$, respectively, and the time of maximum is

$$t_m(x) = \frac{1}{u(x, 0)}\sqrt{1 - \alpha^2 u^2(x, 0)} \quad (24.89)$$

Thus, for different values of x , the amplitudes experience different rates of evolution. The first maximum in the distribution develops at the time of saturation

$$t_m(0) = \frac{1}{u_0}\sqrt{1 - \alpha^2 u_0^2} \quad (24.90)$$

This will be followed by a decrease in the center, accompanied by an increase in the neighboring part. Hence, the peak first developed to reach a maximum at $x = 0$ will move in x -direction in such a way that the next peak occurs with a delay time

$$t_m(x) - t_m(0) = \frac{1}{u(x, 0)} \sqrt{1 - \alpha^2 u^2(x, 0)} - \frac{1}{u_0} \sqrt{1 - \alpha^2 u_0^2} \tag{24.91}$$

If, for example, the initial shape of distribution has a soliton shape (a single hump),

$$u(x, 0) = \frac{u_0}{1 + \kappa x^2} \tag{24.92}$$

where κ is a positive constant. For the time of explosion we have:

$$t_m(x) = \frac{1}{u_0} (1 + \kappa x^2). \tag{24.93}$$

If the time-dependence of initial amplitude is oscillatory, the peaks will become repeated in time for each x value. Figure 24.1 shows the examples of numerical solution for the development of repetitive explosive instability, (a), and occurrence of the explosive instability due to interaction of the negative energy wave with two positive energy waves, (b).

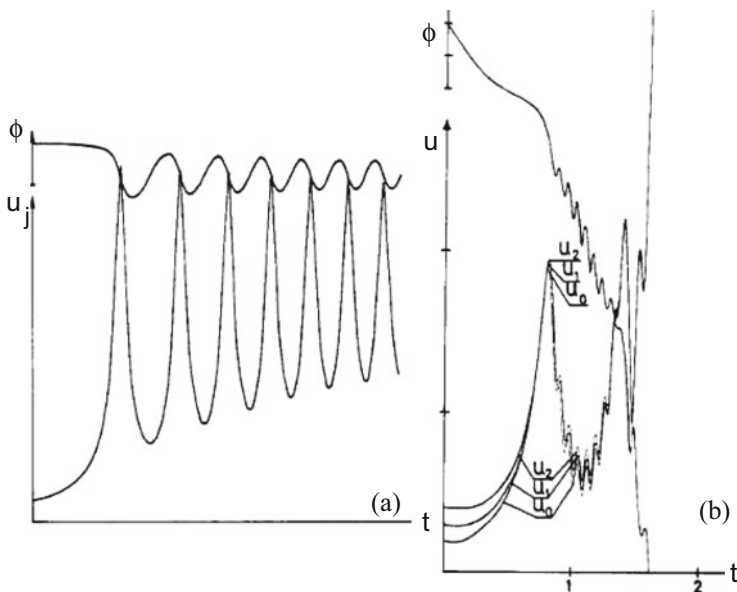


Fig. 24.1 Evolution of repetitive explosive instabilities in space and time. (a) Amplitude and phase development for $\Gamma = 0$ in the presence of dissipation; (b) Explosively unstable interaction between waves of positive and negative energy (Weiland and Wilhelmsson 1977; Wilhelmsson 1984). Courtesy of J. Weiland

24.5 Problems of Chap. 6

6.1 (a) Let us search the solution of the form

$$x(t) = a(t)\cos\omega t + b(t)\sin\omega t \tag{24.94}$$

where $a(t)$ and $b(t)$ are slowly varying functions of time, which according to (6.142) satisfy the following equations:

$$\begin{aligned} \frac{da}{dt} + \left(\omega - \omega_0 + \frac{\alpha\omega_0}{4}\right)b(t) &= 0 \\ \frac{db}{dt} - \left(\omega - \omega_0 - \frac{\alpha\omega_0}{4}\right)a(t) &= 0 \end{aligned} \tag{24.95}$$

If $|\omega - \omega_0| < \alpha\omega_0/4$, the solutions of the above system are

$$a(t) = A_1 (C_1 e^{-\gamma t} + C_2 e^{\gamma t}), \quad b(t) = A_2 (C_1 e^{-\gamma t} - C_2 e^{\gamma t}) \tag{24.96}$$

where

$$\gamma = \frac{1}{4}\sqrt{(\alpha\omega_0)^2 - 16(\omega - \omega_0)^2}, \quad A_{1,2} = \sqrt{\alpha\omega_0 \pm 4(\omega - \omega_0)} \tag{24.97}$$

Now solution of (24.94) takes the form

$$x(t) = D_1 e^{\gamma t} \cos(\omega t - \phi) + D_2 e^{-\gamma t} \cos(\omega t + \phi) \tag{24.98}$$

with $\text{tg}\phi = A_1/A_2$. Thus, the oscillations show unlimited growth in time (Fig. 24.2a). In reality, of course, the stabilization of growing modes will occur due to nonlinear effects, dissipation or appearance of anharmonic terms.

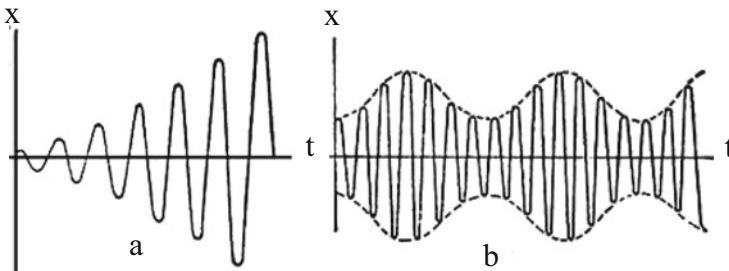


Fig. 24.2 Wave packets: (a) Growing wave packet in region of parametric resonance; (b) Beat waves and slowly varying envelope in the region close to instability

(b) Close to instability threshold $|\omega - \omega_0| \geq \alpha\omega_0/4$, and solution of (6.142) takes the form

$$x(t) = CB_1 \sin(\Omega t + \psi) \cos \omega t + CB_2 \cos(\Omega t + \psi) \sin \omega t, \quad (24.99)$$

where

$$\Omega = \frac{1}{4} \sqrt{16(\omega - \omega_0)^2 - (\alpha\omega_0)^2} \quad (24.100)$$

and

$$B_{1,2} = \left\{ \begin{array}{l} \sqrt{4(\omega - \omega_0) \pm \alpha\omega_0}, \quad \omega > \omega_0 \\ \pm \sqrt{4(\omega_0 - \omega) \pm \alpha\omega_0}, \quad \omega < \omega_0 \end{array} \right\} \quad (24.101)$$

In this case oscillations represent the beat waves:

$$x(t) = C \sqrt{4|\omega - \omega_0| - \alpha\omega_0} \cos(2\Omega t + \psi) \cos \omega t + \cos(\omega t + \theta), \quad (24.102)$$

where θ is the slowly varying phase (Fig. 24.2b). If the frequency approaches to instability threshold, the depth of modulated oscillations approaches to full height and a period of modulation grows infinitely. See Kadomtsev (1968).

6.2 Assume that the wave amplitude is small, so that higher harmonics are small. In this case the main nonlinear effect is the dependence of the phase velocity or the frequency on the amplitude a (Lighthill 1965; Kadomtsev and Karpman 1971). Thus to the first nonvanishing correction we can write for frequency:

$$\omega(k, a) = \omega_0 + \alpha a^2, \quad (24.103)$$

As k and a^2 vary with x , the phase $\phi(x, t) = kx - \omega t$ will no longer be a linear function of space and time. Using $k = \partial\phi/\partial x$, $\omega = -\partial\phi/\partial t$, and (24.103) we can write

$$\frac{\partial k}{\partial t} = -\frac{\partial \omega}{\partial x} = -v_g \frac{\partial k}{\partial x} - \alpha \frac{\partial a^2}{\partial x}, \quad (24.104)$$

where $v_g = \partial\omega_0/\partial k$ is the group velocity. Recalling that the energy of the wave packet is transported with the group velocity, the energy conservation law can be written as

$$\frac{\partial a^2}{\partial t} + \frac{\partial}{\partial x}(v_g a^2) = 0 \quad (24.105)$$

From (24.104)–(24.105) it follows that under certain conditions a plane wave is unstable against breakdown into individual wave packets. Indeed, let us apply a

small perturbation to a monochromatic wave with wave number k_0 and amplitude a_0 :

$$k = k_0 + k' \exp(-i\nu t + i\kappa x), \quad a = a_0 + a' \exp(-i\nu t + i\kappa x) \quad (24.106)$$

where $\nu \ll \omega$ and $\kappa \ll k_0$ are the frequency and wavenumber of the modulation. In the linear approximation from (24.104)–(24.105) we obtain

$$\nu = v_g \kappa \pm \sqrt{\alpha \frac{\partial v_g}{\partial k} a_0^2 \kappa} \quad (24.107)$$

One can see that when

$$\alpha \frac{\partial v_g}{\partial k} < 0 \quad (24.108)$$

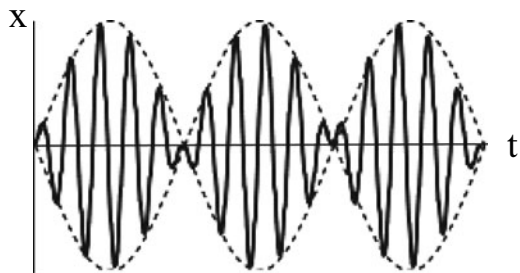
the system is subject to instability and the wave brakes into individual packets. At later stage the wave packets experience self-contraction, i.e., with the growth of the modulation amplitude the depth of modulation grows. This may lead to breaking of the wave into a separate packets (Fig. 24.3). The exemplary case is that of the gravitational waves on the surface of a deep water. The dispersion relation being in linear stage $\omega = \sqrt{gk}$ in weakly nonlinear case becomes

$$\omega(k, a^2) = \sqrt{gk} \left(1 + \frac{a^2 k^2}{2} + \dots \right) \quad (24.109)$$

where a is the amplitude of the oscillations of the surface. For the phase velocity we have

$$v_g = \frac{\partial \omega}{\partial k} = \frac{1}{2} \frac{\sqrt{g}}{\sqrt{k}} + \frac{5}{4} \sqrt{g} k^{3/2} a^2 \quad (24.110)$$

Fig. 24.3 Breaking of the beat wave into separate wave packets



From here for parameter α (24.109) we have

$$\alpha = \frac{1}{2} \sqrt{g} k^{5/2} k^{3/2} a^2 \quad (24.111)$$

Now in the first approximation

$$\alpha \frac{dv_g}{dk} = -\frac{1}{8} g k < 0 \quad (24.112)$$

Thus, the gravitational waves on the surface of deep water are unstable against the longitudinal perturbations. This simple fact is the basics of formation of rogue waves. See also Vedenov and Rudakov (1964).

24.6 Problems of Chap. 7

7.1 The generalization of results described in Sect. 7.1 to the case of a finite number of grid points is quite straightforward. One should replace the integral forms ((7.2)–(7.3)) by their discrete analogue:

$$\bar{\tau}_c^{(n)} = \frac{1}{N} \sum_{i=1}^N \tau_i(\theta_i) \cos n\theta_i \quad (24.113)$$

$$\bar{\tau}_s^{(n)} = \frac{1}{N} \sum_{i=1}^N \tau_i(\theta_i) \sin n\theta_i \quad (24.114)$$

where θ_i stands for a polar angle of the i -th grid point within the annulus. Let $N = 2k$ be the number of points at circle. Denote the angle $\theta_k = 2\pi k/N$ with $k = 0, 1, 2, 3, \dots, N-1$. Let the flow velocity have a direction θ_u . “Correct” distribution of propagation times is

$$\tau_k = \tau_0 + \Delta\tau \cos(\theta_k - \theta_u) \quad (24.115)$$

Assume that the measured values of τ have small errors, $\Delta\tau_k$, i.e., the measured values of τ_k are:

$$\tau_k = \tau_0 + \Delta\tau \cos(\theta_k - \theta_u) + \Delta\tau_k \quad (24.116)$$

Using (24.116) as input data for (24.113) and (24.114) we can find what the values of θ_u and u , and θ_B and B will be.

It is also important to discuss some problems that may appear in analyzing the observational data with a “coarse” grid, when only a few points are situated

within the annulus and/or they are distributed unevenly. In this case, even in the absence of mass flows and magnetic field one could find nonzero values of $\tau_s^{(n)}$ and $\tau_c^{(n)}$. This, however, may have hidden errors. To avoid these errors one must first subtract the average value of τ from the measurements and only then apply relationships (24.113)–(24.114). After that one could apply a further smoothing procedure, by making all calculations in a set of frames turned with respect to the initial one by a sequence of slightly different angles,

$$\theta_k = \frac{k}{N}2\pi, \quad k = 0, 1, \dots, N - 1 \quad (24.117)$$

Note that this problem will not arise if the grid-points, though distributed unevenly over the azimuth of the annulus, are distributed in a symmetric way with respect to the axes $0x$ and $0y$. See Rytova and Scherrer (1997).

24.7 Problems of Chap. 8

8.1 Let us represent the velocity u in two parts:

$$u = \langle u \rangle + \tilde{u} \quad (24.118)$$

where $\langle u \rangle$ is the average velocity and \tilde{u} is the small fluctuating part. The velocity fluctuations must lead to some pressure fluctuations

$$p = \langle p \rangle + \tilde{p} \quad (24.119)$$

The velocity and pressure are related by Bernoulli's equation,

$$p + \frac{\rho u^2}{2} = \text{const} \quad (24.120)$$

Substituting (24.118)–(24.119) into (24.120) we have

$$\langle p \rangle + \tilde{p} + \frac{\rho \langle u \rangle^2}{2} + \rho \langle u \rangle \tilde{u} + \frac{\rho \tilde{u}^2}{2} = \text{const} \quad (24.121)$$

For the average values $\langle u \rangle$ and $\langle p \rangle$ themselves, Bernoulli's equation must also hold

$$\langle p \rangle + \frac{\rho \langle u \rangle^2}{2} = \text{const} \quad (24.122)$$

The quantity $\rho \tilde{u}^2/2$ may be neglected since \tilde{u} is small compared with $\langle u \rangle$. Thus, the pressure fluctuations \tilde{p} are of the order

$$\tilde{p} \simeq \rho \langle u \rangle \tilde{u} \quad (24.123)$$

The pressure fluctuations cause a turbulent fluctuations of frequencies. Note also that in a turbulent stream the acceleration also fluctuates. See Rytova and Persson (1984).

24.8 Problems of Chap. 9

9.1 The original form of KdV equation for long waves on shallow water ($\lambda \gg h_0$ with h_0 being the depth of the layer) has a form

$$\frac{\partial u}{\partial t} + u \frac{\partial u}{\partial x} + \beta_{\text{disp}} \frac{\partial^3 u}{\partial x^3} = 0, \quad (24.124)$$

Here $\beta_{\text{disp}} = c_0/k_0^2$ is the dispersion parameter, determined by the phase velocity, c_0 , and wavenumber, k_0 . Note that $1/k_0$ has meaning of the “dispersion length.”

For very long waves, when the wavelength is much larger than the depth of water, $1/k_0 \gg h_0$, the phase velocity does not depend on the wave number, and is simply equal to $\sqrt{gh_0}$. For the traveling-wave type, when $u = u(x - ct)$, we have

$$\frac{\partial u}{\partial t} = -c \frac{\partial u}{\partial x}, \quad (24.125)$$

and (24.124) changes from a partial differential equation to an ordinary one

$$-c \frac{du}{dx} + \frac{1}{2} \frac{\partial u^2}{\partial x} + \beta_{\text{disp}} \frac{\partial^3 u}{\partial x^3} = 0 \quad (24.126)$$

This equation can be immediately integrated once leading to the following equation

$$\beta_{\text{disp}} \frac{\partial^2 u}{\partial x^2} = A + cu - \frac{1}{2} u^2, \quad (24.127)$$

where A is the integration constant, which can be set to zero, say, by changing over to a moving system of coordinates.

Equation (24.127) can be represented in the form

$$\beta_{\text{disp}} \frac{\partial^2 u}{\partial x^2} = -\frac{\partial W}{\partial u}, \quad (24.128)$$

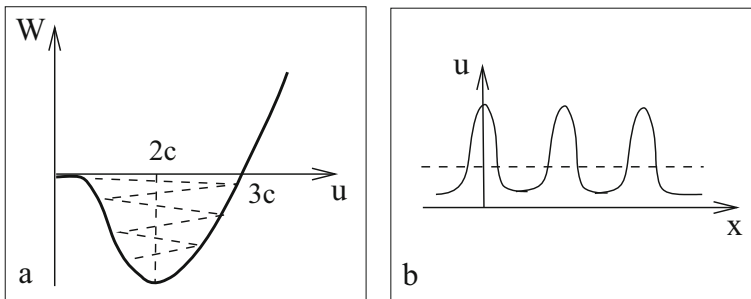


Fig. 24.4 A potential well (a) and Multi-solitons (b)

where

$$W = -\frac{cu^2}{2} + \frac{u^3}{6} \tag{24.129}$$

(24.128) has the form of the equation of motion for a nonlinear oscillator—a material point of mass β_{disp} , moving in a potential well $W(u)$, with the coordinate x playing the role of the time. The plot of $W(u)$ is shown in Fig. 24.4a. It vanishes at $u = 0$, $u = 3c$ and reaches a minimum at $u = 2c$. In case of oscillations about the minimum of the potential energy $W(u)$, the wave is practically harmonic:

$$u = 2c + u_0 \exp \left[i \sqrt{\frac{c}{\beta_{\text{disp}}}} (x - ct) \right] \tag{24.130}$$

One can see that at small amplitudes, u oscillates about the value $2c$. As the oscillation amplitude increases, the wave becomes more and more asymmetric. When the amplitude increases to such an extent that values $u = 0$ become possible, the solution describes a single solitary pulse—a soliton. The corresponding solution is of the form

$$u = A \operatorname{sech}^2 \left(\frac{x - ct}{\Delta} \right) \tag{24.131}$$

where the amplitude A and the width of a soliton Δ are as follows:

$$A = 3c, \quad \Delta = 2\sqrt{\frac{\beta_{\text{disp}}}{c}} = \frac{2}{k_0} \sqrt{\frac{c_0}{c}} \tag{24.132}$$

Thus, the larger the soliton velocity c , the larger its amplitude and the smaller its width. It is interesting that if the wave amplitude A is close to $3c$ (but smaller), then the solution takes a form of multi-solitons: sequence of pulses, close in shape, follow one another periodically (Fig. 24.4b). See Kadomtsev and Karpman (1971).

9.2 The KdV-Bürgers equation

$$\frac{\partial u}{\partial t} + u \frac{\partial u}{\partial x} + \beta_{\text{disp}} \frac{\partial^3 u}{\partial x^3} = \mu \frac{\partial^2 u}{\partial x^2} \quad (24.133)$$

for a traveling wave, $u = u(x - ct)$, after integrating this equation once with respect to x , we get

$$\beta \frac{\partial^2 u}{\partial x^2} - \mu \frac{\partial u}{\partial x} = -\frac{\partial W}{\partial u} \quad (24.134)$$

Now we have an equation for nonlinear damping (μ) oscillator in the same potential, (24.129):

$$W = -\frac{c}{2}u^2 + \frac{1}{6}u^3, \quad (24.135)$$

and a “friction force” with coefficient μ . As earlier, u plays the role of coordinate and the time τ is played by $-x$. If we assume that for $\tau = -\infty$ (i.e., $x = \infty$) the “particle” was located at the coordinate origin ($u = 0$), then at time $\tau = \infty$ (i.e., $x = -\infty$) it appears at the point $u(-\infty) = 2c$ (Fig. 24.4a), corresponding to the minimum energy. Thus (24.134) describes a shock wave whose velocity c is related to the extreme values $u(\infty) = 0$ and $u(-\infty) = u_m$ by

$$c = \frac{u(-\infty) - u(\infty)}{2} = \frac{\Delta u}{2} \quad (24.136)$$

and a solution, bounded at ∞ :

$$u(x - ct) = c_0 + \frac{\Delta u}{1 + \exp[\Delta u/2\mu(x - ct)]}, \quad c = c_0 + \frac{\Delta u}{2} \quad (24.137)$$

where c_0 and Δu are constants, and $\Delta u = u(-\infty) - u(\infty)$. This solution represents a shock wave with a discontinuity Δu and a transition region width $\delta = 2M/\Delta u$. In a reference frame where the medium is at rest, the velocity of the shock wave is

$$c = c_0 + \frac{\Delta u}{2} \quad (24.138)$$

The corresponding Mach number is

$$M = 1 + \frac{\Delta u}{2c_0} \quad (24.139)$$

Because of dissipation, the oscillations in potential $W(u)$ will be damping. Hence, instead of a periodic wave, the solution may take shape of an asymmetric wave train. Altogether the nature of the shock wave depends on the relation between

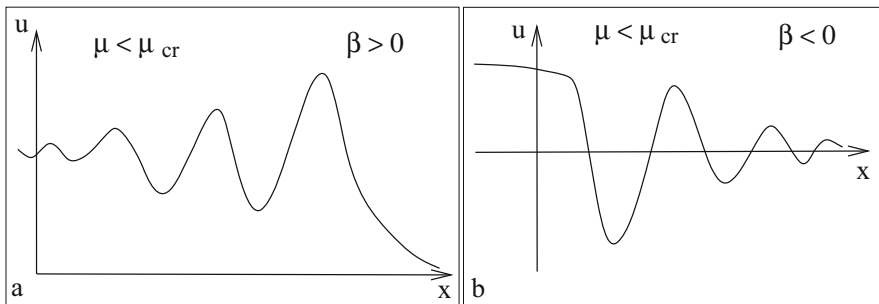


Fig. 24.5 Structure of shock wave in dispersive and dissipative medium with partial soliton regime, i.e., at $\mu < \mu_{cr}$: **(a)** at positive dispersion—the initial phase consists of train of regular solitons; **(b)** at negative dispersion—the initial phase consists of a train of negative solitons

the dispersive and dissipative parameters, β_{disp} and μ . At small dissipation, the “particle” will fall to the bottom of the potential well (Fig. 24.4a), and perform the oscillations between its walls. The energy of the “particle” decreases quite slowly, and first few oscillations at the wave front will be close to solitons moving with velocity (Fig. 24.5a)

$$u \simeq 3c \operatorname{sech}^2 \left[\sqrt{\frac{c}{4\beta_{disp}}} (x - x_0 - ct) \right] \tag{24.140}$$

If the dissipation coefficient is larger than some critical value μ_{cr} , the motion of “particle” will be aperiodic and the shock front will have a monotonic structure as in normal gas dynamic (Fig. 24.5b).

9.3 First, we investigate the asymptotic behavior of the solution of (24.133) for $x \rightarrow -\infty$. Let us represent $u(x)$ as follows:

$$u(x) = \Delta u + f(x) \tag{24.141}$$

where $f(x)$ is a small quantity. Substituting this expression into (24.133) and linearizing it, we obtain for the function $f(x)$ equation:

$$\beta \frac{\partial^3 f}{\partial x^3} - \mu \frac{\partial f}{\partial x} + cf = 0 \tag{24.142}$$

The solutions of this equation are proportional to $\exp(px)$, where

$$p = \frac{\mu}{2\beta_{disp}} \pm \left(\frac{\mu^2}{4\beta_{disp}^2} - \frac{c}{\beta_{disp}} \right)^{1/2} \tag{24.143}$$

We see that expression in brackets may have positive or negative sign providing thus condition for μ_{cr} :

$$\mu_{cr} = \sqrt{4\beta_{disp}c} = \sqrt{2\beta_{disp}\Delta u} \quad (24.144)$$

Thus the shock wave has a monotonic profile for $\mu > \mu_{cr}$ and an oscillating profile for $\mu < \mu_{cr}$.

If $\mu \ll \mu_{cr}$, the asymptotic form of the solution at $\tau \rightarrow \infty$ is as follows:

$$u = \Delta u + A \exp\left(\frac{\mu x}{2\beta_{disp}}\right) \cos\left(\sqrt{\frac{\Delta u}{2\beta_{disp}}}x\right) \quad (24.145)$$

For $\beta_{disp} > 0$ this expression corresponds to the plots shown in Fig. 24.5a, i.e., the oscillatory structure is ahead of the wave front. In case of negative dispersion $\beta_{disp} < 0$, solitons are dark and the largest soliton travels with maximum velocity, while the oscillating tail remains behind the shock front. Such a structure is characteristic, for example, of an oblique shocks in a magnetized plasma (see e.g. Sagdeev 1966). Note that both types of shock waves were observed in laboratory, as well as in the solar atmosphere (see Chaps. 11 and 21).

24.9 Problems of Chap. 10

10.1 Because of the geometry of the problem, the equation of motion has a form:

$$\frac{\partial \mathbf{v}}{\partial t} + \frac{1}{\rho} \nabla p - \nu \Delta \mathbf{v} = 0 \quad (24.146)$$

It follows from the z -component of (24.146) that $\partial p / \partial z = 0$, i.e., $p = \text{const}$, and its x -component becomes ($v_x = v$)

$$\frac{\partial v}{\partial t} = \nu \frac{\partial^2 v}{\partial z^2} \quad (24.147)$$

This is in fact one-dimensional heat conduction equation. For a periodic in z and t solution of the form

$$v = v_0 \exp[i(kz - \omega t)] \quad (24.148)$$

we have from (24.146)

$$i\omega = \nu k^2 \quad (24.149)$$

or

$$k = \frac{1+i}{\delta_p}, \quad \delta_p = \sqrt{\frac{2\nu}{\omega}} \quad (24.150)$$

so that the velocity is

$$v = v_0 e^{-z/\delta_p} e^{i(z/\delta_p - \omega t)} \quad (24.151)$$

The choice of the sign \sqrt{i} corresponds to the requirement that the velocity must decrease into the fluid. The quantity δ_p is the depth of penetration. One can see that this depth decreases with increasing frequency of the wave and increases with the kinematic viscosity of the fluid. It is interesting that in the nonlinear stage of generation of mass flows by the oscillating surface, the effect is independent on the viscosity. This is considered in the next problem.

10.2 To study non-steady flow one needs to include time-derivative terms in the Prandtl's equation. In chosen geometry we have

$$\frac{\partial v_x}{\partial t} + v_x \frac{\partial v_x}{\partial x} + v_y \frac{\partial v_x}{\partial y} - \nu \frac{\partial^2 v_x}{\partial y^2} = U \frac{\partial U}{\partial x} + \frac{\partial U}{\partial t} \quad (24.152)$$

Here

$$U = v_0 \cos kx \cdot \cos \omega t \quad (24.153)$$

where $k = \omega/c_s$. The velocity \mathbf{v} in the boundary layer can be expressed in terms of a stream function $\psi(x, y, t)$:

$$v_x = \partial \psi / \partial y, \quad v_y = -\partial \psi / \partial x \quad (24.154)$$

We will solve (24.152) by successive approximations with respect to the velocity fluctuations in the sound wave. In the first approximation we have

$$\frac{\partial v_x^{(1)}}{\partial t} - \nu \frac{\partial^2 v_x^{(1)}}{\partial y^2} = -i\omega v_0 \cos kx e^{-i\omega t} \quad (24.155)$$

The solution of this equation which satisfies the necessary conditions at $y = 0$ and $y = \infty$ is

$$v_x^{(1)} = \operatorname{Re} \left[v_0 \cos kx e^{-i\omega t} (1 - e^{-ky}) \right] \quad (24.156)$$

where

$$k = \sqrt{\frac{-i\omega}{\nu}} = \frac{1-i}{\delta_p} \quad (24.157)$$

δ_p being a penetration depth (cf. (24.150)). Note that the acoustic streaming is the most efficient when the characteristic length in the problem l is much less than the sound wavelength, λ , but much larger than the penetration depth $\delta_p = \sqrt{2\nu/\omega}$. The stream function corresponding to (24.150) is

$$\psi^{(1)} = \text{Re} \left[v_0 \cos(kx) \cdot \zeta^{(1)}(y) e^{-i\omega t} \right], \quad \zeta^{(1)}(y) = y + \frac{1}{k} e^{-ky} \quad (24.158)$$

This solution satisfies the condition $\psi^{(1)} = 0$ at $y = 0$, which is equivalent to $v_y^{(1)} = 0$. In the next approximation, $\mathbf{v} = \mathbf{v}^{(1)} + \mathbf{v}^{(2)}$, for $v_x^{(2)}$ we have

$$\frac{\partial v_x^{(2)}}{\partial t} - \nu \frac{\partial^2 v_x^{(2)}}{\partial y^2} = U \frac{\partial U}{\partial x} - v_x^{(1)} \frac{\partial v_x^{(1)}}{\partial x} - v_y^{(1)} \frac{\partial v_x^{(1)}}{\partial y} \quad (24.159)$$

The right-hand side contains terms with frequencies $\omega_1 = 2\omega$ and $\omega_2 = 0$. It is just $\omega_2 = 0$ that leads to time-independent terms in $\mathbf{v}^{(2)}$ which correspond to the secondary steady flow generated by the sound.

In what follows, we will consider only this part of velocity under $\mathbf{v}^{(2)}$. Using corresponding stream function

$$\psi^{(2)} = \frac{v_0^2}{c_s} \sin(2kx) \cdot \zeta^{(2)}(y) \quad (24.160)$$

we obtain the equation for $\zeta^{(2)}(y)$:

$$\delta_p^2 \zeta^{(2)'''} = \frac{1}{2} - \frac{1}{2} |\zeta^{(1)'}|^2 + \frac{1}{2} \text{Re}[\zeta^{(1)} \zeta^{(1)''}] \quad (24.161)$$

the primes denote differentiation with respect to y . The solution of this equation must satisfy conditions $\zeta^{(2)} = 0$, $\zeta^{(2)'} = 0$, which are equivalent to $v_x^{(2)} = v_y^{(2)} = 0$ on the solid surface. Far from the surface $v_x^{(2)}$ tends to finite value. Substituting (24.158) in (24.161) and integrating twice one gets for the derivative $\zeta^{(2)'}$:

$$\zeta^{(2)'}(y) = \frac{3}{8} - \frac{1}{8} e^{-2y/\delta_p} - e^{-y/\delta_p} \left\{ \sin(y/\delta_p) + \frac{1}{4} \cos(y/\delta_p) - \frac{y}{4\delta_p} [\cos(y/\delta_p) - \sin(y/\delta_p)] \right\} \quad (24.162)$$

As $y \rightarrow \infty$, it tends to

$$\zeta^{(2)'}(\infty) = 3/8 \quad (24.163)$$

corresponding to a velocity

$$v_x^{(2)}(\infty) = \frac{3v_0^2}{8c_s} \sin 2kx \quad (24.164)$$

Important: outside the boundary layer there is a steady flow whose velocity is independent of the viscosity, whereas the generation of the secondary flows is the result of the action of Reynolds stresses. Flow portrait of Schlichting's solution and corresponding experimental results are shown in Fig. 10.1. The value of $v_x^{(2)}(\infty)$ serves as a boundary condition for determining the main acoustic flow (see the next problem Schlichting (1932); Rayleigh (1883)).

10.3 Since the velocity $v^{(2)}$ of a steady flow is much less than the sound speed, the flow may be regarded as incompressible. Moreover, since v_0 is assumed to be also small, such that $v_0/c_s \ll \delta_p/h$ (as well as $v^{(2)} \sim v_0^2/c_s \ll \delta_p/h$), the quadratic terms in the equation of motion may be neglected. Then equation for the stream function reduces to

$$\left(\frac{\partial^2}{\partial x^2} + \frac{\partial^2}{\partial y^2} \right)^2 \psi^{(2)} = 0 \quad (24.165)$$

We shall seek $\psi^{(2)}$ in the form (24.160). As $h \ll \lambda$, the derivatives with respect to y are much larger than those with respect to x . Neglecting the latter, we obtain for $\zeta^{(2)}(y)$ the equation

$$\zeta^{(2)'''}(y) = 0 \quad (24.166)$$

Because of the symmetry of the problem, the flow is symmetrical with respect to the plane $y = (1/2)h$. Hence

$$v_x^{(2)}(x, y) = v_x^{(2)}(x, h - y), \quad v_y^{(2)}(x, y) = -v_y^{(2)}(x, h - y) \quad (24.167)$$

and therefore

$$\zeta^{(2)}(y) = -\zeta^{(2)}(h - y) \quad (24.168)$$

A solution of (24.166) having this property is

$$\zeta^{(2)}(y) = A(y - h/2) + B(y - h/2)^3 \quad (24.169)$$

The constants A and B are determined from the boundary conditions

$$\zeta^{(2)}(0) = 0, \quad \zeta^{(2)'}(0) = 3/8 \quad (24.170)$$

Thus for the stream function we have

$$\psi^{(2)} = \frac{3v_0^2}{16c_s} \sin 2kx \left[-(y - h/2) + \frac{1}{4}h^2(y - h/2)^3 \right], \quad (24.171)$$

from which follow the velocity distributions:

$$v_x^{(2)} = -\frac{3v_0^2}{16c_s} \sin 2kx \left[1 - \frac{3}{4}h^2(y - h/2)^2 \right], \quad (24.172)$$

and

$$v_y^{(2)} = \frac{3v_0^2 k}{8c_s} \cos 2kx \left[y - h/2 - \frac{1}{4}h^2(y - h/2)^3 \right] \quad (24.173)$$

The velocity $v_x^{(2)}$ changes sign at a distance $(1/2)h(1 - 1/\sqrt{3}) = 0.423(1/2)h$ from the wall. The flow described by these expressions consists of two series of vortices lying symmetrically about the median plane $y = (1/2)h$ and being periodic in the x -direction, with period $(1/2)\lambda$. One of the examples of numerous experiments illustrating the acoustic streaming is shown in Fig. 24.6.

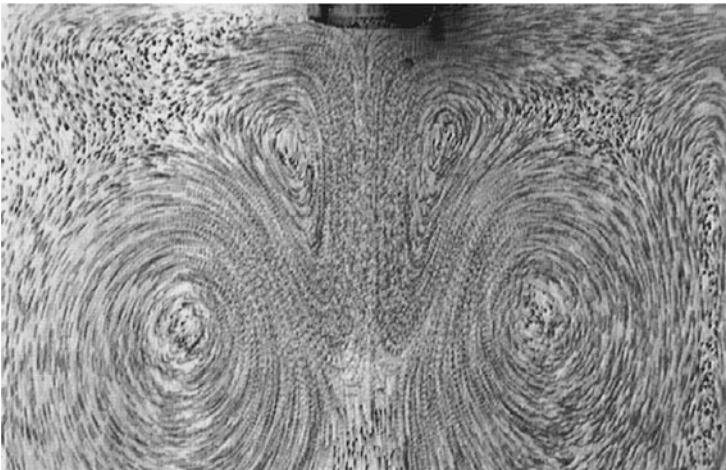


Fig. 24.6 Visualization of acoustic streaming. Ten superimposed images taken at 200 ms interval, created by a transducer 4 mm in diameter (seen at image top center (Reprinted from Nowicki et al. (1998). Copyright (1998), with permission from Elsevier)

24.10 Problems of Chap. 11

11.1 Equation (11.33) can be written in the divergence form as follows:

$$\frac{\partial u}{\partial t} + \frac{\partial}{\partial x} \left(\frac{u^2}{2} + \beta u_{xx} \right) = 0 \quad (24.174)$$

which can be written in form of the “momentum” conservation law:

$$I_1 = \int_{-\infty}^{\infty} u(x, t) dx \quad (24.175)$$

Multiplying both sides of (24.174) by u and making a simple rearrangements we obtain equation which also has the form of an energy conservation law

$$\frac{\partial}{\partial t} \left(\frac{u^2}{2} \right) + \frac{\partial}{\partial x} \left[\frac{u^3}{3} + \beta \left(uu_{xx} - \frac{1}{2} u_x^2 \right) \right] = 0 \quad (24.176)$$

In the same way, multiplying both sides of (24.174) by u^2 , after some algebra we get another conservation law:

$$\frac{\partial}{\partial t} \left(\frac{u^3}{3} - \beta u_{xx} \right) + \frac{\partial}{\partial x} \left[\frac{u^4}{4} + \beta (u^2 u_{xx} + 2u_t u_x) + \beta^2 u_{xx}^2 \right] = 0 \quad (24.177)$$

Although (24.177) does not have such a simple physical interpretation as two previous conservation laws, it leads to amazing discovery that there exists an infinite number of invariants corresponding to the KdV equation,

$$I_m = \int_{-\infty}^{\infty} Q_m(x, t) dx \quad (24.178)$$

whose densities $Q_m(x, t)$ satisfy the equation

$$\frac{\partial Q_m(x, t)}{\partial t} + \frac{\partial P_m(x, t)}{\partial x} = 0, \quad m = 1, 2, 3, \dots \quad (24.179)$$

$Q_m(x, t)$ and $P_m(x, t)$ are polynomials of β and the spatial derivatives of $u(x, t)$. Thus, for example, the first three densities of the conserved quantities are:

$$Q_1[u] = u, \quad Q_2[u] = \frac{u^2}{2}, \quad Q_3[u] = \frac{u^3}{3} - \beta u_x^2 \quad (24.180)$$

Note finally that to the first order of dispersion coefficient β , the expression for $Q_m[u]$ for the infinite number m is quite simple:

$$Q_m[u] = \frac{u^m}{m} - \beta \frac{(m-1)(m-2)}{2} u_x^2 u^{m-3} + O(\beta^2), \tag{24.181}$$

demonstrating a remarkable structural stability of the KdV solutions. See e.g. Miura et al. (1968).

11.2 Like the KdV equation, the MKdV equation is fully integrable, and also has an infinite number of integrals. Consider first a solitary solutions of (11.34) with negative cubic nonlinearity, i.e., when $\alpha < 0$. In this case

$$u = A \operatorname{sech}^2 \left[\frac{1}{2} \sqrt{2A} (x - 2At - x_0) \right] \tag{24.182}$$

where $A = c/2$, c being the soliton velocity. This solution describes a single family of solutions such that $A > 0$. As the wave amplitude increases, it remains bounded by an upper limit given by

$$A_{\max} = \frac{1}{|\alpha|} \tag{24.183}$$

In the limiting case the solution (24.182) describes the so-called thick or table-top solitary wave. The family of the solutions of (24.182) for negative cubic nonlinearity, $\alpha < 0$ is shown in Fig. 24.7, left panel. One can see that entire family consists of the \cap -shaped, bright solitons. Blue line corresponds to A_{\max} of a table-top soliton.

In case of positive cubic nonlinearity, when $\alpha > 0$ there are two possible families of solitary waves having opposite polarities:

$$u(x, t) = A \operatorname{sech}[\sqrt{\alpha} A (x - \alpha A^2 t - x_0)] \tag{24.184}$$

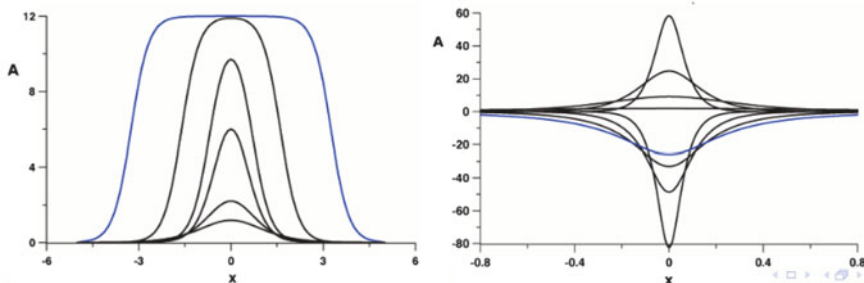


Fig. 24.7 The shape of solitary wave solutions of the dimensionless Gardner equation. Left panel: case of negative cubic nonlinearity; Right panel: case of positive cubic nonlinearity (Grimshaw et al. 1999). Reprinted with permission from IOP publishing

where A can take either sign. In case of negative value of the amplitude we have the \cap -shaped, dark solitons. The amplitude of these solitons is bounded by a lower limit of

$$A_{\text{lim}} = -\frac{2}{|\alpha|}, \quad (24.185)$$

and the wave tends to the soliton shape given by

$$u(x) = \frac{12\alpha A_{\text{lim}}}{12\alpha + x^2} \quad (24.186)$$

The family of solitons at $\alpha > 0$ is shown in Fig. 24.7, right panel. The limiting solutions are shown by the blue line.

11.3 In case of a strong dispersion the wave profile becomes highly oscillatory and instead of the “wave front” we deal with the series of solitons (so-called Low-Frequency Instability). Thus, we need to analyze a behavior of solitons under the conditions

$$\beta \frac{\partial^3 u}{\partial x^3} \sim u \frac{\partial u}{\partial x} \gg \gamma u \sim v \frac{\partial^2 u}{\partial x^2} \quad (24.187)$$

We will use again the method of averaging over stationary waves. The solution of (11.35) is a soliton having an amplitude, $A(t)$, width, $\Delta(t)$ and velocity, $v(t)$ that vary slowly in time (cf. Eqs. (11.7)–(11.9)):

$$u = A(t) \operatorname{sech}^2 \left[\frac{1}{\Delta(t)} \left(x - \int_0^t v(t) dt \right) \right] \quad (24.188)$$

where

$$v(t) = \frac{1}{3} A(t), \quad \Delta^2(t) = \frac{12\beta}{A(t)} \quad (24.189)$$

i.e., the parameters of the soliton are related to one another in the same way as in the conventional KdV (akin magnetic solitons). Multiplying (11.35) by u and integrating over a distance large compared with the size of a soliton (in fact from $-\infty$ to ∞) we obtain the equation for the amplitude:

$$\frac{dA}{dt} = 2\gamma A - \frac{4}{45} \frac{v}{\beta} A^2 \quad (24.190)$$

Solution to this equation is

$$A(t) = \frac{A_0 A_\infty \exp(\alpha t)}{A_0 [\exp(\alpha t) - 1] + A_\infty} \quad (24.191)$$

where A_0 is the initial amplitude, $A_\infty = 5\gamma/nu$, and $\alpha = 4\gamma/3$. From the solution (24.191) it follows that solitons having an initial amplitude $A_0 < A_\infty$ are accelerated to the velocity $v_\infty = (1/3)A_\infty$ and amplified to the amplitude A_∞ . On the other hand, solitons having $A_0 > A_\infty$ are decelerated and dump out to the value A_∞ . Hence, for $t \rightarrow \infty$ low-amplitude solitons have a large width and low-frequency instability leads to their amplification, while narrow solitons, having a large amplitude, dump out due to high-frequency. See Rabinovich and Fabrikant (1976).

24.11 Problems of Chap. 12

12.1 Assume that all magnetic elements have the same radius r_0 and the same field strength B_0 at the photosphere. The magnetic flux of each element is then

$$\Phi_{\text{ph}} = \pi r_0^2 B_0 \quad (24.192)$$

The density n of magnetic elements in the cell, assumed circular, may be found from the conservation equation

$$\frac{1}{r} \frac{d}{dr}(rvn) = S_c \quad (24.193)$$

where S_c is the rate of generation of magnetic elements per unit area. Let magnetic elements appear uniformly at a rate S_c over a supergranular cell of radius R . If the radial outflow velocity v increases linearly from zero at the center to v_c at the boundary of the cell, so that

$$v = v_c r/R, \quad (24.194)$$

(24.193) is satisfied by the following value of the density:

$$n_c = \frac{1}{2} \frac{RS_c}{v_c} \quad (24.195)$$

The rate of generation of flux elements in the cell J_c is given by

$$J_c = \pi R^2 S_c \quad (24.196)$$

We assume that, once flux elements arrive at the network (“boundary”) region, they move randomly with mean speed v_b . Denote the “collision cross section” of each magnetic element as λr_0 , where λ is of the order of unity. If the mean density of flux elements in the network region is n_b , the rate of annihilation of flux elements, per unit area, will be

$$A_b = \frac{1}{\sqrt{2}} v_b n_b^2 \lambda r_0 \quad (24.197)$$

since the mean relative speed is $\sqrt{2}v_b$ and only one-half of the collisions are between elements of opposite polarity. If the width of the network is $2W$, the total rate of annihilation in the network region associated with a single cell will be

$$J_b = 2\pi RW A_b \quad (24.198)$$

to lowest order in W/R . Hence, the balance between the flux generation rate J_c and the annihilation rate J_b leads to the following expression for n_b :

$$n_b^2 = \frac{1}{\sqrt{2}} \frac{RS_c}{\lambda W r_0 v_b} \quad (24.199)$$

When a pair of magnetic elements “collide” and reconnect, the energy in the upper atmosphere is reduced by approximately $2U_{\text{ph}}$ in each collision, where

$$U_{\text{ph}} = \frac{1}{8\pi} B_0^2 \pi r_0^2 \eta r_0 \quad (24.200)$$

here $\eta r_0 \simeq \Lambda$ is the effective scale height. The total energy generation rate is then $J_c U_{\text{ph}}$, so that the average coronal energy flux is given by

$$F = S_c U_{\text{ph}} \quad (24.201)$$

Similarly, the mean magnetic field strength may be calculated by dividing the total magnetic flux by the total area, which leads to

$$B = (n_c + 2R^{-1}Wn_b)\Phi_{\text{ph}} \quad (24.202)$$

If we normalize the mean magnetic field strength according to

$$b = B/B^* \quad (24.203)$$

where

$$B^* = \frac{\sqrt{2}\pi B_0 W r_0 v_c}{\lambda R^2 v_b} \quad (24.204)$$

and normalize the energy flux according to

$$f = F/F^* \quad (24.205)$$

where

$$F^* = \frac{2^{-3/2}\eta B_0^2 W r_0^2 v_c^2}{\lambda R^3 v_b} \quad (24.206)$$

we find that the energy flux is related to the mean field strength by

$$f = [\sqrt{1+b} - 1]^2 \quad (24.207)$$

One can see that the relationship between the photospheric magnetic flux and energy flux in the upper atmosphere is not a simple power law. For weak magnetic fields, the slope of the log-log relationship ($\alpha = d[\log f]/d[\log b]$) is in the range 1.5–2.0. For strong magnetic fields it is in the range 1.2–1.5. See Rabinovich and Fabrikant (1976).

12.2 The speed of magnetic reconnection is usually defined by the speed of inflow, v_{in} , or by the Alfvén Mach number at the inflow region

$$M_i \equiv v_{\text{in}}/v_{Ai} \quad (24.208)$$

$v_{Ai} = B_i/\sqrt{4\pi\rho}$. Denoting the observed specific rate of cancellation of magnetic field by w we can express it through the magnetic field in the inflow region, B_i , and the inflow speed:

$$w = v_{\text{in}}B_i \quad (24.209)$$

Let us now find the inflow speed for both models.

In the Sweet-Parker reconnection model the magnetic field lines are carried by plasma toward the current sheet at the same speed as the magnetic field lines diffuse outward: $v_{\text{in}} = \eta/l$. The speed of outflow in the inflow region is equal to the Alfvén speed, $v_{\text{out}} = v_{Ai}$. The incoming flow of matter must balance the outgoing flow, $Lv_{\text{in}} = lv_{\text{out}}$. Thus for the inflow speed we get

$$v_{\text{in}} = \left[\frac{\eta w}{L\sqrt{4\pi\rho}} \right]^{1/3} \quad (24.210)$$

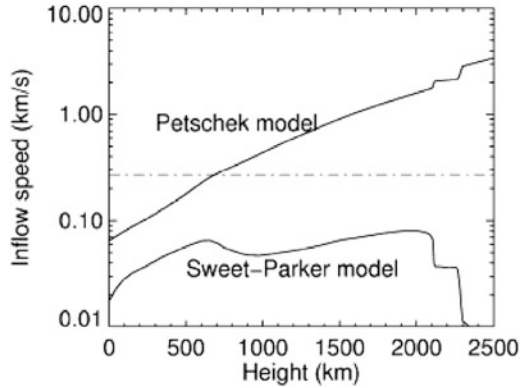
In the Petschek reconnection model the conversion of magnetic energy into kinetic energy occurs in the current layer and is accompanied by the slow shocks that develop outside the reconnection region, $L_e \gg L$. The reconnection rate is measured accordingly as the inflow into the shocks, v_{ext} . The maximum rate of reconnection is now measured by:

$$M_{\text{ext}} = \frac{\pi}{8\ln(8v_{\text{ext}}^2 Re_m/v_{Ae}^2)} \quad (24.211)$$

where Re_m is the magnetic Reynolds number. Using now the observed cancellation rate w we can write

$$v_{\text{ext}} = \left\{ \frac{\pi w}{8\sqrt{4\pi\rho}\ln[8(v_{\text{ext}}/\tilde{v})^3]} \right\}^{1/2} \quad (24.212)$$

Fig. 24.8 Theoretical inflow speeds of magnetic reconnection in the Sweet-Parker and Petschek models. The observed specific cancellation rate is being $w = 1.2 \times 10^6 \text{ G cm s}^{-1}$ (Chae et al. 2002). Reprinted with permission from Korea Institute of Science and Technology Information



where

$$\tilde{v} = \left[\frac{\eta w}{L_e \sqrt{4\pi\rho}} \right]^{1/3} \tag{24.213}$$

For observational comparison of the reconnection rates one needs to specify the parameters L , L_e , ρ , and η . Assume (Chae et al. 2002) that both, L used in Sweet-Parker model and L_e used in Petschek model, are of the order of the local scale height. The velocities v_{in} and v_{ext} may be computed using chromosphere model.

The calculated inflow speeds are shown in Fig. 24.8. One can see that the inflow speed in Sweet-Parker model is less than 0.1 km s^{-1} everywhere throughout the photosphere and chromosphere, and is significantly less than the observed one, $v_{obs} \simeq 0.27 \text{ km s}^{-1}$. As to the Petschek model, here the reconnection rates are, as expected, much faster, and range from 1 km s^{-1} near the photosphere to a few km s^{-1} in the chromosphere. It is interesting that theoretical inflow speed becomes equal to the observed one at about 700 km height, i.e., at about the temperature minimum.

24.12 Problems of Chap. 13

13.1 Let the gas-kinetic pressure be much less than the magnetic pressure. The damping of a fast magnetosonic wave is caused mainly by Ohmic and viscous losses. Let us estimate these effects separately. General equations governing the problem are given by

$$\frac{\partial v}{\partial t} = j \frac{B_0}{\rho c} \tag{24.214}$$

$$j = \sigma \left(E + \frac{v}{c} B_0 \right) \tag{24.215}$$

$$\frac{\partial E}{\partial x} = -\frac{1}{c} \frac{\partial B_0}{\partial t} \quad (24.216)$$

$$\frac{\partial B}{\partial x} = \frac{4\pi}{c} j \quad (24.217)$$

Hence, the equation for the fast wave with Ohmic losses has a form

$$-\frac{\partial}{\partial t} \left(\frac{\partial B}{\partial t} + \frac{c^2}{4\pi\sigma} \frac{\partial^2 B}{\partial x^2} \right) = \frac{B_0^2}{4\pi\rho} \frac{\partial^2 B}{\partial x^2} \quad (24.218)$$

The viscous losses in a laminar plasma can be found from the equations

$$\frac{\partial v}{\partial t} = \nu \frac{\partial^2 v}{\partial x^2} + j \frac{B_0}{\rho c}, \quad E + (v/c)B = 0, \quad (24.219)$$

and the wave equation is

$$\frac{\partial^2 B}{\partial t^2} - \nu \frac{\partial^2}{\partial x^2} \frac{\partial B}{\partial t} = \frac{B_0^2}{4\pi\rho} \frac{\partial^2 B}{\partial x^2} \quad (24.220)$$

Taking into account both, Ohmic and viscous losses, the approximate damping rate at the frequency $\omega = v_A k$ is as follows:

$$\gamma = \left(\nu + \frac{c^2}{4\pi\sigma} \right) k^2 \quad (24.221)$$

The corrugation instability will appear at $\gamma < \omega$, i.e., if

$$\left(\nu + \frac{c^2}{4\pi\sigma} \right) k < v_A \quad (24.222)$$

If we choose for the value of the wave vector the inverse of the width of shock front (with viscous losses), namely if

$$k \rightarrow \frac{v_A}{\nu(M-1)}, \quad (24.223)$$

then the condition for the shock front instability becomes as follows:

$$M - 1 > 1 + \frac{c^2}{4\pi\nu\sigma}. \quad (24.224)$$

13.2 We will assume the gas to be perfect, so that its pressure and specific internal energy may be expressed by the simple relations

$$p = \frac{k_b}{\mu} \rho T, \quad E = \frac{1}{\gamma - 1} \frac{k_b T}{\mu} \quad (24.225)$$

k_b being a Boltzmann constant and μ is molecular weight. We shall assume that the shock propagates from left to right. The x -coordinate will be measured from the shock front compression. The conservation laws in hydrodynamic approximation take the form

$$\rho u = \rho_0 v_{\text{sh}} \quad (24.226)$$

$$p + \rho u^2 = \rho_0 v_{\text{sh}}^2 \quad (24.227)$$

$$E + \frac{p}{\rho} + \frac{u^2}{2} + \frac{S_{\text{rad}}}{\rho_0 v_{\text{sh}}} = \frac{v_{\text{sh}}^2}{2} \quad (24.228)$$

Here S_{rad} is the radiation energy flux, which is directed opposite to the gas flow, so that $S_{\text{rad}} < 0$, whereas $v_{\text{sh}} > 0$ and $u > 0$. Introducing the relative specific volume $\eta = V/V_0$ which is equal to the reciprocal of the density ratio or to the velocity ratio,

$$\eta = \frac{V}{V_0} = \frac{\rho_0}{\rho} = \frac{u}{v_{\text{sh}}}, \quad (24.229)$$

we find from (24.226)–(24.227) that in the regions where flow variables are continuous, the pressure changes along the straight line

$$p = \rho_0 v_{\text{sh}}^2 (1 - \eta) \quad (24.230)$$

The dependence of temperature and flux on the density ratio is obtained from (24.226)–(24.228):

$$T = T_1 \frac{\eta(1 - \eta)}{\tilde{\gamma}(1 - \tilde{\gamma})} \quad (24.231)$$

$$S_{\text{rad}} = -\frac{\rho_0 v_{\text{sh}} k_b T_1}{2\mu} \frac{(1 - \eta)(1 - \tilde{\gamma})}{\tilde{\gamma}^2(1 - \tilde{\gamma})} \quad (24.232)$$

where $\tilde{\gamma} = (\gamma - 1)/(\gamma + 1)$.

Radiation in shock wave plays an important role at high temperatures when the gas is strongly ionized. In the solar atmosphere this effect must be taken into account. For this the energy flux of the shock $v_{\text{sh}} \rho E$ and $\sigma_s T^4$ must be comparable,

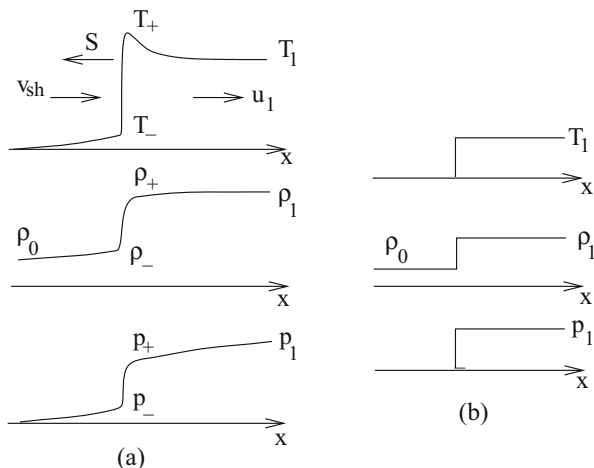


Fig. 24.9 Shock wave profile: (a) temperature, density and pressure in a shock front when radiant heat flux is taken into account; (b) the same for a “classical” shock

i.e., the condition

$$\sigma_s T^4 \simeq \frac{1}{\gamma - 1} v_{sh} n k_b T \quad (24.233)$$

must be met; n being the gas density.

Figure 24.9a shows qualitative profiles of temperature, density and pressure accounting the radiant heat exchange at the shock front. The preheating temperature ahead of the discontinuity T_- is proportional to the radiation flux emerging from the discontinuity surface, $-S \simeq \sigma T_1^4$. Therefore, it increases rapidly with increasing wave strength. To the right the shock profile of a “classical” shock is shown for comparison.

Let us now make a rough estimate for solar atmosphere. At about 3–4 scale-height shocks are easily formed (see Chap. 12). Take, e.g., a chromospheric conditions. At a few scale heights post-reconnection shocks quickly form (see Figs. 14.6 and 14.7). For the temperature $T = 5000$ K and density $n = 10^{16} \text{ cm}^{-3}$, with $\sigma_s = 5.67 \times 10^{-5} \text{ erg cm}^2 \text{ s deg}^4$ we get from (24.233) that the shock velocity should be $v_{sh} = 34 \text{ km/s}$. At this parameter one should expect the influence of the radiation flux on the shock parameters.

13.3 We will follow the method described in Sedov (1959). (a) The gas motion is determined only by two dimensional parameters, the energy E , with dimensions m^2/t^2 and the initial density ρ_0 with dimensions m/l^3 . These parameters cannot be combined to yield scales with dimensions of either length or time. The quantity r/t therefore cannot serve as the similarity variable. The only parameter involving dimensions of length and time is E/ρ_0 or some function of it. The flow is headed

by a shock at $r = R(t)$, where $R(t)$ is a shock front. The only possible form of its dependence on time can be given by

$$R(t) = \xi_0 \left(\frac{E}{\rho_0} \right)^{1/5} t^{2/5} \quad (24.234)$$

Here ξ_0 is a dimensionless parameter. The propagation velocity of the shock wave, $U_{\text{sh}} = dR(t)/dt$, is then

$$U_{\text{sh}} = \frac{2}{5} \xi_0^{5/2} \left(\frac{E}{\rho_0} \right)^{1/2} R^{-3/2} \quad (24.235)$$

Using the strong shock relations

$$\rho_1 = \rho_0 \frac{\gamma + 1}{\gamma - 1}, \quad p_1 = \frac{2}{\gamma + 1} \rho_0 u_{\text{sh}}^2, \quad u_1 = \frac{2}{\gamma + 1} u_{\text{sh}} \quad (24.236)$$

we can find the pressure and velocity immediately behind the blast front:

$$p_1 = \frac{8}{25} \frac{\xi_0^5}{\gamma + 1} \frac{E}{R^3}, \quad u_1 = \frac{4}{5} \frac{\xi_0^{5/2}}{\gamma + 1} \left(\frac{E}{\rho_0} \right)^{1/2} \frac{1}{R^{3/2}} \quad (24.237)$$

(b) For the rough estimate we start with the Rankine-Hugoniot relations in a form

$$\frac{\rho_0}{\rho_1} = \frac{u_1}{u_0} = \frac{\gamma - 1}{\gamma + 1} + \frac{2}{(\gamma + 1)M^2} \quad (24.238)$$

where $M = u_0/c_s$ is the Mach number, which in case of a strong explosion will tend to infinity as the background sound speed is infinitely small. For pressure the Rankine-Hugoniot relations are

$$\frac{p_1}{p_0} = \frac{2\gamma M^2}{\gamma + 1} - \frac{\gamma - 1}{\gamma + 1} \quad (24.239)$$

and in the limit of a strong shock we have

$$p_1 \simeq \frac{2\rho_0 u_0^2}{\gamma + 1} \quad (24.240)$$

The estimate for the thermal energy is then

$$E_{\text{therm}} \sim p_1 R^3 \sim \rho_0 v_0^2 R^3 \sim \rho_0 \frac{R^5}{t^2} \quad (24.241)$$

Suggesting that the thermal energy is of the same order as the kinetic energy, for the total energy $E = E_{\text{therm}} + E_{\text{kin}}$, which is a conserved quantity, we have

$$E \sim \rho_0 \frac{R^5}{t^2}, \quad (24.242)$$

which for the radius $R(t)$ gives a familiar expression (24.234):

$$R(t) \sim \left(\frac{E}{\rho_0} \right)^{1/5} t^{2/5}. \quad (24.243)$$

24.13 Problems of Chap. 14

14.1 Consider first the adiabatic shock. Denote the downstream (behind the shock) parameters by 1 and upstream (in front of the shock) by 0. In the frame moving with the shock, the Rankine-Hugoniot relations are given by

$$\rho_0 u_0 = \rho_1 u_1 = j \quad (24.244)$$

$$p_0 + \rho_0 u_0^2 = \rho_1 u_1^2 + p_1 \quad (24.245)$$

$$\frac{1}{2} u_0^2 + \epsilon_0 + \frac{p_0}{\rho_0} = \frac{1}{2} u_1^2 + \epsilon_1 + \frac{p_1}{\rho_1} \quad (24.246)$$

where ϵ is the internal energy. For a polytropic gas $\epsilon = p/\rho(\gamma - 1)$. Using this expression for ϵ , (24.245)–(24.246) become

$$p_1 + \frac{j^2}{\rho_1} = p_0 + \frac{j^2}{\rho_0} \quad (24.247)$$

$$\frac{1}{2} \frac{j^2}{\rho_1^2} + \frac{\gamma}{\gamma - 1} \frac{p_1}{\rho_1} = \frac{1}{2} \frac{j^2}{\rho_0^2} + \frac{\gamma}{\gamma - 1} \frac{p_0}{\rho_0} \quad (24.248)$$

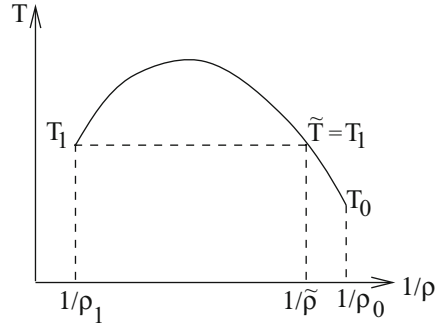
Eliminating j in above equations, one obtains

$$\frac{\rho_1}{\rho_0} = \frac{(\gamma + 1)p_1 + (\gamma - 1)p_0}{(\gamma + 1)p_0 + (\gamma - 1)p_1} \quad (24.249)$$

In the limit of a strong shock, the upstream pressure, p_0 is much smaller than the behind shock pressure $p_0 \ll p_1$, and can be neglected. From (24.249) we then have

$$\frac{\rho_1}{\rho_0} = \frac{\gamma + 1}{\gamma - 1} \quad (24.250)$$

Fig. 24.10 Isothermal jump
(Landau and Lifshitz 1987)



Hence, for $\gamma = 5/3$:

$$\frac{\rho_1}{\rho_0} = 4 \tag{24.251}$$

Thus, we arrived to the well-known result that the compression factor in adiabatic shock is limited by factor 4. Note that $u_1/u_0 = \rho_0/\rho_1$, and upstream density increases by factor 4 (or less), and the velocity falls by the same factor.

In case of an isothermal shock transition from the initial state to final state is considerably different. First, the gas is compressed gradually from the initial density ρ_0 to some density $\bar{\rho}$. This value corresponds to $T(\bar{\rho}) = T_1$. The thickness of this region is determined by thermal conductivity. Further, the compression from $\bar{\rho}$ to ρ_1 occurs discontinuously at the constant temperature T_1 (Fig. 24.10). In the isothermal shock, gas still flows into a shock front for which the Rankine-Hugoniot conditions for mass and momentum flux conservation are the same, but in the energy condition we have to put $T_0 = T_1$. The isothermal sound speed is $c_s^2 = p/\rho$. The conditions isothermality across the discontinuity then give:

$$\frac{p_0}{\rho_0} = \frac{p_1}{\rho_1} = c_s^2 \tag{24.252}$$

With this in mind from (24.244)–(24.245) we get

$$(u_1 - u_0)c_s^2 = u_1 u_0 (u_1 - u_0) \tag{24.253}$$

As $u_1 \neq u_0$, from (24.253) we get

$$\frac{\rho_1}{\rho_0} = \frac{u_0}{u_1} = \left(\frac{u_0}{c_s}\right)^2 = M^2 \tag{24.254}$$

Hence, in an isothermal shock, the shock strength (or compression ratio) is the square of the Mach number of the pre-shocked flow and can be arbitrarily high.

14.2 We follow here Zababakhin and Nechaev (1958). In case of cylindrical symmetry, Maxwell's equations (\mathbf{B} being parallel to the x axis, and \mathbf{E} is circular, are given by

$$\frac{1}{c} \frac{\partial E}{\partial t} = -\frac{\partial B}{\partial r}, \quad \frac{1}{c} \frac{\partial B}{\partial t} = -\frac{1}{r} \frac{\partial(rE)}{\partial r} \quad (24.255)$$

Cross eliminating in these equations B and E , we obtain

$$\frac{1}{c^2} \frac{\partial^2 E}{\partial t^2} - \frac{\partial}{\partial r} \left[\frac{1}{r} \frac{\partial(rE)}{\partial r} \right] = 0 \quad (24.256)$$

$$\frac{1}{c^2} \frac{\partial^2 B}{\partial t^2} - \frac{1}{r} \frac{\partial}{\partial r} \left[r \frac{\partial B}{\partial r} \right] = 0 \quad (24.257)$$

The equation for B is simply the wave equation in the cylindrical symmetry, while the equation for E is not the wave equation. Consider the variation of the cylindrical wave amplitude as it moves towards the axis, treating a wave, as mentioned above, within a cylindrical volume of radius R_{cyl} of an ideal conductor. The total magnetic flux in the cavity is conserved, so that

$$\Phi = 2\pi \int_0^{R_{\text{cyl}}} Br dr = \text{const} \quad (24.258)$$

Differentiating (24.258) twice with respect to time and using (24.257) we obtain the following equation

$$c \left[2R_{\text{sh}} \frac{d(B_{\text{sh}} - B_0)}{dt} - c(B_{\text{sh}} - B_0) \right] + c^2 R_{\text{cyl}} \left. \frac{\partial B}{\partial r} \right|_{\text{cyl}} + \frac{d(B_{\text{cyl}} R_{\text{cyl}} U)}{dt} = 0 \quad (24.259)$$

We used here notations,

$$\frac{dR_{\text{sh}}}{dt} = -c, \quad \frac{dR_{\text{cyl}}}{dt} = -U \quad (24.260)$$

The second and third terms in (24.259) are the quantities at the boundary of region and must vanish:

$$c \left[2R_{\text{sh}} \frac{d(B_{\text{sh}} - B_0)}{dt} - c(B_{\text{sh}} - B_0) \right] = 0, \quad (24.261)$$

which gives

$$B_{\text{sh}} - B_0 = \text{const} \frac{1}{\sqrt{R_{\text{sh}}}} \quad (24.262)$$

Hence the amplitude of the converging cylindrical wave increases without bound as $R_{\text{sh}}^{-1/2}$.

Although we obtained this result for the special case of a wave within a cavity in an ideal conductor, the result is valid for any cylindrical shock wave. Since waves from the surface of the cylinder do not catch up with the shock wave, the wave amplitude on the front is determined entirely by its magnitude (i.e., the initial amplitude at the point at which the wave is formed) and is independent of other field changes on the boundary of the cylinder. On the cylindrical wave front $E_{\text{sh}} - E_0$ also changes according to

$$E_{\text{sh}} - E_0 = \text{const} \frac{1}{\sqrt{R_{\text{sh}}}} \quad (24.263)$$

Note that (24.262) and (24.263) are not approximations valid only for large or small amplitudes; they describe the behavior of a field with the same accuracy as do Maxwell equations.

Finally, the qualitative property of cylindrical cumulation is not only characteristic property of the electromagnetic waves, but it is also a general property of converging cylindrical waves described by any wave equation. It is interesting that for a spherical acoustical wave one may obtain a solution without the assumption that it is self-similar (Zel'dovich and Raizer 1967).

24.14 Problems of Chap. 15

15.1 The finite amplitude Alfvén waves propagating along the uniform magnetic field are described by the derivative nonlinear Schrödinger equation (DNLS)

$$i \frac{\partial \psi}{\partial \tau} - \frac{\partial^2 \psi}{\partial \xi^2} + i \frac{\partial}{\partial \xi} (|\psi|^2 \psi) = 0 \quad (24.264)$$

where ψ is defined as

$$\psi = \frac{1}{2B_0} (B_y + i B_z) \quad (24.265)$$

and the coordinates (ξ, τ) are related to the space and time coordinates (x, t) by

$$\xi = 2 \frac{x - v_A t}{d}, \quad \tau = 2\omega_i t \quad (24.266)$$

where v_A is the Alfvén velocity, ω_i is the ion gyro frequency, and $d = v_A/\omega_i$. It is assumed that waves are propagating along the x -axis.

Let us express the complex function $\psi(\xi, \tau)$ in terms of a real amplitude and a phase

$$\psi(\xi, \tau) = b(\xi, \tau)\exp[i\phi(\xi, \tau)] \quad (24.267)$$

so that the derivative nonlinear Schrödinger equation (24.264) is decomposed into a pair of equations

$$b\phi_\tau = -b_{\xi\xi\xi} + b\phi_\xi^2 - b^3\phi_\xi \quad (24.268)$$

$$b_\tau = 2b_\xi\phi_\xi + b\phi_{\xi\xi} - 3b^2b_\xi \quad (24.269)$$

where the suffixes indicate a partial derivative with respect to the variables. Introducing a moving coordinate

$$z = \xi - u\tau \quad (24.270)$$

we search a solution of the form

$$b(\xi, \tau) = b(z) \quad (24.271)$$

$$\phi(\xi, \tau) = K\xi - \Omega\tau + \theta(z) \quad (24.272)$$

in which the nonlinear amplitude $b(z)$ and phase modulation $\theta(z)$ are subject to the boundary conditions at $z \rightarrow +\infty$

$$\frac{db}{dz} = \frac{d^2b}{dz^2} = 0, \quad \frac{d\theta}{dz} = 0 \quad (24.273)$$

Now, (24.268) for the phase can be integrated to give

$$\frac{d\theta}{dz} = -\frac{1}{2}(u + 2K) + \frac{3}{4}b^2, \quad (24.274)$$

which leads to the nonlinear phase modulation. This equation and the boundary condition $b = 0$ at $z \rightarrow +\infty$ determine the arbitrary velocity to be

$$u = -2K. \quad (24.275)$$

Substituting (24.274) and (24.275) back into the equation for the real amplitude b , (24.269), and carry out integration, one obtains

$$b^2 = \frac{4(\Omega + K^2)}{\sqrt{\Omega + 2K^2}\cosh(z/\Delta) + K} \quad (24.276)$$

which is a stationary Alfvén soliton with the width given by

$$\Delta = \frac{1}{2\sqrt{\Omega + K^2}} \tag{24.277}$$

It is important to note that the wavenumber K may be either positive or negative. The positive sign, $K > 0$ corresponds to the bright soliton (\cap -shaped kink), and $K < 0$ corresponds to the dark soliton (\cup -shaped kink). The bright and dark solitons behave differently as the width parameter $\gamma = \sqrt{\Omega + K^2}$ tends to zero. For bright solitons, the amplitude and energy tend to zero as $\gamma \rightarrow 0$, while for the dark solitons the energy tends to a finite limit.

As an illustration of some properties of Alfvén solitons it is instructive to demonstrate the evolution of the Alfvén solitons for a given shape of an initial pulse. Take for example:

$$\psi(\xi, \tau = 0) = A_0 \operatorname{sech}(\xi/D) \exp i K_0 \xi \tag{24.278}$$

where D is the width of the initial pulse. The Alfvén solitons may be decomposed into a series of solitons whose number is found to be (Ichikawa and Abe 1988, see also Mjølhus and Wyller 1986):

$$N = \frac{1}{2\sqrt{2}} D \psi_0 \sqrt{K_0} + \frac{1}{4} \tag{24.279}$$

Note that the number of solitons depends on the width of the initial pulse D , although it does not play a crucial role in the conservation laws. In Fig. 24.11 the initial pulse is shown in graphical (left panel) and its three-dimensional view. For chosen parameters, Fig. 24.12 illustrates three solitons decomposed from the initial pulse of Fig. 24.11 at the time $\tau = 2$.

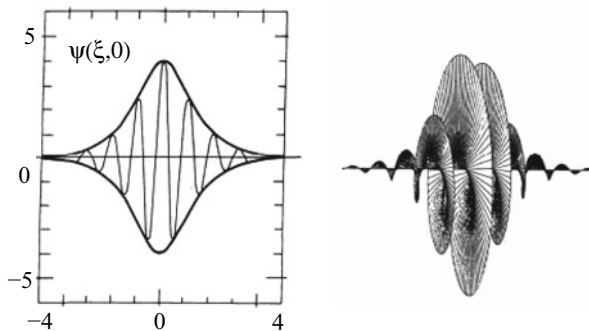


Fig. 24.11 The initial pulse with $\psi_0 = 4$, $K_0 = 6$, and $D = 1$. Left: graphical image, right: 3D image (Ichikawa and Abe 1988)

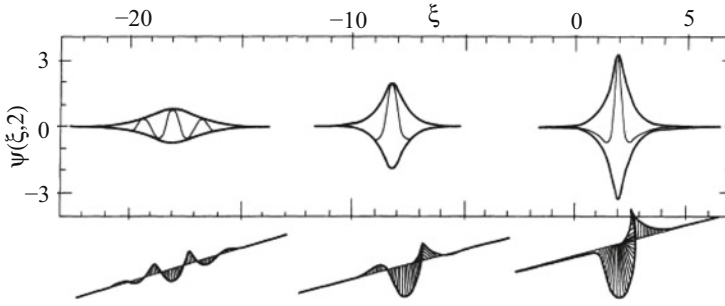


Fig. 24.12 Three solitons at $\tau = 2$, evolved out of the initial pulse shown in Fig. 24.11

15.2 (a) First we consider the magnetic braids with an “infinite” curvature, $R \simeq \infty$. In other words we deal with the magnetic braid whose radius of curvature is much larger than the radius of its cross section, $a: R \gg a$. The force acting along the radius of curvature is given by (Shafranov 1966)

$$F_R = -\frac{V}{R} \left\{ P_{\text{ex}} - \bar{P}_{\text{in}} - \frac{B_{\phi, \text{ex}}^2(a)}{4\pi} \left[\ln \frac{8R}{a} - 1 - \frac{1}{2} \frac{B_{\phi, \text{in}}^2}{B_{\phi, \text{ex}}^2(a)} \right] + \frac{\bar{B}_{z, \text{in}}^2}{8\pi} \right\} \quad (24.280)$$

Here V is the volume of a structure. As $B_{\phi, \text{ex}} \simeq 1/r$ we may assume that $B_{\phi, \text{ex}} \rightarrow 0$. A bar denotes the average value of magnetic field components. Rearranging (24.280) we may write for the force acting along the radius of curvature (per unit volume)

$$f_R = -\frac{1}{R} \frac{\bar{B}_{z, \text{in}}^2}{8\pi} \left(2 - \frac{\bar{B}_{\phi, \text{in}}^2}{B_{\phi, \text{in}}^2(a)} \right) = -\frac{1}{R} \frac{\bar{B}_{z, \text{in}}^2}{8\pi} (2 - \kappa) \quad (24.281)$$

For very long magnetic loops with $R \simeq \infty$, we may replace R by the length of the rope, l

$$f_l = -\frac{1}{l} \frac{\bar{B}_{z, \text{in}}^2}{8\pi} (2 - \kappa) \quad (24.282)$$

We see that for a long loops there is only one equilibrium state with respect to l in which $f_l = 0: \kappa = 0$. Let us investigate its stability with respect to small perturbations:

$$\delta f_l = (\kappa_0 - 2) \delta \left(\frac{\bar{B}_{z, \text{in}}^2}{8\pi l} \right) + \left(\frac{\bar{B}_{z, \text{in}}^2}{8\pi l} \right)_0 \delta \kappa \quad (24.283)$$

or

$$\delta f_l = \frac{1}{l_0} \frac{\bar{B}_{z,0}^2}{8\pi} \left(\frac{\partial \kappa}{\partial l} \right)_0 \delta l \quad (24.284)$$

From this it follows that the general condition for stability of a magnetic braid can be written in the form

$$\left(\frac{\partial \kappa}{\partial l} \right)_0 < 0 \quad (24.285)$$

Using the definition of κ and the equilibrium condition

$$\bar{B}_z^2 = 8\pi(P_{\text{tot}} - \bar{P}), \quad (24.286)$$

where $P_{\text{tot}} = P + B^2/8\pi$ is the total pressure and \bar{P} is the cross-sectional average of gas-kinetic pressure in the braid, we can write the inequality (24.285) as follows:

$$\left[\frac{\partial}{\partial l} \left(\frac{\bar{B}_\phi^2}{P_{\text{tot}} - \bar{P}} \right) \right] < 0. \quad (24.287)$$

(b) To investigate the stability criterion for some given case one should know all the quantities entering in the above condition, i.e., \bar{B}_ϕ^2 , P_{tot} , \bar{P} which may vary in quite a complex ways.

As an example let us consider the Alfvén model of a magnetic braid (Alfvén and Falthammar 1963). If a magnetic flux tube of length l and radius a is twisted at one end through the angle ϕ , then the azimuthal field is created of a strength

$$B_\phi(r) = \frac{r\phi}{l} B_z \quad (24.288)$$

Here B_z does not depend on r . For such braid the twisting index is

$$\kappa = \frac{\phi^2}{2} \left(\frac{a}{l} \right)^2. \quad (24.289)$$

The flux of azimuthal field is given by

$$\Phi_\phi = l \int_0^a B_\phi dr = \frac{\phi}{2} B_z a^2 \equiv \frac{\phi}{2\pi} \Phi_z \quad (24.290)$$

where $\Phi_z = B_z \pi a^2$ is the flux of longitudinal field. If the magnetic field fluxes in braid are conserved, then obviously $\phi = \text{const}$. Let the external medium be homogeneous, $P_{\text{tot}} = \text{const}$. Then with (24.286) we have

$$\delta P_m = -\delta \bar{P}, \quad (24.291)$$

where $P_m = \bar{B}_z^2/8\pi$. Assuming a polytropic law, $\bar{P}V^n = \text{const}$, from (24.288)–(24.291) one finds

$$\frac{\delta l}{l} = -\frac{\delta a}{a} \left(2 + 4P_m \frac{P_m}{\bar{P}} \right) \quad (24.292)$$

Now, since

$$\delta\kappa = \phi^2 \frac{a^2}{l^2} \left(\frac{\delta a}{a} - \frac{\delta l}{l} \right), \quad (24.293)$$

we find that $\delta\kappa < 0$ for $\delta l > 0$, i.e., the system is stable. For magnetic braiding in laboratory and space plasmas see e.g. Stix 1973; Berger et al. 2015; Pontin et al. 2016.

24.15 Problems of Chap. 16

16.1 Consider a circularly polarized transverse wave in a uniform plasma and uniform magnetic field $(0, 0, B_0)$ described by the vector potential

$$\mathbf{A} = (A, iA, 0)\exp[i(kz - \omega t)] \quad (24.294)$$

where ω is real and $k = k_0(\omega) + ik_1(\omega)$. The helicity density associated with the wave is

$$H_\omega = \langle \mathbf{A} \cdot \mathbf{B} \rangle = k_0 A^2 \exp(-2k_1 z) \quad (24.295)$$

For a simple viscous fluid the Ohm's law reads $\mathbf{E} + \mathbf{v} \times \mathbf{B} = \eta \mathbf{J}$. Then for the wave equations we have

$$-\omega \mathbf{B} = (kB_0)\mathbf{v} + i\eta k^2 \mathbf{B} \quad (24.296)$$

$$-\omega \rho \mathbf{v} = (kB_0)\mathbf{B} + i\rho \mu k^2 \mathbf{v} \quad (24.297)$$

where η and μ are the resistivity and viscous coefficients, respectively. The corresponding dispersion equation is

$$(\omega + i\eta k^2)(\omega + i\mu k^2) = k^2 v_A^2 \quad (24.298)$$

When η and μ are small, $k_0 \simeq \omega/v_A$ and the wave damping is given by

$$k_1 = (\eta + \mu) \frac{k_0^2}{2v_A} \quad (24.299)$$

The mean current induced by the wave can be calculated directly from Ohm's law:

$$\eta \langle j_z \rangle = \langle \mathbf{v} \times \mathbf{B} \rangle, \quad (24.300)$$

and if we use (24.296), which itself follows from Ohm's law, we can express \mathbf{v} in terms of \mathbf{B} . Then we have

$$\eta \langle j_z \rangle = (\omega k_1 - \eta |k|^2 k_0) \frac{A^2(z)}{B_0} \quad (24.301)$$

In (24.301), any non-resistive damping appears only through k_1 . Using the value of k_1 given by (24.299) we obtain the expression for the wave-driven current:

$$\eta j_\omega = \frac{k_0 A^2(z)}{B_0} \frac{(\mu - \eta) k_0^2}{2}. \quad (24.302)$$

The helicity balance equation becomes

$$-v_A \frac{\partial H_\omega}{\partial z} = 2\eta \langle j_z \rangle B_0 + 2\eta \langle j_\omega \cdot B_\omega \rangle \quad (24.303)$$

Here, the input of helicity by the wave is

$$-v_A \frac{\partial H_\omega}{\partial z} = 2k_1 v_A H_\omega = (\eta + \mu) k_0^2 H_\omega \quad (24.304)$$

while the helicity dissipated by the fluctuating currents is

$$2\eta \langle j_z \rangle B_0 = (\mu - \eta) k_0^2 H_\omega, \quad (24.305)$$

which fully agrees with (24.302).

These results show that the current driven by wave absorption is not directly related to the helicity input. Other sources of helicity loss must be accounted for. In the present example, current drive depends on the difference between viscous and resistive damping, whereas helicity input depends on their sum. The balance is made up by the helicity lost in fluctuating currents.

It is remarkable that, if only resistivity is important, the loss through fluctuations is exactly twice the input and the helicity dissipated in the current drive is equal in magnitude but opposite in sign to the helicity input. See Taylor (1989).

16.2 Consider the elementary LC network shown in Fig. 24.13 with linear inductors L and nonlinear capacitors $C(V)$ Remoissenet (1999). The equations for current and voltage for each element (including dispersion) are given by

$$L \frac{dI_n}{dt} = V_{n-1} - V_n, \quad C \frac{dV_n}{dt} = I_{n-1} - I_n \quad (24.306)$$

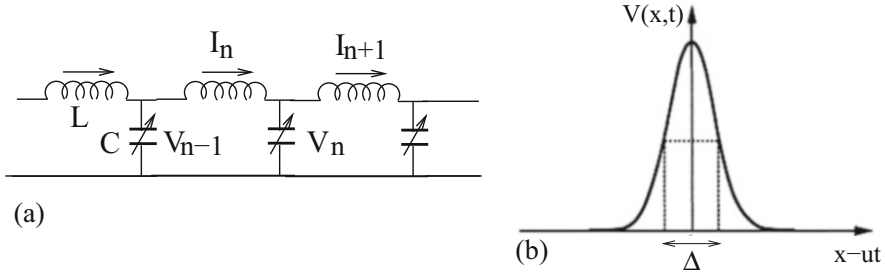


Fig. 24.13 Soliton in the equivalent circuit: (a) Equivalent network circuit with linear inductance L and nonlinear capacitance $C(V_n)$ in each unit section; (b) sketch of the soliton solution $V(x, t)$ given by (24.313) traveling with velocity u

These equations reduce to the following equation

$$\frac{d^2 V_n}{dt^2} = \frac{1}{LC} (V_{n+1} + V_{n-1} - 2V_n) \tag{24.307}$$

let us consider the effect of nonlinearity (ignoring first the dispersion). Now the equations for current and voltage become

$$L \frac{\partial I}{\partial t} = -\frac{\partial V}{\partial x}, \quad C(V) \frac{\partial V}{\partial t} = -\frac{\partial I}{\partial x} \tag{24.308}$$

Expanding the capacitance in V ,

$$C(V) = C_0(1 + a_1 V + a_2 V^2 + \dots) \tag{24.309}$$

we can approximate the capacitance-voltage as follows:

$$C(V_n) = C_0(1 - 2bV_n), \quad b \equiv -2a_1 \tag{24.310}$$

With this we find that

$$LC_0 \frac{\partial^2 V}{\partial t^2} - LC_0 b \frac{\partial^2 V}{\partial t^2} = V_{n+1} + V_{n-1} - 2V_n, \quad n = 1, 2, \dots \tag{24.311}$$

To get approximate solutions, it is convenient to employ the continuum limit and set $x = n\delta$. Combining now (24.307)–(24.311) after a simple algebra we get

$$\frac{\partial^2 V}{\partial t^2} - \frac{\delta^2}{LC_0} \frac{\partial^2 V}{\partial x^2} = \frac{1}{12} \frac{\delta^4}{LC_0} \frac{\partial^4 V}{\partial x^4} + b \frac{\partial^2 V}{\partial t^2} \tag{24.312}$$

This is weakly dispersive, nonlinear wave equation. It describes waves that can travel both to the left and to the right. To order of δ^2 it is just a linear wave equation.

If the nonlinear term is balanced by the dispersive term the solution will be a solitary wave which propagates with constant velocity u . Setting $u_0 = \delta/\sqrt{LC}$, we have:

$$V = \frac{3}{2b} \frac{u^2 - u_0^2}{u^2} \operatorname{sech}^2 \left[\frac{\sqrt{3(u^2 - u_0^2)}}{u_0} \left(n - \frac{ut}{\delta} \right) \right] \quad (24.313)$$

Note that $(n - ut/\delta) = (x - ut)/\delta$. The amplitude of the soliton is given by

$$V_m = \frac{3}{2b} \frac{u^2 - u_0^2}{u^2} \quad (24.314)$$

Let us now find a width of a soliton, Δ , which is defined as a width of pulse at half height, $V_m/2$. Assuming that at $t = 0$ and $x/\delta = \Delta/2$, we have

$$V \left(\frac{\Delta}{2}, 0 \right) = V_m \operatorname{sech}^2 \left(\frac{\sqrt{3(u^2 - u_0^2)}}{u_0} \frac{\Delta}{2} \right) = \frac{V_m}{2} \quad (24.315)$$

Substituting here V_m and evaluating $\operatorname{sech}^{-1}(1/\sqrt{2}) = 0.88$ we obtain

$$\Delta \simeq \frac{u_0}{\sqrt{u^2 - u_0^2}}. \quad (24.316)$$

24.16 Problems of Chap. 17

17.1 The plasma equilibrium is described by magnetostatic equations

$$\nabla \times \mathbf{B} = \frac{4\pi}{c} \mathbf{j} \quad (24.317)$$

$$\nabla p = \frac{1}{c} [\mathbf{j} \times \mathbf{B}] \quad (24.318)$$

For the chosen geometry we obtain

$$-\frac{\partial p}{\partial r} = \frac{1}{c} (j_z B_\phi - j_\phi B_z) \quad (24.319)$$

or

$$-\frac{\partial p}{\partial r} = B_\phi \frac{\partial r B_\phi}{r \partial r} + B_z \frac{\partial B_z}{\partial r} \quad (24.320)$$

Let us multiply (24.320) by r^2 and integrate with respect to r from 0 to expected pinch radius R . Taking into account that at the surface of the pinch $p(R) = 0$ and $B_\phi(R) = 2J/cR$, where J is the total current, we obtain the equilibrium condition for the pinch in the following integral form (Braginskii and Shafranov 1959):

$$2c^2(n_e \bar{T}_e + n_i \bar{T}_i) = J^2 + \frac{c^2 R^2}{4} [B^2(R) - \bar{B}_z^2], \quad (24.321)$$

where n_e and n_i are the number of electrons and ions per unit length of the pinch, \bar{T}_e and \bar{T}_i are the mean temperatures, and

$$\bar{B}_z^2 = \frac{1}{\pi R^2} \int_0^R B_z^2 2\pi r dr \quad (24.322)$$

We may now conclude that the “self-magnetic” field associated with the current J always acts toward pinching the plasma column. The longitudinal magnetic field squeezes the plasma only if the external field is smaller than the internal field.

17.2 If the magnetic field has only z -component, current flows in θ direction and crossed with axial magnetic field can balance a radial pressure gradient. Such configuration is known as θ -pinch. In this case from (24.317)–(24.318) we have

$$\frac{dB_z}{dr} = \frac{4\pi}{c} j_\theta \quad (24.323)$$

and

$$\frac{d}{dr} \left(p + \frac{B_z^2}{8\pi} \right) = 0 \quad (24.324)$$

Thus, total pressure $P = (p + B^2/8\pi)$ is constant for any radial profile of gas-kinetic and magnetic pressure, $p + B^2/8\pi = \text{const}$. The θ -pinch provides a strong stability to plasma column with some restrictions on plasma parameters. One can find the current that holds the plasma column in equilibrium. Indeed, taking cross product of (24.318) and \mathbf{B} ,

$$\nabla p \times \mathbf{B} = \frac{1}{c} [\mathbf{j} \times \mathbf{B} \times \mathbf{B}], \quad (24.325)$$

one obtains

$$j_\theta = \frac{c}{B_z} \frac{dp}{dr} \quad (24.326)$$

This is diamagnetic current generated automatically by the pressure gradient and by the non-uniform spatial distribution of the magnetic moments of the electrons and ions.

17.3 In this case (24.317)–(24.318) give

$$\frac{1}{r} \frac{d}{dr}(r B_\theta) = \frac{4\pi}{c} j_z \quad (24.327)$$

and

$$\frac{dp}{dr} = -\frac{1}{4\pi} \frac{B_\theta}{r} \frac{d}{dr}(r B_\theta) \quad (24.328)$$

Let us integrate these equations over the flux tube cross section. From (24.327) we obtain

$$\int_0^R \frac{1}{r} \frac{d}{dr}(r B_\theta) 2\pi r dr = \frac{4\pi}{c} \int_0^R r j_z 2\pi r dr \quad (24.329)$$

or

$$B_\theta(R) = \frac{2\pi}{c} \bar{j}_z R \quad (24.330)$$

where \bar{j}_z is the average value of current across the flux tube. Multiplying now (24.328) by r and integrating one obtains

$$\int_0^R \frac{dp}{dr} r^2 dr = -\frac{1}{4\pi} \int_0^R r B_\theta \frac{d}{dr}(r B_\theta) dr \quad (24.331)$$

or

$$\bar{p} = \frac{1}{8\pi} B_\theta^2(R) \quad (24.332)$$

where we again used the average value of pressure, \bar{p} , across the flux tube. Equations (24.330) and (24.332) determine the radius of z -pinch:

$$R^2 = \frac{2c^2}{\pi} \frac{\bar{p}^2}{\bar{j}_z^2} \quad (24.333)$$

which shows that the higher the current, the stronger is pinching effect.

17.4 In this case the flux tube acquires screw pinch configuration, which is a combination of θ and z pinches. Equations (24.317)–(24.318) now become

$$j_\theta = -\frac{c}{4\pi} \frac{dB_z}{dr}, \quad j_z = -\frac{c}{4\pi} \frac{1}{r} \frac{d}{dr} r B_\theta \quad (24.334)$$

$$\frac{dp}{dr} = \frac{1}{c} (j_\theta B_z - j_z B_\theta) \quad (24.335)$$

Combining (24.334) and (24.335) we obtain

$$\frac{d}{dr} \left(p + \frac{B_\theta^2 + B_z^2}{8\pi} \right) + \frac{1}{4\pi} \frac{B_\theta^2}{r} = 0 \quad (24.336)$$

Magnetic field lines are now helices of radius r with the trajectories

$$\frac{dr}{dz} = \frac{B_r(r)}{B_z(r)} = 0, \quad \frac{d\theta}{dz} = \frac{B_\theta(r)}{r B_z(r)} = 0 \quad (24.337)$$

When magnetic field line makes one revolution, $\Delta z = 2\pi\lambda$, the change in angle $\Delta\theta$, i.e., the pitch angle is

$$\Delta\theta = \int_0^{\Delta\theta} d\theta = \int_0^{2\pi\lambda} \frac{d\theta}{dz} dz \quad (24.338)$$

or

$$\Delta\theta = \frac{r B_z(r)}{2\pi\lambda B_\theta} \quad (24.339)$$

A “measure of twist,” $q = 2\pi \Delta\theta(r)$, called the safety factor, is expressed as

$$q(r) = \frac{r B_z(r)}{2\pi\lambda B_\theta} \quad (24.340)$$

The safety factor plays an important role in laboratory devices and space plasmas. The most important feature of q is that the magnetic flux tube or torus is stable with respect to screw pinch instability if $q > 1$. On the other hand, at $q < 1$, the plasma column inevitably takes the form of screw pinch configuration (Kruskal-Shafranov limit). In solar atmosphere and space plasmas, magnetic flux tube being thin long filaments is always twisted.

24.17 Problems of Chap. 18

18.1 Assume that the body creating a bow shock has a radius of curvature R_b , and that the bow shock is also in a shape of a circular cylinder with radius R_{sh} (24.341). In two-dimensional cylindrical coordinates R and ϕ with axis $\phi = 0$ directed upstream, the outward mass flow can be expressed through the stream function ψ (Hayes and Probst 1966):

$$\rho U v_r = \frac{\partial \psi}{\partial r} \quad (24.341)$$

$$\rho U v_\phi = -\frac{1}{r} \frac{\partial \psi}{\partial \phi} \quad (24.342)$$

where U is the shock velocity. The stream function immediately behind the shock equals to that immediately in front of it, and we have the condition:

$$\psi_{sh} = \rho_\infty U R_{sh} \sin \phi. \quad (24.343)$$

Here ρ_∞ is the gas density ahead (upstream of) of the shock. The vorticity, $\zeta = \partial v_x / \partial y - \partial v_y / \partial x$ immediately behind the shock (in polar coordinates) is given by

$$\zeta_{sh} = -\frac{U(1-\epsilon)^2 \sin \phi}{\epsilon R_{sh}} \quad (24.344)$$

where $\epsilon = \rho_\infty / \rho_{sh}$ is the density ratio across the shock, which in terms of Mach number is given by (18.12). Since in a steady two-dimensional flow with constant density the vorticity is a function of the stream function alone, we may write

$$\zeta = -\frac{(1-\epsilon)^2}{\epsilon \rho_\infty R_{sh}^2} \psi \quad (24.345)$$

Note that the vorticity ζ must be zero if ψ is zero, and will be zero at the surface of the body.

The stream function satisfies the equation

$$\frac{\partial^2 \psi}{\partial r^2} + \frac{1}{r} \frac{\partial \psi}{\partial r} + \frac{1}{r^2} \frac{\partial^2 \psi}{\partial \phi^2} = \frac{(1-\epsilon)^2}{\epsilon R_{sh}^2} \psi \quad (24.346)$$

One can see from (24.343) that ψ should be a function of $R \sin \phi$. The corresponding general solution may be expressed as follows:

$$\psi = \frac{1}{\epsilon} \rho_\infty U R_{sh} \sin \phi [A I_1(kR) + B K_1(kR)], \quad (24.347)$$

where $I_1(kR)$ and $K_1(kR)$ are modified Bessel functions of the first order, and the parameter k is

$$k = \frac{1 - \epsilon}{\epsilon R_{\text{sh}}} \quad (24.348)$$

The boundary condition on the velocity component normal to the shock is equivalent to (24.343), and the condition on the tangent component (24.341) is

$$\psi_{R_{\text{sh}}} = \frac{1}{\epsilon} \rho_{\infty} U \sin \phi. \quad (24.349)$$

The two boundary conditions (24.343) and (24.349) give

$$A I_1(k R_{\text{sh}}) + B K_1(k R_{\text{sh}}) = \epsilon, \quad A I_1'(k R_{\text{sh}}) + B K_1'(k R_{\text{sh}}) = \frac{\epsilon}{1 - \epsilon}, \quad (24.350)$$

from which the constants A and B may be evaluated:

$$A = K_1 \left(\frac{1 - \epsilon}{\epsilon} \right) - (1 - \epsilon) K_1' \left(\frac{1 - \epsilon}{\epsilon} \right) \quad (24.351)$$

$$B = (1 - \epsilon) I_1' \left(\frac{1 - \epsilon}{\epsilon} \right) - I_1 \left(\frac{1 - \epsilon}{\epsilon} \right) \quad (24.352)$$

The boundary condition and the standoff distance are determined from a condition on the body where $\psi = 0$, which as seen from Fig. 24.14 occurs on the splitting streamline and on the radius R_b , where

$$A I_1(k R_b) + B K_1(k R_b) = 0 \quad (24.353)$$

Fig. 24.14 Geometry of the bow shock formation in front of a cylindrical body

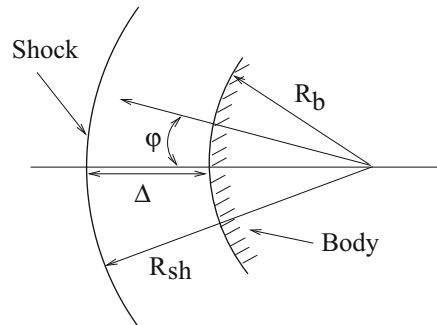
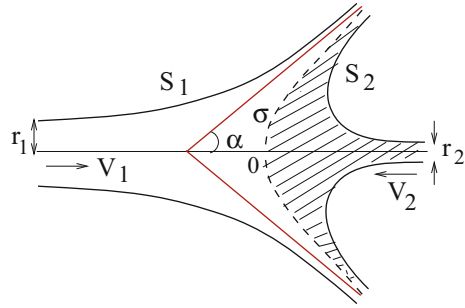


Fig. 24.15 Formation of cumulative jet, akin shaped charge



The approximate solution for small ϵ , i.e. for

$$\epsilon = \frac{2 + (\gamma - 1)M^2}{(\gamma + 1)M^2} < 1, \tag{24.354}$$

the expression for the standoff distance, Δ , is obtained using the asymptotic expansion of the Bessel function which gives:

$$\Delta = R_{sh} - R_b = \frac{1}{2}\epsilon R_{sh} \left[\ln \frac{4}{3\epsilon} + \epsilon \ln \frac{4}{3\epsilon} + O\left(\epsilon^2 \ln \frac{1}{\epsilon}\right) \right]. \tag{24.355}$$

18.2 Statement of the problem is illustrated in Fig. 24.15 (Lavrent'ev 1957). Two jets are moving along the x -axis (line of symmetry). The jet moving from left to right (i.e., from $-\infty$) with velocity V_1 has density ρ_1 and diameter $2r_1$. The jet moving from right to left (i.e., from ∞) has density ρ_2 and diameter $2r_2$, and it has the same velocity, V_1 .

Mass flows shown in Fig. 24.15 have free surfaces S_1 and S_2 . On the separation surface σ the pressure must be continuous

$$\rho_1 V_1^2 = \rho_2 V_2^2 \tag{24.356}$$

Thus the velocity along the surface S_2 is given by

$$V_2 = \sqrt{\frac{\rho_1}{\rho_2}} V_1 \tag{24.357}$$

From the existence of an asymptotic cone (marked by red line in Fig. 24.15) and the conservation of momentum, one can obtain an important relationship between the diameters of the flows, their densities, and the angle α . Indeed, consider two unit lengths of the jet elements in direction $\pm\infty$; their total momentum will be directed along the x axis and is given by

$$J_1 = \pi[\rho_1 r_1^2 V_1 - \rho_2 r_2^2 V_2] \tag{24.358}$$

These elements after collision and a sufficiently long time will be near the asymptotic cone, and projection of their momentum on the axis x will be

$$J_2 = \pi[\rho_1 r_1^2 V_1 + \rho_2 r_2^2 V_2] \cos \alpha \quad (24.359)$$

Due to the momentum conservation, $J_1 = J_2$, we have

$$\cos \alpha = \frac{1 - \eta k^2}{1 + \eta k^2}, \quad k^2 = \frac{1}{\eta} \frac{1 - \cos \alpha}{1 + \cos \alpha} \quad (24.360)$$

where

$$\eta = \sqrt{\frac{\rho_2}{\rho_1}}, \quad k = \frac{r_2}{r_1} \quad (24.361)$$

Let us now consider the collision of two jets in a moving coordinate system with respect to which a thick, left jet is stationary. In this coordinate system, the velocity of the right moving jet will be

$$v = V_1 + V_2 = (1 + \eta) V_2 \quad (24.362)$$

The velocity of the collision line will at the same time be the velocity of penetration (i.e., the velocity of the shaped charge). Denoting it by u , we have

$$u = V_1 = \eta V_2 = \frac{\eta}{1 + \eta} v \quad (24.363)$$

One can see that the penetration velocity is always less than the velocity of the jet. From (24.363) also follows important fact: if some fixed cross section of the jet advances on length l , the shaped charge will penetrate through the distance l_j :

$$l_j = l \frac{u}{v} = \eta L_2 \quad (24.364)$$

Let us now establish dependence of the velocity of penetrating jet on the apex half-angle α . To do so we choose a new coordinate system in which the cone moves along its normal to its surface. In such a system the observer will be moving from right to left with the velocity $V/\cos \alpha$. In new coordinate system the conical veil moves along its normal to its surface with the velocity $v_0 = V \tan \alpha$. Then the velocity of the cumulative jet is given by

$$u = V + \frac{V}{\cos \alpha} = V \frac{1 + \cos \alpha}{\cos \alpha} \quad (24.365)$$

This expression shows that at small angles α one may get jets with very high velocities.

24.18 Problems of Chap. 19

19.1 Consider two rasters with different periods (say two combs with different number of teeth per unit length Kadomtsev (1982)). Let the wave numbers of these rasters (related to the main harmonics) be equal to k_1 and k_2 , respectively. Now, if you cast scattered light on them, then at some distance x from each raster the intensity modulation over the angle θ will obviously have a form

$$\Gamma_0(\theta) = e^{iky+ik\theta x} f(\theta) \tag{24.366}$$

where $k = k_1$ or $k = k_2$, and $f(\theta)$ is the distribution of light in front of rasters (Fig. 24.16).

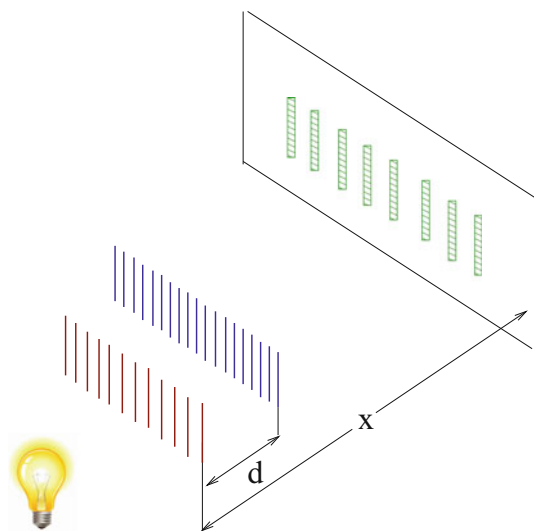
As we move away from the raster, the shadow from it will be more and more blurred as the distribution of intensity of light, that is proportional to $\Gamma(\theta)$, will approach the uniform distribution, due to spreading over the angle. But if we make rasters parallel to each other and place them on the distance d between them so that the shadow from one raster falls on the other, then the distribution of intensity of light will be given by

$$\Gamma = \int e^{ik_1y+ik_1\theta x \pm [ik_2y+ik_2\theta(x-d)]} f(\theta)d\theta \tag{24.367}$$

(24.367) shows that at the distance

$$x_{\text{echo}} = \frac{k_2d}{k_2 - k_1} \tag{24.368}$$

Fig. 24.16 Echo effect produced by scattered light



from the first raster, the exponent in the integrand becomes independent on θ . While on the screen there appears a clear moiré on the wavenumber difference $k_2 - k_1$. As one can see from (24.368), the echo effect arises in this problem only if $k_2 > k_1$.

19.2 We assume that the background electron distribution $f_{e0}(v)$ is stable within the contest of a linear Landau analysis. Suppose that at some instant τ_1 an external pulse with potential

$$\phi_1^{\text{ext}}(x, t) = \Phi_1 \cos(k_1 x) \delta[\omega_{pe}(t - \tau_1)] \quad (24.369)$$

is applied to the plasma, where $k_1 > 0$, ω_{pe} is the electron plasma frequency, and $\Phi_1 = \text{const}$. Since $f_{e0}(v)$ is stable, the electric field excited in the plasma by $\phi_1^{\text{ext}}(x, t)$ Landau-damps and is negligibly small after a damping time $1/|\gamma_{k_1}|$. The electron distribution function, however, is left with a first-order free-streaming modulation of the form

$$F_1(k_1, v) \exp\{\pm i k_1 (x - v[t - \tau_1])\}. \quad (24.370)$$

The free-streaming modulation has no electric field associated with it for large t since the velocity integral of (24.370) phase-mixes to zero. After the electric field associated with the first pulse has Landau-damped, we apply a *second pulse* at time τ_2 of the form

$$\phi_2^{\text{ext}}(x, t) = \Phi_2 \cos(k_2 x) \delta[\omega_{pe}(t - \tau_2)] \quad (24.371)$$

where $\tau_2 - \tau_1 \gg 1/|\gamma_{k_1}|$. The electric field associated with $\phi_2^{\text{ext}}(x, t)$ Landau-damps as in the case of the first pulse, leaving the zero-order electron distribution with a free-streaming modulation of the form

$$F_2(k_2, v) \exp\{\pm i k_2 (x - v[t - \tau_2])\}. \quad (24.372)$$

In addition, the second pulse modulates the free streaming perturbation from the first pulse, giving second-order contributions to the distribution function which includes terms of the form

$$F_1(k_1, v) F_2(k_2, v) \exp\{\pm i [(k_2 - k_1)x - k_2 v[t - \tau_2] + k_1 v[t - \tau_1]]\}. \quad (24.373)$$

for $t > \tau_2$. The velocity integral of above expression phase-mixes to zero except when the coefficient of v in the exponential is near zero. Provided $k_2 > k_1$, this occurs at a time $t \simeq \tau' > \tau_2$, where τ' is the *echo time*,

$$\tau' \equiv [k_1 / (k_2 - k_1)] (\tau_2 - \tau_1) + \tau_2. \quad (24.374)$$

At this time, a second-order electric field, i.e., echo, is generated in the plasma. Here we have a temporal echo. The above arguments may of course be extended to the case of spatial plasma wave echo, as well as to the spatio-temporal echo. See Davidson (1972).

19.3 Consider for illustration the following example. Suppose that there are two sources in a plasma separated by a distance L , generating transverse oscillations of frequencies ω_1 and ω_2 , with the fluctuations in the magnetic field having amplitudes B_1 and B_2 .

If plasma with an electron density n_e contains a certain amount of super-thermal particles with a density n_{th} , such that their mean free path is much larger than the distance between the sources, one should expect occurrence of the following effect. Fast particles traversing regions of both magnetic fields will be modulated by the oscillations. If the transit time of particles is short, there will be no “uncoupling” of phases and the particles will “remember” both modulations. As a result, at a distance

$$L_{echo} = \frac{L\omega_1}{\omega_2 - \omega_1} \quad (24.375)$$

from the second source a strong new disturbance with a frequency $\omega_3 = \omega_2 - \omega_1$ will develop (spatial echo). Longitudinal electric field in the new disturbance will now appear with the amplitude E_l given by

$$\frac{E_l}{B_1} = \frac{\omega_{B_2} L}{c} \frac{\omega_{pe}^2}{\omega_2 \omega_3} \frac{n_e}{n_{th}} \quad (24.376)$$

where $\omega_{B_2} = eB_2/mc$ is the gyrofrequency in the magnetic field of disturbance, and ω_{pe} is the Langmuir frequency.

In a fully developed flare region we may accept $n_{th}/n_e \simeq 10^{-6}$. For the amplitude of fluctuation of the magnetic field, we may roughly take 10 G. Adopting $L \simeq 10^8$ cm, we find that if $\omega_2 \simeq 0.1\omega_{pe}$, the amplitude of the plasma echo will be comparable to the amplitudes of the initial sources, B_1 and B_2 .

24.19 Problems of Chap. 20

20.1 Because of fluid incompressibility the velocity of fluid $u(r, t)$ decreases according to an inverse square law with the distance from the bubble:

$$u(r, t) = \frac{F(t)}{r^2} \quad (24.377)$$

where $F(t)$ is related to $R(t)$ by kinematic boundary condition at the bubble surface. In the idealized case of zero mass transport across the interface, $u(R, t) = dR/dt$ and

$$F(t) = R^2 \frac{dR}{dt} \quad (24.378)$$

The Navier-Stokes equation for motion in r direction,

$$-\frac{1}{\rho_L} \frac{\partial p}{\partial r} = \frac{\partial u}{\partial t} + u \frac{\partial u}{\partial r} - \nu_L \left[\frac{1}{r^2} \frac{\partial}{\partial r} \left(r^2 \frac{\partial u}{\partial r} \right) - \frac{2u}{r^2} \right] \quad (24.379)$$

yields, after substituting u from (24.377):

$$-\frac{1}{\rho_L} \frac{\partial p}{\partial r} = \frac{1}{r^2} \frac{dF}{dt} - \frac{2F^2}{r^5} \quad (24.380)$$

Note that the viscous terms vanish. Indeed, the only viscous contribution to the Rayleigh equation comes from the dynamic boundary condition at the bubble surface. Equation (24.380) can be integrated to give

$$\frac{p - p_\infty}{\rho_L} = \frac{1}{r} \frac{dF}{dt} - \frac{1}{2} \frac{F^2}{r^4} \quad (24.381)$$

where p_∞ is the pressure at $r \rightarrow \infty$.

Now we need to evaluate a dynamic boundary condition on the bubble surface. For this purpose consider a control volume consisting of a small, infinitely thin lamina containing a segment of interface (Fig. 24.17).

The net force on lamina in radially outward direction per unit area is

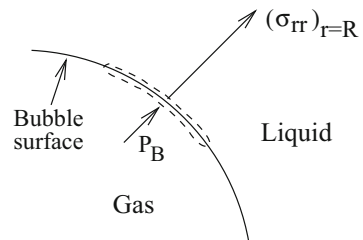
$$\sigma_{rr}|_{r=R} + p_B - \frac{2S}{R} \quad (24.382)$$

or, since $\sigma_{rr} = -p + 2\mu_L \partial u / \partial r$, the force per unit area is

$$p_B - p|_{r=R} - \frac{4\mu_L}{R} \frac{dR}{dt} - \frac{2S}{R} \quad (24.383)$$

In the absence of mass transport across the boundary (evaporation or condensation) this force must be zero. Hence, substitution of the value for $p|_{r=R}$ from Eq. (24.381)

Fig. 24.17 Portion of the spherical bubble surface



with $F = R^2 dR/dt$ yields the generalized Rayleigh-Plesset equation for bubble dynamics:

$$R \frac{d^2 R}{dt^2} + \frac{3}{2} \left(\frac{dR}{dt} \right)^2 = \frac{p_B(t) - p_\infty(t)}{\rho_L} - \frac{2S}{\rho_L R} - \frac{4v_L}{R} \frac{dR}{dt} \tag{24.384}$$

This is a basic nonlinear equation describing the response of a gas bubbles to action of the field of sound or any other oscillatory field. See Davidson (1972).

20.2 For simplicity we will consider a classical case of a liquid droplet formed above an extremely hot surface (Biance et al. 2003; Linke et al. 2006; Brennen 1995). The heat Q brought to the liquid per unit time is proportional to the contact area πr_c^2 , the thermal conductivity of the vapor κ , and the temperature gradient $\Delta T/\lambda$, where λ is the thickness of the vapor layer (Fig. 24.18).

Note that if the drop of radius R is smaller than the capillary length $a = \sqrt{\sigma/\rho g}$ (σ being the liquid surface tension and ρ its density), the drop will be nearly spherical, except at the bottom where it is flattened. Denoting the lowering of the center of mass by δ , we can write: $\sigma \delta \sim \rho g R^3$. For the contact area we can write an estimate as $\pi r_c^2 \sim \pi \delta R$, which yields

$$r_c \sim R^2/a \tag{24.385}$$

Introducing the latent heat of evaporation L_q , we may write for the rate of evaporation

$$\frac{dm}{dt} = \frac{\kappa}{L} \frac{\Delta T}{\lambda} \pi r_c^2, \tag{24.386}$$

The drop weight induces a radial Poiseuille flow of vapor outside the layer. We can calculate its rate from the Navier-Stokes equation and lubrication approximation, which can be used due to the small thickness of the vapor layer. Thus, the flow rate scales as $\lambda^3 \Delta P/\eta r_c$, where ΔP is the pressure imposed by the drop and η is the

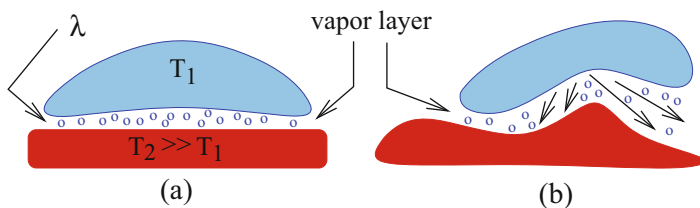


Fig. 24.18 A liquid droplets levitating on their own vapor over extremely hot surface: (a) a small droplet over the smooth surface; (b) a levitating droplet over the uneven surface is subject of self-propelling

vapor viscosity. Integrated over the contact, and written as a mass per unit time, it gives

$$\frac{dm}{dt} = \rho_v \frac{2\pi\lambda^3}{3\eta} \Delta P, \quad (24.387)$$

where ρ_v is the vapor density.

From (24.386)–(24.387) we can determine the film thickness. For small drops, $R < a$, the temperature gradient should be of the order of $\Delta T/R$, and the evaporation process takes place over the whole drop surface R^2 . This gives for the rate of evaporation,

$$\frac{dm}{dt} = \frac{\kappa}{L} \frac{\Delta T}{R} R^2, \quad (24.388)$$

Using (24.387), for the flow rate given by the film thickness we obtain

$$\lambda \simeq \left[\frac{\kappa \Delta T \eta \rho g}{L_q \rho_v \sigma^2} \right]^{1/3} R^{4/3} \quad (24.389)$$

Note that the film thickness is found to increase monotonically with the drop radius, but differently according to the drop size.

Using the similarity criteria between laboratory physics and astrophysics (Ryutov et al. 1999), these estimates can be used for quantitative analysis of the prominence dynamics.

References

- H. Alfvén, C.-G. Fälthamar, *Cosmical Electrodynamics*. Fundamental Principles (Clarendon Press, Oxford, 1963)
- M.A. Berger, M. Asgari-Targhi, E.E. Deluca, J. Plasma Phys. **81**, 395810404 (2015)
- A. Bianche, C. Clanet, D. Quere, Phys. Fluids **15**, 1632 (2003)
- S.I. Braginskii, V.D. Shafranov, *Plasma Physics and the Problem of Controlled Thermonuclear Reactions* (Pergamon Press, New York, 1959)
- C.E. Brennen, *Cavitation and Cavity Dynamics* (Oxford University Press, Oxford, 1995)
- R.A. Cairns, J. Fluid Mech. **92**, 1 (1979)
- J. Chae et al., J. Korean Astron. Soc. **35**, 59 (2002)
- R.C. Davidson, *Methods in Nonlinear Plasma Theory* (Academic, New York, 1972)
- Yu.K. Gol'tsova, M.I. Rabinovich, V.P. Reutov Sov. J. Plasma Phys. **1**, 594 (1975)
- R. Grimshaw et al., Physica D **132**, 40 (1999)
- W.D. Hayes, R.F. Probstein, *Hypersonic Flow Theory* (Academic, New York, 1987)
- Y. Ichikawa, Y. Abe, Prog. Theor. Phys. Suppl. **94**, 128 (1988)
- B.B. Kadomtsev, Sov. Phys. Usp. **11**, 328 (1968)
- B.B. Kadomtsev, *Collective Phenomena in Plasma* (Pergamon, Oxford, 1982)
- B.B. Kadomtsev, V.I. Karpman, Sov. Phys. Usp. **14**, 40 (1971)
- P. Krehl, S. Engemann, D. Schwenkel, Shock Waves **8**, 1 (1998)

- L. Landau, M. Lifshitz, *Fluid Mechanics* (Pergamon Press, Oxford, 1987)
- M. Lavrent'ev, *Usp. Mat. Nauk* **12**, 41 (1957)
- M.J. Lighthill, *J. Inst. Math. Appl.* **1**, 269 (1965)
- H. Linke et al., *Phys. Rev. Lett.* **96**, 154502 (2006)
- R.M. Miura, C.S. Gardner, M.D. Kruskal, *J. Math. Phys.* **9**, 1204 (1968)
- E. Mjølhus, J. Wyller, *Phys. Scr.* **33**, 442 (1986)
- A. Nowicki et al., *Eur. J. Ultrasound.* **7**, 73 (1998)
- D.I. Pontin, S. Candelaresi, A.J.B. Russell, G. Hornig, *Plasma Phys. Control. Fusion* **58**, 054008 (2016)
- E. Priest, *Magnetohydrodynamics of the Sun* (Cambridge University Press, Consultanta Bureau, New York, 1964) (2014), p. 23
- M.I. Rabinovich, A.L. Fabrikant, *Radiophys. Quantum Electron.* **19**, 508 (1976)
- L. Rayleigh, *Proc. Lond. Math. Soc.* **14**, 170 (1883)
- M. Remoissenet, *Waves Called Solitons* (Springer, Berlin, 1999)
- D.D. Ryutov et al., *Astrophys. J.* **518**, 821 (1999)
- M. Ryutova, M. Persson, *Phys. Scr.* **29**, 353 (1984)
- M. Ryutova, P. Scherrer, *Bull. Am. Astron. Soc.* **29**, 893 (1997)
- R.Z. Sagdeev, *Reviews of Plasma Physics* (Consultants Bureau, New York, 1966), p. 23
- H. Schlichting, *Phys. Z.* **33**, 327 (1932)
- L.I. Sedov, *Similarity and Dimensional Methods in Mechanics* (Academic, London, 1959)
- V.D. Shafranov, *Rev. Plasma Phys.* **2**, 103 (1966)
- T.H. Stix, *Phys. Rev. Lett.* **30**, 833 (1973)
- J.B. Taylor, *Phys. Rev. Lett.* **63**, 1384 (1989)
- J. Weiland, H. Wilhelmsson, *Phys. Scr.* **7**, 222 (1973)
- H. Wilhelmsson, *Phys. Scr.* **29**, 469 (1984)
- E.I. Zababakhin, M.N. Nechaev, *JETP* **33**, 442 (1958)
- Ya.B. Zel'dovich, Yu.P. Raizer, *Physics of Shock Waves and High-Temperature Hydrodynamic Phenomena* (Academic, New York, 1967)

Index

- ∩-shaped Flux Tube, 344
- ∩-shaped kink, 290, 320
- U-shaped Flux Tubes, 342
- U-shaped kink, 290, 320

- Ablation shock, 587
- Ablation velocity, 595
- Abrikosov vortices, 38
- Accelerating mass flow, 429
- Acceleration of jets, 374
- Acoustic noise, 152
- Acoustic opacity, 225, 231
- Acoustic streaming, 261, 285, 286, 698
- Acoustic wave packet, 175
- Acoustic wave-trains, 165
- Active filament, 14
- Added mass, 45, 69
- Added-mass effect, 337
- Added mass of cylinder, 676
- Additional heating, 357
- Adiabatic approach, 222
- Advection, 12
- After-shock heating, 360
- Alfvén resonance, 78
- Alfvén shocks, 390
- Alfvén solitons, 423
- Alfvén velocity, 52
- Alfvén waves, 277
- Ambipolar diffusion, 295
- Amorphous emission, 428, 644
- Amorphous structure, 402
- Anaxagoras, 2
- Anomalous dispersion, 111
- Anomalous resonance, 78

- Anti-Stokes satellites, 200
- Archimedes force, 45
- Archimedian force, 227
- Arc-like flows, 438
- Ascending flux tube, 500
- Attracting centers, 367
- Atwood number, 595
- Axisymmetric modes, 155
- Axisymmetric oscillations, 60
- Azimuthal current, 279

- Back-reaction, 448
- Battery mechanism, 589
- Beam-particle interactions, 433
- Beat wave(s), 200, 686
- Behind-shock brightening, 493
- Behind-shock flows, 369
- Behind-shock heating, 364, 368, 493
- Behind shock temperature, 396
- Bernoulli effect, 28
- Bernoulli's equation, 325
- Bessel function, 55
- Bi-directional jets, 371
- Bi-directional plasma jets, 603
- Biermann battery effect, 589
- Bifurcate, 524
- Bifurcation, 449, 658
- Bifurcation point, 111, 297
- Blast wave, 527
- Blinkers/microflares, 626
- Bottom of the fast wind, 399
- Boundary layer, 262, 280
- Boundary value problem, 86, 142
- Bow (detached) shock, 487

- Bow shock(s), 337, 343, 510, 586, 587, 654, 725
 Bow shock formation, 496
 Braided bundle of loops, 643
 Braidlike behavior, 402
 Braidlike coherent structures, 406
 Braidlike structures, 639
 Braid period, 408, 420
 Braking sonic barrier, 105
 Branching, 484
 Branching points, 469
 Brightening of splitting region, 472
 Brightenings, 240
 Bright filaments, 9, 465
 Bright jets, 627
 Brightness enhancements, 623
 Bright point(s), 31, 258, 299, 475
 Bright soliton(s), 293, 309, 700, 715
 Bright transients, 351
 Bright walls, 33, 466
 Brünt-Väisälä frequency, 307, 677
 Bubble competition, 571, 597
 Bubble formation, 595
 Bulk viscosity, 269
 Bullwhip, 90, 105
 Bullwhip behavior, 667
 Buoyancy force, 301, 345, 498
- Cancellation, 367
 Capacitance, 426
 Capacitive reactance, 442
 Cascade of shocks, 333, 380
 Cascade of shock waves, 361
 Catastrophic growth, 69
 Cauchy problem, 51
 Cavity formation, 555
 C-class, 514
 Centrifugal instability, 667
 Chaos, 176
 Chaotic conglomerate, 522
 Chaotic state, 514, 517
 Character of nonlinearity, 99
 Cherenkov condition, 160
 Cherenkov resonance, 50
 Chirality, 482
 Chirality change, 653, 654
 Chirality injection, 654
 Chromosphere, 13
 Chromospheric bright points, 133
 Chromospheric flare(s), 324, 527
 Chromospheric oscillations, 409
 Circuit currents, 426
 Circuit equation, 440
- Circularly polarized kink, 275
 Classes of explosive events, 371
 Climatological heat flux, 195
 Clouds of energy, 147, 162
 Cloudy corona, 148
 Clustering of penumbral microjets, 658
 Coalescence, 626
 Coefficient of nonlinearity, 384
 Coherent braidlike structures, 406
 Collapse, 315, 557
 Collapse in soliton gases, 422
 Collapse of self-organized braidlike structures, 639
 Collective phenomena, 45, 147
 Collimated flows, 433
 Collimated mass upflows, 555
 Collimated plasma flow(s), 427, 459, 584
 Collinear, 157, 335
 Collision layer, 325
 Collisionless plasmas, 537
 Collisionless shock formation, 588
 Collisionless shocks, 589
 Collision rate, 335
 Compact flares, 626
 Compressional shock, 256
 Computed map, 191
 Concave form, 354
 Concentrated cumulative energy, 392
 Condition of steepening, 245
 Confined in loops, 380
 Conservation laws for the KdV equation, 320
 Conserved quantities, 194
 Continuous fragmentation, 333
 Continuous multiple reconnections, 649
 Continuous pump of energy, 632
 Convective cell, 8
 Convective heat flux, 199
 Convective motions, 271
 Converging shock fronts, 355
 Corkscrew motions, 471
 Coronal braiding, 639
 Coronal bright points, 132
 Coronal cavities, 553
 Coronal dissipation region, 426
 Coronal flares, 426, 602
 Coronal hole, 383
 Coronal jets, 415, 636
 Coronal loop braiding, 642
 Coronal loop formation, 318
 Coronal mass ejections (CMEs), 514, 548
 Coronal rain, 646
 Correlation function, 215
 Correlation length, 198
 Corrugation instability, 377, 706

- Counnerstreaming plasma flows, 590
- Counter-propagating flows, 589
- Coupling, 353
- Covariance, 195, 197
- Critical energy level, 525
- Critical incident angle, 359
- Critically damped oscillations, 449
- Critical parameters, 525
- Critical radius, 458, 476, 616, 644, 645
- Critical reflection angle, 359
- Critical wavelength, 564
- Critical wavenumber, 224
- Cross-field shear, 532
- Cubic nonlinearity, 419
- Cumulative jet(s), 510, 728
- Current carrying systems, 426
- Current density, 617
- Current drive, 264, 278, 433, 461, 620
- Current drive rate, 448
- Current generation, 264
- Current sheets, 328
- Cylindrical cumulation, 713
- Cylindrical focusing, 360
- Cylindrical helices, 468

- Damping rate, 51, 118
- Dark-cored filaments, 478
- Dark cores, 466
- Dark filaments, 9, 288
- Dark, negative soliton, 293
- Dark penumbral filaments, 465
- Dark soliton(s), 309, 701, 715
- Decay of bow shock, 508
- Decay regime, 534
- Deficiency of MMFs, 318
- Deficit of MMFs, 312
- Deficit of outgoing power, 229
- Degree of twisting, 423
- Delay times, 502
- Democritus, 2
- Dense conglomerate(s), 39, 147, 207, 239
- Dense plasma jets, 357
- Density of jet, 360
- Developing flare, 527
- Diagnostic goals, 235, 454, 461
- Diagnostic tool(s), 307, 348, 541, 570, 588
- Diamagnetic current, 723
- Diffuse boundary layer, 117
- Diffusive Broadening, 271
- Diffusive dissolution, 264
- Diffusively vanishing limit, 617
- Diffusive regime, 274
- Diffusive vanishing, 284

- Dipole mode, 56
- Direction of energy transport, 383
- Direction of the shock, 632
- Discord of organ, 261
- Dispersion of the wave, 249
- Dispersion relation, 50, 214
- Dispersive media, 103, 259
- Dispersive stretching, 293
- Disruption of prominences, 550
- Disruption of the circuit, 452
- Dissipation rate, 129, 507
- Dissipation region, 427
- Dissipative instabilities, 112
- Dissipative stresses, 441
- Dissolution, 284
- Distribution carrying function, 48
- Doppler gram(s), 12, 203
- Doppler shifted spectral lines, 632
- Double humped peaks, 652
- Double-humped spectrum, 371
- Double structure, 491, 655
- Downward shock, 371
- Drag coefficient, 337
- Drag force, 341, 500
- Drifting transients, 491, 655
- Driving emf, 442
- Dynamic braiding, 642
- Dynamic equation, 251
- Dynamic systems, 525
- Dynamo action, 604
- Dynamo mechanisms, 589

- Echo effect(s), 425, 545, 660
- Echo observations, 541
- Eckart flows, 262
- Eclipses, 1
- Eddy fluxes, 196, 198
- Effective distance, 202
- Effective viscosity, 273
- Effects of gravity, 193
- Elasticity, 49
- Electrical transmission line, 462
- Electromagnetic coupling, 19, 426
- Electromagnetic stresses, 532
- Electro-mechanical coupling, 365
- Electron heating rate, 81
- Electron inertia, 80
- Elemental coronal loops, 645
- Elemental current filaments, 456
- Emerging bipole, 362
- Emitted acoustic power, 202
- Energetically open circuit, 441
- Energetically open oscillator, 450

- Energetically open systems, 110, 287, 642, 648
- Energetically open turbulence, 421
- Energies of different signs, 125
- Energy analysis, 114, 339
- Energy avalanche, 361
- Energy build up, 415
- Energy build up process, 392
- Energy consideration, 49
- Energy distribution, 357
- Energy excess, 631
- Energy extraction, 412
- Energy-production region, 532
- Energy transfer, 57
- Enhanced absorption, 207
- Enhanced brightening, 469
- Enhanced emission, 328
- Enhanced twist, 573
- Enhancement factor, 224, 234
- Enhancement of particle fluxes, 524
- Ensemble of flux tubes, 46
- Ensemble of spins, 536
- Entropy, 210
- Entropy inhomogeneities, 210
- Entry of helical perturbations, 477
- Equation of state, 221
- Equivalent LRC, 439
- Equivalent mutual resistance, 443
- Escape channels, 132
- Euler-Alfvén similarity, 579
- Euler similarity, 579
- Evershed flow, 9, 288, 465
- Evolutionary equation, 102, 293, 419
- Evolutionary kink, 620
- Evolutionary soliton, 304
- Evolution of coronal structures, 429
- Evolution of Current Systems, 449
- Evolution of magnetic structures, 619
- Evolution of shock(s), 330, 370
- Excess of energy supply, 448
- Exploding loop systems, 644
- Explosion time, 294
- Explosive events, 352, 353, 583
- Explosive growth, 141, 294, 313, 569
- Explosive instability, 109, 125, 371, 451, 569, 570, 632
- Explosive phase, 303
- Explosive release of energy, 659
- Explosive time(s), 457, 536
- Extinction, 154

- Families of MMFs, 316
- Fast magnetosonic waves, 60
- Fast solar wind, 379
- Fast wind, 397
- Feature-tracking algorithm, 620
- Fibrills, 14
- Field-aligned current, 470
- Field reversal, 477, 605
- Filamentary structure of sunspot, 611
- Filamentary structure of sunspot umbra, 25
- Filamentary penumbrae, 9
- Filamentary ray-like structures, 383
- Filamentation of electromagnetic fields, 589
- Filamentation process, 281, 532, 608
- Filament branching, 466
- Finger-like plumes, 567
- Finite amplitude wave, 153, 244
- Finite curvature, 341
- Finite dispersion, 251
- Fire hose instability, 667
- Flares, 1, 414
- Flux emergence, splitting, merging and disappearance, 620
- Flux tube oscillations, 43
- Flux tube shredding, 333
- Footpoint brightenings, 636
- Forced Van der Pol equation, 533
- Forerunner, 433
- Formation of a moat, 312
- Formation of the EUV structures, 459
- Form-factor, 97
- Fourier-transformation, 214
- Fractals, 658
- Fragmentation, 54, 283, 329, 616
- Fragmentation process(es), 261, 264, 626
- Frequency detuning, 82
- Frequency shift, 160, 201
- Frictional force, 499
- Friction force, 337
- Frozen-in condition, 122
- Frozen in magnetic field, 268
- Fuzzy emission, 403

- Gardner equation, 320
- Gas discharge filaments, 37
- Gauss's theorem, 29
- Generalized skin depth, 128, 143, 441
- Generated flows, 364
- Generated twist, 472
- Generation of a seed field, 589
- Generation of currents, 427, 648
- Generation of electric currents, 426
- Generation threshold, 448
- Generation upflow/downflows, 616
- Geometrical acoustics, 129, 181
- Geometry of a shock profile, 491

- Geometry of the collision, 336
- Gradient acceleration, 379, 391
- Granular, 12
- Gravitational waves, 687
- Greenhouse-like effect, 547, 572
- Growing hot bulbs, 554
- Growing oscillations, 648
- Growing ripples, 555
- Growing shock front, 91
- Growing wave packet, 685
- Growth rate, 118
- Guderley's effect, 360

- $H\alpha$ flames, 628
- H_α surges, 430
- Hankel function, 55
- Head-on collision, 355
- Heat flux, 197
- Heating power, 85
- HEAT-JET, 359
- HEAT-JET regime, 365
- HEAT regime, 365
- Hedgerow, Loop-kind, Twirl, Fan, 548
- Height of energy release, 127, 130
- Height of shock formation, 387
- Helical instabilities, 469
- Helical motions, 549
- Helices, 470
- Helicity, 40
 - conservation, 461
 - injection, 529
 - input, 719
 - loss, 719
 - of two flux tubes, 40
- Heliopause effects, 189
- Helmholtz resonator, 262
- High β reconnection, 323
- High degree of self-organization, 594
- High-energy particles, 325
- High frequency waves, 176
- High plasma beta, 354
- High quality resonator, 449
- Hodograph, 68
- Hollow temperature profiles, 481
- Homologous flares, 659
- Homologous microflares, 540
- Homologous precursor flares, 660
- Hydrodynamic cumulation, 354
- Hydrodynamic instabilities, 141

- Independent solitons, 252
- Induced coronal flow, 454
- Induced emf, 446
- Induced flows, 265
- Induced power, 434
- Inductance, 426
- Inductive circuit, 426
- Inductive reactance, 442
- Injected current, 452
- Instability dynamics, 589
- Intensity variation, 410
- Interaction of shocks, 651
- Interlaced flux tubes, 465
- Intermittent emission, 144
- Intermittent streamers, 397
- Internetwork magnetic elements (IN), 625
- Inverse damping rate, 85
- Inverse pitch, 479
- Inversion procedure, 195
- Inverted flow and temperature, 197
- Ion heating rate, 81
- Ion temperature jump, 649
- Ion two-stream instability, 589
- Irreversible heating, 80
- Isothermal jump, 711
- Isothermal shock(s), 399, 711

- Jet-ambient plasma interaction, 586
- Jet formation, 359
- Jets, 352
- Joule heating, 481

- KdV-Bürgers equation, 239, 259
- KdV equation, 251, 259
- Kelvin-Helmholtz (KH) instability, 107, 140, 291, 547
 - rolls, 108
- Kinetic coefficients, 277
- Kinetic energy, 340
- Kinked helical shape, 469
- Kink instability, 600
- Kink oscillations, 46, 117, 121
- Kink solitons, 103
- Kruskal-Shafranov, 26
- Kruskal-Shafranov current, 477
- Kruskal-Shafranov law, 555
- Kruskal-Shafranov limit, 477, 724

- Laboratory plasma, 34
- Landau damping, 50, 163
- Laplace inversion, 83

- Laplace transform, 83
- Large wave packet, 166
- Larmor radius, 278
- Lateral jets, 475, 476
- Lax-Wendroff scheme, 253
- Lazy motions, 407
- Left-handed chirality, 653, 654
- Leidenfrost drops, 576
- Level of fluctuations, 213
- Lifetime distribution, 33
- Lifetime of transients, 507
- Light bridges, 258
- Limit cycles, 658
- Limiting currents, 644
- Limiting value, 456
- Linear KH instability, 568
- Linear resonance, 154
- Line-tied, 483
- Local helioseismology, 179
- Localized transients, 407
- Longitudinal electric current, 532
- Longitudinal inhomogeneity, 75
- Longitudinal resonances, 87
- Long-lasting explosive events, 374
- Loop-top reconnection, 602
- Lorentz force, 479
- Loss of radial equilibrium, 87
- Low-frequency Instability, 701, 702
- Lundquist field, 481

- Mach number, 357, 391
- Macroscopic force, 48
- Macroscopic quantum phenomena, 36
- Magnetically driven plasma jets, 579, 584
- Magnetic braid, 717
- Magnetic braiding, 423, 639, 643
- Magnetic buoyancy instability, 69
- Magnetic carpet, 8, 624
- Magnetic cluster, 240
- Magnetic diffusivity, 141
- Magnetic draping, 588
- Magnetic energy avalanche, 398
- Magnetic field generation, 579, 589, 595
- Magnetic field reversal, 482
- Magnetic filling factor, 7, 161, 408
- Magnetic helicity, 438, 532
- Magnetic knots, 24
- Magnetic loop arcades, 380
- Magnetic reconnection, 323
 - in laboratory, 602
 - topology, 602
- Magnetic shear, 24, 529
- Magnetic skeleton, 1

- Magnetic solitons, 701
- Magnetized bow shock, 588
- Magnetosonic streaming, 261, 616
- Mass ejection(s), 98, 667
- Maxwell equations, 28
- M-class, 514
- MDFs, 290, 311
- Measure of shock velocity, 632
- Measure of twist, 724
- Mechanical stressing, 460
- Memory device, 536
- Memory of soliton, 304
- Memory of the system, 169
- Merger processes, 597
- Merging, 284, 367, 405, 466
- Method of characteristics, 383
- Mezgranular, 12
- MHD approximation, 28, 216
- MHD shocks, 360
- MHD similarity in solar flares, 603
- Microflares, 414
- Microjets, 487
- Misuse of reconnection physics, 630
- Mixed polarity plage(s), 10, 401, 417
- Moat region, 484
- Modified sound speed, 250
- Modulated MKdV soliton, 419
- Modulated oscillations, 450
- Modulation instabilities, 419
- Molecular transport, 224
- Momentum flux, 48
- Morphological effects, 162, 417
- Morphology of a heated area, 140
- Mottles, 24, 540
- Mouder Minimum, 5
- Moving Magnetic Features (MMFs), 287, 620
 - deficiency, 621
- Multi-cored entity, 619
- Multiple azimuthal modes, 56
- Multiple branching, 469, 475
- Multiple echoes, 663
- Multiple flares, 544
- Multiple flows, 353
- Multiple fragmentation process, 618
- Multiple reconnection, 332, 635
- Multiple reconnection processes, 475
- Multiple shocks, 506
- Multi-solitons, 691
- Multi-stranded substructures, 645
- Multi-thermal strands, 647
- Multithreaded loop arcades, 513
- Multitude of frequencies, 622
- Multiwired filaments, 471

- Mushroom cap, 555
- Mutual Inductance, 441

- Naked sunspot, 623
- Narrow resonances, 95
- Navier-Stokes equations, 562
- Negative dispersion, 310
- Negative energy kink, 308
- Negative energy waves (NEWs), 107, 109, 114, 140, 291, 371, 568, 684
- Net flow of power, 228
- Network elements (NE), 624
- Newborn flux tube, 264
- New-born kink, 297
- Newborn penumbra, 651
- Next generation bipole, 347
- Non-collinear, 330, 335
- Non-collinear flux tubes, 396
- Non-conservative systems, 12, 287
- Non-inductive current drive, 433
- Non-slinky flares, 517
- Noncollinearity, 31, 53
- Nonconformity, 308
- Nonconservative system, 620
- Nonconvoluted times, 199
- Nonlinear distortions, 384
- Nonlinear evolution of flux tube, 617
- Nonlinear frequency shift, 152
- Nonlinear kink oscillations, 419
- Nonlinear oscillations, 98
- Nonlinear oscillator, 691
- Nonlinear plasma wave echoes, 660
- Nonlinear processes, 330
- Nonlinear Rayleigh-Taylor Instability, 595
- Nonlinear Schrödinger equation (DNLS), 713
- Nonlinear unsteady processes, 444
- Normal dispersion, 111
- N-soliton solution, 420
- Nyquist criterion, 69

- Oblique shocks, 476, 694
- Observable morphological effects, 132
- Observational spectroscopy, 207
- Ocean tomography, 195
- Ohmic dissipation, 217
- Ohmic losses, 84
- Ongoing reconnection, 469, 472, 527
- Onset of absorption, 231
- Opposite parity properties, 184
- Optical depth, 203
- Origin of spicules, 277
- Oscillating shock profiles, 259

- Oscillatory ponderomotive force, 620
- Outgoing waves, 64
- Overdamped oscillations, 449
- Overturning, 244

- Pancakes, 409
- Parametric resonance, 176, 685
- Parental bright points, 488
- Parity of Negative and Positive Energy Waves, 123
- Parity property(ies), 183, 189
- Patchy brightenings, 133
- Penetrating jet, 728
- Penumbral jets, 14
- Penumbral microjets, 657
- Penumbral tadpoles, 608
- Penumbral waves, 611
- Periodically flaring, 425, 644
- Petcheck's mechanism, 326
- Petschek reconnection, 704
- Phase memory of particles, 537
- Phase-mixed Torsional Waves, 83
- Phase mixing, 82, 105, 126, 140
- Phase transition, 525
- Phase velocity, 49
- Photospheric driver, 427, 532
- Photospheric Reconnections, 329
- Piercing plasma flow, 430
- Pinch effect, 485
- Pitch, 468, 556
- Pitch of the helices, 470
- Plages, 7
- Plasma β , 217
- Plasma blob, 69
- Plasma echoes, 513, 536
- Plasma heating, 343
- Plasma instabilities, 16
- Plasma jets, 602
- Plasma streaming, 264, 491
- Plasma turbulence, 127
- Plasmoids, 604
- Plato, 2
- P-mode ridges, 203
- Poincare limit cycle, 450, 455, 534
- Polarity inversion, 526
- Polarity inversion line, 551
- Polarity reversal, 5
- Polar plumes, 12, 17
- Ponderomotive force, 264, 266
- Population of MMFs, 312
- Pores, 10
- Positive dispersion, 293, 309
- Post-flare cooling regime, 457

- Post-flare relaxation, 517
- Post-flare slinky, 660
- Post-reconnection phase, 651
- Post-reconnection processes, 134, 379, 621, 624
- Post-reconnection products, 323, 331, 351
- Post-reconnection shocks, 364, 377, 415, 634
- Potential energy, 340
- Potential well, 346
- Power spectra, 203
- Power spectrum, 229
- Poynting flux, 442
- Prandtl's equation, 695
- Precursor of emerging magnetic field, 644
- Precursors, 392, 410, 513
- Predictability, 522, 535
 - criteria, 516
 - tools, 122
- Pre-flare brightenings, 646
- Pre-flare energy release, 660
- Pre-flare recurrent flushes, 661
- Pre-flare stage, 525
- Preshock plasma, 357
- Pre-shock velocity, 394
- Pressure equilibrium, 46
- Probability distribution, 97
- Probability distribution functions, 33
- Prominence body crush, 664
- Prominence cavities, 548
- Prominence levitating, 576
- Prominences, 1
- Prominence shadow, 551
- Pure JET regime, 365
- Pythagoras, 1

- Quantitative analysis, 227
- Quartz wind, 262
- Quasilinear growth, 566
- Quasi-longitudinal waves, 60
- Quasi-periodic driving force, 444
- Quasi-simple wave, 384
- Quiescent prominences, 14, 16, 547, 597

- Radial inhomogeneity, 75
- Radiant heat exchange, 377, 708
- Radiated energy flux, 59
- Radiation in shock wave, 707
- Radiation of negative-energy waves, 124
- Radiative cooling time, 479
- Radiative damping, 57, 119, 163
- Radiative heat flux, 479
- Radiative transients, 392, 412, 414

- Radio occultation, 383
- Radius of curvature, 339
- Raman spectroscopy, 200
- Raman spectroscopy of p-modes, 179
- Random phases, 164
- Rankine-Hugoniot conditions, 581
- Rankine-Hugoniot relations, 710
- Rarefied ensemble(s), 39, 147, 157
- Rayleigh equation, 267
- Rayleigh-Plesset equation, 561, 576, 666
- Rayleigh-Taylor instability, 547, 595, 666
- Ray trajectory, 129
- Reactance, 442
- Reciprocal travel times, 197
- Reconnecting flux tubes, 361
- Reconnection, 54, 134
 - of filaments, 472
 - outcome, 327
 - rate, 327
- Recurrence of cavities, 560
- Recurrences, 554
- Recurrent explosive events, 634
- Recurrent flares, 536, 542, 658
- Recurrent jets, 635
- Recurrent nature, 563
- Recycling time, 360, 399
- Reflected shocks, 356
- Relaxation regime, 425, 644
- Released thermal energy, 507
- Remnant active regions, 7
- Repeated impulsive events, 643
- Repercussions, 345
- Repetition rate, 141
- Repetitive bursts, 542
- Repetitive explosive events, 367
- Repetitive explosive instability, 684
- Repetitive flare phenomena, 545
- Repetitive pulses, 141
- Resistance, 426, 442
- Resistive coupling, 446
- Resistive load(s), 443, 532
- Resistive stresses, 443
- Resonance condition, 50
- Resonance layer, 266
- Resonance point, 78
- Resonant denominator, 50
- Resonant absorption, 104, 115, 148
- Resonant damping, 78
- Resonant excitation, 70
- Resonant flux tubes, 161
- Resonant interaction, 417
- Resonant layer, 75
- Resonant scattering, 58
- Reverse shock, 588, 614

- Reversed chirality, 482
- Reversible process, 537
- Reynolds number, 127
- Reynolds stresses, 263
- Riemann equation, 384
- Right-handed chirality, 654
- Rippling mode, 547, 555, 569
- Rogue waves, 176, 688
- Rotating prominences, 667
- Rotational mass flows, 264
- Rotational motions, 550
- RT instability growth, 599
- RT-unstable interface, 599
- Rudimentary penumbra, 651
- Running waves, 90

- Safety factor, 26, 470, 555, 724
- Saturation limit, 447, 631
- Saturation regime, 234
- Sausage oscillations, 121
- Sausage mode, 61, 155
- Saw tooth
 - profile, 649
- Saw-tooth shock, 613
- Sawtooth, 394
 - shock, 254
 - weak shocks, 435
- Scale height, 30
- Scale invariance, 525
- Scale-invariant structure, 516
- Scaling, 35
- Scaling criteria, 579
- Scattering centers, 201
- Schlichting's solution, 697
- Schrödinger equation, 419
- Screw pinch configuration, 640
- Screw pinch instability, 26, 478, 550, 642, 653
- Screw-type motion, 468
- Sea-serpent, 289
- Secondary waves, 56, 115
- Second-order spatial echo, 538
- Sedov-Taylor similarity, 579
- Sedov-Taylor solution, 377
- Seed vorticity, 595
- Self-excited oscillations, 448
- Self-focusing, 355, 371, 420
- Self-generation of magnetic fields, 588, 597
- Self-modulation, 420
- Self-organization, 36, 423, 579, 592, 658
- Self-organized critical state, 644
- Self-organized loop arcades, 513
- Self-organized slinky, 644, 661
- Self-organized structures, 421, 642
- Self-similar growth, 597
- Self-similarity, 566, 579
- Self-similarity of Solution, 337
- Self-similar loop arcades, 515
- Self-similar regime, 597
- Sequence of energy transfer, 151
- Sequence of shocks, 648
- Sequences of flares, 522
- Sequential flares, 662
- Series of echoes, 540
- Series of plumes, 554
- Series of reconnection(s), 367, 433
- Series of solitons, 701
- Shafranov's virial theorem, 672
- Shallow soliton, 305
- Shaped charge(s), 510, 728
- Sharp temperature jump, 376
- Shear Alfvén waves, 126
- Shear flow instabilities, 109, 291
- Shear flows, 188
- Shear viscosity, 269
- Shock evolution, 591
- Shock formation, 90
- Shock front, 527
- Shock-like regime, 296
- Shock-related dissipation, 507
- Shock relations, 632
- Shocks, 239
- Shock-shock collision, 633
- Shock-shock interaction, 367, 372, 588
- Shock signatures, 368
- Shock velocity, 396
- Shock waves, 89, 612
- Short-living MMFs, 288
- Short-living UV flashes, 410
- Short wave packet, 166
- Shredding of the magnetic field, 299
- Sigmoidal magnetic structure, 616
- Sign of dispersion, 293
- Signs of the precursors, 524
- Similarity criteria, 579, 734
- Similarity ratio, 566
- Similarity solution, 377
- Similarity theory, 579
- Simple waves, 247
- Singularity, 267
- Singular point, 75
- Sink of wave power, 228
- Skewed shape, 556
- Skewing, 483
- Skewing of the twisted ropes, 642
- Skin-effect, 435
- Slingshot, 386
- Sling-shot effect, 330

- Slinky, 513
- Slinky-producing flare, 659
- Slushing mode, 226
- Slow magnetosonic mode, 182
- Slow magnetosonic waves, 60
- Slow solar wind, 10
- Slow wind, 397
- Small-scale flux tubes, 8
- Smoke ring prominence, 667
- Solar Coronal Plasmoids, 604
- Solar cycle, 5
- Solar interior, 4
- Solar surface driver, 426
- Solar tadpoles, 579
- Solitary wave, 98
- Soliton-like kinks, 296
- Soliton(s), 176, 239, 615
 - in the equivalent circuit, 720
 - formation, 251
 - gas, 420
 - in non-equilibrium media, 320
- Source of emf, 442
- Source region, 427
- Sources and sinks, 201
- Space-time cuts, 44, 312, 404
- Spacetime tracks, 406
- Spatial echo, 537
- Spatial plasma wave echo, 730
- Spatio-temporal braids, 640
- Spatio-temporal echo, 537, 730
- Spatio-temporal echo pattern, 663
- Spatio-temporal periodicity, 425
- Spatio-temporal scale-invariance, 661
- Spectral density, 215
- Spheromak, 36
- Spicules, 14, 402
- Spin echo, 536
- Splitting, 367, 466
 - processes, 405
 - regime, 264
- Spontaneous magnetic field, 602
- Sporadic events, 403
- Sporadic microflares, 408
- Spreading of energy, 168, 176
- Stability boundary, 478
- Stability criteria, 644
- Stability of the KdV solutions, 700
- Stable solitary features, 622
- Stable solitary wave, 297
- Stable soliton, 314
- Stagnation, 137
- Standoff distance, 493, 510, 726
- Stationary vortices, 274
- Statistical analysis, 626, 657
- Statistical properties of MMFs, 317
- Steady energy input, 399
- Steady-state reconnection, 325
- Steepening, 244
- Stochastic field lines, 127
- Stochastisity of umbral oscillations, 614
- Stokes, 200
- Stokes 1st problem, 285
- Strand number density, 645
- Stratified atmosphere, 307, 388
- Stream function, 266
- Stretched variables, 99
- Strong explosive events, 633
- Strong-field reconnections in the photosphere, 628
- Strongly collisional, 435
- Strong shock signatures, 652
- Subsurface flow, 189
- Subsurface layers, 181
- Subsurface motions, 459
- Subtle oscillations, 425, 644
- Sunspot penumbra, 465
- Sunspots, 1
- Superconductivity, 36
- Superfluidity, 36
- Supergranular, 12
- Supernova remnant, 37
- Supersonic jets, 380
- Surface tension, 562
- Surge-like oscillations, 612
- Swaths of caustics, 594
- Sweet-Parker, 326
- Sweet-Parker reconnection, 704
- Symmetry properties, 188
- Sympathetic, 662
- Synchronous lighting, 540
- Table-top soliton, 700
- Tadpole(s), 604, 606
- Tadpol-shaped jets, 604
- Tangential discontinuity, 108
- Tangential motion, 262
- Temperature jump, 94
- Temperature minimum, 356
- Temporal echo, 537
- Temporal plasma echo, 545
- Temporal second-order echo, 538
- Terminal velocity, 559
- Thermal energy, 256
- Thermal losses, 84
- θ -pinch, 722
- Third-order echo, 538
- 3D helical structure, 555

- Three-wave processes, 125
- Time-distance analysis, 179
- Time-distance helioseismology, 205
- Time-distance tomography, 179
- Timescale for the steepening, 254
- Tokamak, 34, 433
- Topographical studies, 236
- Topological effects, 127
- Tornado-like formations, 664
- Tornado-like prominences, 660
- Toroidal currents, 433
- Toroidal vortex, 604
- Torsional Alfvén waves, 83
- Torsional oscillations, 61
- Train of negative solitons, 693
- Transition region, 14
- Transonic velocity, 498
- Transsonic Motion, 340
- Transverse caustics, 594
- Transverse loop oscillation, 647
- Transverse oscillations, 405
- Trapped protons, 525
- Traveling soliton, 292
- Traveling wave, 259
- Triggering mechanism, 415
- True braiding, 639
- True microjet(s), 497, 654
- Turbulent fluctuations of frequencies, 690
- Turbulent pumping, 27
- Turbulent stressing, 440
- Turbulent viscosity, 224
- Turnout time, 272
- Twisted configuration, 466
- Twisted flux tubes, 26
- Twisting motion, 468
- Type I MMFs, 288
- Type I* MMFs, 289
- Type II MMFs, 288
- Type III MMFs, 289
- Type IV MMFs, 289
- Types of MMFs, 309

- Umbral dots, 468
- Umbral oscillations, 611
- Unaccounted energy, 109
- Unbalanced sources and sinks of energy, 620
- Uncombed penumbra, 484
- Uncombed system, 465
- Undamped oscillations, 647
- Underdamped oscillations, 449
- Uneven shock front, 355
- Unified model, 531
- Unipolar features, 311
- Unipolar plages, 10, 401

- Unlimited cumulation, 399
- Unsteady mass flows, 285
- Unsteady wave packets, 162
- Unwinding motions, 653
- Upcoming transient brightening, 651
- Upward and downward shocks, 651
- UV jets, 626

- Validity of soliton solution, 294
- Van der Pol oscillator, 646
- Van der Pol equation, 450, 462, 644, 646
- Van der Pol oscillator, 648
- Varying envelope, 170
- Velocity gradients, 193
- Velocity potential, 55
- Velocity shear maps, 193
- Vibrating plate, 262
- Viscous dissipation, 217
- Viscous friction, 227
- Viscous losses, 84, 141
- Volt-ampere characteristic, 447
- Volume force, 45, 53, 156
- Vortex core, 36
- Vortex rings, 667

- Wave-driven current, 719
- Wave Extinction, 137
- Wave front, 245
- Wave-induced currents, 459
- Wave momentum, 435
- Wave-particle interactions, 433
- Wave phenomena, 611
- Wave train, 263
- Weak Inhomogeneities, 186
- Weakly nonlinear waves, 75
- Weak shocks, 252
- Weibel filamentation, 589
- Weibel filaments, 590
- Weibel instabilities, 588
- Well organized coherent structures, 406
- Whip cracker, 93
- Width of dark cores, 466
- Width of elemental loop, 441
- Width of soliton, 300
- Writhing, 483
- Writhing and skewing, 653

- X-class, 514
- X-ray bright points, 404

- z-pinch, 485